270. WE-Heraeus Seminar on Neutron Stars, Pulsars and Supernova Remnants



January 21-25, 2002, Physikzentrum Bad Honnef (Germany)

Editors: W.Becker, H.Lesch and J.Trümper

MPE-Report 278

MAX PLANCK INSTITUT FÜR EXTRATERRESTRISCHE PHYSIK

Max–Planck–Institut für extraterrestrische Physik

MPE-Report 278

August 2002

Proceedings of the 270. WE-Heraeus Seminar on Neutron Stars, Pulsars and Supernova Remnants

Edited by

W.Becker, H.Lesch & J.Trümper

ISSN 0178-0719

85740 Garching bei München

Preface

Conferences often exhibit time schedules which are so tight that a chairman always has to stop questions since the "show must go on". Such schemes may be appropriate to present in a broad panorama via short (if not to say very short) talks the different specifical advances in a field, but they are not very helpful for a deeper understanding and thorough discussion about the basic questions. For the audience the huge number of short talks on large conferences is often like waiting for a subway in a main station. There are so many different lines so many trains stop and leave the station that it is very difficult to focus the attention.

In the case of neutron stars, pulsars and supernova remnants the number of lines, i.e. the variety of phenomena is so large that sometimes it may be necessary to dwell on some very basic subjects, to clean the mind and to concentrate on very fundamental issues again and get some distance from the steady progression of applications and articles. It may be helpful to have a kind of protected area, in which it may even be allowed to critize the standard pictures apparently accepted from a community and therefore often not a matter of debate, like a dogma.

For such an undertaking a workshop is the optimal forum. A workshop allowing a few scientists to give long talks with long discussional sections with time for doubts and conversations. This was the idea behind our workshop project. Let us invite some experts and give them the opportunity to talk in a complete and comprehensive manner, to review the state of the art about the physics of neutron stars, pulsars and supernova remnants. Especially the critical points should be addressed. Are we investigating into the right direction or are we already too dogmatic in our points of view?

We simply started to invite colleagues who have been working on pulsars, neutron stars and supernova remnants for years. We could do that since we have the HERAEUS-Stiftung in Germany. This foundation is the perfect sponsor for such a workshop - if the case can be presented in a convincing proposal. We got their support since the subject is of high scientific importance. It was great fun to work with HERAEUS since they not only provide the funding but also take over most of the organization. It is our great pleasure to thank Frau Uebel and Dr. Dreissigacker for the perfect support before, during, and in the aftermath of the workshop. Certainly it would not have been half as pleasant and smooth if one of us - or even worse - all of us in an concerted effort had tried to organize that meeting.

As with all proceedings, our collection cannot reproduce the essence of such a meeting: it does not tell about meal conversations, coffee discussions and the really great late night shows down in cellar. They took place after dry throats got well wetted with beer and the excellent wines. The cellar was probably the most significant meeting place at the Physics centre in Bad Honnef on the Rhine. Here the talks of our lecturers which were held during daylight became the starting points of discussions lasting far into the night.

We like to thank all participants for joining us in Bad Honnef and for devoting their precious time and their research activities to our workshop. We like to thank the team of the Physics-Center in Bad Honnef. Their quiet but efficient work in the background provided a perfect basis for a smooth and undisturbed working environment, the protected area, on the one hand side and the very friendly and personal touch of service to us guests on the other.

München, May 2002
W.Becker, H.Lesch and J.Trümper

List of Participants

Bernd Aschenbach
MPI für extraterrestrische Physik
Postfach 1312
D-85741 Garching

Tel. +49 89 30000 3561
Fax: +49 89 30000 3569
E-mail: bra@mpe.mpg.de

Werner Becker
MPI für extraterrestrische Physik
Giessenbachstr. 1
D-85740 Garching

Tel. +49 89 30000 3588
Fax: +49 89 30000 3569
E-mail: web@mpe.mpg.de

Wadim Burwitz
MPI für extraterrestrische Physik
P.O.Box 1312
D-85741 Garching

Tel. +49 89 30000 3585
Fax: +49 89 30000 3569
E-mail: burwitz@mpe.mpg.de

André Crusius-Wätzel
Universität München
Inst. f. Astronomie und Astrophysik
Scheinerstr. 1
D-81679 München

Tel. +49 89 2180 6033
Fax: +49 89 2180 6003
E-mail: arc@usm.uni-muenchen.de

Ernst Dreisigacker
Wilhelm und Else Heraeus-Stiftung
Postfach 15 53
D-63405 Hanau

Tel. +49 6181 923250
Fax: +49 6181 9232515
E-mail: dreisigacker@we-heraeus-stiftung.de

Jean Eilek
New Mexico Tech
Physics Dept.
Socorro, NM 87801
USA

Tel. +1 505 835 5328
Fax: +1 505 835 5707
E-mail: jeilek@aoc.nrao.edu

Jürgen Fath
Drechslerstr. 48
D-85435 Erding

Tel. +49 8122 955 827
Fax:
E-mail: juergen.fath@stud.tu-muenchen.de

Anastasia Y. Gamarova
MPI für extraterrestrische Physik
Giessenbachstr. 1
D-85740 Garching

Tel. +49 89 30000 3584
Fax: +49 89 30000 3569
E-mail: gamarova@mpe.mpg.de

Ulrich R. M. E. Geppert
Astrophysikalisches Institut Potsdam
An der Sternwarte 16
D-14482 Potsdam-Babelsberg

Tel. +49 331 7499 531
Fax: +49 331 7499 200
E-mail: urme@aip.de

Janusz Gil
University of Zielona Góra
Institute of Astronomy
Ul. Lubuska 2,
65-265 Zielona Góra
Poland

Tel. +48 68 320 2863
Fax: +48 68 320 2863
E-mail: jag@astro.ca.wsp.zgora.pl

Christian Gouiffes
DAPNIA/Sap
C. E. Saclay
Service d'Astrophysique
F-91191 Gif-sur-Yvette Cedex
France

Tel. +33 1 6908 44 23
Fax: +33 1 6908 65 77
E-mail: cgouiffes@cea.fr

Dmitri Iakovlev
Ioffe Physical Technical Institute
Dept. of Theoretical Astrophysics
Politekhnicheskaya 26
St. Petersburg 194021
Russia

Tel. +7 812 247-9180
Fax: +7 812 247-1017
E-mail: yak@astro.ioffe.rssi.ru

Axel Jessner
MPI für Radioastronomie
Radioobservatorium Effelsberg
Max-Planck-Str. 28
D-53902 Bad Münstereifel

Tel. +49 2257 301 127
Fax: +49 2257 301 105
E-mail: jessner@mpifr-bonn.mpg.de

Gottfried Kanbach
MPI für extraterrestrische Physik
Giessenbachstr. 1
D-85748 Garching

Tel. +49 89 30000 3544
Fax: +49 89 30000 3606
E-mail: gok@mpe.mpg.de

Aris Karastergiou
MPI für Radioastronomie
Auf dem Hügel 69
D-53121 Bonn

Tel. +49 228 525317
Fax: +49 228 525436
E-mail: akara@mpifr-bonn.mpg.de

Nobuyuki Kawai
Department of Physics, Faculty of Science
Tokyo Institute of Technology
2-12-1 Ookayama, Meguro-ku
Tokyo 152-8551 JAPAN

Tel. +81 3 5734 2390
Fax: +81 3 5734 2389
E-mail: nkawai@hp.phys.titech.ac.jp

Jaroslaw Kijak
University of Zielona Góra
Institute of Astronomy
Ul. Lubuska 2,
65-265 Zielona Gòra
Poland

Tel. +48 68 320 2863
Fax: +48 68 320 2863
E-mail: jkijak@astro.ca.wsp.zgora.pl

John G. Kirk
Max-Planck-Institut für Kernphysik
Postfach 10 39 80
D-69029 Heidelberg

Tel. +49 6221 516 482
Fax: +49 6221 516 549
E-mail: john.kirk@mpi-hd.mpg.de

Bernd Klein
MPI für Radioastronomie
Auf dem Hügel 69
D-53121 Bonn

Tel. +49 228 525 286
Fax: +49 228 525 441
E-mail: bklein@mpifr-bonn.mpg.de

Michael Kramer
Jodrell Bank Observatory
Jodrell Bank
Macclesfield, Cheshire SK 11 9DL
UK

Tel. +44 1477 572622
Fax: +44 1477 571618
E-mail: mkramer@jb.man.ac.uk

Alexander Konopelko
MPI für Kernphysik
Postfach 103980
D-69000 Heidelberg

Tel. +49 6221 516-585
Fax: +49 6221 516-324
E-mail Alexander.Konopelko@mpi-hd.mpg.de

Wolfgang Kundt
Universität Bonn
Institut für Astrophysik
Auf dem Hügel 71
D-53121 Bonn

Tel. +49 228 73 3782
Fax: +49 228 73 3672
E-mail: wkundt@astro.uni-bonn.de

Thomas Kunzl
Universität München
Institut für Astronomie und Astrophysik
Scheinerstr. 1
D-81679 München

Tel. +49 89 21806006
Fax: +49 89 21806003
E-mail: tak@usm.uni-muenchen.de

Harald Lesch
Universität München
Inst. f. Astronomie und Astrophysik
Scheinerstr. 1
D-81679 München

Tel. +49 89 2180 6007
Fax: +49 89 2180 6003
E-mail: lesch@usm.uni-muenchen.de

Oliver Löhmer
MPI für Radioastronomie
Auf dem Hügel 69
D-53121 Bonn

Tel. +49 228 525 315
Fax: +49 228 525 436
E-mail: loehmer@mpifr-bonn.mpg.de

Andrea N. Lommen
2040 Las Canoas Rd.
Santa Barbara, CA 93105
USA

Tel. +1 510 845 1111
Fax: +1 510 642 6111
E-mail: andrea@astro.berkeley.edu

Yury Lyubarsky
Ben-Gurion University
Deptartment of Physics
P.O.Box 653
Beer-Sheva 84105
ISRAEL

Tel. +972 8 647 2177
Fax: +972 8 647 2904
E-mail: lyub@bgumail.bgu.ac.il

Sandro Mereghetti
Instituto di Fisica Cosmica G. Occhialini/CNR
via Bassini 15
I-20133 Milano
Italy

Tel. +39 2 236 99 323
Fax: +39 2 266 6017
E-mail: sandro@ifctr.mi.cnr.it

Mitra
MPI für Radioastronomie
Auf dem Hügel 69
D-53121 Bonn

Tel.
Fax:
E-mail:

Peter Müller
MPI für Radioastronomie
Auf dem Hügel 69
D-53121 Bonn

Tel. +49 228 525 433
Fax: +49 228 525 229
E-mail: peter@mpifr-bonn.mpg.de

Fumiaki Nagase
Institute of Space and Astronautical Science
Center for Planning and Information System
3-1-1 Yoshinodai Sagamihara
Kanagawa 229-8510
JAPAN

Tel. +81 42 759 8351
Fax: +81 42 759 8353
E-mail: nagase@astro.isas.ac.jp

Luciano Nicastro
IFCAI-CNR
Via Ugo La Malfa 153
I-90146 Palermo
Italy

Tel. +39 091 6809562
Fax: +39 091 6882258
E-mail: nicastro@ifcai.pa.cnr.it

Charles Olbert
Columbia University
Astrophysics Laboratory
5124 Lerner Hall
New York, NY 10027
USA

Tel. +1 212 854-3257
Fax: +1 212 854 8121
E-mail: olbert@astro.columbia.edu

Franco Pacini
Osservatorio Astrofisica di Arcetri
Largo Enrico Fermi, 5
I-50125 Firenze
Italy

Tel. +39 055 27 52 232
Fax: +39 055 22 00 39
E-mail: pacini@arcetri.astro.it

George Pavlov
The Pennsylvania State University
Dept. of Astronomy & Astrophysics
525 Davey Lab.
University Park, PA 16802
USA

Tel. +1 814 865 9482
Fax: +1 814 863 3399
E-mail: pavlov@astro.psu.edu

Andrea Possenti
Bologna Astronomical Observatory
via Ranzani 1
I-40127 Bologna
Italy

Tel. +1 814 865 9482
Fax: +1 814 863 3399
E-mail: pavlov@astro.psu.edu

Wolfgang Reich
MPI für Radioastronomie
Auf dem Hügel 69
D-53121 Bonn

Tel. +49 228 525 357
Fax: +49 228 525 229
E-mail: wreich@mpifr-bonn.mpg.de

Olaf Reimer
Ruhr-Universität Bochum
Inst. für Theoretische Physik IV
NB 7/68
D-44797 Bochum

Tel. +49 234 32 22051
Fax: +49 234 32 14177
E-mail: olr@tp4.ruhr-uni-bochum.de

Roger W. Romani
Stanford University
Dept. of Physics, M. C. 4060
Stanford, CA 94305
USA

Tel. +1 650 725 7595
Fax: +1 650 723 4840
E-mail: rwr@astro.stanford.edu

Bronislaw Rudak
Copernicus Astronomical Centre, CAMK PAN
Ul. Rabianska 8,
87-100 Tòrun
Poland

Tel. +48 56 6219 319 ext.13
Fax: +48 56 6219 381
E-mail: bronek@ncac.torun.pl

Daniel Schaudel
MPI für extraterrestrische Physik
Giessenbachstr. 1
D-85740 Garching

Tel. +49 89 30000 3313
Fax: +49 89 30000 3569
E-mail: schaudel@mpe.mpg.de

Rüdiger Schopper
Universität München
Uni-Sternwarte
Scheinerstr. 1
D-81679 München

Tel. +49 89 2180 6005
Fax: +49 2180 6003
E-mail: ruediger.schopper@web.de

Andrew Shearer
National University of Ireland
Computational Astrophysical Lab.
Newcastle Road
Galway
Ireland

Tel. +353 91 512243
Fax: +353 91 750501
E-mail: andy.shearer@unigalway.ie.

Shinpei Shibata
Department of Physics, Yamagata University
1-4-12 Kojirakawa
Yamagata 990-8560
JAPAN

Tel. +81 23 628 4552
Fax: +81 23 628 4567
E-mail: shibata@sci.kj.yamagata-u.ac.jp

Noriaki Shibazaki
Rikkyo University
Department of Physics
3-34-1,Nishi.Ikebukuro,Toshima-ku
Tokyo, 171-8501
JAPAN

Tel. +81 3 3985 2389
Fax: +81 3 3985 2412
E-mail: shibazak@rikkyo.ac.jp

Wolfgang Sieber
Fachhochschule Niederrhein
FB Elektrotechnik
Reinarzstr. 49
D-47805 Krefeld

Tel. +49 2151 822 502
Fax: +49 2151 822 509
E-mail: sieber@fh-niederrhein.de

Joachim Trümper
MPI für extraterrestrische Physik
Giessenbachstr. 1
D-85740 Garching

Tel. +49 89 30000 3559
Fax: +49 89 30000 3315
E-mail: jtrumper@mpe-garching.mpg.de

Vladimir N. Usov
Weizmann Institute of Science
Dept. of Condensed-Matter Physics
76100 Rehovot
ISRAEL

Tel. +972 8 9343751
Fax: +972 8 9465510
E-mail: fnusov@wicc.weizmann.ac.il

Olaf Weidemann
Max-Rothschild-Str. 23
D-81825 München

Tel. +49 89 42 47 14
Fax:
E-mail: olaf.weidemann@ph.tum.de

Martin C. Weisskopf
Space Sciences Department
NASA Marshall Space Flight Center
SD50 MSFC
Huntsville, AL 35812
USA

Tel. +1 256-544-7740
Fax: +1 256-544-5903
E-mail: martin@smoker.msfc.nasa.gov

Richard Wiebelinski
MPI für Radioastronomie
Auf dem Hügel 69
D-53121 Bonn

Tel. +49 228 525 300
Fax: +49 228 525 436
E-mail: rwielebinski@mpifr-bonn.mpg.de

Vyacheslav Zavlin
MPI für extraterrestrische Physik
Giessenbachstr. 1
D-85748 Garching

Tel. +49 89 30000 3558
Fax: +49 89 30000 3569
E-mail: zavlin@mpe.mpg.de

Program:

Sunday, 20 January 2002

17:00 – 21:00	Registration in the Library / Physikzentrum Bad Honnef
from 18:00	Buffet Supper

Monday, 21 January 2002

MORNING SESSION

9:00 – 9:15	**Welcome and Opening Remarks** E. Dreisigacker, Hanau J. Trümper, MPE Garching
9:15 – 10:15	**Radio Observations of Supernova Remnants** W. Reich, MPIfR Bonn
10:15 – 11.15	**X-ray Observations of Supernova Remnants** B. Aschenbach, MPE Garching
11:30 – 12:30	**The Anomalous X-ray Pulsars** S. Mereghetti, CNR Milano/Italy

AFTERNOON SESSION

14:00 – 14:45	**Two Years of Chandra Observations: Neutron Stars and Pulsars with Emphasis on the Pulsar in the Crab Nebula** M. C. Weisskopf, MSFC Huntsville
14:45 – 15:30	**X-ray Pulsars in Binary Systems** E. Nagase, ISAS Kanagawa/Japan
16:00 – 16:30	**New Limits on Gravitational Radiation using Pulsars** A. Lommen, Uni Berkeley/USA
16:30 – 17:00	**Non-linear Magnetic Field Decay in Neutron Stars – Theory and possible Observations** U. Geppert, AIP Potsdam

Tuesday, 22 January 2002

MORNING SESSION

9:00 9:45 **X-ray Observations of Neutron Stars: Recent Results from XMM**
W. Becker, MPE Garching

9:45 – 10:15 **The Chandra LETGS Spectrum of the Neutron Star: RXJ1856.5-3754**
V. Burwitz, MPE Garching

10:45 – 11:45 **Gamma-ray Emission of Pulsars**
G. Kanbach, MPE Garching

11:45 – 12:30 **Optical Observation of Isolated Neutron Stars – The Current Picture and Possibilities**
A. Shearer, NUI Galway/Ireland

AFTERNOON SESSION

14:00 – 14:30 **High-Energy Radiation from Pulsars: A Challenge to Polar-Cap Models**
B. Rudak, CAC Torun/Poland

14:30 – 15:30 **Radiation Mechanisms in the Outer Pulsar Magnetosphere**
R. W. Romani, Uni Stanford/USA

16:00 – 17:00 **Particle Acceleration and Emission Mechanisms in Pulsar Magnetospheres**
A. Crusius-Wätzel, USM München

17:00 – 17:30 **A Wind Model for High-Energy Pulses**
J. Kirk, MPI Heidelberg

17:30 – 18:00 **Vortex Configurations, Oscillations and Pinning in Neutron Star Crusts**
N. Shibazaki, Rikkyo University, Tokio/Japan

Wednesday, 23 January 2002

MORNING SESSION

9:00 – 10:00	**Characteristics of (Normal) Radio Pulsars** R. Wielebinski, MPIfR Bonn
10:00 – 10:30	**Reviewing Pulsar Spectra** W. Sieber, FH Krefeld
11:00 – 12:00	**Radio Emission of Pulsars II: Enlarging the Parameter Space – and our Understanding** M. Kramer, Cheshire/UK
12:00 – 12:30	**New Millisecond Pulsars in Globular Clusters** A. Possenti, Bologna/Italy

FREE AFTERNOON

Thursday, 24 January 2002

MORNING SESSION

9:00 – 10:00	**Plasma Instabilities and Radio Emission** E. Asseo, CNRS Palaiseau/France
10:00 – 10.30	**Simulation of the Free Electron Maser in Pulsar Magnetospheres** R. Schopper, USM München
11:00 – 11:30	**Vacuum Gaps in Pulsars and Related Coherent Radio Emission** J. Gil, Zielona Góra/Poland
11:30 – 12:00	**Emission Altitude in Radio Pulsars** J. Kijak, Zielona Góra/Poland
12:00 – 12:30	**Towards a Consistent Model for Pulsars** W. Kundt, Uni Bonn

AFTERNOON SESSION

14:00 – 14:30 **Natural Limits for Currents in Charge Separated Pulsar Magnetospheres**
A.Jessner, MPIfR Bonn

14:30 – 15:00 **A Current Circuit Model of Pulsar Radio Emission**
T. Kunzl, USM München

15:00 – 16:00 **Coherent Radio Emission from Pulsars**
Y. Lyubarsky, Ben Gurion University, Beer-Sheva/Israel

16:30 – 17.30 **Two-Stream Instability in Pulsar Magnetospheres**
V. V. Usov, Weizmann Institute, Rehovot/Israel

17:30 – 18:30 **The Pair Plasma in Pulsars**
J. Eilek, NRAO New Mexico/USA

Friday, 25 January 2002

MORNING SESSION

9:00 – 9:30 **Modeling Neutron Star Atmospheres**
V. E. Zavlin, MPE Garching

9:30 – 10:30 **Thermal Radiation from Neutron Stars**
G. Pavlov, PSU/USA

11:00 – 12:00 **Cooling of Neutron Stars**
D. G. Yakovlev, Ioffe St. Petersburg/Russia

12:00 – 12:30 **Summary of the Conference and Open Problems**
F. Pacini, ARCETRI Florenz/Italy

Table of Contents

Preface
List of Participants
Program

Radio Observations of Supernova Remnants
W. Reich 1

X-rays from Supernova Remnants
B. Aschenbach 13

Galactic SNR candidates in the ROSAT all-sky survey
D. Schaudel, W. Becker, B. Aschenbach, J. Trümper, W. Reich, M. Weisskopf 26

The Anomalous X–ray Pulsars
S. Mereghetti, L. Chiarlone, G.L. Israel, L. Stella 29

Why study pulsars optically?
A. Shearer, A. Golden 44

PSR B1951+32 and PSR J0537-6910 - where are the optical counterparts?
R.F. Butler, A. Golden, A. Shearer, C. Gouiffes 54

Chandra Observations of Neutron Stars — An Overview
M. Weisskopf 58

X-ray Observations of Neutron Stars and Pulsars: First Results from XMM-Newton
W. Becker, B. Aschenbach 64

The 2-10 keV emission properties of PSR B1937+21
L. Nicastro, G. Cusumano, L. Kuiper, W. Becker, W. Hermsen, M. Kramer 87

Gamma-Ray Pulsars
G. Kanbach 91

Chasing the second gamma-ray bright isolated neutron star: 3EG J1835+5918/RX J1836.2+5925
O. Reimer, K.T.S. Brazier, A. Carramiñana, G. Kanbach, P.L. Nolan, D.J. Thompson 100

Future Pulsar Observations with H.E.S.S.
A. Konopelko 105

Vortex Configurations, Oscillations and Pinning in Neutron Star Crusts
M. Hirasawa, N. Shibazaki 112

New Limits on Gravitational Radiation using Pulsars
A.N. Lommen 114

Non–linear Magnetic Field Decay in Neutron Stars – Theory and Observations
U. Geppert, M. Rheinhardt 126

A wind model for high energy pulses
J.G. Kirk, O. Skjæraasen, Y.A. Gallant 136

High-energy radiation from pulsars: A challenge to polar-cap models
B. Rudak, J. Dyks, T. Bulik 142

On the Field-Aligned Particle Acceleration in the presence of Electron-Positron Pairs
S. Shibata, J. Miyazaki, F. Takahara 155

From Pulsar Spin to Pulsar Wind: The Spectral Connection?
E.V. Gotthelf, C.M. Olbert 159

Emission Mechanisms in High Energy Pulsars: From Gamma Rays to Infrared
A.R. Crusius–Wätzel, H. Lesch 162

The Characteristics of (Normal) Pulsars
R. Wielebinski 167

Reviewing Pulsar Spectra
W. Sieber 171

Enlarging the Parameter Space and our Understanding: Radio Emission of Millisecond Pulsars
M. Kramer 177

The peculiar millisecond pulsars in the globular clusters NGC 6397 and NGC 6752
A. Possenti 183

The Free Electron Maser in Pulsar Magnetospheres
R. Schopper, H. Ruhl, T.A. Kunzl, H. Lesch 193

Emission altitude in radio pulsars
J. Kijak 200

Towards a consistent model for Neutron-Star Sources
W. Kundt 206

Natural Limits for Currents in Charge Separated Pulsar Magnetospheres
A. Jessner, H. Lesch, T. Kunzl 209

Inner vacuum gap formation and drifting subpulses in pulsars
J.A. Gil, G.I. Melikidze 215

A current circuit model of pulsar radio emission
T. Kunzl, H. Lesch, A. Jessner 221

Coherent Radio Emission from Pulsars
Y.E. Lyubarsky 230

Two-stream Instability in Pulsar Magnetospheres
V.V. Usov 240

The Radio-Loud Plasma in Pulsars
J.A. Eilek, P.N. Arendt, Jr., T.H. Hankins, J.C. Weatherall 249

Modeling Neutron Star Atmospheres
V.E. Zavlin, G.G. Pavlov 263

Thermal Radiation from Neutron Stars: Chandra Results
G.G. Pavlov, V.E. Zavlin, D. Sanwal 273

Cooling of Superfluid Neutron Stars
D.G. Yakovlev, O.Y. Gnedin, A.D. Kaminker, A.Y. Potekhin 287

Neutron Stars, Pulsars and Supernova Remnants: concluding remarks
F. Pacini 300

Proceedings of the 270. WE-Heraeus Seminar on: *"Neutron Stars, Pulsars and Supernova Remnants"*
Physikzentrum Bad Honnef, Germany, Jan. 21-25, 2002, eds. W. Becker, H.Lesch & J. Trümper, MPE Report 278, pp. 1- 12

Radio Observations of Supernova Remnants

W. Reich

Max–Planck–Institut für Radioastronomie, Auf dem Hügel 69, 53121 Bonn, Germany

Abstract. Supernovae release an enormous amount of energy into the interstellar medium. Their remnants can observationally be traced up to several ten-thousand years. So far more than 230 Galactic supernova remnants (SNRs) have been identified in the radio range. Detailed studies of the different types of SNRs give insight into the interaction of the blast wave with the interstellar medium. Shock accelerated particles are observed, but also neutron stars left from the supernova explosion make their contribution. X-ray observations in conjunction with radio data constrain models of supernova evolution.

A brief review of the origin and evolution of SNRs is given, which are compared with supernova statistics and observational limitations. In addition the morphology and characteristics of the different types of SNRs are described, including some recent results and illustrated by SNRs images mostly obtained with the Effelsberg 100-m telescope.

1. Introduction

Supernova explosions (SNe) belong to the most spectacular events in space. Historical SNe could be traced by the naked eye. Systematic observations of galaxies reveal several events every year, where the SN is of comparable brightness to the entire galaxy for days up to weeks. SNRs belong to the strongest radio sources observed. The first identification of a SNR in the radio range was published by Bolton et al. (1949), associating the Crab nebula with the radio source Taurus A. Subsequently many more SNRs have been identified and studied in great detail at radio wavelength, which were complemented and extended in recent years by X-ray studies as reviewed by Bernd Aschenbach (this volume). SNe and SNRs have a major influence on the properties of the interstellar medium (ISM) and by their coordinated impact on the evolution of galaxies as a whole. They enrich the ISM by heavy elements, release about 10^{51} ergs and their blast waves shape and heat the ISM, compress the magnetic field and accelerate in their shock waves quite efficiently energetic cosmic rays as observed throughout the Galaxy. They were suggested to trigger star formation and neutron stars are left from SN events.

2. Supernova events

SN have been classified by their optical spectra: SNI with Balmer lines and SNII without Balmer lines. Meanwhile a number of sub-groups have been introduced. Important are their explosion mechanisms depending on the mass of the progenitor stars, as there are thermo-nuclear burning and core collapse events. A core collapse needs a more massive star (SNIb/c, SNII-P) than SN from thermo-nuclear burning (SNIa, SNII-L). Core collapse events leave a neutron star, while from thermo-nuclear burning a pure blast wave results.

SN rates depend on star formation and therefore the different SN rates depend on the type of galaxies (Cappellaro et al. 1999). From these results a SN rate in the Milky Way is expected to be in the range of one SN in about 30 to 50 years. About 80% of SN should be core collapse events and only 20% are expected to release pure blast waves showing up as radio shells.

3. SNR catalogues, statistics and completeness

There are two useful SNR compilations accessible through the web. One is David Green's catalogue (`http://www.mrao.cam.ac.uk/surveys/snrs`), where in its December 2001 version data and references for 231 SNRs are compiled including information also from optical, infrared and X-ray observations. Another useful database is that maintained by Sergei Trushkin (`http://cats.sao.com`) with radio flux densities, spectra and references. A limited number of SNRs is seen at optical, infrared and X-ray wavelength. Increased sensitivity resulted in more detections. In particular in the X-ray range based on the ROSAT all-sky survey a large number of SNR candidates have been identified (Busser Busser 1998). Thus it seems possible that the present fraction of 30% of SNRs showing up at X-rays will be increased, although the low integration times in the ROSAT survey, its relatively soft energy range and significant absorption for objects at larger distances in the Galactic

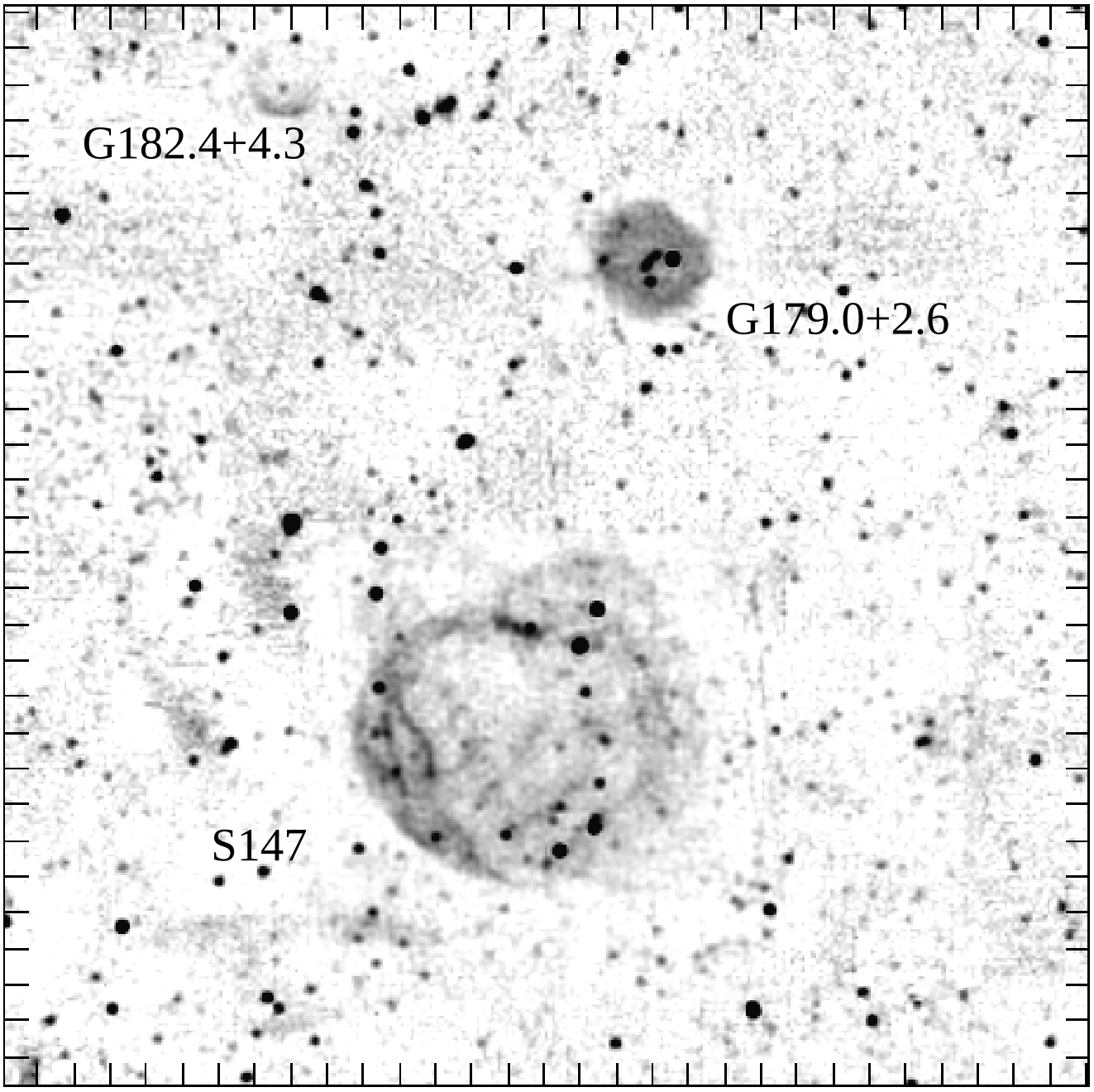


Fig. 1. Section towards the anticentre extracted from the Effelsberg 11 cm survey. The well studied SNR S147 and the two SNRs identified from the 11 cm survey are indicated.

plane are limitations. Meanwhile for some cases subsequent radio observations could prove the SN origin of ROSAT candidates (see Schaudel et al., this volume).

The data in the catalogues are either from dedicated studies or from radio continuum surveys. To what extent are the collected data complete? From statistics about 40 SN should have occurred in the Galaxy within the last two thousand years, although just eight are detected. As expected the two strongest SNRs, which are also the strongest sources in the sky, are Cas A and Tau A from A.D.1680 and A.D.1054, respectively. It is unlikely that the present sensitivity of radio surveys is insufficient to detect such sources throughout the Galaxy when exploding in a typical interstellar environment. Certainly massive stars are clustered and in case they explode within very dense molecular clouds the lifetime of SNRs is reduced substantially. Compact H II regions have a similar spectrum compared to plerions (as discussed in section 7), although the thermal emission from H II regions is unpolarized. However, confusion problems may be present.

For elder SNRs, which are expected to be intrinsically fainter than young SNRs, the fraction of undetected SNRs may be similar or even larger. From the 231 SNRs listed by Green just 9 SNRs are pure plerions and 23 are classified as combined-type objects, e.g. a shell-type SNR with a synchrotron nebula inside being powered by the neutron star. These two groups make up about 15% of all known SNRs, while from SN events about 80% are expected to leave a neutron star and their remnants should be plerions or combined-type SNRs. Beside the selection effects due to very dense material, which largely reduces the SNR lifetime, a number of additional effects have to be considered, which make the available SNR catalogues much likely rather incomplete. The blast wave of SNRs expanding in a hot and thin interstellar medium may reach quite a large size until enough material is swept up to interact with. Faint objects with a diameter of several degrees are difficult to identify in practice, even when offset from the Galactic plane. The task is even more difficult when a regular shell is distorted by fluctuations in the interstellar medium, which are quite likely to be present. In the Galactic plane itself, with a high concentration of sources and diffuse emission, confusion effects are severe and sufficient high intensity and/or an undistorted morphology of the SNR is required to be detected. High depolarization at lower frequencies limits the search for polarized Galactic sources in addition.

4. Identification of SNRs

Radio continuum surveys are the main source for identifying new SNRs. The Effelsberg surveys of the Galactic plane at 1.4 GHz and 2.7 GHz wavelength were quite successful. References and the data are accessible through the web: `http://www.mpifr-bonn.mpg.de/survey.html`. Figure 1 shows a section from the 2.7 GHz survey towards the Galactic anti-center, where the well-known SNR S147 is located, which shows a rather similar morphology at radio and optical wavelength. Two fainter SNRs as indicated in Fig. 1 could be identified (Fürst & Reich 1986a, Kothes et al. 1998). Also the more recent Molonglo survey at 860 MHz covering the southern Galactic plane led to a large number of new identifications (Whiteoak & Green 1996). Of course, the newly detected objects are on average fainter than previously known sources. Surveys at arcmin angular resolution are not able to identify very compact, barely resolved sources and synthesis telescope surveys are required like the VLA 1.4 GHz NVSS (Condon et al. 1989) or the 408 MHz and 1.4 GHz CGPS survey carried out at DRAO (Taylor et al. Taylor et al. 1995). Also the 327 MHz Westerbork survey needs to be mentioned in that context (Taylor et al. 1996). However, synthesis telescope surveys have the disadvantage of being insensitive to large-scale structures and despite their low confusion limit are often not able to measure extended objects reliably.

Morphology, e.g. shell-type sources, linear polarization and non-thermal spectral indices are the classical tools to identify new SNRs. The technique of comparing radio maps from the Effelsberg surveys with those from the IRAS 60μm or 100μm surveys, which have similar angular resolutions, was quite successful in identifying new SNRs, since the ratio of infrared to radio flux for H II regions is about an order of magnitude stronger than that for SNRs (Fürst et al. 1987). Although significant variations in the infrared to radio ratio of H II regions are evident, there is a clear distinction compared to SNRs, which is in addition independent of the type of SNR.

5. Shell-type SNRs

The vast majority of identified SNRs are of shell-type. This morphology is expected when releasing a strong blast wave with an initial expansion velocity of the order of 20000 km/sec. An estimated energy of about 10^{51} ergs is released into the interstellar space. In his classical paper Woltjer (1972) described the following phases of the evolution of a shell-type SNR with an initial energy $E_o = 10^{51}$ ergs into a homogeneous interstellar medium with density n_o [cm^{-3}].

Free expansion: the blast wave expands with its initial velocity and the radius of the SNR increases linear with time. This phase ends until about 1 to 10 $M_\odot$ of material are swept up from the ambient medium in the SNR shell.

Adiabatic expansion or Sedov phase: the energy of the SNR is conserved. The radius R_s [pc] increases as $R_s = 14\ (E_o/n_o)^{1/5}\ t^{2/5}$, with t in units of 10^4 years. The expansion velocity of the SNR decreases accordingly. The density in the shell is $n_s = 4\ n_o$ and its thickness is about 10% of R_s. This phase of SNR evolution ends when about half of its initial energy is released. According to Cox (1972) this phase ends when the age t of the SNR is $t_{rad} = 4.3\ E_o^{4/17}\ n_o^{-9/17}$, its radius is $R_{rad} = 23.1\ E_o^{5/17}\ n_o^{-7/17}$ and its expansion velocity $v_{rad}\ [km\,s^{-1}] = 210\ E_o^{1/17}\ n_o^{2/17}$.

Finally the SNR enters the radiative phase until its initial energy E_o is released to the ISM. In this phase radius and expansion velocity are $R_s = R_{rad}\ (8t/5t_{rad} - 3/5)^{1/4}$ and $v_s = v_{rad}\ (R_{rad}/R_s)^3$. The SNR merges with the interstellar medium at $t_c = 1.23\ t_{rad}$ and $R_c = 1.05\ R_{rad}$.

Although this evolution scenario describes the phases of SNR evolution in principle correctly as proven by observations, it is certainly a simplification. The assumption of a constant density of the ISM during all phases of SNR evolution is not realistic. The effect of the stellar wind from the massive progenitor star modifies the ISM and the young SNR evolves in a quite thin medium and later will encounter the dense material previously swept up by the stellar wind (McKee et al. 1984). Inhomogeneities of the ISM may distort a regular SNR shell, gradients in density may cause an elliptical shape and low density bubbles may lead to "break-out" phenomena. Also the structure and regularity of the ambient interstellar magnetic field

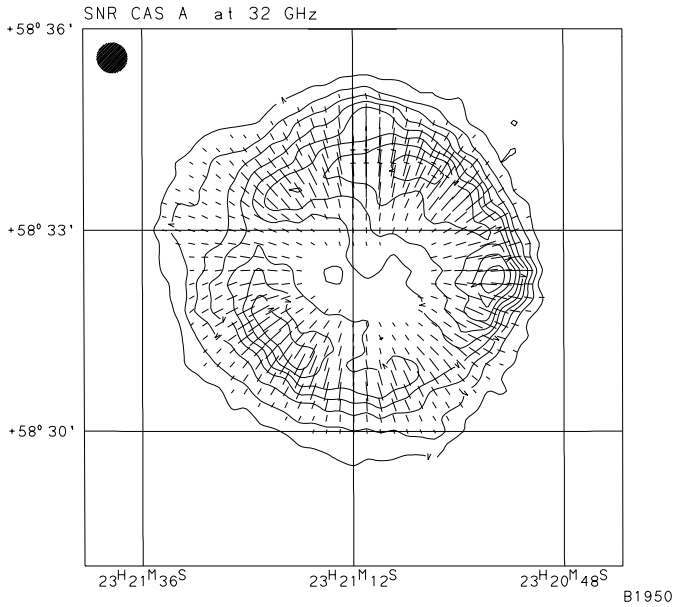


Fig. 2. Cas A observed with the Effelsberg 100-m telescope with $26''$ angular resolution. Polarization bars in B-field direction are superimposed.

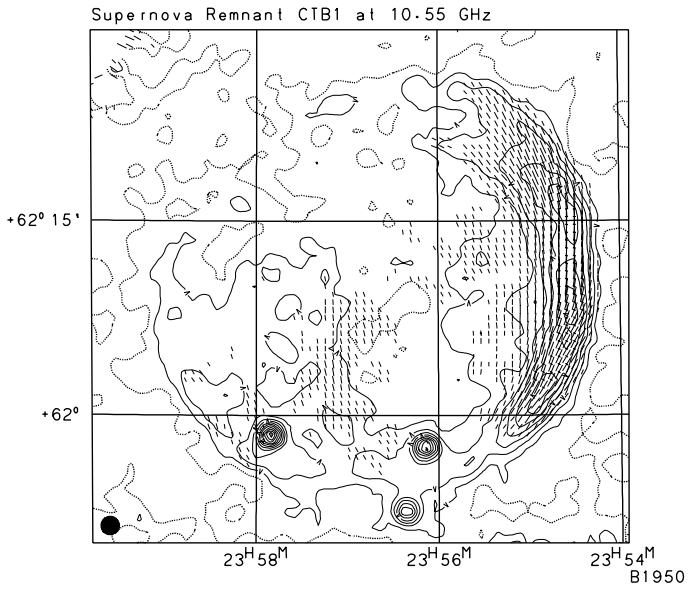


Fig. 3. SNR CTB 1 observed at 10.55 GHz (HPBW = $69''$) with the Effelsberg 100-m telescope. Polarization bars are in B-field direction assuming negligible Faraday rotation.

shapes SNRs (van der Laan 1962) and barrel-shaped structures might result. These in turn indicate the direction and homogeneity of the ambient magnetic field.

5.1. Synchrotron emission

SNRs are strong emitter of synchrotron emission and their spectra can well be described by a power law $S \sim \nu^{\alpha}$, with S the observed flux density and ν the observing frequency. The SNR blast wave sweeps up and compresses the ambient magnetic field B_0 that an enhanced volume emissivity $(B/B0)^{1-2\alpha}$ results. In this case the spectrum of a SNR reflects the cosmic ray electron spectrum, which steepens towards higher energies, and the spectral index α varies accordingly. The strong magnetic field shifts spectral variations towards higher frequencies. In addition the strong shock at the SNR blast wave also induces turbulences, which are able to accelerate particles up to very high energies. Known processes are Fermi I and Fermi II acceleration.

The majority of SNRs are in the adiabatic phase and have spectra around $\alpha = -0.5$. This is expected for a strong shock and a compression factor of 4. Their magnetic field is tangential. Young (historical) SNRs show steeper spectra ($\alpha = -0.6$ to -0.8) on average. Their magnetic field is radial.

5.2. Very young SNRs

Sensitivities in the mJy range are required to observe SN in nearby galaxies and a number of SN events have been measured in recent years. A quite well-studied example is SN1993J (a IIb type) in M81. The first radio detection was about 4 days after the explosion, when about 0.8 mJy were seen at 22 GHz. A steady rise of the flux density to about 1.7 mJy about 50 days later was noted. Afterwards the flux density slowly declined. At lower frequencies radio emission was seen delayed as is expected for an optically thick source. The optical thickness decreases with expansion. Pérez-Torres et al. (2001) fitted the observed radio light curves for a number of frequencies and in fact found evidence for synchrotron self-absorption, however, external free-free absorption was required in addition.

Today's high sensitivity VLBI technique allows to follow also the spatial evolution of young SNRs. Marcaide et al. (1997) analyzed a sequence of VLBI images for the first 42 months of SN1993J and found an increase of its radius with time as $R \sim t^{0.89\pm0.03}$, which is close to – although definitely not identical with – a linear expansion of the blast wave. Although the images show some intensity variations in the shell Marcaide et al. (1997) suggest some residual effect in the image restoration, but take its almost circular shape as evidence for a symmetric explosion.

5.3. Historical SNRs

Until recently historical SNRs resulting from SN events within the last 2000 years were mostly identified via optical flaring events noted in ancient records. There are the shell-type sources SN 1006, Tycho and Kepler. The plerions Tau A and 3C58 and the combined-type SNR G11.2−0.3. In addition the shell-type SNRs Cas A and RXJ0852.0−4622 belong to this group, where the detection of the short living Ti^{44} with a mean lifetime of

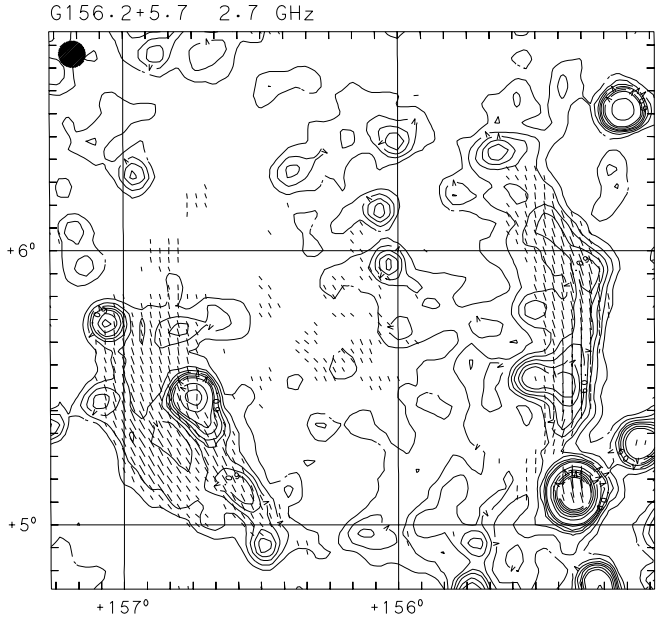


Fig. 4. SNR G156.2+5.7 in the Galactic coordinate system. The Effelsberg 2.7 GHz image is shown convolved to 6′ (HPBW) with polarization bars in B-field direction for the (very likely) case of low Faraday rotation (Reich et al. 1992).

90.4 years proves their young age. Cas A was previously believed to originate from a SN event in 1680, but no clear optical record exists. RXJ0852.0−4622 is not an outstanding radio source, but has been clearly detected in a follow-up search in a highly confused region of the sky (Duncan et al. 1996).

In Figure 2 we show a 32 GHz image of Cas A obtained with the Effelsberg 100-m telescope. Although its spectrum is quite steep with a spectral index of $\alpha = -0.77$, it is nevertheless one of the strongest sources at mm-wavelength. As expected its magnetic field is almost perfectly radial. Along its outer northern rim Gotthelf et al. (2001) recently found evidence for a weak tangential component at its outer shock, indicating that Cas A is leaving free expansion and begins to enter the Sedov phase. The considerable total intensity variations along the shell indicate some influence of an inhomogeneous interacting medium.

5.4. Adiabatic phase

As mentioned earlier most of the detected SNRs are in the adiabatic phase with a spectral index close to $\alpha = -0.5$. Figure 3 shows an image of CTB 1 at 10.55 GHz (Schmidt et al. 1993) with a spectral index of $\alpha = -0.58$. This SNR is located at a distance of about 2 kpc as found from associated neutral hydrogen (Landecker et al. 1982) and has a diameter of about 21 pc. A well-defined shell with a tangential magnetic field is seen along its western periphery. In the south and south-east the shell is still visible, but less pronounced and is almost missing in the north-eastern quadrant. Likely the ISM density is lower in this region, which is supported by X-ray emission extending beyond the circular shell periphery and indicating some kind of 'break-out', where the blast wave expands faster and less material is swept up.

Another example of the 'break-out' phenomenon is indicated for CTA 1, a high latitude SNR at an estimated distance of about 1.4 kpc. CTA 1 has a flat-spectrum non-thermal X-ray core, in addition thermal X-ray emission related to the blast wave of the SNR and seems to be associated to the γ-ray source J000702+7302.9 (Slane et al. 1997). Thus CTA 1 has features not in common to the majority of adiabatic SNRs and may be classified as composite SNR from its X-ray morphology. However, details of its radio emission can well be studied due to its location out of the plane. A 1.4 GHz map (Pineault et al. 1997) is displayed in Fig. 5, where also the spectral indices in the shell and in the 'break-out' region are indicated. There are significant spectral differences of the order of $\alpha = 0.25$ between the intense shells and the diffuse emission extending towards the north-west. Pineault et al. (1997 discuss this effect in terms of Fermi acceleration in shocks and found it possible to account the steepening of the spectrum by expansion of the SNR into a low density region with small compression ratio.

SNRs in the adiabatic phase show a number of effects from their interaction with the ISM, thus reflecting the properties of their environment, which might be additionally largely shaped by the effect of the stellar wind from the progenitor star. Some of these effects are briefly discussed in turn:

The bi-symmetric morphology and the tangential magnetic field in the shell has been used to derive the orientation of the interstellar magnetic field. Objects with the most clear morphology have the most uniform environment. The inclination of the magnetic field to the Galactic plane is small in most cases as expected for a magnetic field orientation along the spiral arms. However, some SNRs show larger deviations. The highly polarized low surface-brightness SNR G156.2+5.7 (Fig. 4), for instance, is inclined by about 70°. Although its distance is not well constrained (1 kpc to 3 kpc), its size ranges between 33 pc and 95 pc and therefore the inferred regular magnetic field orientation holds for a region similar or larger in size.

Rotation measure (RM) observations reveal the direction of the magnetic field $B_{||}$ in the SNR shell of thickness l along the line of sight. RM is calculated: $\mathrm{RM\,[rad/m^2]} = 0.81\ \mathrm{n_e\,[cm^{-3}]\ B_{||}\,[\mu G]\ l\,[pc]}$, where $\mathrm{n_e}$ is the thermal electron density. Polarization angles ϕ at three frequencies are required to get an RM without ambiguity and with the correct sign, where $\phi\,\mathrm{[rad]} = \mathrm{RM\,[rad/m^2]}\ \lambda\,\mathrm{[m]^2}$. Again, in most cases the magnetic field direction agrees with the global field as inferred from averaging RMs of extragalac-

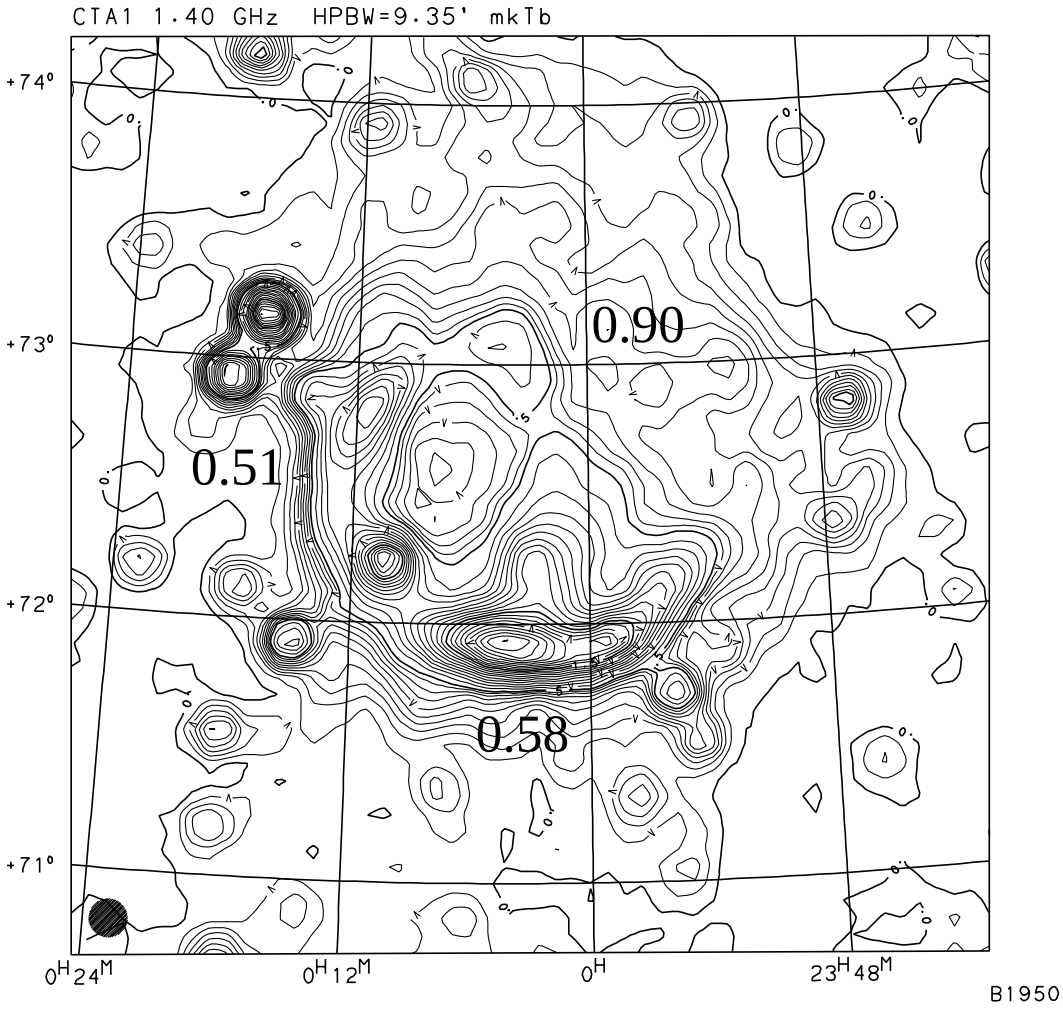


Fig. 5. Effelsberg map of CTA 1 at 1.4 GHz (Pineault et al. (1997). The map is at 9.′35 angular resolution (HPBW). The (absolute) spectral indices for the shell and the 'break-out' region are indicated.

tic sources and pulsars. But there are exceptions as already noted by Fürst & Reich (1990). Recently, Uyaıker et al. (2002) made a detailed analysis of the polarization data of G93.7−0.3 (CTB104A), where a RM gradient across the source was measured. This does not agree with the direction of the global magnetic field at the distance of the SNR of about 1.5 kpc, but agrees with a similar anomaly in the RM data of pulsars. The size of the SNR of about 35 pc is quite likely a rather conservative lower limit of this RM anomaly.

SNRs are supposed to trigger star formation, but just few observations have been made to settle that topic. Molecular clouds interacting with SNRs are the most promising cases where the blast wave may lead to large density enhancements. In a study of G54.4−0.3 Junkes et al. (1992) found evidence for a massive molecular shell surrounding the SNR. While the average density is about 30 [cm^{-3}], a number of higher density clumps (density 100−300 [cm^{-3}] are embedded. A detailed analysis showed that the SNR blast wave is likely not responsible, but the stellar wind of the progenitor star has formed the molecular shell.

Shocked molecular gas in interacting clouds is direct evidence for the interaction of the blast wave. The prototype SNR for associated shocked molecular gas is IC443, but also other SNRs show shocked gas. The association of γ-ray sources with interacting SNRs is clearly established and reflects the absorption of high energy cosmic rays just accelerated in the SNR shock-front with dense gas.

For a larger number of SNRs OH maser emission was clearly detected. These observations indicate small condensations within the SNR shell, where the magnetic field strength ranges up to about 0.5 mGauss (Claussen et al. 1997).

5.5. Evolved SNRs

When the SNR enters the radiative phase its shell is highly compressed, although its interior remains hot as its cooling time is longer and therefore is still detectable by X-ray observations. S147 (see Fig. 1) is an example of this class of SNRs. Its filamentary radio morphology is also seen optically with a perfect correspondence for many substructures (Fürst & Reich 1986b). Evolved SNRs become

faint and their surface brightness Σ [W m^{-2} Hz^{-1} sr^{-1}], which is calculated from $\Sigma = 1.5\ 10^{-19}\,S\,[\mathrm{Jy}]/\Theta\,[']^2$, becomes rather low. Here S is the observed flux density and Θ is the measured diameter of the SNR. For convenience Σ is at most calculated for 1 GHz flux densities. Σ is distance-independent and the Σ–diameter relation was used for distance estimates, assuming the density of the ISM to be fairly uniform. This turns out to be not relevant, and in consequence large density differences reflect in Σ at a certain diameter. However, Berkhuijsen (1983) combined Galactic SNR data with well-defined distances and surface-brightness data from SNRs in nearby galaxies. She concluded that for a given Σ a maximum diameter can be inferred. Accordingly S147 has a rather low surface brightness of $\Sigma_{1\mathrm{GHz}} = 4\ 10^{-22}$ [W m^{-2} Hz^{-1} sr^{-1}]. However, the surface brightness of G179.3+2.6 ($\Sigma_{1\mathrm{GHz}} = 2\ 10^{-22}$ [W m^{-2} Hz^{-1} sr^{-1}]) and G182.4+4.3 ($\Sigma_{1\mathrm{GHz}} = 7.5\ 10^{-23}$ [W m^{-2} Hz^{-1} sr^{-1}]) (see Fig. 1) is even lower, although they do not show the properties of evolved SNRs like S147 (Fürst & Reich 1986a, Kothes et al. 1998). It is most likely that G182.4+4.3 is in the adiabatic phase of expansion. Figure 6 displays a 4.85 GHz Effelsberg image showing a tangential magnetic field and also its spectral index of $\alpha = -0.42 \pm 0.10$ is in agreement with SNRs in the adiabatic phase. It is remarkable that its size of about 45 pc is not much smaller compared to that of S147 (42 pc to 82 pc), despite the large systematic uncertainties for S147.

Evolved SNRs with a compressed magnetic field where no particle acceleration takes place any longer reflect the Galactic electron spectrum with its known bends in their spectra, although the compressed magnetic field shifts the observing frequencies. S147 shows all these characteristics (Fürst & Reich 1986b). Its integrated flux-density spectrum bends at about 1 GHz. However, the spectrum of its filaments is flatter than that of the diffuse emission. Due to the more compressed magnetic field in the filaments radiation from low-energy electrons with a flatter energy spectrum are seen. In the diffuse part of the source the lower magnetic field strength traces emission from electrons with higher energies, which have a steeper energy spectrum.

Despite the remaining uncertainty in classifying a SNR from its low surface brightness, more identifications of these weak sources are of interest to understand SNR evolution and their impact on the ISM. Faint large-diameter objects are filtered out by synthesis telescope observations, while the sensitivity of single-dish observations is limited by confusion of faint unresolved extragalactic sources in their larger beams. An improvement seems possible, when deep-source surveys and single-dish surveys exist at the same frequency and the source contribution can be well subtracted from the single-dish map. An example of such an attempt is shown in Fig. 7, where the noise in the original 1.4 GHz Effelsberg map (Uyanıker et al. 1999) was significantly lowered by subtracting all compact sources visible in the NVSS (Condon et al. 1989). Two shells or partial shells are visible in Fig. 7 with diameter of about 3° or 1°.6. The surface brightness is estimated to about $\Sigma_{1\mathrm{GHz}} = 2.5\ 10^{-23}$ [W m^{-2} Hz^{-1} sr^{-1}] and $\Sigma_{1\mathrm{GHz}} = 3.8\ 10^{-23}$ [W m^{-2} Hz^{-1} sr^{-1}].

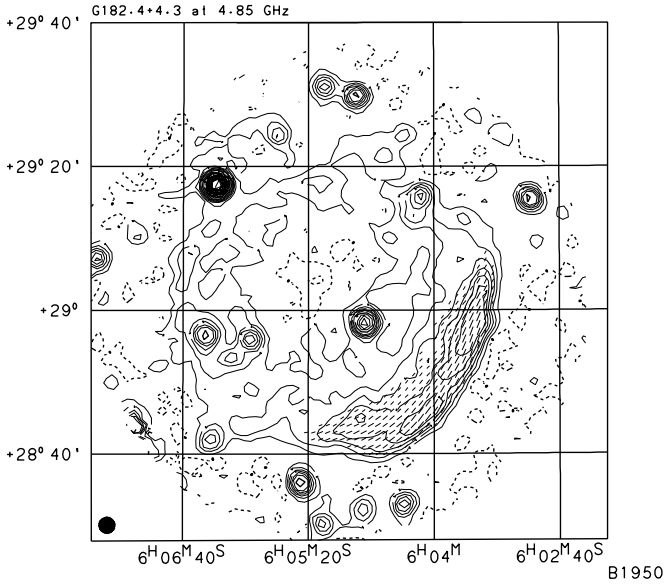


Fig. 6. G182.4+4.3 at 4.85 GHz convolved to a HPBW of 3′ (Kothes et al. 1998). Polarization bars show the B-field direction in case of low Faraday rotation.

6. Pulsar–SNR associations

Although Pulsar (PSR)–SNR associations are expected to be quite common, as they result from a core collapse event, the number of identifications is still small. Before 1980 just Tau A and the Vela SNR were known to have an associated PSR. Since then a number of new detections were made. Until now about 20 associations were identified based on sensitive X-ray as well as on radio observations. Proven associations show young neutron stars, allowing to determine their properties including beaming and birth rate. Better age and distance estimates become possible. PSR distances are inferred from H I absorption, their RM and dispersion measure (DM), while SNR distances are estimated from H I absorption, associated H I clouds or molecular emission structures.

S147, as discussed in the previous section as an example of an evolved SNR, has a 143 msec PSR detected in 1996 at about 40′ from the center of the SNR (Anderson et al. 1996). Another example is G114.3+0.3/PSR2334+61 as shown in Fig. 8. This low surface brightness object has a 0.5 sec PSR close to its center. From combining all available information Fürst et al. (1993) concluded that a distance of 2.2 kpc and an age of $2\ 10^4$ years is most likely for this association. The inferred transverse velocity of the PSR from the geometric center of the SNR is about 125 km/s, well within the range of PSR velocities.

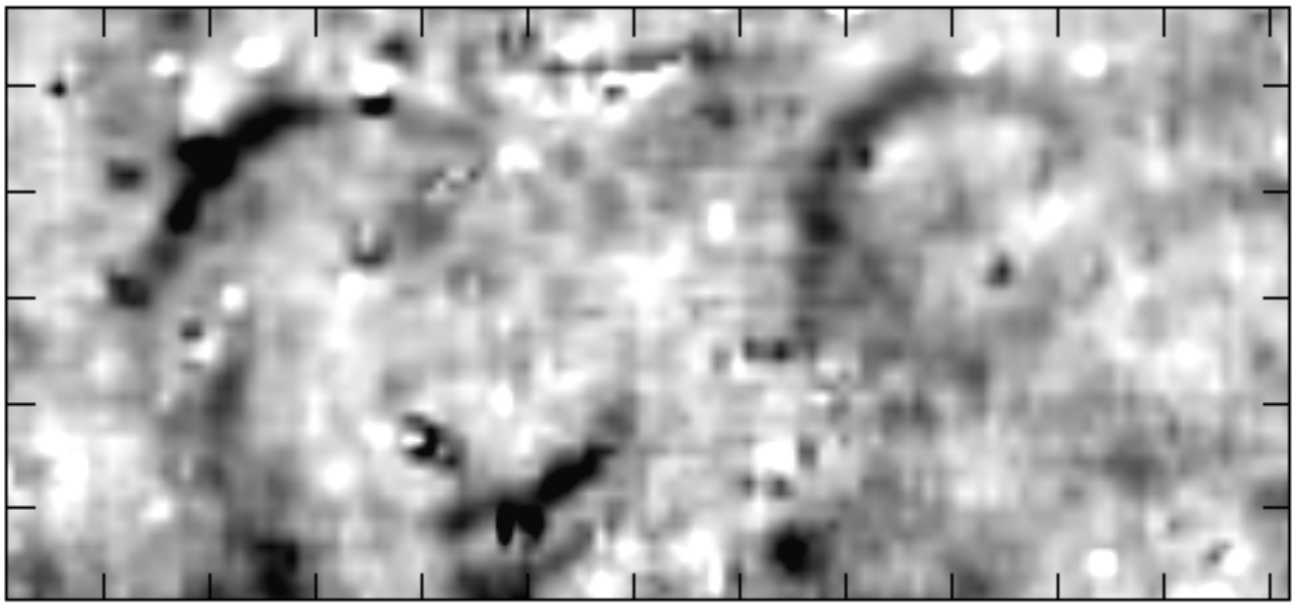


Fig. 7. Two low surface-brightness SNR candidates at 1.4 GHz towards the Galactic anticentre direction (Soberski & Reich, in prep.). The map is a section from the Effelsberg 1.4 GHz Galactic Medium Latitude Survey (extracted from Fig. 12 of Uyanıker et al. 1999) with NVSS sources (Condon et al. 1989) subtracted. The map size is about $8^\circ \times 4.^\circ 7$.

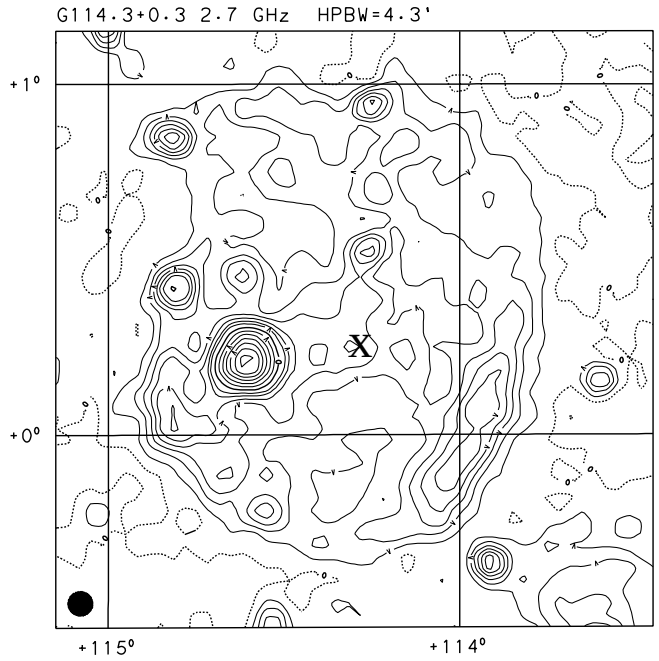


Fig. 8. Image of SNR G114.3+0.3 extracted from the Effelsberg 2.7 GHz Galactic plane survey with indicated position of PSR2334+61 close to its center. The compact sources in the field are extragalactic except the bright source east of the SNR center, which is an unrelated H II region.

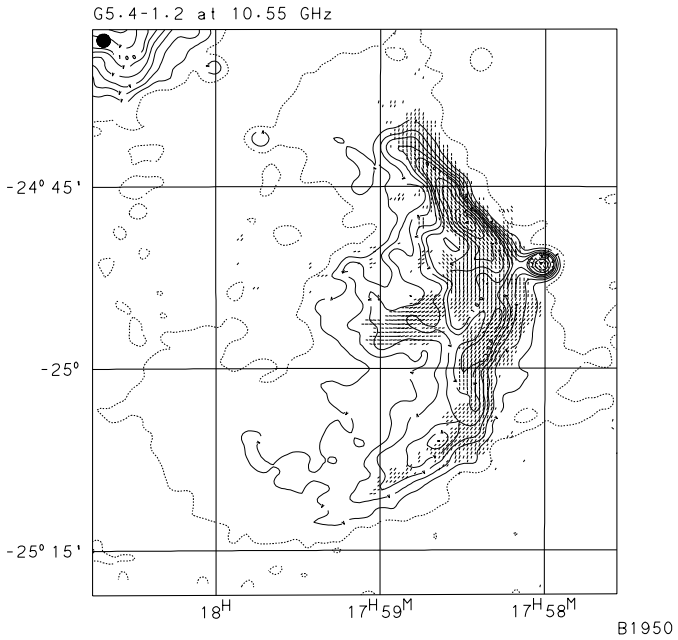


Fig. 9. Effelsberg image of G5.4−1.2 with polarization bars along the B-field direction. The PSR B1757−24 is located just west of its wind nebula, which is located just outside the SNR shell. Its passage causes a clearly visible shell distortion.

A rather interesting case is the association SNR G5.4−1.2/PSR B1757−24. In Figure 9 an image at 10.55 GHz is displayed, where the PSR has overtaken the SNR shell with high velocity. Its cometary tail powered by the pulsar wind is directed towards the SNR center. Gaensler & Frail (2000) were able to limit the proper motion of the PSR from multi-epoch VLA measurements. This results in an age estimate 3 to 10 times larger than

its 'characteristic age', which relates the PSR age to the measured derivative of the rotational frequency.

Recently Kothes et al. (2001) observed the association G106.3+2.7/PSR J2229+6114 and found a highly polarized flat-spectrum structure, the 'boomerang' ahead of the PSR. This bow-shock structure results from an interaction of the PSR wind with surrounding cold and dense material, likely previously swept up from the stellar wind of the progenitor star of G106.3+2.7.

Kothes (1998) found a very close correlation between $\Sigma_{1\mathrm{GHz}}$ of PSR nebula, their diameter and the PSR energy loss rate $\dot{E}$: $\Sigma_{1\mathrm{GHz}} \sim \dot{E}/D$. This correlation holds for about four orders of magnitude of $\Sigma_{1\mathrm{GHz}}$ and must be accounted for by evolutionary models. The correlation seems also useful in predicting PSR parameters from the observed properties of its synchrotron nebula.

7. Plerions and combined-type SNRs

Even in cases where the PSR cannot be detected, its wind of relativistic particles may become pressure-confined and subsequently form isotropically radiating nebula. This classifies the SNR as resulting from a core collapse event. The identification of these flat-spectrum cores within steep non-thermal emission from the SNR shell requires low and high frequency observations to separate both components. An example of this class of objects is G11.2−0.3, believed to be the SNR from the A.D. 386 supernova. An image is displayed in Fig. 10 (Kothes & Reich 2001). Recently a 65 msec X-ray pulsar was detected by Torii et al. (1997), which was later proved by sensitive CHANDRA observations to be precisely in the center of G11.2−0.3 (Kaspi et al. 2001). Thus the supplying source of relativistic particles is identified. Also in this case the characteristic age of about 24000 years largely disagrees with its true age.

Another somewhat different example of a combined-type SNR, where – despite of dedicated searches – so far no PSR has been identified, is G18.95−1.1 as shown in Fig. 11. This object exhibits a number of differences compared to G11.2−0.3 or other combined-type SNR, as it is dominated by flat-spectrum centrally-peaked diffuse emission with filaments running outwards from a central bar-like feature. Its shell is only partial formed. Fürst et al. (1997) compared the Effelsberg 10.55 GHz radio image and the X-ray image obtained with the PSPC of ROSAT. A remarkable similarity of the diffuse emission in the radio and X-ray band was noted, suggesting that the synchrotron emissivity and the thermal emissivity are closely related. In case of pressure equilibrium it could be shown that the tangential magnetic field component decreases radially much faster than the total magnetic field strength. A wound-up magnetic field is suggested. For G18.95−1.1 and also other sources, a simple model of an isotropically expanding PSR-driven synchrotron bubble seems insufficient to account for the observations.

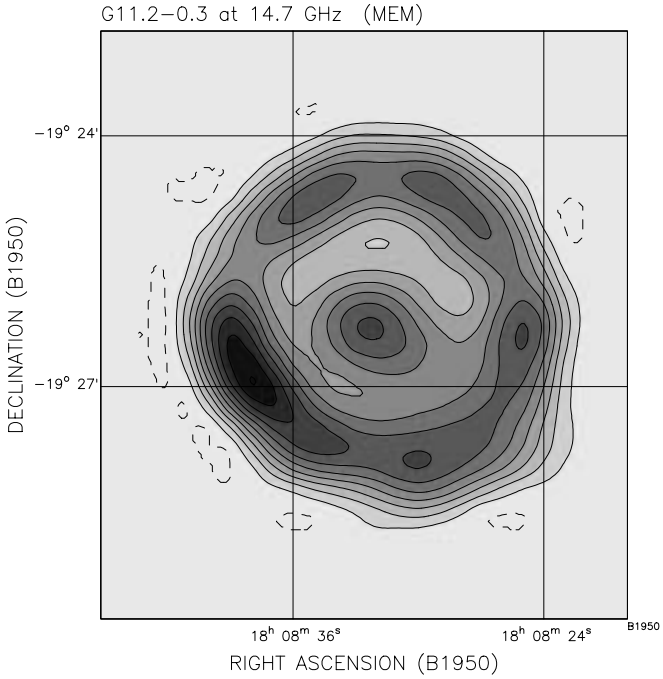


Fig. 10. G11.2−0.3 MEM image from Effelsberg observations (Kothes & Reich 2001) showing the flat-spectrum core inside the steeper spectrum SNR shell.

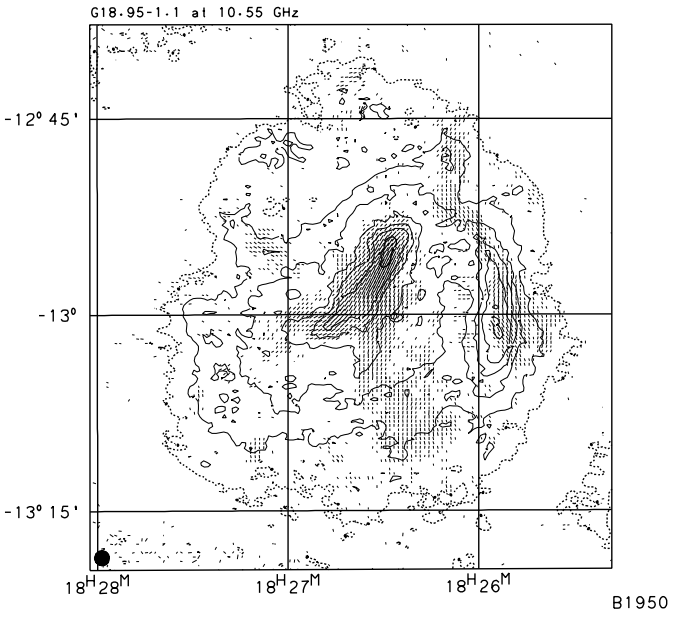


Fig. 11. The combined-type SNR G18.95−1.1 as observed with the Effelsberg 100-m telescope. Polarization percentages up to 30% are seen. Polarization bars are along the B-field.

Plerions or Crab-like SNRs, which show up as pure filled-center objects, have Tau A – the Crab nebula – as the prototype source. An image of Tau A is displayed in Fig. 12. Plerions emit flat-spectrum synchrotron emission and are significantly polarized. Despite very deep searches

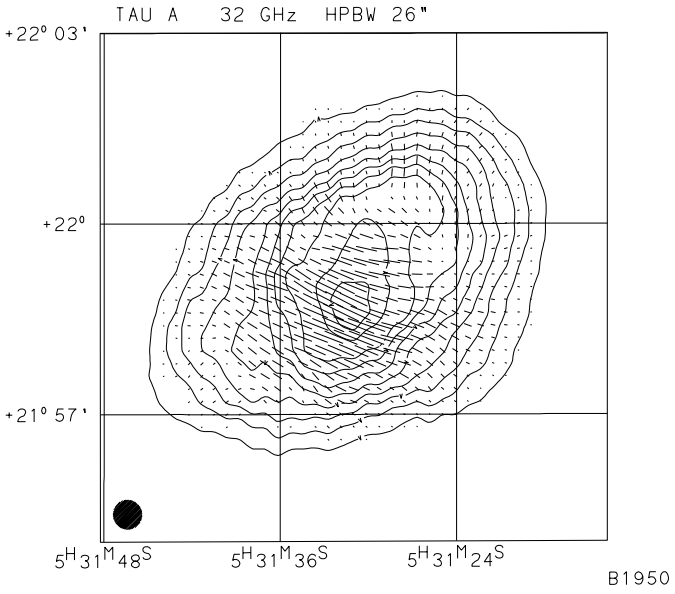


Fig. 12. Tau A as observed with the Effelsberg 100-m telescope. Polarization bars in B-field direction are superimposed.

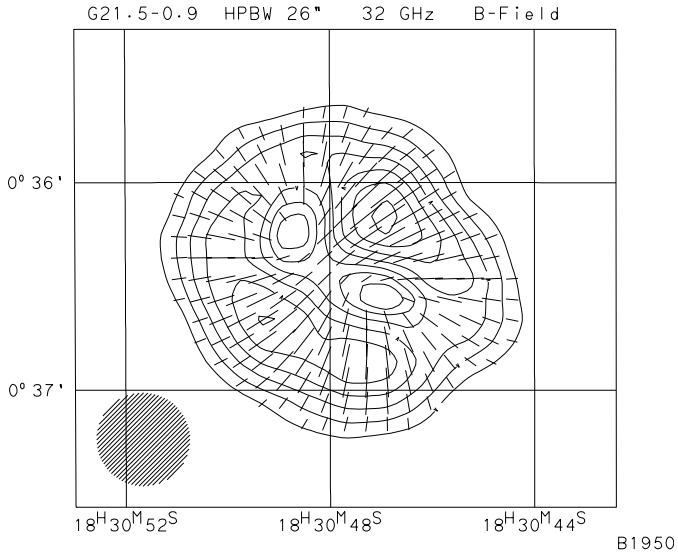


Fig. 14. Contours show the polarized 32 GHz emission of G21.5−0.9 from Effelsberg observations. The radial B-field is shown by the superimposed polarization bars.

for some objects no radio shell could be identified reflecting the impact of the blast wave from the SN explosion with the ISM. Nevertheless plerions might be considered as a subgroup of combined-type SNRs with quite bright

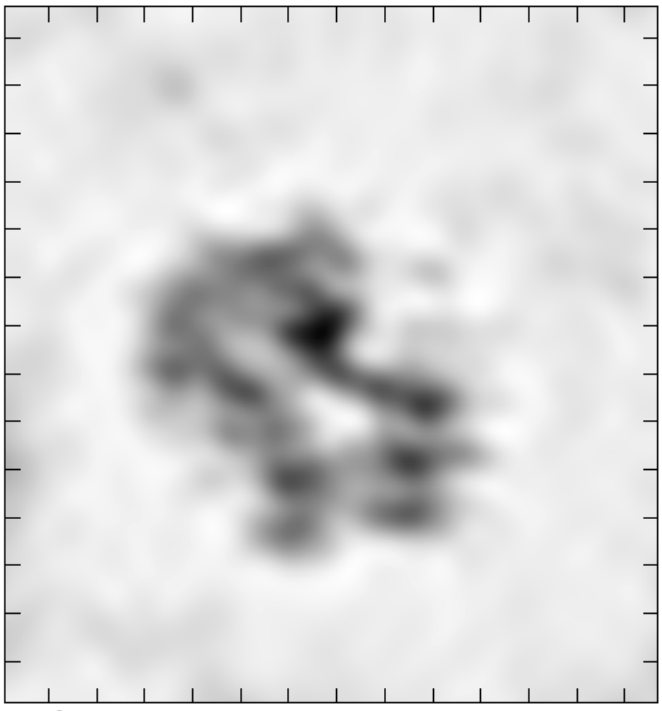


Fig. 13. Small-scale structure of G21.5−0.9 at 22.3 GHz as observed with the Nobeyama Array. The map is convolved to 8″ angular resolution (HPBW) and shows an area of 2′.3 × 2′.5. In the center of the symmetrical double-lobe structure a compact X-ray source is located.

flat-spectrum emission and therefore their low-frequency spectra are better to determine compared to the confused cores of combined-type SNRs. Woltjer et al. (1997) discussed the properties of plerions in comparison to Tau A, which has a radio and X-ray luminosity of about two orders of magnitude larger than all other members of the group. While Tau A can well be described by the PSR-powered expanding sphere model of Pacini & Salvati (1973), which correctly predicts a spectral steepening of $\Delta\alpha = -0.5$ in the infrared due to synchrotron aging, most of the other plerions have spectral breaks in the range of 20 GHz to 50 GHz. This is incompatible with synchrotron aging, and Woltjer et al. (1997) considered cases of a non-standard evolution of the PSR injection.

A well-studied case of a plerion is G21.5−0.9, which was observed with high angular resolution by Fürst et al. (1988) using the Nobeyama Array at 22.3 GHz. 80% of its emission originates from a diffuse slightly elliptical centrally peaked component and 20% comes from a double-cone structure as shown in Fig. 13. A PSR is not visible in the radio, but a non-pulsating X-ray emitting compact source is observed (Slane et al. 2000, Warwick et al. 2001). This source is obviously related to the unseen PSR. The double-cone structure strongly suggests a two-sided collimated outflow from the central PSR along a precessing beam. The diffuse emission shows a very regular radial magnetic field structure as is clearly visible in the Effelsberg 32 GHz image of polarized intensity. Fitting the radial emissivity of G21.5−0.9 Fürst et al. (1988) found as the best solution a constant electron density with a radial linear decrease of the magnetic field, although it must be noted that the fit is not perfect. In any case, G21.5−0.9 defies the explanation in terms of an expanding synchrotron nebula. Recent X-ray observations reveal

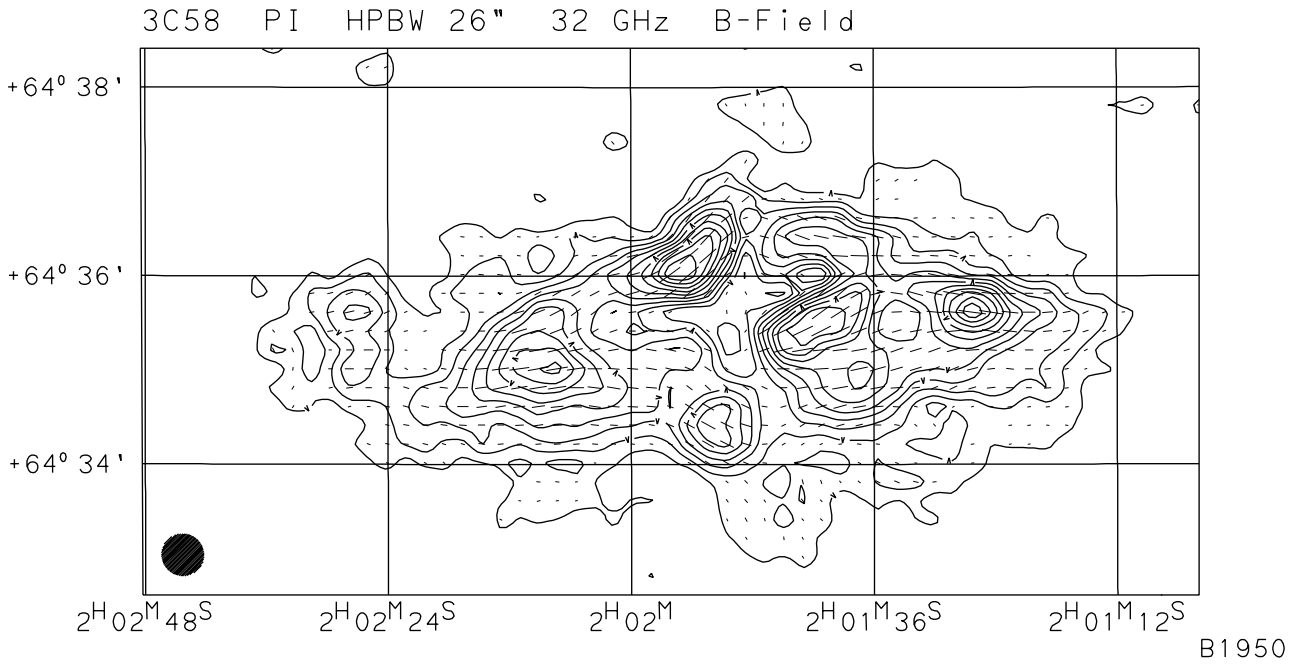


Fig. 15. Effelsberg image of the polarized intensity of 3C58 (Reich et al. 1998). Bars are shown in B-field direction

weak non-thermal diffuse emission extending fairly symmetric beyond the previously known boundaries to about 150″ (Slane et al. 2000, Warwick et al. 2001). The emission is associated with spectral softening of the emission.

G21.5−0.9 was detected in the infrared by Gallant & Tuffs (1998). They tried to describe available radio, infrared and X-ray data with a broken power-law spectrum with a steeping from $\alpha = 0$ to $\alpha = -1$, where the break frequency is at about 200 GHz to 300 GHz. New radio observations with the Effelsberg, Nobeyama and HHT telescopes between 43 GHz and 345 GHz indicate a break frequency at about 20 GHz and a steepening by about $\Delta\alpha = -0.36$ (Reich et al., in prep.), thus incompatible with a single spectral break when including infrared as well as X-ray emission. Since synchrotron aging cannot account for such a spectrum, intrinsic properties of the electron spectrum or an unsteady evolution needs to be considered.

Another plerion known since long to be different from Tau A is 3C58. Its diffuse emission with little small-scale structure is elliptical in shape and shows almost no spatial variations in its spectrum. 3C58 originates from the A.D. 1181 SN event and is located at about 3.2 kpc distance. Recently Camilo et al. (2002) detected a very weak 65 ms radio PSR at the center of the SNR. The flux density of 3C58 was reported to increase by about 0.3%/year (Aller & Reynolds 1985, Aller et al. 1986, Green 1987), which is difficult to understand within current models. 3C58 shows a break in its spectrum around 50 GHz (Salter et al. 1989), which is confirmed by infrared data (Green & Scheuer 1992). An image of the distribution of polarized intensity is shown in Fig. 15, where despite of its rather smooth total-intensity distribution, very patchy polarization is visible. Compared to G21.5−0.9 this reflects a large difference in its internal magnetic field structure from an undisturbed radial magnetic field. The 32 GHz image is rather similar to the 1.4 GHz image of polarized intensities by Wilson & Weiler (1976) at about the same angular resolution. This indicates little internal depolarization and the observed polarization structure reflects regular magnetic field cells of the order of 10% of the size of the SNR. However, this does not imply a strongly enhanced magnetic field in these regions because enhanced total intensities are not observed.

8. More radio observations

High-frequency, high-resolution observations with polarization are of particular importance for the identification of combined-type and plerionic SNRs. It should be stressed again that despite all efforts the number of known sources is quite small. High-sensitivity observations are required for the fainter sources of this class in order to constrain their parameters in a comparable way. Faint flat-spectrum cores seen in projection against steep-spectrum shell emission is difficult to extract. The decomposition of diffuse and small-scale emission provides hints towards the particle injection process and the internal magnetic field structure. Details of the spectral break, its relation to the different components and their spatial variation are of interest to model the source evolution or to constrain the particle injection spectrum including its time dependence. Together with X-ray data from CHANDRA and

XMM models of the observational properties of this class of SNRs will be substantially improved.

Despite the large number of known shell-type SNRs, there are still ongoing identifications, in particular for large-diameter low-surface brightness objects. To make such identifications at high frequencies is difficult and rather time-consuming. A combination of synthesis-telescope data with single-dish observations to reduce the confusion limitations from extragalactic background sources is one way to be successful at low frequencies.

Acknowledgements. I like to thank Roland Kothes, Bülent Uyanıker and in particular Ernst Fürst for many years of common SNR research. Patricia Reich and Ernst Fürst critically read the manuscript. The support of SNR observations at the Effelsberg 100-m telescope by Richard Wielebinski is acknowledged.

References

Aller H.D., Reynolds S.P., 1985, in "The Crab Nebula and Related Supernova Remnants", eds. M.C. Kafatos, B.C. Richards, Cambridge, p. 75
Aller H.D., Aller M.F., Reynolds S.P., 1986, BAAS 18, 1052
Anderson S.B., Cadwell B.J., Jacoby B.A., Wolszczan A., Foster R.S., Kramer M., 1996, ApJ 468, L55
Berkhuijsen, E.M., 1983, AA 120, 147
Bolton J.G., Stanley G.J., Slee, O.B., 1949, Austr. J. Sci. Res. 2A, 139
Busser J.-U., 1998, PhD Thesis, Munich University
Cappellaro E., Evans R., Turatto M., 1999, AA 351, 459
Camilo F., Stairs I.H., Lorimer D.R., et al., 2002, ApJ (in press)
Claussen M.., Frail D.A., Goss W.M., Gaume, R.A., 1997, AJ 489, 143
Condon J.J., Broderick J.J., Seielstad G.A., 1989, AJ 97, 1064
Cox D.P., 1972, ApJ 178, 159
Duncan A.R., Stewart R.T., Haynes R.F., Jones K.L., 1996, MNRAS 280, 252
Fürst E., Reich W., 1986a, AA 154, 303
Fürst E., Reich W., 1986b, AA 163, 185
Fürst E., Reich W., 1990, in "Galactic and Intergalactic Magnetic Fileds", eds. R. Beck, P.P. Kronberg, R. Wielebinski, IAU Symposium 140, Kluwer, p. 73
Fürst E., Reich W., Sofue Y., 1987, AAS 85, 691
Fürst E., Handa T., Morita K., Reich P., Reich W., Sofue Y., 1988, PASJ 40, 347
Fürst E., Reich W., Seiradakis, J.H., 1993, AA 276, 470
Fürst E., Reich W., Aschenbach B., 1997, AA 319, 655
Gallant Y.A., Tuffs R.., 1998, Mem.S.A.It. 69, 963
Gaensler, B.M., Frail D.A., 2000, Nature 406, 158
Green D.A., 1987, MNRAS 225, 11P
Green D.A., Scheuer P.A.G., 1992, MNRAS 258, 833
Gotthelf E.V., Koralesky B., Rudnick L., Jones T.W., Wang U., Petre R., 2001, ApJ 552, L39
Junkes N., Fürst E., Reich W., 1992, AA 261, 289
Kaspi V.M., Roberts, M.E., Vasisht G., Gotthelf E.V., Pivovaroff M., Kawai N., 2001, ApJ 560, 371
Kothes R., 1998, Mem.S.A.It. 69, 971
Kothes R., Fürst E., Reich W., 1998, AA 331, 661
Kothes R., Reich W., 2001, AA 372, 627
Kothes R., Uyanıker B., Pinault S., 2001, ApJ 560, 236
Landecker T.L., Roger R.S., Dewdney P.E., 1982, AJ 87, 1379
Marcaide J.M., Alberdi A., Ros E., et al., 1997, ApJ 486, L31
McKee C.F., Van Buren D., Larareff B., 1984, ApJ 278, L115
Pacini F., Salvati M., 1973, ApJ 186, 249
Pérez-Torres M.A., Alberdi A., Marcaide J.M., 2001, AA 374, 997
Pineault S., Landecker T.L., Swerdlyk C.M., Reich W., 1997, AA 324, 1152
Reich W., Fürst E., Arnal M., 1992, AA 256, 214
Reich W., Fürst E., Kothes, R., 1998, Mem.S.A.It. 69, 933
Salter C.J., Reynolds S.P., Hoog D.E., Payne J.M., Rhodes P.J., 1989, ApJ 338, 171
Schmidt A., Wongsowijoto S., Lochner O. et al., 1993, Kleinheubacher Berichte 36, 99 and Technischer Report No. 73 of MPIfR Bonn
Slane P., Seward F.D., Bandiera R., Torii K., Tsunemi H., 1997, ApJ 485, 221
Slane P., Gaensler B.M., Dame T.M., Seward F.D., 2000, ApJ 533, L29
Taylor A.R., Goss W.M., Coleman P.H., van Leeuwen J., Wallace B.J., 1996, ApJS 107, 239
Taylor A.R., Dewdney P.E., Landecker T.L., et al., 2002, AJ (submitted)
Torii K., Tsunemi H., Dotani T., Mitsuda K., 1997, ApJ 489, L145
Uyanıker B., Fürst E., Reich W., Reich P., Wielebinski R., 1999, AAS 132, 401
Uyanıker B., Kothes, R., Brunt C.M., 2002, ApJ 565, 1022
van der Laan H., 1962, MNRAS 124, 179
Warwick R.S., Bernard, J.-P., Bocchino F., et al., 2001, AA 365, L248
Whiteoak J.B.Z., Green A.J., 1996, AAS 118, 329
Wilson A.S., Weiler K., 1976, AA 49, 357
Woltjer L., 1972, Ann. Rev. AA 10, 129
Woltjer L., Salvati, M., Pacini, F., Bandiera, R., 1997, AA 325, 295

Proceedings of the 270. WE-Heraeus Seminar on: *"Neutron Stars, Pulsars and Supernova Remnants"*
Physikzentrum Bad Honnef, Germany, Jan. 21-25, 2002, eds. W. Becker, H.Lesch & J. Trümper, MPE Report 278, pp. 13- 25

X-rays from Supernova Remnants

B. Aschenbach

Max–Planck–Institut für extraterrestrische Physik, Giessenbachstraße, 85740 Garching, Germany

Abstract. A summary of X-ray observations of supernova remnants is presented including the explosion fragment A of the Vela SNR, Tycho, N132D, RX J0852-4622, the Crab Nebula and the 'bulls eye', and SN 1987A, high-lighting the progress made with Chandra and XMM-Newton and touching upon the questions which arise from these observations and which might inspire future research.

1. Introduction

X-ray research of supernova remnants (SNRs) in the 1990's was dominated by ROSAT and ASCA. Whereas ROSAT put together the first telescopic survey of our Galaxy and produced well resolved images and coarse spectra, ASCA added high quality spectra and extended the spectral range up to 7 keV and more. New scientific grounds were broken on the propagation of SNRs into the interstellar medium (ISM), the physics of supernova explosions by the discovery of fragments of the progenitor stars which shed new light on the question of element mixing in supernova explosions, and on the production of tens of TeV electrons in SNR shells, reviving the discussion of the origin of cosmic rays. Present research is led by the discoveries made with Chandra and XMM-Newton. They produce excellent images and spectra of unprecedented spatial and spectral resolution over a spectral bandpass never accomplished before. Images of various SNRs seem to show a distinction between the matter shocked by either the blast wave rushing into the ISM, more precise the ambient medium, or the reverse shock heating the progenitor's ejecta, which includes differences in elemental abundances and their spatial distribution. A limited selection of new results will be presented. Already now we see new scientific challenges arising which are subject for future research beyond Chandra and XMM-Newton but not only for future X-ray missions but for radio and optical observations as well.

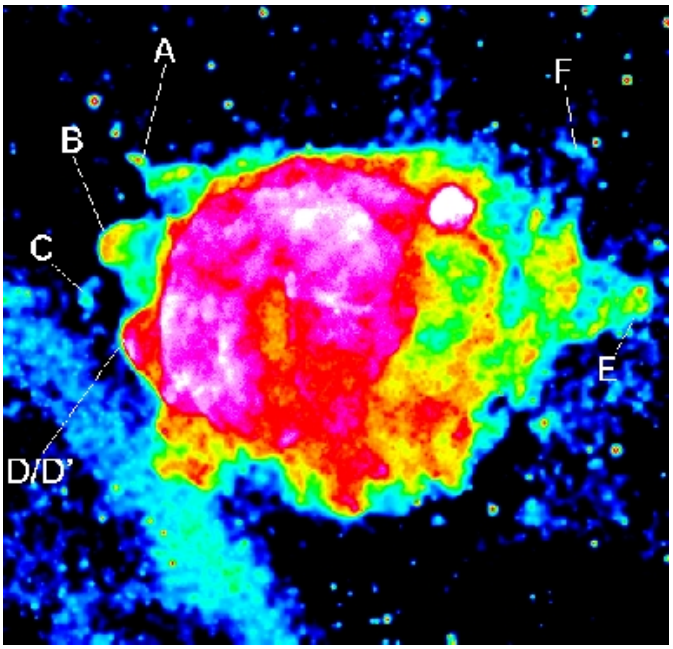


Fig. 1. ROSAT all-sky survey image of the Vela SNR and the fragments A – F (Aschenbach et al., 1995).

2. Compilation of observational results and associated questions

2.1. The explosion fragments of the Vela supernova remnant

A couple (7) of extended X-ray emission regions outside of the general boundary of the Vela SNR have been discovered in the ROSAT all-sky survey, which were suggested to be composed mainly of stellar fragments of the progenitor star (Fig. 1, Aschenbach et al., 1995).

The spectrum of fragment A measured with ASCA indicates a significant overabundance of Si with respect to all other lighter elements (Tsunemi et al., 1999) which is consistent with the view that this fragment originated deep in the interior of the star, but a quantitative analysis was difficult to do. Fig. 2 shows the XMM-Newton EPIC pn-camera image of fragment A, of which the head, $10' \times 5'$ in size, is the brightest part. Both the tail, which extends

back to the SNR boundary, and the head show pronounced structure of surface brightness. Fig. 3 is a display of the XMM-Newton EPIC spectra, i.e. the pn-camera spectrum and the MOS spectra, of the total fragment which reveal the presence of strong Mg (1.38 keV) and Si (1.86 keV) lines but a significant deficit of high ionization emission lines from lighter elements. Nonetheless, weak emission lines from the light elements are present best visible in the MOS spectra: lines from CVI at 0.361 keV and 0.435 keV (seen for the first time from an SNR), NVI and lines from OVII and OVIII, which all are important to fix the abundance of an element to that of oxygen, for instance, the ratio of which is fairly insensitive to spectral models. The spectral analysis demonstrates that the Si/O abundance ratio in the head region is about ten times solar, and that of Mg/O about 4 times solar. This result confirms that fragment A is associated with the ejecta (Aschenbach & Miyata, 2002). It is noted that there is no indication of any sulfur H- or He-like emission lines. The upper limit of the Si/S abundance ratio is just consistent with current core collapse supernova models. The definite determination of this ratio could, however, be a crucial test. Observation times of $>$ 100 ks with XMM-Newton would be needed.

The tip of the head of fragment A is offset from the Vela SNR explosion center by 5.3°, which implies a mean proper motion of 1.7"/yr for an age of $\tau = 11.4$ kyr, which is the age estimated from the spin down rate of the Vela pulsar, or more precise the value of $\frac{P}{2\,\dot{P}}$ with P the current rotation period and $\dot{P}$ its time derivative. Comparison of the ROSAT, Chandra and XMM-Newton images might reveal the current proper motion and whether fragment A has slowed down since its creation. The mean true velocity v is given by the proper motion times the distance and amounts to v = 2000 km/s $\times$ $d_{250}/\tau_{11.4}$ for d = 250 pc. v can be compared with model calculations for core-collapse SNe, like the ones of Shigeyama et al. (1996), who present element resolved mass profiles and velocity profiles for type II-P and II-b SNe. For a 20 $M_\odot$ progenitor without mixing of the Si/Ni^{56} core into the upper layers most of the Si/Ni^{56} is expelled at velocities less than 900 km/s, whereas in the 20 $M_\odot$ progenitor model with mixing the bulk of the Si/Ni^{56} mass moves at ∼1400 km/s. If correct, in either case a reduction of $d_{250}/\tau_{11.4}$ is required by about a factor of 1.5 to 2 or even more if the fragment has decelerated significantly. Since d = 250 pc appears to be a lower limit τ should be increased which would put the age in the range of at least 17 to 23 kyr, an age favored by Aschenbach et al. (1995) and independently by Lyne et al. (1996) by their analysis of the time dependence of the pulsar rotation rate. One of the key questions is, whether pulsars are borne with a rotation rate much faster than the present one. If not, $\frac{P}{2\,\dot{P}}$ is not a reliable measure of the true age.

Obviously, massive sub-stellar, non-core fragments are created in core-collapse SNe, but the immediate question

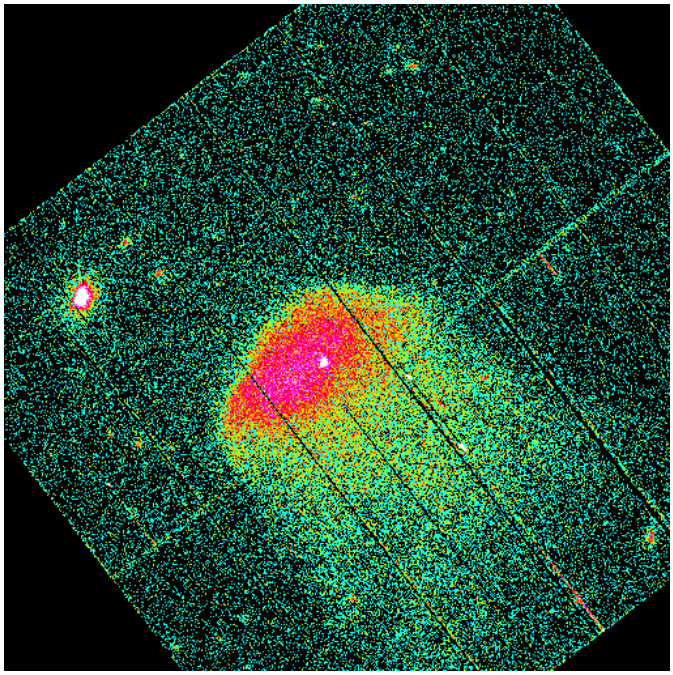


Fig. 2. XMM-Newton EPIC pn-camera unsmoothed image of the Vela SNR fragment A.

is how such an explosion fragment can survive over a distance of ∼20 pc for >11 kyr as in the case for the Vela SNR without being dissolved. Most recent 2-D hydrodynamical codes including time dependent ionization and radiation have been used to follow the fate of such a fragment (Brinkmann, W., 2002). The first results show that the fragment can survive if of sufficiently high Mach number and, more importantly, if the initial matter density of the clump exceeds the ambient matter density by a significant amount. Fig. 4 shows the temperature distribution (10^6 K to a few 10^7 K) of such a clump of matter; note that the x-axis is highly non-linear in scale expanding along x with increasing distance from the central symmetry line. Interestingly, such conditions would favor the survival of high density structures from deep inside the progenitor and rather diffusive large-scale structures are expected to be left from the top layer matter. In that respect X-ray spectral measurements of fragment E (c.f. Fig. 1), which are coming up with XMM-Newton, are interesting.

2.2. The Tycho SNR

The remnant of the supernova observed by Tycho Brahe in 1572 is an excellent target of research concerning the physics of the explosion and expansion of a type Ia supernova for which Tycho has been considered for a long time to be the proto-type. Type Ia supernovae are believed to originate from the deflagration or detonation of an accreting white dwarf most likely living in a binary system. X-rays from Tycho were recorded in the pioneer days of X-ray astronomy, which already revealed the pres-

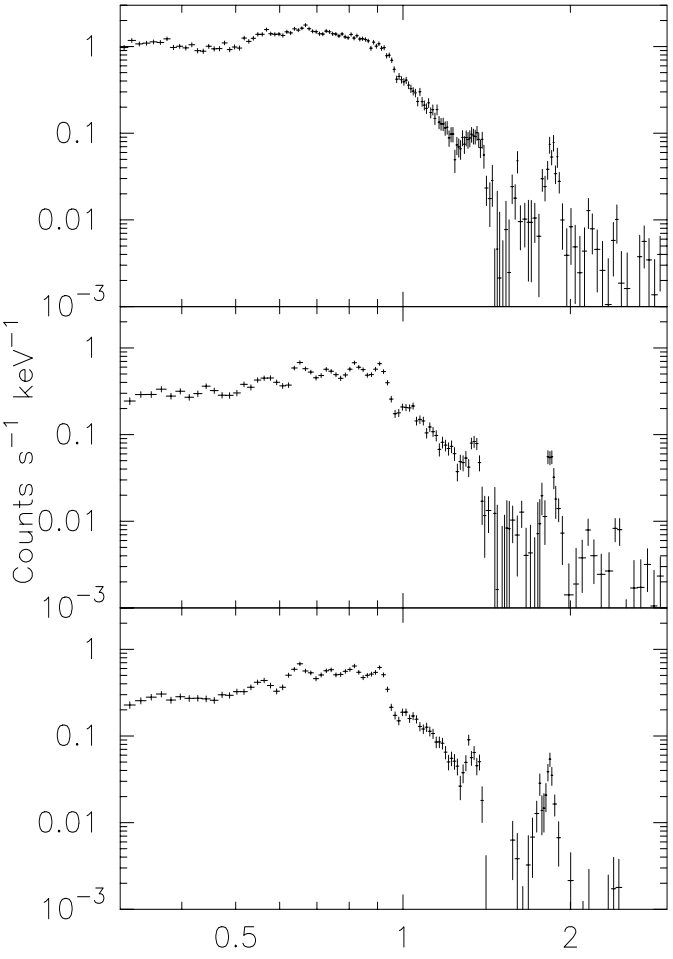


Fig. 3. XMM-Newton EPIC spectra of the Vela SNR fragment A; from top to bottom pn spectrum, MOS1 spectrum, MOS2 spectrum.

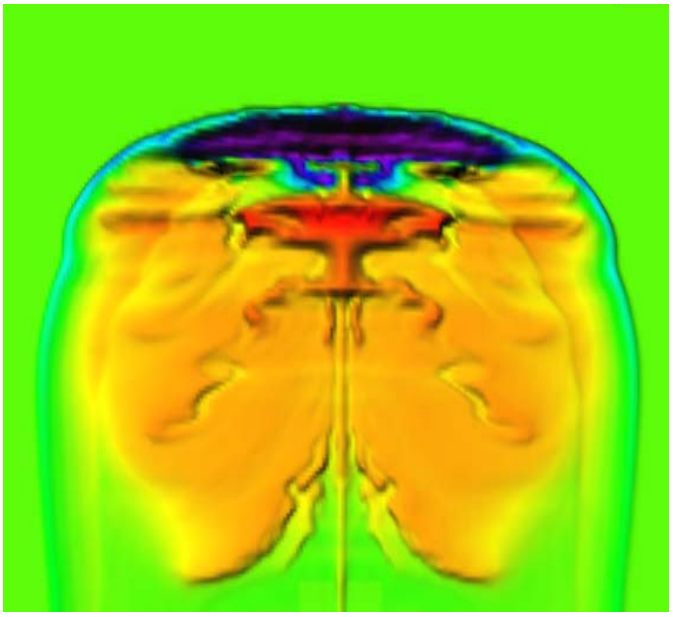


Fig. 4. Temperature distribution of a supersonic clump of matter from 2-dimensional hydrodynamical calculations (Brinkmann et al., 2002).

ence of high temperature plasma and a bright emission line originating from the Fe-K$_\alpha$ transition. High resolution X-ray images were obtained with the *Einstein* and later with the ROSAT HRI. Fig. 5 shows the image of the Tycho SNR obtained with the XMM-Newton MOS1 camera. The remnant has an almost perfect circular appearance with a low surface brightness ring enclosing most of the emission. This appearance has brought forward the idea that the outer annulus is associated with the blast wave shock and that the knotty ring further inside contains the reverse shock heated ejecta. Previous X-ray spectra, compiled from the entire remnant, have shown the presence of many H- and He-like K emission lines up to the Fe and Ni K-lines, including a blend of Fe-L lines. With XMM-Newton spatially resolved spectra have become available. They show a highly non-uniform distribution. For instance, the south-eastern rim, which appears to lead the remnant's expansion there, is dominated by three knots. The spectra of each of the knots can be fitted with the same temperature and the same ionization timescale but the abundances of Si, S and Fe differ remarkably (Decourchelle et al., 2001). The most northern knot shows the highest abundances of S and Si, apparently a few times solar, and some Fe, whereas the most southern knot basically contains no Fe at all demonstrated by the absence of both the Fe-K and Fe-L lines. In comparison with the other two knots a factor of 10 less Fe seems to have been mixed into the Si layer at the explosion when the knots formed. The enhancement of Si and S indicates that the matter is from the deeper ejecta and the abundance variations point to a mixing of the deeper Fe layer changing from place to place. In that sense these knots resemble the fragments observed in the Vela SNR, except that the Tycho knots are much younger and may reflect more directly the explosion physics. The angular separation of the knots along the circumference is $\sim$15° and the linear extent of each knot is $\sim$0.3 pc, which is remarkably close to the elongation of fragment A of the Vela SNR despite their different ages.

On a larger scale the XMM-Newton spectra also provide a much better test bed for the predictions of the deflagration models developed for type Ia SNe. Images taken just in the light of the K emission line of one of the elements demonstrate a generally rather regular stratification such that the lighter elements are found predominantly at large radii and vice versa with the 'Fe ring' having the smallest radius (Fig. 6). Since kinematics studies based on a comparison of the early *Einstein* image, the ROSAT images and the recent XMM-Newton image show that Tycho is expanding still almost undecelerated the images also reflect the velocity distribution of the ejecta. Fig. 6 confirms the onion shell model with the dominant elements ordered in shells following their atomic number (Stadl-

bauer & Aschenbach, 2001). Also, the ejection velocity at the explosion follows a homologous sequence. This was exactly what was predicted by the deflagration models in the early 80's but one should keep in mind that these models were one dimensional and did not allow for radial convection, mixing and instabilities. But it seems that the average ejection velocity of each element was predicted close to correct.

Fig. 7 shows three individual spectra from a radial, 12.5° wide cut through the south-west of the remnant together with the brightness profile. The Fe-K line shows up only at small radii and is absent even at positions where the brightness peaks. In this area lines from Si and S are most prominent. The emission from these areas is clearly associated with shocked ejecta. Going further outside the line emission decreases but the Si and S lines are still present. Given the increase in temperature towards the edge the abundances of Si and S are excessively high by a few times the solar value. This is not at all expected from a region the emission of which should be dominated by blast wave heated interstellar matter, because the abundances should be close to solar. This discrepancy can be explained by that we either do not see the blast wave front at all or there exist high speed precursors of the Si/S shells. The difficulty to verify the one or other option is the fact that Tycho as most of the young SNRs show a high energy continuum which is evident from the spectrum beyond the Fe-L lines. In case of Tycho the spectrum of the outer annulus requires a significant contribution from a power law or bremsstrahlung component, which in the latter case is associated with an emission measure exceeding that of the lower temperature components by a large factor. If the bremsstrahlung option is the correct one the abundance values of Si and S are highly unreliable. A detailed, spatial resolved spectral analysis of the outer annulus along its circumference might shed more light on this issue. Imaging observations at even higher energies beyond 10 keV will help as well.

2.3. N132D in the Large Magellanic Cloud

N132D, a supernova remnant in the LMC is estimated to be ∼3000 years old. The remnant, which resembles the Cygnus Loop in its general surface brightness appearance with intriguing filamentary structure and an apparent blow-out to the north-east, has been imaged by Chandra in great detail. Fig. 8 shows the image obtained with the XMM-Newton EPIC pn-camera. The break-out and the filamentary structure of the limb as well as a bright filament running across the middle of the image are clearly visible. Superimposed is the first high quality broad-band X-ray spectrum of the entire remnant obtained with the XMM-Newton EPIC-pn camera. Emission lines of Si, S, Ar, Ca and Fe are very prominent. By itself this spectrum is amazing because it shows the capability of XMM-Newton: the spectrum covers a flux range of 4.5 orders of magnitude in one exposure. Fig. 9 shows the high-resolution spectrum obtained with the XMM-Newton RGS spectrometer, through which 31 emission lines could be identified (Behar et al., 2001). For the first time lines from H-like N (#24) and C (#31) are seen and they might provide a link to UV observations. Model-

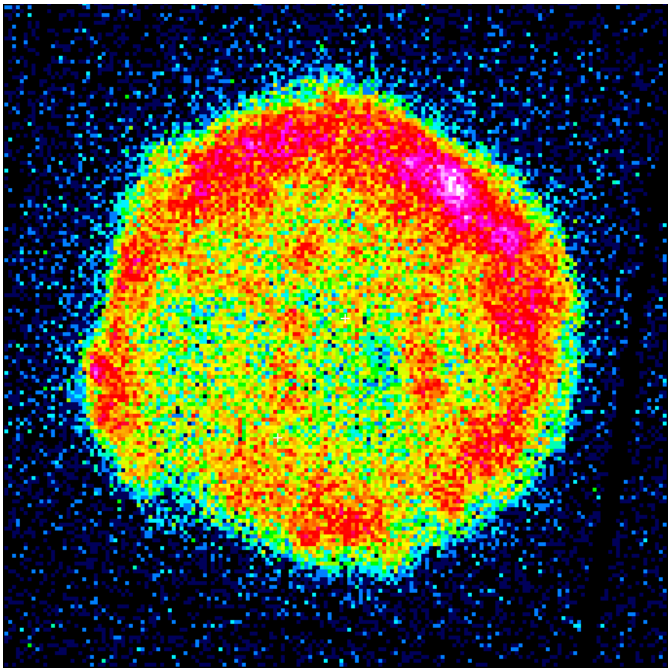


Fig. 5. XMM-Newton EPIC MOS1-camera unsmoothed image of the Tycho SNR.

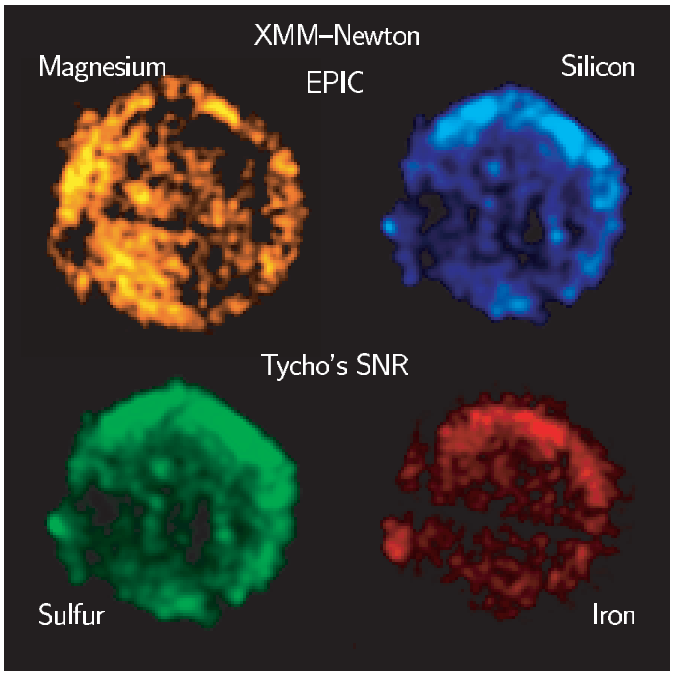


Fig. 6. The XMM-Newton EPIC pn-camera images of the Tycho SNR resolved in the emission lines of Mg, Si, S, Fe. Subimages are at the same scale.

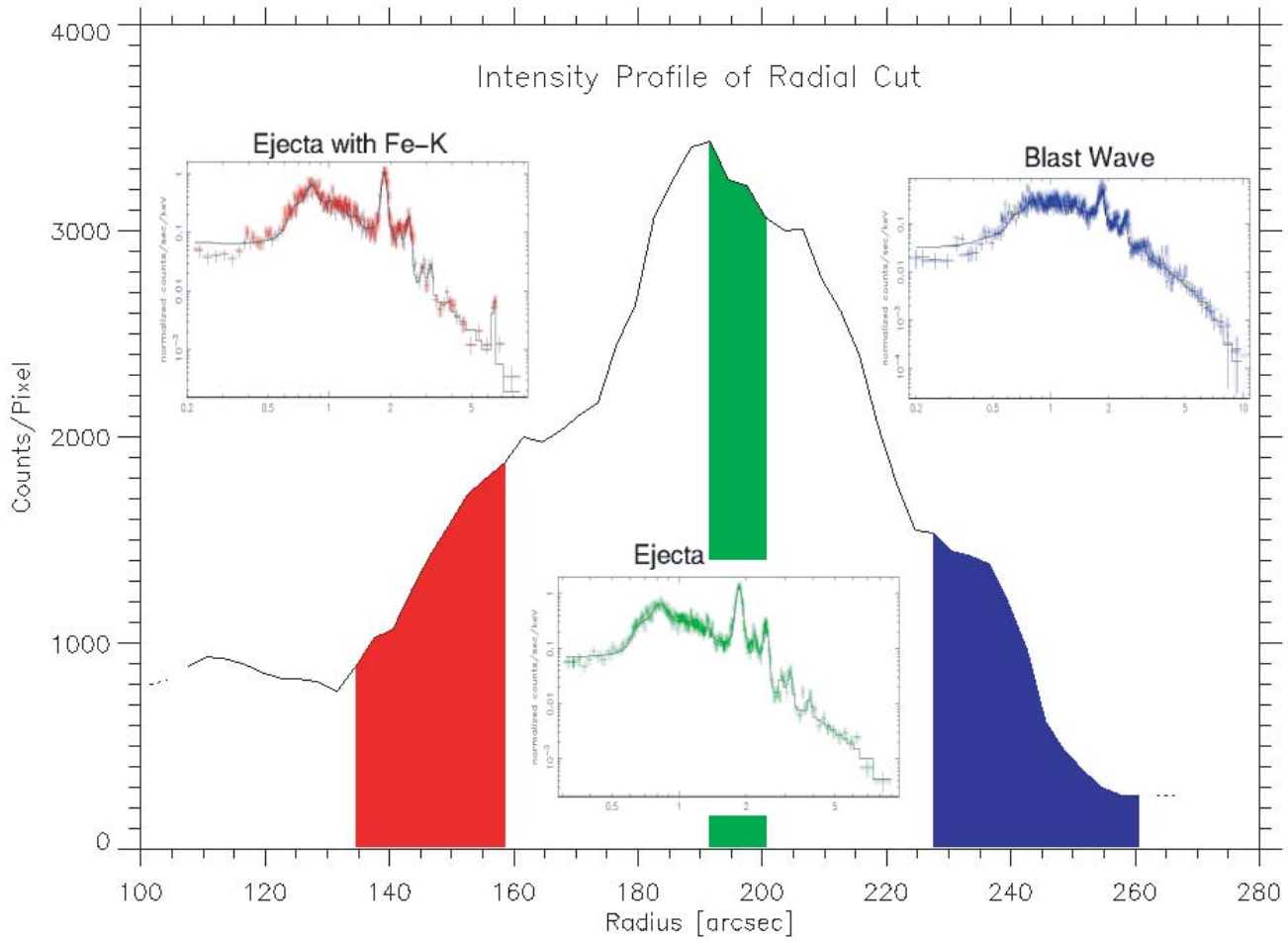


Fig. 7. Three EPIC pn-camera spectra of a narrow cut through the south-west of the Tycho supernova remnant (Stadlbauer & Aschenbach, 2001).

ing of the RGS spectrum indicates a temperature of ∼0.6 keV with a definite upper limit of 1 keV. With this temperature and the abundance of Fe apparent in the RGS spectrum in ionic states from FeXVII to FeXXI essentially no emission of Fe-K is expected, contrary of what the EPIC-pn spectrum shows (c.f. Fig. 8). There must be a high temperature component which produces the high energy continuum and the Fe-K line emission. Interestingly, progressively higher ionic charges of Fe up to FeXXIV are not detected although within the energy range of RGS (strong lines expected at 10.6 and 11.2 Å), which means that plasma of any intermediate temperature between 0.6 keV and a few keV is largely absent. Furthermore, the spatial distributions of the low temperature and high temperature components are totally different. Whereas the images taken at low ionic charge follow the filamentary structure (c.f. Fig. 6, Behar et al., 2001), although different in detail for instance in OVII and OVIII, the high energy continuum and the Fe-K line distributions are fairly uniform across the remnant (Fig. 10). There appears to be a volume filling high temperature plasma whereas the low temperature plasma is in filaments. What causes the temperature stratification with a gap in temperature between 0.6 keV and 2 keV at least? Why are the low Z and high Z but low ionization ions found predominantly found in filaments whereas the high ionization Fe ions and the high energy continuum distributed fairly uniform across the remnant?

The spatial distribution of the high energy continuum is not unique to N132D, a similarly uniform distribution has also been found for Tycho and Cas A (Bleeker et al., 2001, Willingale et al., 2002). It has been suggested that the high energy continuum is at least partly due to synchrotron radiation from highly relativistic electrons (∼10's of TeV) accelerated by diffusive shocks. Diffusive shock acceleration should dominate at the outer shock and the emission should be prominent there which is observed neither for Cas A nor for N132D nor for Tycho. If the high energy continuum is actually due to synchrotron radiation the acceleration mechanism is more likely to be of turbulent nature acting throughout the remnant but on a local scale.

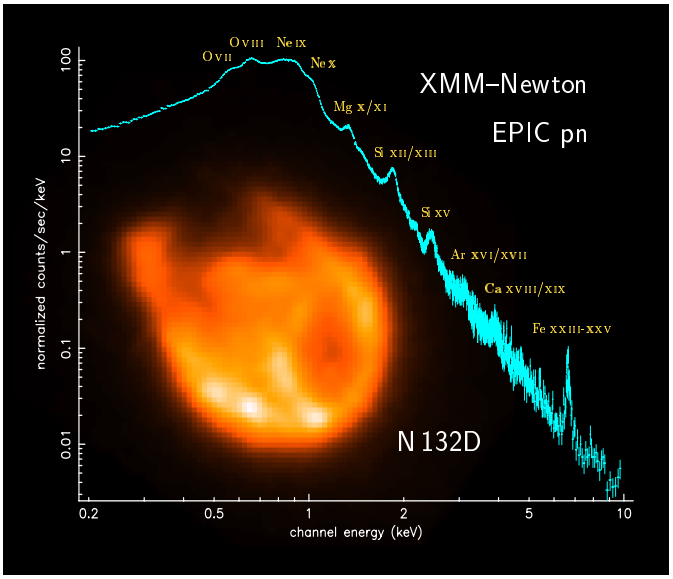


Fig. 8. XMM-Newton EPIC pn-camera image and total spectrum of the SNR N132D in the Large Magellanic Cloud (Behar et al., 2001).

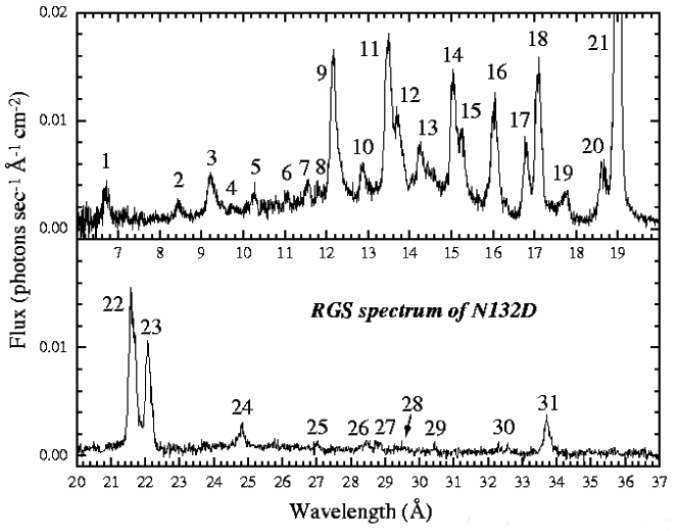


Fig. 9. XMM-Newton RGS spectrum of the SNR N132D in the Large Magellanic Cloud (Behar et al., 2001).

2.4. Shell-type remnants and the high energy non-thermal spectral tails

One of the major surprises of SNR X-ray research has been the discovery of high energy tails in the spectra of shell-type SNRs. After the discovery of Fe-K line emission in the early 1970's the X-emission of shell type remnants has been considered to exclusively arise from shock heated plasma and the radiation is thermal, correspondingly. Although even early measurements with HEAO-1 and EXOSAT indicated hard tails in young SNRs contradicting the straight thermal interpretation the picture has not changed until 1995 when Koyama et al. (1995) using

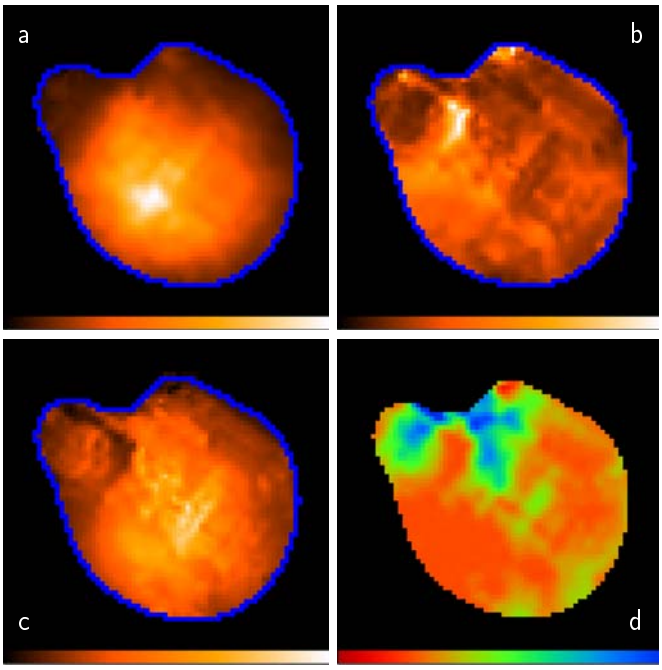


Fig. 10. SNR N132D maps of a) the Fe-K line flux at 6.67 keV, b.) the EW of the Fe-K line, c.) the differential continuum flux at 6.67 keV interpolated from the 4.4 - 10 keV, d.) apparent electron temperature (0.4 - 3.1 keV) derived from just the continuum (Behar et al., 2001).

ASCA measurements and Willingale et al. (1996) analyzing ROSAT PSPC data discovered that the X-spectra of the north-eastern and the south-western caps of the remnant of SN 1006 require a hard tail as well, which is best represented by a power law. If the tail is interpreted as synchrotron radiation electrons with energies of 10's of TeV must be present. The acceleration to these energies, close to the knee of the cosmic ray spectrum but still an order of magnitude or more below, may be provided by diffusive shocks. It seemed that we were close to the solution of a problem which has been standing since 1912 when cosmic rays were discovered. SNRs have always been considered an important site of cosmic ray production. One consequence, however, is that the TeV electrons should also give rise to TeV γ-rays by inverse Compton scattering off the microwave background, and indeed, TeV γ-rays were subsequently detected (Tanimori et al., 1998). Soon after SN 1006 Koyama et al. (1997) added another shell type SNR with a power law spectral tail, i.e. RX J1713.7-3946 or G347.3-0.5, which was originally discovered in the ROSAT all-sky survey (Pfeffermann &Aschenbach, 1996). TeV γ-rays from the north-western quadrant of the remnant were reported recently by Enomoto et al. (2002), who could establish a spectrum from 0.4 - 8 TeV. They conclude from the TeV spectrum and the upper limit obtained with EGRET on GRCO that the γ-rays are not produced by high energy electrons but result from the decay of π^0 mesons which are produced in collisions of high energy

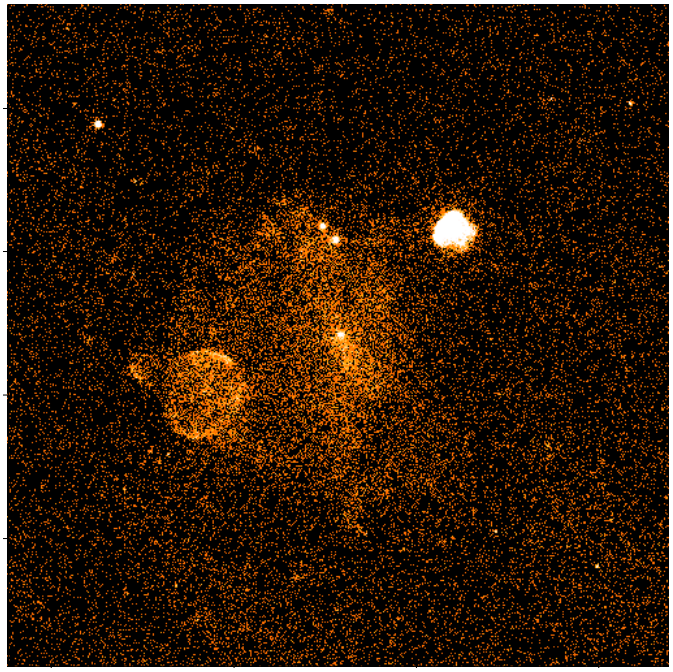


Fig. 11. ROSAT all-sky survey image (E>1.3 keV) of the Vela SNR, which shows the 2° diameter remnant RX J0852-4622 in the south-east (Aschenbach 1998).

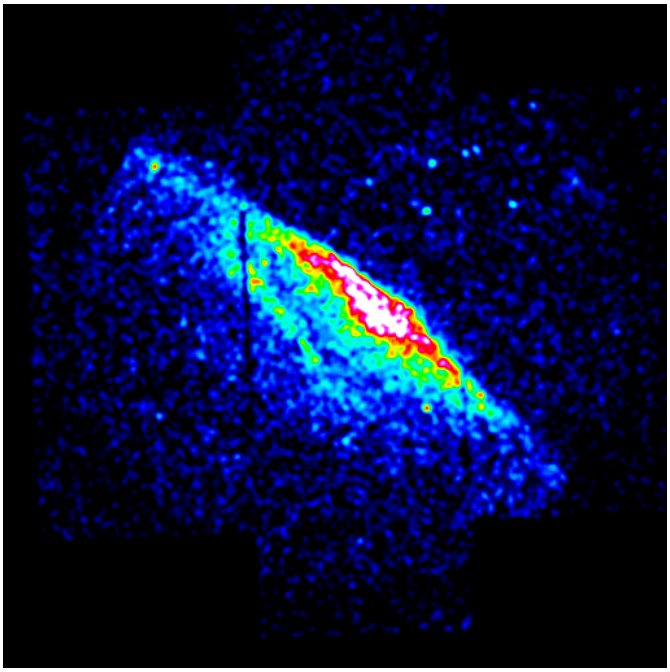


Fig. 12. XMM-Newton EPIC-MOS1 image of the north-section section of the SNR RX J0852-4622. At low energies, in particular at and around the O lines, there is still thermal emission, which mostly likely is from the Vela SNR rather than RX J0852-4622 (Iyudin et al., 2002).

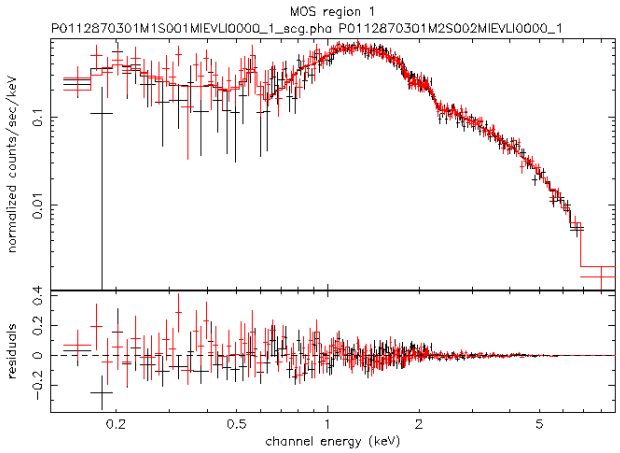


Fig. 13. Spectrum of RX J0852-4622 obtained with the XMM-Newton EPIC-MOS1 camera; the fit shows a power law modified by interstellar absorption (Iyudin et al., 2002).

SNR cosmic rays with nucleons of an adjacent molecular cloud. A revision of the EGRET data which turns the upper limit into a definite flux and a spectrum (Reimer et al., 2002) seems to not exclude electron processes.

From the X-ray point of view these remnants are difficult to analyze because the power law contribution is a minor component of the overall spectrum which is still dominated by thermal radiation. This is different for instance for the supernova remnant RX J0852-4622 or G266.2-1.2 located in the south-east corner of the Vela SNR (Aschenbach 1998, Fig. 11).

The analysis of the ASCA data shows that the spectrum of this shell-type remnant can be represented by a power law without any thermal 'contamination' (Tsunemi et al., 2000, Slane et al., 2001). This is most evident for the north-western section of the shell whereas there may be contributions to the southern spectrum from a thermal component, which, however, could be due to radiation from the Vela SNR. The observations with XMM-Newton have revealed for the first time the topography of the non-thermal shell. The XMM-Newton EPIC pn-camera image is shown in Fig. 12; the section of the shell is broken into a number of filaments which are not aligned as well as condensations and indentations. For energies > 1 keV the spectrum is a clean power law with a photon index of 2.6 (Fig. 13, Iyudin et al., 2002); an improved fit is obtained with the 'srec' model of XSPEC, which takes into account a gradual steepening of the power law towards higher energies attributed to electron leakage and/or synchrotron losses. The fit with a power law requires an interstellar absorption column density to RX J0852-4622 which is significantly higher than that to the Vela SNR, most likely putting RX J0852-4622 behind the Vela SNR. I stress that this is correct in a strict sense only for a power law. So far we don't know the intrinsic shape of the spectrum; in case of a synchrotron spectrum we don't know whether the electron spectrum really follows a power law spectrum.

The only emission line feature in the spectrum is seen at 4.24 keV (Iyudin et al., 2002) assuming an underlying

power law continuum, although at a fairly low significance level. But such a feature was already present in the ASCA spectrum (Tsunemi et al., 2000) although at a slightly lower energy (4.1 keV). This line may result from the ^{44}Ti electron capture decay, which produces a vacation in the K-shell of the daughter nucleus of ^{44}Ca or the line is a blend of lines emitted by Ca and Ti. The line flux observed is consistent with a relatively young and close-by SNR (Aschenbach et al., 1999), and the flux is consistent with the 1.8 MeV γ-ray line flux of radioactive ^{44}Ti reported by Iyudin et al. (1998).

Close to the center of RX J0852-4622 a point-like X-ray source has been found in the ROSAT all-sky survey which was suggested as the neutron star remnant of RX J0852-4622 (Aschenbach 1998). But limited by the large RASS error box which contained three optical sources no identification was possible. This changed when Chandra observed the region and one source now designated CXOU J085201.4-46175 could be singled out (Pavlov et al., 2001). Because of the absence of any radio and optical counterpart down to very faint magnitudes and because of the spectrum, which looks like a blackbody with kT ≈400 eV and an emitting surface of 280 m radius for a distance of 1 kpc the source is very likely a neutron star (Kargaltsev et al. 2002). No significant pulsation in the 0.001 - 100 Hz range have been found. XMM-Newton has observed the central region of RX J0852-4622 as well confirming the absence any other significant X-ray source within a circle of 5 arcmin radius around CXOU J085201.4-46175. Details of the results and the spectrum are presented in these proceedings by W. Becker (2002).

The origin of the high energy X-ray spectral tails is still being discussed controversially, and many more SNRs need to be found to solve the puzzle. Remnants dominated by non-thermal rather than thermal emission in the X-ray band should have a value as large as possible for the ratio of $n_{TeV} \cdot B^{(\gamma+1)/2}/n^2_{therm}$, where n_{TeV} is the density of relativistic electrons in the TeV range, n_{therm} is the thermal electron density, γ is the index of the electron power law distribution, B is the perpendicular component of the magnetic field in which the electrons radiate synchrotron radiation. If there is a coupling between n_{TeV} and n_{therm}, which might depend on the age of the SNR, non-thermal emission is favored in a low density environment. Since the radio emission is proportional to $n_{GeV} \cdot B^{(\gamma+1)/2}$, with not necessarily the same γ, low surface brightness Σ radio remnants are preferred candidates to look for X-ray synchrotron tails, i.e. remnants which show up at the lower end of the Σ-D relation. This is true for SN 1006, RX J0852-4622, RX J1713.7-3946, RX J0459.1+5147 (Pfeffermann et al., 1991), which all demonstrate most clearly the presence of non-thermal X-ray spectra. Interestingly, apart from SN 1006 these remnants were discovered by their X-ray emission, which means that an unbiased survey in the radio band needs much more increased sensitivity to detect these sources. A survey in the X-ray band is severely constrained by interstellar absorption and only a survey at energies above 2 - 3 keV, about 10 times more sensitive than the ROSAT survey at 1 keV, would detect such remnants. Another implication is that if the majority of SNRs is, as expected, from explosion of massive progenitor stars, which have had strong stellar winds sweeping out their environment to very low densities, a large fraction of SNRs may have escaped detection both in the radio and the X-ray bands. And it is this class of remnants which might be the dominant cosmic ray contributor. It would also mean that our estimates of the relative number of SNRs containing a neutron star is severely biased because we haven't seen the majority of remnants because they are actually too faint in general to have been observed so far.

The shell-type power law remnants which have been found so far have typical radio spectra with an index between $\sim$ 0.3 - 0.5 for the energy flux and the corresponding X-ray spectra have an index typically between 1.5 and 2.0, and the fluxes between the radio and X-ray bands are such that the energy output per logarithmic energy interval (the ν F_ν distribution) peaks between the infrared and the EUV, for most of the sources actually in the optical band. In order to check on the synchrotron nature of the X-rays it is suggested to assess the level of any optical continuum radiation and to search for polarization of the optical radiation. This would be an 'experimentum crucis' to decide on the issue of synchrotron radiation up into the X-ray band.

2.5. The Crab Nebula and the 'Bulls Eye'

Although indicated already in the early Einstein HRI image and more clearly in the ROSAT HRI image the detailed structure of the Crab Nebula was revealed only in the superb Chandra images (Fig. 14, Weisskopf et al., 2000). At least three emitting regions can be discerned, which are the torus, the jet and a counter-jet and a more diffuse large scale region, extending far to the north-east, for instance. In particular the region around the pulsar and the main torus exhibit substantial ellipse-like substructure. The existence of the torus-like emission region as an equatorially confined pulsar wind nebula was suggested already in the pre-X-ray telescope era in 1975 by Aschenbach & Brinkmann (1975), interpreting lunar occultation measurements. In 1985 the existence of the polar outflows (jets) was proposed in a paper by Brinkmann et al. (1985) based on a 2-dim Fourier analysis of the *Einstein* HRI image which were even more evident in the ROSAT HRI image if the analysis is restricted to just the spatial high frequency components (Aschenbach 1992). The X-ray images show a brightness asymmetry along the torus such that the north-western part is much brighter than the south-eastern section, which is attributed to Doppler boosting of the electrons leaving the pulsar acceleration zone and hitting the nebula plasma with a speed of $\sim$ one

third of the speed of light. Since the inclination of the torus out of the plane of the sky is $\sim 30^\circ$ (Aschenbach & Brinkmann, 1975) with the north-western section pointing towards the observer, this section should be Doppler brightened (Pelling et al., 1987). It is noted that Aschenbach and Brinkmann (1975) suggested instead that the brightening of the north-western section is due to a compression of the magnetic field in the nebula by the motion of the pulsar against the nebula, the direction of which is pointing fairly close to the position of the maximal X-ray enhancement. Interestingly, the same relation holds for the Vela pulsar and its synchrotron nebula, i.e. the proper motion vector of the pulsar points to the region of maximum brightness. For the polar outflows such large brightness asymmetry has not been measured, and it is definitely significantly lower, which in the Doppler boosting model could be explained by either a geometry where the polar outflows are not perpendicular to the equatorial outflow, or an electron spectrum which is much flatter than the corresponding spectrum in the equatorial wind, or a electron bulk motion velocity along the jets much lower than c/3. The spatially resolved XMM-Newton spectra of the Crab show that the spectra of the polar outflow tend to be steeper than that of the torus region. If the polar outflows are associated with the rotation axis rather than with the magnetic axis the jet electrons move at comparatively low speed.

In the meantime a few more pulsar wind nebulae have been added which show the same structural components, so that highly asymmetric pulsar winds associated with the equatorial and polar regions appear to be the rule. An even more spectacular example is probably the Vela pulsar and its vicinity revealed by the Chandra images which have been discussed at this conference as well.

One of the big puzzles about the Crab is still not solved. Even with the deepest XMM-Newton and Chandra observations thermal X-ray emission, which is expected from the shock heated stellar debris and/or the ambient medium, has still not been found. In other cases of originally proclaimed Crab-like remnants like SNR 0540-69.3 deeper observations revealed in addition to the pulsar and its synchrotron nebula a faint shell of thermal emission (Gotthelf & Wang, 2000, van der Heyden et al., 2001). But recently a second true Crab-like remnant, a close cousin of the Crab Nebula according to the authors, has been identified as such using Chandra (Lu et al., 2002). The remnant G54.1+0.3 has been known for a long time as a radio source and it belongs to the class of centrally filled and strongly polarized remnants with a flat radio spectrum. X-rays have been detected with *Einstein* and ROSAT, the images of the latter observatory show a centrally peaked emission with some structure indicating a jet-like feature (Lu et al., 2001). G54.1+0.3 was then resolved with Chandra observations and spectra of various regions could be obtained (Lu et al. 2002). The Candra image is shown in Fig. 15. The remnant is $\sim$ 2.2' in size at an estimated distance of $\sim$ 5 kpc. It contains a central bright point-like source, a surrounding ring or torus, bi-polar elongations or jets and low surface brightness diffuse emission. The Chandra spectra show that all these components have power law spectra with no evidence of a thermal contribution; a thermal shell is absent as well. The flattest spectrum with a photon spectral index of 1.1 is associated with the point-like source, the torus has a spectrum of slope 1.64 and the outer diffuse regions come close to 2 for the spectral slope; except for the central source the spectra of the other components are pretty close to those in the Crab Nebula, the central source is flatter by 0.4. Spatially resolved X-ray spectra of the Crab are given by Willingale et al. (2001). As in the Crab the brightness of the X-ray torus changes with position vector, i.e. the azimuthal direction. In the framework of the Doppler boosting model the electron bulk velocity at the interface with the nebula amounts to 0.40$\pm$0.12 times the speed of light, which is basically the same as observed for the Crab torus (Lu et al., 2002). It would be interesting to measure the proper motion of the pulsar in G54.1+0.3 to see whether the proper motion vector points to the region of maximum brightness as it does for the Crab and Vela. If so, the Doppler boosting model has to be reviewed because in its current form it does not account for the coincidence of proper motion vector and maximum brightness location.

Recent follow-up observations with the Arecibo radio telescope show the central point-like source to be a radio pulsar with P = 136 ms and a $\dot{P}$ such that the characteristic age $\frac{P}{2\dot{P}} \sim 2900$ yrs and the spin-down luminosity $\dot{E}$ = 1.2×10^{37} erg/s (Camilo et al. 2002). Like in the Crab the pulsar in G54.1+0.3 dominates the picture so that the press has called this object 'bulls eye' (c.f. Fig. 15 and www1.msfc.nasa.gov/NEWSROOM/news/releases/2002/02-159.html). Clearly, based on morphological and spectral similarity the Crab Nebula and G54.1+0.3 belong to the same class of objects. But this discovery together with the low luminosity of the pulsar of just 1 mJy kpc^2, which is among the lowest for known young pulsars, shows that SNR pulsars can be extremely faint and many of them might be present in SNRs but simply have escaped detection so far. New and upgraded radio telescopes like the Arecibo are required to find them.

Another similarity between the Crab Nebula and the nebula of G54.1+0.3 is the mean linear expansion speed defined as the X-ray radius divided by the age. The apparent X-ray expansion rate of the Crab Nebula is 900 km/s versus 550 km/s for G54.1+0.3; they would be identical if G54.1+0.3 were at a distance of 8 kpc, which is not excluded by current data. But there is also a major difference between the Crab and G54.1+0.3, which is the radio extent. Whereas the radio diameter of G54.1+0.3 (Velusamy & Becker, 1988) is about the X-ray diameter the radio Crab is is about twice as large as the X-ray Crab. This could imply that the magnetic field of G54.1+0.3 is significantly less than that in the Crab Nebula, so that

synchrotron losses even in the X-ray band are not important in G54.1+03. On the other hand the steepening of the X-ray spectra with increasing distance from the central pulsar, which for the Crab has usually been attributed to synchrotron losses, is observed in G54.1 +0.3 the same way and level. Concerning the magnitude of the magnetic field strength a simple estimate shows that the nebular magnetic fields are not that much different. The nebular magnetic field scales with the age divided by the pulsar period and divided by the linear extent of the nebula. If I take the numbers given above the mean magnetic field of G54.1+0.3 should not differ from the Crab Nebula magnetic field by more than a factor of two or three. This would mean that the difference of the ratio of the radio versus X-ray size for these two sources is not related to the mean magnetic field strength. Consequently, if the pulsar nebula wind is dominated by electromagnetic losses rather than by particles, the extent of the nebula is not driven by the pulsar wind pressure but is controlled by some outer ambient medium, i.e. its particle and magnetic pressure.

This observation also raises the question whether the spectra we see from the radio range up to the X-ray domain across both the Crab and G54.1+0.3 are intrinsic spectra for this class of source, and that we don't see just the propagation of electrons injected by the pulsar suffering from synchrotron losses. Is there re-acceleration of the electrons inside the nebulae out to their edges?

The frequency dependence of the size of the Crab Nebula has been a long standing issue as it should give insight to the release into and the propagation mechanism of the electrons through the magnetic field. In the Crab Nebula the mean synchrotron lifetime of the electrons in the 0.5 mG field is ∼4 years and increases with frequency as $\nu^{-0.5}$ and a frequency dependent extent is expected. With the EPIC-MOS cameras of XMM-Newton the X-ray spectrum across the nebula has been spatially resolved (Willingale & Aschenbach, 2002). The spectra follow power laws everywhere with a continuous steepening with increasing distance from the pulsar. Fig. 16 shows the spectra for four selected regions in comparison with their optical spectra. Region 1, which is the region inside the torus close to the pulsar, shows a very small increase of the spectral index from the optical to the X-rays by ∼0.1, demonstrating that synchrotron losses are negligible and the electrons are young. But in region 4, which is the far north-west region at a distance of up to ∼ 1.8' from the pulsar the spectrum steepens significantly such that the X-ray flux is far below the extrapolation from the optical about a factor of 60 at 1 keV. This decrement would imply an age of the outermost electrons of at most 25 years, because every 4 years the energy of the electrons drops by a factor of 2 by synchrotron losses when moving away from the pulsar. This is compatible with the large distance of 1.8' from the pulsar only if the electrons move at about 1/7 of the speed of light through the nebula. As discussed above, based on the similarity with G54.1+0.3, the challenge of the high

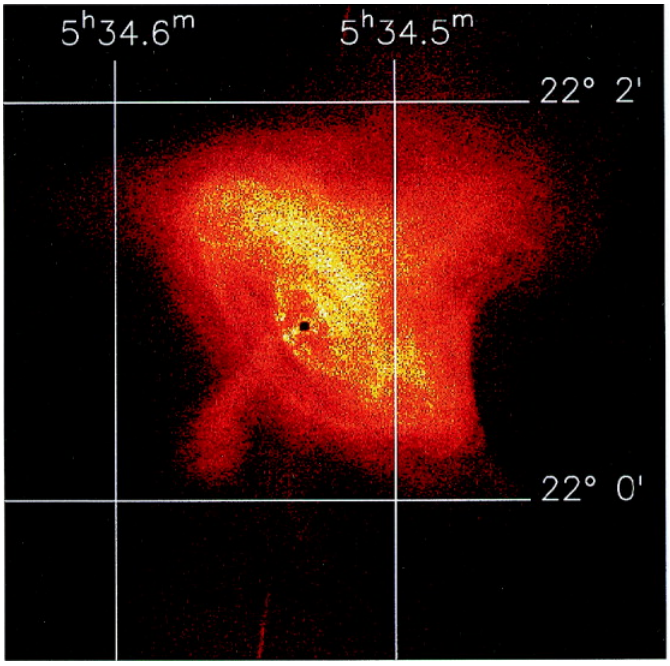


Fig. 14. Chandra image of the Crab Nebula (Weisskopf et al., 2000).

propagation speed would be significantly relaxed if some re-acceleration occurs inside the nebula. The optical filaments might be the sites where diffusive shock acceleration could contribute. Dramatic synchrotron losses could also be significantly reduced if the outer regions of the nebula are fed not so much by the equatorial wind but by the polar winds where jets might transport the electrons at lower loss rates.

As for the Crab Nebula it would be very useful to try to measure the non-thermal radiation of G54.1+0.3 in the optical (narrow band non-thermal flux and/or polarization) and to look for optical filaments.

2.6. SN 1987A

The explosion of SN 1987A was one of the rare historical astronomical events and it has triggered research in many astrophysical fields. In soft X-rays it took a long time, actually almost 3.5 years, to detect soft X-rays. The first attempt which was carried out with a sounding rocket experiment and an imaging X-ray telescope in August 1987, just half a year after the explosion, provided an upper limit of 1.5×10^{36} erg/s, which indicated a very low ambient matter density compliant with a wind of a blue supergiant (Aschenbach et al., 1987). Since the launch of ROSAT SN 1987A has been monitored regularly and the monitoring is now being taking over by Chandra and XMM-Newton. Figure 17 shows the light curve, which can be remarkably well fitted with a t^2 relation up to the end of the ROSAT coverage about 4000 days after the explosion. Soft X-rays are expected from the interaction of the supernova shock

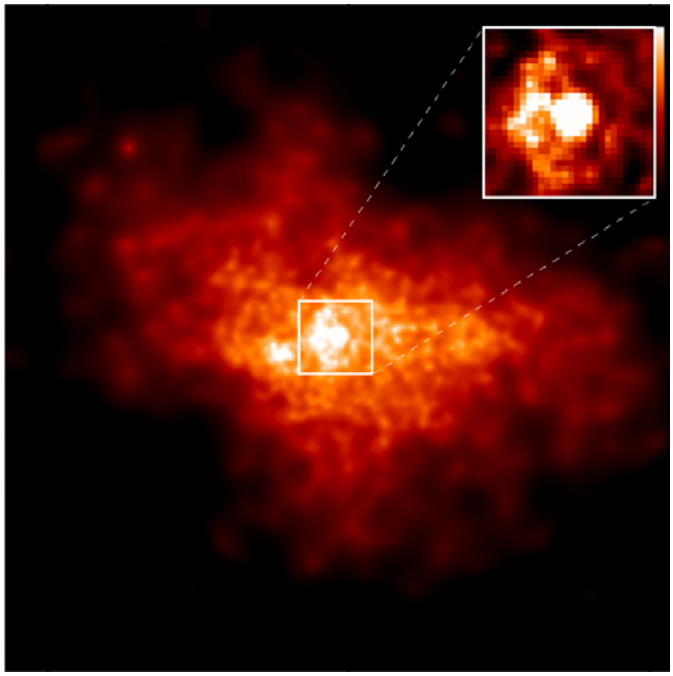


Fig. 15. Chandra ACIS-S image of the SNR G54.1+0.3. Size of the image is 127 arcsec square (Lu et al., 2002).

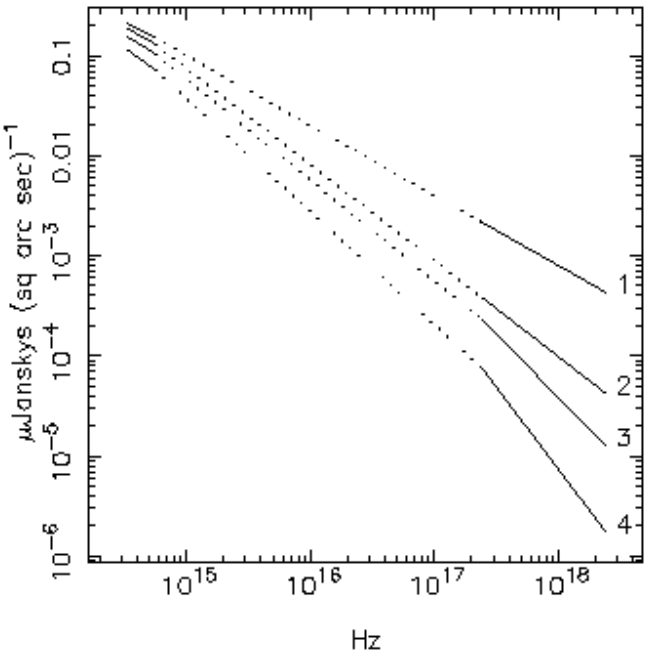


Fig. 16. Optical continuum spectra and X-ray spectra of the EPIC MOS-cameras from four separate regions across the Crab Nebula; region 1 corresponds to the inner edge of the torus, region 2 is the torus, region 3 is the transition region from the torus to the nebula, and region 4 reflects the outskirts of the nebula (Willingale & Aschenbach 2002).

with matter left from the wind of the blue supergiant stage and red supergiant phase of the progenitor inside the ring. The t^2 dependence seems to suggest some cylindrical rather than spherical symmetry of the interaction, which would have implications on the radial distribution of the matter density surrounding SN 1987A. The XMM-Newton and the Chandra data points tend to exceed the t^2 best fit. Whether this is an indication that the shock wave has already reached and partly penetrated the inner ring around SN 1987A remains to be seen. The Chandra images have resolved the supernova indicating that the shock wave has reached the inner surface or is close to contact. The more than proportional increase in flux indicates significant mass concentrations in the ring, the emission measure of which are notable (Park et al. 2002). In order to convert the count rate of the instruments into flux values the spectrum obtained with the XMM-Newton EPIC-pn camera (Fig. 18) has been used except for the Chandra data points. The Chandra data points have been extracted from the paper by Park et al. (2002).

The spectral fits and the derivation of element abundances is not unique. The XMM-Newton data, which cover the energy range from 0.3 - 10 keV can be represented by an optically thin plasma spectrum the temperature of which is $\sim$ 0.36 keV and a second component to fit the spectrum above $\sim$ 3.5 keV. For the thermal component both collisional ionization equilibrium (CIE) and ionization non-equilibrium (NIE) models have been tested and both provide the same parameters for temperature, density and abundances. In the context of the NIE models the plasma appears to be in collisional ionization equilibrium. The high energy component appears to be non-thermal because of the absence of any emission lines and it can be represented by a power law of photon index 2.6. The abundance values associated with the thermal component are about half solar for all elements except Si, S and Fe. Si and S appear to be a few times solar and for Fe only an upper limit of 0.03 times solar could be derived. It is noted that both the Fe-L lines and the Fe-K line are missing. The absence of Fe is remarkable because the modeling of the early hard X-ray lightcurve of SN 1987 A required a substantial mixing of ^{56}Co and Fe from the proto-neutron surface to the upper layers (e.g., Sunyaev et al., 1989). Where has all this Fe gone? Why hasn't it been heated by the reverse shock? And if there is no reverse shock, why are Si and S overabundant, the layers of which should have been contaminated by Fe? A significant condensation of Fe in dust grains is excluded by infrared measurements at about the same epoch of the XMM-Newton measurements. The dust-to-gas ratio in the interaction zone is found to be only 0.01% deduced from ISO measurements (Fischera et al., 2001).

Michael et al. (2001) have fit Chandra ACIS CCD spectra with plane-parallel shock models provided in the XSPEC S/W package. They can fit the spectrum, which covers the range from 0.35 to 4.5 keV, which just one temperature of 2.6 keV, and the abundances of the light elements O, Ne and Mg are significant lower than the abun-

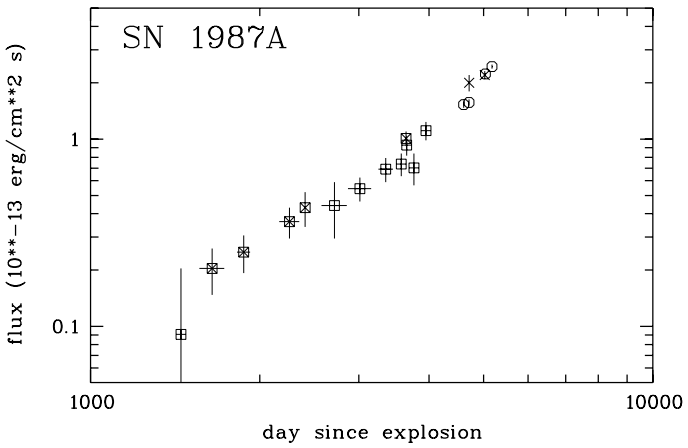


Fig. 17. 0.5 -2.0 keV lightcurve of SN 1987A compiled from ROSAT, Chandra (hexagons, from Park et al., 2002) and XMM-Newton (crosses) measurements.

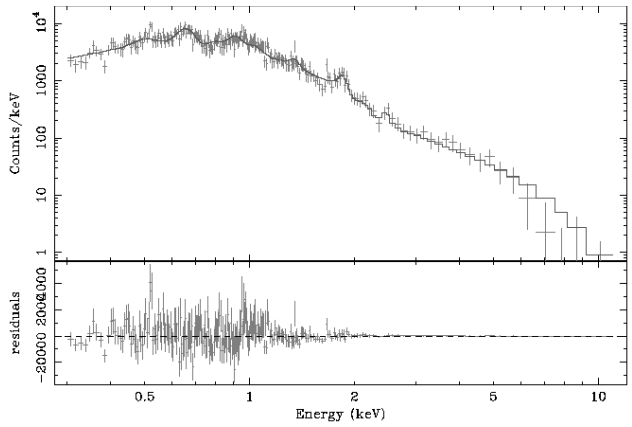


Fig. 18. X-ray spectrum of SN 1987A obtained with the EPIC pn-camera.

dances of Si and S. They are all (except N) lower in absolute terms by a factor of 4 to 5 compared with the XMM-Newton values obtained with a CIE model, but the ratio of Si or S over any light element is about the same. The relative abundances of the medium Z to the low Z elements are independent of the radiation model, the continuum in particular. We have applied the plane-parallel shock model of Michael et al. (2001) with exactly the same best fit parameters to the XMM-Newton data but we failed to get an acceptable fit. Michael et al. (2001) claim that a high energy component is not needed to fit their Chandra ACIS data, which might have to do with the lower high energy cut in the Chandra data compared with the XMM-Newton EPIC pn-data. It is not clear what the high energy tails is to be attributed to. Either it is associated with the putative pulsar, or it is a high energy bremsstrahlung tail or synchrotron radiation from the shell of SN 1987A, as it has appeared in numerous shell-type remnants. Of course, a faint unresolved central synchrotron nebula is not excluded at this stage. Much deeper X-ray observations of SN 1987A with XMM-Newton, both with the EPIC cameras and the reflection grating spectrometer RGS are needed.

Acknowledgements. I thank the Heraeus foundation for financial support.

References

Aschenbach, B. & Brinkmann, W., 1975, A&A 41, 147
Aschenbach, B., Briel, U. G, Pfeffermann, E., 1987, Nature 330, 232
Aschenbach, B., 1992, Zeiss-Info. mit Jenaer Rundsch. 1, 6
Aschenbach, B., Egger, R., Trümper, J., 1995, Nature 373, 587
Aschenbach, 1998, Nature 396, 141
Aschenbach, B., Iyudin, A., Schönfelder, V., 1999, A&A 350, 997
Aschenbach, B. & Miyata, E., 2002, A&A subm.
Becker, W., Aschenbach, B., et al., 2002, in preparation
Behar, E., Rasmussen, A. P., Griffiths, R. G., et al., 2001, A&A 365, L242
Bleeker, J. A. M., Willingale, R., van der Heyden K., et al., 2001, A&A 365, L225
Brinkmann, W., Aschenbach, B., Langmeier, A., 1985, Nature 313, 662
Brinkmann, W., 2002, in preparation
Camilo, F., Lorimer, D. R., Bhat, N. D., R., et al., 2002, astro-ph 0206220
Decourchelle, A., Sauvageot, J. L., Audard, M. et al., 2001, A&A 365, L218
Enomoto, R., Tanimori, T., Naito, T., et al., 2002, Nature 416, 823
Fischera, Jg., Tuffs, R., Völk, H. J., 2001, Astron. Ges. Abstract Ser. 18, #MS 02 13
Gotthelf, E. V. & Wang, Q. D., 2000, ApJ 532, L117
Iyudin, A., Schönfelder, V., Bennett, K., et al., 1998, Nature 396, 142
Iyudin, A., Aschenbach, B., Haberl, F., Freyberg, M., Grupe, D., 2002, in preparation
Kargaltsev, O., Pavlov, G. G., Sanwal, D., Garmire, G. P., 2002, AAS 200, #72.02
Koyama, K., Petre, R. Gotthelf, E. V., et al., 1995, Nature 378, 255
Koyama, K., Kinugasa, K., Matsuzaki., K., et al., 1997, PASJ 49, L7
Lu, F. J., Aschenbach, B., Song., L. M., 2001, A&A370, 570
Lu, F. J., Wang, Q. D., Aschenbach, B., Durouchoux, P., Song, L. M., 2002, ApJ 568, L49
Lyne, A. G., Pritchard, R. S., Graham-Smith, F., Camilo, F., 1996, 381, 497
Michael, E., Zhekov, S., McCray R., et al., 2001, astro-ph 0112261 (2001)
Park, S., Burrows, D. N., Garmire, G. P., et al., 2002, ApJ 567, 314
Pavlov, G. G., Sanwal, D., Kiziltan, B., Garmire, G. P., 2001, ApJ 559, L131
Pelling, R. M., Paciesas, W. S., Peterson, L. E., et al., 1987, ApJ 319, 416
Pfeffermann, E., Aschenbach, B., Predehl, P., 1991, A&A 246, L28

Pfeffermann, E. &Aschenbach, B., 1996, in 'Roentgenstrahlung from the Universe', eds. Zimmermann, H. U. &Trümper, J., MPE Report 263, 267
Reimer, O., Pohl, M., Butt, Y. M., Torres, D. F., Romero, G. E., 2002, astro-ph 0205256
Shigeyama, T., Iwamoto, K., Hachisu, I., Nomoto, K., Saio, H., 1996, Proc. IAU Coll. 145, 129
Slane, P., Hughes, J. P., Edgar, R., J., et al., 2001, ApJ 548, 814
Stadlbauer, T.F.X. & Aschenbach, B., 2001, ASP Conf. Ser., 251, 276
Sunyaev, R. A., Kaniovskii, A. S., Efremov, V. V., et al., 1989, Soviet Astr. Lett. 15, 125
Tanimori, T., Hayami., Y., Kamei, S., et al., 1998, ApJ 497, L25
Tsunemi, H., Miyata, E., Aschenbach, B., 1999, PASJ 51, 711
Tsunemi, H., Miyata, E., Aschenbach, B., Junko, H., Akutsu, D., 2000, PASJ 52, 887
van der Heyden, K. J., Paerels, F., Cottam, J., Kaastra, J. S., Branduardi-Raymont, G., 2001, A&A 365 L254
Velusamy, T., Becker. R. H., 1988, AJ 95, 1162
Weisskopf, M. C., Hester, J. J., Tennant, A. F., et al., 2000, ApJ 536, 81
Willingale, R., West, R. G., Pye, J. P., Stewart, G., C., 1996, MNRAS 278, 749
Willingale, R., Bleeker, J. A. M., van der Heyden, K. J., Kaastra, J. S., Vink, J., 2002, A&A 381, 1039
Willingale, R., Aschenbach, B., Griffiths, R. G., 2001, A&A 365, L212
Willingale, R., Aschenbach, B., 2002, in preparation

Proceedings of the 270. WE-Heraeus Seminar on: *"Neutron Stars, Pulsars and Supernova Remnants"*
Physikzentrum Bad Honnef, Germany, Jan. 21-25, 2002, eds. W. Becker, H.Lesch & J. Trümper, MPE Report 278, pp. 26- 28

Galactic SNR candidates in the ROSAT all-sky survey

D. Schaudel[1], W. Becker[1], B. Aschenbach[1], J. Trümper[1], W. Reich[2] and M. Weisskopf[3]

[1] Max–Planck–Institut für extraterrestrische Physik, Giessenbachstraße, 85740 Garching, Germany
[2] Max–Planck–Institut für Radioastronomie, auf dem Hügel 69, 43121 Bonn, Germany
[3] Marshall Space Flight Center, Space Sciences SD50, Huntsville, Alabama 35812, USA

Abstract. Identified radio supernova remnants (SNRs) in the Galaxy comprise an incomplete sample of the SNR population due to various selection effects. ROSAT performed the first all-sky survey with an imaging X-ray telescope, and thus provides another window for finding SNRs and compact objects that may reside within them. Performing a search for extended X-ray sources in the ROSAT all-sky survey database about 350 objects were identified as SNR candidates in recent years (Busser 1998). Continuing this systematic search, we have reanalysed the ROSAT all-sky survey (RASS) data of these candidates and correlated the results with radio surveys like NVSS, ATNF, Molonglo and Effelsberg. A further correlation with SIMBAD and NED was performed for subsequent identification purposes. About 50 of the 350 candidates turned out to be likely galaxies or clusters of galaxies. We found 14 RASS sources which are very promising SNR candidates and are currently subject of further follow-up studies. We will provide the details of the identification campaign and present first results.

1. Introduction

Supernovae (SNe) are rare events, believed to occur at intervals of $\sim$ 30 – 50 years in the Galaxy (van den Berg & Tamman 1991; Tamman 1994). However, in the past 2000 years, only 7 Galactic SNe have been observed — SN 185 (RCW86), SN 386 (G11.2-0.3), SN 1006, SN 1181 (3C58), Crab SN, Tycho SN, and Kepler SN. Most Galactic SNe appear unobserved owing to visible-band extinction by interstellar dust. When observational techniques in the radio band became available and the SNR Cas A was found to be the brightest radio source in the sky, several surveys and directed searches for SNR were performed at decimeter-wavelengths. Of course, radio observations are unhampered by interstellar dust. Currently, about 250 SNRs have been identified in the radio band (Green 2000 and references therein). Although this catalog represents the result of more than 40 years of intensive search with the largest radio telescopes, it is incomplete and strongly biased by mainly two selection effects: (i) the surface brightness of the remnant must be above the sensitivity limit of the observations, and (ii) the angular size of the remnant must be at least several times the resolution of the observations. These effects mean that not only are old faint remnants missing in the current catalogues, but there is also a deficit of young but distant SNRs (Green 1991). This is only a small fraction of SNRs of the total number expected according to the galactic SNe rate and the life-time of their remnants.
The RASS was performed from 1990 June to 1991 February and is the first (and only) all-sky survey done with an imaging X-ray telescope and thus provides another window that can be exploited to find SNRs as well as the compact objects that may reside within them (Aschenbach 1996). ROSAT was sensitive at soft X-ray energies (0.1-2.4 keV), had an angular resolution in survey mode of $\sim 96''$ and a limiting survey sensitivity of $f_x \sim 3 \times 10^{-13}$erg cm^{-2}s^{-1} (Voges 1999). The exposure time varied between about 400 s and 40,000 s in the ecliptic plane and poles respectively.

2. Analysis and Results

Performing a search for extended ($\geq 5'$) and unidentified X-ray sources in the RASS database at $|b| \leq 15^o$, about 350 objects were identified as potential SNR candidates (Busser 1998). Studying their X-ray morphology and correlating the results with radio catalogues and surveys like NVSS, ATNF, Molonglo and Effelsberg and the optical DSS as well as with SIMBAD and NED, allowed to discriminate between extragalactic background objects and SNR candidates, leaving 230 targets for subsequent identification purpose. About 50 of the 350 candidates turned out to be likely galaxies or clusters of galaxies, whereas $\sim$ 70 were found to be spurious background features. So far, 14 RASS sources were found to be promising SNR candidates and are currently subject of further follow-up studies in the X-ray and radio band. Due to the relatively low photon statistics and spatial resolution of the RASS data, it is not possible to perform a detailed analysis which allows to identify the nature of the objects. Below we briefly

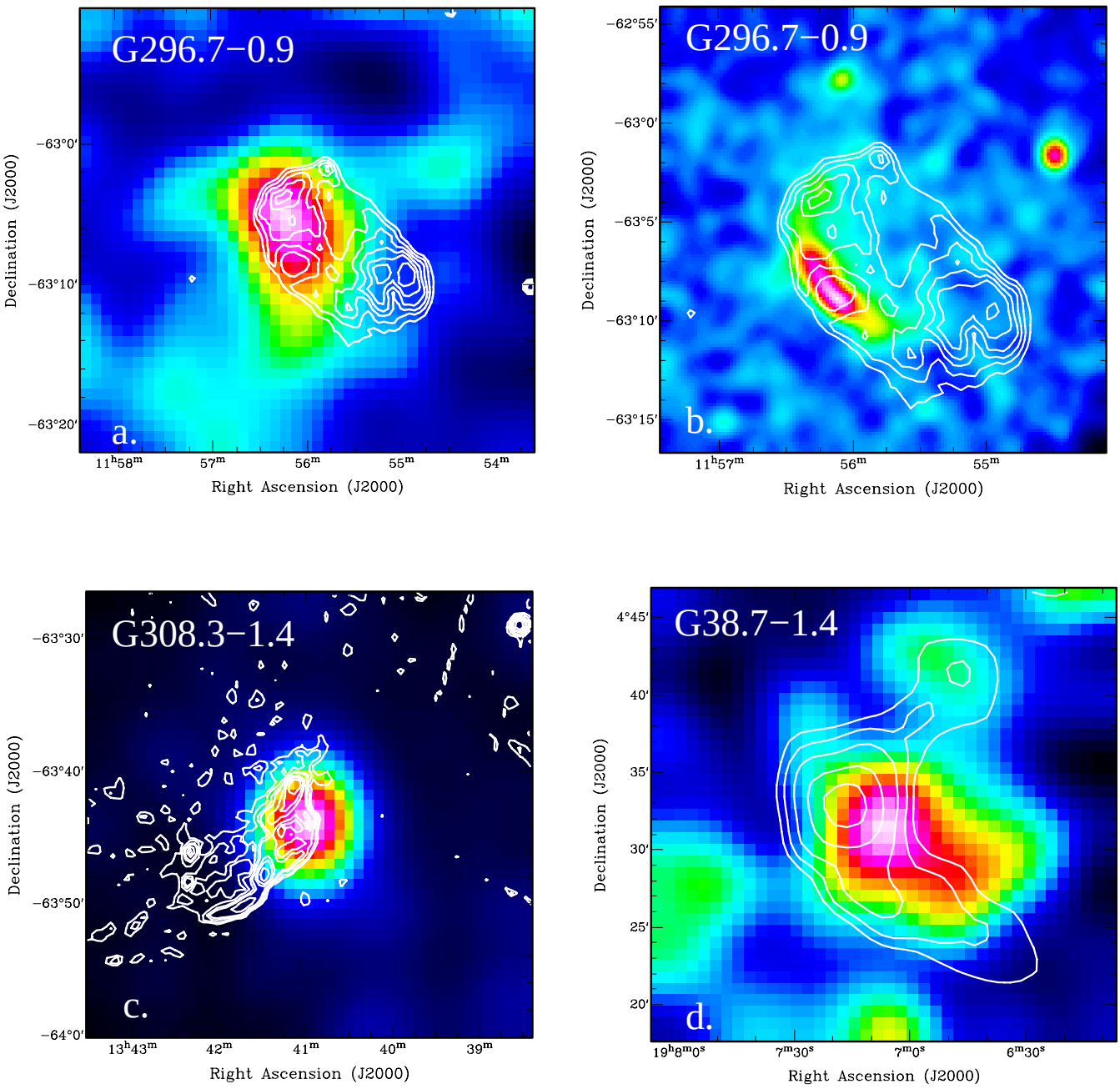


Fig. 1. a.) Grey-scaled RASS image of G296.7-0.9 with superimposed radio contours the MOST data at 843 MHz **b.)** G296.7-0.9 as seen in the ROSAT HRI shown greyscaled. The higher angular resolution resolves the extended X-ray source into a faint arc structure located in the east. **c.)** RASS image of G308.3-1.4 overlaid with MOST data which show an incomplete radio shell. **d.)** RASS image of G38.7-1.4 overlaid with contour lines from the 11 cm Effelsberg survey

mention three targets which turn out to be likely SNRs according to their X-ray and radio morphology.

– G296.7-0.9 is located in a HII region (Russeil 1996) which is overlapping partly the area of radio emission. The target has an extent of about 15′×10′ in X-rays and at radio wavelength. A pointed ROSAT HRI observation which has a 18 times higher angular resolution compared to the survey observation shows an

incomplete shell in the east, supporting strongly the SNR interpretation (Fig. 1a/b).

- G308.3-1.4 is listed as a possible SNR in the MOST supernova remnant catalogue based on the composite radio morphology and the ratio of 60 μm to 843 MHz flux densities (Whiteoak 1992). The RASS PSPC data support this identification showing a hard X-ray source with a diameter of about $10'$ partly overlapping with the radio arcs (Fig. 1c).
- G38.7-1.4 shows X-ray emission in the RASS with an extent of about $12'\times8'$, surrounded by an incomplete radio shell in the Effelsberg galactic plane 11 cm-survey (Reich et al. 1990). A follow-up observation with the Effelsberg 100-m telescope at 6 cm wavelength was recently performed, which shows the shell to be significantly polarized. The spectral index was determined to be $\alpha = 0.76\pm0.34$. This results clearly favor a SNR interpretation of G38.7-1.4 (Fig. 1d).

3. Summary and Prospects

About 70 galactic SNRs are listed in Green's SNR Catalogue (Green 2000) being detected in X-rays. Making use of the spectro-imaging capability provided by ROSAT in its all-sky survey, we reanalyzed a sample of about 350 extended X-ray sources, which were proposed by (Busser 1998) as SNR candidates. Performing a more dedicated imaging analysis and making use of recently updated databases like SIMBAD and the NED we reduced the number of SNR candidates to be about 230. 14 of these targets turn out to be promising SNR candidates based on available data and are subject of follow-up observations for clarification. Two candidates were recently observed with the Chandra observatory and another six candidates with the Effelsberg 100-m telescope. The analysis of these data is currently in progress. We will continue this campaign providing additional observations in X-rays with XMM-Newton and Chandra and in radio with Effelsberg and ATNF telescopes. Optical observations will complete our multi-wavelength studies.

References

Aschenbach, B. 1996, ROSAT Observations of Supernova Remnants, in Röntgenstrahlung from the Universe, eds H.U.Zimmermann, J.Trümper and H.Yorke, MPE Report 263, p213-220

Busser, J.-U. 1998, PhD thesis, Munich

Green, D.A. 2000, 'A Catalogue of Galactic Supernova Remnants', Mullard Radio Astronomy Observatory, Cambridge, United Kingdom

Green, D.A. 1991, PASP, 103, 209

Reich, W., Fürst, E., Reich, P., Reif, K. 1990, A&AS, 85, 633

Russeil, D. 1996, A&A, 319, 788

Tamman, G.A. 1994, The frequency of supernovae in Bludman, S.A., Mochkovitch, R., Zinn-Justin, J., (eds.) Supernovae, Les Houches, 1990, p1

van den Berg & Tamman, G.A. 1991, ARA&A, 29, 363

Voges, W. et al. 1999, A&A, 349, 389

Whiteoak, J.B.Z. 1992, A&A, 262, 251

Proceedings of the 270. WE-Heraeus Seminar on: *"Neutron Stars, Pulsars and Supernova Remnants"*
Physikzentrum Bad Honnef, Germany, Jan. 21-25, 2002, eds. W. Becker, H.Lesch & J. Trümper, MPE Report 278, pp. 29- 43

The Anomalous X–ray Pulsars

S.Mereghetti[1], L.Chiarlone[2,1], G.L.Israel[3] and L.Stella[3]

[1] Istituto di Astrofisica Spaziale e Fisica Cosmica, Sezione di Milano "G.Occhialini", CNR, v.Bassini 15, I-20133 Milano, Italy
[2] Universita' degli Studi di Milano, v.Celoria 16, I-20133 Milano, Italy
[3] Osservatorio Astronomico di Roma, v.Frascati 33, I-00040 Monteporzio Catone, Italy

Abstract. The Anomalous X-ray Pulsars (AXPs) are a small class of pulsars with spin periods in the 6–12 s range, very soft X–ray spectra, secular spin down on time scales of $\sim 10^3 - 10^5$ years, and lack of bright optical counterparts. Two, possibly three, of them are close to the center of shell-like supernova remnants. AXPs are one of the most enigmatic classes of galactic high-energy sources. Isolated neutron stars powered by the loss of rotational energy can be excluded on energetic grounds. The models based on neutron stars involve either accretion (perhaps from a fossil disk around an isolated neutron star) or the decay of a very strong magnetic field ($10^{14} - 10^{15}$ G). We review the models and the observational properties of AXPs, including recent *XMM-Newton* and *Chandra* observations. We also present some unpublished *ASCA* data.

1. Introduction

Bright X–ray sources powered by accretion in a binary system and showing regular pulsations due to the characteristic lighthouse effect from a rotating, magnetized neutron star were discovered in the early seventies. More than one hundred X–ray pulsars are currently known, most of which are optically identified with bright, massive early type stars, or provide other evidence of being in binary systems. The Anomalous X–ray Pulsars (AXPs) were recognized only in the last few years as a separate class of objects, with common characteristics clearly different from those of the normal pulsars. Most remarkable is the lack of signatures for a binary companion, a fact that prompted a variety of models based on isolated neutron stars or white dwarfs.

The interest for this small group (5 or 6) of pulsars has continued to increase in the last few years due to several factors. First, there is the exciting possibility that AXPs could be the neutron stars with the strongest known magnetic field, greater than several 10^{14} G. Second, they share some similarities with the Soft Gamma-ray Repeaters (SGRs, see Hurley 2000 for a review), another class of neutron stars with exceptional properties including super-outbursts with luminosity in excess of 10^{44} erg s^{-1} (assuming isotropic emission). Finally, it has become apparent that the "*textbook*" example of association between a neutron star and a supernova remnant, the Crab, is the exception rather than the rule. Most supernova remnants do not contain "*Crab-like*" pulsars, i.e. neutron stars with high rotational energy loss, magnetic field of several 10^{12} G, small spin period, pulsed radio and non-thermal X/γ-ray emission, and surrounded by bright radio/X-ray synchrotron nebulae. This apparent lack of compact remnants is not considered a problem anymore, since it has been recognized that there are different ways in which young neutron stars manifest themselves. In this context, AXPs are relevant since at least two of them (possibly three) are found right at the center of shell-like supernova remnants.

2. Historical overview

The AXP "*prototype*" 1E 2259+586 was discovered at the center of the SNR G109.1–1.0 back in 1980 (Fahlman & Gregory 1981), and for many years it remained an isolated oddity in the zoo of X–ray pulsars. A small, positive period derivative of 5×10^{-13} s s^{-1}, similar to that of the Crab pulsar, was measured (Koyama et al. 1987), but it was clear that, owing to its long spin period (7 s), the loss of rotational energy was orders of magnitude too small to power the observed luminosity of a few 10^{35} erg s^{-1}. Thus 1E 2259+586 was not a rotation powered Crab-like pulsar and it also seemed different from the majority of accreting pulsars known at the time, due to its soft X-ray spectrum, lack of a bright (and hence massive) companion star, and secular spin-down.

The discovery of several new X–ray pulsars, as well as the extensive efforts to identify and study their optical counterparts, led to the following picture by the end of 1994: out of a total of 39 accreting pulsars known, only three were in Low Mass X–ray Binaries (LMXRBs) with an optically identified companion star: GX 1+4 (with an M giant companion of mass $M_c \sim 0.8 - 2\ M_\odot$), 4U 1626–67 ($M_c \sim 0.02$ or $0.08\ M_\odot$), and Her X–1 ($M_c \sim 2\ M_\odot$). In addition there were four pulsars, without optical identification, but with optical limits excluding a massive com-

Table 1. The AXPs and their associated SNRs

SOURCE	P (s)	$\dot{P}$ (s s^{-1})	SNR	$P/2\dot{P}$ (years)	B$^{(a)}$ (Gauss)	SNR age (kyr)	L$_x^{(b)}$ (erg s^{-1})	D$^{(c)}$ (kpc)
1E 2259+586	6.98	4.88×10^{-13}	G 109.1–0.1 (CTB 109)	227,000	6.1×10^{13}	3 –17	10^{35}	4
1E 1048.1−5937	6.45	(1.5-4)$\times 10^{-11}$	–	$(3-7) \times 10^3$	3.2×10^{14}	–	3.4×10^{34}	5
4U 0142+61	8.69	1.98×10^{-12}	–	70,000	1.4×10^{14}	–	3.3×10^{34}	1
1RXS J1708−4009	11.00	1.9×10^{-11}	–	9,200	4.8×10^{14}	–	6.8×10^{35}	8
1E 1841−045	11.77	4.16×10^{-11}	G 27.4+0.0 (Kes 73)	4,500	7.3×10^{14}	$\lesssim 3$	2.3×10^{35}	7
AX J1845.0−0300 *(AXP candidate)*	6.97	–	G 29.6+0.1	–	–	$\lesssim 8$	$7.4 \times 10^{34(d)}$	8

(a) magnetic field estimated from $B = 3.3 \times 10^{19}\ (P\dot{P})^{1/2}$;
(b) luminosity in the 1-10 keV range, corrected for the absorption;
(c) assumed distance;
(d) assuming the blackbody model, see Table 2.

panion star (1E 2259+586, 4U 0142+61, 1E 1048.1−5937, RX J1838.4–0301). Mereghetti & Stella (1995) pointed out the similarities in their properties and the remarkable fact that they all have spin periods in the narrow interval between 5 and 9 s. For comparison, the High Mass X–Ray Binary (HMXRB) pulsars known at that time had periods from 69 ms to 1450 s: a range spanning more than four decades. Mereghetti & Stella (1995) suggested that, together with 4U 1626–67 (P=7.7 s), these objects belong to a different class of pulsators, probably powered by accretion from a very low mass companion (this was known to be true at least for 4U 1626–67 which has an orbital period of 41 minutes).

Van Paradijs et al. (1995) interpreted these "*6-sec pulsars*"[1] as isolated neutron stars accreting from a residual disk, of course with the exception of 4U 1626–67, which, however, could be considered a close relative in the context of the evolutionary model of Ghosh et al. (1997).

A few years later, pulsations at periods similar to those of AXPs were discovered in the quiescent X–ray counterparts of two SGRs (P=7.5 and 5.2 s, respectively in SGR 1806–20 and SGR 1900+14, Kouveliotou et al. 1998, Hurley et al. 1999a). These sources were found to spin-down with period derivatives $\dot{P} \sim 8$ and 6 $\times 10^{-11}$ s s^{-1}, as expected for dipole magnetic braking in the "*magnetar*" model, developed by Duncan & Thompson to explain the SGR phenomenon. This led, by analogy, to apply the same model also to AXPs (see Section 4.2).

In the meantime, the original list of AXPs had changed, not only for the exclusion of 4U 1626–67, but also because it was found that, contrary to previous claims (Schwentker 1994), RX J1838.4–0301 was not a pulsar (Mereghetti et al. 1997). These losses were balanced by the discovery of two new pulsars with all the characteristics to be included in the AXP group: 1E 1841−045, discovered by Vasisht & Gotthelf (1997) inside the Kes 73 SNR, and 1RXS J170849−400910 (Sugizaki et al. 1997). The last addition to the AXP group is possibly AX J1845.0−0300 (Torii et al. 1998), but for the reasons described below, this should be considered only a "*candidate*" AXP. Table 1 gives the list of currently known AXPs.

[1] the name Anomalous X–ray Pulsars was introduced later, see Duncan (2002)

3. Main properties

The main characteristics that distinguish AXPs from the more common HMXRB pulsars are the following:

a) The absence of a massive companion star in AXPs has been established by means of deep optical and IR observations. Even for the AXPs with the highest interstellar reddening, the current data are sensitive enough to rule out the presence of an early type mass donor. Further evidence comes from the lack of orbital motion signatures, such as periodic intensity variations (eclipses or dips) and pulse arrival times delays (however this analysis has not been carried out yet for all AXPs).

b) The AXPs are characterized by soft X–ray spectra, clearly different from those of HMXRB pulsars. The latter have relatively hard spectra, usually well described by a power law with photon index $\alpha_{ph} \sim 1$ and an exponential cut-off above ∼20 keV. In contrast, AXP spectra require much steeper power laws ($\alpha_{ph} > 3$) and/or blackbody models with low temperature (kT $\lesssim 0.5$ keV).

c) In general, accreting neutron stars tend to spin-up secularly, due to the angular momentum transferred from the accreting material. Indeed this is observed in

many HMXRB pulsars in which there is evidence for an accretion disk. Wind-fed pulsars often show alternating episodes of spin-up and spin-down. on the contrary, the spin periods of AXPs are monotonically increasing at a nearly constant rate (on timescales ranging from ∼5,000 to $\sim 2 \times 10^5$ yrs).

d) Spin period in the range 5–12 s. It is interesting to note that all the pulsars that satisfy the three above criteria (a), (b) and (c) have periods in this very narrow range.

e) Rather constant luminosity, at a level of $\sim 10^{34}$-10^{36} erg s^{-1}. In general, AXPs have relatively steady X–ray fluxes, compared with the kind of variability displayed by other classes of accreting compact objects. As described in Section 5.4, AX J1845.0−0300 showed a flux decrease greater than a factor 14 in observations spaced 3.5 years apart. If further observations will confirm this source as an AXP, the interesting possibility that a class of *transient* AXPs exist should be considered.

f) Two AXPs are clearly associated to SNRs, three if also AX J1845.0−0300 is considered (see Section 8.1).

To summarize, one might define an AXP as "*a spinning down pulsar, with a soft X–ray spectrum, apparently not powered by accretion from a companion star, and with a luminosity larger than the available rotational energy loss of a neutron star*".

4. Models

4.1. Accretion based models

Accretion is a well known powering mechanism that might be at work also for AXPs. Three different reservoirs for the accreting material have been considered: a companion star, the interstellar medium and a residual disk.

The first possibility was originally proposed by Mereghetti & Stella (1995), who suggested that the AXPs were neutron stars with very low mass companions, and characterized by lower luminosities and higher magnetic fields ($B \sim 10^{11}$ G) than classical LMXRBs. However, no detailed binary model for AXPs has been developed yet. Indeed, the lack of evidence for a companion star stimulated more interest in models based on isolated compact objects.

Accretion from the interstellar medium (ISM) was suggested for 4U 0142+61, based on its spatial coincidence with a nearby molecular cloud (Israel et al. 1994). However, it is unlikely that this can explain all AXPs, since ISM accretion can only provide a luminosity

$$L_{acc} \sim 10^{32} \;\; v_{50}^{-3} \;\; n_{100} \qquad \mathrm{erg\ s^{-1}}$$

where v_{50} is the relative velocity between the neutron star and the ISM in units of 50 km s^{-1} and n_{100} is the gas density in units of 100 atoms cm^{-3}. Even for extreme values of v_{50} and n_{100}, this is clearly too small a luminosity, unless all AXPs are nearby objects (∼100 pc), a possibility that seems very unlikely considering their low galactic latitude, high X–ray absorption, and (in at least two cases) the distances of the associated SNRs.

For these reasons, the most promising models are based on "*fossil*" accretion disks (of different origin) around isolated neutron stars.

The scenario of an isolated neutron star fed from a residual disk was first advanced by Corbet et al. (1995) for 1E 2259+586. van Paradijs et al. (1995) proposed that AXPs could be one possible outcome of the common envelope evolution of close HMXRBs, in which a residual accretion disk is formed after the complete spiral-in of the neutron star in the envelope of a giant companion (a so called Thorne-Zytkow object, TZO, Thorne & Zytkow 1977).

According to Ghosh et al. (1997), a HMXRB undergoing common envelope evolution can produce two kinds of objects, depending on the (poorly known) efficiency with which the envelope of the massive star is lost. Relatively wide systems are expected to have enough orbital energy to lead to the complete expulsion of the envelope before the neutron star settles at the center of the massive companion. This results in the formation of tight binaries composed of a neutron star and a helium star, like 4U 1626–67 and Cyg X–3. Closer HMXRB, on the other hand, produce TZOs, as a result of complete spiral in of the neutron star in the common envelope phase, and then evolve into AXPs.

Another possibility for the formation of a disk is through fallback of material from the progenitor star after the supernova explosion. For appropriate values of the neutron star magnetic field, initial spin period, and mass of the residual disk (Chatterjee et al. 2000), these systems can evolve into AXPs with luminosities, periods and lifetimes consistent with the observed values. Due to the steadily declining mass accretion rate, the rotating neutron star evolves through different states. During an initial "*propeller*" phase, lasting a few thousand years, the spin period increases up to values close to those observed in AXPs. In this phase, the AXP progenitors are very faint, undetectable X–ray sources, since accretion down to the neutron star surface is inhibited (or greatly reduced) by the magnetospheric centrifugal barrier. In the following phase, the spin frequency approaches the Keplerian frequency at the inner edge of the disk $\Omega(r_m)$, most of the mass flow is accreted, and the star becomes visible as an AXP. During this quasi-equilibrium phase, the neutron star spins down trying to match $\Omega(r_m)$, which decreases with the declining mass accretion rate in the disk.

Accretion from a fossil disk has also been considered by Alpar (2001) and by Marsden et al. (2001). The latter authors (see also Rothschild et al. 2002) claim that SGRs and AXPs are born in dense regions of the interstellar medium, while the core collapse supernova explosions producing normal neutron stars occur preferentially in super-bubbles of hot and tenuous gas surrounding the

OB associations. In their model, the difference in the environment, rather than intrinsic neutron star properties, are at the origin of the AXP/SGR peculiarities by favoring the disk formation. This could happen in two ways. In the first one, the dense surrounding gas confines the SN progenitor wind, thus favoring a reverse shock in the expanding remnants and the formation of a "*push-back*" disk (Truelove & McKee 1999). The other way applies in the case of a high velocity neutron star which can more easily capture part of the nearly co-moving ejecta slowed down by the prompt reverse shock expected in a dense environment.

This evidence for environmental differences in AXPs and SGRs is based on the uncertain distances and ages of SNRs and has been criticized by Duncan (2002). Furthermore, some of the associations with SNRs considered by Marsden et al. (2001) are very unlikely to be true.

4.2. Magnetar models

Magnetars are neutron stars in which the dominant source of free energy is provided by a strong magnetic field, rather than rotation (as in the ordinary radio pulsars). They are supposed to have internal fields higher, by a factor ten ore more, than the quantum critical value $B_c = \frac{m_e^2 c^3}{e\hbar} = 4.4 \times 10^{13}$ G (at $B > B_c$ the energy between the Landau levels of electrons is greater than their rest mass).

A magnetic field in this range can be produced by an efficient dynamo mechanism that operates if the neutron star is born with a very short (∼1 ms) period (Duncan & Thompson 1992). Although no direct observational evidence for such short initial periods has been found in radio pulsars or in young supernova remnants like SN 1987A, Thompson & Duncan (1995) pointed out that, in the case of the SGRs, a high magnetic field is motivated by several independent requirements (some of which are based on the energetic and spectral properties of the giant flare of 1979 March 5 from SGR 0525–66). Among the different pieces of evidence for a high B field is the magnetic confinement of the hot pair plasma responsible for the long soft tail of the flare and the reduction in photon opacity required to exceed by a factor $\gtrsim 10^3$ the Eddington limit in the soft γ-ray bursts (an argument first applied to SGR 0525–66 by Paczynski 1992). Furthermore, a strong dipole field is required to slow-down the neutron star to the presently long period (8 s) within a time ($\sim 10^4$ yrs) compatible with the age of the associated SNR.

In the magnetar model applied to the SGRs the magnetic field is the main energy source, powering both the normal bursting activity, characterized by brief (< 1 s) and relatively soft (peak photon energy ∼20-30 keV) bursts of super-Eddington luminosity, and the much more energetic flares that have so far been observed only on two occasions: on March 5, 1979 for SGR 0526-66 (Mazets et al. 1979, Cline et al. 1980), and on August 27, 1998 for SGR 1900+14 (Hurley et al. 1999b, Feroci et al. 2001). The diffusion of the magnetic field through the neutron star core causes fractures in the crust that can inject energy in the magnetosphere producing the soft γ–ray bursts, while large-scale magnetic reconnections are responsible for the exceptionally intense flares (see Thompson (2001) for an extensive review).

The discovery of P and the measurement of $\dot{P}$ in SGR 1806–20 (Kouveliotou et al. 1998) and SGR 1900+14 (Hurley et al. 1999a, Kouveliotou et al. 1999) is generally considered as a confirmation of the existence of magnetars. In fact, interpreting the spin-down as due to magnetic dipole radiation losses, the neutron star magnetic field can be derived as B $\sim 3.3\times10^{19}$ $(P\dot{P})^{1/2}$ G, yielding B $\sim 8\times10^{14}$ G and $\sim 6\times10^{14}$ G, respectively for SGR 1806–20 and SGR 1900+14. A more realistic estimate should take into account other contributions to the spin-down torque, such as a particle wind outflow (Thompson & Blaes 1998), either continuous or in the form of sporadic outbursts. Lower magnetic fields are obtained when these effects are considered (Harding et al. 1999).

As mentioned above, other arguments supporting the magnetar scenario are related to the apparent youth of the SGRs, as inferred from their association to SNRs. This is a matter of debate, since, while the SGR 0526–66 / N49 association is generally regarded as very likely, the same is not true for the other proposed associations: SGR 1806–20 / G10.0–0.3 and SGR 1900+14 / G42.8+0.6 (see Gaensler et al. 2001, Duncan 2002).

The magnetar model is very successful to reproduce those temporal and spectral properties of SGRs that are difficult to explain with alternative models like sudden accretion events (see Thompson & Duncan 1996).

The interpretation of AXPs in terms of magnetars is a fairly natural consequence of the analogies between these two classes of objects. Indeed, some similarities between the prototype AXP 1E 2259+586 and SGR 0526–66, for which pulsations at 8 s were observed during the 5 March 1979 giant flare, were immediately pointed out. AXPs and SGRs are similar for what concerns their P and $\dot{P}$ values (and consequently the B inferred from the dipole braking formula), the X-ray luminosity ($\sim 10^{34} - 10^{36}$ erg s^{-1} for SGRs in quiescence, Mereghetti et al. (2000)), and the association with SNRs (at least in some cases).

The enormous magnetic energy available in a magnetar can easily power the steady X–ray luminosity observed in AXPs. The magnetic field decay, on a timescale of $\sim 10^4$ yrs, heats the neutron star surface that emits thermal radiation in the X–ray band (Thompson & Duncan 1996). In addition, the multiple small scale fractures induced by the magnetic field on the neutron star crust produce an emission of Alfvén waves in the magnetosphere that accelerate particles and can produce non-thermal emission.

Heyl & Hernquist (1998) showed that, if B is greater than $\sim 10^{15}$ G, the residual thermal energy of the neutron star is sufficient to power for a few thousand years the observed X–ray luminosity, even without resorting to field

decay. This requires the presence of an envelope of hydrogen and helium (an iron envelope is much more efficient in insulating the core, resulting in a lower luminosity and effective temperature at the neutron star surface). The envelope of light elements, with a mass of $\sim 10^{-11}$–10^{-8} $M_\odot$, could be due to fall-back of material after the supernova explosion and/or accretion from the interstellar medium, if the neutron star were born in a sufficiently dense environment ($\gtrsim 10^4$ cm^{-3}).

Which are the predictions of the magnetar model for AXPs? In the simplest interpretation one would expect a more stable luminosity, spectrum and $\dot{P}$ noise, than in accretion-powered pulsars. The spectra and light curves expected from the surface of highly magnetized neutron stars have been computed by several authors (Özel 2001, Zane et al. 2001, Ho & Lai 2001). As described in Section 6.1, these can reproduce the salient observational properties of AXPs. No detailed predictions exist yet for what concerns the emission at other wavelengths. Accurate timing observations were, somewhat naively, thought to provide a clear discrimination in favor or against the magnetar hypothesis, but, as described in Section 6.2, the situation is not as simple. In conclusion, we believe that the AXPs could be magnetars, but we are still far from a decisive proof, and valid alternative models cannot be ruled out as easily as it has been done for the SGRs.

4.3. Other models

The momentum of inertia of a white dwarf is a factor $\sim 10^5$ larger than that of a neutron star, leading, to a rotational energy loss $\dot{E}_{rot}$ greater than the AXPs luminosity:

$$\dot{E}_{rot} = I_{wd}\Omega\dot{\Omega} \sim 4{\times}10^{37} \left(\frac{P}{10\ s}\right)^{-3} \left(\frac{\dot{P}}{10^{-11} s\ s^{-1}}\right) \mathrm{erg\ s^{-1}}$$

This led Paczynski (1990) to propose that 1E 2259+586 could be a rotation-powered, isolated white dwarf (following an earlier suggestion by Morini et al. (1988)). In order to rotate with such a short period without breaking-up, the white dwarf should have a mass greater than $\sim 1.3\ M_\odot$. Paczynski suggested that a fast spinning, highly magnetized (B$> 10^8$ G) and massive white dwarf could be the result of a recent merger of two white dwarfs. According to this model the AXPs X–ray emission could result either from non-thermal processes powered by rotational energy loss, as in young radio pulsars, or from the thermal emission of a hot white dwarf.

It is not clear whether this model, originally developed for 1E 2259+586, could account for the formation of a SNRs, since the outcome of a white dwarfs merger is highly uncertain. Another problem is that no large $\dot{P}$ variations are expected owing to the large momentum of inertia of a white dwarf.

A different scenario for AXPs (and SGRs), based on strange matter stars, has been proposed by Dar & DeRújula (2000). According to these authors the AXPs are either strange stars or quark stars in which the X–rays are powered by gravitational contraction and the spin-down is due to the emission of relativistic jets.

5. X-ray spectral properties

5.1. Phase–averaged X–ray spectra

AXPs have very soft spectra. Early data of low statistical quality were sufficiently well fit by steep power laws yielding $\alpha_{ph} \gtrsim 3$ (while single blackbody models were unable to reproduce the observed flux above a few keV). When better observations became available with *ASCA* and, especially, *BeppoSAX* (the latter extending to energies as low as 0.1 keV), it became clear that a more complex spectrum, consisting of a blackbody-like component with kT$\sim$0.5 and a steep power law (α_{ph} $\sim$3–4), is required. This spectral decomposition has become the *canonical* AXP spectrum (see the spectral parameters in Table 2), but it should be noted that equivalently good fits can be obtained, e.g., with the sum of two blackbody components (Israel et al. 2002).

It is likely that, due to current instrumental limitations, the canonical two-component model is an oversimplified description of the true underlying spectral continuum. However, it is tempting to interpret the two spectral components in terms of two distinct processes and/or emitting regions in order to infer some physical parameter. For example, the blackbody-like component can be naturally interpreted as thermal emission leading to emitting areas of the order of a few km^2. These are smaller than the whole neutron star surface, but yet much greater than the polar cap hot spots expected in case of magnetically channeled accretion.

Perna et al. (2001) showed that larger emitting areas, consistent with the dimensions of a neutron star, can be obtained with a model for the thermal emission from a light-element atmosphere with magnetic field B $\gtrsim 10^{12}$ G. Such spectra are typically harder than the corresponding blackbodies, thus giving best fits with lower temperatures and higher normalizations. Interestingly, the inclusion of a separate power law component is still required.

There are no clear correlations between the spectral parameters of the canonical model, but some spectral properties have been found to correlate with other quantities. For example, Marsden & White (2001) found that the AXPs with the highest spin-down rate have the hardest spectra, while Israel et al. (2002) noted a correlation between the blackbody contribution to the total luminosity, L_{BB}/L_{tot}, and the pulsed fraction (see Fig.1).

In interpreting correlations of this kind one should always remember that, as mentioned above, there is no compelling evidence for the actual presence of two physically distinct emitting components. In fact, as noted by Özel et al. (2001), the blackbody contribution to the flux is a

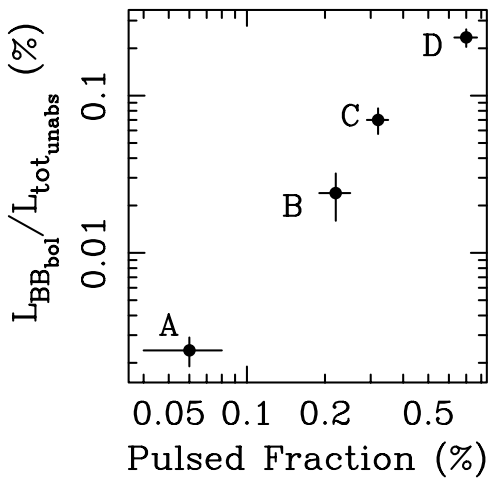


Fig. 1. Correlation between L_{BB}/L_{tot} and the pulsed fraction. L_{BB} is the bolometric luminosity of the blackbody component, L_{tot} is corrected for the absorption and refers to the 0.1–10 keV range. A=4U 0142+61, B=1E 2259+586, C=1RXS J1708−4009, D=1E 1048.1−5937 (Israel et al. 2002).

strong function of the energy, while the pulsed fraction at different energies does not change significantly. In the case of two physically distinct spectral components this would require a rather unlikely a "*ad hoc*" coupling in the pulse profiles of the blackbody and power law components.

5.2. Phase resolved X–ray spectra

Spectral variations as a function of the pulse phase are present in practically all kinds of pulsars and AXPs make no exception, as can be seen at least in some of the light curves of Fig.2 In general these variations are not large enough (or the data lack sufficient statistical quality) to be characterized as significant variations in the spectral parameters derived from the fits (see, e.g., Parmar et al. 1998, Patel et al. 2001, Israel et al. 1999a, Oosterbroek et al. 1998). The best evidence for phase-dependent spectral parameters was found in 1RXS J1708−4009, where Israel et al. (2001) measured a variation of the power law photon index from 3.1 to 1.9 across the pulse (see also Gavriil & Kaspi 2002). In contrast, 1E 1048.1−5937 shows a very energy-independent pulse profile (see Fig.2). However, a recent *XMM-Newton* observation of this source revealed that a "*soft excess*" with respect to the phase-averaged spectrum is present below ∼1.5 keV in correspondence of the pulse minimum (Tiengo et al. 2002).

5.3. Narrow spectral features

Cyclotron resonance features would provide useful diagnostics, but so far no convincing detection has been reported. The energy of the line is

$$E_{Cycl} \approx 11.6\ Z_g \left(\frac{B}{10^{12}\ G}\right)\ \mathrm{keV}$$

for electrons, and

$$E_{Cycl} \approx 0.63\ Z_g \left(\frac{B}{10^{14}\ G}\right)\ \mathrm{keV}$$

for protons, where $Z_g = \sqrt{1 - 2GM/Rc^2}$ is the gravitational redshift at the neutron star surface, typically in the range 0.7–0.85. Model atmosphere calculations (Zane et al. 2001) predict that proton cyclotron features in highly magnetized neutron stars are conspicuous (EW up to ∼ 100 eV) and relatively broad ($\Delta E/E_{Cycl} \sim 0.05$-0.2). However it is clear that the discovery of *a single* line would not permit to easily distinguish between the electron and ion case and thus establish the magnetic field strength in an unambiguous way.

Early reports of a pulse phase-dependent line in 1E 2259+586 (Koyama et al. 1989, Iwasawa et al. 1992) were not confirmed by subsequent higher quality observations. Sensitive line searches with the *XMM-Newton* and *Chandra* satellites have been performed so far only for three AXPs: Tiengo et al. (2002) reported the possible presence of an absorption line at 4.71 keV in 1E 1048.1−5937 during a short (5 ks) *XMM-Newton* observation, but more data are required to confirm this line (note that it was seen only in one of the three EPIC CCD cameras). 4U 0142+61 was observed with the *Chandra* High Energy Transmission Grating Spectrometer by Juett et al. (2002). For absorption lines in the range ∼0.7–5 keV, they reported upper limits from a few eV to a few hundred eV (depending on energy and assumed width of the line). No significant spectral features were found in the range 0.5–7 keV by Patel et al. (2001) who observed 1E 2259+586 with the *Chandra* ACIS instrument.

5.4. Long term variability

Most AXPs have been detected at flux levels consistent with a constant luminosity. However the observations were carried out with different instruments and the limits that one can infer on the absence of variability are subject to systematic uncertainties. Besides the unavoidable (model dependent) uncertainty deriving from conversions between different energy ranges, the fluxes obtained with non-imaging instruments must also be corrected for the (poorly known) contribution of other components in the field of view (e.g. SNRs, diffuse galactic ridge emission, confusing sources, etc...).

Keeping this in mind, we summarize in Table 2 all the measurements obtained with imaging instruments in the ∼ 1–10 keV range. Although small differences in the best fit spectral parameters, in particular N_H and α_{ph}, can result in large variations if one considers the *unabsorbed* luminosity in a range extending to lower energies, no strong

Table 2. Spectral parameters and fluxes of AXPs

Observation date	Satellite	Flux[(a)] (erg cm^{-2} s^{-1})	N_H (10^{22} cm^{-2})	α_{ph} / kT_{BB} (- /keV)	$R_{BB}^{(b)}$ (km)	References
1E 2259+586						
3-4 May 1993	*ASCA*	3.2×10^{-11}	0.45	3.2 / 0.42	$3d_4$	Corbet et al. (1995)
1,11 August 1995	*ASCA*	2.5×10^{-11}	0.52	3.6 / 0.41	$3.1d_4$	This work
16-17 November 1996	*SAX*	2.9×10^{-11}	0.87	3.93 / 0.44	$3.3d_4$	Parmar et al. (1998)
11 January 2000	*Chandra*	3.1×10^{-11}	0.93	3.6 / 0.41	$4.4d_4$	Patel et al. (2001)
1E 1048.1−5937						
2,7 March 1994	*ASCA*	7.0×10^{-12}	1.0	2.9 / 0.57	$0.96d_5$	Paul et al. (2000)
10-11 May 1997	*SAX*	8.3×10^{-12}	1.2	3.3 / 0.62	$0.97d_5$	Tiengo et al. (2002)
26-27 July 1998	*ASCA*	7.0×10^{-12}	1.2	3.2 / 0.56	$1.09d_5$	Paul et al. (2000)
28 December 2000	*XMM*	5.7×10^{-12}	1.0	2.9 / 0.63	$0.74d_5$	Tiengo et al. (2002)
4U 0142+61						
18-19 September 1998	*ASCA*	13.3×10^{-11}	1.10	3.84 / 0.38	$2.3d_1$	Paul et al. (2000)
3 January 1997	*SAX*	9.9×10^{-11}	1.11	3.86 / 0.42	$1.5d_1$	Israel et al. (1999a)
3 February 1998	*SAX*	9.5×10^{-11}	0.98	3.58 / 0.36	$2.1d_1$	Israel et al. (1999a)
21 August 1998	*ASCA*	11.6×10^{-11}	1.17	3.87 / 0.38	$2.2d_1$	Paul et al. (2000)
July/August 1999	*ASCA*	9.3×10^{-11}	1.04	3.92 / 0.40	$1.8d_1$	This work
23 May 2001	*Chandra*	12.1×10^{-11}	0.88	3.3 / 0.42	$2.0d_1$	Juett et al. (2002)
1RXS J1708−4009						
3 September 1996	*ASCA*	4.4×10^{-11}	1.42	2.92 / 0.41	$7.1d_8$	Sugizaki et al. (1997)
1 April 1999	*SAX*	4.5×10^{-11}	1.42	2.62 / 0.46	$6.5d_8$	Israel et al. (2001)
September 1999	*ASCA*	2.9×10^{-11}	1.49	3.1 / 0.45	$5.1d_8$	This work
1E 1841−045						
11-12 October 1993	*ASCA*	1.3×10^{-11}	2.0	3.0 / –	–	Vasisht & Gotthelf (1997)
27 March 1998	*ASCA*	1.1×10^{-11}	2.21	3.38 / –	–	This work
March/April 1999	*ASCA*	1.2×10^{-11}	2.26	3.46 / –	–	This work
AX J1845.0−0300						
12 October 1993	*ASCA*	3.9×10^{-12}	4.6	– / 0.72	$1.5d_8$	Torii et al. (1998)
12 October 1993	*ASCA*	4.3×10^{-12}	9.0	4.6 / –	–	Torii et al. (1998)
28-29 March 1999	*ASCA*	$\lesssim 4 \times 10^{-13}$	–	–	–	Vasisht et al. (2000)

[(a)] Flux in the 1-10 keV range, not corrected for the absorption
[(b)] d_n is the assumed distance in units of n kpc

variability is shown by the values of the *observed* 1-10 keV flux reported in Table 2.

Comparison with some of the data obtained before 1993 (and not reported in Table 2) requires some caution. For instance, the *EXOSAT* data of 4U 0142+61 were clearly contaminated above a few keV by the nearby pulsar RX J0146.9+6121 (Mereghetti et al. 1993); at lower energies they seem to be consistent with the values of Table 2. The flux measured with *Einstein* and *ROSAT* for 1E 1841−045 was found to be constant by Helfand et al. (1994). Several observations exist for 1E 1048.1−5937 and 1E 2259+586, and for both sources evidence for flux variations obtained by comparing data from the same instrument were reported. According to Seward et al. (1986), 1E 1048.1−5937 was at least a factor 10 fainter in December 1978 than at the time of its discovery six months later. Both observations were obtained with the IPC detector on the *Einstein* satellite, but during the first one 1E 1048.1−5937 lied very close to the edge of the field of view and was not detected. A more convincing case for long term variability is given by *GINGA* observations of 1E 2259+586 (Iwasawa et al. 1992). In the August 1990 observation the source was a factor ∼2 brighter than in previous measurements (June 1987 and December 1989). During the higher intensity state the source also showed a different pulse shape (a larger difference in the relative intensity of the two pulses), as well as a variation in the spin-down rate.

Large flux variability was seen in the AXP candidate AX J1845.0−0300. This source had a flux of 4.2×10^{-12} erg cm^{-2} s^{-1} (2-10 keV) during an *ASCA* pointing carried out in December 1993, but was not visible 3.5 years later, implying a flux decrease greater than a factor 14 (Torii et al. 1998). A further *ASCA* observation (March 1999)

revealed only a weak source ($F_x \sim 4\times 10^{-13}$ erg cm^{-2} s^{-1}) at a position consistent with that of the AXP (Vasisht et al. 2000). A search for pulsations could not be performed, due to the small number of counts, thus it is not clear whether this source is really AX J1845.0−0300 in a low state. The possible existence of transient AXPs with low quiescent luminosities has important implications for the total number of AXPs in the Galaxy and their inferred birthrate.

The level of variability in AXPs is of interest since it is expected that some emission processes (e.g. thermal emission from the neutron star surface) produce less variability than others (e.g. those involving mass accretion, which is generally subject to fluctuations). Detailed searches for correlations between luminosity and spin-down variations could provide crucial evidence in favor of accretion, whereby different mass accretion rates are expected to produce different torques on the rotating neutron star. For this reason a regular monitoring of AXPs with the *RXTE* satellite has been carried out for a few years. These observations allow to obtain phase connected timing solution (Section 6.2) and to monitor intensity changes. Unfortunately, due to the non-imaging nature of the PCA instrument and to the uncertain background intensity variations, such data provide a reliable measure only of the pulsed flux component. For 4U 0142+61, 1E 2259+586, and 1RXS J1708−4009 upper limits (1σ) of 20-30% on variations of the pulsed flux have been derived (Gavriil & Kaspi 2002). No variations have been seen in 1E 1841−045 (Gotthelf et al. 2002), while the values of pulsed flux measured in 1E 1048.1−5937 over a 4 years time span have an *rms* at a level of ∼30% of the average, suggesting that this AXP is somewhat less stable than the other ones (Kaspi et al. 2001).

6. Timing properties

6.1. Folded light curves

The folded light curves of all AXPs, derived from *ASCA* GIS data, are shown in Fig.2. They are characterized by broad pulses and rather smooth profiles. The pulsed fractions range from about 7% for 4U 0142+61 and 1E 1841−045 up to ∼70% for 1E 1048.1−5937 and do not depend much on the energy. Two sources, 1E 2259+586 and 4U 0142+61, clearly display a double-peaked profile. The light curve of 1RXS J1708−4009 can be interpreted as the sum of two pulses with different energy spectra (see also Israel et al. 2001, Gavriil & Kaspi 2002).

Large pulsed fractions are generally not expected if the radiation is emitted close to the surface of a neutron star, due to the gravitational light bending. The effect of interstellar absorption is to increase the observed pulsed fractions by preferentially absorbing the softest photons, which for a thermally emitting neutron star have a lower modulation (Page 1995, Perna et al. 2000), but it is not clear that this effect is effective enough for the temperature and N_H values typical of AXPs. According to De Deo et al. (2001), a pulsed fraction as high as that of 1E 1048.1−5937 can be obtained only in the case of a strong beaming, a requirement probably more easily provided by an accreting neutron star.

However, Özel et al. (2001) showed that models of emission from highly magnetized atmospheres can account for the AXPs pulsed fractions, provided that the emission comes from a single hot region on the neutron star surface. More recently Özel (2002) calculated the expected pulse profiles for a variety of model parameters and concluded that magnetars with a single hot emitting region give a better representation of the observations than models involving emission from two antipodal regions.

6.2. Secular spin-down and its fluctuations

The nearly steady spin-down of AXPs, in analogy with radio pulsars, immediately leads to consider their characteristic ages defined as $\tau_c = P/2\dot{P}$ (see Table 1). For a pulsar slowing down according to a braking law of the type $\dot{\nu} \propto -\nu^n$ (or equivalently $\dot{P} \propto P^{2-n}$), the characteristic age gives an upper limit on the true age for n=3. The true age, given by

$$\frac{P}{(n-1)\dot{P}}\left[1-\left(\frac{P_0}{P}\right)^{n-1}\right]$$

can be significantly smaller than τ_c if the initial period P_0 is close to P and/or if n is greater than 3.

Both 1E 1841−045 and 1E 2259+586 have τ_c greater than the ages estimated for the respective SNRs [2]. While in the first case the difference is relatively small, for 1E 2259+586, τ_c is at least ten times larger than the age of G109.1–0.1. A possibility to explain this large discrepancy is to assume that the pulsar suffered a much stronger braking in the past, before the magnetic field decayed to a currently lower value (see, e.g., Colpi et al. 2000).

In principle, the study of $\dot{P}$ fluctuations could discriminate between accretion-based and magnetar models. If accretion is at work one would expect significant $\dot{P}$ variations, possibly correlated with luminosity changes. On the other hand, the period evolution of a magnetar should be much more regular, with the possible exception of glitches, as observed in young radio pulsars (see also Melatos (1999) for magnetars $\dot{P}$ variations caused by precession driven by magnetic dipole radiation torques). Until recently the few available period measurements did not allow to discriminate against alternative possibilities (see, e.g., Baykal & Swank 1996, Heyl & Hernquist 1999). The extensive monitoring now provided by the *RXTE* satellite is producing

[2] in the proposed association between SNRs and SGRs we have the opposite situation, i.e. the τ_c values (∼1500 yrs) are smaller than the SNRs ages.

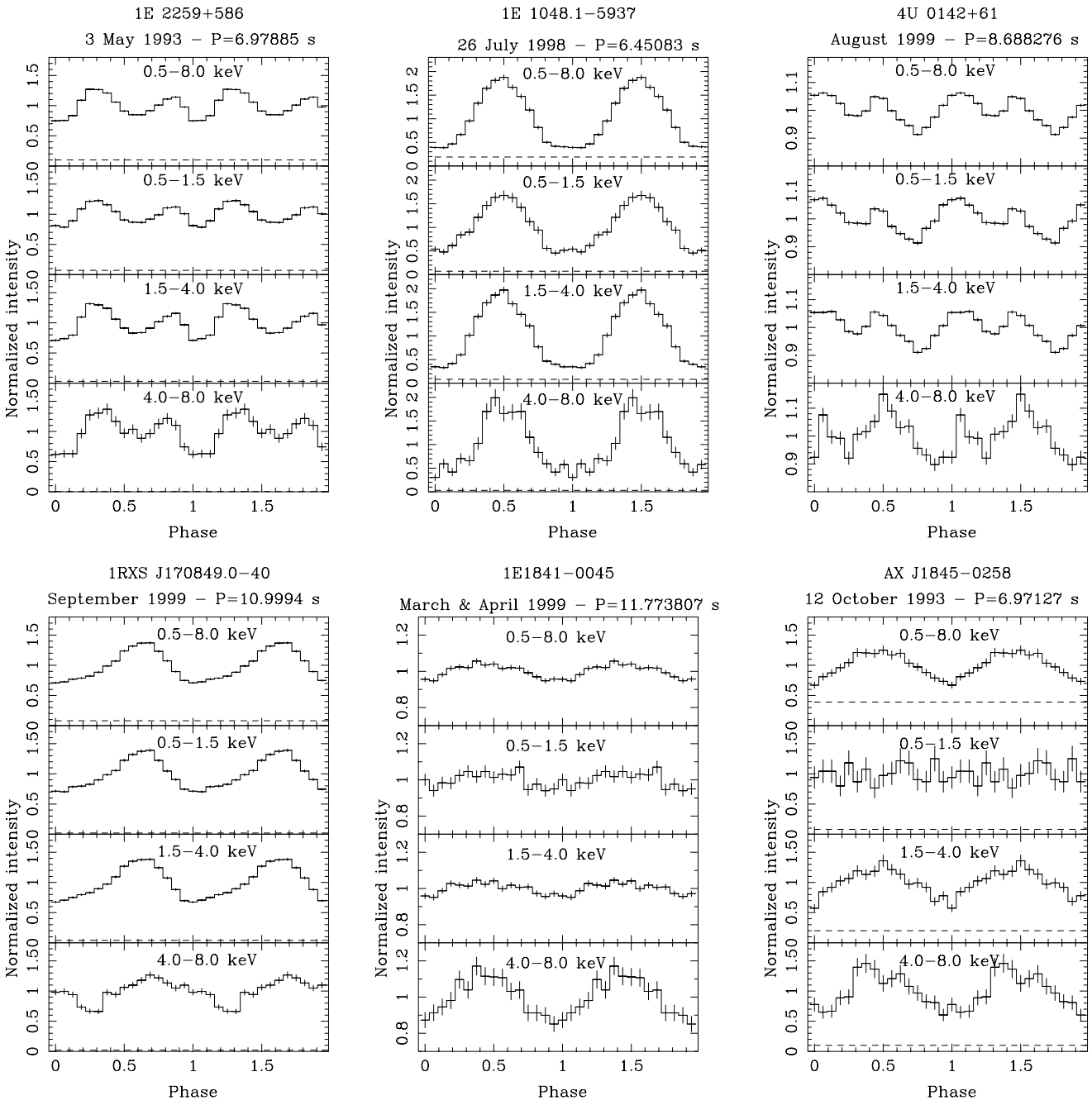


Fig. 2. Folded light curves of the AXPs obtained with the *ASCA* GIS instrument. The dashed lines indicate the level of the background.

more accurate data in which phase-connected timing solutions can be obtained. For 1E 2259+586, these data show a very low level of timing noise during the last few years (Kaspi et al. 1999), contrary to previous results that were based on sparse observations spanning ∼20 years. Also 1RXS J170849−400910 was found to have a similarly low level of timing noise. Both sources had phase residuals of only ∼1%, comparable to or smaller than those measured for most radio pulsars. A sudden spin-up event was detected in 1RXS J170849−400910 in September 1999 and interpreted as a glitch (Kaspi et al. 2000), thus reinforcing the similarity with young radio pulsars.

Another very stable rotator is 1E 1841−045 (Gotthelf et al. 2002), while 1E 1048.1−5937 is characterized by a higher level of timing noise that prevented to find a phase–coherent timing solution for time periods longer than a few months (Kaspi et al. 2001).

The interpretation of this wealth of new data is not straightforward. First, the presence of glitches cannot simply be taken as evidence for the magnetar model: they are

Table 3. Results of orbital motion searches

SOURCE	$a_x \sin i$ (light-s)	Range of P_{orb}	References
1E 2259+586	<0.03	194 s - 1.4 d	(1)
1E 2259+586	<0.07	170 s - 5000 s	(2)
1E 1048.1−5937	<0.06	200 s - 1.5 d	(1)
4U 0142+61	<0.26	70 s - 2.5 d	(3)

(1) Mereghetti et al. (1998); (2) Patel et al. (2001); (3) Wilson et al. (1999).

expected to occur in any neutron star subject to a braking effect (although their detection in accreting systems is hampered by the high level of timing noise). Second, the HMXRB pulsar 4U 1907+09 (P=440 s), which has spun–down constantly since 1983 at a rate only a factor four greater than that of 1E 2259+586, has a long–term noise strength one order of magnitude lower than 1E 2259+586 (Baykal et al. 2000). Another accreting pulsar with small timing noise is 4U 1626–67 (Chakrabarty et al. 1997).

It seems therefore that further precise timing observations and more detailed model predictions are required to distinguish between the various possibilities.

6.3. Limits on orbital motion

The most sensitive searches for orbital Doppler shifts have been carried out with *RXTE*, yielding the upper limits on the projected semi-major axis $a_x \sin i$ reported in Table 3. No sensitive searches for orbital Doppler shifts have been performed for the other AXPs. No periodic intensity variations, like eclipses or dips, that might indicate the presence of a binary system, have been detected in any AXPs.

Although the lack of detectable Doppler shifts seems to support the isolated nature of AXPs, it is worth noting that pulse arrival time delays have remained undetected also in 4U 1626–674, which is in a close binary system (P_{orb} = 42 min) with a very low–mass companion star. For any assumed inclination angle and orbital period the limits on $a_x \sin i$ constrain the possible companion mass. As discussed in Mereghetti et al. (1998), late main sequence stars are extremely unlikely, but He stars with mass $M \lesssim 0.8\ M_\odot$ and white dwarf companions cannot be excluded.

6.4. Period clustering

The clustering of the AXPs periods in the narrow range 6–12 s is remarkable, especially when compared with the large period distribution of pulsars in X–ray binaries. The absence of shorter period AXPs is not surprising given the small sample of AXPs currently known and their secular spin-down. Models, however, should be able to explain why no AXPs with longer periods are observed.

In accretion-based models, AXPs are supposed to rotate at (or close to) the equilibrium period:

$$P_{eq} \sim 2.5 B_{11}^{6/7} L_{35}^{-3/7} \quad \mathrm{s}$$

The observed period distribution and X–ray luminosities can be obtained for neutron stars with magnetic fields below the magnetar range and suitable values of the mass accretion rate (Mereghetti & Stella 1995). It is unclear why only the combination of these two parameters producing periods in the 6-12 s range should be observed. In models based on a fossil disk, in which the equilibrium period increases with the secular decline of the accretion rate, some mechanism must be invoked to turn off the AXPs at periods $\gtrsim 12$ s. Chatterjee et al. (2000) propose that an advection-dominated accretion flow ensues when the accretion rate decreases below a critical value, thus limiting the active lifetime of AXPs to $\gtrsim 5\ 10^4$ yrs.

In the context of the magnetar scenario, the period distribution can be explained if the magnetic field decays on a timescale of $\sim 10^4$ years. Models without a significant field decay would lead to the presence of AXPs with longer periods (Colpi et al. 2000).

7. Multi wavelength observations

7.1. Optical and Infrared counterparts

AXPs lie in the galactic plane, where crowding and severe interstellar absorption complicate the identification work. In the lack of localizations at the arc-second level, studies based on deep multi-color photometry and spectroscopy of the brightest candidates could only establish the high X–ray-to-optical flux ratio of AXPs, thus ruling out the presence of massive counterparts. A typical situation is shown in Fig. 3. The current observational situation is summarized in Table 4.

The recently announced discovery of optical pulsations at the X–ray period (Kern & Martin 2001) has clinched the identification of 4U 0142+61 with a faint, relatively blue object first proposed by Hulleman et al. (2000). A promising candidate has also been found for 1E 2259+586, while only upper limits have been derived for the other objects. These upper limits are less constraining in the AXPs with the highest absorption, such as 1E 1841−045 and 1RXS J170849−400910. Much progress in the identification process is expected in the next few years thanks to the more accurate positions that are becoming available with the *Chandra* satellite.

Both for 4U 0142+61 and the proposed near IR counterpart of 1E 2259+586 the optical/IR flux is higher than an extrapolation of the blackbody like component of the X–ray spectrum, clearly indicating the need for a different origin. An extended accretion disk around an isolated neutron star would probably produce too much optical and IR emission compared to the observed fluxes (Hulleman et al. 2000, Perna et al. 2000). However, these predictions

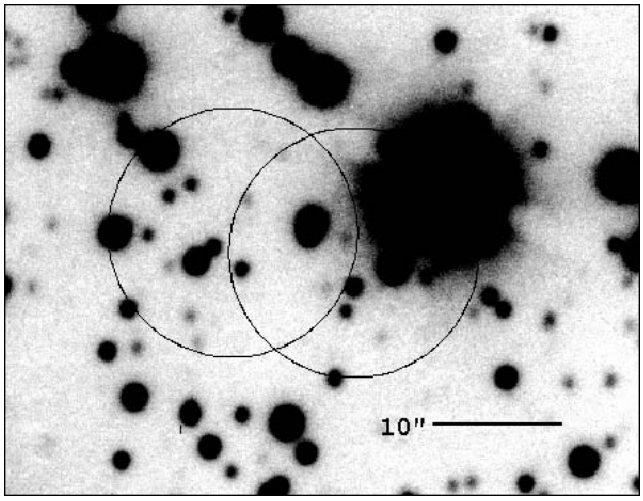


Fig. 3. R band image of the field of 1RXS J1708−4009. The two circles indicate the error regions obtained in two *ROSAT* observations.

Table 5. Upper limits on radio emission at 1.4 GHz

SOURCE	5σ u.l. (mJy)	References
1E 2259+586	0.083	Coe et al. (1994)
1E 1048.1−5937	0.07[(a)]	Israel et al. (2002)
	0.13[(a)]	Crawford et al. (2002)
4U 0142+61	0.27	Gaensler et al. (2001)
1RXS J1708−4009	3	Gaensler et al. (2001)
	0.07[(a)]	Israel et al. (2002)
	0.22[(a)]	Crawford et al. (2002)
1E 1841−045	0.6	Kriss et al. (1985)
	0.07[(a)]	Israel et al. (2002)
	0.25[(a)]	Crawford et al. (2002)
AX J1845.0−0300	0.07[(a)]	Israel et al. (2002)
	0.13[(a)]	Crawford et al. (2002)

[(a)] search for pulsed emission

depend on several very uncertain parameters (e.g. the inclination angle, the inner and outer radius of the disk) and it is not possible to definitely rule out the possibility of accretion, based on current data. The data recently reported by Hulleman (2002) on the flux in the K and B bands for 4U 0142+61 further complicate the interpretation of the optical/IR emission: the K band flux lies above the extrapolation of the shorter wavelength points, while in B only a very tight upper limit has been obtained, implying a spectral turn over.

7.2. (Lack of ?) radio emission

A few searches for radio emission from AXPs have been carried out, some of which concentrated on revealing radio pulsations at the X–ray period. All of them gave negative results. We summarize the upper limits in Table 5. The lack of radio emission is not unexpected if AXPs are powered by accretion; different explanations have been put forward in the context of the magnetar model. An obvious possibility is to invoke an unfavorable beaming angle, also considering that radio pulsars show an anti-correlation between the beam width and the rotation period. Another explanation might be related to the fact that in a high magnetic field ($B \gtrsim 10^{14}$ G) the process of photon splitting becomes competitive with pair creation, thus suppressing the magnetospheric cascades that are at the origin of the radio emission (Baring & Harding 1998, 2001). Gaensler et al. (2001) pointed out, however, that the current upper limits are not very constraining: many radio pulsars have 400 MHz luminosities below those inferred from the AXPs upper limits.

8. Relations with other classes of neutron stars and evolution

8.1. Association with Supernova Remnants

Gaensler et al. (2001) have critically reexamined the evidence for SNRs associated to AXPs and SGRs, concluding that 1E 2259+586 and 1E 1841−045 are indeed the most convincing associations. These sources are located very close to the center of the two well studied shell-like SNRs G109.1–0.1 (CTB 109) and Kes 73 (G27.4+0.0). There is no need to invoke large velocity neutron stars, as in the case of SGRs. For the same reasons also the association between AX J1845.0−0300 and G29.6+0.1, although these objects have not been studied in detail, is quite convincing.

The presence of these SNRs is a very strong argument in favor of an age smaller than a few $\times 10^4$ years for the AXPs. This conclusion is not contradicted by the apparent absence of a SNR around 4U 0142+61 and 1E 1048.1−5937, since several radio pulsars with characteristic ages smaller than $\sim 10^4$ years do not have associated remnants.

8.2. Soft Gamma-ray Repeaters

Having mentioned the similarities between AXPs and SGRs (Section 4.2) we concentrate here on some important differences between these two classes. Quiescent SGRs have rather hard X–ray spectra, that, when fitted with power laws, give photon index $\alpha_{ph} \sim 2$ (see, e.g., Mereghetti et al. 2000). Woods et al. (1999) found that the addition of a blackbody component with kT_{BB}=0.5 keV resulted in a better fit to the X–ray spectrum of SGR 1900+14. Such a component was required only during an

Table 4. Positions and optical counterparts

SOURCE and references	Coordinates (J2000)	Galactic Coordinates	Uncertainty	Optical	Comments
1E 2259+586 (1)	23 01 08.295 +58 52 44.45	109.1 – 0.10	0.6″ *Chandra*	K=21.7±0.2 , R>26.4, I>25.6, J>23.8	Possible IR counterpart at the *Chandra* position
1E 1048.1−5937 (2,3,4)	10 50 06.3 – 59 53 17	288.3 – 0.52	4″ *XMM-Newton*	V>22	No stars with peculiar colors in the error region
4U 0142+61 (5,6,7)	01 46 22.41 +61 45 03.2	129.4 – 0.43	– optical	V=25.6, R=25 I=23.8, K=19.6	Pulsed optical counterpart
1RXS J1708−4009 (8)	17 08 47.24 – 40 08 50.7	346.5 +0.04	10″ Rosat HRI '97	R $\gtrsim$ 18.2	Several stars with R $\gtrsim$ 18 in error region. None has
	17 08 46.52 – 40 08 52.5		10″ Rosat HRI '93		peculiar colors
1E 1841−045 (9,10)	18 41 19.0 – 04 56 08.9	27.4 – 0.005	3″ *Einstein* HRI	R $\gtrsim$ 19	Several very reddened stars in error region. Early
(11)	18 41 19.2 – 04 56 12.5		3″ Rosat HRI		types cannot be excluded if $A_v \gtrsim 8$
AX J1845.0−0300 (12)	18 44 57 – 03 00	29.5 +0.07	120″ *ASCA*		No published optical observations
(13)	18 44 53 – 02 56 40		20″ *ASCA*		Position of AX J184453-025640, a faint source in the error box of the pulsar

(1) Hulleman et al. (2001); (2) Tiengo et al. (2002); (3) Mereghetti et al. (1992); (4) Wang & Chakrabarty (2002); (5) Hulleman et al. (2000); (6) Kern & Martin (2001); (7) Hulleman (2002); (8) Israel et al. (1999b); (9) Kriss et al. (1985); (10) Mereghetti et al. (2001); (11) Helfand et al. (1994); (12) Torii et al. (1998); (13) Vasisht et al. (2000).

observation in which no bursting activity was present, thus supporting the interpretation of AXPs as inactive SGRs. We note however that the blackbody plus power law spectrum of SGR 1900+14 was still harder than the typical AXP spectrum (see Fig.4).

SGRs also differ from AXPs for what concerns their location with respect to the (possibly) associated SNRs, which requires large transverse velocities ($\sim$1000 km s^{-1}). This might imply that AXPs evolve into SGRs as they age and move away from the SNR centre (Gaensler et al. 2001). A difference of 10–100 kyr in the age of AXPs and SGRs would be required in this case, thus making it difficult to explain the similarity of periods in the light of the observed period derivatives.

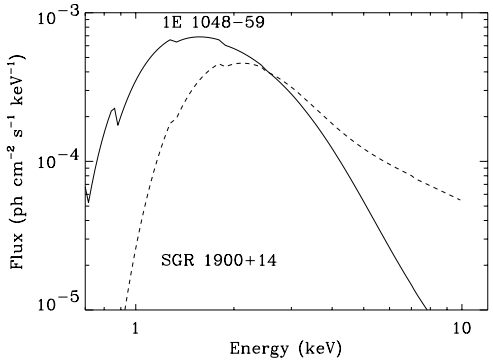


Fig. 4. Comparison of model X–ray spectra for an AXP (solid line, 1E 1048.1−5937, Tiengo et al. (2002)) and a SGR (dashed line, SGR 1900+14, Woods et al. (1999)). 1E 1048.1−5937 is the AXP with the hardest spectrum.

8.3. Compact central objects in SNRs

We list in Table 6 a few X–ray sources that are located within SNRs and have not been detected as radio pulsars. These sources, recently named Compact Central Objects (CCOs, see Pavlov et al. 2002a, for a review), have some similarities with AXPs. It is very likely that all the CCOs are young neutron stars, as indeed confirmed for the ones from which pulsations have been detected. They have soft thermal spectra with temperatures similar to those of the blackbody components of AXPs, but their luminosity is on average smaller (see Fig.5). More sensitive searches for pulsations might lead to classify some of the CCOs as new AXPs (this is certainly not the case for the CCO in G296.5+10.0 which has a short period).

Similar to AXPs, the CCOs have a rather constant X–ray flux, with the interesting exception of 1E 1614–5055, the CCO in RCW 103 (Gotthelf et al. 1999, Garmire et al. 2000). This source, together with AX J1845.0−0300,

Table 6. Other sources possibly related to AXPs

Soft Gamma-ray Repeaters						
SOURCE	P (s)	$\dot{P}$ (s s^{-1})	L$_x$ (erg s^{-1})	α_{ph}	d (kpc)	Comments and references
SGR 0525–66	8.1	–	$\sim 10^{36}$	2	55	in N49 in LMC (1)
SGR 1806–20	7.45	$\sim 8.3\times10^{-11}$	$\sim 4\times10^{35}$	1.95–2.25	15	(1,4,5)
SGR 1900+14	5.16	$\sim 6.1\times10^{-11}$	$\sim 2-8\times10^{34}$	1.9–2.2	5	(1,6,7)
SGR 1627–41	–	–	$\sim 10^{35}$	2.5	11	(1,8)
Compact Central Objects in SNRs						
SOURCE	P (s)	$\dot{P}$ (s s^{-1})	L$_x$ (erg s^{-1})	kT$_{BB}$ (keV)	d (kpc)	Comments and references
RX J0822–4300	–	–	4.7×10^{33}	0.38	2	in Puppis A (2,9,10)
AX J0851.9–4617.4	–	–	9.1×10^{32}	0.4	2	in G266.1-1.2 (2,11,12)
1E 1207.4–5209	0.424	$(2^{+1.1}_{-1.3})\times10^{-14}$	9.5×10^{32}	0.27	2.1	in G296.5+10 (2,13,14)
1E 161348–5055.1	–	–	$(2.1-100)\times10^{33}$	0.6	3.3	in RCW 103 (2,15)
CXO J232327.8+584842	–	–	3.4×10^{33}	0.7	3.4	in Cas A (2,16,17,18)
Dim Thermal Neutron Stars						
RX J0420.0–5022	22.69	–	2.7×10^{30}	0.057	0.1	(3,19)
RX J0720.4–3125	8.39	$(3-6)\times10^{-14}$	2.6×10^{31}	0.079	0.1	(3,20,21)
RX J0806.4–4123	–	–	5.7×10^{30}	0.078	0.1	(3)
RX J1308.8+2127	5.16	$(1.35\pm0.7)\times10^{-11}$	5.1×10^{30}	0.118	0.1	RBS 1223 (3,22,23)
RX J1605.3+3249	–	–	1.1×10^{31}	0.092	0.1	RBS 1556 (3,24)
RX J1836.2+5925	–	–	5.4×10^{30}	0.043	0.4	(25)
RX J1856.5–3754	–	–	1.5×10^{31}	0.057	0.117	(3,26,27)
1RXS J214303.7+065419	–	–	1.1×10^{31}	0.090	0.1	RBS 1774 (28)

(1) Hurley (2000); (2) Pavlov et al. (2002a); (3) Treves et al. (2000); (4) Mereghetti et al. (2000); (5) Kouveliotou et al. (1998); (6) Feroci et al. (2001); (7) Hurley et al. (1999a); (8) Hurley et al. (2000); (9) Petre et al. (1996); (10) Zavlin et al. (1999); (11) Pavlov et al. (2001); (12) Mereghetti (2001); (13) Mereghetti et al. (1996); (14) Pavlov et al. (2002b); (15) Gotthelf et al. (1999) (16) Murray et al. (2002); (17) Chakrabarty et al. (2001); (18) Mereghetti et al. (2002); (19) Haberl et al. (1999); (20) Haberl et al. (1997); (21) Zane et al. (2002); (22) Schwope et al. (1999); (23) Hambaryan et al. (2002); (24) Motch et al. (1999); (25) Mirabal & Halpern (2001); (26) Pons et al. (2002); (27) Walter & Lattimer (2002); (28) Zampieri et al. (2001).

might represent an object with intermediate properties between AXPs and CCOs.

8.4. Dim thermal neutron stars

Another class of neutron stars possibly related to the AXPs are the so called Dim Thermal Neutron Stars (DTNs) discovered as very soft X–ray sources with the ROSAT satellite (for a review see Treves et al. 2000). Pulsations with periods similar to (or slightly longer than) those of AXPs have been detected in four of these sources. This confirms their neutron star nature already suggested by their very high X–ray to optical flux ratio. As shown in Fig. 5, DTNs have softer spectra and lower luminosity than the CCOs and AXPs. Their small distance also implies that they are a much more numerous and probably older population. They are not associated with SNRs. Both accretion from the ISM and internal cooling have been considered to explain their X–ray emission.

Alpar (2001) proposed a unified scenario in which the DTNs, AXPs and CCOs are all interpreted as neutron stars with ordinary magnetic fields (10^{11}-10^{13} G). According to Alpar (2001), isolated neutron stars experience a mass inflow due to the formation of a residual accretion disk from fallback material after the supernova explosion. This causes an evolutionary phase in the propeller regime, before the neutron star turns on as a radio pulsar or as an AXP, depending on the initial rotational period, magnetic field and mass in the residual disk (see also Chatterjee et al. 2000 for a similar model). The DTNs in the lower left corner of Fig.5 are interpreted as examples of sources in the propeller regime, in which the X–ray emission is from cooling powered by internal friction. The CCOs would be the propeller objects with the highest mass inflow. According to this model they are surrounded by an optically thick corona and might evolve into AXPs (Alpar 2001).

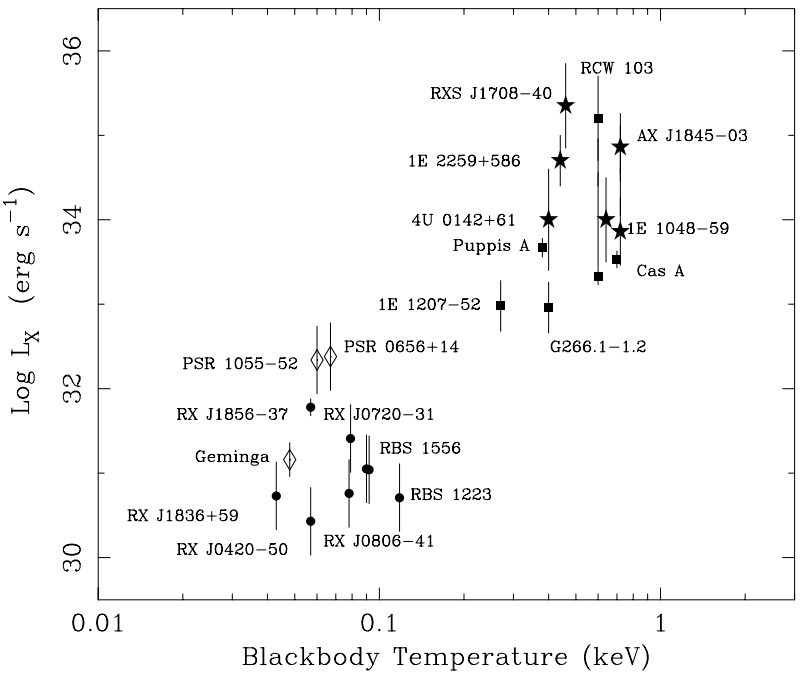


Fig. 5. "Color-Magnitude" diagram for different classes of neutron stars: AXPs (stars), CCOs in supernova remnants (squares), and DTNs (circles). For comparison also a few radio pulsars with thermal X–ray emission are shown (diamonds). For the luminosity of AXPs and radio pulsars only the thermal spectral component has been considered. To facilitate the comparison across different objects we plotted the temperatures inferred from pure blackbody fits; the use of atmospheric models would move all the points to lower temperatures by a factor ∼2-3. The luminosity error bars reflect the distance uncertainties. The two positions for the CCO in RCW 103 and for AX J1845.0−0300 indicate the observed variability range.

9. Conclusions

AXPs are one of the most enigmatic classes of galactic X–ray sources. Although the absence of a massive companion and presence of a neutron star are observationally well established, the current data are unable to discriminate between some of the most promising models which have been proposed for these sources.

The fact that these models involve very peculiar objects, the existence of which is inferred from theoretical considerations, but not yet supported by compelling observational data, is what makes the study of AXPs so exciting.

Much progress is expected in the next few years as deeper optical/IR and radio observations will be carried out, together with more detailed studies with the *Chandra*, *XMM-Newton* and *RXTE* satellites. The X–ray data gathered in the last few years are starting to reveal subtle differences among different AXPs. These might provide crucial information to possibly relate AXPs with other classes of sources such as those mentioned in Section 8, in view of an overall understanding of all the different manifestation of neutron stars.

References

Alpar M.A. 2001, ApJ 554, 1245.
Baring M.G. & Harding A.K. 1998, ApJ 507, L55.
Baring M.G. & Harding A.K. 2001, ApJ 547, 929.
Baykal A. & Swank J.H. 1996, ApJ 460, 470.
Baykal A. et al. 2000, MNRAS 319, 205.
Chakrabarty D. et al. 1997, ApJ 474, 414.
Chakrabarty D. et al. 2001, ApJ 548, 800.
Chatterjee P., Hernquist L., & Narayan R. 2000, ApJ 534, 373.
Cline T.L. et al. 1980, ApJ 237, L1.
Coe M.J., Jones L.R., & Letho H. 1994, MNRAS 270, 178.
Colpi M., Geppert U., & Page D., 2000, ApJ 529, L29.
Corbet R.H.D, Smale A.P., Ozaki M. et al. 1995, ApJ 443, 786.
Crawford F., Pivovaroff M.J., Kaspi V.M. & Manchester R.N. 2002, in *Neutron Stars in Supernova Remnants*, ASP Conference Series, P.O. Slane & B.M. Gaensler, eds., in press
Dar A. & DeRújula A. 2000, Results and Perspectives in Particle Physics, M. Greco ed., Vol. XVII, 13.
De Deo S., Psaltis D. & Narayan R. 2001, ApJ 559, 346.
Duncan R.C. & Thompson C. 1992, ApJ 392, L9.
Duncan R.C. 2002, in Proc. Miniworkshop on Soft Gamma Repeaters and Anomalous X-ray Pulsars, Rome, October 2000, eds. M.Feroci & S.Mereghetti, Mem. S.A.It., in press.
Fahlman G.G. & Gregory, P.C. 1981, Nature 293, 202.
Feroci M. et al. 2001, ApJ 549, 1021.
Gaensler B.M. et al. 2001, ApJ 559, 963.
Garmire G. et al. 2000, AAS HEAD Meeting 32, 32.11.
Gavriil F.P. & Kaspi V.M. 2002, ApJ 567, 1067.
Ghosh P., Angelini L. & White N.E. 1997, ApJ 478, 713.
Gotthelf E.V., Petre R. & Vasisht G. 1999, ApJ 514, L107.
Gotthelf E.V. et al. 2002, ApJ 564, L31.
Haberl F. et al. 1997, A&A 326, 662.
Haberl F. et al. 1999, A&A 351, L53.

Hambaryan V. et al. 2002, A&A 381, 98.
Harding A.K. et al. 1999, ApJ 525, L125.
Helfand D. et al. 1994, ApJ 434, 627.
Heyl J.S. & Hernquist L. 1997, ApJ 489, L67.
Heyl J.S. & Hernquist L. 1999, MNRAS 304, L37.
Ho W.C.G. & Lai D. 2001, MNRAS 327,1081.
Hulleman F. et al. 2000, Nature 408, 689.
Hulleman F. et al. 2001, ApJ 563, L49.
Hulleman F. 2002, in *Neutron Stars in Supernova Remnants*, ASP Conference Series, P.O. Slane & B.M. Gaensler, eds., in press
Hurley K. 2000, Proceedings 5th Huntsville GRB Symposium, AIP Conf. Series 526, 763.
Hurley K. et al. 1999a, ApJ 510, L111.
Hurley K. et al. 1999b, ApJ 510, L107.
Hurley K. et al. 2000, ApJ 528, L21.
Israel G.L., Mereghetti, S., Stella L. 1994, ApJ 433, L25.
Israel G.L. et al. 1999a, A&A 346, 929.
Israel G.L. et al. 1999b, ApJ 518, L107.
Israel G.L. et al. 2001, ApJ 560, L65.
Israel G.L., Mereghetti S. & Stella L. 2002, in Proc. Miniworkshop on Soft Gamma Repeaters and Anomalous X-ray Pulsars, Rome, October 2000, eds. M.Feroci & S.Mereghetti, Mem. S.A.It., in press, astro-ph/0111093
Iwasawa K., Koyama, K., & Halpern, J.P. 1992, PASJ, 44, 9.
Juett A.M. et al. 2002, ApJ 568, L31.
Kaspi V.M., Chakrabarty D. & Steinberger J. 1999, ApJ 525, L33.
Kaspi V.M., Lackey J.R. & Chakrabarty D. 2000, ApJ 537, L31.
Kaspi V.M. et al. 2001, ApJ 558, 253.
Kern B. & Martin C. 2001, IAU Circ. n. 7769.
Kouveliotou C. et al. 1998, Nature 393, 235.
Kouveliotou C. et al. 1999, ApJ 510, L115.
Koyama K., Hoshi R. & Nagase F. 1987, PASJ 39, 801.
Koyama K. et al. 1989, PASJ 41, 461.
Kriss G.A. et al. 1985, ApJ 288, 703.
Marsden D. & White N.E. 2001, ApJ 551, L155.
Marsden D. et al. 2001, ApJ 550, 397.
Mazets E.P. et al. 1979, Nature 282, 587.
Melatos A. 1999, ApJ 519, L77.
Mereghetti S. et al. 1992, A&A 263, 172.
Mereghetti S., Stella, L. & De Nile, F. 1993, A&A 278, L23.
Mereghetti S. & Stella L. 1995, ApJ 442, L17.
Mereghetti S., Bignami G.F. & Caraveo P.A. 1996, ApJ 464, 842.
Mereghetti S., Belloni T. & Nasuti F. 1997, A&A 321, 835.
Mereghetti S., Israel G.L. & Stella L. 1998, MNRAS 296, 689.
Mereghetti S. et al. 2000, A&A 361, 240.
Mereghetti S. 2001, ApJ 548, L213.
Mereghetti S. et al. 2001, MNRAS 321, 143.
Mereghetti S., Tiengo A. & Israel G.L. 2002, ApJ 569, 275.
Mirabal N. & Halpern J.P. 2001, ApJ 547, L137.
Morini M. et al. 1988, ApJ 333, 777.
Motch C. et al. 1999, A&A 351, 177.
Murray S.S. et al. 2002, ApJ 566, 1039.
Oosterbroek T., Parmar A.N., Mereghetti S. & Israel G.L. 1998, A&A 334, 925.
Özel F. 2001, ApJ 563, 276.
Özel F. 2002, submitted to ApJ astro-ph/0201158.
Özel F., Psaltis D. & Kaspi V.M. 2001, ApJ 563, 255.
Paczynski B. 1990, ApJ 365, L9.
Paczynski B. 1992, Acta Astronomica 42, 145.
Page D. 1995, ApJ 442, 273.
Parmar A. et al. 1998, A&A 330, 175.
Patel S.K. et al. 2001, ApJ 563, L48.
Paul B., Kawasaki T., Dotani T. & Nagasake F. 2000, ApJ 537, 319.
Pavlov G.G. et al. 2001, ApJ 559, L131.
Pavlov G.G., Sanwal D., Garmire G.P. & Zavlin V.E. 2002a, in *Neutron Stars in Supernova Remnants*, ASP Conf. Series, P.O.Slane & B.M.Gaensler eds., in press, astro-ph/0112322
Pavlov G.G. et al. 2002b, ApJ 569, L95.
Perna R., Hernquist L. & Narayan R. 2000, ApJ 541, 344.
Perna R., Heyl J., Hernquist L., Juett A. & Chakrabarty D. 2001, ApJ 557, 18.
Petre R., Becker C.M. & Winkler P.F. 1996, ApJ 465, L43.
Pons J.A. et al. 2002, ApJ 564, 981.
Rothschild R.E., Marsden D. & Lingenfelter R.E. 2002, in Proc. Miniworkshop on Soft Gamma Repeaters and Anomalous X-ray Pulsars, Rome, October 2000, eds. M.Feroci & S.Mereghetti, Mem. S.A.It., in press
Schwentker O. 1994, A&A 286, L47.
Schwope A.D. et al. 1999, A&A 341, L51.
Seward F., Charles, P.A., Smale, A.P. 1986, ApJ 305, 814.
Sugizaki M. et al. 1997, PASJ, 49, L25.
Thompson C. & Blaes O. 1998, Phys. Rev. D 57, 3219.
Thompson C. & Duncan R.C. 1995, MNRAS 275, 255.
Thompson C. & Duncan R.C. 1996, ApJ 473, 322.
Thompson C. 2001, in *The Neutron Star – Black Hole Connection*, NATO Science Series C Vol.567, 369.
Thorne K.S. & Zytkow A.N. 1977, ApJ 212, 832.
Tiengo A., Göhler E., Staubert R. & Mereghetti S. 2002, A&A 383, 182.
Torii K. et al. 1998, ApJ 503, 843.
Treves A., Turolla R., Zane S. & Colpi M. 2000, PASP 112, 297.
Truelove J.K. & McKee C.F. 1999, ApJS 120, 299.
van Paradijs J., Taam R.E. & van den Heuvel E.P.J. 1995, A&A 299, L41.
Vasisht G. & Gotthelf E.V. 1997, ApJ 486, L129.
Vasisht G. et al. 2000, ApJ 542, L49.
Walter F.M. & Lattimer J.M. 2002, astro-ph/0204199.
Wang Z. & Chakrabarty D. 2002, in *Neutron Stars in Supernova Remnants*, ASP Conference Series, P.O. Slane & B.M. Gaensler, eds., in press
Wilson C.A. et al. 1999, ApJ 513, 464.
Woods P.M. et al. 1999, ApJ 518, L103.
Zane S., Turolla R., Sella L. & Treves A. 2001, ApJ 560, 384.
Zane S. et al. 2002, MNRAS in press, astro-ph/0203105.
Zampieri L. et al. 2001, A&A 378, L5.
Zaviln V.E., Trümper J. & Pavlov G.G. 1999, ApJ 525, 959.

Proceedings of the 270. WE-Heraeus Seminar on: *"Neutron Stars, Pulsars and Supernova Remnants"*
Physikzentrum Bad Honnef, Germany, Jan. 21-25, 2002, eds. W. Becker, H.Lesch & J. Trümper, MPE Report 278, pp. 44- 53

Why study pulsars optically?

A. Shearer[1], **A. Golden**[1]

Computational Astrophysical Laboratory, National University of Ireland, Galway, Ireland

Abstract. Observations of the five confirmed optical pulsars indicate that the peak emission scales according to the magnetic field strength at the light cylinder. To the accuracy that such low number allows we show that this gives gives further confirmation that a straightforward synchrotron model such as Pacini & Salvati (1987) still has validity. The derived relationships indicates that the emission mechanism is common across all of the pulsars and towards the edge of the light cylinder. In the future observations should include near and far infra red work to determine the long wave self absorption cut-off and polarization observations of all pulsars to restrict (to first order) emission zone geometry

1. Introduction

Since the first optical observations of the Crab pulsar in the late 1960s (Cocke et al (1969) only four more pulsars have been seen to pulsate optically (PSR B0540-69; Middleditch & Pennypacker(1985); Vela: Wallace et al (1977); B0656+14; Shearer et al (1997); Geminga; Shearer et al (1998)). Four of these five pulsars are probably too distant to have any detectable optical thermal emission using currently available technologies. For the fifth (and faintest) pulsar, PSR 0633+17, spectroscopic studies have shown the emission to be predominantly non-thermal (Martin et al (1998)). With these objects we are therefore seeing non-thermal emission, presumably from interactions between the pulsar's magnetic field and a stream of charged particles from the neutron star's surface. Many suggestions have been made concerning the optical emission process for these young and middle-aged pulsars. Despite many years of detailed theoretical studies and more recently limited numerical simulations, no convincing models have been derived which explain all of the high energy properties. There are similar problems in the radio but as the emission mechanism is radically different (being coherent) only the high energy emission will be considered here. However, the most successful analytical model (both in terms of its simplicity and longevity) has been proposed by Pacini (1971) and in modified form by Pacini and Salvati (1983; PS83, 1987; PS87). In general the model proposed that the high energy emission comes from relativistic electrons radiating via synchrotron processes in the outer regions of the magnetosphere, and that the location and approximate dimensions of this emission region scales with the magnetic field in the vicinity of the light cylinder. In this paper we examine the validity of their approach and show that it adequately explains the observed phenomena.

In recent years a number of groups have carried out detailed simulations of the various high-energy emission processes. These models divide into two broad groups - between acceleration and emission low in the magnetosphere (Polar Cap models Daugherty & Harding 1996) and those with the acceleration nearer to the light cylinder (Outer-Gap models Cheng et al (2000) and refs therein). Both models have problems explaining the observed features of the limited selection of high energy emitters. However both models suffer from arbitrary assumptions in terms of the sustainability of the outer-gap and the orientation of the pulsar's magnetic field to both the observers line of sight and the rotation axis. Furthermore some observational evidence, see for example Eikenberry & Fazio (1997), severely limits the applicability of the outer-gap to the emission from the Crab pulsar. However they have their successes - the total polar-cap emission can be understood in terms of the Goldreich and Julian current from in or around the cap; the Crab polarization sweep is accurately produced by an outer-gap variant Romani & Yadigaroglu (1995). Until we have more detailed observations - and in the optical all aspects of the radiation can be measured (intensity, timing, energy and polarization) - on more objects the situation will not improve.

It is the failure of the detailed models to explain the high energy emission that has prompted this work. We have taken a phenomenological approach to test whether Pacini type scaling is still applicable. Our approach has been to try and restrict the effects of geometry by taking the peak luminosity as a scaling parameter rather than the

Table 1. Observed fluxes from the observed optical pulsars in B and scaled to the VLT. Note the sky background is of the order 1300 photons/sec/arcsec^2 for the VLT.

Name	Int. Flux (m_B)	Int. Flux ph/sec/VLT
Crab	17	90,000
PSR 0540-69	23	370
Vela	24	150
Geminga	25.5	37
PSR 0656+14	26	23
(PSR 1509-58	25.7	30)

Table 2. Observed fluxes from the observed thermally emitting pulsars in B and scaled to the VLT. Note the sky background is of the order 1300 photons/sec/arcsec^2 for the VLT.

Name	Int. Flux (m_B)	Int. Flux ph/sec/VLT
PSR 1929+10	>26.2	<20
PSR 0950+08	27.2	7
RXJ 1856.5-37.54	25.5	36
PSR 0656+14	>26.8	<14
Geminga	>27	<10
PSR B1055-52	24.9 (U)	≈50

total luminosity. In this regard we are removing the duty cycle term from PS87. It is our opinion that to first order the peak emission represents the local power density along the observer's line of site and hence reflects more accurately the emission process within the pulsar's magnetosphere. Previous work in this area (see for example Goldoni et al (1995)) looked at the total efficiency, spectral index and found no reasonable correlation with standard pulsar parameters - age, period and spin down rate. Their work was hampered by not including geometry and being restricted to the then three known pulsed emitters. Since then the number of optical pulsars has increased to five. However we are still dealing with very weak statistics in all cases bar that of the Crab pulsar.

2. Current Observations - An Overview

2.1. Introduction

The three brightest pulsars (Crab, Vela and PSR B0540-69) are also amongst the youngest. Tables 1 and 2 show the current observed limitations of optical pulsars. Only the Crab is sufficiently bright for individual pulse work to be performed. For the faintest objects very high throughput instruments (including polarimetry) are needed to do more than simple photometry.

Table 4 shows the basic parameters for these objects. However all these pulsars have very different pulse shapes resulting in a very different ratio between the integrated flux and the peak flux. Table 4 also shows this peak emission (taken as the emission in 95% - 95% portion of the largest peak). Their distances imply that the thermal emission should be low (in all cases < 1% of the observed emission). One observational note the Crab is by far the brightest optical by a factor of 250:1. Only the Crab is bright enough for individual pulse work - of all Stokes' parameters. Furthermore it is the only one for which Stokes' parameters can be accurately measured throughout the pulsar's rotation period.

2.2. The Gold Standard - the Crab pulsar

The Crab pulsar's phase plot is well known - see Figure 1 for R/I (6000-8500 Å) measurements taken with an avalanche photo-diode (APD) on the WHT over 3 nights of observation. Figure 2 shows the peak region indicating the very small plateau. Figure 3 shows 2-d time resolved V band MAMA data - in particular we note emission during the 'off pulse' region (phase 0.77-0.84). This is discussed in more detail below.

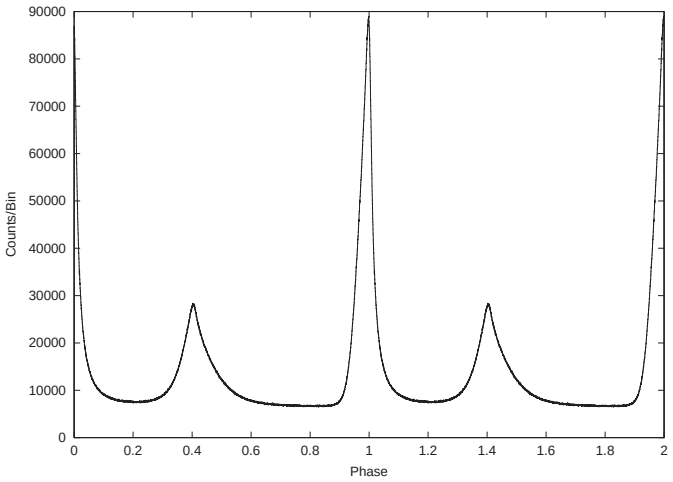


Fig. 1. Crab pulse profile in R and I with 3000 phase bins taken in November 1999 using an APD in the TRIFFID photometer

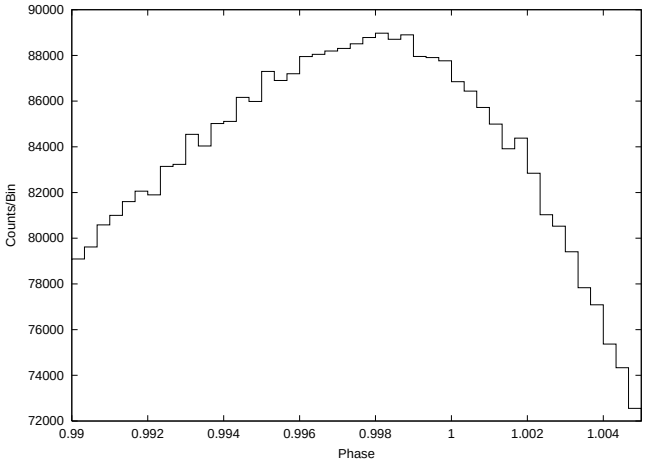


Fig. 2. The peak of the Crab pulse (from the same data set as Figure 1 showing the small or non-existent plateau

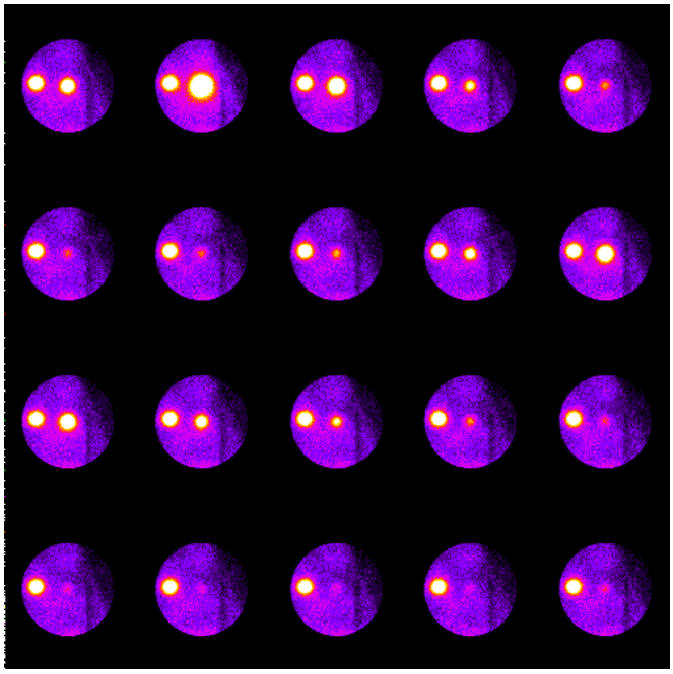


Fig. 3. Phase resolved images taken over three nights using a 2-d MAMA camera in B on the Russian 6m telescope.

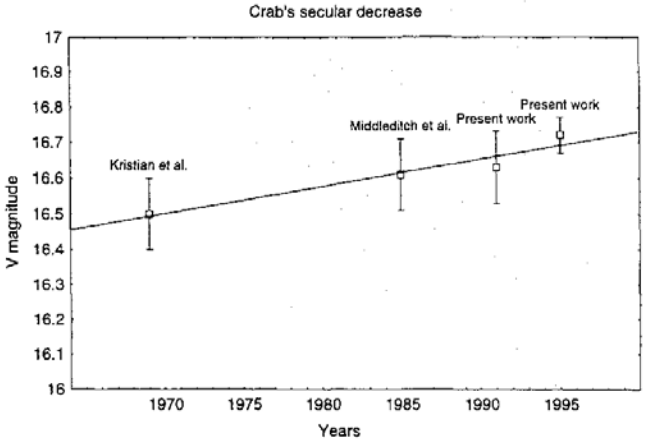


Fig. 4. Secular change on Crab luminosity - from Nasuti et al (1996)

Over the last thirty years the Crab pulsar has been studied more extensively than any other. It is unique in that its age is known accurately, it is relatively close and bright. One of the main predictions of Pacini (1971) was the prediction that the Crab luminosity should reduce by ≈ 0.005 mags/year. Nasuti et al (1996)'s estimate of 0.008 ± 0.004/ year is in agreement with this (see Figure 4). However more detailed observations are required - preferably with the same telescope, detector and filter arrangements to conform this and remove systematic errors.

Smith et al. (1988) made detailed 1-d optical measurements of the phase resolved polarization, displayed in Figures 6 & 7. They noted that the polarization percentage followed the same shape over the main and interpulse. However interestingly they noted that the highest level of polarization was evident in the 'off'-pulse region. Smith et al (1988) went to some considerable lengths to remove the background nebular polarization component, and thus viewed this latter result as a consequence of the 'unpulsed' component being a cusp region between the two pulses. They also noted that the polarization angle swings in similar way through the main and interpulse which they interpreted as indicating a similar source (and geometry) of the radiation for both pulses, but coming from opposite poles. A similar, albeit slightly phase shifted, result has been observed by Romani et al (2001) using the new Transition Edge Detector (see Figure 18).

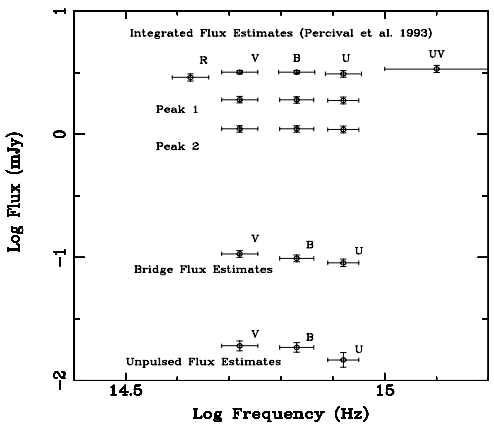


Fig. 5. *UBV* spectrophotometry of the Crab pulsar's light curve components Golden et al (2000)

The Crab's spectrum shows no evidence for a low energy break (see for example Sollerman & Flyckt (2002) and references therein) towards the IR regime, rather some suggestion of a 'levelling' of the spectral index (see Figure 8). Thus far no other optical pulsar has been seen to show evidence for a spectral break at low energies, although we are to some extent constrained by their faintness and the limitations of current high speed detector technology in this waveband. A definitive measurement of the Crab suggested 'roll-over' - indicative of some form of optically thick transition such as self-absorption - in the IR is one of the remaining crucial measurements which should be performed in the next few years.

An unpulsed optical component of emission has been noted for some time, since the work of Peterson et al (1978), although accurate high speed 2-d photometry as always dogged previous efforts to flux the apparent emission. Golden et al (2000) using a MAMA based system obtained sufficient S/N and critically, excellent background statistics to allow for an accurate determination of the flux of this component - clearly apparent in Figure 3, and broad-band spectra in UBV in Figure 5. This unpulsed region, described by Golden et al (2000), can be interpreted in two ways

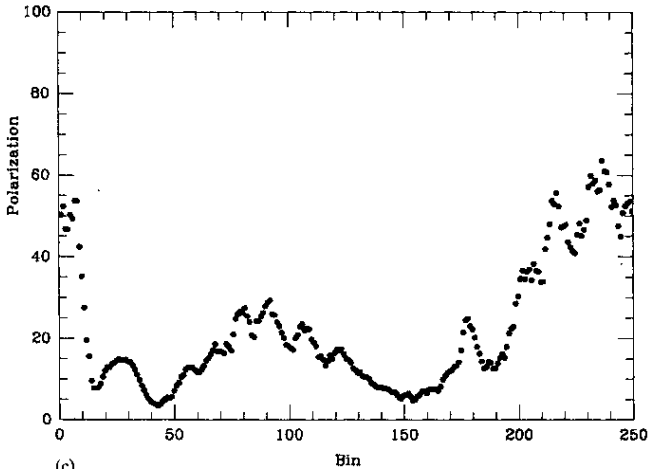


Fig. 6. Crab polarization profile from Smith et al 1988

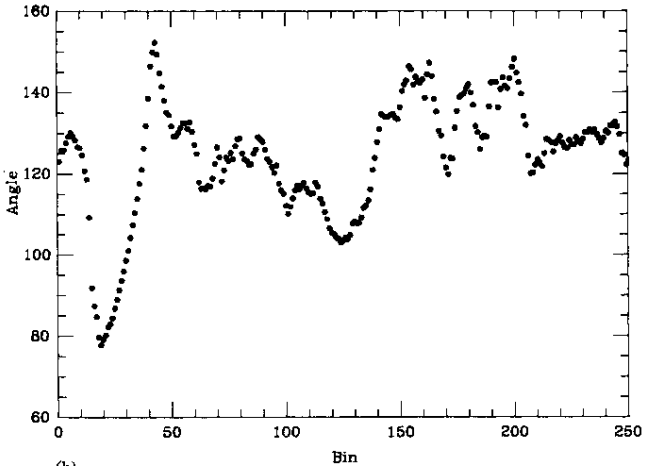


Fig. 7. Crab polarization angle from Smith et al 1988

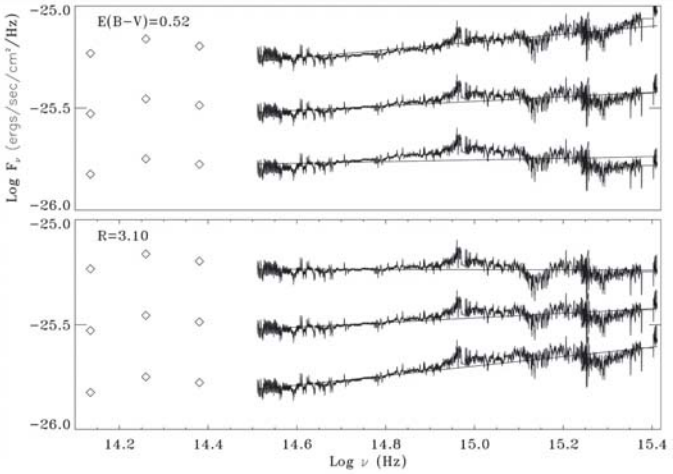


Fig. 8. Crab pulsar spectrum Sollerman et al (2000) with differing values of E(B-V) and R. For E(B-V) = 0.52, fits are [R = 2.9 (top), 3.1 & 3.3], for R = 3.1, fits are [E(B-V) = 0.49 (top), 0.52 & 0.55]. Spectra have been shifted by -0.3, 0.0 & +0.3 dex in 'flux' for clarity. Eikenberry & Fazio (1997) *JHK* data are included - these are consistent with 2MASS photometry for the pulsar.

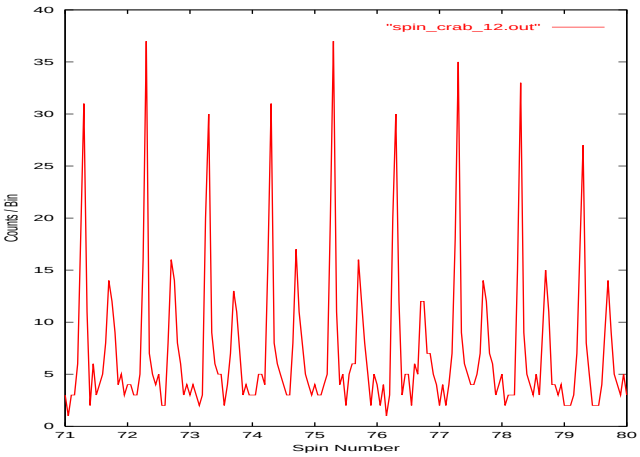


Fig. 9. Individual Crab pulses - statistical analysis shows no deviation from the expectation of Poissonian statistics. There is no observed correlation with the radio giant pulses Shearer et al (2002b)

- either a chance alignment of (e.g. a knot) or as a near constant background component to the emission. The star like point source unpulsed image in Figure 3 showed no significant positional shift compared to the integrated position - a shift of at least 3 pixels would be expected if was associated with the red knot (0".65 from the pulsar) (see Hester et al (1995) and Sollerman & Flyckt (2002)). Furthermore the intensity of the knot given by Sollerman & Flyckt (2002), does not explain the R/I background level shown in Figure 10.

2.3. The Remaining Optical Pulsars

Table 1 gives a summary of the observational data of the 5 pulsars seen to give pulsed magnetospheric emission. Of all the optical pulsars PSR B0633+17 (or Geminga) is perhaps the most controversial. Early observations (Halpern & Tytler (1988); Bignami et al (1988)) indicated that Geminga was an $\approx$ 25.5 m_V object. Subsequent observations including HST photometry appeared to support a thermal origin for the optical emission combined with a cyclotron resonance feature (Mignani et al (1998)). The high-speed optical observations of Shearer et al (1998) combined with spectroscopic observations (Martin et al (1998)) contradict this view. Figure 11 shows the broadband data plotted on top of the Martin et al Keck spectra, we have also included the pulsed B point acquired via a ground-based MAMA system (Shearer et al (1998)) and recent Subaru data (Kawai et al. 2002). This combined dataset indicates a fairly steep spectrum (with spectral index of $\sim$ 1.9) consistent with magnetospheric emission. It was on the basis of these results that Golden & Shearer(1999) were able to give an upper limit of R_∞ of about 10km by considering

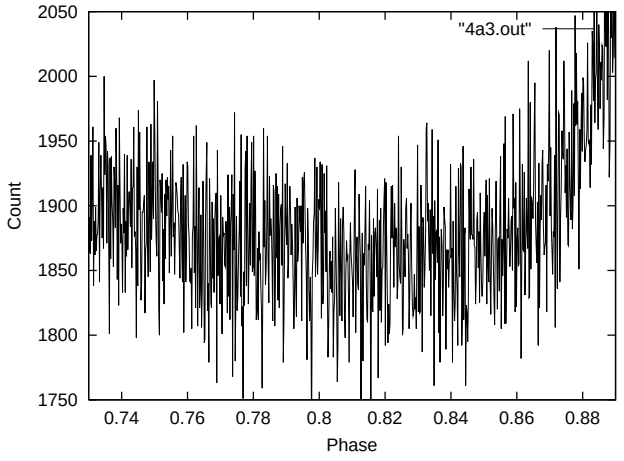


Fig. 10. 'Off' pulse region of Crab pulsar - taken from the full pulse in figure 1. The sky background in this image is at 4390 counts. The knot, see for example Sollerman et al (2000) & Sollerman & Flyckt (2002), situated 0".6 from the pulsar (and within our aperture) would contribute a further 650 counts/bin

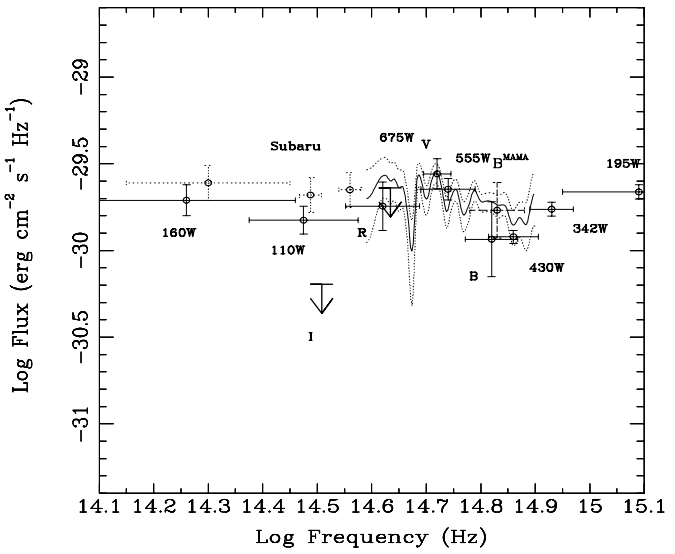


Fig. 11. Spectra and Photometry of Geminga. The spectrum (Martin et al (1998) and the agreement between it and the integrated photometry (Mignani et al (1998)). B is the pulsed flux from Shearer et al (1998). The HST points are from Pavlov, private communication - these are in close agreement with the IR points presented at this workshop Kawai et al. 2002.

the upper limits to the unpulsed fraction of the optical emission from Geminga as an upper limit for the thermal emission. The evolving picture for Geminga is that the soft X-ray and EUV data is predominantly thermal with a magnetospheric component becoming dominant at about 3500 Å.

As regards PSR B0656+14, the pulsar is generally agreed to be predominantly a non-thermal emitter in the optical, becoming a thermal emitter at wavelengths

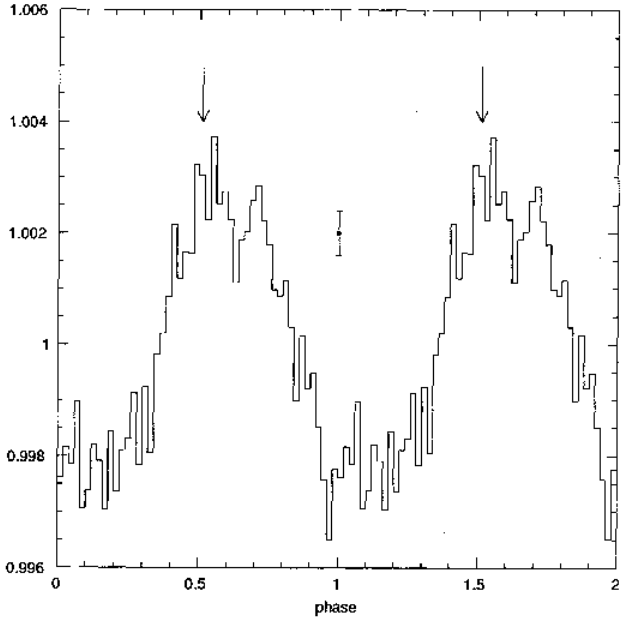


Fig. 12. Light Curve of PSR B0545-69 from Gouiffes et al (1992)

shorter than about 3000 ÅPavlov et al (1997). There is a discrepancy between the radio distance based upon the dispersion measure and the best fits to the X-ray data. From radio dispersion measure a distance of $760 \pm 190pc$ can be derived at odds with the X-ray distance of $250 - 280pc$ from N_H galactic models. A similar low estimate for the distance was given by Kaplan et al (2001). The optical spectrum is best fitted by a two component model with the power law component being significantly steeper than the Crab. Both Geminga and PSR B0656+14 have steep spectra compared their younger cousins. The observed light curve is roughly sinusoidal presumably indicative of closer alignment between the observer and the rotation axis than for the Crab and Geminga.

PSR B0540-69, the second brightest optical pulsar, is also the most distant. It is regarded as a twin of the Crab as it is of similar age, spin-down energy, breaking index and it is embedded within its own plerionic remnant. It has a broad light-curve with two distinct peaks - see figure 12. The difference between its light curve and that of the Crab is likely due to geometry. This pulsar has also had its braking index measured, $n = 2.2 \pm 0.02$ (Boyd et al (1995)). This (like the Crab) differs from the pure dipole value of 3. Middleditch et al (1987) measured no residual polarization from this pulsar - albeit at low significance.

The Vela pulsar has not been studied extensively in the optical. The best light curve from Gouiffes & Ogelman (1996) shows strong similarity between the γ-ray profile and the optical. More data is required to establish both the detailed structure of the light curve and the pulsar's polarization properties.

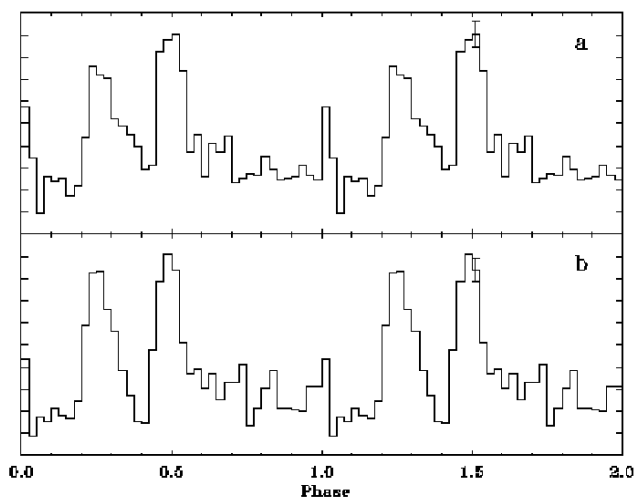


Fig. 13. Vela light curve from Gouiffes & Ogelman (1996)

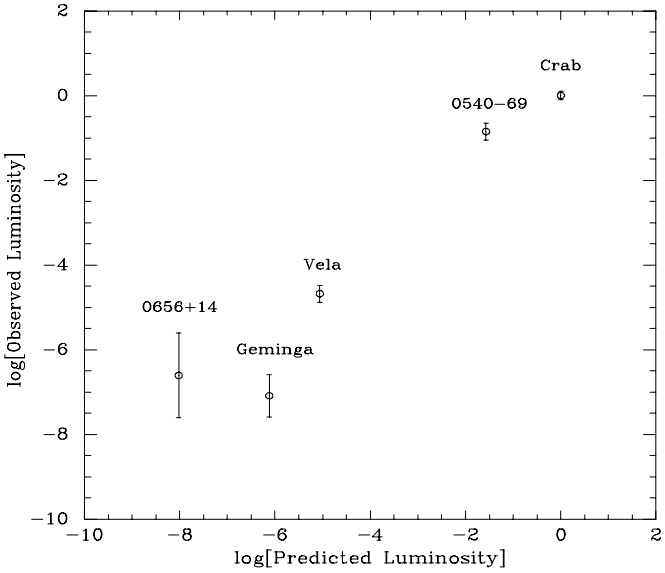


Fig. 14. Observed Peak optical luminosity vs predicted

2.4. Discussion

In Table 1 we have indicated the peak flux normalized to the Crab pulsar. When comparing the individual pulsars (which will have a range of viewing angles and differing magnetic/rotation axes), we have to account for the viewing angle (related to the pulse duty cycle and separation in terms of phase) as well as the total flux. Furthermore for each source, we have to account for the shape of the pulsar's spectrum. PS87 indicates for emission above the low energy cut-off that the ratio of the fluxes from two different pulsars can be given by Equation 1 if one ignores the effect of duty cycle and pitch angle (the suffixes refer to each pulsar). Here $F_{\nu,n}$ refers to the flux at the observed frequency ν for pulsar n (similarly for the magnetic field strength, B, and period, P). The observed energy spectrum exponent is given by α_n. The duty cycle can be accounted for by only considering the peak emission. The pitch angle being beyond the scope of this work and assumed to first order to be invariant. Equation 2 shows the same formulation for the outer field case.

$$\frac{F_{\nu,2}}{F_{\nu,1}} \propto (\frac{\nu_{1,0}}{\nu})^{\alpha_2-\alpha_1}(\frac{B_{2,0}}{B_{1,0}})^{4-\alpha_2}(\frac{P_2}{P_1})^{3\alpha-9} \quad (1)$$

Scaling to the transverse field would give:-

$$\frac{F_{\nu,2}}{F_{\nu,1}} \propto (\frac{\nu_{1,0}}{\nu})^{\alpha_2-\alpha_1}(\frac{B_{2,0}}{B_{1,0}})^{4-\alpha_2}(\frac{P_2}{P_1})^{3} \quad (2)$$

Given the observed peak luminosities we investigated the correlation between the peak emission and the surface field and the tangential light cylinder field. Figure 14 shows the relationship between the peak luminosity with the outer (tangentially at the light cylinder) magnetic field strength, B_T, Goldreich-Julian current and canonical age ($\frac{P}{2\dot{P}}$). A clear correlation is seen with all these parameters. We are interested in investigating the implications of a correlation between the peak luminosity and the transverse field. We accept the the strong correlation with G-J current would under pin both emission from polar as well as outer regions.

A regression of the form:

Peak Luminosity $\propto B_T^{\beta}$

was performed for the empirical peak luminosity this leading to a relationship of the form :-

Peak Luminosity $\propto B_T^{2.86\pm0.12}$

significant at the 99.5% level and consistent with the high average exponent shown in Table 1. Figure 14 shows the predicted peak luminosity from Equation 2 against our observed peaks accounting for the differing observed energy spectrum exponent at 4500 Å. The slope is 0.95 ± 0.04 and significant at the 99 % level. Whilst informative it still goes no further than previous attempts to understand the phenomena of optical emission. Importantly, we note that the flattening of the peak luminosity relationship for the older, slower pulsars is consistent with their having a significantly steeper energy spectrum than the younger pulsars, see Table 2. Whilst this is consistent with the emission zone being optically thick we consider it to be more likely that it reflects a larger emission region for these pulsars rather than the younger ones. This broadly concurs with PS87 argument of Δ (the size of the emission zone) scaling with P.

The polarization of the Crab's 'off-region' can be interpreted as coming from a different source to the main pulsed emission. Smith et al's argument that the off emis-

sion represented a cusp between the two main pulses relies upon the 'off'-pulse being a genuine cusp and not flat as observed by Shearer et al (2002a). The flat region - see Figure 10 - covers the peak of polarization noted by Smith et al. Another explanation is that the net polarization is a combination of two components; the remnants of a pulsed 'normal' magnetospheric component and a secondary unpulsed 'off-pulse' component. The derived polarization profile is then just the intensity normalized combination of these two processes. As the bridge component has twice the intensity of the 'off'-pulse we would expect the degree of polarization to be half that of the off-pulse region - as observed. The swing in polarization can therefore be understood in terms of the unpulsed component becoming dominated by by the pulsed component during the rising edge of each pulse. The relative contributions being due to normal quadratic addition of the Stokes parameters - i.e. dominated by the relative intensity. Figure 17 shows the derived polarization profile if it only comes from a steady low-level background source. The shape agrees well with the previously measured profile from Smith et al, except in the region around the main and inter-pulse - where the main pulsed polarization component will occur.

It seems clear that from both polarization studies (Smith et al (1988); Romani & Yadigaroglu (1995)) and from this work that we expect that optical emission zone is sited towards the outer magnetosphere. Timing studies of the size of the Crab pulse plateau indicates a restricted emission volume ($\approx$ 45 kms in lateral extent) (Golden et al (2000)). This third point, if consistent with the first two, probably points to emission coming from a geometrically defined cusp along our line of sight akin to treatment within the magnetosphere. More importantly the simple relationships we have derived here indicate that there is no need to invoke complex models for this high energy emission. Observed variations in spectral index, pulse shape and polarization can be understood in terms of geometrical factors rather differences in the production mechanism.

We note as well as that similar trends can be seen in γ rays. Figure 16 shows the correlation between the peak γ emission as a function of transverse field. This indicates a regression of the form

$$\text{Peak } \gamma \text{ Luminosity} \propto B_T^{0.89\pm0.15}$$

significant at the 99.6 % level, consistent with the observed steeper distribution seen in the high energy γ-ray band (cf. Table 2).

If we take our results and those of Goldoni et al (1995) we can begin to understand how the high energy emission process evolves with canonically derived pulsar age. Goldoni et al compared the known spectral indices and efficiencies in both the optical and γ-ray regions. They noted that the spectral index flattened with age for the γ-ray pulsars whilst the reverse was true for the optically emitting systems. They also noted a similar trend reversal for the efficiency with the γ-ray pulsars becoming more efficient with age. We note (see the bottom panel in Figures 15 and 16) a similar behaviour with the peak emission. If, as seems likely from the temporal coincidence between the γ-ray and optical pulses, that the source location is similar for both mechanisms. One explanation is that we seem to have a position where by from the same electron population there are two emission processes - expected if we have curvature for the γ-ray photons and synchrotron for the optical ones. It seems likely that the optical photon spectrum has been further modified to produce the reversal in spectral index with age. The region over which the scattering can occur would scale with the size of the magnetosphere and hence with age. With the outer magnetosphere magnetic fields for these pulsars being $< 10^6$ G electron cyclotron scattering is not an option. However synchrotron self-absorption could explain the observed features. In essence we would expect the most marked flattening to be for the Crab pulsar where the outer field strengths are of order 10^6 G and less so for the slower and older systems.

These results (both optical and γ rays) are consistent with a model where the γ and optical emission is coming from the last open-field line at some constant fraction of the light cylinder. The drop in efficiency with age for the production of optical photons points towards an absorbing process in the outer magnetosphere. Clearly more optical and γ-ray observations are needed to confirm these trends.

3. Instrumental Considerations

Table 3 summarizes the current range of detectors available for studies of optical pulsars. To obtain the necessary background measurements 2-d imaging detectors are required - these however (e.g. the MAMA detector used in the TRIFFID photometer, Butler et al (1998)) have limited quantum efficiency. However the limited qe can be offset by reduced effective sky aperture - the TRIFFID photometer uses off-line sky apertures determined by the local seeing conditions.

CCD based detectors, e.g. ULTRACAM (Dhillon & Marsh (2001)), suffer from read-noise problems - which increase with decreasing period/time resolution. These will be effective for AXP studies but 'conventional' pulsars have too short a period. Techniques such as on-chip phase locked image shifting and phase locked moving the secondary mirror have limited application due to field crowding.

Avalanche Photodiodes - as used in OPTIMA (Straubmeier et al (2001)) and TRIFFID - have good quantum efficiency, timing, but, are only single pixel devices. In both Optima and TRIFFID more than one APD is used for different colours and sky background determination. Attempts are currently being made to

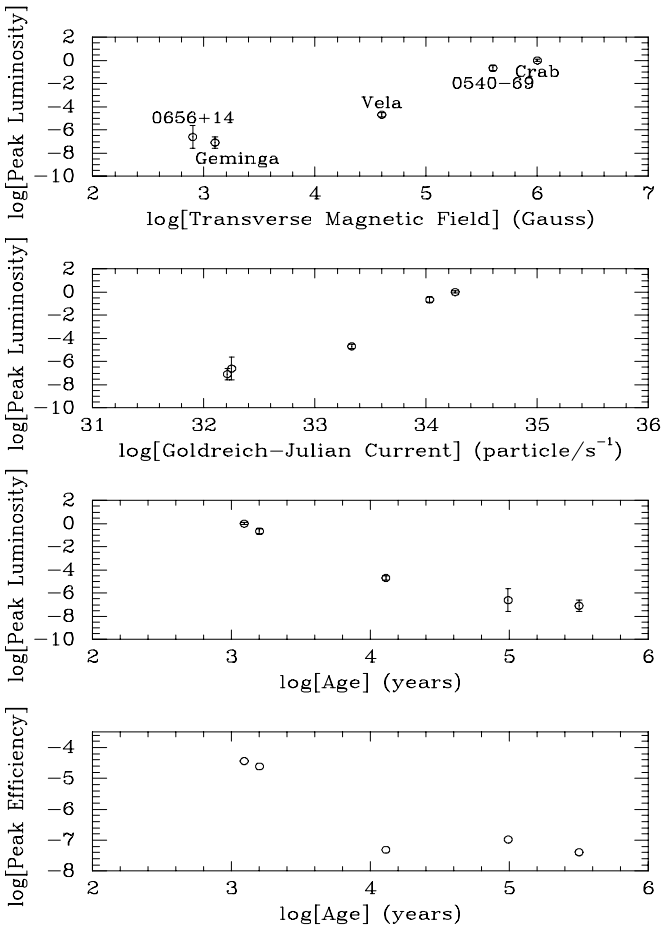


Fig. 15. Peak optical luminosity vs Light Cylinder magnetic field strength, GJ Current and age. Also shown is the optical efficiency as a function of age.

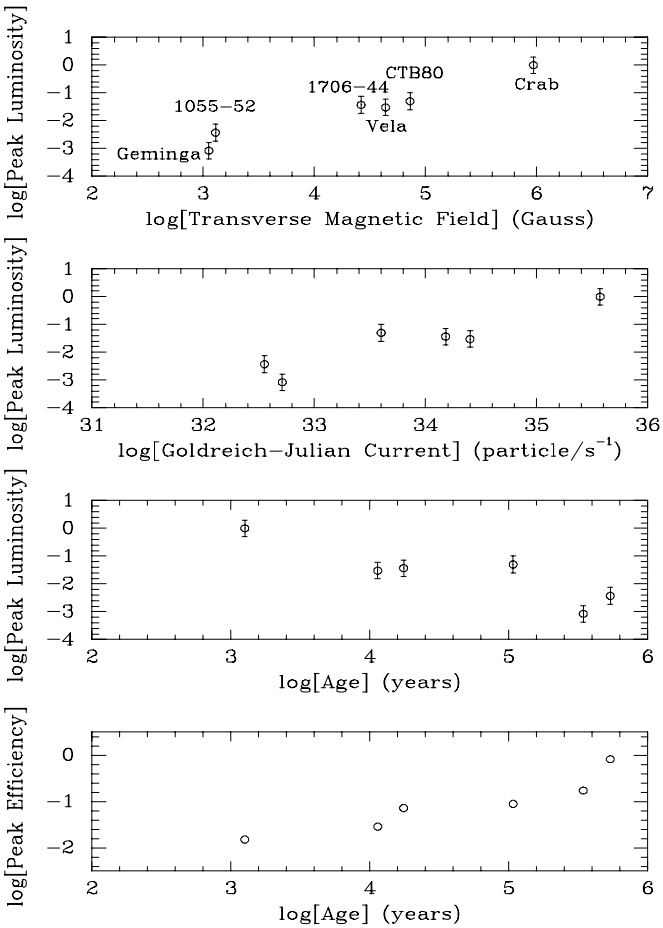


Fig. 16. Outer field strength against peak γ ray luminosity. The γ ray peak luminosity has been inferred from 6, Thompson et al (1996), Thompson et al (1999)

Table 3. Current detector possibilities. The future should lie with the energy sensitive detectors once the number of pixels can be increased

Detector	Time Resulution	Quantum Efficiency	Number of Pixels
CCDs	10 secs +	70%	millions
Fast CCDs e.g. UltraCam	100ms+	70%	millions
APDs Optima	μ secs +	70%	single
TRIFFID	μ secs +	70%	single
Photocathode based systems 2-d - (e.g.) MAMA	μsecs +	<10%	million
Photomultipliers	nsecs +	30% max	single
Energy Sensitive Detectors			
TES	nsecs +	70% max	few
STJ (SCAM)	nsecs +	70%max	few

construct arrays of these items but there are serious cross-talk problems. The next generation of energy sensitive detectors (see for example, Perryman et al (1999) & Romani et al (1999)) will give pulsar observers almost all (with the exception of polarization) flux parameters. However given that these devices are still in their relative infancy there is still a place of APDs and 2-d photocathode based systems.

4. Conclusion

The number of optically emitting pulsar which have been observed is limited. The observed phenomenology points to emission in the outer region of the magnetosphere - this seems more likely to come from an Outer Gap type model rather than a Polar Cap. However the data is sparse and no definitive statement can be made separating these models on the basis of the optical emission alone. Over the next few years as with the advent of larger telescopes and more sensitive detectors, we can confidently expect the number of optical detections of isolated neutron stars to increase. PSR B1055-52 & PSR B1951+32 are likely early candidates.

Table 4. Main Characteristics of Optical Pulsars: B_S & B_{LC} the canonical surface and transverse magnetic field at the light cylinder respectively; Opt. Lum and Peak Lum. refer to the optical luminosity at the indicated distance in the B band.

Name	D (kpc)	P (ms)	$\dot{P}$ 10^{-14} s/s	B_S log(G)	B_{LC} log (G)	Int μCrab	Peak μCrab	Spectral Index at 4500 Å	Cutoff Å
Crab	2	33	40	12.6	6.1	10^6	10^6	-0.11	>20000
Vela	0.5	89	11	12.5	4.8	27	21	0.2	6500(?)
PSR0545-69	49	50	40	12.7	5.7	1.1 10^6	1.4 10^5	0.2	>7000
PSR0656+14	0.76(?)	385	1.2	12.7	3.0	1.8	0.3	1.3	>8000
PSR0633+17	0.16	237	1.2	12.2	3.2	0.3	0.1	1.9	>8000

Table 5. Main Characteristics of γ-ray Pulsars: B_S & B_{LC} the canonical surface and transverse magnetic field at the light cylinder respectively; γ Lum and Peak Lum. refer to the γ luminosity at the indicated distance for E > MeV.

Name	D (kpc)	P (ms)	$\dot{P}$ 10^{-14} s/s	B_S log(G)	B_{LC} log (G)	Int Lumin. Crab=1	Peak Lumin. Crab=1	Spectral Index
Crab	2	33	42.1	12.58	5.97	1	1	2.15
Vela	0.5	89	12.5	12.53	4.64	0.0480	0.0299	1.70
PSR1055-52	49	197	0.6	12.03	3.11	0.0124	0.0037	1.18
PSR1706-44	2.4	102	9.3	12.49	4.42	0.1380	0.0368	1.72
PSR0633+17	0.16	237	1.1	12.21	3.05	0.0019	0.0008	1.50
PSR1951+32	2.5	40	0.6	11.69	4.86	0.0500	0.0187	1.74

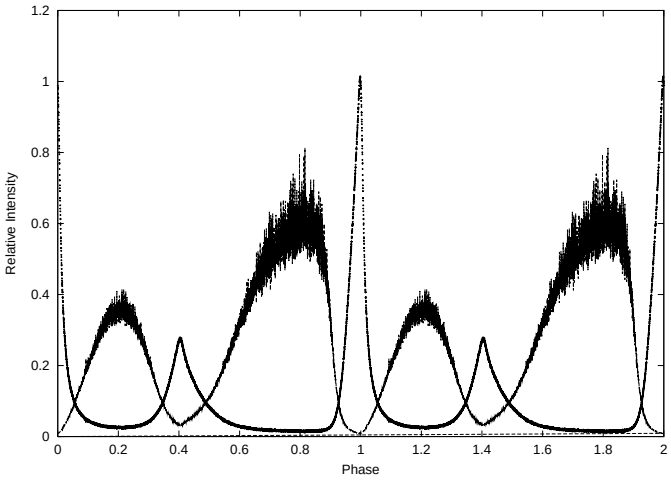


Fig. 17. Crab light curve and inferred polarization fraction using Stokes parameters (Q/U) given by Smith et al (1988) for the off pulse region and then scaled. The contribution from the main pulsar component is not shown.

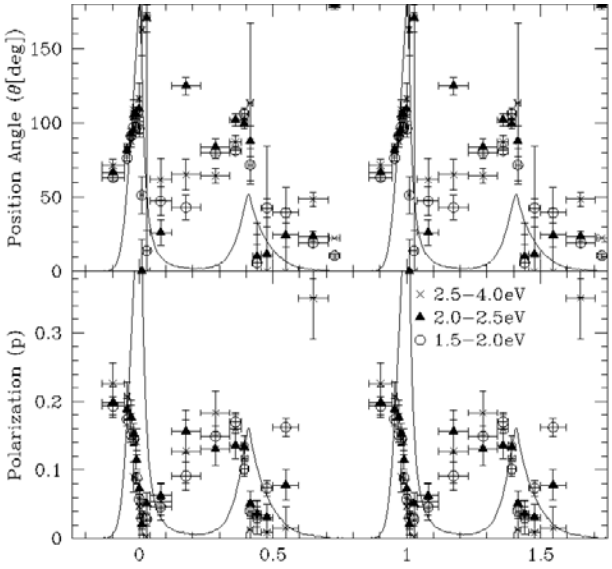


Fig. 18. Crab polarization as a function of pulsar phase measured using the energy sensitive TES from Romani et al (2001)

In the optical any potential thermal component should be separable from the strongly pulsed magnetospheric emission, allowing for reliable estimates of the neutron star radius to be measured with consequent implications for equation of state models. However before this is done with any degree of confidence the nature of the unpulsed emission must be established - is it a synchrotron knot feature or more localized to the pulsar. Is it unique to the Crab pulsar? Of crucial importance in the future will be determination of the low-energy cutoff and the polarization sweep through the optical pulse (significantly modern instruments are capable of measuring the polarization sweep for both PSR B0540-69 and Vela as well as the Crab). Also of interest will be the shape of the pulse - in particular the size of any plateau which scales as the size of the emission zone. All of these parameters are measurable with existing technologies and telescopes for these pulsars. The advent of new detectors and larger telescopes should herald a period of renewed interest in optical pulsar studies, however there are still important questions that can be answered by observation with existing telescope/instrument systems.

5. Acknowledgments

Enterprise Ireland is acknowledged for support under its Basic Research Grant Scheme. Ray Butler and Padraig O'Connor are thanked for help during the preparation of this manuscript. The workshop organizers are thanked for their hospitality.

References

Bignami, G. F., Caraveo, P. A. & Paul, J. A., 1988, A & A, 202, L1
Boyd, P. T. et al, 1995, ApJ, 448, 365
Butler, R. F. & Shearer, A. & Redfern, R. M., Colhoun, M., O'Kane, P., Penny, A. J., Morris, P. W., Griffiths, W.K. & Cullum, M., 1998, MNRAS, 296, 379
Cocke, W. J., Disney, M. J. & Taylor, D. J., 1969, Nature, 221, 525
Caraveo, P. A., Bignami, G. F., Mignani, R. & Taff, L. G., 1996, A & A, 120, 65
Cheng, K. S., Ruderman, M. & Zhang, L., 2000,ApJ, 537, 964
Dhillon, V. & Marsh, T, 2001, NewAR, 45, 91
Daugherty, J. K. & Harding, A. K., 1996, ApJ, 458,278
Eikenberry, S. S. & Fazio, G. G., 1997, ApJ, 476, 281
Fierro, J. M., Michelson, P. F., Nolan, D. C. & Thompson, D. J., 1998, ApJ, 494, 734
Gil, J. A., Khechinashvili & Melikidze, G. I., 2000, to be published in MNRAS
Golden, A. & Shearer, A., 1999, A & A, 342, L5
Golden, A., Shearer, A. & Beskin, G. M., 2000, ApJ, 535, 373
Goldoni, P., Musso, C., Caraveo, P. A. & Bignami, G. F., 1995, å, 298, 535
Gouiffes, C., Finley, J. P. & Oegelman, H., 1992, ApJ, 394, 581
Gouiffes, C. & Ogelman, H., 1996 ASP Conf. Ser. 105: IAU Colloq. 160: Pulsars: Problems and Progress, 299
Halpern, J-P & Tytler, D., 1988, ApJ, 330, 201
Hester, J. J. et al, 1995, ApJ, 448 240
Kaplan, D. L., van Kerkwijk, M. H. & Anderson, J., 2001, astro-ph/011174
Kawai et al, 2002, these proceedings
Nasuti, F. P., Mignani, R., Caraveo, P. A. & Bignami, G. F., 1996, A&A, 314, 849
Martin, C, Halpern, J.P. & Schiminovich, D., 1998, ApJ, 494, L211
Middleditch, J. & Pennypacker, C., 1985, Nature, 313, 659
Middleditch, J., Pennypacker, C. & Burns, M. S., 1987, ApJ, 315, 142
Mignani, R. P., Caraveo, P. A., & Bignami, G. F., 1998, å, 332, L37
Nasuti, F. P., Mignani, R., Caraveo, P. A. & Bignami, G. F., 1996, A&A, 323, 839
Pacini, F., 1971, ApJ, 163,17
Pacini, F. & Salvati, M., 1983, ApJ, 274, 369
Pacini, F. & Salvati, M., 1987, ApJ, 321, 445
Pavlov, G. G., Welty, A. D. & Cordova, F. A., 1997, ApJ, 489, L75
Perryman, M. A. C., Favata, F., Peacock, A., Rando, N. & Taylor, B. G., 1999, A & A, 346, 30
Peterson, B. A., Murdin, P., Wallace, P., Manchester, R. N., Penny, A. J., Jorden, A., Hartley, K. F. & King, D, 1978, Nature, 276, 475
Romani, R. W., & Yadigaroglu, I.-A., 1995, ApJ, 438, 314
Romani, R. W., Millar, A. J., Cabrera, B., Nam, S. W. & Yadigaroglu, I.-A., 2001, astro-ph 0108240
Romani, R. W., Miller, A. J., Cabera, B. & Figueroa-Feliciano, E., 1999, ApJ, 521, L151
Shearer, A., Redfern, R. M., Gorman, G., Butler, Golden, A., R., O'Kane, P., Golden, A., Beskin, G. M., Neizvestny, S. I., Neustroev, V. V., Plokhotnichenko, V. L. & Cullum, M., ApJ, 1997, 487, L181
Shearer, A., Harfst, S., Redfern, R. M., Butler, R., O'Kane, P., Beskin, G. M., Neizvestny, S. I., Neustroev, V. V., Plokhotnichenko, V. L. & Cullum, M., 1998, A & A, 335, L21
Shearer, A. & Golden, A., 2001, ApJ, xxx, yyy
Shearer, A., O Connor, P. & Golden, A., Ryan, O., & Redfern, M., in preparation
Shearer, A., Butler, R. F. & Golden, A., in preparation
Smith, F. G., Jones, D. H. P., Dick, J. S. P. & Pike, C. D., 1988, MNRAS, 233, 305
Sollerman, J., Lundqvist, P., Lindler, D., Chevalier, R. A., Fransson, C., Gull, T. R., Pun, C. S. J. & Sonneborn, G, 2000, ApJ, 537, 861
Sollerman, J. & Flyckt, V., 2002, ESO Messenger, 107, 32
Straubmeier, C., Kanbach, G. & Schrey, F., 2001, Exp Ast, 11, 157
Thompson, D. J., 1996, ApJ, 465, 385
Thompson, D. J., 1999, ApJ, 516, 297
Wallace, P. T. et al. 1977, Nature, 266, 692

Proceedings of the 270. WE-Heraeus Seminar on: *"Neutron Stars, Pulsars and Supernova Remnants"*
Physikzentrum Bad Honnef, Germany, Jan. 21-25, 2002, eds. W. Becker, H.Lesch & J. Trümper, MPE Report 278, pp. 54- 57

PSR B1951+32 and PSR J0537-6910 - where are the optical counterparts?

R. F. Butler[1], A. Golden[1], A. Shearer[1] and C. Gouiffes[2]

[1] National University of Ireland, Galway; University Road, Galway, Ireland
[2] CEA/DSM/DAPNIA/Service d'Astrophysique, Saclay, Paris, France

Abstract. There remain several definitive γ-ray pulsars that are as yet undetected in the optical regime. A classic case is the pulsar PSR B1951+32, associated with the complex CTB 80 SNR. Previous ground based high speed 2-d optical studies have ruled out candidates to $m_V \sim 24$. Hester (2000) has reported an analysis of archival HST/WFPC2 observations of the CTB 80 complex which suggest a compact synchrotron nebula coincident with the pulsar's radio position. Performing a similar analysis, we have identified a possible optical counterpart within this synchrotron nebula at $m_V \sim 25.5$, and another optical counterpart candidate nearby at $m_V \sim 24.2$.

PSR J0537-6910 is a young (canonical age $\approx$ 5000 years), 16ms pulsar in the LMC. We report a search for optical pulsations from the region around the X-ray position. We see no obvious candidate exhibiting optical pulsations at the X-ray period, with a 3σ upper limit of $m_V \approx 23.6$. We have also examined recent Chandra results (Wang et al. 2001) and show that their X-ray-Optical astrometry is in error by about 7".

1. Introduction

The detection of non-thermal high energy magnetospheric emission from isolated pulsars has remained a non-trivial problem, despite great advances in instrumentation and technological expertise. To date, only 7 optical pulsars have been detected with emission believed to be magnetopsherically dominated, and despite considerable effort, only 8 γ-ray pulsars. In contrast to radio emission, which is generally believed to be generated in close proximity to the magnetic poles, no clear theoretical model construct exists as regards the higher energies. The two principal schools of thought place γ-ray emission localized either to the magnetic poles (Daugherty & Harding 1996) or located further out in the magnetosphere (Romani 1996). Considerable problems remain with these two frameworks, in terms of predicted fluxes, spectral indices and light curve morphologies, and it is clear that further work is required on this subject. This is all the more relevant when one attempts to address the growing empirical database of lower energy emission, in particular in the optical regime. A consequence of non-linear processes within the magnetosphere, this synchrotron emission forms a useful constraint with which one can attempt to comprehensively develop a self-consistent theoretical framework.

2. PSR B1951+32

The pulsar PSR B1951+32, located within the complex combination supernova remnant (SNR) CTB 80, was first identified as a steep-spectrum, point-like source in the radio (Strom 1987), and discovery of radio pulses with an unusually fast 39.5-s period quickly followed (Kulkarni et al. 1988). Canonically, the pulsar's age and the estimated dynamical age of the SNR are consistent at $\sim 10^5$ yrs (Koo et al. 1990) and both have been determined to be at a distance of $\sim$ 2.5 kpc. There is thus general agreement that the association is valid. Evidence for pulsed emission was subsequently found in gamma-rays (Ramanamurthy et al. 1995) and possibly in X-rays (Safi-Harb et al. 1995; Chang & Ho 1997). The ROSAT observations in the X-ray regime do indicate a complex light curve strongly dominated by the intense X-ray radiation of a pulsar-powered synchrotron nebula (Safi-Harb et al. 1995; Becker & Truemper 1996). The unambiguous double-peaked γ-ray (EGRET) light curve obtained by Ramanamurthy et al. (1995) at the appropriate spin-down ephemeris suggested that the pulsar had a conversion efficiency, in terms of rotational energy to γ-rays, of ~ 0.004. Consequently there are strong grounds for the possibility of an optical detection. Using a ground-based MAMA detector in the TRIFFID camera, we have previously examined the central field of CTB 80, but could find no evidence of pulsations in either B or V from this region (O'Sullivan et al., 1998).

2.1. Analysis of archival HST/WFPC2 observations

We obtained from the HST archive all existing WFPC2 data of the CTB 80 SNR, as listed in Table 1. The core of the CTB 80 remnant lies on chip WF3 of the WFPC2 camera in every case. Image processing and photometry were performed using the IRAF (Tody 1993), STSDAS,

Table 1. List of WFPC2 observations of the CTB 80 SNR, obtained from the ST-ECF HST archive.

Date	*Filter*	*TotalExptime*	*Notes*
2/10/97	$F656N$	5300	HII
2/10/97	$F673N$	5400	SII
2/10/97	$F502N$	5400	$OIII$
2/10/97	$F547M$	2600	Strömgreny

Table 2. The positions and magnitudes derived by DAOPHOT-II/allstar PSF-fitting for point sources detected in the WFPC2 F547M image of CTB 80. The "Dist." column contains the distance from from each source to the centre of the synchrotron nebula; only sources within 5.0" of this position are listed here.

#	$RA(2000)$ $hh:mm:ss.ss$	$Dec(2000)$ $dd:mm:ss.s$	*Dist.* *arcsec*	MAG_{F547M} *magnitudes*
1_{HST}	19 : 52 : 58.24	32 : 52 : 41.0	0.20	23.93 ± 0.30
2_{HST}	19 : 52 : 58.25	32 : 52 : 41.8	0.97	22.15 ± 0.07
3_{HST}	19 : 52 : 58.23	32 : 52 : 42.0	1.11	21.35 ± 0.07
4_{HST}	19 : 52 : 58.28	32 : 52 : 39.9	1.16	24.21 ± 0.12
5_{HST}	19 : 52 : 58.14	32 : 52 : 39.0	2.23	24.07 ± 0.12
6_{HST}	19 : 52 : 58.14	32 : 52 : 43.4	2.69	21.84 ± 0.07
7_{HST}	19 : 52 : 58.42	32 : 52 : 39.2	2.90	21.61 ± 0.06
8_{HST}	19 : 52 : 58.39	32 : 52 : 38.7	2.95	21.96 ± 0.07
9_{HST}	19 : 52 : 58.48	32 : 52 : 42.6	3.55	23.00 ± 0.09
10_{HST}	19 : 52 : 57.95	32 : 52 : 40.8	3.57	25.73 ± 0.26
11_{HST}	19 : 52 : 58.39	32 : 52 : 44.1	3.73	24.25 ± 0.14
12_{HST}	19 : 52 : 57.97	32 : 52 : 39.1	3.79	25.87 ± 0.47
13_{HST}	19 : 52 : 58.02	32 : 52 : 37.1	4.68	22.90 ± 0.07
14_{HST}	19 : 52 : 58.38	32 : 52 : 36.6	4.74	24.44 ± 0.18

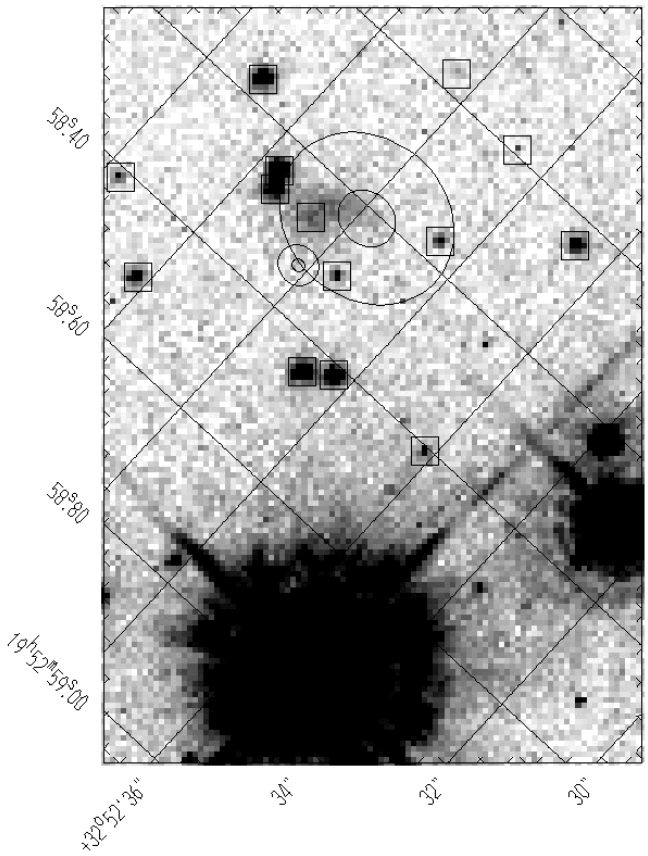


Fig. 1. Section of the HST/WFPC2 F547M image of the core of CTB80. The compact synchrotron nebular knot reported by Hester (2000) can be seen at the upper-centre. The coordinate grid shows our improved astrometric calibration after referencing to the 2MASS point-source catalog. The mapped radio positions for PSR B1951+32 (see text) are marked by black ellipses, the semi-major and semi-minor axes of which are determined by the 1-σ and 3-σ total positional uncertainties in RA and Dec - ie. the quoted error on the radio position, combined with the total rms error on the HST-2MASS fit for 31 stars. The larger pair of ellipses mark the interferometric position. The positions derived by DAOPHOT-II/allstar PSF-fitting for all measured point sources within 5.0" of the centre of the synchrotron nebula are indicated by black squares: counterpart candidate 1_{HST} lies within the nebula and candidate 4_{HST} lies just below it.

and DAOPHOT-II (Stetson 1994) packages. The images in each band were stacked and cleaned of cosmic rays and hot pixels using standard techniques. The F547M intermediate-width band enabled us to perform a deep photometric search for faint stellar sources, to S/N=2 at $\mathrm{MAG}_{F547M} = 26.7$. More details of our reduction procedure, including refinement of the HST astrometry using the 2MASS point-source catalog, can be found in Butler et al. (2002). The photometric and astrometric results are shown in Figure 1 and Table 2.

The two "best" radio positions for PSR B1951+32, from Foster et al. (1990) [interferometric] and Foster et al. (1994) [glitchless timing], are shown overplotting the HST field and its detected point-source content in Figure 1. Two point-sources were found to be the most positionally consistent with these two radio positions; the first (object 4_{HST} in Table 2) is a straightforward point-source measurement at $\mathrm{MAG}_{F547M} = 24.21 \pm 0.12$; whereas the second (object 1_{HST}) is superimposed on the compact synchrotron knot reported by Hester (2000), and required photometric simulations to determine its true magnitude, at MAG_{F547M} between 25.0 - 26.0. Further Monte Carlo simulations to determine the limiting magnitude of the WFPC2 observation showed that an object within this magnitude range is indeed detectable against such nebular background in this data, albeit with S/N of only $\approx$2 - 2.5.

Crucially, the corrected magnitude of $\mathrm{MAG}_{F547M} =$ 25.0 - 26.0 for object 1_{HST} is within the range predicted by the successful mode framework of Pacini & Salvati (1987) and more recently the phenomenological analysis of

Shearer & Golden (2001). The magnitude of object 4_{HST} is also consistent with these models, at the brighter end of the predicted range. Consequently, taken together with their positions with respect to the two radio-position error ellipses, we suggest that these two objects are plausible new optical counterpart candidates to PSR B1951+32.

3. PSR J0537-6910

PSR J0537-6910 was first observed by RXTE satellite (Marshall et al. 1998). ROSAT observations by Wang et al. (1998) showed that the pulsar lies within the SNR N157B near the 30 Doradus star formation region in the LMC. The spin period (16 ms) and age ($\approx$ 5000 years) make it the fastest spinning young pulsar known. Scaling the expected optical emission from the Crab pulsar, using the Pacini & Savati (1987) model, we would expect a pulsed magnitude in the range $m_B \approx$ 19-21. Using archival CCD data, both Mignani et al. (2000) and Gouiffes & Ögelman (2001) show no obvious counterpart candidate down to 23rd magnitude.

3.1. TRIFFID Observations

We observed the region around the ROSAT position in February 2000 using the ESO 3.6m telescope and the TRIFFID 2-d photometer. This instrument consists of a relatively low quantum efficiency MAMA detector, observing in B and V, in combination with a high sensitivity (system QE 25 %) group of avalanche photodiodes (APDs). The primary APD was positioned towards the centre of the X-ray error circle on candidate star 16 on Figure 2. Conditions were not photometric and the seeing varied between 1.1" and 1.6". The region was observed on two nights for a total of 5 hours. No pulsed signal was observed from the APD at a limiting magnitude of $m_R \approx 24$. A timing signal was then searched for in the MAMA data, at the locations of all stars marked within the 7"-radius circle in Figure 2; again no signal was seen. A final search was then performed over the full area of the 7"-radius error circle using a set of multiplexed seeing width apertures; again no signal at the pulsar frequency was observed. Our limiting magnitude is estimated as $m_B = 23.6$ at the 3 σ level. This upper limit implies a pulsed optical / X-ray ratio of about 10^{-3}.

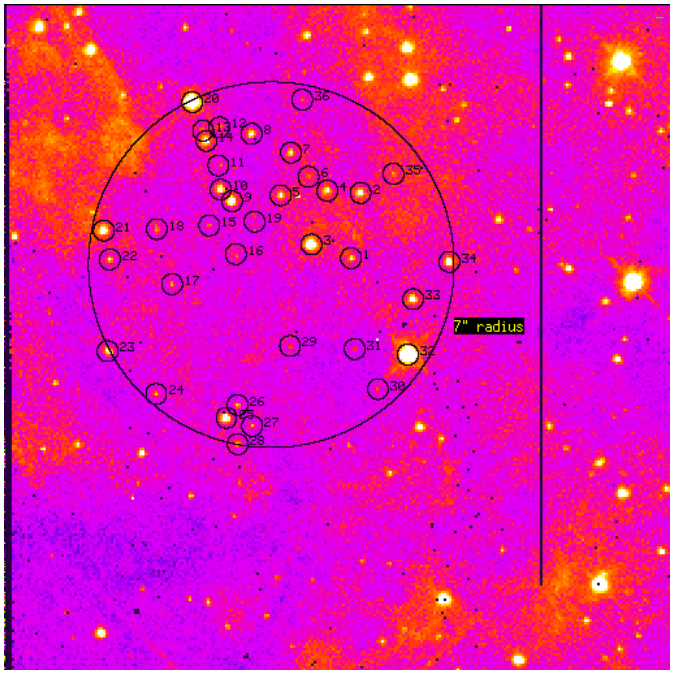


Fig. 2. Section of the HST/WFPC2 F606W image (see Section 4.2) of N157B. This shows the circular region, of 7" radius and centered on the ROSAT position for PSR J0537-6910, which was searched by the TRIFFID photometer.

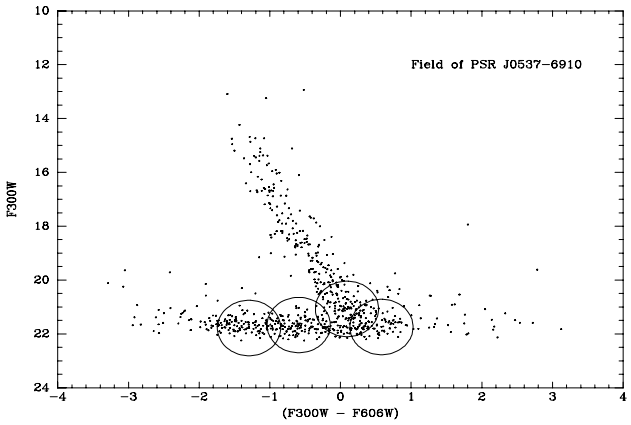


Fig. 3. The HST/WFPC2 colour magnitude diagram (in F300W, F300W-F606W) for stars in the N157B field. Circles mark the stars within the Chandra error circle for PSR J0537-6910 (see Figure 4 below). The bluewards tail at F300W$\approx$22 is an artefact of the different depths in the two filters.

3.2. The Chandra-HST registration of the N157B field

We obtained from the HST archive all WFPC2 images which overlapped the field of N157B. The only moderately deep exposures where in the F606W filter ("wide V-band"). Again, image processing, astrometry, and photometry were performed with STSDAS, IRAF, and DAOPHOT-II. We searched for possible pulsar optical counterpart candidates amongst the stars detected within the ROSAT X-ray error circle for PSR J0537-6910, centred at RA 05:37:47.1 Dec -69:10:23.0, by mapping this coordinate into the astrometric solution in the WFPC2 file headers. Figure 3 shows the colour-magnitude diagram for the stars in the field. A similar analysis, using the RA & Dec derived by Wang et al. (2001) for the pulsar in their Chandra observations, yielded a similar optical (mapped) position, albeit with a somewhat smaller error circle. However a comparison with the same analysis by Wang et al. (2001), shown in their Fig. 2, shows a striking positional

difference of approx. 7 - 8 arcsec. This is very difficult to explain, as the Chandra coordinate for the pulsar should be good to 1 arcsec, based on agreement of this order with the 2 Wolf-Rayet stars in the X-ray field; and the average absolute pointing error for the HST pipeline astrometric solution (based on the Guide Star Catalog) is 0.8 - 1.5 arcsec (Biretta et al. 2000). Furthermore, our astrometry on the HST image (shown in Figure 4) agrees very well with our independent astrometry on NTT-SUSI imagery (Gouiffes & Ögelman, 2001). One must conclude that some error was made in the Chandra-HST registration of the N157B field by Wang et al. (2001).

Indeed, if the X-ray contours in Fig. 2 of Wang et al. (2001) were shifted to agree with our computed position, then these X-ray contours would match the underlying nebulosity structures much better. This would also have the effect of weakening their argument regarding the extended X-ray emission extending "beyond [filament] F4" - the extent would drop back by about 2 contour levels - although it is not entirely incorrect. More seriously, their statement that "the image shows no evidence for the optical counterpart of the pulsar" surely becomes invalid, as they apparently searched the wrong area of the HST image.

Although we can better address the latter question, having searched the correct area of the HST image, we cannot report a convincing optical counterpart either, because the HST exposures were not deep enough - especially in the F300W filter (approx. U-band), which prevented us from obtaining colour indices (U-V) of the fainter F606W sources. This illustrates the need for deeper, high-resolution imaging and time-resolved imaging. The TRIFFID photometer would be capable of reaching 26th magnitude with 10 hours of observation under reasonable conditions.

Acknowledgements. The authors gratefully acknowledge financial support from Enterprise Ireland under the Basic Research Programme. RFB is also grateful for financial support from the Improving Human Potential programme of the European Commission (contract HPFM-CT-2000-00652). This publication is partly based upon Hubble Space Telescope data obtained from the ST-ECF archive, ESO, Garching, Germany. It also makes use of data products from the Two Micron All Sky Survey, which is a joint project of the University of Massachusetts and the Infrared Processing and Analysis Center/California Institute of Technology, funded by the National Aeronautics and Space Administration and the National Science Foundation. Finally, we also wish to thank Richard Strom for useful suggestions and comments while we prepared this paper.

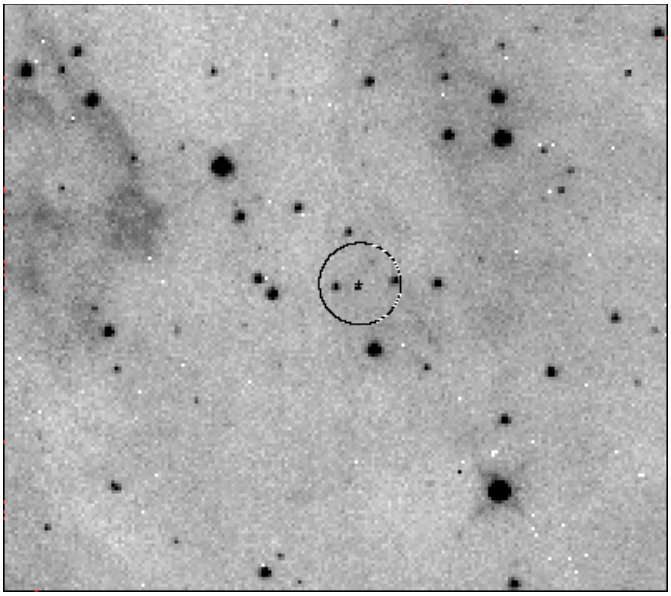


Fig. 4. Aligned HST/WFPC2 field and Chandra X-ray error circle for PSR J0537-6910, from this work.

References

Becker, W., & Trümper, J., 1996, A&AS, 120, 69
Biretta, J. A., et al., 2000, "WFPC2 Instrument Handbook, Version 5.0", (Baltimore: STScI)
Butler, R. F., Golden, A., & Shearer, A., 2002, accepted for publication in A&A
Chang, H.-K., & Ho, C., 1997, ApJ, 479, L125
Daugherty, J.K., & Harding, A. K., 1996, A&AS, 120, 107
Gouiffes, C., & Ögelman, H., 2001, PUAS2000 Conference, ASP 202, 301
Hester J., 2000, AAS, 197, 8216
Koo, B.-C., Reach, W. T., Heiles, C., Fesen, R. A., & Shull, J. M., 1990, ApJ, 364, 178
Kulkarni, S. R., Clifton, T. C., Backer, D. C., Foster, R. S., Fruchter, A. S., 1988, Nature, 331, 50
Marshall, et al., 1998, ApJ, 499, L179
Mignani, R., et al., 2000, A&A, 355,603
O'Sullivan, C., et al., 1998, A&A, 335, 991
Pacini, F., & Salvati, M., 1987, ApJ, 321, 447
Ramanamurthy, P. V., et al., 1995, ApJ, 447, L109
Romani, R. W., 1996, ApJ, 470, 469
Safi-Harb, A., Ögelman, H., & Finley, J. P., 1995, ApJ, 439, 722
Shearer A., & Golden A., 2001, ApJ, 547, 967
Stetson, P. B., 1994, PASP 106, 250
Strom, R. G., 1987, ApJ, 319, L103
Tody, D., 1993, ASP Conf. Ser. 52: Astronomical Data Analysis Software and Systems II, eds. R. J. Hanisch, R. J. V. Brissenden, & J. Barnes, 173
Wang, Q. D. & Gotthelf, E. V., 1998, 509, L109
Wang, Q. D., Gotthelf, E. V., Chu, Y.-H., & Dickel, J. R. 2001, ApJ, 559, 275

Proceedings of the 270. WE-Heraeus Seminar on: *"Neutron Stars, Pulsars and Supernova Remnants"*
Physikzentrum Bad Honnef, Germany, Jan. 21-25, 2002, eds. W. Becker, H.Lesch & J. Trümper, MPE Report 278, pp. 58- 63

Chandra Observations of Neutron Stars — An Overview

M.C.Weisskopf

NASA Marshall Space Flight Center, MSFC/SD50, Huntsville, AL 35812, USA

Abstract. We present a brief review of *Chandra* observations of neutron stars, with a concentration on neutron stars in supernova remnants. The early Chandra results clearly demonstrate how critical the angular resolution has been in order to separate the neutron star emission from the surrounding nebulosity.

1. Introduction

Beginning with the now-famous "first-light" observation of the supernova remnant (SNR) Cassiopeia A and discovery of its central object (Fig. 1), it was evident that the *Chandra X-ray Observatory*'s superb angular resolution would play an important role in advancing our understanding of neutron stars. Now, more than two years into the mission, this promise has been clearly fulfilled, although the full significance of even the currently completed observations is not yet fully realized. Here, I provide a limited (and biased) overview of several *Chandra* observations of neutron stars. In nearly all cases, I summarize work by others, as attributed in the text and figure captions. In addition, I acknowledge the dedication of the entire *Chandra* science team — at the the Smithsonian Astrophysical Observatory, the Marshall Space Flight Center, and the institutions of the Principal Investigators and their colleagues — that has made the *Chandra* mission a such a success.

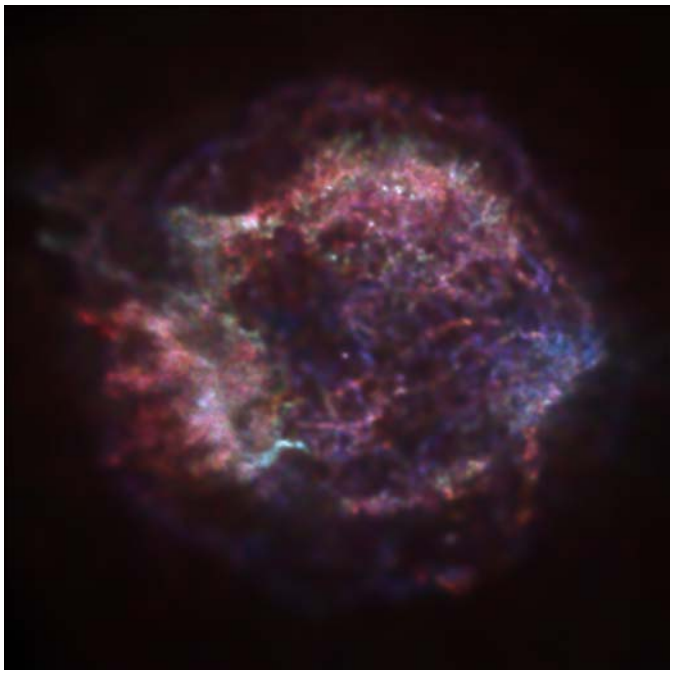


Fig. 1. *Chandra* ACIS spectrometric image of the Cas-A SNR. The red, green, and blue regions in this 6-arcmin-square image show the intensity of low-, medium-, and high-energy X rays, respectively. The red material on the east outer edge is enriched in iron, whereas the bright greenish white region on the southeast is enriched in silicon and sulfur. In the blue region to the west, low- and medium-energy X rays have been filtered out by a cloud of dust and gas. Courtesy NASA/CXC/SAO/Rutgers/Hughes et al. (2000).

2. Neutron Stars in SNR

2.1. Crab Pulsar

A critically important example of *Chandra*'s ability to provide high-contrast images of low-surface-brightness features is the now-classic image (Fig. 2) of the Crab Nebula and Pulsar (Weisskopf et al. 2000), which shows the complex spatial structure of the inner nebula. This image revealed an X-ray inner ring between the pulsar and the X-ray torus. In Tennant et al. (2001), our phase-resolved analysis of an LETG–HRC-S zeroth-order image discovered significant X-ray emission from the pulsar in its "off" phase (Fig. 3). Owing to the high surface brightness and complex structure of the Crab's inner (plerionic) nebula, *Chandra*'s high angular resolution was *essential* to these discoveries. We used the measurement of the pulsar's flux at pulse minimum to establish an upper limit to thermal emission from the surface of the neutron star. At that time we argued that, for a number of reasons, the observed flux was likely to be predominantly non-thermal. First, the detected visible flux at pulse minimum (Golden, Shearer, & Beskin 2000) demonstrates the presence of unresolved non-thermal emission at pulse minimum. Second, the similarity of the relative amplitudes of the X-ray and visible

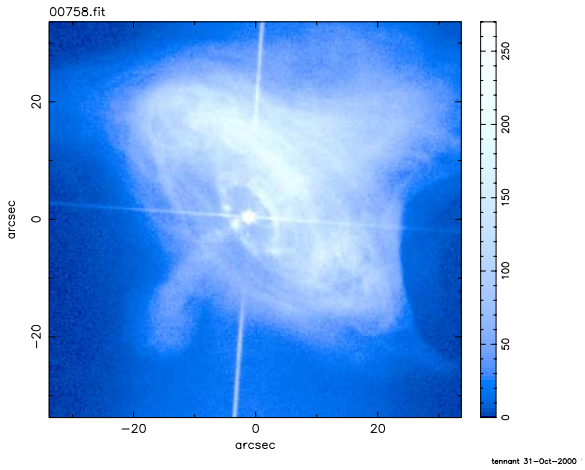


Fig. 2. *Chandra* LETG–HRC-S zeroth-order image of the Crab Nebula and Pulsar. The nearly vertical line is the dispersed spectrum of the pulsar. The nearly horizontal line is the cross-dispersed spectrum produced by the LETG fine support bars.

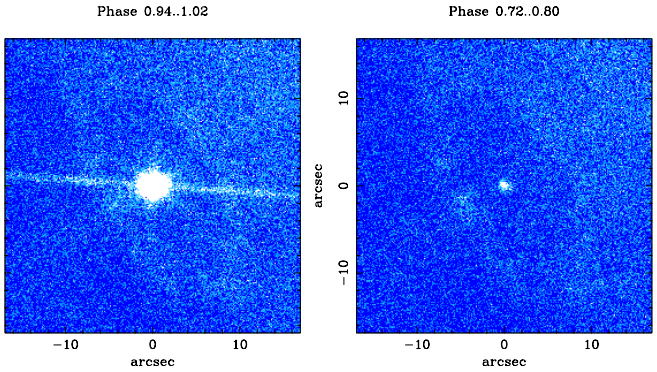


Fig. 3. LETG–HRC-S zeroth-order images of the Crab Pulsar and inner nebula (ObsID 758) at pulse maximum (left) and at pulse minimum (right). The X-ray pulsar is clearly discernible at all pulse phases.

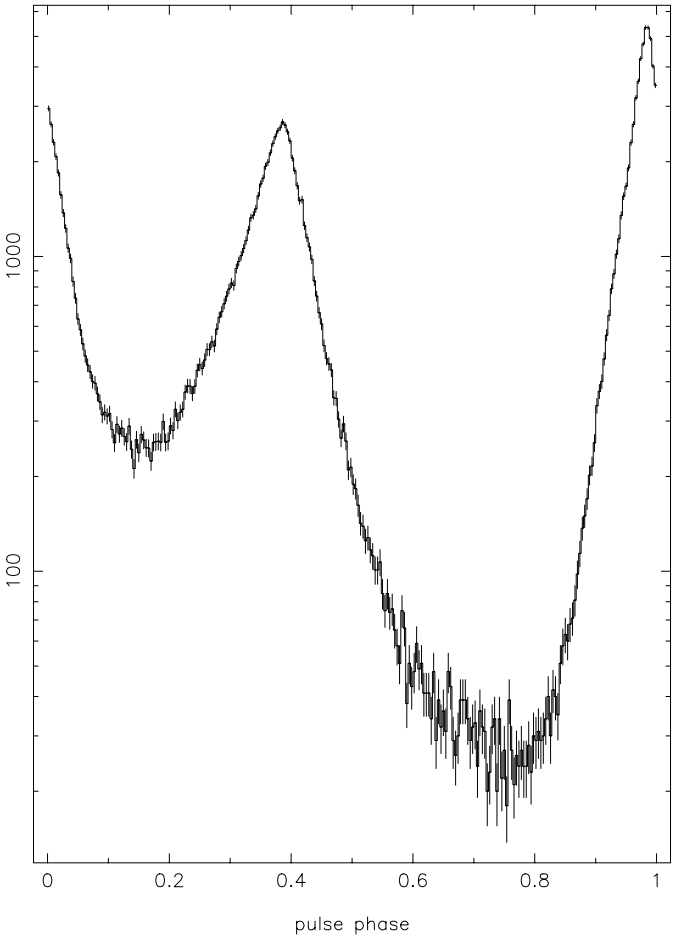


Fig. 4. The light curve of the Crab pulsations from Tennant et al. (2001).

pulsed emission served as another reason — in particular, the ratios of flux at pulse minimum to that at pulse maximum are similar in both bands. The absence of a pronounced floor in the X-ray pulse profile shown in Fig. 4 is another, qualitative consideration.

Subsequently, we (Weisskopf et al. 2002, in preparation) analyzed the dispersed data (ObsID 759), studying the spectral evolution as a function of pulse phase. Our analysis shows a variation of power-law spectral index with pulse phase (Fig. 5) that is in semi-quantitative agreement with previous measurements (e.g., Pravdo, Angelini, & Harding 1997; Massaro et al. 2000) at various different energies. The Chandra results extend the phase coverage through pulse minimum, in that prior observations had to treat the data at pulse minimum as background – a necessary, but incorrect, assumption. These analysis show that there is no reason to invoke a thermal component, and result in an independent upper limit similar to that based only on the imaging data. Unfortunately, neither limit challenges current theories of neutron star cooling. Nevertheless, analysis of these data suggest a new experiment, which we are proposing for Chandra Cycle-4, that can efficiently accomplish this objective.

As part of the spectral analysis, our colleague Frits Paerels emphasized that that scattering of point-source radiation by interstellar dust grains produces a wavelength-dependent (both in intensity and width) scattering halo (Mauche & Gorenstein 1986, and references therein) and that this scattering also requires an aperture correction to the effective-area curve. Fig. 6 compares the energy dependence of interstellar absorption with that of dust scattering. The characteristic scattering angle is of order 10 arcmin and scales approximately as (1 keV)/E. Thus, we effectively measure only the unscattered flux from the point source in our narrow aperture, so that dust scattering produces an energy-dependent modulation of the point-source continuum. Failure to account for dust scattering in the spectral fitting *overestimates* the hydrogen column, in this case by about 20%.

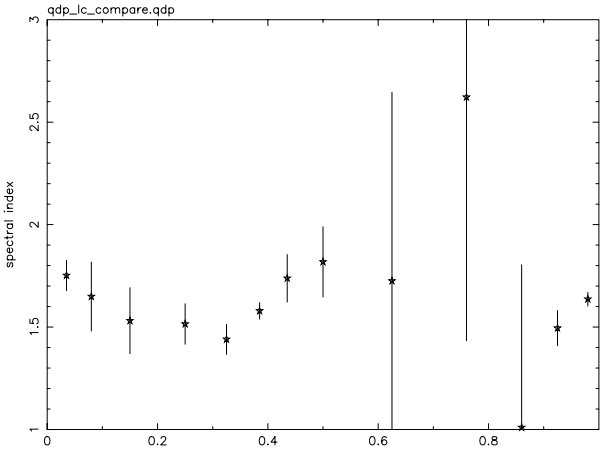


Fig. 5. Spectral index of the Crab Pulsar versus pulse phase.

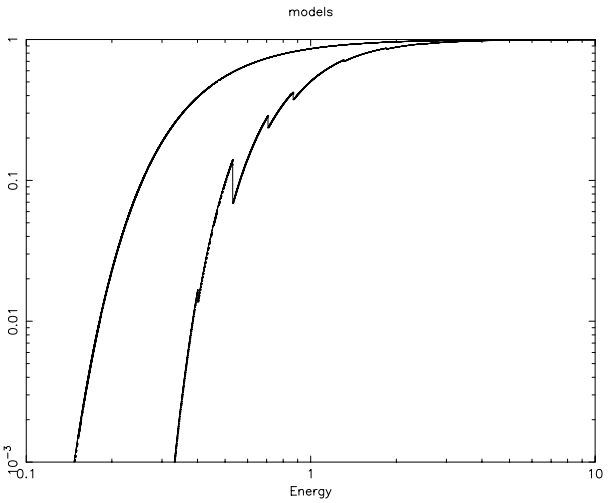


Fig. 6. Spectral dependence of dust scattering (smooth curve) and of interstellar photo-electric absorption.

2.2. Vela Pulsar

Fig. 7 shows the beautiful image (Pavlov et al. 2001a, 2001b) of the Vela Pulsar and the complex morphology — similar to that of the Crab, and B1509-58 (see below) — of its surrounding nebula. In that this symposium concentrates on the neutron stars themselves, I shall not discuss the fascinating morphology of the pulsar-wind driven nebula here. As with the Crab Pulsar, the angular resolution of *Chandra* is essential to probing the detailed spectral properties of the pulsar and to isolate these from those of the nebula. Pavlov et al. performed observations using the Low-Energy Transmission Grating with the High-Resolution Camera (LETGS) and using the Advanced CCD Imaging Spectrometer (ACIS) back-illuminated CCDs, in order to characterize the spectral properties. Separate fits to LETGS and ACIS-S3 data determined the spectral parameters. However, the data were

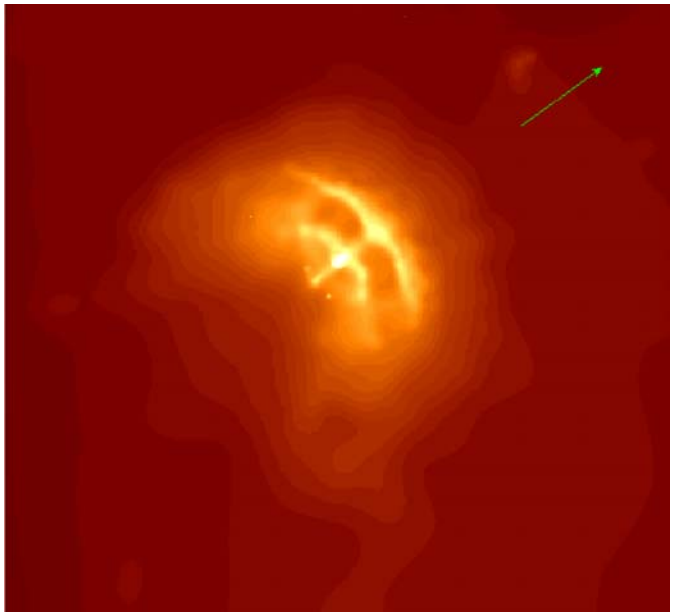


Fig. 7. Smoothed *Chandra* image of the Vela Pulsar. In this 3.5-arcmin-square image, the green arrow denotes the proper-motion direction. The image is courtesy of NASA/PSU/Pavlov et al. (2001a).

insufficient to discriminate fully between various spectral models — blackbody plus power law versus a hydrogen atmosphere plus power law. Nevertheless, an important result was the evidence for a harder spectral component — a thermal interpretation leading to "an implausibly small size" of 10 m (stretching even a quark-star interpretation!!) — thus indicating spectral similarities with middle-aged ($10^5 - 10^6$-y) X-ray pulsars.

2.3. B1509-58

Fig. 8 shows the young pulsar B1509-58, within SNR G230.4-1.2 in the constellation Circinus. This is another example of a pulsar-driven (plerionic) synchrotron nebula, the complex structure of which *Chandra* resolves dramatically.

2.4. G292.0+1.8

Along with Cas A and Puppis, SNR G292.0+1.8, with a 1700-y estimated age (Murdin & Clark 1979; Braun et al. 1983) is one of three known oxygen-rich supernovae in the Galaxy. Hughes et al. (2001) performed a moderately long ACIS–S3 observation (Fig. 9), detecting a bright, spectrally hard, point source within an apparently extended region. This suggested the presence of a pulsar and its pulsar-wind nebula. Indeed, subsequent radio observations (Camillo et al. 2002) detected a 135-ms pulsar, noting that "X rays provide an important complement to the radio band, the traditional hunting ground of pulsar studies." Camillo et al. (2002) also report that follow-up

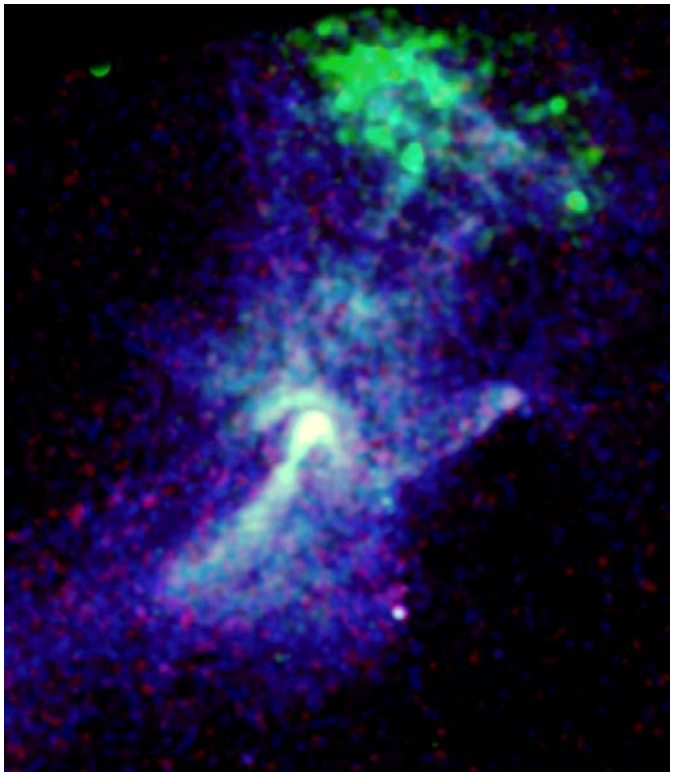


Fig. 8. *Chandra* ACIS image of pulsar B1509-58 in SNR G230.4-1.2. The colors in this 10×14-arcmin image indicate relative intensity. The image is courtesy NASA/MIT/Gaensler et al.

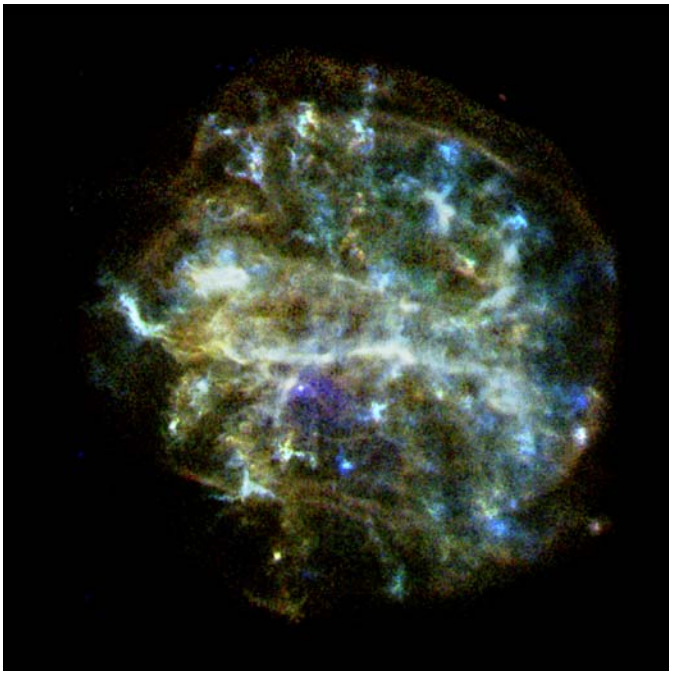


Fig. 9. *Chandra* ACIS-S image of the oxygen-rich SNR G292.0+1.8, with the pulsar lying southeast of the center. In this 9-arcmin-square image, the colors indicate relative intensity. The image is courtesy NASA/CXC/Rutgers/Hughes et al.

X-ray observations (Hughes et al. 2002, in preparation) confirm the presence of X-ray pulses with a period consistent with the radio observations. The X-ray spectroscopy is consistent with a simple power law, although, as with Vela, the model fit is not unique. It is interesting to note that the spin-down age is 2900 years, in contrast to the 1600–1700 years inferred from the supernova remnant.

2.5. G11.2-0.3

Kaspi et al. (2001) used *Chandra* to obtain the precise location of the 65-ms pulsar at the center of G11.2-0.3. The X-ray image (Fig. 10) reveals the presence of a pulsar-wind nebula around the pulsar, which lies within 8 arcsec of the center of the SNR shell, consistent with the historical supernova of 386. Because the spin-down age exceeds the historical age (as with G292.0+1.8) by a factor of 12, Kaspi et al. (2001) argue against the assumption that all pulsars are born with a very short period, as was the Crab Pulsar. Invoking a larger birth period (closer to 62 ms) obviates the need for non-conventional spin-down.

2.6. IC443

A sociologically, as well as scientifically, interesting *Chandra* result was the detection of a point source in SNR IC443 (Fig. 11) by high-school students from the (Durham) North Carolina School of Mathematics and Science. Their efforts led to winning the team award of the 2000 Siemens–Westinghouse Science and Technology Competition. (One of these students — Mr. Olbert, now at Columbia University — is presenting a poster paper at this symposium.) The limited spectral data from this short (10-ks) observation are consistent, but not uniquely, with a 0.7-keV blackbody. (See, however, Bocchino & Bykov 2001 for an XMM-*Newton* viewpoint.)

2.7. Others

The above examples indicate the significance and utility of *Chandra* observations of compact objects in SNRs. See also Kaspi et al. (2002) for a discussion of the detection of PSR B1757-24 and Pavlov et al. (2001b) for a discussion of the compact object in the RX J0852.0-4622 SNR. I apologize for failing to reference other papers relevant to this topic.

3. Transients in Quiescence

X-ray transients spend a considerable fraction of their time in quiescence. Data from *Chandra* observations have been used to test models of the emission mechanism in the quiescent state. We discuss here *Chandra* observations of Cen X-4, Aquila X-1, and KS 1731-260.

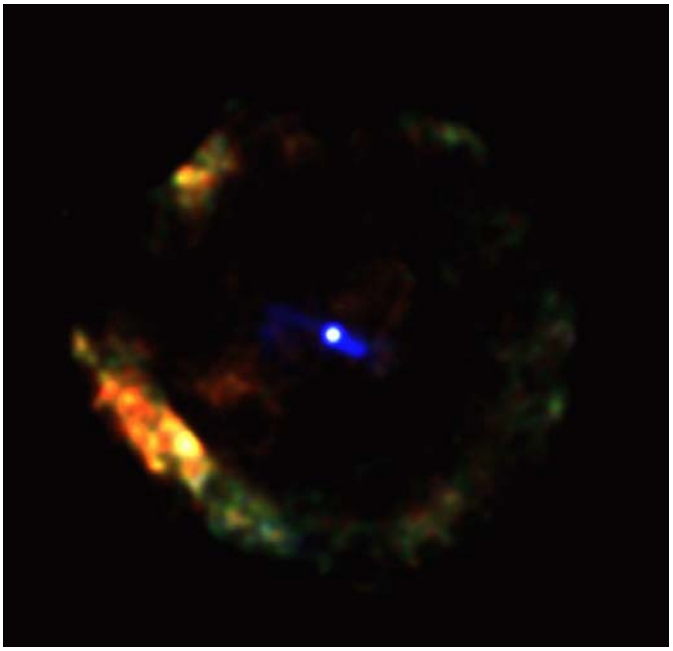


Fig. 10. *Chandra* ACIS image of SNR G11.2-0.3, with its central pulsar and faint pulsar-wind inner nebula. In this 5.8×5.4-arcmin image, the colors denote 0.6–1.65-keV (red), 1.65–2.25-keV (green), and 2.25–7.5-keV (blue) energy bands. The image is courtesy NASA/McGill/Kaspi et al. (2001)

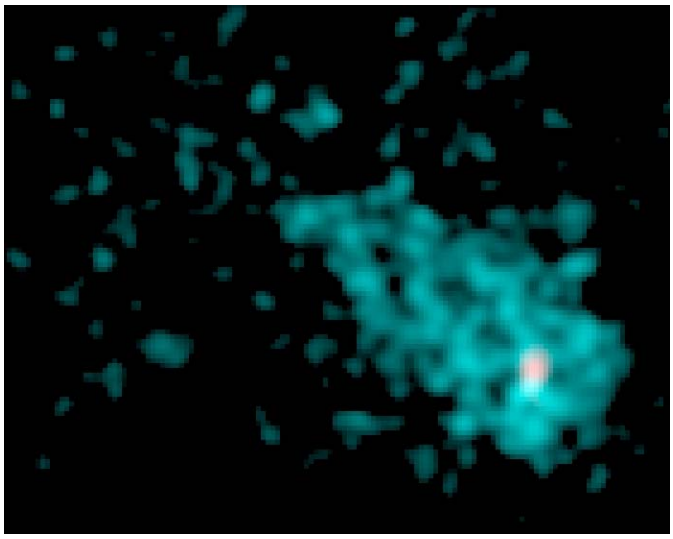


Fig. 11. *Chandra* ACIS image of SNR IC443. In this 1.0 × 0.8-arcmin image, the colors denote intensity. The image is courtesy NASA/NCSSM/Olbert et al.

3.1. Centaurus X-4 and Aquila X-1

Rutledge et al. (2001a, 2001b) have analyzed *Chandra* observations of Cen X-4 and Aquila X-1 in quiescence. Their analysis — discussed in terms of the detailed model by Brown, Bildsten, & Rutledge (1998) — emphasizes that a blackbody spectrum is not an appropriate description of a weakly magnetic transient in quiescence. For Cen X-4, the authors find that no single-component spectral model produces a statistically acceptable fit. While there is no unique two-component model, the authors use astrophysical arguments to interpret the data in terms of thermal plus power-law emission, deducing a radius for the neutron star.

For Aquila X-1, the spectral situation is both simpler and more complicated. Although the data are consistent with thermal emission from a pure hydrogen atmosphere on the neutron star, models that include an additional power-law component (indicated by non-*Chandra* observations) give equally acceptable fits. As with Cen X-4, the authors invoke astrophysical arguments to down-select spectral models.

3.2. KS 1731-260

KS 1731-260 differs from the above-mentioned two X-ray transients, in the duration of the transient activity. The observation of type-I X-ray bursts from KS 1731-260 substantiate it's neutron-star identification. The principal difference between this source and Cen X-4 and Aquila X-1 is that its outburst phase is apparently longer — perhaps more than 12 years. Wijnands et al. (2001), who performed a 20-ks *Chandra* ACIS-S observation during quiescence, summarize these and other characteristics. The spectral fits do not distinguish statistically between a blackbody (kT = 0.3 keV) and a pure, very soft power-law model (photon index > 4). Their discussion, based on the blackbody fit and other assumptions, concludes that either the star has spent much of its life in quiescence for it to cool, or that neutrino cooling has been enhanced compared to Aquila X-1.

4. Isolated Neutron Star RX J1856.5-3754

Burwitz et al. (2001) obtained a 56-ks LETGS observation of the isolated neutron star RX J1856.5-3754. They found that none of the possibly relevant neutron-star atmosphere models, at least those neglecting magnetic fields, yield as good a spectral fit as a simple blackbody. Furthermore, they found no evidence for electron cyclotron resonance lines. Subsequent to these observations, *Chandra* Director's Discretionary time increased the exposure to over 500 ks, with the data being immediately public. Early analysis of these data (Walter (2001); Burwitz, these proceedings) confirm the original results and set more stringent limits on the presence of any line features. I am convinced that we have not begun to appreciate the implications of this observation. (Subsequent to the symposium, Drake et al. (2002) made the bold suggestion that these data may be interpreted as evidence for a quark star. However, see Pons et al. (2002) for an opposite view.)

5. Conclusions

High-spatial-resolution spectrometric images — such as those obtained by *Chandra* — are necessary to enhance our understanding of neutron stars in SNR and of pulsar-wind nebulae. Higher-throughput but lower-angular-resolution X-ray missions — such as XMM-*Newton* and the planned Constellation X — will benefit from the complementary capabilities of *Chandra*'s high angular resolution.

I am somewhat concerned that much of the current data do not adequately distinguish between spectral models. Certainly, one factor is simply the limited statistics of the earliest and typically short observations. As mentioned above, using *Chandra* data to guide analysis of the far less photon-starved XMM-*Newton* data will help, if statistical limitations underlie these ambiguities. As high-throughput missions drive down the statistical errors, it will be necessary to reduce uncertainties in the instrumental response and to develop even more detailed and accurate astrophysical models. These are areas that obviously need more work. Nevertheless, these early *Chandra* results are clearly stimulating and exciting. As we should expect, the wealth of *Chandra* and XMM-*Newton* data is challenging current views of pulsar and pulsar-wind-nebula emission mechanisms.

Acknowledgements. I gratefully acknowledge support by NASA, by the Heraeus Foundation, and by the Max-Planck-Institut für Extraterrestriche Physik in Garching. In addition I thankfully acknowledge the comments and clarifications to the manuscript made by my colleague Steve O'Dell whose abilities to express his thoughts is writing are outstanding.

References

Bocchino, F. & Bykov, A.M. 2001, A&A, 376, 248
Braun, R., Goss, W.M., Danziger, I.J. & Boksenbeg, A. 1983, in IAU Symposium 101, Supernova Remnants and their X-Ray Emission, ed. P. Gorenstein & J. Danziger (Dordecht: Reidel) 159
Brown, E.F., Bildsten, L.& Rutledge, R.E. 1998, ApJ, 504, L95
Burwitz, V., Zavlin, V.E., Neuhauser, R., Predehl, P., Trumper, J. & Brinkman, A.C. 2001, A&A, 379, L35
Camilo,F. Manchester,R.N., Gaensler,B.M., Lorimer,D.R. & Sarkissian,J. 2002, ApJ, 576, L71
Drake, J.J., Marshall, H.L., Dreizler, S., Freeman, P.E., Fruscione, A., Juda, M., Kashyap, V., Nicastro, F., Pease, D.O., Wargelin, B.J. & Werner, K. 2002, ApJ, accepted for publication
Golden, A., Shearer, A. & Beskin, G.M. 2000, ApJ, 535, 373.
Gaensler, B.M., Arons, J., Kaspi, V.M., Pivovaroff, M.J., Kawai, N. & Tamura, K. 2002, ApJ, 569, 878
Hughes, J. P., Rakowski, C. E., Burrows, D. N. & Slane, P. O. 2000, ApJ, 528, L109
Hughes, J.P., Slane, P.O., Burrows, D.N., Garmire, G.P., Nousek, J.A., Olbert, C.M. & Keohane, J.W. 2001, ApJ, 559, L153
Kaspi, V.M., Roberts, M.E., Vasisht, G., Gotthelf, E.V., Pivovaroff, M. & Kawai, N. 2001, ApJ, 560, 371
Massaro, E., Cusumano, G., Litterio, M. & Mineo, T. 2000, A&A, 361, 695
Murdin, P. & Clark, D.H. 1979, MNRAS, 328, 17
Olbert, C.M., Clearfield, C.R., Williams, N.E., Keohane, J.W. & Frail, D.A., Apj, 554, L205
Pavlov, G.G., Kargaltsev, O.Y., Sanwal, D. & Garmire, G.P. 2001, ApJ, 554, L189
Pavlov, G.G., Zavlin, V.E., Sanwal, D., Burwitz, V. & Garmire, G.P. 2001, ApJ, 552, L129
Pavlov, G.G., Sanwal, D., Kiziltan, B. & Garmire, G.P. 2001b, ApJ, 559, L131
Pons, J.A., Walter, F.M., Lattimer, J.M., Prakash, M., Neuhauser, R. & An, P. 2002, ApJ, 564, 981
Pravdo, S.H., Angelini, L. & Harding, A.K. 1997, ApJ, 491, 808
Rutledge, R.E., Bildsten, L., Brown, E.F., Pavlov, G.G. & Zavlin, V.E. 2001, ApJ, 551, 921
Rutledge, R.E., Bildsten, L., Brown, E.F., Pavlov, G.G. & Zavlin, V.E. 2001, ApJ, 559, 1054
Tennant, A.F., Becker, W., Juda, M., Elsner,R.F., Kolodziejczak,J.J., Murray,S.S., O'Dell,S.L., Paerels,F., Swartz,D.A., Shibazaki,N., & Weisskopf,M.C. 2001a, ApJ, 554, L173
Walter, F.M. 2001, BAAS, 109, 105.3
Weisskopf, M.C., Hester, J.J., Tennant, A.F., Elsner, R.F., Schulz, N.S., Marshall, H.L., Karovska, M., Nichols, J.S., Swartz, D.A., Kolodziejczak, J.J., & O'Dell, S.L. 2000, ApJ, 536, L81
Wijnands, R., Miller, J.M., Markwardt, C., Lewing, W.H.G. & Van der Klis, M. 2001, 560, L159

Proceedings of the 270. WE-Heraeus Seminar on: *"Neutron Stars, Pulsars and Supernova Remnants"*
Physikzentrum Bad Honnef, Germany, Jan. 21-25, 2002, eds. W. Becker, H.Lesch & J. Trümper, MPE Report 278, pp. 64- 86

X-ray Observations of Neutron Stars and Pulsars: First Results from XMM-Newton

W.Becker, B.Aschenbach

Max–Planck–Institut für extraterrestrische Physik, Giessenbachstraße, 85741 Garching, Germany

Abstract. The X-ray Multi-Mirror Mission XMM-Newton is ESA's largest observatory so far; it is dedicated to explore the Universe in the $0.2 - 15$ keV X-ray band of the electromagnetic spectrum. Because of its large collecting area very faint sources not accessible before can be observed and it is therefore the long awaited instrument to study young pulsars and neutron stars in supernova remnants, cooling neutron stars and millisecond pulsars at X-ray energies. The high throughput of the instruments, which all are operated simultaneously, provide high resolution spectral, spatial and temporal information from a source during a single observation and make XMM-Newton unique and best suited for pulsar studies. In this article we briefly describe the instrument capabilities useful for pulsar observations and provide information on the timing accuracy on the relative and absolute scale. We further provide scientific results from observations of the Crab-pulsar, PSR J1617-5055 near RCW 103, of young neutron stars in the supernova remnants RX J0852-4622, Puppis-A and RCW 103 including 1E161348-5055.1 which is identified to be the second binary in a supernova remnant. In addition we report on observations of the cooling neutron star PSR B1055-52 and on the millisecond pulsar PSR J0030+0451 which all were observed by XMM-Newton during the first two years of scientific operation.

1. Introduction

X-ray observatories like ROSAT, ASCA, BeppoSAX and RXTE have achieved an important progress in neutron star and pulsar astronomy. The identification of Geminga and of cooling neutron stars (Halpern & Holt 1992; Ögelman 1995 and references therein), the discovery of pulsed X-ray emission from millisecond pulsars (Becker & Trümper 1993) and of the first accreting X-ray ms-pulsar SAX J1808.4-3658 (in't Zand et al. 1998; Wijnands & van der Klis) are only a few of the fascinating results. ROSAT's predominant contribution was due to its favorable soft response down to 0.1 keV, which permitted to observe the very soft thermal emission from the neutron stars' surface, but the relatively small bandwidth of up to 2.5 keV precluded any broad band study of the pulsar emission. Any conclusive identification of the nature of the 'hard tails' indicated in various X-ray spectra of cooling neutron stars and ms-pulsars was therefore not possible. ASCA and the Narrow Field Instruments on BeppoSAX, on the other hand, were sensitive up to 10 keV and were very successful in discovering young neutron stars in SNRs by their hard X-ray emission (cf. Torii 1998; Saito 1998). The lack of high resolution imaging, however, did in most cases not allow to resolve any central compact X-ray source from the surrounding plerion or supernova remnant.

The expectations from an observatory like XMM-Newton, with its enormous collecting area, multi-instrumentation and wide energy bandwidth are therefore high, especially in the field of neutron star astronomy where the targets (apart from a few Crab-like objects) are known to be relatively faint X-ray emitters.

XMM carries three identical X-ray telescopes, each of which is equipped with an X-ray CCD camera in the focal planes, called EuroPean Imaging Camera (EPIC). Two of the cameras are constructed using Metal Oxide Semiconductor technology (MOS1 & MOS2) and the third camera is built in Positive-Negative depleted Silicon Semiconductor technology, therefore called PN-camera. About half of each of the beams of the two telescopes operating with the MOS's is intercepted by Reflection Grating Spectrometers (RGS1 & RGS2), which diffract the X-rays to two dedicated CCD detectors. Optical observations can be made with a separate co-aligned optical telescope called Optical Monitor (OM). The instruments can be operated in parallel and they provide various observation modes which are very well suited for pulsar studies. Table 1 summarizes the timing modes available for the PN and MOS detectors. Also listed are the detectors' field of view (in units of detector pixels and angular units) and the associated temporal resolution. Useful is the PN small-window mode which provides imaging information for a sky field of $\sim 4.4' \times 4.4'$ along with spectral and a ~ 6 ms temporal resolution. This mode has its benefit for timing studies of sources located in crowded regions or in supernova remnants. It prevents source confusion which often is found to be the limiting factor when using the faster timing modes.

Table 1. Instrument modes available on XMM-Newton for timing studies of pulsars. The image size is given in detector pixels and angular units. FOV is the full field of view.

EPIC PN Mode	Image size / pixel / FOV arcmin	Temporal resolution
Small window	2D - 64 × 64 / 4.4′ × 4.4′	5.67 ms
Fast-timing	1D - 64 × 199 / 4.4′ × 13.75′	0.02956 ms
Burst	1D - 64 × 199 / 4.4′ × 13.75′	0.0072 ms

EPIC MOS Mode	Image size / pixel / FOV arcmin	Temporal resolution
part. window1	2D - 100 x 100 / 1.8' x 1.8'	200 ms
part. window2	2D - 300 x 300 / 5.5' x 5.5'	700 ms
timing	1D - user defined pixel area	$\geq$ 1.5 ms

Note: In PN timing modes only CCD #4 (of 12 CCDs in total) is active whereas in MOS timing modes only the central CCD provides timing information and the remaining 6 chips are operated in imaging mode. Burst mode is designed for very bright sources up to 6.3 Crab only. The efficiency of the PN small-window mode is $\sim$ 30% of that of the PN timing mode. In burst mode it is only 3%. XMM's spatial resolution is $\sim$ 15" (HEW). The size of a CCD pixel is 1.1" × 1.1" and 4.125" × 4.125" for the MOS and PN camera, respectively.

For the PN fast-timing and burst modes the spatial and spectral information from a 64 × 199 CCD pixel array is condensed into a one dimensional 64 × 1 pixel array (1D-image), i.e. the spatial information in Y-direction is lost due to the continuous read-out of the CCD. In these modes, the complete photon flux (source plus DC emission from foreground or background sources located along the read-out direction) is accumulated and collapsed in the final 1D-image, severely reducing the signal-to-noise ratio and preventing the detection of X-ray pulsations from the target of interest. Soft-proton flares which are known to happen on various time scales and frequencies almost unpredictable can likewise produce enough DC flux to prevent the detection of X-ray pulsations from a pulsar of intermediate X-ray brightness if the fast-timing mode was selected for the observation. For pulsars with periods longer than $\sim$ 60 ms, the PN small-window mode is a good choice even in view of a $\sim$ 30% reduced efficiency compared with the fast-timing mode. For millisecond pulsar observations, however, the fast-timing mode is the only one which provides sufficient temporal resolution for timing studies.

The strong interest in XMM-Newton, especially for neutron star and pulsar research, is supported by the large list of sources accepted for observations in AO1 (cf. Table 2). The proposed science and accepted targets cover a wide range of different categories, from young pulsars in supernova remnants to cooling neutron stars, binary-pulsars, old but nearby pulsars and millisecond pulsars. Even a small survey for potentially X-ray bright rotation-powered pulsars is included.

In the following sections we will report on the first XMM observations of pulsars, browsing through the various categories from young Crab-like pulsars and neutron star candidates in supernova remnants to the very old millisecond pulsars, summarizing the most exciting results. Before we do so, however, we will briefly review the various emission processes discussed to be the source for the observed X-ray emission.

2. High-energy X-ray Emission Processes

As a result of observations with the satellite observatories ROSAT, ASCA and Chandra, the number of rotation-powered pulsars seen at X-ray energies has reached 51 (as of June 2002). Almost half of the detected pulsars are ms-pulsars. Several of these objects have been detected at optical wavelengths and at gamma-ray energies (cf. Tab.3 and Tab.4 for a summary), advocating for multi-wavelength studies of the pulsar emission. This approach is of great benefit as the physical processes which cause the emission in different wavelength bands are obviously related to each other. Although the quality of the data obtained with different instruments and/or in different wavebands is inevitably rather inhomogeneous, and the conclusions drawn on these data are to some extent unlikely to be solid in a number of cases, there is general consensus that the X-radiation detected from rotation-driven pulsars has to be attributed to various thermal and non-thermal emission processes including the following:

- Non-thermal emission from charged relativistic particles accelerated in the pulsar magnetosphere. This emission is characterized by power-law like spectra over a broad energy band. The emitted radiation can be observed from the optical to the gamma-ray band.
- Extended emission from pulsar-driven synchrotron nebulae. Depending on the local conditions (e.g., matter density of the ambient medium), these nebulae can be observed from radio through hard X-ray energies.
- X-ray and gamma-ray emission from interaction of relativistic pulsar winds with a close companion star or with the wind of a companion star.
- Photospheric emission from the hot surface of a cooling neutron star. In this case a modified blackbody spectrum and smooth, low-amplitude intensity variations with the rotational period are expected, observable from the optical through the soft X-ray range.

In many pulsars the observed X-ray emission is due to a mixture of different thermal and non-thermal processes. The available data do not always allow to discriminate between the different emission scenarios. This was true for

Table 2. List of Pulsars which are accepted for observations by XMM-Newton during AO1. Also listed is the main instrument (PN, MOS, RGS or OM) and the proposed exposure time in ksec. CAL indicates calibration targets which are observed at regular time intervals for calibration purposes and in various instrument modes and setups. *obs* indicates whether a target has been observed by June 2002. Category C-Targets are supposed to be optional and not guaranteed to be observed.

Young Pulsars	Status	Instrument	Exposure
PSR B0531+21	obs	EPIC PN/MOS	CAL
PSR 0540-69	obs	EPIC PN/MOS	CAL
PSR 1509-58	obs	EPIC PN/MOS	20
PSR B0833-45	obs	EPIC RGS	90
PSR B1811-19	obs	EPIC PN/MOS	30
PSR J0537-6909	obs	EPIC PN/MOS	40
PSR J1709-4428	obs	EPIC PN/MOS	90
PSR B1046-58		EPIC PN/MOS	30
PSR B1823-13	obs	EPIC PN/MOS	55
PSR J1119-6127		EPIC PN/MOS	C60
PSR B1800-21		EPIC PN/MOS	C40
ms-Pulsars			
PSR J0030+0453	obs	EPIC PN/MOS	30
PSR J0437-4715		EPIC PN/MOS	70
PSR J1024-0719		EPIC PN/MOS	80
PSR J2124-3358	obs	EPIC PN/MOS	70
PSR J0218+42	obs	EPIC PN/MOS	35
PSR J1012+53	obs	EPIC PN/MOS	20
PSR J0034-0534	obs	EPIC PN/MOS	30
PSR J0751+18	obs	EPIC PN/MOS	40
Binary Pulsars			
PSR B1259-63	obs	EPIC PN/MOS	10
PSR B1259-63	obs	EPIC PN/MOS	10
PSR B1259-63	obs	EPIC PN/MOS	10
PSR B1259-63	obs	EPIC PN/MOS	10
PSR B1259-63		EPIC PN/MOS	10
PSR B1259-63		EPIC PN/MOS	10
PSR B1259-63		EPIC PN/MOS	10
PSR B1259-63		EPIC PN/MOS	10

Cooling NS	Status	Instrument	Exposure
PSR B0656+14	obs	EPIC PN/MOS	40
Geminga	obs	EPIC RGS	40
PSR B1055-52	obs	EPIC PN/MOS	80
PSR J0358+5413	obs	EPIC PN/MOS	30
PSR J0538+2817		EPIC PN/MOS	20
Old nearby NS			
PSR B1929+10		EPIC PN/MOS	35
PSR 0950+08		EPIC PN/MOS	100
PSR B0823+26	obs	EPIC PN/MOS	50
PSR J1908+0734		EPIC PN/MOS	C30
PSR J2043+2740		EPIC PN/MOS	20
Mini Survey			
PSR B0136+57		EPIC PN/MOS	5
PSR B0540+23		EPIC PN/MOS	5
PSR B0611+22	obs	EPIC PN/MOS	5
PSR J0631+1036	obs	EPIC PN/MOS	5
PSR B0740-28	obs	EPIC PN/MOS	5
PSR B0906-49	obs	EPIC PN/MOS	5
PSR B1221-63		EPIC PN/MOS	5
PSR B1449-64	obs	EPIC PN/MOS	5
PSR B1634-45	obs	EPIC PN/MOS	5
PSR B1719-37	obs	EPIC PN/MOS	5
PSR B1742-30	obs	EPIC PN/MOS	5
PSR J1757-2421	obs	EPIC PN/MOS	5
PSR B1757-244		EPIC PN/MOS	5
PSR J0117+5914		EPIC PN/MOS	5
PSR J1705-1906		EPIC PN/MOS	5
PSR J1730-3350		EPIC PN/MOS	5
PSR J1825-0935		EPIC PN/MOS	5
PSR J1856+0113		EPIC PN/MOS	5

ROSAT and ASCA observations and might still be true for Chandra and XMM data.

It is well established, however, that magnetospheric emission from charged particles, accelerated in the neutron star magnetosphere along the curved magnetic field lines, dominates the radiation from young *rotation-powered* pulsars with ages $\lesssim 5000$ years. Middle aged pulsars such as the three Musketeers PSR B0656+14, PSR B1055-52 and Geminga are seen to have composite spectra consisting of two or three components which are a soft thermal (cooling) and a hotter polar-cap component as well as some hard emission associated with non-thermal processes (cf. §4). For the millisecond pulsars, ROSAT and ASCA did not allow to conclusively clarify whether their emission is purely due to the presence of hot/heated polar-caps, due to non-thermal magnetospheric emission or a mixture of both or whether there exists even a dichotomy among the emission properties which correlates with the pulsar's spin-parameters. Chandra and XMM-Newton observations of the two ms-pulsars PSR J0437-4715 and PSR J0030+0451 (cf. §5) as well as the detection of 11 ms-pulsars in the Globular Cluster 47TUC seem to suggest that both, a thermal and a non-thermal emission component are present in all ms-pulsars though it is difficult to accomplish the gross similarity between the radio and X-ray pulse profiles with these two (or even more) different components at work.

3. Young Neutron Stars in Supernova Remnants

3.1. The Crab- and Vela-like Pulsars

The majority of the young Crab- and Vela-like pulsars have been observed by XMM-Newton during AO1 with the aim to study the pulsars' temporal emission properties along with a study of the pulsars' wind nebulae or a search for it. While a large fraction of data was delivered to the PIs only recently and are still in the process of data analysis, the Crab, PSR 0540-69 and PSR 1509-58 were

observed for the purpose of instrument calibration (clock and mirrors), and have undergone a first scientific analysis already.

Although the Crab has been observed with almost every instrument since its discovery, it is amazing to see how many new results were obtained with Chandra and XMM-Newton. First images taken with the Advanced CCD Imaging Spectrometer (ACIS) aboard Chandra have already provided spectacular details of the inner nebula structure associated with the pulsar-wind outflow — in addition to the torus ($r \approx 0.38$ pc) the *inner ring* ($r \approx 0.14$ pc), *jet* and *counter-jet* have been identified (Weisskopf et al. 2000). In the same observation, systematic variations of the X-ray spectrum were discovered throughout the nebula. A more detailed study of the spectral variations became possible with the XMM data, taken in March 2000 with the EPIC detectors (Willingale et al. 2001). Figure 1 shows an X-ray image of the Crab nebula in which the color coding is associated with the photon-index α of the nebula's X-ray spectrum, $dN/dE \propto E^{-\alpha}$. This image impressively illustrates the different shape of the spectra of the torus ($\alpha = 1.8 \pm 0.006$), the jet ($\alpha = 2.1 \pm 0.013$) and the outer nebula regions ($\alpha = 2.34 \pm 0.006$). Similar results were obtained by Chandra, measuring the hardness ratio distribution throughout the nebula (Weisskopf et al. 2000). For the pulsar, a photon spectral index of $\alpha = 1.63 \pm 0.09$ is determined from out-of-time events selected along the read-out direction of the CCDs, and thus not affected by pile-up. The spectral difference between the jet and the torus is found to be likely due to an intrinsically steeper electron spectrum of the jet. The outer regions of the nebula show the steepest spectrum, which is likely to be due to enhanced synchrotron losses of the electrons during their ride from the pulsar to the outskirts (Willingale et al. 2001).

Observations with the High Resolution Imager (HRI) aboard ROSAT has already shown that at least $\sim 75\%$ of the Crab-pulsar's total soft X-ray flux is emitted from the co-rotating magnetosphere (Becker & Trümper 1997). Recent observations with the High Resolution Camera aboard Chandra by Tennant et al. (2001) at an angular resolution of ≤ 1 arcsec has improved this number in showing that in the $0.5 - 10$ keV band the pulsed fraction is $\sim 85\%$. The high pulsed fraction along with the monthly published radio ephemeris (Lyne et al., 2002) makes the Crab therefore an excellent target for the XMM-clock calibration. The Crab-pulsar was observed for that reason in March 2000, 2001 and 2002 with the PN in timing and burst mode, respectively. Because of the pulsar's brightness only the burst mode provides accurate spectral information not affected by pile-up effects, though the detector life time in that mode is only 3%. We have analyzed the Crab data from all orbits (cf. Fig.2) and found that the pulsar period deduced from the XMM data matches to better than 2.5×10^{-10} s the radio period given in the Jodrell Bank monthly Crab ephemeris (Lyne et al., 2002).

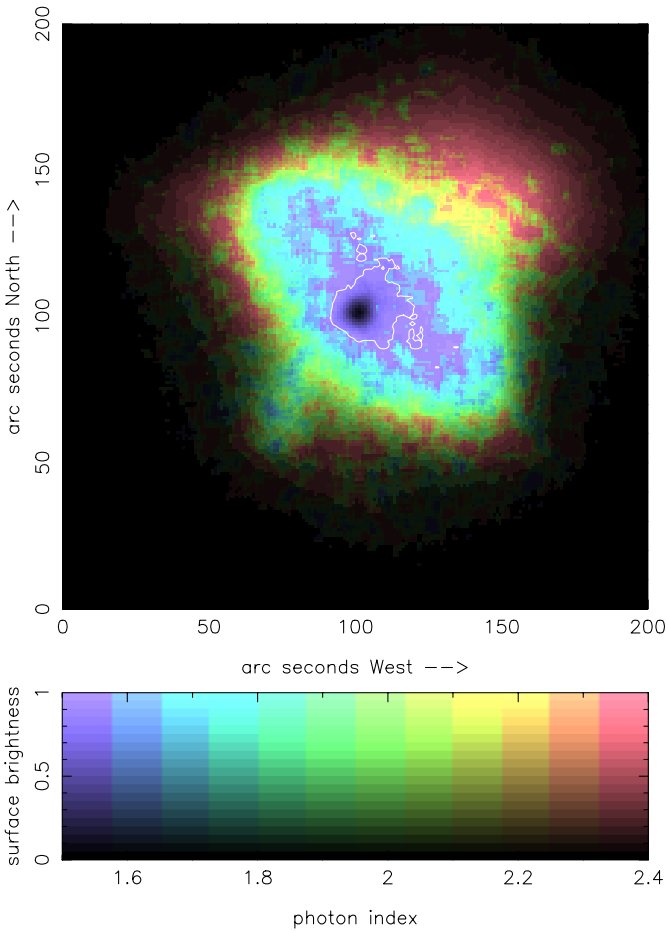


Fig. 1. The Crab as observed with the European Imaging Camera aboard XMM-Newton. The image has been spatially oversampled, using a bin size of 1 arcsec (instrument HEW $\sim$ 15 arcsec). The color coding of surface brightness and photon index is shown in the lower panel. The white contour encircles the region compromised by pile-up. (From Willingale et al. 2001)

The difference is within the expected statistical uncertainty[1].

In addition to the relative timing we checked the accuracy of the XMM clock on the absolute scale by comparing the arrival time of the Crab pulsar's main peak with that measured in the radio band (Lyne et al., 2002). We find that for all XMM data the arrival of the main peak leads the arrival of the main radio peak by 0.047 ± 0.001 in phase (modulo the pulsar period), corresponding to a time difference of 1.57 ms (modulo the pulsar period). Rots et al. (2000) have analyzed all Crab data taken with RXTE since the start of the mission in January 1996 and found that the phase of the main X-ray peak is different from the

[1] In previous versions of XMM-SAS the barycenter correction code was erroneous, leading to discrepancies of periods derived from EPIC data and compared to, e.g. radio ephemeris of up to $\Delta P/P = 7 \times 10^{-6}$ (Kuster et al. 2002). The code was fixed recently (SAS 5.3 and later versions) which improved the EPIC relative timing by three orders of magnitude.

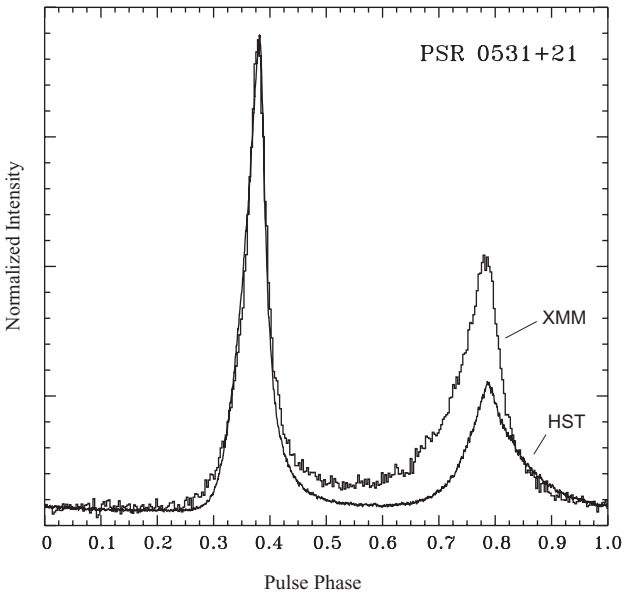


Fig. 2. The Crab pulse profile observed with the XMM-Newton and Hubble Space observatories. Peaks of the main pulse have been co-aligned in phase. A slight phase difference between the main and the second peaks is apparent which suggests a small energy dependence of the phase shift between main and secondary pulse peak.

radio peak by $\sim 300\mu$s. Depending on whether this phase difference observed in RXTE data is real or only reflects the accuracy of the RXTE timing, the phase alignment between radio and X-ray pulses measured by XMM is uncertain by $1.27 - 1.57$ ms on the absolute scale. Careful analysis of all modules involved in XMM's timing are currently in progress in order to improve the absolute clock accuracy.

Besides the Crab several other young pulsars have been observed by XMM during the first two years of scientific observations. One of these pulsars is PSR J1617 − 5055, which is a 69 ms pulsar located about 7 arcmin outside the boundary of the young supernova remnant RCW 103 (cf. Fig.9). The spin-down age of the pulsar is $\tau \sim 8000$ years (cf. Table 3) placing it among the youngest known radio pulsars. An association of RCW 103 and the pulsar was discussed but found to be unlikely (Dickel & Carter 1998; Kaspi et al. 1998). The pulsar distance is not very well constrained. The radio dispersion measure yields a distance of $6.1 - 6.9$ kpc (Taylor & Cordes 1993) whereas Kaspi et al. (1998) conclude from a comparison between dispersion measure based distances and distances obtained from HI absorption measurements of PSR 1641-45 and PSR 1718-35 - which are both located within 20° of PSR J1617−5055 - that the pulsar could be as close as ~ 4.5 kpc.

PSR J1617 − 5055 was discovered by its X-ray pulses in archival GINGA data (Torii et al. 1998). It was then detected also in the radio domain (Kaspi et al. 1998). With ASCA it was not possible to separate the pulsar from the close by RCW 103 supernova remnant, which limited modeling of the pulsar spectrum to energies > 3 keV (Torii et al. 2000). XMM-Newton has observed the pulsar in September 2001 for 30 ksec and for another 20 ksec but off-center because the target was RCW 103 (cf. §3.2). The XMM data of PSR J1617−5055 provide the first detailed pulsar spectrum in the $0.3 - 10$ keV band. Among various spectral models a power-law spectrum with a photon index of $\alpha = 1.1 - 1.4$ (90% confidence range) is found to be the simplest but acceptable description of the spectrum up to 10 keV ($\chi^2_\nu = 0.93$ for 121 dof). Thus the X-ray emission is classified as non-thermal. The emission turns out to be highly absorbed, with $N_H = (2.8 - 3.6) \times 10^{22}\,\mathrm{cm}^{-2}$, prohibiting any measurement of the softer cooling emission from the neutron star surface. Figure 3 shows the energy spectrum as observed by the EPIC MOS1/2. The X-ray flux in the 0.5−10 keV band is $f_x = (4.9 - 5.4) \times 10^{-12}\,\mathrm{erg\,s^{-1}cm^{-2}}$, implying a luminosity of $L_x = (2.1 - 2.3) \times 10^{34}\,\mathrm{erg\,s^{-1}}$ for a distance of $d = 6$ kpc. The inferred X-ray conversion efficiency is $L_x/\dot{E} = 1.4 \times 10^{-3}$ and 3.6×10^{-4} in the $0.5 - 10$ keV and $0.1 - 2.4$ keV band, respectively.

Diffuse X-ray emission associated with PSR J1617−5055, either because of the presence of a plerion or a supernova remnant, has not been detected in the XMM-Newton data (cf. Fig.9). Chandra observed PSR J1617−5055 in September 1999 and February 2000. We analyzed the public archive data, and found no indication of diffuse extended emission surrounding PSR J1617−5055 either (Becker et al., 2002a).

In order to investigate the pulsar's temporal X-ray emission properties we used the data from the EPIC-PN camera which was operated in timing mode with a temporal resolution of 0.03 ms (cf. Tab.1). The presence of the nearby RCW 103 supernova remnant required a tight roll-angle constraint of $268° - 270°$ for the lower and upper position angles in order to minimize source confusion with photons being recorded along the read-out direction of the CCD columns in which PSR J1617 − 5055 was placed. To extract the pulsar events we selected an area of 8×199 pixels from the central CCD #4 of the PN camera. According to the fractional encircled energy function this means that we sample about 70% of the source photons in x- and 100% in y-direction. After barycentrisation (we used the source position RA=16:17:29.45, DEC=-50:55:13.61) and correcting for the satellite orbit we searched for the pulsar period using an fft-based algorithm. To optimize the pulsar signal we blocked off all emission below 2.5 keV as the DC level at these energies is found to exceed the pulsar signal due to the emission from the nearby RCW 103, which reduced the signal-to-noise ratio and the detectability of the X-ray pulses significantly. But still with the remaining events we detected strong pulsed emission up to 15 keV. The pulse profile shows a single peak with a duty cycle of $\sim 50\%$ and it shows a pronounced similarity with the radio profile at 1.4 GHz reported by Kaspi et

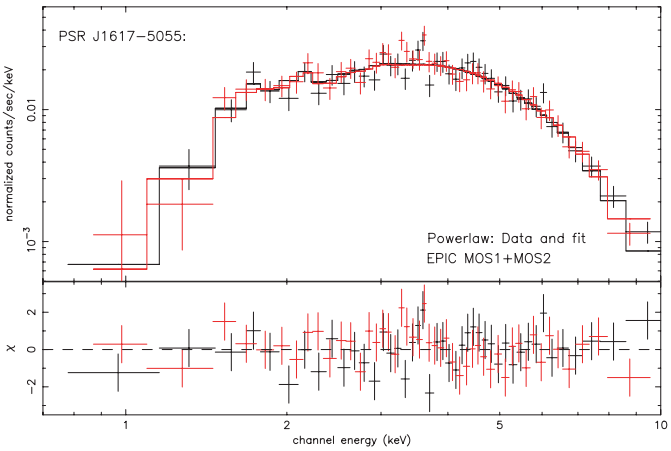


Fig. 3. X-ray spectrum of PSR J1617-5055 taken with MOS1/2 and fit by a power-law.

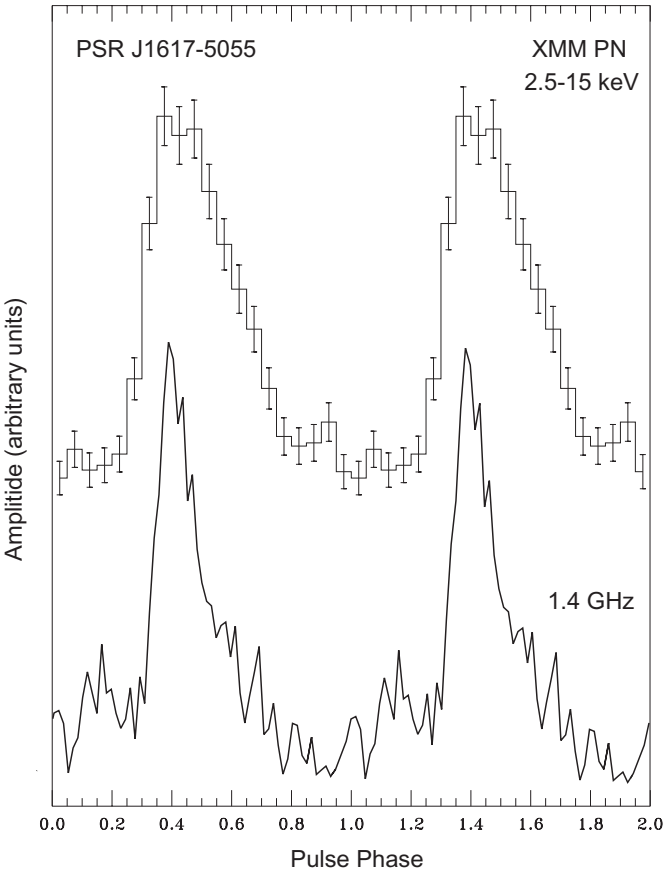


Fig. 4. X-ray and radio pulse profiles of PSR J1617-5055 as observed in the 2.5−15 keV band with the XMM EPIC-PN and at 1.4 GHz with the Parkes Radio Telescope. Both the X-ray and the radio profile show a single peak. The X-ray pulse has a duty cycle of ∼ 50% in the 2.5-15 keV band.Two pulsation cycles are shown for clarity. (The radio pulse profile has been adopted from Kaspi et al. 1998)

al. (1998). This suggests a close correlation between the radio and X-ray emission mechanisms (cf. Fig.4). Comparing the X-ray pulse profile of PSR J1617 − 5055 with those observed from other young pulsars we find a striking similarity with PSR 1509-58 and PSR 0540-69. For the epoch MJD=52155.5992851784, which is the mean epoch of the XMM observation in TDB at the solar system barycenter, we measure a period of $P = 69.37252615720$ ms. The accuracy of the XMM clock against UTC is good enough to measure the arrival time of the X-ray pulse which we find at phase 0.65 (center of mass of the pulse) for the epoch given above.

In order to investigate the energy dependence of the X-ray pulse we performed a timing analysis separately for the $2.5 - 4.5$ keV, $4.5 - 9.0$ keV and $9.0 - 15$ keV bands. Neither the overall shape of the pulse nor its phase is found to change with energy. The pulsed fraction we measured in the different energy bands using a bootstrap method (Swanepoel et al. 1996) is $48 \pm 4\%$, $57 \pm 4\%$ and $69 \pm 19\%$ in the $2.5 - 4.5$ keV, $4.5 - 9.0$ keV and $9.0 - 15$ keV bands, respectively. The fraction of the pulsed flux in the $2.5 - 15$ keV band is $53 \pm 3\%$.

3.2. Radio-silent Neutron Stars in Supernova Remnants

A fascinating result reflecting the advantage of wide-field spectro-imaging observations provided by ROSAT in its all-sky survey (RASS) is the discovery of the supernova remnant RX J0852.0-4622 by Aschenbach (1998). The remnant is located along the line of sight towards the south-east corner of the Vela supernova remnant (cf. Fig.5). Because the Vela SNR dominates the emission in the soft band, RX J0852.0-4622 is best visible in the RASS data at energies above ∼ 1 keV. The remnant has a circular shell-like shape with a diameter of 2 degrees. Although the distance to the remnant is quite uncertain, its free-expansion age ($t \sim 3.4 \times 10^3 v_{5k}^{-1} d_{1kpc}$ yr, with v_{5k} as expansion velocity in units of 5000 km/s) suggests a remnant age much younger than that of Vela. RX J0852.0-4622, often denoted as *Vela-Junior* because of its young age, turns out to be remarkable in several aspects. COMPTEL data suggest that the remnant has a 1.157 MeV γ-line from the radioactive isotope ^{44}Ti exclusively produced in supernovae (Iyudin et al. 1998). If true, the remnant could be as young as ∼ 620 years and as close as ∼ 200 pc (Aschenbach et al. 1999), making it the closest and youngest supernova remnant among the ∼ 250 remnants known today (Green 2000). However, as the detection of the ^{44}Ti line is of low significance, it leaves the age and distance estimates of the remnant widely unconstrained, but see Aschenbach et al. (1999) for a detailed discussion. ASCA observations have shown that the X-ray emission of the brightest parts of the remnant are dominated by non-thermal emission (Tsunemi et al. 2000; Slane et al. 2001) with a column density about one order of magnitude larger than what is known for the Vela supernova remnant. Together with SN1006 and G347.3-0.5, RX J0852.0-4622 thus form the first

Characteristics of the optical, X-ray and gamma-ray detected rotation-powered field pulsars.

Pulsar	Comment	detected						$\dot{E}/(4\pi d^2)$	$\log\dot{E}$	$\log L_x^{tot}$	$\log L_x^{puls}$	$\log L_x^{pn}$	$\log L_{bol}^{\infty}$	$\log(P/2\dot{P})$	P	$\dot{P}\times10^{-15}$	d	$\log B_{\perp}$
		R	O	X_s	X_h	γ_s	γ_h	erg/s/cm^2	erg/s	erg/s	erg/s	erg/s	erg/s	years	ms	s s^{-1}	kpc	Gauss
B0531 + 21	Crab	p	p	p	p	p	p	$9.3\cdot10^{-7}$	38.65	35.98	35.85	37.3	$\leq$ 34.1	3.10	33.40	420.96	2.00	12.58
B0833 − 45	Vela	p	p	p	p	p	p	$2.3\cdot10^{-7}$	36.84	32.25	31.25	32.95	$\sim$ 32.3	4.05	89.29	124.68	0.30	12.53
J0205 + 6449	in 3C58	-	-	p	-	-	-	$3.2\cdot10^{-8}$	37.42	32.20		34.31		3.73	65.67	193.52	2.60	12.55
J2229 + 6114	in G106.6+2.9	p	-	p	-	-	d	$2.0\cdot10^{-8}$	37.34	33.01				4.02	51.62	78.27	$\geq$ 3	12.30
J1617 − 5055	near RCW 103	p	-	p	-	-	-	$1.3\cdot10^{-8}$	37.20	33.76	33.48			3.91	69.33	136.05	3.30	12.49
B0633 + 17	Geminga	p	p	p	-	-	p	$1.1\cdot10^{-8}$	34.51	31.10	30.62		31.2	5.53	237.09	10.97	0.16	12.21
B1706 − 44	in G343.1-02.3	p	-	p	-	-	p	$8.6\cdot10^{-9}$	36.53	33.15			$\leq$ 33.5	4.24	102.45	93.04	1.82	12.49
B1509 − 58	in MSH 15-52	p	-	p	p	p	-	$7.7\cdot10^{-9}$	37.25	34.29	34.10	35.3	$\leq$ 33.9	3.19	150.23	1540.19	4.30	13.19
B1951 + 32	in CTB 80	p	-	d	-	-	p	$5.0\cdot10^{-9}$	36.57	33.44		34.0	$\leq$ 33.9	5.03	39.53	5.85	2.50	11.69
J1930 + 1852	in G54.1+0.3	p	-	p	-	-	-	$4.0\cdot10^{-9}$	37.08					3.46	136.85	750.20	$\sim$ 5	13.00
J1811 − 1926	in G11.2-0.3	-	-	p	-	-	-	$2.4\cdot10^{-9}$	36.80					4.38	64.67	44.00	$\geq$ 5	12.23
B1046 − 58	Vela twin	p	-	d	-	-	p	$1.9\cdot10^{-9}$	36.30	$\leq$32.11			$\leq$ 32.7	4.31	123.65	95.92	2.98	12.54
B1259 − 63*	Be-star/bin	p	-	d	d	d	-	$1.7\cdot10^{-9}$	35.92	32.95			$\leq$ 33.8	5.52	47.76	2.27	2.00	11.51
J0537 − 6909	in N157B/LMC	p	-	p	-	-	-	$1.6\cdot10^{-9}$	38.68					3.71	16.11	51.24	49.4	11.96
J1420 − 6048		p	-	p	-	-	-	$1.4\cdot10^{-9}$	37.00	34.46				4.11	68.18	82.85	7.70	12.38
B1823 − 13	Vela like	p	-	d	-	-	-	$1.4\cdot10^{-9}$	36.45	33.39			$\leq$ 33.9	4.33	101.45	74.95	4.12	12.45
B1800 − 21	G8.7−0.1	p	-	d	-	-	-	$1.2\cdot10^{-9}$	36.35	33.06			$\leq$ 33.8	4.30	133.61	134.32	3.94	12.63
B1929 + 10		p	d	p	-	-	-	$1.1\cdot10^{-9}$	33.59	30.00	29.5		$\leq$ 31.4	6.49	226.51	1.16	0.17	11.71
B0656 + 14	cooling NS	p	p	p	-	-	?	$5.5\cdot10^{-10}$	34.58	32.98	32.15		32.9	5.05	384.87	55.03	0.76	12.67
B0540 − 69	in N158A,LMC	p	p	p	p	-	-	$5.1\cdot10^{-10}$	38.17	36.21	36.1	37.2	$\leq$ 36.1	3.22	50.37	479.06	49.4	12.70
J1105 − 6107		p	-	d	-	-	-	$4.3\cdot10^{-10}$	36.40					4.80	63.19	15.80	7.00	12.00
B0950 + 08		p	?	d	-	-	-	$3.3\cdot10^{-10}$	32.75	29.35			$\leq$ 31.0	7.24	253.06	0.23	0.12	11.39
B1610 − 50		p	-	d	-	-	-	$2.5\cdot10^{-10}$	36.20					3.87	231.60	492.54	7.26	13.03
J0538 + 2817	in G180.0−1.7	p	-	d	-	-	-	$1.3\cdot10^{-10}$	34.69	32.74			$\leq$ 33.6	5.79	143.15	3.66	1.50	11.87
B1055 − 52	cooling NS	p	d	p	-	-	p	$1.1\cdot10^{-10}$	34.48	33.42	32.57		33.5	5.73	197.10	5.83	1.53	12.03
B0355 + 54		p	-	d	-	-	-	$8.8\cdot10^{-11}$	34.66	31.96			$\leq$ 33.8	5.75	156.38	4.39	2.07	11.92
B2334 + 61	G114.3+0.3	p	-	d	-	-	-	$8.6\cdot10^{-11}$	34.79	31.86			$\leq$ 33.4	4.61	495.24	191.91	2.46	12.99
B0823 + 26		p	-	d	-	-	-	$2.6\cdot10^{-11}$	32.66	29.83			$\leq$ 31.0	6.69	530.66	1.72	0.38	11.99

Table 3. List of rotation-powered pulsars that have been detected in the radio, optical, X- and/or γ-ray wavebands, ordered according to their spin-down flux density at Earth $\dot{E}/4\pi d^2$. The individual columns are as follows: 1. Pulsar name; 3-8. Energy ranges in which pulsed (p), unpulsed (d) radiation has been detected: R – radio, O – optical, X_s – soft X-rays ($E_\gamma \sim$ 1keV), X_h – hard X-rays ($E_\gamma \sim$ 10keV), γ_s – soft γ-rays ($E_\gamma \sim$ 1MeV) and γ_h – hard γ-rays ($E_\gamma >$ 100MeV). Possible detections are indicated by a question mark. $\dot{E}$ is the pulsar spin-down power $I\Omega\dot{\Omega}$; $L_x^{tot} = 4\pi d^2 f_x$ is the sum of the pulsed and unpulsed X-ray luminosity. L_x^{puls} is the pulsed luminosity; L_x^{pn} is the total X-ray luminosity including synchrotron nebula emission. All luminosities L_x are calculated for the ROSAT energy range 0.1 − 2.4 keV. For Geminga, PSR 0656+14 and 1055-52 thermal and non-thermal contributions are included. L_{bol}^{∞} is the bolometric luminosity. The upper limits have been computed for a neutron star with a medium stiff equation of state (FP-Model, $M = 1.4$ M$_\odot$ and $R = 10.85$ km). *PSR 1259-63 was observed $\sim 13°$ post-apastron. For references see Becker & Trümper (1997; 1999) and Becker & Pavlov (2002) and references therein. Radio pulsar parameters have been taken from Manchester et al. (2002). A summary of the optical and γ-ray observations can be found in Caraveo et al. (2002) and Kanbach (2002, this proceedings).

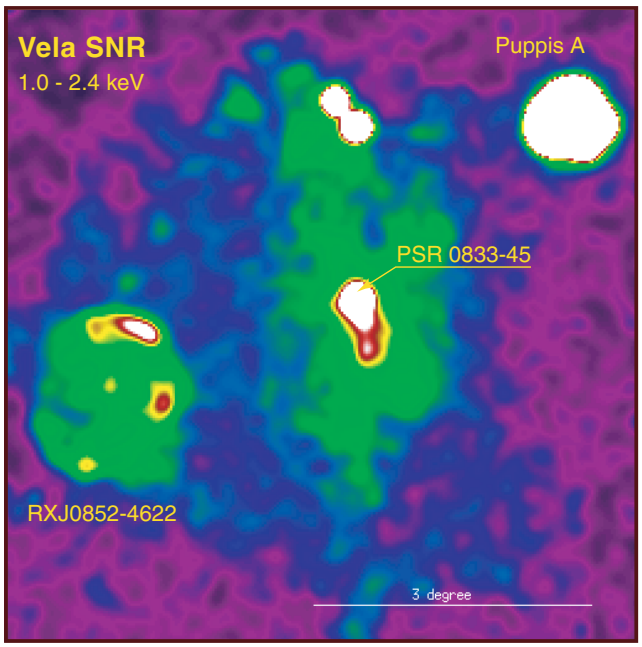


Fig. 5. Vela and friends: The two supernova remnants Puppis-A and RX J0852.0-4622 are both located at the edge of the Vela supernova remnant. Emission from the neutron star CXOU J085201.4-461753 is clearly visible in the ROSAT all-sky survey image near to the center of RX J0852.0-4622.

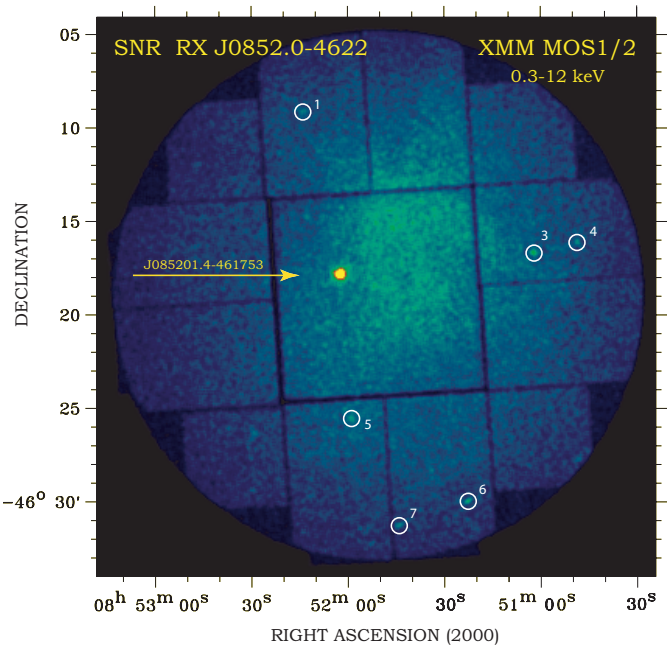


Fig. 6. XMM's view of the ~ 30 arcmin diameter part centered on RX J0852.0-4622. Data from MOS1 and MOS2 have been merged to produce the image. A few other faint and point-like sources, indicated by circles, are detected in the field of view.

members of the exclusive group of non-thermal shell-type supernova remnants, believed to be accelerators of cosmic rays. The lack of strong variation in N_H across RX J0852.0-4622 further indicates that the remnant cannot be more distant than the Vela Molecular Ridge (Slane et al. 2001), locating it most likely behind the Vela remnant at a distance between 1-2 kpc.

The remnant and its emission properties are interesting by its own and justify deep and detailed X-ray studies, but a compact central X-ray source has been detected in the remnant as well. First recognized as a 5σ excess in the RASS data by Aschenbach et al. (1998) its existence was supported by the detection of a hard, somewhat extended X-ray source in the ASCA data (Tsunemi et al. 2000; Slane et al. 2001). To conclusively identify this source as the compact remnant of the supernova explosion that created RX J0852.0-4622 was not possible because of the presence of two foreground stars (HD 76060 and Wray 16-30) which could be responsible for at least part of the central X-ray emission. But a recent observation with the Chandra ACIS-I has clearly invalidated the association with either one of these stars (Pavlov et al. 2001) and another faint but hard X-ray source found by Mereghetti (2001) in a recent BSAX observation. In view of this, there is little doubt that the central X-ray source CXOU J085201.4-461753, located only 4 arcmin off the geometrical center of RX J0852.0-4622, indeed is the compact remnant of the supernova explosion. This is further supported by the f_x/f_{opt} ratio as the source has no optical counterpart brighter than $m_B \sim 22.5$. The short 3 ksec Chandra observation provides only an accurate position for CXOU J085201.4-461753. Spectral analysis is strongly hampered by small photon statistics and pile-up effects (Pavlov et al. 2001). There is no extended X-ray emission reported from this short Chandra observation.

The central part of RX J0852.0-4622 was observed on 2001 April 27 by XMM-Newton in the course of the guaranteed time program (Becker et al. 2002a). The exposure time was ~ 25 ksec. In all observations, the MOS1/2 and the PN cameras were operated in full-frame and extended full-frame mode, respectively. An image of the central part of RX J0852.0-4622 as seen with the MOS1/2 is displayed in Fig.6. CXOU J085201.4-461753 is the brightest source in the field. It is located at the eastern edge of a faint diffuse and irregularly shaped X-ray structure. The extended emission was already visible in ASCA images, but less resolved from the neutron star because of ASCA's wider point spread function. As the whole remnant emits non-thermal X-ray emission along with a small thermal contribution from the Vela remnant, it was not possible to conclusively identify the extended structure in the ASCA images as plerionic (Slane et al. 2001). The XMM-Newton observation thus allowed for the first time a somewhat more detailed view of the field. The extended source has a size of $\sim 9' \times 14'$ and emits mostly in the soft band below ~ 2 keV. A MOS1/2 image showing the field in the 2.0-12 keV band is displayed in Fig.7. No significant emission from the extended structure is visible beyond ~ 2 keV.

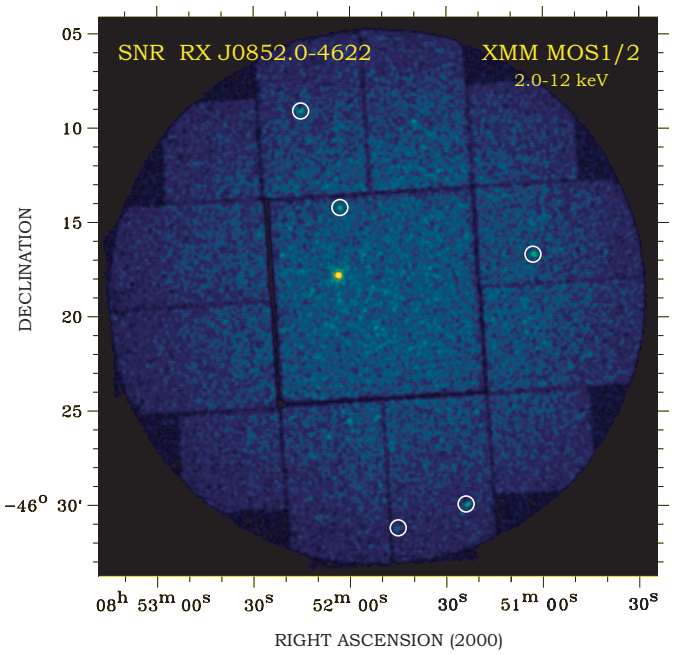


Fig. 7. The central part of RX J0852.0-4622 in the energy band 2.0 – 12 keV. Only very faint residual emission from the extended structure surrounding CXOU J085201.4-461753 is visible.

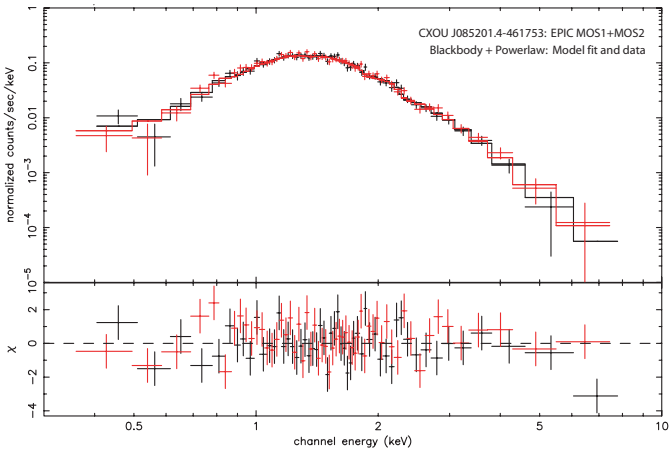


Fig. 8. The spectrum of CXOU J085201.4-461753 obtained with XMM MOS1/2 and fitted with a blackbody plus power-law model. The residuals of the fit are shown.

Fitting model spectra to the data from CXOU J085201.4-461753, we tested the usual blackbody and power-law models as well as models consisting of two blackbody components and a blackbody and power-law component, respectively. With a reduced χ^2 of 0.952 (for 218 dof) the single blackbody model provides an excellent fit to the data, implying a column density of $N_H = (3.7 - 4.3) \times 10^{21}\mathrm{cm}^{-2}$, a temperature in the range $(4.28 - 4.50) \times 10^6$ K and a formal emitting area of $R_{bb} = (0.31 - 0.36)$ km for an assumed distance of 1 kpc. The unabsorbed X-ray flux and luminosity are $f_x = (1.82{-}2.96) \times 10^{-12}\,\mathrm{erg\ cm^{-2}s^{-1}}$ and $L_x(\mathrm{d{=}1\ kpc}) = (2.17 - 3.53) \times 10^{32}\,\mathrm{erg\ s^{-1}}$ in the 0.5 – 10 keV band, respectively. All parameters are given for a 90% confidence range. Compared with the blackbody fit, the power-law model is invalidated by a larger reduced χ^2 of 1.21 and residuals which indicate systematic deviations from the measured data points. The fitted photon index of $\alpha = 4.38 - 4.62$ is much steeper than what is usually found in other young neutron stars which are well known for their non-thermal emission. The blackbody fit, however, indicates a small unmodeled emission in the hard band beyond ~ 3 keV. We therefore tested a compound model consisting of a blackbody and an additional power-law component and fitted the non-thermal spectrum with a photon index of $\alpha = 2.85 \pm 1.5$. The flux and luminosity of these component are $f_x = 3.7 \times 10^{-13}\mathrm{erg\ s^{-1}cm^{-2}}$ and $L_x(\mathrm{d{=}1\ kpc}) = 4.4 \times 10^{31}$ erg/s.

The temperature along with the small size of the emitting region invalidates the interpretation that the thermal radiation is emission from cooling of the entire neutron star surface. If the blackbody model is the right description it points towards emission from a hot polar cap region on the neutron star surface. In the literature various models have been proposed to produce hot spots on the neutron star surface. Almost all magnetospheric emission models predict a bombardment of the polar cap regions by energetic particles accelerated in the magnetosphere backwards to the neutron star surface (cf. Cheng, Ho & Ruderman 1982; Harding & Muslimov 2002 and references therein). Though CXOU J085201.4-461753 is not known to be a radio pulsar it still could be possible that the hot polar caps are heated by particle bombardment while the radio emission itself is undetected due to an unfavorable beaming geometry. This is not an unlikely scenario. The opening angle of a radio beam is inversely proportional to the square root of the pulsar's rotation period so that the radio beams of slowly rotating pulsars can easily miss the observers line of sight and thus keep undetected.

The heat transport in neutron stars is accomplished by electrons and positrons. A strong magnetic field is therefore expected to have an essential impact on the neutron star cooling as it channels the heat transport along the magnetic field lines and suppresses it in the perpendicular direction. Neutron star cooling with a full treatment of a strong magnetic field thus should lead to an anisotropic heat flow and subsequently to an anisotropic surface temperature distribution, with the polar cap regions hotter than the equatorial regions.

A great advantage of the CCD based EPIC detectors aboard XMM is that they not only provide spatial and high resolution spectral information but have observing modes which are fast enough for timing studies even of millisecond pulsars (Becker et al. 2002; Kuster et al. 2002, Kendziorra et al. 2002). During the observation of CXOU J085201.4-461753 the MOS1/2 and PN cameras were operated in full frame and extended full frame mode, provid-

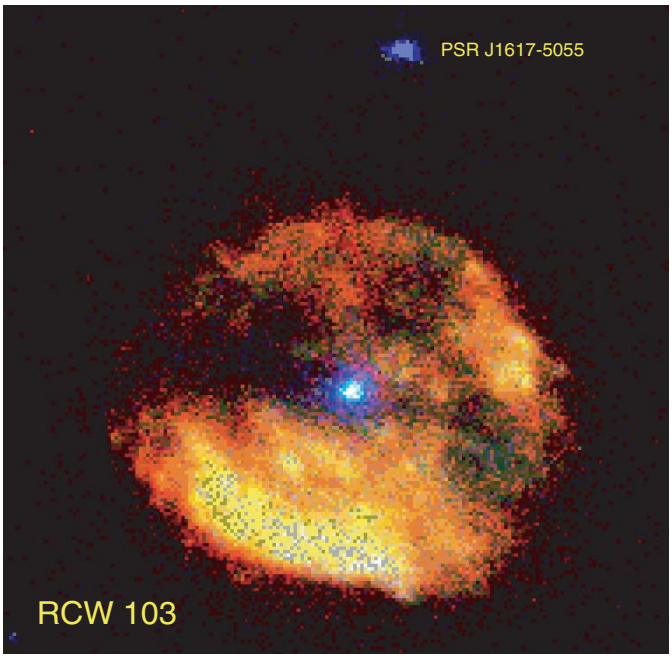


Fig. 9. XMM MOS1/2 image of the supernova remnant RCW 103. The red color represents photons in the $0.3-0.75$ keV band, green and blue correspond to $\sim 0.75-2$ keV and $2-10$ keV, respectively. The neutron star candidate is the hardest X-ray source in the remnant. The 69 ms pulsar PSR J1617−5055 is located 7 arcmin off the supernova center. The remnant extent is $\sim 10'$.

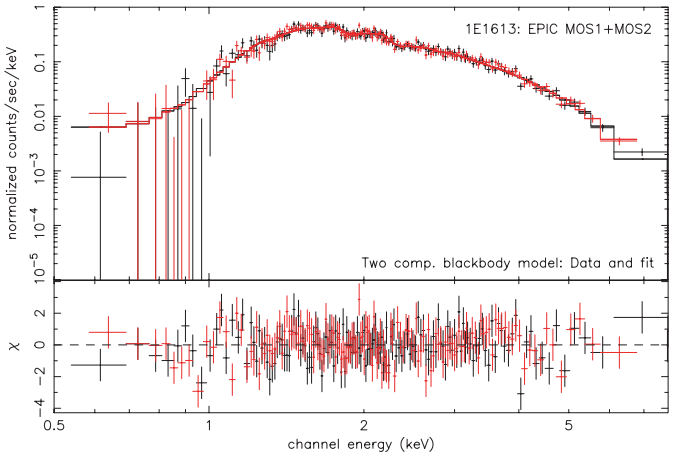


Fig. 10. X-ray spectrum of 1E 161348−5055 in RCW 103 obtained from XMM MOS1/2 data. The spectrum is fitted by a two component blackbody model. Red and black data points are from the MOS1 and MOS2 cameras, respectively. A small spectral feature is seen at ~ 0.98 keV.

ing a temporal resolution of 2.6 s and 200 ms, respectively. While this is not fast enough to search for coherent pulsations on a millisecond time scale, it allows to search the signal for periodicities in a period range in which anomalous X-ray pulsars (AXPs) are seen. Application of fft-based search algorithms along with a more detailed periodicity search around possible frequency candidates, however, did not result in a detection of a significant periodic signal.

Another example of a radio silent neutron star in a supernova remnant is 1E 161348−5055, the projected location of which is in RCW 103 (cf. Fig.9). This source was discovered with the Einstein Observatory (Tuohy & Garmire 1980) and has an estimated age of ~ 2000 yrs. The remnant is mostly known for its central point source, which was considered for many years to be the prototype of a cooling neutron star. No X-ray pulsations and no radio or optical counter part could be detected. ROSAT observations suggested that the source emits hard X-rays (Becker et al. 1993). Comparing two ASCA observations of RCW 103 Gotthelf, Petre & Vasisht (1999) found an order-of-magnitude decrease in luminosity over four years, which suggests that this object may be an accreting source rather than a cooling neutron star. Likewise puzzling is the ~ 6h periodicity of its flux reported by Garmire et al. (2000) from Chandra observations and archival ASCA data.

XMM has observed RCW 103 in September 2001 for an exposure time of 20 ksec. Figure 9 shows a false color image of the remnant, derived from the XMM MOS1/2 data. These data provide for the first time detailed spectral information on the central point source. Chandra has observed the remnant in September 1999 and February 2001. Albeit superior imaging, small counting statistics in the first observation and severe pile-up effects in the second observation preclude a meaningful spectral analysis. The energy spectrum of 1E 161348−5055 extracted from XMM MOS1/2 data is shown in Fig. 10. The status of the detector response matrix which is available for the EPIC-PN small-window mode and which is still preliminary, did not allow to include this data in the analysis up to now, but will provide additional spectral information in the $0.3-10$ keV band. Fitting various spectral models to the MOS data a simple blackbody was found to describe the data almost up to ~ 5 keV, but leaving unmodeled hard emission beyond. A single power-law fit is acceptable on statistical grounds but requires a photon spectral index of $4.1-4.2$. Testing two component models, a double blackbody is found to describe the data best ($\chi^2_\nu = 1.0$ for 287 dof), resulting in $N_H = (1.5-1.8)\times 10^{22}\,\mathrm{cm}^{-2}$, temperatures of $T_1 = (4.1-5.1)\times 10^6$ K and $T_2 = (8.3-10)\times 10^6$ K with $R_1^{bb} = 1.7-3$ km and $R_2^{bb} = 220-500$ m for the blackbody radii of the emitting areas (assuming a distance of $d = 3.3$ kpc). The given numbers represent the 90% confidence range. This result suggests that the first thermal component is emitted from a rather large fraction of the surface, whereas the second component requires a much smaller emitting area like a polar cap region. Compared with the surface temperatures predicted by neutron star cooling models, T_1 is much higher than what is expected for a ~ 2000 yr young neutron star.

In addition to the long term flux change the Chandra data suggested a ~ 6h periodicity. Archival ASCA data were found to be consistent with this. However, a

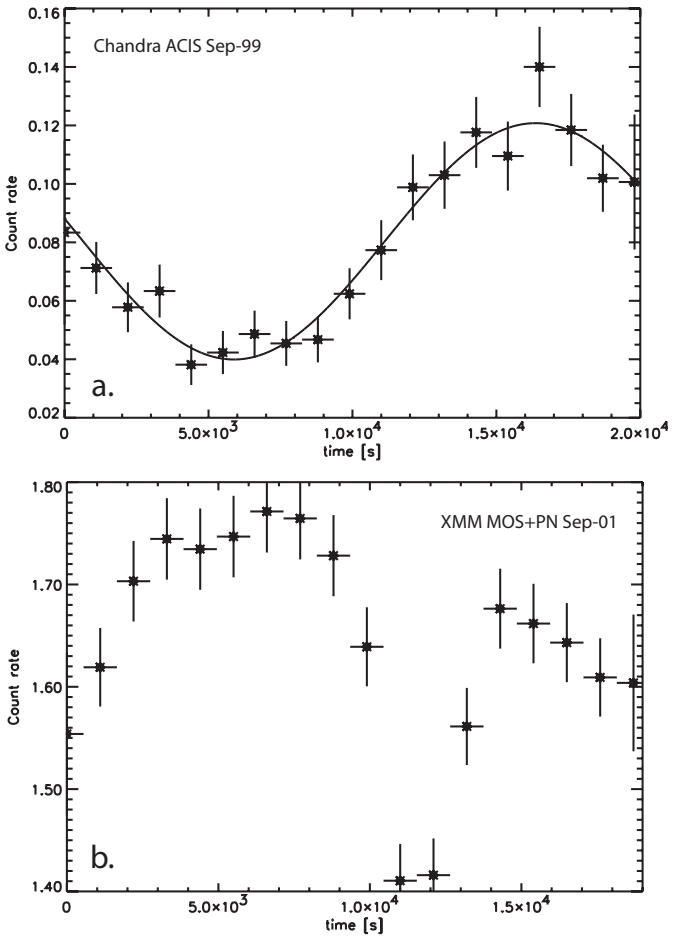


Fig. 11. X-ray lightcurve of 1E 161348−5055 observed with Chandra (a.) and XMM-Newton (b.) in September 1999 and 2001, respectively. The Chandra lightcurve indicates a sinusoidal modulation with a period of $\sim$ 6h. The lightcurve observed by XMM-Newton shows for the first time clear indication of an eclipse and thus identifies 1E 161348−5055 as a neutron star in a binary system (Becker 2001).

second Chandra observation taken in Feb 2000 did not really confirm this periodicity and was more consistent with a $\sim$ 4h period, although 1E 161348−5055 was about ten times brighter at that time than in September 1999. It was therefore of special interest to see the lightcurve of 1E 161348−5055 taken with XMM-Newton in September 2001. Figure 11 shows the lightcurve taken with Chandra and XMM-Newton in September 1999 and 2001, respectively. The lightcurve taken by XMM-Newton does not show the $\sim$ 6h periodicity but discovers an eclipse about 3h after the start of the observation, identifying 1E 161348−5055 as the second accreting binary in a supernova remnant. The companion most likely is a low-mass companion. Chandra observations taken in March 2002 confirm the XMM findings (Sanwal et al., 2002). The discovery of a candidate optical counterpart in the near-IR was reported by Pavlov et al. (these proceedings).

Similar to the previous examples is the point source RX J0822−4300 in Puppis-A (cf. Fig.5). With a distance of about 2.2 kpc the remnant is further away than the Vela supernova remnant. The kinematic age is estimated to $\sim 3500 - 4000$ years, and is therefore a factor of about three younger than the Vela SNR. Discovered in Einstein data, it became evident with ROSAT that RX J0822−4300 is most likely the neutron star expected to form in the SN event (Petre, Becker & Winkler 1996). As for CXOU J085201.4-461753 there is no radio emission detected from this source down to 0.75 mJy and no optical counterpart could be detected down to an observation limit of about 24 mag.

In order to study the nature of RX J0822-4300 in greater detail, the central part of Puppis-A was observed by XMM-Newton in April and December 2001 for 20 kec and 30 ksec, respectively. Figure 12 shows the false color image of the central part of the remnant taken with the two MOS1/2 cameras in April 2001. Like in RCW 103, the neutron star candidate is the hardest X-ray source in the remnant.

The analysis of the RX J0822−4300 emission reveals an X-ray spectrum similar to that observed for 1E 161348−5055. Fitting the data with a simple blackbody model doesn't describe the spectrum beyond $\sim$ 3 keV. A two component blackbody model and a model consisting of a blackbody and a power-law are fitting the spectrum equally well. The double blackbody spectrum yields $N_H = (3.6 - 4.4) \times 10^{21}\,\mathrm{cm}^{-2}$, temperatures of $T_1 = (3.4 - 4) \times 10^6$ K and $T_2 = (0.6 - 1.3) \times 10^7$ K with $R_1^{bb} = 1.4{-}1.8$ km and $R_2^{bb} = 40{-}310$ m for the blackbody radii of the corresponding emitting areas (assuming a distance of $d = 2.2$ kpc). A model consisting of a blackbody and a power-law yields similar results for the dominating blackbody component ($N_H = (2.9 - 3.6) \times 10^{21}\mathrm{cm}^{-2}$, $T = (4.3 - 4.5) \times 10^6$ K, $R^{bb} = 1.1 - 1.3$ km) but fits the hard emission with a power-law of photon-index $\alpha = 2.0 - 2.7$ (90% confidence). This slope is in agreement with what is observed for other young pulsars showing magnetospheric emission.

Zavlin et al. (1999) have modeled the ROSAT data of RX J0822−4300 including a hydrogen atmosphere on top of the neutron star. These models reduce the temperature of the thermal component by a factor of ~ 2 and require a somewhat larger size for the emitting region. Spectral fits which take into account models of a non-magnetic neutron star atmosphere of pure H or He are currently in progress. The X-ray luminosities based on the two component models are in the range $L_x = (3 - 4) \times 10^{33}$ erg/s.

The EPIC-PN camera observed RX J0822−4300 in small-window mode restricting the field of view to $4' \times 4'$ but with a time resolution of 6 ms. Using archival ROSAT data of RX J0822−4300 Zavlin et al. (1999) found evidence for X-ray pulsations with a period of $\sim$ 75.3 ms. The XMM-Newton data, however, which are of much better statistical quality than the ROSAT data do not confirm

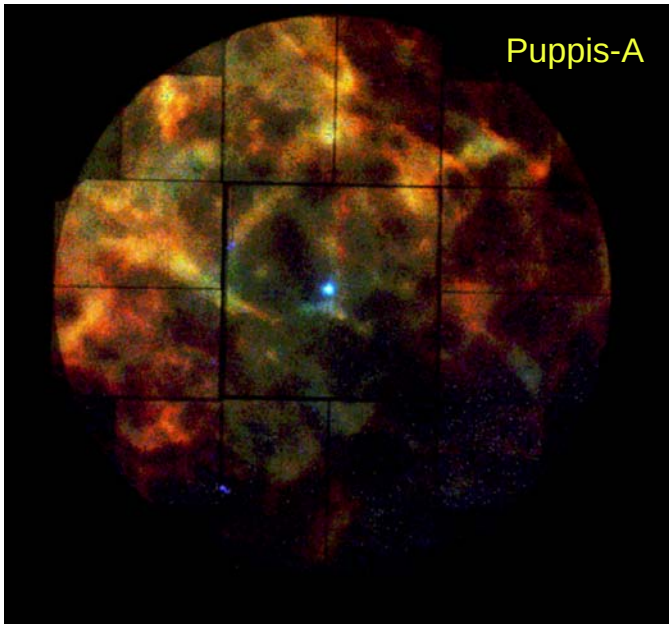


Fig. 12. False color image of the central part of Puppis-A, depicting an area of 15 arcmin in radius centered on RX J0822−4300. The red color represents photons which are detected in the $0.3-0.75$ keV band, green and blue correspond to $\sim 0.75-2$ keV and $2-10$ keV, respectively. Note the amazing honeycomb structure seen in the remnant emission.

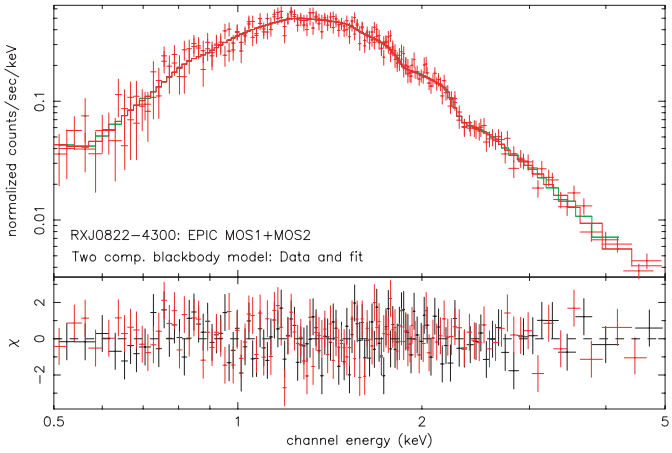


Fig. 13. X-ray spectrum of the point source RX J0822−4300 in Puppis-A derived from XMM MOS1/2 data. The spectrum is fitted by a two component blackbody model. Red and black data points represent the data taken with the MOS1 and MOS2 cameras, respectively. The residuals of the fits shown below shown amount to a reduced χ^2_ν value of 0.9444 for $\nu = 244$ degrees of freedom.

this periodicity, leaving the rotation period of the neutron star candidate unknown.

From the observations of radio-silent compact objects in supernova remnants one can conclude that the emission properties of such sources are quite different compared to ordinary radio pulsars. On the other hand, it is very plausible that they are more common than radio pulsars, and the relatively small number of the members of this class discovered so far is mainly due to observational selection effects. It is much easier to detect and identify active radio or X-ray pulsars than these "radio-quiet" sources observable only in the X-ray band and located in a patchy X-ray bright supernova remnant environment.

4. The cooling neutron stars

As discussed in §2, soft X-ray radiation of rotation-powered pulsars of an age between $\sim 10^5 - 10^6$ yrs should be dominated by emission from the cooling hot neutron star surface. These pulsars are old enough for their magnetospheric emission to become fainter than the thermal surface emission, but they are still young and hot enough to be detectable in the soft X-ray range. There are three middle-aged pulsars, i.e. Geminga, PSR B0656+14 and B1055−52, from which thermal X-ray radiation from the surface of the cooling neutron star has certainly been observed. Because of the similarity of their emission properties, they were dubbed as *the three Musketeers* by Becker & Trümper (1997). It follows from the ROSAT and ASCA observations of the brightest middle-aged pulsar B0656+14 that the thermal component cannot be described by a single temperature blackbody spectrum, i.e. the neutron star surface temperature is not uniform (Greiveldinger et al. 1996). In a simple model the thermal component consists of a soft thermal component (TS) from most of the neutron star surface (at $E \lesssim 0.5-1$ keV) and a hard thermal component (TH) from hot polar caps, heated by relativistic particles, for instance. Alternatively, the temperature non-uniformity can be due to an anisotropic heat conductivity in the neutron star crust caused by the anisotropic magnetic field — the heat flux across the field is reduced whereas it is preferred in directions perpendicular to the field, so that the magnetic poles are expected to be hotter than the equatorial regions (Potekhin & Yakovlev 2001). The thermal component dominates in the UV through the soft X-ray range (up to $1-2$ keV), whereas the non-thermal component described by a power-law (PL) spectrum prevails in the IR, optical, hard X-ray and gamma-ray bands.

PSR 1055-52 and Geminga are not as luminous as PSR 0656+14. Their spectra measured by ROSAT and/or ASCA are well described by a two component model consisting of a blackbody (TS) and a non-thermal (PL) component. Whether a second thermal spectral component (TH) was not detected because of poor counting statistics or whether the component is intrinsically absent has been a pending question which prompted observations with XMM-Newton.

PSR 1055-52 was observed by XMM-Newton for about 96 ksec in December 2000. The X-ray spectrum is shown in Figure 14. It is interesting to note that the two component spectral model which describes the ROSAT and

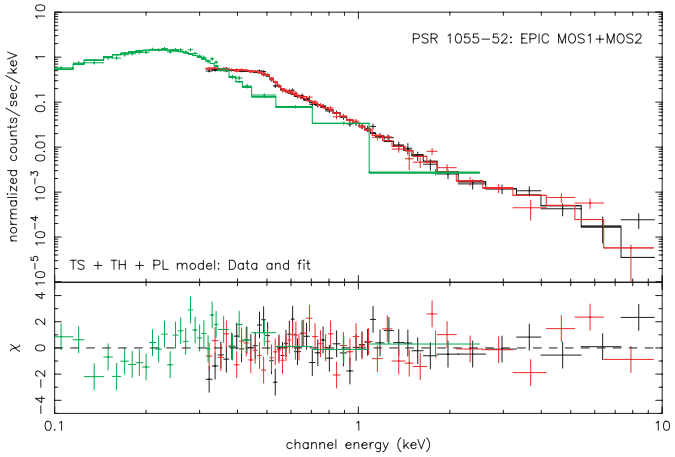


Fig. 14. X-ray spectrum of PSR 1055−52 derived from ROSAT and XMM MOS1/2 data. As for PSR 0656+14 the spectrum requires three components consisting of two thermal (TS+TH) and a harder non-thermal power-law component (PL). The green points represent ROSAT data. Red and black points represent MOS1 and MOS2 data, respectively.

ASCA data does not fit the pulsar spectrum observed by XMM-Newton (Becker 2001). Including the ROSAT data in the spectral analysis, 3 spectral components are required to fit the spectrum in the wide band from 0.1−10 keV. The pulsar's spectral properties are thus indeed found to match those observed in PSR 0656+14. The soft thermal component (TS) yields a blackbody temperature of $T_{TS} = (7.1 \pm 0.3) \times 10^5$ K, similar to what was obtained from the ROSAT data with a somewhat smaller error, though. The second and harder thermal component (TH) is described by $T_{TH} = (1.4 \pm 0.1) \times 10^6$ K. The corresponding blackbody emitting areas are $R_{TS} = 31 \pm 2$ km and $R_{TH} = 2.6 \pm 0.3$ km, respectively, assuming a distance of 1.5 kpc. The non-thermal component (PL) is described by a power-law with a photon index of $\alpha = 1.89 \pm 0.32$. The column absorption is $N_H = (2.1-2.4) \times 10^{20}\,\mathrm{cm}^{-2}$ (all errors represent 90% confidence limits). For the unabsorbed flux in the 0.5−10 keV band we obtain for each of the three components $f_x^{TS} = 2.3 \times 10^{-13}\,\mathrm{erg\ s^{-1}cm^{-2}}$, $f_x^{TH} = 2.1 \times 10^{-13}\,\mathrm{erg\ s^{-1}cm^{-2}}$ and $f_x^{PL} = 1.4 \times 10^{-13}\,\mathrm{erg\ s^{-1}cm^{-2}}$. The corresponding bolometric luminosities are $L_{TS} = 1.74 \times 10^{33}\,\mathrm{erg\ s^{-1}}$ and $L_{TH} = 1.9 \times 10^{32}\,\mathrm{erg\ s^{-1}}$. For the luminosity of the non-thermal component we obtain $L_x = 3.8 \times 10^{31}\,\mathrm{erg\ s^{-1}}$. More detailed results on the pulsar spectrum as well as the results of a phase resolved spectral analysis are given in Becker et al. (2002b).

It should be stressed that the inferred effective temperatures, and hence the radius-to-distance ratios, depend on the model used to describe the thermal component. For instance, if one assumes that the neutron star surface is covered by a hydrogen or helium atmosphere, the effective temperatures are lower than those derived from the simple blackbody fits by a factor of $1.5 - 3$ (Pavlov et al. 1995). Atmospheres dominated by heavy elements give temperatures close to the blackbody temperatures. However, the heavy element atmosphere spectra should show numerous absorption lines and photo-ionization edges (Rajagopal & Romani 1996; Zavlin et al. 1996). Recent observations by Chandra and XMM-Newton of PSR 0656+14 (Marshall & Schulz 2001) as well as of the neutron stars RXJ 1856.5-3754 (Burwitz et al. 2001) and RX J0720.4-3125 (Paerels et al. 2001) have not shown any sign for line emission from a neutron star atmosphere but are perfectly consistent with a pure blackbody like emission.

The X-ray pulses of PSR 1055−52 were discovered by Ögelman & Finley (1993) using ROSAT data. The temporal emission properties were found to indicate a phase shift of about 100° at $0.5 - 0.6$ keV accompanied by an apparent increase in the pulsed fraction from $\sim 10\%$ to $\sim 65\%$. Although the narrow bandwidth of ROSAT along with a decreasing sensitivity beyond 1 keV resulted in large errors of the energy dependent pulsed fraction and phase shift, it was suggested that this dichotomy is associated with the thermal and non-thermal emission components seen in the pulsar's X-ray spectrum. The non-thermal magnetospheric emission is expected to be stronger beamed than the thermal one. Magnetospheric emission thus could show up with a pulsed fraction of up to 100%, depending on the viewing geometry.

XMM-Newton has observed PSR 1055-52 with the EPIC-PN camera set up in timing mode. As described in the introduction (cf. §1), this mode is very sensitive to any enhanced background emission which is accumulated over the whole CCD and condensed along with the source signal into a 1D-image. After barycentering the photon arrival times and correcting for the satellite orbit, the timing signal is detected with high significance. The X-ray pulse profiles, which are shown for different energy bands in Fig.15, are all approximately sinusoidal. A reason for this sinusoidal shape could be the non-uniformity of the surface temperature due to the presence of a strong magnetic field of $\sim 5 \times 10^{12}$ G, as discussed above.

Figure 16a shows the pulsed fraction P_f as a function of photon energy. P_f increases from $\sim 15\%$ in the 0.3−0.4 keV band up to $\sim 80\%$ in the 1.1−1.2 keV band. The fraction of the pulsed flux at higher energies is undetermined in the EPIC-PN data. The observed decrease at $E \geq 1.3$ keV is due to an enhanced background signal, caused by soft proton flares which contaminate the observation and which can not be corrected for. The high background together with a fast decline of the pulsar emission beyond ~ 2 keV causes a strong reduction of the signal-to-noise ratio in the hard energy band, preventing the detection of X-ray pulsations in the EPIC-PN data from most of the non-thermal (PL) emission component. The phase angles of the X-ray pulses observed in different energy bands is shown in Figure 16b. The XMM data indicate that the energy dependence of the pulse phase is by far not as strong

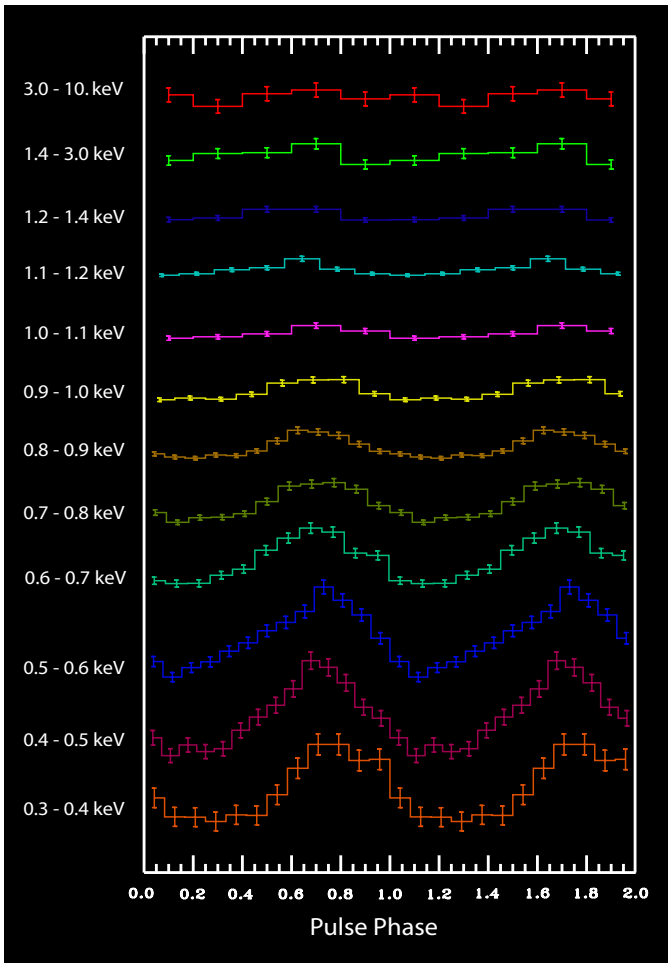


Fig. 15. X-ray pulse profiles of PSR 1055−52 for different energy bands. The pulse profile is sinusoidal. Two complete cycles are shown for clarity. The energy dependent phase shift in the 0.3−3 keV band is not as significant as suggested from ROSAT observations.

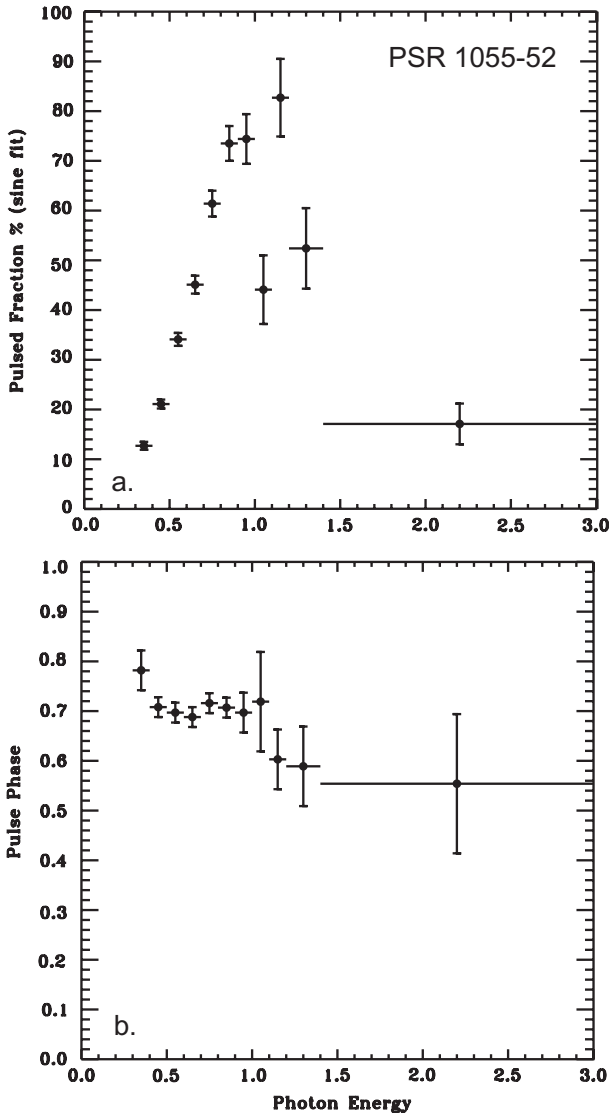


Fig. 16. a. Fraction of pulsed flux vs. photon energy observed for PSR 1055−52 by XMM-Newton. The pulsed fraction peaks at ∼ 1.1 keV and decreases beyond that energy. The decrease goes along with a decreasing signal-to-noise ratio which we suggest to be caused by the fading pulsar signal at higher energies in combination with a high DC level from soft-proton flares which are present over the whole observation. Note the dip in the pulsed-fraction at ∼ 1 keV. **b.** Pulse phase vs. photon energy. The XMM-Newton data are in agreement with no significant phase shift in the 0.4-3 keV band. A significant pulsed signal is seen up to ∼ 3 keV only.

as indicated by ROSAT. This can also be seen in the pulse profiles shown in Fig. 15.

Since all active pulsars are powerful sources of strong winds, one should expect that they generate pulsar-wind nebulae (PWNe), similar to those observed around the Crab-like and Vela-like pulsars. The PWN sizes should scale as $(\dot{E}/p_0)^{1/2}$, where p_0 is the pressure of the ambient medium. The existence of X-ray bright PWNe (albeit of much larger sizes) around several pulsars, including the three musketeers, was reported by Kawai & Tamura (1996) based on ASCA observations. In addition, the suggestion of a clumpy pulsar-wind nebula near to PSR B1055−52 was made by Shibata et al. (1997). The authors proposed the "clumps" of X-ray emission to be created by the interaction of a pulsar-wind outflow with the local interstellar environment. The very low signal-to-noise ratio of the "clumps", however, limited any detailed analysis based on just the ASCA data. In an analysis combining BeppoSAX and ROSAT data, Becker et al. (1999) confirmed the existence of X-ray sources surrounding PSR 1055−52 but came to a different conclusion with respect to its interpretation. With ROSAT, and partly with BeppoSAX, the clumpy X-ray emission was resolved as the superposition of a number of point sources, well separated from the pulsar and unlikely to be associated with it. Several of these sources were found to have optical and radio counterparts using the DSS2 and a radio image taken by Stappers et al. (1999) at 1.4 GHz.

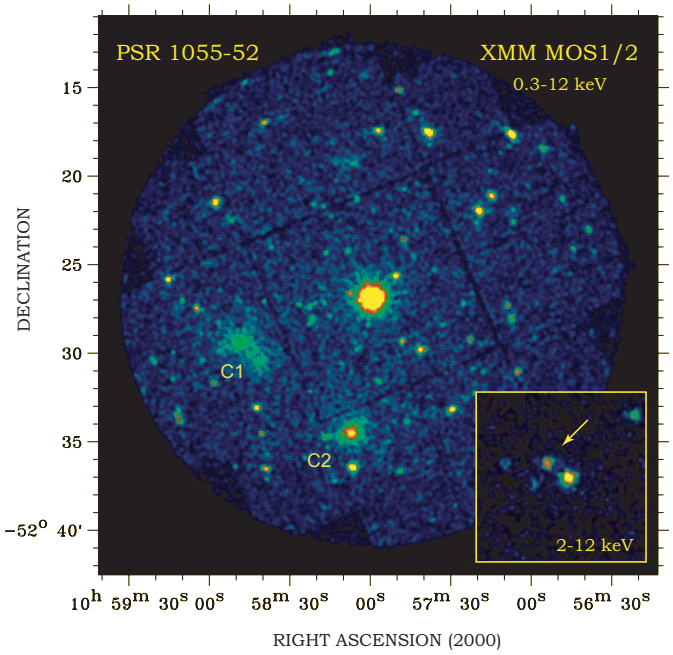


Fig. 17. The X-ray sky around PSR 1055-52 as seen by the MOS1/2 detectors in the $0.3-12$ keV band. The inset in the lower-right corner is a zoomed view on the central $4' \times 4'$ field around PSR 1055-52 for 2-12 keV. The arrow indicates the X-ray source XMMU J105801.8-522639 which is located ~ 30" offset from PSR 1055-52 which is the brightest source in the image.

The ROSAT data in the $1.0-2.4$ keV band were quite limited as far as the photon statistics of the X-ray sources neighboring PSR 1055−52 is concerned. It was therefore of special interest so see this sky region observed by XMM-Newton, which provides a sensitivity about a factor of 10 higher than ROSAT. The X-ray sky around PSR 1055-52 as seen by XMM-Newton in the $0.3-12$ keV band is shown in Fig.17. Apart from the many X-ray sources detected in the field the source denoted by Becker et al. (1999) as C1 appears to be extended by about 1×4 arc-minutes. Its location coincides with that of four faint radio point sources some of which have optical counterparts detected in the DSS2 (Becker et al. 1999). Similar results are found for the other putative X-ray clump C2. Interesting to note is an X-ray source located 30" offset from the pulsar position (cf. the inset in Fig.17). This source, denoted as XMMU J105801.8-522639, shows up only in the hard band and was not recognized in any other observation of PSR 1055-52 so far. Inspecting the data from the XMM-Newton optical monitor we found that XMMU J105801.8-522639 has no optical counter part down to $m_v \sim 22$. The radio image of Stappers et al. (1999) shows a faint radio source near to PSR 1055-52 which roughly matches with the position of XMMU J105801.8-522639. It might be the radio counterpart of XMMU J105801.8-522639.

5. The millisecond Pulsars

By the middle of 2002, about 100 millisecond pulsars have become known, out of which 57 are located in the galactic plane (Camilo 1999; Lommen et al. 2000; Manchester et al. 2000). The others are in globular clusters (Kulkarni & Anderson 1996; Camilo et al. 2000, D'Amico et al. 2001) which provide a favorable environment for the recycling scenario (Rasio, Pfahl & Rappaport 2000). Only 10 of the 57 galactic plane ms-pulsars are solitary (including PSR B1257+12 which has a planetary system); the rest are in binaries, usually with a low-mass white dwarf companion.

Millisecond pulsars were studied exclusively in the radio domain until the early 1990's when PSR B1957+20 was detected by ROSAT (Kulkarni et al. 1992; Fruchter et al. 1992). Unfortunately only a handful of counts were recorded from this object so that no detailed data analysis was possible. The identification was based on the positional coincidence with the radio pulsar. The first ms-pulsar with X-ray pulsations was PSR J0437−4715 (Becker & Trümper 1993). Since then further detections followed (Halpern 1996; Verbunt et al. 1996; Danner et al. 1997; Saito et al. 1997; Takahasi et al. 1999; Becker et al. 1998a; Becker et al. 1998b; Becker et al. 1999; Mineo et al. 2000, Becker et al. 2000, Grindlay et al 2002) which three years after the launch of Chandra and XMM-Newton sum up to almost 50% of all X-ray detected rotation-powered pulsars. Table 4 provides an up-to-date summary.

Although for most of these objects no detailed spectral and temporal information is available, the number of detected counts allows at least an estimate of the X-ray flux and luminosity assuming a standard X-ray spectrum (cf. Tab.4). XMM-Newton will observe several of these pulsars during AO1 (cf. Tab.2) and hopefully will provide the required spectral and temporal information to finally identify the emission mechanism responsible for the observed X-ray emission. Chandra and HST observations of the ms-pulsars detected in 47TUC are scheduled for October 2002 so that also for these objects more detailed information will become available in the near future. For the remaining pulsars, data of six objects provide sufficient spectral and/or temporal information to identify the origin of their X-ray emission (Becker & Trümper 1999 and references therein; Sakuray et al. 2001; Mineo et al. 2000). Observations by Chandra and XMM-Newton have provided the missing spectral information for some of them only recently (Kuiper et al. 2002; Zavlin et al. 2002, Becker et al. 2002c).

The X-ray emission observed from PSR B1821−24, PSR B1937+21 and PSR J0218+4232 ($P \sim 1.5-3$ ms, $\log \dot{E} \sim 35-36$ erg s^{-1}) is produced by non-thermal processes (Kawai & Saito 1999, Takahashi et al. 1998; 2001, Mineo et al. 2000, see also Nicastro et al. 2002, these proceedings). This is concluded from their power-law spectra (photon-index $\alpha \sim 1.5-2$) and pulse profiles with narrow peaks and pulsed fractions of up to $\sim 90\%$

Characteristics of the optical, X-ray and gamma-ray detected rotation-powered millisecond pulsars.

Pulsar	Comment	detected						$\dot{E}/(4\pi d^2)$	$\log\dot{E}$	$\log L_x^{tot}$	$\log L_x^{puls}$	$\log(P/2\dot{P})$	P	$\dot{P}\times10^{-15}$	d	$\log B_\perp$
		R	O	X_s	X_h	γ_s	γ_h	erg/s/cm^2	erg/s	erg/s	erg/s	years	ms	s s^{-1}	kpc	Gauss
J0437 − 4715	bin	p	-	p	-	-	-	$1.0\cdot10^{-9}$	33.62	30.86	30.3	9.50	5.75	$2.0\cdot10^{-5}$	0.18	8.54
B1937 + 21	sol	p	-	p	-	-	-	$7.1\cdot10^{-10}$	36.04	$\leq$ 32.10		8.37	1.55	$1.0\cdot10^{-4}$	3.60	8.61
B1821 − 24	sol, M28	p	-	p	p	-	-	$6.2\cdot10^{-10}$	36.35	33.24		7.48	3.05	$1.6\cdot10^{-3}$	5.50	9.35
J0030 + 0451	sol	p	-	p	-	-	-	$5.4\cdot10^{-10}$	33.53	30.56	30.26	9.88	4.86	$1.0\cdot10^{-5}$	0.23	8.32
J2124 − 3358	sol	p	-	p	-	-	-	$4.7\cdot10^{-10}$	33.55	30.35	29.8	9.86	4.93	$1.1\cdot10^{-5}$	0.25	8.36
B1957 + 20	bin	p	-	d	-	-	-	$4.1\cdot10^{-10}$	35.06	31.93		9.32	1.60	$1.2\cdot10^{-5}$	1.53	8.14
J1024 − 0719	sol	p	-	d	-	-	-	$3.6\cdot10^{-10}$	33.72	29.48		9.76	5.18	$1.8\cdot10^{-5}$	0.35	8.49
J1744 − 1134	sol	p	-	d	-	-	-	$2.4\cdot10^{-10}$	33.28	29.30		9.86	4.07	$8.6\cdot10^{-6}$	0.26	8.27
J1012 + 5307	bin	p	-	d	-	-	-	$1.2\cdot10^{-10}$	33.60	30.20		9.76	5.25	$1.4\cdot10^{-5}$	0.52	8.45
J0218 + 4232	bin	p	-	p	-	-	?	$6.5\cdot10^{-11}$	35.37	32.75		8.66	2.32	$8.0\cdot10^{-5}$	5.85	8.63
J0751 + 1807	bin	p	-	d	-	-	-	$1.5\cdot10^{-11}$	33.88	31.60		9.84	3.47	$8.0\cdot10^{-6}$	2.02	8.23
J0024 − 7205E	bin, 47Tuc	p	-	d	-	-	-	$1.1\cdot10^{-11}$	34.50	30.6		$\geq$ 8.47	3.53	$\leq 3.0\cdot10^{-4}$	4.60	$\leq$ 9.00
J0024 − 7204F	sol, 47Tuc	p	-	d	-	-	-	$8.4\cdot10^{-12}$	34.40	30.5		$\geq$ 8.34	2.63	$\leq 2.1\cdot10^{-4}$	4.60	$\leq$ 8.90
47Tuc S	bin, 47Tuc	p	-	d	-	-	-			30.2			2.83		4.60	
J0023 − 7203J	bin, 47Tuc	p	-	d	-	-	-	$8.4\cdot10^{-12}$	34.40	30.3		$\geq$ 9.15	2.10	$\leq 1.1\cdot10^{-4}$	4.60	$\leq$ 8.69
J0024 − 7204O	bin, 47Tuc	p	-	d	-	-	-	$8.4\cdot10^{-12}$	34.40	30.6		$\geq$ 8.38	2.64	$\leq 1.8\cdot10^{-4}$	4.60	$\leq$ 8.84
J0024 − 7203U	bin, 47Tuc	p	-	d	-	-	-	$5.3\cdot10^{-12}$	34.20	30.3		$\geq$ 8.60	4.34	$\leq 3.4\cdot10^{-4}$	4.60	$\leq$ 9.07
J0024 − 7204N	sol, 47Tuc	p	-	d	-	-	-	$4.2\cdot10^{-12}$	34.10	30.2		$\geq$ 8.81	3.05	$\leq 1.5\cdot10^{-4}$	4.60	$\leq$ 8.84
J0024 − 7204I	bin, 47Tuc	p	-	d	-	-	-	$2.7\cdot10^{-12}$	33.90	30.2		$\geq$ 8.72	3.48	$\leq 1.5\cdot10^{-4}$	4.60	$\leq$ 8.84
J0024 − 7204G	sol, 47Tuc	p	-	d	-	-	-	$1.6\cdot10^{-12}$	33.70	30.1		$\geq$ 8.69	4.04	$\leq 1.9\cdot10^{-4}$	4.60	$\leq$ 8.95
J0024 − 7204D	sol, 47Tuc	p	-	d	-	-	-	$1.6\cdot10^{-12}$	33.70	30.3		$\geq$ 8.83	5.75	$\leq 3.0\cdot10^{-4}$	4.60	$\leq$ 9.11
J0023 − 7205M	sol, 47Tuc	p	-	d	-	-	-	$1.1\cdot10^{-12}$	33.50	30.1		$\geq$ 9.51	3.67	$\leq 1.7\cdot10^{-4}$	4.60	$\leq$ 8.90
J0024 − 7204H	bin, 47Tuc	p	-	d	-	-	-	$5.3\cdot10^{-13}$	33.20	30.1		$\geq$ 8.88	3.21	$\leq 1.8\cdot10^{-4}$	4.60	$\leq$ 8.90

Table 4. List of rotation-powered ms-pulsars that have been detected in the radio, optical, X- and/or γ-ray wavebands, ordered according to their spin-down flux density at Earth $\dot{E}/4\pi d^2$. The individual columns are as follows: 1. Pulsar name; 2. Comment: bin=binary, sol=solitary; 3-8. Energy ranges in which pulsed (p), unpulsed (d) radiation has been detected: R – radio, O – optical, X_s – soft X-rays ($E_\gamma \sim$ 1keV), X_h – hard X-rays ($E_\gamma \sim$ 10keV), γ_s – soft γ-rays ($E_\gamma \sim$ 1MeV) and γ_h – hard γ-rays ($E_\gamma >$ 100MeV). Possible detections are indicated by a question mark. $\dot{E}$ is the pulsar spin-down power $I\Omega\dot{\Omega}$; $L_x^{tot} = 4\pi d^2 f_x$ is the sum of the pulsed and unpulsed X-ray luminosity. L_x^{puls} is the pulsed luminosity; L_x are calculated for the ROSAT energy range 0.1 − 2.4 keV. For references see Becker & Trümper (1997; 1999), Becker & Pavlov (2002) and references therein, Grindlay et al. (2002). Radio pulsar parameters have been taken from Taylor et al. (1995), Navaro et al. (1995), Bailes et al. (1997), Toscano et al. (1998), Toscano et al. (1999), Lommen et al. (2000), Camilo et al. (2000), Lange et al. (2001), van Straten et al. (2001), Freire et al. (2001). Proper motion corrected period derivatives have been used for all those pulsars for which this effect is of significance and has been measured.

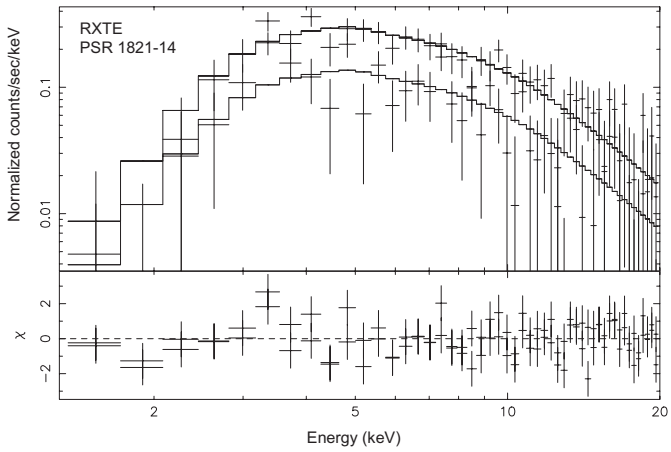


Fig. 18. X-ray spectrum of the millisecond pulsar PSR 1821-24 extracted from XTE data. A power-law spectrum yields a valid description of the data of up to 20 keV (Saito, priv. com.).

(cf. Fig. 22). PSR B1821−24 was detected by RXTE up to ~ 20 keV (cf. Fig. 18). All these pulsars show relatively hard X-ray emission, which made it possible to study some of their emission properties already with ASCA, BeppoSAX and RXTE. For the remaining pulsars ($P \geq 4$ ms, $\log \dot{E} \sim 33 - 34$ erg s^{-1}) the X-ray emission is found to be much softer, which in the absence of definite spectral information led to the conclusion that in these pulsars thermal polar-cap emission dominates. The argument for this second group being purely thermal emitters was that their pulse profiles are broad, and that the pulsed fraction is small ($\sim 20 - 30\%$) in comparison to the non-thermal sources (pulsed fraction $\geq 50-60\%$). The argument is not unreasonable − thermal polar-cap emission should result in broad sinusoidally modulated soft emission with a pulsed fraction $\leq 50\%$ (Pavlov & Zavlin 1998), whereas magnetospheric emission is expected to create narrow pulse-peaks and large pulsed fractions.

But, of course, given the limited amount of data the physical interpretation is not fully justified and therefore not at all unique. Becker & Trümper (1997; 1999) have emphasized that the radiation cone confining the magnetospheric emission is likely to yield sharp peaks at one aspect angle but may be less well defined when viewed from other directions producing a less strong modulation. Thus a broad, weakly modulated pulse profile does not provide unambiguous evidence for thermal emission. Indeed, based on the L_x vs $\dot{E}$ relation (most of the X-ray pulsars lie close to the line $L_x \sim 10^{-3}\dot{E}$, cf. Becker & Trümper 1997) one can argue on phenomenological grounds that the X-ray emission from all ms-pulsars is dominated by magnetospheric emission. The gross similarity between the X-ray and radio pulse profiles is part of this argument.

For the nearest and brightest millisecond pulsar, PSR J0437−4715, it was already evident in the ROSAT and ASCA data that the X-ray emission consists at least of two different spectral components. Either a two temperature thermal model or a model composed of a blackbody ($T \sim 1.2 \times 10^6$ K) and a power-law (photon-index $\alpha = 2.9$) fitted these data but also a broken power-law spectrum gives a valid description (Becker & Trümper 1999). The emitting area deduced from the blackbody fits was found to be very small ($R_{bb} \sim 510\,\mathrm{m}\,(d/180\,\mathrm{pc})$), implying the existence of relatively small hot-spots on the neutron star surface from which the X-rays are emitted (Becker & Trümper 1997; 1999).

Chandra observed PSR J0437−4715 in May 2000 (Zavlin et al. 2002, cf. also Zavlin et al. and Pavlov et al., these proceedings). These data, together with the ROSAT data, provide the most significant spectral information available from this pulsar by now and suggest the presence of a power-law component and two thermal components in the pulsar's X-ray spectrum. The thermal components are interpreted as emission from a hot polar cap, having a non-uniform temperature distribution with a hot core ($T_{core} = 2.1 \times 10^6$ K, $R_{core} = 0.12$ km) and a cooler rim ($T_{rim} = 0.54 \times 10^6$ K, $R_{rim} \sim 2.0$ km). The power-law component yields a photon index of $\alpha \sim 2.2$. The size of the polar cap is found to be roughly in agreement with the theoretical predictions. Defined as the area of open field lines in which the bombardment by relativistic particles is expected, it is $R_{pc} = R(R\,\Omega/c)^{1/2}$. Assuming $R = 10$ km for the neutron star radius and $\Omega = 1.09 \times 10^3$ for the pulsars angular frequency $R_{pc} = 1.9$ km. It is interesting to mention that the pulsar spectrum measured by Chandra is still consistent with a broken power-law with properties similar to those fitted to ROSAT and ASCA data by Becker & Trümper (1999); $N_H = 0.3^{+0.5}_{-0.2}\,\mathrm{cm}^{-2}$, $\gamma_1 = 2.0 \pm 0.2$, $\gamma_2 = 3.6 \pm 0.1$ keV below and above the break energy $E_b = 1.1 \pm 0.1$ keV. Zavlin et al. (2002) argue against the broken power-law model because of an apparent discrepancy between the flux estimated from this model and observed by EUVE DSI - despite a known discrepancy in the cross-calibration between ROSAT and EUVE. If the broken power-law model is relevant, and this is not excluded presently by the Chandra data, it would imply that the purely non-thermal pulsar spectrum would bend down significantly in the X-ray band, which could be due to a deficit of high-energy charged particles in the pulsar's magnetosphere.

A pulsar with spin parameters similar to those observed in PSR 0437−4715 is the solitary ms-pulsar PSR 0030+0451 (cf. Table 4 and Fig.19). X-ray emission from this pulsar was discovered during the final ROSAT PSPC observations (Becker et al. 2000). Though the "dying" PSPC detector had lost most of its spectral capability a timing analysis revealed strong X-ray pulsations with a pulsed fraction of $69 \pm 18\%$. This and the gross similarity between the double peaked X-ray pulse profile and the Crab-like radio profile taken at 1.4 GHz suggested that the X-rays from PSR 0030+0451 were most likely of non-thermal origin, although its spin-parameters appear very similar to those of PSR J0437−4715 suggesting a soft pul-

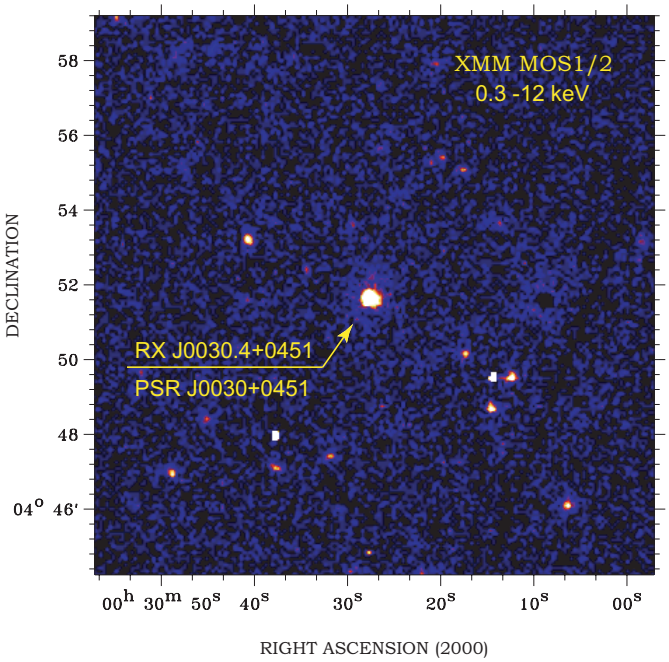


Fig. 19. The X-ray sky around PSR J0030+0451 as seen by the MOS1/2 detectors in the $0.3-12$ keV band. The position of PSR J0030+0451 is marked. There is no evidence for any extended emission.

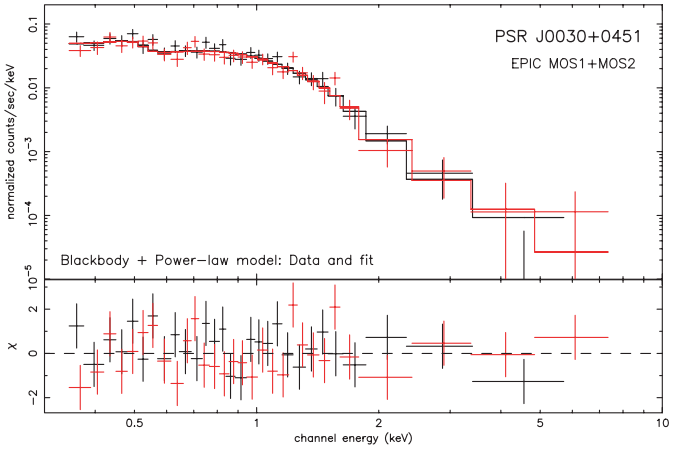


Fig. 20. X-ray spectrum of the millisecond pulsar PSR J0030+0451 extracted from XMM data. The read and black points correspond to data extracted from the MOS1 and MOS2 detectors, respectively. The data are fitted by a composite model consisting of a blackbody and power-law model. The residuals of the fits are shown at the bottom.

sar spectrum (Becker et al. 2000). It was therefore important to observe this pulsar with XMM-Newton in order to identify the emission mechanism by the spectrum rather than from just the pulse profile and the similarity of the spin-parameters with PSR J0437−4715.

PSR 0030+0451 was observed by XMM-Newton in 2001 June 19−20 for a duration of ~ 30 ksec. The MOS1/2 and the PN cameras were operated in full-frame and fast-timing mode, respectively. The latter mode required to constrain the satellite roll angle to $67-68$ degrees in order to prevent source confusion in the PN data (cf. §1). The thin filters where used for the MOS1/2 and the PN cameras in order to block stray light and optical leakage from bright foreground stars. The observation is affected by several soft-proton flares covering the whole observation. Cleaning the data for the times of excessive background reduced the effective exposure time to 17.8 ksec. For the spectral analysis we selected all events in the MOS1/2 within a circle of 38 arcsec radius, containing $\sim 87\%$ of the encircled energy of a point source. The X-ray flux and luminosity were corrected accordingly. The data are not affected by pile-up.

Figure 20 shows the energy spectrum of PSR 0030+0451 observed with XMM-MOS1/2. The spectrum is rather flat in the soft band. The pulsar is detected up to ~ 7 keV. Motivated by the results obtained for PSR J0437−4715 we tested various thermal and non-thermal spectral models such as blackbody and power-law models and combinations of them as well as broken- and curved power-law spectra. A single blackbody model did not yield a valid description of the spectrum because of severe systematic deviations and a rather large reduced χ^2 of $\chi^2_\nu = 1.4$ (for 56 dof). In comparison to this, a single power-law model fits the observed spectrum ($\chi^2_\nu = 0.92$ for 56 dof) but requires a high column absorption of $N_H = (2.1-3.46)\times 10^{21}\,\mathrm{cm}^{-2}$ with a rather steep power-law slope of $\alpha = (4.2-5.1)$ for the photon-index (90% confidence range). For comparison, the column density along the pulsar's line of sight through the entire Galaxy is just $N_H = 3\times 10^{20}\,\mathrm{cm}^{-2}$ (Dickey and Lockman 1990). Models consisting of a combination of a blackbody and a power-law as well as of a two component blackbody model all yield an acceptable description of the observed spectrum. For the blackbody plus power-law model ($\chi^2_\nu = 0.87$ for 54 dof) we obtain $N_H = (0-2.5)\times 10^{20}\,\mathrm{cm}^{-2}$, $T = (2.2-2.7)\times 10^6$ K, $R_{bb} = (50-100)$ m and a photon index of $\alpha = 2.65-3.45$ (90% confidence range). The pulsar distance was assumed to be 0.23 kpc (Lommen et al. 2000). The corresponding total flux and luminosity in the 0.1–2.4 keV band is $f_x \sim 5.7\times 10^{-13}\,\mathrm{erg\,s^{-1}cm^{-2}}$ and $L_x \sim 3.6\times 10^{30}\,\mathrm{erg\,s^{-1}}$. For the 0.5–10 keV band we compute $f_x \sim 1.9\times 10^{-13}\,\mathrm{erg\,s^{-1}cm^{-2}}$ and $L_x \sim 1.2\times 10^{30}\,\mathrm{erg\,s^{-1}}$, respectively. The two component blackbody model fits the spectrum with comparable quality and yields $N_H = (0-1.9)\times 10^{20}\,\mathrm{cm}^{-2}$, $T_{bb1} = (2.6-3.7)\times 10^6$ K, $T_{bb2} = (1-1.8)\times 10^6$ K, $R_{bb1} = (20-60)$ m and $R_{bb2} = (130-340)$ m. For the X-ray conversion efficiency in the 0.1-2.4 keV band we find $L_x/\dot{E} = 1.1\times 10^{-3}$, in agreement with the general trend found by Becker & Trümper (1997). In addition to these composite models we tested a broken power-law and a curved power-law spectrum (Fossati et al. 2000) either of which provides an excellent fit to the data ($\chi^2_\nu = 0.93$ for 55 dof and $\chi^2_\nu = 0.92$ for 51 dof for the broken and curved

power-law model, respectively). Fixing the column absorption to zero, we find the spectral break point at $E_b = (0.97 - 1.28)$ and photon indices of $\alpha_1 = (1.98 - 2.4)$ and $\alpha_2 = (3.88 - 5.36)$, respectively. The unabsorbed flux and luminosity obtained from this model for the 0.1–2.4 keV band are $f_x \sim (4.3 - 6.8) \times 10^{-13}\,\mathrm{erg\ s^{-1}cm^{-2}}$ and $L_x \sim (2.7 - 4.3) \times 10^{30}\,\mathrm{erg\ s^{-1}}$, respectively. For the 0.5-10 keV band we find $f_x \sim (1.5 - 2.1) \times 10^{-13}\,\mathrm{erg\ s^{-1}cm^{-2}}$ and $L_x \sim (0.95 - 1.3) \times 10^{30}\,\mathrm{erg\ s^{-1}}$. The fitted parameters are very similar to those found in the analysis of the Chandra data of PSR J0437-4715. Broken power-law fits thus provide an attractive alternative to describe the X-ray spectrum of PSR J0437-4715 and PSR J0030+0451 in a pure non-thermal scenario. More detailed results on the spectral analysis are presented in Becker et al. (2002c).

The rotation period of PSR J0030+0451 is 4.86 ms. The temporal resolution of the EPIC-PN camera in timing mode is 0.03 ms and thus is sufficient to measure the pulse profile and pulsed fraction as a function of photon energy. To extract the events from PSR J0030+0451 we selected an area of 8×199 pixel from the central CCD #4 of the PN camera. According to the fractional encircled energy this means that we sample about 70% of the point-spread function in x- and 100% in y-direction. Applying the usual corrections for the barycentering and the satellite orbit, a strong pulsed signal is detected in the $\sim 0.3 - 2.5$ keV band. Below and beyond that bandwidth the cumulative instrument and sky-background contribution per pixel exceeds that of the pulsar signal which prevents a detection at those energies (see Becker et al. 2002c for further details). The pulse profiles obtained from events in the 0.3–1.0 keV, 1.0–2.5 keV and 0.3–2.5 keV bands are displayed in Fig.21. Each lightcurve shows two rather narrow peaks which are separated in phase by ~ 0.5. XMM thus confirms our findings obtained in the final ROSAT observation (Becker et al. 2000). The pulsed fraction is found to to be $(49 \pm 3)\%$ in the $0.3 - 1.0$ keV and $(66 \pm 12)\%$ in the $1.0 - 2.5$ keV band (errors are 1σ) using a bootstrap method (Swanepoel et al.,1996). For the $0.3 - 2.5$ keV bandwidth we obtain $51 \pm 3\%$. The gross similarity between the X-ray and radio pulse profiles becomes even more striking with these new pulse profiles obtained with XMM. As can be seen in Fig.22, the peak separation of the radio and X-ray lightcurves of PSR J0030+0451 appear to be in agreement with each other, suggesting a close relation between the X-ray and radio emission mechanism. It is evident that this holds for all the other pulse profiles shown in the chart. It is straight forward to understand this gross similarity in terms of a common non-thermal emission mechanism but it is hard to understand how a mixture of thermal and non-thermal emission mechanisms can produce this similarity. In the case of PSR J0437-4715, for which the *broad* X-ray pulse profile often is taken as an additional argument for the thermal origin of its soft X-radiation, it should be noted that also the radio emission has a duty cycle of $\sim 80\%$ so that the radio pulse itself appears rather broad.

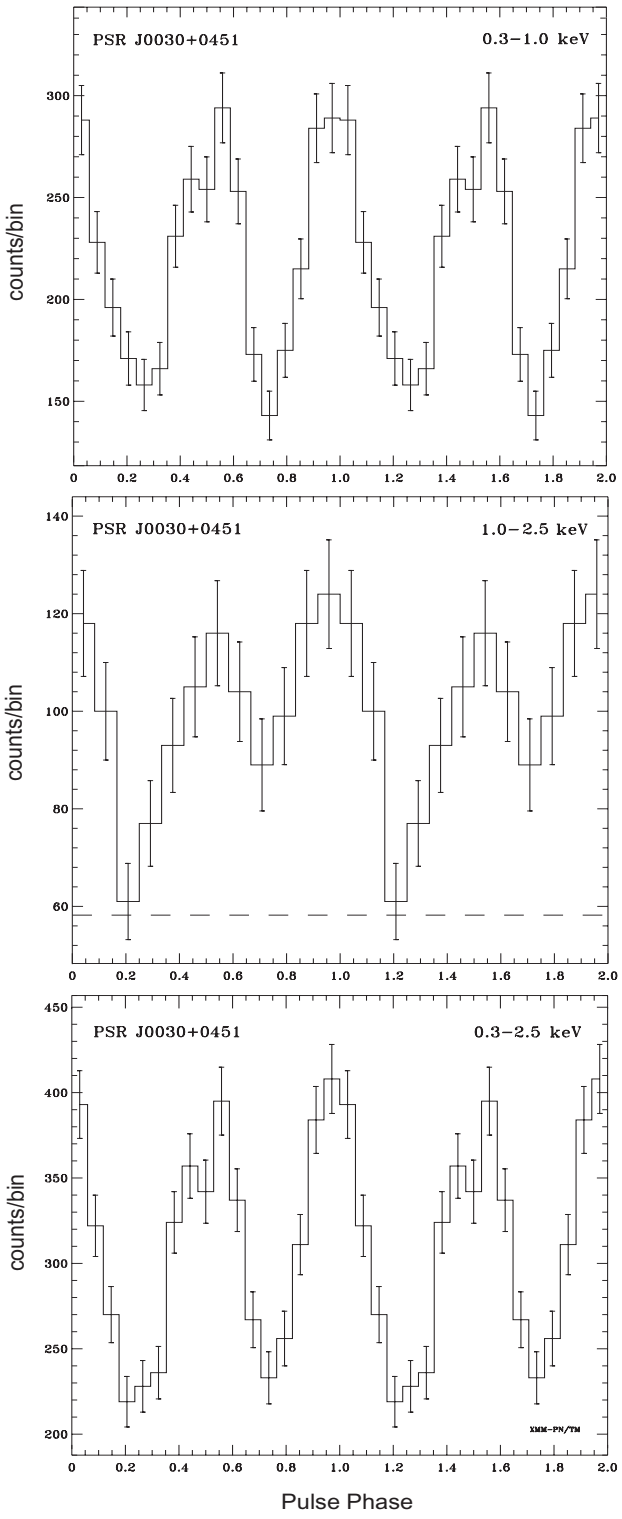


Fig. 21. Pulse profiles of PSR J0030+0451 observed by XMM-Newton. Two full pulse cycles are shown for clarity. The profile appears double peaked with a pulsed fraction of $50 \pm 3\%$ in the $0.3 - 2.5$ keV band.

In the light of these new results it will be interesting to see the data from more millisecond pulsars observed by XMM-Newton and Chandra in order to further explore these interesting objects and their emission mechanisms.

6. Concluding remarks

In spite of the first impressive achievements summarized above, lots of questions still remain. First, the evolution of neutron stars, beginning with their violent birth in supernova explosions, is far from being well understood. Until recently, a common prejudice had been that all neutron stars are born as active, fast spinning rotation-powered pulsars, which slow down their rotation, eventually stop their activity and, after crossing a "death line", get into the "pulsar graveyard". A former pulsar remains in the graveyard forever, cool and quiet, unless it is captured by a flying-by star (e.g., in a globular cluster) and forms a close binary, where accretion onto the neutron star can spin it up (recycle) to periods that short that it again becomes an active pulsar. However, as the results from XMM-Newton and Chandra have shown, it is likely that the picture is not as simple as that. In particular, it appears that several very young neutron stars (like those in Puppis-A and RCW 103) are not active pulsars at all. Others are found to have spin periods longer than the canonical limit of 4 seconds. Were those objects born with such a slow spin-period or did they spin down rapidly after their formation because of the presence of an ultra-strong magnetic field? Or is it simply an unfavorable beaming which precludes to see the pulsed emission? Since such objects are not seen in radio, and are extremely faint in optical, they could not be observed until the onset of the X-ray astronomy era, which means that our perception of neutron star early evolution was strongly biased in favor of much easier observable radio pulsars. Why are many (perhaps, the majority of) nascent neutron stars not active pulsars? Is it because they are indeed magnetars, whose super-strong magnetic field inhibits the pulsar activity? Or, on the contrary, are their magnetic fields so weak and/or is their rotation so slow that the pulsar does not turn on? Or is their pulsar activity quenched by accretion of debris of the supernova explosion? Are the (apparently young) anomalous X-ray pulsars and soft gamma-ray repeaters indeed magnetars or are their unusual observational properties due to quite different reasons, like a residual disk?

Observing middle aged neutron stars at X-ray energies has provided valuable information on the pulsars' surface temperature for some objects. The XMM data have provided further evidence that the surface temperature distribution is not uniform and several, at least two, thermal components are required to describe the observed spectra. The question remains what mechanisms are responsible for the non-uniform surface temperature distribution? Is the presence of the strong magnetic field already sufficient to channel the heat flow in the star to produce the observed non-uniformity, or is it due to the presence of polar caps which are heated by a bombardment of energetic particles accelerated in the neutron star's magnetosphere? Other questions are related to the chemical composition of the neutron star surface layer and the presence of a neutron star atmosphere. Why does none of the data taken so far show any direct evidence for the existence of a neutron star atmosphere except 1E1207-5209 (cf. Pavlov et al., these proceedings; Mereghetti et al., 2002 and references therein)? No emission or absorption features are observed in the LETG spectrum taken from the nearby isolated neutron star RX J1856-3754, but a blackbody was measured with very high accuracy (Burwitz et al. 2001; cf. Pavlov et al.,these proceedings).

Crucial for building a consistent evolutionary scenario of pulsar emission properties at X-ray energies are older pulsars in the age bracket $10^6 - 10^7$ years. What is the dominant emission process producing their X-rays? Only a few of these objects turn out to be bright enough to be observable at all. None of them has been observed by XMM-Newton or Chandra so far but a few objects are scheduled for XMM's AO1 (cf. Tab.2). These pulsars are of particular importance for the study of particle acceleration and high energy radiation processes on the neutron star surface and in the magnetosphere. This is because of their outstanding location in the $P - \dot{P}$ parameter space, where they are found in the area of strong magnetic fields ($\sim 10^{11} - 10^{12}$ G) but spin-down ages which are intermediate between the middle aged cooling neutron stars and the very old $\sim 10^9 - 10^{10}$ years millisecond pulsars. Will the thermal emission observed in cooling neutron stars simply fade away with increasing age due to the neutron star cooling or will the star be kept hot at about $(0.5 - 1) \times 10^5$ K over millions of years due to energy dissipation by processes such as internal frictional heating ($\dot{E}_{diss} \sim 10^{28} - 10^{30}$ erg/s) and crust cracking or by vortex pinning and creeping?

As far as millisecond pulsars are concerned, what are the pulsar parameters which determine the relative strength of the thermal and non-thermal emission components? Or is the pulsar emission non-thermal for all detected objects? Why do the pulse profiles observed in the radio and X-ray bands show this strong gross similarity, even when their X-ray emission appears to be emitted mainly from heated polar-caps like proposed for PSR J0437-4715? What is causing the relation between the emission properties and energy spectra, which is observed in the radio and X-ray band?

In this paper we have shown that observatories like XMM-Newton provide very exciting new results on all classes of neutron stars and that this observatory will be able to provide the answer for many of the open questions mentioned above. We are confident that XMM-Newton and Chandra will have a similar strong impact on our understanding of neutron star emission mechanisms as ROSAT had few years ago. With respect to this it might

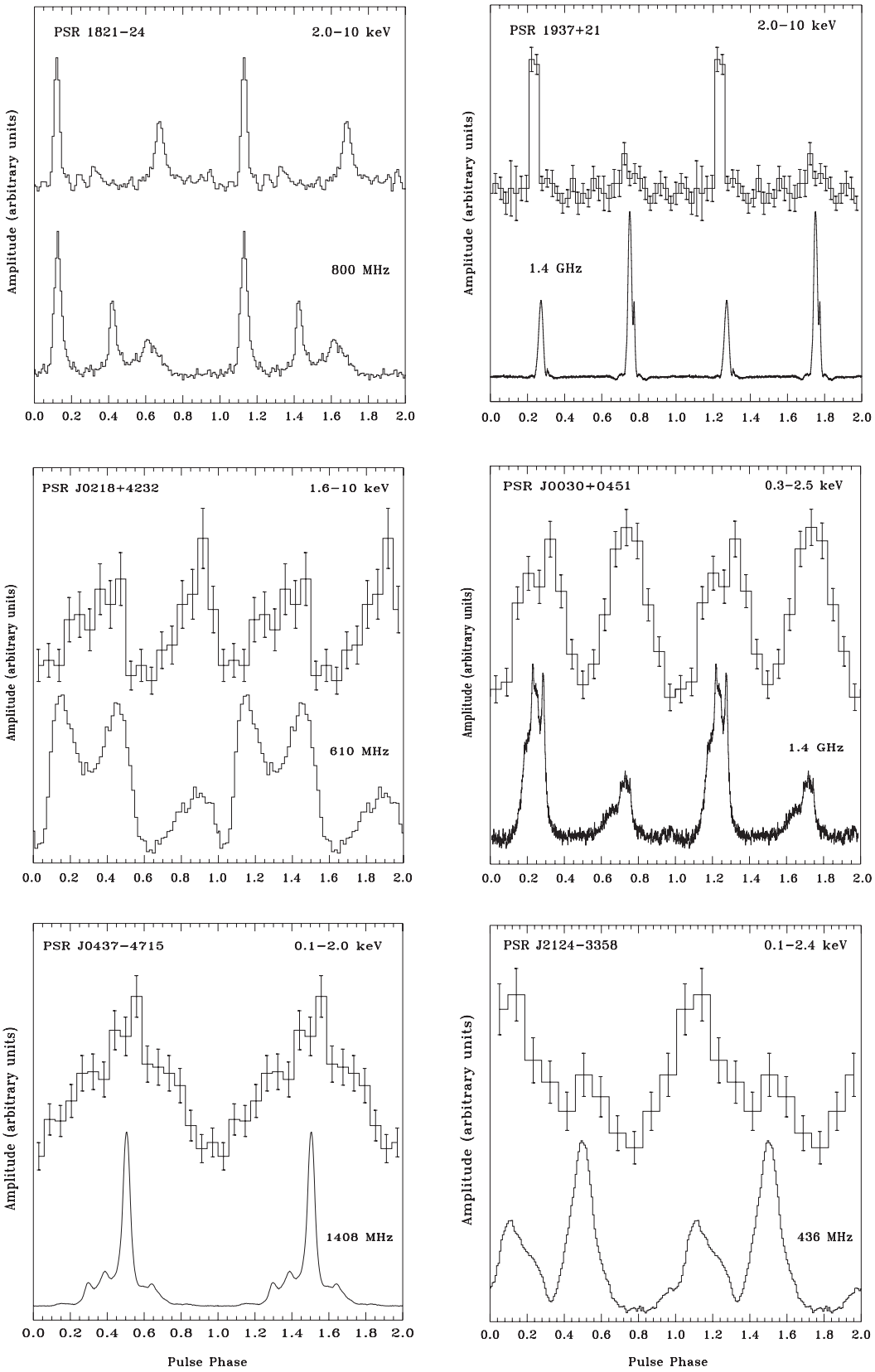


Fig. 22. Integrated lightcurves for all ms-pulsars for which X-ray pulses have been detected. The upper panel phase histograms show the pulse profiles for the energy bands noted. The radio profiles are shown in the lower panel for comparison. Two full pulse cycles are shown for clarity. The relative phase between the radio and X-ray pulses is only known for PSR 1821-24, B1937+21, 0218+4232 and PSR J0437-4715. The phase alignment in all other cases is arbitrary due to the lack of accurate clock calibration.

be worth to mention that we still use the soft photons detected by ROSAT to explore the X-ray spectra of pulsars because none of the new instruments can compete in the soft band down to energies of 0.1 keV.

Acknowledgements. We would like to thank the XMM team at ESTEC and MPE for their help with the data analysis, especially Dirk Grupe for the compilation of the data analysis cookbook and Michael Freyberg for his help during the data processing and analysis. Uwe Lammers, Eckhard Kenziora, Markus Kuster, Tim Oesterbroek and Ed Serpell for the help with the clock calibration. WEB is thankful for discussion with M.Weisskopf and J.Grindlay.

References

Aschenbach, B., 1998, Nat, 396, 141
Aschenbach, B., Iyudin, A., Schönfelder, V., 1999, A&A, 350, 997
Bailes, M., Johnston, S., Bell, J.F., et al, 1997, ApJ, 481, 386
Becker, W., & Trümper, J. 1993, Nat, 365, 528
Becker, W., Trümper, J., Hasinger, G., Aschenbach, B, 1993, in *Isolated Pulsars*, eds. K.A. Van Riper, R.I. Epstein & C. Ho, p116, Cambridge University Press
Becker, W., Trümper, J., 1997, A&A, 326, 682
Becker, W., Trümper, J., 1998a, IAU Circular No. 6829
Becker, W., Trümper, J., Hasinger, G., 1998b, IAU Circular No. 6845
Becker, W., Trümper, J. 1999, A&A, 341, 803
Becker, W., Kawai, N., Brinkmann, W., Mignani, R., 1999, A&A, 352, 532
Becker, W., Trümper, J., Lommen, A.N., Backer, D.C., 2000, ApJ, 545, 1015
Becker, W., 2001, Talk presented at the second XMM Symposium *New Vision of the X-ray Universe in the XMM-Newton and Chandra Era*', Nov. 2001, ESTEC
Becker, W., Pavlov, G.G., 2002, in *The century of Space Science*, eds. J.Bleeker, J.Geiss & M.Huber, Kluwer Academic Press, in press, astro-ph/0208356
Becker, W., Aschenbach, B., Iyudin, A., 2002a, A&A, submitted
Becker, W., et al., 2002b, A&A, submitted
Becker, W., et al., 2002c, ApJ, submitted
Burwitz, V., Zavlin, V.E., Neuhäuser, R., Predehl, P., Trümper, J., Brinkman, A. C., 2001, A&A, 379, 35L
Camilo, F. 1999, in *Pulsar Timing, General Relativity and the Internal Structure of Neutron Stars*, ed. Z. Arzoumanian, F. Van der Hooft, & E.P.J. van den Heuvel, Amsterdam: Koninklijke Nederlandse Akademie van Wetenschappen, p. 115
Camilo, F., Lorimer, D. R., Freire, P., Lyne, A. G., & Manchester, R. N., 2000, ApJ, 535, 975
Caraveo, P.A., Mignani, R., Pavlov, G.G., Bignami, G.F., 2002, in *A decade of HST science*, Space Telescope Science Institute Symposium, eds. M.Livio, K.Noll and M.Stiavell, p13
Cheng, K.S., Ho, C. & Ruderman, M.A., 1986, ApJ, 300, 500
Danner R., Kulkarni S.R., Saito Y., Kawai N., 1997, Nat 388, 751
D'Amico, N., Lyne, A.G., Manchester, R.N., Possenti, A., Camilo, F., 2001, ApJ, 548, L171
Dickel, J.R., Carter, L.M., Memorie della Societa Astronomia Italiana, Vol. 69, p.845
Dickey J. M., Lockman F. J., 1990, ARA&A., 28,215
Freire, P.C., Camilo, F., Lorimer, D.R., Lyne, A.G., Manchester, R.N., D'Amica, N., 2001, MNRAS, 326, 901
Fruchter A.S., Bookbinder J., Garcia M.R., Bailyn C.D., 1992, Nat, 359, 303
Fossati, G., Celotti, A., Chiaberge, M., et al., 2000, ApJ, 541, 166
Garmire, G.P., Pavlov, G.G., Garmire, A.B., Zavlin V.E. 2000, IAU Circ. #7350
Green, A.,2000, *A Catalogue of Galactic Supernova Remnants*, Mullard Radio Astronomy Observatory, Cambridge, UK
Greiveldinger, C., Camerini, U., Fry, W., et al. 1996, ApJ, 465, L35
Grindlay, J.E., Camilo, F., Heinke, C.O., Edmonds, P.E., Cohn, H., Lugger, P., 2002, to apper in ApJ
Gotthelf, E.V., Petre, R., Vasisht, G. 1999a, ApJ. 514, L107
Halpern, J.P., Holt, S.S., 1992, Nat, 357, 222
Halpern J.P., 1996, ApJ, 459, L9
Harding, A.K., Muslimov, A.G., 2002, ApJ, 568, 862
in't Zand, J.J.M., et al.,1998, A&A, 331, L25
Iyudin, A.F., Schönfelder, V., Bennett, K., Bloemen, H., Diehl, R., Hermsen, W., Lichti, G.G., van der Meulen, R.D., Ryan, J., Winkler, C., 1998, Nat, 396, 142
Johnston S., Lorimer D.R., Harrison P.A., et al. 1993, Nat, 361, 613
Kawai, N., Tamura, K., 1996, in *IAU Colloquium 160*, eds S.Johnston, M.A.Walker and M.Bailes, p367
Kawai, N., Saito, Y., 1999, Astro. Lett. and Communications, 38, 1
Kaspi, V.M., Crawford, F., Manchester, R.N., Lyne, A.G., Camilo, F., D'Amico, N., Gaensler, B.M., 1998, ApJ, 503, L161
Kendziorra E., Kuster, M., Kirsch, M., Risse, P., Straubert, R., Becker, W., Strüder L., Treis, J., Lechner, P., Holl, P., 2002, SPIE Conference 4851,
Kuiper, L., Hermsen, W., Verbunt, F., Ord, S., Stairs, I., Lyne, A., 2002, ApJ, in press, astro-ph/0206081
Kulkarni, S. R., Anderson, S. B. 1996, in *Dynamical Evolution of Star Clusters – Confrontation of Theory and Observations*: IAU Symposium 174, Kluwer Academic Publisher, p.181
Kulkarni S.R., Phinney E.S., Evans C.R., Hasinger G., 1992, Nat, 359, 300
Kuster, M., Kendziorra, E., Benlloch, S., Becker, W., Lammers, U., Vacanti, G., Serpell, E., 2002, in the Proceedings of *New Vision of the X-ray Universe in the XMM-Newton and Chandra Era*', Nov. 2001, ESTEC, in press
Lange, C., Camilo, F., Wex, N., Kramer, M., Backer, D.C., Lyne, A.G., Doroshenko, O., MNRAS, 326, 274
Lyne, A.G., Jordan, C.A., Roberts, M.E., 2002, Jodrell Bank Crab Pulsar Timing Results, Monthly Ephemeris, University of Manchester
Lommen, A.N., Zepka, A., Backer, D.C., Cordes, J.M., Arzoumanian, Z., McLaughlin, M., & Xilouris, K. 2000, ApJ, 545, 1007
Manchester, R. N., Lyne, A. G., Camilo, F., Kaspi, V. M., Stairs, I. H., Crawford, F., Morris, D. J., Bell, J. F., & D'Amico, N., 2000, in *Pulsar Astronomy - 2000 and Beyond*, ed. M.Kramer, N.Wex, and R.Wielebinski, San Francisco: ASP, p.49

Manchester at al., 2002, Catalog of pulsars, unpublished
Marshall, H.L., Schulz, N.S., 2001, AAS, 199, #119.05
Mereghetti, S., 2001, ApJ, 548, L213
Mereghetti, S., De Luca, A., Caraveo, P.A., Becker, W., Mignani, R., Bignami G.F., 2002, accepted for ApJ, astro-ph/0207296
Mineo, T., Cusumano, G., Kuiper, L., Hermsen, W., Massaro E., Becker, W., Nicastro, L., Sacco, B., Verbunt, F., Lyne, A.G., Stairs, I.H., Shibata, S. 2000, A&A, 355, 1053
Navaro, J., de Bruyn, G., Frail, D., Kulkarni, S.R., Lyne, A.G., 1995, ApJ, 455, L55
Ögelman, H., Finley, J.P., 1993, ApJ, 413, L31
Ögelman, H.B., 1995, in *The Lives of Neutron Stars*, eds M.Alpar et al., NATO ASI Series Vol. 450, Kluwer Academic Pblisher, p101-120
Paerels, F., Mori, K., Motch, C., Haberl, F., Zavlin, V.E., Zane, S., Ramsay, G., Cropper, M., Brinkman, B.,2001, A&A, 365, 298L
Pavlov, G.G., Shibanov, Y.A., Zavlin, V.E., 1995, in *The Lives of Neutron Stars*, eds. A.Alpar, U.Kilizoglu & J. van Paradijs, KLuwer Academic Publishers, p71
Pavlov, G.G., Sanwal, D., Kiziltan, B., G.Garmire, 2001, ApJ, 559, 131
Petre, R. Becker, C.M., Winkler, P.F. 1996, ApJ, 465, L43
Potekhin, A., Yakovlev, D., 2001, A&A, 374, 213
Rajagopal, M., Romani, R.W. 1996, ApJ, 461, 327
Rasio, F.A., Pfahl, E.D., & Rappaport, S. 2000, ApJ, 532, L47
Rots, A.H., Jahoda, K., Lyne, A.G., 2000, AAS, HEAD meeting #32, #33.08
Saito Y., Kawai N., Kamae T., et al., 1997, ApJ, 477, L37
Saito, Y., 1998, Ph.D. thesis, Tokio Univ. (ISAS Research Note 643)
Sakurai, I., Kawai, N., Torii, K., Negoro, H., Nagase, F., Shibata, S., Becker, W., 2001, PASJ, 53, 535
Sanwal, D., et al., 2002, AAS 200, 7201
Slane, P., Hughes, J.P., Edgar. J., et al., 2001, ApJ, 548, 814
Stappers, B.W., Gaensler, B.M., Johnston S., 1999, MNRAS, 308, 609
Swanepoel J.W.H., de Beer C.F., Loots H., 1996, ApJ, 467, 261
Takahashi M., Shibata S., Torii K., Saito Y., Kawai N. 1998, IAU Circ. 7030
Takahashi, M., Shibata, S., Torii, K., Saito, Y., Kawai, N., Hirayama, M., Dotani, T., Gunji, S., Sakurai, H., Stairs, I.H., Manchester, R.N., 2001, ApJ, 554, 316
Tennant, A.F., Becker, W., Juda, M., Elsner, R.F., Kolodziejczak, J.J. Murray, S.S., O'Dell, S.L., Paerels, F., Swartz, D.A., Shibazaki, N., Weisskopf, M.C., 2001, ApJ, 554, L173
Torii, K., 1998, Ph.D. thesis, Osaka Univ. (ISAS Research Note 650)
Torii, K., Kinugasa, K., Toneri, T., Asanuma, T., Tsunemi, H., Dotani, T., Mitsuda, K., Gotthelf, E. V., Petre, R., 1998, ApJ, 494L, 207
Torri, K., Gotthelf, E.V., Vasisht, G., Dotani, T., Kinguasa, K., ApJ, 2000, 534, L71
Toscano, M., Bailes, M., Manchester, R., Sandhu, J.S., 1998, ApJ, 506, 863
Toscano, M., Britton, M.C., Manchester, R., Bailes, M., Sandhu, J.S., Kulkarni, S., Anderson, S.B., 1999, ApJ, 523, L171
Tsunemi, H., Miyata, E., Aschenbach, B., Hiraga, J., Akutsu, D., 2000, PASJ, 52, 887
Tuohy, I.R., Garmire, G.P. 1980, ApJ, 239, L107
van Straten, W., Bailes, M., Britton, M., Kulkarno, S.R., Anderson, S.B., Manchseter, R.N., Sarkissian, J., 2001, Nat, 412, 158
Verbunt F., Kuiper L., Belloni T., et al, 1996, A&A, 311, L9
Wijnands, R., van der Klis, M., 1998, Nat, 394, 344,
Weisskopf, M.C., Hester, J.J., Tennant, A.F., et al. 2000, ApJ, 536, L81
Willingale, R., Aschenbach, B., Griffiths, R. G., Sembay, S., Warwick, R. S., Becker, W., Abbey, A. F., Bonnet-Bidaud, J.-M., 2001, A&A, 365, L212
Zavlin, V.E., Pavlov, G.G., Shibanov, Y.A., 1996, A&A, 315, 141
Zavlin, V.E., Trümper, J., Pavlov, G.G., 1999, ApJ, 525, 959
Zavlin, V.E., Pavlov, G.G., Sanwal, D., Manchester, R.N., Trümper, J., Halpern, J.P., Becker, W., 2002, ApJ, 569, 894

Proceedings of the 270. WE-Heraeus Seminar on: *"Neutron Stars, Pulsars and Supernova Remnants"*
Physikzentrum Bad Honnef, Germany, Jan. 21-25, 2002, eds. W. Becker, H.Lesch & J. Trümper, MPE Report 278, pp. 87- 90

The 2-10 keV emission properties of PSR B1937+21

L. Nicastro[1], G. Cusumano[1], L. Kuiper[3], W. Becker[2], W. Hermsen[3], and M. Kramer[4]

[1] IASF–CNR, Via U. La Malfa 153, 90146 Palermo, Italy
[2] Max–Planck–Institut für extraterrestrische Physik, Giessenbachstraße, 85740 Garching, Germany
[3] SRON National Institute for Space Research, Sorbonnelaan 2, 3584 CA Utrecht, The Netherlands
[4] University of Manchester, Jodrell Bank, Macclesfield SK11 9DL, United Kingdom

Abstract. We present the results of a *Beppo*SAX observation of the fastest pulsar known: PSR B1937+21. The $\sim$ 200 ks observation (78.5 (34) ks MECS (LECS) exposure times) allowed us to investigate with high statistical significance both the spectral properties and the pulse profile shape. The absorbed power law spectral model gave a photon index of ~ 1.7 and $N_{\rm H} \sim 2.3 \times 10^{22}$ cm^{-2}. These values explain both *a.* the ROSAT non-detection and *b.* the deviant estimate of a photon index of ~ 0.8 obtained by ASCA. The pulse profile appears, for the first time, clearly double peaked with the main component much stronger than the other. The statistical significance is 10σ (main peak) and 5σ (secondary peak). The 1.6–10 keV pulsed fraction is consistent with 100%; only in the 1.6–4 keV band there is a $\sim 2\sigma$ indication for a DC component. The secondary peak is detected significantly only for energies above $3 \div 4$ keV. The unabsorbed (2–10 keV) flux is $F_{2-10} = 3.7 \times 10^{-13}$ erg cm^{-2} s^{-1}, implying a luminosity of $L_X = 4.6 \times 10^{31}\,\Theta\,(d/3.6\ {\rm kpc})^2$ erg s^{-1} and an X-ray efficiency of $\eta = 4 \times 10^{-5}\,\Theta$, where Θ is the solid angle spanned by the emission beam. These results are in agreement with those obtained by ASCA.

1. Introduction

The various X-ray satellites, from Rosat to Chandra, observed about 10 millisecond pulsars (MSPs) (see e.g. Becker 2001), but good spectral and temporal informations exist only for half of them. In fact MSP X-ray observations are usually affected not only by low statistics but also by insufficient time accuracies to perform detailed periodicity and timing analysis. X-ray observations demonstrate that the X-ray emission from MSPs is generally not of thermal origin, and those with the hardest spectra appear to be objects with strong magnetic fields at the light-cylinder B_L ($R_L = cP/2\pi$; see Saito et al. 1997, Kuiper et al. 1998, Kuiper et al. 2000, Becker 2001). Given the correlation between spin-down power and X-ray luminosity (see Verbunt et al. 1996, Becker and Trümper 1997 and Takahashi et al. 2001), another important quantity is the spin-down flux density at Earth ($\dot{E}/4\pi d^2$).

PSR B1937+21, with a period $P = 1.56$ ms, was the first and still the fastest MSP known. In spite of its low surface magnetic field strength of $B_S = 4.1 \times 10^8$ G, its magnetic field at the light-cylinder is the highest of all known pulsars: $B_L \simeq 1 \times 10^6$ G, very similar to that of the Crab pulsar. Its spin-down flux density is $\sim 2 \times 10^{-10}$ erg cm^{-2} s^{-1}, which is 3 times higher than for PSR J0218+4232 but 3 times lower than for PSR B1821−24.

Here we report on the results obtained by a *Beppo*SAX observation in the energy range 1.6–10 keV.

2. Observation and spatial analysis

*Beppo*SAX observed PSR B1937+21 on May 1$^{\rm st}$ 2001. The $\sim$ 200 ks observation time resulted in a total effective on-source time of $\sim$ 78.5 ks ($\sim$ 34 ks) with the MECS (LECS). To extract the source photons from LECS (0.1–10 keV) and MECS (1.6–10 keV), we used:

- a standard spatial analysis with optimized extraction radius and energy range;
- a Maximum Likelihood (ML) approach to extract the number of counts assigned to the pulsar taking into account the presence of other sources and the background simultaneously.

In the first case we estimated the local background (in a circular region in the field of view 10′ away from the pulsar) and compared the results with the standard one from archival blank sky usually used in the spectral fitting. We found that the local background is 50% and 15% higher for LECS and MECS respectively. The extraction radii which optimized the signal to noise ratio were 3′ (LECS) and 2′ (MECS) resulting in a collection of 106 (0.5–8 keV) and 369 (1.6–10 keV) photons. In spite of the lower exposure time and sensitivity of LECS we were able to detect a significant signal in the 0.5–8 keV range for this instrument. Inclusion of these softer photons in the spectral fit allowed us to better constrain the hydrogen column density toward the pulsar ($N_{\rm H}$). Using the ML approach we could extract the source photons modeling the contribution to the total counts from additional field sources and

the (assumed flat) background. This method was successfully used in several other cases of weak source (see e.g. Kuiper et al. 1998, Mineo et al. 2000).

3. Temporal analysis

The arrival times of the extracted photons were converted to the Solar System Barycentric (SSB) Frame using the BARYCONV[1] code and then searched for periodicities by folding them with trial frequencies around the radio one (see updated radio ephemeris in Table 1). The χ^2 value plotted versus trial frequency is shown in Fig. 1. The distribution had a clear maximum, but we found the corresponding pulse frequency deviating from the radio value by $\simeq -7.6 \times 10^{-6}$ Hz ($f_R - f_X$). This is about ten times the statistical error of $\sim 8 \times 10^{-7}$ Hz. To investigate this discrepancy we first verified the correctness of the SSB conversion code by also using independent software. We verified that all the routines involved in the processing were working properly. We then verified the OBT (On-Board Time) to UTC time conversion routine. To this aim we:

1. analyzed separately two sections of the observation; the results confirmed those of the full observation;
2. used different polynomial order for the OBT–UTC fit and various high deviation points (de-)selection criteria; in all cases the results were the same;
3. verified the (X-ray) pulse frequency of the Crab during the observation performed on April 2000 and on September 2001; these observations are shorter than the PSR B1937+21 one (in particular the 2001 observation), nevertheless in the first case we found a discrepancy which is outside the statistical errors.

We concluded that the difference had likely to be attributed to incorrect photon time markers. We investigated the possible reasons of that with the *Beppo*SAX mission director. The answer was that, excluding an unlikely (and unobserved) UTC clock drift (which comes out of the Malindi ground station GPS clock), the only likely explanation could be an on-board electronics problem. In particular it could be an internal drift of the clock which tags the "base band" packets. Performance degradation with time of the clock is not unexpected and usually not considered critical for detectors not specifically built for high precision timing. Also, as we verified with the Crab, the problem is less severe (or not visible) for pulsar with relatively long periods or for relatively short observations. Even though other (we believe more unlikely) explanations could be found, we decided to correct the (possible) clock drift by estimating the required additional slope to add in the OBT–UTC conversion. The result was a constant slope of $\sim 1 \times 10^{-8}$ s s^{-1}. We verified this value (actually a value slightly lower) could also correct the 2000 Crab observation ($\sim$ 70 ks elapsed time) while it had no effect on the 2001 observation ($\sim$ 24 ks elapsed time).

[1] see http://www.sdc.asi.it/software/saxdas/baryconv.html

Table 1. Ephemeris of PSR B1937+21 (from observations performed at Effelsberg).

Parameter	Value
Right Ascension (J2000)	$19^h\ 39^m\ 38^s.560$
Declination (J2000)	$21°\ 34'\ 59''.14$
Epoch validity start/end (MJD)	51639 – 52047
Frequency	641.928246349481 Hz
Frequency derivative	-4.331×10^{-14} Hz s^{-1}
Epoch of the period (MJD)	51843.0
RA proper motion	-0.15 mas yr^{-1}
Dec proper motion	-0.47 mas yr^{-1}

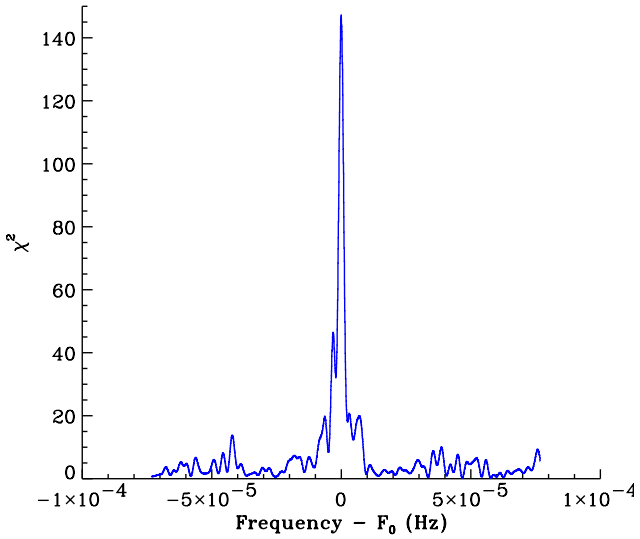


Fig. 1. The χ^2 significance as function of trial folding frequency. The 0 is aligned with the maximum.

Counting statistics allowed us to perform temporal analysis only for the MECS data (actually a search on the LECS photons didn't reveal any significant modulation). As already mentioned, a periodicity search analysis was performed on the 369 photons (1.6–10 keV) around the nominal radio period, after converting the arrival times to the SSB. Figure 2 shows the folded light curve together with the radio one (from the EPN archive[2] – Kramer et al. 1998). The primary peak (P1) is detected at 10σ level and, for the first time, we also detect the secondary peak (P2 – significance $\sim 5\sigma$) and estimate a relative phase separation of 0.48 ± 0.04. Data collected by ASCA allowed Takahashi et al. (2001) to claim an alignment of the main X-ray peak with the radio interpulse. We then arbitrarily aligned the two profiles (the BSAX on-board clock absolute calibration does not allow to do it for a

[2] see http://www.mpifr-bonn.mpg.de/pulsar/dat/

Table 2. Power law fit parameters using photons extracted with the standard and the Maximum Likelihood methods.

Method	K[a]	α	$N_{\rm H}$ (10^{22} cm^{-2})	F_{2-10}[b]
STD	0.85	$1.66^{+0.07}_{-0.06}$	$2.27^{+0.58}_{-0.47}$	3.7 ± 0.4
ML	$1.12^{+0.10}_{-0.10}$	$1.71^{+0.06}_{-0.08}$	$2.10^{+0.56}_{-0.42}$	3.7 ± 0.4

Note: all quoted uncertainties are 1σ confidence. It is $N_{ph}(E) = K \times E^{-\alpha}$.
[a] Normalization at 1 keV (10^4 ph s^{-1} cm^{-2}).
[b] Unabsorbed flux in 2–10 keV (10^{-13} erg cm^{-2} s^{-1}).

MSP). The vertical dashed lines in the figure are exactly 0.5 apart. The radio peaks separation is instead 0.4794(8) so it would be tempting to consider the ASCA result incorrect and consider P1 be coincident with the main radio peak. The X-ray peak widths are compatible with the instrument time resolution limit (~ 100 μs). Figure 3 shows the X-ray pulse profile in 3 energy ranges. In an attempt to quantify the evidence for a pulsar DC component, we applied the bootstrap method proposed by Swanepoel et al. (1996), which allows us to estimate the DC level (sky background and possibly a source component) in the pulse profile. We can then determine the DC and pulsed fractions of the pulsar by taking the background level from the spatial analysis into account. However, in the available form, the bootstrap method is able to find only one unpulsed interval and cannot account for systematic errors. One should therefore realize that the quoted errors on the calculated parameters are only statistical. Note in Fig. 3 how the DC level is compatible with the background level. We find that over the total energy range 1.6–10 keV the source is consistent with being 100% pulsed; the 2σ lower limits for the pulsed fraction in the energy ranges 1.6–10, 1.6–4 and 4–10 keV are 88%, 66% and 95%, respectively. Only for the lower 1.6–4 keV energy interval we find an indication for a DC component of (18.7 ± 7.7)%. An increase of P2 compared to P1 with energy is clearly visible.

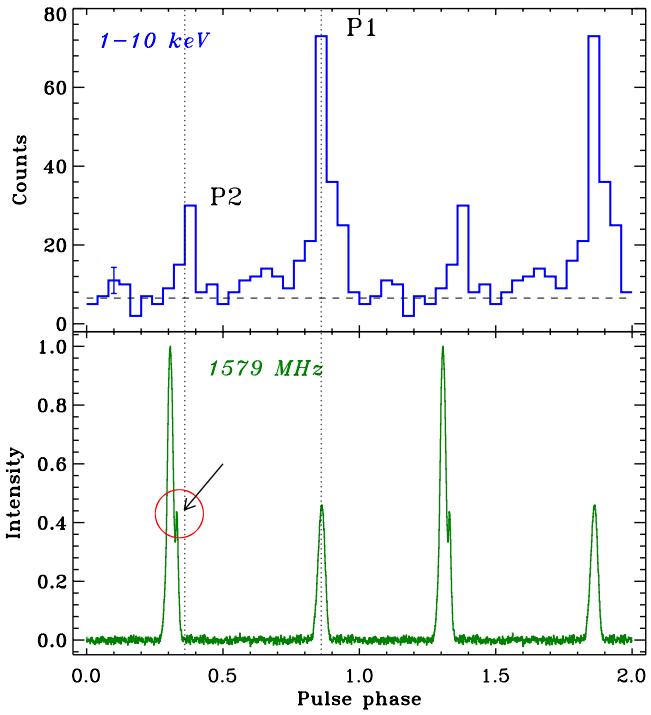


Fig. 2. The 1.6–10 keV X-ray profile and the radio one arbitrarily aligned using the main X-ray peak. The two vertical dotted lines are 0.5 apart. The X-ray phase separation is 0.48 like for the radio but 0.5 shifted in phase (if the ASCA result is correct). In this case we can also confidently exclude that the secondary X-ray peak is associated with the feature visible in the main radio peak (which instead would mimic the X-ray feature in P1).

4. Spectral analysis

The spectral analysis was performed using photons extracted in two different ways: *a.* those in a (S/N optimized) circular region centered on the pulsar position (standard method); *b.* those from the ML analysis, which consider simultaneously the source, the background and a number of field sources. In both cases the best fitting model was an absorbed power law. A Black Body model did not fit the data satisfactorily. The two methods gave consistent results and are summarized in Tab. 2. The absorbed flux (2–10 keV) is 3.1×10^{-13} erg cm^{-2} s^{-1}.

The derived (unabsorbed) luminosity is $L_X = 4.6 \times 10^{31}\,\Theta\,(d/3.6\ {\rm kpc})^2$ erg s^{-1} while the X-ray conversion efficiency is $\eta = L_X/\dot{E} = 4 \times 10^{-5}\,\Theta$, where Θ is the solid angle spanned by the emission beam. Note that the column density is 10 times greater than the radio DM derived one (by assuming 10 H atoms for each e$^-$) and is only marginally consistent (within 2σ) with the Galactic value 1.4×10^{22} cm^{-2}. In addition the photon index is significantly softer than that found for PSR J0218+4232 (0.94 ± 0.22) and PSR B1821−24 (~ 1.1 using RXTE data, Kawai and Saito 1999). Also for the latter pulsar (placed in the globular cluster M28, at a distance of ~ 5 kpc, galactic latitude $-5.^\circ6$) its $N_{\rm H} \simeq 3 \times 10^{21}$ cm^{-2}, consistent both with the Galactic and DM derived one. Being the line of sight to PSR B1937+21 tangent to the Galactic spiral arms ($l \simeq 57.51$, $b \simeq -0.29$, see Taylor and Cordes 1993) one can invoke a particularly low e$^-$/$N_{\rm H}$ ratio in that direction due to the lack of ionizing sources. However, using the relation $N_{\rm H} = 1.79 \times 10^{21} A_V$ of Predehl and Schmitt (1995), Verbunt at al. (1996) set an upper limit of 2.2×10^{21} cm^{-2} for the column density, i.e. in agreement with the DM value. More simply, the measured high $N_{\rm H}$ could suggest for PSR B1937+21 a true distance greater than the 3.6 kpc derived from the Taylor and Cordes (1993) model. If instead this value is correct

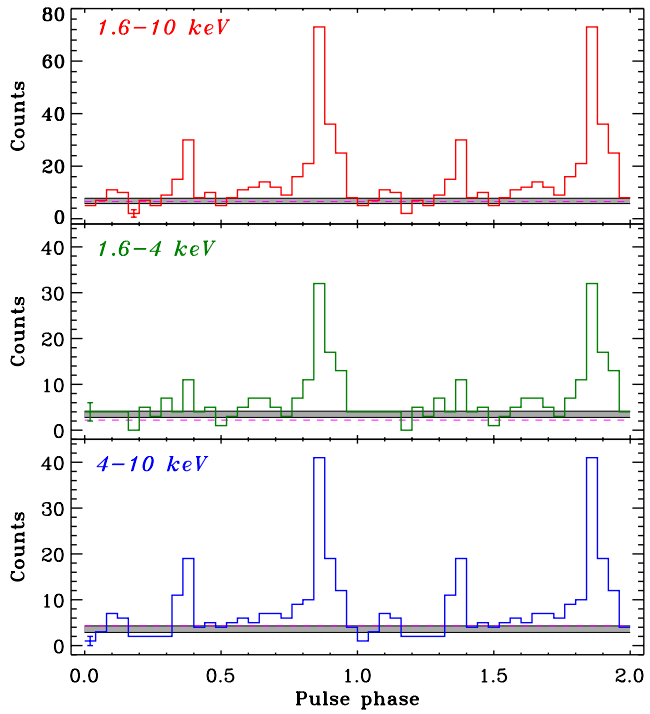


Fig. 3. The X-ray pulse profile in the full MECS X-ray band 1.6–10 keV and two sub-bands. The shaded areas show the estimated DC level ($\pm 1\sigma$), while the dashed lines indicate the measured background level. In the 1.6–4 keV energy band the secondary peak is detected at $\lesssim 3\sigma$ level and is compatible with the DC level. In the 4–10 keV band instead the detection level is 4σ (above background or DC level).

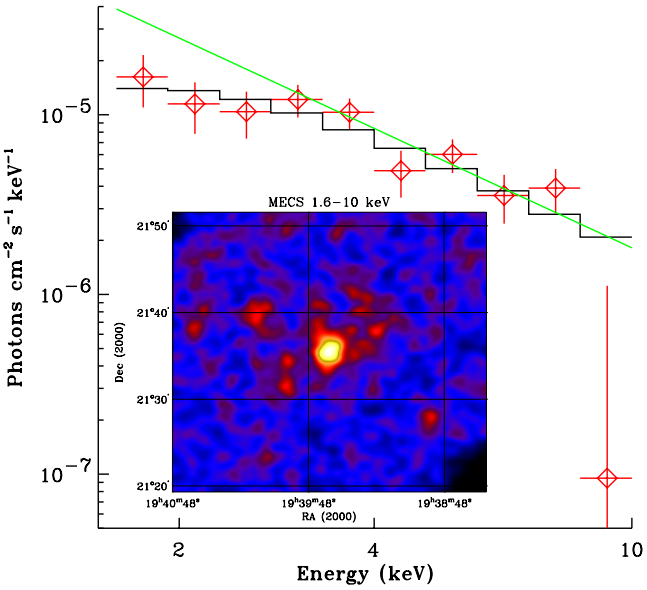


Fig. 4. The 1.6–10 keV spectrum and best fit model with the unabsorbed power law ($\alpha = 1.66$). It is evident the strong absorption below ~ 3 keV. In the inset the smoothed MECS image around the PSR position is shown.

then the continuing radio timing measurements should be able to detect its effect on the timing fit residuals very soon. We also note that the fit parameters are consistent with the non-detection in the ROSAT HRI energy range (0.1–2.4 keV).

5. Conclusions

We detected the double peak profile of the fastest pulsar known. The 1.6–10 keV pulsed fraction is consistent with 100%, only for the band 1.6–4 keV there is an indication for a DC component (18.7 ± 7.7 %). The secondary (X-ray) peak is significantly detected only above 3–4 keV and the ratio primary/secondary decreases with energy. It was not possible to perform an absolute phase comparison with the radio profile, but, *purely* morphologically, a phase separation comparison suggests alignment of the main X-ray peak with the main radio one, contrary to the ASCA finding by Takahashi et al (2001) which claim an alignment with the radio interpulse. An accepted Rossi-XTE observation will clarify this point.

We measure a soft power law spectral index ($\alpha \simeq 1.7$), different from those measured for PSR J0218+4232 and PSR B1821−24. The $N_{\rm H} \sim 2.3 \times 10^{22}$ cm^{-2} is marginally consistent with the Galactic value in the direction of the pulsar and gives a $e^-/N_{\rm H}$ ratio of 1/100, 10 times smaller than the canonical average value. This could be justified by the position of PSR B1937+21 in the Galaxy w.r.t. our line of sight but could also suggest a larger distance than the DM derived one. Radio timing should settle this issue soon.

Acknowledgements. This research is supported by the Italian Space Agency (ASI) and Consiglio Nazionale delle Ricerche (CNR). BeppoSAX is a major program of ASI with participation of the Netherlands Agency for Aerospace Programs (NIVR).

References

Becker W., Trümper J., 1997, A&A 326, 682
Becker W., 2001, in *X-ray Astronomy '99: Stellar Endpoints, AGN & the Diffuse X-ray Background*, eds N. White et al., AIP Conference Proceedings 599, p. 13-24
Kawai N., Saito Y., 1999, Proc. 3rd INTEGRAL Workshop, Taormina, Astroph. Lett. & Comm. Vol. 38, I, p.1.
Kramer M., et al., 1998, ApJ 501, 270
Kuiper L., Hermsen W., Verbunt F., Belloni T., 1998, A&A 336, 545
Kuiper L., Hermsen W., Verbunt F., et al. 2000, A&A 359, 615
Mineo T., Cusumano G., Kuiper L., et al., 2000, A&A 355, 1053
Predehl P., Schmitt J., 1995, A&A 293, 889
Takahashi M., Shibata S., Torii K., et al., 2001, ApJ 554, 316
Saito Y., Kawai N., Kamae T., et al., 1997, ApJ 477, L37
Swanepoel J.W.H., de Beer C.F., Loots H., 1996, ApJ 467, 261
Taylor J.H., Cordes J.M., 1993, ApJ 411, 674
Verbunt F., Kuiper L., Belloni T., et al., 1996, A&A 311, L9

Proceedings of the 270. WE-Heraeus Seminar on: *"Neutron Stars, Pulsars and Supernova Remnants"*
Physikzentrum Bad Honnef, Germany, Jan. 21-25, 2002, eds. W. Becker, H.Lesch & J. Trümper, MPE Report 278, pp. 91- 99

Gamma-Ray Pulsars

Gottfried Kanbach

Max–Planck–Institut für extraterrestrische Physik, Giessenbachstraße, 85741 Garching, Germany

Abstract. Gamma-ray photons from young pulsars allow the deepest insight into the properties and interactions of high-energy particles with magnetic and photon fields in a pulsar magnetosphere. Measurements with the Compton Gamma-Ray Observatory have led to the detection of nearly ten γ-ray pulsars . Although quite a variety of individual signatures is found for these pulsars, some general characteristics can be summarized: (1) the γ-ray lightcurves of most high-energy pulsars show two major peaks with the pulsed emission covering more than 50% of the rotation, i.e. a wide beam of emission; (2) the γ-ray spectra of pulsars are hard (power law index less than 2), often with a luminosity maximum around 1 GeV. A spectral cutoff above several GeV is found; (3) the spectra vary with rotational phase indicating different sites of emission; and (4) the γ-luminosity scales with the particle flux from the open regions of the magnetosphere (Goldreich-Julian current).

1. Introduction

If the perceptiveness of Jocelyn Bell had not led to the discovery of radio pulsars in 1967, the three brightest localized γ-ray sources would have certainly attracted the attention of the astronomical community. The first high-energy γ-ray maps of the Galaxy (SAS-2, Fichtel et al.,1975; COS-B, Mayer-Hasselwander et al., 1982) are dominated by the sources now known as the young pulsars Crab, Vela and Geminga. Unlike in any other waveband these young pulsars outshine other sources at energies above 100 MeV. The sky survey performed with the Compton Gamma-Ray Observatory (CGRO) from 1991 to 2000 led to the detection of at least 4 more gamma-ray pulsars, raising the total number to 7 sources. Listing also some detections of lower significance we now have about a dozen potential γ-ray pulsars . This is still a small number compared to the known population of radio ($\sim$1500) or X-ray ($\sim$30) pulsars. However the γ-radiation should provide the deepest insights into the physics of the extreme astrophysical site characterized by magnetic fields close to the quantum-mechanical scale ($B_{cr} = m^2c^3/e\hbar = 4.414 \times 10^{13}$ G), space-time near to a fast rotating neutron star, and relativistic speeds in the outer co-rotating magnetosphere. As we will see, the number of detected γ-ray pulsars is quite in agreement with expectations based on sensitivities of current telescopes. Moreover, it is quite likely that several of the unidentified γ-ray sources, which belong mostly to a galactic population and are strongly correlated with population II regions (i.e. molecular clouds, OB associations, SNRs), are γ-ray pulsars without radio emission.

2. High Energy Pulsar Physics

Why can, indeed must, we expect high-energy emissions from young pulsars? Goldreich and Julian (1969) have shown that the magnetosphere of a pulsar is filled with a charge-separated plasma. A rotating, magnetized, conducting neutron star works as a unipolar inductor. The positive and negative charges inside the star, redistributed by the Lorentz forces, arrange themselves such that the electric field from charge separation counterbalances the magnetic forces and no permanent currents flow inside the star. The interior charge distribution determines the electric fields outside the star, requiring continuity for the potentials and tangential electric fields at the stellar surface. The radial components of this magnetospheric electric field ($\sim 6 \times 10^{10} P_s^{-1}$ V cm^{-1}) have a discontinuity on the stellar surface which implies a surface charge layer. The electric fields close to the surface greatly surpass the gravitational attraction as well as the exit work functions of charges from the star. Therefore the magnetosphere of the neutron star is filled with a charge separated plasma which tends to compensate the induced electric fields until $\mathbf{E} \cdot \mathbf{B} = 0$ is achieved and the magnetosphere comes to equilibrium. The required charge density, called the Goldreich–Julian density, is given by

$$n_{GJ} \simeq -\frac{\boldsymbol{\omega} \times \boldsymbol{B}}{2\pi c} = 7 \times 10^{10} B_{\parallel,12} P_s^{-1} \text{ cm}^{-3}, \qquad (1)$$

where $B_{\parallel,12}$ (units of 10^{12} G) is the field component parallel to $\boldsymbol{\omega}$ and P_s is the rotation period in s.

However there can be no static equilibrium in the co-rotating magnetosphere of a pulsar. At a distance of

$r_c = c/\omega \sim 5 \times 10^4 P_s$ km from the axis of rotation (the 'light cylinder'), particles and fields would have to co-rotate with the speed of light. Relativistic effects of retardation and plasma mass loading will severely distort the pulsar magnetosphere close to the light cylinder and field lines trying to extend across r_c are forced open to the outside. Regions of the magnetosphere threaded by these field lines ('open regions') release their charges into the pulsar wind zone. The outflow leads to a deficit of charges in the regions above the magnetic poles ('polar cap') and between the zero charge density surfaces ($n_{GJ} = 0$) and the equatorial magnetosphere close to r_c ('outer gaps'). In these gaps the electrostatic potential of the rotating dipole is not balanced by charges and is available to accelerate particles to very high energies. Additional accelerating potentials are generated by relativistic effects ('frame dragging') close to the neutron-star surface (Muslimov and Tsygan, 1990, 1992). As a consequence of the described electrodynamics, high-energy particles (Lorentz factors $\sim 10^6 - 10^7$ in most theories, $\sim 10^3$ in some) are accelerated in the gap regions and propagate along the magnetic field. Radiation losses due to magnetic bremsstrahlung (synchro-curvature radiation) and inverse Compton scattering on a low energy photon environment counterbalance the acceleration. If the energies in the particle/photon cascade exceed the threshold for pair creation ($\gamma - \gamma$ and $\gamma - \boldsymbol{B} \rightarrow e^+e^-$), the extent of the acceleration region is further limited by the formation of a dense electron–positron plasma (pair formation front) which screens the open potentials. The high-energy cascade of particles and photons propagates through the magnetosphere until the photons decouple from the particles ('pulsar photosphere') and reachinfinity, i.e. our telescopes. The observation of pulsed high-energy radiation allows us therefore to look directly at the particle spectra and magnetic field geometries on the 'pulsar photosphere'. This high-energy photosphere can be visualized as a complex three-dimensional radiating surface with high directivity. Its properties should depend critically on pulsar parameters like field strength, inclination of the magnetic axis, aspect angle of observer, etc. and of course on the model assumptions. Although the scenario of magnetospheric high-energy cascades in the open zones is generally accepted, a fully self-consistent, quantitative theory has not yet been achieved. The terminal energies and spectra reached by the radiating particles depends on many uncertain assumptions and the debate on the relative importance of 'polar cap' and/or 'outer gap' emission continues, with occasional suggestions that the pulsar wind zone could be an additional source of γ-rays . A good set of observational facts, including multi-wavelength spectra and lightcurves, will certainly help to clarify our understanding of these fascinating high-energy machines.

In the following, we qualitatively scale the high-energy radiation output with the current of relativistic particles flowing from the polar cap ('PC'). The Goldreich–Julian current, formed by n_{GJ} particles flowing with c from the PC area $A_{PC} \sim \pi r_{NS}^2 (\frac{r_{NS}}{r_c})$ is given by

$$\dot{N}_{GJ} = A_{PC} \cdot n_{GJ} \cdot c \sim 1.7 \times 10^{38} \dot{P}^{\frac{1}{2}} P^{-\frac{3}{2}} \text{ s}^{-1}. \quad (2)$$

If this particle flow consists mainly of electrons with Lorentz factor $\sim 10^6$ the outflowing power is of the order of $\sim 10^{38} \dot{P}^{\frac{1}{2}} P^{-\frac{3}{2}}$ erg s^{-1}. It should be noted that the product $\dot{P}^{\frac{1}{2}} P^{-\frac{3}{2}}$ is proportional to $\sqrt{\dot{E}_{rot}}$ and also to the total voltage available over the pulsar's open field lines Φ.

We can now estimate the energy flux observable from a pulsar at distance d:

$$F_E = (\eta \cdot \dot{E}_{rot}^{\alpha})/4\pi f_\Omega d^2 \quad (3)$$

where η is an efficiency factor that describes the conversion of the energy input (rotational energy loss or GJ current) into γ-radiation, α an exponent for the energy source (=0.5 if $\dot{N}_{GJ}$ dominates, =1 if $\dot{E}_{rot}$ relates directly to the γ-ray luminosity), and f_Ω describes the solid angle fraction illuminated by the pulsar beam (a canonical value of $f_\Omega = 1/4\pi$, i.e. beaming into 1 sr is assumed). Figure 1 shows the distribution of expected fluxes from a current list of radio pulsars with different assumptions for their luminosities. Rough sensitivity limits for past (COS-B, EGRET) and future (GLAST) telescopes are also shown in fig. 1. COS-B with 4-5 pulsars and EGRET with about a dozen detections are at the expected level. For GLAST we would estimate between 30 and 100 new radio pulsar detections.

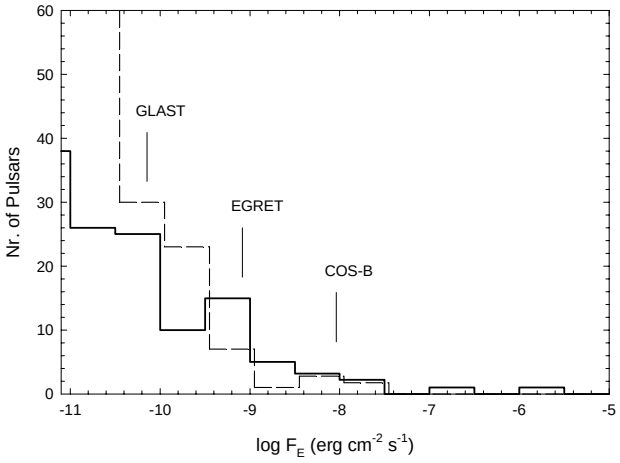


Fig. 1. Distribution of F_E for radio pulsars. For the γ-ray efficiency η two assumptions are used: η = const = 0.01(*solid line*) and $\eta \dot{E}_{rot}^{\alpha} \approx \sqrt{\dot{E}_{rot}}$ (*dashed line*). Approximate sensitivity limits for COS-B, EGRET and GLAST are shown

These predictions for high-energy emission from radio pulsars were published early after their discovery and the search for pulsars outside the radio range began. Detections were first reported for the Crab pulsar at X-ray (from balloon-borne detectors) and at optical wavelengths. Today more than 30 pulsars are known at X-ray energies. In

Table 1. High-energy pulsars: multi-wavelength detections, candidates, and positional coincidences
Notes: P: pulsed emission; D: positional coincidence; ?: low significance pulsed detection

PSR	P (ms)	$\dot{E}/d^2$ rank	Radio	Optical	EUV	X_{low}	X_{hi}	γ_{low}	γ_{hi}
High-confidence γ-ray detections									
B0531+21 (Crab)	33.4	1	P	P		P	P	P	P[1]
B0833-45 (Vela)	89.3	2	P	P		P		P	P[3]
J0633+1746 (Geminga)	237.1	3	?	?	P	P		?[9]	P[7]
B1706-44	102.5	4	P			P			P[4]
B1509-58	150.7	5	P	D		P	P	P[2]	
B1951+32	39.5	6	P			P		P[10]	P[5]
B1055-52	197.1	33	P	D		P		P[11]	P[8]
Candidate γ-ray detections									
B0656+14	384.9	18	P	?	D	P		?[10]	?[6]
B0355+54	156.4	36	P			D			?[12]
B0631+10	287.7	53	P						?[13]
B0144+59	196.3	120	P						?[14]
Candidate ms-pulsars γ-ray detections									
J0218+4232	2.32	43	P			P			?[15]
B1821-24	3.05	14	P			P			?[16]
Likely pulsar–γ-ray source coincidences									
B1046-58	123.7	8	P			D			?[18]
J1105-6107	63.2	21	P[17]			D			
B1853+01	267.4	27	P			?			?

References:
[1] Nolan et al.(1993); [2] Matz et al.(1994), Kuiper et al.(1999a); [3] Kanbach et al.(1994);
[4] Thompson et al.(1992, 1996); [5] Ramanamurthy et al.(1995); [6] Ramanamurthy et al.(1996);
[7] Mayer-Hasselwander et al.(1994); [8] Fierro et al.(1993); [9] Kuiper et al.(1996);
[10] Hermsen et al.(1997); [11] Thompson et al.(1999); [12] Thompson et al.(1994);
[13] Zepka et al.(1996); [14] Ulmer et al.(1996); [15] Kuiper et al.(1999b);
[16] Thompson et al.(1997); [17] Kaspi et al.(1997); [18] Kaspi et al.(2000)

the optical range, four to five pulsating counterparts and a similar number of optical candidates based on positional coincidence have been found.

3. Detections

Table 1 (Kanbach, 2001) gives an overview of the high-energy pulsars and their multi-frequency detections, ranging from the radio band to gamma rays, after the decade of discoveries with the CGRO instruments. Next to the column with the spin period the rank of the quantity $\dot{E}/d^2$, i.e. the spin-down power over the square of the distance as a measure of the apparent brightness, is given. It is evident that the detections in the gamma-ray range follow closely the ranking derived from the spin-down luminosity. Therefore we might conclude that gamma-ray emission is a common phenomenon of pulsars. However, since so far most detections of gamma-ray pulsars require the detection in the radio or X-ray regime in order to provide the periodicity ephemeris, we must be careful not to discard the possibility that many pulsars might exist that emit dominantly at high energies and so far have only been detected as unidentified γ-ray sources.

4. Emission Characteristics

4.1. Lightcurves

The regular brightness variation of pulsars ('lightcurves'), with periods ranging from $\sim ms$ to nearly 10s, was the primary characteristic of this new astrophysical object. The lightcurve of a pulsar can be regarded as the cross-section through a rotating beaming pattern cut along the line of sight to the observer. The full beaming pattern on the sphere around a pulsar would give us a direct view of the sites of origin and beaming directions and allow us to derive the luminosity of such a 'highly' non-isotropic source. But of course we are restricted to our singular view of individual sources. In order to gain a better understanding of high energy pulsars we can follow two routes: (1) rely on theoretical modeling or (2) observe a sufficient number of pulsars to get a statistical relevant sample with different aspect angles. The rather limited number of detections has not yet allowed a full population treatment. But some common traits for the γ-ray emission from young pulsars become already apparent. Figure 2 displays the high-energy lightcurves of the brightest 6 EGRET pulsars. We note that the pulsed emission extends over more

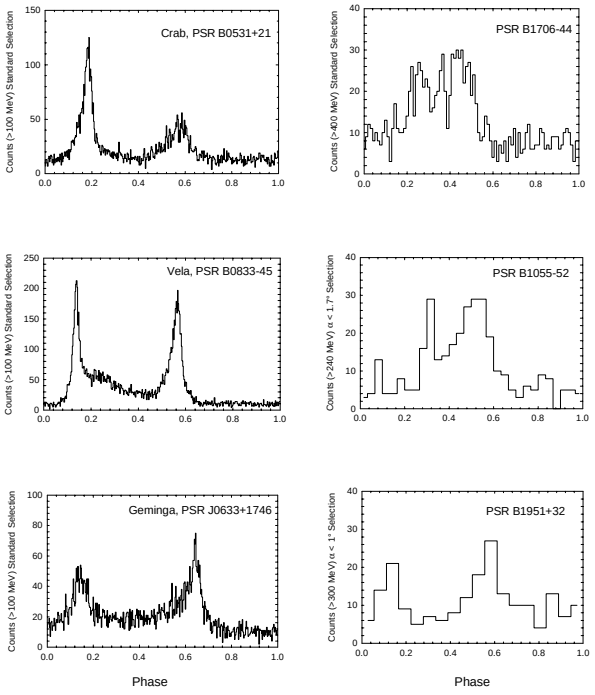


Fig. 2. High-energy light curves of γ-ray pulsars (> 100 MeV, unless indicated differently)

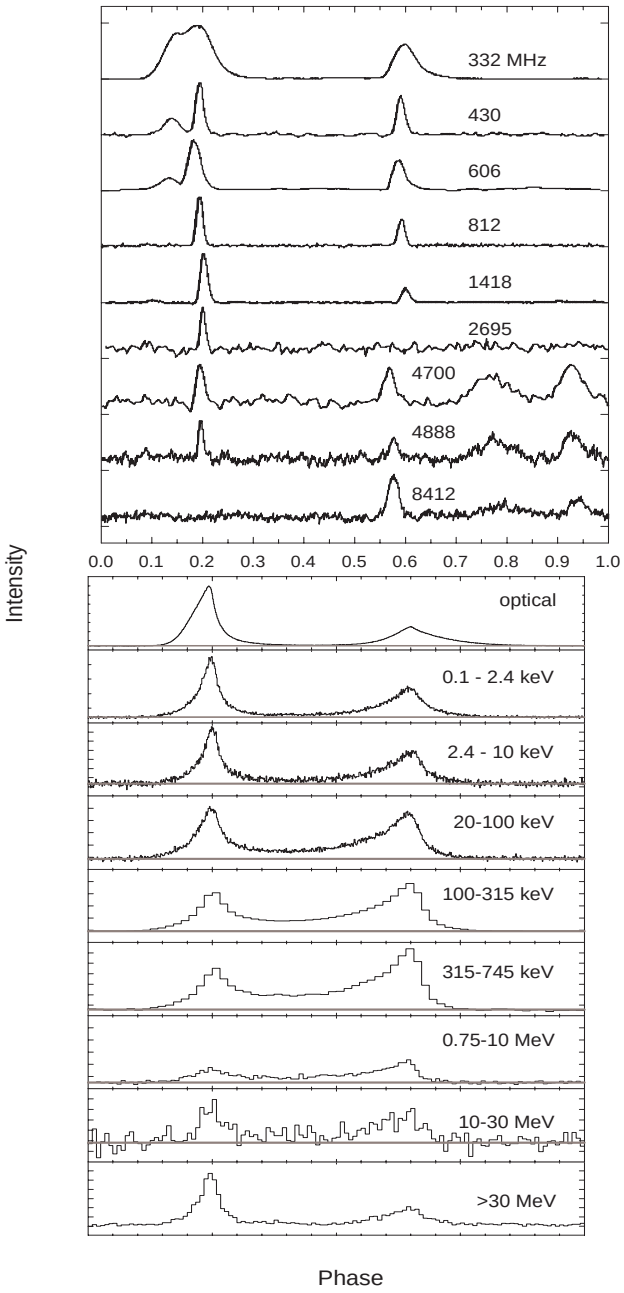


Fig. 3. Multi-wavelength lightcurves of the Crab pulsar in the radio range (top, Moffett & Hankins, 1996) and at high energies (bottom, Kuiper et al., 2001).

than 50% of rotation and sharp peaks (generally 2) limit the 'pulsed' phase interval. The width and dominance of the peaks led to the conventional assumption of a beaming solid angle of 1 sr for luminosity estimates. The likely beaming pattern inferred from these γ-ray lightcurves is in the shape of a cone with high intensity on the rim and lower levels inside ('hollow cone'). Both leading models, polar cap and outer gap, generate this kind of pattern, although the 2-dimensional shape for the outer gap model could be far from circular. The bright rims of the emission cones indicate the location of intense particle-photon cascades in the magnetospheres. The emission inside the cones is often found to have a harder spectrum, which could indicate that this radiation has been propagated along magnetic field lines with less curvature (polar cap region) avoiding the cascading processes.

In the following we compare the γ-ray lightcurves of the three brightest γ-ray pulsars with their emission at lower energies. These multi-wavelength comparisons serve to distinguish different emission processes. Figure 3 (right panel) shows the Crab pulsar between optical and γ-ray energies. The overall shape of the double-peaked lightcurve remains similar over this range but spectral differences between the components are clearly visible: the bridge region between the two peaks and the second peak are very strong between 100 keV and $\sim$10 MeV. Also in the radio range (left panel figure 3) we find additional structures besides the two peaks: two trailing peaks around 5 GHz and a so-called precursor peak at frequencies below 400 MHz. No comprehensive model has yet been proposed that can explain this complex spatial and spectral emission but it is apparent that several components must exist in the radiation zones of the Crab pulsar.

The same conclusions can be derived for the older pulsars Vela and Geminga. Their multi-wavelength lightcurves are shown in figure 4. Vela is clearly detected as a pulsating source from radio to γ-ray energies. The lightcurves below the γ range are however, in contrast

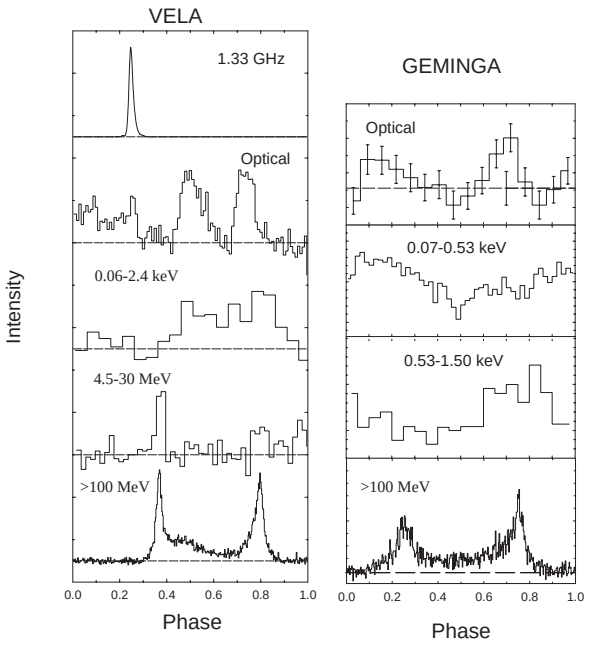


Fig. 4. Multi-wavelength lightcurves of the Vela and Geminga pulsars

to the Crab case, completely at different phase angles of emission. The same finding applies to the Geminga pulsar. In this case significant pulsed emission has only been detected in the X- and γ-ray region. The present optical and radio detections of Geminga are considered to be of marginal significance and need to be confirmed. We conclude again, that the available multi-wavelength lightcurves show that the magnetospheres of young pulsars contain several additional emitting regions with different spectral and beaming characteristics on top of a basic two-peaked structure.

4.2. Spectra

Thompson et al., 1999 have compiled multi-wavelength spectra for the pulsed emission of γ-ray pulsars as shown in figure 5. The spectral intensities are displayed in terms of νF_ν , which is equivalent to the power emitted per unit interval of $ln(\nu)$. The spectra emphasize that emission in the X- and γ-ray regions dominates the radiation budget of these pulsars and that the pulsed emissions are generally harder than power-laws with index -2 (which would be a horizontal line in this spectral display). In several cases the spectra are curved in the γ-ray range and lead up to a cut-off or turn over at a few GeV. The pulsar spectra are arranged in order of increasing rotational age ($\tau \sim \frac{P}{\dot{P}}$) with Crab ($\tau \sim 10^3 y$) as the youngest and PSR B1055-52 ($\tau \sim 5 \times 10^5 y$) as the oldest object.

The **Crab** pulsar emits the maximum power at about 100 keV and the spectrum can be described by a broad peak extending from the optical band (≈ 1 eV) to about 100 MeV. Above 100 MeV the pulsed spectrum continues with a harder power law distribution up to a few GeV, where the spectrum goes into a steep decline (Kuiper et al., 2001). In addition to the pulsed emission, the Crab shows a strong unpulsed component at high energies. This component has been interpreted to come from the inner Crab nebula as synchrotron radiation below a few GeV and as inverse Compton radiation, up-scattered from optical photons, up to TeV energies.

PSR B1509-58 has been detected in the hard X-ray range by Ginga and at low γ-ray energies up to 30 MeV by BATSE, OSSE and COMPTEL. EGRET may have a marginal detection of this pulsar between 30-70 MeV but places significant upper limits on the flux above this energy range, which indicates that this spectrum must turn over in the $\sim$ 10 MeV range. This low energy spectral cut-off in PSR B1509-58 has been explained as an absorption effect for high-energy photons in the magnetic field. PSR B1509-58 has one of the strongest inferred magnetic fields ($\sim 2 \times 10^{13}$ Gauss, about 40% of B_{crit}) and could be called a 'magnetar'. Harding et al., 1997 have modelled polar cap photon cascades in such strong fields and find that the second order quantum-mechanical process of 'photon splitting' ($\gamma \rightarrow \gamma\gamma$) would limit the energy of emitted γ-rays to several 10's of MeV.

The **Vela** pulsar (PSR B0833-45) has a pronounced spectral break at 2 GeV. Due to the strength of this source, very detailed spectra for the individual phase components, e.g. the peaks and the interpulse emission, are available. The spectra of the emission peaks are generally softer than the spectra of the inter-peak regions. The softest components are observed in the leading and trailing wings of the peaks, which has been explained as a low-energy spill-out from the main γ-ray cascades in the outer magnetosphere.

PSR B1706-44, a γ-ray source that had been detected with COS-B 25 years ago (2CG342-02), was identified in 1992 as a radio pulsar with a 102 ms pulsation period. Although an X-ray source is found coincident with the pulsar no pulsation is found at keV energies. Also at TeV energies the source is detected only as a steady emitter, similar to the Crab. The maximum power of PSR1706-44 is emitted around 1 GeV.

PSR B1951+32 is found as a weak γ-ray source at energies above 300 MeV. After extended EGRET observations, pulsational analysis was successful and confirmed the identification of this γ-ray source with the radio pulsar. The spectrum of this pulsar shows the characteristic spectral break above several GeV only marginally, because of the limited statistics for this source .

Geminga (PSR B0633+17) was the most enigmatic γ-ray source since its detection with SAS-2 in 1972. After long and patient searches with X-ray and optical telescopes Geminga was finally identified as a pulsar in 1992. ROSAT observations revealed a 237 ms pulsations in Geminga (Halpern and Holt, 1972) and the corresponding γ-ray signal was found in data from EGRET, COS- B,

and SAS-2. The spectrum of the pulsed emission is generally very hard and shows marked variations over the rotation period. The maximum power of Geminga is emitted at about 1 GeV. Above a few GeV the spectrum breaks off sharply. Geminga is the first specimen of a true high-energy pulsar. The power in optical ($m_v \sim 25.5$, pulsation marginally detected) and radio emissions (marginal detections of pulsed emission at 102 MHz) is lower than the γ-ray emission by more than 6 orders of magnitude, justifying the designation 'radio-quiet pulsar' for Geminga. Speculations that many of the other unidentified galactic γ-ray sources, which appear with comparable brightness, are similar 'Geminga-like' pulsars have been discussed widely. One must realize however that Geminga is a very close (~ 160 pc), low-luminosity pulsar and that the other γ-ray sources, based on their galactic distribution are at least 10 times more distant and therefore should be a hundred times more luminous than Geminga. If the above hypothesis is maintained one has to assume that much younger, high-luminosity pulsars can also operate in a 'Geminga-like' mode. The absence of significant radio- and X-ray counterpart detections for most of the unidentified γ-ray sources requires also that the emission patterns at different wavelengths would not coincide with the γ beams.

PSR B1055-52 also has a very hard energy spectrum that seems to extend from X-rays into the γ-ray range. Again the maximum power is emitted around 1 GeV. No clear break in the spectrum is visible up to 4 GeV. Above that energy a break is required by upper limits at TeV energies.

Figure 6, with an enlarged version of the pulsed spectrum from the Crab, shows the current concept of spectral components in high-energy pulsars. The low energy spectrum, with a peak around 100 keV, is thought to result from synchrotron emission. Based on the spectral maximum of emission from a relativistic electron ($E = \gamma mc^2$) in a magnetic field $B_\perp$ which is at $\nu_{max} \sim 1.2\ MHz \cdot B_\perp(G) \cdot \gamma^2$ an order of magnitude estimate for the peak at 100 keV demands that the product $B_\perp(G) \cdot \gamma^2$ is about 2×10^{13}. Such values could be achieved either with very energetic electrons ($\gamma \sim 10^{6-7}$) in outer magnetospheric fields of ~ 1 Gauss or with electrons of ($\gamma \sim 10^{2-3}$) in inner polar fields with $B_\perp \sim 10^8$ Gauss. The high energy peak could result from inverse Compton scattering of energetic electrons on low energy radiation of energy ε. The typical energy of the inverse Compton photons is then $E_\gamma = \frac{4}{3}\epsilon\gamma^2$, which means that electrons with Lorentz factors $\sim 10^4$ could boost 10 eV photons into the GeV range.

As we saw from the multi-wavelength lightcurves pulsars show spectral changes as they rotate, i.e. the lightcurves look different for adjacent energy bands. This phase dependent spectroscopy can be extended to the γ-ray range also. In figure 7 a hardness ratio, defined as the ratio between the number of photons above 300 MeV to those in the band 100-300 MeV, is shown as a function of

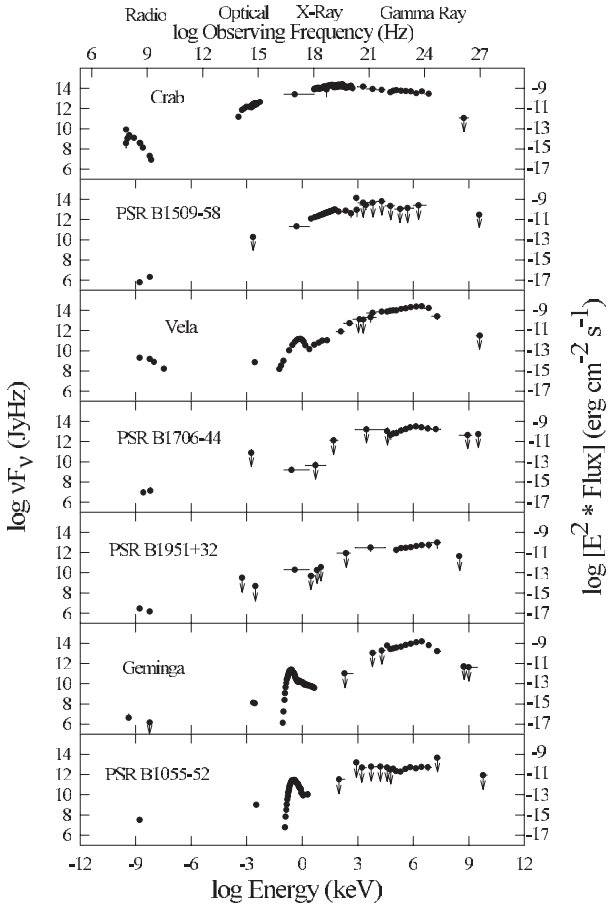


Fig. 5. Multi-wavelength spectra (pulsed emission only) of γ-ray pulsars (Thompson et al., 1999).

the pulsar's rotation. We notice that in the prominent '2-peak' pulsars the first peak has a softer spectrum than the interval region. The second peak is generally also harder than the first peak. Model calculations for polar cap cascades (Daugherty and Harding, 1996) as well as the outer-gap model of Romani, 1996 have successfully reproduced these phase-dependent spectra for Vela.

4.3. Luminosities and Energetics

The energy budget of high-energy of pulsars is derived from the pulsed emission spectra by integration from optical wavelengths (∼1 eV) to the cut-off at GeV energies. The result is given in table 2 where F_E is the observed high-energy flux. For the calculation of the efficiency η, with which the pulsar generates energetic photons from the loss of rotational energy, we assume that the emission is beamed into a solid angle of 1 sr. This could be a problematic assumption especially for the wide beaming patterns generated in outer gap models. Figure 8 shows plots of the correlation of the high-energy properties, spectral index and efficiency (≥ 100 MeV) with some derived pul-

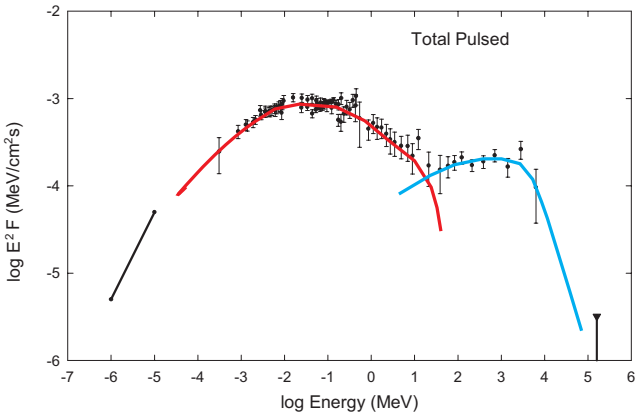


Fig. 6. Pulsed emission from the Crab pulsar with theoretical spectra corresponding to emission via the synchrotron process (low energy peak) and the inverse Compton or curvature radiation peak at higher energies (data from Kuiper et al., 2001).

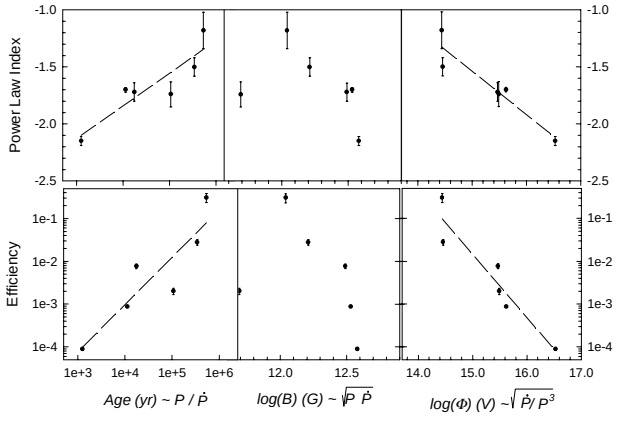


Fig. 8. Correlation of several derived pulsar parameters (rotational age, magnetic field strength, and potential across the polar cap, which is also proportional to the Goldreich-Julian current) with the observed intensity and hardness of γ radiation above $\sim 100 MeV$.

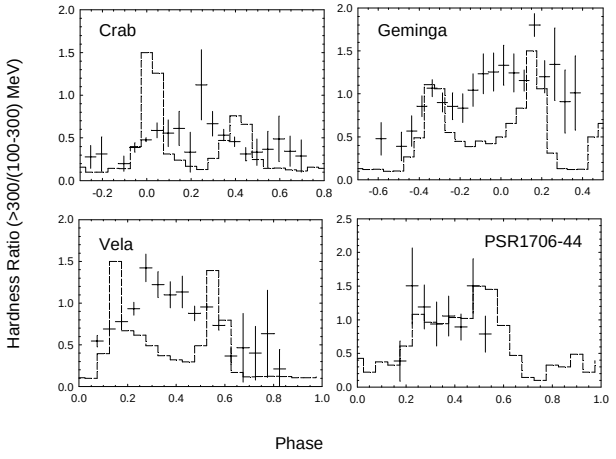


Fig. 7. Spectral hardness as a function of rotation phase for 4 bright γ-ray pulsars . The location of the emission peaks is shown in the underlying lightcurves.

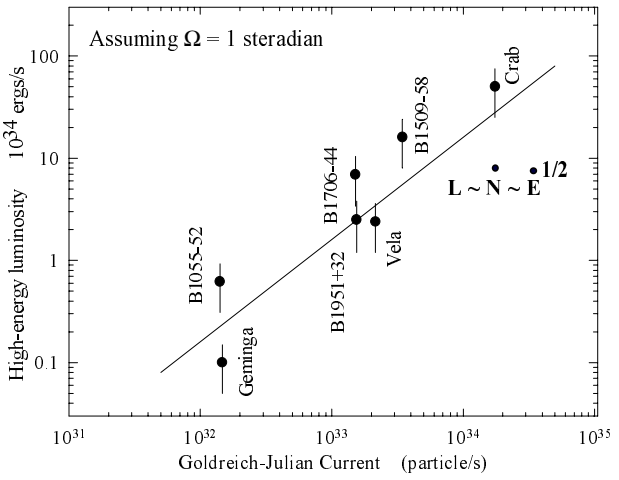


Fig. 9. Pulsar luminosity above $\sim$ 1 eV, assuming a beaming pattern solid angle of 1 sr, versus the Goldreich–Julian current flowing from the open magnetosphere. (Thompson et al., 1999).

sar parameters: the rotational age ($\tau \propto P/\dot{P}$), the magnetic field ($B \propto \sqrt{P\dot{P}}$) and the total voltage available over the pulsar's open field lines ($\Phi \propto \sqrt{\dot{P}/P^3}$). As many previous investigations have shown, both the efficiencies and the spectral indices for radiation above 100 MeV correlate well with the apparent age and the open field line potentials of pulsars. Pulsars become more efficient in their conversion of rotational energy into $E > 100$ MeV radiation and their spectra become harder with increasing age or decreasing potential values. The correlation with the inferred magnetic field is not as clear. Indeed, there seems to be an indication of a decreasing efficiency for both the highest B fields and for low B values. Similarly the spectra appear softer at the marginal magnetic field values. Figure 9 shows directly the correlation between the total high-energy luminosity ($\geq$1 eV) and the Goldreich-Julian current. The direct proportionality of $L_\gamma \propto \dot{E}^{0.5}$ is in contrast to the relation at soft X-ray energies $L_X \propto \dot{E}$ (Becker and Trümper, 1997), which could indicate different emission mechanisms in the two bands. As we see in figure 8, the efficiency of some older pulsars appears already quite high ($\sim$ 20%) and a limit tothe conversion of rotational energy into γ-rays must be reached at some value of the open field line potential ($\Phi \leq 10^{14}$ V). Such a condition could indicate the termination of γ-ray production in old pulsars and form a so-called 'death-line' in the conventional $P - \dot{P}$ diagram. Only future, more sensitive, γ-ray observations will be able to define this transition from a 'γ-ray -active' to a 'γ-ray -dead' pulsar more clearly.

Table 2. Properties of high-energy pulsars (Thompson et al., 1999)

Name	P (ms)	τ (10^3 yr)	$\dot{E}$ (10^{36} erg s^{-1})	F_E (erg cm^{-2} s^{-1})	d (kpc)	L_{HE} (erg s^{-1})	η ($E > 1$eV)
Crab	33	1.3	450	1.3×10^{-8}	2.0	5.0×10^{35}	0.001
B1509-58	150	1.5	18	8.8×10^{-10}	4.4	1.6×10^{35}	0.009
Vela	89	11	7.0	9.9×10^{-9}	0.5	2.4×10^{34}	0.003
B1706-44	102	17	3.4	1.3×10^{-9}	2.4	6.9×10^{34}	0.020
B1951+32	40	110	3.7	4.3×10^{-10}	2.5	2.5×10^{34}	0.007
Geminga	237	340	0.033	3.9×10^{-9}	0.16	9.6×10^{32}	0.029
B1055-52	197	530	0.030	2.9×10^{-10}	1.5	6.2×10^{33}	0.207

5. Conclusions and Outlook

After the mission of the Compton Gamma Ray Observatory we know about a dozen (7 definitely and a few more as likely candidates) γ-ray pulsars. These are objects in which the most extreme electromagnetic and gravitational conditions in the universe act to accelerate highly relativistic particles, leading to high-energy luminosities of the order of 10^{35} erg/s. Young γ-ray pulsars can in principle be observed throughout the Galaxy because γ-rays suffer neither absorption nor dispersion of the pulsed signals. High-energy radiation from magnetized rotating neutron stars is not only a fascinating astrophysical topic in itself – a thorough understanding of the radiation processes also opens the way to uncover the true nature of some of the presently unidentified γ-ray sources. The majority of these objects are galactic (their distribution correlates well with the galactic disk) but the ~ 170 objects of the EGRET catalog ($\sim 60\%$ of all γ-ray sources) pose a major challenge and puzzle to astronomy. It is known that the γ-ray sources correlate generally with regions containing young populations like molecular clouds, star forming regions, OB associations, HII regions, or SNRs. We can safely assume that these regions also contain young pulsars that have not yet been revealed, either being hidden inside their birth places or for a lack of emission at other wavelengths. As described above, Geminga can be taken as a rôle model for such a population of pure γ-ray pulsars. The discovery of individual young γ-ray pulsars will certainly support our theoretical understanding of pulsar physics, but their population will also provide us with new insights into active star forming regions and the processes leading to the formation of neutron stars. Overall the contribution of unresolved, distant pulsars to the diffuse galactic γ-ray emission could be in the range of 5–30%.

The next generation of γ-ray telescopes, especially the GLAST project as a successor to EGRET (Michelson, 1996), will be much more sensitive and is expected to discover 30 - 100 new γ-ray pulsars based on the catalog of radio pulsars alone. With the much higher sensitivity of GLAST and the resulting high photon detection rate it will also be possible to investigate many unidentified γ-ray sources for periodicities independent of observations at other wavelengths. For EGRET this capability for independent periodicity detection has been demonstrated only for Geminga (Brazier and Kanbach, 1996; Chandler et al., 2001). None of the other EGRET sources has a signal/noise ratio with a high photon detection rate similar to Geminga and the powerful investigation for periodicities in some strong EGRET sources carried out by Chandler et al., 2001 was unsuccessful. Thus the next generation of γ-ray telescopes has the potential to reveal the radiation physics of pulsars with a wide range of ages and to discover a new population of pure high-energy pulsars.

References

Becker, W., and Trümper, J., 1997, A& A, **326**, 682
Brazier, K.T.S., and Kanbach, G., 1996, A& A Suppl., **120**, 85
Chandler, A.M., et al.,2001, ApJ, **556**, 59
Daugherty, J.K., and Harding, A.K., 1996, ApJ, **458**, 278
Fichtel, C.E., et al.,1975, ApJ, **198**, 163
Fierro, J.M., et al.: 1993, ApJ, **413**, L27
Goldreich, P., and Julian, W., 1969, ApJ, **157**, 869
Harding, A.K., Baring, M.G., and Gonthier, P.L., 1997, ApJ, **476**, 246
Halpern, J.P., and Holt, S.S., 1992, Nature, **357**, 222
Hermsen, W., et al., 1997, in *The Transparent Universe*, Proc. 2nd INTEGRAL Workshop, St. Malo, France, ESA SP-382, 287
Kanbach, G., 2001, Gamma-Ray Pulsars. In: The Universe in Gamma Rays, (Ed.) V. Schönfelder. Springer Verlag, Berlin, 127
Kanbach, G., et al., 1994, A& A, **289**, 855
Kaspi, et al., 1997, ApJ, **485**, 820
Kaspi, et al., 2000, ApJ, **528**, 445
Kuiper, et al., 1996, NATO-ASI No.515, p.211
Kuiper, L., et al., 1999a, A& A, **351**, 119
Kuiper, L., et al., 1999b, Astrophys.Lett. and Comm., **38**, 33
Kuiper, L., et al., 2001, A& A, **378**, 918
Matz, S.M., et al., 1994, ApJ, **434**, 288
Mayer-Hasselwander, H.A., et al., 1982, A& A, **105**, 164
Mayer-Hasselwander, H.A., et al., 1994, ApJ, **421**, 276
Michelson, P.F., 1996, SPIE, **2806**, 31
Moffett, D.A., and Hankins T.H., 1996, ApJ, **468**, 779
Muslimov A.G. and Tsygan A.I.: 1990, Astron.Zh., **67**, 263
Muslimov A.G. and Tsygan A.I.: 1992, MNRAS, **255**, 61
Nel, H.I., et al., 1996, ApJ, **465**, 898
Nolan, P.L., et al., 1993, ApJ, **409**, 697
Ramanamurthy, P.V., et al., 1995, ApJ, **447**, L109
Ramanamurthy, P.V., et al., 1996, ApJ, **458**, 755

Romani, R.W., 1996, ApJ, **470**, 469
Thompson, D.J., et al., 1992, Nature, **359**, 615
Thompson, D.J., et al., 1994, ApJ, **436**, 229
Thompson, D.J., et al., 1996, ApJ, **465**, 385
Thompson, D.J., et al., 1997 Proc. of the 4^{th} Compton Symp.,
eds. C.D. Dermer et al., Williamsburg, Va., AIP CP410, 39
Thompson, D.J., et al., 1999, ApJ, **516**, 297
Ulmer, M.P., et al., 1996, ApJ, **448**, 356
Zepka, A., et al., 1996, ApJ, **456**, 305

Proceedings of the 270. WE-Heraeus Seminar on: *"Neutron Stars, Pulsars and Supernova Remnants"*
Physikzentrum Bad Honnef, Germany, Jan. 21-25, 2002, eds. W. Becker, H.Lesch & J. Trümper, MPE Report 278, pp. 100-104

Chasing the second gamma-ray bright isolated neutron star: 3EG J1835+5918/RX J1836.2+5925

O.Reimer[1], K.T.S.Brazier[2], A.Carramiñana[3] G.Kanbach[4], P.L.Nolan[5], and D.J.Thompson[6]

[1] Ruhr-Universität, Theoretische Physik IV, Bochum, Germany,
[2] University of Durham, Durham, DH1 3LE, England,
[3] INAOE, 72000 Puebla, Mexico,
[4] MPE, D-85740 Garching, Germany,
[5] Stanford University, Stanford, CA 94395, USA,
[6] NASA GSFC, Greenbelt, MD 20771, USA

Abstract. The EGRET telescope aboard NASAs Compton GRO has repeatedly detected 3EG J1835+5918, a bright and steady source of high-energy gamma-ray emission with no identification suggested until recently. The long absence of any likely counterpart for a bright gamma-ray source located 25° off the Galactic plane initiated several attempts of deep observations at other wavelengths. We report on counterparts in X-rays on a basis of a 60 ksec ROSAT HRI image. In order to conclude on the plausibility of the X-ray counterparts, we reanalyzed data from EGRET at energies above 100 MeV and above 1 GeV, including data up to CGRO observation cycle 7. The gamma-ray source location represents the latest and probably the final positional assessment based on EGRET data. The X-ray counterparts were studied during follow-up optical identification campaigns, leaving only one object to be likely associated with the gamma-ray source 3EG J1835+5918. This object, RX J1836.2+5925, has the characteristics of an isolated neutron star and possibly of a radio-quiet pulsar.

1. Gamma-Ray Observations

3EG J1835+5918 was first discovered at photon energies above 100 MeV by the EGRET instrument aboard NASAs Compton GRO during regularly scheduled observations in 1991. The source was repeatedly seen whenever it was in the field of view of the EGRET instrument. However, the first observation performed with a close on-axis pointing towards 3EG J1835+5918 using EGRET was only made in CGRO observation cycle 7 in 1998. EGRET observations performed at large off-axis viewing angle are problematic due to the degradation of the instrumental point spread function (PSF). The first report on GRO J1837+59 (Nolan et al. 1994) included only data from EGRET observations between 1991 and 1993. The source has been subsequently listed in the EGRET catalogs as GRO J1837+59 (Fichtel et al. 1994) and 2EG J1835+5919 (Thompson et al. 1995). With the appearance of the Third EGRET catalogue (E > 100 MeV) (Hartman et al. 1999) and GeV source compilations (E > 1 GeV) (Lamb & Macomb 1997, Reimer et al. 1997), results from a total of 12 individual observations of 3EG J1835+5919 were reported. This source remained the brightest unidentified EGRET source outside the Galactic plane.

In order to extend the coverage of 3EG J1835+5919 to its maximum, we finally used all gamma-ray data taken by EGRET through the CGRO mission, including the observations made at a small off-axis angle in observation cycle 7. Generally one needs to distinguish between observations in which the angle between 3EG J1835+5918 and the instrument pointing direction was within or without 25°. This distinction has been recommended by the EGRET instrument team for using the standard PSF (sources within 25° of the instrumental pointing) or using the wide-angle PSF if outside. The EGRET observations from CGRO observation cycle 7 extend significantly beyond the catalogued observations. They are separated by more than 3 years from the previous observations of 3EG J1835+5918. Both the long-term observational aspect and the quality of the observation have been improved: despite the lower efficiency of the EGRET spark chamber, the 1998 observations were the first on-axis observations, unbiased from effects which most of the earlier EGRET observations of 3EG J1835+5918 could suffer from. The narrow field-of-view mode, used in EGRET viewing periods 710 and 711, does not introduce additional problems in this respect.

The best source location was obtained from EGRETs highest energetic photons, where the instrumental PSF is significantly smaller than at lower energies. Using a likelihood method (Mattox et al. 1996), Reimer et al. 2001 determined the best position (> 1 GeV) to be l = 88.80°, b = 25.02°, which is consistent with the position from an analysis above 100 MeV (l = 88.76°, b = 25.09°), the posi-

tion given in 3EG and GEV catalogues, and the elliptical fit from Mattox, Hartman & Reimer 2001 (l = 88.74°, b = 25.08°, a = 9.7′, b = 7.8′, Φ = 13°). However, the additional data gave positional errors of only 6′ and 8′ for the 68% and 95% confidence region, respectively.

Nolan et al. 1994 and McLaughlin et al. 1996 indicated flux variability for 3EG J1835+5918 on the basis of smaller data sets than presented lastly. The most recent variability study (Tompkins 1999) puts 3EG J1835+5918 clearly among the non-variable sources, similar to the identified gamma-ray pulsars. Tompkins made use of an algorithm especially adopted for the characteristics of the observations by EGRET, i.e. sparse data sets from individual observations, often widely separated in time and characterized by different background levels. In addition, data from individual EGRET observations up to CGRO observation cycle 4 were used in this study. A strict data selection (only within 25° on-axis) among the gamma-ray observations was used, assuring a data set of comparable quality.

We complemented the flux history of 3EG J1835+5918 with the data from 13-27 January 1998, the last high-energy gamma-ray data on this source to be taken for some years. Due to the generally lower efficiency of the EGRET spark chamber towards the end of the EGRET mission, the early 1998 viewing periods were evaluated using adjusted normalization factors (Esposito et al. 1999). These factors were checked quantitatively by means of a similar on-axis observation of Geminga during 7-21 July 1998. Assuming that the instrumental sensitivity has not changed appreciably between these observations and that Geminga remains the stable gamma-ray emitter previously observed, this normalization for Geminga could be applied to the flux of 3EG J1835+5918 in the cycle 7 observations. In addition, one needs to consider observations with up to 25° off-axis separately from observations outside 25°. The fluxes above 100 MeV and above 1 GeV appear to be linearly correlated, considering the uncertainties in individual viewing periods arising from photon statistics, especially for the sparse data of the detections above 1 GeV.

We concluded, there is no indication of flux variability after all for 3EG J1835+1918, neither above 100 MeV nor above 1 GeV. Given the differing quality of the EGRET observations within their statistical and systematical uncertainties, we find 3EG J1835+5918 compatible with a non-variable source of an average flux of 5.9×10^{-7} cm^{-2} s^{-1} (E > 100 MeV).

After realizing that 3EG J1835+5918 is consistent with having constant gamma-ray flux throughout the EGRET mission, the issue of its spectral variability still remains. Nolan et al. 1996 reported evidence for spectral variability between individual EGRET viewing periods. Apparently, no correlation between spectral index and flux was found. Hence, we re-examined the EGRET data on 3EG J1835+5918 for indication of spectral variability. Individual spectra in each of the relevant viewing periods were determined by simultaneously analyzing likelihood excesses of 3 σ detection significance and above. We derived a flux value or upper limit in each of ten energy intervals (30 MeV to 10 GeV) using a likelihood method. In cases when poor count statistics gave a spectrum dominated by upper limits, the ten energy intervals were recombined into four (30-100, 100-300, 300-1000, >1000 MeV), followed by the appropriate determination of the spectral slope. Also, when the source position determined from likelihood analysis of an individual observation differed from the GeV-position, both positions were individually considered for consequences for the resulting spectrum. None of them introduces relevant modifications in the resulting spectral slope. Therefore, the determined individual spectra could be compared at the best level currently achievable for an unidentified high-energy gamma-ray source.

We find that the spectra of 3EG J1835+5918 determined from individual viewing periods are fully compatible within their statistical and systematic uncertainties throughout the entire EGRET mission. A single power law spectral index of 1.73 ± 0.07 is consistent within 1 σ for all individual spectra.

With the consistency of the individual spectra throughout the EGRET observations established, we coadded the data from cycles 1 to 7 in order to determine the best overall spectrum of 3EG J1835+5918. A single power-law fit appears to be inadequate for this source. The spectrum of 3EG J1835+5918 resembles the gamma-ray spectra of known gamma-ray pulsars like Vela or Geminga and the spectra of candidate gamma-ray pulsars 3EG J2020+4017, 3EG J0010+7309, and 3EG J2227+6122: the hard power law spectral index, as determined to be -1.7 ± 0.06 between 70 MeV and 4 GeV, the high-energy spectral cut-off or turnover as well as a possible spectral softening at the low energies. Upper limits from COMPTEL do not constrain the shape of the spectrum at lower energies. The TeV upper limits as reported by Whipple are consistent with a rollover at 4 GeV, but certainly not with a simple extrapolation of the EGRET measured power law spectrum to even higher energies.

2. Radio Observations

Deep searches in radio (770 MHz) at the position of 2EG J1835+59 could not detect any object above 0.5 Jy (Nice & Sayer 1997). This is in agreement with the correlation study between unidentified EGRET sources and catalogued flat-spectrum radio sources (Green Bank 4.85 GHz/Parkes-MIT-NRAO 4.85 GHz), not suggesting any radio counterpart for 3EG J1835+59 (Mattox, Hartman & Reimer 2001).

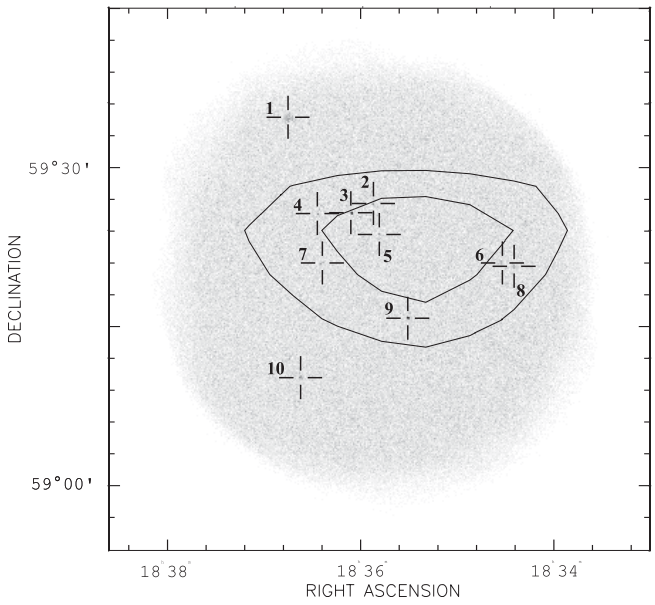


Fig. 1. The long ROSAT HRI (0.1 - 2.4 keV) observation of the field of 3EG J1835+5918 from December 1997/January 1998. The X-ray image is overlaid with source location contours (68% and 95%) of the high-energy gamma-ray source, determined above 1 GeV. The detected X-ray sources are indicated and were subject of a optical follow-on identification campaign.

3. X-Ray Observations

With the analysis of the 60 ksec ROSAT High Resolution Imager observation from December 1997/January 1998, the earlier coverage of this source in X-rays could be increased by a factor of 12. For the first time, counterparts have been discovered in X-rays between 0.1 -2.4 keV (Reimer et al. 1999). The sources are all faint with HRI count rates of 1-3 ksec^{-1}. Only sources 1 and 10 are excluded due to positional disagreement with the EGRET source, see Fig. 1

4. Optical Observations

The discovered X-ray sources were subject of deep optical studies, performed at the 2.1 m telescope at the Guillermo Haro observatory at Cananea, Mexico. The instrumentation is aimed for ROSAT counterpart identifications and served well for our purpose. The observations were accompanied by studies of the DSS-2 images and use of the USNO A2.0 catalog. Independently, Halpern & Mirabal studied these counterparts at the 2.4 m Hilter telescope, the 3 m Shane reflector at Lick and the Hobby-Eberle telescope. The following optical counterparts were found:

1) positional disagreement, QSO with z = 0.46
2) QSO, z = 1.87
3) U > 22.3,B > 23.4,V > 25.2,R > 24.5
4) V = 18.9, R = 19.2, QSO with z = 1.75
5) V = 19.3, R =19.1, QSO with z = 1.865
6) M5V star
7) QSO with z = 1.36
8) G7V dwarf star
9) bright object in center (V = 15.6), M type star, fainter object out of X-ray source error box, G type dwarf
10) K5V-star, in positional disagreement

5. Conclusions

3EG J1835+5918 is a persistent high-energy gamma-ray source located at high Galactic latitudes and has been observed repeatedly by EGRET. It is characterized by a hard power law and a spectral break or turn-over above 4 GeV. It appears to be a non-variable source in terms of its flux as well as its spectral shape throughout the entire EGRET mission, despite suggestions of variability from earlier analysis. Its gamma-ray properties are typical of those observed from other gamma-ray pulsars and candidate radio-quiet neutron stars. The deep ROSAT HRI observation revealed several X-ray sources consistent with the location of the observed GeV-emission of 3EG J1835+5918. As a result of the identification campaigns independently carried out by Mirabal & Halpern 2000 and ourselves, only one of the ten X-ray sources still attracts interest to be considered further for an association with the γ-ray source. This source, RX J1836.2+5925, is characterized by an obvious lack of radio-emission, indetectibility by means of an UV-excess identification technique, lack of optical counterpart up to V$\sim$25 mag, and location well inside the 68% likelihood test statistic contours of 3EG J1835+5918. Our HRI observation contain no information on the X-ray spectrum of RX J1836.2+5925. Hence, assuming that this X-ray source is the most likely counterpart to 3EG J1835+5918, we are restricted to using the X-ray flux of RX J1836.2+5925 and the gamma-ray properties of 3EG J1835+5918 to investigate the characteristics of the object.

To do so, we can use its multi-frequency properties to ascertain its characteristics. The high F_γ/F_{radio} value seems to rule out a blazar origin. The already noted similarities in the gamma-ray characteristics with known gamma-ray pulsars or radio-quiet pulsar candidates preferably suggests a neutron star nature for 3EG J1835+5918/RX J1836.2+5925. We have reexamined the gamma-ray and X-ray fluxes for all the known and candidate pulsars, using a consistent energy range in both bands. Comparing the flux of 3EG J1835+5918 in γ-rays (E > 100 MeV) and RX J1836.2+5925 in X-rays (0.12 - 2.4 keV), this source falls among the candidates currently considered for associations between gamma-ray sources and X-ray sources with proven or suspected neutron star origin, see Fig.5. Nearly all of the candidate gamma-ray pulsars lie at the bottom end of the sensitivity feasible for the last generation of X-ray instruments like ROSAT, ASCA, and SAX. Obviously, only deep observa-

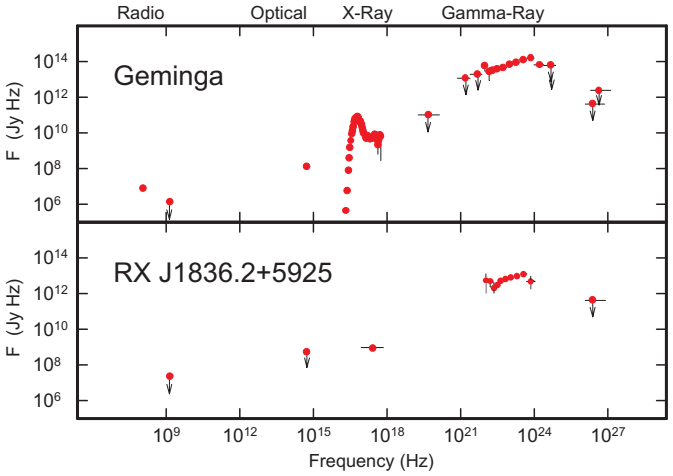


Fig. 2. Multi-frequency energy spectra of Geminga and RX J1836.2+5925/3EG J1835+5918. Similarities could easily be seen, however the spectral energy distribution is not nearly as good covered in the case of RX J1836.2+5925. Completing the SED in X-rays between 0.1 and 10 keV or revealing an optical counterpart will be the most promising way to confirm RX J1836.2+5925/3EG J1835+5918 as the 2nd gamma-ray bright radio-quiet isolated neutron star.

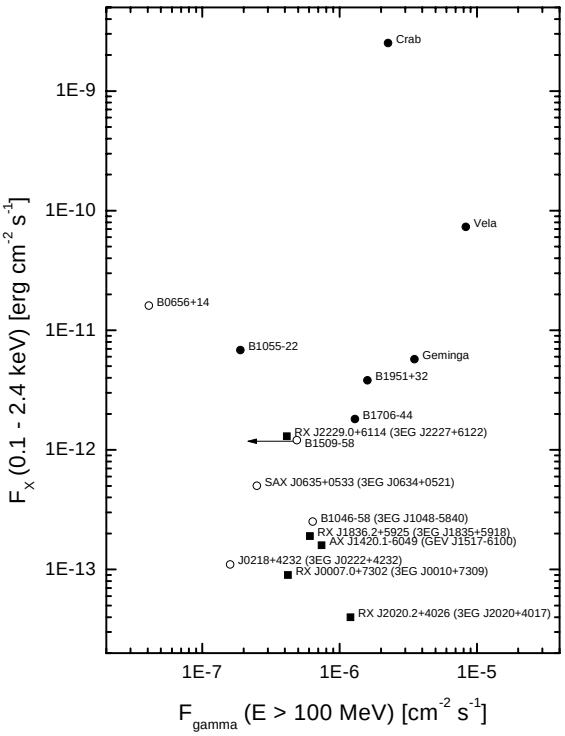


Fig. 3. X-ray and gamma-ray fluxes of high-confidence pulsar detections (filled circles), probable associations between pulsars and high-energy gamma-ray sources (open circles), and candidate radio-quiet pulsars (filled squares). All X-ray fluxes are given for the 0.1 to 2.4 keV energy band, in cases of different energy band quoted in the literature, the flux is normalized into the chosen energy band. The gamma-ray fluxes are given above 100 MeV, in cases where different event selection criteria were used the appropriate gamma-ray flux above 100 MeV has been determined for the energy band desired here.

tions could reveal counterparts at all or with features not easily explained by any other astronomical objects. The lack of optical counterparts up to V∼25 mag and radio emission for RX J1836.2+5925 is a further characteristic signature for isolated, radio-quiet neutron stars, and ideally demonstrated by Geminga as its gamma-ray bright prototype.

Although many of the candidate radio-quiet pulsars beside Geminga itself are located within or near SNRs, 3EG J1835+5918 does not. Neither radio observations nor the X-ray data yield any hint of a SNR in the vicinity of this object, and the high Galactic latitude seems to rule out the possibility of obscuration that might hide one.

If 3EG J1835+5918/RX J1836.2+5925 is not of quasar origin and also not the first candidate of an hypothesized extragalactic astronomical object bright and steady in gamma-rays, faint in X-rays, and yet undetectable at optical and radio wavelengths, it will reside within our Galaxy. We therefore have to suspect an isolated radio-quiet neutron star candidate. With Geminga as the only established pulsar of a predicted class of radio-quiet pulsars, a comparison of observational parameters in analogy with 3EG J1835+5918/RX J1836.2+5925 might be appropriate. Fig 2 compares the multi-frequency $\nu F\nu$-spectrum of Geminga and 3EG J1835+5918, respectively.

First, Geminga is three times brighter in gamma-rays and about fifty times brighter in X-rays. To extrapolate from the distance to Geminga using the observed fluxes, 3EG J1835+5918 would lie between 250 pc (scaling from gamma-rays) and 1.1 kpc (scaling from X-rays), assuming the same beaming as Geminga. Besides, pulsars tend to begin their life in the Galactic plane. A pulsar moving with a typical velocity of about 350 km/s would move only 300 pc, even in a lifetime of 106 years, while an object seen at b = 25° would have to move more than 420 pc from the plane if it were at a distance greater than 1 kpc. As pointed out by Yadigaroglu & Romani 1995 discussing the beaming evolution of pulsars in the outer-gap model, the beaming fraction becomes rather small as the pulsars age increases. Therefore a distant but old pulsar would have to be immensely powerful or exceptionally beamed. If 3EG J1835+5918 is more distant, then its gamma-ray luminosity would exceed that of Geminga, but if closer, then the surface brightness in X-rays of the neutron star would have to be lower than Gemingas. This indicates, that either the efficiency of the emission mechanism is different and/or the parameter space which radio-quiet pulsar candidates could occupy is wide spread. In contrast to ener-

getic pulsars like Vela or B1706-44, non-thermal emission or PWN features have not been observed here so far. Nor is it an extended source in X-rays. The lack of an associated SNR as well as the rare chance to find a similar pulsar at such high Galactic latitude (to say: nearby) argues against a young pulsar in the case of 3EG J1835+5918. However, the striking similarities in the gamma-ray properties between Geminga, other candidate radio-quiet pulsars and 3EG J1835+5918, the absence of a radio and optical counterpart of RX J1836.2+5925, points toward its nature of an old but radio-quiet neutron star.

Certainly, neither the X-ray data nor the gamma-ray data currently allow wide range period scans for pulsations without known ephemeris (Jones 1998, Chandler et al. 2001). Any (potentially) successful search for periodicity will have to be postponed until more sensitive instruments like XMM in the X-rays or GLAST in the gamma-rays will have observed 3EG J1835+5918. However, if a restrictive set of parameters can be predicted from pulsar models or if a lightcurve can be derived from another wavelength, the archival EGRET data will permit the discovery of pulsations in the gamma-rays. The long observational history presented here will certainly assist in any such effort. Finally, RX J1836.2+5925 might be identified as a neutron star by extremely deep optical imaging/spectroscopy, as already in progress using the Subaru telescope (Kawai et al. 2002).

To unambiguously relate 3EG J1835+5918 to a known class of astronomical objects would be of extreme importance for any collective studies of gamma-ray sources, and a gain for general pulsar physics if the existence of another isolated neutron star in gamma-rays will be confirmed.

References

Chandler, A.M. et al., ApJ 556, (2001), 59
Esposito, J.A. et al., 1999, ApJS, 123, 203
Fichtel, C.E. et al., ApJS, 94, 551,
Hartman, R.C. et al., 1999, ApJS, 123, 79
Jones, B.B., 1998, PhD thesis, astro-ph/0202088
Kawai, N., Totani, T. and Kawasaki, W., these proceedings
Lamb, R.C. and Macomb, D.J., 1997, ApJ, 488, 872
Mattox, J.R. et al., 2001, ApJS 135, 155
Mattox, J.R. et al., 1996, ApJ, 461, 369
McLaughlin, M.A. et al., 1996, ApJ, 763
Mirabal, N. and Halpern, J., 2000, ApJ 541, 180
Nice, D.J. and Sawyer, R.W., 1997, ApJ, 476, 261
Nolan, P.L. et al., in Proc. 2nd Compton Symposium, 1994, AIP Conference Proceedings 304, 360
Nolan, P.L. et al., 1996, ApJ, 459, 100
Reimer, O. et al., in Proc. 25th ICRC, 1997, Vol.3, 97
Reimer, O. et al., in Proc. 5th Compton Symposium, 1999, AIP Conference Proceedings 510, 489
Reimer, O. et al., 2001, MNRAS 324, 772
Thompson, D.J. et al., 1995, ApJS, 101, 259
Tompkins, W., 1999, PhD thesis, astro-ph/0202141
Yadigaroglu, I.A. and Romani, R.W., 1995, ApJ, 449, 211

Proceedings of the 270. WE-Heraeus Seminar on: *"Neutron Stars, Pulsars and Supernova Remnants"*
Physikzentrum Bad Honnef, Germany, Jan. 21-25, 2002, eds. W. Becker, H.Lesch & J. Trümper, MPE Report 278, pp. 105-111

Future Pulsar Observations with H.E.S.S.

A. Konopelko

Max–Planck–Institut für Kernphysik, D-69029 Heidelberg, Germany

Abstract. Since their discovery at radio wavelengths pulsars have been persistent targets for widespread multi-wave observations throughout optics, radio, X-rays, and high-energy γ-rays. Observations with the EGRET γ-ray telescope, on board Compton GRO satellite, confirmed the expectation of a pulsed high-energy emission up to a few GeV. Presently, at least seven objects are known as well established high-energy γ-ray pulsars. A few of those emit γ-rays well above 1 GeV. Forthcoming ground-based Cherenkov telescopes will enable observations of γ-rays well below 100 GeV, finally reaching the yet unexplored energy gap at tens of GeV. H.E.S.S. (*High Energy Stereoscopic System*) is one of such instruments which is planned to be operational in 2004. Here I summarize the basic scientific motivations, the H.E.S.S. sensitivity, and the first targets for future pulsar observations at high energies from the ground.

1. Introduction

It is generally accepted that pulsars are produced from massive progenitor stars with a masses of $M \geq 8\ M_{\odot}$ and typical radii $R_o \simeq 10^{11}$ cm, collapsing at the end of their evolution to neutron stars in an explosion, which ejects the outer envelope forming a supernova remnant. A pulsar is a rotating neutron star (Baade & Zwicky 1934) with a mass of $M \simeq 1.4\ M_{\odot}$, a radius of $R \simeq 15$ km, and a rotational period typically of order $P \simeq 1$ s. Pulsars are slowing down and loosing their rotational energy with the rate

$$\dot{E} = 4\pi^2 I \dot{P}/P^3 \tag{1}$$

where $\dot{P} = dP/dt$ is the measured rate of a pulsar slow-down, and $I = 10^{45}$g cm^2 is a generic moment of inertia of a pulsar. Assuming that the pulsar releases its mechanical energy in form of magnetic dipole radiation (Ostriker & Gunn 1969) one can estimate the pulsar surface magnetic field

$$B_s \cong 3.2 \cdot 10^{19} (P\dot{P})^{1/2}, \tag{2}$$

which appears to be very strong and for a typical pulsar is of the order of 10^{12}G. Assuming a constant magnetic field throughout the pulsar lifetime, the characteristic age of a pulsar can be determined from its rotational period and slow-down rate

$$\tau = P/(2\dot{P}). \tag{3}$$

The γ-ray luminosity of a pulsar, L_γ erg s^{-1}, can be roughly estimated using the measured flux of high-energy γ-rays, F_γ photon cm^{-2} s^{-1}:

$$L_\gamma(> E_\gamma) \simeq \omega d^2 F_\gamma(> E_\gamma) E_\gamma \tag{4}$$

where ω is the solid angle into which the pulsar beams and d is the distance to the pulsar. The γ-ray luminosity is widely supposed to be proportional to the total loss of pulsar rotational energy

$$L_\gamma \simeq \epsilon \dot{E} \tag{5}$$

where ϵ is the efficiency of converting the rotational energy of neutron star into γ-rays. On the other side the γ-ray flux of a particular pulsar can be estimated as

$$F_\gamma \propto \epsilon (\dot{E}/d^2) {E_\gamma}^{-1}\ \text{ph cm}^{-2}\,\text{s}^{-1}. \tag{6}$$

The conversion efficiency, ϵ, could be, in zero approximation, assumed as a phenomenological function of pulsar age, even though this function is not unique and not universal. The observed γ-ray flux depends at first on the size of the pulsar beam. Finally the spin-down powered pulsars can be characterized by a set of five parameters $(P, \dot{P}, B_s, \tau, \dot{E}/d^2)$, which allow to predict approximate γ-ray luminosity of a particular pulsar for a given $\dot{E}/d^2$ and ϵ. More accurate calculations of γ-ray fluxes, light-curves and energy spectra can be performed using elaborated models of spinning down pulsars.

2. Models of high-energy pulsars

There are two major classes of models dealing with high-energy γ-ray emission from the pulsars. They differ primarily by the initial assumptions on where the particle acceleration and radiation take place, either near the surface of neutron star at its *polar caps* or in the *outer gaps*, which may occur in the outer magnetosphere of a pulsar

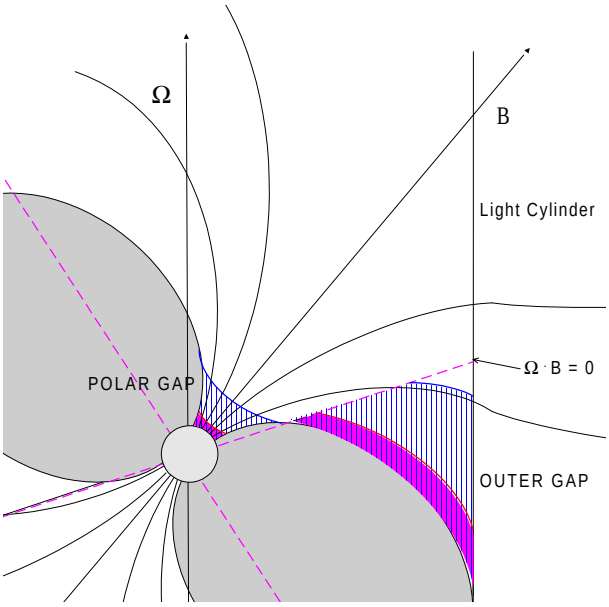


Fig. 1. Schematic view onto the pulsar environment. Courtesy of A.K. Harding (NASA/GSFC).

at relatively large distance from the surface of the neutron star (see Figure 1).

Polar cap model. A fast spinning, magnetized neutron star can generate a huge electric field, which induces an electrostatic potential $U \propto P^{-3/2}(\dot{P})^{1/2} \cong 10^{12}$V right above the polar caps of a pulsar. As suggested by Goldreich & Julian (1969) the corresponding electrostatic force may overcome gravity and pull out the charged particles from the surface of the neutron star, forming the current given by $I_{GJ} \propto B_s/P^2$. In addition charged particles may escape from the surface of the neutron star because its surface temperature $T_s = 10^5 - 10^6$K (Becker & Trümper 1997) may exceed the electron thermal emission temperature. The electrons can be accelerated in the regions above the poles where the open magnetic field lines[1] originate (Sturrock 1971; Ruderman & Sutherland 1975). Those electrons may emit high-energy γ-rays in three major processes: *(i)* synchrotron emission induced by electrons spinning around the magnetic field lines; *(ii)* curvature radiation generated by the electrons moving along magnetic field lines; *(iii)* inverse Compton emission produced by high-energy electrons, which up-scatter low energy photons to γ-ray energies. The γ-rays interact with the pulsar magnetic field ($\gamma \rightarrow e^- e^+$) initiating the pair cascade (Harding 1981; Daugherty & Harding 1982). The pair formation fronts occur at 0.5-1 stellar radii above the surface of the neutron star where the magnetic field is rather strong (for a typical pulsar $B \simeq 10^{12}$G). For such magnetic fields only the γ-rays below a certain energy (a few GeV for typical pulsars) may freely escape from the pair production region. The super-exponential cut-off in the high-energy γ-ray spectrum is an intrinsic feature the of polar cap model.

[1] magnetic field lines, which are crossing the light cylinder of a radius $R_{LC} = c/\Omega$, where Ω is an angular velocity of a pulsar.

Table 1. High-energy γ-ray pulsars.

Pulsar	$P(ms)$	$-log\dot{P}$	$logB_s$	$log\tau$	$d\ (kpc)$	$log\dot{E}/d^2$	R^1
$B0531+21$	33	12.4	12.6	3.1	2.0	−4.9	1
$B0833-45$	89	12.9	12.5	4.1	0.5	−5.5	2
$B1706-44$	102	13.0	12.5	4.2	1.8	−7.0	3
$B1509-58^2$	150	11.8	13.2	3.2	4.4	−7.0	4
$B1951+32$	39	14.2	11.7	5.0	2.5	−7.2	5
$J0633+1746$	237	14.0	12.2	5.5	0.2	−7.3	6
$B1055-52$	197	14.2	12.0	5.7	1.5	−8.9	29

[1] R is a rank given according to the derived value of $\dot{E}/d^2$.
[2] *PSR* $B1509-58$ was seen only with COMPTEL (Kuiper et al. 1999) up to an energy of about 30 MeV, and not with EGRET.

Outer Gap model. A vacuum gap may occur in the outer magnetosphere of a pulsar (Cheng, Ho & Ruderman 1986; Romani 1996), which is limited by the null charge surface $\mathbf{\Omega} \cdot \mathbf{B} \equiv 0$ and the light cylinder. Charged particles can flow out through the light cylinder, whereas they could not run through the null charge surface. The γ-rays (curvature or inverse Compton photons) penetrating into the vacuum gap can produce a pair ($\gamma\gamma \rightarrow e^- e^+$) by interacting with non-thermal X-rays or infrared photons, which fill the gap. The secondary electrons can be accelerated in the vacuum gap electric field and emit synchrotron and curvature γ-ray photons. The γ-rays of energy at least up to 10 GeV may escape from the vacuum gap. This model is suggestive of pulsed TeV γ-ray emission induced by the inverse Compton up-scattering of infrared photons by high-energy electrons (Romani 1996).

Even though both of the models can fit the variety of light-curves of radio pulsars as well as the photon spectra over the optical, radio, X-ray, and high-energy wavelengths, they inevitably predict very different spectra at energies above 10 GeV. The harder spectra of high-energy γ-rays are more plausible for outer gap model, whereas such spectra are almost excluded in the polar cap model (see Harding 2000) except for millisecond pulsars. Future pulsar observations from the ground with Cherenkov telescopes will allow to measure the spectral shape of a pulsed emission in the relevant energy range (above 10 GeV), which will be tightly constraining the choice of an appropriate model of high-energy γ-ray emission.

There are a few other models, which do not fit into the two classes mentioned above, for instance a *neutron star wind model* suggested recently by Kirk, Skjaeraasen, Gallant (2002). The energy of the pulsar magnetic field may be converted into energy of accelerated particles within

Table 2. Spectral parameters[1] of high-energy γ-ray pulsars[2].

Object	$K(\times 10^{-8})$ $(cm^{-2}s^{-1}GeV^{-1})$	α	E_o (GeV)	β
$B0531+21$	24.0	2.08	30	2.0
$B0833-45$	138.0	1.62	8	1.7
$B1706-44$	20.5	2.10	40	2.0
$B1951+32$	3.8	1.74	40	2.0
$J0633+1746$	73.0	1.42	5	2.2
$B1055-52$	4.0	1.80	20	2.0

[1] see for details de Jager et al. (2001)
[2] Spectral references from Macomb & Gehrels (1999)

the magnetic field reconnections, which do occur at the null current sheet extending rather far from the surface of the neutron star beyond the light cylinder. Spectra of γ-ray emission computed using such a model might be challenging future observations at high-energies from the ground.

3. EGRET pulsars

The discovery of the first radio pulsar $PSR\ B1919+21$ (Hewish et al. 1968) has triggered further large-scale search for radio pulsars, which brought us a lot more detections. These days the catalogs of radio pulsars account for more than 1400 objects. About 50 of those have been seen in X-rays, but only 7 at high energies ($E_\gamma \geq 30$ MeV) (Kanbach 2002), recently observed with EGRET[2]. It is remarkable that most of the EGRET pulsars have got a top rank when they are listed according to the value of $\dot{E}/d^2$ (see Table 1).

Most of the high-energy γ-ray pulsars have been seen at radio wavelengths, except Geminga ($PSR\ J0633+1746$), which appears to be radio-quiet. The light-curves of pulsed high-energy γ-ray emission generally do not resemble the light-curves of radio emission, even though they can be rather similar, e.g. for the Crab pulsar ($PSR\ B0531+21$). Three pulsars, Crab, Vela ($PSR\ B0833-45$), and Geminga, have a double-peaked light-curve with a substantial contribution of a bridge (inter-peak) emission. The peculiar behavior of the light-curves reveals a complicated geometry of the pulsed emission, which is evidently not always similar to the light-curves at other wavelengths (for detailed discussion see Thompson 2000).

Six γ-ray pulsars show a clear evidence of the pulsed emission above 5 GeV. Spectral energy distributions (SED) of γ-ray emission from the high-energy pulsars (νF_ν, Jy Hz) peak in the hard X-ray or γ-ray range. The

[2] EGRET is the high-energy γ-ray telescope on board *Compton Gamma Ray Observatory (CGRO)*

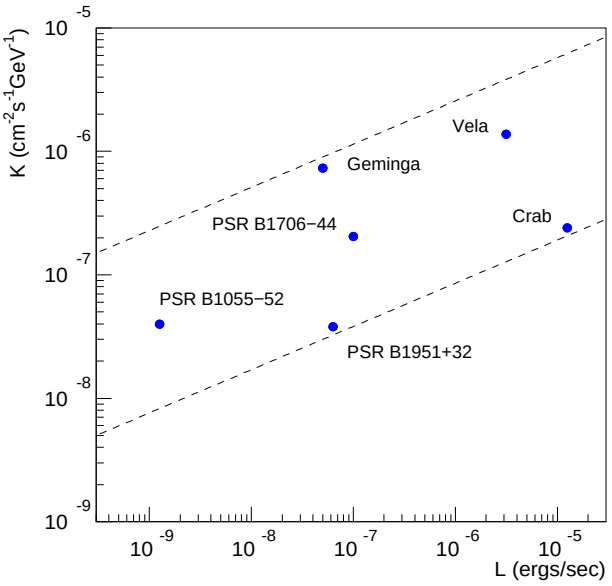


Fig. 2. The γ-ray photon flux at 1 GeV versus rescaled total loss of rotational energy $L = \dot{E}/d^2$.

SED breaks at GeV energies, which is an established distinctive feature of γ-ray emission from the pulsars, which was predicted by the polar cap model.

The energy spectra of EGRET pulsars can be well fitted by power laws with spectral indices within the range α=1.4–2.1 plus a super-exponential cut-off at the energy about $E_o = 5-40$ GeV (de Jager et al. 2001)

$$dF_\gamma/dE = K \cdot E^{-\alpha}\exp(-(E/E_o)^\beta),\ \beta \simeq 2 \qquad (7)$$

where E is in units of GeV. Parameters of the fit for six EGRET pulsars are summarized in Table 2.

The normalization constant K in Eqn.(7) corresponds to the photon flux at energy of 1 GeV, and is an approximate measure of the pulsar luminosity in high-energy γ-rays, L_γ. One can expect that L_γ correlates with the total loss of the rotational energy of a pulsar ($\dot{E}/d^2$). In Figure 2 the scatter plot of K over $\dot{E}/d^2$ for six GeV EGRET high-energy γ-ray pulsars is shown. Even though the current sample of high-energy γ-ray is very poor one can see an evident trend, which can be fitted as $L_\gamma \propto (\dot{E}/d^2)^{1/3}$. Pulsar luminosity in high-energy γ-rays is determined not only by the total loss of its rotational power but in addition by the efficiency of energy conversion from slow-down into high-energy γ-rays (see Eqn.(6)). In fact, even a pulsar with a rather low value of $\dot{E}/d^2$ and low Rank (see Table 1) could appear to be a powerful γ-ray emitter. For instance γ-ray pulsar $PSR\ B1055-52$ has rather low Rank $-$ 29. Naturally the efficiency $\epsilon = L_\gamma/L \propto K/(\dot{E}/d^2)$ could be a function of pulsar age. The efficiency of energy conversion from rotational slow-down into high-energy γ-rays can be determined at most by the increase of current flow out of the neutron star for elder pulsars (Harding 1981), or by the corresponding increase in size of a particle acceleration region in the magnetosphere around the

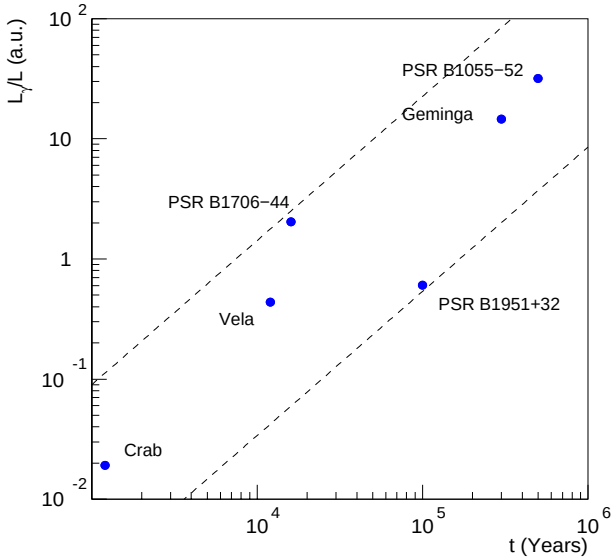


Fig. 3. Efficiency of energy conversion of a rotational energy of a pulsar into high-energy γ-ray emission.

star (Ruderman, Cheng 1988). The measure of conversion efficiency as a function of pulsar apparent age is shown in Figure 3. The general tendency can be approximated by $\epsilon \propto \tau^{1.2}$.

For a better understanding of pulsar workings a substantially more representative sample of γ-ray pulsars is needed. Future observations from space with GLAST[3] and from the ground with future Cherenkov instruments may significantly increase the sample of γ-ray pulsars.

de Jager et al (2001) have estimated the minimal exposure for a 5σ detection of EGRET high-energy γ-ray pulsars. Pulsar $PSR\ B1706-44$ appeared to be the best candidate for the future observations with H.E.S.S. (for a description of the experiment, see Hofmann 2001). A 10 hours exposure with H.E.S.S. will enable to resolve a pulsed high-energy γ-ray emission above 30 GeV from $PSR\ B1706-44$.

4. Pulsar observations at very high energies

Based on the outer gap model of γ-ray emission (see discussion above) Romani (1996) predicted a pulsed very high energy (VHE) TeV emission through the inverse Compton (IC) up-scattering of synchrotron photons on the primary electrons accelerated in the strong electric field of a pulsar. It motivated numerous observations of pulsars with ground-based imaging and non-imaging atmospheric Cherenkov telescopes (Ong 1998; Catanese & Weekes 1999). Note that the ground-based instruments are approaching the energy range covered by satellite detectors and already nowadays achieve an energy threshold as low as 60 GeV. Basic results of these observations are summarized in Table 2. Except for recent evidence for a detection of Geminga with still low level of confidence (Neshpor & Stepanian 2001) none of the observations have resolved a pulsed VHE γ-ray emission. The outer gap model could easily accommodate the non-detection of pulsed VHE γ-ray emission by assuming higher fluxes of the microwave seed photons which cause the pair production of TeV γ-rays within the vacuum gap (Hirotani & Shibata 2001). Predicted fluxes of pulsed IC TeV γ-rays rely heavily on the spectral energy distribution of the microwave seed photons, which is currently purely known. A detailed search for the IC component of VHE γ-ray emission from pulsars will be performed with the ground-based imaging Cherenkov telescopes of the next generation with drastically improved flux sensitivity.

[3] GLAST: The Gamma ray Large Area Space Telescope

Table 3. Summary of a search for pulsed VHE γ-ray emission from the ground.

Pulsar	*Telescope* :	$E_{th}(GeV)$	*U.L.*[1]	*Ref.* :
$B0531+21$	$HEGRA$	10^3	$\leq 5.6 \times 10^{-13}$	1
	$Whipple$	250	$\leq 4.8 \times 10^{-12}$	33
	$STACEE$	190	$\leq 1.2 \times 10^{-11}$	37
	$CELESTE$	60	$\leq 7.4 \times 10^{-11}$	19
$B0833-45$	$CANGAROO$	2.5×10^3	$\leq 3.7 \times 10^{-13}$	48
	$Durham$	300	$\leq 1.3 \times 10^{-11}$	11
$B1706-44$	$Durham$	300	$\leq 7.8 \times 10^{-12}$	10
$B1951+32$	$Whipple$	260	$\leq 6.7 \times 10^{-12}$	43
$J0633+1746$	$HEGRA$	1.5×10^3	$\leq 1.0 \times 10^{-12}$	1
	$Whipple$	500	$\leq 6.5 \times 10^{-12}$	4
	$CrAO$[2]	10^3	$\simeq 2.4 \times 10^{-11}$	35
$B1055-52$	$Durham$	300	$\leq 6.8 \times 10^{-11}$	11

[1] U.L. is an upper limit measured in photon $\mathrm{cm}^{-2}\,\mathrm{s}^{-1}$.
[2] Neshpor & Stepanian (2001) claim the detection of Geminga pulsar at 4.4σ confidence level.

5. Plerions

What sets the puzzle is that the Crab Nebula (Hillas et al. 1998; Aharonian et al. 2000), Vela (Yoshikoshi et al. 1997; Chadwick et al. 2000), and $PSR\ B1706-44$ (Kifune et al. 1995; Chadwick et al. 1998), are well established sources of DC GeV-TeV γ-ray emission in the 60 GeV - 50 TeV energy range. This steady flux emission might be associated possibly with the X-ray synchrotron nebula around the pulsar (de Jager & Harding. 1992; de Jager et al. 1996; Aharonian, Atoyan, Kifune 1997). However the spectral behavior of both, pulsed and unpulsed, components of high-energy γ-rays within the energy range from 10 GeV up to 100 GeV remains unknown. This energy range can be effectively studied from the ground with the forthcoming imaging atmospheric Cherenkov light telescopes (see for a review Catanese, Weekes 1999). Spectral measurements over this energy range will severely constrain

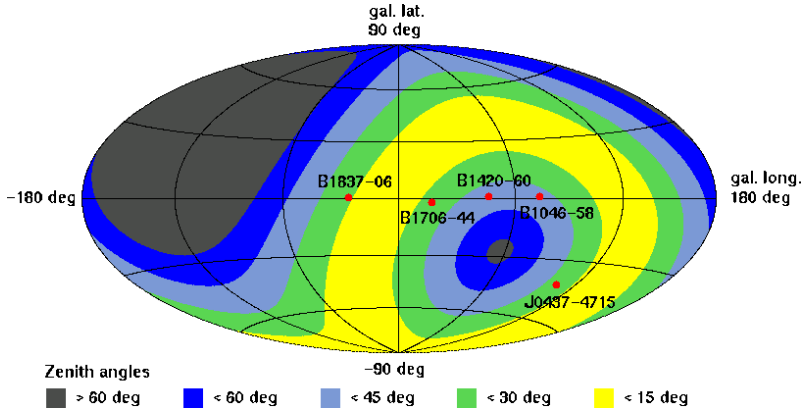


Fig. 4. H.E.S.S. visibility. Courtesy of S. Gillessen (MPI-K, Heidelberg).

the physics of particle injection and acceleration in a pulsar and within the surrounding pulsar nebula. Note that H.E.S.S. could detect a Crab like source of DC VHE γ-rays after a few minutes of observation (Konopelko 2000).

6. Millisecond pulsars

Most of the radio pulsars detected so far have their rotational periods within the range from 10 ms to 10 s, whereas a few of them form a separate sample of millisecond pulsars with rotational periods in the range from 1 ms to 10 ms. $PSR\ 1937+214$ is the first detected millisecond pulsar, and has a rotational period of 1.5 ms (Backer et al. 1982). For such a short period it has a surprisingly small value of $\dot{P} \simeq 10^{-19}$. Using the relation given by Eqn.(3), one can estimate the pulsar age as $\tau \geq 10^7$ years. Being rather old, the millisecond pulsars do not fit the general scheme of pulsar evolution, and most probably are re-accelerated by some external mechanism (e.g. by accretion from a companion star in a binary system). The millisecond pulsars should have smaller surface magnetic field (see Eqn.(2)), $B_s \sim 10^9$ G, and that makes them particularly interesting with respect to the high-energy γ-ray emission. Given such a low magnetic field, the cut-off energy of curvature photons due to the pair production (see discussion in section 2) shifts to higher energies, and the maximum radiation of the millisecond pulsars should correspond to photons with energy $\sim 10^{11}$ eV (Usov 1983). The value of the photon flux above 100 GeV, estimated for $PSR\ 1937+214$ by Usov (1983), is approximately an order of magnitude higher than that of the Crab pulsar, $J_\gamma(\geq 100\ \mathrm{GeV}) \simeq 2\times10^{-10}\,\mathrm{ph\,cm^{-2}\,s^{-1}}$. Recent detailed calculations of the energy spectra of high-energy and very high energy γ-ray emission from millisecond pulsars (Bulik, Rudak, Dyks 2000) in general have confirmed early expectations.

Pulsar $J0437-4715$ ($P = 5.75$ ms, $d = 140$ pc) is a prime candidate for observations in the energy range above 100 GeV. Its integral γ-ray flux above 100 GeV is expected to be as high as $\simeq 10^{-11}\,\mathrm{ph\,cm^{-2}\,s^{-1}}$ (Bulik, Rudak, Dyks 2000), which is above the sensitivity limit of H.E.S.S. (Konopelko 2000). Assuming rather conservative γ-ray flux for $J0437-4715$ one needs a 50 hour exposure with H.E.S.S. in order to detect the pulsed γ-rays. Another millisecond pulsar, $PSR\ B1821-24$, is a good candidate for pulsed high-energy γ-ray emission seen by EGRET, and it is certainly a valuable target for future observations with H.E.S.S.

7. Young pulsars

In addition to seven well established high-energy γ-ray pulsars EGRET discovered a large number of unidentified γ-ray sources at low Galactic latitudes (see Kanbach 2002). The recent Parkes multi-beam radio surveys allowed to resolve a number of young energetic radio pulsars with some of those being in rather good positional coincidence with unidentified EGRET γ-ray sources (Torres, Butt, Camilo 2001). Such associations resemble in many ways the established EGRET γ-ray pulsars. For instance pulsar $PSR\ B1046-58$ could be a counterpart of high-energy γ-ray source $3EG\ J1048-5840$ (Kaspi et al. 2000). It has the ninth highest value of $\dot{E}/d^2$, and its γ-ray light-curve morphology is similar to other known γ-ray pulsars, namely, two narrow peaks separated by ~ 0.4 in the light-curve phase. $3EG\ J1048-5840$ has a rather flat energy spectrum ($\alpha \simeq 2.0$) without clear evidence for a cut-off. Two other young radio pulsars $PSR\ J1420-6048$ (P=68 ms) and $PSR\ J1837-0604$ (P=96 ms) are located $\sim 10'$ away from the position of the EGRET unidentified sources $3EG\ J1420-6038$ and $3EG\ J1837-0606$, respectively (D'Amico et al. 2001). In the energy range from 100 MeV to 10 GeV, the spectra of these two sources can be fitted with power laws of photon spectral index $\alpha = 2.02$ and 1.82, respectively, which are inside the spectral index range of the known γ-ray pulsars. A 20 hour exposure with H.E.S.S. for this source may be sufficient for a clear detection of very high energy γ-ray emission (de Jager et al. 2001) from both of these pulsars, assuming the energy cut-off at 40 GeV. About 30 young energetic

radio pulsars are currently known as positional associations with unidentified EGRET γ-ray sources (D'Amico 2001). In addition some of those pulsars are within the X-ray nebula, which confirms that they are plerions (see Roberts, Romani, Kawai 2001), and may well be in addition the sources of DC high-energy γ-ray emission coming from the X-ray nebula, surrounding the pulsar. Such sources could be effectively studied at very high energies from the ground with an instrument like H.E.S.S.

8. H.E.S.S.

H.E.S.S. (*High Energy Stereoscopic System*) is one of the next generation ground-based instruments for very high energy γ-ray astronomy (Hofmann 2001). In its 1st phase it will consist of four 12 m Cherenkov telescopes deployed in the Khomas Highland of Namibia. H.E.S.S. will have an energy threshold in the range of 50 - 100 GeV (Konopelko 2000), an angular resolution for individual photons of 0.1°, and an energy resolution better than 20%. According to the current sensitivity estimate, H.E.S.S. will need a 50 hour exposure to detect a γ-ray point source with photon fluxes $J_\gamma \simeq 10^{-11}\,\mathrm{ph\,cm^{-2}\,s^{-1}}$ and $\simeq 10^{-13}\,\mathrm{ph\,cm^{-2}\,s^{-1}}$ above 100 GeV and 1 TeV, respectively. The first observations with two telescopes are being currently planned in early 2003. The complete system is due in 2004. The visibility of H.E.S.S. along with a few selected pulsars as the potential targets for future observations is shown in Figure 4.

9. Summary

Pulsars are objects with an extreme physics environment. They are offering physics processes to be studied by plasma electrodynamics, nuclear physics, cosmic ray physics, *etc.* Understanding the pulsar physics could substantially benefit from the enrichment of the presently very small sample of high-energy γ-ray pulsars. Measurements of energy spectra for already established, as well as for newly discovered γ-ray pulsars, will constrain the modeling of high-energy emission and in particular the location of the emitting regions with respect to the neutron star. Future observations at high-energies, which can be effectively done with the ground-based Cherenkov instruments, will stretch the existing models and will help to understand the physics of millisecond pulsars. Observations of associations of the energetic young radio pulsars at low Galactic latitudes with unidentified EGRET γ-ray sources will allow to prove that pulsars are in general powerful emitters of high-energy γ-rays. Finally, a rich sample of γ-ray pulsars can be used for better understanding the conversion of pulsar rotational energy into γ-ray emission, which is determined by the size and geometry of emitting regions.

H.E.S.S. is one of the forthcoming ground-based Cherenkov detectors, such as CANGAROO, MAGIC, and VERITAS, and the present discussion is entirely relevant for the future observations with any of those instruments.

Acknowledgements. I would like to thank Werner Becker, Alice Harding, Okkie de Jager, Gottfried Kanbach, John Kirk, Yury Lyubarsky, Roger Romani, Bronislaw Rudak, Vladimir Usov, and Heinz Völk, for discussions on pulsar physics.

References

Aharonian, F., et al. 1999, *A&A*, 346, 913
Aharonian, F., et al. 2000, *ApJ*, 539, 317
Aharonian, F., Atoyan, A., Kifune, T. 1997, *MNRAS*, 291, 162
Akerlof, et al., 1993, *A&A*, 274, L17
Baade, W., Zwicky, F. 1934, *Proc. Nat. Acad. Sci. USA*, 20, 254
Backer, D.C., et al. 1982, *Nature*, 300, 615
Becker, W., Trümper, J. 1997, *A&A*, 326, 682
Bulik, T., Rudak, B., Dyks, J. 2000, *Mon. Not. R. Astron. Soc.*, 317, 97
Catanese, M., Weekes, T. 1999, *Pub. Astron. Soc. of Pacific*, 111, 764, 1193
Chadwick, et al., 1998, *Astropart. Phys.*, 9, 131
Chadwick, et al., 2000, *ApJ*, 537, 414
Cheng, K.S., Ho, C., Ruderman, M.A. 1986, *ApJ*, 300, 500
D'Amico N., et al. 2001, *ApJ*, 552, L45
D'Amico, 2001, *Talk at Gamma Ray Astrophysics Symposium*, Baltimore
Daugherty, J.K., Harding, A.K. 1982, *ApJ*, 252, 337
de Jager O.C., et al. 1992, *ApJ*, 396, 161
de Jager O.C., et al. 1996, *ApJ*, 457, 253
de Jager O.C., Konopelko, A., Raubenheimer, B.C., Visser, B. 2001, *Proc. ICRC, Hamburg*, vol. 6, 2432
de Naurois, et al. 2002, *ApJ*, 566, 343
Goldreich, P., Julian, W.H. 1969, *ApJ*, 157, 869
Harding, A.K. 1981, *ApJ*, 245, 267
Harding, A. et al. 2000, *Proc. Int. Symp. High Energy Gamma Ray Aston., Heidelberg, Eds. F.A. Aharonian, H.J. Völk, AIP Conf. Proc.*, vol. 558, 115
Hewish, A., et al. 1968, *Nature*, 217, 709
Hillas, A.M., et al. 1998, *ApJ*, 503, 744
Hirotani, K., Shibata, S. 2001, *ApJ*, 558, 216
Hofmann, W. 2001, *Proc. 27th ICRC, Hamburg*, vol. 7, 2785
Kanbach, G. 2002, *This proceedings*
Kaspi, V.M., et al. 2000, *ApJ*, 528, 445
Kifune, T., et al., 1995, *ApJ*, 438, L91
Kirk, J., Skjaeraasen, O., Gallant, Y. 2002, *submitted to A&A*
Konopelko, A., 2000, *Proc. Int. Symp. High Energy Gamma Ray Aston., Heidelberg, Eds. F.A. Aharonian, H.J. Völk, AIP Conf. Proc.*, vol. 558, 569
Kuiper, L., et al. 1999, *A&A*, 351, 119
Lessard, et al., 2000, *ApJ*, 531, 942
Macomb, D.J., Gehrels, N. 1999, *ApJS*, 120, 335
Neshpor, Yu., Stepanian, A., 2001, *Astron. Letters*, 27, 12, 794
Ong, R. 1998, *Phys. Reports*, 305, 93
Oser, et al., 2001, *ApJ*, 543, 949
Ostriker, J.P., Gunn, J.E. 1969, *ApJ*, 157, 1395
Roberts, M., Romani, R., Kawai, N. 2001, *ApJS*, 133, 451
Romani, R. 1996, *ApJ*, 470, 469
Ruderman, M., Cheng, K.S. 1988, *ApJ*, 335, 306
Ruderman, M.A., Sutherland, P.G. 1975, *ApJ*, 196, 51

Srinivasan, R., et al. *ApJ*, 489, 170
Sturrock, P.A., 1971, *ApJ*, 164, 529
Thompson, D.J. 2000, *Proc. Int. Symp. High Energy Gamma Ray Aston., Heidelberg, Eds. F.A. Aharonian, H.J. Völk, AIP Conf. Proc.*, vol. 558, 103
Torres, D., Butt, Y., Camilo, F. 2001, *ApJ*, 560, L155
Usov, V.V. 1982, *Nature*, 305, 409
Yoshikoshi, et al., 1997, *ApJ*, 487, L65

Proceedings of the 270. WE-Heraeus Seminar on: *"Neutron Stars, Pulsars and Supernova Remnants"*
Physikzentrum Bad Honnef, Germany, Jan. 21-25, 2002, eds. W. Becker, H.Lesch & J. Trümper, MPE Report 278, pp. 112-113

Vortex Configurations, Oscillations and Pinning in Neutron Star Crusts

M.Hirasawa[1] **and N.Shibazaki**[2]

[1] Department of Physics, Rikkyo University, Nishi-Ikebukuro, Tokyo 171-8501, Japan
[2] Department of Physics, Rikkyo University, Nishi-Ikebukuro, Tokyo 171-8501, Japan

Abstract. The rotating neutron superfluid in the inner crust of a neutron star is threaded by quantized vortex lines. The pinning force from lattice nuclei and the Magnus force from neutron superfluid act onto a vortex line that has a finite tension. The configuration of a vortex line in equilibrium comprises a number of pinned straight lengths separated by unpinned kinks when the rotation axis is slightly inclined to the major axis of a crystal lattice and the Magnus force is not so strong. Energy of $\sim$ 4 MeV is required to form a kink at densities of $\sim 3.4 \times 10^{13}$ g cm^{-3}. Magnus force makes the vortex line parabolic on global scale. There exist two modes, rotational and helical (Kelvin), for oscillations allowed on a vortex line. The vortex oscillations in the pinned straight segments are possible only above a minimum frequency. We find no unstable mode that grows with time. Hence, the vortex configurations with kinks may be stable and yield the strongly pinned state. The essence of our results may not be altered even when we consider the vortex behaviors in a polycrystalline structure. Our studies suggest that pinning of a vortex line in a polycrystalline structure would be still strong enough to explain the large glitches.

We show the equilibrium configuration of a vortex line in Fig. 1, where we adopt the coordinates fixed in the lattice nuclei. The z-axis is chosen to be parallel to one of the major axes of a body-centered cubic lattice and the neutron superfluid is assumed to flow in the y-direction. The horizontal coordinate ϕ expresses displacement of a vortex segment from the z-axis. All coordinates are multiplied by $g = 2\pi/a$, where a is the lattice constant. Here the Magnus force is ignored for simplicity. The numbers on the curves denote the inclination angle between the rotation and main crystal axes. We find that when the inclination angle is small, vortex lines in equilibrium configurations move from one lattice plane to the next by forming a kink and a number of kinks increases with increasing inclination angle. Note that the average orientation of a vortex line corresponds to the direction of the rotation axis. A vortex line can orient its average direction to the direction of the rotation axis by adjusting a number of kinks. Apart from the kink parts, the vortex lines are straight

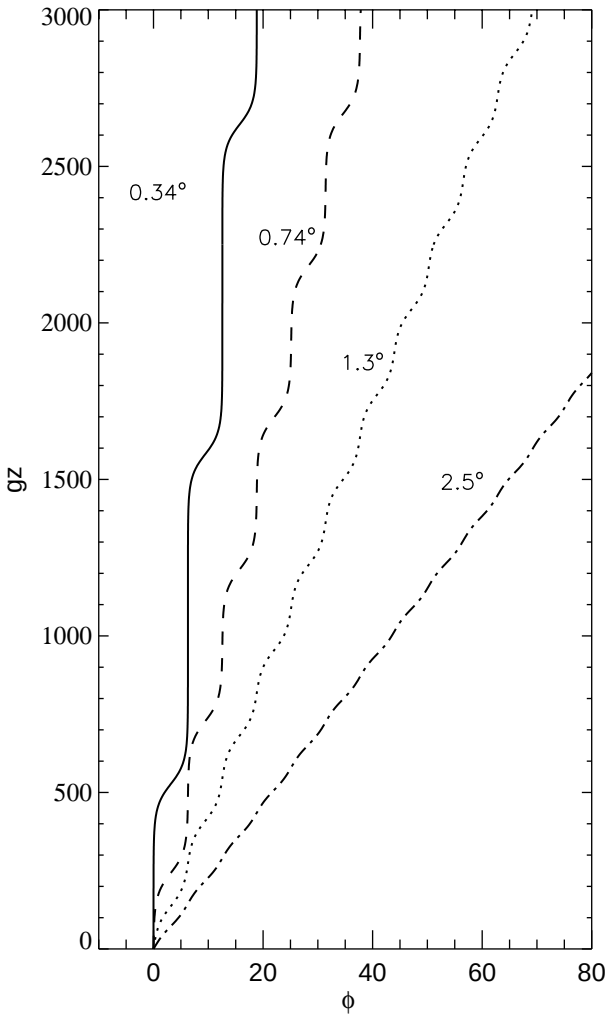


Fig. 1. Vortex equilibrium configurations with kinks for different inclination angles of a rotation axis against the z-axis. Here the Magnus force is ignored. The numbers on the curves denote the inclination angle. The average orientation of a vortex line corresponds to the direction of a rotation axis of the star. The main lattice planes are located at the horizontal coordinate of $\phi = 2n\pi$.

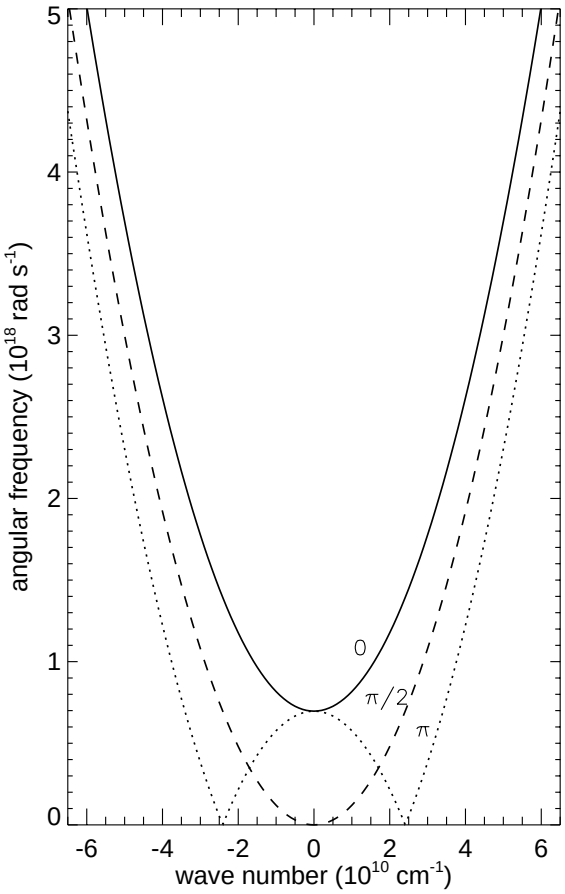


Fig. 2. Dispersion relations for oscillations allowed on a vortex line. The numbers by the curves denote displacement of the vortex segment, ϕ, from the z-axis in equilibrium configuration. The oscillations in the pinned segments are possible only above a minimum frequency.

and in parallel to the z-axis, and are firmly pinned to the lattice nuclei. Even though the extra energy is required to create kinks, the total energy of a vortex line with kinks is much lower than that of the inclined straight vortex line without kinks since except for kink parts the vortex line lies in the bottom region of the pinning potential.

Figure 2 illustrates the dispersion relations for oscillations excited on a vortex line. The numbers by the curves denote a displacement of the vortex segment, ϕ, in equilibrium. We find that there exist two oscillation modes, rotational and helical (Kelvin) modes. At lower wave numbers the angular frequency of oscillations is determined mainly by the rotational mode, while at higher wave numbers mainly by the Kelvin mode. We should note that there exists the minimum frequency for the oscillations especially when ϕ is close to $2n\pi$. The oscillations with frequencies lower than the minimum cannot be excited on and cannot propagate in the pinned part of a vortex line, whereas the oscillations with frequencies higher than the minimum can propagate along a vortex line, varying the wave length.

Recently, Jones (1998) argues that vortex interaction with a polycrystalline structure does not provide pinning strong enough to explain the large glitches observed in the Vela pulsar, considering the kink motion along a vortex line. Our results, however, show that the vortex equilibrium configurations with static kink structure are stable. Hence, the kink motion as required by Jones is less likely. The kink solution can be expressed as a sum of Fourier components of different wave numbers. The dispersion relation shows that the phase velocity of vortex waves depends on the wave number. Hence, even if a kink is formed and starts to move, the kink feature will be smeared out during propagation. The vortex equilibrium configuration is composed of the static kink and straight segments. A vortex line in equilibrium lies deep in the pinning potential well and is strongly pinned to the lattice nuclei in its most part. We conclude from these results that pinning may be strong enough to explain the large glitches observed in the Vela pulsar.

References

Jones, P. B. 1998, MNRAS, 296, 217

Proceedings of the 270. WE-Heraeus Seminar on: *"Neutron Stars, Pulsars and Supernova Remnants"*
Physikzentrum Bad Honnef, Germany, Jan. 21-25, 2002, eds. W. Becker, H.Lesch & J. Trümper, MPE Report 278, pp. 114-125

New Limits on Gravitational Radiation using Pulsars

A. N. Lommen

Astronomy Department & Radio Astronomy Laboratory, University of California, Berkeley, CA 94720-3411, USA
currently at Sterrenkundig Instituut, University van Amsterdam, Kruislaan 403, 1098 SJ Amsterdam, the Netherlands
email: alommen@astro.uva.nl

Abstract. We calculate a new gravitational wave background limit using timing residuals from PSRs J1713+0747, B1855+09, and B1937+21. The new limit is based on 17 years of continuous data pieced together from 3 different observing projects: 2 at the Arecibo Observatory and 1 at the 140ft Green Bank Telescope. This project represents the earliest results from the 'Pulsar Timing Array' which will soon be able detect the stochastic background from early massive black hole mergers.

1. Introduction

There are two categories of sources that could produce a detectable level of stochastic gravitational radiation from the distant Universe. One is of cosmological origin and the other involves galaxy evolution. First, low-frequency ($10^{-20\text{ to }0}$ Hz) relic gravitational radiation may be generated during inflation, according to string theory models of the early Universe, via both early evolution of the extra dimensions and decay of cosmic strings. Cosmic strings, while now disfavored as the driver behind structure formation in the Universe, still arise in many grand unified theories of particle physics after the epoch of inflation (Caldwell, Kamionkowski, & Wadley 1998; Hogan 2000; see also Maggiore 2000). Second, the coalescence of massive black holes (MBHs) during galaxy evolution could also produce a detectable level of Gravitation Waves (GWs). (See Lommen & Backer 2001 for more on this.) Three cosmology experiments are being conducted or planned by a number of investigators around the globe to either detect or place new limits on the stochastic background of gravitational radiation: polarization of the Cosmic Microwave Background Radiation (pCMBR), Pulsar Timing Array (PTA), and Laser Interferometer Space Array (LISA).

The PTA consists of a regular observing schedule on a handful of the millisecond pulsars that are most accurate as clocks. So far, we have used the Arecibo Telescope in conjunction with the Green Bank 140ft telescope, but we plan on including the new Green Bank 100-m telescope that has just been commissioned and a collection of other European and Australian telescopes to maximize the observation time and the range of observations available.

Pulsar timing residuals are sensitive to gravitational radiation of wavelengths of about 1 yr, making the PTA complementary to LISA which will measure much shorter wavelengths, and the pCMBR which will measure much longer wavelengths.

Using timing residuals from Arecibo Observatory observations of PSRs B1937+21 and B1855+09 over 8 yr, Kaspi,Taylor, & Ryba (1994, hereafter KTR94) placed a limit of

$$\Omega_g h^2 < 6 \times 10^{-8} \quad (95\%\text{confidence})$$

where Ω_g is the fractional energy density in gravitational waves per logarithmic frequency interval and the Hubble constant $\mathrm{H}_o = 100h$ km s^{-1} Mpc^{-1}. We have connected the KTR94 data to 10 years of Green Bank 140ft telescope data and 3 years of Arecibo Observatory data. The overlapping data sets span a total of nearly 17 years, doubling the baseline of Kaspi et al's results. The sensitivity of the PTA is proportional to $1/(timespan)^4$, and therefore we expect an increase in sensitivity of about 16 over the KTR94 results.

First, in §2 we describe the 3 different sets of observations that have gone into calculating the limits presented in this article. In §4 we connect the three data sets. In §5 we show the calculation of the new gravitational wave limit. §6 compares the precision of pulsar clocks to those of atomic time standards. §7 is an update of the relationship between $\dot{P}$ and timing noise presented by Arzoumanian et al. (1994). In §8 we discuss the possibility that a planet orbits pulsar PSR B1937+21. Finally in §10 we present our conclusions.

2. Observations

At the NRAO[1] 140-foot (42.7 m) telescope we observed PSR J1713+0747, PSR B1855+09, and PSR B1937+21 in

[1] The National Radio Astronomy Observatory (NRAO) is operated by Associated Universities, Inc., under contract with the National Science Foundation.

addition to others 4-6 times per year at radio frequencies near 800 and 1400 MHz from 1989 October to 1999 July. For details on the analysis of these data see the report by Backer et al. (1993) on results from the first half of the data set. Observations of PSR J1713+0747 started after its discovery in 1994 (Camilo, Thorsett, & Kulkarni, 1994).

We have been conducting monthly observations at 0.43 GHz, 1.4 GHz and 2.4 GHz of an array of MSPs using the NAIC[2] Arecibo Observatory 300 m telescope since December 1997. These data are used to make precision arrival time measurements for a variety of astrophysical goals. We used the Arecibo-Berkeley Pulsar Processor (ABPP), which is a multi-channel, coherent dispersion removal processor[3] with 112-MHz total bandwidth capability (For a detailed technical description of the hardware see Backer et al.(1997.) For PSRs J1713+0747 and B1855+09 we use 56-MHz bandwidth for observations at 1.4 GHz, and 112-MHz for 2.4 GHz, while for PSR B1937+21 we use 45-MHz bandwidth at 1.4 GHz and 56-MHz at 2.4 GHz.

Calibrated total intensity profiles were formed from signals with orthogonal circular polarization. The profiles were then cross correlated with a template to measure times of arrival (TOAs) relative to the observatory atomic clock. Small errors in the observatory UTC clock, of order 1 μs, were corrected based on comparison of local time to transmissions from the Global Positioning System of satellites (GPS). The templates used for cross correlations were constructed by fitting a set of Gaussian components to long-term averages of observations, using the software described in Kramer et al. (1994) and Kramer (1994). This model fitting scheme is described extensively in Lommen (2001). We use the model to generate noise-free templates with a specific common fiducial point at all frequencies. Lommen (2001) shows that the templates generated in this manner have at most 2 μs of error in the fiducial point between 1400 and 2380 MHz.

In addition to the two data sets mentioned above, we also have incorporated the archival Arecibo data from KTR94 on PSR B1855+09 and B1937+21 into our analysis. See the original paper for details on these data.

3. Analysis

As we just mentioned, TOAs are calculated calculated via cross-correlation with a template. Before these TOAs can be analyzed several corrections are required:

$$TOA' = TOA + \Delta_{clock} + \Delta_{DM} + \Delta_{backend}$$

Δ_{clock} is comprised of a number of clock corrections which in our case transform a TOA which is referenced against an observatory maser, to one which is referenced against UTC. Δ_{DM} causes TOA$'$ to be the time that the pulse would have arrived had it been at infinite frequency (lower frequencies are delayed more by the ISM). $\Delta_{backend}$ corrects for any delays that are dependent on the observing backend used. In our case we have a digital latency which is dependent on channel bandwidth and a mid-scan correction which is a result of our on-line folding. After all of these corrections, TOA$'$ is independent of observatory clock, frequency, and observing backend. TOA$'$ marks the space-time event of the arrival of a defined fiducial point of the pulse at the telescope on a defined time scale.

4. Connection of Data Sets

In the TEMPO analysis arrival time of pulses at the observatory is referred to that at the barycenter of the solar system. The solar time corresponding to the rotation of the earth is known as UT1. UT1 is tabulated by measuring the difference between UT1 and UTC. UTC is a solar time scale that runs at the rate of TAI, international atomic time. BIPM tables of (UT1-UTC) are used to orient the observatory in inertial space and make the translation from observatory to earth-center. (UT1-UTC) is between 7 and 32 seconds over the course of our observations, and is known to 0.1 ms at all times. This translates to an uncertainty in TOA of only ~ 0.1 ns. To calculate the earth's position TEMPO uses standard JPL ephemerides DE405.1950.2050. We know the geodetic position of each observatory to within meters. The delays that remain, that are most difficult to account for, are the delays between the arrival of the pulse at the fiducial point of the antenna as defined by VLBI coordinates and the completion of its transmission through the 'back-end' of the receiving system. These are typically in the range of 100-3500 ns. At Arecibo, for example, we know that the travel time for a signal from the control room to the Gregorian receivers and back is approximately 7 μs [4] largely resulting from the $\sim$1200 ft of fiber-optic cabling through which the signal must travel from the platform to the control room. This would give us a ~ 3.5 μs delay in the TOAs. Typically, we ignore these delays because we take data from a single observatory, with a single operating system, and any constant delay such as this is seemingly irrelevant.

However, these delays become important for connecting multi-observatory data sets. If all such delays at all observatories engaged in pulsar timing were known, it would be possible to have a "Universal Pulsar Timing Array (UPTA)" in which all TOAs from all pulsar data from all over the world could be combined a priori in single meaningful data base. This would necessitate the need for uniform template fiducial point processing. For example, if the world's pulsar astronomers could piece together 17-year data sets on 10 different MSPs with comparable pre-

[2] The National Astronomy and Ionosphere Center Arecibo Observatory is operated by Cornell University under contract with the National Science Foundation.

[3] 'coherent' means that the dispersion is removed in the voltage domain prior to power detection.

[4] Mike Nolan, private communication, 2001 Aug 19

Table 1. Offsets, in μs, between data sets.

Pulsar	KTR94-GB[a]	GB-ABPP[b]
J1713+0747	···	−3.2
B1855+09	−56.9	1.4
B1937+21	−14.4	−0.12

[a] GB=Green Bank data
[b] ABPP=ABPP data (post-upgrade Arecibo)

cision, the sensitivity of the UPTA would go down by a factor of $1/\sqrt{10}$.

In our comparatively small experiment, we attempt this, but can only account for everything but the final 15-60 μs, and so in the end we end up doing a bootstrap connection. We have 3 overlapping data sets. For each pulsar, the average separation between two overlapping sections is used as the offset between the two data sets. These offsets, which will be included in the ITOA format that we will make publicly available, are shown for each pulsar and for each adjacent data set in Table 1. In the case of the Green Bank and ABPP data sets, the TOAs were generated using the same series of Gaussians with the same fiducial point, so all template discrepancies are removed to within 2 μs (see Lommen 2001 for more on this subject). 2 μs in fact, represents the maximum error in going between 1400 and 2380 MHz. The data we have connected is centered from 1330 MHz to 1420 MHz, and the error roughly scales with the size of the bandwidth over which one must construct templates (see Lommen 2001). Therefore the maximum error in connecting our range of data, due to our template cross-correlation is roughly a tenth of 2 μs, or 0.2 μs. In the case of the offset between the KTR94 data sets and the Green Bank data sets, we added, a priori, an amount of offset corresponding to the difference between our fiducial point and the fiducial point of KTR94, who used the peak of the template. These a priori numbers were a phase of 0.443259 for B1855+09 and 0.353460 for B1937+21. The numbers shown in the table, are the offsets in addition to these template offsets. The sign of the offsets are meaningful, e.g. the numbers under the column "GB-ABPP" are the quantities acquired from subtracting the average ABPP residual from the average Green Bank residual during the epoch while they overlap. The offsets between data sets that we processed ourselves (GB - ABPP) are all less than 8 μs.

In order to perform a weighted fit across multiple data sets, it is necessary to be very careful of the average weighting of one data set relative to another. Said another way, with a single set of data, all taken with a single observing system and analyzed uniformly, one need not worry about, for example, overestimating all the error bars by a factor of 3. However, when one is combining two such data sets, if one has overestimated error bars, and a second has underestimated error bars, the fit will

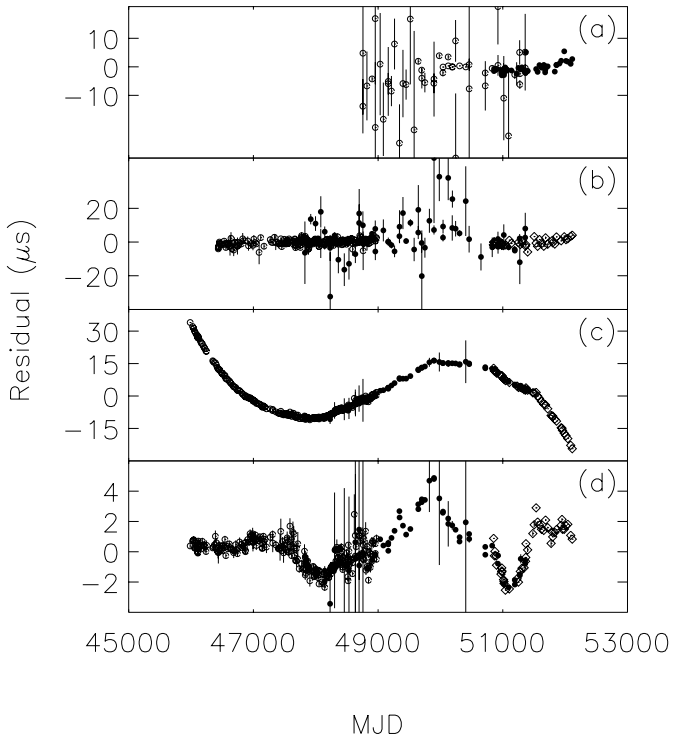


Fig. 1. (a) PSR J1713+0747, (b) PSR B1855+09, (c) PSR B1937+21 and (d) PSR B1937+21 fit for $\ddot{P}$. The open circles are KTR94 data, the filled circles are Green Bank data, and the open diamonds are ABPP data.

tremendously favor the latter. In order to account for this problem, we normalized the error bars in each data set by the total variance per day in those data, i.e.

$$\sigma_{\rm normalized} = \sigma_{\rm original} \times \frac{\sqrt{\sum_i 1/{\rm err}_i^2}}{L}$$

where L is the length of the data set, in days, and $\sigma_{original}$ are the error bars that were published by KTR or calculated by us, using the method created by Christophe Lange (private communication) which was adapted from Downs & Reichley (1983).

We used the standard TEMPO package[5] to perform weighted fits to α, δ, μ_α, μ_δ, P, and $\dot{P}$, in each of the 3 pulsars. Additionally in J1713+0747 and B1855+09 we fit for the 5 Keplerian parameters and the Shapiro delay parameters, m_2 and $\sin i$ (See Stairs, 1998 for an excellent summary of the process of fitting for the Shapiro delay).

We show the resulting residuals in Figure 1. In (a), (b), and (c), we show J1713+0747, B1855+09, and B1937+21, respectively, fitted for the parameters not marked with footnote "c" in the table. Additionally, in panel (d), we show B1937+21 fitted for $\ddot{P}(\ddot{\nu})$.

In the next three sections, we discuss various implications of the residuals resulting from these fits. First, we

[5] http://pulsar.princeton.edu/tempo

assume the residuals shown in Figure 1 are the result of GWs and use them to place new limits on the GWB. Second, we assume the same residuals are the result of timing noise intrinsic to the pulsars, and determine whether these pulsars are more or less noisy than expected based on the characteristics of the population at large. Finally, we consider the possibility that the residuals in B1937+21 are the result of a planet orbiting that body.

5. Limit on Gravitational Radiation

These data, representing a continuous 17-y set, provide a new limit on the level of background gravitational radiation present throughout the galaxy, and ostensibly the universe. In short, we assume that all the observed fluctuations in the timing residuals are due to the stochastic background of gravitational radiation. This yields the maximum possible gravitational wave spectrum present.

To determine the limit they place, we first need to measure the spectrum of fluctuations that we observe in the timing residuals. The process of computing an observed noise spectrum from irregularly sampled data has been given much consideration by previous authors (Groth 1975; Deeter & Boynton 1982; Deeter 1984; Cordes & Downs 1985; KTR94). These authors are particularly concerned with "red" spectrum where imperfect sampling leads to coupling of spectral estimates at low frequency. Deeter (1984) compares the various methods and determines that the method of fitting the data to orthonormal polynomials produces the most meaningful results. We therefore use this method, as did both Stinebring et al. (1990) and KTR94 in previous generations of this experiment.

Stinebring et al. (1990) and KTR94 start with a calculation which shows that the energy density of background gravitational radiation per frequency octave would have a frequency dependency $\propto \nu^{-5}$ and they go about putting limits on that assumed spectrum. We do the same. However, Rajagopal & Romani (1995), Phinney (2001), and Jaffe & Backer (2002) recently show that the energy density per frequency octave would be proportional to $\nu^{-4.3}$ rather than ν^{-5}. Either way, this is steep compared to the intrinsic spectrum observed in young pulsars, and would not change our results significantly.

A series of polynomials, $p_i(t)$ where i is of the set 0, 1, 2, 3 of corresponding order, is generated orthogonally over the sampling of the timing residuals. We started with the following set:

$$p_{j=0,1,2,3}(t) = \sum_{i=0}^{j} t^i$$

The process of orthogonalization is done via standard Gram Schmidt reduction. A linear combination of the p_i's is found which minimizes the quantity

$$\chi^2 = \frac{1}{\sigma^2} \sum_{n=1}^{N} \left(r(t_n) - \sum_{j=0}^{3} C_j p_j(t_n) \right)^2$$

where $r(t_n)$ is the measured residual at time t_n. The first three C_j's are covariant with the fitting of the phase, period, and period derivative in the pulsar model. C_3, however, is a measure of the amplitude of the spectral density of the variance in the timing residuals at a frequency corresponding to 1/T where T is the length of the data set. $S_m =< C_3^2 >$ is the corresponding estimate of the power(variance) contained near frequency 1/T. In order to sample the spectrum of S_m over multiple frequencies, we divide the data into smaller and smaller subsets in time, by factors of 2. We refer to the divisor as the frequency index. A frequency index of 2 implies the data set was divided in half, and that therefore we are measuring frequencies of 2/T, or periods of about 8.5 years.

The results of the spectral measurements are shown in the solid line Figure 2 for PSRs J1713+0747, B1855+09, and B1937+21, using the fits corresponding to parts a, b, and c of Figure 1, i.e. fits through $\dot{\nu}$ only. Though this method works well for irregularly sampled data, the value of the S_ms are still dependent on sampling. In order to gauge the extent of this dependence we have simulated data sets of various spectral indices, with the same sampling as the actual data. Randomly distributed Gaussian noise was transformed into the Fourier domain, multiplied by a function with spectral index 0,2,3, or 5, normalized to 1 μs^2 y at a frequency of 1 y^{-1}, and transformed back to a time series. Once in the time domain, the data were sampled identically to the actual data. 10,000 such realizations were created for each of the 4 spectral indices. The power spectra of each was measured using the method of orthonormal polynomials described above. The results of this analysis are shown in dotted lines in Figure 2 for each of the 4 spectral indices.

The average value of the spectral estimator, S_m, with spectral index 5 represents the estimate of S_m in the presence of a gravitational radiation, $< S_m(\Omega_g h^2) >$, where Ω_g is the energy density in GWs, ρ, expressed as a fraction of the closure density, ρ_c of the universe:

$$\Omega_g = \frac{\rho}{\rho_c} = \frac{8\pi G\rho}{3H_o^2}$$

where H_o is the Hubble constant. We generally express Ω_g in terms of h, i.e. $\Omega_g h^2$ where $H_o = 100\ h$ km s^{-1} Mpc^{-1}. We need to translate the normalizing amplitude, (1 μs^2 y at a frequency of y^{-1}) into a particular value of $\Omega_g h^2$. We use the relationship derived from the definition of Ω_g (from Stinebring et al. 1990)

$$P_g(f) = \frac{H_0^2}{8\pi^4} \Omega_g f^{-5}.$$

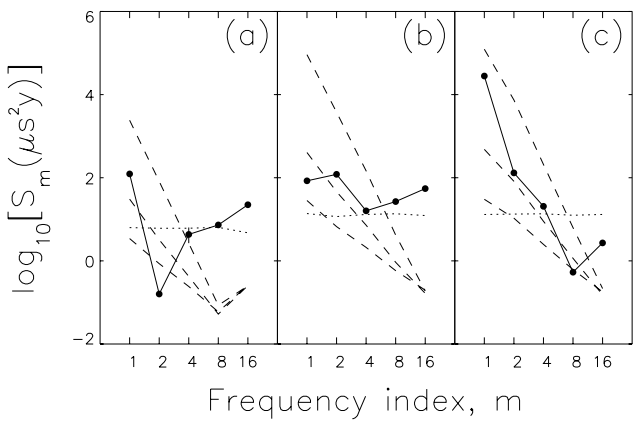


Fig. 2. $\log S_m$ vs frequency index. Solid line shows measured values for each pulsar. Dotted lines show simulated data for spectral index 0. Dashed lines show simulated data for spectral indices 2, 3, and 5. (a) PSR J1713+0747, (b) PSR B1855+09, and (c) PSR B1937+21. Frequencies corresponding to frequency index are m/L where L is the length of the data set: (a) 9.2 yr, (b) 15.6 yr, and (c) 16.8 yr.

Table 2. Observed and computed spectral densities.

Pulsar	m	S_m	$< S_m >_w$	$< S_m >_g$
J1713+0747	1	348	538	3.21
	2	6.20	435	0.108
	4	22.4	410	3.52×10^{-3}
	8	4.17	420	1.14×10^{-4}
	16	111	278	3.34×10^{-4}
B1855+09	1	84.8	137	121
	2	120	182	5.01
	4	15.6	210	0.195
	8	26.6	204	5.57×10^{-3}
	16	54.7	155	2.51×10^{-4}
B1937+21	1	29379	0.025	164
	2	203	0.028	9.87
	4	11.8	0.035	0.277
	8	7.93	0.035	8.39×10^{-3}
	16	3.43	0.034	2.87×10^{-4}

[a] GB=Green Bank data
[b] ABPP=ABPP data (post-upgrade Arecibo)

where $P_g(f)$ is spectral density, i.e. the same quantity we are attempting to measure with S_m. This means that values of $< S_m(\Omega_g h^2) >$ from data with 1 μs y at a frequency of y^{-1} need to be divided by 752 in order to represent the spectral density when $\Omega_g h^2 = 10^{-7}$ which is the value we represent in Table 2.

Figure 2 shows that the measured spectra of both J1713+0747 and B1855+09 are both quite flat compared to the spectral index 5 model. We would expect J1713+0747 to be somewhat flatter than the others simply by virtue of the plot representing a higher frequency region of the spectrum. PSR B1937+21 demonstrates a steep spectrum, comparable to the spectral index 5 model spectrum, but this may be due to other sources as we will discuss later (e.g. see §8).

In order to calculate the expected influence of gravitational waves on the spectral measurements, S_m, we needed to know the contribution from purely white noise. To this end, we simulated residuals that were only influenced by our known quantities of instrumental noise. We created white noise at the same sampling as that of the three pulsars we are considering. The white data from each observatory were normally distributed random numbers normalized such that their RMS matched the median of instrumental noise from that pulsar at that observatory. The value used for instrumental noise was the standard deviation of the mean of the timing residuals about the mean for a particular day, i.e.

$$stdev = \frac{\sqrt{\sum_i (r_i - u)^2}}{N}$$

where r_i is a single residual of which there are N averaged to form a daily average and u is the mean of the residuals on that day. We created 10,000 random realizations for each of the 3 pulsars, and measured their spectrum using the same technique shown above. The average value of these data we call $< S_m >_w$.

The values of S_m, $< S_m >_w$, and $< S_m >_g$ for each value of the frequency index, m, are given in Table 2.

In order to attempt to rigorously calculate an upper limit to background gravitational radiation present in our residuals, we duplicate the analysis of Thorsett & Dewey (1996, hereafter TD96). There is significant controversy around this method, which we address following the results. TD96 create a statistic, $Stat_1 = mS_m/[< S_m >_w + < S_m(\Omega_g h^2) >_g]$, which is normally distributed with m degrees of freedom. The statistic is essentially the measured value of the spectral estimator divided by the predicted value, based on Monte Carlo simulations.

We use a Neyman-Pearson test to determine whether the distribution of $Stat_1$, for various values of $\Omega_g h^2$ is significantly different than the corresponding statistic in the absence of gravitational radiation. The validity of the Neyman-Pearson test is complicated, but it has a simple construction. Consider a particular measurable, A, with probability distribution S1. Correspondingly, consider another measurable, B, with probability distribution S2. The Neyman-Pearson test essentially tests the extent to which the distributions overlap. If they have considerable overlap, they are indistinguishable, if not, they aren't. The quantitative test of 'considerable' involves computing the line which delineates 5% of the area under the curve, representing the least likely outcomes of measuring A. Consider Figure 3 which shows two probability distributions. The area to the left of the dotted line is 5% of the total area of the solid curve. The mean value of the dotted curve, falls just to the left of the dotted line. Thus, we can say

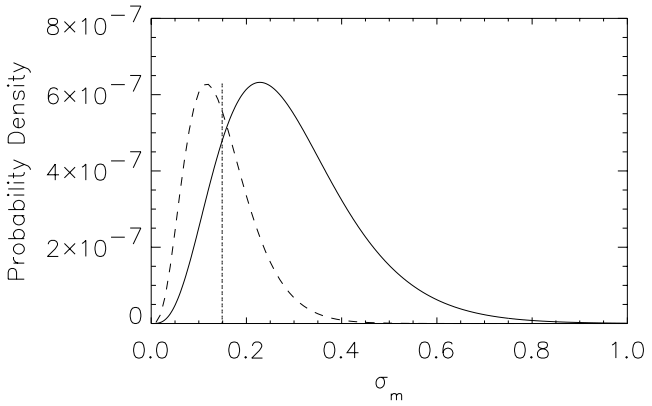


Fig. 3. An example of two different probability density distributions. 5% of the area under the solid curve is to the left of the dotted line.

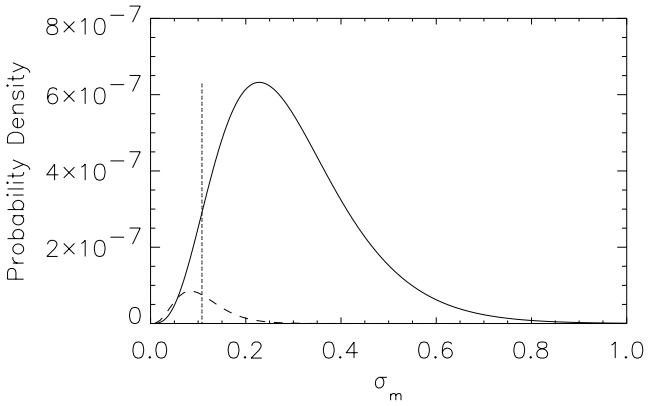


Fig. 4. The solid line shows the probability density of the null statistic, S0, while the dashed curve shows the probability density of the S1 statistic at the 95% confidence value. The dotted line is the same as in Figure 3

that these two distributions are different from each other at the 95% confidence level.

One of the subtleties of the Neyman-Pearson test is that one of the two hypothesis is considered the 'null' hypothesis, and this is the hypothesis one accepts unless the data compels one to choose otherwise. Thus, the Neyman-Pearson test, by conjecture has a preferred answer, i.e. whatever you choose as the null hypothesis. Our null hypothesis will be that there is no gravitational radiation in the universe. This is of course incorrect. This is the first issue McHugh et al. (1996) have with this method. We are inclined to agree that this is not a good construction.

TD96 used a likelihood ratio, which is an unnecessarily complicated way to construct the Neyman-Pearson test. We merely need to compare the two distributions that are shown in the numerator and the denominator of the ratio TD96 use.

$$S1 = \Pi_{m=1,2,4,8}\chi^2_m \left(\frac{mS_m}{< S_m >_w + < S_m(\Omega_g h^2) >_g} \right)$$

$$S0 = \Pi_{m=1,2,4,8}\chi^2_m \left(\frac{mS_m}{< S_m >_w} \right).$$

S0 represents the null statistic, and is shown in the solid line of Figure 4. S1 represents the statistic when a certain amount of gravitational radiation $\Omega_g h^2$ is present. We have plotted S1 in Figure 4 when its value is equal to the 5% limit that we calculate, namely, $\Omega_g h^2 \leq 2.8 \times 10^{-6}$ at a 95% confidence level.

TD96 calculated $\Omega_g h^2 \leq 1.0 \times 10^{-8}$ at a 95% confidence level using only the KTR94 B1855+09 data. Using the technique of TD96 our expanded set of B1855+09 data actually place a weaker limit than the KTR94 data alone, because of the large scatter in the Green Bank data points. The technique separates the data into smaller and smaller sections in order to measure shorter frequencies. The average of these shorter frequency sections is therefore falsely enlarged in our calculations. Using only the $m = 1$ term of our data we have: $\Omega_g h^2 \leq 9.8 \times 10^{-6}$ at a 90% confidence level.

McHugh et al. (1996) rejected the analysis of TD96 because of their use of hypothesis testing rather than parameter estimation. They completed a full Bayesian analysis of the same data which resulted in a much less restrictive limit, $\Omega_g h^2 < 9.3 \times 10^{-8}$, than the analysis of TD96 using the same data.

These opaque calculations cover up the essential nature of the results. After KTR94 we can make a much more simple estimate of the limit these data place on the GWB. We use KTR94 equation 6 which relates the energy density, ρ, in gm cm^{-3} of a gravitational wave to its affect on TOA in μs, A, and a frequency, f, in Hz.

$$\rho = \left(\frac{243\pi^3}{416G} \right) A^2 f^4.$$

The largest amplitude sinusoid that one could conceivably fit to the B1855+09 data has $A = 3$ μs and $f = 1/17\ yr = 1.9 \times 10^{-9}$ Hz. This gives $\rho = 3.2 \times 10^{-38}$ gm cm^{-3}, or using

$$\frac{\rho}{\rho_c} = \frac{8\pi G\rho}{3H_o^2} = 2 \times 10^{-9} h^{-2},$$

which is more than an order of magnitude smaller than the limit found by KTR94. We assume $H_o = 100\ h$ km s^{-1} Mpc^{-1}.

As explained in Lommen & Backer (2001), a gravity wave propagating through the galaxy would have an effect both on the emitting site (the pulsar) and the receiving site (the Earth). Neglecting geometrical considerations for a moment, this could imply that the limit we have just derived will on average be a factor of 2 too high, i.e., that the response that we see in the pulsar timing, since it results from effects at both sites, is essentially doubled. The factor is not so simple, but depends on (a) the direction

of propagation and polarization of the impinging gravitational wave, and (b) the geometrical relationship of the pulsars to the Earth. For a stochastic background of gravitational waves, however, we can calculate the expected effect. If the GW at the emission and reception sites constructively interfere then C_3 will increase by a factor of 2, and S_m will increase by a factor of 4. If emission and reception destructively interfere then S_m will be close to 0 (it will certainly be non-zero due to irregular sampling). The expectation value, i.e. the ensemble average over the 4π directions of propagation, and over the wavelengths in question is a factor of 2, so the limit is actually half what we, or any of these other groups, measure. This of course leaves aside the issue of the variance in the GWB. The background value we measure using these data place a limit on the GWB in a specific place and epoch: in our galaxy and during the 2 decades in which this experiment took place. Jaffe & Backer (2002) are working on a realistic version of the GWB which takes these specifics into account.

We have assumed up until now, that PSR B1855+09 produces the best limit on the GWB since it demonstrates the most stable timing and a long baseline. However, what if there was a geometrical situation in which B1937+21 was experiencing a large perturbation due to GWs while a null occurred at PSRs J1713+0747 and B1855+09? We first need to consider that the limited range of data on J1713+0747 was preventing our detection of any cubic therein. In Figure 5 we performed the same fit that we did for part (c) of Figure 1 but using only the limited range of the J1713+0747 data. The obvious cubic is gone but there is a 'sawtooth' present at the level of 2 μs that we do not see in the J1713+0747, so we conclude that we are seeing no comparable gravitational wave in J1713+0747.

To attempt to find a geometrical situation which produces an approximate null in J1713+0747 and B1855+09 we inspected the range of possible geometrical multiplicative factors, $(1-\gamma)/2$ over the 4π sphere of possible gravitational wave directions for each of the three pulsars. See Lommen & Backer (2001) for an explanation of this factor. Figure 6 shows the factor for 2π values of RA while DEC=0° for each of the 3 pulsars. B1937+21 is shown by the solid line. J1713+0747 is the dotted line, and B1855+09 is the dashed line. The three pulsars are close enough together in the sky that $(1-\gamma)/2$ is highly correlated over the sphere. We chose the DEC=0 line to show because it essentially produces the most favorable spot on the sphere for a B1937+21 gravity wave enhancement with a near-null in J1713+0747 and B1855+09. At DEC=80° J1713+0747 has $(1-\gamma)/2 = 0.005$, B1855+09 has $(1-\gamma)/2 = 0.05$, while B1937+21 has $(1-\gamma)/2 = 0.12$. That gives B1937+21 a 2.4× enhancement over B1855+09 and a 24× enhancement over J1713+0747. The relative strengths of J1713+0747 and B1855+09 can be exchanged somewhat as you can see in Figure 6. We conclude that it would be very difficult to arrange for the 'deviant' residuals we see in B1937+21 to be produced by gravitational radiation without producing a similar, but slightly smaller, $\sim$ 10 μs effect, in either J1713+0747 or B1855+09. In addition, a gravitational wave disturbance, which, when reduced by a factor $(1-\gamma)/2 = 0.12$ still yields a 30 μs residual deviation is unrealizable using any known gravitational wave producer in the universe (see Lommen & Backer 2001).

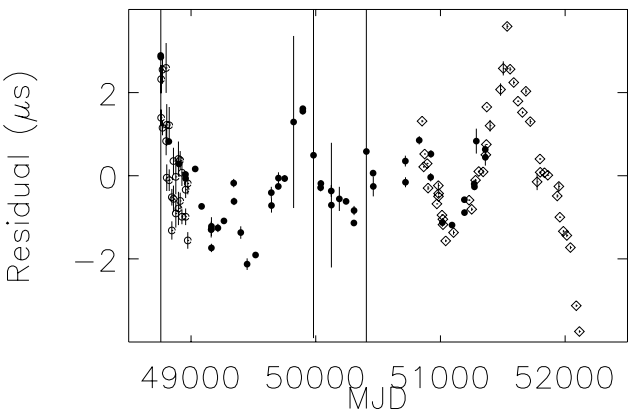


Fig. 5. Residuals from B1937+21 with no $\ddot{\nu}$ removed, fitted only to the range of the J1713+0747 data.

Finally, we consider whether emission and reception site disturbances could be destructively interfering in the case of B1855+09 and constructively interfering in the case of PSR B1937+21. The stochastic GWB can be thought of as "crinkled" space-time. We approximate the crinkling as a sine-wave of equal amplitude but arbitrary phase near each of the 2 pulsars and also near the earth. We begin by computing the enhancement of the amplitude of a sine wave by adding two equal sine-waves together, with a variable displacement, ϕ, between the two. This enhancement we call $E(\phi)$. Thinking of B1937+21 and the earth as emitter and receiver, we may, for example, calculate the probability that $E(\phi)$ will be 5 or greater: 0.001. To obtain the probability that B1937+21's perturbation will be enhanced over B1855+09's perturbation by a factor of 25 (roughly the ratio of their peak deviations) or greater we compute the quotient:

$$Q(\Delta\phi) = \frac{E(\phi)}{E(\phi - \Delta\phi)}$$

for $\Delta\phi = [0, 2\pi]$. The probability that $Q(\Delta\phi) > 25$, 0.016, is the probability that the disturbance in B1937+21 is 25 times that in B1855+09. Thus, the residuals we observe in B1855+09 render it highly unlikely that the large amplitude quasi-sinusoid observed in B1937+21 is the result of a GW. Consideration of PSR J1713+0747 would suppress the probability further but not by an equal factor.

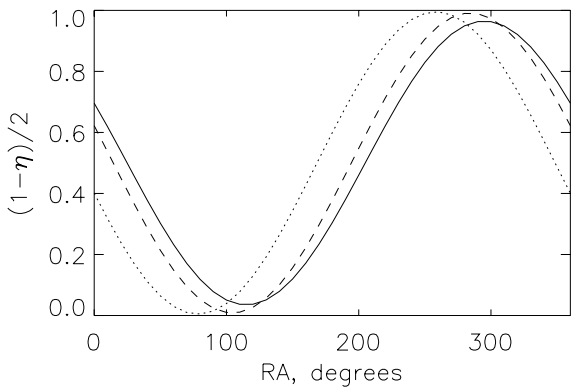


Fig. 6. $(1-\gamma)/2$ vs RA for DEC=0 for each of the 3 pulsars. B1937+21 is shown by the solid line. J1713+0747 is the dotted line, and B1855+09 is the dashed line.

6. Fractional Stability of Terrestrial Atomic Time Standards vs. Fractional Stability of Neutron Star Rotations

At the baselines considered in this paper, namely longer than 10 years, the fractional stability of neutron star rotations rivals that of terrestrial atomic time standards. To make the comparison quantitative we used the statistic σ_z proposed by Matsakis, Taylor, & Eubanks (1997) for describing pulsar and clock stabilities. The recipe for computing σ_z given in Matsakis, Taylor, & Eubanks (1997) is very complete. We only give a bare outline of the computation process here. We divide the timing residual or clock comparison, $X(t)$, into smaller and smaller subsections of time, starting with the full length, T, and going to T/2, T/4, T/8, etc. To each subset we fit the function

$$X(t) = c_o + c_1(t-t_0) + c_2(t-t_0)^2 + c_3(t-t_0)^3.$$

σ_z is related to the average of c_3^2 by the following formula

$$\sigma_z(\tau) = \frac{\tau^2}{2\sqrt{5}} < c_3^2 >^{1/2}$$

where the angular brackets denote the average, and τ is the length of the subset of data. Figure 7 shows the fraction stability, σ_z vs. dataspan for [UTC-GPS], [TAI-PTB], [TAI-USNO], and [PSR-TAI] for PSRs B1855+09, B1937+21. To compute the error we used the estimate provided by Matsakis, Taylor, & Eubanks (1997), which underestimates the error in the case of data with significant red noise, as is evident in the pulsar data.

Figure 7 shows that PSR B1855+09 beats the [TAI-USNO] time scale at the longest time periods, and is essentially equally as accurate as [TAI-PTB] at timescales of 19 years. Since the fractional stability of B1855+09 improves steadily with increased dataspan, we expect that as additional data on B1855+09 is acquired, this pulsar will easily beat [TAI-PTB] at ∼25 year timescales unless

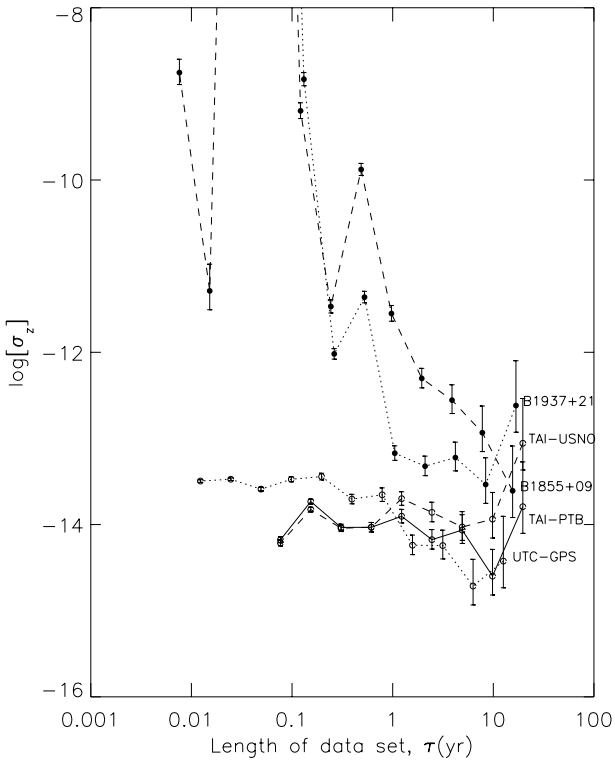


Fig. 7. Fractional Stability of 3 terrestrial timescales, and 2 MSPs.

TAI and PTB improve or the pulsar becomes less stable. Note that TAI is significantly better than USNO alone even though TAI is an aggregate that contains USNO, and similarly, for TT(BIPM) which contains TAI. It is also interesting to note that the PTA allows the possibility of ignoring the earth clock altogether; one degree of freedom in the PTA can be used to solve for time, i.e., PSR vs PSR.

7. Update on Timing Noise as a Function of Period Derivative

Pulsar astronomers have long wondered whether the noise they see in timing residual plots, such as we show in Figure 1 is due to intrinsic instability in the rotation of the pulsar, or is an error in the model, such as a missing planet or unmodeled DM variations. Arzoumanian et al. (1994) published a compendium of measurements of "timing noise" in a number of slow and millisecond pulsars, and suggested that there is a relationship between timing noise and $\dot{P}$, i.e., the larger the $\dot{P}$ the larger the timing noise. This implies first that the noise is intrinsic to the pulsar, and second that for each pulsar there is a minimum RMS in the residuals that no amount of accounting for systematics will lessen. This has obvious implications for the PTA, and our effort to achieve sub-μs RMSs on a collection of MSPs. The data presented here along with recently pub-

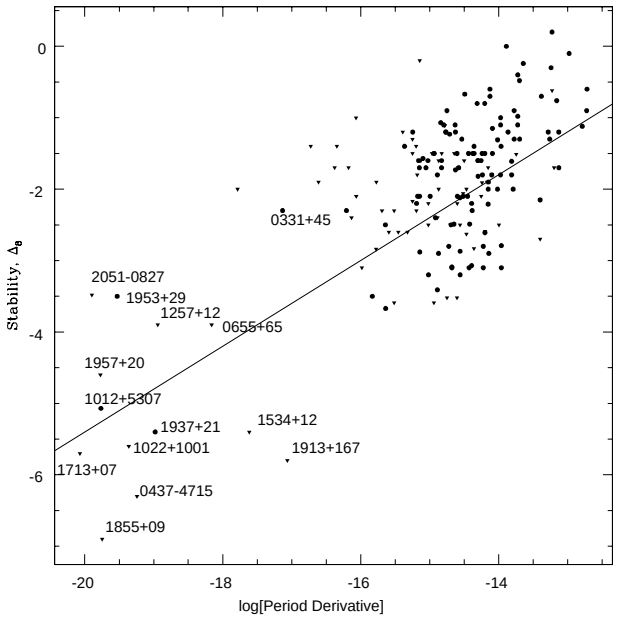


Fig. 8. The timing noise parameter, Δ_8, as a function of $\log \dot{P}$. Values used are courtesy of Zaven Arzoumanian, except those shown in Table 3, and 1957+20 (Arzoumanian, Fruchter, & Taylor, 1994), B1534+12 (Stairs et al, 1998).

lished results on MSPs allow us to update the picture of timing noise in MSPs as a function of period derivative. This was most recently done by Arzoumanian et al. (1994) who quantified the noisiness of a pulsar using the noise parameter, Δ_8, defined by

$$\Delta_8 = \log\left(\frac{1}{6\nu}|\ddot{\nu}|t^3\right),$$

where $t = 10^8$ s. Arzoumanian et al. (1994) quote the best fit result to the scatter plot

$$\Delta_8 = 6.6 + 0.6\log\dot{P}$$

which brought forth the rather depressing notion that we would never achieve better than 1 μs accuracy for the MSPs owing to the fact that $\dot{P}$ for the population is $\sim 10^{-20}$ or higher.

We are happy to report that some of the MSPs used to create the low $\dot{P}$ end of the spectrum have been determined to have lower Δ_8's than were presented in Arzoumanian et al. (1994). We present the new MSP data in Table 3 and the corresponding plot in Figure 8.

The value used for PSR B1937+21 is the best fit to $\ddot{\nu}$ letting all the parameters vary. Arzoumanian et al. (1994) were only able to place an upper limit on Δ_8 for PSR B1855+09 and so are we, but ours is significantly lower, -6.9, down from -6. This comes from the best-fit value of $\ddot{\nu}$ of $-8 \pm 4 \times 10^{-29}$, where the uncertainty quoted is that given by TEMPO. This is significantly smaller than the value previously obtained by KTR94, $\ddot{\nu} = -1.0 \pm 0.9 \times 10^{-27}$. The value for $\ddot{\nu}$ that we use to calculate Δ_8 is different from the value one obtains by only allowing $\ddot{\nu}$ to vary. With only 1 degree of freedom, the value is not an appropriate upper limit. For J1713+0747 the fit refines nicely to give $\ddot{\nu} = -2.6 \pm 0.2 \times 10^{-27}$.

PSR J0437-4715 was discovered by Johnston et al. (1993). This 5.8-ms pulsar is very bright and has been shown to be very good for timing. The RMS of the residuals, folded and averaged at the binary orbital period, is only 35 ns.

Since a third body was discovered around PSR B1257+12, a new upper limit on $\ddot{\nu} < -1.35 \times 10^{-25}$ has been published by Wolszczan et al. (2000). The value is an upper limit since Wolszczan suggests the distinct possibility of a fourth body. While these new measurements do not change the value of Δ_8 significantly from the value reported by Arzoumanian et al. (1994), it is now clear that the value represents an upper limit.

PSR B1534+12 has an updated $\ddot{\nu} < 6 \times 10^{-28}$ (I.Stairs, private communication) which yields $\Delta_8 < -5.4$.

PSR B1957+20 is possibly influenced by DM variations, and also by an instable orbital system, as shown by Applegate & Shaham (1994) and Arzoumanian, Fruchter, & Taylor (1994). On the basis of the relationship between DM and RMS DM shown by Backer et al. (1993) we would expect PSR B1957+20, with a DM of 29, to have an RMS DM of about 0.0002 cm^{-3}pc. We can calculate the expected influence of these DM variations on the estimation of $\ddot{\nu}$ which was done on single-frequency data at 430 MHz. A DM of 0.0002 cm^{-3}pc corresponds to a timing residual of 5 μs. A 5 μs trend over the course of the observations performed by Arzoumanian, Fruchter, & Taylor (1994) for example, could produce a false $\ddot{\nu}$ of $\sim 1 \times 10^{-25}$ given the 5-year observation length. This $\ddot{\nu}$ corresponds $\Delta_8 = -4.6$, which is the value attributed to B1957+20 by Arzoumanian et al. (1994). In other words, the timing noise measured by Arzoumanian et al. (1994) could be entirely due to unmodeled DM variations. We therefore make this point an upper limit and emphasize that the true value is probably much smaller.

It seems, then, that a significant fraction of MSPs fall below the line fitted by Arzoumanian et al. (1994). Either the relationship is not well described by a line, or the line has a steeper slope than was published. Either way, this bodes well for the PTA, which relies on submicrosecond accuracy in a handful of pulsars.

Figure 8 is somewhat misleading in that it makes the $\ddot{\nu}$ measured in B1937+21 look average. Many of the $\ddot{\nu}$'s measured are from single-frequency timing, so DM variations may be contributing to what we are calling 'timing noise.' There is, in fact, no MSP that displays such a convincing, significant $\ddot{\nu}$. We measure $\ddot{\nu}$ in B1937+21 to 4 significant digits, where as most other MSP measurements are upper limits or at best known to 20%. It is possible that B1937+21 is displaying noise whose source is internal to the neutron star crust. Alternatively, perhaps B1937+21

Table 3. Timing Noise Parameter vs $\ddot{\nu}$ for the MSPs for which they are available.

Pulsar	$\dot{P}$	$\ddot{\nu}$ (s^{-3})	Δ_8	Source
J0437+4715	5.72906(5)	$< 5 \times 10^{-28}$	<-6.3	vs[a]
J1012+5307	$1.7134(1) \times 10^{-20}$	$-9.8(2.1) \times 10^{-27}$	-5.1	la[b]
J1022+1001	$4.341(4) \times 10^{-20}$	$< 1 \times 10^{-27}$	<-5.6	kr[c]
B1257+12	$11.4223(7) \times 10^{-20}$	$< -1.35 \pm 0.04 \times 10^{-25}$	<-3.9	wz[d]
J1713+0747	8.54×10^{-19}	$< -2.6 \pm 0.1 \times 10^{-27}$ [c]	-5.6	tw[e]
B1855+09	1.78×10^{-18}	$1 \pm 6 \times 10^{-29}$	< -6.9	tw[f]
B1937+21	1.05×10^{-19}	$1.515 \pm 0.001 \times 10^{-26}$	-5.4	tw[f]
J2051-0827	$1.2737(5) \times 10^{-20}$	$< 2 \times 10^{-26}$	<-3.5	do[g]

[a] vs=van Straten et al. (2001) Although van Straten et al. (2001) did not calculate a limit $\ddot{\nu}$ we have estimated this quantity by taking the maximum deviation of their timing residuals (100 ns), converting this to a phase, and dividing by the cube of length of their data set, 3.4 y

[b] la=Lange et al. (2001)

[c] kr=Kramer et al. (1999) See note above[a]. We do the same for this pulsar using 50 μs and 1700 d.

[d] wz=Wolszczan et al. (2000)

[e] To calculate an upper limit we have allowed all the other parameters to vary along with $\ddot{\nu}$.

[f] tw=this work

[g] do=Doroshenko et al. (2001)

has a magnetic field structure that is evolving with a 20-y timescale, but we see such evolution at this magnitude in no other object. As an alternative we consider the possibility that B1937+21 is hosting a planet.

8. Planet Around PSR B1937+21?

The residuals shown in part (c) of Figure 1 are the result of a best-fit model α, δ, μ_α, μ_δ, P, and $\dot{P}$, and includes daily corrections for DM. One possible source of their cubic structure is the existence of a planet of binary period, $P_b = 17.6 \pm 0.2$ y which yields an orbital separation of 8 AU, using Kepler's Law with a central mass of 1.4 $M_\odot$. The residuals after including the planet in the model are shown in Figure 9. A$\sin i$ is $27.1 \pm 0.7\mu$s, yielding a companion mass of $0.08/\sin i$ $M_\oplus$, where i is the inclination of the orbit to the line of sight. If real, this planet would be the smallest known extrasolar planet besides the lunar-mass planet around PSR B1257+12 (Wolszczan et al., 2000). A planet of similar mass ($0.15/\sin i$ $M_\oplus$) has been found around PSR B1257+12 but is much closer to the pulsar (0.20 AU vs 8 AU) Wolszczan (1994).

The planetary model adds 3 free parameters to the standard fit, T_o, P_b, and A$\sin i$. We compare the goodness of this model to adding the three parameters, $\ddot{\nu}$, $\dddot{\nu}$, and $\ddot{\dddot{\nu}}$. The best-fit planetary model fits the data minutely better than the best $\ddot{\nu}$ through $\dddot{\nu}$ fit (RMS of 1.14 μs vs 1.18 μs). The best fit parameters are $\ddot{\nu} = 1.07(2) \times 10^{-26}\mathrm{s}^{-3}$, $\dddot{\nu} = 1.68(5) \times 10^{-34}\mathrm{s}^{-4}$, and $\ddot{\dddot{\nu}} = -1.42(3) \times 10^{-42}\mathrm{s}^{-5}$. We show in Figure 10 the χ^2 as a function of orbital period, and RMS as a function of orbital period, both of which show a minimum near 17 years, which is the length of our data set. The dotted line in both parts of the figure shows the value of the quantity when the fit to $\ddot{\nu}$ is turned on instead of the addition of the planet. Only ν, $\dot{\nu}$, T_0, and asin$i$ were allowed to vary in the fits. We did not allow α, δ, μ_α and μ_β to vary for consistency with the 2-step fitting process described for B1937+21 in §4.

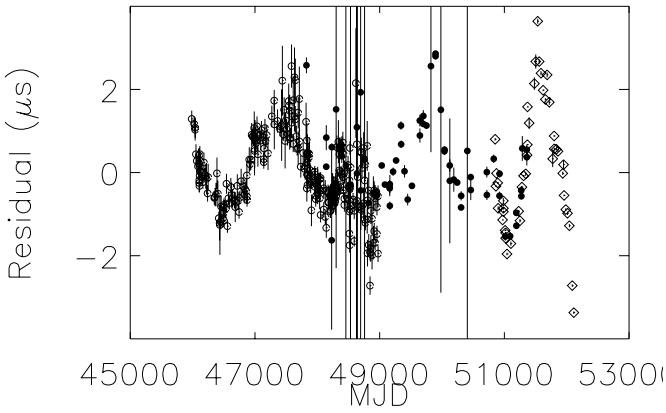


Fig. 9. PSR B1937+21 residuals after fit for a planet.

It is possible that the residuals you see in Figure 1 are the result of some intrinsic property of the pulsar (see §7). For years this pulsar was thought to have significant "timing noise" causing the phase to wander as it does (KTR94). We were concerned that there may always be a well in the figure of χ^2 vs P_b (e.g. Figure 10) where P_b is roughly equal to the length of the data set. We tested this possibility by doing the following. We simulated an extended data set, N years into the future, by assuming that $\ddot{\nu}$ is fixed. We then fit a planet to each data set and looked at the position of the well (in other words, the best-fit P_b) vs N. What we found was that a 'planet' will produce a constant $\ddot{\nu}$ up through the year 2020, which is

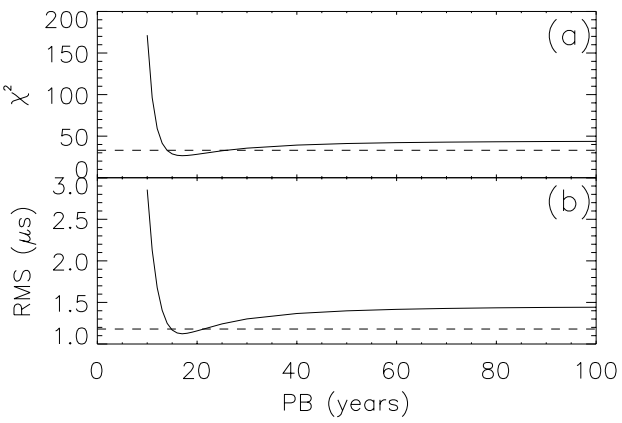


Fig. 10. (a)ξ^2 vs orbital period, and (b) RMS vs orbital period for the model using a planet around B1937+21. The dotted line shows the value of the quantity when $\ddot{\nu}$ is used instead.

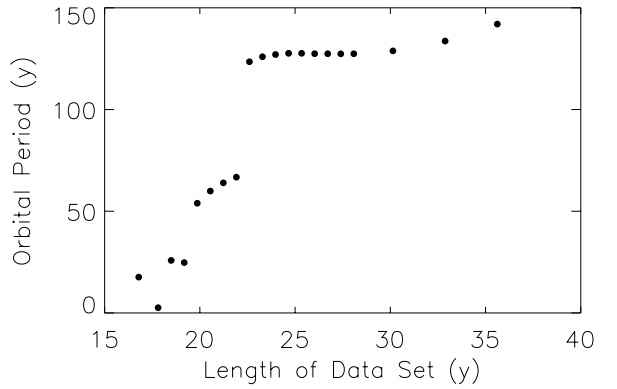


Fig. 11. Best-fit Planetary Orbital Period vs Length of Data Set for simulated extensions of PSR B1937+21 data, assuming a constant $\ddot{\nu}$.

as far as we tested. There is a correlation between orbital period and the length of the data set, as shown in Figure 11. Some of the fits are not stable, such as the point at data span=18 y which yields a 3-y period. Notice that in general, the best-fit planetary orbit is much longer than the data set. This is easily understood if you consider that the planetary model needs to imitate the $\ddot{\nu}$ and can do so by extracting a fraction of an orbit from a putative planet. The non-continuous jumps to a higher P_b shown in Figure 11 are doublings of the orbital period. The χ^2 and RMS for these simulated fits remains very similar to what we observe. We conclude that we could be fooled by a constant $\ddot{\nu}$ into supposing the presence of a planet. However, the previous section, §7, shows that the large and highly significant $\ddot{\nu}$ in B1937+21 is strange relative to the population of MSPs. The only thing that will resolve this is additional $\sim$ 10 years of data, assuming the orbit is about 20 years.

PSR B1937+21 is regarded as having too large a $\dot{P}$ for being a recycled pulsar, i.e. its large $\dot{P}$ alone implies it is a 'young' pulsar although it is generally regarded as old Backer et al. (1993). We wondered if perhaps the unknown existence of an orbiting planet could have been skewing the measurement of $\dot{P}$ since the discovery of the pulsar. In fact, it could not. Our best fit $\dot{P}$ without the planet, and without assuming a $\ddot{\nu}$ is slightly smaller, by 1 part in $\sim 10^6$ than our best fit $\dot{P}$ with the planet.

9. Implications of Planet on Possible Evolutionary Scenarios of PSR B1937+21

Millisecond pulsars are thought to be created in supernovae and spun up by accretion from a companion star during the red-giant phase of the companion. Forming planets around such objects is complex and is the subject of much debate (Wolszczan 1998 and references therein). In fact, finding planets, such as this one, in similar millisecond pulsars helps to solve the mystery in the creation of isolated millisecond pulsars. At the present, of the ~70 known millisecond pulsars, 9 are solitary systems, meaning the presence of a companion has not been detected. Given that we suspect these objects have been spun-up by a companion, this presents an inconsistency. However, if planets are somehow the remains of an ablated or otherwise significantly reduced companion, then we would expect to find similar planets around the other 8 known millisecond pulsars. A planet with a 17-y orbit or longer, as we describe would not have been found in any other system, simply by lack of dataspan.

10. Conclusion

We have demonstrated that connection of data sets with sub-μs accuracy across multiple telescopes and many years is possible and yields high precision results for pulsar model parameters. The new limit that our data place on the energy density in background gravitational radiation, $\frac{\rho}{\rho_c} = 2 \times 10^{-9} h^{-2}$, is below that yielded by the work of KTR94 by more than an order of magnitude.

The data suggest the existence of a small (< 1 $M_\oplus$) planet around B1937+21. The best-fit orbital period is currently 17.6 y but that may change with the addition of more data. We have ruled out the possibility that the cubic present in B1937+21's residuals are due to a GW that has geometrically escaped detection in both J1713+0747 and B1855+09. We also show that if the cubic is due to a $\ddot{\nu}$ intrinsic to the pulsar, that B1937+21 is unique. We find this alternative therefore unlikely.

References

Applegate, J. H., & Shaham, J. 1994, ApJ, 436, 312
Arzoumanian, Z., Fruchter, A. S., & Taylor, J. H. 1994, ApJ, 426, L85

Arzoumanian, Z., Nice, D. J., Taylor, J. H., & Thorsett, S. E. 1994, ApJ, 422, 671
Backer, D. C., Kulkarni, S. R., & Taylor, J. H. 1983, Nat, 301, 314
Backer, D. C., Hama, S., van Hook, S., & Foster, R. S. 1993, ApJ, 404, 636
Backer, D. C., Dexter, M. R., Zepka, A., Ng, D., Werthimer, D. J., Ray, P. S., & Foster, R. S. 1997, PASP, ,, 109, 61
Caldwell, R., Kamionkowski, M., & Wadley, L. 1998, Phys Rev, D59, 27101
Camilo, F., Thorsett, S. E., & Kulkarni, S. R. 1994, ApJ, 421, L15
Cordes, J. M., & Downs, G. S. 1985, ApJS, 59, 343
Deeter, J. E. 1984, ApJ, 281, 482
Deeter, J. E., & Boynton, P. E. 1982, ApJ, 261, 337
Doroshenko, O., Lohmer, O., Kramer, M., Jessner, A., Wielebinski, R., Lyne, A. G., & Lange, C. 2001, A&A, submitted
Downs, G. S., & Reichley, P. E. 1983, ApJS, 53, 169
Groth, E. J. 1975, ApJS, 29, 443
Hogan, C. 2000, Phys. Rev. D., 62, 121302
Jaffe, A., & Backer, D. C. 2002, submitted to ApJ
Johnston, S., Lorimer, D. R., Harrison, P. A., Bailes, M., Lyne, A. G., Bell, J. F., Kaspi, V. M., Manchester, R. N., D'Amico, N., & Nicastro, L. 1993, Nat, 361, 613
Kaspi, V. M., Taylor, J. H., & Ryba, M. F. 1994, ApJ, 428, 713
Kramer, M. 1994, A&AS, 107, 527
Kramer, M., Wielebinski, R., Jessner, A., Gil, J. A., & Seiradakis, J. H. 1994, A&AS, 107, 515
Kramer, M., Xilouris, K. M., Camilo, F., Nice, D. J., Backer, D. C., Lange, C., Lorimer, D. R., Doroshenko, O., & Sallmen, S. 1999, ApJ, 520, 324
Lange, C., Camilo, F., Wex, N., Kramer, M., Backer, D. C., Lyne, A. G., & Doroshenko, O. 2001, MNRAS, ,, 326, 274
Lommen, A. 2001, PhD Thesis, UC Berkeley
Lommen, A. N., & Backer, D. C. 2001, ApJ, 562, 297
Maggiore, M. 2000, Phys. Rep., 331, 283
Matsakis, D. N., Taylor, J. H., & Eubanks, T. M. 1997, A&A, 326, 924
McHugh, M. P., Zalamansky, G., Vernotte, F., & Lantz, E. 1996, Phys. Rev. D, 54, 5993
Phinney, E. 2001, MNRAS, submitted, astroph, 0108028
Rajagopal, M., & Romani, R. W. 1995, ApJ, 446, 543
Stairs, I. H., Arzoumanian, Z., Camilo, F., Lyne, A. G., Nice, D. J., Taylor, J. H., Thorsett, S. E., & Wolszczan, A. 1998, ApJ, 505, 352
Stinebring, D. R., Ryba, M. F., Taylor, J. H., & Romani, R. W. 1990, Physical Review Letters, 65, 285
Thorsett, S. E., & Dewey, R. J. 1996, Phys. Rev. D, 53, 3468
van Straten, W., Bailes, M., Britton, M., Kulkarni, S. R., Anderson, S. B., Manchester, R. N., & Sarkissian, J. 2001, Nat, 412, 158
Wolszczan, A. 1994, Science, 264, 538
Wolszczan, A. 1997, In ASSL Vol. 223: Visual Double Stars : Formation, Dynamics and Evolutionary Tracks, p. 221
Wolszczan, A., Hoffman, I. M., Konacki, M., Anderson, S. B., & Xilouris, K. M. 2000, ApJ, 540, L41

Proceedings of the 270. WE-Heraeus Seminar on: *"Neutron Stars, Pulsars and Supernova Remnants"*
Physikzentrum Bad Honnef, Germany, Jan. 21-25, 2002, eds. W. Becker, H.Lesch & J. Trümper, MPE Report 278, pp. 126-135

Non–linear Magnetic Field Decay in Neutron Stars – Theory and Observations

U. Geppert and M. Rheinhardt

Astrophysikalisches Institut Potsdam, An der Sternwarte 16, 14482 Potsdam, Germany

Abstract. There exists both theoretical and observational evidence that the magnetic field decay in neutron stars may proceed in a pronounced non–linear way, at least episodically. In the presence of a strong magnetic field the Hall–drift may dominate the field evolution in the crust and/or the superfluid core of neutron stars. Analysing observations of P and $\dot{P}$ for sufficiently old isolated pulsars we gain strong hints for a significantly non–linear magnetic field decay. Under certain conditions with respect to the geometry and strength of a large–scale magnetic background field an instability is shown to occur which rapidly rises small–scale magnetic field modes. Their growth rates increase with the background field strength and may reach $\sim 10^4$ of the ohmic decay rate. Consequences for the rotational and thermal evolution as well as for the cracking of the crust of neutron stars are discussed.

1. Introduction

There is still an ongoing scientific debate whether the magnetic fields of pulsars decay (see e.g. Regimbau and de Freitas Pacheco (2001) and references therein). Thus, the question whether this questionable decay proceeds in a non–linear way seems to be somewhat academic. However, the neutron star magnetic fields are the strongest known in the universe and already this very fact suggests the idea that, if there is a field evolution at all, it should be a non–linear one. As we will show, there exist both theoretical and observational evidences that the field decay may be in its essence a non–linear one, at least in certain regions of the star and during certain episodes of its life.

In order to be able to deal with well defined physical conditions we will consider here the evolution of sufficiently old isolated neutron stars (SOINSs). We characterize them by the following properties:

- the supernova fall–back accretion phase is finished and a stable density stratification $\rho(r)$ has been established;
- the rediffusion of the magnetic field has been completed;
- the rotation is slow enough so that the irradiation of gravitational waves does practically not contribute to the spin down;
- the appearance of glitches is less probable;
- the crust is almost completely crystallized;
- the temperature profile has become flat enough, to avert convection in the outermost thin liquid layer and in the core region and the occurrence of a thermoelectric instability in the crust;
- the electron relaxation time is already so large that the magnetization parameter may reach values large enough for considerable non–linear electron transport effects;
- the absence of accretion, as a consequence of isolation, ensures that there are neither external sources of angular momentum nor of heating;
- likewise there is a stable compactness ratio M/R and no screening of the magnetic field can happen.

All these constraints are met by the majority of neutron stars the age of which is $\gtrsim 10^5$ years. Therefore, if any magneto–thermal and rotational evolution of SOINSs is observed it *must* be caused with a high probability by an evolution of its magnetic field. Particularly, the dominance of non–linear effects is given for those stars even if the standard, i.e., the slowest cooling scenario is assumed.

Here, we intend to consider as the non–linearity of the field evolution the *Hall–effect* or *Hall–drift*, as it occurs in the crust (see e.g. Shalybkov and Urpin, 1997), i.e., both ambipolar diffusion and any convective motion of the neutron star matter is excluded.
The effect of the Hall–drift on the magnetic field evolution of isolated neutron stars has been considered by a number of authors (see e.g. Haensel, Urpin and Yakovlev 1990; Goldreich and Reisenegger 1992; Muslimov 1994; Naito and Kojima 1994; Shalybkov and Urpin 1995, 1997, ; Urpin and Shalybkov 1995, 1999, and Vainshtein et al. 2000). They discussed the redistribution of magnetic energy from an initially large–scale (e.g. dipolar) field into small–scale components via the Hall–term. Though the Hall–drift itself is a non–dissipative process, the changes in the field geometry and the tendency to redistribute the magnetic energy into small scales may in principle accel-

erate the field decay. However, the results presented in Naito and Kojima (1994), Shalybkov and Urpin (1997), Urpin and Shalybkov (1999), and Muslimov (1994) suggest the conclusion that the field decay is not modified drastically.

Goldreich and Reisenegger (1992) developed the idea of the *Hall–cascade*, i.e., when starting with a large–scale magnetic field that cascade will generate small–scale field components down to a scale-length $l_{\rm crit}$, where the ohmic dissipation begins to dominate the Hall–drift.

In some of the above–mentioned investigations numerical instabilities are reported if either the field structure becomes too complex (Urpin and Shalybkov, 1995) or the initial field is too strong (Naito and Kojima, 1994; Urpin and Shalybkov, 1999). Also, when considering the thermomagnetic field generation in the crust of young neutron stars (Wiebicke and Geppert, 1996), where small–scale modes are the first ones to be excited, numerical instabilities occurred caused exclusively by the Hall–drift.

Recently the authors (Rheinhardt and Geppert, 2002) showed that all the observed instabilities are in their essence very likely not of numerical origin but have physical reasons: A sufficiently strong and inhomogeneous large–scale background field is unstable with respect to small–scale perturbations, which rise very rapidly in comparison with the relevant ohmic decay time of the background field. This rapid transfer of energy from the background into small–scale field components proceeds *not* via a cascade but jumps across wide spectral distances. The unstable perturbations show small radial structures close to the neutron star's surface whereas their lateral structures are medium sized. Of course, this Hall–instability will act only during an episode of the field decay, which unavoidably leads to a zero field. This episode, however, may have observable consequences.

In the following we will present the theoretical and observational hints for the non–linear field decay in isolated neutron stars and than, after a description of the Hall–drift induced field instability, discuss their effect on observable quantities of the above introduced SOINSs.

2. Theoretical motivation

Under which conditions becomes the evolution of the magnetic field non–linear? In quasi–stationary approximation the field evolution is determined by Maxwell's equations

$$\dot{\boldsymbol{B}} = -c\,\mathrm{curl}\,\boldsymbol{E}\,, \quad \mathrm{div}\,\boldsymbol{B} = 0\,, \quad \boldsymbol{j} = \frac{c}{4\pi}\,\mathrm{curl}\,\boldsymbol{B} \qquad (1)$$

together with Ohm's law, which has in the absence of convective motions the form

$$\boldsymbol{E} = \hat{\sigma}^{-1}\boldsymbol{j} = \hat{R}\boldsymbol{j}\quad . \qquad (2)$$

In the presence of a magnetic field both the electric conductivity, $\hat{\sigma}$, and the resistivity, $\hat{R}$, become tensors whose components parallel and perpendicular to the magnetic field along with their Hall–component are represented by

$$\hat{\sigma} = \begin{pmatrix} \sigma_\perp & \sigma_H & 0 \\ -\sigma_H & \sigma_\perp & 0 \\ 0 & 0 & \sigma_\parallel \end{pmatrix} = \hat{R}^{-1} = \begin{pmatrix} R_\perp & R_H & 0 \\ -R_H & R_\perp & 0 \\ 0 & 0 & R_\parallel \end{pmatrix}^{-1}, \qquad (3)$$

if $\boldsymbol{B}$ goes along the $\boldsymbol{z}$–axis.

Let us consider the evolution of a magnetic field completely confined in the crust of the neutron star. There, the field could be generated either by convection in the outermost layers of the proto–neutron star or by a thermoelectric instability during the early period of the neutron star's life, when the temperature gradient in the liquid crust is extremely large (see e.g. Urpin et al., 1986 and Wiebicke and Geppert, 1996). A peculiarity of the transport processes in the crust is that the components of the resistivity tensor parallel and perpendicular to the magnetic field coincide, $R_\perp = R_\parallel$ (see Yakovlev and Shalybkov, 1991), because the electrons move as a degenerate gas through the crystal lattice of the crust. In relaxation time approximation they found

$$\sigma_\parallel = \sigma_0\,, \quad \sigma_\perp = \frac{\sigma_0}{1+(\omega_B\tau)^2}\,, \quad \sigma_H = \omega_B\tau\,\sigma_\perp, \qquad (4)$$

where $\omega_B = eB/m_e^*c$ is the Larmor frequency of the electrons, m_e^* their effective mass, and τ their relaxation time between two collisions with the phonons or impurities of the crustal lattice. The coincidence of the parallel and perpendicular components of the resistivity tensor in the crust implies

$$R_\parallel = R_\perp = \frac{\sigma_\perp}{\sigma_\perp^2+\sigma_H^2} = \sigma_0^{-1}\,, \quad R_H = \frac{\sigma_H}{\sigma_\perp^2+\sigma_H^2}. \qquad (5)$$

The scalar electric conductivity σ_0 as well as the relaxation time τ are complicated functions of the density $\rho(r)$, the temperature $T(r,t)$, the impurity concentration Q and of the chemical composition (charge number $Z(r)$ and mass number $A(r)$ (see e.g. Urpin and Yakovlev, 1980).

Ohm's law (2) together with Eq. (3) allows of representing the electric field by use of the unit vector of the magnetic field $\boldsymbol{b} = \boldsymbol{B}/|\boldsymbol{B}|$ as

$$\boldsymbol{E} = R_\parallel(\boldsymbol{b}\cdot\boldsymbol{j})\boldsymbol{b} + R_\perp(\boldsymbol{b}\times\boldsymbol{j})\times\boldsymbol{b} + R_H(\boldsymbol{j}\times\boldsymbol{b}), \qquad (6)$$

which yields because of $R_\perp = R_\parallel$

$$\boldsymbol{E} = R_\parallel\boldsymbol{j} + R_H\boldsymbol{j}\times\boldsymbol{b} = \sigma_0^{-1}\big(\boldsymbol{j} + \omega_B\tau(\boldsymbol{j}\times\boldsymbol{b})\big). \qquad (7)$$

Taking now the curl of $\boldsymbol{E}$ and using Ampere's law we arrive at the *Hall–induction equation* for the crystallized neutron star crust:

$$\dot{\boldsymbol{B}} = -\frac{c^2}{4\pi}\,\mathrm{curl}\left(\frac{1}{\sigma_0}\big(\,\mathrm{curl}\,\boldsymbol{B} + \omega_B\tau\,(\,\mathrm{curl}\,\boldsymbol{B} \quad \times\boldsymbol{b})\big)\right) \qquad (8)$$

which makes immediately clear that the field decay will proceed in a significantly non–linear manner as soon as

$$\frac{eB(r,t)}{m_e^*(r)c}\tau\big(\rho(r), T(r,t), Q, A(r), Z(r)\big) > 1\,, \qquad (9)$$

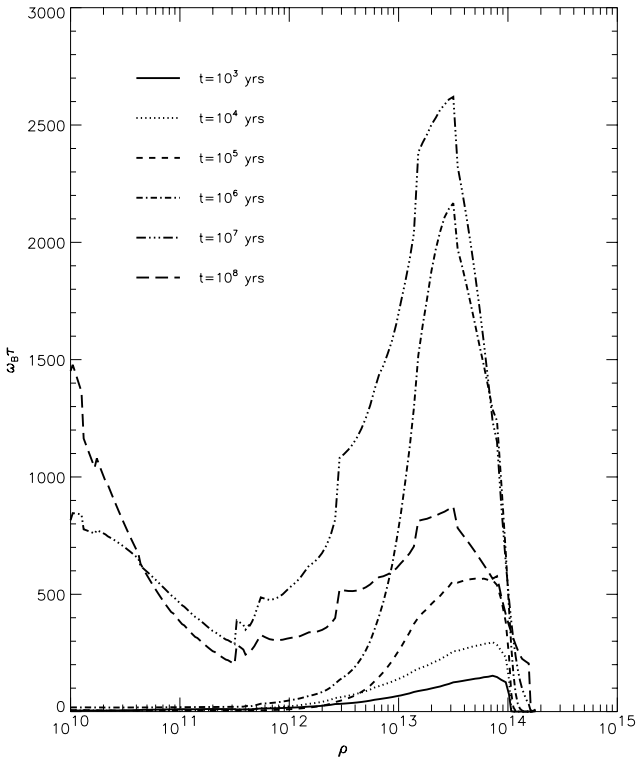


Fig. 1. The magnetization parameter $\omega_B\tau$ as a function of the density at different moments of neutron star's life.

i.e., the strength of the non–linearity depends not only on the field but on all the complex physical conditions in the crust!

In order to get an impression how the magnetization parameter $\omega_B\tau$ in the crust of an isolated neutron star evolves we present here results obtained by Page et al. (2000) for a neutron star whose state of matter in the core is described by a medium equation of state. The initial polar surface field strength is assumed to be 10^{13} G, the density up to which the field is initially penetrating is $\rho_0 = 10^{14}$g cm^{-3}; for the impurity concentration $Q = 0.01$ is supposed and the chemical composition of the crust should be that of cold catalyzed matter. Since the field decay as presented by Page et al. (2000) has been calculated just by neglecting the non–linear effects, i.e., considering only the linear ohmic decay, Fig. 1 does not present the "real" evolution of $\omega_B\tau$ because $\boldsymbol{B}(r,t)$ certainly evolves differently under the influence of a strong Hall drift. Nevertheless, these results may serve as a strong hint that the latter may play an important role for the magnetic field decay in neutron stars. When, e.g., $\omega_B\tau$ becomes as large as 1000, especially as a consequence of the star's cooling down due to which the electron relaxation time rises by orders of magnitude, a linear description of the field decay is surely no longer justified.

3. Observational motivation

The best known observational quantities of SOINSs are obtained when they appear as radiopulsars: their pulsation period $P = 2\pi/\Omega$ (Ω being the related rotational velocity), its time derivative $\dot{P}$ and, unfortunately only in a few cases, its second time derivative $\ddot{P}$. The spin–down behavior is to a high accuracy determined by

$$\dot{E}_{\rm rot} = I\Omega\dot{\Omega} \approx \dot{E}_{\rm mmr}, \tag{10}$$

i.e., the loss of rotational energy $E_{\rm rot} = I\Omega^2/2$ (I is the moment of inertia of the neutron star) is equal to the power of the magneto–multipole radiation $\dot{E}_{\rm mmr}$, irradiated away by the rotating magnetized neutron star, i.e., the radio pulsar. Here, the attenuation of the radiation by magnetospheric currents has been neglected. As already discussed above, for pulsars older than $\approx 10^5$ years, the spin–down as a consequence of the radiation of gravitational waves can surely be neglected, and the loss of angular momentum due to a relativistic wind of charged particles (caused by the pulsar mechanism) shows the same functional dependences on the neutron star radius R, the magnetic field and the rotational velocity as the magneto–multipole radiation (Shapiro and Teukolsky, 1983). Clearly, Eq. (10) is not valid during glitches.

According to Krolik (1991) the power of the magneto–multipole radiation is given by

$$\dot{E}_{\rm mmr} = \frac{c}{8\pi}\sum_{l,m} S_{lm}^{-2}\left[\frac{2^l l!}{(2l)!}\right]^2\left(\frac{mR\Omega}{c}\right)^{2(l+1)} R^2\langle|\boldsymbol{B}_{lm}|\rangle^2, \tag{11}$$

where $\langle|\boldsymbol{B}_{lm}|\rangle$ is the average of the multipole component of the magnetic field, defined by its multipolarity l and projection m, across the spherical surface. S_{lm} is a constant reflecting the geometry of $\boldsymbol{B}_{lm}$ (see Krolik, 1991). Since R and I are fixed for SOINSs, we have with Eqs. 10 and (11) an unambiguous relation between the observational quantities P and $\dot{P}$ and the magnetic field. In other words, once we could calculate all the multipole components of the magnetic field as functions of time and they would together with the exactly measured quantities $P(t)$ and $\dot{P}(t)$ satisfy Eq. (10), we had understood the field decay. However, as a consequence of the sum occurring in Eq. (11) it is impossible to infer from $P(t)$ and $\dot{P}(t)$ all the $\langle|\boldsymbol{B}_{lm}|\rangle$ in an unambiguous way. Therefore, we consider here only one term of the sum to be responsible for the spin–down and denote the corresponding $\langle|\boldsymbol{B}_{lm}|\rangle$ simply by B. (Usually, the dipolar term, $l = m = 1$, is chosen.) Then, by equating Eq. (10) with Eq. (11), the change of the neutron star's rotation can be written as

$$\dot{\Omega} = -K\Omega^n \tag{12}$$

where the constant K comprises the geometrical constant S_{lm} as well as radius and moment of inertia. The exponent n is called the "*braking index*", where $n = 2l + 1 = 3$ for a pure rotating dipole. The standard way to calculate the

braking index is to take the time derivative of Eq. (12) resulting in

$$n = \frac{\ddot{\Omega}\Omega}{\dot{\Omega}^2} = 2 - \frac{\ddot{P}P}{\dot{P}^2} \,. \tag{13}$$

However, $\ddot{\Omega}$ (or $\ddot{P}$) can be obtained with sufficient accuracy for a few young pulsars only.

Johnston and Galloway (1999) suggested an alternative way to calculate n without employing $\ddot{P}$. By direct integration of Eq. (12) over a time interval $T \gg P$

$$\int_{\Omega_1}^{\Omega_2} \frac{\mathrm{d}\Omega}{\Omega^n} = -K \int_t^{t+T} \mathrm{d}t' \tag{14}$$

they calculate the braking index by

$$n = 1 + \frac{\Omega_1\dot{\Omega}_2 - \Omega_2\dot{\Omega}_1}{\dot{\Omega}_1\dot{\Omega}_2 T} \,, \tag{15}$$

i.e., knowing the rotational period and its time derivative of two observations, separated by T, they are able to obtain the braking index without needing $\ddot{P}$. For the Crab pulsar and B 1509–58 they found a good coincidence of the values of n obtained with both methods. Thus, there exists a certain warranty that the application to other radio pulsars will yield reliable results, too. In their Table 1 Johnston and Galloway (1999) present the braking index n, calculated according to Eq. (15) along with P and $\dot{P}$ for 20 pulsars. Six of them have negative braking indices which possibly could be understood as due to the occurrence of glitches during the observational periods. The eight pulsars with the smallest error bars for n (B0540+23, B0611+22, B0656+14, B0740–28, B1915+13, B2002+31, B2148+52 and B2334+61) have all positive braking indices, five of them with $n > 20$. Because of their similar braking indices B0919+06, B1221-63 and B1907+10 may belong to that group too, but their error bars are much larger. Two further pulsars, B0154+61 and B1356-60, with $n > 3$ have unacceptably large error bars. All of them have an active age $\tau_a = P/2\dot{P}$ between $4.13 \cdot 10^4$(B2334+61) and $1.7 \cdot 10^6$ (B1907+10) years, i.e., are just at the range of ages, the SOINSs should be.

A supposition basic for both methods to calculate the braking index is that the coefficient K in Eq. (12), by virtue of Eq. (11) proportional to B^2, is really a constant. Now let us relax that assumption in so far as we will allow for a varying field while the other quantities entering K remain constant, in agreement with our concept of SOINSs. Than we can rewrite Eq. (12) into

$$\dot{P} = \mathcal{K} B^2(t) P^{-n+2} \,, \tag{16}$$

where for a standard neutron star ($R = 10^6$cm, $I = 10^{45}$gcm^2) the constant $\mathcal{K} \approx 10^{-39}$ cm s^{3}g^{-1} if $n = 3$. Nevertheless, we will assume in the following that the rotational evolution is still quite well described by a power–law similar to Eq. (12), where, of course, the quantities K and n have to be replaced by modified ones:

$$\dot{\Omega} = -\hat{K}\Omega^{\hat{n}} \,. \tag{17}$$

The description of the rotational behaviour by a power law seems to be sufficiently precise as long as the time T (see Eq. (15)) is small in comparison with the characteristic time of the magnetic field evolution. Of course, a final justification for that assumption can only be obtained for each individual pulsar by considering its actual time series of P and $\dot{P}$. Re–evaluating now Eq. (13) with n replaced by $\hat{n}$ we find with $\ddot{P} = \mathcal{K} B P^{-n+1} \left(2\dot{B}P \; - \; (n-2)B\dot{P}\right)$ the up or down scaling of n to the "observed" $\hat{n}$ to be proportional to the time derivative of the magnetic field:

$$\hat{n} = n - 2\frac{\dot{B}P}{B\dot{P}} = n - 2\frac{\tau_P}{\tau_B} \,. \tag{18}$$

Here we introduced τ_P and τ_B as characteristic times of the rotational period and the magnetic field, respectively. How should this equation be interpreted? In case there is no magnetic field decay, that is $\dot{B} = 0$, pulsars with $n < 3$ are not understandable in the framework of the magneto–multipole radiation model, because the neutron star will certainly be not a rotating monopole (though possibly with small higher multipole contributions). In case we assume that the spin–down is completely due to magneto–*dipole* radiation, an assumption perhaps not completely wrong for SOINSs, we have $n = 3$ and $\hat{n} < 3$ indicates an increasing field while $\hat{n} > 3$ is the signature of a decaying field. The interpretation of $\hat{n} < 3$ as caused by an increasing field is supported by the fact, that such braking indices are observed especially for very young pulsars (Lyne et al. 1996), in which both rediffusion of a field submerged during the supernova fallback (Geppert et al., 1999) and/or thermoelectric field generation may still proceed. Alternatively, deviations of $\hat{n}$ from its classical value 3, even values of either sign up to 10^6, can be understood as due to internal frictional instabilities occurring between the crust and the superfluid (Shibazaki and Hirano, 1995; Shibazaki and Mochizaki, 1995; Kundt, 200110). Also processes in the magnetosphere may cause values of $\hat{n}$ different from 3.

Here, however, we intend to investigate, whether the observed relatively large $\hat{n}$ may indicate a *non–linear field decay*. For that purpose let us consider as a typical example B0740-28, found in Table 1 of Johnston and Galloway (1999), with $\hat{n} \approx 26$. From its observed $P = 0.167$s, $\dot{P} = 1.68 \cdot 10^{-14}$ we can infer a dipolar surface magnetic field strength $B_\mathrm{d} = 6.4 \cdot 10^{19}\sqrt{P\dot{P}} \approx 3.4 \cdot 10^{12}$ G which is more or less standard for such "middle aged" radio pulsars. Using the standard formula for the active age $\tau_a = P/2\dot{P}$ we find $\tau_a \approx 1.6 \cdot 10^5$ years, but this relies on the assumption that the rotational evolution follows all the time the power law (17) with $\hat{n} = 3$. Of course, this τ_a is at best an upper limit for the star's age, since we just argue in favour of an $\hat{n} > 3$ during some (unknown) period of the rotational evolution still lasting. On the other hand a much shorter active age is unlike because none but one of the mentioned pulsars is reported to be associated with a

PSR	P [s]	$\dot{P}$ [10^{-14}]	$\hat{n}$	τ_a [10^5 yrs]	B_d [10^{12}G]	$\dot{B}_\mathrm{d}$ [10^8G/yr]
0540+23	0.246	1.531	12	2.55	3.93	0.35
0611+22	0.334	5.921	20	0.89	9.00	4.28
0656+14	0.385	5.507	15	1.11	9.32	2.52
0740−28	0.167	1.687	26	1.57	3.40	1.25
0919+06	0.431	1.375	29	4.97	4.93	0.65
1221−63	0.216	0.493	19	6.94	2.09	0.12
1907+10	0.284	0.265	24	17.6	1.75	0.05
1915+13	0.195	0.724	36	4.28	2.40	0.46
2002+31	2.128	7.562	23	4.46	25.7	2.88
2148+52	0.332	1.005	50	5.24	3.70	0.83
2334+61	0.495	19.02	9	0.41	19.6	7.13

Table 1. SOINSs supposed to be in the phase of non–linear magnetic field decay. Rotational period P and its time derivative $\dot{P}$ are taken from Table 1 of Johnston and Galloway (1999), $\hat{n}$ is the rounded mean value given there. The active age, polar dipole field strength and field decay rate are calculated as described in Sect. 3.

supernova remnant. The only exception, B2334+61, with $\tau_a = 4.1 \cdot 10^4$ yrs, is associated with the fairly old SNR G114.3+0.3 (see e.g.Becker et al. 1996; thus the active age seems to be a sound estimate of the real age.

If we exclude the possibility of magnetic field decay we have for our example B0740-28 $\hat{n}=n\approx 26$, i.e., the neutron star magnetic field structure must, because of $l \approx 12$, be that of a 2^{12}–pole. This implies, considering Eq. (11), that the surface magnetic field strength of such a field must be many orders of magnitudes stronger than that of a dipolar field which could explain the observed spin–down. Therefore, the assumption of a constant magnetic field seems not to be very likely. If we instead assume that the spin–down is caused by magneto–dipole radiation, that is $n = 3$, we can easily estimate the rate of the magnetic field decay. Rearranging Eq. (18) and inserting the observed or inferred values for $P, \dot{P}$ and B_d we find

$$\dot{B}_\mathrm{d} = (n-\hat{n})\frac{B_\mathrm{d}\dot{P}}{2P} \approx 4\mathrm{G/s} \approx 1.25 \cdot 10^8 \mathrm{G/yr}\,. \quad (19)$$

This rate of the dipolar–field decay should now be compared with the typical ohmic decay rate of a crustal magnetic field in such middle–aged neutron stars. The ohmic decay time of a crust of thickness $L = 10^5$cm and an averaged electric conductivity $\sigma_0 = 10^{27}\mathrm{s}^{-1}$ is

$$t_\mathrm{ohm} = \frac{4\pi\sigma_0 L^2}{c^2} \approx 4.4 \cdot 10^9 \mathrm{yrs}, \quad (20)$$

providing an upper bound for the real field decay times. By use of the above estimated $B_\mathrm{d} = 3.4 \cdot 10^{12}$ G we can now compare

$$\dot{B}_\mathrm{d} = 1.25 \cdot 10^8 \mathrm{G/yr} \gg \frac{B_\mathrm{d}}{t_\mathrm{ohm}} \approx 7.7 \cdot 10^2 \mathrm{G/yr}. \quad (21)$$

This comparison is robust, i.e., even if we somewhat overestimated L or σ_0 (which, because of the unknown impurity concentration, could indeed also be underestimated),

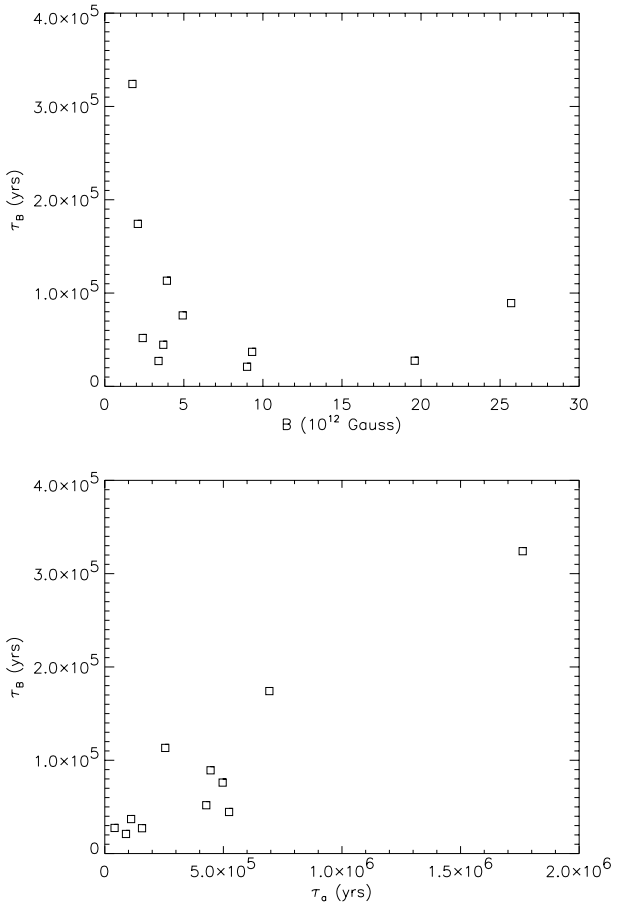


Fig. 2. Characteristic time of the magnetic field, τ_B, over the magnetic field B itself (upper panel) and over the active age τ_a (lower panel) for the SOINSs given in Table 1.

the magnetic field decay proceeds obviously much faster than would be predicted for a (linear) ohmic decay. What has been demonstrated here for a single example proves to be valid for the complete selection of SOINSs specified above, see Table 1.

As demonstrated in Sect. 2 the only possible modification of the ohmic decay in the context of our model is due to the Hall–drift. *That is, any significant acceleration of the magnetic field decay is explainable then and only then, if the Hall drift can be shown to cause time scales of the field evolution significantly smaller then the ohmic one.*

In order to visualize the clear signs of non–linear field decay for the selected SOINSs we present in the upper panel of Fig. 2 the correlation of the characteristic time of the magnetic field τ_B with the magnetic field B_d itself. Bearing in mind, that eleven objects form only a very small statistical ensemble, there nevertheless seems to exist a pronounced trend indicating non–linearity of the field decay: Evidently, $\tau_B = B_\mathrm{d}/\dot{B}_\mathrm{d}$ falls significantly with increasing B_d which is compatible with the idea that the stronger the field the faster proceeds the redistribution of

energy into smaller modes by the Hall–drift and, consequently, the faster the energy is drained from the dipolar field mode. In addition, we show in the lower panel of Fig. 2 the correlation of τ_B with the active age τ_a suggesting the conclusion that the acceleration of the field decay by the Hall–drift acts only temporarily. This makes sense because this effect of course destroys its own basis, namely the dominance of the Hall–drift over the ohmic decay.

In the following chapter we will present an instability which proceeds on time–scales much smaller than the ohmic scale.

4. A Hall–drift induced magnetic field instability

4.1. Hints for the occurrence of an instability

Now, let us return to Eq. (8) which together with $\operatorname{div}\boldsymbol{B} = 0$ and appropriate boundary conditions determines the magnetic field evolution in the crust of isolated neutron stars. As already mentioned in the introduction, this equation has been considered in the context of neutron star physics by a number of authors. It is generally accepted that the non–linear Hall–term causes a re–distribution of magnetic energy, when it is at a certain "initial" state stored in the mode characterized by the largest spatial scale, say a dipolar field mode. Goldreich and Reisenegger (1992) coined the term *Hall–cascade* for that process by stressing an analogy to the vorticity equation for an incompressible fluid. As they noted, this analogy is incomplete at least as far as one curl operator has to be replaced by its inverse, which makes the conclusions about the Kolmogoroff spectrum questionable.

Attempts performed by the present authors to solve the non–linear Eq. (8) in a full sphere assuming a constant density profile reproduced the results of Shalybkov and Urpin (1997) for moderate values of the magnetization parameter $\omega_B\tau$. Starting with a dipolar field modes of smaller scales were excited and helicoidal waves were observed. But, as soon as $\omega_B\tau$ exceeded a certain value, typically about 100, the spectral resolution, attainable by the numerical code was no longer sufficient to ensure convergence. This motivated us to search for possible physical reasons for that apparent numerical instability .

For simplicity we assume the conductive properties of the matter to be constant in space and time, that is, we assume constant σ and τ_e/m_e^*. Thus, Eq. (8) can be rewritten in dimensionless variables such that it no longer contains any parameter and the evolution of the magnetic field is solely determined by its initial configuration $\boldsymbol{B}(\boldsymbol{x},0)$. For that purpose we normalize the spatial coordinates by a characteristic length L of the model (e.g., the neutron star's radius or the thickness of its crust), the time by the ohmic decay time $4\pi\sigma L^2/c^2$ and the magnetic field by $B_N = m_e^* c/e\tau_e$. The governing equations in these dimensionless variables read

$$\dot{\boldsymbol{B}} = \Delta\boldsymbol{B} - \operatorname{curl}(\operatorname{curl}\boldsymbol{B}\times\boldsymbol{B})\ ,\quad \operatorname{div}\boldsymbol{B} = 0\ , \qquad (22)$$

where the differential operations have to be performed with respect to the now dimensionless spatial and time coordinates x, y, z and τ, respectively.

Let us first have a look onto energetics. Using standard arguments one can immediately state that in the absence of currents at infinity the total energy of any solution of Eq. (22) is bound to decrease monotonically to zero since the Hall–term $\operatorname{curl}\boldsymbol{B}\times\boldsymbol{B}$ is unable to deliver energy (nor to consume it). That is, all these solutions are asymptotically stable in a strict mathematical sense following Lyapunov's definition of stability. However, this applies also to a lot of slowly time varying processes for which nevertheless the transient occurrence of instabilities is a generally accepted idea (e.g., the temporary convection in a cooling liquid). Therefore, it seems reasonable to adopt as a criterion of instability the following: Define a steady reference (equilibrium) state in the spirit of the usual stability analysis to be a snapshot of the transient process. If the analysis detects growing, that is, unstable perturbations with a time increment large enough in comparison with the time decrement of the transient process under consideration the latter may be accounted unstable in a short enough period of time around the instant of the snapshot.

Of course, when adopting this concept a necessary condition for the occurrence of an instability is as well the existence of terms in the linearized equation which are potentially able to deliver energy to the perturbations. Linearization of Eq. (22) about the *background field* $\boldsymbol{B}_0$ yields

$$\begin{aligned}\dot{\boldsymbol{b}} &= \Delta\boldsymbol{b} - \operatorname{curl}(\operatorname{curl}\boldsymbol{B}_0\times\boldsymbol{b} + \operatorname{curl}\boldsymbol{b}\times\boldsymbol{B}_0)\\ \operatorname{div}\boldsymbol{b} &= 0\end{aligned} \qquad (23)$$

describing the behavior of small perturbations $\boldsymbol{b}$ of the reference state $\boldsymbol{B}_0$.

Indeed, here along with the energy–conserving term $\operatorname{curl}\boldsymbol{b}\times\boldsymbol{B}_0$ now as a second Hall–term $\operatorname{curl}\boldsymbol{B}_0\times\boldsymbol{b}$ occurs which may well deliver or consume energy (from/to $\boldsymbol{b}$!) since in general the integral $\int_V(\operatorname{curl}\boldsymbol{B}_0\times\boldsymbol{b})\cdot\operatorname{curl}\boldsymbol{b}\,dV$ will not vanish. Of course, this is due to the fact that the linearized equation describes the behavior of only a part of the total magnetic field. Actually, perturbations may grow only on expense of the energy stored in the background field.

Considering Eq. (23), we can determine a scale below which the ohmic dissipation dominates the Hall–drift. Estimating $|\operatorname{curl}\boldsymbol{B}_0|$ and $|\operatorname{curl}\boldsymbol{b}|$ by $\bar{B}_0$ and $\bar{b}/l$, respectively, we find the critical scale of $\boldsymbol{b}$ to be $l_{\rm crit} \lesssim 1/\bar{B}_0$, which is de–normalized $l_{\rm crit} \lesssim L/(\omega_{\bar{B}_0}\tau_e)$, identical with the expression derived by Goldreich and Reisenegger (1992) considering the Hall–cascade in analogy with the turbulent flow of an incompressible fluid.

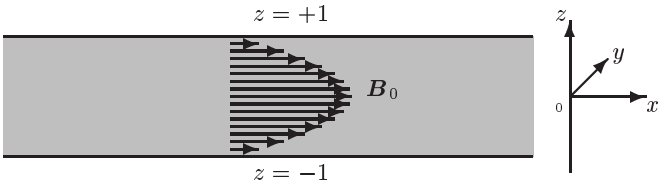


Fig. 3. Sketch of the model and background field geometry. In $z < -1$ a perfect conductor, in $z > 1$ vacuum is assumed.

4.2. Analogy with the $\boldsymbol{\Omega} - (\boldsymbol{\omega} \times \boldsymbol{j})$–dynamo

A strong support for the idea of a Hall–drift induced magnetic field instability is provided by the analogy of the linearized Hall–induction equation (23) to the mean–field induction equation including the so–called $(\boldsymbol{\omega} \times \boldsymbol{j})$–effect found by Rädler (1969).

$$\dot{\bar{\boldsymbol{B}}} = \Delta\, \bar{\boldsymbol{B}} - \operatorname{curl}\left(-\boldsymbol{u}_\Omega \times \bar{\boldsymbol{B}} + \operatorname{curl} \bar{\boldsymbol{B}} \times \boldsymbol{\omega} \right). \quad (24)$$

Here, $\bar{\boldsymbol{B}}$ is the averaged magnetic field, $\boldsymbol{u}_\Omega$ describes a (large–scale) differential rotation and $\boldsymbol{\omega}$ is a turbulence–related coefficient, which reflects the offset of the isotropy of the turbulence by Coriolis forces. Eq. (24) has been proved to allow for a magnetic instability (dynamo; see Rädler, 1969).

Comparing Eq. (23) with Eq. (24) when letting correspond $\boldsymbol{b}$ to $\bar{\boldsymbol{B}}$ it becomes clear, that $\operatorname{curl} \boldsymbol{B}_0$ (then corresponding to $-\boldsymbol{u}_\Omega$) must not be a constant, since $-\boldsymbol{u}_\Omega$ is a shear velocity. This implies that not all second derivatives of $\boldsymbol{B}_0$ with respect to the spatial co–ordinates may vanish. It should be noted that the analogy lacks completeness only insofar that the dynamo acts even with a constant $\boldsymbol{\omega}$. Note that $\boldsymbol{\omega}$ enters the term which is energy conserving.

4.3. Mathematical treatment

Let us now specify the geometry of our model and the background field. We consider a slab which is infinitely extended both into the x– and y–directions but has a finite thickness $2L$ in z–direction.

The background field $\boldsymbol{B}_0$ is assumed to be everywhere parallel to the surface of the slab pointing, say, in x–direction and to depend on the z–coordinate only, i.e., $\boldsymbol{B}_0 = f(z)\boldsymbol{e}_x$ ($\boldsymbol{e}_x$ being the unit vector in x–direction). Note, that by this choice $\operatorname{curl} \boldsymbol{B}_0 \times \boldsymbol{B}_0$ represents a gradient. Thus, the unperturbed evolution of the background field is not at all affected by the Hall–drift; in the absence of an e.m.f. it would decay purely ohmically!

Further on we decompose a perturbation $\boldsymbol{b}$ into its poloidal and a toroidal components, $\boldsymbol{b} = \boldsymbol{b}_p + \boldsymbol{b}_t$, which can be represented by scalar functions S and T, respectively, by virtue of the definitions

$$\boldsymbol{b}_p = -\operatorname{curl}\left(\boldsymbol{e}_z \times \nabla S \right) \;,\; \boldsymbol{b}_t = -\boldsymbol{e}_z \times \nabla T\,, \quad (25)$$

ensuring $\operatorname{div} \boldsymbol{b} = 0$ for arbitrary S, T.

For the sake of simplicity we will confine ourselves to the study of plane wave solutions with respect to the x– and y–directions, thus making the ansatz

$$\left\{ \begin{matrix} S \\ T \end{matrix} \right\} (\boldsymbol{x}, \tau) = \left\{ \begin{matrix} s \\ t \end{matrix} \right\} (z) \exp\left(i\tilde{\boldsymbol{k}}\tilde{\boldsymbol{x}} + p\tau \right) \;, \quad (26)$$

where $\tilde{\boldsymbol{k}} = (k_x, k_y) \neq \boldsymbol{0}$, $\tilde{\boldsymbol{x}} = (x, y)$ and p is a complex time increment. This ansatz guarantees as well the uniqueness of the poloidal–toroidal decomposition since from $\overset{\Delta}{@!@!@!@!}(S, T) = 0$ it follows $(S, T) = 0$ with $\overset{\Delta}{@!@!@!@!}$ being the two–dimensional lateral Laplacian (see Bräuer and Rädler, 1988). With Eq. (26) we obtain from Eq. (23) two coupled ordinary differential equations

$$\begin{aligned} pt - t'' + \tilde{k}^2 t &= ik_x f(s'' - \tilde{k}^2 s) - ik_x f'' s \\ ps - s'' + \tilde{k}^2 s - ik_y f' s &= -ik_x f t\,, \end{aligned} \quad (27)$$

where dashes denote derivatives with respect to z. Together with appropriate boundary conditions Eqs. (27) define an eigenvalue problem with respect to p.

Having in mind that the neutron star's crust is neighboured upon the superconducting core on the one and a region with very low conductivity on the other side we choose the following simplified boundary conditions: Outside the star we assume vacuum, that is, $\operatorname{curl} \boldsymbol{B} = \boldsymbol{0}$ above the slab. Because of the finite conductivity inside the slab we require continuity of all components of $\boldsymbol{B}$ across this boundary. Considering the crust–core boundary an electric field must be prevented from penetrating into the perfectly conducting region below the slab, $z < -1$, that is, the normal magnetic and tangential electric field components must vanish. In terms of the scalars s and t this means $[s] = [s'] = t = 0$ for the vacuum boundary and $s = t' = 0$ for the perfect conductor boundary where $[.]$ denotes the jump across a boundary. Note, that for $t' = 0$ to be valid the vanishing of $\boldsymbol{B}_0$ at the perfect conductor boundary is required. Making use of the vacuum solution for the upper halfspace, $z \geq 1$, vanishing at infinity, the vacuum boundary condition for s can be expressed as $s' = -\tilde{k}s$ at $z = 1$, with $\tilde{k} = |\tilde{\boldsymbol{k}}|$.

Finally we specify the background field profile: Guided by the conditions under which the above discussed $\boldsymbol{\Omega} - (\boldsymbol{\omega} \times \boldsymbol{j})$–dynamo may work we conclude that $f(z)$ has to be at least quadratic in z. Taking into account the boundary conditions we choose $f(z) = B_0(1 + z)(1 - z^2)$. Hence, the magnitude of B_0 is the only free parameter of the eigenvalue problem.

4.4. Numerical results

For certain ranges of the wave numbers k_x, k_y and for $B_0 \gtrsim 3$ we found eigenvalues p with a positive real part, i.e., exponentially growing perturbations. The dependence of the growth rate $\Re(p)$ on the wave numbers for $B_0 = 1000$ is shown in Fig. 1.

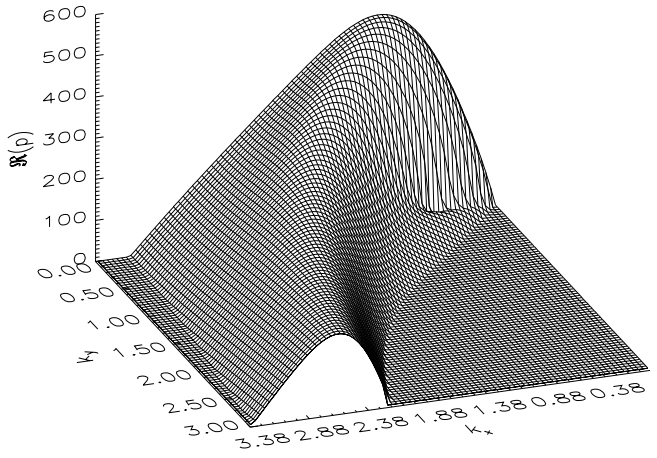


Fig. 4. Growth rate as a function of k_x and k_y for $B_0 = 1000$. Negative values were set to zero.

Figure 2 shows the dependence of growth rate and wave number k_x of the fastest growing mode on B_0. An interesting feature is, that the maximum growth rates occur for all B_0 considered at $k_y = 0$. Of course this asymmetry is due to the choice of the background field: once it was chosen parallel to the y–direction the maximum growth rates would occur at $k_x = 0$. Note that the most unstable eigenmodes are always non–oscillatory, though oscillating unstable ones exist.

Evidently, for each B_0 above a certain threshold (say, $B_0 = 50$) there exists a range of wave numbers within which the obtained growth rates are in agreement with the constraint, formulated above: In comparison with the background field decay the growth of the most unstable perturbations is a fast process; thus we may consider it as "episodically unstable".

With respect to the asymptotic behavior $\sigma \to \infty$ for a fixed (unnormalized!) background field one has to note that the time increment p is normalized on the ohmic decay rate ($\propto \sigma^{-1}$). From Fig. 2 it can be inferred $\Re(p) \propto B_0^q$, $q < 1$ for $B_0 \geq 100$, which means that in the limit of negligible dissipation the growth rate in physical units tends to zero.

Figure 5 shows the eigensolutions $(s,t)(z)$ of the fastest growing mode for three different values of B_0. One can observe that with increasing B_0 the toroidal field becomes more and more small–scale and concentrated towards the vacuum boundary. In contrast, the corresponding poloidal field remains large–scale. The magnetic field structure of the fastest growing mode for $B_0 = 2000$ is shown in Fig. 6. Assuming a ratio of crust thickness and neutron star radius R equal to 0.1 the shown lateral period of that mode fits ≈ 20 times into the circumference of the star.

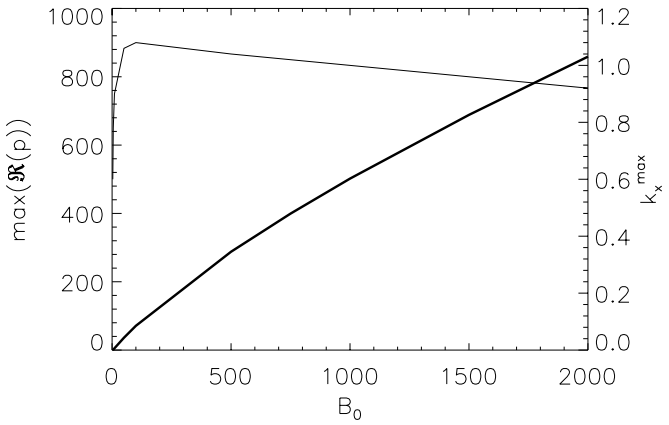


Fig. 5. Growth rate and wave number $k_x^{\max}$ of the fastest growing mode as functions of B_0. Thick and thin lines correspond to growth rates and $k_x^{\max}$, respectively.

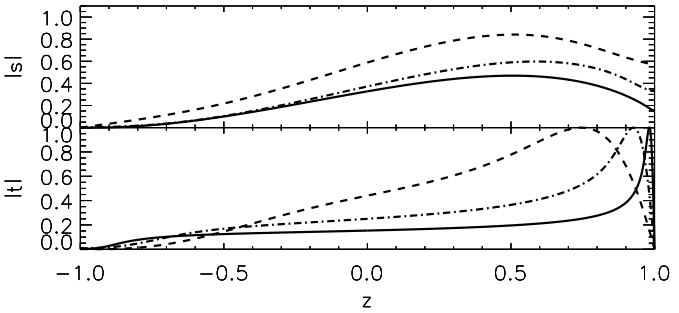


Fig. 6. Moduli of $(s,t)(z)$ of the fastest growing mode. Solid, dash–dotted and dashed lines refer to $B_0 = 2000$, $B_0 = 100$ and $B_0 = 10$, respectively.

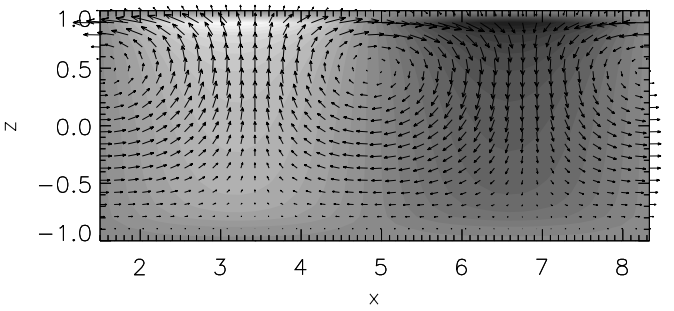


Fig. 7. Field structure of the fastest growing mode for $B_0 = 2000$. Arrows: $b_{x,z}$, grey shading: value of b_y, dark — into, light — out of the plane.

5. Discussion and Conclusions

Clearly, any assignment of the results gained by help of a very simplified model to neutron stars has to be done with great care. Even when accepting the plane layer as a reasonable approximation of the crust one has to concede

that the very specific profile of $\boldsymbol{B}_0$ assumed above may only exemplify the crustal field's structure.

An acceptable approximation of the radial profile of a dipolar crustal field as given e.g. in Page et al. (2000) will in general have to allow for non–zero values at the boundaries which cause more complicated boundary conditions. Moreover, the strong dependence of the conductive properties on the radial co–ordinate should anyway be taken into account.

To get an impression of possible consequences for the evolution of neutron stars we now simply assume, that the real $\boldsymbol{B}$–profile is sufficiently "curved" (i.e., its second derivative is big enough) and associate the parameter B_0 with a typical value of the field.

Assuming further electric conductivity and chemical composition to be constant, $\sigma = 5 \times 10^{26}\mathrm{s}^{-1}$ and the relative atomic weight $A/Z = 25$, respectively, we find the normalization field at a density $\rho = 10^{14}\mathrm{g\ cm}^{-3}$ to be 7×10^{10}G (see e.g. Page et al., 2000). That is, for typical (inner) crustal magnetic fields ranging between 7×10^{12}G and 1.4×10^{14}G we find a B_0 between 100 and 2000 and the e–folding time of the most rapidly growing unstable mode to be 0.0035 and 0.0003 times the ohmic decay time, respectively. Note, that the assumption about B_0 may well be in agreement with the surface field data given in Table 1. Hence, an initial perturbation will quickly evolve to a level at which the linear analysis is no longer feasible, that is, at which it starts to drain a remarkable amount of energy out of the background field.

We want to emphasize again that a sufficient curvature of the background field profile is a necessary condition for the occurrence of an unstable behavior. Therefore neither the derivation of the well–known helicoidal waves (whistlers) nor its modification presented in Vainshtein et al. (2000) could reveal it because a homogeneous background field was used there.

With even more care we may speculate about possible observational consequences. For SOINSs, the small–scale field modes initially generated or existing in the crust have already been decayed and the magnetic field is concentrated almost completely in the large–scale, say, dipolar mode. Simultaneously, in the process of cooling the coefficient $m_e^* c/e\tau_e$, i.e., the normalization field B_N, becomes smaller and smaller until the Hall term in Eq. (22) dominates the linear ohmic term. From that moment the Hall–instability may rise small–scale perturbations down to scale lengths $\gtrsim l_{\mathrm{crit}}$ on expense of the dipolar mode. This may lead to a spin–down behaviour of SOINSs as discussed in Sect. 3.

Another possible observational consequence follows from the dissipative effects of the rapidly excited small–scale field modes, that is, enhanced Joule heating. As can be seen in the upper panel of Fig. 7, the growing perturbations cause heat sources located close to the surface of the crust which, in turn, may produce a patchy neutron star surface. Note, that in Fig. 7 only the linear part of the heat source distribution is depicted, since the non–linear part $(\mathrm{curl}\,\boldsymbol{b})^2/\sigma_0$ has to be dropped in the linear analysis. These heat sources are concentrated in a very thin layer comprising only less than 5 % of the crustal thickness. Clearly, conclusions about the observability of that hot spots are impossible to be drawn from our simple model, since to infer the temperature distribution from the heat sources demands the knowledge of the absolute perturbation amplitudes. Anyway, we expect the neutron star's surface to be warmer during the episode of the Hall–instability than standard cooling calculations predict.

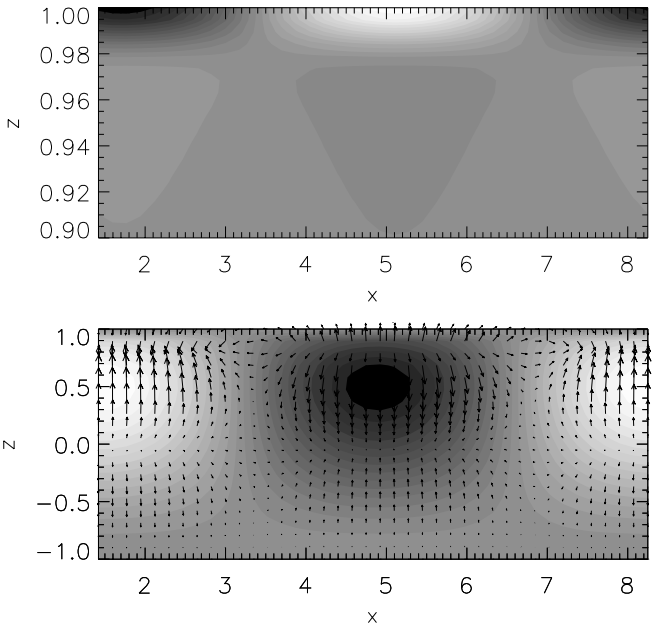


Fig. 8. Heat source density perturbation $2\boldsymbol{B}_0 \cdot \mathrm{curl}\,\boldsymbol{b}/\sigma_0$ (upper panel) and Lorentz force density perturbation $(\mathrm{curl}\,\boldsymbol{B}_0 \times \boldsymbol{b} + \mathrm{curl}\,\boldsymbol{b} \times \boldsymbol{B}_0)/4\pi$ (lower panel) of the fastest growing mode for $B_0 = 2000$ in arbitrary units. Upper panel: dark and light shading denotes cooling and heating by the perturbation, respectively; note the stretched z–scale. Lower panel: arrows denote x– and z–force components, grey shading the value of the y–component (dark — into, light — out of the plane).

Third, strong small–scale field components cause small–scale Lorentz forces. The lower panel of Fig. 7 shows that the maximum of the Lorentz force density perturbation is concentrated in deeper regions of the crust (at about 25 % of the thickness). From their pattern one may infer shear, both in y– and z– directions, to be the prevailing type of deformation. Thompson and Duncan (1995) discussed a scenario in which the helicoidal waves, being a consequence of the Hall drift, ignite high energetic bursts by cracking the crust. From our results we can hope that the unstable modes of the Hall instability act even more efficiently than the at best undamped, but never growing helicoidal waves.

However, all the questions connected with the actual influences of the presented instability on spin–down, cool-

ing and crust–cracking can be decided only by performing non–linear calculations in a realistic spherical–shell geometry taking into account a realistic density profile and chemical composition of the crust.

Acknowledgements. We gratefully acknowledge the support by the Heraeus foundation.

References

Becker W., Brazier,K., and Trümper, J., 1996, Astron. Astrophys. 306, 464
Bräuer, H.–J. and Rädler, K.–H., 1988, Astron. Nachr. 309, 1
Geppert, U., Page, D., and Zannias, T., 1999, Astron. Astrophys. 345, 847
Goldreich, P. and Reisenegger, A., 1992, Astrophys. J. 395, 250
Haensel, P., Urpin, V., and Yakovlev, D., 1990, Astron. Astrophys. 229, 133
Johnston, S. and Galloway, D., 1999, Mon. Not. R. Astron. Soc. 306, L50
Krolik, J., 1991, Astrophys. J. 373, L69
Kundt, W., 2001, Bull. Astr. Soc. India 29, 283
Lyne, A., Pritchard, R., Graham–Smith, F., and Camilo, F., 1996, Nature 381, 497
Muslimov, A.G., 1994, Mon. Not. R. Astron. Soc. 267, 523
Naito, T. and Kojima, Y., 1994, Mon. Not. R. Astron. Soc. 266, 597
Page D., Geppert U., and Zannias T., 2000, Astron. Astrophys. 360, 1052
Rädler, K.–H., 1969, Monatsber. Dt. Akad. Wiss. 11, 194
Regimbau, T. and de Freitas Pacheco, J. A., 2001, Astron. Astrophys. 374, 182
Rheinhardt, M. and Geppert, U., 2002, Phys. Rev. Lett. 88, 101103
Shalybkov, D. and Urpin, V., 1995, Mon. Not. R. Astron. Soc. 273, 643
Shalybkov, D. and Urpin, V., 1997, Astron. Astrophys. 321, 685
Shapiro, S. and Teukolsky, S., 1983, Black Holes, White Dwarfs and Neutron Stars (New York: John Wiley & Sons)
Shibazaki, N. and Hirano, S., in: 17th Texas Symposium. Annals of New York Academy of Sciences 759, 295
Shibazaki, N. and Mochizuki, Y., 1995, Astrophys. J. 438, 288
Thompson, C. and Duncan, R., 1995, Astrophys. J. 473, 322
Urpin, V. and Yakovlev, D., 1980, Sov. Astron. 24, 425
Urpin, V., Levshakov, S., and Yakovlev, D., 1986, Mon. Not. R. Astron. Soc. 219, 703
Urpin, V. and Shalybkov D., 1995, Mon. Not. R. Astron. Soc. 294, 117
Urpin, V. and Shalybkov D., 1999, Mon. Not. R. Astron. Soc. 304, 451
Vainshtein S., Chitre S., and Olinto A., 2000, Phys. Rev. E 61, 4422
Wiebicke, H.–J. and Geppert, U., 1996, Astron. Astrophys. 309, 203
Yakovlev, D. and Shalybkov D., 1991, Astrophys. Space Sc. 176, 191

Proceedings of the 270. WE-Heraeus Seminar on: *"Neutron Stars, Pulsars and Supernova Remnants"*
Physikzentrum Bad Honnef, Germany, Jan. 21-25, 2002, eds. W. Becker, H.Lesch & J. Trümper, MPE Report 278, pp. 136-141

A wind model for high energy pulses

J. G. Kirk[1], O. Skjæraasen[1], and Y. A. Gallant[2]

[1] Max-Planck-Institut für Kernphysik, Postfach 10 39 80, 69029 Heidelberg, Germany
[2] Service d'Astrophysique, CEA-Saclay, F–91191 Gif-sur-Yvette, France

Abstract. A solution to the σ problem — that of finding a mechanism capable of converting Poynting energy flux to particle-borne energy flux in a pulsar wind — was proposed several years ago by Coroniti and Michel who considered a particular prescription for magnetic reconnection in a striped wind. This prescription was later shown to be ineffective. In this paper, we discuss the basic microphysics of the reconnection process and conclude that a more rapid prescription is permissible. Assuming dissipation to set in at some distance outside the light-cylinder, we compute the resulting radiation signature and find that the synchrotron emission of heated particles appears periodic, in general showing both a pulse and an interpulse. The predicted spacing of these agrees well with observation in the case of the Crab and Vela pulsars. Using parameters appropriate for the Crab pulsar — magnetization parameter at the light cylinder $\sigma_{\rm L} = 6 \times 10^4$, Lorentz factor $\Gamma = 250$ — reasonable agreement is found with the observed total pulsed luminosity. This suggest that the high-energy pulses from young pulsars originate not in the co-rotating magnetosphere within the light cylinder (as in all other models) but from the radially directed wind well outside it.

Key words: Pulsars: general – pulsars: Crab – MHD – radiation mechanisms: non-thermal

1. Introduction

Recently, the non-axisymmetric "striped pulsar wind" investigated by Coroniti (1990) and Michel (1994) has been reexamined (Kirk & Lyubarsky 2001). A striped wind is a structure similar to a Parker spiral, which is produced by the outward radial advection of magnetic field lines whose foot points are anchored on the surface of the rotating neutron star. However, if the field lines originate from the poles of an obliquely rotating dipole, there exists a region around the equatorial plane where the polarity of the field at a fixed radius reverses at the rotation period of the star, producing stripes of alternating magnetic field direction. Magnetic energy is dissipated into particle energy if reconnection occurs at the stripe boundaries. Coroniti (1990) proposed that this kind of dissipation proceeds at a rate sufficient to maintain the thickness of the current sheet approximately equal to the gyro radius of the heated particles. Michel (1994) used essentially the same criterion, phrased in terms of the velocity of the current carriers. These early papers concluded that observations of the Crab Nebula, which indicate conversion of Poynting flux to particle-borne energy flux within $10^9 r_{\rm L}$, (where $r_{\rm L}$ is the radius of the light cylinder) could be explained by this mechanism. However, Lyubarsky & Kirk (2001) point out that reconnection is accompanied by acceleration of the wind. Both processes occur on the same timescale when the Coroniti/Michel prescription is used for reconnection. This is also the timescale on which the plasma expands. As a result, time dilation in the accelerated flow has to be taken into account and the dissipation rate is significantly reduced — in the case of the Crab, conversion of Poynting flux to particle-borne energy flux is not achieved until roughly $10^{12} r_{\rm L}$, which is too slow to account for the observations (the so-called σ-problem; see Melatos (1998) and references therein).

In Sect. 2 we discuss the physics of the dissipation process and the prescriptions used to model it. We conclude that it may proceed much more rapidly than suggested by Coroniti and Michel. If rapid reconnection in fact occurs, it will be accompanied by radiation losses (Melatos 1998) that may give rise to an observable signature. In this paper, and in an accompanying letter (Kirk et al. 2002) we adopt this hypothesis. We assume that dissipation is triggered at a surface $r = r_0$ well outside the light cylinder in the supersonic MHD wind of a pulsar and takes place rapidly, so that the plasma does not have time to expand significantly. Using two simple models of the electron distribution we show (i) that for parameters thought typical of the winds from young pulsars (e.g., the Crab) the predicted emission is pulsed, with, in general, a pulse and interpulse that are not symmetrically spaced in phase and (ii) that the predicted synchrotron luminosity in the pulses agrees to order of magnitude with that observed from the high energy emission of the Crab pulsar.

Our calculations suggest that the high energy pulses emitted by young pulsars originate as synchrotron emis-

sion in the pulsar wind, far outside the light cylinder. This is in marked contrast with conventional models of high-energy pulse production at an inner or outer gap — for a review see Harding (2001) — and also with magnetospheric synchrotron based models Machabeli et al (2000), Crusius-Wätzel et al. (2001). The current sheet just beyond the region of closed field lines in the magnetosphere has also been proposed as the source of high energy radiation from the Crab pulsar (Lyubarsky1996). But, in common with the others, this model relies for pulse production on the co-rotation with the star of a beam of radiation emitted from within the light cylinder.

2. Dissipation in the current sheet

An equilibrium solution of the Maxwell-Vlasov equations describing a magnetic reversal across a current sheet was found many years ago (Harris 1962) and was subsequently generalized to apply also to the case of relativistic particle temperatures and drift speeds (Hoh 1968). If, in the special case in which the plasma is composed solely of positrons and electrons the magnetic field strength far from the sheet is B', the central density of particles of each charge is N' and the sheet width is a, (all measured in the frame of reference in which the sheet is stationary and the electrons and positrons have equal and opposite drift speeds) then the temperature T, which is independent of position in the sheet, is given by

$$T = \frac{B'^2}{16\pi N'} \tag{1}$$

The Debye radius is

$$\lambda_{\rm D} = \left(\frac{T}{4\pi N' e^2}\right)^{1/2} \tag{2}$$

and is, to within a factor of the order of unity, equal to the gyro radius of a particle of energy T in the magnetic field B'. The speed $\pm c\beta$ with which each component drifts is also independent of position in the sheet and is obtained from

$$\beta = \frac{\lambda_{\rm D}}{a} \tag{3}$$

The magnetic field reverses across the sheet and the density goes to zero far from the sheet — simple explicit expressions for these quantities as functions of position are available.

This solution is well-known to be unstable to the excitation of a variety of waves — see, for example, Daughton (1999). The standard scenario is that the current sheet first filaments because of the growth of the tearing mode, producing magnetic islands separated by neutral lines. These then lead to magnetic reconnection and its associated dissipation (Melrose 1986). This scenario has largely been developed in the context of the geomagnetic tail of the Earth. Particle-in-cell simulations appear to confirm its validity ([Zhu & Winglee 1996; Pritchett et al. 1996), although the 3-dimensional picture is more complicated (Büchner & Kuska 1999; Hesse et al. 2001).

The key question in the application to pulsar winds is that of how quickly and, therefore, whereabouts in the wind the dissipation occurs. The linear growth rate $\gamma_{\rm t}$ of the tearing instability has been calculated in the relativistic case by Zelenyi & Krasnosel'skikh (1979). For $T \gg mc^2$ they find for the most unstable mode, which has a wavelength approximately equal to the sheet thickness,

$$\gamma_{\rm t} = \beta^{3/2} c/a = \lambda_{\rm D}^{3/2} c/a^{5/2} \tag{4}$$

The magnetic field far from the sheet and the total number of particles per unit area of sheet ($\approx aN'$) suffice to determine the drift speed. A single additional parameter is then needed to fix the sheet properties. This can be chosen, for example, as the thickness a or the temperature T; the thinner (cooler) the sheet, the faster the tearing mode grows.

In his model of the high-energy emission from pulsars, Lyubarsky (1996) argues that the rate of dissipation is controlled by the timescale associated with the growth of the tearing mode. Specifically, he assumes that magnetic flux is swept into the sheet and annihilated at a speed given by $a\gamma_{\rm t}$. This scenario is plausible, although it is not certain that the field dissipation, which presumably occurs at null points created during the field filamentation, proceeds on the timescale of the tearing mode growth. If it operates, it results in strong radiation from the innermost parts of the sheet. The geometry of the flow in this region is, however, uncertain.

Another, simpler, prescription for the speed of dissipation was (implicitly) adopted by both Coroniti (1990) and Michel (1994) and, later, also by Lyubarsky & Kirk (2001). In terms of the magnetic field and the number of particles per unit area in the sheet, the drift speed can be written

$$\beta = \frac{B'}{8\pi a N' e} \tag{5}$$

If the wind expands radially without any dissipation ($a =$ constant), then its speed remains constant so that $B' \propto r^{-1}$ and $N' \propto r^{-2}$. Equation (5) then implies that the drift speed β grows linearly with radius. At a radius where, according to this equation, $\beta > 1$, no equilibrium of the Harris type can exist; the Coroniti/Michel prescription consists in assuming that the sheet thickness grows at a rate just sufficient to avoid this happening. Dissipation

is thus assumed to maintain the current sheet very close to an equilibrium in which $\beta \approx 1$. This enables reconnection to be incorporated straightforwardly into a set of MHD equations describing the pulsar wind. Provided the sheet does not radiate significantly, conservation of energy, momentum and particle number, together with Eq. (3) in which β is set to unity, determine the dynamics of the wind. However, in this case dissipation proceeds on a time scale corresponding to the length r, which is the same scale on which adiabatic expansion of the sheet operates. A careful analysis of the dynamics shows that the wind accelerates and, as a result, the dissipation becomes rather ineffective (Lyubarsky & Kirk 2001).

On the other hand, an instability in the current sheet can communicate itself to the rest of the pulsar wind at the speed of the fast magnetosonic wave, which, for a cold plasma is roughly equal to the Alfvén speed. Recent investigations of reconnection in a relativistic pair plasma (Zenitani & Hoshino 2001) indeed indicate that the relevant timescale is related to the crossing time of a magnetosonic wave. In the case of a transsonic pulsar wind, a magnetosonic wavefront could appear almost stationary in the frame of the observer, so that dissipation could be completed within a few pulsar periods. This is the prescription we adopt in this paper. Energy is assumed to be released in the current sheet at a fixed radius, the position of which is taken as a free parameter. After energy release, we assume the plasma cools slowly as the wind moves radially outwards.

3. Geometry of the emission region

Any radial, relativistic flow containing a periodic modulation of the emissivity is likely to appear pulsed to an observer because of two effects. Firstly, the strong Doppler boosting of approaching parts of the flow means that only a small cone of the flow is visible, propagating within an angle of roughly $1/\Gamma$ with respect to the line of sight, where $\Gamma = (1-\beta^2)^{-1/2}$ is the Lorentz factor and $c\beta$ the radial speed. The spread in arrival times at the observer of photons emitted at the same radius but at different parts within this cone is roughly $r/(c\Gamma^2)$. Secondly, if emission is restricted to a range Δr in radius, the fact that the photons move only slightly faster than the flow when seen in the laboratory frame means that the spread in arrival times is roughly $\Delta r/(c\Gamma^2)$. For a wind modulated at the period $P = 2\pi r_{\rm L}/c$ of a rotating star, the approximate condition for the observation of pulsed emission is therefore

$$\Delta r,\ r \lesssim \Gamma^2 r_{\rm L} \qquad (6)$$

If this is fulfilled, the observed pulse shapes appear similar to the pattern of modulation of the flow. In particular, for a flow containing the corrugated spiral current sheet of an oblique rotator (Fig. 1), there should in general be

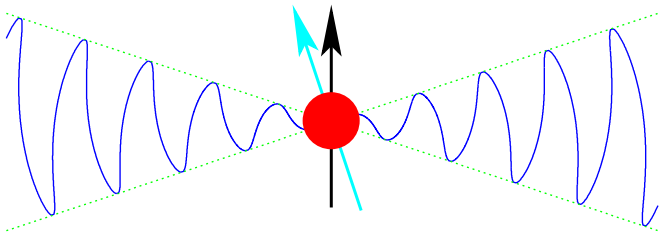


Fig. 1. A meridional section of the current sheet of an oblique rotator with a radial wind. The thin lines limiting the extent of the sheet in latitude depict the plane of the magnetic equator when the magnetic axis lies in the plane of the section.

two components (pulse and interpulse) which are symmetrically placed if the pulsar is viewed from the equatorial plane, but are asymmetrical when viewed from higher latitudes. Denoting by α the angle between the rotation axis and the magnetic axis, and by ζ the angle between the rotation axis and the viewing direction, these pulses appear only for $90^{\rm o} - \alpha < \zeta < 90^{\rm o} + \alpha$.

To improve on the estimate (6) and calculate the expected pulse shapes we adopt the following model of the volume emissivity ϵ of the wind:

(i) The emission region is located on the current sheet in the super-magnetosonic MHD wind of a rotating neutron star with an oblique, split-monopole magnetic field.
(ii) The dependence on frequency ν of the volume emissivity is a power-law: $\epsilon \propto \nu^{-a}$.
(iii) The emission switches on abruptly as plasma in the sheet crosses the surface $r = r_0$. Thereafter the volume emissivity decays as a power law in radius: $\epsilon \propto r^{-2-q}$.

Outside the light cylinder, assumption (i) should be a good approximation, independent of the actual configuration of the magnetic field close to the pulsar surface. The assumption that emission occurs only at the exact position of the current sheet is an idealization — in reality, the entire flow may be modulated, making the observed pulse more complex. In this case, our computations provide the Greens function with which the pattern is to be folded to find the observed pulse shape. In the ultra-relativistic limit, a simple wind solution is available (Bogovalov 1999) in which the velocity is radial and constant and the magnetic field is almost toroidal. The thin current sheet in such a wind is described by the equation

$$\begin{aligned} r &= r_{\rm s}(\theta,\phi,t) \\ &= \beta r_{\rm L}\left[\pm \arccos\left(-\cot\alpha\cot\theta\right) + ct/r_{\rm L} - \phi + 2n\pi\right] \end{aligned} \qquad (7)$$

(Kirk & Lyubarsky 2001), where (r,θ,ϕ) are polar coordinates, t is the observer-frame time and n is an integer.

Assumption (ii) is an idealization that ensures the pulse shape is independent of frequency. In reality, the

electron distribution may exhibit breaks and cut-offs, which will be translated into different pulse shapes at different frequencies. Our assumption, however, ensures that all parts of the flow can contribute to the emission at a given frequency, making it harder to obtain sharply defined pulses.

The dependence of the observed flux F on t, α and the direction of observation $\hat{\boldsymbol{n}}$ is:

$$F \propto \int_{-\infty}^{+\infty} \mathrm{d}t' \int_{r_0}^{\infty} \mathrm{d}r \int_{90^\circ-\alpha}^{90^\circ+\alpha} \mathrm{d}\theta \int_0^{2\pi} \mathrm{d}\phi \; r^{-q} D^{2+a} \delta\left[r - r_\mathrm{s}(\theta,\phi,t')\right] \delta\left(t' - t + \hat{\boldsymbol{n}}\cdot\boldsymbol{r}/c\right) \qquad (8)$$

where $D = 1/(1-\beta\hat{\boldsymbol{r}}\cdot\hat{\boldsymbol{n}})$ is the conventionally defined Doppler factor, apart from a (constant) factor of Γ. Choosing $a = 0$ and $q = 3$, which is appropriate for the synchrotron radiation of a fixed number of particles that undergo predominantly adiabatic losses in the expanding plasma, we present sample pulses for various Lorentz factors in Fig. 2. For the higher Lorentz factors this figure also displays the effect of a faster fall-off of the emissivity towards higher radii ($q = 6$), mimicking the effect of an accelerating wind. The asymmetry in time of the pulses is produced by our assumption of a sudden switching on of the emission and is reduced by a more rapid switching off. The parameters of this figure have been chosen to correspond to the Crab Pulsar. The radio emission of this object is complex, but is known to display 'core emission' in the radio precursor (Rankin (1990), which strongly suggests that the magnetic axis passes within a few degrees of the line of sight. This indicates that the inclination angle α of the magnetic axis to the rotation axis roughly equals the angle ζ between the rotation axis and the line of sight. The latter is determined by X-ray and optical observations of the 'torus' (Aschenbach & Brinkmann 1975; Hester et al. 1995) to be 60°. In Fig. 2 the emission has been assumed to switch-on at $r_0 = 30r_\mathrm{L}$ and pulses appear for $\Gamma > 5$, in rough agreement with the estimate (6). At higher Lorentz factors, the pulses sharpen. From Eq. (7) it can be seen that the emission splits naturally into two contributions, corresponding to different signs of the term $\arccos(-\cot\alpha\cot\theta)$. In the first two plots of Fig. 2 these contributions are plotted separately as dotted lines. Although the detailed pulse shapes will depend on the structure of the reconnecting sheets in the Crab wind, as well as the details of the switching on mechanism and the amount of acceleration of the wind, the separation of the two peaks is not sensitive to these unknowns, being determined by the location of the sheets. This separation in phase equals $\arccos(\cot\alpha\cot\zeta)/180^\circ$, corresponding to 0.39 for the Crab Pulsar, in good agreement with observation (e.g., Kanbach (1998)).

In the case of the Vela pulsar, conflicting interpretations of the polarization sweep and the X-ray morphology

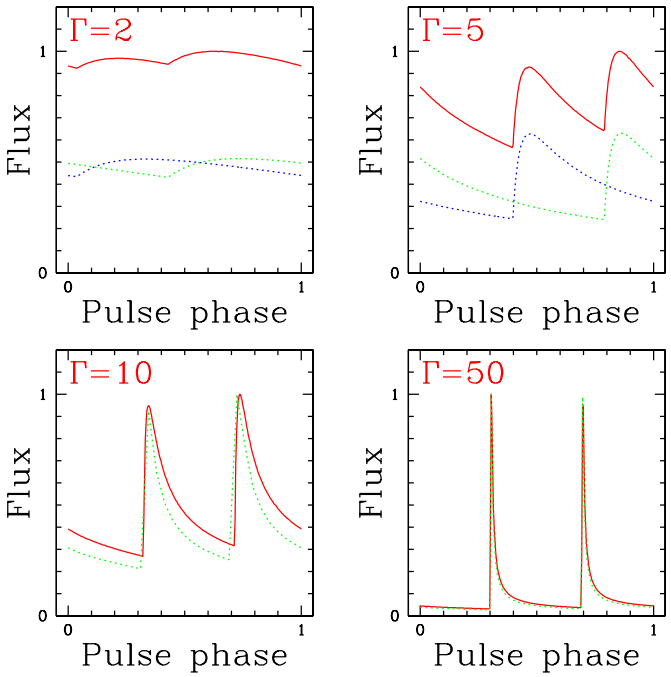


Fig. 2. Pulse shapes obtained by a numerical integration of Eq. (8). Four values of the Lorentz factor (Γ) are shown, the remaining parameters are: $\alpha = 60^\circ$, $\zeta = 60^\circ$, $r_0 = 30r_\mathrm{L}$, $a = 0$ and $q = 3$ (see text). The total emission is shown as a solid line. For $\Gamma = 2$ and 4, the contributions of the current sheets of different polarity are shown as dotted lines. For $\Gamma = 10$ and 50, the dotted line shows the effect of a more rapid fading of the emissivity to larger radius ($q = 6$).

have yielded $\alpha \approx 71^\circ$, $\zeta \approx 65^\circ$ in one case (Radhakrishnan & Deshpande 2001) and $\alpha \approx \zeta = 53^\circ$ in the other (Helfand et al. 2001). These imply separations of the gamma-ray (sub-)pulses of 0.45 and 0.31 of a period respectively, so that the observed spacing of 0.4 marginally favors the former interpretation.

4. Luminosity estimates

Electrons heated in the current sheets will enter the surrounding magnetic field and emit synchrotron radiation. A rough estimate of the power radiated can be found by assuming a monoenergetic electron population of Lorentz factor γ ($\gg 1$) and requiring pressure equilibrium between the hot plasma and the surrounding magnetic field. Taking the single particle synchrotron emissivity to be a delta function in frequency, the luminosity at frequency ν into a solid angle Ω is given by

$$\frac{\mathrm{d}L}{\mathrm{d}\nu\mathrm{d}\Omega} \approx \int_{r_0}^{\infty} \mathrm{d}r\, r^2 \Delta\Gamma n'_\mathrm{h} P_\mathrm{s.p.} \delta\left(\nu - \nu_0\right) \qquad (9)$$

(Skjæraasen & Kirk 2001), where Δ (≤ 1) is the fraction of a wavelength of the wind pattern occupied by hot electrons of proper density n'_h, $P_\mathrm{s.p.} = (4/3)c\sigma_\mathrm{T}\gamma^2(B'^2/8\pi)$ is

the synchrotron power emitted by a single electron, and ν_0 is the characteristic frequency of emission, measured in the observer frame ($\sigma_{\rm T}$ is the Thomson cross section). The condition of pressure equilibrium gives $n'_{\rm h}\gamma mc^2/3 = B'^2/8\pi$, where B' is the magnetic field in the co-moving frame and m the electron mass. Well outside the light cylinder, but before energy release begins; i.e., at $r_{\rm L} < r < r_0$, the density and magnetic field scale as r^{-2} and r^{-1} respectively, and can be characterizes by the values $n_{\rm L}$ and $B_{\rm L}$ obtained by extrapolating back to $r = r_{\rm L}$. Provided the flow does not accelerate significantly whilst emitting synchrotron radiation, these same scalings, which imply γ independent of r, can be used in the integration in Eq. (9). This is convenient for a rough estimate of the luminosity, but is sensitive to the assumption that the wind does not accelerate upon reconnection.

If we identify the ratio of Poynting flux to kinetic energy (at the light cylinder) $\sigma_{\rm L} = B_{\rm L}^2/(4\pi\Gamma n_{\rm L} mc^2)$, define an average fraction of hot particles $\bar{\Delta} = r_0\int_{r_0}^{\infty} {\rm d}r\Delta/r^2 \lesssim 1$, and use the standard relation $B_{\rm L} = 2.9\times10^8\dot{P}^{1/2}P^{-5/2}\,{\rm G}$, the luminosity becomes

$$\frac{{\rm d}\hat{L}}{{\rm d}\Omega} \;=\; 3.9\times10^7\left(\frac{\sigma\bar{\Delta}r_{\rm L}\dot{P}}{\Gamma^3 r_0 P^4}\right)\;\;(P\text{ in secs}) \qquad (10)$$

where ${\rm d}\hat{L}/{\rm d}\Omega$ is the synchrotron luminosity per steradian divided by the total wind luminosity per steradian. Similarly, the characteristic frequency is

$$h\nu_0(r) \;=\; 2.6\times10^{-6}\left(\frac{r_{\rm L}}{r}\right)\sigma^2\dot{P}^{1/2}P^{-5/2}\;({\rm MeV}). \qquad (11)$$

The spectrum produced by this simple model with monoenergetic electrons extends to a maximum frequency given by Eq. (11) with $r = r_0$ and is flat: ${\rm d}L/{\rm d}\nu{\rm d}\Omega \propto \nu^0$. However, this aspect is sensitive to the way in which the plasma expands and accelerates after reconnection. If, in a more realistic scenario, the electron density is a power law $N(\gamma) \propto \gamma^{-p}$, with $p > 2$, then most of the energy resides in the particles with lowest γ and the above estimate (11) refers to the photons emitted by these particles. The emission at frequencies $\nu < \nu_0(r_0)$ is dominated by the same low energy particles radiating at larger radius in a weaker magnetic field, and is determined by the expansion and acceleration of the hot plasma. In the absence of acceleration, the flat spectrum derived above prevails. However, the intrinsic spectrum, which is a power law ${\rm d}L/{\rm d}\nu{\rm d}\Omega \propto \nu^{-a}$, with $a > 0.5$, is revealed at frequencies $\nu > \nu_0(r_0)$, where particles radiating at r_0 dominate. In the case of the Crab pulsar, the optical to X-ray emission is consistent with a flat spectrum (Shearer & Golden 2001), which steepens to $a > 1$ at a photon energy of approximately 1 MeV (Kanbach 1998; Kuiper et al. 2001). Equation (11) therefore implies $\sigma = 1.1\times10^4\sqrt{r_0/r_{\rm L}}$. Observations suggest ${\rm d}\hat{L}/{\rm d}\Omega \approx 10^{-3}$ for this object, which, from Eq. (10), is consistent with a mildly supersonic flow, $\Gamma \approx 250$, that starts to radiate at $r_0 = 30r_{\rm L}$. This is consistent with the lower limit of $5r_{\rm L}$ found by (Bogovalov & Aharonian 2000) for the radius at which the conversion of Poynting flux to particle-born flux may occur.

5. Discussion

Current models of the high energy emission from rotation powered pulsars fall loosely into two groups: "polar cap" and "outer gap" models (for a recent review see Harding (2001)). Each of these places the emission region in the corotating magnetosphere of the star. The predicted pulse shapes depend sensitively on the uncertain geometry of the magnetic field in this region, which is usually assumed dipolar. In contrast, in the model presented above, pulses are emitted well outside the co-rotation region. Provided the pulsar drives a supersonic, MHD wind, the field geometry approaches a simple asymptotic solution (Bogovalov 1999), which determines the basic properties of the pulses.

In a series of papers, Pacini (1971), Pacini & Salvati (1983), Pacini & Salvati (1987) suggested that particles close to the light cylinder emit synchrotron radiation and are responsible for the optical pulses of the Crab and other pulsars — a theory which appears to be in reasonable agreement with observation (Shearer & Golden 2001). The model presented here is similar in that the radiation mechanism is synchrotron emission and the scaling of Eq. (10) is close to that originally given by Pacini (1971). It goes further, however, by specifying for the emission region a precise geometrical structure and location.

It is known that the dilution of the plasma in the wind must lead to non-ideal MHD behavior (Usov 1975, Michel 1982) and so can be responsible for triggering the emission. The position at which this occurs depends on the initial concentration of charges in the current sheet and is taken as a free parameter. The major uncertainty in the model is the speed with which dissipation proceeds. Our computations implicitly assume rapid dissipation (over a scale small compared to the radius). In this case, it is possible to make a rough estimate of the synchrotron luminosity which is in agreement with observations. A more detailed comparison with the wealth of relevant observations of optical, X-ray and gamma-ray pulsars must await further modeling. It is also conceivable that at least part of the radio emission could be produced in the wind region, as is suggested by the similarity of the pulse profiles at all frequencies seen in the Crab pulsar. However, until a candidate coherent mechanism can be identified, this connection remains very speculative. Nevertheless, the wind scenario is a viable alternative to current theories of gamma-ray, X-ray and optical pulses from rotation-driven pulsars and has the advantage of making specific predictions of the pulse properties.

Acknowledgements. This work is a collaboration of the TMR Network "Astroplasmaphysics" of the European Commission,

contract FMRX-CT-98-0168. Y.G. is supported by a Marie Curie Fellowship from the European Community, contract no. HPMFCT-2000-00671 under the IHP programme. J.K. thanks the Wilhelm and Else Heraeus-Stiftung and the conference organisers for their invitation to attend and their hospitality at the meeting, and thanks the other participants for stimulating discussions.

References

Arons J. 1996 Space Science Reviews, 75, 235
Aschenbach B., Brinkmann W. 1975 A&A 41, 147
Bogovalov S.V., 1999 A&A 349, 1017
Bogovalov S.V., Aharonian F.A. 2000 MNRAS 313, 504
Büchner J., Kuska J.P. 1999 Ann. Geophys. 17, 604
Coroniti F.V. 1990 ApJ 349, 538
Crusius-Wätzel A.R., Kunzl T., Lesch H. 2001 ApJ 546, 401
Daughton W. 1999 Phys. Plasmas 6, 1329
Harding A.K. 2001 in 'High energy gamma-ray astronomy' eds: F. Aharonian, H.J. Völk, AIP.
Harris E.G. 1962 Nuovo Cimento 23, 115
Helfand D.J., Gotthelf E.V., Halpern J.P. 2001 ApJ 556, 380
Hesse M., Kuznetsova M., Birn J. 2001 J. Geophys. Res. Space Phys. 106, 29831
Hester J.J. et al. 1995 ApJ 448, 240
Hoh F.C. 1968 Physics Fluids 9, 277
Kanbach G., 1998 Adv. Space Res. 21, 227
Kirk J.G., Lyubarsky Y. 2001 Publ. Astron. Soc. Aust. 18, 415
Kirk J.G., Skjæraasen O., Gallant Y.A. 2002 A&A letters, submitted.
Kuiper L., Hermsen W., Cusumano G., Diehl R., Schönfelder V., Strong A., Bennett K., McConnell M.L. 2001 to appear in A&A (astro-ph/0109200)
Lyubarsky Y. 1996 A&A 311, 172
Lyubarsky Y., Kirk J.G. 2001 ApJ 547, 437
Machabeli G.Z., Luo Q., Melrose D.B., Vladimirov S. 2000 MNRAS 312, 51
Melatos A. 1998 Mem. Soc. Ast. It., 69, 1009
Melrose D.B. 1986 "Instabilities in space and laboratory lasmas", Cambridge University Press, Cambridge
Michel, F.C., 1982 Rev. Mod. Phys. 54, 1
Michel, F.C., 1994 ApJ 431, 397
Pacini F. 1971 ApJ 163, L17
Pacini F., Salvati M. 1983 ApJ 274, 369
Pacini F., Salvati M. 1987 ApJ 321, 447
Pritchett P.L., Coroniti F.V., Decyk V.K. 1996 J. Geophys. Res. Space Phys. 101, 27413
Radhakrishnan V., Deshpande A.A. 2001 A&A 379, 551
Rankin J.M. 1990 ApJ 352, 247
Skjæraasen O., Kirk J.G. 2001 in "Similarities and universality in relativistic flows" Eds: Georganopoulos, Guthmann, Manolakou, Marcowith (Logos Verlag, Berlin)
Shearer A., Golden A. 2001 ApJ 547, 967
Usov V.V., 1975 Astrophys. & Space Sci. 32, 375
Zelenyi L.M., Krasnosel'skikh V.V. 1979 Sov. Phys. A.J. 56, 819
Zenitani S., Hoshino M. 2001 ApJ 562, L63
Zhu Z.W., Winglee R.M. 1996 J. Geophys. Res. Space Phys. 101, 4885

Proceedings of the 270. WE-Heraeus Seminar on: *"Neutron Stars, Pulsars and Supernova Remnants"*
Physikzentrum Bad Honnef, Germany, Jan. 21-25, 2002, eds. W. Becker, H.Lesch & J. Trümper, MPE Report 278, pp. 142-154

High-energy radiation from pulsars: a challenge to polar-cap models

B. Rudak, J. Dyks and T. Bulik

Nicolaus Copernicus Astronomical Center, Warsaw - Toruń, Poland

Abstract. Spectacular results of pulsar observations in X-ray and gamma-ray domains gave a new boost to theoretical models of pulsar magnetospheric activity. A challenging aspect of these efforts is that lightcurves and broadband energy spectra of the brightest HE sources exhibit unexpected richness of features, making each object almost a unique case to be interpreted with a custom-made model. This review offers our subjective account of how the models of high-energy radiation used within the framework of SCLF polar-cap scenarios tackle with these challenges. We describe major characteristics of all radiative processes relevant for modeling the observed features. Then we address successes as well as noticeable disadvantages of these models upon their confrontation with the available data.

1. Introduction

A large fraction of galactic X-ray and gamma-ray sources is associated with neutron stars, in particular with rotation powered pulsars (RPP). Spectacular results of observational campaigns of RPP with ROSAT, ASCA and CGRO, and recently with RXTE and CHANDRA induced a new wave of interest in theoretical models of pulsar magnetospheric activity. A challenging aspect of these efforts is that lightcurves and broadband energy spectra of the brightest HE sources exhibit unexpected richness of features making thus each object a unique case pending special treatment.

The pair creation paradigm is a pivotal element in virtually all models of magnetospheric activity of radio pulsars (which at the moment constitute a vast majority of known RPPs). Electron-positron pairs ($e^{\pm}$-pairs) are thought to be responsible for radio emission observed in radio pulsars which is interpreted as the coherent curvature radiation of $e^{\pm}$ plasma. Pairs can be produced in magnetospheric environments either via photon absorption in a dense field of soft photons (photon-photon collision) or via photon absorption in a strong magnetic field. In either case a supply of hard gamma photons is required in order to fulfill stringent threshold conditions for pair creation. Not all of these photons would be subject to absorption; many will escape the magnetosphere without any attenuation. This leads us to expect that all radio pulsars (including low-B millisecond objects) should be the sources of gamma radiation. It is up to theoretical models to show whether the expected flux of the radiation is interestingly high with respect to the sensitivity of recent and future gamma-ray telescopes. One should keep in mind, however, that the pair creation paradigm remains just a paradigm for the time being: recently it was questioned by (Jessner et al. 2001), who presented arguments that for a wide range of surface temperature, magnetic field strength and spin period, the electrons supplied by neutron star surface via thermionic and field emission will screen out the accelerating electric field $\mathcal{E}_{\|}$, limiting it to a residual value. In consequence, no favorable conditions would exist for magnetic pair production.

This review offers our subjective account of how the models of high-energy radiation do perform within the framework of polar-cap models with space-charge-limited-flow (SCLF). First, we introduce all ingredients of polar-cap models with SCLF and we describe major characteristics of all radiative processes relevant for physical conditions in pulsar magnetospheres. Then we address successes as well as noticeable disadvantages of these models upon their confrontation with the data.

2. Basic parameters

For the sake of completeness, we recall in this section basic quantities used throughout the review. A neutron star of radius $R_{\rm s}$ and moment of inertia I, spinning with angular velocity $\Omega = 2\pi/P$ which decreases in time (for whatever the reason) at a rate $\dot{\Omega} = -2\pi P^{-2}\dot{P} < 0$, loses its rotational energy at the rate

$$L_{\rm sd} \simeq 4 \times 10^{31}\, I_{45} \dot{P}_{-15} P^{-3} {\rm erg\ s^{-1}}, \qquad (1)$$

where P is in seconds, $\dot{P}_{-15} \equiv \dot{P}/10^{-15}$ and $I_{45} \equiv I/10^{45}$ g cm^2, and $L_{\rm sd}$ is the so called spin-down luminosity. If a magnetic dipole is anchored at the center of a neutron star, with its magnetic moment $\boldsymbol{\mu}_B$ inclined at angle α to the spin axis $\boldsymbol{\Omega}$, then the strength of the field at the stellar equator is $B_{\rm s} = \mu_B/R_{\rm s}^3$ (and twice as high at the poles). The dipole, rotating in a vacuum will lose energy at the rate

$$L_{\rm magn} = \frac{2}{3c^3} B_{\rm s}^2 \sin^2\alpha\, R_{\rm s}^6\, \Omega^4. \qquad (2)$$

The quantity $B_{\rm s}\sin\alpha$ can be thus inferred from P and $\dot{P}$ for a neutron star with known values of I and $R_{\rm s}$. Another model, where the dipolar radiation is replaced with a magnetospheric wind of particles (1), gives a similar result as (2) for an orthogonal case:

$$L_{\rm wind} \approx \frac{1}{c^3} B_{\rm s}^2\, R_{\rm s}^6\, \Omega^4 \qquad (3)$$

and therefore is independent of the angle α. Since no observational support exists for $\dot{P}$ depending on $\sin\alpha$, the standard approach is to apply the latter model ($L_{\rm sd} = L_{\rm wind}$) to derive the strength of the dipolar component of magnetic field

$$B_{12}^2 = 10^{15}\, I_{45}\, R_6^{-6}\, P\, \dot{P} \qquad (4)$$

where $B_{12} \equiv B_{\rm s}/10^{12}$G, and $R_6 \equiv R_{\rm s}/10^6$cm. It is likely that neutron star magnetic fields contain high-order multipoles which may dominate the dipolar component at the surface level. Their relative amplitudes as well as distribution remain, however, unknown. It will be assumed throughout the paper that the magnetic field is a static-like dipole, not distorted by rotational effects or by presence of strong outflowing wind of particles (the latter effect has been recently invoked to decrease very high values of $B_{\rm s}$ inferred from P and $\dot{P}$ for two SGRs (Harding et al. 1999). The field is therefore approximated with axisymmetric field lines satisfying $r\sin^{-2}\theta = R_{\rm dc}$ in polar coordinates r and θ, with the dipole constant $R_{\rm dc}$. A dipole constant for which a rigid rotation with the angular velocity Ω reaches the speed-of-light limit (it occurs for $R_{\rm dc} = c/\Omega$ and this particular value is denoted as $R_{\rm lc}$) determines the so called light cylinder of radius $R_{\rm lc}$. All field lines which cross the light cylinder are then considered as open lines, and their footpoints on the stellar surface define two polar caps of radius $R_{\rm pc} \approx R_{\rm s}\cdot(R_{\rm s}/R_{\rm lc})^{1/2}$, where the latter factor is the sine function of the magnetic colatitude $\theta_{\rm pc}$ for the outer rim of the polar cap:

$$\sin\theta_{\rm pc} = (R_{\rm s}/R_{\rm lc})^{1/2}. \qquad (5)$$

3. Properties of pulsars in X-rays and gamma-rays

For more than 1500 pulsars known to date only about ~ 40 positive detections in X-rays and no more than 10 detections in gamma-rays have been achieved (Becker 2002, Kanbach 2002). CGRO provided seven high-confidence detections (of *Seven Samurai*) with three other cases classified as 'likely' detections. The gamma-ray sources were identified by virtue of flux pulsations with previously known P and $\dot{P}$. Crab and Vela are the only pulsars seen by all three instruments of CGRO. No trace of pulsed signal in VHE range (300 GeV – 30 TeV) has been found so far for the gamma-ray pulsars (Sako et al. 2000, Weekes 2000). However, strong steady VHE emission is associated with 3 out of 10 gamma-ray pulsars. Two plerionic sources of the steady VHE radiation – The Crab Nebula and the plerion around B1706-44 – may serve as standard candles, with 'grade A' according to Weekes 2000. A third plerion – around the Vela pulsar – was given 'grade B' in the same ranking. All 10 gamma-ray pulsars are strong X-ray emitters.

The positions of these HE pulsars are shown in the $P-\dot{P}$ diagram of Fig.1 along with positions of about 700 radio pulsars for which $\dot{P}$ values were available. A remarkable fact is that the location of X-ray sources does not correlate with the inferred strength of magnetic field $B_{\rm s}$; at least not in a naively anticipated way that high-B objects would emit HE radiation, whereas low-B objects would not. In particular, 10 millisecond pulsars – about thirty percent of all millisecond pulsars (the objects with $P \lesssim 0.01$s and $\dot{P} \lesssim 10^{-17}$, i.e. with low B values: $B_{\rm s} \lesssim 10^9$G) known to date – have been detected as X-ray sources. So far, millisecond pulsars have eluded the detection

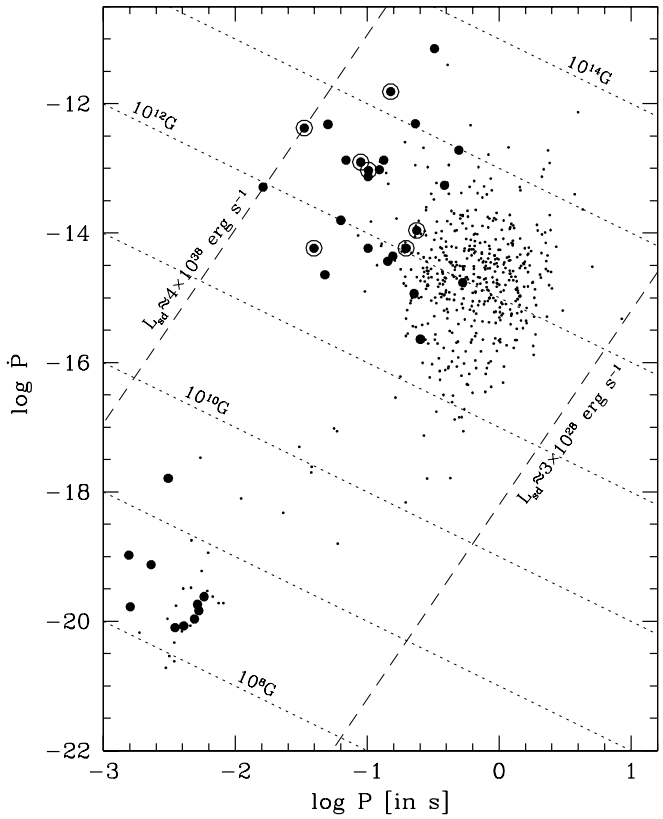


Fig. 1. $P-\dot{P}$ diagram for Rotation Powered Pulsars. The pulsars detected exclusively in radio are indicated with dots; they are taken mostly from the data base of Taylor et al. 1995. Thirty five pulsars emitting X-rays are indicated with bullets. These include two objects recently discovered with RXTE: J0537-6910 in SNR N157B in LMC (Marshall et al. 1998) is the fastest young pulsar known, spinning twice as fast as the Crab pulsar but with similar value of spin down luminosity; J1846-0258 in SNR Kes-75 (Gotthelf et al. 2000), with $P = 0.32$s, the highest $\dot{P}$ among all RPP. Seven bullets in circles indicate seven gamma-ray pulsars of high confidence. Dashed lines correspond to constant values of spin down luminosity $L_{\rm sd}$. The upper line ($L_{\rm sd} \approx 4\times10^{38}$erg s^{-1}) includes the Crab pulsar and J0537-6910, the lower one ($L_{\rm sd} \approx 3\times10^{28}$erg s^{-1}) includes J2144-3933 – the slowest ($P = 8.5$s) radio pulsar detected so far (Young et al. 1999). Dotted lines correspond to constant values of the dipolar component of the surface magnetic field as inferred from P and $\dot{P}$ through (4) with $R_6 = 1$.

in gamma rays (possibly with one exception, see below) and just upper limits were available for a handful of them from EGRET observations (Nel et al. 1996). In the case of J0437-4715 the upper limit is interestingly tight – in disagreement with the empirical relation $L_\gamma \propto L_{\rm sd}^{1/2}$ (see Fig.3).

Empirical evidence that pulsars must somehow tap their high-energy activity from rotation comes from a strong correlation between the success of detection in X and/or γ-rays and the position in the lists of targets ranked by spin-down flux values $L_{\rm sd}/D^2$, which is presented in a graphical form in Fig. 2.

Spectral analysis for pulsars detected with ROSAT PSPC (0.1 keV to 2.4 keV) shows that in most cases a power-

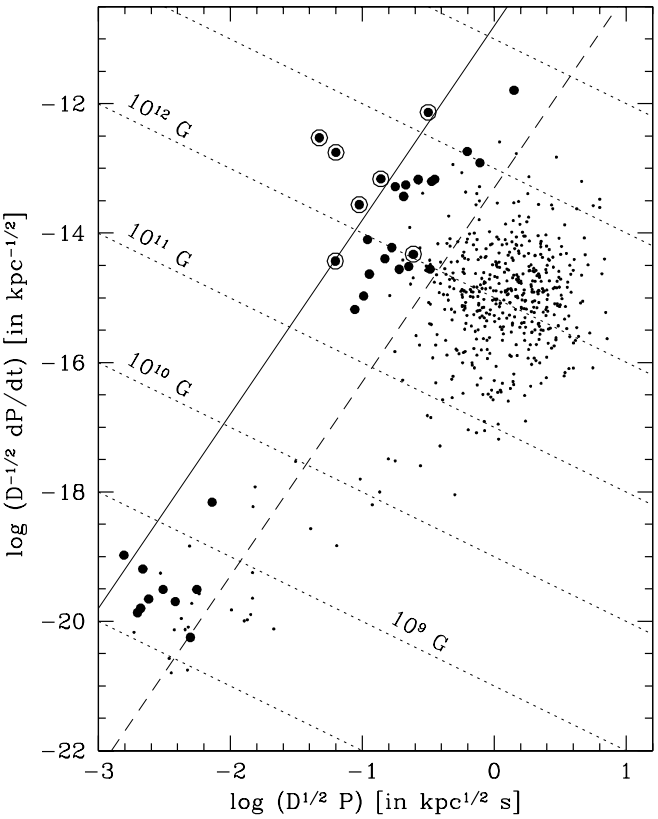


Fig. 2. The ranking of RPPs by their spin-down flux $L_{\rm sd}/D^2$. The units of abscissa and ordinate are chosen to keep the resemblance with the $P-\dot{P}$-diagram: the lines of constant spin-down flux (two such lines - continuous and dashed – are shown as examples) have the same slope with respect to the abscissa (+3) as the lines of constant $L_{\rm sd}$ in Fig. 1; the lines of constant $B_{\rm s}$ (dotted) have the same slope (-1) with respect to the abscissa in both figures; the range of values for coordinates is also identical. Crab and Vela sticking out well above the continuous line posses the highest spin-down fluxes among the RPPs. The continuous line is trained on B1951+32 with $L_{\rm sd}/D^2 \approx 7\times10^{-8}$ erg s^{-1} cm^{-2}; the dashed line is for the millisecond X-ray pulsar J0751+1807 with $L_{\rm sd}/D^2 \approx 2\times10^{-10}$ erg s^{-1} cm^{-2}. Note a low overall position of the gamma-ray pulsar B1055-52. (From Kluźniak & Rudak 1996, with recent updates).

law spectral model provides acceptable fits to the data (Becker & Truemper 1997). Moreover, an intriguing empirical relation between inferred X-ray luminosity and spin down luminosity was found, $L_X \approx 0.001\,L_{\rm sd}$, confirming rotational origin of most of the X-ray activity. An interesting point is that the relation was obtained for all the sources regardless their temporal characteristics (about 50 % of all pulsars detected with ROSAT are unpulsed sources). A complementary empirical relation was found for pulsed emission from 19 pulsars observed with ASCA (0.6keV to 10keV). Assuming opening angle of X-rays to be one steradian, the inferred pulsed X-ray luminosity correlates with spin-down luminosity as

$$L_X = 10^{34}\left(\frac{L_{\rm sd}}{10^{38}\ {\rm erg\ s^{-1}}}\right)^{3/2}\ {\rm erg\ s^{-1}}, \qquad (6)$$

according to Saito et al. 1998.

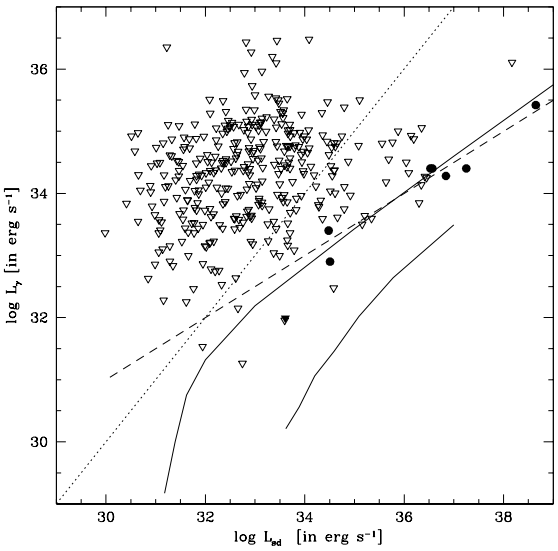


Fig. 3. Gamma-ray luminosity versus spin-down luminosity for seven pulsars (filled dots) detected with the CGRO instruments. Opening angle of one steradian was assumed for the gamma-ray emission. Open triangles are the EGRET upper limits after Nel et al. 1996 for 350 objects, including seven millisecond pulsars. The filled triangle indicates the upper limit for J0437-4715 (Fierro et al. 1995). Note, that most of the upper limits are well above the maximum possible value for L_γ set by $L_\gamma = L_{\rm sd}$ (dotted line). The dashed line marks the empirical relation derived for the CGRO pulsars: $L_\gamma \propto L_{\rm sd}^{1/2}$. Solid lines show evolutionary tracks for a classical pulsar with $B_{\rm s} = 10^{12}$G (upper line) and a millisecond pulsar with $B_{\rm s} = 10^{9}$G (lower line) according to the phenomenological model of Rudak & Dyks 1998.

A similar power-law empirical relation holds for gamma-rays (cf. Fig.3), but with a different power-law index (e.g. Thompson et al. 1999):

$$L_\gamma \simeq 10^{35}\left(\frac{L_{\rm sd}}{10^{38}\ {\rm erg\ s^{-1}}}\right)^{1/2}\ {\rm erg\ s^{-1}}. \qquad (7)$$

Important conclusion from (6) and (7) is that neither L_X nor L_γ becomes a sizable fraction of $L_{\rm sd}$. The most efficient conversion of spin-down luminosity into high-energy radiation is taking place for B1055-52 – the oldest pulsar among *Seven Samurai* – with $L_\gamma \simeq 0.1\,L_{\rm sd}$.

High energy lightcurves differ significantly from those in radio. Their most striking feature are relatively long duty cycles as well as phase shifts in comparison to the radio pulses. Only for the Crab pulsar the peaks in gamma-rays as well as in radio wavelengths occur at the same rotational phases. The light-curve shapes fall into two categories. The Crab pulsar, Vela and Geminga show two sharp peaks separated in phase by $0.4-0.5$ and connected by an interpeak bridge of considerable level. B1706-44 shows two peaks separated by 0.2 in phase, with some hints of a third component in between. Other pulsars exhibit broad single pulses. Unknown opening angles for gamma-ray emission introduce a factor of uncertainty when inferring the gamma-ray luminosities. Broad peaks in gamma-ray pulses do not necessarily mean large opening angles for

gamma-ray emission. Polar cap models, which rely on purely dipolar magnetic fields postulate nearly aligned rotators, where inclination of magnetic axis to spin axis is comparable to the angular extent of the polar cap (Daugherty & Harding 1994).

With a discovery of sharply peaked pulsed X-ray emission in the fastest millisecond pulsar B1937+21 an apparently separate group of millisecond X-ray pulsars emerges, with its members – B1821-24 (Saito et al. 1997), J0218+4232 (Kuiper et al. 2000), and B1937+21 (Takahashi et al. 2000) – being scaled-down versions of the Crab pulsar as far as sharp pulse profiles and hard power-law X-ray spectra are concerned. An astonishing common feature within the group is the same strength of the magnetic field estimated at the light cylinder and the fact that it matches the strength of the Crab pulsar magnetic field at the light cylinder.

It is, however, lightcurves and broadband energy spectra extending from optical to X-rays and to gamma-rays, available for *Seven Samurai* (e.g. Thompson et al. 1999, Thompson 2001) that are particularly impressive and challenging for any models of pulsar activity. These observations are reviewed in details by Kanbach 2002 (this volume).

4. Unipolar induction

Consider a neutron star of radius $R_{\rm s}$ and surface magnetic field $B_{\rm s}$ as a perfect conductor. For the rotating star with its dipolar magnetic field immersed in a vacuum an external quadrupole electric field $\boldsymbol{\mathcal{E}}$ develops, with non-zero component along magnetic field lines at the surface. The corresponding electrostatic potential Φ in polar coordinates r and θ reads (Michel 1991)

$$\Phi(r,\theta) = -\frac{Q}{r^3}\,\left(3\cos^2\theta - 1\right), \tag{8}$$

where $Q = \pi B_{\rm s} R_{\rm s}^5/(3\,c\,P)$ is the quadrupole moment. Maximal electromotive force will then be induced between the pole of the star and the outer rim of the polar cap due to:

$$\Delta\Phi_{\rm pc} = \Delta\Phi_{\rm equator}\left(\frac{R_{\rm pc}}{R_{\rm s}}\right)^2, \tag{9}$$

where

$$\Delta\Phi_{\rm equator} = \frac{1}{2c}\,B\,\Omega\,R_{\rm s}^2 \tag{10}$$

denotes a (huge but unavailable) potential drop between the pole and the equator. In terms of voltage, polar caps offer then $\Delta V_{\rm pc} \approx 7\times10^{12}\,B_{12}\,P^{-2}$ Volt

4.1. Potential drops in SCLF gaps

Potential drop (9) sets a firm upper limit for all (model-dependent) realistic potential drops $\Delta\Phi_{\parallel}$, including vacuum gap model of Ruderman & Sutherland, as well as outer gap models of e.g. Cheng et al. 1986. In fact,

$$\Delta\Phi_{\parallel} \ll \Delta\Phi_{\rm pc} \tag{11}$$

for most cases. We will concentrate hereafter on a class of models where the supply of charged particles from a neutron star surface along open field lines is not limited by either binding or cohesive energy of the particles and therefore can reach the Goldreich–Julian rate close to the surface ('Space Charge Limited Flow' – Sturrock 1971, Arons & Scharlemann 1979). A concise but to-the-point account of essential properties of the SCLF models has been presented by Arons 2000.

Three boundary conditions essential to the electrodynamics above the polar cap are (Muslimov & Tsygan 1992):
1) $\boldsymbol{\mathcal{E}}\cdot\boldsymbol{B} = 0$ for the magnetosphere within the closed field lines,
2) $\Phi = 0$ at the surface and at the interface between the closed magnetosphere and the open field lines,
3) $\mathcal{E}_{\parallel} = 0$ at the surface level,
where $\mathcal{E}_{\parallel}$ is the electric field component parallel to the magnetic field.
Last but not least, it is assumed that the outflow is stationary and the magnetosphere remains axisymmetric.

The electric field $\boldsymbol{\mathcal{E}}$ required to bring a charged particle into co-rotation satisfies the following equation

$$\boldsymbol{\mathcal{E}} + \frac{1}{c}((\boldsymbol{\Omega}-\boldsymbol{\omega}_{\rm LT})\times\boldsymbol{r})\times\boldsymbol{B} = 0 \tag{12}$$

where the inertial-frame dragging effect is included (Beskin 1990, Muslimov & Tsygan 1992) with $\boldsymbol{\omega}_{\rm LT} = \kappa_{\rm g}(R_{\rm s}/r)^3\,\boldsymbol{\Omega}$, where $\kappa_{\rm g} = I/(M_{\rm s}R_{\rm s}^2)\cdot R_{\rm g}/R_{\rm s}$, and $R_{\rm g} = 2GM_{\rm s}/c^2$.

Charge density necessary to support this local $\boldsymbol{\mathcal{E}}$ is

$$\varrho_{corot} = \frac{1}{4\pi}\boldsymbol{\nabla}\cdot\boldsymbol{\mathcal{E}} \approx -\frac{\boldsymbol{\Omega}\cdot\boldsymbol{B}}{2\pi c}\,[1-\omega_{\rm LT}] \tag{13}$$

The charge density ϱ_{corot} due to SCLF at $r = R_{\rm s}$ is called the Goldreich–Julian charge density:

$$\varrho_{\rm GJ} \approx -\frac{\boldsymbol{\Omega}\cdot\boldsymbol{B}}{2\pi c}\,[1-\kappa_{\rm g}]. \tag{14}$$

As charged particles flow out along the open field lines a deviation of the local charge density $\varrho_{\rm local}$ from the local co-rotation density ϱ_{corot} develops. By using now two relations satisfied in the dipolar structure, $B(r)\propto r^{-3}$ and $\varrho(r)\propto r^{-3}$, one obtains a simple formula for local deviation from the co-rotation charge density:

$$\varrho_{\rm local} - \varrho_{corot} \approx \frac{\boldsymbol{\Omega}\cdot\boldsymbol{B}}{2\pi c}\,\kappa_{\rm g}\,\left[1-\left(\frac{R_{\rm s}}{r}\right)^3\right]. \tag{15}$$

Accordingly, the accelerating potential drop in SCLF reads

$$\Delta\Phi_{\parallel} \approx \Delta\Phi_{\rm pc}\,\kappa_{\rm g}\,\left[1-\left(\frac{R_{\rm s}}{r}\right)^3\right], \tag{16}$$

where $\Delta\Phi_{\rm pc}$ is given by (9) and $\kappa_{\rm g} = 0.15\,I_{45}$. This is a remarkable result obtained by Muslimov & Tsygan 1992: the potential drop due to inertial-frame dragging is significantly larger than the drop induced by curvature of magnetic field lines ('flaring', Arons & Scharlemann 1979), or – useless to say - by particle inertia (Michel 1974)).

5. Electric field structure in SCLF gaps

The model with frame dragging effects presented in a simplified form above, does not take into account possible feed-back effect due to $e^{\pm}$-pairs formed via photon absorption within open magnetic field lines. Copious pair creation occurs in a relatively thin layer – a pair formation front (PFF). The creation of pairs leads to the screening of the accelerating field $\mathcal{E}_{\parallel}$ within the layer of PFF. A detailed picture of this effect would

require to follow the dynamics of electrons and positrons in a self-consistent way. Instead, it is reasonable to assume, that the field is shorted out at the height were the first $e^{\pm}$-pair is created (hereafter denoted as h_c): $\mathcal{E}_{\parallel}=0$ for $h \geq h_c$.

The problem of electric field structure in the context of SCLF with boundary condition $\mathcal{E}_{\parallel}=0$ set at $h_0=0$ (stellar surface) and at $h \geq h_c$ (PFF) was formulated and solved by Harding & Muslimov 1998a. The solution is rather lengthy and includes special functions. It is however possible to obtain simple but quite accurate analytical approximations. As long as the length h_c of the accelerator is of the order of polar cap radius $R_{\rm pc}$, the accelerating electric field may be approximated according to Dyks & Rudak 2000a as

$$\mathcal{E}_{\parallel} \approx -1.46 \ \frac{B_{12}}{P^{3/2}} \ h \left(1-\frac{h}{h_c}\right) f_1(\xi) \cos\chi \ \text{Gauss}, \qquad (17)$$

where $B_{12}=B_{\rm s}/10^{12}$G, P is the spin period in seconds, χ is the angle between the spin axis and the magnetic moment of the rotating star, h is expressed in cm, and $M=1.4\,M_{\odot}$, $R_{\rm s}=10^6$cm. The magnetic colatitude $\xi \equiv \theta/\theta(\eta)$ is scaled with the half-opening angle of the polar magnetic flux tube $\theta(\eta)$, where $\eta \equiv 1+h/R_{\rm s}$. The magnetic colatitude function $f_1(\xi)$ is a monotonically decreasing function, with $f_1(0) \simeq 1$ and $f_1(1)=0$.

Vertical structure of the electric field depends (via the location of PFF) on radiative processes which induce the pair creation: curvature radiation (CR) and inverse Compton scattering (ICS) on soft X-ray photons from the stellar surface (brief characteristics of these processes is presented in the next section).

An interesting way to avoid immediate screening of the electric field by created pairs, relevant in strong magnetic fields $\gtrsim 0.1\,B_{\rm crit}$, was proposed by Usov & Melrose 1995 who noticed that pairs are created then near the energy threshold, most favorable in bound states – as atoms of positronium – which then move to high altitudes before being ionized.

6. Radiative processes in pulsar magnetospheres

Cooling of ultrarelativistic electrons via curvature radiation (CR) and magnetic inverse Compton scattering (ICS) are the most natural ways of producing hard gamma-rays capable of inducing cascades of $e^{\pm}$-pairs and secondary HE photons. These two processes dominate within two distinct ranges of Lorentz factors γ of primary electrons.

When $\gamma \lesssim 10^6$, magnetic inverse Compton scattering plays a dominant role in braking the electrons and it is the main source of hard gamma-ray photons (Sturner et al. 1995). Energy losses due to resonant ICS limit the Lorentz factors of the particles to a level which depends on electric field strength $\mathcal{E}_{\parallel}$, temperature T and size of hot polar cap, and magnetic field strength $B_{\rm s}$ (Xia et al. 1985, Sturner 1995). The Lorentz factors can then be limited even to $\sim 10^3$. This stopping effect becomes more efficient for stronger magnetic fields, and it was suggested as an explanation for the observed cutoff at $\sim$ 10MeV in the spectrum of B1509-58 (Sturner 1995). ICS was also found to be able (under some circumstances) to smear out the monotonic energy distribution of electrons significantly, with interesting consequences for the cascades (Dyks & Rudak 2000b).

However, in their modern versions the accelerators of particles are strong enough to outpower the ICS cooling. In consequence, very high Lorentz factors – $\gamma \gtrsim 10^6$ – are achieved by electrons, limited by CR. The first detailed scenario of radiative processes in CR-induced cascades was presented by (Daugherty & Harding 1982) and despite many modifications and additions its basic features remain valid. The model assumes that primary electrons accelerated to ultrarelativistic energies emit curvature photons which in turn are absorbed by the magnetic field and $e^{\pm}$-pairs are created. These pairs cool off instantly via synchrotron radiation process. Whenever the SR photons are energetic enough they may lead to further creation of pairs, etc. ICS can still be incorporated to the models with CR-induced cascades as the process relevant for $e^{\pm}$-pairs, since typical Lorentz factors of theirs do not exceed $\sim 10^3$. According to the analytical model of Zhang & Harding 2000a the empirical relations for X-ray and gamma-ray luminosities of pulsars (presented in Sect.3) can be reproduced satisfactorily when the ICS involving $e^{\pm}$-pairs is included.

Processes relevant for generation and transfer of high-energy photons in pulsar magnetospheres are therefore:
- curvature radiation,
- magnetic inverse Compton scattering,
- magnetic pair creation $(\gamma \rightarrow e^{\pm})$
- synchrotron radiation,
- photon splitting $(\gamma \rightarrow \gamma+\gamma,)$
- photon-photon pair creation $(\gamma+\gamma \rightarrow e^{\pm})$.

Their basic properties are given below, except for $\gamma+\gamma \rightarrow e^{\pm}$: in practice it is treated exactly as in free space. This is justified in models of 'thick outer gaps' (Cheng & Zhang 1999) but within the framework of polar cap models this is not the case, in general. However, no handy formula is available for the cross section of this process in the limit of high B and standard non-magnetic formulae are in use (e.g. Zhang & Qiao 1998).

To illustrate how these processes contribute to the high-energy radiation of a pulsar the numerically calculated components (due to the first four processes in the list) are presented in Figs.4 and 5 (after Dyks & Rudak 2002a and Dyks et al. 2001) along with overlaid data points for the Vela pulsar. The dipolar field in the Vela pulsar does not exceed 10^{13}G and photon splitting was neglected as non-competitive to the magnetic pair creation. The electric field structure of the accelerator used in these calculations is taken after Harding & Muslimov 1998a.

6.1. Curvature radiation

Relativistic electron of energy γmc^2 (we take $\gamma \gg 1$) sliding along the magnetic field line of curvature $\varrho_{\rm cr}$ will emit photons with a continuum energy spectrum peaked at the characteristic energy

$$\varepsilon_{\rm cr}=\frac{3}{2}\,c\,\hbar\,\frac{\gamma^3}{\varrho_{\rm cr}}. \qquad (18)$$

The radius $\varrho_{\rm cr}$ for a purely dipolar line attached to the outer rim of the polar cap can be approximated not far away from the NS surface as $\varrho_{\rm cr} \approx \sqrt{R_{\rm s}\cdot R_{\rm lc}} \approx 10^8\sqrt{P}$cm. The cooling rate of that electron is

$$\dot{\gamma}_{\rm cr}=-\frac{2}{3}\,\frac{e^2}{mc}\,\frac{\gamma^4}{\varrho_{\rm cr}^2}. \qquad (19)$$

For a monoenergetic injection function of electrons $Q(\gamma) \propto \delta(\gamma-\gamma_0)$ and their cooling due solely to CR the electrons

will assume a single power-law distribution in energy space $N_\gamma(\mathrm{el.}) \propto \gamma^{-4}$ for $\gamma < \gamma_0$ as long as they stay within the region of the cooling. Their escape introduces a natural low-energy cutoff $\gamma_{\rm cutoff}$ in $N_\gamma(\mathrm{el.})$. Therefore, the unabsorbed CR energy spectrum $f_\varepsilon(\varepsilon)$ due to the injected electrons has a broken power-law shape, with a high-energy limit set by γ_0 and the break at some energy $\varepsilon_{\rm break}$. For $\varepsilon > \varepsilon_{\rm break}$ the energy spectrum is $f_\varepsilon(\varepsilon) \propto \varepsilon^{-2/3}$, and $f_\varepsilon(\varepsilon) \propto \varepsilon^{+1/3}$ for $\varepsilon < \varepsilon_{\rm break}$. Since nonthermal spectra cover ususally many decades in energy it is more convenient to use $\varepsilon f_\varepsilon(\varepsilon)$ for easy comparison of power in different parts of energy space (see Fig. 4). Accordingly, $\varepsilon f_\varepsilon(\varepsilon) \propto \varepsilon^{+1/3}$ above the break, and $\propto \varepsilon^{+4/3}$ below the break.

The cutoff limit $\gamma_{\rm cutoff}$ can be found by comparing the characteristic cooling time scale $t_{\rm cr} \equiv \gamma/|\dot\gamma_{\rm cr}|$ with the estimated time of escape $t_{\rm esc}$, which we take as $t_{\rm esc} \approx \varrho_{\rm cr}/c$. Therefore

$$\varepsilon_{\rm break} \approx \frac{9}{4}\,\hbar\,\frac{c}{r_0} \approx 150\,\mathrm{MeV}, \qquad (20)$$

where r_0 is the classical electron radius (Rudak & Dyks 1999). Note, that photon energy $\varepsilon_{\rm break}$ at which the cooling break occurs does not depend on any pulsar parameters.

The spectrum of CR calculated numerically to model the Vela pulsar (Dyks et al. 2001) is shown in Fig.4 as dot-dashed line. High-energy cutoff due to one-photon magnetic absorption occurs around 10 GeV. Note the importance of gamma-ray detectors capable to operate above 10 GeV for (in)validating the model. The low-energy CR spectral break $\varepsilon_{\rm break}$ is prominent at $\sim$ 40MeV. Below $\varepsilon_{\rm break}$ the power of CR decreases and eventually becomes unimportant at $\sim$ 1MeV where the synchrotron component takes over.

6.2. Magnetic pair creation

Pair creation via magnetic photon absorption ($\gamma + \boldsymbol{B} \to e^\pm + \boldsymbol{B}$) is kinematically correct because the magnetic field can absorb momentum. To ensure high chances for the process to occur it is not enough for a photon propagating at a pitch angle ψ to local $\boldsymbol{B}$ to satisfy the energy threshold condition, $\sin\psi \cdot \varepsilon \geq 2mc^2$, but high optical thickness $\tau_{\gamma B}$ of the magnetosphere is required. In fact the condition $\tau_{\gamma B} = 1$ is used as a criterium for the so called death-line for radio pulsars in the $P - \dot P$ diagram. Maximal values of $\sin\psi$ for curvature photons in the dipolar field do not exceed $\sim 0.1 \sin\theta_{\rm pc} \approx 0.0014\,P^{-1/2}$ (Sturrock 1971), and, therefore, both conditions are difficult to be met for long-period pulsars.

The absorption coefficient for the process as described in Erber 1966 and used to calculate $\tau_{\gamma B}$ reads

$$\eta(\varepsilon) = \frac{1}{2}\,\frac{\alpha}{\lambda\!\!\!^{-}_{\rm c}}\,\frac{B_\perp}{B_{\rm crit}}\,T(\chi) \qquad (21)$$

where α is a fine structure constant, $\lambda\!\!\!^{-}_{\rm c}$ is a Compton wavelength, $B_{\rm crit} = m^2c^3/e\hbar \simeq 4.4 \times 10^{13}$G, $B_\perp$ is the component of the magnetic field perpendicular to the photon momentum, and $\chi \equiv \frac{1}{2}\frac{B_\perp}{B_{\rm crit}}\frac{\varepsilon}{m_e c^2}$ is the Erber parameter χ. The function $T(\chi)$ is then approximated as $T(\chi) \approx 0.46\exp(-4f/3\chi)$, which is valid for $\chi \lesssim 0.2$; for $\chi \gtrsim 0.2$ this approximation starts to overestimate $\eta(\varepsilon)$ significantly. The function f is a near-threshold correction introduced by Daugherty & Harding 1983, important in the case of high local B. Electron-positron pairs created through the magnetic absorption emit synchrotron photons (SR) and also may get involved in ICS with soft photons.

Taking advantage of the dipolar character of the magnetic field, it straightforward to find analytical approximation of the condition $\tau_{\gamma B} = 1$. A photon created at a radial distance r from the neutron star center, with its momentum parallel to the local magnetic field line will undergo magnetic absorption if its energy exceeds the following local cutoff energy (after Baring & Harding 2000, Baring 2001)

$$\varepsilon_{\rm cutoff} \approx 0.4\,P^{1/2}\left(\frac{r}{R_{\rm s}}\right)^{1/2} \times \max\left\{1,\ \frac{0.1B_{\rm crit}}{B_{\rm pc}}\left(\frac{r}{R_{\rm s}}\right)^3\right\}\mathrm{GeV}. \qquad (22)$$

This formula is valid for the magnetic field lines with their footpoints at the outer rim of the polar cap, of colatitude $\theta_{\rm pc}$ (eq. 5), hence the dependence on $\sqrt{P}$. For other colatitudes θ the formula should be multiplied by $\theta_{\rm pc}/\theta$.

6.3. Synchrotron radiation

Consider a particle of energy γmc^2 gyrating around a local field line at a pitch angle ψ. Let $\gamma_\parallel$ denotes the Lorentz factor of the reference frame co-moving with the center of the gyration. As long as $\gamma_\parallel \gg 1$ it relates to the pitch angle ψ via $\sin\psi \approx \gamma_\parallel^{-1}$. The energy available for synchrotron emission at the expense of the particle is $\gamma_\perp mc^2$, and $\gamma = \gamma_\perp\,\gamma_\parallel$.

The rate of SR cooling reads

$$\dot\gamma_{\rm sr} = -\frac{2}{3}\,\frac{r_0^2}{m_{\rm e}c}\,B^2\gamma_\perp^2 = -\frac{2}{3}\,\frac{r_0^2}{m_{\rm e}c}\,B^2\sin^2\psi\,\gamma^2. \qquad (23)$$

In comparison to the CR cooling it is enormous (due to much smaller curvature radius).

Critical photon energy (analogous to (18)) reads

$$\varepsilon_{\rm sr} = \frac{3}{2}\,\hbar\,\frac{eB}{m_{\rm e}c}\gamma^2\sin\psi. \qquad (24)$$

For a monoenergetic injection function of particles ($e^\pm$-pairs in the context of this review) and their cooling due to SR the energy spectrum of SR spreads between a high-energy limit $\varepsilon_{\rm sr}(\gamma_0)$ set by γ_0 of the injected (created) particles, and a low-energy turnover $\varepsilon_{\rm ct}$ determined by the condition $\gamma_\perp \sim 1$:

$$\varepsilon_{\rm ct} \equiv \varepsilon_{\rm sr}(\gamma = \gamma_\parallel) = \frac{3}{2}\,\hbar\,\frac{eB}{m_{\rm e}c}\,\frac{1}{\sin\psi}. \qquad (25)$$

The spectrum assumes a single power-law shape $f_\varepsilon(\varepsilon) \propto \varepsilon^{-1/2}$ (and accordingly – $\varepsilon f_\varepsilon(\varepsilon) \propto \varepsilon^{+1/2}$) above the turnover. Below $\varepsilon_{\rm ct}$, the spectrum f_ε changes it slope, asymptotically reaching $\propto \varepsilon^{+2}$. It is built up by contributions from low-energy tails emitted by particles with $\gamma_\perp \gg 1$, and each low-energy tail cuts off at local gyro-frequency, which in the reference frame co-moving with the center of gyration is $\omega_B = \frac{eB}{m_e c\,\gamma_\perp}$. The spectrum of SR calculated with Monte-Carlo method to model the Vela pulsar is shown in Fig.4 as a dashed line. The low-energy part of the SR spectrum at $\varepsilon_{\rm ct}$ seems to be essential for connecting the RXTE and the OSSE points.

Synchrotron as well as cyclotron emission become prohibited at strong local magnetic fields $B \gtrsim 0.1\,B_{\rm crit}$ (Usov & Melrose 1995, Arendt & Eilek 2001) – the magnetic photon absorption proceeds here close to the threshold, and

the pairs created do not occupy excited Landau levels. In consequence, electromagnetic cascades are expected to be notably weaker than for $B < 0.1\,B_{\rm crit}$. Along with photon splitting (Baring & Harding 2001), this may explain why do radio pulsars avoid the high-B region in the $P-\dot{P}$ diagram.

6.4. Magnetic Inverse Compton Scattering

Consider an electron with a Lorentz factor γ moving along a magnetic field line $\boldsymbol{B}$ and a photon of energy $\varepsilon = \epsilon mc^2$ moving at angle $\arccos\mu$ to the field line. In the reference frame comoving with the electron (primed symbols) the counterpart of the free-space Compton formula, due to energy-momentum conservation appropriate for collisions with the electron at the ground Landau level both in the initial and final state, reads

$$\epsilon'_s = \left(1-{\mu'_s}^2\right)^{-1}\left\{1+\epsilon'(1-\mu'\mu'_s) - \left[1+2\epsilon'\mu'_s(\mu'_s-\mu')+{\epsilon'}^2(\mu'_s-\mu')^2\right]^{1/2}\right\} \quad (26)$$

where $\epsilon' = \epsilon\gamma(1-\beta\mu)$ (Herold 1997), and symbols with no subscript and with the subscript 's' refer to the state before the scattering and after the scattering, respectively. A longitudinal momentum of the electron in the electron rest frame changes due to recoil from zero to $(\epsilon'\mu' - \epsilon'_s\mu'_s)mc$.

The polarization-averaged relativistic magnetic cross section in the Thomson regime may be approximated with a non-relativistic formula (Dermer 1990):

$$\sigma = \frac{\sigma_T}{2}\left(1-{\mu'}^2+(1+{\mu'}^2)\left[g_1+\frac{g_2-g_1}{2}\right]\right) \quad (27)$$

where σ_T is the Thomson cross section, and g_1 and g_2 are given by

$$g_1(u) = \frac{u^2}{(u+1)^2}, \qquad g_2(u) = \frac{u^2}{(u-1)^2+a^2} \quad (28)$$

where $u \equiv \epsilon'/\epsilon_B$, $a \equiv 2\alpha\epsilon_B/3$, $\epsilon_B \equiv \hbar eB/m^2c^3$ and α is a fine-structure constant. The resonance condition for the scattering is therefore the cyclotron resonance $\epsilon' = \epsilon_B$. The factor a represents a 'natural' broadening of the resonance due to finite lifetime at the excited Landau level.

In the Klein-Nishina regime ($\epsilon' > 1$) the relativistic magnetic cross section for the $|\mu'| \approx 1$ case becomes better approximated with the well known Klein-Nishina relativistic non-magnetic total cross section σ_{KN} (Daugherty & Harding 1986, Dermer 1990).

The rate $\mathcal{R}$ of scatterings subject by an electron moving across the field of soft photons, measured in the lab frame is

$$\mathcal{R} = c\int d\Omega \int d\varepsilon\ \sigma\left(\frac{dn_{\rm ph}}{d\varepsilon d\Omega}\right)(1-\beta\mu) \quad (29)$$

where $\Omega = d\mu d\phi$ is the total solid angle subtended by the source of soft photons, $\mu = \cos\theta$, σ is a total cross section for the process, and $dn_{\rm ph}/d\varepsilon/d\Omega$ is the local density of the soft photons.

The properties of the field of soft photons are usually simplified by taking $dn_{\rm ph}/d\varepsilon/d\Omega$ as for the blackbody radiation. This simplification should be taken with care since magnetised atmospheres of neutron stars introduce strong anisotropy as well as spectral distortions to the outgoing radiation (Pavlov et al. 1994). Effectively it means that the ICS effects obtained with this simplification are just upper limits to the actual effects.

To estimate electron cooling rate $\dot{\gamma}_{\rm ICS}$ due to the ICS the differential form of (27) is necessary:

$$\frac{d\sigma}{d\Omega'_s} = \frac{3\sigma_T}{16\pi}\left[(1-{\mu'}^2)(1-{\mu'_s}^2) + \frac{1}{4}(1+{\mu'}^2)(1+{\mu'_s}^2)(g_1+g_2)\right] \quad (30)$$

(eg. Daugherty & Harding 1989), where $d\Omega'_s = d\phi'_s d\mu'_s$ is an increment of solid angle into which outgoing photons with energy ϵ'_s in the electron rest frame are directed. The mean electron energy loss rate then reads

$$\dot{\gamma}_{\rm ICS} = -c\int d\epsilon \int d\Omega\left(\frac{dn_{\rm ph}}{d\epsilon d\Omega}\right)(1-\beta\mu)\times \times \int d\Omega'_s\left(\frac{d\sigma}{d\Omega'_s}\right)(\epsilon_s-\epsilon) \quad (31)$$

where $\epsilon_s = \epsilon'_s\gamma(1+\beta\mu'_s)$ is the scattered photon energy in the lab frame (e.g. Dermer 1990).

The spectrum of magnetic ICS calculated numerically to model the Vela pulsar is shown in Figs.4 and 5 with thin solid line. The blackbody soft photons originating at the stellar surface (dotted line) are upscattered by secondary $e^{\pm}$-pairs at the expense of their "longitudinal" energy $\gamma_{\|}mc^2$, assumed to remain unchanged during the burst of synchrotron emission. Without the ICS component due to the $e^{\pm}$-pairs the RXTE data for the Vela pulsar would be difficult to reproduce within the model. It is worth to note, that the magnetic ICS component due to primary electrons (not shown in Fig.4) is energetically insignificant comparing to the CR component.

6.5. Photon splitting

Photon splitting into two photons in the presence of magnetic field B is a third-order QED process with no energy threshold (Adler 1971). The attenuation coefficient, after averaging over the polarization states, reads (Harding et al. 1997)

$$T_{\rm split}(\epsilon) \approx \frac{\alpha^3}{10\pi^2}\frac{1}{\lambda\!\!\!^{-}_{\rm c}}\left(\frac{19}{315}\right)^2\left(\frac{B\sin\theta_{\rm kB}}{B_{\rm crit}}\right)^6\epsilon^5\ {\rm cm}^{-1}, \quad (32)$$

(provided B does not exceed $B_{\rm crit}$ substantially) where α is a fine structure constant, ϵ is the photon energy in units of mc^2, $\theta_{\rm kB}$ is the angle between photon momentum vector and the local magnetic field. The process, therefore, strongly depends on magnetic field strength B.

Photon splitting has attracted substantial interest in recent years due to the discovery of neutron stars with supercritical magnetic fields (Mereghetti 1999). It has been analyzed in details by Harding et al. 1997 and incorporated in a Monte Carlo code tracing the propagation of electromagnetic cascades in the magnetospheres of high-B pulsars. The effect was found to explain satisfactorily the unusual cut-off observed in the gamma-ray spectrum of B1509-58 (see Sect.3). Generally, it becomes competitive to the magnetic pair creation for dipolar magnetospheres with $B_{\rm s} \gtrsim 0.3B_{\rm crit}$ (Harding et al. 1997). The degradation of photon energy in the course of splitting inhibits also any development electromagnetic cascades. In consequence, high-B RPP should not emit coherent radio emission. Indeed, there exists a high-B region in the $P-\dot{P}$ diagram void of radio pulsars. Even though three recently discovered (during The Parkes Multibeam Pulsar survey) high-B ra-

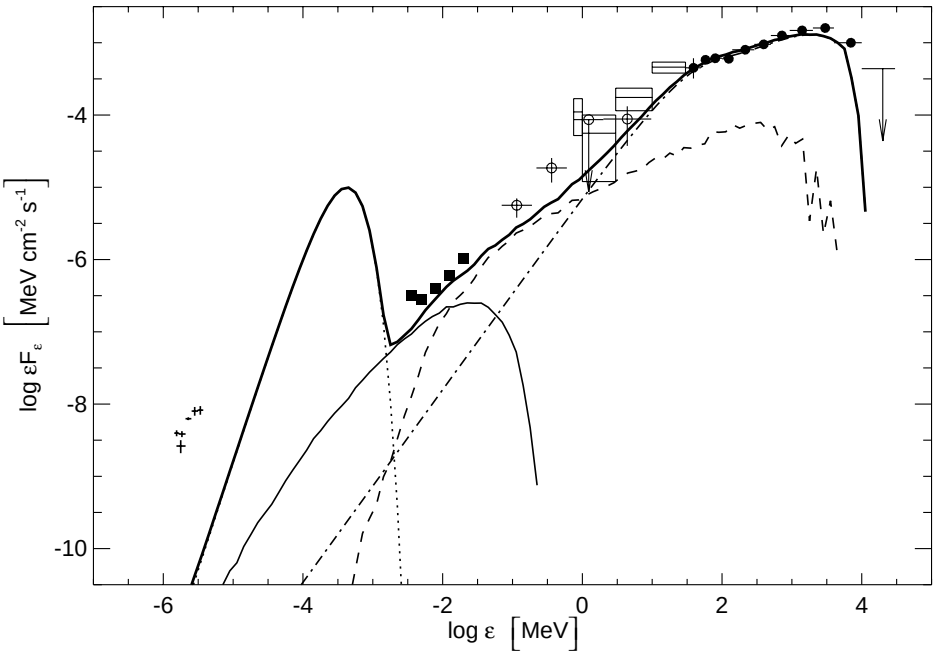


Fig. 4. The model energy spectrum calculated by Dyks & Rudak 2002a to reproduce the spectral features of the Vela pulsar ($P = 89$ ms, $B_s = 6 \times 10^{12}$G). The accelerator is located at $h_0 = 3R_s$ above the surface (see Sect.6). The broad–band spectrum consists of four components due to: curvature radiation of primary electrons (dot-dashed), synchrotron radiation of secondary $e^{\pm}$–pairs (dashed), inverse Compton scattering of surface X-ray photons on the $e^{\pm}$–pairs (thin solid) and the blackbody surface emission (dotted). The surface temperature $T_s = 1.26 \times 10^6$K was assumed for the neutron star. Total spectrum is given by a thick solid line. Phase-averaged data points for Vela from different telescopes are indicated: crosses – multicolor photometry with NTT and HST (Mignani & Caraveo 2001); filled squares – RXTE (Strickman et al. 1999); open circles – OSSE (Strickman et al. 1996); rectangles – COMPTEL (Schönfelder et al. 2000); filled circles plus an upper limit just above 10 GeV – EGRET (Thompson et al. 1997).

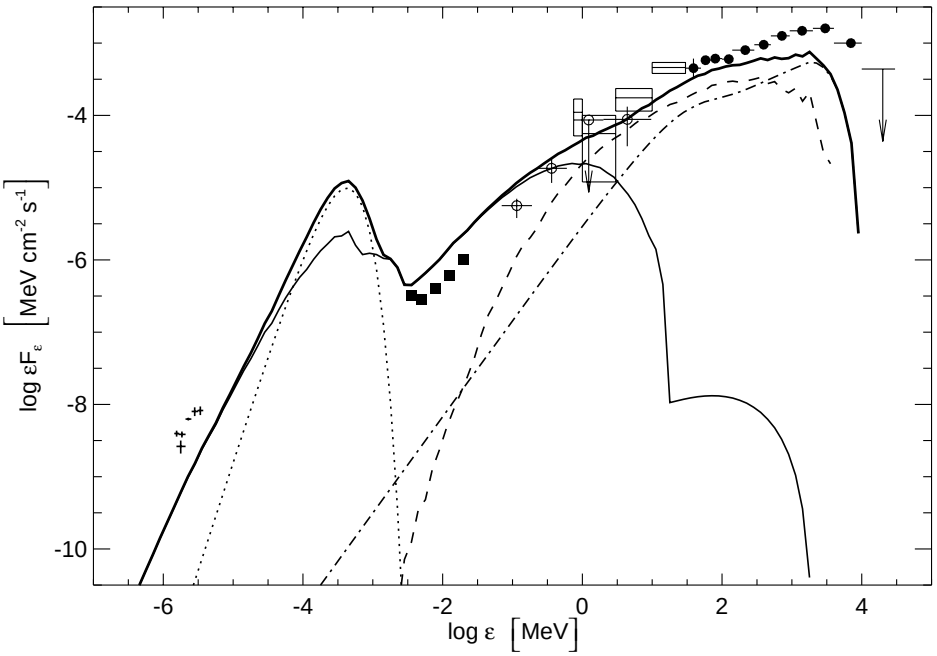


Fig. 5. Same as Fig. 4 but with two parameters changed drastically ($B_s = 0.6 \times 10^{12}$G, $h_0 = 0$) in order to obtain as much power in the optical range as possible by modifying the ICS component due to $e^{\pm}$–pairs (thin solid line). Despite unrealistically favorable conditions to down-scatter some of the blackbody photons, the low-energy tail of the ICS component falls short by a factor of ~ 3 below the observed optical flux level (crosses).

dio pulsars (Camilo et al. 2000) are located above the formal limiting line derived in Barring & Harding 1998 (and elaborated in Baring & Harding 2001), the general argument that magnetars are expected to be radio-quiet RPP remains valid (Zhang & Harding 2000b).

7. Facing the Vela pulsar

In order to fit our model to the phase averaged spectrum of Vela over almost 8 decades in energy (see Fig.4) we were forced to locate the accelerator at the altitude of $h_0 \simeq 3\,R_{\rm s}$, i.e. unrealistically high for any version of polar-cap models. The same problem was encountered by Daugherty & Harding 1996 when modeling the CGRO data points of Vela.

Physical justification for lifting the accelerator up to $\sim 1\,R_{\rm s}$ might rely on a mechanism proposed by Harding & Muslimov 1998a. They considered a sandwich-like structure of two pair formation fronts (PFF), controlled by either CR or ICS, where the lower PFF would be formed due to positrons returning from the upper PFF. With reasonable surface temperatures ($T_{\rm s} \sim 5 \times 10^5$K) it is ICS which dominates (comparing to CR) in generating high-energy quanta at the energetic expense of upward moving electrons and downward moving positrons. Such a situation is not symmetrical and not stable, therefore. Accordingly, the lower PFF tends to elevate until the CR-cooling takes over, which happens at $h_0 \sim 1\,R_{\rm s}$. Unfortunately, this mechanism – rather promising in the context of required $h_0 \simeq 3\,R_{\rm s}$, even though $3\,R_{\rm s}$ is still notably more than $\sim 1\,R_{\rm s}$ – has been invalidated by recent numerical calculations: Harding & Muslimov 2002 concluded the inability of ICS-controlled upper PFFs to develope lower PFFs because of too low multiplicities in such cases.

The requirement of high-altitude accelerator for Vela is likely to be extended to other gamma-ray pulsars. A piece of hint for such a requirement comes from a strong correlation for known gamma-ray pulsars between the inferred magnetic field strength and the value of high-energy cutoff (Baring & Harding 2000). [*Note, that this empirical correlation speaks in favor of high-energy cutoffs in pulsar spectra originating due to magnetic absorption of gamma-rays – a signature of polar-cap models.*] This is shown in Fig.6 along with the dependence of $\varepsilon_{\rm cutoff}$ on the location of photon emission point r according to eq.(22).

Last but not least – a real challenge for all contemporary models for Vela comes from the phase-resolved spectral analysis of pulsed hard X-rays and the phasing of the lightcurves in optical, X-rays and gamma-rays, presented by Strickman et al. 2001 and Harding et al. 2002. The strong double-peak lightcurve in optical (fig.1 in these refs.) is particularly enigmatic. The peak-to-peak separation is notably smaller than in HE domain. Moreover, the leading peak has no counterpart in any other energy range (including the radio). The trailing optical peak seems to be associated with the trailing RXTE peak and with the trailing gamma-ray peak, though the latter lags behind the trailing optical by about 0.1 in phase. Extrapolation of the gamma-ray spectrum taken for either of the two gamma-ray peaks falls below the phase-averaged optical flux level (by a factor ~ 10 in the case of the trailing gamma-ray peak).

The problem of optical emission is also difficult to solve in the framework of our phase-averaged approach to model the spectrum of Vela. A difficult task we have faced was to find a component (without referring to any ingredients external to the model) that would account for the optical emission, at least in some particular circumstances. Fig.5 gives an example of what can be achieved at best in the optical domain of the model spectrum, but at the price paid at the high-energy end of the spectrum.

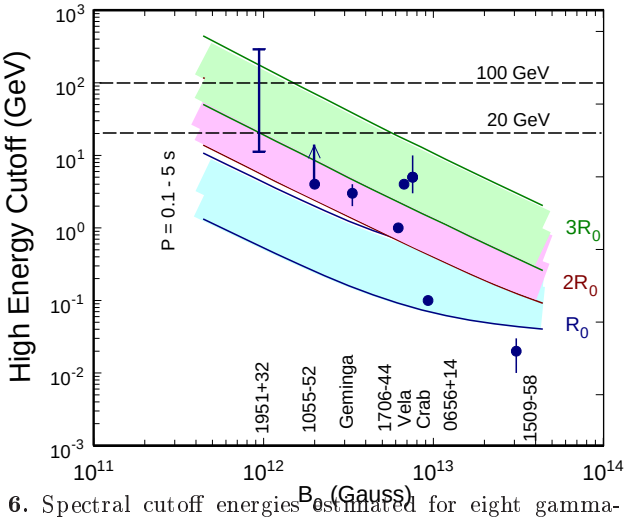


Fig. 6. Spectral cutoff energies estimated for eight gamma-ray pulsars are plotted against inferred surface magnetic field strengths $B_{\rm s}$. Three shaded bands (note the overlaps) indicate the location of $\varepsilon_{\rm cutoff}$ according to eq.(22) for three values of the emission altitude ($r = R_{\rm s}$, $2R_{\rm s}$ and $3R_{\rm s}$) and for the range of spin periods P between 0.1 and 5 s. (From Baring & Harding 2000 and Baring 2001; courtesy of Matthew Baring.)

8. Millisecond pulsars

The question of whether millisecond pulsars (i.e. with low magnetic fields) do emit gamma-rays will be hopefully answered within the next five years with GLAST. On theoretical side, there had been some attempts to address this problem. For instance, Wei et al. 1996 presented broad-band spectra of both pulsed and unpulsed emission expected in their version of the outer-gap model. In the framework of polar-cap scenarios, Sturner & Dermer 1994 made their predictions for gamma-ray luminosity L_γ by scaling down with B their analytical formulae for L_γ for classical pulsars. Rudak & Dyks 1998 proposed a modification of the model by Daugherty & Harding 1982; this modification incorporates a contribution of electron-positron pairs to L_γ, which becomes a non-monotonic function of B (see Figs. 7 and 8 of Dyks 1998). One of the consequences of this modification is that expected values of L_γ for millisecond pulsars, including J0437-4715, are typically about one or two orders of magnitude lower than for classical pulsars (see Fig.3 in section 3). Quantitatively similar estimate, though for a different reason, comes from the model of Dermer & Sturner 1994. If these estimates are correct then some millisecond pulsars, including J0437-4715 (see Fig.7), should be detected with next-generation experiments, providing thus a testing ground for magnetospheric models relevant for millisecond pulsars. GLAST is expected to have sensitivity above 100MeV about

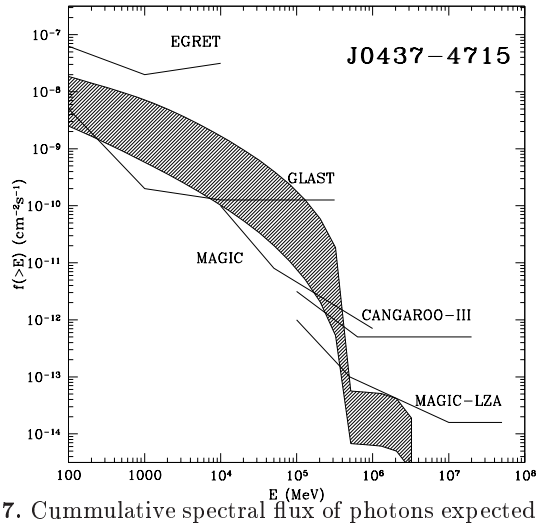


Fig. 7. Cummulative spectral flux of photons expected for the millisecond pulsar J0437-4715 at a distance of 140 pc. The shaded region shows the range of flux levels due to uncertainty in the maximal energy of primary electrons. The main part of the spectrum is due to curvature radiation of the electrons. The additional feature reaching the VHE domain is due to inverse Compton scattering of soft photons from the surface with the temperature 4×10^5K. Sensitivities of EGRET as well as three major HE and VHE experiments of the future are also indicated. MAGIC–LZA denotes sensitivity of MAGIC in its Large Zenith Angle mode. (After Bulik et al. 2000).

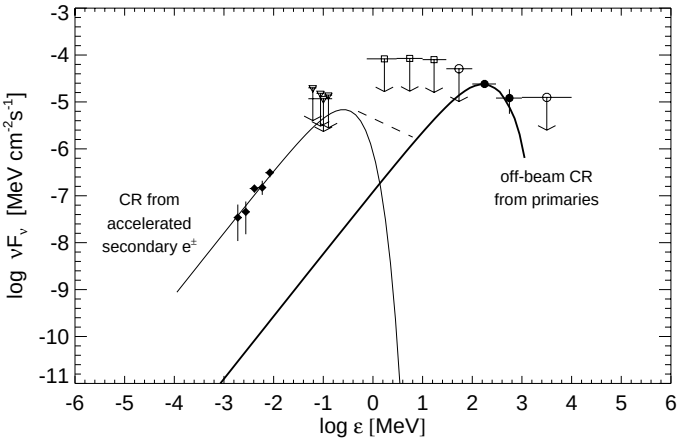


Fig. 8. Two-component theoretical spectrum for the off-beam geometry (continuous lines) is compared with the spectrum observed for PSR J0218+4232 (diamonds – BeppoSAX, triangles – OSSE, squares – COMPTEL, circles – EGRET). The low energy component is due to curvature radiation from secondary $e^{\pm}$ pairs (with energy $\sim 10^5$MeV acquired upon their acceleration in a residual electric field), whereas the high-energy component is due to curvature radiation from primary electrons (with energy $\sim 10^7$MeV). (From Dyks & Rudak 2002.)

30 times higher then EGRET, and it will reach high-energy limit at 300GeV - closing thus for the first time the energy gap between the VHE (very high energy) domain accessible with ground-based Cherenkov techniques and the HE (high energy) domain of satellite experiments (Kamae et al. 2000). Moreover, millisecond pulsars are expected to radiate mostly in the range between 10GeV and 100GeV, this class of objects should be of interest for the upcoming IAC telescope MAGIC (Blanch et al. 1998).

For the time being, the only millisecond pulsar marginally detected above 100 MeV (at $3.5\,\sigma$ level) is PSR J0218+4232, with the spin period $P = 2.3$ ms and the inferred magnetic field $B_{\rm pc} \simeq 8.6 \times 10^8$ G, (Verbunt et al. 1996). The inferred luminosity of the pulsed emission for 1 steradian opening angle reaches $L_\gamma \simeq 1.64 \times 10^{34}$erg s^{-1} $\simeq 0.07\,L_{\rm sd}$. Broad-band spectrum of this pulsar differs from the HE spectra known for young gamma-ray pulsars: above 100 MeV the photon index $\alpha_{\rm ph} \sim -2.6$ (Kuiper et al. 2000) and the spectrum resembles soft spectra of EGRET UID sources; within the BeppoSAX range the spectrum is extremely hard, with $\alpha_{\rm ph} \simeq -0.61 \pm 0.32$ (Mineo et al. 2000). Off-beam geometry (i.e. the line of sight misses the hollow cone beam) was recently proposed (Dyks & Rudak 2002) for this pulsar. In such a situation the high energy "cutoff" occurs at a relatively low energy ~ 100 MeV (marked by two EGRET points, see Fig.8). Unlike in on-beam cases, this cutoff is not due to magnetic absorption; it corresponds to a maximum energy of those electrons which emit curvature photons towards the observer. The shape of the apparent cut-off can easily mimic very soft spectra (Harding & Zhang 2001 used similar viewing geometry arguments to explain very soft spectra of EGRET UID sources). The BeppoSAX points are explained in this model as due to curvature radiation of secondary $e^{\pm}$ pairs accelerated within the polar gap. Upon the acceleration in a residual electric field, the $e^{\pm}$ pairs should reach the energy $\gamma_{\parallel}$ between 1.5×10^5 and 6×10^5, which is about 1% of the primary electron energy. A few hundred of pairs per primary electron are required to be accelerated in order to reproduce the BeppoSAX level. According to Harding & Muslimov 2001 and 2002, acceleration of such a large number of pairs within the polar gap is difficult to achieve.

9. Viewing geometry effects

Viewing geometry has been recognized as an important factor in shaping the lightcurves as well as broadband energy spectra of particular objects (like e.g. the Vela pulsar, see Harding & Muslimov 1998) as well as in the context of EGRET UID galactic sources (e.g. recent review by Baring 2001).

To taste a variety of apparent pulsar characteristics accessible upon changing the viewing angle ζ we present here two cases: of a classical pulsar in Fig.9 and a millisecond pulsar in Fig.10. The lightcurves (these are energy-integrated above 100 MeV) and the gamma-ray spectra were calculated with our numerical code. The spectra are two-component: due to curvature and synchrotron emission; inverse Compton scattering was neglected. The effects of aberration and light travel delays were included. These effects are important for millisecond pulsars, and affect their lightcurves, especially at large inclination angles α (the case not shown here). Whenever the line of sight misses outer rim of the polar cap, the observed spectra become soft with an apparent exponential (and not super-exponential) decay, mimicking thus an outer-gap candidate. The millisec-

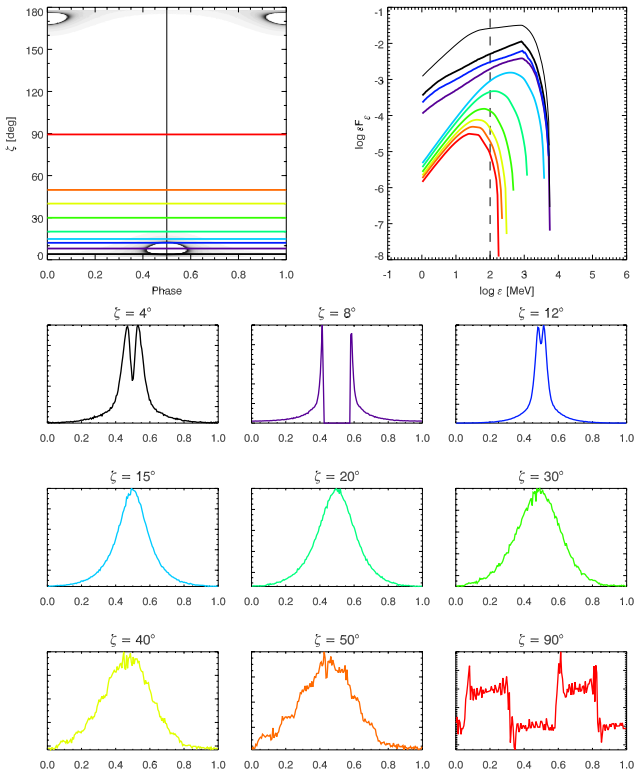


Fig. 9. The characteristics of high energy radiation expected from a classical pulsar with $P = 0.1$ s, $B = 10^{12}$ G and the magnetic dipole inclination $\alpha = 8^{\circ}$. The top left panel shows the intensity distribution for radiation above 100 MeV as a function of rotational phase ϕ and viewing angle ζ. Horizontal color-coded lines correspond to the position of nine observers located at different angles ζ. For each ζ the phase-averaged spectrum drawn with color-coded line is shown in top right panel. The corresponding pulse profiles are shown in small panels labelled with ζ. The spectrum of total luminosity from the pulsar (thin solid line in top right panel) is plotted (at an arbitrary level relative to the phase-averaged spectra) for comparison of the shapes. (From Woźna et al. 2002).

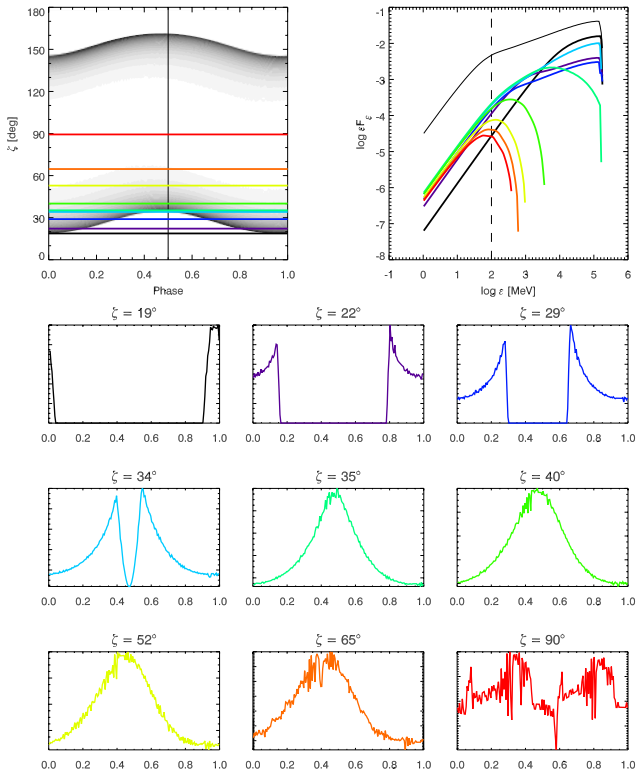


Fig. 10. Same as fig.9, but for a millisecond pulsar with $P = 2.3$ ms, $B = 10^{9}$ G and different set of viewing angles ζ. (From Woźna et al. 2002).

ond gamma-ray pulsar J0218+4232 (Fig.8) is probably a good example of such a case.

10. Concluding remarks

High-energy astrophysics of pulsars was challenged by unexpected richness of spectral and temporal properties found for the brightest gamma-ray pulsars. Numerous modifications (both, minor and major) to the existing models of magnetospheric activity are being invented to accommodate at least some of these properties. It is clear, however, that we actually need good quality high-energy data for much weaker sources. Only then it will be possible to asses on statistical grounds the significance of those properties (the argument used by many authors, recently reiterated strongly by Baring 2001). Chances are that it may have happen in a few years time.

The planned observatory GLAST (Kamae et al. 2000) will be superior to EGRET in two aspects. First, its sensitivity at 10 GeV will be more than two orders of magnitude better than that of EGRET. Second, it will reach energy of 300 GeV, closing thus for the first time the energy gap between satellite and ground-based observatories (HE and VHE, respectively). The MAGIC Telescope (Blanch et al. 1998) – a 17 m diameter Imaging Air Cherenkov Telescope (IACT) – is expected to operate with sensitivity about three orders of magnitude higher at 10 GeV than EGRET. Its advanced technology will make possible to cover energy range between 10 GeV and 1 TeV, and to reach ~ 50 TeV in the Large Zenith Angle mode. Energy ranges of GLAST and MAGIC will overlap over more than one decade in energy.

We expect that the question of whether millisecond pulsars emit gamma-rays at all, will be answered relatively easily with these high-sensitivity observatories, verifying at first the status of J0218+4232.

In the context of numerous positive detections anticipated at hard gamma-rays, inclusion of viewing geometry effects will be of particular importance to properly interpret the observed shapes of spectral turnovers at high-energy ends.

To tackle high-quality data of the future in the most effective way, numerical 3D codes should be developed, capable of fast tracing the development and propagation of electromagnetic cascades in variety of non-dipolar realizations of magnetic field structure. Relaxing the centered-dipole assumption as a first step would be very much in line with recent conclusions from the soft X-ray data analysis for neutron stars

(Pavlov et al. 2002). Optical to gamma-ray properties of Vela (section 7) are in our opinion a signature of a strongly non-axisymmetric hollow cone of radiation around the magnetic axis. Strong deviations of the actual magnetic field structure from a pure dipole at the stellar surface may well be responsible for inducing this axial asymmetry already at the site of electron acceleration. (Recently, multipolar character of open field lines has been considered in a quantitative way by Gil et al. 2002 to justify radio pulsars with vacuum gap solutions in pulsars with super-strong magnetic fields.) An advantage of incorporating multipolar components to the polar-cap models is twofold:

1) magnetic field strength may locally be lowered slightly, opening thus windows for GeV photons to escape without magnetic attenuation; postulating high-altitude accelerators would be then unnecessary.

2) directional characteristics of high-energy radiation would change notably with respect to the dipolar axis at higher altitudes, where radio emission is generated.

Acknowledgements. This work was supported by the KBN grants: 2P03D02117 (BR, TB) and 5P03D02420 (JD).

References

Adler, S.L., 1971, Ann.Phys., 67, 599

Arendt, P.N.,Jr., Eilek, J.A., 2000, In: *IAU Coll. 177, Pulsar Astronomy - 2000 and Beyond* ed. M. Kramer, N. Wex, R. Wielebinski (ASP Conference Series, 202, 445

Arons, J., 2000, In: *IAU Coll. 177, Pulsar Astronomy – 2000 and Beyond* ed. M. Kramer, N. Wex, R. Wielebinski (ASP Conference Series, 202, 449

Arons, J. & Scharlemann. E.T., 1979, ApJ, 231, 854

Baring, M.G., 2001, Proc. Tonantzintla Workshop, eds. A. Carramiñana et al. (Kluwer Academic, Dordrecht), astro-ph/0106161

Baring, M.G. & Harding, A.K., 1998, ApJ, 507, L55

Baring, M.G. & Harding, A.K., 2000, Bull. AAS, 32, 12.43

Baring, M.G. & Harding, A.K., 2001, ApJ, 547, 929

Becker, W., 2002, this proceedings

Becker, W. & Truemper, J., 1997, A&A, 326, 682

Becker, W. & Truemper, J., 1999, A&A, 341, 803

Beskin, V.S., 1990, Sov. Astron. Lett., 16(4), 286

Blanch, O. et al., 1998, 'The MAGIC telescope', Letter of Intent

Bulik, T., Rudak, B., Dyks, J., 2000, MNRAS, 317, 97

Camilo, F. et al., 2000, ApJ, 541, 367

Chen, K. & Ruderman, M., 1993, ApJ, 402, 264

Cheng, K.S. & Zhang, L., 1999, Fundamentals of Cosmic Physics, 20, 177

Cheng, K.S., Ho, C., Ruderman, M.A., 1986, ApJ, 300, 500

Cheng, K.S., Ho, C., Ruderman, M.A., 1986, ApJ, 300, 522

Daugherty, J.K. & Harding, A.K., 1982, ApJ, 252, 337

Daugherty, J.K. & Harding, A.K., 1983, ApJ, 273, 761

Daugherty, J.K. & Harding, A.K., 1986, ApJ, 309, 362

Daugherty, J.K. & Harding, A.K., 1989, ApJ, 336, 861

Daugherty, J.K. & Harding, A.K., 1994, ApJ, 42, 325

Daugherty, J.K. & Harding, A.K., 1996, ApJ, 458, 278

Dermer, C.D., 1990, ApJ, 360, 197

Dermer, C.D. & Sturner, S.J., 1994, ApJ, 420, L75

Dyks, J., 1998, Acta Astron., 48, 355

Dyks, J. & Rudak, B., 2000a, A&A, 362, 1004

Dyks, J. & Rudak, B., 2000b, A&A, 360, 263

Dyks, J. & Rudak, B., 2000c, MNRAS, 319, 477

Dyks, J. & Rudak, B., 2002, *XXIInd Moriond Meeting 'The Gamma-Ray Universe'*, in press (astro-ph/0205222)

Dyks, J. & Rudak, B., 2002a, in preparation

Dyks, J., Rudak, B., Bulik, T., 2001, Proc. of the 4th INTEGRAL Workshop, ESA SP, 459, 191,

Erber, T., 1966, Rev.Mod.Phys., 38, 626

Fierro, J.M. et al., 1995, ApJ, 447, 807

Gil, J., Melikidze, G.I., Mitra, D., 2002, A&A, 388, 235

[Goldreich & Julian 1969]Goldreich, P. & Julian, W.H., 1969, ApJ, 157, 869

Gotthelf, E.V. et al., 2000, ApJ, 542, L37

Halpern, J.P. & Wang, F.Y.-H., 1997, ApJ, 477, 905

Harding, A.K., Baring, M.G., Gonthier, P.L., 1997, ApJ, 476, 246

Harding, A.K., Contopoulos, I., Kazanas, D., 1999, ApJ, 525, L125

Harding, A.K. et al., 2002, ApJ, in press (astro-ph/0205183)

Harding, A.K. & Muslimov, A.G., 1998, ApJ, 500, 862

Harding, A.K. & Muslimov, A.G., 1998a, ApJ, 508, 328

Harding, A.K. & Muslimov, A.G., 2001, ApJ, 556, 987

Harding, A.K. & Muslimov, A.G., 2002, ApJ, 568, 862

Harding, A.K. & Zhang, B., 2001, ApJ, 548, L37

Herold, H., 1979, Phys.Rev.D, 19, 2868

Jessner, A., Lesch, H., Kunzl, T., 2001, ApJ, 547, 959

Kamae, T. et al., 2000, Adv.Sp.Res., 25, 905

Kanbach, G., 2002, this proceedings

Kluźniak, W. & Rudak, B., 1996, unpublished

Kuiper, L. et al., 1999, A&A, 351, 119

Kuiper, L. et al., 2000, A&A, 359, 615

Marshall, F.E. et al., 1998, ApJ, 499L, 179

Mereghetti, S., 1999, In: *NATO ASI The Neutron Star - Black Hole Connection*

Michel, F.C., 1974, ApJ, 192, 713

Michel, F.C., 1991, *Theory of Neutron Star Magnetospheres* (The University of Chicago Press, Chicago)

Mignani, R.P. & Caraveo, P.A., 2001, A&A, 376, 213

Mineo, T. et al., 2000, A&A, 355, 1053,

Muslimov, A.G. & Tsygan, A.I., 1992, MNRAS, 255, 61

Nel, H.I. et al., 1996, ApJ, 465, 898

Pavlov, G.G. et al., 1994, A&A, 289, 837

Pavlov, G.G. et al., 2002, this proceedings

Rudak, B. & Dyks, J., 1998, MNRAS , 295, 337

Rudak, B. & Dyks, J., 1999, MNRAS , 303, 477

Ruderman, M.A. & Sutherland, P.G., 1975, ApJ, 196, 51

Saito, Y. et al., 1997, ApJ, 477, L37

Saito, Y. et al., 1998, In: *Neutron Stars and Pulsars: Thirty Years after the Discovery* ed. N. Shibazaki, et al. (Universal Academy Press: Tokyo) pp.295-298

Sako, T. et al., 2000, ApJ, 537, 422

Schönfelder, V. et al., 2000, A&AS, 143, 145

Schroeder, P.C. et al., 1995, ApJ, 450, 784

Strickman, M.S. et al., 1996, ApJ, 460, 735

Strickman, M.S., Harding, A.K., de Jager, O.C., 1999, ApJ, 524, 373

Strickman, M.S. et al.. 2001, In: *Gamma-Ray Astrophysics 2001* ed. S. Ritz et al. (AIP), 570

Sturner, S.J., 1995, ApJ, 446, 292

Sturner, S.J. & Dermer, C.D., 1994, A&A, 281, L101

Sturner, S.J., Dermer, C.D., Michel, F.C., 1995, ApJ, 445, 736
Sturrock, P.A., 1971, ApJ, 164, 529
Takahashi, M. et al., 2000, In: *IAU Coll. 177, Pulsar Astronomy – 2000 and beyond* ed. M. Kramer, N. Wex, R. Wielebinski (ASP Conference Series , 202: 2000) pp.353-354
Taylor, J.H. et al., 1995, 'The Princeton Pulsar Database' (http://pulsar.princeton.edu)
Thompson, D.J., 2001, In: *International Symposium on High Energy Gamma-Ray Astronomy*, ed. F. A. Aharonian, & H. J. Völk, AIP Conference Proceedings, vol. 558, 103
Thompson, D.J. et al., 1997, In: *Fourth Compton Symposium* ed. by C.D. Dermer, M.S. Strickman, J.D. Kurfess (New York: AIP 1997) 410
Thompson, D.J. et al., 1999, ApJ, 516, 297
Usov, V.V. & Melrose, D.B., 1995, Aus.J.Phys., 48, 571
Verbunt, F. et al., 1996, A&A, 311, L9
Seward, F.D. & Wang, Z.-R., 1988, ApJ, 332, 199
Wei, D.M., Cheng, K.S., Lu, T., 1996, ApJ, 468, 207
Weekes, T.C., 2000, In: *GeV-TeV Gamma Ray Astrophysics Workshop: Towards a major atmospheric Cherenkov detector VI* ed. B.L. Dingus, M.H. Salamon, D.B. Kieda: AIP Conference Proceedings, Vol. 515., p.3 (New York: AIP)
Woźna, A. et al., 2002, *XXIInd Moriond Meeting 'The Gamma-Ray Universe'*, in press (astro-ph/0205224)
Xia, X.Y. et al., 1985, A&A, 152, 93
Young, M.D., Manchester, R.N., Johnston, S., 1999, Nature, 400, 848
Zhang, B. & Harding, A.K., 2000a, ApJ, 532, 1150
Zhang, B. & Harding, A.K., 2000b, ApJ, 535, L51
Zhang, B. & Qiao, G.J., 1998, A&A, 338, 62

Proceedings of the 270. WE-Heraeus Seminar on: *"Neutron Stars, Pulsars and Supernova Remnants"*
Physikzentrum Bad Honnef, Germany, Jan. 21-25, 2002, eds. W. Becker, H.Lesch & J. Trümper, MPE Report 278, pp. 155-158

On the Field-Aligned Particle Acceleration in the presence of Electron-Positron Pairs

S. Shibata[1], **J. Miyazaki**[2], **and F. Takahara**[2]

[1] Department of Physics, Yamagata University, 1-4-12 Kojirakawa, Yamagata 990, Japan
[2] Department of Earth and Space Science, Osaka University, 1-1 Machikaneyama, Toyonaka, Osaka 560-0043, Japan

Abstract. We study self-consistency for the pulsar polar cap model. In general, there will remain an unscreened electric field at the pair production front (PPF). We have derived the condition of electric field screening by pairs in the presence of returning particles. A previous belief that pairs with a density higher than the Goldreich-Julian density immediately screen out the electric field beyond PPF is unjustified. Pairs have little contribution on screening the electric field, and the geometrical screening is the only known way of getting a finite potential drop.

1. Introduction

One of the promising models for the pulsar action is the polar cap model where the field-aligned electric field accelerates charged particles up to TeV energies, and causes an electromagnetic shower. The potential drop is normally thought to be confined in a small region: the field-aligned electric field is screened out at the both ends of the accelerator (Fig. 1). The polar cap potential drop is a part of the electromotive force produced by the rotating magnetic neutron star. The voltage drop is a few percent of the available voltage for young pulsars, while it becomes some important fraction for older pulsars. The localized potential is maintained by a pair of anode and cathode regions, the formation mechanism of which is the long issue of the polar cap accelerator.

2. Pair Production Front (PPF) and Screening

If the field-aligned electric field is formed to accelerate particles up to the Lorentz factor of $10^6 - 10^7$, then a number of curvature gamma-photons convert into electron-positron pairs under strong magnetic field $\sim 10^{12}$ G above a surface, which may be called the pair production front (PPF). The expected multiplicity — number of pairs produced by one primary particle — is typically 10^3 within a distance $\sim 10^5$ cm.

In a number of literatures, it is assumed that the field-aligned electric field is screened out above PPF because the density of pairs is higher than the Goldreich-Julian (GJ) density. However, this screening process had not been studied in detail. Shibata, Miyazaki & Takahara (1998) showed that pair polarization is not efficient even if pair density is much higher than the GJ density. In their work, presence of the particles reflected backward by unscreened electric field was ignored. In this paper, taking the backward-moving particles into account, we derive an expression for the steady screening at PPF.

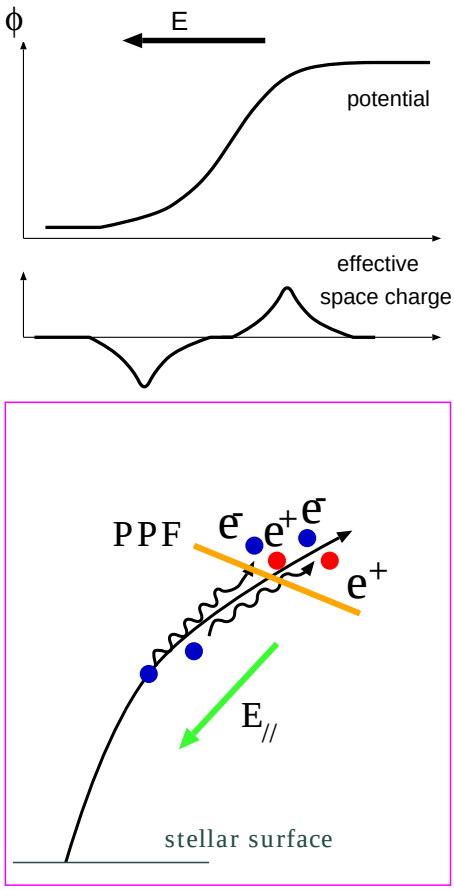


Fig. 1. localized potential drop

3. Model

Let us consider a model for the steady accelerator which has a finite potential drop along the magnetic field with the electric field screened at the both ends. For definite sign of charge, let us assume electrons are accelerated outwards, i.e., the electric field points toward the star. γ-rays emitted by the electrons convert into pairs beyond PPF continuously.

Schematic picture of the screening region is shown in Fig. 2. At the top panel, electrons are accelerated to the right, so the electric field points to the left. The gamma-rays emitted by the electrons are converted in to pairs above PPF (the right side of PPF in the figure). Since the pairs are created almost continuously in a half space to the right of PPF, the pair-flux monotonically increases with the coordinate x along the magnetic lines of force, where curvature is ignored since the scale considered here is very short.

The second panel indicates the pair flux $F(x)$, which is defined as the number of pairs created below x. The multiplication factor $m(x)$ may be much convenient: $F(x) = m(x)j_0$ where j_0 is the primary flux of electrons coming up from a region below PPF.

Here, it must be reminded that why the accelerating electric field is formed below PPF. The electric field well within the light cylinder is conveniently decomposed by the co-rotational and non-corotational fields:

$$\boldsymbol{E} = -\frac{\boldsymbol{\Omega} \times \boldsymbol{r}}{c} \times \boldsymbol{B} - \boldsymbol{\nabla}\Phi, \tag{1}$$

where Φ is the non-corotational electric potential, and field aligned electric field is given by $E_\parallel = -\boldsymbol{B} \cdot \boldsymbol{\nabla}\phi/B$. The Poisson equation for Φ reads

$$-\nabla^2\phi = 4\pi(\rho - \rho_0), \tag{2}$$

where $\rho_0 \approx \Omega B_z/2\pi c$ is the GJ charge density. From this expression it follows that the anode region is formed where $\rho > \rho_0$, and the cathode region is formed where $\rho < \rho_0$. In the screened region, $\rho = \rho_0$.

In our sign convention, the GJ density is negative, and electronic flow with super-GJ density can produce cathode (negative) region, which is located above the stellar surface (see Fig. 1). There must be such a negative region below the PPF. Above PPF, created pair positrons will be returned back by the electric field, so they can destroy the cathode region. This fact sets a constraint to the flux of pair positrons. In the problem of electric field screening, one needs an anode region where the effective charge $\rho - \rho_0$ is positive. There are two possible ways of producing the anode region. One is the 'geometrical effect', and the other is pair polarization.

The geometrical effect is cased by the fact that the GJ charge density is proportional to the magnetic component along the rotation axis B_z while the charge density of the electronic flow is proportional to the magnetic field strength, or equivalently inversely proportional to the cross sectional area of the magnetic flux tube if the flow velocity is $\approx c$ (constant). Therefore, if the flow is curving toward the rotation axis, the GJ density decreases slower than the primary electronic charge density so that the electronic charge is insufficient to compensate the GJ density, and the anode is formed. This effect is effective, and the accelerating electric field can be terminated without pair creation. Although geometrical screening is effective, PPF can in general appear before geometrical screening. If this is the case, dynamics of pairs just after PPF will be important.

Our interest in this paper is not the geometrical screening but the pair effect. In general, at PPF, whatever values of the effective charge can be; it can even be negative so that anode formation relay only on pair polarization.

As shown in Fig. 2, pair electrons are accelerated while pair positrons are decelerated after their birth. As far as the speed of pair positron is relativistic, net space charge due to pairs are essentially zero. However, once the pair positron become non-relativistic, positive space charge appears owing to charge conservation. This is the effect which produces anode charge. If the electric field is strong enough, some positrons are reflected backward and weaken the cathode space charge. Assuming steadiness, one can relate the strength of the electric field to the pair creation rate, the returning positron flux, and the effective space charge before PPF. If the pair creation rate is more or less uniform, one can do this analytically as shown in the following section. Then, we have an screening condition.

4. Results

If the pair creation rate is more or less uniform, the screening condition with returning positron can be derived analytically. Detailed calculation will be published near future, but main results are discussed below.

The field-aligned electric field $E_\parallel$ at PPF is screened if the following two conditions are satisfied:

$$\frac{1}{2}E_{\rm f}^2 = j\alpha_\phi[\phi_1(2-\phi_1)+\zeta] - (j - j_0 - jM_1)\phi_{\rm s}. \tag{3}$$

$$\rho_{\rm s} = j\alpha_\phi(1-2\phi_1) - (j - j_0 - M_1 j) > 0. \tag{4}$$

(3) is just the result of Gauss' law: a condition for giving the column positive charge to screen the electric field. (4) is the positiveness of the space charge density at the screening surface where $E_\parallel$ vanishes.

$E_{\rm f}$ is the normalized electric field to be screened: $E_{\rm f} \equiv (e\lambda_0/mc^2)E_\parallel$, where $\lambda_0 = \sqrt{c^2/2\Omega\Omega_B} = 2.0$ cm $B_{12}^{-1/2}P^{1/2}$ is the Debye length of typical GJ plasma. For 10^{12} Volt acceleration in 10^4 cm, $E_{\rm f} \sim 100$. j is the primary electronic current density in units of the typical GJ density: $j = J/(-\Omega B/2\pi)$. α_ϕ is the pair multiplicity — number of pairs produced by one primary electron — in an unit breaking distance λ_*, with which a non-relativistic particle turns by the unscreened electric field, i.e., $eE_\parallel\lambda_* = mc^2$. In non-dimensional form, this distance is $1/E_{\rm f}$. ϕ_1 is defined in such a way that a pair positrons produced in between $\phi = 0$ (PPF) and ϕ_1 are reflected backward, and therefore $M_1 = \alpha_\phi\phi_1$ gives the returning multiplication factor, i.e., $jM_1 = j\alpha_\phi\phi_1$ gives the returning positron flux. j_0 is the normalized (local) GJ charge density: $j_0 = B_{\rm z}/B$. ζ: a numerical factor determined by the Lorentz factor at the birth of pairs; e.g., for $\gamma_{\rm birth} \sim 100$, $\zeta = 1.7$.

5. Application

Positive space charge by pair polarization is little. A previous belief that pair creation with a pair density higher than the Goldreich-Julian density immediately screen out the electric field is unjustified. This is because

(1) only the non-relativistic positrons can provide positive space charge,

(2) the non-relativistic positrons are reflected backward by the electric field and leave the pair electrons behind, so that a negative space charge is produced in the screening region where the positive charge is required.

In the case where geometrical screening is ineffective, more specifically, $j - j_0 - jM_1 > 0$, we have a condition on the

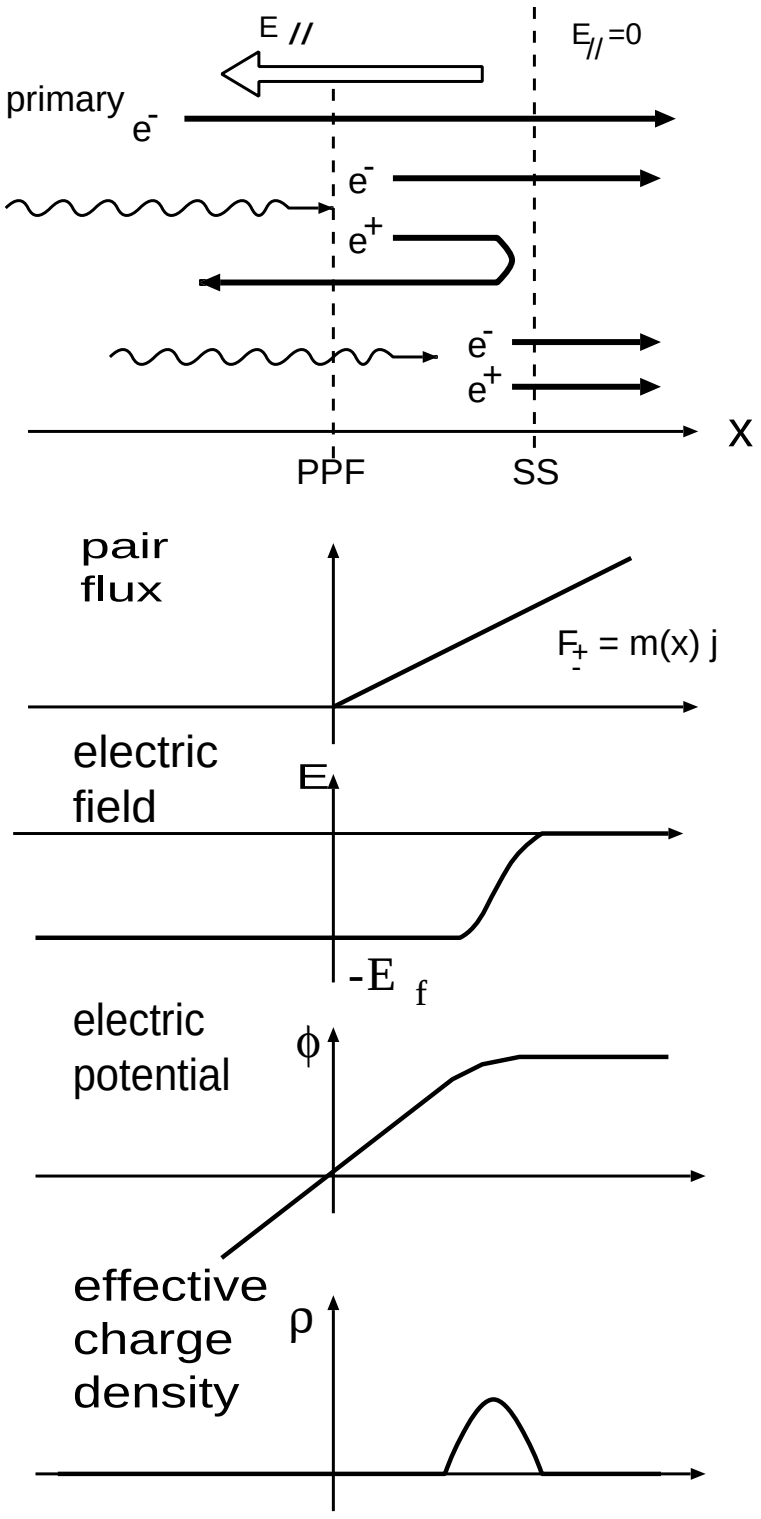


Fig. 2. Schematic picture of screening region

multiplication factor produced in unit breaking distance λ_* at PPF:

$$\Delta M_{\rm screen} \geq \frac{E_{\parallel}^2}{8\pi mc^2 n_0 \zeta' j}, \qquad (5)$$

which indicates that if $j \sim 1$, a multiplication factor of 10^3 is required in 0.01 cm. This condition will not be satisfied in the pulsar magnetosphere.

Thus the geometrical screening (toward curvature) is the only known way of screening, i.e., in (3), the positive effective charge $-j + j_0 + jM_1 > 0$ last in an appropriate distance

(until the electric field is screened out or weakened enough to be screened by pair polarization). Even on toward curved field lines, if the current density is super-GJ, or if $E_{\parallel}$ at PPF is not so weakened, then there is no way of maintaining a steady potential drop along field lines.

Difficulty in pair screening is always true for field lines curving away from the rotation axis regardless of the strength of the current density.

In our analysis, we do not take interaction between the particle beams into account. Beam instability may produce some frictional force on returning positrons and enlarge positive space charge. Time dependent behavior such as repetition of acceleration and screening may be an alternative way for a self-consistent model.

References

Shibata S., Miyazaki J., Takahara F., 1998, MNRAS 295, L53

Proceedings of the 270. WE-Heraeus Seminar on: *"Neutron Stars, Pulsars and Supernova Remnants"*
Physikzentrum Bad Honnef, Germany, Jan. 21-25, 2002, eds. W. Becker, H.Lesch & J. Trümper, MPE Report 278, pp. 159-161

From Pulsar Spin to Pulsar Wind: The Spectral Connection?

E.V. Gotthelf and C.M. Olbert

Columbia Astrophysics Laboratory, Columbia University, 550 West 120th Street, New York, NY 10027

Abstract. We present preliminary results from a systematic spectral study of pulsars and their wind nebulae using the *Chandra X-Ray Observatory*. The superb spatial resolution of *Chandra* allows us to differentiate the compact object's spectrum from that of its surrounding nebulae. Specifically, for six Crab-like pulsars, we compare spectral fits of the averaged pulsar wind nebulae (PWN) emission to that of the central core using an absorbed power-law model. These results suggest an empirical relationship between the bulk averaged photon indices for the PWNe and the pulsar cores; $\Gamma_{PWN} = 0.8 \times \Gamma_{Core} + 0.8$. The photon indices of PWNe are found to fall in the range of $1.3 < \Gamma_{PWN} < 2.3$. We propose that the morphological and spectral characteristics of the pulsars observed herein seem to indicate consistent emission mechanisms common to all young pulsars. We point out that the previous spectral results obtained for most X-ray pulsars are likely contaminated by PWN emission.

1. Introduction

Recent observation of pulsars associated with supernova remnants obtained with the *Chandra* X-ray observatory (Weisskopf, O'Dell & van Speybroeck 1996) are providing an unprecedentedly detailed view of pulsar wind nebulae. For the first time, emission features involving wisps, co-aligned toroidal structures, and axial jets are fully resolved in X-rays on arcsecond scales. These features, similar to those seen from the optical Crab nebula, are now found to be common to young, energetic pulsar in supernova remnants (Gotthelf 2001). Herein we present preliminary spectral analysis of several PWNe observed with *Chandra*, which, collectively, suggest a fundamental observational relationship between the spectral characteristics of pulsars and their pulsar wind nebulae.

Table 1 presents spectral results from a sample of *Chandra* pulsars which have characteristic wind nebulae. A summary of these objects along with references and images can be found in Gotthelf (2001). All observations were obtained with the ACIS-CCD camera which is sensitive to X-rays in the 0.2–10 keV band with an energy resolution of $\Delta E/E \sim 0.1$ at 1 keV. The on-axis point spread function is slightly undersampled by the CCD pixels ($0.5''$) allowing us to isolate the pulsar emission from that of the nebula. Except for N157B, which serendipitously fell on ACIS-I0, all data were obtained with ACIS-S3. The data were collected in nominal spectral ("FAINT") and timing (3.24 s) mode and reduced and analyzed using the latest version of CIAO (CIAO 2.2/CALDB v.2.9). Starting with the Level 1 processed event files we corrected the event data for CTI effects (Townsley et al. 2001) and applied the standard Level 2 filtering criteria, then further rejected time intervals of anomalous background rates.

For each object listed in Table 1, we extracted spectra from the PWN, pulsar core, and background, when available, or obtained spectral parameters from the literature as indicated. For the core spectra, the brightest central pixels were extracted based upon data above 4.0 keV, where the core emission is substantially greater than that of the surrounding nebula. The nebula itself was then extracted from the region above which the background was constant, excluding the core. Large variations in background rates and size of both the nebula and the central source amongst observations precluded the use of a standard extraction aperture. Custom spectral response matrix functions (RMFs) were provided with the CTI correction software, and ancillary response functions (ARFs) were created according to standard CIAO 2.2 procedures, using the QEU calibration files similarly provided. All spectra were grouped to a minimum of 50 counts per spectral bin.

We fit the resultant background-subtracted pulsar and PWN spectra with a power-law model above 2 keV using the latest version of `XSPEC` (v11.1). The spectral fits to the core included a convolution model to account for pileup effects on the spectra. Table 1 lists the spectral parameters obtained for each object; the values for the Crab and N157B have been obtained from the literature (Willingale et al. (2001), Wang & Gotthelf 1998, respectively). No measurement of the pulsed spectrum for 3C58 is currently available. Absorption values were obtained by fitting the nebula spectra with an absorbed power-law above 0.6 keV, and were subsequently frozen for all future fits.

The best-fit linear relationship between core and PWN photon indices is shown in Figure 1. We expect that the linear relationship seem in Fig. 1 may steepen slightly as we more fully account for pileup effects in the spectra. We note that the pileup corrected photon indices are likely subject to change due to the preliminary nature of the pileup model implementation, and suggest caution until these issues are resolved, but expect the basic result to remain unchanged.

We also note that due to extreme pileup effects and the brightness of its nebulae compared to the brightness of its core, SNR 0540-69 has not been included pending a more detailed analysis of the available data.

Table 1. Spectral Properties of Pulsars and their Wind Nebulae[a]

Remnant	$\Gamma_{\rm PWN}^{\rm Averaged}$	$\Gamma_{\rm Core}^{b}$	$\Gamma_{\rm Pulsed}^{c}$	$\log L_{\rm x\,NS}$	$\log L_{\rm x\,PWN}$
G11.2 − 0.3	1.28 ± 0.15	0.63 ± 0.12	0.60 ± 0.60	33.9	34.2
Vela XYZ	1.50 ± 0.04	0.95 ± 0.24	0.93 ± 0.26	31.2	32.6
Kes 75	1.88 ± 0.04	1.13 ± 0.11	1.10 ± 0.30	35.2	36.0
3C 58	1.92 ± 0.11	1.73 ± 0.15	...	33.0	...
Crab Nebula	2.11 ± 0.05	1.63 ± 0.09	1.86 ± 0.07	35.9	37.3
N157B Nebula	2.28 ± 0.12	2.07 ± 0.21	1.60 ± 0.35	35.9	36.1

[a] Ranked by increasing **averaged** PWN photon index.
[b] The value for the Crab pulsar has been obtained from the literature (Willingale et al. 2001). The measured photon-indices have been corrected for pile-up as discussed in the text.
[c] Pulsed PI value references: Vela: Strickman, Harding & Jager (1999);G11.2-0.3: Torii et al. (1997); Kes 75: Gotthelf et al. (2000); Crab: Pravdo, Angelini & Harding (1997); N157B: Marshall et al. (1998).

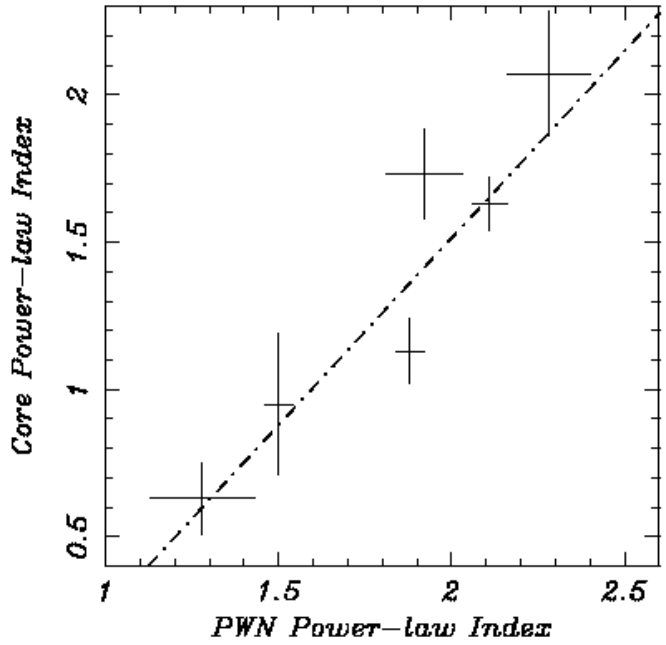


Fig. 1. $\Gamma_{\rm PWN}^{\rm Averaged}$ vs. $\Gamma_{\rm Core}$ – A plot of the power-law photon indices of the average pulsar wind nebulae spectra versus the pileup-corrected core photon indices for the collection of objects presented in Table 1. A dashed-line indicates the best-fit linear regression (i.e. $\Gamma_{PWN} = 0.8 \times \Gamma_{Core} + 0.8$). The physical origin of this relationship is yet to be determined.

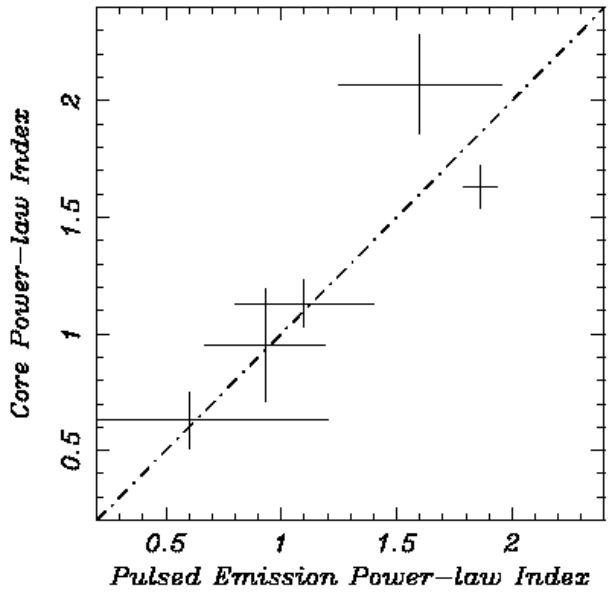


Fig. 2. $\Gamma_{\rm Core}^{\rm Pulsed}$ vs. $\Gamma_{\rm Core}$ – A comparison between the subset of measured power-law photon index for the core emission of objects presented in Table 1 and the pulsed emission for each of these source obtained from the literature (from ASCA or XTE fits). A one-to-one correspondence is indicated by the dashed line.

As a check to our final spectral results and to look for any systematic effect due to pile-up, we compare our measured power-law indices with those obtained from the literature for the pulsed emission for each source (Figure 2). Although they need not be the same, it is reassuring that they agree to within measurement errors.

2. Results

The photon indices obtained from this analysis show a trend that the average PWNe photon indices are consistently steeper than their core's photon indices by a factor of one-half to one. We suggest that this relationship is linear, with the form $\Gamma_{PWN} = 0.8 \times \Gamma_{Core} + 0.8$. This trend may be due to a number of factors. It may imply that the synchrotron spectrum frequency break occurs close to the neutron star, that there is a fundamental difference in emission mechanisms between the two regions, or that the nebula is being powered by the core and that the steepening is due to synchrotron burn-off or a comparable aging mechanism.

Though pulsations have not yet been discovered in the nebulae in supernova remnants G21.5-0.9 and G54.1+0.3, we note that their spectral indices are in the range predicted by this formula (Slane et al. 2000, Lu et al. 2002, respectively).

Chandra is the first telescope able to spatially resolve the neutron star from the nebula. Previous spectral observation of pulsars are likely to be strongly contaminated by PWN emission. For example, we see no clear relationship between the power-law spectral index obtained for these pulsars by *ASCA* with any of those measured by *Chandra*. As more crab-like pulsars are observed and analyzed, a more complete picture of their morphological and spectral characteristics comes into view, paving the way for future models and simulations.

Acknowledgements. We gratefully acknowledge the support by the Heraeus foundation. This work made possible by NASA LTSA grant NAG 5-7935. C.M.O. also acknowledges the support of the I.I. Rabi Scholars Program at Columbia University.

References

Gotthelf, E. V., Vasisht, G., Boylan-Kolchin, M., et al. 2000, ApJL, 542, L37

Gotthelf, E. V. 2001, Proc. The 20th Texas Symposium on Relativistic Astrophysics, AIP Press; astro-ph/0105128

Lu, F. J., Wang, Q. D., Aschenbach, B., Durouchoux, P., & Song, L. M. 2002, ApJL, 568, L49

Marshall, F. E., Gotthelf, E. V., Zhang, W., et al. 1998, ApJL, 499, L179

Pravdo, S. H., Angelini, L., & Harding, A. K. 1997, ApJ, 491, 808

Slane, P., Chen, Y., Schulz, N. S., Seward, F. D., Hughes, J. P., & Gaensler, B. M. 2000, ApJL, 533, L29

Torii, K., Tsunemi, H., Dotani, T., & Mitsuda, K. 1997, ApJL, 489, L145

Townsley, L. K., Broos, P. S, Garmire, G. P., Nousek, J. A., ApJL, 534, L139

Strickman, M. S., Harding, A. K., & de Jager, O. C. 1999, ApJ, 524, 373

Wang, Q. D. & Gotthelf, E. V. 1998, ApJL, 509, L109

Weisskopf, M. C. O'Dell, S. L., van Speybroeck, L. P. 1996, Proc. SPIE 2805, Multilayer and Gazing Incidence X-ray/EUV Optics III, 2

Willingale, R., Aschenbach, B., Griffiths, R. G., et al. 2001, A&A, 365, L212

Proceedings of the 270. WE-Heraeus Seminar on: *"Neutron Stars, Pulsars and Supernova Remnants"*
Physikzentrum Bad Honnef, Germany, Jan. 21-25, 2002, eds. W. Becker, H.Lesch & J. Trümper, MPE Report 278, pp. 162-166

Emission Mechanisms in High Energy Pulsars: From Gamma Rays to Infrared

André R. Crusius–Wätzel and Harald Lesch

Institut für Astronomie und Astrophysik der Universität München, Scheinerstr. 1, 81679 München, Germany

Abstract. We present a model for the gamma-ray emission of pulsars in terms of curvature radiation by highly relativistic particles. It is shown that the injection of power-law primary particles from an outer gap and subsequent cooling by curvature radiation losses reproduces the high energy spectrum and the luminosity of pulsars. As a result a spectral break is to be expected at a photon energy of $\sim 1\,\mathrm{GeV}$. This value does not depend on the surface magnetic field strength or on the period of the neutron star, but only involves a geometric factor. The predicted change of the spectral index by 1 explains in particular the spectral shape of PSR B1706–44. We find that according to this model the luminosity of pulsars in the high energy band varies according to $L_\gamma \propto B_0/P^{5/3}$, which is in good agreement with the observations.

A model for the infrared, optical and soft X-ray emission of pulsar is also presented. It is based on anisotropic synchrotron emission by relativistic particles in an outer gap scenario with a single energy distribution $N(\gamma) \propto \gamma^{-2}$. It is shown that this synchrotron model is able to reproduce the spectral shape between the infrared and soft X-rays and also the corresponding luminosities for the Crab pulsar. In particular, the long standing problem of the rapid spectral decline towards infrared frequencies is understandable as emission at very small pitch angles from low energy particles with $\gamma \gtrsim 10$. It is also shown that the scaling of the synchrotron model explains the observed correlation between the X-ray luminosity and the spin-down luminosity of the neutron star $L_\mathrm{x} \sim 10^{-3}\dot{E}$.

1. Gamma-Ray Emission of Pulsars

There are now at least seven spin-powered pulsars known to be emitting pulsed gamma radiation. Detailed spectral information has been obtained by observations with the *Compton Gamma Ray Observatory* in the energy range of up to 10 GeV. Several of these pulsars have a break in the spectrum at about $1-2\,\mathrm{GeV}$. This is also the energy where the gamma-ray pulsars emit most of the spectral power. The gamma ray luminosity is correlated to the square root of the spin-down power of these pulsars (with some scatter). For specific informations about the properties of individual gamma ray pulsars we refer to Thompson et al. (1996), Fierro et al. (1998), Thompson et al. (1999), and Kanbach (2001).

The models proposed for high-energy pulsars can be devided into polar cap models (e.g., Daugherty and Harding 1996; Sturner and Dermer 1994, Usov and Melrose 1996) and outer gap models (e.g., Romani and Yadigaroglu 1995; Romani 1996). In the first group the acceleration of particles and the gamma ray production is done in the open field line region above the magnetic pole of the neutron star. In the second group this takes place in the vacuum gaps between the neutral line and the last open field line in the outer magnetosphere, near the light cylinder. Depending on the distribution of the electric field parallel to the magnetic field along and across the gap, a power-law energy distribution of primary particles can be expected that emit gamma radiation. Here we discuss the effects of subsequent cooling by curvature radiation.

1.1. Primary Particles, and Particle Energy Spectrum

Particles entering the starvation gap will be accelerated by the strong electric field along the magnetic field. The accelerating electric field given in Cheng, Ho, and Ruderman (1986) can be rewritten as

$$E_0 = \delta^2 B \ , \tag{1}$$

where $\delta \sim 0.3$ is the ratio of the gap thickness to the light cylinder radius. The particles gain energy at a rate $P_\mathrm{gain} = ceE_0$. The energy of these primary particles is limited by curvature radiation losses, that depend on the bending of the field lines. The equilibrium between gains and losses determines the maximum energy. The curvature radius R_c of the last open field line is of the order of the light cylinder radius $R_\mathrm{lc} = c/\Omega$, with $\Omega = 2\pi/P$, and increases towards the neutral line. This becomes even more important for a (nearly) perpendicular rotator. By setting $R_\mathrm{c} = kR_\mathrm{lc}$, with $k \sim 1$, the power emitted by a single particle is then

$$P_\mathrm{cr} = \frac{2e^2c}{3R_\mathrm{c}^2}\gamma^4 = \frac{2e^2}{3c}k^{-2}\Omega^2\gamma^4 \ . \tag{2}$$

The typical frequency emitted is

$$\nu_\mathrm{c} = \frac{3c}{4\pi R_\mathrm{c}}\gamma^3 = \frac{3}{4\pi}k^{-1}\Omega\gamma^3 \ . \tag{3}$$

Equating P_gain with $P_\mathrm{loss} = P_\mathrm{cr}$, this results in an equilibrium Lorentz factor for the primaries of

$$\gamma_\mathrm{max} = 4.6 \times 10^7 \ (k\delta)^{1/2}\kappa^{-3/4}\left(\frac{B_{0,12}}{P_{-1}}\right)^{1/4} \ , \tag{4}$$

where $\kappa \sim 0.5$ is the ratio of the inner starting radius of the gap to the light cylinder radius.

The emission of gamma ray photons by the primaries leads to a pair creation cascade. These pairs, if produced inside the gap, will also be accelerated, start to shield the electric potential in the gap. As their density increases and becomes of the order of the Goldreich-Julian density $n_{\rm GJ} = \Omega B/2\pi ec$ this finally closes the gap. The outward moving particles are no longer accelerated and only loose energy via curvature radiation.

The pairs generated outside the gap with a finite pitch angle due to aberration effects will emit synchrotron radiation that can be seen in the MeV, X-ray and optical bands (Romani, 1996; Crusius-Wätzel, Kunzl, and Lesch, 2001). The electric field available for the acceleration of particles depends on the details of the cascade process, which leads to a quasi stationary state where the electric field is a function of the location along and across the gap. Although attempts have been made to understand the cascade and outer gap closure, no solid model exists. Therefore we just assume a power-law energy distribution of the accelerated particles,

$$Q(\gamma) \propto \gamma^{-s} \ , \ \gamma_{\rm min} < \gamma < \gamma_{\rm max} \ , \tag{5}$$

with an index s, that must be determined from the observations, rather than from theory in the light of the considerations given above. Since $\nu \propto \gamma^3$ the ratio $\gamma_{\rm max}/\gamma_{\rm min}$ needs to be only about 5 to cover a frequency range of more that two decades.

1.2. Curvature Radiation Cooling

The timescale for curvature cooling of relativistic electrons or positrons near the light cylinder of the pulsar magnetosphere is given by

$$\tau = \frac{\gamma}{\dot\gamma} = 4.1 \times 10^{-2} k^2 P_{-1}^2 \gamma_7^{-3} \ {\rm s} \ , \tag{6}$$

where $\dot\gamma = P_{\rm cr}/mc^2$ and equation (2) has been used. We estimate the Lorentz factor $\gamma_{\rm b}$ above which we expect a spectral break by setting the cooling timescale equal to the time needed for the particle to move out of the magnetosphere into the wind region, $t_{\rm esc} = fR_{\rm lc}/c = f/\Omega$, where $f \sim 0.1$ is the fraction of the light cylinder radius, corresponding to the outer gap region in which the particles are not accelerated anymore but only radiate. From this consideration we find that cooling will be important for particles with $\gamma > \gamma_{\rm b}$, where

$$\gamma_{\rm b} = \left(\frac{3mc^3k^2}{2e^2 f\Omega} \right)^{1/3} = 2.9 \times 10^7 k^{2/3} f_{-1}^{-1/3} P_{-1}^{1/3} \ . \tag{7}$$

The frequency at which the spectral break occurs is then

$$\nu_{\rm b} = \frac{3\Omega}{4\pi k}\gamma_{\rm b}^3 = \frac{9mc^3}{8\pi e^2} \cdot \frac{k}{f} \ , \tag{8}$$

which corresponds to a frequency and photon energy of $\nu_{\rm b} = 3.8 \times 10^{23} (k/f_{-1}) {\rm Hz}$ and

$$E_{\rm b} = h\nu_{\rm b} = 1.6 \ {\rm GeV} \frac{k}{f_{-1}} \ , \tag{9}$$

respectively, depending only on the geometrical factors k and f. In particular, **the break energy is independent of the magnetic field strength and period**.

1.3. Gamma-Ray Spectrum

For frequencies below the break $\nu_{\rm b}$ the spectrum can be calculated from the particle energy distribution according to equation (5). By using the monochromatic approximation for the spectral power of a single lepton, $P_\nu(\gamma) = P_{\rm cr}(\gamma)\delta[\nu - \nu_{\rm c}(\gamma)]$, it follows that

$$\begin{aligned} I_\nu \ &\propto \ \int d\gamma \, Q(\gamma) P_\nu(\gamma) \\ &\propto \ \int d\gamma \, \gamma^{-s} \gamma^4 \left| \frac{d(\nu - \nu_{\rm c})}{d\gamma} \right|^{-1} \delta(\gamma - \gamma_0) \ , \end{aligned} \tag{10}$$

where $\gamma_0 \propto \nu^{1/3}$ is the Lorentz factor at which the argument of the δ-function becomes zero. We then find that

$$I_\nu \propto \nu^{-(s-2)/3} \quad (\nu < \nu_{\rm b}) \ . \tag{11}$$

This corresponds to a photon energy index of $\phi(\nu < \nu_{\rm b}) = -(s+1)/3$, where $N_{\rm E} \propto E^\phi$. The Crab, Geminga, and Vela pulsar have photon indices -2, -1.4, and -1.6, respectively, below the spectral break (Fierro, et al., 1998). This then gives the particle energy indices s of the primaries below the break energy as 5, 3.2, and 3.8, respectively.

For frequencies above the break we first have to find the distribution function modified by radiation losses. Assuming that a spectrum $Q(\gamma)$ is injected at a rate $\dot Q(\gamma) = Q(\gamma)/t_{\rm esc}$, the cooled spectrum is given by the following expression

$$N(\gamma) = \frac{1}{|\dot\gamma|} \int_\gamma^{\gamma_{\rm max}} d\gamma' \, \dot Q(\gamma') \ , \tag{12}$$

from which we find $N(\gamma) \propto \gamma^{-(s+3)}$. By using the monochromatic approximation again, we finally get

$$I_\nu \propto \nu^{-(s+1)/3} \quad (\nu > \nu_{\rm b}) \ , \tag{13}$$

corresponding to a photon index of $\phi(\nu > \nu_{\rm b}) = -(s+4)/3$. Therefore the spectral index of the gamma radiation changes by

$$\Delta\phi = -1 \tag{14}$$

at the break frequency (eqn. 8) in the direction of increasing frequencies.

The pulsar PSR B1706–44 shows exactly this behavior (Thompson et al., 1996). The gamma ray photon spectrum changes by $\Delta\phi = -1$, from $\phi = -1.25$ below 1 GeV to $\phi = -2.25$ above 1 GeV, with the spectrum extending for more than a decade in energy, both, below and above the break. From this we find $s = 2.75$ for this pulsar.

The emitted power per logarithmic frequency band scales as $\nu I_\nu \propto \nu^{(5-s)/3}$ below the break and $\nu I_\nu \propto \nu^{(2-s)/3}$ above the break. For $2 < s < 5$ the gamma ray energy distribution thus is rising below and is falling above the break energy. The maximum power is then emitted at the break energy.

The highest frequencies are produced by the primary particles that feel the vacuum potential. The spectrum of the radiation emitted by them cuts off exponentially above

$$\begin{aligned} \nu_{\rm max} \ &= \ \frac{3\Omega\gamma_{\rm max}^3}{4\pi k} \\ &= \ 1.5 \times 10^{24} \delta^{3/2} k^{1/2} \kappa^{-9/4} B_{0,12}^{3/4} P_{-1}^{-7/4} \ {\rm Hz} \ . \end{aligned} \tag{15}$$

The change in the spectrum is dominated by cooling only if the exponential cutoff is at higher energies than the break, $\nu_{\rm max} > \nu_{\rm b}$. The cooled spectrum is nicely seen in PSR B1706–44, where the cutoff must be above 10 GeV. The situation is

less clear for the other gamma ray pulsars, where the energy range between the break and the cutoff is either smaller or not existent. It can be expected that with the GLAST mission more pulsars with a clear break will be found and also that a smaller range of the cooled spectrum can be detected.

1.4. Luminosity Estimates for the Gamma-Ray Emission

We now estimate the power L_γ emitted by pulsars in the gamma-ray region at the break frequency very roughly as the product of the volume, the Goldreich-Julian number density near the light cylinder $n_{\rm GJ} \propto B_0/P^4$, and the radiation power of a single particle $P_{\rm cr} \propto \gamma^4/P^2$,

$$L_\gamma = V n_{\rm GJ} P_{\rm cr} \ , \tag{16}$$

where the volume is assumed to be a shell near the light cylinder with $V = 4\pi f R_{\rm lc}^3 \propto P^3$. From this we find

$$L_\gamma = 4.2 \times 10^{34} \, \frac{k^{2/3}}{\kappa^3 f_{-1}^{1/3}} \frac{B_{0,12}}{P_{-1}^{5/3}} \ {\rm erg\,s^{-1}} \ , \tag{17}$$

where the break Lorentz factor from equation (7) has been used in the curvature radiation power (2). Since the spin-down luminosity $\dot{E}$ of a pulsar is proportional to B_0^2/P^4, the gamma luminosity thus scales according to $L_\gamma \propto \dot{E}^{1/2} P^{1/3}$. The observed high-energy luminosities of the seven gamma ray pulsars indicate a trend $L_\gamma \propto \dot{E}^{1/2}$, and the small additional dependence on $P^{1/3}$ is still in agreement with this correlation. If we instead insert the maximum Lorentz factor (4) into the power formula, the result is

$$L_\gamma = 7.9 \times 10^{34} \, \frac{\delta^2 f_{-1}}{\kappa^6} \frac{B_{0,12}^2}{P_{-1}^4} \ {\rm erg\,s^{-1}} \ , \tag{18}$$

and is thus linearly dependent on $\dot{E}$.

In Figures (1) and (2) we compare the model results with the data points. The latter have been taken from Thompson et al. (1999). These observed luminosities are integrated fluxes above 1 eV. It is clearly seen in Figure (1) that if the maximum of the luminosity is determined by the break, a reasonable correlation is found, not only for the slope but also for the absolute values. However, the observed luminosity of Geminga is smaller by about a factor of 5, which might be due to the fact that this pulsar emits 20% of its spin-down power in gamma rays. This means that the model curve would give an efficiency of 100%, which then causes a significant nonlinear back-reaction on the rotation of the pulsar and on the formation of outer gaps, with the effect that the gamma luminosity of Geminga is reduced below the expectation from the linear model. Another point worth to note is that the Crab pulsar emits it maximum spectral power at ~ 100 keV. Therefore the data point of the Crab pulsar that gives the luminosity in the GeV range is actually somewhat lower than plotted here. With these remarks in mind our simple model is in good agreement with the data. In Figure (2) the luminosity is plotted versus B_0^2/P^4. The solid line represents the dependence $\log L_\gamma = 20 + 0.5 \, \log(B_0^2/P^4)$, and the dotted line is the relation found, if the peak luminosity would be reached at the cutoff energy. The latter clearly overpredicts the observed values, especially for the high B – low P pulsars, since the slope of the curve is too steep.

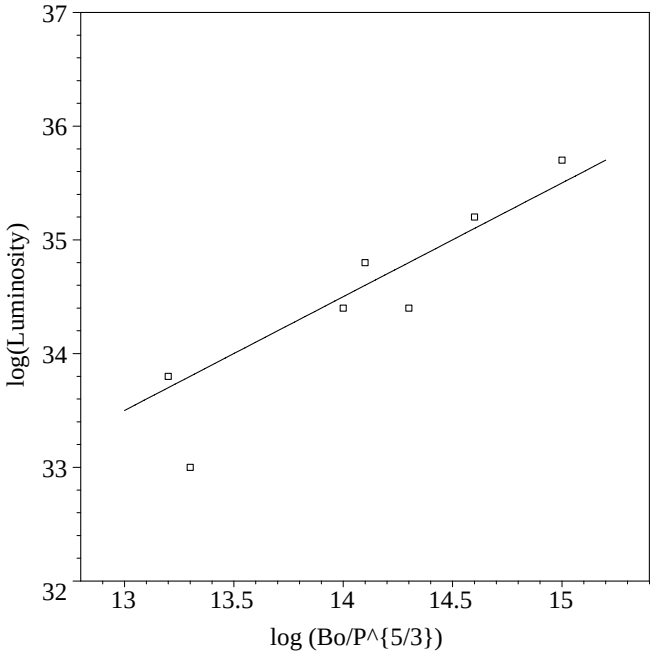


Fig. 1. The squares show the observed high energy luminosities versus the parameter combination $B_0/P^{5/3}$. The line represents the predicted luminosity at the break frequency (equation 8), i.e., when radiative cooling is important.

2. Synchrotron Model for the Infrared, Optical and X-Ray Emission of the Crab pulsar

The Crab pulsar has a continuous spectrum from the optical to X-rays and γ-rays with different power-laws (Lyne & Graham-Smith 1990). The spectral index α, defined as $I_\nu \propto \nu^{-\alpha}$, varies from $\alpha = 1.1$ in the γ-region via 0.7 in the hard X-ray region to 0.5 at soft X-rays (Toor & Seward 1977) and zero at optical frequencies (Percival et al. 1993). In the far infrared region the spectrum is inverted $\alpha = -2$ and cuts off sharply towards lower frequencies. This behavior is not accompanied by dramatic pulse profile changes, as one would expect from saturation or self-absorption effects. Self-absorption should first influence the peak intensity. The infrared spectrum measured by Middleditch, Pennypacker, & Burns (1983) is still not explained. In the following it is shown that the theory of optically thin synchrotron radiation at very small pitch angles gives a possible solution to this problem.

2.1. Synchrotron Emission at Small Pitch Angles

The emissivity at very low pitch angles ($\Psi < 1/\gamma$) of a single particle is given by (Epstein 1973)

$$\epsilon_\nu(\theta,\gamma) = \frac{\pi e^2 \gamma \Psi^2 \nu^3}{\nu_B c} \left[1 - \frac{\nu}{\gamma\nu_B} + \frac{\nu^2}{2\gamma^2\nu_B^2}\right] \times \delta\left(\nu - \frac{2\gamma\nu_B}{1+\theta^2\gamma^2}\right) \tag{19}$$

with $\nu_B = eB/2\pi mc = 2.80 \times 10^{12} B_6$ Hz. This formula has to be applied when angles $\theta < 1/\gamma$ are resolved in the observations, i.e. when the pulse width $\Delta\phi$ becomes comparable to the emission cone angle of the particles, $1/\gamma > 2\pi\Delta\phi$. Since the

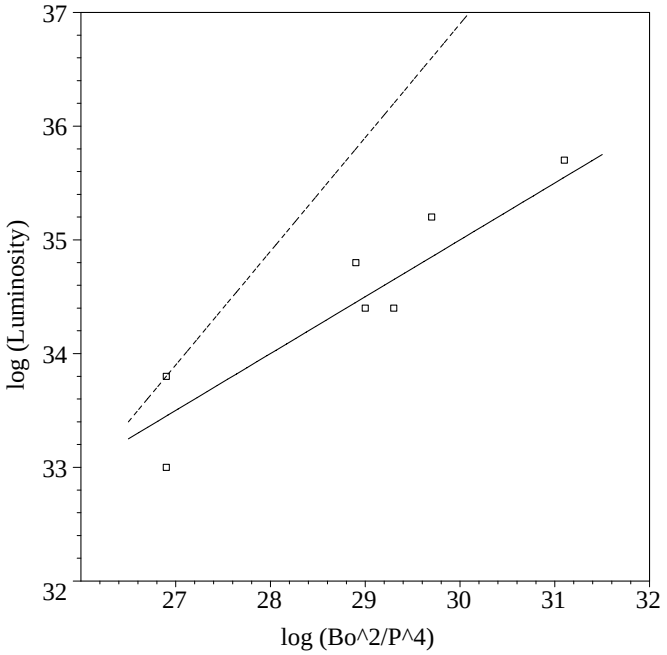


Fig. 2. Here the data points are plotted versus B_0^2/P^4. The solid line is given by $L_\gamma \propto \dot{E}^{1/2} \propto B_0/P^2$ and the dotted line represents the predicted luminosity at the maximum frequency (equation 15), i.e., when radiative cooling is not important.

maximum of the emission is in the forward direction ($\theta = 0$) the emission is dominated by the field lines that point towards the observer at each phase of the pulse. When the typical angle of emission θ is small compared to the pulse width it is useful to integrate the emissivity over all angles (averaging):

$$\begin{aligned}\varepsilon_\nu(\gamma) &= 2\pi \int \epsilon_\nu \sin\theta \; d\theta \\ &= \frac{2\pi^2 e^2 \Psi^2}{c} \nu \left[1 - \frac{\nu}{\gamma\nu_B} + \frac{\nu^2}{2\gamma^2\nu_B^2}\right] \; . \end{aligned} \tag{20}$$

2.2. Infrared Spectrum

The emission from a power law distribution of relativistic particles, $N(\gamma) = N_0\gamma^{-s}$, in the direction along the magnetic field $\theta = 0$ is given by

$$\begin{aligned} I_\nu &\propto \int \epsilon_\nu(0,\gamma) N(\gamma) \, d\gamma \\ &\propto \frac{\pi e^2 \Psi^2 N_0 \nu^3}{2\nu_B^2 c} \int \delta\left(\gamma - \frac{\nu}{2\nu_B}\right) \gamma^{1-s} \, d\gamma \end{aligned} \tag{21}$$

so that

$$I_\nu \propto \frac{4N_0 \pi e^2 \Psi^2 \nu_B}{c} \left(\frac{\nu}{2\nu_B}\right)^{4-s} \; . \tag{22}$$

The spectrum rises very steeply, in fact $I_\nu \propto \nu^2$ for $s = 2$. The Lorentz factors in the case of the Crab then have to be of the order of $\gamma \sim 1/2\pi\Delta\phi \sim 20$, which is is consistent with the requirement that $2\gamma\nu_B$ lies in the infrared part of the spectrum.

2.3. Optical Spectrum

In case of somewhat higher Lorentz factors the single particle beam angle becomes smaller than the phase angle of the pulse and the total (or angle averaged) power spectrum has to be applied. For simplicity the monochromatic approximation is used:

$$\varepsilon_\nu \approx -\frac{dE}{dt} \, \delta(\nu - 2\gamma\nu_B) \; . \tag{23}$$

This is a good approximation since the emission is sharply peaked at $2\gamma\nu_B$ and one may just put all the emission at this frequency. The result for the optical emission is then

$$I_\nu \propto \int \varepsilon_\nu N(\gamma) \; d\gamma = \frac{4\pi^2 e^2 N_0 \nu_B^2 \Psi^2}{3c} \left(\frac{\nu}{2\nu_B}\right)^{2-s} \; . \tag{24}$$

In the case of $s = 2$ this gives the observed flat, $\alpha \approx 0$, optical/UV spectrum of the Crab pulsar, with $\gamma \sim 10^2$.

2.4. Soft X-ray Spectrum

Soft X-ray emission in this model comes from the particles with larger pitch angles ($\Psi \gg 1/\gamma$), radiating at a typical frequency $\nu_c = \frac{3}{2}\nu_B \Psi \gamma^2$ The spectrum in this large pitch angle limit is given by $I_\nu \propto \nu^{-(s-1)/2}$. This yields the observed $I_\nu \propto \nu^{-0.5}$ at soft X-rays for $s = 2$.

2.5. Luminosity Estimates for the Optical and X-Ray Emission

The energy radiated by the pulsar in the optical and in the X-ray band can be estimated simply as the number of particles times the energy radiated by one particle $L = M n_{\rm GJ} V P_{\rm syn}$, where $M = \gamma_{\rm p}/\gamma$ is the multiplicity of the relativistic particle density within the volume V as compared to the Goldreich-Julian density $n_{\rm GJ}$. The volume is estimated as a spherical shell within a fraction f of the light cylinder radius $V = 4\pi R_{\rm lc}^2 \cdot f R_{\rm lc} = 1.4 \times 10^{30} f P^3$ cm^3. The frequency of the optical emission (at small pitch angles) is given by

$$\nu_{\rm opt} = 5.6 \times 10^{14} \gamma_{\rm opt,2} B_6 \text{ Hz} \tag{25}$$

and the optical luminosity:

$$\begin{aligned} L_{\rm opt} &= 10^{33} \alpha \delta_{-1} f_{-1} \Psi_{\rm p,-3}^{-1} \Psi_{\rm opt,-2}^2 \nu_{\rm opt,14.7} \\ &\quad \times B_{0,12.5}^{3/2} P_{-1.5}^{-5/2} \text{ erg s}^{-1} \; . \end{aligned} \tag{26}$$

The frequency of the X-ray emission is

$$\nu_{\rm x} = 2.8 \times 10^{17} \Psi_{\rm x,-1} \gamma_{\rm x,3}^2 B_6 \text{ Hz} \tag{27}$$

and the soft X-ray luminosity evaluates to

$$\begin{aligned} L_{\rm x} &= 6 \times 10^{35} \alpha \delta_{-1} f_{-1} \Psi_{\rm p,-3}^{-1} \Psi_{\rm x,-1}^{3/2} \nu_{\rm x,17}^{1/2} \\ &\quad \times B_{0,12.5}^2 P_{-1.5}^{-4} \text{ erg s}^{-1} \; . \end{aligned} \tag{28}$$

This can now be compared with the spin-down luminosity $L_{\rm sd}$ of the Crab pulsar due to magnetic dipole radiation:

$$L_{\rm x} \approx 2 \times 10^{-3} \alpha \delta_{-1} f_{-1} \Psi_{\rm p,-3}^{-1} \Psi_{\rm x,-1}^{3/2} \nu_{\rm x,17}^{1/2} \dot{E} \; . \tag{29}$$

Since this relation is now independent of B_0 and P, it should apply to any pulsar. Becker & Trümper (1997) have found such a relation observationally for X-ray selected pulsars. More details of the model presented here can be found in Crusius-Wätzel, Kunzl, & Lesch (2001).

3. Discussion and Conclusions

We have found that curvature radiation cooling results in a universal spectral break energy in the photon spectrum at ~ 1 GeV in gamma ray pulsars. This break depends only on geometric factors, but does not depend on other pulsar parameters as the magnetic field strength or the rotation period. The maximum power is emitted at this energy. In fact in several of the gamma-ray pulsars a spectral break or cut-off can be observed at this energy. A photon spectral index change of $\Delta\phi = -1$ is expected, when going from lower to higher energies. This is clearly seen in PSR B1706–44 (Thompson et al., 1996) and we expect that during the GLAST mission more pulsars with this spectral feature will be detected.

The high energy luminosity calculated with cooling is proportional to $B_0/P^{5/3}$, which compares well with the observed values. Romani (1996) has obtained cutoff energies from a curvature radiation model without cooling that also lie in the observed range, but they depend on the pulsar parameters B_0 and P, since they are connected to the maximum energy of the primaries. Using the cutoff particle energies for the luminosity estimate we find that the power output of pulsars in high energy photons scales as $\propto B_0^2/P^4$, i.e. as a constant fraction of the spin-down power $\dot{E}$, which overpredicts the γ-ray luminosity for young pulsars. But note that in deriving this result it was assumed that the density of the emitting particles is of the order of the Goldreich-Julian density, which might not be true in general. Harding (1981) estimated the gamma ray luminosity from a polar cap model by assuming that the power put into particles is completely converted into radiation and found a scaling $\propto B_0 P^{-2}$. In the outer gap model with a power-law energy distribution of relativistic particles (due to gap closure), the "luminosity" in particles is dominated by the density at the lowest energy. On the other hand the maximum spectral power is dominated by the high energy particles with $\gamma = \gamma_{\rm b}$ or $\gamma = \gamma_{\rm max}$. So it is not immediately clear what fraction of the particle luminosity is converted into radiation.

According to Kanbach (2001) the observed luminosity trend $L_\gamma \propto \dot{E}^{1/2}$ can be caused either by a proportionality to the number of particles, which would all be accelerated to the same energy, or by the same particle flow from different pulsars with correspondingly different acceleration energies. In our opinion the reality is somewhere in between, depending on the details of the pair cascade and the gap closure. Only when the energy (depending on the locally available electric field and curvature radius) and the density of the relativistic particles, including its spacial dependence is known, we can get more insight into the spectrum and the luminosity of gamma-ray pulsars.

Synchrotron emission of particles with small pitch angles with a single power-law energy distribution, $N(\gamma) \propto \gamma^{-2}$ reproduces the key properties of the Crab pulsar spectrum and the luminosity from the infrared up to soft X-rays.

Acknowledgements. This work was supported by the Deutsche Forschungsgemeinschaft with the grant LE 1039/6 (C.-W.).

References

Becker, W., Trümper, J. 1997, A&A, 326, 682
Crusius-Wätzel, A.R., Kunzl, T., Lesch, H. 2001, ApJ, 546, 401
Cheng, K.S., Ho, C., Ruderman, M. 1986, ApJ, 300, 500
Daugherty, J.K., Harding A.K. 1996, ApJ, 458, 278
Epstein, R.I. 1973, ApJ, 183, 593
Fierro, J.M. et al. 1998, ApJ, 494, 743
Harding, A.K. 1981, ApJ, 245, 267
Kanbach, G. 2001, The Universe in Gamma Rays, V. Schönfelder, Berlin: Springer, 127
Lyne, A.G., Graham-Smith, F. 1990, Pulsar Astronomy (Cambridge University Press)
Middleditch, J., Pennypacker, C., Burns, M.S. 1983, ApJ, 273, 261
Percival, J.W., et al. 1993, ApJ, 407, 276
Romani, R.W. 1996, ApJ, 470, 469
Romani, R.W., Yadigaroglu, I.-A. 1995, ApJ, 438, 314
Sturner, S.J., Dermer, C.D. 1994, ApJ, 420, L79
Thompson, D.J. et al. 1996, ApJ, 465, 385
Thompson, D.J. et al. 1999, ApJ, 516, 279
Toor, A., Seward, F.D. 1977, ApJ, 216, 560
Usov, V.V., Melrose, D.B. 1996, ApJ, 464, 306

Proceedings of the 270. WE-Heraeus Seminar on: *"Neutron Stars, Pulsars and Supernova Remnants"*
Physikzentrum Bad Honnef, Germany, Jan. 21-25, 2002, eds. W. Becker, H.Lesch & J. Trümper, MPE Report 278, pp. 167-170

The Characteristics of (Normal) Pulsars

Richard Wielebinski

Max–Planck–Institut für Radioastronomie, Auf dem Hügel 69, 53121 Bonn, Germany

Abstract. Pulsars have now been studied for 34 years. We know of the existence of some 1500 objects at radio frequencies. Many of the characteristics of pulsars such as pulsar period, period derivative, spectrum, polarization, etc., have been catalogued for many objects. Still we do not know the details of the pulsar emission mechanism. The present review will give an up-to-date description of the characteristics of (normal, slow) radio pulsars. Millisecond pulsars will be dealt with by M. Kramer (this volume).

1. Introduction

The discovery of pulsars by Hewish et al., made at the low radio frequency of 81.5 MHz, stunned the astronomical community. In the discovery paper the authors speculated already on the possibility that we had either white dwarfs or neutron stars showing the pulsations. Virtually every radio telescope around the world was observing pulsars in 1968. Many of the important parameters of pulsars like the exact period, the period derivative, pulse shape, the polarization and spectrum were determined in the earliest papers already. Also the Galactic distribution of pulsars was found after the discoveries with the Molonglo telescope (Large et al. 1968a) increased rapidly the number of known objects. The Pulsar – Supernova correlation was suggested by the discovery of PSR 0833−45 near the Vela X SNR (Large et al. 1968b) and conclusively confirmed by the discovery of the pulsar in the Crab nebula (Clomella et al. 1969; Zeissig & Richards 1969). This gave the theory of pulsar formation great impulse. The measurement of the pulsar polarization in PSR 0833−45 by Radhakrishnan & Cooke (1969), that showed a vector sweep, finally clinched the argument that we were observing the magnetic poles of a rotating neutron star. Further important discoveries at radio frequencies were the binary pulsar (Hulse & Taylor 1975), the millisecond pulsar (Backer et al. 1982) and the planets around a pulsar (Wolszczan & Frail 1992).

The early discoveries made way to large search programmes and to surveys of pulsar characteristics. All the large radio telescopes have been involved in finding new objects. In particular, the recent Parkes multibeam survey (e.g. Manchester et al. 2001), led to the discovery of more than 600 new pulsars. To determine the pulsar spectra we require the collection of data over a wide frequency range. In this area the Effelsberg radio telescope was most prominent since it was the only instrument able to observe pulsars at high radio frequencies. Pulsar polarization is a very important parameter that has to be known for any serious emission theory discussion. This was observed by many telescopes but also in particular in Effelsberg. Pulsar emission shows many details, like drifting sub-pulse emission, pulsar modes or microstructure. I will not discuss these details because of lack of time. I will concentrate on pointing out what I consider to be the important connections of known pulsar parameters. Towards the end of this talk I will describe some promising new avenues of observational pulsar research.

2. Pulsar period

The periods of pulsars are remarkably stable, in the range 0.0015 sec to 8.51 sec. The pulsar period has been found to change (increase) as a result of loss of rotational energy. This period derivative P(dot) is a very important parameter for the determination of the pulsar age. The 'normal' pulsars are found in the period range of 0.033 sec for the Crab pulsar and up to 8.51 sec for PSR J2144−3933 (Young et al. 2000). The peak of the period distribution of pulsars lies around 0.7 sec. A second population of pulsars, the millisecond pulsars, is to be found in the period range 1.558 millisec to 20 millisec. These objects have very small period derivative and are considered to be 'recycled' pulsars. These are the best clocks in the universe.

3. Pulse shapes

One of the very characteristic parameters of a radio pulsar is its pulse shape. The pulse shape is due to the emission region that is close to the magnetic pole in a dipolar magnetic field of the rotating neutron star. This emission region sweeps past the observer giving, depending on the geometrical orientations of the rotation axis and the magnetic axis forming a pulsar beam. It is common knowledge that after the addition of some thousand of pulses a stable pulse shape appears. This pulse to space ratio is mostly a few % with some exceptions. Some pulsars have a duty ratio of more than 50%. The pulse shapes can be single double, triple or even more complex. The single pulse shape is considered to be due to an inner 'core'. In triple pulse shapes we observe the 'core' and two 'cones' being cut by the line of sight. The most complex pulse shapes show up to nine components. Interpulses are observed in some pulsars, being interpreted as the emission from the opposite pole. The stability of pulse shapes has to be taken with a great BUT! When an observer can discern single pulses a huge variety of behavior

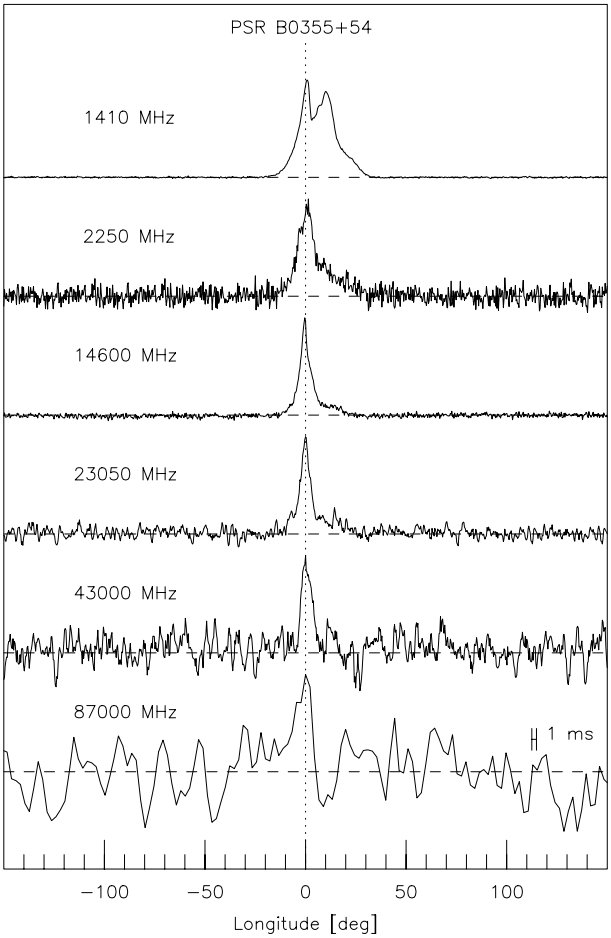


Fig. 1. Pulse shape of PSR B0355+54 aligned by timing

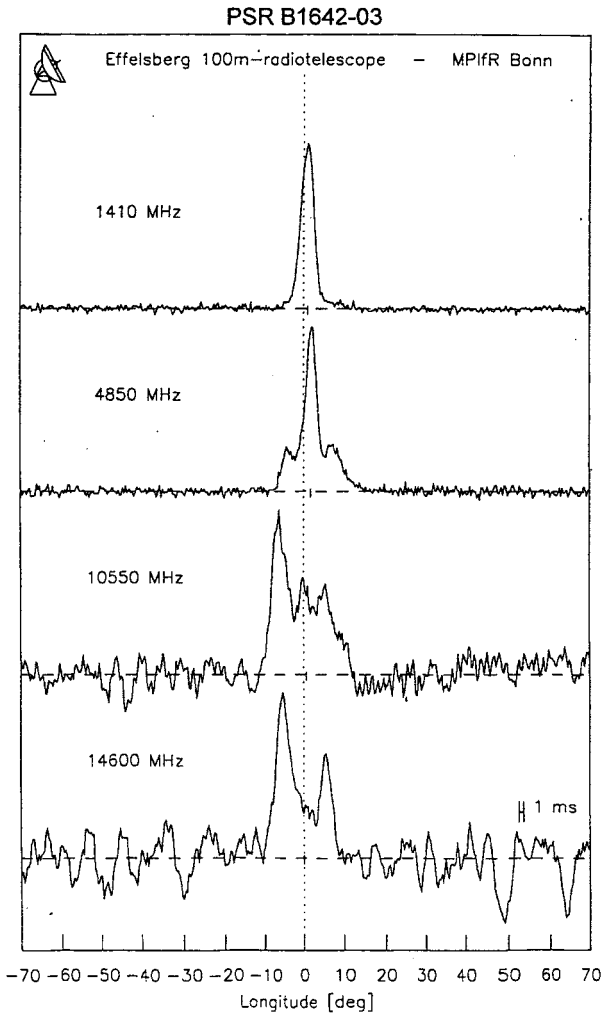


Fig. 2. Pulse shape of PSR B1642−03. Note the unusual frequency evolution of this pulsar

is seen. Each single pulse is formed from a series of sub-pulses. These sub-pulses can show microstructure which seems to be limited only by the temporal resolution of the recording equipment. Sub-pulses can drift within the integrated pulse shape envelope giving multiple (non-integral) periodicities. The description of all these effects becomes even more complicated when one considers the evolution of pulse shape with radio frequency. The general evolution is to a narrower pulse shape at higher radio frequencies that is often cited as the Radius–to–Frequency mapping. At higher radio frequencies emission is thought to come from regions closer to the neutron star surface. A large collection of pulse shapes is to be found in Seiradakis et al. (1995) and in Kijak et al. (1998). The evolution of pulse shape with frequency is documented in Sieber et al. (1975), Kramer et al. (1997) or Kuzmin et al. (1998). I present the pulse shapes for the pulsars 0355+54 (Fig. 1) and 1642−03 (Fig. 2) to illustrate the different evolutions of pulse shape with frequency. Finally there are moding pulsars where a stable pulse shape changes for some time to an abnormal mode, returning to normal after an unpredictable length of time.

4. Pulsar spectra

Observing at five frequencies (four of them simultaneously) with the Parkes telescope, Robinson et al. (1968) established the spectrum of CP1919+21 from 85 MHz to 2.7 GHz. This 'classical' spectrum showed a steep spectral index at decimeter wavelengths ($\alpha \sim 1.5$) with a spectral break with the spectral index increasing to $\alpha \sim 3.0$ at the highest frequencies. The continuation of gathering of data at many frequencies was a prerequisite of determining pulsar spectra. Here a serious problem must be mentioned, namely that there are huge flux variations due to interstellar scattering, but possibly also due to internal variations in the pulsar emission. Pulsars with high dispersion measure exhibit particularly strong 'fading' at high radio frequencies. To determine a flux of a pulsar at a frequency repeated observations are necessary. In spite of these difficulties several large data sets are available (e.g. Malofeev et al. 1994; Lorimer et al. 1995; Toscano et al. 1998; Maron et al. 2000). The older data on pulsar spectra were derived for flux density measurements in the frequency range 85 MHz to 1400 MHz. The newer data have extended the spectra of hundreds of pulsars up to 4.8 GHz and down to 102 MHz. For the strongest

objects data are available at 10 GHz and even at mm wavelengths. Here a surprise has been found: the spectrum of some pulsars did not continue fall but showed a surprising 'flattening' or even 'turn-up' (e.g. Wielebinski et al. 1993; Kramer et al. 1997). The spectra of eight strongest pulsars with detected flux values at mm wavelengths are shown in Figure 3. One pulsar could be detected at 87 GHz (Morris et al. 1997). A change in the pulsar emission mechanism?

5. Pulsar polarization

The earliest observations (e.g. Lyne & Smith 1968) showed that sub-pulse components had very high degree of polarization. At first it was only the linear polarization that was studied showing the characteristic position angle sweep that indicated rotating objects. Later circular polarization was also detected (e.g. Manchester 1971). A surprising result was the observation by Manchester et al. (1973) that pulsar polarization remains high up to some critical frequency and then falls rapidly. Orthogonal polarization modes were postulated (e.g. Manchester 1975) based on the observation that in some pulsars the position angle sweep has jumps of $\sim 90^\circ$. Recent surveys of integrated polarization of pulsars at many frequencies (e.g. von Hoensbroech & Xilouris 1997; Gould & Lyne 1998; Weisberg et al. 1999; von Hoensbroech 1999) showed us the great diversity in polarization morphology. A type of pulsar has been discovered (von Hoensbroech 1999) in which the linear polarization falls to high frequencies with a corresponding increase of circular polarization. This was interpreted as a propagation effect (von Hoensbroech & Lesch 1999). The early conclusion that the linear polarization drops suddenly after reaching some critical frequency has been confirmed. This is shown in Figure 4. This drop in linear polarization seem to occur when the spectrum (compare Figures 3 and 4) of the pulsar changes. Does the loss of coherence (polarization) occur when another emission mechanism (incoherent one) begins to dominate?

6. Discussion

In this talk many of the integral characteristics of pulsars were discussed. I presented a summary about pulsar periods, their spectra, the polarization and pulse shapes. I have not dealt with the characteristics of millisecond pulsars since they are presented elsewhere in this volume. I want to bring to your attention the importance of studying single pulses at many frequencies simultaneously. Such observations require the use of many telescopes simultaneously. A contribution by Karastergiou (this volume) describes recent four-station experiments. The single pulse data, with full polarization, taken over a wide frequency range may hold the key to understanding the pulsar emission process. Also the extension of pulsar observations to yet higher radio frequencies (into the sub-mm wavelength range) may finally allow us to 'join' the radio to infrared spectra and hence understand how pulsars work.

References

Backer D.C,, Kulkarni S.R, Heiles, C., et al., 1982, Nature 300, 615

Clomella J.M., Craft jun. H.D., Lovelace R.V.E., et al., 1969, Nature 221, 453

Gould D.M., Lyne A.G., 1998, MNRAS 301, 235

Hewish A., Bell, S.J., Pilkington J.D.H., et al., 1969, Nature 217, 709

Hulse R.A., Taylor J.H., 1975, ApJ 195, L51

Kijak J., Kramer M., Wielebinski R., Jessner A., 1998, A&AS 127, 153

Kramer M., Jessner A., Doroshenko O., Wielebinski R., 1997, ApJ 488, 364

Kuzmin A., Izvekova V.A., Shitov Yu.P., et al., 1998, A&AS 127, 355

Large M.I., Vaugham A.E., Wielebinski R., 1968a, Nature 220, 753

Large M.I., Vaugham A.E., Mills B.Y., 1968b, Nature 220, 340

Lorimer D.R., Yates J.A., Lyne A.G., Gould D.M., 1995, MNRAS 273, 411

Lyne A.G., Smith F.G., 1968, Nature, 218, 124

Malofeev V.M., Gil J.A., Jessner A., et al., 1994, A&A 285, 201

Manchester R.N., 1971, ApJS 199, 283

Manchester R.N., 1975, Proc ASA 2, 334

Manchester R.N., Taylor J.H., Huguenin G.R., 1973, ApJ 179, L7

Manchester R.N., Lyne A.G., Camilo F., et al., 2001, MNRAS 328, 17

Maron O., Kijak J., Kramer M., Wielebinski, R., 2000, A&AS 147, 195

Morris D., Kramer M., Thum C., et al., 1997, A&A, 322, L17

Radhakrishnan V., Cooke D.J., 1969, Astrophys. Lett. 3, 225

Robinson B.J., Cooper B.F.C., Gardner F.F., et al., 1968, Nature 218, 1143

Seiradakis J.H., Gil J.A., Graham D.A., et al., 1995, A&AS 111, 205

Sieber W., Reinecke R., Wielebinski R., 1975, A&A, 38, 169

Toscano M., Bailes M., Manchester R.N., Sandhu J.S., 1998, ApJ 506, 863

von Hoensbroech A., Xilouris K.M., 1997, A&AS 126, 121

von Hoensbroech A., 1999, PhD thesis, Bonn University

von Hoensbroech A., Lesch H., 1999, A&A 342, L57

Weisberg J.M., Cordes J.M., Lundgren S.C., et al., 1999, ApJS 121, 171

Wielebinski R., Jessner A., Kramer M., Gil J.A., 1993, A&A, 272, L13

Wolszczan A., Frail D.A., 1992, Nature 355, 145

Young M.D., Manchester R.N., Johnston S., 2000, ASP Conf. Ser. Vol 202, p. 185

Zeissig G.A., Richards D.W., 1969, Nature 222, 150

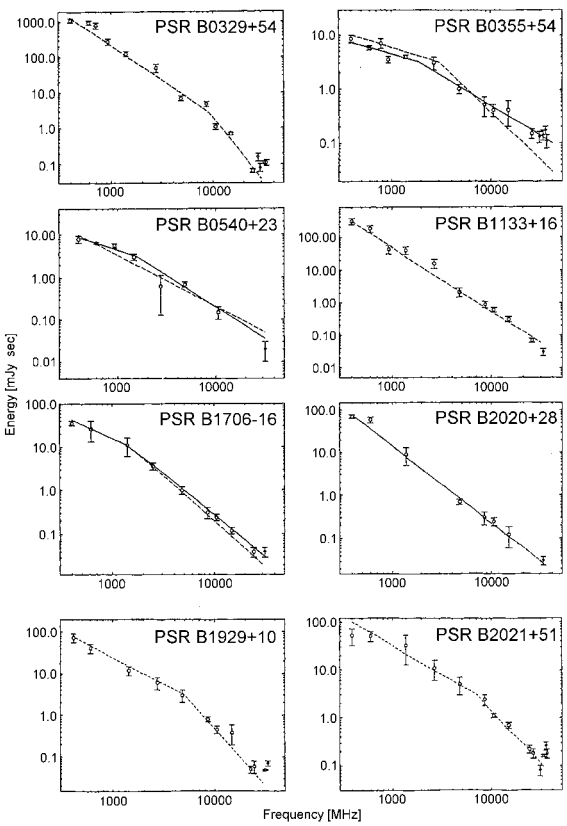


Fig. 3. The spectra of eight pulsars detected at mm-wavelengths

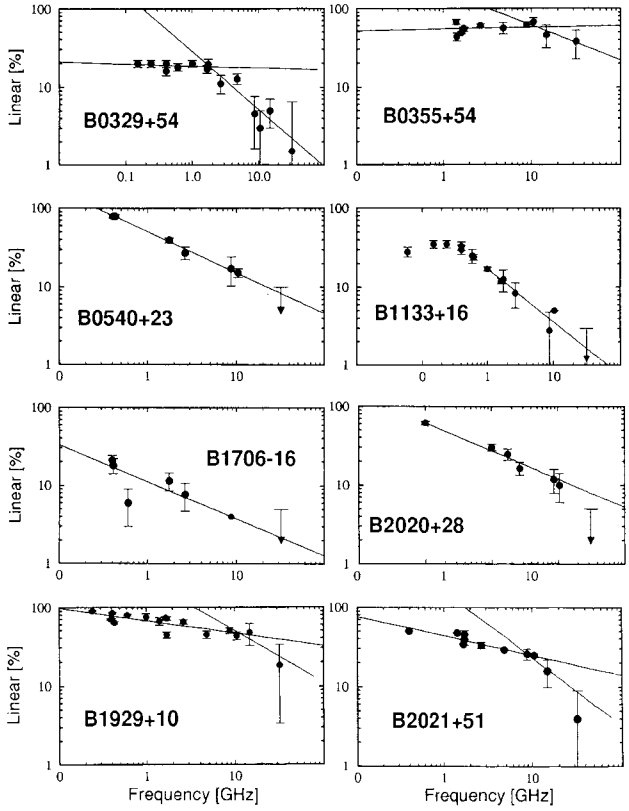


Fig. 4. The polarization of the eight pulsars shown in Figure 3. Note the sudden break in polarization and the corresponding change in the spectrum

Proceedings of the 270. WE-Heraeus Seminar on: *"Neutron Stars, Pulsars and Supernova Remnants"*
Physikzentrum Bad Honnef, Germany, Jan. 21-25, 2002, eds. W. Becker, H.Lesch & J. Trümper, MPE Report 278, pp. 171-176

Reviewing Pulsar Spectra

W. Sieber

Hochschule Niederrhein, University of Applied Sciences Reinarzstr. 49, D-47805 Krefeld, Germany

1. Problems solved?

Pulsar research must be considered - 35 years after the detection of pulsars - a mature science, where the basic questions have been raised and discussed. One would hope that many if not all generic and important problems have found some kind of answer and that scientific work can concentrate now on specific details requiring more in depth investigation. We know, however, that this picture is not true. Even well studied areas did in the past not always lead to a general accepted model and some were investigated at the beginning with enthusiasm but left behind.

This paper will concentrate on one narrow topic, pulsar radio spectra. It is the attempt to work out, what features are now generally accepted, but also what features are still in discussion after so many years of pulsar research. In this sense the paper will enlighten in a personal view those aspects which are still under discussion.

2. The spectrum, indicator of the emission mechanism

The spectrum, i.e. the total emitted energy in specific radio bands, was considered from the beginning as an easy to measure generic characteristic of the emission mechanism, especially since one could hope to learn something about an exciting new type of coherent amplification. Comella (1971) collected and published the first data points from measurements made at Arecibo, a work which was carried on by Sieber (1973) covering a wider compilation of observations from different observatories. Later on comprehensive data collections were published by Izvekova et al. (1981) and Lorimer et al. (1995) who extended the compilation to several hundreds of pulsars, albeit concentrated on few frequency bands. More recently wide collections of data were published by Malofeev (2000) and Maron et al. (2000).

From the beginning it was clear that pulsar spectra are characterizes by a "steep" spectral index, steeper than e.g. measured for supernova remnants, which explains why they were detected at rather low - below 1 GHz - frequencies. There were in addition indications that the spectra even steepen in some cases at higher frequencies beyond 1 GHz, although the measurement uncertainty was high. Undoubtedly, some pulsars showed a "low-frequency turnover", a decrease of the emitted energy at low frequencies, typically around 100 MHz, whereas other pulsars had a straight spectrum down to the lowest observable frequencies. The cause of this decrease - some kind of absorption in the magnetosphere or a loss of efficiency of the emission mechanism was discussed - remained unclear.

The problem with all the measurements was a high variability of the pulsar emission on many time scales, which resulted in a high uncertainty of the data points and which made it questionable, if a constant, time invariable spectrum exists at all. Investigations of pulsar spectra have, therefore, to face this problem and to look into the various possible contributions to the variability.

3. Variability

3.1. Intrinsic variability

Emission within a pulse during the pulse window is - depending on the pulsar - highly structured showing sometimes features as short as microseconds (microstructure) or even nanoseconds. Most pulsars have clearly visible sub-pulses extending over milliseconds, which in some rare cases are well organized with a shift from pulse to pulse, the so called drifting sub-pulses, Fig. 1.

This effect can now be quantitatively explained by the occurrence of an ExB force in the magnetosphere working on the out streaming particles. The drift bands cause a well defined periodic modulation (variability) of the received emission from pulse to pulse called P3 with characteristic time scale of several periods. Interestingly, some pulsars exhibit periodic modulations without recognizable drifting sub-pulses, where the duration extends over many periods, a kind of memory of the radiation mechanism which seems to be poorly understood so far.

Also poorly understood seems to be the producing mechanism for a sudden drop of the emission to zero (at least below the detection limit) called nulling, an effect which can be found for many pulsars. These nulls can stretch over many periods, even dominating the emission pattern, so that the emission occurs only in well defined bursts; an effect, which obviously results in a strong modulation of the radiation which may extend over many minutes of time.

Measurements show that the mentioned intensity variations are essentially broadband ($>$ 100MHz) and with high probability related to the emission mechanism or the structure of the magnetosphere or the surface of the neutron star. The time scales extend from nanoseconds to minutes. It is the hope (we will come to this point later) that averages of the

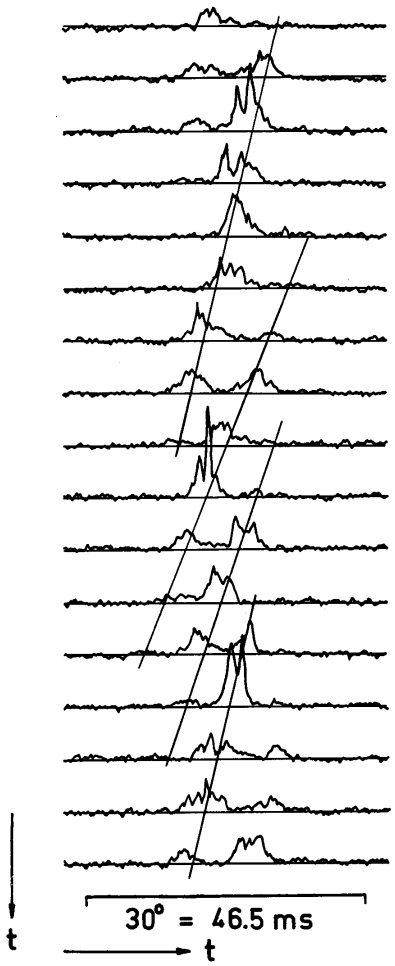


Fig. 1. Drifting sub-pulses of PSR B2016+28

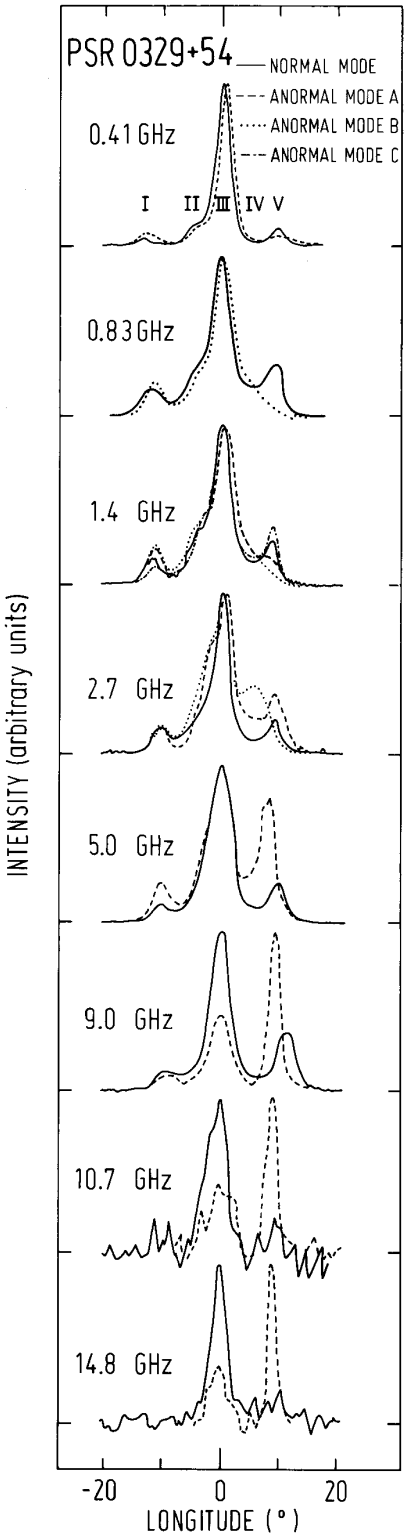


Fig. 2. Mode switching of PSR B0329+54

received signal over many minutes will "smooth out" all these variations.

There is less confidence with respect to another effect, which was called mode switching: In contrast to the well known behavior that the average of many pulses results in a stable average pulse profile, some pulsars show sudden variations of the average profile normally correlated with a change in intensity (Fig. 2). The times of variation are unpredictable and may occur suddenly even after e.g. several hours (Fig. 3).

For mode switching pulsars, time stable intensity values are obtainable only after some hours of integration, depending on the degree of accuracy which one would like to reach (see e.g. the investigation of Helfand et al. (1975) on the stability of integrated pulse profiles). Nevertheless, the hope is, that the intrinsic intensity variations can be averaged out by measurements lasting long enough - at least many minutes, for some pulsars even several hours. Least stable seem to be the mode switching pulsars whose long-term behavior has not yet been investigated very well.

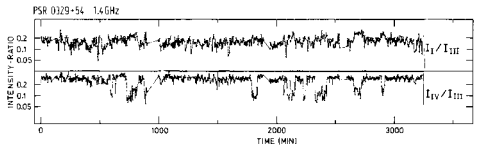


Fig. 3. Mode switching for PSR B0329+54; designation of components explained in Fig. 2

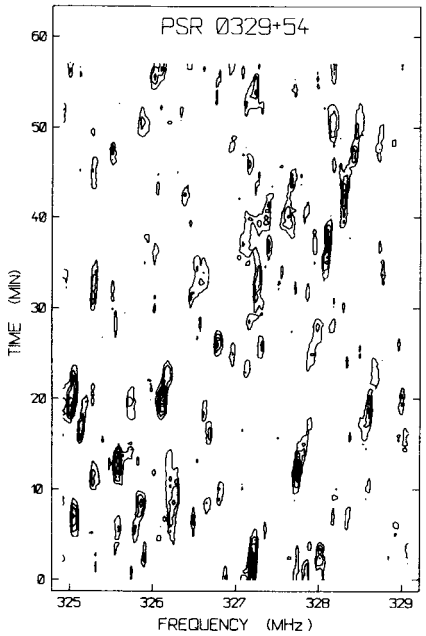


Fig. 4. Dynamic spectrum of PSR B0329+54 at ca. 327 MHz

3.2. External influence

3.2.1. Diffractive interstellar scintillation DISS

Scheuer (1968) showed as early as 1968 that interstellar scintillation may be the cause of the modulation of the received pulsar signal on time scales around several minutes, mainly because the small extent of the emission region makes pulsars ideal "point sources". Rickett (1969) could later proof that indeed features of strong and weak scintillation can be found in the received emission of pulsars, a decorrelation of the received signal in frequency and time being the clearest signature of this scintillation process, now being called diffractive interstellar scintillation DISS. The decorrelation is best represented by way of "dynamic spectra" (Fig. 4), where the average emission of one or several pulses is analyzed in a spectrometer and displayed as intensity contours. Successive spectra then depict the development of the structure in time.

Typical time scales for diffractive scintillation range from seconds to hours and frequency scales from about 100 kHz to a few 100 MHz. Since scattering parameters are now known for many pulsars, at least in the strong scintillation regime - albeit by far not for all and not for each frequency range - it is in principle possible to remove the strong intensity variations caused by DISS. Carefully planned observations, extending over much more than the decorrelation bandwidth, and/or with durations much longer than the decorrelation time should "average out" the variations so that the intrinsic emitted signal becomes measurable.

Alternatively one could take many observations of the emitted energy at a certain frequency - even if bandwidth and duration are smaller than the decorrelation scales - and average these scintillation modulated signals afterwards. The averaging process should smooth out the variations if enough samples are taken. Interestingly enough, this was more or less the procedure which was taken intuitively by the first observers, who just collected the measurements of many authors or observing periods.

3.2.2. Refractive interstellar scintillation RISS

For years it was known that pulsars show intensity variations even if diffractive scintillation effects are removed. The cause of the remaining long-term variations was unclear until Sieber (1982) could show, that they are correlated with the dispersion measure and due to the interstellar medium. The theoretical foundation was laid by Rickett, Coles and Bourgois in 1984, who showed that focussing and defocussing by features large compared to the Fresnel scale are the origin, an effect which is now called refractive interstellar scintillation RISS. The effect is rather broadband and the times scales rather large, extending perhaps even up to months or years as demonstrated e.g. by long-term observations of Stinebring et al. (2000) and Ramesh Bhat et al. (1999).

The results of Ramesh Bhat et al. (1999) shook, unfortunately, the confidence that diffractive scintillation effects may be easily removable by averaging over the decorrelation time or frequency scale, because they showed that the time and frequency scale is also variable, being influenced by the longer lasting RISS. Only really long-term observations are apparently able to tell the truth about the emitted signal strength.

The measurements of Stinebring et al. (2000) contained also good news: Their observations demonstrate quite clear that some pulsars, like PSR B0736-40, B1641-45 and B1859+03 exhibit very stable intensity over many years of observations. This means that the intrinsic emission at least for these pulsars must be stable. The observations give a clear hint, that the intrinsic emission of perhaps all pulsars is stable on long terms (intrinsic effects being excepted as demonstrated in Sec. 3.1). So that we have good hope that we can talk about stable intrinsic (emitted) pulsar radio spectra (on time scales as discussed above); which means that the original, naive, approach to the problem of pulsar spectra - being based on the assumption of stable intrinsic spectral behavior - has found a justification. There remains the problem, that very few pulsars are known so far whose emission has been measured to be stable on long terms. Far more long-term observations are needed to create a sound basis for accurate pulsar spectra determinations.

4. Spectra

4.1. Spectral index

0n the basis of the discussion in the preceeding sections, it seems appropriate to talk about pulsar spectra as a well-defined intrinsic characteristic of pulsars. Observations of the first years showed already the steep character of the spectra

Table 1. Compilations of pulsar spetra

Author	Number of Pulsars	Mean Spectral Index	Remarks
Sieber 1973	27	- 1.62	
Izvekova et al. 1981	52	- 2.0	
Lorimer et al. 1995	280	- 1.6	small frequency range
Malofeev 2000	340	- 1.71	wide frequency range
Maron et al. 2000		- 1.8	more high frequency values

(Sieber 1973), with an exponent of -1.62 for the high-frequency, power law part of the spectrum (not taking into account the low-frequency turnover found for some pulsars and without considering the high-frequency steepening). These first investigations were based on few sources (27), a number, which was increased later on by Izvekova et al. (1981) (52 sources) and then in a big step to 280 by Lorimer et al. (1995), Malofeev (1996, 2000) and Maron et el. (2000).

The computed mean spectral indices vary for these investigations between -1.6 and -2.0, underlining the steep character of the emitted spectra, but showing also a remaining uncertainty in the determination of the average value (which makes it not very sensible to give error bars). There is a wide scatter of measured spectral indices apparent for individual pulsars, ranging from 0.0 (or even slightly positive) to -3.1, which may explain also the scatter in the compiled average spectral index. There is also some uncertainty due to the fact that the frequency range used for the determination of the exponent is often limited either by lack of data or because one has to exclude either the low-frequency or the high–frequency turnover.

The spectral index is only weakly correlated with any other measurable pulsar parameter, as e.g. P, dP/dt etc., the clearest correlation being given to the characteristic age (Lorimer et al. 1995). It remains to theories of the emission mechanism to explain the physical reasons for the differences in spectral index for different pulsars (See however section 6).

4.2. Low-frequency turnover

A high percentage of those (normal) pulsars, where flux values below 100 MHz have been measured, show a low-frequency drop (turnover) in intensity (see Fig. 5); and it is known that correlations between for example the maximum frequency and the pulsar period exist.

Several mechanism have been proposed to explain this drop in intensity, often related to the radiation mechanism. Since the debate on the most probable emission mechanism is still ongoing, there is also still no definite answer to the cause of this low-frequency turnover.

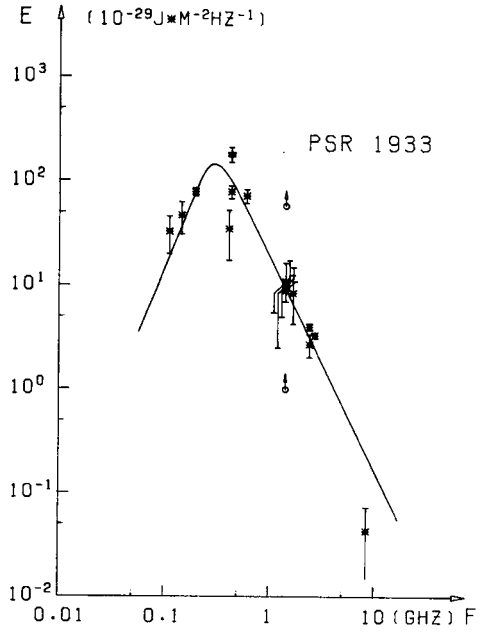


Fig. 5. Low-frequency turnover of PSR B1933+16

It is interesting to note, that some pulsars on the contrary show definitely no low-frequency turnover, although accurate measurements are available for them down to very low frequencies (10 MHz). Famous examples are the Crab pulsar (Fig. 6) and the millisecond pulsar PSR B1937+214 (Erickson & Mohany 1985). Explanations for the low-frequency turnover should also clearly state, why some pulsars obviously show increasing intensity down to very low frequencies.

4.3. Break in the power law spectrum

There were already at the beginning of the investigation of pulsar spectra indications, that also the high-frequency part of the spectrum may not completely be describable by just one power law. Very few pulsars showed indications of a steepening of the spectrum (see e.g. Fig. 7), which could be fitted by two power laws. The fact that pulsar emission is highly variable on many time scales (Sec. 3), makes it difficult to firmly proof such a break in the spectrum and to separate clearly intrinsic effects from e.g. long-time refraction effects. It should, however, be mentioned, that a break in the spectrum is a natural consequence of some theoretical radiation emission mechanisms; see e.g. Ochelkov & Usov (1984).

Most interesting appears also the fact that some pulsars show obviously an increase of their emission intensity at very high frequencies; this effect will be discussed in detail in the contribution of Wielebinski (2002) in these proceedings.

5. Millisecond pulsars

The detection of millisecond pulsars opened up a new era in the investigation of pulsars. Millisecond pulsars occupy a different region in the parameter space and build therefore a severe test

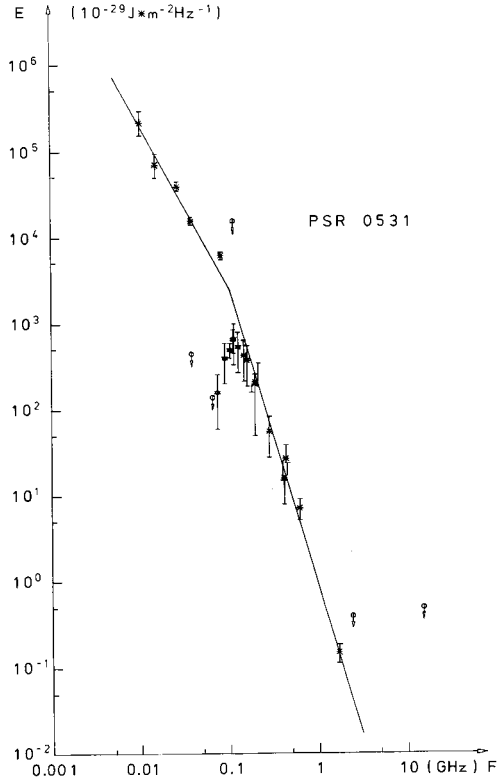


Fig. 6. Spectrum of PSR B0531+21, the Crab pulsar

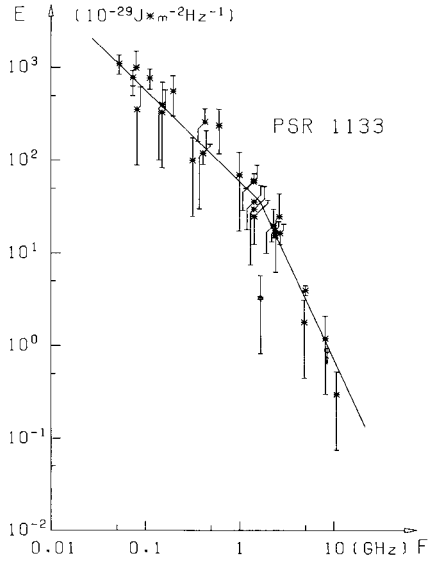


Fig. 7. Spectrum of PSR B1133+16

for every theory of radio emission. Comparisons between the characteristics of normal pulsars and millisecond pulsars were therefore eagerly expected. Kramer et al. (1998) published the spectra of 32 millisecond pulsars and found an exponent of = -1.8 if no distance limit was applied. Nearer pulsars (distance less then 1.5 kpc) showed a bit flatter spectrum with = - 1.6. They compared this result with 346 normal pulsars,

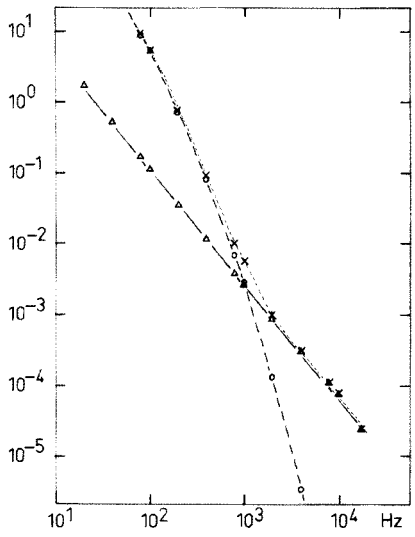


Fig. 8. Simulation of the steepening of the spectrum (Sieber 1997): A gaussian core component is assumed (circles) and a cone component (triangles). The measured intensity of the core component and of the whole profile (crosses) drops rapidly just due to the shrinking of the profile width at high frequencies

which showed an exponent of = -1.6 for all distances and of = - 1.7 for distances < 1.5 kpc. In correspondence to the result of Toscano et al. (1998), who measured an index of = -1.9 for southern millisecond pulsars, one comes to the conclusion that there exists no real difference in the spectral index between normal pulsars and millisecond pulsars. It seems that the same radiation mechanism works in both environments.

5.1. Low-frequency turnover

Kuzmin & Losovsky (2001) were able to extend the spectral frequency range of quite a collection of millisecond pulsars down to 100 MHz. Interesting enough no low-frequency turnover (drop at low frequencies) was detected, with one exception, PSR J1012+5307. Together with the fact that the millisecond pulsar PSR B1937+214 shows a straight spectrum down to 10 MHz, there is the indication, that low-frequency turnovers might be rarer in millisecond pulsars than in normal pulsars.

6. Geometry

The geometry of the hollow-cone must have a direct impact on the spectrum, if the radio emission is - as we believe - concentrated in a hollow cone with a frequency dependent width. Kramer et al. (1994) and Sieber (1997) could demonstrate that the observed spectrum may be indeed steeper than the emitted one, the steepening being caused by the shrinking of the hollow-cone width at high frequencies.

An emitted spectrum with exponent = -1.5 could - depending on the specific geometry - be observed as a spectrum with = -2. This would mean, that the radiation mechanism itself must not produce such steep spectra as we observe them.

In addition, the received intensity may depend on several more geometrical factors, e.g. the curvature radius of the field

lines, the emission hight over the neutron star surface and the orientation of magnetic field axis and rotation axis. Kuzmin & Solov'ev (1986) worked out an curvature radiation emission model which reflects quite well as an example the spectral characteristics of PSR B1133+16, including the low-frequency turnover and taking into account all these geometrical effects.

It appears obvious that geometrical effects influence the shape of the received spectrum; but it is much harder to determine the exact impact in individual cases, since then the precise geometry has to be known, e.g. the angle between rotation axis and magnetic field , as well as the impact angle . Normally the geometry is derived from measurements of the polarization angle sweep across the profile; these measurements are, however, often spoiled by orthogonal polarization angle jumps and may give unreliable results. Most promising are polarization angle histograms which often allow to determine at least the angle sweep with good precision.

7. Conclusions

From the arguments presented one is led to the conclusion that astonishingly few problems found an answer so far. One of these is obviously the question of the stability of the intrinsic spectrum which seems to be settled in the sense, that we can now indeed assume a stable emitted spectrum being heavily modulated by transmission effects on all time scales extending up to months. Also the intrinsic variations manifested as drifting sub-pulses and P3 modulation can now be explained more and more in the framework of geometrical mapping to the polar cap of the neutron star.

To the still debated problems belongs e.g. the question of the cause of the low-frequency turnover in the spectra of pulsars - normal and millisecond - the cause of the high-frequency break in some spectra and the turn-up at extreme high frequencies. And finally it would be of great help if the geometry of the emission geometry of more and more pulsars could be determined with higher confidence.

Acknowledgments: The support of the Wilhelm und Else Heraeus-Stiftung is very much acknowledged. This work was also supported by INTAS grant no. 2000-849.

References

Comella J.M., 1971, Ph.D. thesis

Erickson W.C., Mahoney M.J., 1985, ApJ 299, L29

Helfand D.J., Manchester R.N., Taylor J.H.: observations of pulsar radio emission. III. Stability of integrated profiles, 1975 ApJ 198, 661-670

Izvekova V.A., Kuzmin A.D., Malofeev V.M. et al., 1981, Ap&SS 78, 45

Kramer M., Wielebinski R, Jessner A., Gil J.A., Seiradakis J.H.: 1994, A&ASS 107, 515

Kramer M., Xilouris K.M., Lorimer D.R. Doroshenko O., Jessner A., Wielebinski R., Wolszczan A., Camilo F.: The characteristics of millisecond pulsar emission. I. Spectra, pulse shapes, and the beaming fraction, 1998 ApJ 501, 270-285

Kuzmin A.D., Losovsky B.Ya.: No Low Frequency Turn-over in the Spectra of Millisecond Pulsars, 2001 A&A

Kuzmin A.D., Solovev A.G.: Model pulsar radio spectra and pulse profiles, 1986, Sov. Astron. 30, 38

Lorimer D.R., Yates, J.A., Lyne A.G., Gould D.M.: Multifrequency flux density measurements of 280 pulsars, 1995 MNRAS 273, 411-421

Malofeev V.M., 1996, PASPC 105, 271

Malofeev V.M., 2000, PASPC 202, 221

Maron O., Kijak J., Kramer M., Wielebinski R.: Pulsar spectra of radio emission, 2000, A&ASS 147, 195-203

Ochelkov Yu.P., Usov V.V.: The nature of low-frequency cutoffs in the radio emission spectra of pulsars, 1984, Nature 309, 332-333

Ramesh Bhat N.D., Pramesh Rao A., Yashwant Gupta: Long-term scintillation studies of pulsars. I. Observations and basic results, 1999, ApJS 121, 483-513

Rickett B.J., 1969 Nature 221, 158

Rickett B.J., Coles W.A., Bourgois G., 1984, A&A 134, 390

Scheuer P.A.G., 1968 Nature 218, 920

Sieber W.: Pulsar spectra: A summary, 1973 A&A 28, 237-252

Sieber W.: Causal relationship between pulsar long-term intensity variations and the interstellar medium, 1982, A&A 113, 311

Sieber W.: Geometrical effects on radio pulsar profiles and spectra, 1997, A&A 321, 519-522

Stinebring D.R., Smirnova T.V., Hankins T.H., Hovis J.S., Kaspi V.M., Kempner J.C., Myers E., Nice D.J.: Five years of pulsar flux density monitoring: refractive scintillation and the interstellar medium, 2000, ApJ 539, 300-316

Toscano M., Bailes M., Manchester R.N. et al., 1998, ApJ 506, 863

Wielebinski R.: Characteristics of (normal) radio pulsars, in: Becker et al. (eds.), Neutron Stars, Pulsars and Supernova Remnants, Proceedings of the 270 WE-Heraeus-Seminar 2002

Proceedings of the 270. WE-Heraeus Seminar on: *"Neutron Stars, Pulsars and Supernova Remnants"*
Physikzentrum Bad Honnef, Germany, Jan. 21-25, 2002, eds. W. Becker, H.Lesch & J. Trümper, MPE Report 278, pp. 177-182

Enlarging the Parameter Space and our Understanding *or* The Radio Emission of Millisecond Pulsars

Michael Kramer

University of Manchester, Jodrell Bank Observatory, UK

Abstract. The understanding of pulsar radio emission demands a close look at all regions of the huge parameter space present for pulsar observations. In this review we concentrate on the space given by the range of observed pulse periods, spanning four orders of magnitude. A comparative study of the emission properties of millisecond pulsars and normal pulsars, both at radio and high energy frequencies, promises to shed light on the still poorly understood emission theory.

1. Introduction

The search for a theoretical framework that is able to explain the radio emission of pulsars, has been largely unsuccessful. This is due to the difficulty to include all the different phenomena and time scales observed in radio pulsars into a working model. It is essential to isolate the bigger picture, and one way of doing this, is to enlarge the parameter space. Rather than making the picture even more complicated by more observations that are difficult to explain, the aim must be to study the emission properties by pushing the known parameter space to new boundaries to provide solid and obvious constraints.

The parameter space relevant for pulsar radio emission is large. Obvious parameters are the period and its increase, determining important values like magnetic field, or potential drop above the surface. Further parameters are time resolution, frequency coverage in the radio, but also from the radio regime to high energies, eventually simultaneously, and sensitivity. A large neglected part of the parameter space in pulsar studies is that of observing length – quite naturally as many time allocation committees do not appreciate long-term projects. However, some new phenomena will only be discovered, when sources – not only pulsars, that is — are monitored for a long time span. In this review I will concentrate on the period space, and the implication that can be derived from studying emission of millisecond pulsars. For the other aspects, the reader may be referred to other contributions (e.g. Karastergiou et al.) or recent literature (e.g. Kramer et al. 2002).

2. Millisecond Pulsars

Despite a manifold increase in the number of known pulsars, the smallest period of any known pulsar is still that of PSR B1937+21 discovered by Backer et al. (1982) with 1.56 ms. As a consequence of their small periods millisecond pulsars (MSPs) are surrounded by magnetospheres which are 6 to 7 orders of magnitude more compact than those of slower rotating pulsars. Inferred magnetic fields close to the surface of MSPs are 3 to 4 orders weaker than in normal pulsars. In contrast, charges at these regions experience an accelerating potential similar to that of normal pulsars. The impact of the different environment on the emission processes in MSPs magnetospheres has been a question addressed already shortly after their discovery. With the plethora of MSPs detected over the years, a better understanding of not only MSPs (as radio sources and tools) but slower rotating (normal) pulsars as well. Recent addressing the radio emission of pulsars are those by Kramer et al. (1998, Paper I) on spectra, pulse shapes and beaming fraction, by Xilouris et al. (1998, Paper II) on polarimetry of 24 MSPs, by Sallmen (1998) and Stairs et al. (1999) on multi-frequency polarimetry, by Toscano et al. (1998) on spectra of Southern MSPs, by Kramer et al. (1999b, Paper III) on multi-frequency evolution, and Kramer et al. (1999a, Paper IV) on profile instabilities of MSPs. A number of contributions can also be found in the proceedings of IAU Colloquium 177.

2.1. Flux Density Spectra

Prior to the investigations leading to Paper I it was commonly believed that the spectra of millisecond pulsars were steeper than those of normal pulsars. It was demonstrated in Paper I that the distribution of spectral indices for MSPs is in fact not significantly different, finding an average index of -1.76 ± 0.14 (Paper III). The initial impression was due to a selection effect, since the first MSPs were discovered in previously unidentified steep spectrum sources. Results presented in Paper III also suggest that most spectra can be represented by a simple power law, i.e. clear indications for a steepening at a few GHz as known from normal pulsars are not seen.

It is interesting to note that the current data suggest a similar mean flux density spectrum but the distribution spectral indices seems to be somewhat narrower for MSPs than for normal pulsars (Fig. 1).

[1] Upper row: MSPs (PSRs J0218+4218, J0621+1001, B1534+12, J1640+2224, J1730−2304), lower row: normal pulsars (PSRs B1831−04, B2045−16, B2110+27, B2016+28, B1826−17)

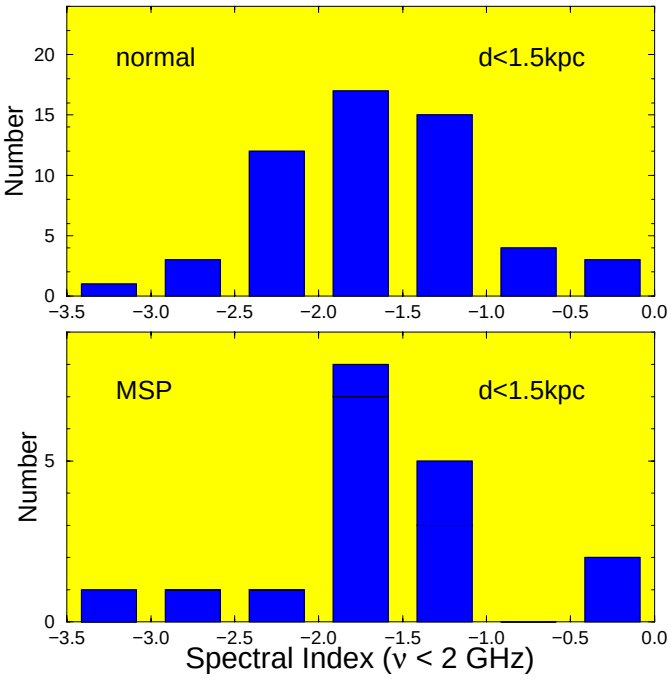


Fig. 1. Distribution of spectral indices for normal pulsars and MSPs, measured in a frequency range below 2 GHz. Note that all data have been derived from distance limited samples in order to avoid selection effects (see text for details).

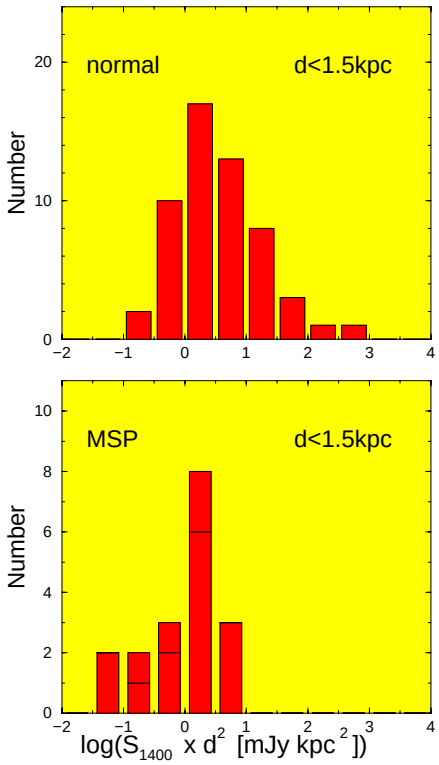


Fig. 2. Luminosity of normal pulsars and MSPs derived from the flux density measured at 1400 MHz. Note that all data have been derived from distance limited samples in order to avoid selection effects (see text for details).

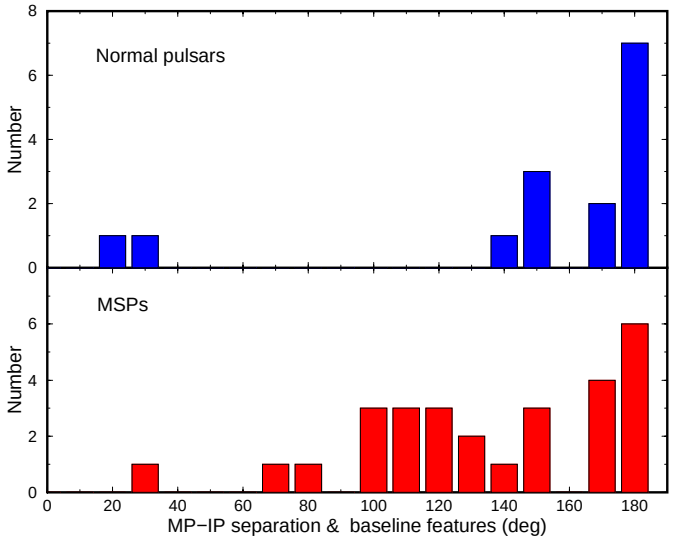


Fig. 4. Location of addition pulse feature across the pulse period for normal pulsars and MSPs.

2.2. Radio Luminosity

When comparing the spectra and radio luminosity of normal pulsars and MSPs, one has to take extra care that selection effects do not bias the result. The sample of MSPs in the galactic plane is limited by scattering effects, resulting in the discovery of mostly nearby MSPs. In contrast, normal pulsars are also affected by scattering, but the longer period allows their detection to larger distances. It is therefore useful to compare only a distance limited sample that can be assumed to be sampled adequately. A distance of 1.5 kpc is appropriate, as outlined in Paper I. As a result one obtains that MSPs are slightly less luminous, being also slightly less efficient in converting spin-down luminosity into radio emission (Fig. 2)

Bailes et al. (1997) pointed out that isolated MSPs are less luminous than those in binary systems, pointing towards a possible relation between radio luminosity and birth scenarios. We have compared a distance limited sample of normal and MSP and came to a similar result with the MSPs as a whole being weaker sources than normal pulsars.

2.3. Pulse Profiles – Complexity, Interpulses and Beaming Fraction

For a long time it was also believed that MSP pulse profiles are more complex than those of normal pulsars. Using a large uniform sample of profiles for fast and slowly rotating pulsars, we showed in Paper I that the apparent larger complexity is due to the (typically) larger duty cycle of MSPs. MSP profile can hence studied in greater detail, facilitating the recognition of detailed structure. In fact, blowing up normal pulsar profiles in a similar manner leads to very similar profiles. A quantitative proof is given in Paper I, while Fig. 3 provides an illustration.

Despite this similarity, there is a profound difference to the profiles of normal pulsars! Additional pulse features like interpulses, pre- or post-cursor are much more common for MSPs. While only $\sim 2\%$ of all normal pulsars are known to show such features, we detect them for more than 30% of all (field) MSPs.

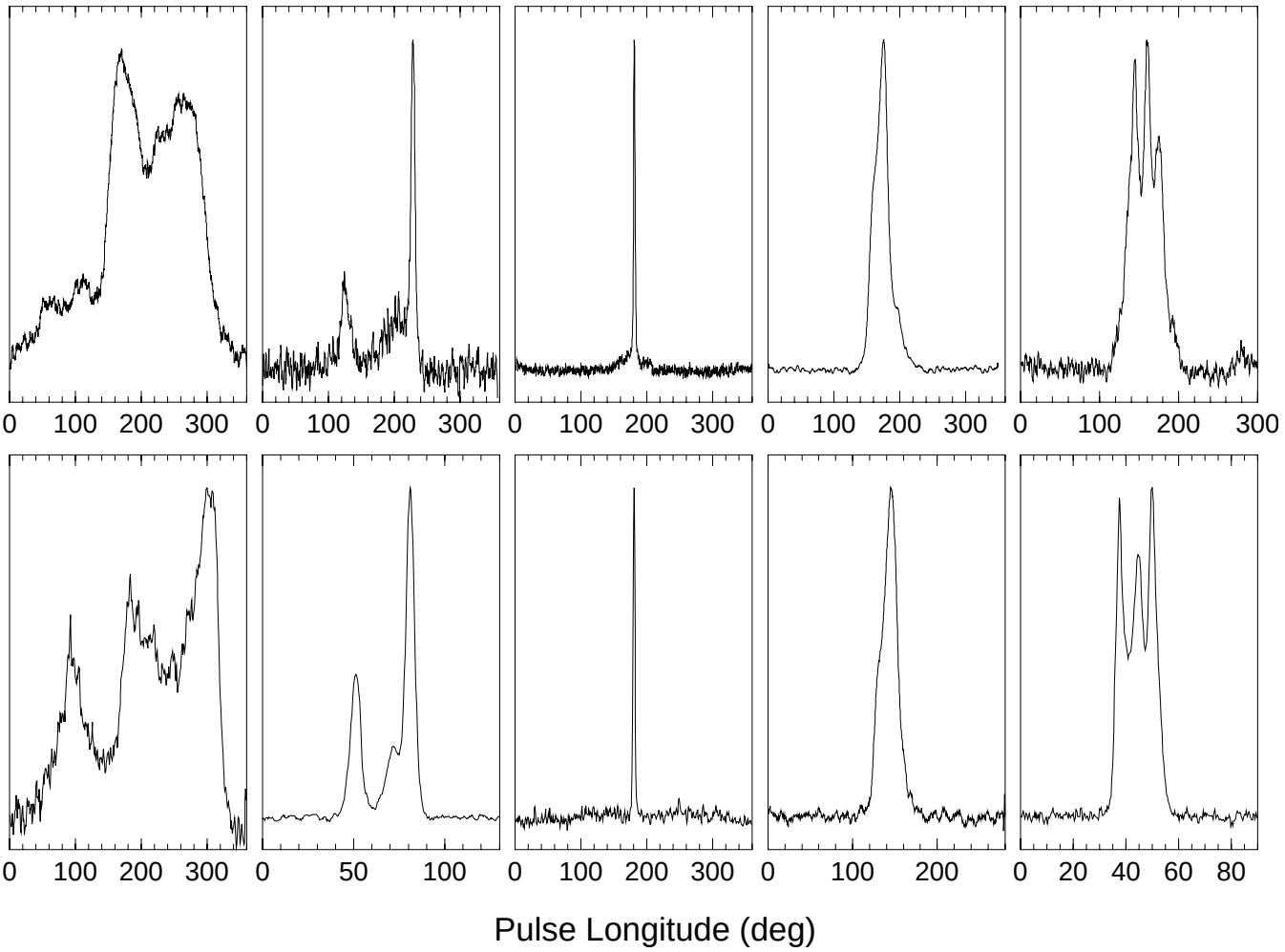


Fig. 3. Pulse profiles for a selected sample of MSPs and normal pulsars (Paper I and EPN database). Note the similarity and make a guess which is which! See footnote[1] for the solution.

They also appear at apparently random positions across the pulse period than we see for normal pulsars (Fig. 4). Their frequent occurrence and location makes one wonder — given the similarity of the main pulse shapes otherwise — whether these components are of the same origin as the main pulse profile or whether other sources of emission are responsible.

One interpretation of these additional pulse features is related to a model first put forward for some young pulsars by Manchester (1996), who interpreted some interpulses as the results of cuts through a very wide cone. This is an interesting possibility also for MSPs, since their beam width appears to be much smaller than predicted from the scaling law derived for normal pulsars. The beam width of normal pulsars, ρ, i.e. the pulse width corrected for geometrical effects (see Gil et al. 1984), follows a distinct $\rho \propto P^{-0.5}$-law (e.g. Rankin 1993, Kramer et al. 1994, Gould 1994). Using polarization information to determine the viewing geometry and also applying statistical arguments, we calculated ρ (at a 10% intensity level) for MSPs and showed (Paper I) that they are not only much smaller than the extrapolation of the known law to small periods, but that – under the assumption of dipolar magnetic fields – the emission of some MSPs seems to come even from within the neutron star — a really disturbing result! While we discuss the possibility of non-dipolar fields and the used the polarization information below, one explanation would be that (perhaps below a critical period) the emission beam does not fill the whole open field line region ("unfilled beam"). The situation improves a bit when we consider the additional pulse features as regular parts of the pulse profile (Fig. 5). In fact, those MSPs with interpulses may indicate an additional inner scaling parallel to that known for normal pulsars, which could be a result of unfilled beams.

Another explanation of the additional pulse features could be the possibility that so-called "outer gap" emission is responsible (see Paper II). A number of MSPs are detected as X-ray sources (see contribution by Becker) and those with magnetospheric emission are probably detected by emission created in the outer magnetosphere, i.e. "outer gaps" (see contribution by Romani). As MSPs have very compact magnetospheres, the usual location of radio emission in some distance to the star could well coincide with the location of outer gaps, enabling the detection of "classical" polar-cap radio emission and that of outer gaps at the same time. This is similar to the circum-

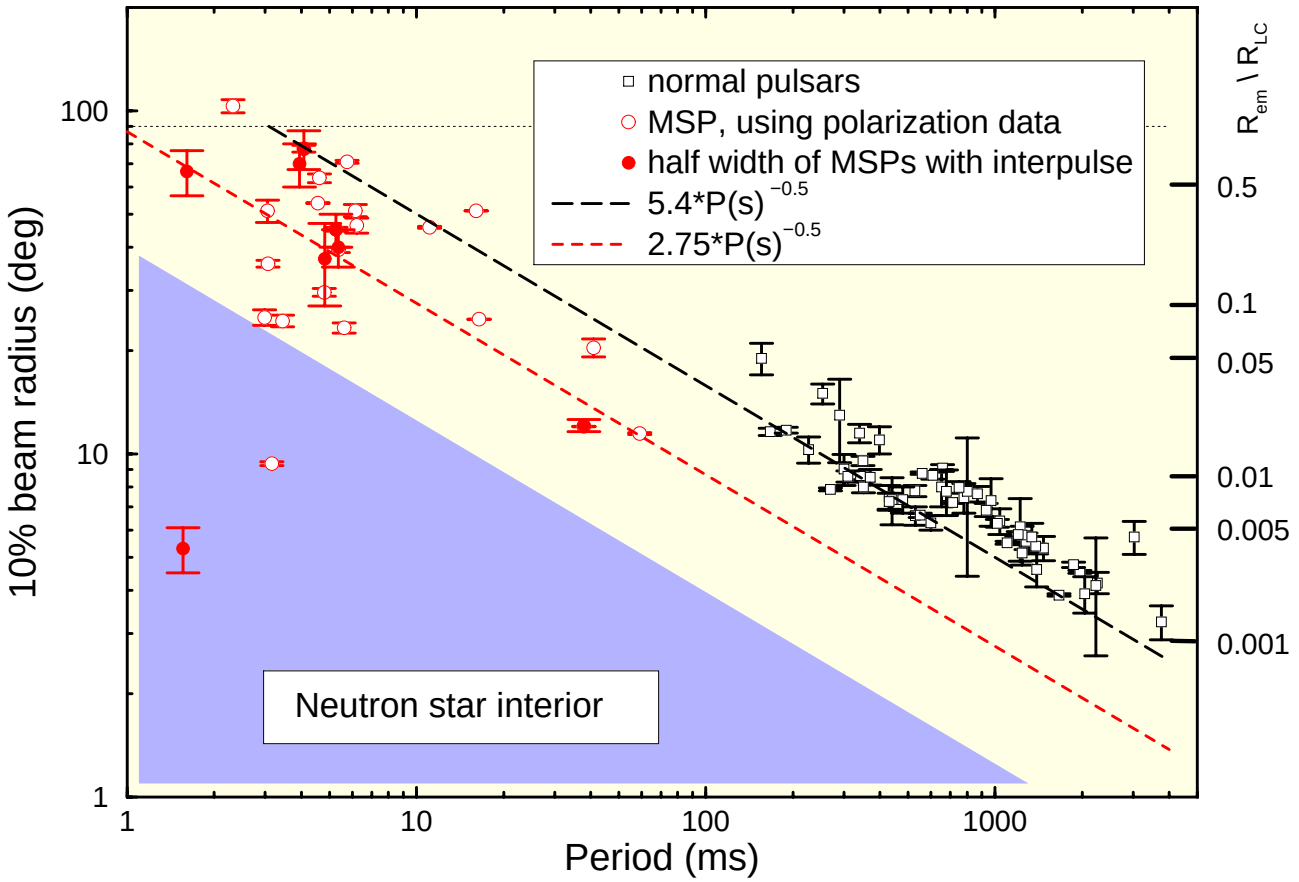


Fig. 5. The beam radius, ρ, for normal pulsars and MSPs. MSPs do not follow the scaling law of normal pulsars (here Gould 1994) but their beaming fraction is much smaller. For MSPs with interpulses an "inner" relationship is indicated.

stances probably responsible for the additional high-frequency components seen in the Crab pulsar (Moffett & Hankins 1996).

Finally, it should be pointed out that the much smaller beam width has consequences for population studies, which usually utilize the $\rho - P$ scaling as found for normal pulsars. The failure of this law leads to an overestimated beaming fraction and an underestimation of the birth rate of recycled pulsars (see Paper I).

2.4. Polarization Properties

The radio emission of MSPs shows all polarization features known from normal pulsars, i.e. circular polarization which is usually associated with core components, linear polarization which is usually associated with cone components, and also orthogonal polarization modes (see Paper II, Sallmen 1998, Stairs et al. 1999). Despite the qualitative similarities, the position angle (PA) swing is often strikingly different. While normal pulsars show typically a S-like swing, which is interpreted within the rotating vector model (RVM; Radhakrishnan & Cooke 1969), the PAs of many MSPs often appear flat (see e.g. Fig. 6). This could be interpreted in terms of non-dipolar fields, but Sallmen (1998) noted that larger beam radii lead to a larger probability for outer cuts of the emission cones, i.e. flatter PA swings according to the RVM. Although one should bear in mind the limitations of the ρ-scaling law and another *caveat* discussed later, this interpretation justifies the geometrical interpretation of the data. Magnetic inclination angles derived from RVM fits are important for binary evolution models and determinations of the companion mass (Fig. refincl).

2.5. Frequency Evolution

The radio properties of normal pulsars show a distinct frequency evolution, i.e. with increasing frequency the profile narrows, outer components tend to dominate over inner ones, and the emission depolarizes. The emission of MSPs, which at intermediate frequencies tends to be more polarized than that of normal pulsars (Paper II), also depolarizes at high frequencies (Fig. 8; Paper III). Simultaneously, the profile width hardly changes or remains constant (see Fig. 9). This puts under test attempts to link both effects to the same physical origin (i.e. birefringes). In fact, many profiles also exhibit the same shape at all frequencies, while others evolve in an unusual way, i.e. the spectral index of inner components is not necessarily steeper, so that a systematic behavior as seen for normal pulsars is hardly observed. This can be understood in terms of a compact emission region, an assumption further supported by a simultaneous arrival of the profiles at all frequencies. We emphasize that we have not detected any evidence for the existence of non-dipolar fields (Paper III).

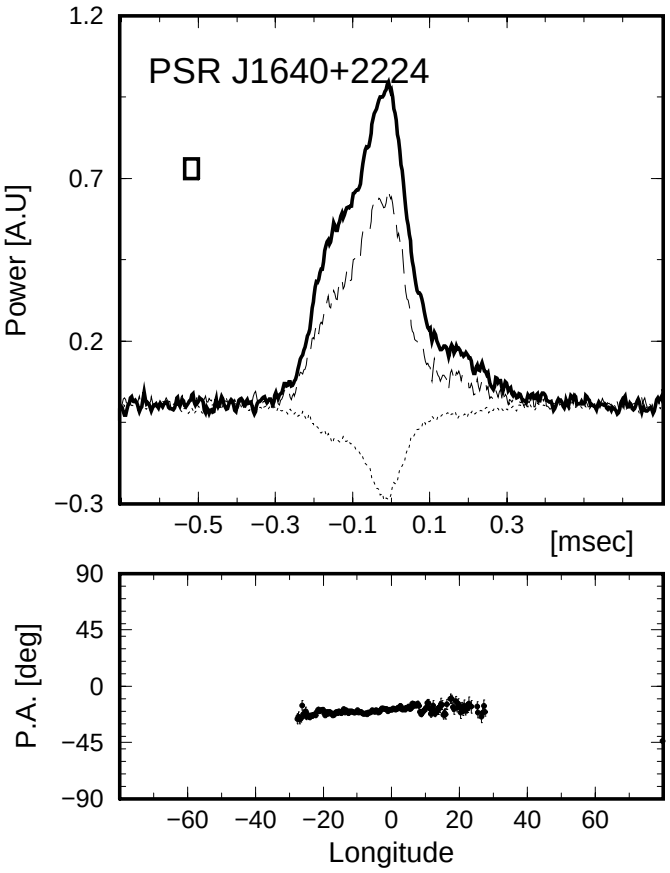


Fig. 6. Profile of PSR J1640+2224 as an example for a MSP exhibiting a flat PA swing.

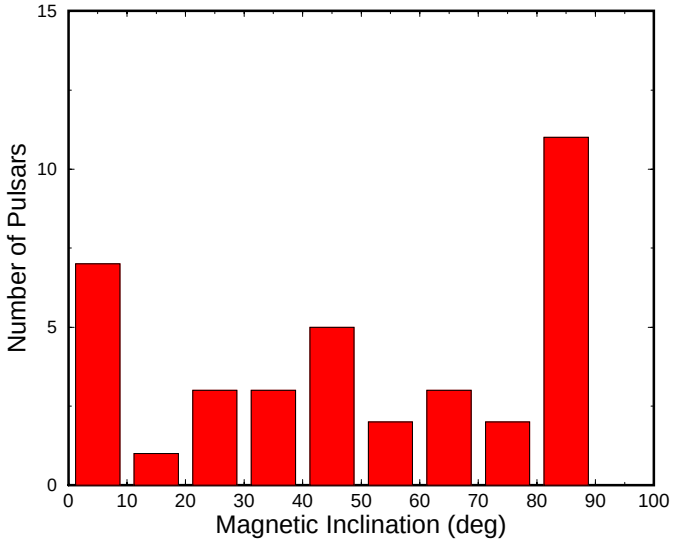


Fig. 7. Distribution of magnetic inclination angles derived from RVM fits.

2.6. Profile and Polarization Instabilities

The amazing stability with time of MSP profiles has enabled high precision timing over the years. However, in Paper IV we discussed the surprising discovery that a few MSPs do

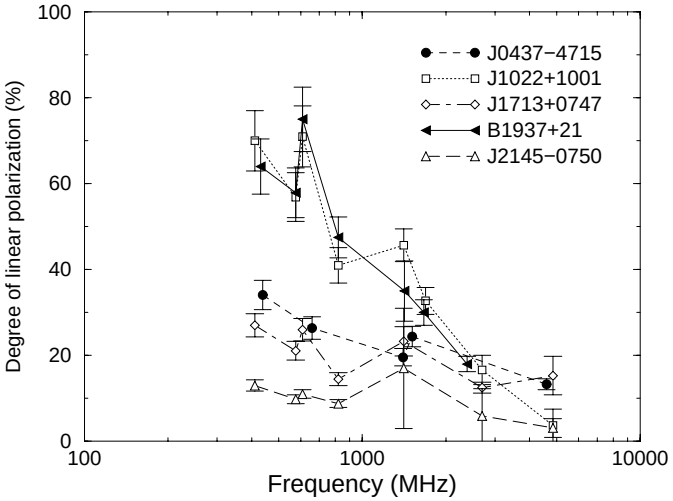


Fig. 8. Degree of polarization for some MSPs as a function of frequency.

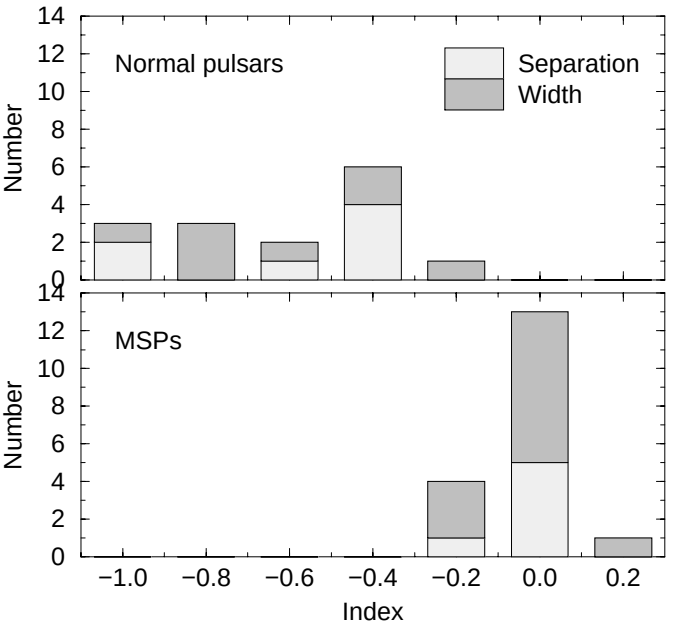


Fig. 9. Power law index of profile narrowing with frequency (see Paper III for details).

show profile changes caused by an unknown origin. These time scales of these profile instabilities are inconsistent with the known mode-changing. In particular, PSR J1022+1001 exhibits a narrow-band profile variation never seen before (Paper IV), which could, however, be the result of magnetospheric scintillation effects described by Lyutikov (2001). With the pulse shape the polarization usually changes as well, and hence this effect is possibly related to phenomena which we discovered in Paper II. Some pulsars like PSR J2145–0750 (Paper II) or PSR J1713–0747 (Sallmen 1998) show occasionally a profile which is much more polarized than their usual pulse shape. In the case of PSR J2145–0750, the PA changes from some distinct (though not S-like) swing to some very flat curve. This is a strong indication that some of the flat PA swings discussed above may not be of simple geometrical origin alone.

3. Summary and Conclusions

The emission properties of millisecond pulsars are in many respects similar to those of slowly rotating pulsars. However, there are a few remarkable differences like additional profile components and a very week frequency evolution for most MSPs, which can be attributed to the smaller, compact magnetosphere. The additional pulse components may be representatives of outer gap emission, providing an interesting link to the X-ray properties of MSPs. This motivates a close inspection of their joint radio and high energy characteristics. Results of this work in progress will be presented elsewhere.

Acknowledgements. The author gratefully acknowledges the support by the Heraeus foundation and thanks the organizers for a wonderful meeting.

References

Backer et al. 1982, Nature, 300, 615
Bailes, M., et al 1997, ApJ, 481, 386
Gil, J.A., et al. 1984, A&A, 132, 312
Gould, D.M. 1994, PhD thesis, University of Manchester
Lyutikov, M., 2001, Ap&SS, 278, 81
Kramer M., Xilouris K. M., Lorimer D. R., et al. 1998, ApJ, 501, 270 (Paper I)
Kramer M., Xilouris K. M., Camilo F., et al. 1999a, ApJ, 520, 324 (Paper IV)
Kramer M., Lange, Ch., Lorimer, D.R., et al. 1999b, ApJ, 526, 975 (Paper III)
Manchester, R.N. 1996, in Proc of IAU Colloq. 177, ASP Conf. Series, p. 193
Moffett, D.A., Hankins, T.H., 1996, ApJ, 468, 779
Radhakrishnan, V., & Cooke, D.J., 1969, ARA&A, 32, 591
Rankin, J.M. 1993, ApJ, 405, 285
Sallmen, S. 1998, PhD thesis, University of California at Berkeley
Stairs ,I. H., Thorsett, S. E., & Camilo, F. 1999, ApJS, 123, 627
Toscano, M., Bailes, M., Manchester, R.N., & Sandhu, J. 1998, ApJ, 506, 863
Xilouris, K. M., Kramer, M., Jessner, A., et al. 1998, ApJ, 501, 286 (Paper II)

Proceedings of the 270. WE-Heraeus Seminar on: *"Neutron Stars, Pulsars and Supernova Remnants"*
Physikzentrum Bad Honnef, Germany, Jan. 21-25, 2002, eds. W. Becker, H.Lesch & J. Trümper, MPE Report 278, pp. 183-192

The peculiar millisecond pulsars in the globular clusters NGC 6397 and NGC 6752

Andrea Possenti[1]

Osservatorio Astronomico di Bologna, Via Ranzani 1, 40127 Bologna, Italy

Abstract. The millisecond pulsars discovered in globular clusters are diagnostic tools for studying the dynamics of the clusters, the intracluster ionized gas and the evolution of the binaries embedded in the cluster. In the first two years of a search at 1.4 GHz in progress at the Parkes radio telescope 12 new millisecond pulsars have been discovered in 6 globular clusters in which no pulsars were previously known. The scientific fall-back of these discoveries is here discussed for the case of two globular clusters: NGC 6397 and NGC 6752.

1. Introduction

Millisecond pulsars (MSPs) are old neutron stars *recycled* through transfer of matter and angular momentum from a mass losing companion in a binary system (e.g. Alpar et al. 1982; Smarr & Blandford 1976; Bhattacharya & van den Heuvel 1991; Kulkarni & Anderson 1996). They are massive and almost pointlike objects, appearing very good test masses for probing gravitational effects. Most of them are also extremely stable clocks, allowing very accurate measurements of their rotational parameters and position in the sky. Finally they are the endpoints of a complex stellar evolution in binary systems, involving not yet completely understood mechanisms like common envelope, accretion disk instabilities, magnetic braking, irradiation, evaporation.

Besides evolution of a primordial binary, in a Globular Cluster (GC) another formation channel for the MSPs is available: in fact exchange interactions in the ultra-dense stellar environment of the cluster core can sustain the formation of various kinds of binaries suitable for recycling neutron stars (Davies & Hansen 1998; Rasio, Pfahl & Rappaport 2001). As a consequence, despite the large difference in total mass between the disk of the Galaxy and the Globular Cluster system, about 50% of the entire MSP population has been found in the latter.

In particular millisecond pulsars found in globular cluster have proven to be valuable tools for studying:

- the potential well of the globular cluster (e.g. Phinney 1992; Camilo et al. 2000);
- the dynamical interactions in the globular cluster core (e.g. Phinney & Sigurdsson 1991);
- the gas content in the globular cluster (e.g. Freire et al. 2001)
- the neutron star retention in the globular cluster (e.g. Rappaport et al. 2001);
- the binary evolution in a crowded environment (e.g. Rasio et al. 2000).

Unfortunately, the MSPs in GC are sources difficult to be detected. The main reason for their elusiveness is that *GC-MSPs are often distant pulsars in close binary systems.* Their large distances *(i)* make their fluxes typically very small and *(ii)* strongly distort their signals due to the dispersive effects of propagation through the interstellar medium. Their inclusion in tight binaries *(iii)* causes Doppler-shift changes of the apparent spin period and sometimes *(iv)* makes the radio signal periodically obscured by eclipses.

As a consequence, except for the relevant case of 47 Tucanae (Camilo et al. 2000), the discovery rate of these objects strongly declined in the second half of the 1990s: in the 7 years from 1987 (when the first GC-MSP, B1821−24, was discovered in M28 at Jodrell Bank: Lyne et al. 1987) to 1994 (Biggs et al. 1994) 32 GC-MSPs entered the catalog, whereas no new source was published in the following 5 years.

Since two years a new deep search has been running at the Parkes radio telescope; it involves people from the Cagliari Astronomical Observatory (N. D'Amico), from the Australia Telescope National Facility (R. N. Manchester and J. Sarkissian), from the Jodrell Bank Observatory (A. G. Lyne), from the Columbia Astrophysics Laboratory (F. Camilo), and the author of this review. As a result, to date a dozen new pulsars have been discovered in 6 globular clusters, none of which had previously known pulsars associated. More recently, 3 further millisecond pulsars have been detected in one of these clusters (namely NGC 6266) by Jacoby et al. (2002), exploiting the sensitivity of the new Green Bank Radiotelescope. So the total number of known millisecond pulsars in globular cluster is now 57.

In the following I will focus on the globular clusters NGC 6397 and NGC 6752, summarizing the main scientific results obtained so far, sometimes combining radio data with optical and X-ray observations. What I will review here have been originally reported in seven different papers: D'Amico et al. (2001b) and Possenti et al. (2001) described the new hardware and software systems adopted in the Parkes search for GC-MSPs, the current status of the experiment and its perspectives. D'Amico et al. (2001a) announced the discovery of the first 4 millisecond pulsars detected during the Parkes search for GC-MSPs. D'Amico et al. (2001c) and Ferraro et al. (2001)

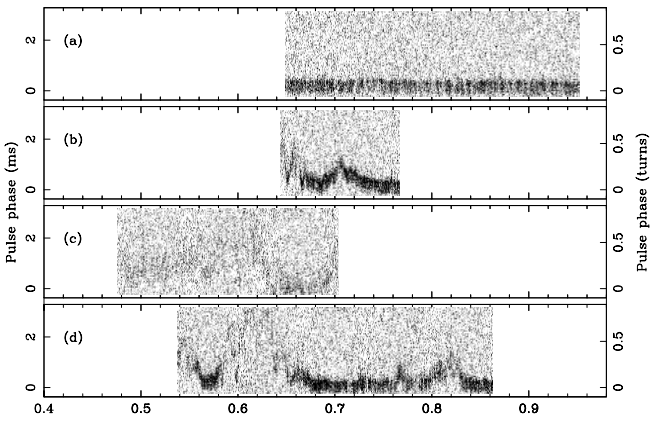


Fig. 1. Observed signal intensity at 1.4 GHz as a function of orbital phase and pulsar phase for four long observations away from the nominal eclipse region. The data are processed in contiguous integrations of 120 s duration. (a) $\sim$ 10 hr observation starting on 2000 December 3 at 22:23 UT; (b) $\sim$ 4 hr observation starting on 2001 March 1 at 22:32 UT; (c) $\sim$ 7 hr observation starting on 2001 March 5 at 18:31 UT; (d) $\sim$ 11 hr observation starting on 2001 March 12 at 15:02 UT (from D'Amico et al. 2001c).

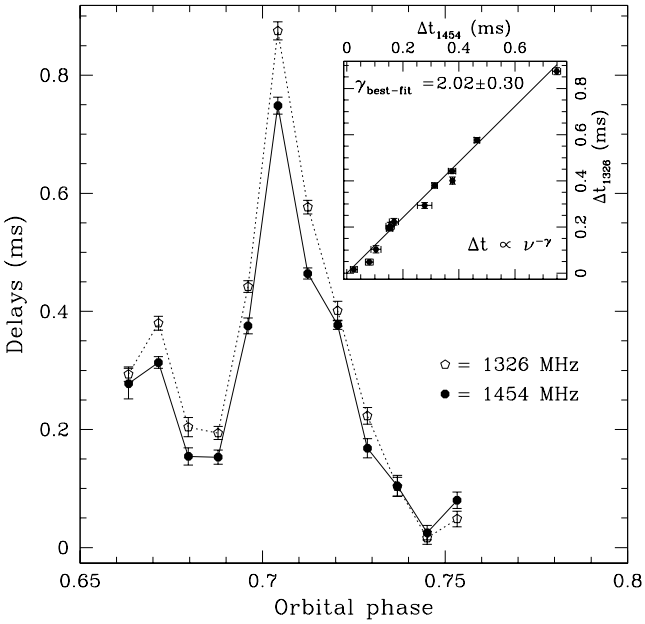


Fig. 2. Excess group delays measured in two 128 MHz-wide bands centered at 1454 MHz (*filled symbols*, connected by a *solid line*) and at 1326 MHz (*open symbols*, connected by a *dotted line*) for an event occurring at orbital phases 0.65−0.75 on 2001 March 1 (see Fig. 1b). The delays in the two subbands are fitted (*inserted panel*) with a straight line of slope 1.21±0.04, corresponding to a frequency dependence for the delays ($\Delta t \propto \nu^{-\gamma}$) with a best-fit power-law index $\gamma = 2.02 \pm 0.30$ (from D'Amico et al. 2001c).

presented the timing solution and the optical observations for the binary millisecond pulsar in NGC 6397. D'Amico et al. (2002) and Colpi, Possenti & Gualandris (2002) investigated the case of NGC 6752.

2. The millisecond pulsar in NGC 6397

NGC 6397 is one of the most promising targets for searching MSPs in GCs: in fact, it is one of the closest clusters, at a distance of 2.6 kpc $\pm$ 6% (Reid & Gizis 1998) and probably has a collapsed core with hints of mass segregation (King, Sosin & Cool 1995). It lies in fourth place in the list of GCs ranked according to central luminosity (Harris 1996). In this cluster only one millisecond pulsar has been discovered so far: PSR J1740−5340, a binary MSP with a spin period of 3.65 ms (D'Amico et al. 2001a). Its X-ray counterpart has been identified by Grindlay et al. (2001) among the $\sim$ 20 X-ray sources detected with *Chandra* within $2'$ of the cluster center (8 of which probably being CVs).

2.1. Observed features of PSR J1740−5340

It displays eclipses at 1.4 GHz for more than 40% of the orbital phase. Ten eclipsing systems containing a MSP are known (Fruchter et al. 1990; Lyne 1990; Stappers et al. 1996; Nice, Arzoumanian & Thorsett 2000; Camilo et al. 2000; D'Amico et al. 2001a) and in one of them (PSR B1744−24A: Nice & Thorsett 1992) the eclipses show duration and irregularities similar to those of PSR J1740−5340. However this new system is $2-3$ times wider (with an orbital separation of ~ 6.5 $R_\odot$) than any other known eclipsing pulsar binary, and has a heavier minimum mass for the companion (> 0.19 $M_\odot$) than any known eclipsing system.

In addition, the radio signal exhibits strong fluctuations (delays and intensity variations) over a wide range of orbital phases (see Figure 1), indicating that the MSP is orbiting within a large envelope of matter released from the companion with a high mass loss rate. The frequency-dependent behavior of the observed delay events have been studied by splitting the 256-MHz bandwidth available at 1.4 GHz into two adjacent subbands. Figure 2 shows an example of the measured excess delays in the two subbands. The small panel also shows these measurements plotted against each other. The best-fitting straight line corresponds to $\Delta t \propto \nu^{-2.02\pm0.30}$ for the excess delays, consistent with the ν^{-2} dependency expected if the delays are due to dispersion in an ionized medium. If entirely due to dispersion, the excess propagation delays of up to ~ 3 ms visible in Figure 1 would correspond to electron column density variations of $\sim 1.5 \times 10^{18}$ Δt_{-3} cm^{-2}, or ΔDM ~ 0.47 Δt_{-3} cm^{-3}pc (Δt_{-3} being the delay at 1.4 GHz in ms). This corresponds to a pulse broadening of 0.10 P $\Delta t_{-3} = 0.36\Delta$ t_{-3} ms over the receiver bandwidth (to be compared with an intrinsic pulse FWHM of 0.17 P) and may be responsible for most of the signal attenuation and pulse broadening observed near the delay peaks.

When combined with the typical duration of the eclipse at 1.4 GHz ($\sim$ 13 hr), these parameters imply an eclipse radius $R_{\rm ECL}$ ($\sim$ 7.5 $R_\odot$) larger than the orbital separation $a \sim 6.5$ $R_\odot$ for any value of the orbital inclination i. $R_{\rm ECL}$ is defined as the chord subtended on the orbital circumference of radius

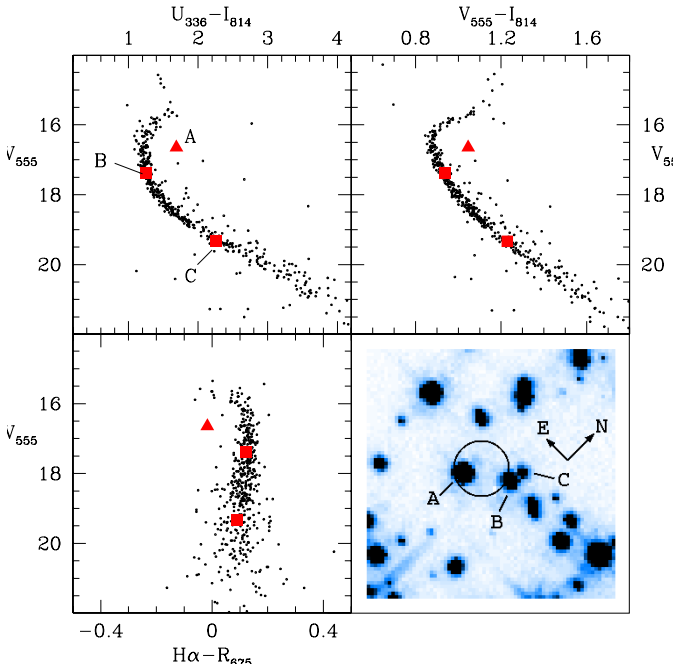


Fig. 3. *Bottom right panel*: A portion of a median-combined F675W HST WFPC2 image (chip WF4) of NGC 6397, centered near the MSP position. The region covers about $7'' \times 7''$. Star A is the companion to the MSP PSR J1740−5340. *Remaining three panels*: Multiband CMDs for stars detected in a region of the WF4 chip ($40'' \times 40''$) containing the MSP position. The three stars found in the vicinity of the MSP error box are marked with different symbols (a triangle for star A and squares for stars B and C) and labeled with their names in the first panel (from Ferraro et al. 2001).

a by the angle between the orbital phase of eclipse ingress (or egress) and the orbital phase 0.25 (see also Figure 5).

According to different values of the orbital inclination, the values of the Roche lobe radius R_L span the interval 1.3–2.2 $R_\odot$ (Eggleton 1983). Because $R_{\rm ECL} > a > R_L$, the matter causing the eclipses escapes the gravitational influence of the companion star and therefore must be continuously replenished. Assuming isotropic emission, mass continuity implies that the companion star releases mass at a rate $\dot{M}_c = 4\pi R_{\rm ECL}^2 \rho(R_{\rm ECL}) v_f$. Using the values at the eclipse radius inferred from the observation of the excess delays assuming completely ionized matter ($\rho[R_{\rm ECL}] \sim 3 \times 10^{-18} \Delta t_{-3}$ g cm^{-3}), it results a mass loss rate from the companion $\dot{M}_c \sim 1.5 \times 10^{-11}\ \Delta t_{-3}\ v_{f,8}\ {\rm M}_\odot {\rm y}^{-1}$ where $v_{f,8}$ is the wind velocity at $R_{\rm ECL}$ in units of 10^8 cm s^{-1} (typical order of magnitude of the escape velocity from the surface of the companion).

The large position offset of PSR J1740−5340 with respect to the center of NGC 6397 ($r \sim 0.'55$) limits the unknown contribution to the observed period derivative $\dot{P}$ due to acceleration in the globular cluster potential. Thus $\dot{P}$ can be used to infer the rotational energy loss of the pulsar, $\dot{E} \sim 1.4 \times 10^{35}$ ergs s^{-1}. At the distance of 6.5 $R_\odot$, the power impinging on a white dwarf companion (of typical radius $R_{wd} = 0.033$ $R_\odot$) would be $W_{wd} \lesssim 10^{30}$ ergs s^{-1}. This would allow release of an ionized wind from the degenerate companion at a maximum rate $\dot{M}_{wd,max} = W_{wd}(R_{wd}/GM_{wd}) \lesssim 1.6 \times 10^{-12}$ ${\rm M}_\odot {\rm y}^{-1}$. Thus, for realistic terminal velocity of the wind ($v_f \sim 1000$ km s^{-1}) the pulsar flux cannot sustain the observed releasing of mass, $\dot{M}_c$, from a white dwarf companion.

This conclusion suggested that more likely the companion could be a bloated main-sequence star or a sub-giant, prompting a deep optical search for it. Using a series of public *Hubble Space Telescope* archive exposures taken in 1996 March and 1999 April, Ferraro et al. (2001) found a bright, ~ 16.6 mag, variable star (hereafter Star A) with an anomalous red color and optical variability (~ 0.2 mag), which nicely correlates to the orbital period of the pulsar (see Figures 3 & 4). This variable had been already discovered by Taylor et al. (2001); however on the basis of the unusual colors and time variability, Taylor et al. (2001) had classified this object as a BY Draconis star. Radius $R_c \sim 1.3 - 1.8$ $R_\odot$ and effective surface temperature $T_{eff} \sim 5500-5800$ K for the companion to PSR 1740-5340 can be derived by comparing the color-magnitude diagram in Fig. 3 with the isochrones by Silvestri et al. (1998) and by Vanderberg (2000) for metallicity [Fe/H]=−2.00 and ages of $t = 12-14$ Gyr (compatible with the values observed for NGC 6397).

2.2. The nature of PSR J1740−5340

The red color of PSR-A shows that it is not an undisturbed main sequence star. Its peculiar nature can be unveiled inspecting the amplitude and the shape of its light curves (insert in Figure 4). Two other eclipsing millisecond pulsars, both in the Galactic field, have measured light curves: PSR B1957+20 (Callanan, van Paradijs & Rengelink 1995) and PSR J2051-0827 (Stappers et al. 2001). In both cases, the optical companions show strong modulations, which are readily explained by the heating of one side of the companion by radiation from the pulsar. The optical maximum is at orbital phase 0.75, where the heated side of the companion faces the earth. A similar trend, though with a much smaller degree of modulation, is seen in 47 Tuc U_{opt}, the first identified MSP companion in a GC (Edmonds, et al. 2001).

The light curves of Star A are completely different. In Figs. 4 & 5, the phase 0.0 is located at the ascending node of the MSP orbit; thus at the phase 0.75 the side of the companion facing the pulsar is visible. In contrast to the other known variable MSP companions, the light curves of Star A display there a minimum instead of a maximum (see Figure 4). Within the limits in the available orbital period coverage, the best-fit light curve of Figure 4 shows two maxima and two minima during each binary orbit: thus, tidal distorsions appear the more natural responsible for this pattern. If this is the correct interpretation, the observed modulation can be reproduced only if the companion has almost filled up its Roche lobe and the orbital plane is nearly edge-on ($i \sim 90^o$).

In summary, as roughly depicted in Figure 5, this binary appears the first example of a system comprising an active MSP whose companion keeps on pouring mass in the binary system through the inner Lagrangian point of its Roche lobe.

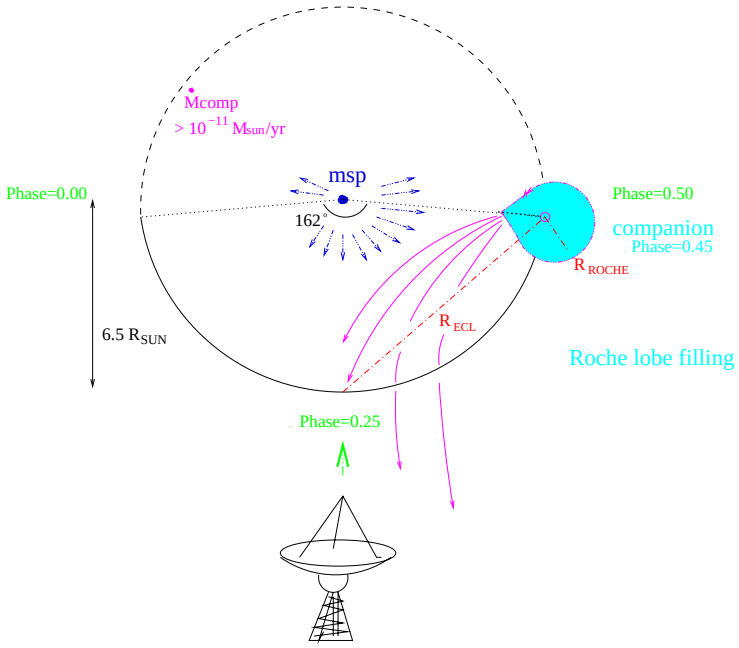


Fig. 5. Sketch of the binary system containing PSR J1740−5340 at the phase of the egress of the millisecond pulsar from the eclipse at 1.4 GHz. $R_{\rm ECL}$ represents the eclipse radius, greater than the orbital separation of the system. The maximum of the eclipse occurs at phase 0.25 (lower side of the figure). The eclipse ingress is roughly located at phase 0.05, whereas the eclipse egress is at phase 0.45.

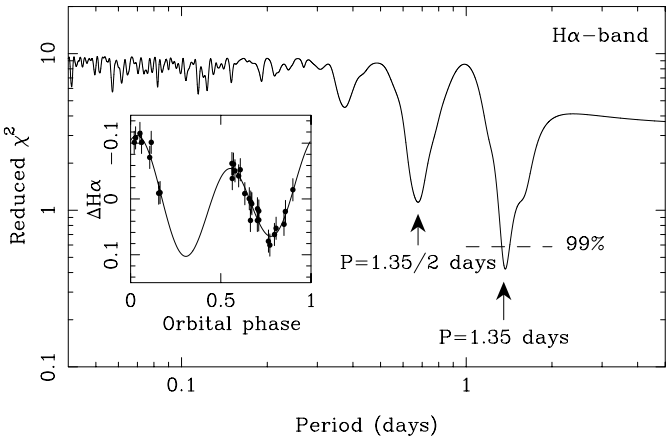


Fig. 4. Reduced χ^2 resulting from the fit of two Fourier harmonics to the Hα data as a function of the modulation period. *Small panel*: same Hα data folded using the period and the reference epoch of the radio ephemeris, and best fit (solid line) of the spectral amplitudes of the 1^{st} and 2^{nd} harmonics to the data (from Ferraro et al. 2001)

2.3. The origin of PSR J1740−5340

Three hypotheses have been suggested for explaining the origin of this system:

(a) that Star A is a main sequence (MS) star perturbed by the energetic flux emitted from the MSP;
(b) that PSR J1740−5340 is a new-born MSP, the first one observed just after the end of the process of recycling (D'Amico et al. 2001c; Burderi, D'Antona & Burgay 2002; Ergma & Sarna 2002);
(c) that PSR J1740−5340 is a re-born MSP, which has already experienced many phases of recycling (Grindlay et al. 2002).

Given the relatively large orbital separation, it seems energetically difficult to explain an increasing of both the effective temperature and of the radius of a main sequence companion: however further detailed simulations are required before excluding the scenario *(a)*. The hypothesis *(b)* is particularly stimulating because could be the first example of a binary in the so-called *radio-ejection* phase (Burderi, D'Antona & Burgay 2002) in which the Roche-lobe overflow stage is not ended yet, but the MSP is already active and sweeps away the infalling matter preventing accretion onto its surface. In particular (Burderi, D'Antona & Burgay 2002) Star A could have been originally a main sequence star of ~ 1 M$_\odot$, whose evolution triggered mass transfer towards the compact companion, spinning it up to millisecond periods (Alpar, et al. 1982). Irregularities in the mass transfer rate from the companion, $\dot{M}_c$, are common in the evolution of these systems (e.g. Tauris & Savonije 1999): even a short decreasing of $\dot{M}_c$ can have easily allowed PSR J1740−5340 (having a magnetic field $\sim 8 \times 10^8$ G and a rotational period $\lesssim 3.65$ ms) to become source of relativistic particles and magnetodipole emission, whose pressure *(i)* first swept the environment of the "neutron stars (NS), allowing coherent radio emission to be switched on (Shvartsman 1970) and *(ii)* then kept on expelling the matter overflowing from the Roche lobe of Star A (Ruderman, Shaham & Tavani 1989). For a wide enough binary system, once the radio pul-

sar has been switched on, any subsequent restoration of the original $\dot{M}_c$ cannot quench the radio emission (Burderi et al. 2001). Remarkably, for the parameters of PSR J1740−5340, the orbital period at which *radio-ejection* dominates is $\sim$ 39 hrs, very close to the observed value of $\sim$ 32.5 hrs (Burderi, D'Antona & Burgay 2002).

As already noticed, the signal from PSR J1740−5340 is eclipsed for about 40% of the time at 1.4 GHz and strongly disturbed along all the orbit (D'Amico et al. 2001c) and this suggests a bias against the detection of this kind of radio sources. On the other hand, the occurrence of the *radio-ejection* mechanism can strongly shorten the duration of the bright X-ray phase in the recycling scenario. Hence, if this *radio-ejection* phase is common in the formation of the MSPs, the birth-rate of the Low-Mass X-ray Binaries (depending on their observed number in the Galaxy and on the supposed lifetime) should be revised upwards. This could help solving the apparent slight discrepancy between the observed birth-rate of the MSPs and that of the Low-Mass X-ray Binaries, which are their supposed progenitors.

Finally, hypothesis *(c)* calls for the high rate of dynamical interactions between single stars and binaries allowed by the crowded environment of the central regions of a globular cluster. Due to such interactions, a neutron star in a globular cluster could undergo many phases of *recycling*, accreting mass from different companion stars acquired at different times along the cluster evolution. These repeated stages of accretion could affect e.g. the evolution of the surface magnetic field of the MSPs in globular cluster and their X-ray luminosity (Grindlay et al. 2002).

3. The five millisecond pulsars in NGC 6752

NGC 6752 is one of the globular clusters with the more precise distance measurement: 4.1 kpc $\pm$ 5%, obtained fitting the white dwarf (WD) sequence (Renzini et al. 1996). It is classified as a core-collapsed cluster with evidence of mass segregation (Ferraro et al. 1997). Rubenstein & Bailyn (1997) estimated a binary fraction for main sequence stars in the range 15%−38% inside the inner core radius ($< 11''$), decreasing to less than 16% beyond that. At least 6 dim X-ray sources had been identified on the basis of ROSAT pointings (Verbunt & Johnston 2000), whereas a more recent *Chandra* observation revealed 19 sources within the half-mass radius of the cluster (Pooley et al. 2002).

In this cluster a 3.26 ms binary pulsar was first discovered, and originally labeled PSR J1910−59A (D'Amico et al. 2001a). Amplification due to scintillation helped in the detection of four additional MSPs in the same cluster (hereafter PSRs B, C, D, E). All of them are isolated with spin periods in the range 4.6 − 9.0 ms. X-ray counterparts for PSR−D, PSR−C and PSR−B have been detected (Pooley et al. 2002, D'Amico et al. 2002) using a 28700 sec long exposure taken with the ACIS-S detector aboard the *Chandra* X-ray observatory.

3.1. The three inner millisecond pulsars

PSRs B, D and E are located close to the cluster center, as expected as a consequence of mass segregation in the cluster (see Figure 6). In particular, PSR−D has the third largest period derivative, $\dot{P} = 9.6 \times 10^{-19}$, among known MSPs (after

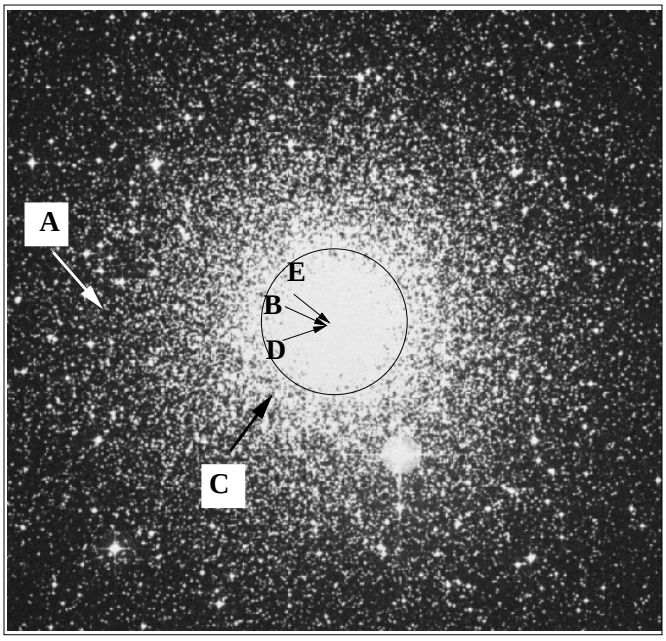


Fig. 6. Positions of the 5 millisecond pulsars (arrows) in NGC 6752, superimposed on an optical image retrieved from the Digital Sky Survey. The circle indicates the half-mass radius region ($\theta_{hm} = 115''$).

PSR B1820−30A in NGC 6624 and PSR B1821−24 in M28), suggesting that the $\dot{P}$ is dominated by the line-of-sight acceleration in the cluster gravitational field. This interpretation is supported by the large negative $\dot{P}$ values observed for PSR−B and E, which allow to directly derive lower limits to the line-of-sight accelerations, $a_l/c = \dot{P}/P = -9.6 \pm 0.1 \times 10^{-17}$ s^{-1}. This value is the largest known after those of PSRs B2127+11A and D in the core of M15 (Anderson et al. 1990). Other contributions to a_l/c are all negligible (D'Amico et al. 2002) and thus the inferred high values of $|a_l/c|$ unambigously calls for the effects of the potential well of NGC 6752.

3.2. Central Mass-to-Light ratio in NGC 6752

A lower limit to the mass-to-light ratio in the inner regions of NGC 6752 can be derived from the following rule, which holds to within $\sim$10% in all plausible cluster models (Phinney 1992):

$$\left|\frac{\dot{P}}{P}(\theta_\perp)\right| < \left|\frac{a_{l,max}(\theta_\perp)}{c}\right| \simeq$$

$$\simeq 1.1 \frac{G}{c} \frac{M_{cyl}(<\theta_\perp)}{\pi D^2 \theta_\perp^2} = 5.1 \times 10^{-18} \frac{\mathcal{M}}{\mathcal{L}_V} \left(\frac{\Sigma_V(<\theta_\perp)}{10^4\ \mathrm{L_{V\odot}\,pc^{-2}}}\right) \mathrm{s}^{-1}.$$

Here $\Sigma_V(<\theta_\perp)$ is the mean surface brightness within a line of sight subtended by an angle $\theta_\perp$ with respect to the cluster center, $M_{cyl}(<\theta_\perp)$ is the mass enclosed in the cylindrical volume of radius $R_\perp = D\theta_\perp$ and $\mathcal{M}/\mathcal{L}_\mathcal{V}$ is the mean *projected* mass-to-light ratio in the V-band. In Figure 7 the curves of maximum $|a_l/c|$ for different values of $\mathcal{M}/\mathcal{L}_\mathcal{V}$ have been plotted, using the most recent published brightness profile for this cluster (Lugger, Cohn & Grindlay 1995), normalized to the central surface brightness in the V-band reported by Djorgovski (1993). In particular, in Figure 7 the histogram represents the data for $\mathcal{M}/\mathcal{L}_\mathcal{V}$=1.1, the mass-to-light ratio suggested by Pryor & Meylan (1993) for the central regions of NGC 6752. This greatly

underestimates the observed values of $\dot{P}/P$. The dashed lines are good analytical fits to the observed data, scaled according to increasing values of $\mathcal{M}/\mathcal{L}_\mathcal{V}$. Only $\mathcal{M}/\mathcal{L}_\mathcal{V} \gtrsim 9$ can account for the observed $|\dot{P}/P|$ of PSRs B and E. An even larger $\mathcal{M}/\mathcal{L}_\mathcal{V} \gtrsim 13$ is required if PSR-D has a negligible intrinsic $\dot{P}/P$ (see caption of Figure 7). It is worthwhile noting that these estimates of the projected $\mathcal{M}/\mathcal{L}_\mathcal{V}$ are independent of modeling of the cluster potential and of distance, excepting the effects of extinction. Being E(B−V) very small for NGC 6752 (= 0.04 according to Harris 1996) the latter affects negligibly the result.

It provide the first direct dynamical evidence for a high density of unseen remnants in the core of a globular cluster, suggesting a mass-to-light ratio $\gtrsim 10$ in the core region. Typical mass-to-light ratios for the central regions of the globular cluster span the interval $\mathcal{M}/\mathcal{L}_\mathcal{V}$=1−3.5 (Pryor & Meylan 1993). NGC 6256, the GCs at the top of a list ordered according to $\mathcal{M}/\mathcal{L}_V$ (Pryor & Meylan 1993), has $\mathcal{M}/\mathcal{L}_V \sim 6$, but this value is quite uncertain due to the high level of reddening. Using the same method applied to NGC 6752, a much smaller value ~ 3, was obtained by Phinney (1993) in the case of M15, a core-collapsed GC long suspected to host a central black-hole (see e.g. van der Marel & Roeland 1999).

The nature of the remnants in the core of NGC 6752 is not clear as it strongly depends on assumptions about the initial mass function of the cluster. However, the possibility that they are black holes, or that many stellar remnants have collapsed into a massive (binary?) black hole, is intriguing.

3.3. The millisecond pulsar in the outskirts of the cluster

When a coherent timing solution became available, PSR−A (the only binary pulsar known in the cluster) resulted located at $6'.4$ from the globular cluster center (R.A.=$19^{\rm h}\ 10^{\rm m}\ 51^{\rm s}.8$, Dec.=$-59^\circ\ 58'\ 55''$, eqx 2000, Harris 1996) equivalent to 3.3 half-mass radii or $\sim$ 57 core radii. Hence, it is the farthest objects from the GC center known in the catalogue of 41 pulsars in GC with accurately determined positions. Previously, the largest offset of an associated pulsar from a GC center was for PSR B2127+11C (Prince et al. 1991), a member of a double-neutron-star eccentric binary in M15, located at $\sim$ 0.8 half-mass radii. Given this large radial offset, one could question the association of PSR−A with the cluster. However, the probability of chance superposition of a Galactic field MSP with a flux density of $S_{1400} \gtrsim$ 0.2 mJy within $6'.4$ of the center of NGC 6752 is at most 10^{-5}. This probability is further reduced by noting that all five pulsars have very similar DM values.

The companion to PSR−A is a dwarf (probably degenerate) star of mass $m_{\rm c}^* \sim 0.2 M_\odot$, moving with period $P_{\rm orb}$ = 0.86 days on a circular orbit around PSR−A (the eccentricity is $< 10^{-5}$, D'Amico at al. 2002). The orbital separation is $a_{\rm PSR-A} \sim 0.0223$ AU, and the binary has a gravitational binding energy $E_{\rm PSR-A} \sim 10^{47}$erg. The inferred magnetic field is $\sim 10^8$ Gauss and the characteristic age $\tau_{\rm PSR-A} \sim 15$ Gyr (given the large offset from the GC center, the period derivative of PSR−A is not significantly affected by the GC potential well); in short, it looks like a "canonical" recycled MSP (Lorimer 2001).

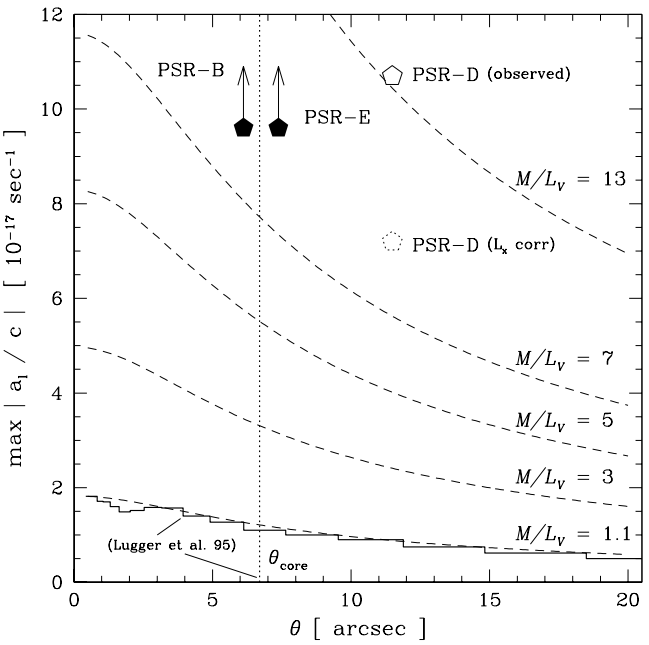


Fig. 7. Maximum line-of-sight acceleration $|a_{l_{max}}/c| = |\dot{P}/P|$ versus displacement θ with respect to the center of NGC 6752. The histogram represents the prediction based on the available optical observations. The dashed lines are analytical fits to the optical observations, labeled according to the adopted mass-to-light ratio. The filled pentagons represent lower limits to the line-of-sight acceleration based on the observation of PSRs B and E. The open pentagon shows the value of $\dot{P}/P$ for PSR-D assuming a negligible intrinsic $\dot{P}$. If various observed scalings (Becker & Trümper 1997; Possenti et al. 2002; Grindlay et al. 2002) between X-ray luminosity and spin-down power for the MSPs are used to estimate the intrinsic $\dot{P}$, $\dot{P}/P$ for PSR-D assumes values in the interval between the open and the dotted pentagon (from D'Amico et al. 2002).

3.4. The origin of PSR J1911-5958A

Colpi, Possenti & Gualandris (2002) explored three possible explanations for the unprecedented position of PSR J1911−5958A (this is the correct name given to the pulsar after the determination of its precise position):

(a) that PSR−A, remnant of a massive star, was the component of a truly *primordial binary* born in the GC halo or expelled from the GC core due to the natal kick imparted by the supernova explosion;
(b) that it was ejected from the core via *scattering* or *exchange* interaction(s) with cluster *stars*;
(c) that it was propelled into the cluster halo by a *scattering* event involving a *black hole binary* (hereafter [BH+BH]).

3.4.1. Case *(a)*

Hypothesis *(a)* is the simplest among the three. It requires orbit stability against dynamical friction (having a characteristic time scale $\tau_{\rm df}$), and a low recoil speed at the moment of the neutron star (NS) formation.

If the binary has been kicked from the globular cluster central regions into a highly eccentric orbit ($e_{\rm ec} \gtrsim 0.9$) at the time of NS formation, it would remain at the periphery for a time $\tau_{\rm df} \gtrsim 7 \times 10^8 (1.6 M_\odot/M)$ yr before returning to the core. Hence, if the supernova took place in the central regions, the binary of PSR−A (of mass $\gtrsim 2.5 M_\odot$ after the NS has formed) would have been driven back to the core by dynamical friction within $\lesssim$1 Gyr. As the supernova must have occurred in the first Gyr since GC formation, the binary would not have survived in the halo until present time.

For a centrophobic halo orbit ($e_{\rm ec} \lesssim 0.5$) the dynamical friction timescale $\tau_{\rm df}$ is $\gtrsim 10^{11} (1.6 M_\odot/M)$ yr in NGC 6752, implying stability of the orbit of PSR−A and of its progenitor halo binary. However, if PSR−A indeed descends from a binary born in the cluster outskirts and following an almost circular orbit in the cluster potential, it must have experienced the faintest supernova kick ever observed: in fact the escape velocity $V_{\rm esc}$ is only $\sim 10\,{\rm km\,s^{-1}}$ in the halo of NGC 6752. Conversely, it is known from current proper motion measurements of 13 MSPs belonging to the Galaxy (Toscano et al. 1998) and from statistical studies (Cordes & Chernoff 1997) that MSPs have relatively large mean transverse velocities of $85 \pm 13\,{\rm km\,s^{-1}}$ implying peculiar speeds with a 3-D dispersion of 84 $\rm km\,s^{-1}$. Moreover, theoretical studies estimates that the minimum recoil speeds $V_{\rm rec}$ for a MSP binary is $\gtrsim 60\,{\rm km\,s^{-1}}$ (Tauris & Bailes 1996). As a consequence, scenario *(a)* calls for the NS of PSR−A being probably formed from the accretion-induced collapse of a massive white dwarf (Grindlay et al. 1988), in which a large kick velocity is not expected.

A difficulty of this scenario is related with the probability that a MSP is formed in the outer halo of a globular cluster. It contains only a small fraction of the total mass of the cluster and the relatively small stellar density does not permit the occurrence of a significant number of dynamical interactions. Hence the only available channel for the formation of a MSP is just the evolution of a primordial binary, similar to the formation scenario holding in the Galactic field. Given the estimated number $N_{\rm gal} \sim 4 \times 10^4$ of MSPs in the Galactic field (e.g. Lorimer 2001) and the ratio $\mu \lesssim 5 \times 10^{-4}$ between the mass in all the globular clusters to that of the Galaxy, it turns out that at most $N_{\rm gcs} = N_{\rm gal} \mu f_r \sim 20 f_r$ MSPs born from a primordial binary should be hosted by the GCs system (comprising $\sim$ 200 objects) at radii larger than r. Here f_r is the fraction of the total mass in a typical GC which resides at a distance greater than r from the center. Taking r equal to 3 half-mass radii, $f_r \sim 0.15$ and thus $N_{\rm gcs} \sim 3$. The very low number $N_{\rm gcs}$ makes improbable the detection of a MSP at its offset position, when descending from a primordial binary born in the GC halo.

3.4.2. Case *(b)*

Ejection of PSR−A away of the core *via* a dynamical interaction with a cluster *star* calls for two possible scenarios: *(b1)* inelastic scattering or *(b2)* three-body exchange. Scattering can occur either before or after recycling as it preserves, to a high degree, the circularity seen in our binary pulsar. In both cases, a recoil kinetic energy of $2-3 \times 10^{46}$erg is requested for ejecting [$\rm NS_A$+co] (comprising either PSR−A or the not yet recycled NS and its companion) into its halo orbit. This energy must be extracted from the [$\rm NS_A$+co] binding energy: inspecting the tables of Sigurdsson & Phinney (1993) it is easy to conclude that this energetic requirement imposes an upper limit on the orbital period $P_{\rm orb,up}$ of [$\rm NS_A$+co] which is $\lesssim$0.4 days.

At the onset of recycling a "bifurcation" orbital period, $P_{\rm bif} \sim 2$ days, separates the formation of a converging binary (which evolves with decreasing orbital period $P_{\rm orb}$ until the mass-losing star becomes degenerate and a short-period binary pulsar is formed) from a diverging one (which evolves with increasing $P_{\rm orb}$ forming a long period binary pulsar; Tauris & Savonije 1999). Given this scenario, PSR−A should result from a converging binary and thus its period can not have ever been shorter than its current value of 0.86 days and this exclude the scattering hypothesis *(b1)*.

Exchange (scenario *(b2)*) alters the nature of the interacting system and makes the new binary rather eccentric and with a longer orbital period. Thus due to the very long circularization time between compact stars, a three-body exchange must occur before recycling (reminding that the upper limit on the eccentricity of the orbit of PSR−A is 10^{-5}). The simplest and most probable case in this scenario is that of a main sequence binary [MS+ms] (MS heavier than ms) interacting with the $\rm NS_A$ (slowly rotating not yet recycled progenitor of PSR−A) flying by (given the similar masses of MS and $\rm NS_A$, the results are almost unaffected when swapping their roles). In such a three-body encounter the energetic requirement on the recoil kinetic energy of [$\rm NS_A$+co] can be accomplished, provided that the original main sequence binary is tight enough. On the other hand the tables of Sigurdsson & Phinney (1993) show that after the exchange, the [$\rm NS_A$+co] binary has an orbital period suspiciously close to the currently observed value, considering that recycling (and hence shrinking of the orbit) has not occurred yet. Even more disturbing is the value of the characteristic time ($\sim$ 18 Gyr > age of the cluster) for an interaction of this kind to take place in the core of NGC 6752.

3.4.3. Case *(c)*

Partly motivated by the unusual high mass-to-light ratio discovered in the inner region of NGC 6752 (see previous section), Colpi, Possenti & Gualandris (2002) investigated a more exotic scenario, involving the presence of a binary black-hole in the centre of the cluster. In effect, dynamical studies (Portegeis Zwartz & McMillan 2000) show that some clusters could still retain one binary, the last which has not been kicked out. This would be the consequence of repeated exchange interactions and ejections (Sigurdsson & Hernquist 1993; Portegeis Zwartz & McMillan 2000), occurring early in the cluster lifetime among the initially rich population (of few hundreds) of BHs, born from the most massive stars in the cluster. As they sink toward the center by dynamical friction (on a timescale $\lesssim 10^6$ yr), BH−[BH+BH] interactions become overwhelmingly important. Binaries hardens progressively in virtue of these encounters and eventually leave the cluster due to recoil. As a result, many clusters lose their original BHs on a time scale of $\sim$ Gyr. But the outcome of the last encounter (which could involve two single BHs or a single BH and a binary BH system) depends on the specific and unpredictable parameters of the interacting corpses and thus could either eject all the 3 bodies or leave a single BH or leave a binary BH. Following

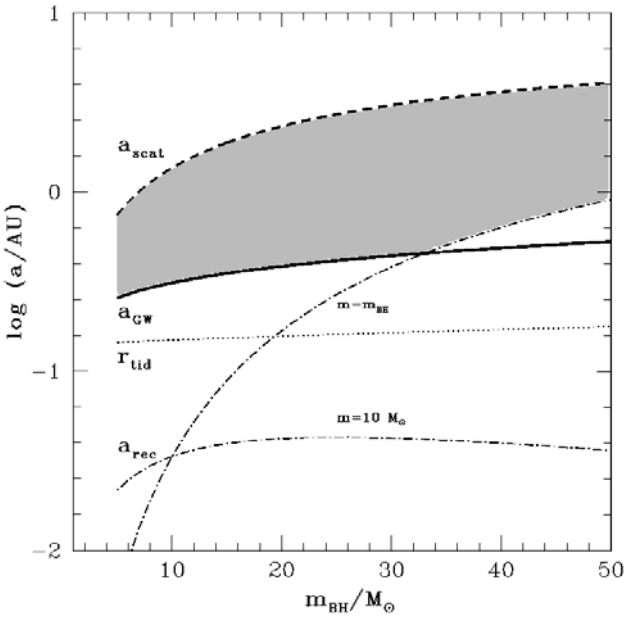


Fig. 8. [BH+BH] binary separation a against $m_{\rm BH}/M_\odot$ for $M_{\rm BH} = 50M_\odot$; $a_{\rm GW}$ (*heavy solid line*), $a_{\rm rec}$ (*heavy dot-dashed lines*) and $a_{\rm scat}$ (*heavy dashed line*) are computed from the related equations presented in the paragraph 3.4.3. In particular $a_{\rm rec}$, is computed for the case of light $m = 10M_\odot$ black-hole intruders and for the case of intruders as massive as the secondary black-hole, namely $m = m_{\rm BH}$. The *dotted line* gives the tidal disruption radius for [NS_A+co]. The shaded area indicates the values of a for ejection of PSR−A during the last Gyr, compatible with its detection (from Colpi, Possenti & Gualandris 2002).

Miller & Hamilton (2002a), the supposed binary that avoided ejection should likely have unequal masses and could harbor the heaviest BH that NGC 6752 ever had.

The scenario *(c)* is fully consistent and viable provided that:

- *i* the [BH+BH] binary that survived the early ejection from the GC, later avoided also coalescence by emission of gravitational waves (GWs), at least for a time $\tau_{\rm GW} \geq 10$ Gyr;
- *ii* the separation of the [BH+BH] binary is sufficiently large to have prevented ejection from the cluster due to a single interaction with a much lighter stellar intruder;
- *iii* the hardening of the [BH+BH] binary due to the encounters with the bath of the cluster stars impinging on it does not reduce its orbital separation enough for triggering coalescence by emission of GWs (point *i*) or ejection (point *ii*);
- *iv* during the scattering interaction, the [NS_A+co] binary is not ionized by the [BH+BH] binary tidal field;
- *v* the [BH+BH] binary can have transferred enough kinetic energy to propel PSR−A into the cluster halo;
- *vi* both the probability of occurrence of the scenario *(c)* and the probability of detection of PSR−A at the present offset position are not negligible.

Indicating with $M_{\rm BH}$ and $m_{\rm BH}$ the masses of the two BHs in the binary, with $M_{\rm BH,t}$ and $\mu_{\rm BH}$ their total and reduced mass, and with m the mass of an intruder, a [BH+BH] binary (with typical eccentricity of 0.7) satisfies the condition *i)* if its separation a exceeds a critical value $a_{\rm GW}$, that is

$$a > a_{\rm GW} \sim 0.4 \left(\frac{M_{\rm BH,t}}{100M_\odot}\right)^{1/2} \left(\frac{\mu_{\rm BH}}{10M_\odot}\frac{\tau_{\rm GW}}{10^{10}{\rm yr}}\right)^{1/4} {\rm AU}\ .$$

On the contrary the condition *ii)* imposes the inequality

$$a > a_{\rm rec} \sim 0.01 \left(\frac{\mu_{\rm BH}}{10M_\odot}\right)\left(\frac{m}{10M_\odot}\frac{100M_\odot}{M_{\rm BH,t}}\frac{35\,{\rm km\,s^{-1}}}{V_{\rm esc}}\right)^2 {\rm AU}\ .$$

For the parameters of NGC 6752, the (very approximate) number of stars impinging onto the target binary over a time $t \sim 10^{10}$ yr is

$$\mathcal{N}_* \lesssim 2 \cdot 10^3\ ,$$

whereas the minimum required number of encounters for triggering the coalescence of the [BH+BH] binary due to gravitational waves emission is

$$\mathcal{N}_{\rm GW} \sim 5 \cdot 10^3\ .$$

Hence condition *iii)* is accomplished. The condition *iv)* requires that the distance of closest approach between the two binaries satisfies the relation

$$r_{\rm min} \sim a > r_{\rm tid} \simeq 0.2 \left(\frac{M_{\rm BH,t}}{100M_\odot}\frac{1.6M_\odot}{m_{\rm PSR-A}+m_{\rm c}}\right)^{1/3} {\rm AU}\ .$$

The condition *v)* on the conversion of the binding energy of the BH binary into kinetic energy for the ejection (with initial velocity $V_{\rm ej}$) of the [NS_A+co] binary can be accomplished if

$$a < a_{\rm scat} \sim \left(\frac{G\mu_{\rm BH}}{V_{\rm ej}^2}\right) \sim 1.3 \left(\frac{\mu_{\rm BH}}{10M_\odot}\right)\left(\frac{35\,{\rm km\,s^{-1}}}{V_{\rm ej}}\right)^2 {\rm AU}\ .$$

Finally, one can estimate a rate for MSP ejection $\mathcal{R}_{MSP}$ of $\sim 0.5\ {\rm Gyr}^{-1}$, implying a probability of detection of about $\sim 50\%$ considering a life-time for the current orbit of ~ 1 Gyr. The value of $\mathcal{R}_{MSP}$ can be derived on the basis of the flux of stars on the [BH+BH] over the cluster lifetime (see the equation for $\mathcal{N}_*$), assuming that about 1/30 of these encounters should have involved a NS and that $\sim 5\%$ of the NSs is in the state of a MSP. These figures are calculated adopting a Salpeter-like initial mass function (giving $\sim 1\%$ of NSs) and a mass segregation enhancement of ~ 6 in the density (Sigurdsson & Phinney 1995). If the IMF is flatter (as suggested by the observations of D'Amico et al. 2002), this rate could be higher, enhancing the likelihood of this scenario. Once ejected into an halo orbit, [NS_A+co] spends only $\sim 1/50$ of its life in the dense GC core and thus has negligible probability to undergo further interactions.

Figure 8 summarizes the results of all the previous considerations, showing that a dynamical interaction with a [BH+BH] binary in a mass range of $\sim 3-100M_\odot$ and separation of ~ 0.3-2 AU can propel PSR−A into the cluster halo, being consistent with the conservation both of energy and linear momentum. In particular an unequal mass binary with a heavy $\gtrsim 100M_\odot$ BH and a lighter companion $\sim 10M_\odot$ is preferred, as it can form in a GC (Miller & Hamilton 2002b) and can provide the right statistics for explaining PSR−A.

4. Conclusion

During the last two years, the detection of 15 millisecond pulsars in six globular clusters which contained no previously known pulsars (Possenti et al. 2001; Jacoby et al. 2002) broke a 7 years long hiatus in such discoveries. More recently, the first stage of timing observations for most of the new objects has been completed, opening the possibility of investigating both their properties and the characteristics of the globular clusters in which they are embedded. Here I have presented the first results of these studies in the cases of the globular clusters NGC 6367 and NGC 6752. They confirm that the efforts devoted to the search and timing of millisecond pulsars in globular clusters, when combined with observation at other wavelengths, can deserve a significant and often surprising scientific pay-back.

Acknowledgements. We gratefully acknowledge the support by the Heraeus foundation.

References

Alpar, M. A., Cheng, A. F., Ruderman, M. A., and Shaham, J., 1982, Nature, 300, 728
Anderson, S. B., Gorham, P. W., Kulkarni, S. R., Prince, T. A., & Wolszczan, A., 1990, Nature, 346, 42
Becker, W., & Trümper, J., 1997, A&A, 326, 682
Bhattacharya, D., van den Heuvel, E. P. J., 1991, Phys. Rep., 203, 1
Biggs, J. D., Bailes, M., Lyne, A. G., Goss, W. M., Fruchter, A. S., 1994, MNRAS, 267, 125
Burderi, L., et al., 2001, ApJ, 560, L71
Burderi, L., D'Antona, F., & Burgay, M., 2002, ApJ, in press, astro-ph/0203387
Callanan, P. J., van Paradijs J., & Rengelink R., 1995, ApJ, 439, 928
Camilo, F., Lorimer, D. R., Freire, P., Lyne, A. G., Manchester, R. N., 2000, ApJ, 535, 975
Colpi, M., Possenti, A., & Gualandris, A., 2002, ApJ, in press
Cordes, J.M., & Chernoff, D.F., 1997, ApJ, 482, 971
D'Amico, N., Lyne, A. G., Manchester, R. N., Possenti, A., & Camilo, F., 2001a, ApJ, 548, L171
D'Amico, N., Possenti, A., Manchester, R. N., Sarkissian, J., Lyne, A. G., & Camilo, F., 2001b, in Proc. of the 20th Texas Symposium, 586, 526
D'Amico N., Possenti A., Manchester R. N., Sarkissian J., Lyne A. G., Camilo F., 2001c, ApJ, 561, L89
D'Amico, N., Possenti, A., Fici, L., Manchester, R.N., Lyne, A.G., Camilo, F., & Sarkissian, J., 2002, ApJ, in press
Davies, M. B., Hansen, B. M. S., 1998, MNRAS, 301, 15
Djorgovski, S., 1993, in Structure and Dynamics of Globular Clusters, ed. S. G. Djorgovski & G. Meylan, ASP Conf. Ser. 50, 373
Edmonds, P. D., Gilliland, R. L., Heinke, C. O., Grindlay, J. E., Camilo, F., 2001, ApJ, 557, L57
Eggleton, P. P., 1983, ApJ, 268, 368
Ergma, E., & Sarna, M. J., 2002, A&A, submitted, astro-ph/0203433
Ferraro, F. R., Carretta, E., Bragaglia, A., Renzini, A., Ortolani, S., 1997, MNRAS, 286, 1012
Ferraro, F. R,, Possenti A., D'Amico N., Sabbi E., 2001, ApJ, 561, L93
Freire, P. C., Kramer, M., Lyne, A. G., Camilo, F., Manchester, R. N., D'Amico, N., 2001, ApJ, 557, L105
Fruchter, A. S. et al., 1990, ApJ, 351, 642
Grindlay, J.E., & Bailyn, C.D., 1988, Nature, 336, 48
Grindlay, J. E., Heinke, C. O., Edmonds, P. D., Murray, S., Cool, A., 2001, ApJ, 563, L53
Grindlay, J. E., Camilo, F., Heinke, C. O., Edmonds, P. D., Cohn, H., & Lugger, P., 2002, ApJ, submitted
Harris, W E., 1996, AJ, 112, 1487
Jacoby, B. A., Chandler, A. M., Backer, D. C., Anderson, S. B., & S. R. Kulkarni, 2002, IAUC 7783
King, I. R., Sosin, C., Cool, A. M., 1995, ApJ, 452, L33
Kulkarni, S. R., Anderson, S. B., 1996, in *Dynamical Evolution of Star Clusters - Confrontation of Theory and Observations*, eds. P. Hut & J. Makino, (Dordrecht: Kluwer), 181
Lorimer, D., 2001, in Living Reviews in Relativity, astro-ph/0104388
Lugger, P. M., Cohn, H. N., & Grindlay, J. E., 1995, ApJ, 439, 191
Lyne, A. G., Brinklow, A., Middleditch, J., Kulkarni, S. R., Backer, D. C., 1987, Nature, 328, 399
Lyne, A G., 1990, Nature, 347, 650
Miller, C.M., & Hamilton, D.P., 2002a, MNRAS, 330, 232
Miller, C.M., & Hamilton, D.P., 2002b, astro-ph/0202298
Nice, D. J., Thorsett, S. E., 1992, ApJ, 397, 249
Nice, D. J., Arzoumanian, Z., Thorsett, S. E., 2000, in *Pulsar Astronomy - 2000 and Beyond*, IUA Coll. 177, ed. M. Kramer, N. Wex, R. Wielebinski, ASP, 67
Phinney, E. S., & Sigurdsson, S., 1991, Nature, 349, 220
Phinney, E. S., 1992, Phil. Trans. Roy. Soc. A, 341, 39
Phinney, E. S., 1993, in Structure and Dynamics of Globular Clusters, ed. S. G. Djorgovski & G. Meylan, ASP Conf. Ser. 50, 141
Pooley, D. et al., 2002, ApJ, in press, astro-ph/0110192
Portegies Zwart, S.F., & McMillan, S.L.W., 2000, ApJ, 528, L17
Possenti, A., D'Amico, N., Manchester, R. N., Sarkissian, J., Lyne, A. G., & Camilo, F., 2001, Aspen Proc., astro-ph/0108343
Possenti, A., Cerutti, R., Colpi, M., & Mereghetti, S., 2002, A&A, in press, astro-ph/0109452
Prince, T. A., Anderson, S. B., Kulkarni, S. R., & Wolszczan, W., 1991, ApJ, 374, L41
Pryor, C., & Meylan, G., 1993, in Structure and Dynamics of Globular Clusters, ed. S. G. Djorgovski & G. Meylan, ASP Conf. Ser. 50, 357
Rappaport, S., Pfahl, E., Rasio, F. A., & Podsiadlowski, P., 2001, in Evolution of Binary and Multiple Star Systems, eds. P. Podsiadlowski, S. Rappaport, A. R. King, F. D'Antona, L. Burderi, ASP Conf. Ser. 229, 409
Rasio, F. A. Pfahl, E. D., Rappaport, S., 2000, ApJL, 532, 47
Renzini, A. et al., 1996, ApJ, 465, L23
Reid, I. N., Gizis, J. E., 1998, ApJ, 116, 2929
Rubenstein, E. P., Bailyn, C. D., 1997, ApJ, 474, 701
Ruderman, M., Shaham, J., & Tavani M. 1989, ApJ, 336, 507
Shvartsman, V. F. 1970, Radiofizika, 13, 1852
Sigurdsson, S., & Hernquist, L., 1993, Nature, 364, 423
Sigurdsson, S., & Phinney, S., 1993, ApJ, 415, 631
Sigurdsson, S., & Phinney, S., 1995, ApJS, 99, 609
Silvestri, F., Ventura, P., D'Antona, F., & Mazzitelli, I., 1998, ApJ 509, 192

Smarr, L. L., & Blandford, R., 1976, ApJ, 207, 574
Stappers, B. W. et al., 1996, ApJ, 465, L119
Stappers, B. W., van Kerkwijk, M. H., Bell, J. F., & Kulkarni, S. R., 2001, ApJ, 548, L183
Taylor, J. M., Grindlay, J. E., Edmonds, P. D., & Coll, A. M., 2001, ApJ, 553, L169
Tauris, T.M., & Savonije, G.J., 1999, A&A, 350, 928
Tauris, T.M., & Bailes, M., 1996, A&A, 315, 432
Toscano, M. et al., 1998, MNRAS, 307, 925
VanderBerg, D.A., 2000, ApJS, 129, 315
van der Marel, R. & Roeland, P., 1999, in Black-Holes in Binaries and Galactic Nuclei, eds. L. Kaper, E.P.J. van den Heuvel, P. A. Woudt, Springer, 246
Verbunt, F., Johnston, H. M., 2000, A&A, 358, 910

Proceedings of the 270. WE-Heraeus Seminar on: *"Neutron Stars, Pulsars and Supernova Remnants"*
Physikzentrum Bad Honnef, Germany, Jan. 21-25, 2002, eds. W. Becker, H.Lesch & J. Trümper, MPE Report 278, pp. 193-199

The Free Electron Maser in Pulsar Magnetospheres

R. Schopper[1,4], H. Ruhl[2], T.A. Kunzl[3] and H. Lesch[4]

[1] Max–Planck–Institut für extraterrestrische Physik, Giessenbachstraße, 85740 Garching, Germany
[2] General Atomics, San Diego, CA, USA
[3] Max Planck Institut für Quantenoptik, Garching, Germany
[4] Universitäts–Sternwarte München, Scheinerstraße 1, 81679 München, Germany, Centre for Interdisciplinary Plasma Science

Abstract. We present the numerical simulations of coherent inverse Compton scattering (CICS) in a highly magnetized plasma process by means of a full three dimensional particle in cell code (PIC), which is mass and energy conservative. We used the parameters of a pulsar magnetosphere where CICS is one of the most promising models for the generation of the observed highly coherent radio emission. First we show details of the onset and time evolution of strong Langmuir turbulence driven by a relativistic electron beam penetrating a strongly magnetized background plasma. The Langmuir turbulence acts as self-generated wiggler fields which bunch the beam electrons thereby inducing strong coherent emission of the bunches at frequency γ^2 times the plasma frequency. The emitted power is about 10 GW in a few nanoseconds. This radiation is interpreted in terms of inverse Compton scattering on nonlinear density fluctuations. CICS is the longitudinal version of a laboratory free electron laser and is applicable in strongly magnetized plasmas like pulsars.

1. Introduction

A strong source for coherent radiation in laboratory is the free electron laser (FEL) (O'Shea and Freund 2001). Its principle is the interaction of a relativistic electron beam (REB) and a magnetic wiggler system. The beam of high energy electrons with energy $\gamma m_e c^2$ passes between permanent magnets of alternating polarity and periodicity λ_W. The energy of the REB is efficiently converted by electron bunching. In the observer's frame the bunches emit the relativistically Doppler-shifted wavelength $\lambda = \lambda_W/\gamma^2$. A comparable effect can be driven by a REB penetrating a strongly magnetized plasma. In phase space such a configuration corresponds to a two-stream-instability. In the plasma version the free energy of the emitted radiation is supplied by the REB, as it is in the case of the FEL, but the positive gradient of the momentum distribution function $df/dp > 0$ is the source of the instability which excites strong density fluctuations. In a strongly magnetized plasma such density oscillations are predominately longitudinal Langmuir waves which grow to nonlinear amplitudes (Benford and Weatherall 1991), (Kato et al. 1983), (Weatherall 1988). The interaction of the REB with the electrostatic fluctuations of the Langmuir waves results in very strong coherent electromagnetic waves (Kato et al. 1983), (Levron et al. 1987). In the rest frame of the beam electrons, they experience the Doppler shifted electrostatic wave moving towards them. The nonlinear waves force the REB to wiggle and to emit dipole radiation of the same frequency as the waves. In the laboratory frame this Hertz' dipole radiation is again Doppler boosted and strongly beamed in forward direction due to the relativistic lighthouse effect. This interaction can be viewed as coherent inverse Compton scattering (CICS) off Langmuir waves (Benford and Weatherall 1991). Coherence occurs due to the bunch structure of the beam which means a phase coupled electrostatic field and density modulation.

2. Computational Details

Since CICS has been discussed to be promising candidate for the origin of the extremely coherent radio emission from pulsars (Kunzl et al. 1998), (Melrose and Gedalin 1999), (Melrose 2000), we use the physical parameters of a pulsar magnetosphere as an instructive application. Radio observations indicate that at about 500 km from the strongly magnetized neutron star the coherent pulsed radio emission is produced. The coherence is proved by pulse substructures on time scales down to a few tens of nanoseconds with increasing flux densities(Rickett 1995). In these regions of a pulsar magnetosphere typical values are: background electron density $n_e = 10^{12}\,\mathrm{m}^{-3}$, beam electron density equal to the plasma density $n_b = 10^{12}\,\mathrm{m}^{-3}$, beam electron Lorenz factor $\gamma = \sqrt{5}$ ($\gamma\beta = 2$) and an extremely strong background magnetic field B of about 1000 T. Especially the strong guiding field is important for the efficiency of the CICS-process. It reduces the electron dynamics to the spatial dimension along the magnetic field lines which greatly improves the stability of the excited Langmuir waves and thus leads to strong and stable electrostatic wiggler fields (Pelletier et al. 1988). For the temperature of both the beam– and background electrons values we take the value of $e = T_b = 100\,\mathrm{eV}$, typical polar cap temperature of neutron stars derived from their thermal X-ray-emission (Pavlov and Petekhin 1995). The PIC–code used for this numerical simulation is fully three dimensional and it conserves mass and energy. In the simulation the direction of electron beam propagation $\gamma\boldsymbol{\beta}$ and of the magnetic field $\boldsymbol{B}$ is the positive z–direction, which is also called the longitudinal direction. The simulated box has a numerical extension of $80 \times 80 \times 200$ grid points and a physical extension of $100\,\mathrm{m} \times 100\,\mathrm{m} \times 250\,\mathrm{m}$, which corresponds to the size of the expected features. The resolution of $\delta x = \delta y = \delta z = 1.25\,\mathrm{m}$ is more than sufficient to resolve the expected maximum wave-

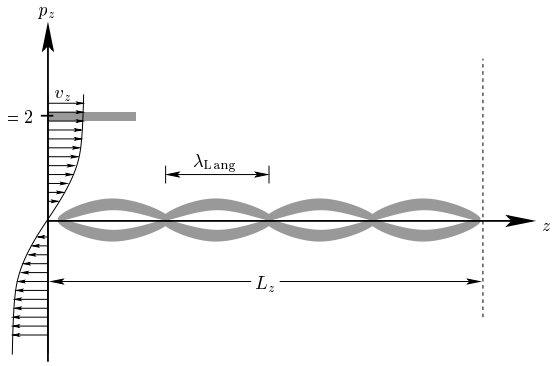


Fig. 1. The initial configuration of electron phase space including the beam. The initial disturbance of the background plasma is heavily exaggerated for reasons of better display.

lengths of approximately $\lambda_{\mathrm{Rad}} = 2\pi/k_{\mathrm{Rad}} = 2\pi c/\gamma^2\omega_{\mathrm{pe}} \approx 6.7\,\mathrm{m}$. A particle density of $10^{12}\,\mathrm{m}^{-3}$ is approximated by 10 quasi particles per cell, leading to 16 million background quasi electrons that are accompanied by a varying number of beam quasi electrons of not more than 2.5 million, which eventually enter the computational box. Those numbers are doubled, since for quasi neutrality an equally large number of positive particles are required.

The initial condition is given by a homogeneous background plasma of density n_{e}, temperature e and a longitudinal magnetic field $B_z = 0.1\,\mathrm{T}$. This value is found to be sufficiently high to represent a much stronger field of 1000 T. Initially there is no beam in the computational box. The beam is injected later at the $z = 0$ plane of the box with a density profile of $n(r) = n_{\mathrm{b}}/\left(1 + \exp\left[\frac{r-R}{\Delta R}\right]\right)$. Here r denotes the distance from the x–y center of the box and $R = 20\,\mathrm{m}$ and $\Delta R = 3\,\mathrm{m}$ give the radius and the sharpness of the electron beam. The homogeneous background plasma is disturbed in phase space (see Fig. 1) in order to accelerate the excitation of Langmuir waves by giving the system a hint of the relevant length scales. We used the wave length of the fastest growing Langmuir mode, which follows from an analytic calculation of the linear growth rate. The disturbance is chosen not to induce any finite charge or current densities, thus leaving the background plasma initially homogeneous, neutral and current free.

The boundary conditions during the simulation are quite simple. In the transversal directions x and y we chose periodic boundaries and in the longitudinal direction z the box is open, which means that plasma particles and fields can leave the box unaffected. In addition at the lower z plane ($z = 0$) an electron component is continuously injected with the density profile mentioned above, a mean $\gamma\beta$ of 2 and the temperature T_{b}.

The simulation runs for 600 time steps with $\delta t = 2.41\,\mathrm{ns}$. The total time simulated was $1.44\,\mu\mathrm{s}$, after which the growing nonlinear Langmuir waves saturate and a quasi stationary situation had developed as it is shown in the next section.

3. Results

The beam particles entering the computational box interact with the faint traces of fluctuations we introduced in our initial setup and excite the appropriate modes to grow. In Fig. 6 on page 197 the temporal evolution of the electrons phase space in z–direction is presented by showing phase diagrams for the time steps 150, 300, 325 and 400. In the first plot (upper left) the penetrating electron beam can be seen together with the background plasma, both are still nearly undisturbed. In the following plots the development of strong Langmuir waves can be observed. After 781 ns, the disturbance in the beam and the background has grown so strong, that both components start to mix, i.e. there is no distinction between beam and background electrons anymore. Beam electrons are strongly decelerated even until $v \simeq 0$, whereas background electrons are accelerated up to a Lorenz factor of 5. This can be seen best in Fig. 7 on page‘197, where each of the both components are plotted in separate diagrams for the time step 400. In Fig. 7 left the phase space of the beam electrons is shown. Clearly visible are the ring structures of fully developed Langmuir waves. Some of beam electrons are accelerated up to a $\gamma\beta$ of 4–5 as it is the case for the background electrons, which is shown in Fig. 7 right. On the other hand the beam electrons are also decelerated to zero momentum during their interaction with the Langmuir waves. The extremely strong accelerations are due to the strong electrostatic fields of the excited Langmuir waves. Since the Langmuir turbulence structure in Fig. 6 moves with a much lower speed (which is even continuously decreasing throughout the simulation) than the yet unaffected beam electrons, it acts as the wiggler field that stimulates the CI CS-emission. The electrostatic fluctuations directly correspond to electron density fluctuations (solid curve in Fig. 6), which reach a value of $\sim +100\%/-50\%$ oriented at $n = n_{\mathrm{e}} + n_{\mathrm{b}} = 2 \cdot 10^{12}\,\mathrm{m}^{-3}$. The structure of the electron density is better seen in Fig. 8 (page 198) and Fig. 9 (page 199), where the temporal evolution of contour surfaces at $n = 1.5 \cdot 10^{12}\,\mathrm{m}^{-3}$ and $n_{\mathrm{e}} = 1.9 \cdot 10^{12}\,\mathrm{m}^{-3}$ and of a cut through the electron beam is shown. The electron density varies between 4 and 1 times $10^{12}\,\mathrm{m}^{-3}$, which implies the strong electrostatic fields. It can be clearly seen, that the beam decays in a series of "pancakes". Such pancakes are absolutely necessary to explain the coherent nature of the pulsed radio emission of neutron stars. Why? Since the emission from relativistic particles is confined to a forward cone with half angle $\sim 1/\gamma$ and the emission is nearly along the magnetic field. Thus, in Fourier space bunching emission corresponds to the component $k_\perp$ to the fields being smaller than the component $k_\parallel$ along the field line by a factor $1/\gamma$. This corresponds to flat pancake shaped bunch with the normal within an angle $1/\gamma$ of B (Melrose 2000). This is exactly what we observe in our simulations! We briefly note that our simulations are the first ones which show this kind of pancake bunches! The number of particles in such a pancake corresponds to the the maximum coherence achievable for CICS and it should be noted, that in our simulation the thickness of such a pancake is significantly larger ($\gtrsim 1\,\mathrm{m}$) than the Debye length which is usually used in analytical models. A typical volume of one bunch is about $10m^3$ giving a total number of particles per bunch of about 10^{13}. Our simulations prove, that a much higher coherence is achievable than expected from analytical models.

The growth of Langmuir waves can be deduced by the Fourier transform of the electrostatic field $\tilde{E}_z$. In Fig. 2 the energy density of the electrostatic modes is plotted versus the corresponding wavenumber k and time t. The $k \simeq 0.25\,\mathrm{m}^{-1}$ mode is growing by four orders of magnitudes within some ten nanoseconds. It should be noted however, that the fastest

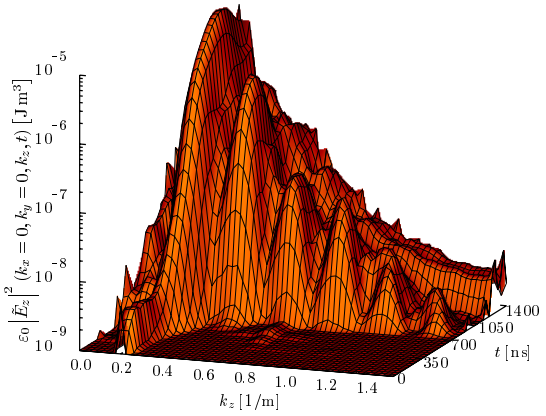


Fig. 2. The electrostatic mode energy density is plotted against wavenumber k and time t.

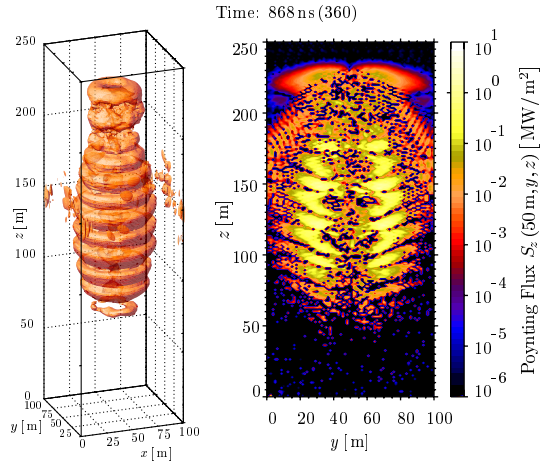


Fig. 3. Structure of the emitted pointing flux as 3D contour surface of the value $2.5 \cdot 10^4$ W/ m^2 (left) and as a cut through the center of the beam at $x = 50$ m (right).

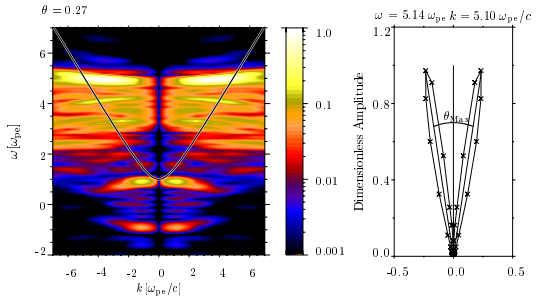


Fig. 4. Dispersion relation (left) and emission characteristic (right) of the emitted radiation. For the left plot the angle θ_M, the angle of maximum intensity, has been used. The curve in the left plot gives the dispersion branch of electromagnetic radiation in a plasma. The right diagram presents the intensity of the radiation for a given θ in a polar plot. θ is the angle between beam direction and direction of emission. The values in both diagrams are normalized to a value of one.

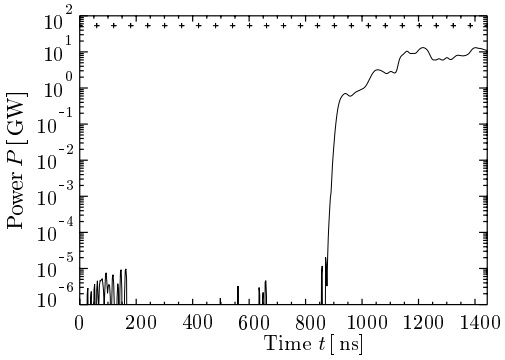


Fig. 5. Total integrated poynting flux leaving the computational box at the top ($z = 250$ m) against time. The + symbols show the total power injected as kinetic energy of the beam electrons.

growing mode is slightly off compared to the initially given wave number can be seen in Fig. 2 as the small peak at early times. This means, that for our simulation the analytical value for the fastest growing mode is not precisely correct and it proves, that although the initial disturbance has given a hint to the system it has not forced it towards an unphysical solution. We note that the wave energy density is distributed to higher k when it exceeds a value of about 10^{-7} J m^3, driven by nonlinear wave–wave interactions.

It is important to recognize that the generated electrostatic fluctuations react on the beam electrons similar to the wiggler fields in the laboratory FEL, with one major difference. In our case the wave wiggling self-consistently excited is along the propagation direction of the beam, whereas in the FEL-case the external magnetic wiggling is perpendicular to the beam propagation. The strongest emission originates in regions with the largest density gradients Fig. 3. Every de– and acceleration region forces the beam electrons to emit Hertz' dipole radiation, which is beamed in forward direction, as can be seen in Fig. 4 (right). θ_M represents the angle of maximum intensity, expected from theoretical consideration ($\tan\theta_M = 1/2\gamma\beta$) with a $\gamma\beta = 2$. The striking resemblance with a relativistically beamed Hertz' dipole is obvious, but the emission characteristic in our simulation also gives precisely the expected opening angle of the emission cone, which is proposed for a CICS-process. In Fig. 4 (left) the "spectrum" of the emitted radiation is shown, which has a strong peak at $\omega = 5\omega_{pe}$ and a couple of minor peaks at $4\omega_{pe}$ and $3\omega_{pe}$ due to nonlinear wave coupling. Again we find rather precisely the theoretically expected value of $w = \gamma^2\omega_{pe}$. The total power emitted by the simulated computational box is shown in Fig. 5. It is the escaping poynting flux at the top of the computational box ($z = 250$ m) integrated over the top surface. After about 850 ns the emitted power rises within some ten nanoseconds by more than 6 orders of magnitude to a value of 1 GW. Afterwards the total output power increases more slowly by one more order of magnitude and reaches a maximum of 10 GW continuous radiative power at the end of the simulation. This is a significant fraction of the power injected by kinetic energy of the beam particles, shown in Fig. 5 as + symbols at a constant value of 50 GW. The rest of the energy leaves the box as kinetic energy

of beam electrons, which would probably be also emitted if the computational would have a greater size in z-direction.

4. Discussion

We have shown that in a strongly magnetized plasma a relativistic electron beam can be forced to emit highly coherent radio emission by self-induced nonlinear density fluctuations. Such slowly moving nonlinear structures oscillate with the local plasma frequency at which the relativistic electrons are scattered. Beam electrons dissipate a significant amount of their kinetic energy by inverse Compton radiation at a frequency of about $\gamma^2\omega_{\rm pe}$. Since the beam is sliced into pancake structures which experience the same electric field the inverse Compton scattering is coherent. Such a process is a very promising candidate for the coherent radio emission of pulsars.

Acknowledgments

Acknowledgements. The authors would like to thank the John von Neumann Institute for Computing (NIC) and the Leibniz Rechenzentrum München for the granted computational time and the Deutsche Forschungsgemeinschaft which supported our work through the grant LE 1039/3-1.

References

Benford, G., Weatherall, J.C., 1991, ApJ, 378, 543
Kato, K., Benford, G., Tzach, D., 1983, Phys. Fluids, 26, 3636
Kunzl, T., Lesch, H., Jessner, A., von Hoensbroch, A., 1998, ApJ, 505, L139
Levron, P., Benford, G., Tach, D., 1987, PRL, 58, 1336
Melrose, D.B., 2000, in Pulsar AstronomyIAU Colloq. 177, ASP. Conf. Series 202, 721
Melrose, D.B., Gedalin, M., 1999, ApJ, 521, 351
O'Shea, P.G., Freund, H.P., 2001, Science, 292, 1853
Pavlov, G.G., Petekhin, A.Y., 1995, ApJ, 450, 883
Pelletier, G., Sol, H., Asseo, E. 1988, Phys. Rev. A, 38, 2552
Rickett, B.J., 1995, ApJ, 197, 185
Weatherall, J.C., 1988, PRL, 60, 1302

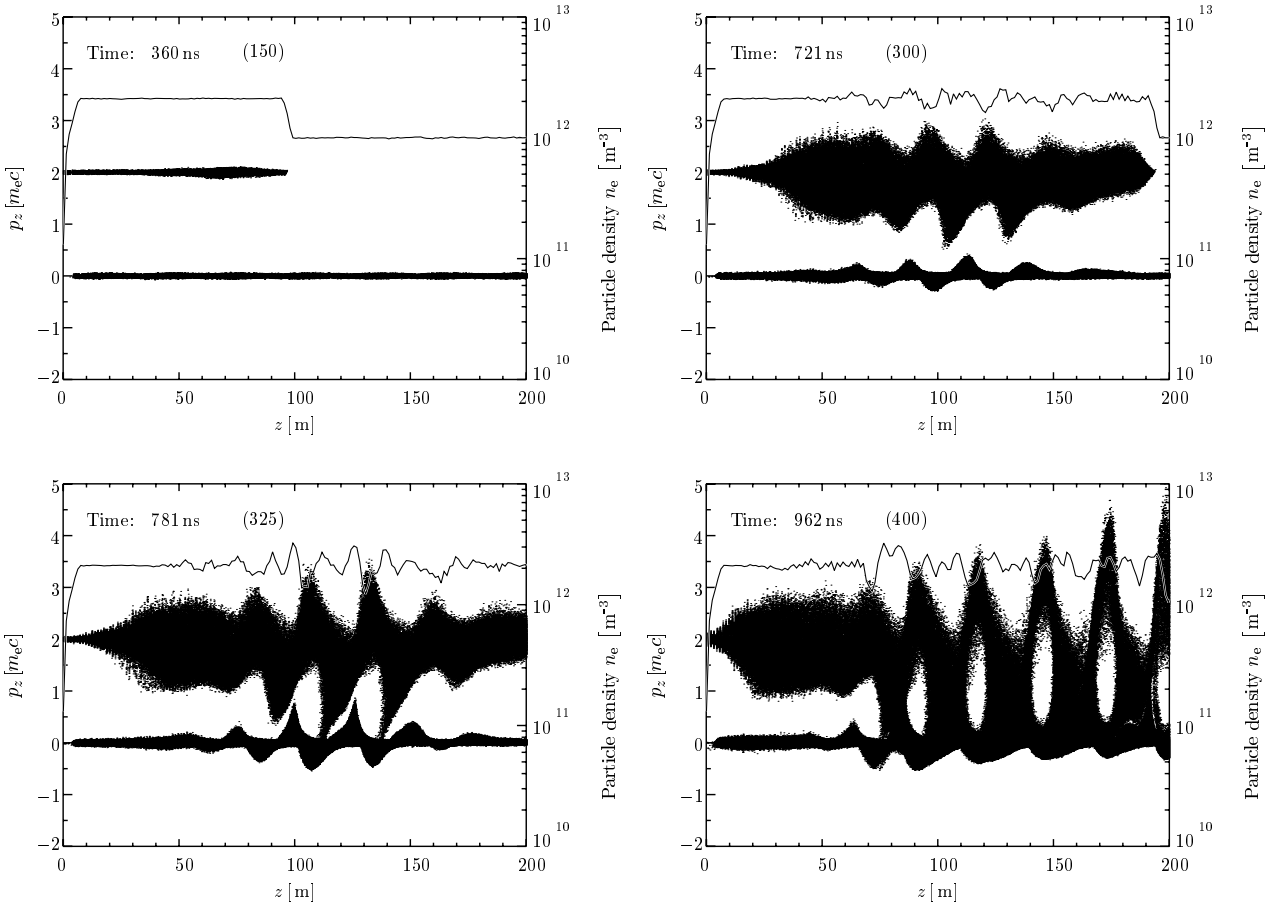


Fig. 6. Electron phase space in z–direction after 150, 300, 325 and 400 timesteps. The quasi particles are plotted as dots according to their corresponding position in z (ordinate) and their momentum p_z (left abscissa). The solid curves present the particle density of the electrons (right abscissa).

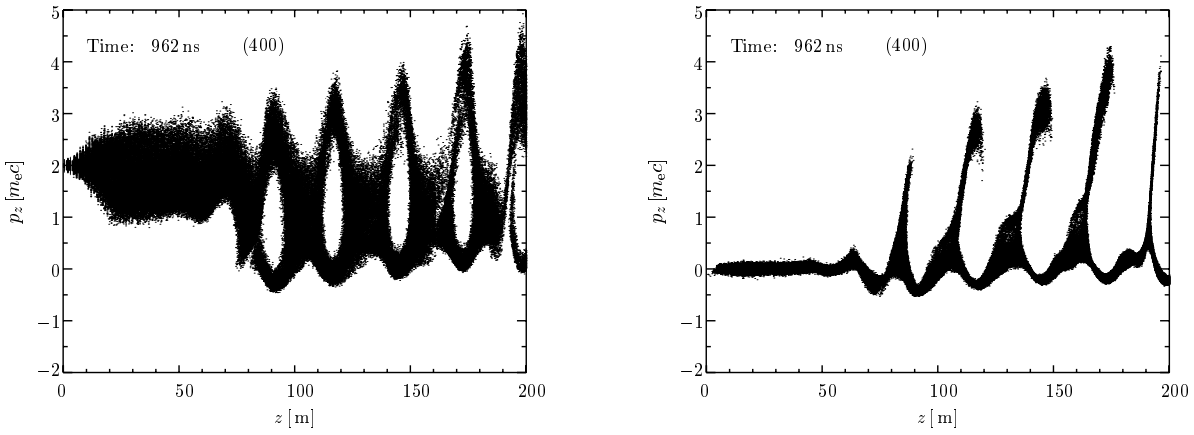


Fig. 7. Electron phase space in z–direction after 400 timesteps separated for beam (left) and background (right) electrons.

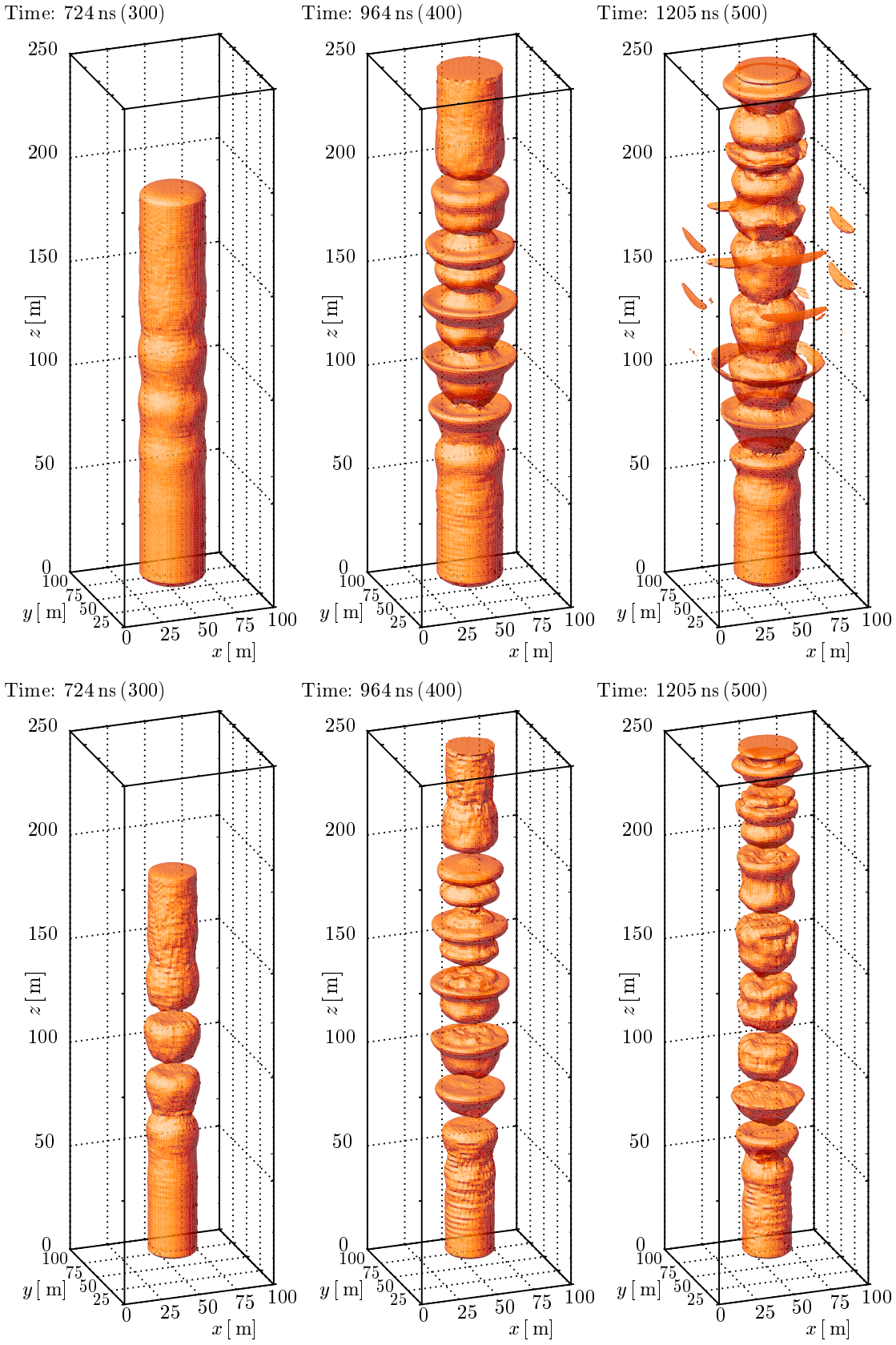


Fig. 8. Three dimensional contour plots of the electron particle density. For the timesteps 300, 400 and 500 (left to right) the surfaces are shown, where the density is $n = 1.5 \cdot 10^{12}\,\mathrm{m}^{-3}$ (top) and $n_e = 1.9 \cdot 10^{12}\,\mathrm{m}^{-3}$ (bottom) respectively.

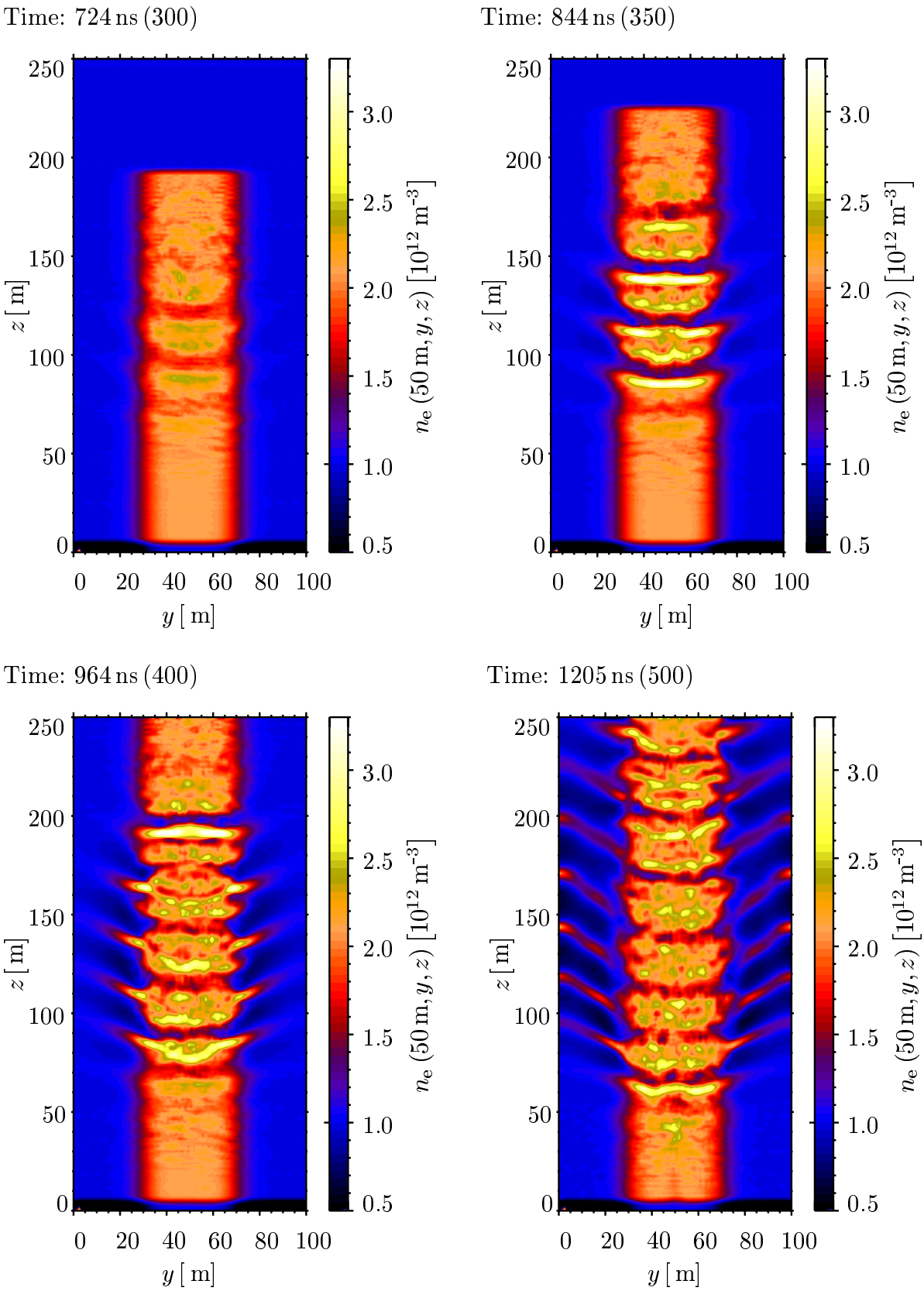


Fig. 9. two dimensional contour plots of the electron particle density at timesteps 300,350,400 and 500. Shown is a cut through the center of the penetrating electron beam at $x = 50$ m.

Proceedings of the 270. WE-Heraeus Seminar on: *"Neutron Stars, Pulsars and Supernova Remnants"*
Physikzentrum Bad Honnef, Germany, Jan. 21-25, 2002, eds. W. Becker, H.Lesch & J. Trümper, MPE Report 278, pp. 200-205

Emission altitude in radio pulsars

Jarosław Kijak

Institute of Astronomy, University of Zielona Góra, Lubuska 2, 65-265 Zielona Góra, e-mail: jkijak@ia.uz.zgora.pl

Abstract. This paper presents a method of estimation of emission altitudes using observational data - precise measurements of pulse profile widths at low intensity level. The analysis of emission altitudes obtained using this method for a large number of pulsars gives constraints that should be useful for theory of coherent pulsar emission. It seems that radio emission originates at altitudes of about few percent of the light cylinder and that they depend on frequency ν, pulsar period P and period derivative $\dot{P}$.

1. Introduction

It is thirty five years since the first pulsar was discovered, but the mechanism of coherent radio emission in pulsars is still not well known. In the polar cap model (e.g. Goldreich & Julian 1969, hereafter GJ; Ruderman & Sutherland 1975), the observed emission of radio pulsars is a coherent radiation of relativistic particles flowing along dipolar field lines. This radiation is generated not far from the surface of the neutron star (NS). The emission altitude $r_{\rm em}$, which is the distance from NS to a place where radiation is generated, is a crucial parameter of emission region. It is commonly believed that $r_{\rm em}$ dependes on the observed frequency. This view, supported by the systematic narrowing of average pulse width with increasing frequency (Thorsset 1991), is described by a radius-to-frequency mapping (RFM). It is obvious that all observational limits for emission altitude can be crucial for understading the physical mechanism generating pulsar radiation. One of the ways to estimate the emission altitude (Cordes 1978, 1993) involves an analysis of observational data concerning the average pulse profiles. This method was adopted and developed by Kijak & Gil (1997, 1998, hereafter Papers I and II) and Kijak (2001, hereafter Paper III), using precise measurements of pulse profile width for the largest available data set (about 40 PSRs). Three straightforward assumptions were used: (1) the pulsar radiation is narrow-band, with a radius-to-frequency mapping operating in the emission region (that is, a narrow-band frequencies $\Delta\nu \ll \Delta\nu_{\rm tot}$ are emitted at given altitude $r_{\rm em}$, where $\Delta\nu_{\rm tot} \sim 30$GHz is a total band of pulsar radiation), (2) the elementary pulsar emission is relativistically beamed tangentially to dipolar magnetic field lines (beaming angle $\theta \sim 1/\gamma$; $\gamma \sim 100$), (3) the extreme profile wings originate at or near the last open dipolar field lines. The estimation of emission altitude is correct (i.e. valid for describing the actual physical phenomenon) as long as the above assumptions are true. In other words, if we question one of these assumptions, our estimation of emission altitude can be questioned too. The first two assumptions are in agreement with basic pulsar electrodynamics (GJ; Sturrock 1971; Ruderman & Sutherland 1975) and with the observed narrowing of profiles with increasing frequency (Thorsset 1991; Mitra & Rankin 2002). These two assumptions are commonly accepted. In the third assumption, the edge of pulsar radio beam is determined by the boundary of the GJ polar cap. This assumption is not widely accepted and will be discussed details in §3.

2. Geometry of emission region

The pulsar beam originates within the open dipolar field lines at altitudes much smaller than the radius of the light-cylinder $r_{\rm LC} = c/\Omega$ (Lyne & Smith 1998). The last open field lines define the polar cap on the neutron star surface. The radiating plasma streams outwards along the open field lines. Let us consider the case of a neutron star with aligned rotation and magnetic axes (see Fig. 1). The equation of dipolar magnetic field lines in polar coordinates $(\mathbf{r}, \vartheta)$ has a form $r = (R^3/d^2) \cdot \sin\vartheta^2$. For the last open field line $\vartheta = \pi/2$ and $r = c/\Omega$, therefore $d = \sqrt{R^3(2\pi/cP)}$ and the radius of polar cap is $r_{\rm p} = 1.45 \cdot 10^4 P^{-1/2}$[cm], for the neutron star radius $R = 10^6$ cm.

2.1. Geometry on the celestial sphere

The geometry of pulsar radio emission as defined by Manchester & Taylor (1977) is presented in Fig. 2. The rotation and magnetic axes are inclined by an angle α. The observer's angle $\xi = \alpha + \beta$, where β is the impact angle of the closest approach of the line-of-sight (l-of-s) to the magnetic axis. The beam radius (corresponding to a pulse profile) is $\rho \geq \beta$ and the observed pulse width is $W = 2\varphi$, where φ is the longitude of the beam edge. The fiducial plane containing the rotation $\mathbf{\Omega}$ and magnetic $\mathbf{m}$ axes defines the so called fiducial phase, which is usually taken as the longitude $\varphi = 0^\circ$ (Fig. 2).

2.2. The method of estimating emission altitude

The opening angle of the pulsar beam corresponding to the pulse width W is given by

$$\rho = 2\sin^{-1}\left(\sin^2\frac{W}{4}\sin\alpha\cdot\sin(\alpha+\beta) + \sin^2\frac{\beta}{2}\right)^{1/2}, \qquad (1)$$

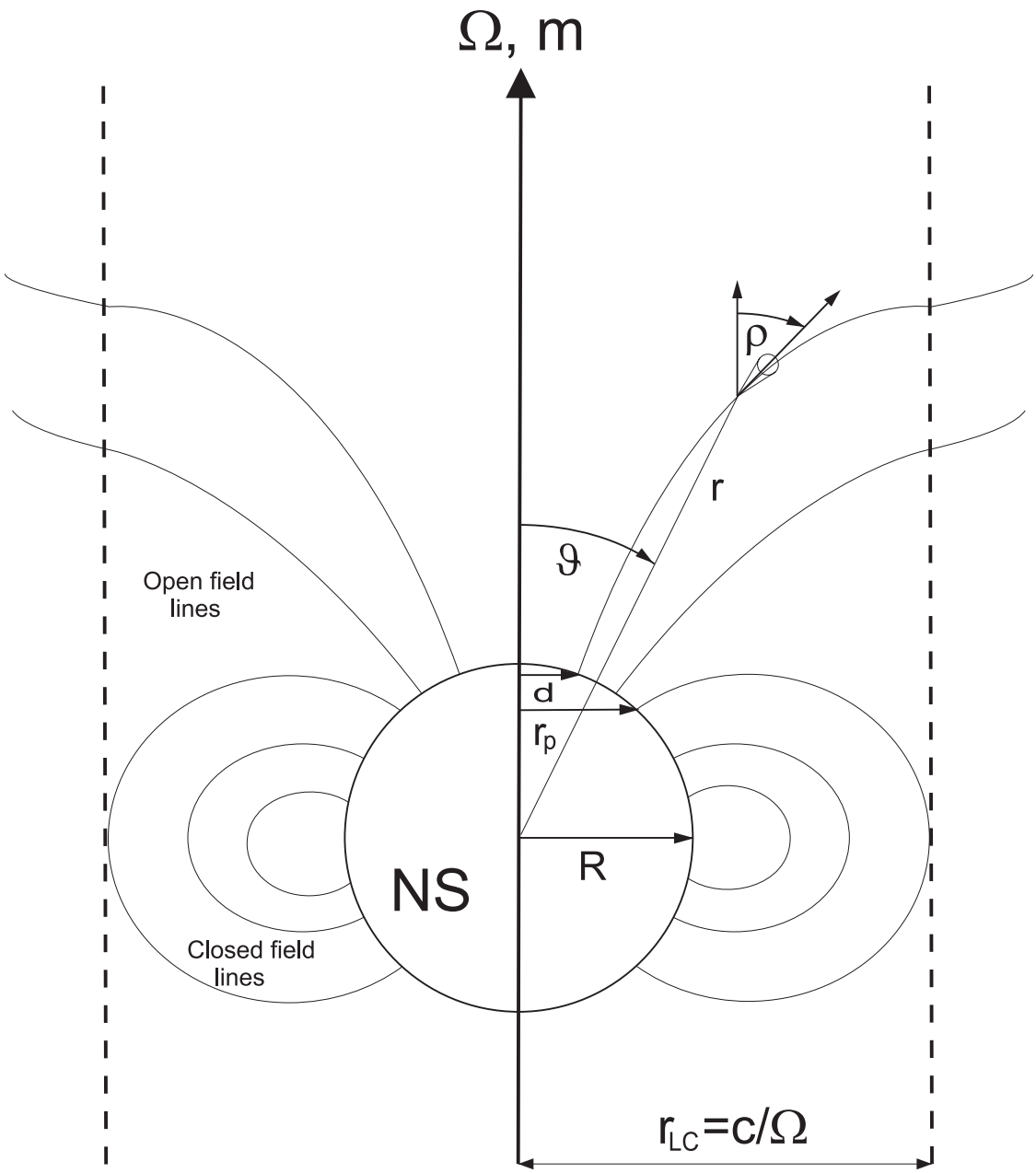


Fig. 1. Geometry of dipole field lines of the neutron star

where α is the inclination angle between the rotation and magnetic axes and β is the impact angle (Gil, Gronkowski & Rudnicki 1984). This formula is independent of the shape of the pulsar beam (circular, elliptical, patchy, etc.) when the beam is symmetric with respect to the fiducial plane. This of course assumes that the edge of beam is close to circular or elliptical in shape.

The opening angle ρ expressed above is also the angle between **m** axis and the tangent to magnetic field lines at points where the emission corresponding to the apparent pulse width W originates. For dipolar field lines (see Fig. 1)

$$\rho = 1.24^\circ s (r/R)^{1/2} P^{-1/2} \ , \qquad (2)$$

where P is the pulsar period, r is the emission altitude (at which radiation at a given frequency ν is generated), $R = 10^6$cm is the neutron star radius and the mapping parameter $s = d/r_p$ describes the locus of corresponding field lines on the polar cap ($s = 0$ at the pole and $s = 1$ at the edge of the polar cap. Finally, we calculate the emission altitude as follows

$$r_{\rm em} = R \left(\frac{\rho}{1.24^\circ s} \right)^2 P \quad . \qquad (3)$$

3. Precise measurements of pulse profile and the edge of the radiation beam

The most important question is what we mean by the edge of pulsar beam and the edge of an average pulse profile. First of

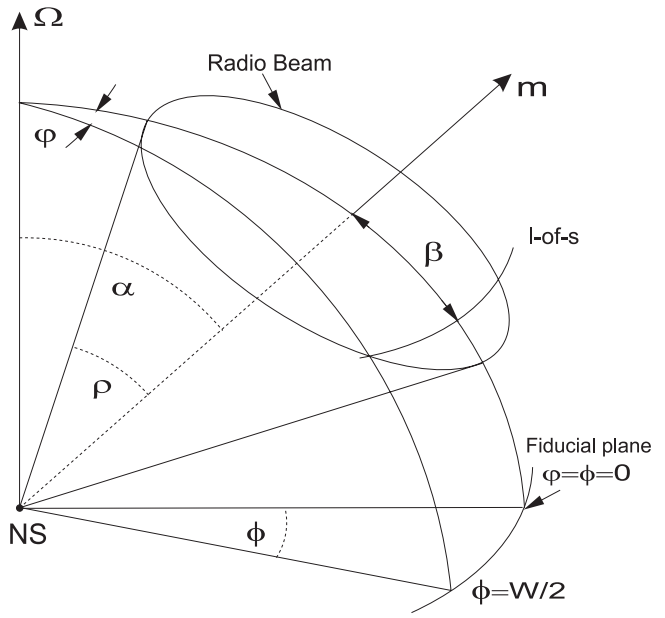


Fig. 2. Geometry on the celestial sphere.

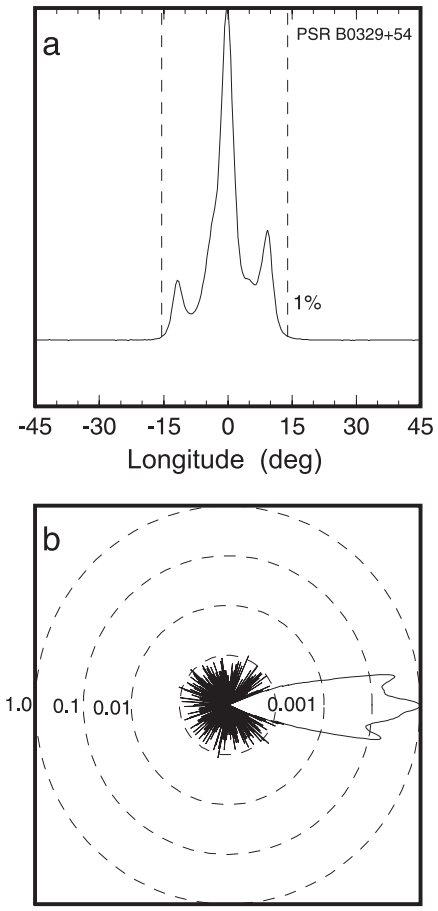


Fig. 3. (a) A plot of profile of PSR B0329+54 at 1.4 GHz, (b) the profile of the same pulsar in the log-scale and the polar coordinates. The dynamic range is 10^4.

all, the edge of pulsar beam is related to the edge of a pulse profile in the following term: when the pulsar beam starts passing through the radiotelescope, then we start observing a weak coherent signal in the receiver. The moment at which the pulsar beam enters the radiotelescope corresponds to the moment at which the recorded noise rapidly becames a coherent signal (and signal becames a noise when the beam leaves the radiotelescope). In studies on emission regions (Papers I, II and III) we used precise measurements of the longitude corresponding to these events. The egde of the beam is defined as the longitude at which recorded signals are distinguished from the noise and have the instensity at least 0.1% of the maximum intensity. Since the pulsar radiation is relativistically beamed along dipolar field lines, we can attempt to calculate which field lines should be tagged as coming from the emission region. This should be easiest for the last open magnetic field lines, which are believed to be associated with the lowest detectable level of radio emission - i.e. at the profile wings.

The radio emission from pulsars is characterized by a short time of duration, typically 3-10% of its period. However, a few objects demonstrate the emission through the entire pulsar period. Hankins et al. (1993) showed, using the VLA, that the emission through the entire pulsar period is observed only in cases when the inclination angle α is smaller than the beam radius ρ (see Fig. 2), that is, the l-of-s is always inside the emission beam (Gil 1985). In general, there is a transition from the noise to the weak emission at the extreme profile wings (Fig. 3 and 4). In our analysis of emission altitudes (Paper I, II and III), we measured pulse widths at the extremely low intensity level corresponding to about 0.05 per cent of the maximum intensity (see Fig. 3), using the polar-log-scale technique (Hankins & Fowler 1986).

It is not certain that the entire GJ polar cap is involved in the emission process thus, the edge of pulsar beam is emitted at or near the last open field lines (which correspond to $s = 1$). It is possible that a forbidden area exists at the outer parts of the GJ polar cap. Evidently, we cannot give a theoretical answer to these questions. Recently, Gangadhara & Gupta (2001) found new outermost weak components in the pulse window of pulsar B0329+54 at frequencies of 320 and 610 MHz. The separation $\Delta\phi$ between the newly detected components is 34°. In Fig. 5 the profile of PSR B0329+54 at 320 MHz is presented, which was used by Kijak & Gil (1998) in their measurement of pulse width and corresponding estimation of emission altitude (Paper II, Fig. 2). Let us note that the pulse width measurement W at 0.05% level is about 49°. A comparison of these two measurements ($\Delta\phi = 34°$ and $W = 49°$) clearly shows that the profile width presented in Fig. 5 includes new components found by Gangadhara & Gupta (2001). Thus, the reported new outermost components in the profile of PSR B0329+54 do not contradict our assumption that $s \approx 1$ at the pulse edges. Our method of profile width measurements has proven to be sensitive to very weak radio emission at profile wings originating at the edge of the beam, most probably close to the last open field lines. These outermost components are clearly visible in Fig. 5 at the level of about 0.1% of the maximum intensity.

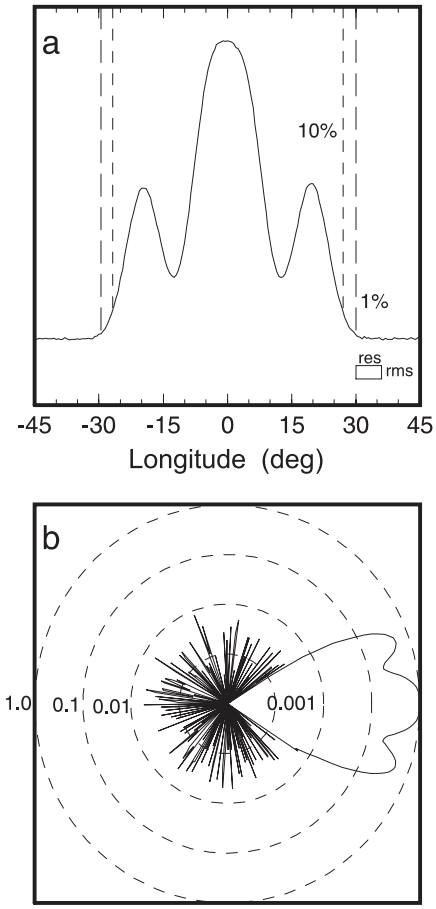


Fig. 4. The syntetic data with pulsar signal which comes from open field lines. The noise was obtained using a random generator. Error box is marked as an example (see details in Paper I).

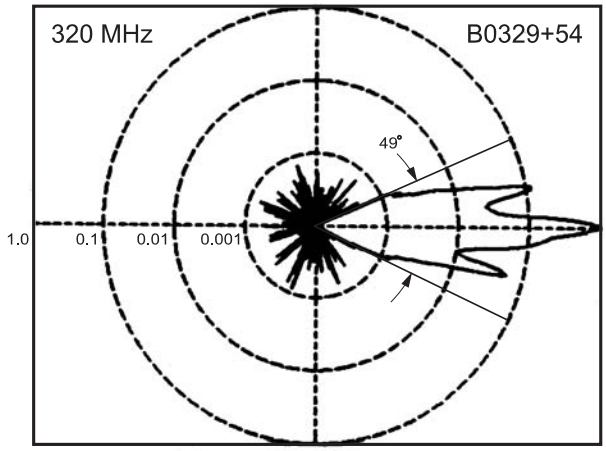


Fig. 5. A pulsar profile of B0329+54 at 320 MHz in the log-scale and the polar coordinates. The data come from Jodrell Bank Observatory.

4. Emission altitude estimation

In our research of radio emission regions we used the high quality average pulse profiles in the wide frequency range. We selected pulsars for which some information about α and β angles was available. For this purpose, observations were performed between 1995 and 1998 using the Effelsberg 100-m radio telescope (Lorimer et al. 1998) and the Jodrell Bank data (Gould & Lyne 1998) were used as well. As a result, the high quality average profiles were obtained with the signal-to-noise ratio S/N$\sim$ 1000 in the frequency range between 0.3 and 20 GHz. These profiles were used to obtain precise measurements of pulse profile widths and to estimate the emission altitudes.

4.1. Results

The result of emission altitude analysis (Papers I, II and III) indicated clearly that the emission altitude $r_{\rm em}$ depends not only on the observing frequency ν, but also on the basic pulsar parameters: pulsar period P and period derivative $\dot{P}$. Here, we present the analysis of emission altitudes at 1.4 GHz for the largest available data set (37 PSRs). An apparent period dependence of emission altitudes is visible in Fig. 6, where a formal fit to all data points gives $r_{\rm em} = (45 \pm 3) R P^{0.37\pm0.05}$. This result confirms the previous analysis of the emission altitude at different frequencies for a smaller data set presented in Papers I and II. Figure 6 also shows a weak dependence $r_{\rm em}$ on pulsar characteristic age τ_6 (in 10^6 yrs), which is discussed in Paper III (see its Fig. 2 and Table 2). For this analysis, a formal fit to the same data set (37 PSRs) at 1.4 GHz yields $r_{\rm em} = (33 \pm 1) R \tau_6^{-0.07\pm0.03}$. In Paper II, the RFM was derived for 16 pulsars covering the frequency range between 0.3 and 20 GHz. The average frequency dependence on emission altitude is represented by the formal fit $r_{\rm em} \propto \nu^{-0.26\pm0.09}$. Generally, the pulsar emission altitude depends on frequency ν, pulsar priod P and pulsar age τ.

4.2. The semi-empirical formula for emission altitude

The radial location of the emission regions was discussed in Papers I, II and III. A general form of the formula for the emission altitude is

$$r_{\rm KG} = \mathcal{A} R \nu_{\rm GHz}^{-a} \tau_6^{-b} P^c \quad , \qquad (4)$$

where $\mathcal{A} \sim 55$, $R \cong 10^6$cm, $\nu_{\rm GHz}$ is observing frequency (in GHz), τ_6 is characteristic age (in 10^6 yrs), P is pulsar period (in sec).

The study on emission region in Paper I carried out for about 10 PSRs at two frequencies $\nu = 0.4$ and 1.4 GHz yielded $\mathcal{A} = 55 \pm 5$, $a = 0.21 \pm 0.07$, $b = 0.07 \pm 0.03$ and $c = 0.33 \pm 0.05$. Here we verify these values for a larger data set, as well as for a wider frequency range. Taking into account results of § 4.1, we obtain

$$r_{\rm KG} = (50 \pm 10) R \nu_{\rm GHz}^{-0.26\pm0.09} \tau_6^{-0.07\pm0.03} P^{0.37\pm0.05} \quad , \qquad (5)$$

or

$$r_{\rm KG} \approx (40 \pm 8) R \nu_{\rm GHz}^{-0.26\pm0.09} \dot{P}_{-15}^{0.07\pm0.03} P^{0.30\pm0.05} \quad , \qquad (6)$$

where $\tau_6 = 16 P / \dot{P}_{-15}$ and $\dot{P}_{-15} = \dot{P}/10^{15}$ is the period derivative. The uncertainties given for various quantities in the above

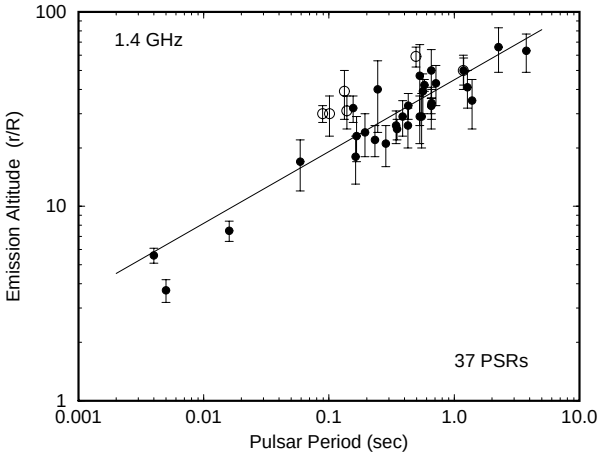


Fig. 6. Emission altitude at 1.4 GHz versus pulsar period. Open circles correspond to young objects (see Paper III for details).

equations follow from systematic errors in the pulse width W measurements and random errors in estimations of the inclination angle α and the impact angle β.

5. Discussion and Conclusions

As it follows from Eqs. (5) or (6), the radio emission of pulsars originates at the narrow altitude range below 10 per cent of the light-cylinder radius. In millisecond pulsars, the radio emission region is much more compact, consistent with their small light-cylinder radii, and is located closer to the neutron star surface (see Paper II). Previously, it was thought that millisecond pulsars have different characteristics of radio emission from those of normal pulsars. However, it was recently argued (Gil & Sendyk 2000; Kramer 1999, and this proceedings) that millisecond pulsar emission properties do not differ from those of typical pulsars.

Recently, Gil et al. (2002) analysed simultaneous dual-frequency single pulse observations of PSR B0329+54 at 240 and 610 MHz. The phase shifts of the leading and the trailing conal components are not equal at these frequencies. This is caused by the retardation-aberration effects. In fact, since the conal beams at different frequenies are emitted at different altitudes, lower frequencies arrive earlier. The retardation-aberration shift of 0.39° translates into a difference of emission altitudes of $\Delta r \sim 2.3\times10^7$cm. This is consistent with the result obtained using the semi-empirical formula $\Delta r_{\rm KG} = 2 \times 10^7$cm (Eqs. 5 or 6).

Mitra & Rankin (2002) found the RFM using outer-conal components data. In Fig. 7 we present a comparison between their results and calculation from Eqs. (5) or (6). Emission altitudes represented by open and filled circles were calculated from $r_{\rm em} = h \cdot s^{-2}$, where h was the emission height for conal component and s was taken as the average value from Mitra & Rankin's paper for each pulsar, respectively. The open circles represent calculations for the first group of their fitted procedure, and filled circles were calculated using the index of $-2/3$ (see Mitra & Rankin 2002, their Table 4). Figure 7 shows that the semi-empirical formula describes quite fr

well the radio emission region in pulsars, consistenly with other results.

The main conclusions from the work on radio emission regions are as follows:

(i) A radius-to-frequency mapping operates in the emission region.

(ii) Pulsar radio emission is typically generated at altitudes lower than a few per cent of the light-cylinder radius $r_{\rm LC}$ and the ratio $r_{\rm KG}/r_{\rm LC}$ decreases with incresing period. The total size of the emission region is below $500R$ in longer period pulsars and correspondingly smaller in shorter period pulsars.

(iii) The emision region in old pulsars is located at correspondingly lower altitudes than in young pulsars with approximately the same period.

Qq cx

Acknowledgements. I gratefully acknowledge the support by the Heraeus foundation.

References

Cordes J. M., 1978, ApJ, 222, 1006
Cordes J. M., 1993, in van Riper K. A., Epstein R., Ho C. eds, Proc. Los Alamos Workshop Cambridge Unov. Press, Cambridge, p. 182
Gangadhara R. T., Gupta Y., 2001, ApJ, 555, 31
Gil J., Gronkowski P., Rudnicki W., 1984, A&A 132, 312
Gil J., 1985, ApJ 299, 154
Gil J., Sendyk M., 2000, ApJ, 541, 351
Gil J., Gupta Y., Gothoskar P.I., & Kijak J., 2002, ApJ, 565, 500
Goldreich P., Julian W. H., 1969, ApJ, 157, 869
Gould M., Lyne A. G., 1998, MNRAS, 301, 235
Hankins T. H., Fowler L. A., 1986, ApJ, 304, 256
Hankins T. H., Moffett D. A., Novikow A., Popov M., 1993, ApJ, 417, 735
Kijak J., Gil J., 1997, MNRAS, 288, 631 (Paper I)
Kijak J., Gil J., 1998, MNRAS, 299, 855 (Paper II)
Kijak J., 2001, MNRAS, 323, 537 (Paper III)
Kramer M., Lange C., Lorimer D. R., Backer D. C., Xilouris K. M., Jessner A., Wielebinski R., 1999, ApJ, 526, 957
Lorimer D. R., Jessner A., Seiradakis J. H., Lyne A. G., D'amico N., Athanasopoulos A., Xilouris K. M., Kramer M., Wielebinski R., 1998, A&AS, 128, 541
Lyne A. G., Graham-Smith F., 1998, Pulsar Astronomy, Cambridge University Press, Cambridge, p. 173
Menchester R. N., Taylor J. H., 1977, Pulsars, Freeman, San Francisco
Mitra D., Rankin J.M., A&A 2002, in press
Ruderman M. A., Sutherland P. G., 1975, ApJ, 196, 51
Sturrock P. A., 1971, ApJ, 164, 529
Thorsett S. E., 1991, ApJ, 377, 263

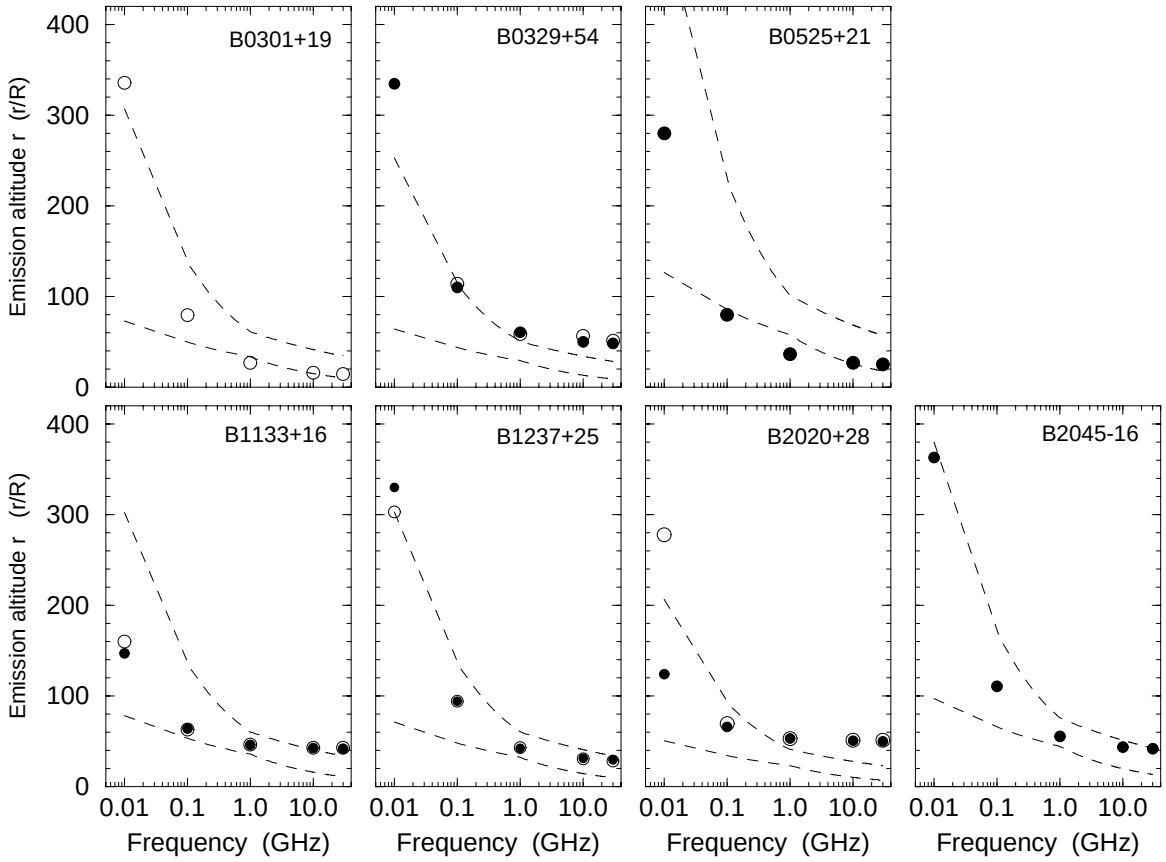


Fig. 7. The multifrequency study of emission altitude. Data points represent calculations from the paper of Mitra & Rankin (2002). The dashed lines show upper and lower limits, calculated from equation (5), corresponding to limiting values of parameters in the semi-empirical relationship.

Proceedings of the 270. WE-Heraeus Seminar on: *"Neutron Stars, Pulsars and Supernova Remnants"*
Physikzentrum Bad Honnef, Germany, Jan. 21-25, 2002, eds. W. Becker, H.Lesch & J. Trümper, MPE Report 278, pp. 206-208

Towards a consistent model for Neutron-Star Sources

W.Kundt

Institut für Astrophysik der Universität, Auf dem Hügel 71, 53121 Bonn, Germany

Abstract. We are still far from understanding how pulsars pulse, how neutron stars are born, what neutron stars can emit, and in which way they do this. In this short communication, I list 18 alternatives – several of them old, a few of them new – which are handled differently by different authors but all of which are crucial for a model of neutron stars to be viable.

1. Ten Alternatives related to Pulsars

• (1) We speak of pulsars as of 'radio pulsars' even though the spectra νS_ν *vs* ν of at least seven, perhaps already sixteen γ*-ray pulsars* peak at hard γ-rays, between $\lesssim$ MeV and $\gtrsim 30$ GeV photon energies. Uncertain in the spectra is their beaming fraction f = f(ν), which may well be frequency dependent. Is it justified to estimate the emitted power L via L := S d^2, rather than via L = 4 π S d^2 ? The factor 4 π matters in particular when we compare the bolometric luminosity of a pulsar with its spin-down power: What fraction of the spin-down power escapes as radiation, and what fraction in the wind?

For a clarification, on the observational side we need a larger number of broadband spectra; and on the theoretical side we need an insight into how and at what *separations* these spectra are emitted. Ever since Kundt & Krotscheck (1980), it is my reinforced conviction that the (coherent) radio pulses are emitted somewhere inside the magnetosphere (as is widely agreed), logarithmically halfway between the stellar radius R and the speed-of-light distance c/Ω, but that the much larger power at γ-rays (and X-rays) relies on a (further) transfer of spin-down power, downstream beyond c/Ω, from the co-rotating magnetosphere to the outgoing, radiating leptons, i.e. that the γ-rays are emitted in the "rural areas" of a pulsar's wind-zone – in the language of Ruderman (1980) – via inverse-Compton losses of the charges (Kundt 1998b). This interpretation is consistent with an often encountered phase shift between the radio and the hard pulses. For similar reasons, I expect all the other (incoherent) pulsar emissions, between high radio frequencies and γ-rays, to be emitted beyond the light cylinder.

• (2) How strong are *pulsar winds*, measured in units of the Goldreich-Julian rate $\dot{N}_{GJ} := \mu_\parallel \Omega^2/ec$, ($\mu := BR^3$)? Are they leptonic? Mapped bowshocks of $\gtrsim 13$ pulsars indicate $\dot{N} = \xi \dot{N}_{GJ}$ with $\xi \approx 10^4$, (Kundt 1998a). The alternative interpretation of the bowshocks – as driven by the pulsar's outgoing Poynting flux – is at variance with our understanding of plasma electrohydrodynamics according to which a convected (toroidal) magnetic flux would require an at least comparable inertia in the flux-anchoring plasma, and a strong outgoing wave would fail to sweep the blocking CSM.

Such strong winds are independently thought to be required for the high *coherence* of the radio pulses, $T_b \lesssim 10^{30\pm2}K$, wanting some 10^{14} electrons to radiate in phase (Kundt 1998a). They need not conflict with the rule that a medium does not allow wave propagation below its plasma frequency: A layered density profile of the (luminally!) outgoing wind would have the high plasma frequency in the high-density layers – the antennae – not in the low-density medium which fills the space between them.

• (3) How do pulsars *drive* their strong winds, inferred under (2), with a *neutral excess plasma* measured by $\xi \approx 10^4$? It has been clear from the beginning of pulsar physics that gravitational forces are too weak for driving a wind, and have the wrong sign, so that electric forces must be at work. But there is no stationary wind solution for (radial) electric forces of uniform sign, because the star would charge up in a light-crossing time, and halt further escape; cf. Pétri et al. (2002).

Instead, *oscillatory discharges* are required during which negative and positive electrons are sucked out alternatingly from the polar caps, and accelerated in the form of space-charge-limited flows. Each (highly relativistic) primary electron transfers its outward momentum to $\xi e^\pm$-pairs, via ξ inverse-Compton and/or curvature photons each of which, in turn, is converted into one pair via the Erber mechanism, a photon collision with the strong, transverse magnetic field (Chang 1985). Weak – though energetic – downward currents to the polar caps, by charges of the opposite sign, guarantee ample production of $e^\pm$-pairs which have been predicted to form a *pair corona*, of temperature $T = 10^{6.5}$K, dense enough for the forming wind to draw its alternating charges therefrom, irrespective of the work function of the surface (Kundt & Schaaf 1993). A derivation from first principles of these 1-d flows – along the open magnetic field lines through the star's center (w.r.t. which the flow is symmetrical) – is now under construction, combining the textbook treatment of a long cable with the driving, largely screened unipolar-induction voltage whose AC discharges satisfy a time-dependent, relativistic Child's Law with electron energies being limited by inverse-Compton and curvature-radiation losses.

These pair coronae, of scale height $\lesssim 10^4$cm, may explain why recent attempts at detecting a neutron star's surface chemistry (via X-rays) have resulted in perfect *blackbody spectra*, (deviations $\lesssim 10^{-2}$), in the case of more than seven nearby neutron stars (Burwitz et al. 2001). These coronae are thought

to grow (rapidly) in column density until they get opaque to pair annihilation, of cross section σ_{ann}, at which column density their optical depth τ to photon scattering is given by $\tau \approx \sigma_T/\sigma_{ann}$. In strong magnetic fields, pairs approaching each other cannot easily get rid of their angular momentum because they are trapped in the Landau ground level of gyrations, and only suffer straight-line accelerations along $\boldsymbol{B}$ (via mutual attraction) during flyby, with reduced radiation by about a factor of 2^{-2} (compared to the non-magnetic case); hence their capture cross section σ_{ann} will be of the order of $\pi r_0^2/4 \lesssim 10^{-1}\sigma_T$. *Pair coronae* are therefore expected to be *opaque* to the heat radiation from a neutron star's surface: $\tau \gtrsim 10$. Note that strong, pulsed pair annihilation from the polar caps of the Crab pulsar has been observed by Massaro et al. (1991), $10^{39.9}$ annihilations per second, consistent with above estimates.

• (4) Strong *electric currents* in the wind-zone – compared with the Goldreich-Julian current density $j_{GJ} := e\boldsymbol{B\Omega}/2\pi$ – are in conflict with (i) a plausible driving mechanism, (ii) their closure across the polar caps, via Pedersen currents, and (iii) the (moderate) X-ray intensities (from the polar caps).

• (5) How strong are pulsar *surface magnetic fields* B_*? Pure dipole fields would be (i) unstable (inside a fluid star: Flowers & Ruderman (1977), hence are inconsistent. During a neutron star's birth, (ii) the increasing angular velocity of the collapsing progenitor star's core is expected to result in a (stabilizing) *toroidal bandage*, forming a 'strangled dipole', or 'bandaged dipole', with large, higher multipoles of odd order. Such strong higher multipoles are also required by (iii) the indispensable Erber mechanism (for pair formation), which needs high field strengths: $B_\perp \geq 10^{12.6}\mathrm{G}\ m_e c^2/h\nu$ for the conversion of a photon of frequency ν, and (iv) small curvature radii R_c ($\lesssim R_*$), (Kundt 1998a). This insight requires a recalculation of the emission heights of the radio pulses, so-called 'radius-to-frequency mapping', which has so far only been done for dipole fields.

However, I see no indication of surface field strengths B_* above $10^{14}G$, as have been proposed for magnetars by Thompson & Duncan (1996).

• (6) How do pulsars achieve their high *radio brightnesses*, $T_b \lesssim 10^{32}K$? The Lorentz-Dirac-Abraham-Laue equation of motion allows for coherent *small-pitchangle synchro-curvature radiation*, whose radiative term gains importance for $Z\tau_e \approx$ ns, (Kundt 1998a), with a significant conversion of kinetic into radiation energy.

• (7) How strongly *beamed* is pulsar radio radiation? A bulk beaming fraction $f \lesssim 0.5$ would be inconsistent with (i) the pulsar *birthrate* $(\Delta t)^{-1}$, where $\Delta t = tf/N = 10^{1.3\pm0.3}f$ yr is the average pulsar birth interval, $t = 10^{6.4}yr =$ average pulsar age (determined from the distribution of $P/\dot{P}$), and $N =$ number of detected pulsars $\gtrsim 10^{5.1}$, corrected for incompleteness of detection (by means of the N vs distance distribution). Note that pulsars are likely the younger twins in their cradle binaries, concluded from the high occurrence rate of – both progenitor, and neutron-star – binaries, and from their large peculiar velocities. The birthrate of neutron stars is then twice the birthrate of pulsars, one in 10 f yr in the Galaxy, unpleasantly high if f were $\lesssim 0.5$.

Another argument against significant bulk beaming is (ii) the missing *synchrotron nebulae* without detected central sources. The high dynamic ranges of pulsar radio emission, $\Delta I/I = 10^{2\pm2}$, indicate a *spiky* instantaneous radiation, both in space and time, but not an avoidance of large spherical angles in the sky.

• (8) Are the *msec pulsars recycled*? I don' t think so. The *distribution* of pulsar periods is certainly *two-humped*, but there is a clear bridge region, between the two humps – containing more than 12 pulsars – and there is (i) no other property that would allow to draw a dividing line (between 'ordinary' and 'recycled' ones). Recycling (ii) ignores a braking torque, (iii) conflicts with the missing (X-ray luminous!) progenitor systems, and (iv) is at variance with the predicted much higher masses of recycled pulsars ($> 2M_\odot$). Note that not only the rotational but also the potential (oblateness) energy grows increasingly with the spin rate. A stellar core collapse is required to create a msec pulsar. The msec pulsars need not be old: their spin-down ages are probably large overestimates of their true ages, by factors of $\approx 10^3$, (Kundt 1998a).

There is a small subset of (six) *anomalous X-ray pulsars* (=AXPs), of spin period $(9 \pm 3)s$, not spin-powered, but with glitches, whose ages are not known. The AXPs range at the opposite end of the 2-humped period distribution (to the ms pulsars). Were they born slow?

• (9) Why are pulsar clocks *noisy*, with both discrete 'glitches', and continuous spin-down noise? In (Kundt 1998a) I have shown that both inaccuracies can be understood as due to a mild *super-rotation*, $\Delta\Omega/\Omega \lesssim 10^{-3}$, of their neutral, superfluid component, of relative moment of inertia $\Delta I/I \lesssim 0.1$, which couples to the normal component in a stochastic way. It is possible that the gradual decay of the higher (than dipole) magnetic multipole moments yields an independent contribution to a pulsar's noisiness.

• (10) Can pulsars act as *jet sources*? The recent, repeated X-ray maps by the CHANDRA satellite, of the near surroundings of the 4 pulsars: Crab, Vela, B1509-58 (in MSH 15-5*2*, = G320.4-1.2), and B1951+32 (in CTB 80), show a wealth of time-varying detail involving (i) a large number of expanding (segments of) ellipses, (ii) symmetric arrays of bright spots, and (iii) two fuzzy, antipodal, jet-like protrusions along the symmetry axis; all this out to distances of $\lesssim 2$ lyr from the pulsar. What goes on?

The outer ellipses have been interpreted, for some 25 yr, as due to enhanced radiation from the (equatorial) inner edge of the pulsar nebula, at the injection shock, where the pulsar wind is decelerated – from supersonic to subsonic – as it joins the outward motion of earlier generations of injected relativistic $e^\pm$-pairs. New are in particular the jets, but also the bright spots, and an inner ring.

The jets look like of *Eilek-type B*, i.e. like relativistic jets whose (decelerated) heads move subsonically w.r.t. their CSM, so that they get defocussed, and lack hot-spots at their outer ends. Jet-sources are thought to evolve from (edge-brightening) type A to (edge-dimming) type B, as a consequence of a decreasing ram pressure and (perhaps) an increasing ambient sound speed with increasing jet length (Kundt 2001). In the present case (of pulsars), the jets form an energetically minor constituent inside a relativistically hot environment, hence look weak already at their young ages. They look very different from the strong jets of, say, SS 433, or of some of the black-hole candidates, which latter I understand as neutron stars surrounded by heavy accretion disks.

These new *pulsar jets* tell me that our earlier understanding of pulsars has been overidealized, as isolated neutron stars

inside clear skies which have swept clean a cavity around them, of radius some lightyear. Pulsar winds are too light to achieve this. Rayleigh-Taylor instabilities allow debris from the SN explosion to hang around and/or fall back, to halt the pulsar wind near its polar caps, confine it, and get it re-started, as a feeble twin jet. The transiently trapped, highly relativistic pairs escape supersonically through a self-rammed, narrow channel, and blow lobes whose intersections with the nozzle are seen glowing at X-rays, as rings and bright spots, the latter at local density enhancements of the debris. X-ray movies which have been prepared from successive maps are reported to show perplexing variability: We see locally heated matter pushed around by new generations of escaping pulsar-wind leptons.

2. Eight further Alternatives related (more generally) to Neutron Stars

• (11) Do (essentially) all *supernovae* give birth to a neutron star? Are they thick-walled explosions, i.e. splinter bombs, implying that their remnants glow via the collisional heating of their CSM, as maintained, e.g., in (Kundt 2001)? Note the particular morphology of the Vela remnant, with its large protrusions seen at X-rays (Aschenbach et al. 1995).

• (12) Must supernova remnants be distinguished from *pulsar nebulae* – like CTB 80, or G 5.3-1.0, the 'Bird' – the latter illuminated by a pulsar wind (Kundt & Chang 1992)? Of particular concern are the *soft γ-ray repeaters* (= SGRs), whose distances can be largely overestimated, and ages largely underestimated if assumed inside SNRs.

• (13) Can neutron stars act as *ejectors* – in distinction to pulsars, or (accreting) binary X-ray sources – like SS 433, and create pair-plasma bubbles which escape as *jets* (Kundt 1998a; 2001)? I.e. neutron stars may behave in many different ways: like pulsars, accretors, ejectors, and 'dead neutron stars', among them perhaps the cosmic-ray boosters, the black-hole candidates, and the γ-ray bursters. Note that SS 433 has recently shown that (even) jet formation need not be without losses: Blundell et al. (2001) find radio emission in the orbit plane, at distances $\gtrsim 10^2$ AU. Those who do not believe in in-situ acceleration must conclude that spillover relativistic pairs are convected outward by an equatorial wind.

• (14) Are the *cosmic rays* generated by the corotating magnetospheres of neutron stars, via *relativistic slingshot* ejections (Kundt 2001)? Note that 20 % of all CRs above 10^{20}eV are *repeaters*, i.e. come from the same direction (within 1^0), asking for nearby compact sources, and that the CRs are hydrogen- and helium-deficient.

• (15) Are the (bright) *supersoft X-ray sources* – with energies between 20 and 60 eV – emitted by forming massive accretion disks (between 1 and 20 $M_\odot$, typically 5 $M_\odot$), rather than by white dwarfs (Kundt 1996)? I think so. The record in mass is presently held by GRS 1915+105, (Greiner et al. 2001).

• (16) How to explain the *super-Eddington sources*, mostly (agreed) neutron-star binaries with X-ray powers $\lesssim 10^{41}$erg/s? Are they due to 'blade' accretion from forming massive disks, i.e. due to magnetically confined, clumpy accretion in the orbit plane (Kundt 1996)?

• (17) Are the *black-hole candidates* neutron-star binaries with massive accretion disks, filling the gap between the low-mass and high-mass X-ray binaries (Kundt 2001)?

• (18) Are the *γ-ray bursts* emitted by spasmodically accreting old, nearby (Galactic) neutron stars, via clumpy accretion, as is signaled by the ($\gtrsim 6$) repeaters? The SGRs are the nearest among them, from which we receive both the rare, ordinary GRBs and, in addition, the frequent softer and vastly weaker repetitions. Their afterglows – whose relativistic redshifts are reminiscent of the transverse Doppler shifts of SS 433 – would be *light echos* from their transient hadronic winds as well as from their CSM.

Acknowledgements. There were times in modern sciences when one could use a significant fraction of one's working hours for doing research, with no extra education required in how to please a group of malicious PCs; these times now belong to the past. This communication owes its existence to my younger colleagues Robindro Dutta-Roy, Jürgen Päpke, and Gernot Thuma for whose repeated help I thank them warmly.

Concerning the science part, my thanks go to Bernd Aschenbach, Joachim Trümper, and to Gernot Thuma for in-depth, undoubtedly honest, and always ready discussions respectively.

References

Aschenbach B., Egger R., Trümper J., 1995, Nature 373, 587-590

Blundell K.M., Mioduszewski A.J., Muxlow T.W.B., Podsiadlowski P., Rupen M.P., 2001, ApJ 562, L79-L82

Burwitz V., Zavlin V.E., Neuhäuser R., Predehl P., Trümper J., Brinkman A.C., 2001, A&A 379, L35-L38

Chang H.-K., 1995, A&A 301, 456-462

Flowers E., Ruderman M.A., 1977, ApJ 215, 302-310

Greiner J., Cuby J.G., McCaughrean M.J., 2001, Nature 414, 522-524

Kundt W., 1996, in Supersoft X-Ray Sources, ed. J. Greiner, Lecture Notes in Phys. 472, 45-50

Kundt W., 1998a, Fundamentals of Cosmic Phys. 20, 1-119

Kundt W., 1998b, Mem. Soc. Astron. Ital. 69, 911-917

Kundt W., 2001, Astrophysics - A Primer, Springer

Kundt W., Chang H.-K., 1992, Ap&SS 193, L145-L154

Kundt W., Krotscheck E., 1980, A&A 83, 1-21

Kundt W., Schaaf R., 1993, Ap&SS 200, 251-270

Massaro E., Matt G., Salvati M., Costa E., Mandrou P., Niel M., Olive J.F., Mineo T., Sacco B., Scarsi L., Gerardi G., Agrinier B., Barouch E., Comte R., Parlier B., Masnou J.L., 1991, ApJ 376, L11-L14

Pétri J., Heyvaerts J., Bonazzola S., 2002, A&A 384, 414-432

Ruderman M., 1980, in Ninth Texas Symposium on Relativistic Astrophysics, eds. J. Ehlers, J. Perry, & M. Walker, Ann. New York Acad. Sci. 336, 409-428

Thompson C., Duncan R., 1996, ApJ 473, 322-342

Proceedings of the 270. WE-Heraeus Seminar on: *"Neutron Stars, Pulsars and Supernova Remnants"*
Physikzentrum Bad Honnef, Germany, Jan. 21-25, 2002, eds. W. Becker, H.Lesch & J. Trümper, MPE Report 278, pp. 209-214

Natural Limits for Currents in Charge Separated Pulsar Magnetospheres

A. Jessner[1], H. Lesch[2] and T. Kunzl[2]

[1] Max–Planck–Institut für Radioastronomie, Radio-Observatorium Effelsberg, Max-Planck-Str. 28, D-53902 Bad Münstereifel, Germany
[2] Centre for Interdisciplinary Plasma Science
Universitäts-Sternwarte München, Scheinerstr.1, D-81679 München, Germany

Abstract. Rough estimates and upper limits on current and particle densities form the basis of most of the canonical pulsar models. Whereas the surface of the rotating neutron star is capable of supplying sufficient charges to provide a current that, given the polar cap potential, could easily fuel the observed energy loss processes, observational and theoretical constraints provide strict upper limits to the charge densities. The space charge of a current consisting solely of particles having only one sign creates a compensating potential that will make the maximum current dependent on potential and distance. In the non-relativistic case this fact is expressed in the familiar Child-Langmuir law. Its relativistic generalization and subsequent application to the inner pulsar magnetosphere provides clear limits on the strength and radial extension of charged currents originating on the polar cap. Violent Pierce-type oscillations set in, if one attempts to inject more current than the space charge limit into a given volume. These considerations apply wherever there is a significant amount of charged current flow, in particular in the gap regions. There they can be used to derive limits on the size of such gaps and their stability.

1. Introduction

All pulsar models require charges to be drawn from the pulsar surface, accelerated, and possibly multiplied by pair production, as being the medium that will be responsible for the great variety of observational features currently known from many pulsars. Common to all models is a rotating heavily magnetized ($10^8 - 10^{12}$G) neutron star. As early as 1955 it was recognized by A. Deutsch that a sufficiently strongly magnetized fast rotator in a vacuum would be surrounded by an envelope (magnetosphere) of charged particles. Because of their fundamental importance, the electrodynamical aspects of pulsar models have been of interest from the early days of pulsar research until now.

In all cases, the number density of particles available is the decisive factor for the self-consistency and hence viability of any pulsar model.

Starting from the surface of the neutron star, it is recognized that its very composition plays a crucial role in determining the number charges emitted (Usov & Melrose 1996). The controlling factor is the surface work function, representing the potential barrier to be overcome by the charges that are to be emitted from the pulsar surface. Usually, the work function is of the order of the Fermi-energy of the solid lattice, which in itself depends on the electron density. Using a Thomas-Fermi-Dirac-Weizsäcker approximation Abrahams & Shapiro (1992) calculated the cold ($T = 0$) surface density ρ_{Fe} to be about $2.9 \cdot 10^6\,\mathrm{kgm}^{-3}$. That result enabled us (Jessner et. al. 2001) to estimate the Fermi energy at the surface as

$$E_F(\rho_{Fe}) = \frac{2 \cdot \pi^4 \hbar^4 c^2}{e^2 B^2 m_e} \cdot \left(\frac{\rho_{Fe} \cdot (28-2)}{56 \cdot m_p} \right)^2 \qquad (1)$$

which amounts to $E_F = 4.17 \cdot 10^2$ eV. For such a low work function, even field emission can supply enough charges to provide a relativistic flow of electrons at the co-rotation value given by the Goldreich-Julian-density (Jessner et. al. 2001). But the estimated value for E_F should be taken as an upper limit, since the thermal X-ray emission indicates that pulsars have surface temperatures well above $3 \cdot 10^5$K and are surrounded by a thin gaseous surface layer which would not entail any significant barrier for the extraction of electrons (Pavlov and Zavlin 1998). In that case the surface properties themselves will not influence the primary charge densities (free charge emission scenario).

Recently (Jessner et. al 2001), we proceeded to calculate the Lorentz factors and pair production rates of electrons accelerated along field lines of an aligned dipole taking due account of radiation losses due to inverse Compton scattering on thermal photons (as was proposed by Sturner 1995) and curvature radiation. This was done under the simplifying assumption of a relativistic flow which resulted in constant shielding of the accelerating field by the primary charges below the pair production region. In addition, the field and density enhancements described by Muslimov and Tsygan (1992) were also not implemented. To be complete we will now give an estimate of the initial (primary) current that can be drawn from a pulsar polar cap and on its stability by solving Poisson's equation with constant current density, but with a velocity dependent charge density.

2. The Child-Langmuir Equation

Space charge limitations play an important role in the conduction of currents across otherwise empty space, their detailed study in first half of the 20^{th} century provided the foundation of much of our electronic technology. In order to illustrate the

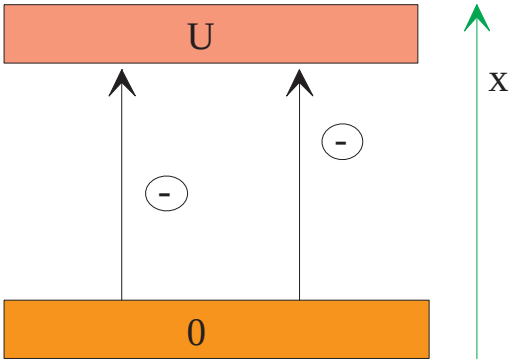


Fig. 1. Simple one dimensional flow of electrons between two electrodes.

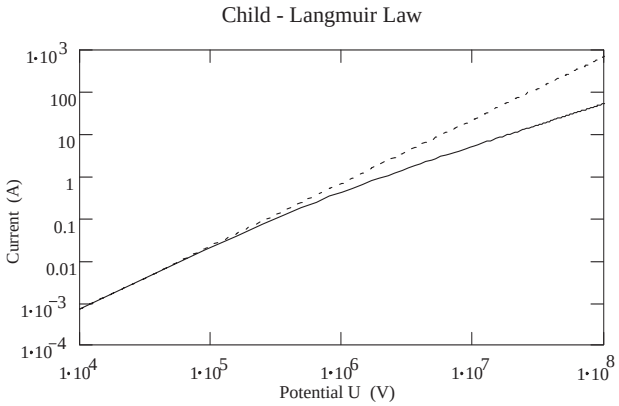


Fig. 2. Current flowing between two parallel 1cm^2 electrodes (spacing 1 m) as a function of the potential difference U (solid line). The dashed line shows the usual non-relativistic relationship which is invalid for $U > \frac{m_e c^2}{q_e}$.

principle, we will briefly review a simple classical 1-dimensional case: Take two large electrodes (Fig. 1) of equal area A_0 separated by a distance x, one at zero potential and the other at $U = U_0$. We assume that we can supply an arbitrary amount of charge for the flow in the direction of x, so that the current will limit itself as soon as the potential at the lower surface vanishes. The velocity of an electron, accelerated by a potential U is given by

$$\beta(U) \cdot c = \frac{\sqrt{q_e^2 U^2 + 2 q_e U m_e c^2}}{q_e U + m_e c^2} \tag{2}$$

In the non-relativistic case ($U << 511$ kV) this simplifies to

$$v(U) = \sqrt{\frac{2 \cdot q_e U}{m_e}} \tag{3}$$

If the potential $U > 0$, then a current I will flow from the lower to the upper electrode. This current is conserved along the upward (x) direction. Such a current moving in a vacuum obeys Poisson's law:

$$\frac{d^2}{dx^2} U = \frac{I}{\epsilon_0 c A_0 \beta(U)} \tag{4}$$

In the non-relativistic case we replace $c\beta$ with $\sqrt{\frac{2 \cdot q_e U}{m_e}}$, integrate twice and solve for the current to obtain the canonical expressions for the maximum current I_0 and the internal resistance $R_0 = U/I_0$ of a planar vacuum diode (Child, 1911, Langmuir 1913) that has a potential U w.r.t. the cathode.

$$I_0(U,x) = \frac{4\sqrt{2}}{3} \sqrt{\frac{q_e}{m_e}} \epsilon_0 A_0 U^{3/2} x^{-2} \tag{5}$$

The resistance follows as

$$R_0(U,x) = \frac{3}{4\sqrt{2}\epsilon_0 A_0 \sqrt{\frac{m_e}{q_e}}} U^{-1/2} x^2 \tag{6}$$

Hence a very important, but often overlooked consequence of Poisson's equation and the equation of motion is the fact, that a charged current requires a potential to flow through a vacuum. In the non-relativistic regime, the required potential increases as the 4/3 power of the longitudinal distance and the 2/3 power of the current.

The solution to the fully relativistic equation

$$\frac{d^2}{dx^2} U = \frac{I \cdot (q_e U + m_e c^2)}{\epsilon_0 c A_0 \sqrt{q_e^2 U^2 + 2 q_e U m_e c^2}} \tag{7}$$

is slightly more complicated,

$$I(U,x) = \frac{\epsilon_0 c A_0}{q_e x^2} \left(2\sqrt{q_e^2 U^2 + 2 q_e U m_e c^2} + m_e c^2 \left(2 \sin^{-1} \left(\frac{m_2 c^2}{q_e U + m_e c^2} - \pi \right) \right) \right) \tag{8}$$

but the general dependence of the space charge limited current on the inverse squared distance remains unchanged. In fig. 2 we give a quantitative example of the current that will flow between two electrodes of 1cm^2 crossection, spaced apart by one meter. In the relativistic regime, the current rises linearly with the applied potential, hence the potential required to drive a particular current density over a distance x now increases as x^2. Although this example appears to be somewhat remote from the expected conditions at a pulsar's polar cap, one easily recognizes, that for a typical Pulsar (B = 10^{12}G, P = 0.5s), the relativistic Goldreich-Julian current density approaches [1] $q_e n(r_{ns}) c = 498$ Acm^{-2}. A potential of 10^9 V is required to drive such a current over the distance of 1 meter. For a height of i.e. $h = 100$m we have exhausted the available potential difference ($\sim 10^{13}$ V) on the polar cap! The square law dependence of the required potential makes it impossible to have a far reaching *charged* current of appreciable density within the pulsar magnetosphere.

[1] Here we used the general relativistic surface density $n(r_{ns})$ as defined in section 3

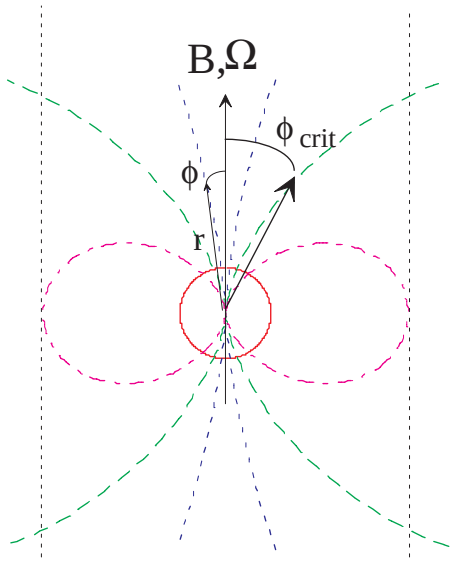


Fig. 3. Aligned magnetic rotator

3. Space charge limits for an aligned relativistic pulsar magnetosphere

For reasons of simplicity we will now use the model of an aligned rotator as described by Goldreich and Julian (1969). Fig. 3 outlines the geometry of the rotating neutron star field. Near the surface of the neutron star, the space-time metric is affected by the presence of the heavy compact rotator leading to the general relativistic effects of the Lense-Thirring dragging of field lines and a radial dependence of the volume elements. Muslimov and Tsygan (1992) introduced an auxiliary function to account for the general relativistic distortion of the field lines:

$$f(r) = -3\left(\frac{r}{r_{ns}\epsilon_{MT}}\right)^3\left[\ln\left(1-\frac{\epsilon_{MT}r_{ns}}{r}\right) + \frac{\epsilon_{MT}r_{ns}}{r}\left(1+\frac{\epsilon_{MT}r_{ns}}{2r}\right)\right] \quad (9)$$

here we used the compactness $\epsilon_{MT} = \frac{2\Gamma M_{ns}}{c^2 r_{ns}}$ where $\frac{2\Gamma M_{ns}}{c^2} = r_g$ is the canonical Schwarzschild radius of the neutron star. A magnetic field line starting with a colateral angle ϕ_0 at the pulsar surface is given by

$$\sin(\phi) = \sqrt{\frac{r}{r_{ns}}\frac{f(1)}{f\left(\frac{r}{r_{ns}}\right)}}\sin(\phi_0) \quad (10)$$

As an example we use the well known pulsar PSR B2021+51 from the catalogue of Taylor, Manchester and Lyne (1995) with a period of $P = 0.529$s and a surface magnetic field of $B_0 = 10^{12.11}$G which for simplicity we treat as if it were an aligned rotator. Then the colateral angle of the rim of the polar cap turns out to be $\phi_{crit} = \sin^{-1}\left(\sqrt{\frac{2\pi r_{ns}\sin^2(\pi/2)}{Pcf(1)}}\right) = 0.94^\circ$ and the area of the polar cap is $A_{pole} = 2\pi r_{ns}^2(1-\cos(\phi_{crit})) = 8.5\cdot 10^4\mathrm{m}^2$. The opening angle ϕ and thus the surface area enclosed by the limiting field lines increases with increasing distance from the surface. Using the equation of field lines (10), we can subsequenty replace $\cos(\phi(r))$ with

$$\zeta(r) = \sqrt{1-\frac{r}{r_{ns}}\frac{f(1)}{f\left(\frac{r}{r_{ns}}\right)}\sin^2(\phi_{crit})} \quad (11)$$

The Goldreich-Julian charge density compensates the induced electric field parallel to the magnetic field line and is classically given for the pole by $n_0(r) = \frac{B_0\Omega\epsilon_0}{q_e}\left(\frac{r_{ns}}{r}\right)^3$ yielding $n_0(r_{ns}) = 8.5\cdot 10^{16}\mathrm{m}^{-3}$ on the surface of the centre of the polar cap. Following Beskin (1999) we can use

$$f_0(r) = \frac{1-\left(\frac{r_g}{r}\right)^3}{\sqrt{1-\frac{r_g}{r}}} \quad (12)$$

to describe the G.R. correction of the co-rotation density n as a function of distance. Because of the higher electric field at the surface, the density has to increase by a factor of $f_0(r_{ns}) = 1.21$ to a value of $n_0(r_{ns})\cdot f_0(r_{ns}) = 1.03\cdot 10^{17}\mathrm{m}^{-3}$. $f_0(r)$ decays quickly with r, i.e. to 1.021 at $r = 10r_{ns}$. Assuming relativistic velocities, the total polar cap current can roughly account for the observed spin-down energy loss of the pulsar:

$$I_{cap} = n(r_{ns})q_e c A_0 \frac{1}{\phi_{crit}}\int_0^{\phi_{crit}}\left(3\cos^2(\theta)-1\right)d\theta = 1.01\cdot 10^{12}\mathrm{A} \quad (13)$$

Together with the polar cap potential $U_{cap} = \frac{-B_0\Omega r_{ns}^2}{2}\left(\cos^2(\phi_{crit})-1\right) = 2.07\cdot 10^{13}$V we obtain an electrical power of $I_{cap}U_{cap} = 2.09\cdot 10^{25}$W which, for such a coarse model, agrees surprisingly well with the observed energy loss of $10^{32.9}\frac{\mathrm{erg}}{\mathrm{s}} = 7.9\cdot 10^{25}$W.

For a pulsar with an electron current flowing out of the polar cap, the radial part of Poisson's equation can now be written in spherical polar coordinates:

$$\frac{1}{r^2}\frac{d}{dr}r^2\frac{d}{dr}U = \frac{-I}{\epsilon_0 2\pi r_{ns}^2 c\beta(u)(1-\zeta(r))} + \frac{q_e}{\epsilon_0}n_0(r_{ns})f_0(r)\left(\frac{r_{ns}}{r}\right)^3(3\zeta(r)^2-1) \quad (14)$$

The first term on the right hand side of the equation contains the charge density due to the current of electrons and the second term the equivalent co-rotation charge density. Here we have assumed a uniform current density across the cap and we neglect the transverse dependence of the potential (all other derivatives in Poission's equation are assumed to vanish). But the divergence of field lines as a function of distance is accounted for by $\zeta(r)$. Furthermore, it is quite reasonable to assume that the electrons will leave the surface with thermal velocities. For $T = 3\cdot 10^5$K their kinetic energy corresponds to an initial potential of $U_0 = \frac{kT}{q_e} = 25.9$V, and a velocity of $0.01c$. Come what may, the boundary condition at the surface $0 < U < U_0$ dictates that the flow starts in the non-relativistic regime. As current densities are conserved along the field lines, and charges are accelerated, the first (current) term in (14) will decrease on acceleration, leading to further increase of the accelerating potential (and vice versa). If we therefore have a space charge limited flow with full shielding at the surface ($n = n(r_{ns})$) and $\beta = 0.01$, the charge density will decrease by a factor of $\sim\beta$ along the field lines if relativistic potentials are encountered, a point already made by Fawley, Arons and Scharleman (1977).

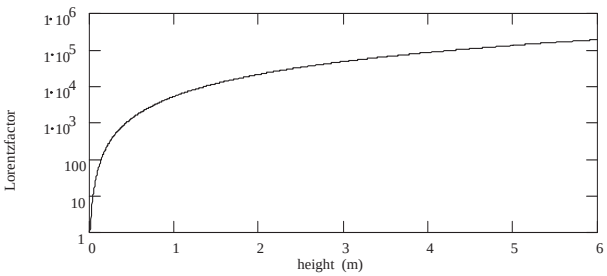


Fig. 4. Lorentz factor reached by particles in a current that is limited by the space charge density being equal to the co-rotation density at the pulsar surface.

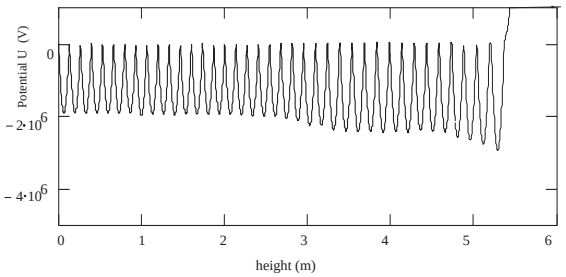


Fig. 5. Effective potential along a central field line for an enforced current of about 0.8 of the relativistic co-rotation current I_0.

4. Numerical Solutions of the Pulsar Poisson Equation

A Bulirsch-Stoer algorithm (provided by MATHCAD) was employed with typically 2048 steps to solve (14) for a range of up to 6m above the pulsar surface where the boundary conditions were set to $U(r_{ns}) = U_0$ and $\frac{dU}{dr} = 0\mathrm{Vm}^{-1}$. The results were checked by increasing the resolution and sometimes with another algorithm (adaptable Runge-Kutta method).

4.1. Strict space charge limitation at the surface

With a constant current over the polar cap that is in equilibrium at the surface, fulfilling the above boundary conditions, we get a massive increase in particle energies with height (fig. 4). But in the same vein, the charge density falls to about 1% of the surface value after about $\frac{c}{\omega_{pl}} = c\sqrt{\frac{\epsilon_0 m_e}{q_e^2 n_0}} = 15\mathrm{mm}$ in agreement with Fawley, Arons and Scharleman (1977). In this and all following cases we neglected energy losses of particles by inverse Compton scattering and curvature radiation. These losses will start to limit the attainable particle energies in the surface layer as soon as Lorentz factors of about a few 1000 are attained (Jessner et.al. 2001).

4.2. Enforced current at about 0.8 times the relativistic co-rotational current

The extremely low relativistic charge densities of $0.01n(r_{ns})$ obtained from the steady-state solution make pulsar models unworkable, if they require a primary current of co-rotational density (Ruderman & Sutherland 1975) to supply the energy for the magnetospheric processes. Following the reasoning in section 3 we now find that $\beta I_{cap} V_{cap}$ is more than two orders of magnitude smaller than the observed energy loss. The high, unshielded $E_{||}$ may aid pair creation, but unless the secondary charges themselves are accelerated by an unshielded field, they will not contribute to the energy balance.

It is therefore of interest to see what happens when the strict boundary condition $U(r_{ns}) = U_0$ is relaxed by forcing a charge overdensity to be drawn from the surface yielding a relativistic current density of the order of the co-rotation density. Fig. 5 shows the strongly fluctuating potential distribution that will be the result. The current breaks into slabs of $\sim$ 10cm thickness until the particles have obtained enough energy so that their charge density becomes low enough for the accelerating field to take over, in this case after $\sim$ 5m. Such oscillations are common in flows that exceed the space charge limit locally and the stationary solutions of similar cases have been described by Mestel et. al. (Mestel et. al. 1985) and Shibata (1997). Haeff noted the time variability of the instability in 1939, Pierce described it in 1949 and Eilek presented (this volume) a time dependent solution showing how the oscillatory patterns evolve and propagate with time. Schopper presented a 3-D PIC simulation (this volume) showing how an initially steady particle beam breaks into the noted charged slabs.

4.3. Enforced currents with an additional positively charged relativistic inflow

The local charge overdensity on the surface, required by strong relativistic currents, can be neutralized by an inflowing current of the same magnitude, but with opposite sign of the charges. The simplest case would be a highly relativistic current I_r with $\gamma m_e c^2 >> q_e U$. Then we can set $\beta = 1$ for the return current and solve the following differential equation:

$$\frac{1}{r^2}\frac{d}{dr}r^2\frac{d}{dr}U = \frac{-1}{\epsilon_0 2\pi r_{ns}^2 c(1-\zeta(r))}\left(\frac{I}{\beta(u)} - I_r\right) + \frac{q_e}{\epsilon_0} n_0(r_{ns}) f_0(r) \left(\frac{r_{ns}}{r}\right)^3 (3\zeta(r)^2 - 1) \quad (15)$$

The positively charged current will not neutralize the space charge in an extended region above the polar cap, leading to strong acceleration, similar to that shown in fig. 4. But, not unexpectedly, as soon as one relaxes the neutrality condition at the surface, density oscillations will appear. For closely matched inflowing and outflowing currents a second boundary with $U = 0$ will exist higher up in the magnetosphere. Fig. 6 shows an example where the effects of a positively charged current of $0.9I_0$ and a negative thermal current of $1.8I_0$ are calculated. Further simulations with different flowrates have shown that the location of the second boundary is very sensitive to the matching of the currents. A decrease of the outflow by one percent moves the second boundary outward by several hundred meters. Figs. 7 and 8 show the oscillations near the surface. Mildly relativistic potential fluctuations of a few 10^6V are encountered with wavelengths of about 40cm and the densities (Fig. 8) show positive values with narrow gaps.

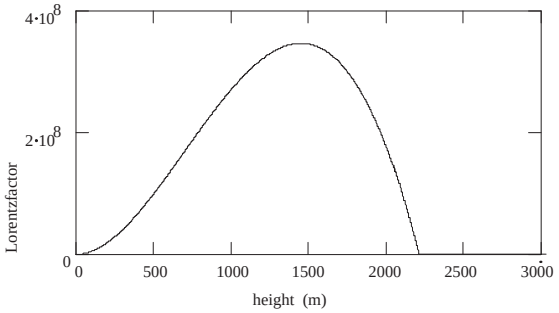


Fig. 6. Lorentz factor of outflowing particles with 1.8 of the relativistic co-rotation current I_0 and a positive inflow of $0.9I_0$. Particles come to rest at $h \sim 2200$m!

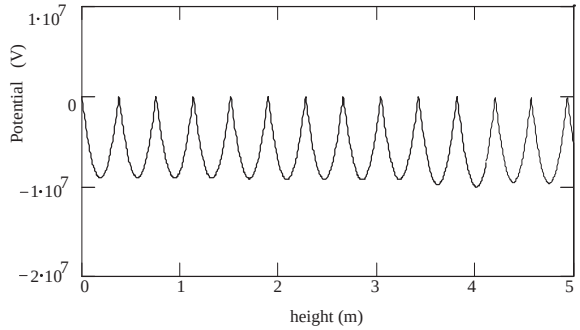


Fig. 7. Potential oscillations caused by outflowing particles with 1.8 of the relativistic co-rotation current I_0 and a positive inflow of $0.9I_0$.

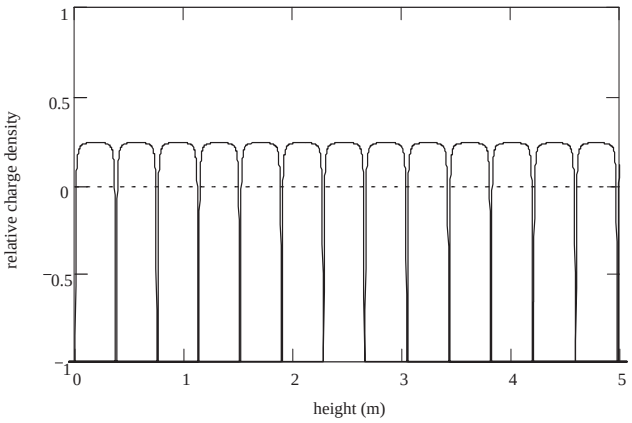


Fig. 8. Charge densities for outflowing particles with 1.8 of the relativistic co-rotation current I_0 and a positive inflow of $0.9I_0$.

5. Conclusions

Charged currents cannot propagate in a vacuum without an outer potential, for a fixed current density the required potential increases as the square of the distance. In the case of pulsars, the available potential on the polar cap allows for a relativistic electron current of co-rotation density only up to a height of a few hundred metres.

Particles start from the neutron star with thermal velocities. An electron current, if limited by non-relativistic space charges at the surface, will encounter an outwardly increasing potential along the field lines. This accelerates the charges and decreases the available current density. Hence a thermal current of non-relativistic surface density cannot compensate the parallel electric field once it leaves the surface. In a steady-state regime, relativistic currents from the polar cap can only be a small fraction $O(0.01)$ of a co-rotational current. Standard pulsar models *assume* a relativistic current of co-rotational density and become unworkable when the primary currents are as low as shown. The available power in the magnetospheric current system is insufficient if the current is space charge limited. Due to the unshielded $E_{||}$ Lorentz factors would become too high for radio emission at the observed heights and if pair production were to take place, another boost of at least a hundred in the multiplicity factor would be required to reach the frequently assumed $10^{3-4} n_0(r)$. We take this as evidence against a steady state description of the pulsar mechanism and a large scale charged current flow out to i.e. the light cylinder.

Forcing a current that locally exceeds the co-rotation charge density leads to strong Pierce type oscillations. The presence of a relativistic inflow of opposite charges does not alter the picture significantly, mainly the outflowing density can be increased by the inflowing amount. A second boundary with $U = 0$ (inner gap) can be formed for particular combinations of inflow and outflow, where the outflow exceeds the inflow. In these cases the current and the potentials fluctuate with wavelengths of a few 10cm in a region of a few metres above the surface. The density is strongly modulated, showing narrow gaps in the flow. Such fluctuations are inevitable whenever the density exceeds the space charge limits. It may happen at a boundary as in our case, or whenever a relativistic current is strongly perturbed so that it may become non-relativistic in places and by that way exceed the space charge limit. Work by Eilek (this volume), Schopper (also this volume) , Shibata (this volume and 1995), Mestel et. al. (1985) does indicate that the Pierce instability is of importance in the pulsar magnetosphere.

Acknowledgements. We like to thank J. Arons, V. Beskin and A. Tsygan for drawing our attention to the fact that shielding of $E_{||}$ cannot be uniform along the field lines. Valuable discussions with Y. Lyubarski, R. Schopper and the particular interest in the subject shown by D. Mitra and J. Eilek were inspiring and encouraging. We gratefully acknowledge the support by the Heraeus foundation.

References

A.M. Abrahams, S.L. Shapiro, ApJ, 374, 655 (1991)
V.S. Beskin, Physics-Uspekhi, 42(11), 1071 (1999)
C.D. Child, Phys. Rev. 32 (1911), 324
A. Deutsch, Ann. Astrophys. 18,1, 1 (1955)
P. Goldreich, W.H. Julian, ApJ, 157, 869 (1969)
A.V. Haeff, Proc. I.R.E., 27, 586 (1939)
W.M. Fawley, J. Arons, E.T. Scharleman, ApJ, 217,227-243 (1977)
A. Jessner, H. Lesch, T. Kunzl, ApJ, 547, 959 (2001)
I. Langmuir, Phys. Rev. 2 (1913)

L. Mestel, J.A. Robertson, Y.M. Wang, K.C. Westfold, MNRAS, 217, 443 (1985)
A.G. Muslimov and A.I. Tsygan, MNRAS,255, 61 (1992)
G.G. Pavlov, V.E. Zavlin in Neutron Stars and Pulsars, ed. N. Shibazazaki et. al (Tokyo 1998)
J.R. Pierce, The Theory and Design of Electron Beams, van Nostrand, (Toronto, New York, London 1949)
M.A. Rudermann, P.G. Sutherland, ApJ, 196, 51-72 (1975)
S. Shibata, ApJ, MNRAS, 276, 537 (1995)
S.J. Sturner, ApJ, 446, 292 (1995)
J.H. Taylor, R.N. Manchester, A.G. Lyne, ApJS,88,529 (1993)
V.V. Usov, D.B. Melrose, ApJ 464, 306 (1996)

Proceedings of the 270. WE-Heraeus Seminar on: *"Neutron Stars, Pulsars and Supernova Remnants"*
Physikzentrum Bad Honnef, Germany, Jan. 21-25, 2002, eds. W. Becker, H.Lesch & J. Trümper, MPE Report 278, pp. 215-220

Inner vacuum gap formation and drifting subpulses in pulsars

Janusz A. Gil & George I. Melikidze

Institute of Astronomy, University of Zielona Góra, Lubuska 2, 65-265, Zielona Góra, Poland

Abstract. The problem of formation of the inner vacuum gap in neutron stars with $\mathbf{\Omega}\cdot\mathbf{B}<0$ is considered. It is argued by means of the condition $T_i/T_s>1$, where T_i is the melting temperature of surface $^{56}_{26}$Fe ions and T_s is the actual temperature of the polar cap surface, that the inner vacuum gap can form, provided that the actual surface magnetic field is extremaly strong ($B_s\gtrsim 10^{13}$ G) and curved ($\mathcal{R}<10^6$ cm), irrespective of the value of dipolar component measured from the pulsar spin down rate. The calculations are carried out for pulsars with drifting subpulses and/or periodic intensity modulations, in which the existence of the quasi steady vacuum gap discharging via $\mathbf{E}\times\mathbf{B}$ drifting sparks is almost unavoidable.

1. Introduction

The subpulses in single pulses of a number of pulsars change phase systematically between adjacent pulses, forming apparent driftbands of the duration from several to few tenths of pulse periods. The subpulse intensity is also systematically modulated along driftbands, typically increasing towards the pulse centre. In some pulsars, which can be associated with the central cut of the line-of-sight trajectory, only periodic intensity modulation is observed, without a systematic change of subpulse phase. On the other hand, the clear subpulse driftbands are found in pulsars with grazing line-of-sight trajectories. These characteristics strongly suggest an interpretation of this phenomenon as a system of subpulse associated beams rotating slowly around the magnetic axis. Ruderman & Sutherland (1975; hereafter RS75) proposed a natural explanation of the origin of subpulse drift, that involved a number of isolated $\mathbf{E}\times\mathbf{B}$ drifting sparks discharging the quasi steady vacuum gap formed above the polar cap of the so-called anti-pulsar with $\mathbf{\Omega}\cdot\mathbf{B}<0$, in which $^{56}_{26}$Fe ions were strongly bound at the surface. Although the original idea of RS75 associating the rotating sub-beams with the circulating sparks is still regarded as the best qualitative model of drifting subpulse phenomenon, their vacuum gap was later demonstrated to suffer from the so-called binding energy problem (for review see Abrahams & Shapiro 1991). In fact, the cohesive energies of $^{56}_{26}$Fe ions used by RS75 proved to be largely overestimated and the inner vacuum gap envisioned by RS75 was impossible to form. However, it is worth to emphasize that RS75 considered the canonical surface dipolar magnetic fields with values determined from the pulsar spindown rate, although they implicitly assumed small radii of curvature $\mathcal{R}\sim 10^6$ cm, inconsistent with purely dipolar field. Recently Gil & Mitra (2001; hereafter GM01) revisited the binding energy problem an found that formation of vacuum gap is in principle possible, although it requires extremely strong non dipolar surface magnetic field $B_s=bB_d$, where the coefficient $b>>1$ in typical pulsar, $B_d=6.4\times10^{19}(P\dot{P})^{0.5}\mathrm{G}=2\times10^{12}(P\dot{P}_{-15})^{0.5}$ G is the dipolar field at the pole, P is the pulsar period in seconds, $\dot{P}$ is the period derivative and $\dot{P}_{-15}=\dot{P}/10^{-15}$.

In a superstrong surface magnetic field $B_s>0.1B_q$, where $B_q=4.414\times10^{13}$ G, the asymptotic approximation of Erber 1966 used by RS75 in derivation of the height of quasi steady vacuum gap is no longer valid. In fact, in such strong field the high energy $E_f=\hbar\omega$ photons produce electron-positron pairs at or near the kinematic threshold $\hbar\omega=2mc^2/\sin\theta$, where $\sin\theta=h/\mathcal{R}$, h is the gap height, and $\mathcal{R}=\mathcal{R}_6 10^6$ cm is the radius of curvature of surface magnetic field lines (e.g. Daugherty & Harding 1983), $\hbar$ is the Planck constant, c is the speed of light, m and e are the electron mass and charge, respectively. The vacuum gap formed under such conditions was called the Near Threshold Vacuum Gap (hereafter NTVG) by GM01. They considered two kinds of high energy seed photons dominating the e^-e^+ pair production: the Curvature Radiation (CR) photons with energy $\hbar\omega=(3/2)\hbar\gamma^3c/\mathcal{R}$ (RS75; Zhang & Qiao 1996), and resonant Inverse Compton Scattering (ICS) photons with energy $\hbar\omega=2\gamma\hbar eB_s/mc$ (**?**), where γ is a typical Lorentz factor of particles within the gap. The corresponding vacuum gap is called the Curvature Radiation dominated (CR-NTVG) and the Inverse Compton Scattering dominated (ICS-NTVG), respectively. GM01 estimated the characteristic heights of both CR-NTVG and ICS-NTVG. In this paper we will further refine these estimates by including the general relativistic (GR) effects of inertial frame dragging (IFD) and considering the heat flow conditions within the thin uppermost surface layer of the polar cap. Moreover, we will use broader range of cohesive energies of surface $^{56}_{26}$Fe ions. The obtained VG models are applied to pulsars with drifting subpulses and/or periodic intensity modulations, in which the presence of $\mathbf{E}\times\mathbf{B}$ drifting spark discharges seems almost unavoidable (Deshpande & Rankin 1999; 2001; Vivekanand & Joshi 1999 and Gil & Sendyk 2000).

2. Near threshold vacuum gap formation

If the cohesive energy of $^{56}_{26}$Fe ions is large enough to prevent them from thermionic (this section) or field emission (Ap-

pendix A), a vacuum gap forms right above the polar cap. Jessner et al. (2001) pointed out that the GR effect of IFD (?) should affect the RS75 type models with a vacuum gap above the polar cap. Although Jessner et al. (2001) did not investigate the problem, they implicitly suggested that the electric fields distorted by GR effects make formation of "starved" inner magnetospheric regions even more difficult than in the flat space case. However, Zhang et al. (2000) demonstrated that although the GR-IFD effect is small, it nevertheless slightly helps formation of VG above the polar caps. In other words, the GR modified potential drop within the VG is slightly lower than in the flat space case. Below we confirm this finding for NTVG conditions, with a very strong and complicated surface magnetic field.

The gap electric field $\mathbf{E}_{\|}$ along $\mathbf{B}_s$ results from a deviation of the local charge density $\rho \approx 0$ from the co-rotational charge density $\rho_c = (\zeta/\alpha)\rho_{GJ}$, where $\rho_{GJ} = -\mathbf{\Omega}\cdot\mathbf{B}_s/(2\pi c)$ is the flat space-time Goldreich-Julian (1969) charge density, $\Omega = 2\pi/P$, $\zeta = 1-\kappa_g$, $\kappa_g \sim (r_g/R)(I/MR^2)$, $\alpha = (1-r_g/R)^{1/2}$ is the redshift factor, r_g is the gravitational radius, M is the neutron star mass and I is the neutron star moment of inertia. The potential V and electric fields $E_{\|}$ within a gap are determined by GR-analog (Muslimov & Tsygan 1992) of the one dimensional Poisson's equation $(1/\alpha)d^2V/dz^2 = -4\pi(\rho-\rho_c) = 2\Omega B_s\zeta/(c\alpha)$, with a boundary condition $E_{\|}(z=h)=0$, where h is the height of infinitesimal gap. The solution of Poisson's equation gives

$$E_{\|}(z) = \zeta(2\Omega\frac{B_s}{c})(h-z), \qquad (1)$$

and

$$\Delta V = \zeta\frac{\Omega B_s}{c}h^2. \qquad (2)$$

In further calculations we will adopt a typical value of the correction factor $\zeta \sim 0.85$ (corresponding to $M = 1M_\odot$, $R = 10^6$ cm and $I = 10^{45}$g cm^2), although its value can be as low as 0.73 (Zhang et al. 2000). Thus, the potential drop within the actual gap can be 15 to 27 percent lower than in the conventional RS75 model.

The polar cap surface of the anti-pulsar ($\mathbf{\Omega}\cdot\mathbf{B} < 0$) is heated by a back-flow of relativistic electrons (accelerated in the parallel electric field $E_{\|}$) to the temperature $T_s = k^{1/4}(e\Delta V\dot{N}/\sigma\pi r_p^2)^{1/4}$, where ΔV is described by equation (2), $\dot{N} = \pi r_p^2 B_s/eP$ is the Goldreich-Julian kinematic flux and the heat flow coefficient $0.2\lesssim k<1$ is described in the Appendix B. The thermal condition for the vacuum gap formation can be written in the form $T_i/T_s > 1$, where T_s is the actual surface temperature described above, and $T_i = \Delta\varepsilon_c/30$k is the iron critical (melting) temperature above which $^{56}_{26}$Fe ions are not bound on the surface (?), where $\Delta\varepsilon_c$ is the cohesive energy of condensed $^{56}_{26}$Fe matter in the neutron star surface and k$= 1.38\times10^{-23}JK^{-1}$ is the Boltzman constant. The properties of condensed matter in very strong magnetic fields characteristic for the neutron star surface have been investigated by many authors using different examination methods (for review see Usov & Melrose 1995). There exists a lot of discrepancy in determination of the cohesive energy $\Delta\varepsilon_c$ and in this paper we refer to the two most useful papers, representing the limiting extreme cases. Abrahams & Shapiro (1991; AS91 henceforth) estimated $\Delta\varepsilon_c = 0.91$ keV, 2.9 keV and 4.9 keV for $B_s = 10^{12}$ G, 5×10^{13} G and 10^{13} G, respectively. These values were approximated by Usov & Melrose 1995 in the form $\Delta\varepsilon_c \simeq (0.9\text{keV})(B_s/10^{12}\text{ G})^{0.73}$, which leads to melting temperatures

$$T_i = (3.5\times10^5\text{K})(B_s/10^{12}\text{G})^{0.73} = (6\times10^5)b^{0.73}(P\dot{P}_{-15})^{0.36}\text{ K}. \qquad (3)$$

On the other hand, Jones (1986; J86 henceforth) obtained much lower cohesive energies $\Delta\varepsilon_c = 0.29$ keV, 0.60 keV and 0.92 keV for $B_s = 2\times10^{12}$ G, 5×10^{12} G and 10^{13} G, respectively. This can be approximated by $\Delta\varepsilon_c \simeq (0.18\text{ keV})(B_s/10^{12}\text{G})^{0.7}$ and converted to melting temperatures

$$T_i = (0.7\times10^5\text{K})(B_s/10^{12}\text{G})^{0.7} = (1.2\times10^5)b^{0.7}(P\cdot\dot{P}_{-15})^{0.36}. \qquad (4)$$

Below we consider the condition $T_i/T_s > 1$, using both expressions for melting temperatures described by equations (3) and (4), for CR- and ICS-dominated NTVG models, separately.

2.1. CR-NTVG

In this case the gap height $h = h_{CR}$ is determined by the condition that $h = l_{ph}$, where $l_{ph} \approx \sin\theta\ \mathcal{R} = (B_\perp/B_s)\mathcal{R}$ is the mean free path for pair production by photon propagating at an angle θ to the local surface magnetic field (RS75). The CR-NTVG model is described by the following parameters: the height of quasi steady gap

$$h_{CR} = (3\times10^3)\zeta^{-3/7}\mathcal{R}_6^{2/7}b^{-3/7}P^{3/14}\dot{P}_{-15}^{-3/14}\text{ cm}, \qquad (5)$$

(notice typographical errors in eq. [6] of GM01, which are corrected here), the gap potential drop

$$\Delta V = (1.2\times10^{12})\zeta^{1/7}\mathcal{R}_6^{4/7}b^{-1/7}P^{-1/14}\dot{P}_{-15}^{1/14}\text{ V}, \qquad (6)$$

and the surface temperature

$$T_s = (3.4\times10^6)\zeta^{1/28}k^{1/4}\mathcal{R}_6^{1/7}b^{2/7}P^{-1/7}\dot{P}_{-15}^{1/7}\text{ K}. \qquad (7)$$

The thermal condition $T_i/T_s > 1$ for the formation of CR-NTVG leads to a family of critical lines on the $P-\dot{P}$ diagram (see Fig. 1 in GM01)

$$\dot{P}_{-15} \geq \mathcal{A}^2\zeta^{0.16}k^{1.14}\mathcal{R}_6^{0.64}b^{-2}P^{-2.3}, \qquad (8)$$

where $\mathcal{A} = (2.7\times10^3)^{1/2} = 52$ for AS91 case (eq. [3]) and $\mathcal{A} = (3.96\times10^6)^{1/2} = 1990$ for J86 case (eq. [4]). Alternatively, one can find a minimum required surface magnetic field $B_s = bB_d$ expressed by the coefficient b in the form

$$b_{min}^{CR} = \mathcal{A}\zeta^{0.08}k^{0.57}\mathcal{R}_6^{0.32}P^{-1.15}\dot{P}_{-15}^{-0.5}. \qquad (9)$$

2.2. ICS-NTVG

In this case the gap height $h = h_{ICS}$ is determined by the condition $h = l_{ph} \sim l_e$, where l_e is the mean free path of the electron to emit a photon with energy $\hbar\omega = 2\gamma\hbar eB_s/mc$ (GM01, Zhang et al. 2000). The ICS-NTVG model is described by the following parameters: the height of quasi steady gap

$$h_{ICS} = (5\times10^3)\zeta^{0.14}k^{-0.07}\mathcal{R}_6^{0.57}b^{-1}P^{-0.36}\dot{P}_{-15}^{-0.5}\text{ cm}, \qquad (10)$$

the gap potential drop

$$\Delta V = (5.2\times10^{12})\zeta^{0.72}k^{-0.14}\mathcal{R}_6^{1.14}b^{-1}P^{-1.22}\dot{P}_{-15}^{-0.5}\text{ V}, \qquad (11)$$

and the surface temperature

$$T_s = (4 \times 10^6)\zeta^{0.18} k^{0.25} \mathcal{R}_6^{0.28} P^{-0.43} \text{ K}. \quad (12)$$

The thermal condition $T_i/T_s > 1$ for the formation of ICS-NTVG leads to a family of critical lines on the $P - \dot{P}$ diagram (see Fig. 1 in GM01)

$$\dot{P}_{-15} \geq \mathcal{B}^2 \zeta^{0.5} k^{0.7} \mathcal{R}_6^{0.8} b^{-2} P^{-2.2}, \quad (13)$$

where $\mathcal{B} = (2 \times 10^2)^{1/2} = 14$ for AS91 case (eq. [3]) and $\mathcal{B} = (1.69 \times 10^4)^{1/2} = 130$ for J86 case (eq. [4]). Alternatively, one can find a minimum required surface magnetic field $B_s = bB_d$ expressed by the coefficient b in the form

$$b_{min}^{ICS} = \mathcal{B}\zeta^{0.25} k^{0.34} \mathcal{R}_6^{0.39} P^{-1.1} \dot{P}_{-15}^{-0.5}. \quad (14)$$

2.3. NTVG development in pulsars with drifting subpulses

GM01 examined the $P - \dot{P}$ diagram (their Fig. 1) with 538 pulsars from the Pulsar Catalog (Taylor et al. 1993) with respect to the possibility of VG formation by means of the condition T_i/T_s, with T_i determined according to AS91 (eq. [3]). They concluded that formation of VG is in principle possible, although it requires very strong and curved surface magnetic field $B_s = b \cdot B_d \gtrsim 10^{13}$ G, irrespective of the value of B_d. Here we reexamine this problem by means of equations (9) and (14), with melting temperatures corresponding to both the AS91 case ($\mathcal{A} = 52$ and $\mathcal{B} = 14$) and J86 case ($\mathcal{A} = 1990$ and $\mathcal{B} = 130$), for CR and ICS seed photons, respectively. Therefore, we cover practically almost the whole range of melting temperatures between the two limiting cases, which differ by a factor of five between each other. We adopt the GR-IFD correction factor $\zeta = 0.85$ (**?**), the normalized radius of curvature of surface magnetic field lines $0.01 \leq \mathcal{R}_6 \leq 1.0$ (GM01 and references therein) and the heat flow coefficient $0.2 \leq k \leq 1.0$ (Appendix B).

The results of calculations of NTVG models for 42 pulsars with drifting subpulses and/or periodic intensity modulations (after Rankin 1986) are presented in Fig. 1. We calculated the ratio $B_s/B_q = 0.0453\, b(P\dot{P}_{-15})^{0.5}$, where $B_q = 4.414 \times 10^{13}$ G and the coefficient b is determined by equation 9 and equation 14 for CR and ICS seed photons, respectively. Noting that the functional dependence on P and $\dot{P}_{-15}$ in both equations is almost identical, we sorted the pulsar names (shown on the horizontal axes) according to the increasing value of the ratio B_s/B_q (shown on the vertical axes). Calculations were carried out for $B_s/B_q \geq 0.1$, since below this value the NT conditions are no longer valid. On the other hand, the values of B_s/B_q are limited from above by the photon splitting threshold, which is roughly about 10^{14} G (see also astro-ph/0102097, **?**). Therefore, the physically plausible NTVG models lie within the grey areas, which correspond to surface magnetic fields 4.4×10^{12} G $\leq B_s \leq 10^{14}$ G. The left hand side of Fig. 1 corresponds to AS91 case ($\mathcal{A} = 52$ and $\mathcal{B} = 14$ in eqs. [9] and [14], respectively) and the right hand side of Fig. 1 corresponds to J86 case ($\mathcal{A} = 1930$ and $\mathcal{B} = 130$ in eqs. [9] and [14], respectively). Four panels in each side of the figure correspond to different values of the radius of curvature $\mathcal{R}_6 = 1.0$, 0.1. 0.05 and 0.01 from top to bottom, respectively (indicated in left upper corner of each panel). Two sets of curved lines in each panel correspond to the CR (thin upper lines) and ICS (thick lower lines) seed photons, respectively. Three different lines within each set correspond to different values of the heat flow coefficient $k = 1.0$ (dotted), $k = 0.6$ (dashed) and $k = 0.2$ (long dashed).

A visual inspection of the model curves within grey areas in Fig. 1 shows that in AS91 case the ICS-NTVG is favored for larger radii of curvature $\mathcal{R}_6 > 0.05$, while the CR-NTVG requires lower values of $\mathcal{R}_6 < 0.1$. In J86 case, only the ICS-NTVG corresponding to $\mathcal{R}_6 < 0.1$ can develop. If the actual cohesive energies correspond to some intermediate case between the AS91 and J86 cases, they will also be associated with the ICS-NTVG. Therefore, we can generally conclude that the ICS-NTVG model is apparently favored in pulsars with drifting subpulses. The CR-NTVG is also possible although it requires an extremely strong ($B_s/B_q \sim 1$) and/or extremely curved ($\mathcal{R}_6 \sim 0.01$) surface magnetic field at the polar cap.

3. Conclusions

There is a growing evidence that the radio emission of pulsars with systematically drifting subpulses (grazing cuts of the line-of-sight) or periodic intensity modulations (central cuts of the line-of-sight) is based on the inner vacuum gap developed just above the polar cap (**?**). To overcome the binding energy problem (**?**) put forward an attractive but exotic conjecture that pulsars showing the drifting subpulses represent bare polar cap strange stars (BPCSS) rather than neutron stars. However, as demonstrated in this paper, invoking the BPCSS conjecture is not necessary to explain drifting subpulse phenomenon. The quasi steady vacuum gap, with either curvature radiation or inverse Compton scattering seed photons, can easily form in pulsars with $\mathbf{\Omega} \cdot \mathbf{B} < 0$, provided that the actual surface magnetic field at the polar cap is extremely strong $B_s \sim 10^{13}$ G and curved $\mathcal{R} < 10^6$ cm, irrespective of the value of dipolar component measured from the pulsar spindown rate.

The pulsars with drifting subpulses and/or periodic intensity modulation do not seem to occupy any particular region of the $P - \dot{P}$ diagram (see Fig. 1 in GM01). Rather, they are spread uniformly all over the $P - \dot{P}$ space, at least for typical pulsars. Therefore, it seems tempting to propose that radio emission of all pulsars is driven by vacuum gap activities. An attractive property of such proposition is that the nonstationary sparking discharges induce the two-steam instabilities that develop at relatively low altitudes (**?**), where the pulsars radio emission is expected to originate (**?**). It is generally believed that the high frequency plasma waves generated by the two-stream instabilities can be converted into coherent electromagnetic radiation at pulsar radio wavelengths (e.g. Melikidze et al. 2000). In such a scenario, all radio pulsars would require a strong, non-dipolar surface magnetic field at their polar caps (e.g. Gil et al. 2002 a, b).

Acknowledgements. We gratefully acknowledge the support by the Heraeus foundation. We are grateful to Prof. V. Usov and dr B. Zhang for helpful discussions. We also thank E. Gil, U. Maciejewska, and M. Sendyk for technical help.

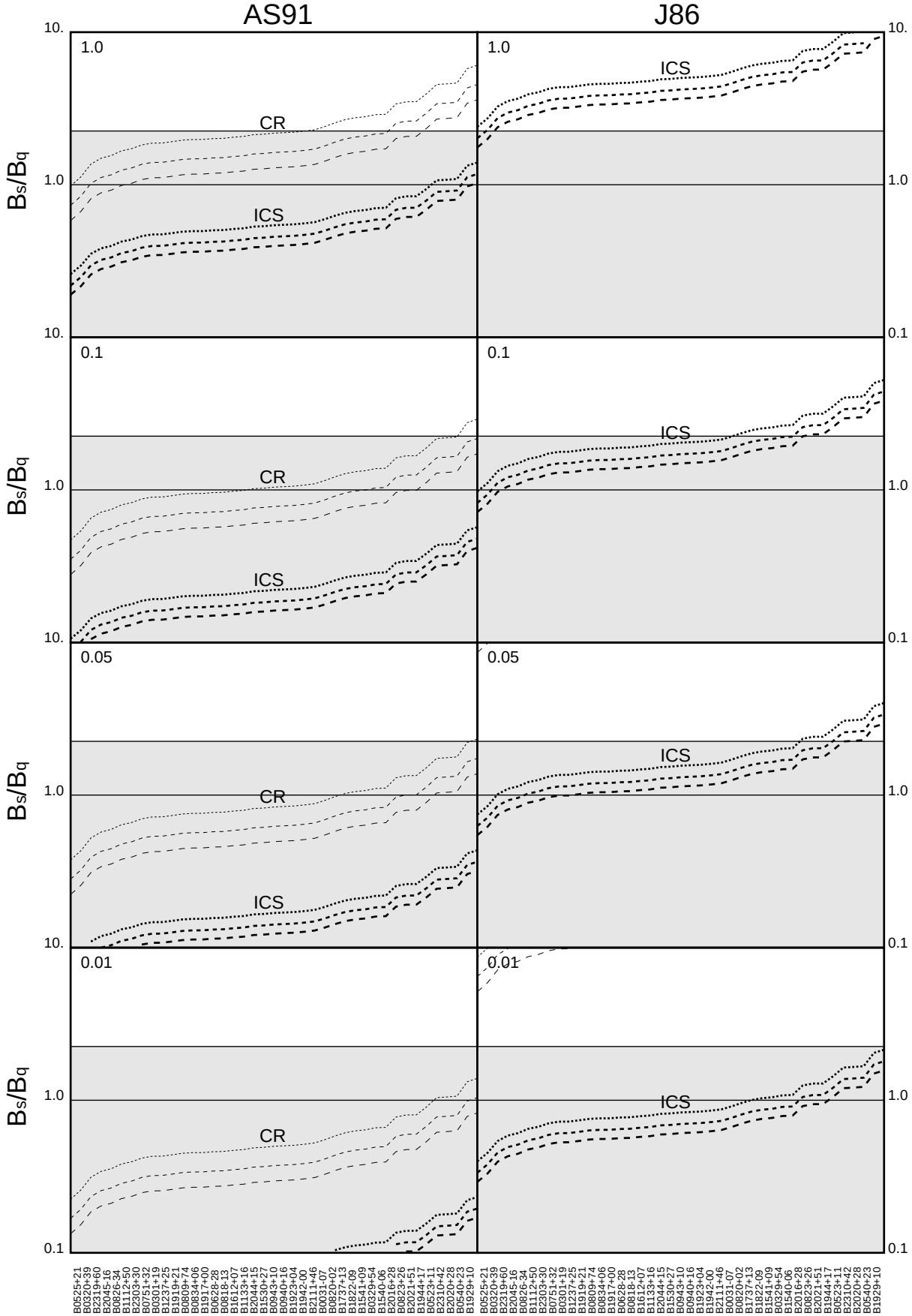


Fig. 1. Models of NTVG for 42 pulsar with drifting subpulses and/or periodic intensity modulations (see text for explanations).

Appendix A: Field emission

The vacuum gap can form in pulsars with $\mathbf{\Omega} \cdot \mathbf{B} < 0$ if the actual surface temperature T_s is not high enough to liberate $^{56}_{26}$Fe ions from the polar cap surface by means of thermal emission. Now we will examine the field (cold cathode) emission, which is possibly important when thermionic emission is negligible (e.g. Zhang & Harding 2000). The maximum electric field (along $\mathbf{B}_s$) at the NS surface $E_{\parallel}(max) = \zeta(4\pi/cP)B_s h_{ICS} = (1.25 \times 10^9)\zeta^{0.86} b^{-1} \mathcal{R}_6^{0.57} P^{0.14}$ V/cm, or taking into account that $\zeta = 0.85$ and $b \gtrsim 2(P \cdot \dot{P}_{-15})^{-0.5}$, $E_{\parallel}(max) \leq (5 \times 10^8)\mathcal{R}_6^{0.57} P^{0.64} \dot{P}_{-15}^{0.5}$ V/cm. The critical electric field needed to pull $^{56}_{26}Fe$ iron ions from the NS surface is $E_{\parallel}(crit) = (8 \times 10^{12})(\Delta\epsilon/26 \text{ keV})^{3/2}$ V/cm (?), where the cohesive (binding) energy of iron ions in strong surface magnetic field $B_s \sim 10^{13}$ G is $\Delta\epsilon = 4.85$ keV (Abrahams & Shapiro 1991). Thus, $E_{\parallel}(crit) = 6.4 \times 10^{11}$ V/cm $>> E_{\parallel} \sim 10^9$ V/cm and no field emission occurs. It is possible that the cohesive energy is largely overestimated and $\Delta\varepsilon_c$ can be much smaller than about 4 keV even at $B_s > 10^{13}$ G. We can thus ask about the minimum value of $\Delta\varepsilon_c$ at which the field emission is still negligible. By direct comparison of $E_{\parallel}(max)$ and $E_{\parallel}(crit)$ we obtain $\Delta\varepsilon_c > 40x^{0.67}$ eV, where $x = \mathcal{R}_6^{0.57} P^{0.64} \dot{P}_{-15}^{0.5}$ is of the order of unity. Therefore, contrary to the conclusion of Jessner et al. (2001), no field emission is expected under any circumstances.

Appendix B: Heat flow conditions at the polar cap surface

Let us consider the heat flow conditions within the uppermost surface layer of the pulsar polar cap above which NTVG can develope. The basic heat flow equation is (e.g. Eichler & Cheng 1989)

$$C\frac{\partial T}{\partial t} = \frac{\partial}{\partial x}\left(\kappa_{\parallel}\frac{\partial T}{\partial x}\right), \qquad (15)$$

where C is the heat capacity (per unit volume) and $\kappa_{\parallel} >> \kappa_{\perp} \sim 0$ is the thermal conductivity along ($\parallel$) surface magnetic field lines (which are assumed to be perpendicular ($\perp$) to the polar cap surface). The heating of the surface layer of thickness Δx is due to sparking avalanche with a characteristic development time scale Δt. We can write approximately $\partial T/\partial t \approx T/\Delta t$, $\partial T/\partial x \approx T/\Delta x$, $\partial/\partial x(\partial T/\partial x) \approx T/\Delta x^2$ and thus $C/\Delta t \approx \kappa_{\parallel}\Delta x^2$. Therefore, the crust thickness Δx heated during Δt is approximately $\Delta x \approx \left(\kappa_{\parallel}\Delta t/C\right)^{1/2}$ (within an uncertainty factor δx of 2 or so), where the time scale corresponds to the spark development time $\Delta t \approx 10\mu$s (RS75). The energy balance equation is $Q_{heat} = Q_{rad} + Q_{cond}$, where $Q_{heat} = en_{GJ}\Delta V_{max}$ (e.g. RS75), $Q_{rad} = \sigma T_s^4$ (T_s is the actual surface temperature and $\sigma = 5.67 \times 10^{-5}$ erg cm$^{-2}K^{-4}s^{-1}$), and $Q_{cond} = -\kappa_{\parallel}\partial T/\partial x \approx -\kappa_{\parallel}T_s/\Delta x$. We can now define the heat flow coefficient $k = Q_{rad}/Q_{heat} < 1$, which describes deviations from the black-body conditions on the surface of the sparking polar cap. In other words, the value of k describes the amount of heat conducted beneath the polar cap which cannot be transferred back to the surface from the penetration depth Δx during the time-scale Δt. The coefficient k can be written in the form

$$k = \frac{1}{1 + \kappa_{\parallel}/(\sigma T_s^3 \Delta x)} = \frac{1}{1 + (\kappa_{\parallel}C)^{1/2}/(\sigma T_s^3 \Delta t^{1/2})}, \qquad (16)$$

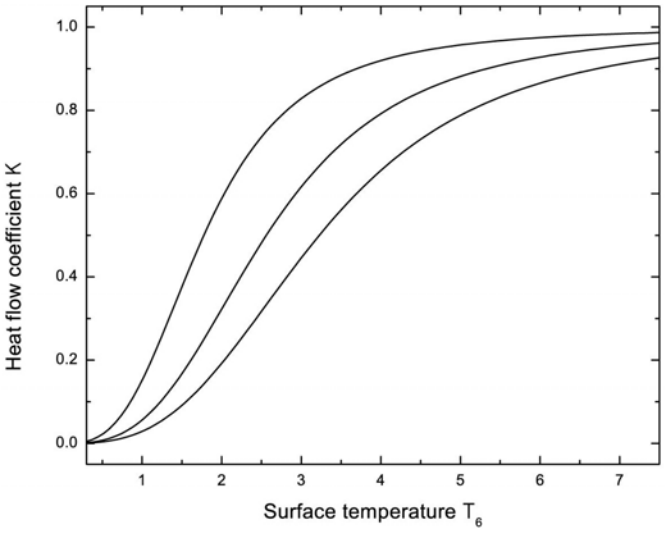


Fig. 2. Heat flow coefficient k versus surface temperature T_6 (see text for explanations).

whose value can be estimated once the parameters C, $\kappa_{\parallel}$ and T_s as well as Δx or Δt are known.

The matter density at the neutron star surface composed mainly of $^{56}_{26}$Fe ions (e.g. Usov & Melrose 1995) is $\rho(B_s) \simeq 4 \times 10^3 (B_s/10^{12}\text{ G})^{6/5}$g cm^{-3} (Flowers et al. 1977). Thus for $B_s \sim (1 \div 3) \times 10^{13}$ G we have $\rho \sim (0.6 \div 2.4) \times 10^5$g cm^{-3}. The thermal energy density of $^{56}_{26}$Fe is $U_{Fe} \simeq 2.2 \times 10^{19}\rho_5 T_8$ erg cm^{-3} (Eichler & Cheng 1989), where $\rho_5 = \rho/(10^5\text{g cm}^{-3})$ and $T_8 = T_s/(10^8$ K). Thus, the heat capacity $C = dU_{Fe}/dt = 10^{-8}dE_{Fe}/dT_8 = (1 \div 5) \times 10^{11}\rho_5$ erg cm^{-3}K^{-1}. For $\rho_5 \approx 1$ we have $C \approx 2 \times 10^{11}$erg cm^{-3}K^{-1}. The longitudinal thermal conductivity can be estimated as $\kappa_{\parallel} \approx (2 \div 4) \times 10^{13}$ erg s^{-1}cm^{-1}K^{-1} (see Fig. 5 in Potekhin 1999). Thus $\kappa_{\parallel}/C \approx 1.5 \times 10^2$ cm^2 and the penetration depth $\Delta x \approx 10\Delta t^{1/2} s^{-1/2}$ cm. Since $\Delta t \sim 10\mu = 10^{-5}$ s (spark characteristic time scale) then $\Delta x \approx 0.03$ cm. More generally, the penetration depth can be written as

$$\Delta x = 0.03\,\delta x \left(\frac{\kappa_{13}}{C_{11}}\right)^{1/2}, \qquad (17)$$

where $\kappa_{13} = \kappa_{\parallel}/10^{13} \approx 2 \div 4$ and $C_{11} = C/10^{11} \approx 1 \div 5$ and the uncertainty factor $\delta x \approx 0.5 \div 2$. Now the heat flow coefficient can be written as

$$k = \frac{1}{1 + 5.6\Delta/T_6^3}, \qquad (18)$$

where $T_6 = T_s/10^6$ and $\Delta = (\kappa_{13}C_{11})^{1/2}/\delta x \approx 0.7 \div 6.3$. Figure 2 shows variations of the heat flow coefficient k versus the surface temperature T_6 (in 10^6 K) for three values of $\Delta = 1$ (upper curve), $\Delta = 3$ (middle curve) and $\Delta = 6$ (lower curve). As one can see, for realistic surface temperatures of few times 10^6 K, the values of the heat flow coefficient k are in the range $0.2 \div 0.9$. Gil et al. 2002a found from independent considerations that in PSR B0943+10 the heat flow coefficient $k < 0.8$, in consistency with the results obtained in this paper.

References

Abrahams, A.M., Shapiro, S.L. 1991, ApJ, 374, 652

Asseo, E., Melikidze, G. 1998, MNRAS 301, 59
Cheng, A. F., & Ruderman, M. A. 1977, ApJ, 212, 800
Cheng, A. F., & Ruderman, M. A. 1980, ApJ, 235, 576
Cordes, J. M. 1978, ApJ, 222, 1006
Barring, M.G., Harding, A.K. 1998, ApJ, 507, L55
Barring, M.G., Harding, A.K. 2001, ApJ, 547, 926
Daugherty, J., Harding, A.K. 1983, ApJ, 273, 761
Deshpande, A.A., & Rankin, J.M. 1999, ApJ, 524, 1008
Deshpande, A.A., & Rankin, J.M. 2001, MNRAS, 322, 438
Eichler, D., Cheng, A.F. 1989, ApJ, 336, 360
Erber, T. 1966, Rev. Mod. Phys., 38, 626
Flowers, E.G., Ruderman, M.A., Lee J-F. et al. 1977, ApJ, 215, 291
Gil, J., & Sendyk, M. 2000, ApJ, 541, 351
Gil, J., & Mitra, D. 2001, ApJ, 550, 383 (GM01)
Gil, J., Melikidze, G.I., & Mitra, D. 2002a, A&A Letters, in press
Gil, J., Melikidze, G.I., & Mitra, D. 2002b, A&A, in press
Harding, A.K., Muslimov, A.G. 1998, ApJ, 508, 328
Jessner, A., Lesch, H., & Kunzl., T. 2001, ApJ, 547, 959
Jones, P.B. 1986, MNRAS, 218, 477 (J86)
Kijak, J., & Gil, J. 1997, MNRAS, 288, 631
Kijak, J., & Gil, J. 1998, MNRAS, 299, 855
Melikidze, G.I, Gil, J., & Pataraya, A.D. 2000, ApJ, 544, 1081
Muslimov, A.G., Tsygan, A.I., 1992, MNRAS, 255, 61
Muslimov, A.G., Harding, A. 1997, ApJ, 485, 735
Potekhin, A.Y. 1999, A&A, 351, 787
Rankin, J.M. 1986, ApJ, 301, 901
Ruderman, M.A., & Sutherland, P.G. 1975, ApJ 196, 51 (RS75)
Taylor, J. H., Manchester, R. N., & Lyne, A. G. 1993, ApJs, 88, 529
Usov, V.V. 1987, ApJ, 481, L107
Usov, V.V., & Melrose, D.B. 1995, Australian J. Phys. 48, 571
Usov, V.V., & Melrose, D.B. 1996, ApJ, 463, 306
Usov, V. 2001, ApJ, 559, L135
Vivekanand, M., Joshi, B.C. 1999, ApJ, 515, 398
Xu, R.X., Qiao, G.J., & Zhang, B. 1999, ApJ, 522, L109
Xu, R.X., Zhang, B. & Qiao, G.J. 2001, Astropart.Phys., 15(1),101
Zhang, B., Qiao, G.J. 1996,A&A, 310, 135
Zhang, B., Qiao, G.J., Lin, W.D., et al. 1997, ApJ, 478, 313
Zhang, B., & Harding, A.K. 2000, ApJ, 535, L51
Zhang B., Harding, A., & Muslimov, A.G. 2000, ApJ, 531, L135
Zhang, B. 2001, ApJ, 562, L59

Proceedings of the 270. WE-Heraeus Seminar on: *"Neutron Stars, Pulsars and Supernova Remnants"*
Physikzentrum Bad Honnef, Germany, Jan. 21-25, 2002, eds. W. Becker, H.Lesch & J. Trümper, MPE Report 278, pp. 221-229

A current circuit model of pulsar radio emission

Th Kunzl[1,2], H. Lesch[2] and A. Jessner[3]

[1] Max–Planck–Institut für Quantenoptik, Hans-Kopfermann- Straße, 85748 Garching, Germany
[2] Institut für Astronomie und Astrophysik der Universität München, Scheinerstr. 1, D-81679 München
[3] Max–Planck–Institut für Radioastronomie, Auf dem Hügel 69, D-53121 Bonn

Abstract. We present the outline of a new model for the coherent radio emission of pulsars that succeeds in reproducing the energetics and brightness temperatures of the observed radio emission from the observationally deduced distances of 50-100 pulsar radii above the neutron star in a narrow region.

The restrictions imposed by energy conservation, plasma dynamics of the coherent radiation process and propagation effects are used to apply the action of a plasma process like coherent inverse Compton scattering (CICS) (see Benford, 1992). In accordance with our findings (Kunzl et al. 1998a) this process requires Lorentz factors of about 10 which are lower than in most other radio emission models. This implies that no significant pair production can take place near the surface and we expect charge densities close to the Goldreich-Julian value (Goldreich & Julian (1969)).

To fulfill the energetic and electrodynamic constraints the model requires constant re-acceleration in dissipation regions which can be interpreted as a voltage drop similar to that in a resistive current circuit built of a battery, connecting copper wires and a resistive load.

Using the emission heights for PSR 0329+54 published by Mitra and Rankin (2002) and the spectral data from Malofeev et al. (1994) we find that a constant depth of the dissipation region of about $2r_{\rm NS}$ can account for the observed luminosities and spectral behavior.

The extremely high peak fluxes in the substructures of single pulses can be explained by beaming effects as discussed in Kunzl et al. (1998b).

1. Introduction

Pulsars are generally accepted to be rotating neutron stars having $10^4 - 10^8$T magnetic fields that induce electric potential drops along the magnetic field lines which allow efficient particle acceleration of thermally emitted electrons in the region of open field lines (Goldreich and Julian (1969); Sturrock (1971); Ruderman and Sutherland (1975), Arons (1981)). Although the emitted radio luminosity in comparison to the spin-down power of a rotating neutron star is tiny (only the 10^{-5}- 10^{-6} part of the spin-down power is emitted in the radio regime) one of the most striking features about pulsars is their very intense pulsed radio emission, the physical origin of which is still poorly understood. The wealth of observational data (intensity, polarization, shape of the radio spectrum) clearly indicates that the pulsar radio emission cannot be of incoherent origin, but must be due to some coherent radiation mechanism (e.g. Lyne and Graham-Smith 1998; Kramer, Wex and Wielebinski (2000) and references therein). Especially at low frequencies (below 1 GHz) a very high degree of coherence is needed to explain the observed intensities in terms of brightness temperatures. Therefore a pulsar emission model has to explain how a large number of phase coupled particles can be stimulated to radiate in a coherent manner.

Currently the most favored models for radio emission mechanism are curvature radiation (e.g. Rankin (1992); Radhakrishnan and Rankin (1990); Gil (1992)) or maser process due to strong turbulence, like the free electron maser, (hereafter FEM) (e.g. Melrose (1978), Rowe (1992a,b)).

Since there are severe difficulties with coherent curvature radiation (Lesch et al. (1998) pointed out that the energetic requirements can hardly be matched, Melrose (1992) discussed the absence of an appropriate bunching mechanism to build up a coherent curvature radiation) we propose a process directly coupled to the most significant eigenfrequency of the magnetospheric plasma: the electron plasma frequency. It has been shown by Melrose (1978) that such an amplified linear acceleration emission (ALAE) process could produce sufficient growth rates i.e. is fast enough to explain the observations. But it needs low Lorentz factors of the emitting particles to work. This model requires low energy particles with energies of a few MeV.

Recently, support for such a low energy scenario came from various criticisms on the so-called standard model with an inner gap where a highly relativistic pair plasma is created:

It was argued by Kunzl et al. (1998a) and confirmed by Melrose and Gedalin (1999, 2000) that the observed radio emission would not escape from a magnetosphere filled with a dense relativistic pair plasma. Additional problems with the production of high energy particles close to the pulsar were discussed by Arendt & Eilek (2000), Lesch et al. (2000) and Jessner et al. (2001). They commonly concluded that the assumption of strong electric fields at the pulsar surface that ultimately result in ultrarelativistic particle energies is at least questionable.

Thus, we introduce an entirely different approach here, which has first been promoted by Shibata (1991) for an analysis of the global magnetospheric structure of rotation-powered neutron stars. In contrast to the standard model assuming a shielding of the electric fields by massive pair production we propose that in the inner region of the magnetosphere (i.e. the open field lines inward of the neutral surface) the situation is similar to the multiple scatterings in a solid state conductor.

In other words we have a current whose time average is the same at all cross sections through the open field line region. There is neither acceleration close to the surface (as indicated by our recent findings (Jessner et al. 2001) nor deceleration in the dissipation region (as indicated by the very small dissipation rate given by small the radio luminosity in comparison to the total spin down power).

In this conducting wire model any dissipation region corresponds to a resistance where electric potentials are present. The "deceleration" caused by the losses is balanced by the "acceleration" due to the electric field. The most important consequence of this scenario is that the energy loss per particle is no longer limited by the average kinetic energy of the electron in the same way as the kinetic energy of the electrons in a copper wire current circuit is no indicator for the dissipated energy. The one-dimensional approach with a constant voltage applies, because the resistivity perpendicular to the magnetic field is small inside the pulsar (to allow sufficient supply of charged particles for a Goldreich-Julian DC current) and large enough in the magnetosphere (to avoid "leakage", meaning current closure across the field lines in the inner magnetosphere) (see Ewart et al. 1975; Itoh 1975).

Our aim is now to obtain the constraints on the dissipation field in such a model and see whether we can explain the luminosities in the radio frequency range at the emission heights given by the observations from a thin radiating layer.

2. The model

In a current-carrying collisionless plasma waves are known to introduce resistivity via fluctuating electric fields. These fields present the deviations from the ideal plasma state with an infinitely high electrical conductivity. For an incoming current I the locations of a significant high plasma wave intensity act as a resistance R. The emitted power of such a resistive region is given by $L = I^2R$. In a time averaged picture the current has to be divergence-free. So if a DC current flows through a region in which plasma waves generate a resistance the particles lose their kinetic energy meaning that their velocities decline. Although for relativistic particles this effect is small it cannot be entirely neglected.

In a dense pair plasma this energy loss of the particles presents no difficulties since the velocities of the two components can adjust in an adequate way to fulfill both energy and current conservation. However, in a single charge plasma deceleration has to be accompanied by a density rise. So if the particle beam would gradually lose energy the relative density would have to increase all the time. This is totally incompatible with the outer boundary condition of a Goldreich-Julian magnetosphere.

The latter point is the main difference to the argumentation by Shibata (1997) who also assumes a current outflow determined by the system. In Shibata's model curvature effects causes space charges to accumulate that cannot be removed by acceleration on some field lines as the particle velocity is limited by c. We assume that these curvature effects do not play a significant role as they will be balanced by particles of the opposite charge drifting inwards from the neutral line and therefore only deceleration by losses will result in a space charge. This would mean that radiation losses produce a global deviation from the GJ case if there was no acceleration of the particles. So such a description would immediately turn out to be inconsistent (non-idealities induce electric fields which accelerates or decelerates particles).

Nevertheless there is a consistent description of a single charge plasma distribution if we recall that the rotating neutron star induces the vacuum electric field. The electric charges *on the neutron star surface* are displaced in such a way that the field that has to be shielded by the GJ charge and the field is actually anchored in the neutron star. Thus, the vacuum field can be interpreted as a stationary distribution of infinitely heavy positive particles whose strength is given by the entire pulsar system.

This means that electrons that suffer losses will immediately be dragged on by the electric field that builds up in such a way that just an electrostatic wave is produced. A particle transversing this wave is accelerated by this non-vanishing potential drop and looses the gained energy by non-thermal radiation.

In this case the particles have to pile up which means that their velocity has to decrease. Where the density goes down, the velocity has to increase accordingly to keep the current stable ($\mathrm{div}\, \boldsymbol{j} = 0$).

Then the resulting electric field is able to accelerate particles and varies with half the wavelength of the density variation (as follows directly from the Poisson equation).

Such a system is similar to a battery whose poles are the region of the open field lines (acting as the negative pole in the parallel rotator) and the edge of the polar cap being the anode. If a particle starts close to the pole and returns on the last closed field line it encounters a voltage drop of typically 10^{13} V. But, of course, this does not mean that the particle has to be accelerated **by the full potential in one step** anywhere along its path.

As will be motivated in sect. 7 it is likely that the outer magnetosphere itself provides a constant minimum resistance which clearly dominates all plasma induced resistances so that the latter are only minor corrections. In other words, if the main voltage drop occurs close to the light cylinder almost all of the energy is dissipated there and transformed into high energetic radiation and ultrarelativistic particles. A schematic view of the model is shown in fig. 1..

Of course, there are two basic assumptions in this model, which have to be checked carefully. On the one hand, the pulsar is described as a voltage source. This description requires that the generator's internal resistance is negligible compared to the total resistance. It will be shown in section 6 that the maximum current allowed would be a highly relativistic Goldreich-Julian current over the entire two polar caps. The corresponding resistance is about $5\,\Omega$ which is huge in comparison with the transverse resistance of about $10^{-8}\,\Omega$ (Itoh, 1975) Thus the first assumption appears to be quite reasonable.

The second assumption, namely the one-dimensional current flow in the inner magnetosphere is also very natural. The conductivity can be expressed by a mean collision time τ using the formula

$$\sigma = \frac{ne^2\tau}{m_\mathrm{e}\varepsilon_0}\,. \qquad (1)$$

The transverse collision time τ can be estimated by $1/\omega_\mathrm{c}$ (the inverse gyro frequency) whereas the collision time for the parallel current cannot exceed the inverse plasma frequency

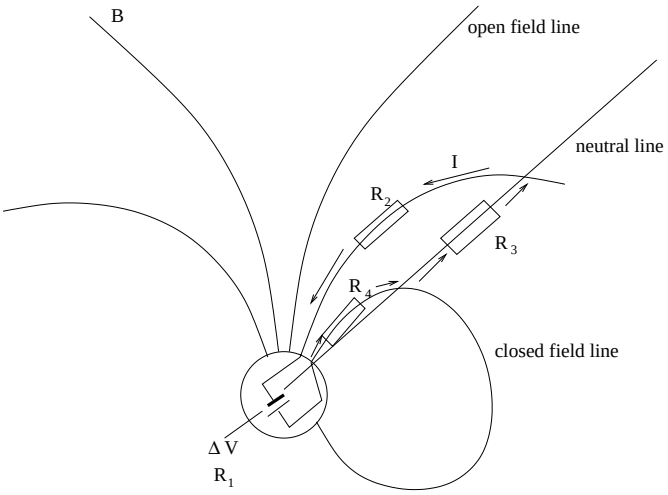


Fig. 1. Schematic view of the current circuit model. The current is determined by the applied voltage ΔV and the resistances R_1 to R_4. R_1 is the battery's resistance which is assumed to be small. R_2 stands for plasma resistance effects, mainly the losses by radio emission. The vastly dominating resistance is R_3 which limits the current to a relativistic GJ current over the two polar caps. In R_4 we combine other possible resistances which are also assumed to be small (e.g. curvature radiation losses or similar effects)

$1/\omega_\mathrm{p}$ (see below). As in the inner magnetosphere $\omega_\mathrm{p} \ll \omega_\mathrm{c}$, the one-dimensional approach is appropriate. Another way of confirming this is to calculate the maximum (transverse) drift velocity in the inner magnetosphere. Taking the maximum plasma wave electric field (see below) and typical pulsar parameters ($P = 0.5$ s, $B_0 = 10^8$ T) we find a drift velocity of

$$v_\mathrm{drift} = 0.359 \frac{\mathrm{m}}{\mathrm{s}} x_\mathrm{em}^{3/2} \gamma^{1/2} \qquad (2)$$

which is far below c for typical emission heights and particle energies used in the model ($x_\mathrm{em} \approx 50$, $\gamma = 10$). Particles move almost perfectly along the field lines as long as relativistic parallel outflow is possible (on the neutral line the situation is a bit different as a pure electron flow cannot cross this border easily).

An important consequence of our description is that the total energy a particle radiates along its path is in no way limited by its own kinetic energy as the actually dissipated energy comes from the inductor, *i. e.* the battery. Here, the analogy to a battery with a bulb attached through copper wires can be helpful. In a metal conductor the current carrying electrons have velocities of only some millimeters per second which means a kinetic energy of only 10^{-16} eV because of the small path length of electrons in a solid state conductor. Nevertheless each of them converts a total of 1.5 eV into heat on its way from the cathode to the anode. The only restriction which is given by the kinetic energy is the potential difference of the electrostatic field in one elementary radiation cell. As we will point out in sect. 4 this limit directly leads to the maximum possible resistivity in the plasma and therefore is never exceeded anyway.

The accelerating fields occurring in the outer magnetosphere do not invalidate the current circuit model, however as the circuit is open (high resistance) near the light cylinder.

Another advantage of this description is that our model uses particle inertia as the source for an accelerating field near the pulsar surface to get relativistic particles. So a very small acceleration region has to occur as the electrons have non-relativistic velocities inside the neutron star; therefore an overdense thin charge layer develops just above the surface where the electrons reach their terminal energy.

Therefore is no need for a "gap" (meaning a starved region near the neutron star) but inertia naturally provides the fields necessary to reach the mildly relativistic energies, and the terminal energy is determined by the global current instead of some large-scale space charge field (cf. sect. 6).

3. Application to radio emission

In the following we derive a quantitative model for the radio emission of pulsars. The particular aim is to explain the energetics of the radiation, from observed or observationally derived pulsar parameters such as

- the period P
- the dipolar surface magnetic field B
- the brightness temperature T_B of the low frequency emission
- the emission height x_em
- the total luminosity in the radio band L

With these input parameters we derive the radial width of the emission region, which should be small to be consistent with observations. A narrow radiation zone is suggested by both the highly structured emission in space and time as seen by many microstructure experiments (Boriakoff, 1992).

3.1. Plasma beams and coherent emission

Emission processes in relativistic plasmas are always connected with the electron plasma frequency, which is (Kunzl et al. 1998a; Melrose and Gedalin 1999)

$$\omega_\mathrm{pe} = \sqrt{\frac{ne^2}{\gamma \varepsilon_0 m_e}}$$

As a very promising candidate for the origin of coherent radio emission of pulsars we consider the collective inverse Compton mechanism, which was detected first in a number of laboratory experiments in which relativistic electron beams with a number density n_b penetrate into a background plasma with density n_p and in which extremely intense coherent microwave emission has been observed (Kato et al. 1983; Levron et al. 1987; Yoshikawa et al. 1993; 1994). The detected radiation has been explained in terms of collective inverse Compton scattering of strong Langmuir turbulence (Benford and Weatherhall 1992; Benford 1992). Relativistic electron beams interact with self-excited strong density fluctuations in the background plasma if the beam-plasma-density ratio $n_\mathrm{b}/n_\mathrm{p}$ exceeds 0.1 for a beam Lorentz factor of about 3. The beam electrons are bunched by the electric field of the density fluctuations and radiate coherently in their reference system at $\gamma\omega_\mathrm{pe}$, transformed into the observer's frame this gives an emitted frequency of

about $\gamma^2\omega_{\rm pe}$. The efficiency of this energy transfer of beam energy into photon energy is up to 30%.

The general scaling law from laboratory experiments for the relation between beam Lorentz factor and density ratio is (Benford 1992)

$$\gamma_{\rm crit} = \left(1 + \frac{9}{20}\lg\left(\frac{n_{\rm b}}{n_{\rm p}}\right)\right)^{-1}$$

As shown in Fig. 2 for large beam energies the required density ratios is quite small, whereas for small beam energies the beam density must be comparable to that of the background plasma to drive collective inverse Compton scattering. For a given beam energy one can calculate the required density ratio.

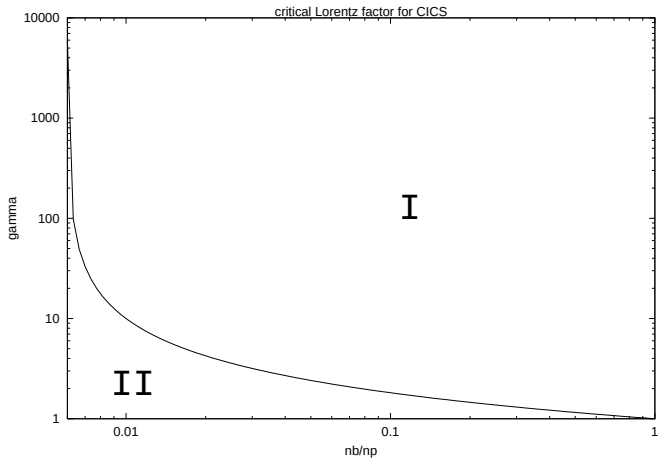


Fig. 2. Minimum Lorentz factor that allows coherent inverse Compton scattering (CICS) as a function of the ratio of beam density $n_{\rm b}$ to background plasma density $n_{\rm pl}$ (see Benford, 1992). For strong beams ($n_{\rm b} \approx n_{\rm pl}$) even low relativistic particles can cause coherent radiation (region I). In region II no coherent emission is possible.

The underlying physics of this mechanism has been investigated in all details and the general consensus is, that a relativistic electron beam with sufficient energy and particle density penetrates into a background plasma the collective inverse Compton scattering is the unavoidable coherent radiative power output (Benford 1992 and references therein). Based on these findings we transfer this process into a neutron star magnetosphere and investigate, whether this process matches the required properties.

Collective inverse Compton scattering is a nonlinear scattering processes whose radiative output in first order does not depend on the origin of the density fluctuations. In contrast, direct excitation mechanisms like maser or beam radiation depend sensitively on the form of the beam energy distribution and the time evolution of the beam (Ursov & Usov 1988; Melrose & Gedalin 1999; Melrose et al. 2001).

For comparison with alternative processes, we give a general scaling of the emitted frequency with the nonrelativistic plasma frequency $\omega_{\rm pe}^{(0)}$ for the different radiation mechanisms

$$\nu = \frac{\omega_{\rm pe}^{(0)}}{2\pi}\gamma^{\alpha/2}\,. \qquad (3)$$

In this notation the value of α for the collective inverse Compton scattering is 3, whereas for direct emission it is 1. In the next chapter we will debate an argument why the description of the pulsar system as a resistive current circuit makes $\alpha = 1$ less likely than a higher value. Inserting the expressions for the Goldreich-Julian density and the plasma frequency, we can solve this equation for γ:

$$\gamma = \left[\frac{\omega_{\rm p}(x_{\rm em})}{2\pi\nu}\right]^{-2/\alpha} = \left(\frac{B_0\Omega e}{2\pi^2\nu^2 m_{\rm e} x_{\rm em}^3}\right)^{-1/\alpha}\,. \qquad (4)$$

According to the usual estimates, an incoherent process from an electron with a Lorentz factor of γ cannot produce radiation with a brightness temperature exceeding $10^{10}\,{\rm K}\gamma$. However, in the case discussed here, this argument is not applicable, because there is no absorption. The emitted power of a radiation process is not limited any more if the radiation produced further inside is not absorbed on its way out of the magnetosphere.

Consider a cylindrical plasma column of radius R, length l, particle density n and single particle power output $P_{\rm single}$ in forward direction. Then the total power adds up to

$$P_{\rm ges} = lR^2\pi n P_{\rm single}. \qquad (5)$$

Thus the brightness temperature can reach arbitrarily high values on the condition that l is large enough no matter, whether the emission process is coherent or not.

Consequently we use a different estimate for the brightness temperature. The average flux is received from an area that corresponds to the polar cap moved and expanded along the field lines up to the emission height:

$$A = A_{\rm cap}x_{\rm em}^3\,. \qquad (6)$$

The total radio luminosity over a frequency band of $\Delta\nu$ around the frequency ν can therefore be equated to the thermal flux of a blackbody with the appropriate brightness temperature. For broadband emission ($\nu = \Delta\nu$) and using the definition of the brightness temperature we find

$$L = F_\nu \Delta\nu A_{\rm cap} x^3 \approx \frac{2\pi\nu^3}{c^2}k_{\rm B}T_{\rm B}A_{\rm cap}x_{\rm em}^3 \qquad (7)$$

which yields a brightness temperature of

$$T_{\rm B} = \frac{Lc^2}{2\pi\nu^3 k_{\rm B}A_{\rm cap}x_{\rm em}^3} = \qquad (8)$$

$$= 1.87\cdot 10^{23}\,{\rm K}\left(\frac{L}{10^{20}\,{\rm W}}\right)\left(\frac{\nu}{400\,{\rm MHz}}\right)^{-3}\left(\frac{P}{\rm s}\right)\left(\frac{x_{\rm em}}{50}\right)^{-3}\,.$$

Note that there is no additional geometric factor as the estimate of the total radio luminosity already averages over some typical pulse profile. The values for the brightness temperature found in (8) are consistent with observationally deduced results (Sutherland, 1979, Kramer, 1995) as the same principal method has been used in both cases.

High coherence is required for a different reason, namely that the radiating volume is small enough. In the next step we show that our model is able to reproduce these fluxes under the assumption of a thin layer emitting highly coherent radiation, but where the coherence factor is kept below the limit imposed by the model. As already mentioned, we propose a mechanism of the relativistic plasma emission type.

For the discussed process, particles are scattered by strong, nonlinear plasma waves (solitons) excited by the two-stream instability. Such a radiation mechanism can be described as an inverse Compton scattering (ICS) of solitons by relativistic electrons.

For each particle coherent ICS radiates a power of

$$P_{\rm rad}^{\rm coh} = N\sigma_{\rm T}c\cdot\frac{E_{\rm wave}^2\varepsilon_0}{2}\gamma^2 \tag{9}$$

with the wave electric field $E_{\rm wave}$ if $\hbar\omega_{\rm wave} \ll m_{\rm e}c^2$, which is the case for radio emission[1]. N is the coherence number, and γ^2 comes from the Lorentz transfomation of $E_{\rm wave}$. As long as the wave electric field is small, the wave can be treated linearly as a small density fluctuation. But in an unstable situation the wave grows exponentially. The growth saturates quickly because the wave will also accelerate particles as a back reaction. Thus, the wave growth has to be calculated using nonlinear methods (Benford & Weatherall, 1992). As a result, the strongest possible wave has an electrostatic field energy comparable to the kinetic energy of the plasma. In the extreme, these two energy densities are equal

$$n_{\rm GJ}\gamma m_{\rm e}c^2 = \frac{1}{2}\varepsilon_0 E_{\rm wave}^2 \tag{10}$$

which means (9) can be rewritten as

$$P_{\rm rad}^{\rm coh} = N\sigma_{\rm T}cn\gamma^3 m_{\rm e}c^2\,. \tag{11}$$

As particles are not assumed to change their longitudinal momentum in the radio emission region, we can interpret the radiated power as an electric dissipation field (which is the field necessary to balance radiation losses). Its strength is

$$E_{\rm diss} = \frac{P_{\rm rad}^{\rm coh}}{ec} = \frac{2N\sigma_{\rm T}\Omega B_0\varepsilon_0 m_{\rm e}c^2}{e^2x_{\rm em}^3}\gamma^3\,. \tag{12}$$

3.2. Extension of the radiation region and the maximum luminosity

Now we calculate the radial width of the radiation zone. This is an important test of the model, as the very small RFM taken from the observations requires a fairly narrow emission zone. Apart from that, the highly modulated radiation observed in the radio band would be hard to explain for large widths.

In (12) the only the free parameter left is N. However, this number cannot directly be fixed from the brightness temperature as mentioned before. Nevertheless there are upper limits for the coherence factor which serve to derive a minimum radial width of the emission region.

As we consider a plasma wave being the cause of coherence, the maximum volume of coherently radiating particles is a sphere of around one Debye volume. Taking into account relativistic effects, Melrose (1992) finds a maximum coherence volume of

$$V_{\rm coh} = \left(\frac{c}{\omega_{\rm p}}\right)^3\frac{\gamma^2}{\pi} \tag{13}$$

and therefore

$$\begin{aligned} N_{\rm max} &= n_{\rm GJ}\left(\frac{c}{\omega_{\rm p}}\right)^3\frac{\gamma^2}{\pi} = \sqrt{\frac{m_{\rm e}^3c^6\varepsilon_0\gamma^7x_{\rm em}^3}{2\Omega}B_0e^5} = \\ &= 6.41\cdot10^{13}\gamma^{7/2}\left(\frac{P}{\rm s}\right)^{1/2}B_8^{-1/2}\left(\frac{x_{\rm em}}{50}\right)^{3/2}\,. \end{aligned} \tag{14}$$

Another upper limit is found by equating the particle and the field energy density, since in the optimal case those quantities are comparable. More detailed calculations (Lesch & Schlickeiser, 1987) show that the field energy density is less than half of the particle energy density (as already used in eq. (10)).

Inserting this result into (12) we find a maximum coherence number of

$$\begin{aligned} N &= \sqrt{\frac{e^3x_{\rm em}^3}{2\gamma^5\Omega B_0m_{\rm e}c^2\varepsilon_0^2\sigma_{\rm T}^2}} = \\ &= 3.79\cdot10^{15}\,\gamma^{-5/2}\left(\frac{P}{\rm s}\right)^{1/2}B_8^{-1/2}\left(\frac{x_{\rm em}}{50}\right)^{3/2}\,. \end{aligned} \tag{15}$$

Comparing the maximum coherence numbers from (14) and (15) we find that the latter is smaller whenever $\gamma \geq 1.97$. Therefore it is a good approximation to use (15) for determining the maximum coherence number.

For estimates of the radial extension of the radio emission region we take the total radio power and calculate the radiating volume necessary to reproduce the observed luminosities.

The total energy loss in a resistive current reads

$$L = \int\limits_{V_{\rm rad}} E_{\rm diss}j\,{\rm d}V \tag{16}$$

where $V_{\rm rad}$ denotes the dissipation volume.

$E_{\rm diss}$ is given by (12) and (15), $j(x) = n_{\rm GJ}(x)ec$, and by assuming that the non-ideality extends over the entire cross-section of open field lines; using a dipolar geometry and neglecting angular corrections to the GJ- density all quantities in (16) only depend on the radial coordinate. The volume element ${\rm d}V$ can be transformed to

$${\rm d}V = r_{\rm NS}A_{\rm cap}x^3\,{\rm d}x\,. \tag{17}$$

Here we have used (6), as the cross-section is a simple function of x. Therefore (16) reduces to a one-dimensional integral.

Inserting all the previous expressions the integral reads

$$\begin{aligned} L &= \left(\frac{2\pi^2\nu^2m_{\rm e}}{B_0\Omega e}\right)^{1/(2\alpha)}\sqrt{\frac{2\Omega B_0m_{\rm e}c^2}{e}}\,\frac{2\Omega B_0\varepsilon_0}{e}ec \\ &\quad r_{\rm NS}\,\frac{\pi\Omega r_{\rm NS}^3}{c}\int\limits_{x_{\rm em}}^{x_{\rm em}+\tilde{l}_0}x^{3/(2\alpha)}x^{-3/2}\,{\rm d}x \end{aligned} \tag{18}$$

where $\tilde{l}_0$ denotes the radial extension of the radiation region in units of $r_{\rm NS}$, whereas $x_{\rm em}$ stands for the height of its inner edge in pulsar radii.

Evaluating the integral and inserting numbers for a frequency of $\nu = 400$ MHz we find

$$L = 5.56\cdot10^{22}{\rm W}\left(\frac{P}{\rm s}\right)^{1/\alpha-5/2}B_8^{3/2-1/\alpha}F_\alpha \tag{19}$$

where

[1] For higher wave energies the cross section is no longer described by $\sigma_{\rm T}$, so that the Klein-Nishina cross section ($\sigma_{\rm KN} \approx \sigma_{\rm T}(\ln\gamma)/\gamma$) must be used.

$$F_\alpha = 0.0286^{1/\alpha} \begin{cases} \tilde{l}_0 & \text{for } \alpha = 1 \\ 4\left[\left(x_{\rm em}+\tilde{l}_0\right)^{1/4} - x_{\rm em}^{1/4}\right] & \text{for } \alpha = 2 \\ \ln\frac{x_{\rm em}+\tilde{l}_0}{x_{\rm em}} & \text{for } \alpha = 3 \end{cases} \quad (20)$$

Solving this equation for $\tilde{l_0}$ in the case $\alpha = 3$ renders

$$\tilde{l_0} = x_{\rm em} \left\{ \exp\left[5.88\cdot 10^{-3}\left(\frac{P}{s}\right)^{13/6} B_8^{7/6}\left(\frac{L}{10^{20}\,\mathrm{W}}\right)\right] - 1 \right\} \quad (21)$$

which, for typical parameters ($L = 10^{20}$ W, $P = 1$ s, $B_8 = 1$, $x_{\rm em} = 50$) yields $\tilde{l_0} = 0.295$ which justifies the assumption of a narrow emission region. The dependence of $\tilde{l_0}$ and L is shown in fig. 3.

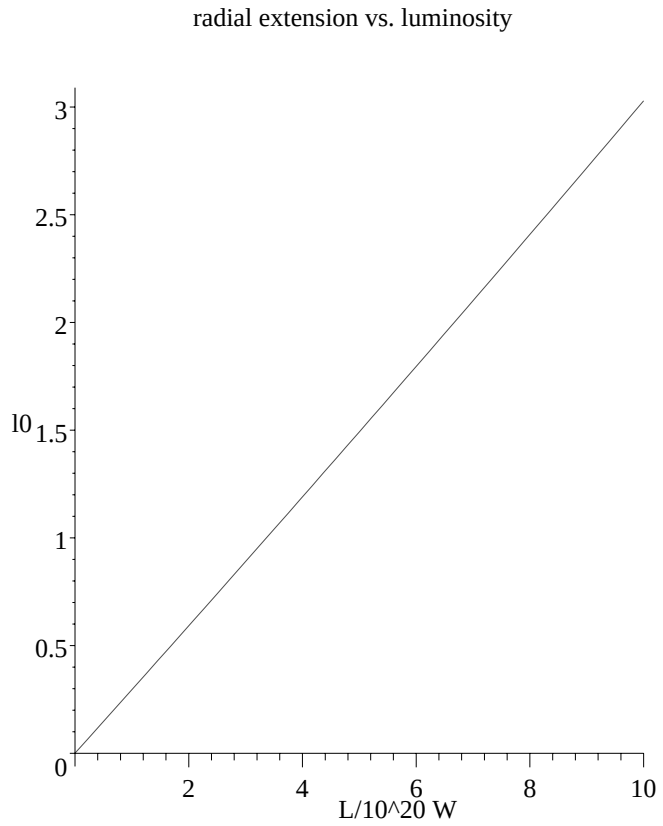


Fig. 3. Radial extension of the radio dissipation region (in units of pulsar radii) versus luminosity for a standard pulsar ($P = 1$ s, $B_8 = 1$). The emission height $x_{\rm em}$ has been set to 50 pulsar radii.

From the result above one can obtain sufficient luminosity even for slow pulsars. However, for small Ω the radial extension of the emission region increases. Especially, the corresponding electric field (12) can even exceed the vacuum field ($E_{\rm vac} = \Omega B_0 r_{\rm NS} x^{-4}$) locally. In a shielded magnetosphere the kinetic energy density and by equipartition the dissipated electric field, may exceed the energy density of the vacuum field.

4. Application to PSR 0329+54

The pulsar PSR 0329 is an extensively researched object and one of the few where the spatial orientation of magnetic and spin axis is well determined (Rankin, 1983). Assuming that the profile peaks occur on the same field lines for all frequencies enabled Mitra and Rankin (2002) to obtain revised effective opening angles and emission heights for PSR 0329+54 amongst others. A good fit to the surface opening angle (including relativistic corrections) for the field lines that provide the two outer peaks of the profile is $\phi_0 = 0.66^\circ$. For any angle ϕ between those peaks we can find an emission height of a profile at a specific frequency using the parametric equation of dipole field lines:

$$r(\phi) = \frac{r_{ns}}{f_1}\frac{\sin(\phi)}{\sin(\phi_0)} \quad (22)$$

Mitra and Rankin (2002) found that the emission heights range from about 500 km for frequencies above 1 GHz up to 1100 km for the lowest frequency of 100 MHz. Together with the known radio fluxes (Kramer et al. 1997) we were able to match the described model to the data and determine the dissipation length scales for frequencies between 100 MHz and 30 GHz. To enhance the realism of the fit, the relativistic (Muslimov & Tsygan, 1992) corrections to the Goldreich-Julian densities and effective areas were also included. In this case we calculated the local Goldreich-Julian density through

$$n(r) = 2\epsilon_0 B_0 \left(\frac{r_{\rm NS}}{r}\right)^3 \cdot \frac{f(r)}{f_1 \cdot \sqrt{1-\frac{r_{\rm g}}{r}}} \quad (23)$$

Here

$$f(r) = -3(\frac{r}{r_{\rm g}})^3 \cdot \left(\ln(1-\frac{r_{\rm g}}{r}) + \frac{r_{\rm g}}{r}\cdot(1+\frac{1}{2}\frac{r_{\rm g}}{r})\right)$$

and $f_1 = f(r_{\rm NS})$ are the corrections due to general relativity (Muslimov & Tsygan). In this context $r_{\rm g} = \frac{2\Gamma m_{ns}}{c^2}$ denotes the Schwarzschild radius of the neutron star.

Assuming that the observed emission is indeed caused by coherent inverse Compton scattering, we can calculate the Lorentz factor of the emitting electron current as a function of distance from the pulsar.

$$\gamma(\omega_{\rm obs}) = \left(\frac{\epsilon_0 m_{\rm NS}}{n(r_{\rm em}(\omega_{\rm obs}))e^2}\right)^{\frac{1}{3}} \omega_{\rm obs}^{\frac{2}{3}} \quad (24)$$

It varies from 13 (100 MHz) to 267 (30 GHz). Using the relativistically corrected values for distance, density and Lorentz factor we obtain an improved estimate of the dissipation scale λ which is given by

$$\lambda = \frac{L}{P_{\rm coh}(r,\gamma)\cdot n(r)\cdot 2\pi r^2\,(1-\cos(\phi))} \quad (25)$$

Here L and ϕ are the observed luminosity and opening angles of the pulsar beam at a given frequency and $P_{\rm coh}$ means the emitted power per coherently radiating particle. We estimated the luminosity as an upper limit from the radio flux by assuming that the smaller cap area given by the peak flux opening angle is filled with uniform emission can be a good representation of the conal beam structure.

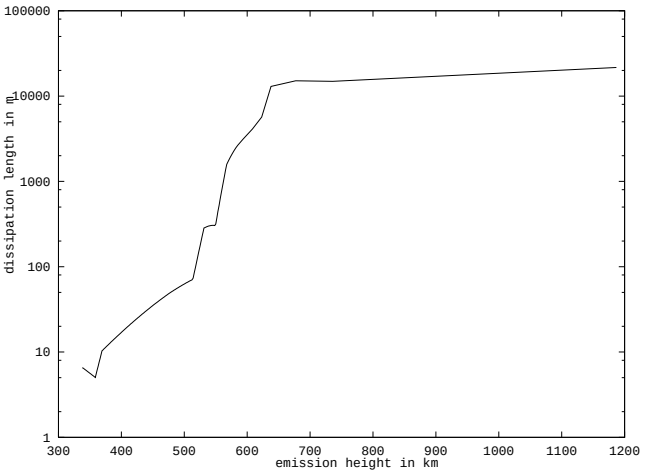


Fig. 4. Dissipation length λ as a function of emission height.

Fig. 4 shows the development of the the dissipation scale with emission height. After a steep rise at 500 km ($\nu >$ 1000 MHz), λ stays around 20 km up to a height 1100 km (100 MHz). Thus we have evidence for a quick onset of a strong and stable coherence at a height of 600 km, lasting for another 600 km. This is also borne out by the fact that the brightness temperatures of the source vary only a little in this regime where most of the pulsar radio luminosity is created. A typical fluctuation time scale of $\gamma \cdot \lambda/c = 1$ms is associated with the dissipation scale below 1 GHz. Above that frequency it is expected to decrease monotonically to 20μs at 20 GHz. These timescales are in good agreement with observational evidence (Lange et al. 1998) where typical microstructure timescales were found to range within $600 - 1200\mu s$ for that pulsar at 4.85 GHz. There is also some observational evidence for a decrease in microstructure timescales with increasing frequency for the pulsars PSR B1133+16 and PSR B2016+28 (Lange et al. 1998).

5. Micropulse flux enhancement by beaming effects

In this section we discuss anisotropy effects for pulse substructures which may enhance the observed brightness temperatures by up to several orders of magnitude. It is very unlikely that the flux enhancement only arises from a growth of the dissipation region. For the nanosecond giant pulses of the Crab pulsar this is even impossible (if the width of the radio emission region jumped from only 0.001 – which is extremely narrow – to around 1 pulsar radius, the peak would occur on a timescale of $\tau_{\rm mic} \approx r_{\rm NS}/c \approx 3 \cdot 10^{-5}$ s). But as such small time scales also mean highly localized emission, the anisotropy of the elementary radiation process has to be considered. For an isotropic process there is a simple connection between the radiated power and the observed flux:

$$S_{\rm obs}(\nu) = \frac{1}{4\pi d^2} \frac{\partial}{\partial \nu} P_{\rm rad}(\nu) \tag{26}$$

where $P_{\rm rad}(\nu)$ is the total power emitted in frequencies below ν, whereas d denotes the transverse extension of the radiation region. For a rough quantitative estimate, we can set $P_{\rm rad}(\nu_{\rm crit}) = L$, and replace the derivative by a quotient. Thus we obtain the simpler equation

$$S_{\rm obs}(\nu_{\rm crit}) = \frac{L}{4\pi \nu_{\rm crit} d^2}\,. \tag{27}$$

This flux is drastically enhanced by two effects, producing a strongly anisotropic emission pattern. The first is the well-known relativistic lighthouse effect (Rybicki & Lightman, 1979). A relativistically moving source of isotropic radiation emits most of the power in a narrow cone with an angular opening of about $1/\gamma$ for $\gamma \gg 1$, as can easily be verified by performing the Lorentz transformation. The exact result is

$$\theta' = \arctan\left(\frac{1}{\gamma}\,\frac{\sin\theta}{(\cos\theta + \beta)}\right) \tag{28}$$

with θ being the angle between the direction of the flux and source velocity in the co-moving frame and θ' denoting this angle in the observer's system. For $\theta = 90^{\rm o}$ and $\gamma \gg 1$ the approximation $\theta' \approx 1/\gamma$ is a good one.
Therefore we find a flux enhancement of

$$\xi_1 = \frac{4\pi}{\pi/\gamma^2} = 4\gamma^2 \tag{29}$$

by the lighthouse effect.

Another anisotropy factor is the coherent radiation process itself, as has been shown by Kunzl et al. (1998b). To understand this effect, one has to recall that coherent emission requires a phase coupling of the emitting particles in one direction. For relativistic plasma emission, the preferred direction obviously is the direction of the streaming velocity (forward direction).

As long as the spatial dimension of the coherently radiating volume is small compared to the emitted wavelength, the interference is still constructive even under large angles to the forward direction. However, as soon as the extension of the coherence region becomes comparable to the wavelength, the coherent emitter can be seen as a phased antenna field producing intrinsically beamed emission.

The quantitative analysis of this effect has been performed by Kunzl *et al.* (1998b). The first minimum appears under the angle

$$\alpha_{\rm min} = \sqrt{1 + \frac{2\pi}{T}} - 1\,. \tag{30}$$

Here $T := 2\pi d/\lambda$ with d being the transverse extension of the emission region. The angle of the minimum is much smaller than unity for $T \gg 1$.

Similar to the lighthouse effect, we can use this angular extension to estimate the enhancement factor by coherence beaming. Thus the flux grows by a factor of

$$\xi_2 = \frac{4\pi}{\pi \alpha_{\rm min}^2} = \frac{4}{\left(\sqrt{1 + \frac{2\pi}{T}} - 1\right)^2}\,. \tag{31}$$

A more realistic treatment of the geometry uses a cylindrically symmetric soliton with a density profile proportional to $\cosh^{-2}(R_0/R)$ where $R_0 \approx \lambda_{\rm D}$ is the typical length scale. Numerical calculations for this structure show a much stronger anisotropy (Kunzl et al. 1998b)

Combining the two anisotropy effects we find the total beaming factor

$$\xi := \xi_1 \xi_2 = 16\gamma^2 \left(\sqrt{1 + \frac{2\pi}{T}} - 1 \right)^{-2} \quad (32)$$

which, even with quite moderate parameters (like $\gamma = 10, x_{\rm em} = 50, N = 10^{13}$ for a typical pulsar), causes an enhancement of some 10^3. Therefore it can easily explain strong substructures, and micropulse brightness temperatures that are some 10^3 times above the mean value (Boriakoff, 1992).

As these beaming effects apply only to the elementary emission process, but do not enhance the mean flux significantly, it is an important check on whether the model can reproduce the observed brightness temperatures of up to 10^{31} K (Hankins, 1996) observed in *giant pulses* of the Crab pulsar.

Therefore we take the maximum possible number of coherently radiating particles, and the corresponding beaming effects. Let A be an arbitrary cross section. Then starting with eq. (8) one can express the integrated flux $I := I_\nu \Delta\nu = L_{\rm radio,A}/A$ by the brightness temperature:

$$I := \frac{L_{\rm radio,A}}{A} = \frac{2\pi\nu^3 k_{\rm B} T_{\rm B}}{c^2} \,. \quad (33)$$

Inserting the critical frequency of the Crab pulsar $\nu = \nu_{\rm crit} = 160$ MHz and $T_{\rm B} = 10^{31}$ K, the integrated flux is

$$I = 3.95 \cdot 10^{16} \, \frac{\rm W}{\rm m^2} \,. \quad (34)$$

As this value means the beamed flux, the actual power per area is only

$$I_{\rm real} := \frac{I}{\xi} = 2.47 \cdot 10^{15} \frac{\rm W}{\rm m^2} \, \gamma^{-2} \left(\sqrt{1 + \frac{2\pi}{T}} - 1 \right)^2 \,. \quad (35)$$

Now we can compute the minimum thickness of a layer producing the power per cross-section. To obtain the lower limit we take the strongest dissipation field possible (see eq. (12)) and assume a coherence cell with a lateral extension of $c/\nu_{\rm p}$, so that $T = 2\pi\gamma$.

The total dissipated power from a volume with the cross-section A and the radial extension d is

$$P_{\rm diss} \stackrel{!}{=} I_{\rm real} A = E_{\rm diss} \, d \, j \, A \,. \quad (36)$$

For a relativistic Goldreich-Julian current $j = j_{\rm GJ} = n_{\rm GJ}(x) e c$ eq. (36) can be solved for d. Inserting the Crab pulsar parameters ($P = 33.4$ ms, $B = 3.8 \cdot 10^8$ T, $\nu = 160$ MHz, $x_{\rm em} = 80$) and additionally using eq. (4) we obtain

$$d = 3.85 \, {\rm m} \left(\frac{T_{\rm B}}{10^{31} \, {\rm K}} \right) \quad (37)$$

which corresponds to a time scale of

$$\tau := \frac{d}{c} = 1.28 \cdot 10^{-8} \, {\rm s} \left(\frac{T_{\rm B}}{10^{31} \, {\rm K}} \right) = 12.8 \, {\rm ns} \left(\frac{T_{\rm B}}{10^{31} \, {\rm K}} \right) \,. \quad (38)$$

Thus we can expect to see giant pulses on nanosecond timescales, with brightness temperatures above 10^{30} K, from far inside the light cylinder in the Crab pulsar, although the relative emission height will be considerably larger than for average pulsars.

6. Densities in the radiation region

Here we briefly discuss if the model described above could also work for particle densities significantly above or below the GJ value. We will show that even if there were a mechanism producing a current density and particle energies matching the requirements to produce the low radio frequencies, such a scenario would be very unlikely.

Assuming that the particle density was much larger than the value predicted by Goldreich & Julian (1969), the Lorentz factor corresponding to a certain frequency would drop according to (4). Especially for young pulsars this would quickly require $\gamma < 1$ which is, of course, not possible (even $\beta\gamma \geq 1$ should be fulfilled as the particles are definitely relativistic). This important fact has already been pointed out by Kunzl *et al.* (1998a).

A relativistic current significantly below the GJ current (meaning that the particle density is smaller than $n_{\rm GJ}$ faces even more difficulties. On the one hand, accelerating fields are incompletely shielded (the equilibrium Lorentz factor where acceleration and radiation losses – now including coherent radio emission – balance is extremely high, so coherence is highly doubtful). Furthermore the one-dimensional approach would no longer account as a permanent strong deviation from ideality allows efficient $\boldsymbol{E} \times \boldsymbol{B}$ drift. But also the existence of strong γ -pulsars provides an argument against this solution:

As we observe *pulsed* γ-emission of pulsars whose high energetic luminosity reaches up to 10% of the spindown luminosity, some mechanism must efficiently convert *particle energy* into (hard) radiation (Kanbach, 2001). But the potential difference a particle can suffer is limited by the polar cap potential. Since the power dissipated by a relativistic GJ current flowing over the entire polar cap area with the polar cap voltage is comparable to the spindown power of the neutron star, a large fraction (well above 10%) of the generator's power must be pumped into particles. This, of course, is only possible for currents of about the GJ current and thus for particle densities comparable to the Goldreich-Julian value.

7. Discussion

We have presented the outline of a model which may explain the creation of radio emission within the energy constraints of the observationally deduced emission heights of 50-100 pulsar radii. (e.g. Blaskiewicz et al. 1991; Taylor et al. 1993; Kijak and Gil 1997,1998; Kramer et al. 1997). Several other pulsar models fail to explain this feature, e.g. the model of Lyutikov et al. (1999) which uses Cherenkov drift resonance, but predicts the radiation zone to be in some 1000 pulsar radii.

One of the main differences to the standard model is that we do not assume an inner gap which accelerates particles to ultrarelativistic energies and is saturated by a pair avalanche. Instead we suggest a conducting wire model with a quasi-stationary, low relativistic current that suffers fluctuations on short time scales. Such a model is supported by calculations on particle densities available from the polar cap by thermal and field emission (Jessner et al. 2001) which show that inner gap models have severe difficulties in producing particles energetic enough to start pair cascades for parallel or nearly parallel rotators.

We showed that the brightness temperatures for the mean pulse can be reproduced by our model and also micropulse fluxes can be explained by appropriate beaming assumptions.

The radiation process in the framework of such a model could be some relativistic plasma emission like the ALAE process described by Melrose (1978). This mechanism requires mildly relativistic particles to be efficient. As shown also in Kunzl et al. (1998a) any plasma process responsible for the low frequency emission in the Crab pulsar must work with mildly relativistic particles. Von Hoensbroech et al. (1998) showed that in a Goldreich-Julian magnetosphere with low relativistic particles propagation effects can also qualitatively explain the observed polarization properties.

Finally we would like to note that our model does not rule out pair production in general. As can be seen from several observations of the Crab pulsar a dense particle wind is needed which transports energy to the nebula. The calculations of Hirotani and Shibata (1999) show that a significant fraction of the vacuum potential drop can occur in an outer gap if the X-ray photon density is not too high. For a detailled geometric examination of the outer gap structure see Cheng et al. (2000).

It has been shown that for reasonable parameters an outer gap model could easily explain the observed energy and particle fluxes in the pulsar wind. Recently Crusius et al. (2000) have shown that an outer gap model can explain the observed spectrum and energy output of the Crab pulsar from the infrared to X-ray frequencies which provides another hint that the main dissipation region is in the outer magnetosphere.

We gratefully acknowledge constructive discussions with J. Arons, D.B. Melrose M. Kramer, D. Mitra and A. von Hoensbroech. In addition D. Mitra and M. Kramer provided us with access to their radio flux- and emission height measurements for PSR 0329+54 for which we are particularly grateful.

References

Arendt, P.N., Eilek, J.A., 2000 in: Pulsar Astronomy – 2000 and beyond, eds. Kramer, M., Wex, N., Wielebinski, R., IAU Colloq. **177**, p. 445

Arons, J., 1981, in Origin of Cosmic Rays, eds. Setti, G., Spada, G., Wolfendale, A.W., p. 175

Benford, G., 1992, IEEE Trans. on Plasma Sci., 20, 3

Benford, G., Weatherhall J.C., 1992, Phys. Fluid B, 4, 4111

Blaskiewicz, M., Cordes, J.M., Wasserman, I., 1991, ApJ 370, 643

Boriakoff, V., 1992, in The Magnetospheric Structure and Emission Mechanisms of Radio Pulsars, eds. Hankins, T.H., Rankin, J.M. and Gil, J.A., IAU Colloq. **128**, p. 343

Cheng, K.S., Ruderman, M., Zhang, L., 2000, ApJ 537, 964

Crusius-Wätzel, A.R., Kunzl, T., Lesch, H., 2000, ApJ, 546, 401

Ewart, G.M., Guyer, R.A., Greenstein, G., 1975, ApJ, 202, 238

Gil, J.A., 1992, in: The Magnetospheric Structure and Emission Mechanisms of Radio Pulsars, eds. Hankins, T.H., Rankin, J.M. and Gil, J.A., IAU Colloq. **128**, p. 395

Goldreich, P., Julian, W.H., 1969, ApJ 157, 869

Hankins, T.H., 1996 in: Pulsars: problems and progress, Astronomical Society of the Pacific Conference Series, Vol. 105; eds. Johnston, S., Walker, M.A., Bailes, M., p. 181

Hirotani, K, Shibata, S., 1999, MNRAS 308, 54

von Hoensbroech, A., Lesch, H., Kunzl, T., 1998, A&A, 336, 209

von Hoensbroech, A., Lesch, 1999, A&A, 342, L57

Itoh, N., 1975, MNRAS, 173, 1P

Jessner, A., Lesch, H., Kunzl, T., 2000, ApJ, *in press*

Kanbach, G., 2001, in: The Universe in γ-rays

Kato, K.G., Benford, G., Tzach, D., 1983, Phys. Fluid 26, 3636

Kijak, J., Gil, J.A., 1997, MNRAS 288, 631

Kijak, J., Gil, J.A., 1998, MNRAS 299, 855

Kramer, M., 1995, PhD thesis, University Bonn, Germany

Kramer, M., Xilouris, K.M., Jessner, A., Lorimer, D.R., Wielebinski, R., Lyne, A.G., 1997, A&A, 322,846

Kramer, M., Wex, N., Wielebinski, R., 2000, Pulsar Astronomy – 2000 and beyond, eds. Kramer, M., Wex, N., Wielebinski, R., IAU Colloq. **177**, p. 381

Kunzl, T., Lesch, H., Jessner, A., von Hoensbroech, A., 1998a, ApJ,505, L139

Kunzl, T., Lesch, H., Jessner, A., 1998b, A&A, 339, 917

Lange, C., Kramer, M., Wielebinski, R., Jessner, A., 1998, A&A 332, 111

Lesch, H., Schlickeiser, R., 1987, A&A, 179, L93

Lesch, H., Jessner, A., Kramer, M., Kunzl, T., 1998, A&A 332, L21

Lesch, H., Kunzl, T., Jessner, A., 2000, in: Pulsar Astronomy – 2000 and beyond, eds. Kramer, M., Wex, N., Wielebinski, R., IAU Colloq. **177**, p. 381

Levron, D., Benford, G., Tzach, D., 1987, Phys. Rev. Lett, 58, 1336

Lyne, A.G., Graham-Smith, F., 1998, Pulsar Astronomy, Cambridge University Press

Lyutikov, M., 1999, ApJ, 525, L37

Malofeev, V.M., Gil, J.A., Jessner, A., et al., 1994, A& A 285, 201

Melrose, D.B., 1978, ApJ, 225, 557

Melrose, D.B., 1992, in The Magnetospheric Structure and Emission Mechanisms of Radio Pulsars, eds. Hankins, T.H., Rankin, J.M., Gil, J.A., IAU Colloq. **128**, p. 306

Melrose, D.B., Gedalin, M.A., 1999, ApJ 521, 351

Melrose, D.B., Gedalin, M.A., 2000, in Pulsar Astronomy – 2000 and beyond, eds. Kramer, M., Wex, N., Wielebinski, R., IAU Colloq. **177**, p. 381

Muslimov, A.G., Tsygan, A.I., 1992, MNRAS, 255, 61

Radhakrishnan, V., Rankin, J.M., 1990, ApJ 352, 258

Rankin, J.M., 1992, in The Magnetospheric Structure and Emission Mechanisms of Radio Pulsars, eds. Hankins, T.H., Rankin, J.M. and Gil, J.A., IAU Colloq. **128**, p. 133

Rowe, E.T., 1992a, Aust. J. Phys., 45, 1

Rowe, E.T., 1992b, Aust. J. Phys., 45, 21

Ruderman M.A., Sutherland P.G., 1975, ApJ 196, 51

Rybicki, G.G., Lightman, A.P., 1979, *Radiative Processes in Astrophysics*, Wiley, New York

Shibata, S., 1991, ApJ, 378, 239

Shibata, S., 1997, MNRAS, 287, 262

Sturrock, P.A., 1971, ApJ 164, 529

Sutherland, P.G., 1979, Fundamentals of Cosmic Physics, Vol. 4, p.95

Taylor, J.H., Manchester, R.N., Lyne, A.G., 1993, ApJS 88, 529

Ursov, V.N., Usov, V.V., 1988, APSS 140, 325

Yoshikawa, M., Ando, R., Masuzaki, M., 1993, Japan J. Appl. Phys., 32, 969

Yoshikawa, M., Masuzaki, M., Ando, R., 1994, J. Phys. Soc. Japan, 64, 3303

Proceedings of the 270. WE-Heraeus Seminar on: *"Neutron Stars, Pulsars and Supernova Remnants"*
Physikzentrum Bad Honnef, Germany, Jan. 21-25, 2002, eds. W. Becker, H.Lesch & J. Trümper, MPE Report 278, pp. 230-239

Coherent Radio Emission from Pulsars

Y.E.Lyubarsky

Ben-Gurion University, P.O.B. 653, Beer-Sheva 84105, Israel

Abstract. Generation of the pulsar radio emission from plasma waves excited by the two-stream instability is considered. Special attention is given to propagation effects.

1. Introduction

Strong coherent radio emissions from pulsars are believed to result from the development of plasma instabilities in the magnetosphere of the neutron star. The theory should explain a) what plasma instability excites collective plasma motions in the pulsar magnetosphere; b) how these collective motions generate radio waves and c) how the generated radio waves propagate through the magnetosphere. Such a complete theory has not available yet; moreover there is still no consensus on the basic emission mechanism. The two-stream instability, which readily excites strong plasma oscillations, is among the most widely discussed. Pulsar magnetospheres are believed to be filled with an electron-positron plasma generated in a cascade process from a primary particle beam accelerated in the rotationally induced electric field (see the recent work by Hibschman & Arons 2001 and references therein). This plasma streams along the open magnetic field lines, which extend beyond the light cylinder. Oscillations generated in this plasma may be a source of a powerful radio emission.

Conditions for the development of the two-stream instability in pulsar magnetospheres are not trivial. The plasma flow should involve streams with markedly different velocities. Usov (1987) pointed out that such a configuration arises if plasma production is extremely unsteady. Then the plasma flow is built up from separate clouds following each other along the magnetic field line and slower particles from a cloud would be overtaken by faster particles from the subsequent cloud giving rise to the two-stream instability (see also Ursov & Usov 1988; Asseo & Melikidze 1998). A two-stream configuration arises also because the adjustment of electric current and charge density in the open field line tube requires a certain flow of particles to be directed downwards, against the main plasma flow (Lyubarskii 1992a,b; 1993a). At last conditions for the two-stream instability may arise as a result of interaction of the secondary pair plasma with the thermal emission from the neutron star surface (Lyubarskii & Petrova 2001). Discussion of these scenarios is out of the scope of my talk; it is enough to mention that in the plasma flow within the open magnetic line tube, the two-stream instability develops readily. Therefore let us assume that the instability does develop and consider the formation of pulsar radio emission from the excited plasma waves and the properties of the outgoing radiation.

2. Generation of radio emission from plasma oscillations in pulsar magnetospheres

2.1. Waves in the plasma embedded in a super strong magnetic field

Let us first outline qualitative properties of waves in the electron-positron plasma embedded in a super strong magnetic field. The pulsar radio beam is believed to originate from deep inside the magnetosphere, where the magnetic field may be considered as effectively infinite. Namely particles in such a field may be considered as beads on a wire; they move freely along the magnetic field lines and do not shift in the transverse direction. Properties of this plasma are relatively simple. They are especially simple if plasma is cold therefore below all estimates will be made in this limit. In the relativistically hot plasma properties of the waves are qualitatively the same (see, e.g., Volokitin et al. 1985; Arons & Barnard 1986; Lyubarskii 1996; Melrose & Gedalin 1999; Asseo & Riazuelo 2000).

Let us first consider waves in the plasma rest frame (all the quantities in this frame will be marked by prime). It is evident that a transverse wave propagating along the magnetic field does not interact with the plasma because the electric field in this wave is perpendicular to the background magnetic field and plasma particles are unable to move in this direction. Therefore transverse waves propagate along a super strong magnetic field just like in vacuum; for these waves $\omega = kc$. On another hand, there exist longitudinal, electrostatic waves propagating along the magnetic field and these waves are just the same as Langmuir waves in a nonmagnetized plasma because particles oscillating along the magnetic field do not "feel" this field. So frequency of such a wave is equal to the plasma frequency (in the plasma rest frame) independently of the wavelength,

$$\omega_p = \sqrt{\frac{4\pi e^2 n'}{m}}, \qquad (1)$$

just as in a nonmagnetized plasma. Here n' is the plasma number density in the proper frame, e and m the electron charge and mass, respectively.

The dispersion curves of the waves propagating along the magnetic field are shown in Fig. 1 by solid lines. The horizontal line corresponds to the longitudinal plasma wave and the bisector corresponds to the transverse wave. Intersection of the

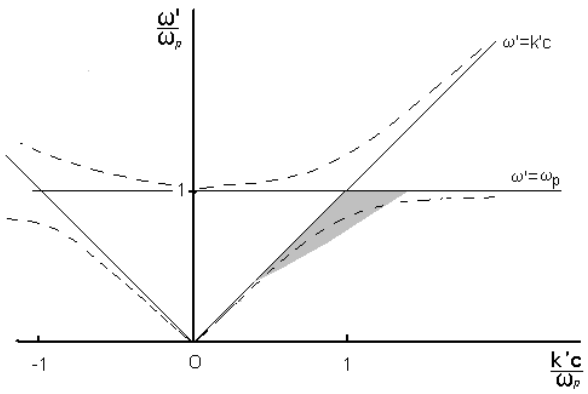


Fig. 1. Dispersion curves in the proper plasma frame. Solid lines correspond to the waves propagating along the magnetic field and dashed, to those propagated obliquely. The two-stream instability excites waves in the shaded region.

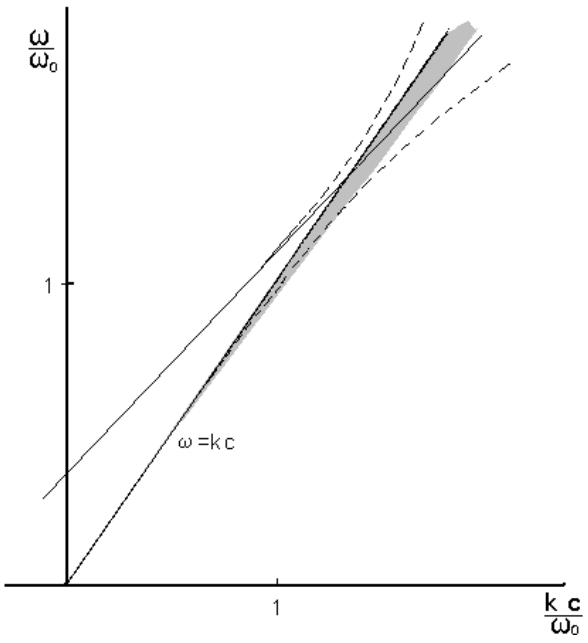


Fig. 2. Dispersion curves in the pulsar frame.

dispersion curves (degeneracy) is possible because the system is axisymmetrical for the waves propagating along the magnetic field. The dispersion curves of the oblique waves can not intersect because axisymmetry is broken in this case. Taking into account that properties of waves propagating at small angles to the magnetic field should be close, by continuity, to properties of waves propagating strictly along the magnetic field, one can sketch the dispersion curves of oblique waves (dashed lines in Fig.1). Of course this simple qualitative picture is confirmed by calculations (see the above-mentioned papers). One can see that the dispersion curves of the oblique waves are split into superluminous ($\omega' > k'c$) and subluminous ($\omega' < k'c$) branches, the separation between the branches being larger for waves propagating at larger angle to the magnetic field. Polarization of oblique waves is neither purely longitudinal nor transverse however polarization of waves propagating at small angle to the magnetic field is close to longitudinal or transverse in the corresponding parts of the dispersion curve. At $\omega' \gg \omega_p$ the superluminous wave becomes nearly transverse wave with the vacuum dispersion law, $\omega = kc$. It is very important that a single branch of the dispersion curve for the oblique wave links nearly longitudinal and nearly transverse waves.

In pulsars plasma streams with a Lorentz factor $\gamma \sim 100$ along the open magnetic field lines. The dispersion curves in the pulsar frame may be obtained by Lorentz transformation of the curves shown in Fig. 1. The result is plotted in Fig. 2. The dispersion law of the transverse wave propagating along the magnetic field, $\omega = kc$, evidently remains unchanged whereas the horizontal line $\omega' = \omega_p$, corresponding to the longitudinal waves, transforms into an inclined line such that the frequencies of the longitudinal plasma waves may vary significantly. The reason is that not only the frequency but also the wavelength enter the Lorentz transformation therefore the waves with different wavelengths and the same frequency in the proper plasma frame have different frequencies in the pulsar frame. The wave $\omega' = \omega_p$, $k' = 0$ have the frequency

$$\omega_0 = \omega_p \sqrt{\gamma} \tag{2}$$

in the pulsar frame. The waves with $\omega < \omega_0$ are those propagating in the proper frame upstream the plasma flow. The dispersion curves of the transverse and longitudinal waves propagating along the magnetic field intersect at the point $\omega = 2\omega_0$, $k = 2\omega_0/c$; above this point the longitudinal wave is subluminous. The dispersion curves for the oblique waves are also split into superluminous and subluminous branches. At $\omega \gg \omega_0$ the superluminous wave becomes the vacuum transverse electromagnetic wave.

The waves resonantly interact with particles if the phase velocity, ω/k, coincides with the particle velocity (more exactly the resonance condition reads as $\omega = \mathbf{k} \cdot \mathbf{v}$). Of course only subluminous waves participate in such an interaction. In the presence of a particle beam, such a resonant interaction leads to the two-stream instability, which predominantly excites waves with the phase velocities close to the beam velocity. The region where waves are generated by a high velocity particle beam is shaded in Fig. 1. Waves with low enough phase velocities are heavily damped because they are in resonance with the thermal plasma particles (Landau damping).

Up to now only so called ordinary waves were considered. There is also an extraordinary wave; in this wave the electric field is perpendicular both to the background magnetic field and to the wave vector $\mathbf{k}$. In the limit of infinitely strong magnetic field this wave evidently does not interact with the plasma and propagates like in vacuum.

2.2. Escape of waves

The crucial question is what waves can escape from the pulsar magnetosphere and form the observed radio beam. The answer is evident for the nonmagnetized plasma where the purely longitudinal as well as purely transverse waves exist. Namely the longitudinal wave, which is electrostatic, do not escape whereas the transverse wave escapes freely. There is no purely transverse waves in the strongly magnetized plasma and therefore one should ask what wave becomes the vacuum transverse electromagnetic wave when it propagates outward, in the plasma of decreasing density (Arons & Barnard 1986).

Let us consider propagation of a superluminous wave. In a steady state medium with smooth density gradients, the wave frequency remains constant while the wavelength is adjusted in order to satisfy the dispersion equation at any point. In the (ω, k) plane, the point representing a wave moves along the dispersion curve upward because plasma frequency decreases together with plasma density. If the wave propagates strictly along the magnetic field, it transits along the dispersion curve to the subluminous region. Eventually the wave phase velocity, ω/k, decreases such that the wave decays through the Landau damping. In the oblique propagation case, the wave remains superluminous and at $\omega \gg \omega_0$ transforms into the vacuum transverse electromagnetic wave, which escapes freely [1]. Finally it should be noted that in a curved magnetic field, a wave becomes oblique, even if it was initially directed along the magnetic field (Barnard & Arons 1986, Lyubarskii & Petrova 1998). Therefore the superluminous longitudinal waves eventually escape from pulsar magnetospheres in the form of the vacuum transverse electromagnetic waves.

Applying the same consideration to the subluminous waves, one can see that such waves do not escape. When they propagate in the plasma of decreasing density, their phase velocities decrease and eventually the waves decay through the Landau damping. So in the strong magnetic field the superluminous wave escapes even if it was initially purely longitudinal (in the curved magnetic field) whereas the subluminous waves does not escape even though these waves are nearly transverse at $\omega \ll \omega_0$.

The two-stream instability generates predominantly longitudinal waves, which are in Cherenkov resonance with the particle beam, $\omega = kv$. This waves are evidently subluminous, $\omega/k < c$ (the region where the waves are generated is shaded in Figs. 1, 2). Such waves are unable to escape from plasma unless nonlinear processes redistribute the wave energy into the superluminous region. High brightness temperature of pulsar radio emission implies high wave energy density in pulsar magnetospheres and therefore nonlinear effects should be of paramount importance.

2.3. The second order processes

As the first step in studying of the nonlinear effects, one should consider the processes of the lowest order in the wave energy density, W. These are the wave-wave interaction and induced scattering by the plasma particles (see, e.g., Tsytovich 1970; Melrose 1980). The wave-wave interactions involve, in the lowest order in W, merging of two waves into one and decay of a wave into two waves. All three interacting waves should satisfy the dispersion equation, $\omega = \omega(\mathbf{k})$, and also the energy and momentum conservation laws,

$$\omega(\mathbf{k}_1) + \omega(\mathbf{k}_2) = \omega(\mathbf{k}_3);$$

$$\mathbf{k}_1 + \mathbf{k}_2 = \mathbf{k}_3;$$

which place severe restrictions on the process. Therefore this process is rather ineffective in pulsar conditions (Bliokh & Lyubarskii 1997) [2] .

In contrast to wave-wave interactions, there is no restrictions on induced scattering and therefore this process is of crucial importance. At rather general conditions, the induced scattering redistributes the wave energy towards large wavelengths (in the plasma rest frame). One can easily see from Fig. 1 that when a longitudinal wave from the shaded region moves towards small k (larger wavelengths) it eventually becomes superluminous. However it was shown above that superluminous waves escape freely in the form of vacuum transverse waves if they propagate in the curved magnetic field in the plasma of decreasing density. So the observed radio emission may be generated through the induced scattering of the longitudinal waves excited by the two-stream instability.

Redistribution of the wave energy is described by the kinetic equation; in the plasma in the infinite magnetic field it may be presented in the form

$$\frac{\partial W_{\mathbf{k}}}{\partial t} + \mathbf{v}_g \frac{\partial W_{\mathbf{k}}}{\partial \mathbf{r}} \tag{3}$$

$$= W_{\mathbf{k}} \int w_p(\mathbf{k}, \mathbf{k_1}) W_{\mathbf{k_1}} \frac{k_z - k_{z1}}{\omega_1} \frac{\partial f}{\partial p} dp d\mathbf{k}_1,$$

where $W_{\mathbf{k}}$ is the spectral energy density of waves, $f(p)$ the particle distribution function, $w_p(\mathbf{k}, \mathbf{k_1})$ the probability of the scattering of the wave $\mathbf{k_1}$ into the wave $\mathbf{k}$, $\mathbf{v}_g$ the group velocity of the wave; the field is directed along z axis. The scattering probability was calculated by Lominadze et. al (1979) for waves propagating along the magnetic field and by Lyubarskii (1993b) in the general case.

One can conveniently analyze the plasma processes in the proper plasma frame. In this frame (more exactly, in the frame of reference moving with the maximum of the particle distribution function) $\frac{\partial f}{\partial p} \leq 0$ and the right-hand side of Eq.(3) is positive if $k_z < k_{k1}$, so the wavelength increases in the scattering process. Kinetics of the induced scattering in the one-dimensional relativistic plasma was considered by Lyubarskii (1996). Of course in the presence of a particle beam, one more maximum appears in the distribution function and, provided the beam is strong enough, the above statement violates and the wave frequency may significantly increase (e.g., Weatherall 2001, Schopper et al. 2002). In this case the beam plays the role of the main plasma and, switching to the frame of the beam, we come to the same conclusion: the wavelength increases. In the frame of the beam this is accompanied by changing of the wave propagation direction and therefore the wave frequency grows in the laboratory frame. One should also note that the so called amplified linear acceleration emission (Melrose 1978; Rowe 1995) actually represents the induced scattering of a longitudinal, electrostatic wave into a (quasi) transverse one.

[1] Of course an infinitely small angle between the magnetic field and the propagation direction is insufficient for free escape of a longitudinal wave. If the angle is small enough, the superluminous branch approaches closely to the subluminous one near the point $\omega = 2\omega_0, \quad k = 2\omega_0/c$ and the wave may jump, because of linear coupling, onto the subluminous branch. However in pulsar magnetospheres, this effect is of no importance because the corresponding critical angle is very small (Bliokh & Lyubarskii 1996).

[2] There are more degrees of freedom for wave-wave interactions in a finite magnetic field (Machabeli 1983; Lyutikov 1999) however probabilities of these processes are rather small.

For a rough estimate, one can present the kinetic equation (3) in the simple form

$$\frac{dW}{dt} \sim \eta W, \tag{4}$$

where $W = \int W_{\mathbf{k}} d\mathbf{k}$ is the total wave energy density. In the proper plasma frame, the redistribution rate may be roughly presented as

$$\eta \sim \frac{W'}{n'mc^2}\,\omega_p. \tag{5}$$

The structure of this simple estimate is common for any second order process: the corresponding redistribution rate is proportional to the ratio of the wave energy to the plasma energy density and some relevant frequency. In the case of interest, the characteristic plasma "temperature" is about of the electron rest energy and all frequencies are about the plasma frequency therefore the estimate is especially simple and may be in fact obtained from dimensional considerations.

2.4. Emission power

The mechanism under consideration generates electromagnetic waves with $k' < \omega_p/c$ (see Fig. 1); in the pulsar frame the frequencies of these wave are about ω_0 (Eq.(2)). So the observed frequency is determined, via the plasma frequency, by the plasma density at the emission point. The electron-positron plasma is assumed to be generated at the base of the open field line tube; the generation rate is conveniently characterized by the multiplicity parameter, κ, such that the plasma density at the base of the open field line tube is normalized by the Goldreich-Julian (1969) density,

$$n = \kappa \frac{B}{ecP}, \tag{6}$$

where B is the surface magnetic field, P the pulsar period. Continuity of the plasma flow in the tube implies that the plasma density falls off as the tube cross section; for the dipole field, $n \propto 1/r^3$. Now the radiation frequency may be estimated as

$$\nu = \frac{\omega_0}{2\pi} = 1.4\sqrt{\frac{\kappa_2\gamma_2 B_{*12}}{P}\left(\frac{30r_*}{r}\right)^3}\ \mathrm{GHz}, \tag{7}$$

where $B_* \equiv 10^{12}B_{*12}$ G is the surface magnetic field, r_* the stellar radius, $\kappa_2 \equiv \kappa/10^2$, $\gamma_2 \equiv \gamma/10^2$. Observational data suggest that the radio emission is generated at altitudes about few hundreds km (e.g., von Hoensbroech & Xilouris 1997; Kijak & Gil 1998; Kijak 2001). At such altitudes, the width of the open field line tube is about the observed beam width, the last being estimated as $\vartheta = 0.1P^{-1/2}$ (Rankin 1993). The estimate (7) shows that the radio emission may be generated at the plasma frequency provided the multiplicity is about 100. Note that the presented radius-to-frequency mapping does not mean that the emission is narrow band. Plasma at a given radius radiates in the range $\Delta\nu \sim \nu$.

Because nonlinear redistribution rates depend on the wave energy density, one can easily estimate the radiation power comparing the redistribution rate with the escape rate. The two-stream instability generates Langmuir waves in the region shaded in Fig. 2. These waves propagate upward in the plasma of decreasing density; without nonlinear redistribution, the phase velocity of the waves would decrease and the waves would eventually decay. Phase velocity decreases with plasma density at the characteristic scale r; in the proper plasma frame, the corresponding time is about $r/(c\gamma)$. Emission of radio waves is possible if the induced scattering transforms the waves into superluminous ones for a lesser time, $\eta \geq r/(c\gamma)$. Making use of Eq. (5), one can estimate the minimal wave energy density necessary for the emission as

$$\frac{W'}{n'mc^2} = \frac{W}{\gamma nmc^2} = 0.016\,\frac{\gamma_2^{5/3}P^{1/3}}{(\nu_9\kappa_2 B_{*12})^{1/3}}. \tag{8}$$

Here the radius-to-frequency mapping (7) was used to eliminate the radius in favor of the radiation frequency. If the plasma wave density is less then the above value, nonlinear processes are ineffective and the waves eventually decay. The pulsar radiates if the two-stream instability generates waves with the energy density exceeding the minimal value; then the generated waves are transformed into superluminous ones and may escape. The corresponding luminosity may be estimated multiplying the wave energy density by the speed of light and the cross section of the polar tube, $S = \pi r_*^3\Omega/c$; for the two tubes one gets

$$L_{min} = 2WcS = 5\cdot 10^{26}\,\frac{(\kappa_2 B_{*12})^{2/3}\gamma_2^{8/3}}{P^{5/3}\nu_9^{1/3}}\ \mathrm{erg/s}. \tag{9}$$

The presented estimate roughly corresponds to the luminosity of weak pulsars. The radiation spectrum in this case may be estimated as $\frac{dL}{d\nu} \propto \nu^{-4/3}$.

The pulsar luminosity is limited from above by the total energy of the plasma flow. So the maximal pulsar luminosity may be estimated as

$$L_{max} = 2nmc^3\gamma S = 2.5\cdot 10^{28}\,\frac{\kappa_2 B_{*12}\gamma_2}{P^2}\ \mathrm{erg/s}. \tag{10}$$

This estimate is compatible with the observed pulsar luminosities.

According to Eq.(7), the plasma multiplicity factor should be not large, $\kappa \leq 100$, for radio emission to be emitted not too high in the magnetosphere. Originally the plasma production models predicted $\kappa \sim 10^3 - 10^4$ and even more (Ruderman & Sutherland 1975; Daugherty & Harding 1982; Arons 1983). However recent calculations, which take into account the resonant scattering of the thermal radiation from the surface of the star, favor for smaller κ (Hibschman & Arons 2001), which are in better agreement with the assumption that the emission is generated at the plasma frequency. On the other hand, the observed pulsar luminosities require, according to Eq.(10), $\kappa \geq 100$. Whilst these estimates are not incompatible, one would nevertheless fill more comfortable if the plasma could emit at frequencies well below the plasma frequency or if there was an additional energy source such that a low density plasma could provide the observed radiation power.

Radiation at $\nu \ll \nu_p$ is possible, in principle, in the subluminous mode (Arons & Barnard 1986; Lyutikov 2000; Melikidze et al. 2000). This wave propagates along the magnetic field preserving original direction of the wave vector. Being emitted at a level where the plasma density is high, the wave is ducted upwards along the magnetic field line and eventually decays when the phase velocity reaches the particle velocities (Barnard & Arons 1986). The outgoing radiation may be generated if the wave is transformed into the superluminous wave

before the decay takes place. One should expect that then the beam width will be determined by the width of the tube at the transformation level, which is in fact the level where $\nu \sim \nu_p$. So if κ is large, the beam should be too wide even if it was emitted at low altitudes. The beam will remain narrow only if the transformation process does not affect the original direction of $\mathbf{k}$ however up to now nobody has proposed such a transformation process.

The possibility that the plasma in the open field line tube gains energy from an external source may not be ruled out because the electromagnetic energy in the pulsar magnetosphere greatly exceeds the plasma energy. True, plasma with $\kappa > 1$ screens electric fields and therefore the huge electric potential generated in the open field line tube seems to remain beyond the reach of the plasma flow. Nevertheless adjustment of the electric charge density in the open field line tube requires some longitudinal electric field (Scharlemann 1974; Cheng & Ruderman 1977). It is possible that the plasma flow may gain some energy from this field; then the pulsar luminosity may exceed that of Eq.(10).

2.5. Strong turbulence

If the wave energy density is about Eq.(8), the induced scattering rate is comparable with the propagation time and therefore the waves are transformed into superluminous ones and escape. If the wave energy is larger, the induced scattering rate exceeds the escape time, which means that the effective optical depth becomes large. In this case the waves may be locked in the system therefore another nonlinear processes come into play.

The most important effect is the modulation instability. A spatially uniform distribution of plasma waves becomes unstable with respect to formation of regions with enhanced energy density of the waves (e.g., ter Haar & Tsitovich 1981; Goldman 1984). In the nonrelativistic plasma, this instability develops already at rather small plasma wave energy densities. The threshold of the instability is

$$\frac{W}{W_{pl}} \sim (kD)^2, \tag{11}$$

where W_{pl} is the plasma energy density, D the Debye length. The waves are excited by a particle beam with the velocity v_b at the resonance $k = v_b/\omega_p$ therefore the right hand side of Eq. (11) may be presented as $(v_{th}/v_b)^2$, where v_{th} is the electron thermal velocity. Taking into account that typically $v_b \gg v_{th}$, one can see that the threshold of the instability is rather low. In the relativistic plasma, $v_b \sim v_{th} \sim c$ and $W'_{pl} \sim n'mc^2$ therefore the modulation instability develops only when the wave energy density becomes comparable with the plasma energy density. In this case the induced scattering rate (5) is comparable with the plasma frequency and therefore can not be neglected. Interplay between the two effects should be considered, which has not been done yet. One can only anticipate that the induced scattering makes the development of the modulation instability easier because the wavelength increases.

It is still unclear how formation of cavities with the enhanced wave energy density influences the emission properties of the pulsar plasma. Evidently the effect results in a short term variability. However it is still unclear how outgoing waves are generated. Asseo et al. (1990), Asseo (1993), Melikidze et al. (2000) considered emission from the cavities, or solitons, assuming that they are stable. However Weatherall (1997, 1998) found numerically that the longwave Langmuir solitons collapse like in the nonmagnetized plasma. He suggested that the waves escape from the collapsing cavities because longitudinal electrostatic waves evolve into oblique electromagnetic waves in the course of the collapse. However these waves may be locked within the cavity surrounded by a higher density plasma. More careful analysis is necessary, both numerical and analytical, to clarify the situation. Comparing analytical estimates with the results of numerical simulations, one will be able to find reliable scalings, which may be applied to real pulsars.

3. Propagation effects

3.1. Polarization limiting radius

If the radio emission is generated by the two-stream instability, the wave frequency should be of the order of the plasma frequency at the emission point. Then many observed characteristics of the outgoing radiation, first of all polarization, are dictated by the wave propagation in the magnetospheric plasma. Whatever the emission mechanism, radiation propagates in the plasma in the form of two orthogonally polarized normal waves. Deep inside the magnetosphere, normal waves are linearly polarized; the ordinary wave is polarized in the plane defined by the ambient magnetic field, $\mathbf{B}$, and the wave vector, $\mathbf{k}$, and the extraordinary wave in the $\mathbf{k} \times \mathbf{B}$ direction. The polarization pattern follows, along the ray, the local orientation of the $\mathbf{k} \times \mathbf{B}$ plane; Cheng & Ruderman (1979) used the term "adiabatic walking" to describe the evolution of the ray polarization in this regime. Ultimately the plasma density falls to an extent that the medium no longer affects wave propagation. The observed polarization is fixed in the transition region, at the so called polarization-limiting radius, which is determined by the condition

$$kL\Delta n = 1, \tag{12}$$

where L is the characteristic scale length for changing polarization of the normal waves, Δn the difference in index of refraction between the normal waves. Because all characteristic scales in the pulsar magnetosphere are large as compared with the wavelength, $kL \gg 1$, Δn should be small at the polarization limiting radius, which typically means that both indexes are close to unity, i.e. the local plasma frequency is much lower then the wave frequency. So the polarization-limiting altitude should be significantly higher then the emission altitude.

In pulsar magnetospheres, the polarization-limiting radius was estimated by Cheng & Ruderman (1979), Melrose (1979), Barnard (1986). Unfortunately this value depends not only on the plasma density, which itself is rather uncertain, but also on the angle the wave vector makes with the magnetic field. Since this angle is small, even small deviation of the magnetosphere structure from the pure dipole is of crucial importance. Therefore one cannot firmly fix the polarization-limiting radius until the self-consistent model for the relativistic, rotating magnetosphere will be available.

Observations of the polarization position angle swing, i.e. of the smooth rotation of the plane of linear polarization through the pulse, place limits on the polarization limiting radius. The

observed polarization position angle is determined by the projection of the magnetic field on the plane perpendicular to the ray direction at the polarization limiting radius. Deviations of the magnetosphere structure from the pure dipole at the polarization-limiting radius, as well as the aberration and retardation effects, should affect the position angle vs. pulse longitude curve. The success of the simple rotating vector model in description of the position angle swing (Radhakrishnan & Cooke 1969; Manchester & Tailor 1977) suggests that the polarization-limiting radius is small as compared with the light cylinder radius. In particular, the position angle sweep decreases with the altitude; this was demonstrated by Barnard (1986) for the Deutch magnetosphere but this effect is of general nature (Fig. 3). Large position angle sweeps, which are not uncommon in pulsars, favor for a small polarization limiting radius. Large sweeps may be obtained at large altitudes only if the magnetosphere sweepback caused by rotation is exactly compensated by the rotation itself, so the plasma motion is strictly radial and the magnetic field in the proper plasma frame is also radial. In this case the magnetic axis has exactly the form of the Archemedean spiral. Since the self-consistent model of the pulsar magnetosphere has not available yet, such a possibility cannot be excluded however below the general picture sketched in Fig. 3 is assumed.

The position angle sweep decreases with increasing ratio of the polarization-limiting radius to the light cylinder radius. Therefore the sweep should decrease, in average, with decreasing pulsar period (Barnard 1986). This conclusion agrees with shallow polarization swing observed in millisecond pulsars (Xilouris et al. 1998).

3.2. Circular polarization

The radiation from many pulsars contains detectable circular polarization, although the amounts are generally much less than the degree of linear polarization (e.g., Radhakrishnan & Rankin 1990; Han et al. 1998). The circular polarization naturally arises at high altitudes where the cyclotron frequency is already not too large as compared with the radiation frequency. The normal waves are elliptically polarized in this region if the distribution functions of electrons and positrons are different. This is always the case because the Goldraich-Julian charge density should be maintained in pulsar magnetospheres. Therefore the circular polarization in the outgoing radiation may be attributed to the dispersive properties of the magnetospheric plasma provided the polarization-limiting radius is about the light cylinder radius (Melrose & Stoneham 1977; Cheng & Ruderman 1979; Melrose 1979; von Hoensbroech et al. 1998; von Hoensbroech & Lesch 1999; Gedalin et al. 2001). However large position angle sweeps imply a small polarization limiting radius, at least in significant fraction of pulsars. At such radii, the normal waves are linearly polarized and elliptical polarization may arise from the wave mode coupling in the polarization-limiting region (Cheng & Ruderman 1979).

Deep inside the polarization-limiting radius, where the plasma density is high enough, the normal waves propagate independently and their polarization plane is adjusted to the local orientation of the $\mathbf{k}\times\mathbf{B}$ plane. Outside this region, the plasma density is too low and the waves propagate as in vacuum. In the polarization limiting region, the normal waves are still influenced by the plasma but this influence is insufficient to make the wave polarization follow the orientation of the $\mathbf{k}\times\mathbf{B}$ plane. Provided the $\mathbf{k}\times\mathbf{B}$ plane turns along the ray path, wave mode coupling takes place resulting in the elliptical polarization of the outgoing waves. The $\mathbf{k}\times\mathbf{B}$ plane turns along the ray path due to rotation of the magnetosphere, or due to sweepback of the magnetic field lines caused by the rotation or if the initial co-planarity between $\mathbf{k}$ and the field line fails because of refraction.

The quantitative treatment of the polarization transfer in the rotating magnetosphere was held by Lyubarskii & Petrova (1999) and Petrova & Lyubarskii (2000). They found significant circular polarization of the outgoing radiation, in some cases with the sense reversal near the pulse center. The degree of circular polarization depends on the limiting polarization radius and reaches large values, $V\sim 1$, if this radius is about $r_L\vartheta$, where ϑ is the beam width, r_L the light cylinder radius.

Circular polarization is generally larger in the central part of the pulse profile, in the core beam according to Rankin's (1983a) classification. This property may be naturally explained if the polarization limiting radius is small, $< r_L\vartheta$, such that the magnetic axis remains within the beam (see Fig. 3). In this case the angle between the ray and the magnetic field decreases towards the center of the beam. The lesser this angle, the larger variation in the orientation of the $\mathbf{k}\times\mathbf{B}$ plane may be caused by a small deviation from co-planarity between $\mathbf{k}$ and the field line (Fig. 4). Therefore the circular polarization increases towards the center of the beam. Moreover violation of the regular position angle swing, which is commonly observed in the core beams (e.g., Rankin 1990), may be naturally explained by the same reason. One should also note that the angle between the magnetic field and the ray direction in the cone beam is also not large, therefore the difference between the polarization characteristics of the cone and core beams is not qualitative but only quantitative. This also explains why there is no abrupt transition from the cone to the core emission but merely a gradation of properties across the whole emission beam (Lyne & Manchester 1988; Han et al. 1998).

3.3. Orthogonal polarization modes and depolarization

The plasma in the pulsar magnetosphere is birefringent; the orthogonally polarized ordinary and extraordinary waves propagates independently producing the abrupt orthogonal transitions in polarization position angle that are commonly observed in studies of individual pulse polarization (Manchester et al. 1975; Stinebring et al. 1984a,b; Gil & Lyne 1995; Gangadhara 1997; McKinnon, Stinebring 1998, 2000). The observed depolarization of pulsar average profiles with increasing radio frequency (Manchester et al. 1973; Morris et al. 1981; Xilouris et al. 1996; von Hoensbroech et al. 1998; Kramer et al. 1999) may be attributed to merging of the ordinary and extraordinary beams at high frequency. McKinnon (1997) assumed, following Barnard & Arons (1986), that pulsars emit originally in both radiation modes and all the emission comes from a narrow range of heights above the stellar surface. The extraordinary mode propagates along straight ray paths, while the ordinary waves may be deflected from the original direction by refraction. At low frequencies, refraction separates the two modes resulting in a net polarization. At high frequencies

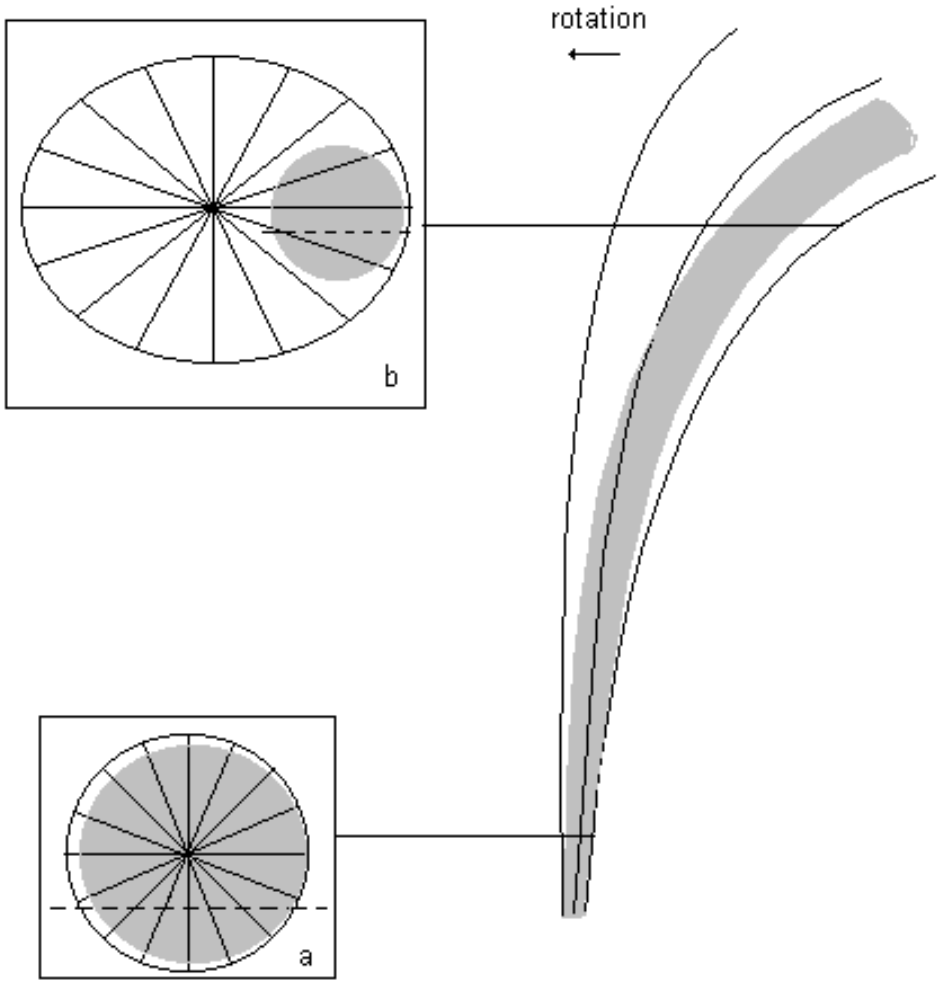


Fig. 3. Propagation of the radio beam within the magnetosphere. The open field line tube is swept back because of rotation. The shaded region traces the beam path within the rotating magnetosphere. In the cross sections *a* and *b*, solid lines show the magnetic planes, the dashed lines trace the path of the line of sight in the course of the magnetosphere rotation. One can see that in the low altitude cross section *a*, the sweep of the magnetic planes, which determines the polarization position angle sweep, may be large whereas in the high altitude cross section *b* the sweep is always small.

(above the local plasma frequency), refraction is negligible and both modes merge producing a non-polarized beam.

It is still unclear if it is possible to generate the extraordinary waves deep inside the magnetosphere where the magnetic field is effectively infinite. In this case, the extraordinary wave, whose electric vector is orthogonal to the background magnetic field, does not interact with the plasma and cannot be emitted, at least in the homogeneous magnetic field. In principle, interaction is possible in a curved magnetic field, especially if one takes into account that the characteristic frequency of the curvature emission in pulsars is of the order of the emitted radio frequency. Unfortunately, nonlinear wave processes in a curved, super strong magnetic field have not been considered yet.

The extraordinary wave may appear in the outgoing radiation due to propagation effects even if initially only ordinary waves were emitted. Because the plasma production process in pulsars may be unsteady, the plasma flow in the open field line tube may be strongly inhomogeneous. One can naturally assume that the plasma is gathered in clouds separated by regions of the very low density such that the condition $\Delta nkL \ll 1$ is satisfied in the inter-cloud space and the waves propagate there preserving the polarization position angle. Now let us consider an ordinary wave emitted within some cloud. Because the frequency of this wave is of the order of the local plasma frequency, refraction deviates the ray from the initial direction such that the ray may come to another plasma cloud where the orientation of the local magnetic field is different from that in the original cloud. Because adiabatic walking ceases in the inter-cloud space, the ray enters the second cloud not in a normal mode corresponding to the local orientation of the magnetic field. Therefore the wave is split into two independently propagating normal waves. This process may produce orthogonal polarization modes and may result in depolarization of the outgoing radiation.

The depolarization mechanism outlined above works if the refraction angle is comparable with the angular width of the open field line tube. Taking into account that the refraction

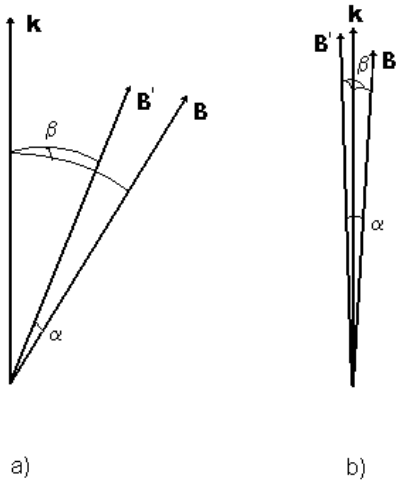


Fig. 4. The turn of the $\mathbf{k} \times \mathbf{B}$ plane caused by a variation of the magnetic field along the ray path. If the angle between the wave direction and the magnetic field is large (a), a turn of $\mathbf{B}$ by a small angle α result in a turn of the $\mathbf{k} \times \mathbf{B}$ plane by a small angle β. If the angle between $\mathbf{k}$ and $\mathbf{B}$ is small (b), a small turn of $\mathbf{B}$ may result in a large turn of the $\mathbf{k} \times \mathbf{B}$ plane.

angle is determined by the transverse density gradient, which decreases with the increasing of the tube width, one can state a general trend: the narrower the open field line tube the less degree of polarization. Then the radius-to-frequency mapping implies that the high frequency radiation, which is emitted at lower heights where the tube is narrow, should be less polarized, what is indeed observed. Another observational finding may be considered as a partial case of the above general trend. Namely because the width of the open field line tube decreases with the increasing pulsar period, depolarization should be more pronounced in slow pulsars. The observed high frequency polarization actually decreases with the pulsar period (Morris et al. 1981; von Hoensbroech et al. 1998).

Recently Petrova (2001b) considered another mechanism for the conversion of ordinary waves into extraordinary ones. Due to refraction, the ray may for a short while become nearly aligned with the local magnetic field. In this degenerate situation, refraction indexes of the two waves become equal and the conversion takes place. Calculations were made in the assumption that the plasma distribution in the open field line tube is axisymmetric, then the refracted ray remains in the plane of the magnetic field line. In the general case, co-planarity between the refracted beam and the field line fails and the ray may never become aligned with the magnetic field. Nevertheless this effect may reveal itself at some phases of the pulsar period.

3.4. Refraction

Refraction was already invoked in the above discussion of the depolarization. Of course the shape of pulses should be also strongly affected by refraction. The observed pulse widths typically broaden with decreasing frequency however at high frequencies (> 1 GHz) the beam width vs. frequency curve commonly flattens (Sieber et al. 1975; Rankin 1983b; Thorsett 1991). Barnard & Arons (1986) attributed this behavior to the refraction. They assumed that all the pulsar emission comes from the same height; then the frequency dependence of the beam width follows the frequency dependence of the refraction angle: at high frequencies refraction is negligibly small and the beam width is constant whereas at low frequencies the beam widens with decreasing frequency due to increasingly strong refraction.

In the model advocated here, radiation is emitted at about the local plasma frequency, which implies the standard radius-to-frequency mapping $\nu \propto r^{-3/2}$. In this case the refraction index, which depends on the ratio ν/ν_p, is the same for any ray at the emission point. However the emission height and the width of the open field line tube increases with decreasing frequency therefore the relative contribution of the refraction into the beam width decreases. Lyubarskii & Petrova (1978) considered the impact of refraction upon the beam width assuming the standard radius-to-frequency mapping and the axisymmetrical plasma distribution in the tube. The ray deviation occurs mainly on account of the density gradient across the tube. If the plasma density decreases towards the edge of the tube, the rays deviate outwards. Then at high frequencies the refraction angle exceeds the angular width of the open field tube and the beam width becomes independent of the frequency whereas at low frequencies the beam widens together with the open field line tube. If the plasma density increases towards the edge of the tube (the density is minimal at the magnetic axis), the ray deviate towards the magnetic axis and, provided the tube is narrow enough, may even reflect from the opposite side of the tube. As a result a trough arises at the beam width vs. frequency curve, which resembles the so called "absorption feature" observed in some pulsars (Rankin 1983b).

Assuming a hollow cone distribution of the plasma in the open field line tube (the plasma density is small at the axis, increases outwards and then decreases towards the edge) one can obtain pulse profiles with three components (Petrova & Lyubarskii 2000; Petrova 2000) resembling those observed in real pulsars. The rays deviating towards the axis form the core beam whereas the rays deviating outwards form the cone beam. Petrova (2001a) demonstrated that the refraction may also account for the unusual apparent structure of the emission region inferred from the observations of the interstellar scintillations (Wolszczan & Cordes 1987; Gupta et al. 1999).

The refraction may affect also the observed pulsar spectrum. Sieber (1997) demonstrated that many properties of the observed spectra may be attributed to the geometry of the beam. Petrova (2002) studied these effects in case the geometry of the beam is determined by refraction.

Of course the assumption about the hollow cone plasma distribution is rather restrictive. The plasma density at the axis should be small if the magnetic field is strictly dipolar down the stellar surface; then the plasma production rate is small at the magnetic axis. However it is naturally to believe

that higher order multipoles contribute to the field at the surface (see however Arons 1993) and then the plasma distribution across the tube is not so regular. Nevertheless one can anticipate that many qualitative features of the ray behavior remain in more general configurations. Let us assume, for example, that the instant plasma distribution in the tube is clumpy because the plasma production process is unsteady. Refraction in such a clumpy medium results in some scatter in the ray directions, which provides a minimal beam width even if the tube becomes very narrow. So saturation of the beam width vs. frequency curve at high frequencies (Sieber et al. 1975; Rankin 1983b; Thorsett 1991) seems to be a rather general feature.

4. Conclusion

It was demonstrated above that a large variety of the observed properties of the pulsar radio emission may be explained self-consistently, at least at the qualitative level, assuming that the emission is generated by the two-stream instability. Of course the theory falls far short of being complete. Evidences for a large transverse size of the emission region inferred from the observations of the interstellar scintillations (Smirnova et al. 1996; Gwinn et al., 1997, 2000; Hirano & Gwinn 2001; Smirnova & Shishov 2001) make a challenge. A possible solution is the scattering of the beam on the plasma inhomogeneities in the upper pulsar magnetosphere (Lyutikov & Parikh 2000; Lyutikov 2001). Another difficult problem is posed by the recent finding that the Vela pulsar emits in the extraordinary polarization mode (Lai et al., 2001). Plasma processes in an effectively infinite magnetic field are believed to emit predominantly in the ordinary mode, at least in the straight magnetic field. Possible emission of the extraordinary mode in the curved magnetic field should be considered.

Acknowledgements. The support by the Heraeus foundation is gratefully acknowledged.

References

Arons J., 1983, ApJ 266, 215
Arons J., 1993, ApJ 408, 160
Arons J., Barnard J.J., 1986, ApJ, 302, 120
Asseo E., 1993, MNRAS 264, 940
Asseo E., Melikidze G. I., 1998, MNRAS 301, 59
Asseo E., Pelletier G., Sol H., 1990, MNRAS 247, 529
Asseo E., Riazuelo A., 2000, MNRAS 318, 983
Barnard J.J., 1986, ApJ 303, 280
Barnard J.J., Arons J., 1986, ApJ 302, 138
Bliokh K.Y., Lyubarskii Y.E., 1996, Astron. Lett., 22, 482.
Bliokh K.Y., Lyubarskii Y.E, 1997, Plasma Phys.Rep. 23, 416
Cheng A.F., Ruderman M.A., 1977, ApJ 212, 800
Cheng A.F., Ruderman M.A., 1979, ApJ 229, 348
Daugherty J. K., Harding A. K., 1982, ApJ 252, 337
Gangadhara R. T., 1997, A&A 327, 155
Gedalin M., Gruman E., Melrose D. B., 2001, MNRAS 325, 715
Gil J., Lyne A.G., 1995, MNRAS 276, L55
Goldman M.N., 1984, Rev.Mod.Phys. 56, 709
Goldreich P., Julian W.H., 1969, ApJ 157, 869
Gupta Y., Bhat N. D. R., Rao A. P., 1999, ApJ 520, 173
Gwinn C. R., Ojeda M. J., Britton M. C., et al., 1997, ApJ 483, L53
Gwinn C. R., Britton M. C., Reynolds J. E., et al., 2000, ApJ 531, 902
Han J.L., Manchester R.N., Xu R.X., Qiao G.J., 1998, MNRAS 300, 373
Hibschman J.A., Arons J., 2001, ApJ 560, 871
Hirano C., Gwinn C. R., 2001, ApJ 553, 358
Kijak J., 2001, MNRAS 323, 537
Kijak J., Gil J., 1998, MNRAS 299, 855
Kramer M., Lange C., Lorimer D. R., et al. 1999, ApJ 526, 957
Lai D, Chernoff D. F., Cordes J.M. 2001, ApJ 549, 1111
Lominadze D.G., Mikhailovskii A.B. & Sagdeev R.Z., 1979, Sov. Phys.-JETP 50, 927 (1979)
Lyne A.G., Manchester R.N., 1988, MNRAS 234, 477
Lyubarskii Y.E., 1992a, A&A 261, 544
Lyubarskii Y.E., 1992b, A&A 265, L33
Lyubarskii Y.E., 1993a, Astron.Lett. 19, 14
Lyubarskii Y.E., 1993b, Astron.Lett. 19, 208
Lyubarskii Y.E., 1996, A&A, 308, 809
Lyubarskii Y.E., Petrova S.A., 1998, A&A 333, 181
Lyubarskii Y.E., Petrova S.A., 1999, Ap&SS 262, 379
Lyubarskii Y. E., Petrova S. A., 2000, A&A 355, 406
Lyutikov M., 1999, ApJ 525, L37
Lyutikov M., 2000, MNRAS 315, 31
Lyutikov M., 2001, Ap&SS 278, 81
Lyutikov M., Parikh A., 2000, ApJ 541, 1016
Machabeli G.Z., 1983, Soviet J.Plasma Phys. 9, 1177
Manchester R.N., Tailor J.H., 1977, Pulsars. W.H.Freeman and Company, San Francisco
Manchester R.N., Tailor J.H., Huguenin G.R., 1973, ApJ 179, L7
Manchester R.N., Tailor J.H., Huguenin G.R., 1975, ApJ 196, 83
McKinnon M.M., 1997, ApJ 475, 763
McKinnon M.M., Stinebring D.R., 1998, ApJ 502, 883
McKinnon M.M., Stinebring D.R., 2000, ApJ 529, 435
Melikidze G. I., Gil J. A., Pataraya A. D., 2000, ApJ 544, 1081
Melrose D.B., 1978, ApJ 225, 557
Melrose D.B., 1979, Austr.J.Phys, 32, 61
Melrose D.B., 1980. Plasma Astrophysics. Gordon and Breach, NY
Melrose D. B., Gedalin M. E., 1999, ApJ 521, 351
Melrose D.B., Stoneham R.J., 1977, Proc.Astr.Soc.Austr. 3, 120
Morris D., Graham D.A., Sieber W., 1981, A&A 100, 107
Petrova S.A., 2000, A&A 360, 592
Petrova S.A., 2001a, MNRAS 324, 931
Petrova S.A., 2001b, A&A 378, 883
Petrova S.A., 2002, A&A 383, 1067
Petrova S.A., Lyubarskii Y. E., 2000, A&A 355, 1168
Radhakrishnan V., Cooke D.J., 1969,Astrophys.Lett., 3, 225
Radhakrishnan V., Rankin J.M., 1990, ApJ 352, 258
Rankin J.M., 1983a, ApJ 274, 333
Rankin J.M., 1983b, ApJ 274, 359
Rankin J.M., 1990, ApJ 352, 247
Rankin J.M., 1993, ApJ 405, 285
Rowe E.T., 1995, A & A 296, 275
Ruderman M.A., Sutherland P.G., 1975, ApJ 196, 51
Scharlemann E. T., 1974, ApJ 193, 217
Schopper R.,Kunzl T.A., Ruhl H., Lesch H., 2002, these proceedings
Sieber W., 1997, A&A 321, 519

Sieber W., Reinecke R., Wielebinski R., 1975, A&A 38, 169
Smirnova T. V., Shishov V. I., 2001, Ap&SS 278, 71
Smirnova T. V., Shishov V. I., Malofeev V. M., 1996, ApJ 462, 289
Stinebring D.R., Cordes J.M., Rankin J.M., Weisberg J.M., Boriakoff V., 1984a, ApJS 55, 247
Stinebring D.R., Cordes J.M., Rankin J.M., Weisberg J.M., Boriakoff V., 1984b, ApJS 55, 279
ter Haar D., Tsytovich V.N., 1981, Phys.Rep. 73, 175
Thorsett S. E., 1991, ApJ 377, 263
Tsytovich V.N., 1970, Non-linear Effects in Plasma. Plenum Press
Ursov V.N. & Usov V.V., 1988, Ap&SS 140, 325
Usov V.V., 1987, ApJ 320, 333
Volokitin A.S., Krasnoselskikh V.V., Machabeli G.Z., 1985, Sov.J.Plasma Phys. 11, 531
von Hoensbroech A., Kijak J., Krawczyk A., 1998, A & A 334, 571
von Hoensbroech A., Lesch H., 1999, A & A 342, L57
von Hoensbroech A., Lesch H., Kunzl T., 1998, A & A 336, 209
von Hoensbroech A., Xilouris K. M., 1997, A & A 324, 981
Weatherall J. C., 1997, ApJ 483, 402
Weatherall J. C., 1998, ApJ 506, 341
Weatherall J. C., 2001, ApJ 559, 196
Wolszczan A., Cordes J. M., 1987, ApJ 320, L35
Xilouris K. M., Kramer M., Jessner A., et al., 1996, A & A 309, 481
Xilouris K.M., Kramer M., Jessner A., et al., 1998, ApJ 501, 286

Proceedings of the 270. WE-Heraeus Seminar on: *"Neutron Stars, Pulsars and Supernova Remnants"*
Physikzentrum Bad Honnef, Germany, Jan. 21-25, 2002, eds. W. Becker, H.Lesch & J. Trümper, MPE Report 278, pp. 240-248

Two-stream Instability in Pulsar Magnetospheres

V.V. Usov

Department of Condensed Matter Physics, Weizmann Institute of Science, Rehovot 76100, Israel

Abstract. Creation of electron-positron pairs near the pulsar surface and the parameters of plasma in pulsar magnetospheres are discussed. It is argued that the pair creation process is non-stationary, and the pair plasma that flows out from the pulsar environment is strongly non-homogeneous and gathers into separate clouds. Plasma instabilities in the outflowing plasma are reviewed. The two-stream instability that develops due to strong non-homogeneity of the outflowing plasma is the most plausible reason for the generation of coherent radio emission of pulsars. The development of the two-stream instability in pulsar magnetospheres is considered.

1. Introduction

Current models for the generation of coherent radio emission of pulsars require the development of plasma instabilities in the pulsar magnetospheres, the most studied of which is the two-stream instability (for a review, see Arons 1981a,b; Melrose 1981, 1993, 1995; Usov 1981; Asseo 1996). The two-stream instability in the pulsar magnetospheres has been considered in many papers (e.g., Ruderman & Sutherland 1975; Benford & Buschauer 1977; Buschauer & Benford 1977; Cheng & Ruderman 1977; Arons 1981; Usov 1987; Ursov & Usov 1988; Asseo 1993; Asseo & Melikidze 1998; Melikidze, Gil & Pataraya 2000).

The two-stream instability can arise when two plasma flows travel through each other:

$$\Longleftarrow \quad \mathbf{v}_1,\, n_1$$
$$\mathbf{v}_2,\, n_2 \quad \Longrightarrow$$

If the density of one flow is much higher than the density of the other (for example, $n_1 \gg n_2$), the low-density flow (component 2) calls the beam while the high-density flow (component 1) calls the plasma. In the magnetospheres of pulsars, both the plasma-beam interaction and the interaction of two plasmas with more or less equal densities may occur (see below). The two-stream instability may lead to formation of plasma bunches that generate the radio emission via curvature mechanism (Ruderman & Sutherland 1975; Cheng & Ruderman 1980; Ochelkov & Usov 1984). Besides, the radio emission of pulsars may be generated directly in the process of the instability development (Asseo, Pellat & Rosado 1980; Asseo, Pellat & Sol 1983). Before to discuss the two-stream instability in the pulsar plasma and the generation of coherent radio emission of pulsars, we review both the physical processes that are responsible for the filling of pulsar magnetospheres with plasma and the plasma parameters.

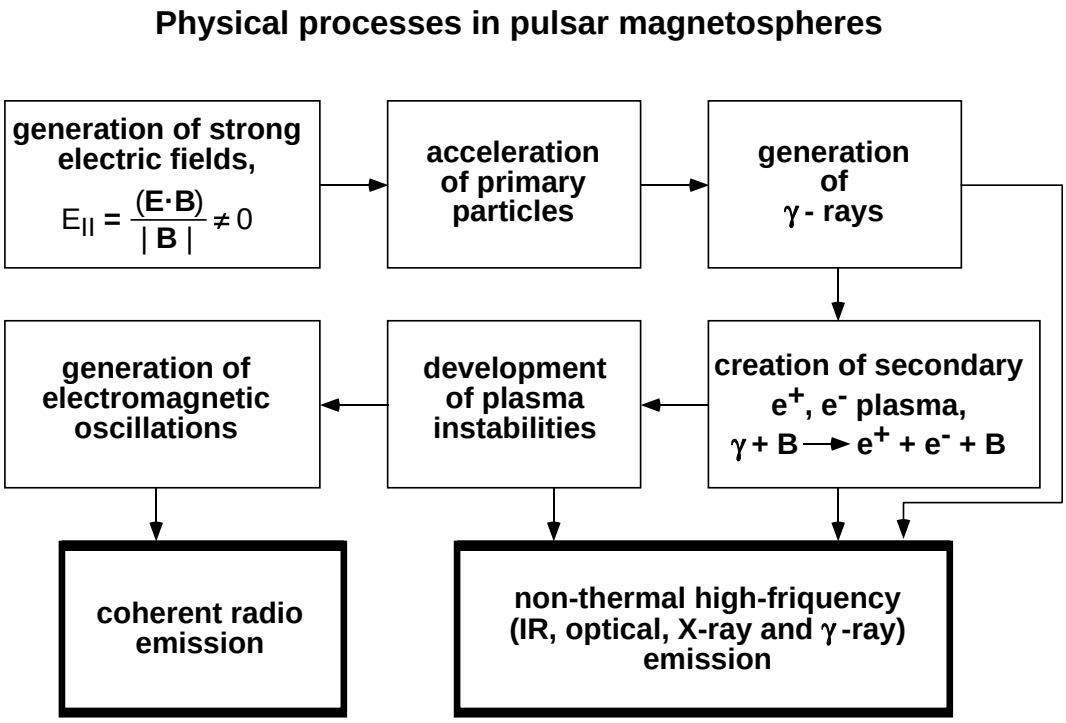
2. Physical processes and parameters of plasma in pulsar magnetospheres

A common point of all acceptable models of pulsars is that the spin-down power of strongly magnetized neutron stars is the energy source of non-thermal emission of pulsars. The rotational energy of the neutron star is transformed into the pulsar emission by a long sequence of processes.

2.1. Physical processes in pulsar magnetospheres

Strong electric fields are generated in the magnetospheres of rotating magnetized neutron stars (for a review, see Michel 1991). The component of the electric field $\mathbf{E}_{\|} = (\mathbf{E}\cdot\mathbf{B})\mathbf{B}/|\mathbf{B}|^2$ along the magnetic field $\mathbf{B}$ is non-zero. Primary particles are accelerated by this electric field to ultrarelativistic energies and generate γ-rays. Some of these γ-rays are absorbed by creating secondary e^+e^- pairs. The created pairs screen the electric field $\mathbf{E}_{\|}$ in the pulsar magnetosphere everywhere except for compact regions. The compact regions where $\mathbf{E}_{\|}$ is unscreened are called gaps. These gaps are "engines" that are responsible for the non-thermal radiation of pulsars. The gaps are located either near the magnetic poles of pulsars (polar gaps) or near their light cylinders (outer gaps). Outer gaps may act as a generator of non-thermal radiation of pulsars only if the period of the pulsar rotation is small enough, $P < P_{\rm cr} \simeq$ a few $\times\, 0.1$ s. For typical pulsars with $P > P_{\rm cr}$, the polar gap model has no an alternative. In the polar gap model the sequence of processes that leads to the generation of non-thermal emission of pulsars is the following:

The density of primary particles accelerated in the polar gap is about the Goldreich-Julian density $n_{\rm GJ} = |\mathbf{\Omega}\cdot\mathbf{B}|/2\pi ce$, where $\mathbf{\Omega}$ is the angular velocity of the pulsar rotation. The value of $n_{\rm GJ}$ is determined so that the electric field $E_{\|}$ in the outflowing plasma is screened completely if the charge density is equal to $en_{\rm GJ}$. Therefore, the accelerating field $E_{\|}$ arises from deviations from this density. Such a deviation may be because of (1) the inertia of particles (Michel 1974), (2) the curvature of the magnetic field lines (Arons 1981), the General Relativity effects (Muslimov & Tsygan 1992, Beskin 1992), and the



binding of particles within the solid surface of a strongly magnetized neutron star (Ruderman & Sutherland 1975; Cheng & Ruderman 1980; Usov & Melrose 1995, 1996). When both the neutron star surface is cold enough and the surface magnetic field is strong enough, there is no emission of particles from the neutron star surface, and the binding of particles is responsible for the $E_{\|}$ field in the polar gaps (e.g., Usov & Melrose 1996). In the case when particles flow freely from the stellar surface, the field $E_{\|}$ is mainly due to the General Relativity effects (i.g., Harding & Muslimov 1998). The second case is applicable to typical pulsars while the former case may be applied to pulsars with very strong magnetic fields at their surface, $B_{\rm S} \sim 10^{13}$ G or more.

Ultrarelativistic primary particles in the process of their outflow move practically along the magnetic field lines and generate γ-rays via both curvature radiation and magnetic Compton scattering. These γ-rays are absorbed in strong magnetic fields of pulsar magnetospheres and create e^+e^- pairs. Created pairs very quickly lose the momentum component transverse to the magnetic field due to synchrotron losses, and their distribution becomes one-dimensional, i.e., $\mathbf{v} \parallel \mathbf{B}$. Hence, to develop the theory of coherent radio emission of pulsars it is necessary to investigate both the parameters of ultrarelatistic one-dimensional plasma outflowing from the polar cap regions and instabilities of this plasma.

2.2. Parameters of pulsar plasma

Electrons and positrons that flow away from the neutron star vicinity with relativistic speeds may be divided into two components: a secondary e^+e^- plasma and an extremely high-energy beam of primary particles (see Fig. 1). Particles of the beam may be either electrons or positrons, depending on the direction of the electric field $\mathbf{E}_{\|}$ in the polar gap. For the e^+e^- plasma (denoted by p) and the ultrarelativistic beam (denoted by b) the typical values of the Lorentz factor Γ and the density n are, respectively, (Ruderman & Sutherland 1975; Arons 1981a,b, 1984; Machabeli & Usov 1989; Michel 1991)

$$\Gamma_p \simeq (2-3)R_c/R \simeq \text{a few} \times (1-10^2)\,, \qquad (1)$$

$$\Gamma_b \simeq e\Delta\varphi/m_e c^2 \simeq \text{a few} \times 10^6\,, \qquad (2)$$

$$n_p \simeq (\Gamma_b/2\Gamma_p)n_b\,, \qquad (3)$$

$$n_b \simeq n_{\rm GJ} = \Omega B/(2\pi ce) \simeq 10^{11}(R/r)^3 \text{ cm}^{-3}\,, \qquad (4)$$

We have adopted here the following characteristic values for the pulsar parameters: $\Omega \simeq 10$ s^{-1}; $B \simeq 10^{12}(R/r)^3$ G is the magnetic field in the magnetosphere; R_c is the curvature radius of the magnetic field lines in the polar cap; $R \simeq 10^6$ cm is the neutron star radius; and $\Delta\varphi$ is the potential drop across the polar gap.

2.3. Nonstationarity of the plasma outflow

It was suggested long time ago that the process of pair creation near the pulsar surface is strongly nonstationary (Sturrock 1971; Alber et al. 1975; Ruderman and Sutherland 1975). Such a nonstationarity was discussed in detail in the outstanding paper by Ruderman and Sutherland (1975) where the first self-consistent model of pulsar radiation was presented. In the Ruderman-Sutherland model, the creation of pairs occurs in narrow spark discharges, separated from one another by a distance of the order of the polar gap height H (characteristic value of H is $\sim 10^4$ cm). The secondary e^+e^- plasma, produced by absorption of γ-rays in a spark discharge, gathers into an outflowing jet that has the discharge at its base. Such a discharge is strongly nonstationary on a time scale of $\sim 30(H/c)$

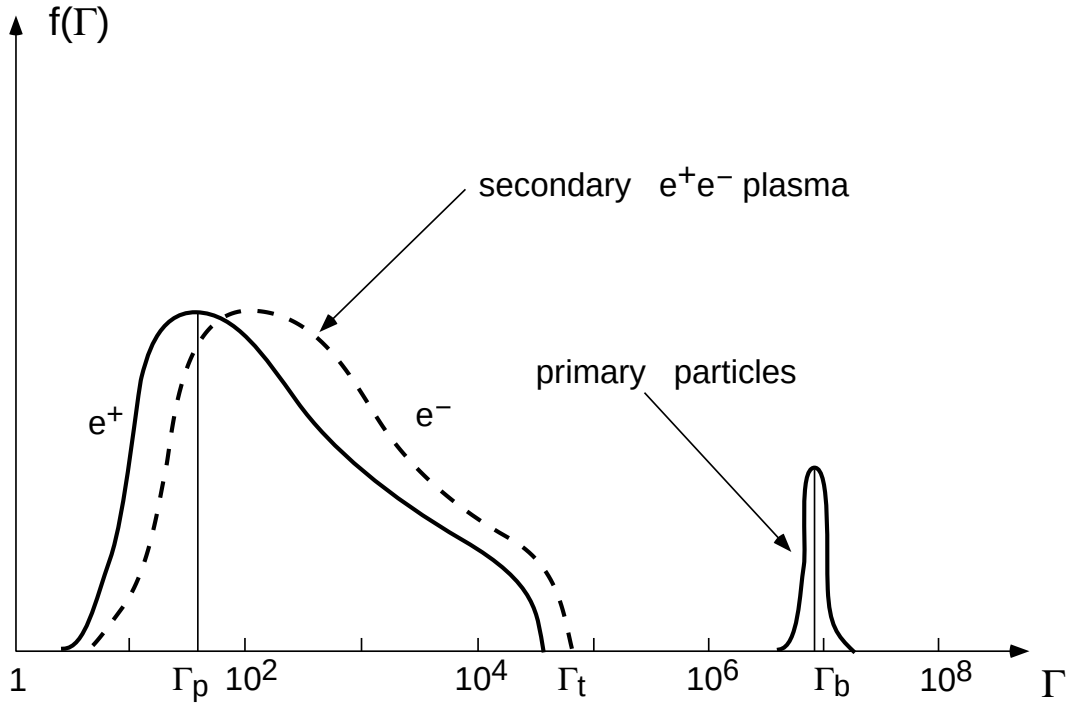


Fig. 1. The energy spectrum of the basic components of the plasma particles ejected from the polar gap region into the pulsar magnetosphere. The spectra of secondary electrons (dashed line) and secondary positrons (solid line) are shifted relatively each other.

(Ruderman & Sutherland 1975; Cheng & Ruderman 1980). The discharge nonstationarity results in a strong modulation of the outflowing pair plasma along the jet. In fact, these jets consist of plasma clouds spaced by $L_1 \simeq 30H \simeq 0.3R$.

However, it is not only the nonstationarity of discharges that can lead to inhomogeneity of the outflowing plasma along the fixed magnetic field lines. Another reason for such a inhomogeneity is the displacement of discharges caused by the curvature of the magnetic field lines (Ruderman & Sutherland 1975). The displacement is directed toward the magnetic axis of the pulsar. The speed with which a spark discharge moves across the polar cap is estimated (Ruderman & Sutherland 1975; Cheng & Ruderman 1980) as $v_d \simeq cH/2R_c$. As already noted above, the average distance between two discharges is $\sim H$. During the time $\tau_d \simeq H/v_d \simeq 2R_c/c$, a discharge is displaced by the distance of $\sim H$ and takes a position close to the initial position that of a neighboring discharge, which during the same time is also displaced by $\sim H$ toward the pulsar magnetic axis. As a result of these displacements of discharges, the plasma outflowing along any fixed magnetic field lines becomes modulated with a characteristic length $L_2 \simeq c\tau_d \simeq 2R_c$. Since, according to Ruderman and Sutherland (1975) and Beskin (1982), in the polar gap the discharges are separated by intervals within which the process of pair creation is suppressed, the plasma density in between the clouds falls down almost to zero. Therefore, the outflowing plasma gathers into separate clouds spaced by $L_2 \simeq 2R_c$ along the direction of the plasma outflow. In turn, these large clouds consist of small clouds with the lengths and the spaces between them about $L_1 \simeq 0.3R$.

The idea that the process of pair creation near the polar caps of pulsars is nonstationary has got recently the strong support (e.g., Muslimov & Harding 1997; Harding & Muslimov 1998). In these papers, the model of the polar gaps of typical pulsars which is rather close to reality is developed. In this model, it was shown that both stable acceleration of primary particles and stable creation of pairs are not possible. The characteristic length of the outflowing plasma modulation is expected more or less comparable with L_1.

3. Possible instabilities in pulsar plasma

Development of instabilities in a magnetized plasma when transverse electromagnetic waves (t-waves) are generated depends on the ratio ω_p/ω_B, where

$$\omega_p = \sqrt{\frac{4\pi e^2 n_p}{m_e}} \simeq 5.64 \times 10^4 n_p^{1/2} \ \mathrm{s}^{-1}\,, \tag{5}$$

$$\omega_B = \frac{eB}{m_e c} \simeq 1.76 \times 10^7 B \ \mathrm{s}^{-1}\,, \tag{6}$$

are the Langmuir frequency of the plasma and the cyclotron frequency, respectively. At the pulsar surface for the typical parameters of both the pulsar plasma and the strength of the magnetic field ($n_{p_0} \sim 10^{14}$ cm^{-3} and $B_{\mathrm{S}_0} \sim 10^{12}$ G), from equations (5) and (6) we have $\omega_{p_0}/\omega_{\mathrm{B}_0} \sim 10^{-7}$.

Since the difference between the phase velocity (v_{ph}) of t-waves and the speed of light is extremely small at the pulsar surface (e.g., Lominadze, Machabeli & Usov 1983),

$$c - v_{\mathrm{ph}} \sim c(\omega_{p_0}/\omega_{\mathrm{B}_0})^2 \Gamma_p \sim 10^{-13} c \tag{7}$$

in the frame of the pair plasma, particles of both the plasma and the beam cannot be in a resonance with t-waves that prop-

agate in the pulsar plasma, and resonance instabilities (for example, the cyclotron instability) do not develop in the neutron star vicinities.

Besides, the energy density of plasma ($\varepsilon_p \simeq m_e c^2 n_p \Gamma_p$) is very small in comparison with the energy density of the magnetic field ($\varepsilon_{\rm B} = B^2/8\pi$),

$$\varepsilon_p/\varepsilon_{\rm B} \sim 2(\omega_{p_0}/\omega_{\rm B_0})^2 \Gamma_p \sim 10^{-13} \qquad (8)$$

Therefore, hydrodynamic instabilities are also suppressed near the pulsar surface by the strong magnetic field.

In the near zone of the pulsar magnetosphere ($r < c/\Omega$), we have $n_p \propto B \propto r^{-3}$. The ratio $\omega_p/\omega_{\rm B}$ increases with increase of the distance from the pulsar, $\omega_p/\omega_{\rm B} \propto r^{3/2}$. Near the light cylinders of pulsars the ratio $\omega_p/\omega_{\rm B}$ is of the order of unity, and the outflowing plasma may be unstable with respect to excitation of t-waves (e.g., Machabeli & Usov 1979, 1989; Lominadze et al. 1983; Lyutikov, Machabeli & Blandford 1999 and references therein). At the distance from the pulsar in the range $R \leq r \ll c/\Omega$ only the two-stream instability may be developed.

Observations of pulsars suggest that the radio emission regions are far inside the light cylinder (e.g., Gil & Kijak 1993; Kramer et al. 1994; Kijak & Gil 1997),

$$r_{\rm radio} \simeq 50R \simeq (0.02 - 0.04)\, c/\Omega \ll c/\Omega\,, \qquad (9)$$

Therefore, the development of the two-stream instability in the magnetospheres of pulsars is the most plausible reason of their extremely intense radio emission.

4. Two-stream instability

The two-stream instability may occur only if (1) there is a "hump" on the momentum distribution function $f(p)$, i.e. a region having $\partial f/\partial p > 0$, and (2) in the frame where plasma is at rest the mean momentum of the "hump" particles ($p_{\rm b}$) is large enough in comparison with the mean momentum of the plasma particles (the Penrose criteria). Particles, which are in the inside slope of the "hump" where $\partial f/\partial p > 0$, produce longitudinal ($l$) waves with the frequency $\omega = (\mathbf{k}, \mathbf{v})$ (the Cherenkov resonance), where $\mathbf{k}$ is the wave vector (see Fig. 1). These particles thus lose their energy. As a result the inside slope of the "hump" begins to move into the region of even lower velocities, and the distribution function of the "hump" particles becomes "plateau-shaped" (see, Fig. 1). The further generation of l-waves is cut off. The plateau formation and the cut-off in the plasma wave generation is called the quasi-linear relaxation. The energy density of l-waves generated in the process of quasi-linear relaxation is of the order of the energy density of the "hump" particles.

A strong magnetic field has no an influence on the development of the two-stream instability in the one-dimensional plasma outflowing from the polar cap regions of pulsars, and therefore, this instability may occur everywhere in the pulsar magnetosphere if the mentioned above conditions for its development are realized. Since there are several components of particles in the pulsar plasma that move with different speeds, the idea that the two-stream instability is responsible for the coherent radio emission of pulsars is very natural.

The two-stream instability could be developed due to the following three reasons. The first one is the interaction between the beam of primary particles and the secondary e^+e^- plasma (Ruderman & Suthermand 1975). The second one is the interaction between electrons and positrons of the secondary plasma itself (Cheng & Ruderman 1977). At last, the two-stream instability may be triggered in the inhomogeneous pulsar plasma when the outflowing plasma clouds disperse and overlap each other (Usov 1987; Ursov & Usov 1988; Asseo & Melikidze 1998).

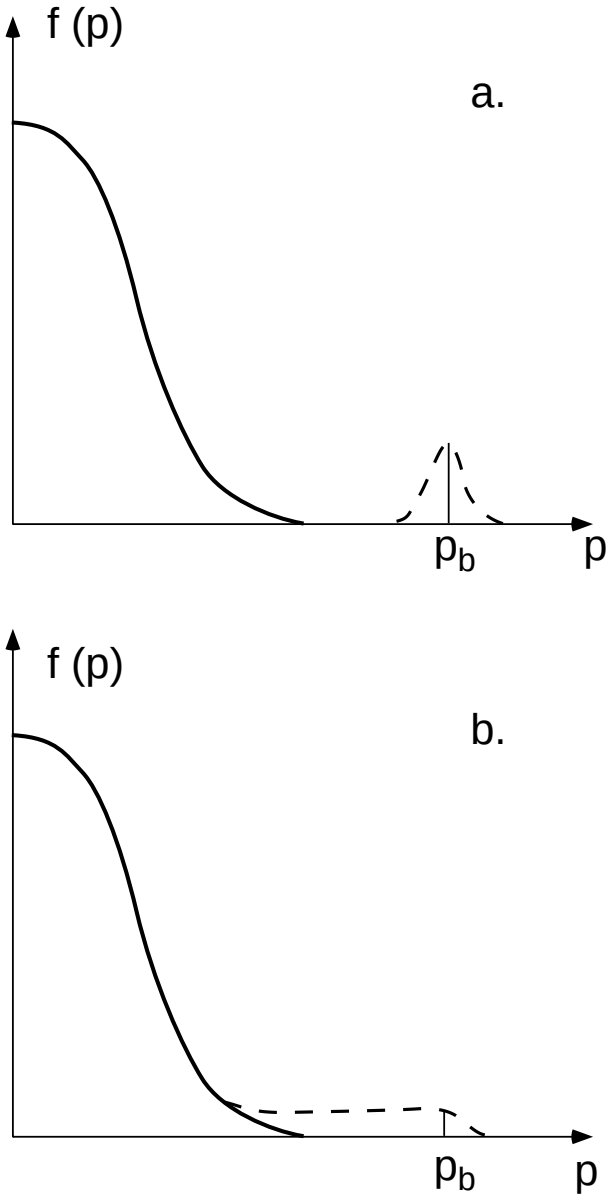


Fig. 2. The momentum distribution function of particles for a plasma-beam system: (a) prior and (b) after the development of the two-stream instability.

4.1. The interaction between the primary beam and the secondary plasma

The ultrarelativistic beam of primary particles has the distribution function that obeys the conditions that are necessary

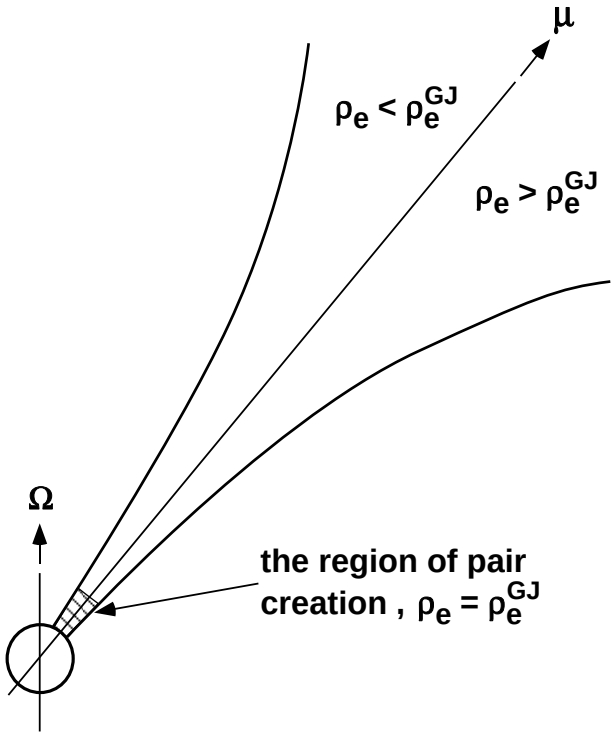


Fig. 3. Charge flow separation of the pulsar plasma moving outward along the curved magnetic field lines; μ is the magnetic dipole moment.

for the two-stream instability development (see Fig. 1). Therefore, the generation of radio emission of pulsars was initially associated with the ultrarelativistic beam of primary particles (Ruderman & Sutherland 1975). However, further more precise estimates of the instability growth rate have shown that it is impossible. Indeed, the characteristic time for development of the two-stream instability in the pulsar frame is (Benford & Buschauer 1977; Egorenkov, Lominadze & Mamradze 1983)

$$\tau_i \simeq (n_p/n_b)^{1/3}\Gamma_b\Gamma_p^{1/2}\omega_p^{-1}. \qquad (10)$$

From equations (1)-(4), (5) and (10), for typical pulsars the value of τ_i is about $10^{-4}(r/R)^{3/2}$ s at the distance r from the neutron star. For the instability development, it is necessary that τ_i is, at least, a few times less than $\tau_0 = r/c \simeq 3\times10^{-5}(r/R)$ s, the characteristic time of the plasma outflow from the distance r. However, the reverse relation between τ_i and τ_0 holds. Hence, the two-stream instability that, in principal, could be caused by the primary beam because its distribution function forms a "hump" with $\partial f/\partial p > 0$, in fact, has not enough time to be developed in the pulsar magnetospheres. This is because both the beam density is too low and the Lorentz-factor of the beam is too high.

4.2. The interaction between the electrons and the positrons of the secondary plasma

The secondary e^+e^- plasma produced by photons initially has identical distribution functions in its components (electrons and positrons). In this case, the pair plasma is neutral, and the charge density ρ_e is determined by the primary beam and equals to $\rho_e^{\rm GJ} = en_{\rm GJ}$. In the process of the plasma outflow the charge density ρ_e is $\propto n \propto B$ while $\rho_e^{\rm GJ}$ is $\propto B\cos\chi$, where χ is the angle between $\mathbf{\Omega}$ and $\mathbf{B}$. The magnetic field lines are curved, and therefore, the angle χ varies with the distance from the pulsar. This leads to a deviation of ρ_e from $\rho_e^{\rm GJ}$ and generation of the electric field along the magnetic field (see Fig. 3). This field accelerates one of the components of the secondary plasma and decelerates the other, and the distribution functions of these components shift to each other. The difference between the mean velocities of the electrons and the positrons is (Cheng & Ruderman 1977)

$$|v_+ - v_-| \simeq \frac{n_b}{n_p}\left[\frac{\mathbf{\Omega}\cdot\mathbf{B}}{(\mathbf{\Omega}\cdot\mathbf{B})_0} - 1\right]c, \qquad (11)$$

where $(\mathbf{\Omega}\cdot\mathbf{B})_0$ is the $\mathbf{\Omega}$ and $\mathbf{B}$ product taken at the region of pair creation.

Far the neutron star ($r \gg R$), equations (3) and (11) yield

$$\frac{|\Gamma_+ - \Gamma_-|}{\Gamma_p} \simeq \frac{r\Omega}{c}\frac{\Gamma_p^3}{\Gamma_b} \qquad (12)$$

where

$$|\Gamma_+ - \Gamma_-| \simeq \frac{|v_+ - v_-|}{c}\Gamma_p^3. \qquad (13)$$

Using a relativistic generalization of the Penrose criteria (Buschauer & Benford 1977; Krall & Trivelpiece 1986) and equation (12), the condition for development of the two-stream instability may be written as

$$\Gamma_p > 2\times10^2(c/r\Omega)^{1/3}. \qquad (14)$$

From equation (14) we can see that the two-stream instability, which develops because of the relative motion of the secondary plasma components, may occur only rather near the light cylinder of pulsars. Besides, the magnetic field near the pulsar surface must be close to the dipole field when the Lorentz-factor of the secondary particles is equal to its maximum (see, equation (1)).

4.3. The interaction between clouds of the secondary plasma

Here the nonstationarity of plasma ejection from the polar gap regions is modeled as follows. Plasma particles (electrons and positrons) are ejected along the z-axis from $z = 0$ during the time T with Lorentz-factors ranging from $\Gamma_{\rm min}$ to $\Gamma_{\rm max}$, so that $\Gamma_{\rm max} \gg \Gamma_{\rm min} \gg 1$. Then over the time τ no particles are ejected, after that everything is repeated. In other words, we assume that the secondary e^+e^- plasma is ejected in the form of separate isolated clouds with the length cT along the z-axis, and the space between these clouds is $c\tau$.

At $z = 0$, the distribution of ejected particles over Lorentz-factors is described by the function $f_o(\Gamma)$ determined from the condition that the number of particles dn_p per volume dV with energies from $m_ec^2\Gamma$ to $m_ec^2(\Gamma + d\Gamma)$ is equal to

$$dn_p = n_p dV f_o(\Gamma)d\Gamma. \qquad (15)$$

The distribution function thus determined is normalized to unity, i.e.,

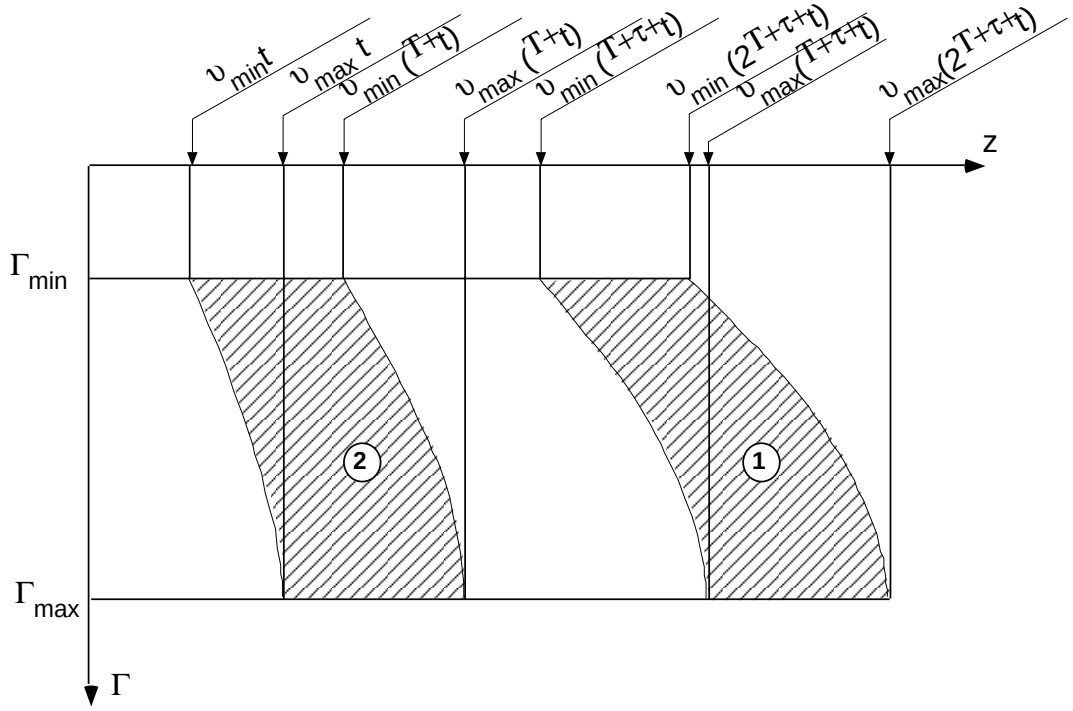


Fig. 4. Particle distribution over the plane with coordinates z and Γ at the instant t. The regions with particles are shaded. The first and the second clouds of plasma are numerated by 1 and 2.

$$\int_{\Gamma_{\min}}^{\Gamma_{\max}} f_o(\Gamma) d\Gamma = 1\,. \tag{16}$$

The pulsar plasma can be regarded as collisionless. Therefore, the spatial and energy distribution of outflowing particles at $z > 0$ may be found from simple kinematic relations.

To study the dispersion of plasma clouds and their mutual overlapping it is sufficient to consider the outflow of two successively ejected clouds. It is expedient to draw the distribution of particles in the z- and Γ-coordinates (see Fig. 4). In our case the initial time ($t = 0$) is the moment when the ejection of particles of the second cloud is just finished.

At the time

$$t_o = \frac{v_{\min}(T+\tau) - v_{\max} T}{v_{\max} - v_{\min}} \simeq 2\Gamma_{\min}^2 \tau \tag{17}$$

determined from the equation

$$v_{\min}(T + \tau + t_o) = v_{\max}(T + t_o)\,, \tag{18}$$

the fast particles of the second cloud catch up with the slow particles of the preceding cloud, and mutual overlapping of the clouds begins, where

$$v_{\min} = [1 - (1/\Gamma_{\min})^2]^{1/2} c\,, \tag{19}$$

$$v_{\max} = [1 - (1/\Gamma_{\max})^2]^{1/2} c\,. \tag{20}$$

The width of the overlapping region at $t > t_o$ is

$$\Delta = v_{\max}(T + t) - v_{\min}(T + \tau + t)\,. \tag{21}$$

The distribution function of particles in the overlapping region is (see Fig. 5)

$$f(\Gamma, z, t) = \begin{cases} 0\,, & \Gamma < \Gamma_1\,, \\ f_o(\Gamma)\,, & \Gamma_1 < \Gamma < \Gamma_2\,, \\ 0\,, & \Gamma_2 < \Gamma_3\,, \\ f_o(\Gamma)\,, & \Gamma_3 < \Gamma < \Gamma_4\,, \\ 0\,, & \Gamma_4 < \Gamma\,, \end{cases} \tag{22}$$

where

$$\Gamma_i = [1 - (v_i/c)^2]^{-1/2}, \quad i = 1, 2, 3, 4, \tag{23}$$

$$v_1 = v_{\min}, \quad v_2 = \frac{z}{T + \tau + t}\,, \tag{24}$$

$$v_3 = \frac{z}{T + t}, \quad v_4 = v_{\max}. \tag{25}$$

In the overlapping region, there are, in fact, two streams of slow and fast particles (see Fig. 5). This may lead to development of the two-stream instability. A simple approximation where plasma is one-dimensional and homogeneous may be employed for consideration of this instability in the overlapping regions of plasma clouds in the magnetospheres of pulsars (Usov & Ursov 1988). In this approximation, the dispersion equation for l-waves with $\mathbf{k} \parallel \mathbf{v} \parallel \mathrm{B}$ is

$$1 - \frac{4\pi e^2 n_p}{m_e} \int \frac{f(\Gamma, z, t) d\Gamma}{\Gamma^3 (\omega - kv)^2} = 0 \tag{26}$$

At the initial stage of clouds overlapping, when the width of the overlapping region is much smaller than the width of the clouds, along the z-axis, $\Delta \ll cT$, the function $f(\Gamma, z, t)$ describes two groups of practically monoenergetic particles at velocities v_2 and v_4. Taking this into account, equation (26) may be written as

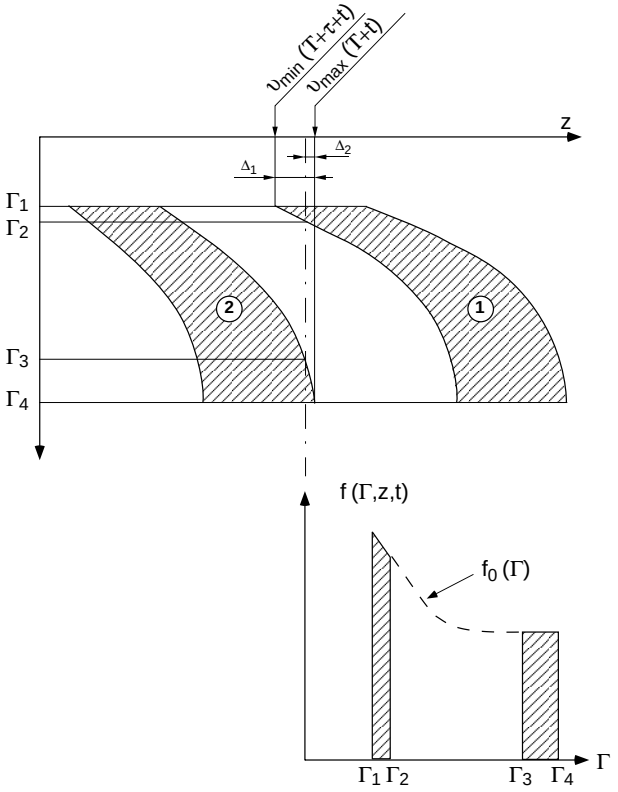


Fig. 5. Overlapping of plasma clouds at $t > t_0$. The regions with particles are shaded. In the overlapping region, z meets the condition $v_{\min}(T+\tau+t) < z < v_{\max}(T+t)$. The distribution function of particles in the overlapping region at the distance z from the pulsar surface is shown in the bottom.

$$1 - \omega_p^2 \left[\frac{\alpha}{(\omega - k v_2)^2} + \frac{\beta}{(\omega - k v_4)^2} \right] = 0 \qquad (27)$$

where

$$\alpha = \int_{\Gamma_1}^{\Gamma_2} \frac{f_o(\Gamma)}{\Gamma^3} d\Gamma \,, \quad \beta = \int_{\Gamma_3}^{\Gamma_4} \frac{f_o(\Gamma)}{\Gamma^3} d\Gamma \,. \qquad (28)$$

From equation (27), the maximum growth rate of l-waves is (Ursov & Usov 1988)

$$\mathrm{Im}\,\omega_{\max} = \frac{\sqrt{3}}{2} \alpha^{1/2} \left(\frac{\beta}{2\alpha} \right)^{1/3} \omega_p \,, \qquad (29)$$

and occurs for the wave vector

$$k_{\rm res} = \frac{\alpha^{1/2} \omega_p}{v_4 - v_2} \qquad (30)$$

that corresponds to a resonance between plasma oscillations of the slow ($\Gamma_1 < \Gamma < \Gamma_2$) flow and high-energy particles of the fast ($\Gamma_3 < \Gamma < \Gamma_4$) flow.

Since for the slow and fast flows the Γ ranges of plasma particles are narrow for slightly overlapping clouds ($\Delta \ll c\tau$), the function $f_0(\Gamma)$ in equations (28) can be factored out the integral sigh and then to integrate:

$$\alpha \simeq \frac{f_o(\Gamma_1)}{2} \frac{\Gamma_2^2 - \Gamma_1^2}{\Gamma_1^2 \Gamma_2^2} = \frac{v_2 - v_1}{c} f_o(\Gamma_1) \simeq \frac{\Delta_1}{c t_o} f_o(\Gamma_{\min}) \qquad (31)$$

$$\beta = \frac{f_0(\Gamma_4)}{2} \frac{\Gamma_4^2 - \Gamma_3^2}{\Gamma_3^2 \Gamma_4^2} = \frac{v_2 - v_3}{c} f_o(\Gamma_4) \simeq \frac{\Delta_2}{c t_o} f_0(\Gamma_{\max}), \qquad (32)$$

where (see Fig. 5)

$$\Delta_1 = z - v_{\min}(T + \tau + t) \,, \quad \Delta_2 = v_{\max}(T + t) - z \qquad (33)$$

in the overlapping region,

$$v_{\min}(T + \tau + t) < z < v_{\max}(T + t) \,. \qquad (34)$$

Substituting equations (31) and (32) into equation (29), we obtain

$$\mathrm{Im}\,\omega_{\max} = \frac{\sqrt{3}}{2^{4/3}} \omega_p [f_o(\Gamma_{\min})]^{1/6} [f_o(\Gamma_{\max})]^{1/3} \times \left(\frac{\Delta - \Delta_2}{c t_o} \right)^{1/6} \left(\frac{\Delta_2}{c t_o} \right)^{1/3} . \qquad (35)$$

The growth rate (35) depends on the distance Δ_2 to the leading front of the cloud overlapping and reaches the maximum

$$(\mathrm{Im}\,\omega_{\max})_{\max} = \frac{\omega_p}{2} [f_o(\Gamma_{\min})]^{1/6} [f_o(\Gamma_{\max})]^{1/3} \times (\Delta / c t_o)^{1/2} \qquad (36)$$

at $\Delta_2 = (2/3)\Delta$.

The distribution function of plasma particles in the magnetospheres of pulsars may be roughly approximated by the following law (Arons 1981)

$$f_o(\Gamma) = \begin{cases} A\,\Gamma^{-3/2} & \Gamma_{\min} < \Gamma < \Gamma_* \,, \\ A\,\Gamma_*^{-3/2} & \Gamma_* < \Gamma < \Gamma_{\max} \,, \end{cases} \qquad (37)$$

where A is the constant determined from the normalization condition (16) and written as

$$A = \frac{\Gamma_{\min}^{1/2}}{2} \left[1 + \frac{1}{2} \left(\frac{\Gamma_{\min}}{\Gamma_*} \right)^{1/2} \left(\frac{\Gamma_{\max}}{\Gamma_*} - 3 \right) \right]^{-1} . \qquad (38)$$

Substituting equation (37) into equation (36) and taking into account that $c t_o \simeq 2 L \Gamma_{\min}^2$, we have the characteristic time of the instability development

$$\tau_i = (\mathrm{Im}\,\omega_{\max})_{\max}^{-1} = \frac{2^{3/2} \Gamma_{\min}^{5/4} \Gamma_*^{1/2}}{\omega_p A^{1/2}} \left(\frac{L}{\Delta} \right)^{1/2} , \qquad (39)$$

where $L = c\tau$ is the space between the plasma clouds.

An instability manages to develop if the lifetime of the unstable system exceeds the characteristic time of the instability development by more than an order. In our case, the unstable system is the overlapping region, and its lifetime is Δ/c. With a similar criterion, $10\tau_i = \Delta_i/c$, we get the value of Δ at which the two-stream instability is developing to be given by

$$\Delta_i \simeq (30 c \omega_p^{-1} A^{-1/2} \Gamma_{\min}^{5/4} \Gamma_*^{1/2} L^{1/2})^{2/3} . \qquad (40)$$

We now estimate the quantities that characterize the development of the two-stream instability in the magnetospheres of pulsars. The following parameters of the secondary e^+e^-

plasma may be assumed: $\Gamma_{\min} \simeq 5$, $\Gamma_* \simeq 10^2$, $\Gamma_{\max} \simeq 10^3$ (Arons 1981) and $L = c\tau \simeq cT \simeq R \simeq 10^6$ cm (Usov 1987). From equations (3)-(5), (38) and (40), we have $\Delta_i \simeq 0.8 \times 10^5$ cm. Hence, the development of the two-stream instability already occurs when the cloud overlapping is very small ($\Delta_i \ll L$). Further overlapping of the plasma clouds ($\Delta > \Delta_i$) could be considered only beyond the scheme of our linear approximation.

The distance from the neutron star to the region where the two-stream instability occurs is

$$r_i \simeq 2c\tau\Gamma_{\min}^2 = 2L\Gamma_{\min}^2 \qquad (41)$$

or numerically $r_i \simeq 5 \times 10^7$ cm for $L \times 10^6$ cm and $\Gamma_{\min} \simeq 5$. The value of r_i is consistent with the distance from the neutron stars to the radio emission regions (see equation (9)).

The existence of several scales of the outflowing plasma modulation (e.g., $L_1 \simeq 0.3R$ and $L_2 \simeq 2R_c$ in the Ruderman-Sutherland model) may lead to the situation that in the magnetospheres of pulsars there are several regions where the two-stream instability develops and the generation of coherent radio emission occurs. From the observational data on radio emission of pulsars it follows that such a situation is possible for some pulsars (e.g., Gil 1985).

5. Discussion

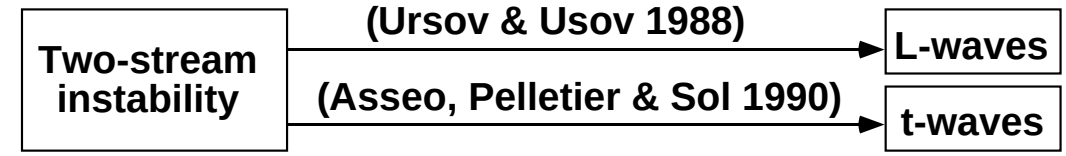
The mechanism of coherent radio emission of pulsars is closely connected with the location of the radio emitting regions in the pulsar magnetospheres. If it is confirmed that the distances from the neutron stars to the radio emitting regions are $\ll c/\Omega$ (Gil & Kijak 1993; Rankin 1993; Kramer et al. 1994; Kijak & Gil 1997), i.e., these regions are far inside the light cylinder, then most probably, the two-stream instability developed in the outflowing strongly nonhomogeneous plasma (Usov 1987; Ursov & Usov 1988; Asseo & Melikidze 1998) is responsible for the generation of the pulsar radio emission. It is worth noting that if the process of pair creation near the pulsar surface in strongly nonstationary indeed, the development of this instability in the magnetospheres of pulsars is almost inevitable.

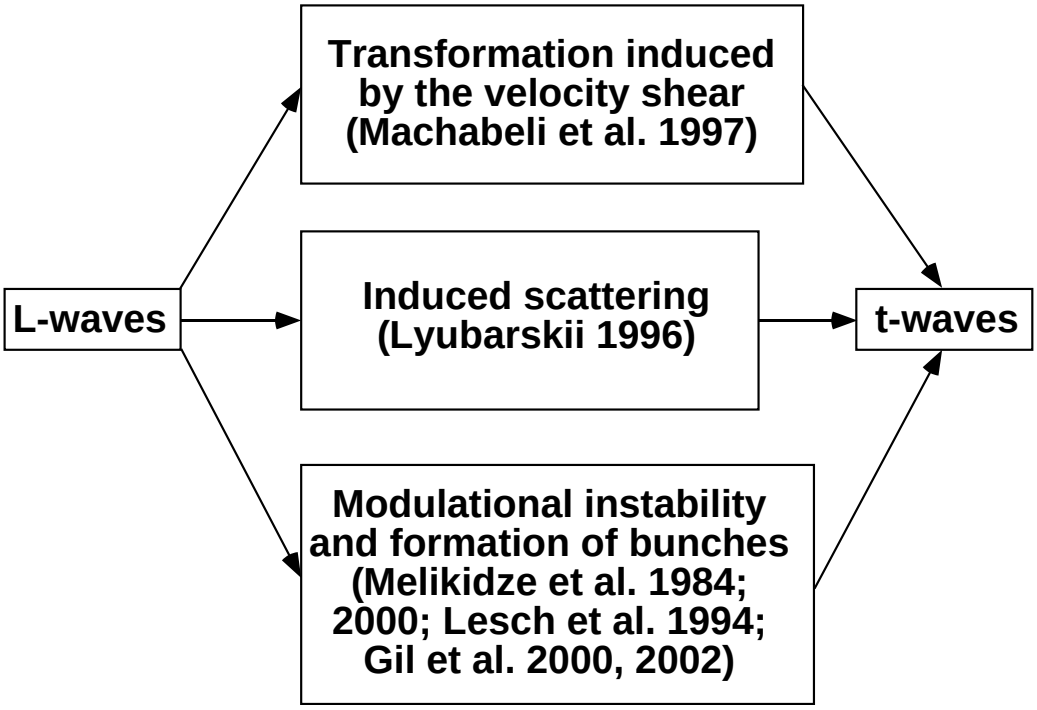
Longitudinal (nonescaping) Langmuir waves are generated in the process of development of the two-stream instability. Then, these waves may be converted into t-waves, that can escape from the pulsar magnetosphere, by means of the following nonlinear effects:

Acknowledgements. I gratefully acknowledge the support by the Heraeus foundation. This work was supported by MINERVA Foundation, Munich, Germany.

References

Alber Ya.I., Krotova Z.N., Eidman V. Ya., 1975, Astrophizika 11, 283
Arons J., 1981a, in Proc. Internat. Summer School and Workshop in Plasma Physics, ed. T.D. Guyenne (ESA SP-161), 273
Arons J., 1981b, in Proc. IAU Symp. 95, Pulsars, eds. W. Sieber and R. Wielebinski, Reidel, Dordrecht, 69
Arons J., 1981c, ApJ 248, 1099
Arons J., 1984, Adv. Space Res. 3, 287
Asseo E., 1993, MNRAS 264, 940
Asseo E., 1996, in Proc. Pulsars: Problems and Progress, ASP Conf. Ser. 105, eds. S. Johnston, M.A. Walker and M. Bailes, 147
Asseo E., Melikidze G.I., 1998, MNRAS 301, 59
Asseo E., Pelletier, G., Sol, H., 1990, MNRAS 247, 529
Asseo E., Pellat R., Rosado M., 1980, ApJ 239, 661
Asseo E., Pellat R., Sol H., 1983, ApJ 266, 201
Benford G., Buschauer R., 1977, MNRAS 179, 189
Beskin V.S., 1982, Soviet Astron. 26, 443
Beskin V.S., 1992, Soviet Astron. Lett. 16, 286
Buschauer R., Benford R., 1977, MNRAS 179, 99
Cheng A.F., Ruderman M.A. 1977, ApJ 212, 800
Cheng K.S., Ruderman M.A. 1980, ApJ 235, 576
Egorenkov V.D., Lominadze J.G., Mamradze P.G., 1983, Astrophizika 19, 753
Gill J.A., 1985, ApJ 299, 154
Gil J.A., Kijak J., 1993, A&A 273, 563
Gil J.A. et al., 2002, these proceedings
Harding A.K., Muslimov A.G., 1998, ApJ 508, 328
Kijak J., Gil J.A., 1997, MNRAS 288, 631
Krall N.A., Trivelpiece A.W., 1986, Principles of Plasma Physics, San Francisco Press
Kramer M., Wielebinski R., Jessner A., Gil J.A., Seiradakis J.H., 1994, A&AS 107, 515
Lesch H., Gil J.A., Shukla P.K., 1994, Space Sci. Rev. 68, 349
Lominadze J.G., Machabeli G.Z., Usov V.V., 1983, A&SS 90, 19
Lyubarsky Yu.E., 1996, A&A, 308, 809
Lyutikov M., Machabeli G.Z., Blandford R.D., MNRAS 305, 338
Machabeli G.Z., Mahajan S.M., Rogova A.D., 1997, ApJ 478, L129
Machabeli G.Z., Usov V.V., 1979, Soviet Astron. Lett. 5, 238
Machabeli G.Z., Usov V.V., 1989, Soviet Astron. Lett. 15, 393
Melikidze G.I., Gil J.A., Pataraya A.D., 2000 ApJ 544, 1081
Melikidze G.I., Pataraya A.D., 1984, Astrophizika 20, 157
Melrose D.B., 1981, in Proc. IAU Symp. 95, Pulsars, eds. W. Sieber and R. Wielebinski, Reidel, Dordrecht, 133
Melrose D.B., 1993, in Pulsars as Physics Laboratories, eds. R.D. Blandford, A. Hewish and L. Mestel, Oxford University Press, 105
Melrose D.B., 1995, J. Astrophys. Astr. 16, 137
Michel F.C., 1974, ApJ 192, 713
Michel F.C., 1991, Theory of Neutron Star Magnetospheres, UCP
Muslimov A.G., Harding A.K., 1997, ApJ 485, 735
Muslimov A.G., Tsygan A.I., 1992, MNRAS 255, 61
Ochelkov Yu.P., Usov V.V., 1984, Nature 309, 332
Renkin J.M., 1993, ApJ 405, 285
Ruderman M.A., Sutherland P.G., 1975, ApJ 196, 51
Sturrock P.A., 1971, ApJ 164, 529
Ursov V.N., Usov V.V., 1988, Ap&SS 140, 325
Usov V.V., 1981, Adv. Space Rec. 1, 125
Usov V.V., 1987, ApJ 320, 333
Usov V.V., 1996, in Proc. Pulsars: Problems and Progress, ASP Conf. Ser. 105, eds. S. Johnston, M.A. Walker and M. Bailes, 323
Usov V.V., Melrose D.B., 1995, Australian J. Phys. 48, 571
Usov V.V., Melrose D.B., 1996, ApJ 464, 306


Two-stream instability
(Ursov & Usov 1988)
L-waves
(Asseo, Pelletier & Sol 1990)
t-waves


L-waves
Transformation induced by the velocity shear (Machabeli et al. 1997)
Induced scattering (Lyubarskii 1996)
Modulational instability and formation of bunches (Melikidze et al. 1984; 2000; Lesch et al. 1994; Gil et al. 2000, 2002)
t-waves

Proceedings of the 270. WE-Heraeus Seminar on: *"Neutron Stars, Pulsars and Supernova Remnants"*
Physikzentrum Bad Honnef, Germany, Jan. 21-25, 2002, eds. W. Becker, H.Lesch & J. Trümper, MPE Report 278, pp. 249-262

The Radio-Loud Plasma in Pulsars

J. A. Eilek[1], P. N. Arendt, Jr.[1], T. H. Hankins[1] and J. C. Weatherall[1]

New Mexico Tech, Socorro NM 87801, USA

Abstract. The pulsar magnetosphere contains a strongly magnetized, relativistic plasma. We need to understand the physics of that plasma if we want to connect the data to the models. Our group in Socorro is mixing theory and observations in order to study the radio-loud pulsar plasma. In this paper we report on several aspects of our current work.

1. Introduction

We know pulsars produce radio emission at high brightness temperatures. It is very likely that this arises in a plasma. We also know that high-$T_{\rm B}$ emission is created by dynamical, non-equilibrium plasma processes elsewhere in space or astrophysical plasmas. Therefore, we can safely guess that the process by which pulsars shine involves a plasma. This is, however, not saying much. We know very little about the origin or dynamics of the radio-loud plasma. This is unfortunate, because understanding the pulsar plasma is critical to understanding the star. The radiation from that plasma is the only data we can get from these interesting stars. If we want to connect the observations to the physics (including the wealth of new, high-quality data becoming available, such as presented at this meeting), we need to study the plasma.

This paper is organized around two questions. What do we know about the radio-loud plasma in the pulsar? Can insight and methods from other areas of plasma astrophysics be applied here? More specifically, can we understand the dynamical state of the plasma (which connects back to the electrodynamics of the system), and how it produces the observed radiation (which is a consequence of its dynamical state)?

We begin with an overview (§2-5) of standard pulsar theory and what that theory requires, or suggests, about the plasma. One common assumption is that the radio emission comes from a lepton pair plasma. In §6-7 we report on work carried out by two of us (Arendt & Eilek) which follows the pair cascade numerically and determines the details of the lepton plasma produced by the cascade. After that, in §8-9 we suggest that time variability might be the best observational diagnostic of the plasma, and we report on ongoing work by two of us (Weatherall, Eilek) to model the plasma dynamics on short timescales. We close with a report (§10) on ultra-high time resolution observations of the Crab pulsar carried out by one of us (Hankins) which we believe begin to address some basic theoretical issues regarding plasma dynamics and the emission mechanism.

2. The standard model and its Limitations

To set the stage, we review the standard model, with an eye to its consequences for plasma formation and dynamics. This model has been carefully developed by many people over the years, and has had good success. But it also has its limitations; now that we have a common theoretical ground, and now that we have some excellent new data (including single-pulse work, polarimetry, multifrequency studies and millisecond pulsar studies), it is time to review the model with a critical eye. The areas where it fails will be the areas which can be fruitfully revisited. In this paper we limit ourselves to the radio emission region, and leave high-altitude, high-energy issues to others.

2.1. A co-rotating magnetosphere

A strong magnetic field is tied to a rapidly rotating neutron star. It contains and structures a plasma-filled magnetosphere. Most of the field lines which leave the star's surface reverse direction within the light cylinder and return to the star (as illustrated in Figure 1). It is natural to consider a steady atmosphere in this region, *i.e.*, one which rotates with the star. This can be maintained if an electric field exists, $\mathbf{E}_{\rm co}$, which satisfies

$$\mathbf{E}_{\rm co} + \frac{1}{c}\left(\mathbf{\Omega}\times\mathbf{r}\right)\times\mathbf{B} = 0 \qquad (1)$$

Such a field produces an $\mathbf{E}_{\rm co}\times\mathbf{B}$ drift equal to the co-rotation speed. This field must be supported by a nonzero charge density,

$$\rho_{\rm GJ} = \frac{1}{4\pi}\nabla\cdot\mathbf{E}_{\rm co} \simeq -\frac{\mathbf{\Omega}\cdot\mathbf{B}}{2\pi c} \qquad (2)$$

This is called the "co-rotation" or "GJ" density. Note that the plasma must be non-neutral in order to co-rotate; most of the magnetosphere is usually assumed to contain a single sign of charge.

2.2. The acceleration region

Conditions are different in the polar flux tube (PFT). This is the narrow region defined by field lines which do not close within the light cylinder. In this region, relativistic outflow from star's surface is thought to occur, driven by deviations from the co-rotation density. These deviations can support an $\mathbf{E}$ field with a non-zero component parallel to the $\mathbf{B}$ field; $\mathbf{E}_{\|}$ can accelerate particles to high energies.

The standard model now has a branch point, with two specific but different variants proposed (*e.g.*, Ruderman & Suther-

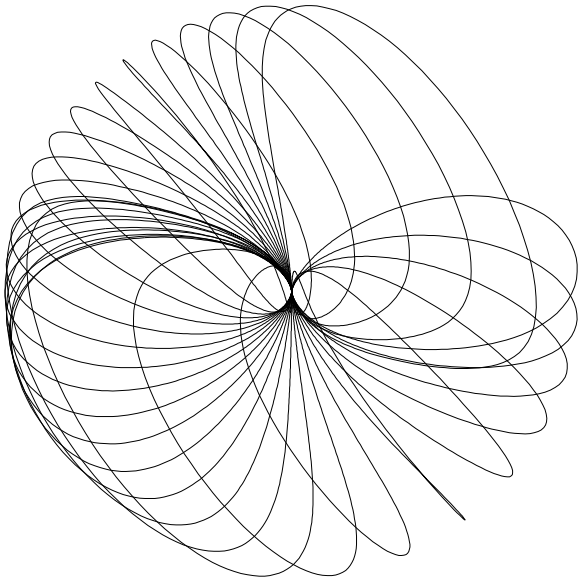


Fig. 1. The magnetosphere of a pulsar, illustrated by the last open field lines in a rotating vacuum magnetic dipole, at an 45° inclination angle to the rotation axis, viewed looking down the rotation axis. Relativistic effects distort the field lines close to the light cylinder. Most of the magnetosphere, within the closed field lines, is assumed to co-rotate with the star. The open field line region (or polar flux tube, PFT) allows a current-carrying outflow from the star, is thought to contain a dense electron-positron plasma, and to be the origin of the radio emission. Despite the high-altitude field distortions due to relativity, the PFT is nearly circular in cross section at radio emission altitudes. From Arendt (2002).

land 1975, Arons & Scharleman 1979). One variant assumes that charges cannot freely leave the star's surface, and thus a "vacuum gap" exists just above the surface. Strong $\mathbf{E}_{\|}$ in this gap accelerates particles to relativistic energies, perhaps in a non-steady fashion (sparking, breakdown). Another variant assumes that charges can freely leave the star's surface. If the charge density deviates from co-rotation, $\mathbf{E}_{\|}$ created by these charges will enable their acceleration, also to relativistic energies.

This low-altitude acceleration creates a highly relativistic "primary beam", which gains significant fraction of the maximum potential drop in a short distance. Most authors assume the acceleration region is limited by pair formation, which is believed to shield $\mathbf{E}_{\|}$. Alternatively, the acceleration may be limited by radiative losses before the energies required for pair formation are reached (Sturmer 1995; Jessner *et al.* 2001).

2.3. The Pair Cascade

A very important step is taken here. Radiation from the primary beam charges is assumed to seed a γB pair cascade. Either curvature radiation (if the charges reach $\gamma \sim 10^7$) or magnetic-resonant Compton scattering (if they reach $\gamma \sim 10^4$ and the star is a thermal X-ray source) produces energetic photons. These photons, in the star's strong B field, can produce an electron-positron pair. Further photon production by these daughter leptons leads to further pair production, thus initiating a cascade of particle creation. The end point of this cascade is often assumed to be total conversion of the primary beam energy to much slower (but still relativistic) leptons, with very high multiplicities ($\mathcal{M}$, defined as the number of daughter leptons per primary beam particle).

Two additional important assumptions follow; neither of them has been clearly established to be true. One is that the pair plasma terminates the acceleration region, by shielding the accelerating E field. The second is that the pair plasma is the means by which the free energy available in the primary beam is converted to coherent radio emission. We discuss both in more detail later.

3. Annoying Issues and Inconsistencies

Some problems remain in this picture.

3.1. The Density is a Problem

We do not know the details of the radio emission mechanism, but the local plasma frequency, $\nu_{\rm p}$, is likely to be important. Plasma turbulent models predict emission at close to $\nu_{\rm p}$. Signal propagation is suppressed below $\nu_{\rm p}$ (except at angles very close to $\mathbf{B}$). However, the numbers do not work. (Others have also noticed this problem: *cf.* Kunzl *et al.* 1998, or Melrose 2000).

Consider a plasma of number density n, moving at bulk Lorentz factor γ. It supports plasma waves with frequency $\nu_{\rm p}^2 = \gamma n e^2/\pi m$ (all quantities measured in the star's frame). The standard model predicts the number density is at least that required by co-rotation, $n_{\rm GJ} = \rho_{\rm GJ}/e$; pair creation amplifies this by the multiplicity $\mathcal{M}$. If we use (2) and scale to the field at the stellar surface, this predicts a plasma frequency

$$\nu_{\rm p} = \left(\frac{\gamma e B \mathcal{M}}{4\pi m c P}\right)^{1/2} \simeq 1.2 \left[\frac{\gamma B_{*,12}\mathcal{M}}{P(r/r_*)^3}\right]^{1/2} \text{GHz} \qquad (3)$$

Now, $\gamma\mathcal{M} \gg 1$ in most models, and $r \sim 3 - 30 r_*$ is the typical range of emission altitudes. Thus, the standard model predicts $\nu_{\rm p} > 1$ GHz, and we should see little radiation at lower frequencies. On the other hand, pulsars are strong radio sources down to frequencies ~ 10 MHz. We consider this a problem.

To resolve this problem, either the radiation must emerge well below the plasma frequency, or the plasma density in at least part of the radio-loud region is much lower than commonly thought. We think the latter case is more likely. It must follow that steady co-rotation is not obeyed; the plasma will be dynamically variable.

3.2. The Plasma is not Steady

We note two further hints of an unsteady plasma.

No pulsar has steady radio emission. We see modulation on all time scales where we've looked, from sub-μs flickering to mode changes and nulls on multi-period timescales. Coherent radio emission is a very nonlinear-gain process, so we expect small fluctuations in the plasma to be strongly amplified.

Nonetheless, this observed variability tells us that the plasma flow cannot be as steady as in most of the models. As with the density problem, this suggests to us that the plasma does not satisfy coloration. Density deviations lead to a net force in the co-rotating frame, and these forces should lead to nonsteady flows.

Furthermore, the assumption of a steady, co-rotating magnetosphere with no flows is only self-consistent for an aligned rotator. We note two interesting features of a star whose magnetic axis is not aligned with its rotation axis. (1) The $\mathbf{E} \times \mathbf{B}$ drift velocity has a component along $\mathbf{B}$. Unless the plasma is charge-neutral (recall $\rho_{\rm GJ}$ carries a sign), this will drive field-aligned currents even in co-rotating regions. (2) The "GJ current", $j_{\rm GJ} \propto \rho_{\rm GJ}$, has a non-zero divergeance. Non-steady flows are therefore required by charge conservation, unless the magnetosphere is fully static (which is highly unlikely). Both of these effects may be small, but they also hint at non-steady plasma flows in the magnetosphere.

3.3. Where is the acceleration region?

The standard model predicts a very low-altitude acceleration and pair cascade region. On the other hand, the radio-loud region is thought to be at least several stellar radii above the surface. The emission altitude is determined from the data through a quasi-universal set of assumptions: that the radio emission arises only in the PFT, that the magnetic field is dipolar, and that the mean profile width is due to the star rotating past one's sightline. Details of the deprojection vary between authors (*e.g.*, Rankin 1993, Kijak & Gil 1998, or Eilek & Hankins 2002), but there is general agreement that the emission altitude lies between a few and a few tens of stellar radii.

We find this unsatisfying. Once the pair plasma is formed it should radiate almost immediately. The plasma turbulence thought to lead to radio emission should develop quickly. Thus, if the acceleration and pair formation region is indeed close to the star, the radiation must remain confined in the PFT plasma until it escapes at a few tens of stellar radii. Plasma trapping of the radiation, when the wave frequency is below the local plasma frequency, has of course been assumed to explain this. However, we now know that the density distribution of the PFT is not as simple as was once thought. We also note that radiation wavevectors at small angles to $\mathbf{B}$ can propagate below the local plasma frequency. The entire situation would be simpler if the radio emission region were also the acceleration and pair formation region (*e.g.*, Shibata 1991).

3.4. Do all pulsars have a pair cascade?

The pair cascade is an important part of the standard model. Its onset is determined by the acceleration rate in the "gap" region. The dense plasma it produces is assumed to shield the accelerating $\mathbf{E}$ field, and thus end the gap. But this cartoon is not self-consistent. When the standard model is made quantitative, one finds that the pair cascade is unlikely to occur in pulsars with magnetic field $\lesssim 10^{11}$G (Arendt & Eilek 2002; details below). This means that neither old, isolated pulsars, nor msec pulsars, should show pair formation, if they obey the standard model.

How can this be resolved? Either (i) not all pulsars have a dense pair atmosphere (and thus are "pairless" radiators), or (ii) our standard model is seriously lacking; or perhaps (iii) both of the above are true.

3.5. Is Magnetic Field Dipolar?

The assumption that the magnetic field is dipolar lies at the heart of the standard model. Detailed development of that model usually assumes a purely dipolar field. There are various hints, however, that this is not the full picture. Some authors have suggested that the low-altitude field is more complicated – a stronger field with more complex structure near the surface may help the problem of pair formation in weak-field pulsars. Such ideas may well be supported by the data. There has been some very good work on polarization in recent years (*e.g.*, van Hoensbroech & Xilouris 1997, or Hankins & Rankin 2002) We now know (*e.g.*, Eilek & Hankins 2000) that the linear polarization in an interesting subset of bright pulsars is *not* well explained by the usual rotating-vector model. Thus, the field is very likely to deviate from dipolar, *even in the radio emission region.*

4. Larger Unsolved Questions

The standard picture contains (at least) two major, unsolved questions. These are not new questions, and work continues on each – with no consensus as to the answer.

4.1. The Pulsar Circuit

An outflow of relativistic charged particles, along open field lines, is a fundamental part of the pulsar model. This constitutes a current. The nature of the pulsar circuit is still far from understood: where does the current return to the star? Is the circuit open (to the ISM) or closed? How is the current driven (that is, how does the rotational potential of the star couple to the current flow?) The literature contains two approaches to this problem. Models of the low-altitude acceleration region (possibly with pair formation) describe in detail the dynamics of individual charges in that region. This region is assumed also to drive the current. If the outflowing plasma is relativistic, fills the PFT, and is at the corotation density, then the magnitude of the current follows directly: $I = \rho_{\rm GJ} c A_{PFT}$. These models rarely address the rest of the circuit.

An alternative approach is to consider the global circuit. The dynamo must still be the star's rotation, which creates a potential drop in any plasma which is not co-rotating with the star.[1] This approach allows the possibility of localized resistive regions ("loads"; possibly the inner or outer gaps) where energy is dumped into plasma, then radiation (*e.g.*, Kunzl *et al.* 2002). In principle, the combination of the driving voltage and the resistance of the circuit will determine the magnitude of the current. We see no *a priori* reason for this to be the GJ current (Shibata, 1991, has made this point nicely.).

[1] This may be the magnetosphere, which some authors assume rotates at a slightly different rate from the star itself, or could be the ambient ISM, which is magnetically connected to the star *via* the open field lines.

These models have not yet been developed at the level of the low-altitude acceleration region models, but we find them attractive. One might hope that observational diagnostics could be developed (of such quantities as current density or circuit length). We return to this issue in §8-9.

4.2. The Radiation Mechanism

How does the pulsar shine? We do not have a simple model of how the plasma produces the very high brightness temperatures characteristic of the radio emission. Most authors believe either the primary beam or the pair plasma will be susceptible to plasma instabilities (such as beam bunching or the two-stream instability). Some of these instabilities will grow to nonlinearity and couple to electromagnetic radiation which can escape the system.

Within this general picture much variety is possible. Models abound, and some have been developed in great detail, but with no consensus as to which is the most relevant to real pulsars, and with hardly any useful observational discriminants proposed. (For instance, *cf.* Melrose 1992, or Lyubarski, this meeting). We might group the models currently being discussed into three categories. One starts with *coherent charge bunches*. Early emission models assumed that such bunches produced curvature emission in the radio range. An interesting recent variant is Compton scattering of plasma emission by such bunches (*e.g.*, Kunzl *et al.* 2002). A second class of models invoke strong *plasma turbulence*, in which soliton growth and possible collapse convert plasma wave energy into escaping radiation (*e.g.*, Asseo *et al.* 1990, Weatherall 1997). A third type of model uses *maser-like* mechanisms, which convert internal energy of the plasma to radio emission (*e.g.*, Luo & Melrose 1995, Kazbegi *et al.*1991, Weatherall 2001)

All of these models differ in their details, and often in their deductions about the significant properties of the emission (such as its spectrum, spatial location, or relation to local plasma conditions). One might also hope that observational tests of the models could be developed. We also return to this question in §8-9, below.

5. The State of the Radio-Loud Plasma

To return to our original question: what do we know, or assume, about the plasma in the radio-loud region?

Composition. The plasma is probably dominated by electron-positron pairs in the radio-loud region (although this is not established for slow and msec pulsars). It is also not charge neutral (in order to maintain corotation).

Number density. The plasma is assumed either to be at the co-rotation density, $n_{\rm GJ} = \rho_{\rm GJ}/e$, or to be increased over this by the pair multiplicity $\mathcal{M}$. Both of these assumptions are common in the literature; as we point out above, both assumptions are inconsistent with observed low-frequency radio emission. We suspect (in agreement with Melrose 2000) that the plasma is highly inhomogeneous, with radio emission coming from the lower-density regions, and the co-rotation density possibly being met in some average fashion.

Plasma "beta". The plasma is highly magnetized, with $B \sim 10^{11} - 10^{13}$G at the surface of single pulsars. It is therefore strongly field dominated; the inertia and energy density of the plasma are tiny compared to the magnetic field.

Flows. The plasma flow is highly relativistic and one-dimensional: $\gamma \sim 100 - 10^7$ (depending on author). The flow is nearly along the magnetic field, with slow cross-field drifts in regions where transverse **E** fields exist. The gyromotion of individual charges is quantized, with most particles in the lowest Landau levels.

Dynamical state. The plasma is very likely to be inhomogeneous and unsteady. We know collective effects are needed to produce coherent radio emission. Thus the plasma is likely to be strongly turbulent on microscales. We also infer a nonsteady state from the nonsteady radio emission. Finally, if the plasma contains low-density regions, we expect the unshielded electric field to keep the plasma dynamically active.

Plasma distribution function. This important part of any plasma physics study has remained unconstrained until recently. Previous authors have either assumed analytically convenient forms, or tried to quantify semi-heuristic arguments. New work, on which we report below, shows that the pair plasma is well described by a relativistic Maxwellian, at $k_{\rm B}T \sim mc^2$, *in the comoving frame.*

6. The Cascade and the Plasma it Produces

We now turn to the pair cascade: when and how does it occur, and what is the nature of the plasma it produces? The cascade begins with a seed photon, of energy $\epsilon = h\nu/mc^2$, which pair creates *via* $\gamma + B \rightarrow e^+ + e^- + B$. The newly created leptons will emit synchrotron radiation if they are created in upper Landau levels. If this is the case the synchrotron photons will themselves pair create, thus extending the cascade to several generations.

This is an inherently nonlinear process, not well suited to analytic methods (although progress can be made with heroic effort, *e.g.*, Hibschman & Arons 2001). Numerical simulation are called for. Daughtery and Harding (1982) led the way with simulations which determined the spectrum of hard photons escaping from a cascade region. We revisited the subject in order to learn more about the pair plasma. Our goal was to simulate a cascade produced according to the standard models. That is, we did not attempt a self-consistent treatment of the plasma electrodynamics within the acceleration region. Rather, we assumed the primary beam particles had energies typical of what is found in the literature, and they produce seed energetic photons either by curvature radiation (CR) or inverse Compton scattering (ICS). We summarize our results here; more details can be found in Arendt (2002), and Arendt & Eilek (2002).

6.1. Details of the calculation

Our calculations were based on monoenergetic photon "kernels". For each of these, we started with photons of a fixed energy, moving at a small range of angles (such as given by

relativistic beaming) relative to the local **B**. We followed each in time and space (assuming linear propagation relative to a non-rotating frame, ignoring general relativistic effects) until it had a unit opacity to pair creation. At that point the differential cross section and Monte Carlo methods were used to create daughter leptons. We followed each lepton in time and space (assuming guiding-center motion along **B**, ignoring acceleration by any local $\mathbf{E}_{\|}$) until it had unit opacity to synchrotron radiation. At that point Monte Carlo methods were again used to create new photons. This process continued, following all quanta in time and space, until all the action had stopped—that is until no further pair or photon creation occured. The end of such a calculation gave us one "kernel".

We convolved the kernels with the seed photon distributions produced by CR or ICS to determine the plasma and photon distributions predicted by cascades in a pulsar. We chose primary beam energies $\gamma_{\rm p} \sim 10^6 - 10^7$ for cascades seeded by CR, and $\gamma_{\rm p} \sim 10^3 - 10^5$ for cascades seeded by magnetic-resonant ICS. We simulated full cascades for magnetic fields $B = 10^{12}$G and 10^{13}G. We also explored cascades in $B = 10^{11}$G fields, but found they were very expensive in computer time, due the large numbers of soft photons created for each lepton pair produced. Thus we only included the two larger field strengths in our final results.

6.2. Onset of the Cascade

The cascade can be understood in terms of the two governing principles, energetics and opacity. Recall that an electron at energy $\gamma_{\rm p}$ produces a curvature radiation spectrum which peaks at a photon energy $\epsilon_{\rm CR} = \hbar\omega_{\rm CR}/mc^2 \sim 3c\hbar\gamma^3/2\rho mc$, where ρ is the radius of curvature of the field line. Magnetic resonant ICS produces photons in the range $\epsilon_{\rm B}/2\gamma_{\rm p} \le \epsilon \le 2\gamma_{\rm p}\epsilon_{\rm B}$, where $\epsilon_{\rm B} = \hbar\omega_{\rm B}/mc^2 = B/B_{\rm c}$.

Consider a seed photon, of energy ϵ, moving at an angle θ relative to **B**. Two conditions must be satisfied if it is to pair produce. The first condition is energetics. The available photon energy must satisfy $\epsilon > 2mc^2$. Relativistic kinematics expands this as

$$\epsilon_\perp = \epsilon \sin\theta > 2. \qquad (4)$$

(in the star's frame). We found that most of the pair creation in our high-field runs was governed by energetics. Photons travelling nearly parallel to **B** propagate freely until field line curvature finally establishes $\epsilon_\perp > 2$. Pair creation then proceeds immediately. Most of the newly created leptons are in the ground Landau state, so they cannot create further photons, and the cascade ends.

The second condition that must be met for pair creation is opacity. The photon must have a significant chance of creating a pair. Using the basic cross section, one can show that this requires

$$\epsilon B \gtrsim 0.1 B_{\rm c} \sim 4 \times 10^{12}{\rm G} \qquad (5)$$

again in the star's frame (this is the best case, that of $\theta = \pi/2$, a right angle crossing of the magnetic field line). We found that our lower field runs, and some initial creation events in our high field runs, were opacity dominated. The parent photons have more than enough energy to produce a pair, but the probability of pair production is low until they propagate to an angle such that $\epsilon_\perp \lesssim 0.1 B_{\rm c}/B$. The newly created leptons in this case tend to be born in excited Landau levels. They then decay *via* the production of energetic synchrotron photons, which extend the cascade to several further generations.

These two conditions make it clear that the magnetic pair cascade does not necessarily occur in all pulsars. In particular, stars with a weak B field need very energetic photons to satisfy the opacity condition; such high energies are not produced by the two standard seed-photon radiation models (*e.g.*, Weatherall & Eilek 1997). It is traditional to invoke highly curved fields in old and millisecond pulsars, assuming that this will enable pair production. We caution, however, that the acceleration of the primary beam charges, and the spectrum of their radiation, must be shown to work quantitatively before the pair cascade can be demonstrated to occur in all pulsars.

6.3. Development and Decay of the Cascade

We found, as expected, that pair formation is enhanced towards the edge of the PFT, due to the larger field line curvature there. We would thus expect "conal" emission from the pair plasma; as others have pointed out, "core" emission does not easily fit into this picture.

We continued our simulations until all reactions had stopped – until there were no remaining photons with energy and opacity to create further pairs. In all cases the cascade ended before the quanta reached one stellar radius from their injection point. Thus, the pair cascade is a rapid process, with the time from seed photon emission to cascade completion being less than $R_*/c \sim 30\mu$s. If the seed photon production is sporadic, the pair plasma should be highly nonuniform within the PFT.

6.4. Efficiency and Multiplicity of the Cascade

The fraction of the primary beam energy converted into the pair plasma, and the abundance of that plasma, are key parameters in many models of the pulsar magnetosphere and its interaction with the ambient ISM. *Our numerical results do not support assumptions commonly made in the literature.*

One common assumption is that the entire energy of the primary beam is transferred to the plasma. We found this is not always the case. Instead, much of the beam energy escapes as photons. The fraction of beam energy going into the pairs ranges from $f_{e^+e^-} \lesssim 1.0$ in higher magnetic fields, to $f_{e^+e^-} \lesssim 0.1$ in lower magnetic fields. Another common assumption is that the multiplicity (the number of pairs produced per primary beam particle) is high; a value $\mathcal{M} \sim 10^4$ is often found in the literature. We found much lower values. The high-field runs, with Compton seeds, were strongly limited by energetics and produced only a few pairs per primary charge. Multiplicities for the lower field and curvature-seed runs ranged from $O(10)$ to $O(1000)$, and increased strongly with primary beam energy. Table 1 summarizes the range of $f_{e^+e^-}$ and $\mathcal{M}$ found in our runs; more details can be found in the original papers.

6.5. Lepton Distribution from the Cascade

One of our primary goals in these simulations was to determine the momentum distribution function (DF) of the pair plasma created by the cascade. We found a very simple result. Despite

Table 1. Summary of results from cascade simulations

Curvature Radiation:

$\mathbf{B = 10^{12}}$G:	$\mathbf{B = 10^{13}}$G:
$\gamma_{\rm p} \sim 5 - 10 \times 10^6$	$\gamma_{\rm p} \sim 2 - 10 \times 10^6$
$\mathcal{M} \sim 300 - 1000$	$\mathcal{M} \sim 500 - 2000$
$f_{e^+e^-} \sim 0.03 - 0.1$	$f_{e^+e^-} \sim 0.4 - 0.5$
$\gamma_{\rm CM} \sim 80 - 480$	$\gamma_{\rm CM} \sim 60 - 600$
$f_\nu \sim 0.02 - 1.0$	$f_\nu \sim 0.001 - 0.03$

Inverse Compton:

$\mathbf{B = 10^{12}}$G:	$\mathbf{B = 10^{13}}$G:
$\gamma_{\rm p} \sim 2 - 50 \times 10^4$	$\gamma_{\rm p} \sim 2 - 10 \times 10^4$
$\mathcal{M} \sim 10 - 100$	$\mathcal{M} \sim 2 - 10$
$f_{e^+e^-} \sim 0.1 - 0.3$	$f_{e^+e^-} \sim 0.8 - 1.0$
$\gamma_{\rm CM} \sim 60 - 400$	$\gamma_{\rm CM} \sim 100 - 900$
$f_\nu \sim 0.1 - 0.8$	$f_\nu < 0.01$

$\gamma_{\rm p}$ is the energy of the primary beam charges.
$\mathcal{M}$ is the multiplicity: the number of pairs per primary charge.
$f_{e^+e^-}$ is the energy efficiency: the fraction of the primary beam energy that goes into leptons.
$\gamma_{\rm CM}$ is the center of momentum energy of the created leptons.
f_ν is the photon energy efficiency: the fraction of the primary beam energy that goes into photons.
Full details can be found in Arendt & Eilek (2002), or Arendt (2002).

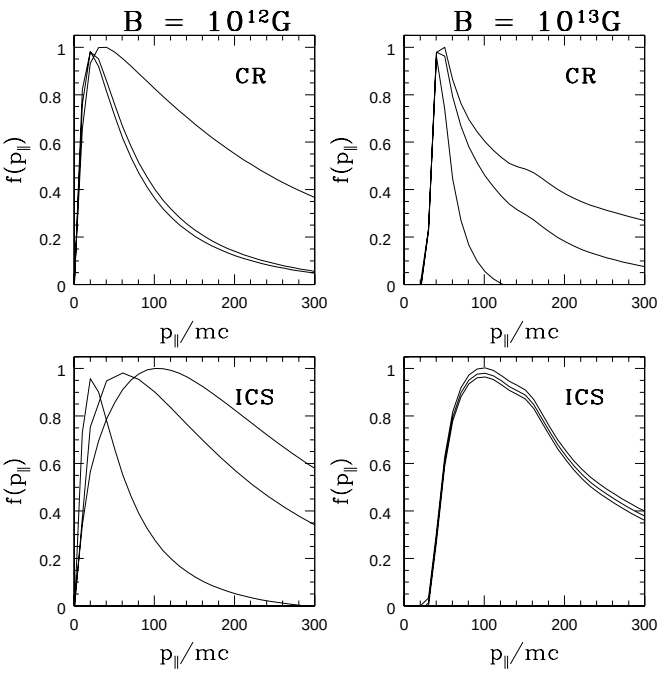


Fig. 2. The one-dimensional momentum distribution function of the pair plasma created in the cascade, *as viewed in the star's frame*. The results are shown for two magnetic fields, for cascades seeded by CR with $\gamma_{\rm p} = 1, 2, 5 \times 10^6$, and by ICS with $\gamma_{\rm p} = 2, 5, 10 \times 10^4$. From Arendt & Eilek (2002).

the wide range in cascade parameters and pair creation efficiencies encountered, the final DF's have remarkably similar shapes. Figure 2 shows some examples of DF's seeded by both CR and by ICS, *as viewed in the star's frame*. The DF's are all broadly similar, with a strong peak at moderate energies and an extended high-energy tail. There are slight differences due to the magnetic field. In the $B = 10^{13}$G runs, there are no slow leptons; all DF's have a low-$p_\parallel$ gap below $\sim 20mc$. In contrast, all of the $B = 10^{12}$G runs have leptons down to $p_\parallel < .01mc$. (This difference is due to the importance of synchrotron losses, and the energy degrading of multiple lepton generations, in the lower-field runs).

The numerical results simplify nicely if the DF's are transformed to the center-of-momentum (CM) frame of the plasma. (We found that $\gamma_{\rm CM} \sim 10 - 100$ over the set of runs). Figure 3 shows the same DF's as in Figure 2, but seen in the CM frame. In this frame, the DF's are remarkably close to a *thermal* distribution, *i.e.* a relativistic Maxwellian:

$$f(p_\parallel) \propto \exp\left[-\zeta\gamma(p_\parallel)\right] \qquad (6)$$

The parameter ζ can be identified with the inverse temperature of the plasma. We carried out numerical fits of this expression to our CM-frame DF's, and found that $k_{\rm B}T/mc^2 \sim 0.8 - 2$ describes the full range of our results.

Thus, the DF of the cascade-produced pair plasma is remarkably simple. It is a warm ($k_{\rm B}T \sim mc^2$) relativistic Maxwellian when viewed in a frame moving with the plasma. The distorted shape as seen in the lab is simply due to the Lorentz boost when passing to that frame.

6.6. Photon Distribution from the Cascade

We also determined the spectrum of the energetic photons which remained after the end of the cascade. This is a composite of secondary photons, produced by synchrotron emission of the pairs, and seed photons which never pair produced.[2] Figure 4 shows a selection of these spectra, presented as number counts (not energy spectra). The photon spectra tended to be steeper in lower magnetic fields, due to secondary synchrotron emission being more important in those cascades. Conversely, the spectra are flatter in the high field runs, where synchrotron photons are rare and the photon spectra are dominated by the seed photons which escaped pair creation. All spectra show a high-energy turnover which comes from the input seed photon distribution.

The fraction of the primary beam power that remained in the photons, f_ν, was quite low for the high-field runs, especially those with ICS seed; nearly all of the beam energy did go into leptons in those cases. The lower-field runs ended with a large fraction of the beam energy in photons: $f_\nu \sim 0.1 - 1$ in those runs. The large numbers of photons produced in our exploratory runs at $B = 10^{11}$G suggest f_ν would be quite large there as well.

[2] Some photons never satisfied the opacity and energy criteria. We distributed the seed photons over angle, within a small range identified with $1/\gamma_{\rm p}$; those at lower angles had a good chance of escaping the region without pair producing.

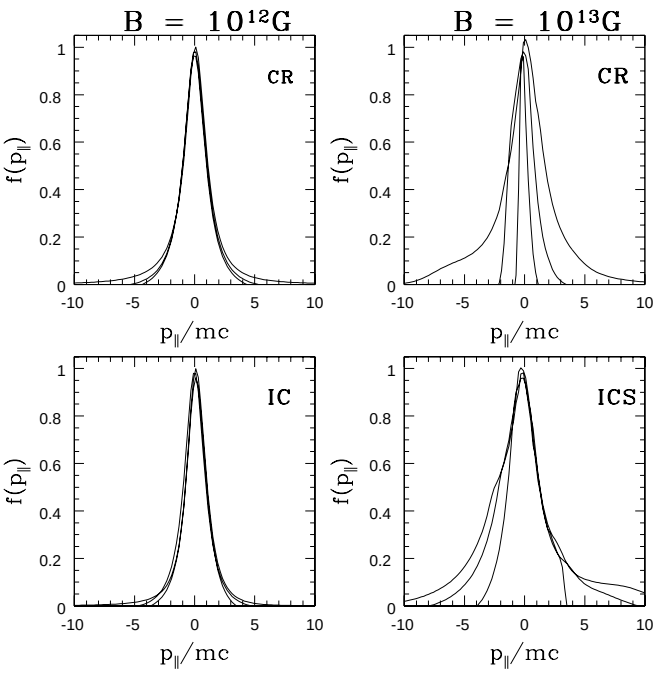


Fig. 3. The one-dimensional momentum DF of the pair plasma created in the cascade, *as viewed in the comoving frame*. See Figure 2 for details. From Arendt & Eilek (2002).

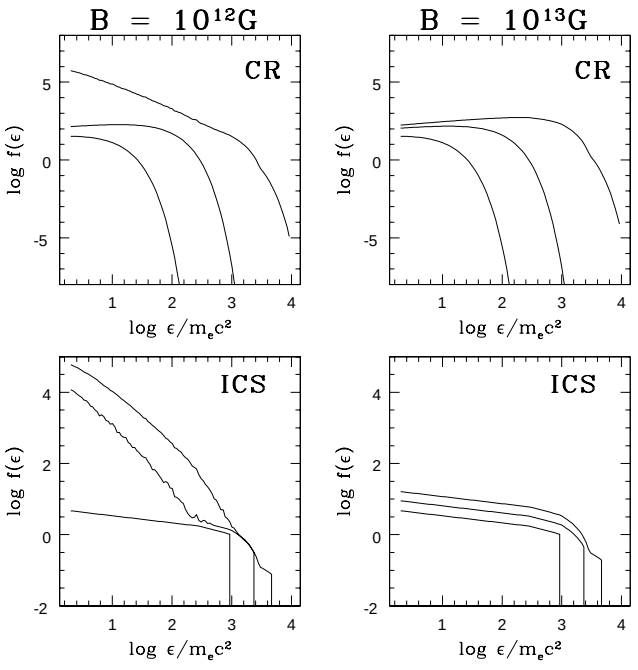


Fig. 4. The photon number counts (not the energy spectrum) resulting from the pair cascade, in the star's frame. See Figure 2 for details. From Arendt & Eilek (2002).

7. Why does the DF matter?

The reader who is not a plasma theorist may wonder at our emphasis on the plasma DF. Our answer is that it is crucial to understanding the emission and propagation of the radio signal, and that it may have important consequences for the electrodynamics of the emission region.

7.1. Coherent Radio Emission

As we noted above, the means by which pulsars produce coherent radio emission are still unknown. There is a general sense that some plasma process converts the energy of that beam to radio emission. But the details are critical. What plasma process (that is, which instability) is involved? What conditions are necessary in the plasma for it to happen? Where in the magnetosphere does it go?

These questions can only be answered with a detailed knowledge of the plasma DF. Consider the ongoing discussion about the two-stream instability, and whether or not it can occur in pulsars. The instability goes only if the two plasmas moving relative to each other are are "cool", that is with momentum width less than their separation. In the pulsar context, the two streams are either the electrons and positrons of the pair swarms, or the primary beam moving through the pair swarms. The onset of plasma turbulence is governed by the temperature and relative motion of the different plasma species (*e.g.*, Weatherall 1994; Usov, this proceedings.). In other words, we need to know the DF.

But this DF has been unclear; in fact, "theorist's freedom" has prevailed. Some calculations of plasma wavemodes and instabilities have assumed analytically convenient forms (such as boxcars, cold plasma, or relativistic Maxwellians in the star's frame). Other work has attempted to quantify a plausible, but heuristic, DF introduced by Arons (1981). We hope that our simulations of the true DF will be of use to future work in this area.

7.2. Magnetospheric Propagation

The radio emission must travel through the pair plasma, between its emission point and its escape from the star. This propagation can involve "shunting" of radiation along **B**, evolution of the polarization state, and dispersive and scattering effects. The details of the transport, and observable signatures, depend critically on the details of the plasma DF. A familiar example is propagation through the ISM, for which the frequency dependence of scattering and propagation are well known. These signatures can easily be derived from the DF for the ISM, that is a cold, ion-electron plasma, with plasma frequency well below the frequency of the observed radiation. A similar calculation for propagation in a relativistically moving, cold pair plasma predicts that dispersion and scattering in that plasma could be distinguished from ISM propagation at high frequencies (Eilek, 2002; also Lyutikov & Parikh, 2000, or Petrova & Lyubarskii, 2000). We are not aware of any such studies that include a warm plasma, which we now know to be the case.

7.3. Shielding

Models of the acceleration region usually assume that the pair plasma can adjust itself to maintain the corotation density, and thus reduce the local **E** to zero, as soon as pair formation goes.

This is a great help mathematically, as it allows for straightforward analytic solutions in the acceleration region. However, it may not be supported by more careful consideration of the cascade.

Such shielding depends on two things: the multiplicity of the cascade, and the DF of the pair plasma. If the plasma is cold, and if the electrons and positrons are given a large enough relative streaming velocity (such as a local $\mathbf{E}_{\|}$ would create), number conservation leads to a finite charge density which can satisfy co-rotation. Shibata *et al.* (1998) go further, and show that steady space-charge-limited flow is possible for a cold plasma only if the pair multiplicity is very high. This is because newly created opposite-sign charges change the field structure of the acceleration region, and too few pairs (too low an $\mathcal{M}$) cannot support a self-consistent $\mathbf{E}_{\|}$ field. Their numerical examples require much higher $\mathcal{M}$ values than our simulations predict. The issue is further complicated by the creation of warm plasma, as in our simulations. Arendt (2002) applied $\mathbf{E}_{\|}$ fields to induce relative streaming in the post-cascade electron and positron distributions. He found that quite low fields will, indeed, produce a net charge density of the opposite sign, which admits the possibility of shielding. However, a somewhat larger E field will reverse some of the opposite-sign charges, and thus enhance the original density, because of charges leaving the system.

We are therefore not confident that the pair cascade will always adjust to shield the accelerating $\mathbf{E}_{\|}$. We suspect pair formation will induce more interesting, non-steady behavior in the plasma.

8. How might we observe the plasma?

Theories need to be tested by observations. Is there any way in which we can observe the pulsar plasma?

8.1. Indirectly: radio emission and propagation

We observe the plasma indirectly *via* its radio emission. In more conventional astrophysics this allows a simple approach – incoherent emission is well understood. The radio power and spectrum allow the type of emission (synchrotron, bremsstrahlung, *etc.*) to be identified, and the physical conditions (such as density or temperature) in the emitting region to be determined.

This is not so easy for pulsars. We do not have a unique model for coherent radio emission, let alone a simple one. The coherent power is likely to be extremely sensitive to detailed conditions in the plasma, so that modest changes in, say, local density or DF will result in large changes in the instantaneous radio power. Furthermore, the detected pulsar signal probably arises from a highly inhomogeneous region, stratified in density and possibly distributed over altitude.

The situation is further complicated by the fact that the radio signal may have traversed an extended region of the plasma before escaping into "space" and thence to our detectors. The effects of propagation through the ISM are reasonably well understood, but this is not the case for propagation effects within the pulsar magnetosphere.

Thus, interpreting observations of radio power or spectrum directly in terms of the conditions in the emitting region is very difficult. We need alternative methods.

8.2. Quasi-directly: temporal fluctuations

Anyone who has looked at pulsar radio data knows that the signal is intrinsically variable on many time scales. The variability can be categorized in terms of observables, and arranged in order of variability timescale.

Nulls, modes and the mean profile. The pulsar signal varies dramatically from pulse to pulse, in an apparently random fashion, and yet each star has a meaningful and stable emission profile when averaged over enough rotation periods (tens to hundreds, depending on the star; *e.g.*, Rathnasree & Rankin 1995). In addition, some stars show nulls or mode changes which persist for many rotation periods. Thus a large-scale order clearly exists within the emission region.

Drifting subpulses. Some stars show another type of striking long-term order: drifting subpulses. These are easily identifiable features which drift through the mean profile (*e.g.*, Ramachandran *et al.* 2002). In a few cases they are known to be long-lived, lasting tens of rotation periods, and to circulate around the star's magnetic axis (Deshpande & Rankin 2001). These occur in some but not all stars; we do not know why.

Microstructure. Going to smaller timescales, some stars show microstructure, *i.e.*, significant power on $\delta t \sim 1 - 100\mu$s (*e.g.*, Lange *et al.* 1998). Once again, microstructure does not exist in all stars (Hankins & Fowler 1982, unpublished) and we do not understand why. The associated scale size $\lesssim 0.3 - 30$ km $\sim .03 - 3R_*$. We may be seeing plasma dynamics on scales up to the size of the emission region, or we may be seeing a nonsteady pair cascade.

Nanostructure. On even smaller time scales, nanostructure has been detected in giant pulses from the Crab pulsar. There is power on $\delta t \sim 10 - 100$ ns. We do not know whether this occurs in other stars; only the Crab pulsar has been studied at this time resolution. The associated spatial scale is $\lesssim 3 - 30$ m; we are "seeing" quite small structures.

8.3. Are these temporal or spatial fluctuations?

There has been much discussion of whether the short-term variability is temporal (due to true time changes in the emitting plasma) or spatial (as a narrow emission beam moves across the sight line). We believe it is temporal, and we argue as follows.

Consider the longer timescales. We can follow individual drifting subpulses for many rotation periods. They are surely due to long-lived plasma structures, moving within the polar cap. The fact that we can identify these structures as they move around the radio emission region (Deshpande & Rankin 2001), means that their emission beam cannot be extremely narrow.

Compare this to the shortest timescales known. If the Crab nanostructure were spatial (as tiny features move past our sightline) the emitting plasma would have to be bunched in very narrow columns, $\lesssim 1$ cm in width, moving at bulk Lorentz factors of $\sim 10^7$. This seems unlikely to us, and contradicts the evidence from drifting subpulses. If microstructure were

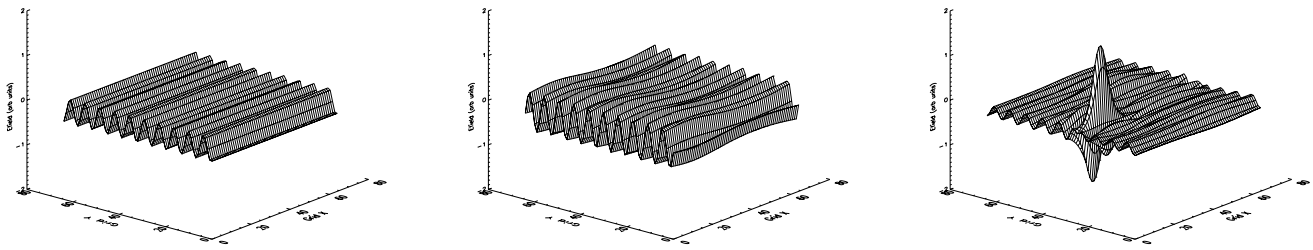


Fig. 5. Numerical simulation of the the electric field in strong plasma turbulence. The simulation spans a time interval of $200/\nu_{\rm p}$, and illustrates wave growth by beam-instabilty (left), modulational instability (center), and wavepacket collapse (right). The extent of the spatial grid is $64c/\omega_{\rm p}$, which scales to to 60γ cm at an observing frequency of 5 GHz. The radiation field produced by this collapse is shown in Figure 6. From Weatherall (1997).

spatial, the size and Lorentz factors of the required plasma columns would be less extreme, but would still disagree with the subpulse evidence. Based on this, we believe the short-term variability reflects time variability in the emitting plasma.

9. Dynamical Variability and Timescales – examples

We know that other plasmas, in the lab and in space, are dynamic and highly variable. We expect the pulsar plasma to be so as well. Thus, our observations of variability in the pulsar signal are indirect observations of the plasma dynamics. With an eye to the general models of the pulsar emission region, described above, we consider time and space scales on which we expect variability.

9.1. Micro-scale: the radiating entities

On the smallest space and time scales, the plasma variability will be that which produces coherent radiation. As we noted above, the specific emission process remains a mystery, and several competing models have been suggested. What these models have in common is sensitivity to the microscale dynamics of the underlying plasma. The large-scale structure of the radio-loud region sets the broad stage, but coherent radio emission is generated by evolving plasma structures on much smaller scales. We suspect that each emission process will have a characteristic timescale, which can in principle be observed.

Numerical simulations are needed to follow the plasma evolution and determine the time signature of each model. Weatherall (1997, 1998) has carried out such simulations for the plasma turbulent emission model. In this picture, a two-stream instability drives electrostatic plasma turbulence. When the turbulence becomes nonlinear, the modulation instability produces filamentation of the initial beam-resonant wave, which is followed by "collapse" of the wave along the field direction. Thus, the wave energy accumulates in transient, spatially localized regions. Figure 5 shows an example of this growth and collapse. Mode conversion during the explosive collapse phases generates radio emission (the coherence comes from the spatial localization of the plasma oscillation). The simulations reveal a distinctive time signature (Figure 6 shows one example) which comes from the coupling of the radiation modes to

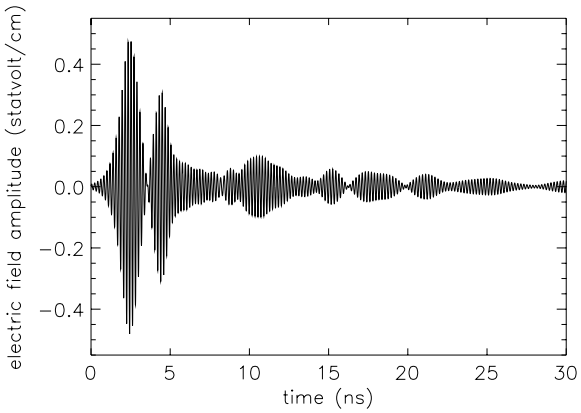


Fig. 6. Numerical simulation of a nanopulse: the amplitude of the radiation burst emitted by the strong-turbulence region shown in Figure 5. The characteristic time for radiation emitted at ν_o is $\nu_o \delta t \sim O(10)$; this figure has been scaled to an observing frequency of 5 GHz. From Weatherall (1998).

the beam-resonant wave. The simulations predict quite narrow band emission, $\Delta\nu/\nu \sim 0.2$, centered on the *comoving* plasma frequency; and predict timescales given by $\nu\delta t \sim O(10)$ (thus, a few ns at 5 GHz).

Other competing emission mechanisms will have their own characteristic timescales and temporal signatures associated with the "shots". For instance, curvature emission from coherent plasma bunches might evolve on a particle trapping timescale, *e.g.*, $(m\lambda/eE)^{1/2}$, where λ is the bunch length and the field is limited by $E^2 \lesssim 8\pi\gamma_{\rm p} mc^2 n_{\rm p}$. In addition, the bunch life may be limited by magnetic field curvature (*e.g.*, Melrose 1992). Combining these, we estimate this process has a longer timescale, $\sim 0.01 - 0.1\mu$s; but numerical simulations are required to confirm such speculation.

As the emission region is very likely inhomogeneous, containing many microscopic emitting structures (growing and collapsing wave packets, or coherent bunches which grow and dissipate), an observed pulse will be an incoherent collection of such nanobursts. Each nanoburst will contibute an impulse in a shot noise-type model. The individual impulses may be

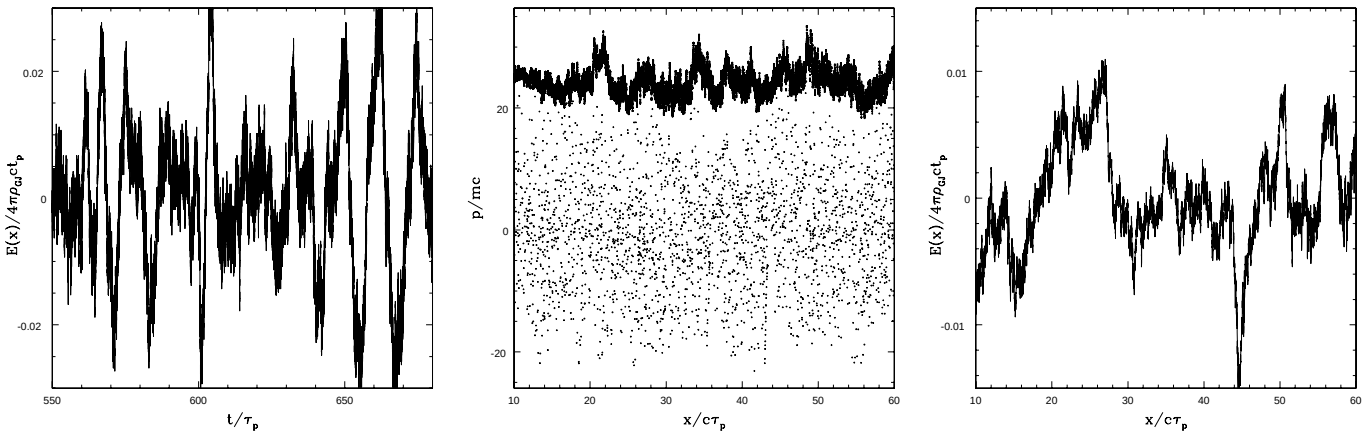


Fig. 7. Excitation of strong waves in a sub-GJ current. In this example, which is typical of our numerical experiments, a current density $j = 0.95 j_{\rm GJ}$ flows from the surface of the star ($x = 0$ on the grid). The simulation follows the positions and momenta of individual charges, and the electric field evolution in time and space. Left, a partial time series of the E field at one point of the grid. Center, a phase plot showing the resultant particle trapping. Right, a snapshot of the strong waves in the electric field, at one time during the run. We find that the frequency of the waves excited decreases as $j/j_{\rm GJ}$ approaches unity.

observable if their density is low enough; however a full understanding of the pulse nanostructure requires an understanding of the statistics of such shots. This also requires numerical simulation, and we are extending our plasma-turbulence work to address this issue.

9.2. Meso-scale: dynamical fluctuations.

When we consider the intermediate timescales of microstructure, we have likely left the regime of the fundamental radiation process. The associated length scales are comparable to the dimensions of the region (the acceleration region or the radio emission region). Thus, we are "seeing" the dynamical behavior of the radio-loud plasma, as it responds to local forces.

As an example of mesoscale dynamics, consider plasma flow in the acceleration region. The general $\mathbf{E}$ field in this region, whose divergence is the physical charge density ρ, can be separated into "corotation" and "other" parts:

$$\tilde{\mathbf{E}} = \mathbf{E} - \mathbf{E}_{\rm co} \qquad \nabla \cdot \tilde{\mathbf{E}} = 4\pi\,(\rho - \rho_{\rm GJ}) \tag{7}$$

The easiest way to follow plasma dynamics in this region is to work in the rotating frame, where the difference field, $\tilde{\mathbf{E}}$, controls particle motion. (Compare equation 1, where $\mathbf{E} = \mathbf{E}_{\rm co}$ was assumed). Thus, if $\mathbf{E} \neq \mathbf{E}_{\rm co}$ (that is if $\rho \neq \rho_{\rm GJ}$), the plasma feels a net force in the co-rotating frame.

Now, let the acceleration region sit within a pulsar circuit, so that the local current density is determined by the voltages and resistive loads of the full circuit. This density can easily differ from GJ. If it exceeds GJ (in absolute value), simple space-charge-accelerated flow can occur. If it is somewhat below GJ, however, the situation becomes more complicated. Several authors (*e.g.*, Shibata 1997, or Jessner *et al.*, this proceedings) have noted that steady-flow solutions display strong spatial oscillations when the current is sub-GJ.

We revisit this problem, allowing for time variability. We use a one-dimensional particle-in-cell code to model the space-charge acceleration of plasma escaping from the star's surface. The simplest situation starts with an external vacuum and a background (co-rotation) field. For super-GJ flow we verify that the system reaches the steady, space-charge-limited situation, $\Phi(z) \propto \gamma(z) \propto z^2$ (where Φ is the potential and z is the space coordinate; described *e.g.* by Shibata). In the interesting case of slightly sub-GJ flow, we also find oscillations, but now they are temporal as well as spatial. The outflowing plasma rapidly develops strong waves in the density and E field, in which feedback and nonlinear growth tends to trap the particles between the wave crests. This trapping slows, but does not stop, the advance of the charge front. A quasi-steady state is reached, in which the current is modulated by strong "trapping" waves. Figure 7 shows an example of this flow. Shibata predicted the spatial wave frequency would depend on the current density; we find this is true also of the temporal frequency. As the current approaches the co-rotation value, the oscillations slow down. We have found oscillation periods $\sim 10 - 100 \nu_{\rm p}^{-1}$ in our simulations to date, which could be observable as microstructure if $\nu_{\rm p}$ is identified with the observing frequency.

Our simulations do not include emission of escaping radiation. Thus, we cannot directly predict the time signature of the coherent radiation emitted by this plasma. That radiation will arise through the interaction of plasma charges and waves riding within the meso-scale structure which these simulations describe. We anticipate, however, that the density and field modulations seen in this non-stable system will be echoed in the escaping radiation. Thus, pulsars with strong microstructure signatures may be ones in which the current is close to but below the co-rotation current.

We expect similar results in other situations. One example is pair formation, which might disrupt an initially steady flow. Laboratory diodes are difficult to maintain in a steady state, because plasma formation at the diode disrupts the current, leading to strong waves and breakdown of the steady flow. We expect that pair formation in a pulsar acceleration region will have a similar effect. Rapid injection of new plasma in a steady-

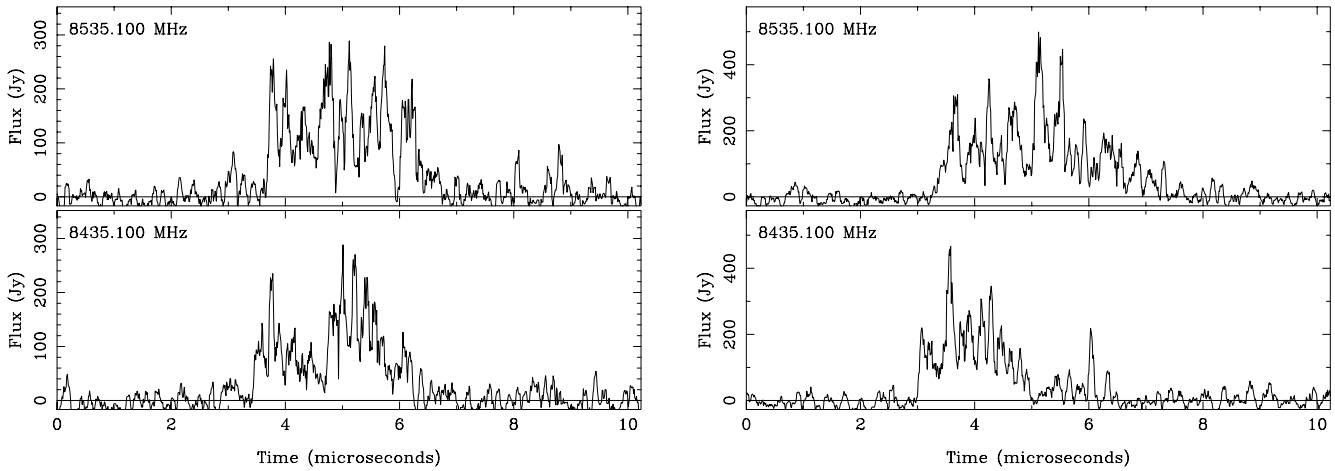


Fig. 8. Two single giant pulses from the interpulse of the Crab pulsar, each recorded simultaneously at 8.4 and 8.5 GHz. The data were obtained (after coherent dedispersion; §10.1) at 10 ns time resolution, and have been block smoothed to 80 ns. The dispersion delay has been removed.

flow region will disrupt the flow, leading to temporal variability that may be observable.

9.3. Macro-scale: self organization.

On longer timescales, many rotation periods, we leave plasma microphysics and go to larger-scale, MHD effects. These timescales are the most accessible observationally, and perhaps the most daunting theoretically.

One striking example is the long-lived drifting subpulses seen in some stars. Their drift rate is consistent with the $\mathbf{E}\times\mathbf{B}$ drift due to the non-corotation $\mathbf{E}$ field predicted by well-known models of the acceleration region (*e.g.*, Ruderman & Sutherland, 1975, or Arons & Scharlemann, 1978). The mystery of the drifting subpulses is their stability; the analysis of Deshpande & Rankin (2000) suggests that individual radio-loud structures retain their identity for 10–100 rotation periods. They have been modeled as "sparks" of localized pair creation, which may partially shield their immediate surroundings (*e.g.*, Ruderman & Sutherland). This does not seem to be the entire picture, however. Why should such sparks be so long-lived?

It is tempting to speculate that these long-lived plasma filaments are the result of a saturated plasma instability. Such features – for instance, quasi-stable, current-aligned filaments – are common in other plasma environments. The problem is how to make them. The radio-loud pulsar plasma is very highly magnetized, as shown by the energy ratio

$$\beta = \frac{8\pi\gamma nmc^2}{B^2} \sim 1\times10^{-18}\frac{\gamma n}{n_{\rm GJ}}\frac{(r/r_*)^3}{PB_{*,12}} \qquad (8)$$

(we have scaled the number density to the co-rotation value, the B field to its value at the star's surface, and assumed a dipole field). This shows that one must go to quite high altitudes before the plasma inertia becomes comparable to the magnetic energy density (so that normal MHD instabilities might be expected). Resistive instabilities are tempting; they are known to occur in low-β plasmas and can lead to field-aligned filaments. We agree with Melrose (2000) who suggested such structures in the context of the density problem. It may be that filaments exist in all pulsars at some level, and happen to be stronger or longer-lived in those with clear subpulse drift. However, without a good understanding of such details as cross-field resistivity in this environment, we can do no more than speculate on this interesting question.

10. A Case Study: Giant Pulses in the Crab pulsar

The Crab pulsar emits occasional "giant" pulses which can be thousands of times more intense than an average pulse. One of us (Hankins, with his colleagues) is making ultra-high time resolution observations of these giant pulses. The data can give us insight into the emission mechanism and the dynamics of the emitting plasma. In this section we present preliminary results which bear on the physics of the emission region.

10.1. Observations and Pulse Structure

Using the VLA in phased-array mode minimizes the signal from the surrounding nebula, and allows us to study individual giant pulses at time resolution down to a few ns. To achieve this we used coherent dedispersion. The incoming voltage is Nyquist sampled at 100 MHz. The samples are recorded for later, off-line processing which removes dispersion distortion. The signals are passed through a filter whose transfer function is the inverse of the (frequency-dependent) phase change imposed by propagation through the ISM. This technique allows us to recover the full time resolution of the emitted signal, limited only by the receiver bandwidth.

We reached 10 ns resolution at several frequencies from 1.4 to 15 GHz, making single frequency observations and also doing simultaneous observations at two frequencies. Individual pulses are quite complex when seen at this resolution. They often contain clear subpulses, which usually have a "Fred" shape ("*F*ast *R*ise, *E*xponential *D*ecay"). Figures 8 - 11 show some examples. The subpulse widths are typically $\sim 1\mu$s at 5 GHz, and $\sim 0.1\mu$s at 8 GHz. (We note that unresolved features can be found down to our resolution limit of 10 ns.)

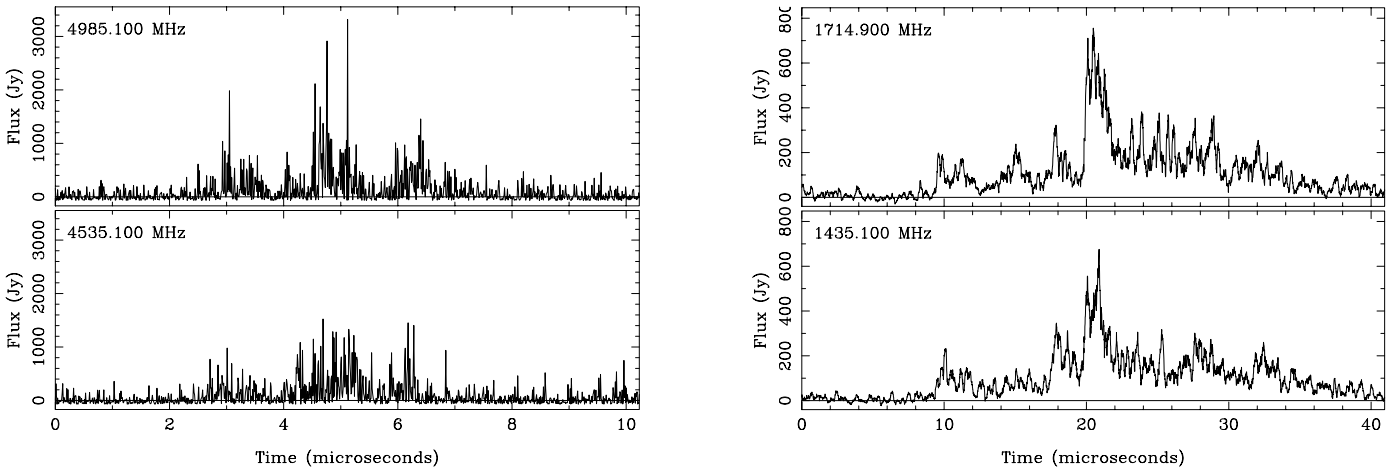


Fig. 9. Two single giant pulses from the Crab pulsar. Left, a pulse recorded simultaneously at two frequencies within C band, with time resolution 10 ns. Right, a (different) pulse recorded simultaneously at two frequencies within L band; the data have were obtained at 10 ns time resolution and have been smoothed to 200 ns. The dispersion delay has been removed for each pulse. These pulses illustrate the typical behavior of the star. The subpulses and micro-bursts are similar but not identical. Such data suggest that the intrinsic bandwidth of an individual "burst" of emission is at least $\delta\nu/\nu \sim 0.2$.

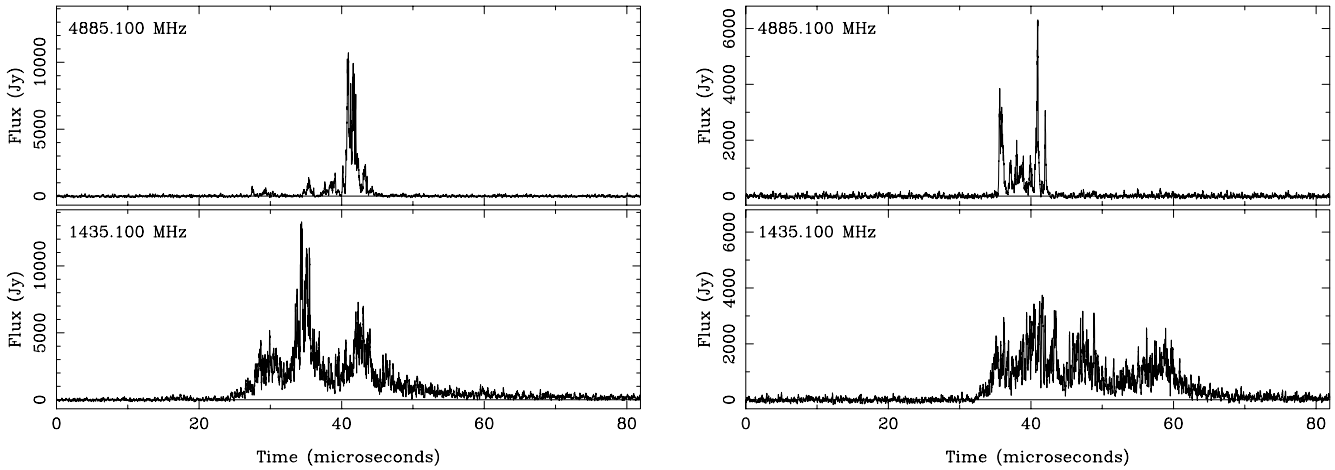


Fig. 10. Two more single giant pulses from the Crab pulsar. Each was recorded simultaneously at 5 and 1.4 GHz, obtained at 10 ns time resolution and smoothed to 100 ns. The dispersion delay has been removed. These two pulses are not as well correlated, over this larger frequency separation, as are the two illustrated in Figure 9. This behavior is typical of the star. We infer that the emission bandwidth of the microbursts which constitute an individual "giant pulse" is narrower than this frequency separation. Comparing this with data such as in Figure 9, we infer the intrinsic emission bandwidth obeys $0.2 \lesssim \Delta\nu/\nu < 1$, and that a giant pulse contains a collection of many such microbursts, distributed over a range of central emission frequencies.

Above $\sim$ 2 GHz we clearly see the intrinsic pulse shape; below $\sim$ 1 GHz the pulse width is dominated by nebular or interstellar scattering (ISS). In the range $\sim 1-2$ GHz single pulses or subpulses show the "Fred" shape characteristic of scattering, but have widths which do not follow the ν^{-4} law expected for ISS, and are strongly variable on a timescales less than an hour (too short to be from variations in the ISM). The average pulse width at high frequencies decays only slowly with frequency, and may obey $\Delta t(\nu) \propto \nu^{-2}$ (Moffett, 1997). We suspect that propagation through the magnetosphere broadens high-frequency subpulses and give them the "Fred" shape. Turbulent scattering in a cold, relativistically streaming pair plasma in fact gives the observed frequency signature (Eilek, 2002).

10.2. Emission bandwidth

Giant pulses in the Crab pulsar occur simultaneously over a broad frequency range, at least from 1.4 to 4.8 GHz. Thus, in some sense the emission is broad-band.

However, the situation becomes more complex if we consider substructure within a giant pulse. Our simultaneous two-frequency data suggest that the intrinsic emission bandwidth of *substructure* is narrow band. Compare Figures 8-10 in which we present simultaneous dual-frequency measurements of individual giant pulses. While we have not yet completed a statistical analysis of our two-frequency observations, our impression after working with the data is that the substructure in a giant pulse is well correlated if the two frequencies are close: 1.4 and 1.7 GHz, 4.5 and 5.0 GHz, or 8.4 and 8.5 GHz. However, the

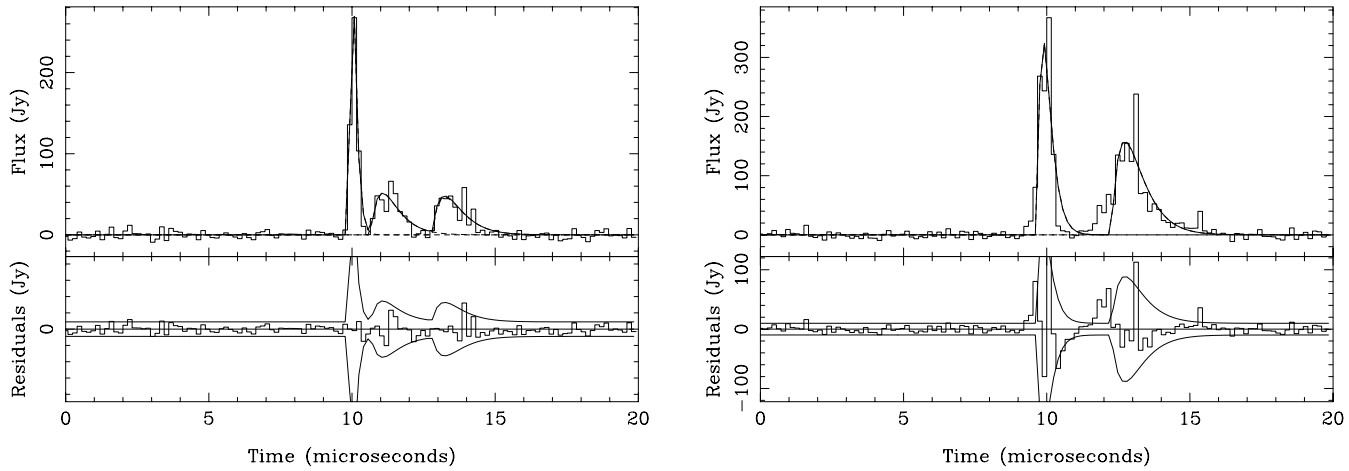


Fig. 11. Two representative X band pulses, illustrating "Fred" fits to subpulses. The data were fitted with a function $I(t) \propto I_o t e^{-t/\tau}$. (Thus, I_o measures the pulse height, τ the width, and the total energy $\propto I_o \tau$.) The upper plot shows the original data, taken at 8415 MHz and smoothed to 160 ns resolution, and the result of the "Fred" fits. The lower plot shows the 2σ estimation error of the fit and the fit residuals. The intensity I_o and width τ for a set of these fits are plotted in Figure 12.

substructure is less well correlated over a broader frequency range, such as 1.4 and 4.8 GHz. This suggests that the bandwidth of a given *subpulse* obeys $0.2 \lesssim \Delta\nu/\nu < 1$. Comparing this to the simulations by Weatherall (1998), we note that the observations are consistent with what his model predicts.

10.3. Energy content

Another interesting hint in the data is that individual subpulses conserve total energy, $E = \int I(t)dt$. We have fitted several data sets at 1.4, 4.8 and 8.4 GHz with the "Fred"-like function $I(t) = I_o t e^{-t/\tau}$, allowing multiple subpulses per giant pulse. Figure 11 shows examples of such fits. Typical results are shown in Figure 12. A plot of intensity I_o against width τ shows an upper envelope, which is consistent with $E \propto I_o \tau =$ constant. This is what one would expect if each subpulse results from a "collect and release" process, in which internal energy is stored until a threshold is reached, then suddenly released. The constant-energy envelope of the distribution then describes the total energy released in the burst, and the points below the envelope are what we would expect if the released energy is relativistically beamed at some angle to the line of sight.

We caution the reader that these results are preliminary, and require a careful statistical analysis of a larger, complete sample of high-frequency subpulses (currently underway). If further work supports our speculation, that the subpulses in giant pulses have an upper limit to their energy content, then the difference between this conclusion and the energy distribution of giant pulses presented by Lundgren *et al.* (1995) must be addressed. We note two differences between our work and theirs. We are considering subpulses, several of which may be contained in a giant pulse. In addition, our higher time resolution allows us to separate subpulse width and height, which may make the upper energy limit more apparent.

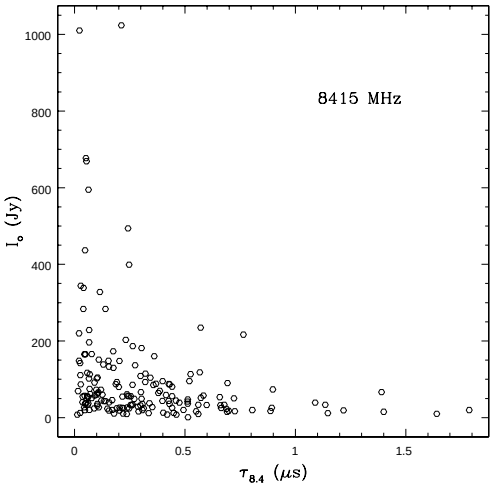


Fig. 12. Intensity *vs.* width for subpulse fits for one data set. The plot shows (τ, I_o) from fits to 180 subpulses identified in a set of 60 giant pulses, recorded within a bit over an hour at 8.4 GHz at the VLA. There is a tendency for weak pulses to be broad and strong pulses to be narrow; a constant energy ($I_o \propto 1/\tau$) envelope seems to exist.

10.4. The emission region in the Crab pulsar

From these data, we begin to draw a picture of the radio-loud plasma in the Crab pulsar. It is inhomogeneous and fluctuates on quite short timescales. Any given piece of the plasma is a narrow-band radio emitter; the larger frequency range of an individual giant pulse probably comes from the variable density within the region. A giant pulse seems to trace the simultaneous excitation of an extended region of plasma, in which different sub-regions independently reach some critical threshold and then release their stored energy in sudden, observable bursts.

Acknowledgments. We have learned a great deal about pulsar physics through discussion with a number of people, including Jon Arons, Gregory Benford, Janusz Gil, Wolfgang Kundt, Harald Lesch, Leon Mestel, Don Melrose and Dipanjan Mitra. We particularly appreciate the enthusiastism and hard questions supplied by Jeff Kern and Axel Jessner, and we thank Axel for his careful reading of this long paper. Work by the Socorro pulsar group has been partially supported by NSF grants AST-9315285 and AST-9618408. JE appreciates support and hospitality from the Heraeus foundation and the MPIfR while this paper was being written.

References

Arendt, P. N. Jr, 2002, Ph.D. thesis, New Mexico Tech
Arendt, P. N. Jr. & Eilek, J. A., 2002, submitted to ApJ.
Arons, J., 1981, in Proc. Varenna Summer School on Plasma Astrophysics, ed. T. D. Guyenne & G. Lévy (Noordwijk: ESA), 273
Arons, J. & Scharlemann, E. T., 1979, ApJ, 231, 854
Asseo, E., Pelletier, G. & Sol, H., 1990, MNRAS, 247, 529
Eilek, J. A., 2002, submitted to ApJ
Eilek, J. A. & Hankins, T. H., 2000, in IAU Colloquium 177, Pulsar Astronomy–2000 and Beyond, eds., M. Kramer, N. Wex & R. Wielebinski (San Francisco: ASP), 721
Eilek, J. A. & Hankins, T. H., 2002, in preparation
Daughtery, J. K. & Harding, A. K., 1982, ApJ, 252, 337
Deshpande, A. A. & Rankin, J. M., 2001, MNRAS, 322, 438
Hankins, T. H. & Rankin, J. R., 2002, in preparation.
Hibschman, J. A. & Arons, J., 2001, ApJ, 560, 871
Jessner, A., Lesch, H. & Kunzl, T., 2001, ApJ, 547, 959
Kazbegi, A. Z., Machabeli, G. Z. & Melikidze, G. I., 1995, MNRAS, 253, 377
Kijak, J. & Gil, J., 1997, MNRAS, 288, 631
Kunzl, T., Lesch. H., Jessner, A. & von Hoensbroech, A., 1998, ApJ, 505, L139
Kunzl, T., Lesch, H. & Jessner, A., 2002, submitted to A&A
Lange, C., Kramer, M., Wielebinski, R. & Jessner, A., 1998, A&A, 332, 111
Lundgren, S. C., Cordes, J. M., Ulmer, M., Matz, S. M., Lomatch, S., Foster, R. S. & Hankins, T. H., 1995, ApJ, 453, 433
Luo, Q. & Melrose, D. B., 1995, MNRAS 276, 372
Lyutikov, M. & Parikh, A., 2000, ApJ, 541, 1016.
Melrose, D. B., 1992, in IAU Colloquium 128, ed. T. H. Hankins, J. M. Rankin & J. A. Gil (Zielona G'ora: Pedaogical Univ. Press), 307
Melrose, D. B., 2000, in IAU Colloquium 177, eds., M. Kramer, N. Wex & R. Wielebinski (San Francisco: ASP), 721
Moffett, D., 1997, Ph.D. thesis, New Mexico Tech
Petrova, S. A. & Lyubarskii, Y. E., 2000, A&A, 355, 1168
Ramachandran, R., Rankin, J. M., Stappers, B.W., Kouwenhoven, M.L. A., & van Leeuwen, A. G. J., 2002, submitted to A&A
Rankin, J. R., 1993, ApJ, 405, 285
Rathnasree, N. & Rankin, J. R., 1995, ApJ, 452, 814
Ruderman, M. A. & Sutherland, P. G., 1975, ApJ, 196, 51
Shibata, S., 1991, ApJ, 278, 239
Shibata, S., 1997, MNRAS 287, 262
Shibata, S., Miyazaki, J. & Takahara, F., 1998, MNRAS 295, L53
Sturmer, S., 1995, ApJ, 446, 292
van Hoensbroech, A. & Xilouris, K. M., 997, A&A, 126, 121
Weatherall, J. C., 1994, ApJ, 428, 261
Weatherall, J. C., 1997, ApJ, 483, 402
Weatherall, J. C., 1998, ApJ, 506, 341
Weatherall, J. C., 2001, ApJ, 559, 196
Weatherall, J. C. & Eilek, J. A., 1997, ApJ, 474, 407

Proceedings of the 270. WE-Heraeus Seminar on: *"Neutron Stars, Pulsars and Supernova Remnants"*
Physikzentrum Bad Honnef, Germany, Jan. 21-25, 2002, eds. W. Becker, H.Lesch & J. Trümper, MPE Report 278, pp. 263-272

Modeling Neutron Star Atmospheres

V.E. Zavlin[1] **and G.G. Pavlov**[2]

[1] Max–Planck–Institut für extraterrestrische Physik, Giessenbachstraße, 85748 Garching, Germany
[2] The Pennsylvania State University, 525 Davey Lab, University Park, PA 16802, USA

Abstract. Models of thermal emission of neutron stars, presumably formed in their atmospheres, are needed to infer the surface temperatures, magnetic fields, chemical composition, and neutron star masses and radii from the observational data. This information, supplemented with model equations of state and neutron star cooling models, is expected to move us further in understanding the fundamental properties of the superdense matter in the neutron star interiors. The neutron star atmospheres are very different from those of usual stars due to the immense gravity and huge magnetic fields. In this presentation we review the current status of the neutron star atmosphere modeling and present most important results.

1. Introduction

A systematic study of X-ray emission from isolated neutron stars (NSs), including radio pulsars, has started after the launch of the *Einstein* and *EXOSAT* space observatories. These studies have shown that, generally, there are two different components of the NS X-ray emission — thermal and nonthermal. The nonthermal component with a power-law spectrum, observed from many radio pulsars, is believed to originate from the pulsar's magnetosphere, while the thermal component is emitted from the NS surface layers (atmospheres). The thermal radiation is particularly interesting because it can provide important information about the NS: its surface temperature, magnetic field, and chemical composition, as well as the NS radius and mass. Measuring these parameters for a sample of NSs is necessary for studying the thermal evolution of NSs and constraining the equation of state and composition of the superdense matter in the NS interiors (see the review by Yakovlev et al. in these Proceedings).

Thermal X-ray emission from the NS surface had been discussed by Chiu & Salpeter and Tsuruta in 1964, before NSs were discovered, and well before their thermal emission was detected with *Einstein* and *EXOSAT* (e.g., Cheng & Helfand 1983; Brinkmann & Ögelman 1987; Córdova et al. 1989; Kellet at al. 1987). Many new observational results on the NS thermal radiation were obtained in 1990' with the *ROSAT*, *ASCA*, and *EUVE* satellites (see Becker & Pavlov 2002 for a review). Thermal radiation from a few NSs was also detected in the optical-UV energy range with the *Hubble Space Telescope* (e. g., Pavlov, Stringfellow & Córdova 1996; Walter & Matthews 1997). Currently operating X-ray observatories, *Chandra* and *XMM*-Newton, are providing new excellent data on X-rays from NSs (see the contributions by Weisskopf, Becker, and Pavlov, Zavlin & Sanwal in these Proceedings).

To interpret these observations, one needs reliable models for the NS thermal radiation. The fact that the spectrum of radiation emergent from a NS atmosphere can be very different from a blackbody spectrum, and the angular distribution can be very far from isotropic, particular in a strong magnetic field, has been recognized long ago. For instance, Pavlov & Shibanov (1978) calculated spectra and angular distributions of radiation from a strongly magnetized NS atmosphere assuming the source function grows inward linearly in the emitting layers. First self-consistent models for NS atmospheres were developed by Romani (1987), for low magnetic fields, and Shibanov et al. (1992), for strong magnetic fields. Since then, various aspects of the NS atmosphere modeling have been investigated in many papers. Below we will overview the current status of this field and summarize some important results.

2. Distinctive features of NS atmospheres

The NS thermal radiation emerges, as in usual stars, in superficial layers which can be in a gaseous state (atmosphere) or a condensed state (liquid or solid surface), depending on surface temperature, magnetic field and chemical composition. A condensed surface forms at low temperatures and very strong magnetic fields. For instance, according to the estimates by Lai & Salpeter (1997), hydrogen is condensed in surface layers if $T \lesssim 1\times10^5$ K at $B = 1\times10^{13}$ G ($T \lesssim 1\times10^6$ K at $B = 5\times10^{14}$ G). At higher temperatures and/or lower magnetic fields, hydrogen does not condensate and forms an atmosphere.

In both usual stars and NSs the properties of radiation emergent from an atmosphere strongly depend on its chemical composition. The difference between usual stars and NSs is that in NSs we expect the emitting layers to be comprised of just one, lightest available, chemical element, not a mixture of elements, because heavier elements sink into deeper layers due to the immense NS gravitation (Alcock & Illarionov 1980). For instance, even a small amount of hydrogen (with a surface density of ~ 1 g cm^{-2}) is sufficient for the radiation to be indistinguishable from that emitted from a purely hydrogen atmosphere. Such an amount of hydrogen, $\gtrsim 10^{-20} M_\odot$, can be delivered onto the NS surface by, e. g., accretion from the interstellar medium and/or fallback of a fraction of the envelope ejected during the supernova explosion. If no hydrogen is present at the surface, a heavier chemical element is responsible for the radiative properties of the NS atmosphere. However,

a mixture of elements can be observed in the emitting layers if the NS is experiencing accretion with such a rate that the accreting matter is supplied faster than the gravitational separation occurs. Therefore, it is important to construct the NS atmosphere models for a variety of surface compositions, both 'pure' and mixed.

The gravitational separation of elements is one of the consequences of the enormous gravity at the NS surface, with the gravitational acceleration $g \sim 10^{14} - 10^{15}$ cm s^{-2}. The gravity makes NS atmospheres very thin, $\sim 0.1-10$ cm, and dense, $\rho \sim 10^{-2} - 10^{2}$ g cm^{-3}. Such a high density causes strong nonideality effects (pressure ionization, smoothed spectral features) which must be taken into account (e. g., Pavlov et al. 1995). In addition, the strong gravitational field bends the photon trajectories near the NS surface (Pechenick, Ftaclas & Cohen 1983), as illustrated by the sketch in Figure 1. This effect depends on the gravitational parameter $g_{\rm r} = (1 - 2GM/c^2R)^{1/2}$, and it can even make the whole NS surface visible if the NS is massive enough, $M > 1.8\,(10\,{\rm km}/R)\,M_\odot$. In particular, the gravitational bending strongly affects the observed pulsations of thermal emission (Zavlin, Shibanov & Pavlov 1995a).

Huge magnetic fields, $B \sim 10^{11} - 10^{14}$ G, in the surface layers of many NSs change the properties of the atmospheric matter and the emergent radiation even more drastically. Strongly magnetized NS atmospheres are essentially anisotropic, with radiative opacities depending on the magnetic field and the direction and polarization of radiation. Moreover, since the ratio of the cyclotron energy, $E_{\rm ce} = \hbar eB/m_{\rm e}c$, to the Coulomb energy is very large (e.g., $\gamma \equiv E_{\rm ce}/(1\,{\rm Ry}) = 850\,(B/10^{12}\,{\rm G})$ for a hydrogen atom), the structure of atoms is strongly distorted by the magnetic field. For instance, the binding (ionization) energies of atoms are increased by a factor of $\sim \ln^2\gamma$ (e. g., the ionization potential of a hydrogen atom is about 310 eV at $B = 10^{13}$ G). This, in turn, significantly modifies ionization equilibrium of the NS atmospheric matter. Another important effect is that the heat conductivity of the NS crust is anisotropic (it is higher along the magnetic field). This results in a nonuniform surface temperature distribution (Greenstein & Hartke 1983), which leads to pulsations of the thermal radiation due to NS rotation.

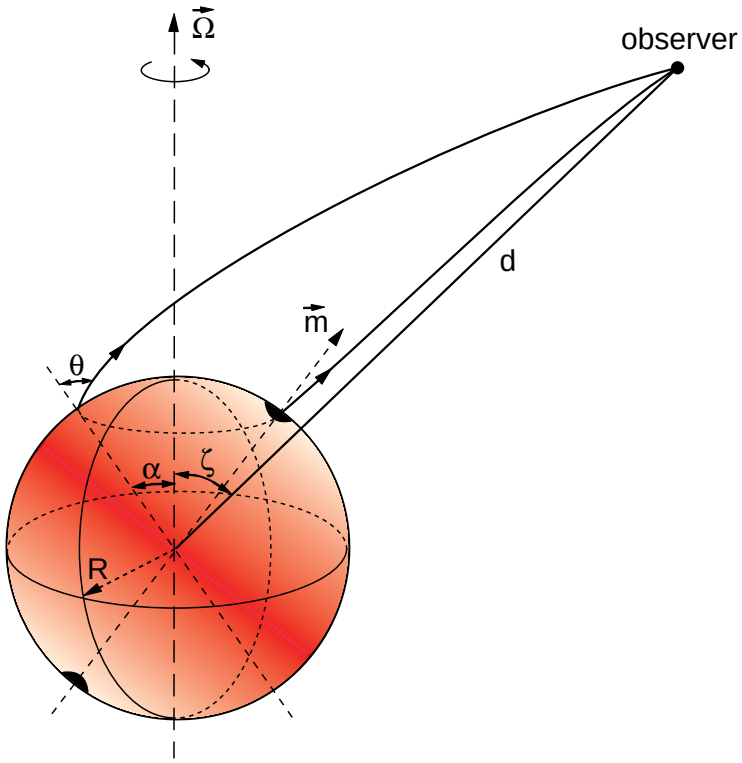


Fig. 1. Bending of photon trajectories in a strong gravitational field near the surface of a NS with rotational and magnetic axes $\boldsymbol{\Omega}$ and $\boldsymbol{m}$, respectively.

3. Atmosphere models with low magnetic fields

Some NSs (e.g., millisecond pulsars) have relatively low magnetic fields, $B \lesssim 10^9$ G. In such magnetic fields the electron cyclotron energy, $E_{\rm ce} \lesssim 0.01$ keV, is lower than the binding energy of atoms and thermal energy of particles. As a result, the effect of the field on the radiative opacities and emitted spectra is negligible, at X-ray energies, $E \gtrsim 0.1$ keV. Hence, to model low-field NS atmospheres, one can merely put $B = 0$. These models are applicable to millisecond pulsars, NS transients in quiescence (e.g., Rutledge et al. 2002), and, perhaps, to some radio-quiet isolated NSs. One should remember, however, that the magnetic field effects on spectral opacity at optical wavelengths must be included even for these low fields if the models are applied for interpreting the optical spectra.

First models of low-field NS atmospheres were presented in the pioneering work by Romani (1987). Since then, models for various surface chemical compositions have been developed by Rajagopal & Romani (1996), Zavlin, Pavlov & Shibanov (1996), Pavlov & Zavlin (2000a), Werner & Deetjen (2000), Pons et al. (2002), Gänsicke, Braje & Romani (2002).

3.1. General approach

As the thickness of a NS atmosphere is much smaller than the NS radius, $R \approx 10$ km, NS atmospheres can be considered in the plane-parallel approximation. In addition, rather high densities of the surface layers allow one to consider the atmospheres to be in local thermodynamic equilibrium.

The standard approach for the atmosphere modeling includes solving of three main equations. The first one is the radiative transfer equation for the specific spectral intensity I_ν (e. g., Mihalas 1978):

$$\mu \frac{{\rm d}}{{\rm d}y} I_\nu = k_\nu (I_\nu - S_\nu)\,, \qquad (1)$$

where μ is cosine of the angle θ between the normal to the atmosphere and the wave-vector of radiation, y is the column density (${\rm d}y = \rho\,{\rm d}z$, with z being the geometrical depth), $k_\nu = \alpha_\nu + \sigma_\nu$ is the total radiative opacity which includes the 'true absorption' (α_ν) and scattering (σ_ν) opacities, $S_\nu = (\sigma_\nu J_\nu + \alpha_\nu B_\nu)k_\nu^{-1}$ is the source function, $J_\nu = \frac{1}{2}\int_{-1}^{1} I_\nu\,{\rm d}\mu$ is the mean spectral intensity, and B_ν is the Planck function. The boundary

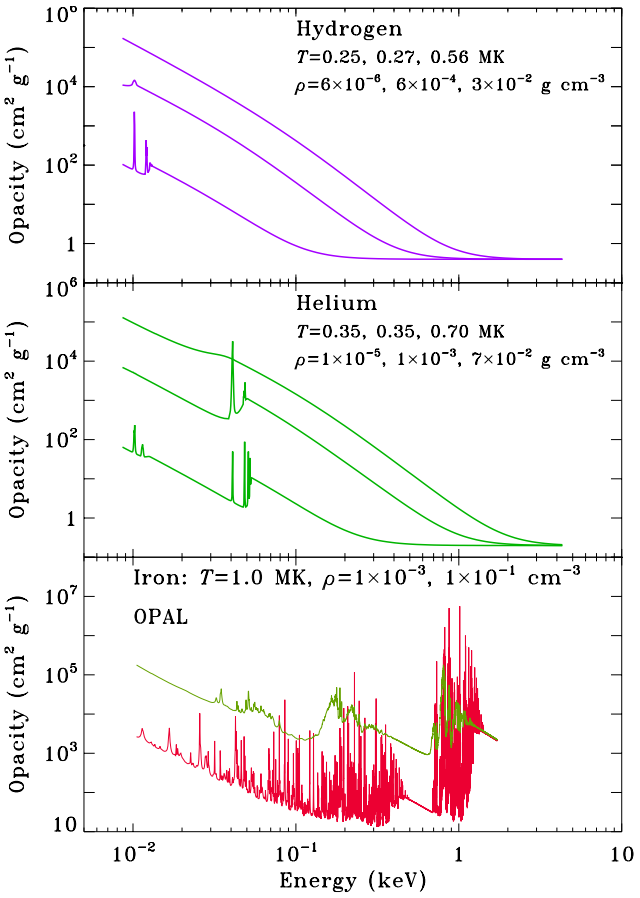


Fig. 2. Radiative spectral opacity k_ν for hydrogen, helium and iron plasmas at different temperatures and densities (magnetic field $B = 0$). The iron opacity is provided by the OPAL group (Rogers & Iglesias 1994).

condition for this equation is $I_\nu = 0$ for $\mu < 0$ at $y = 0$, assuming no incident radiation at the NS surface.

NS atmospheres are usually considered to be in radiative and hydrostatic equilibrium. The first condition implies that the total energy flux through the atmosphere is constant and transferred solely by radiation,

$$\int_0^\infty \mathrm{d}\nu \int_{-1}^{1} \mu I_\nu \, \mathrm{d}\mu = \sigma_{\rm SB}\, T_{\rm eff}^4 \,, \qquad (2)$$

where $T_{\rm eff}$ is the effective temperature, and $\sigma_{\rm SB}$ is the Stefan-Boltzmann constant. The second condition means that the atmospheric pressure is $P = g\,y$ (the radiative force is insignificant unless $T_{\rm eff} \gtrsim 10^7$ K). Finally, these three equations are supplemented with the equation of state for the atmospheric plasma and equations of ionization equilibrium. The latter is needed for computing the electron number density and the fractions of ions in different stages of ionization to obtain the radiative opacity with account for free-free, bound-free and bound-bound transitions (see examples in Fig. 2)[1]. A detailed description of the model computations can be found, e.g., in Zavlin et al. (1996).

[1] Opacities of heavy chemical elements used in this work were calculated by the OPAL group:
`http://www-phys.llnl.gov/Research/OPAL/index.html`

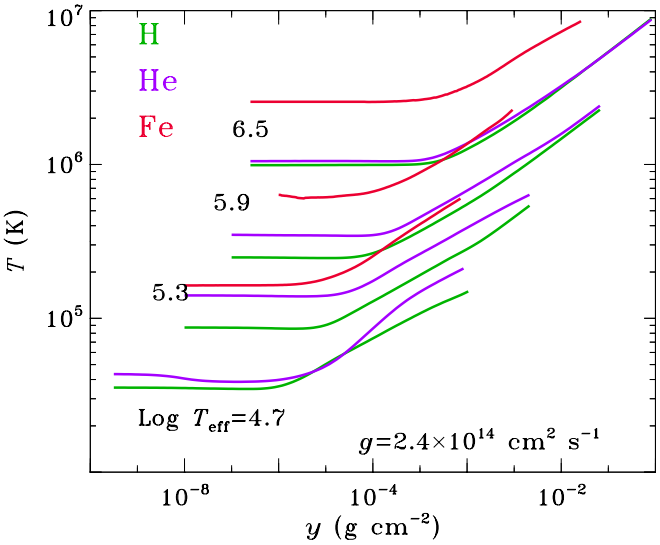


Fig. 3. Temperature dependences $T(y)$ in nonmagnetic atmosphere models with different effective temperatures and chemical compositions.

3.2. Results

To explain the main properties of the atmosphere emission, we first present in Figure 3 the most important property of the atmospheric structure responsible for the emergent radiation — the depth dependence of the temperature in the NS surface layers, $T(y)$.

Figure 4 presents the spectral fluxes of emergent radiation at a local surface point, $F_\nu = \int_0^1 \mu I_\nu \mathrm{d}\mu$ (at $y = 0$), for several effective temperatures and chemical compositions (pure hydrogen, helium and iron, and a solar mixture), together with the blackbody spectral fluxes at the same $T_{\rm eff}$. The model spectra differ substantially from the blackbody spectra, particularly in high-energy tails of the spectra of light-element (hydrogen and helium) atmospheres[2]. The reason for such behavior is in the rapid decrease of the light-element opacities with energy ($\sim E^{-3}$, see the upper and middle panels in Fig. 2), so that the high-energy radiation is formed in deeper and hotter layers (Fig. 3). Since the radiative opacity is large at lower energies, the low-energy photons escape from very superficial layers with a temperature $T(0) < T_{\rm eff}$. Therefore, the low-energy tails of the model spectra are suppressed with respect to the Rayleigh-Jeans spectra at the same $T_{\rm eff}$.

The spectra emitted from the heavy-element atmospheres (iron and solar mixture) exhibit numerous spectral lines and photoionization edges (e. g., M, L and K spectral complexes in the iron spectra) produced by ions in various ionization stages. Generally, they are closer to the blackbody radiation because the energy dependence of the heavy-element opacities is, on

[2] The nonmagnetic hydrogen atmosphere models are available at `http://legacy.gsfc.nasa.gov/docs/xanadu/xspec`

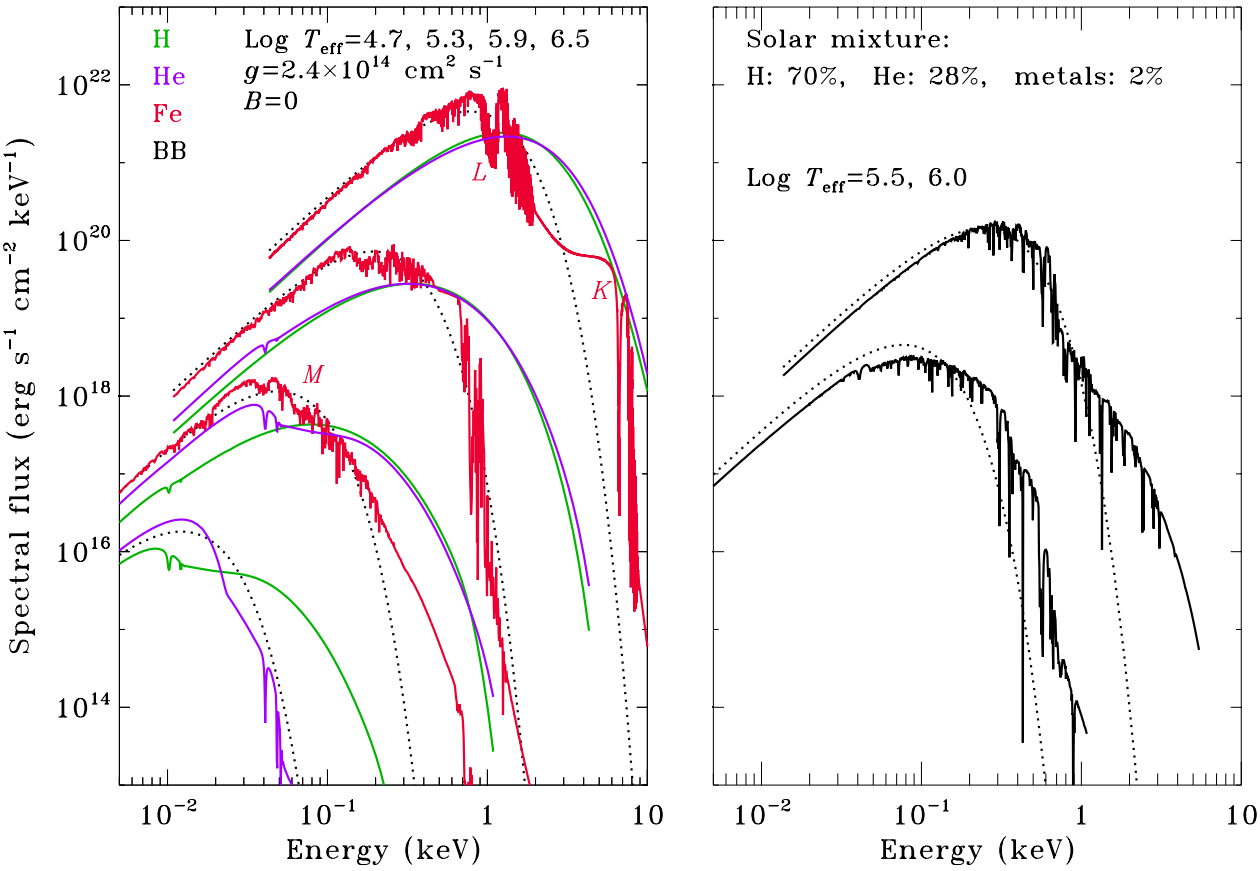


Fig. 4. Spectral fluxes of emergent radiation in nonmagnetic atmosphere models for several effective temperatures and chemical compositions.

average, flatter than that for the light elements (see examples in the bottom panel of Fig. 2). However, local deviations from the blackbody spectra can be very substantial. Moreover, the spectral features can be rather strong even if metals contribute as little as 0.05% of the total NS atmosphere composition (see Fig. 5).

Although the opacity of the atmospheric plasma is isotropic in the nonmagnetic case, the emitted radiation show substantial anisotropy, i. e., the specific intensity I_ν depends on the direction of emission due to the limb-darkening effect (Fig. 6). At large values of the angle θ between the normal to the surface and the wave-vector the emerging photons are produced in shallow layers with lower temperatures. The anisotropy depends on photon energy and chemical composition of the atmosphere. This effect should be taken into account to model thermal radiation from a nonuniform NS surface (see Section 5).

The emergent radiation depends also on the surface gravity: a stronger gravitational acceleration increases the density of the atmospheric plasma and enhances the nonideality effects, which results in weaker (more smoothed) spectral features (see examples in Fig. 6 of Zavlin et al. 1996). However, this effect is rather small and might be important only for analyzing observational data of extremely good statistics.

4. Atmosphere models with strong magnetic fields

It is commonly believed that most NSs (at least active radio/X-ray/γ-ray pulsars) have rather strong surface magnetic fields, $B \sim 10^{10}$–10^{14} G. Such fields drastically change the properties of NS atmospheres, as discussed above. Magnetic hydrogen models have been developed by Shibanov et al. (1992), Pavlov et al. (1994), Shibanov & Zavlin (1995), Pavlov et al. (1995), and Zavlin et al. (1995b). These models use simplified radiative opacities of strongly magnetized, partially ionized plasma, which do not include the bound-bound transitions. However, they are considered to be reliable enough in the case of high temperatures ($T_{\rm eff} \gtrsim 10^6$ K at typical radio-pulsar fields $\sim 10^{12}$ G), when the atmospheric plasma is almost fully ionized even in the strong magnetic fields. Recently, completely ionized hydrogen models for superstrong magnetic fields, $B \sim 10^{14}$–10^{15} G, have been presented in a number of papers (Bezchastnov et al. 1996; Bulik & Miller 1997; Özel 2001; Ho & Lai 2001; Zane et al. 2001), concerned mainly with the vacuum polarization effects (Pavlov & Gnedin 1984) and the ion cyclotron lines whose energies get into the X-ray band at $B \gtrsim 2 \times 10^{13}$ G. A set of magnetic iron models was constructed by Rajagopal, Romani & Miller (1997), with the use of rather crude approximations for the very complicated properties of iron ions in strong magnetic fields. The iron atmosphere spectra show many prominent

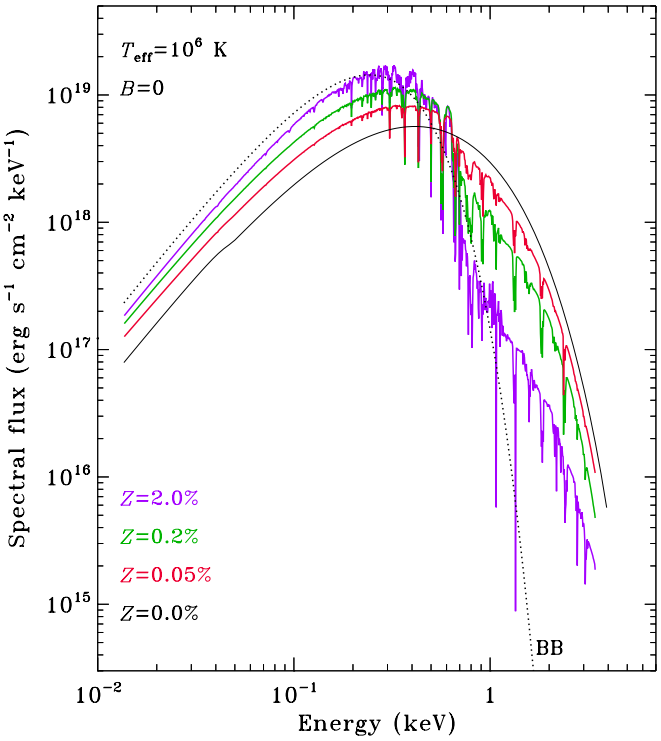


Fig. 5. Spectral fluxes of emergent radiation in nonmagnetic models with different metal abundances Z (Z = 2.0% corresponds to the standard solar mixture of elements — see Grevesse & Noels 1993).

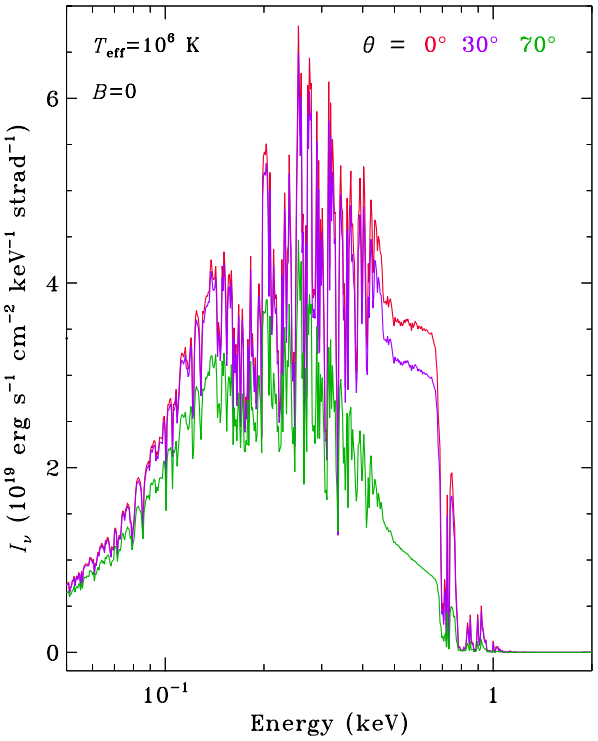


Fig. 6. Spectra of specific intensities I_ν emitted from an iron atmosphere with $T_{\rm eff} = 1 \times 10^6$ K, at different angles θ ($\mu = \cos\theta$).

spectral features which could be very useful to measure the NS magnetic field and the mass-to-radius ratio.

4.1. General approach

Modeling magnetic NS atmospheres is generally similar to the nonmagnetic case. The main difference is that the atmospheric radiation is polarized, and the radiative opacities depend on the polarization and direction of radiation. Gnedin & Pavlov (1974) described the radiative transfer in a strongly magnetized plasma in terms of coupled equations for specific intensities of two normal modes, $I_{\nu,1}$ and $I_{\nu,2}$, with different polarizations and opacities:

$$\mu \frac{\mathrm{d}}{\mathrm{d}y} I_{\nu,j}(\boldsymbol{n}) = k_{\nu,j}(\boldsymbol{n}) I_{\nu,j}(\boldsymbol{n}) -$$

$$- \left[\sum_{i=1}^{2} \oint \mathrm{d}\boldsymbol{n}'\, I_{\nu,i}(\boldsymbol{n}')\, \sigma_{\nu,ij}(\boldsymbol{n}', \boldsymbol{n}) + \alpha_{\nu,j}(\boldsymbol{n}) \frac{B_\nu}{2} \right], \qquad (3)$$

where $\boldsymbol{n}$ is the (unit) wave-vector, $\alpha_{\nu,j}$ is the absorption opacity for the j-th mode, and $\sigma_{\nu,ij}$ is the scattering opacity from mode i to mode j. It should be noted that the opacity depends on the angle between the wave-vector and the magnetic field, so that I_ν depends not only on θ, but also on $\Theta_{\rm B}$, the angle between the local magnetic field and the normal to the NS surface. Similar to the nonmagnetic case, equations (3) are supplemented with the equations of radiative and hydrostatic equilibrium. To overcome the problems with the sharp angular dependence of the radiative opacities (Kaminker, Pavlov & Shibanov 1982), a two-step method for modeling of magnetic NS atmospheres was developed (Pavlov et al. 1994; Shibanov & Zavlin 1995). At the first step, the radiative transfer is solved in the diffusion approximation for the mean intensities $J_{\nu,j} = (4\pi)^{-1} \oint I_{\nu,j}(\boldsymbol{n})\, \mathrm{d}\boldsymbol{n}$:

$$\frac{\mathrm{d}}{\mathrm{d}y} d_{\nu,j} \frac{\mathrm{d}}{\mathrm{d}y} J_{\nu,j} = \bar{\alpha}_{\nu,j} \left[J_{\nu,j} - \frac{B_\nu}{2} \right] + \bar{\sigma}_\nu \left[J_{\nu,j} - J_{\nu,3-j} \right], \qquad (4)$$

where $d_{\nu,j}$ is the diffusion coefficient, $\bar{\alpha}_{\nu,j}$ and $\bar{\sigma}_\nu$ are the angle-averaged absorption and scattering opacities (see Pavlov et al. 1995 for details). Next, the atmospheric structure obtained at the first step is corrected using an iterative procedure applied to the exact equations of the radiative transfer.

4.2. Results

Figure 7 shows polarization-summed spectral fluxes of the emergent radiation, $F_\nu = \int_0^1 \mu (I_{\mu,1} + I_{\mu,2})\, \mathrm{d}\mu$, emitted by a local element of the NS surface, for several values of effective temperature and magnetic field perpendicular to the surface ($\Theta_{\rm B} = 0$). The main result is that the magnetic model spectra are harder than the blackbody radiation of the same $T_{\rm eff}$, although they are softer than the low-field spectra. Similar to the low-field case, this is explained by the temperature growth with depth and the opacity decrease at higher energies, which is more gradual ($\propto E^{-1}$ for the mode with smaller opacity) compared to the nonmagnetic case. At lower effective temperatures, $T_{\rm eff} \lesssim 10^6$ K, the photoionization opacity is important, and the dependence of the spectra on magnetic field becomes

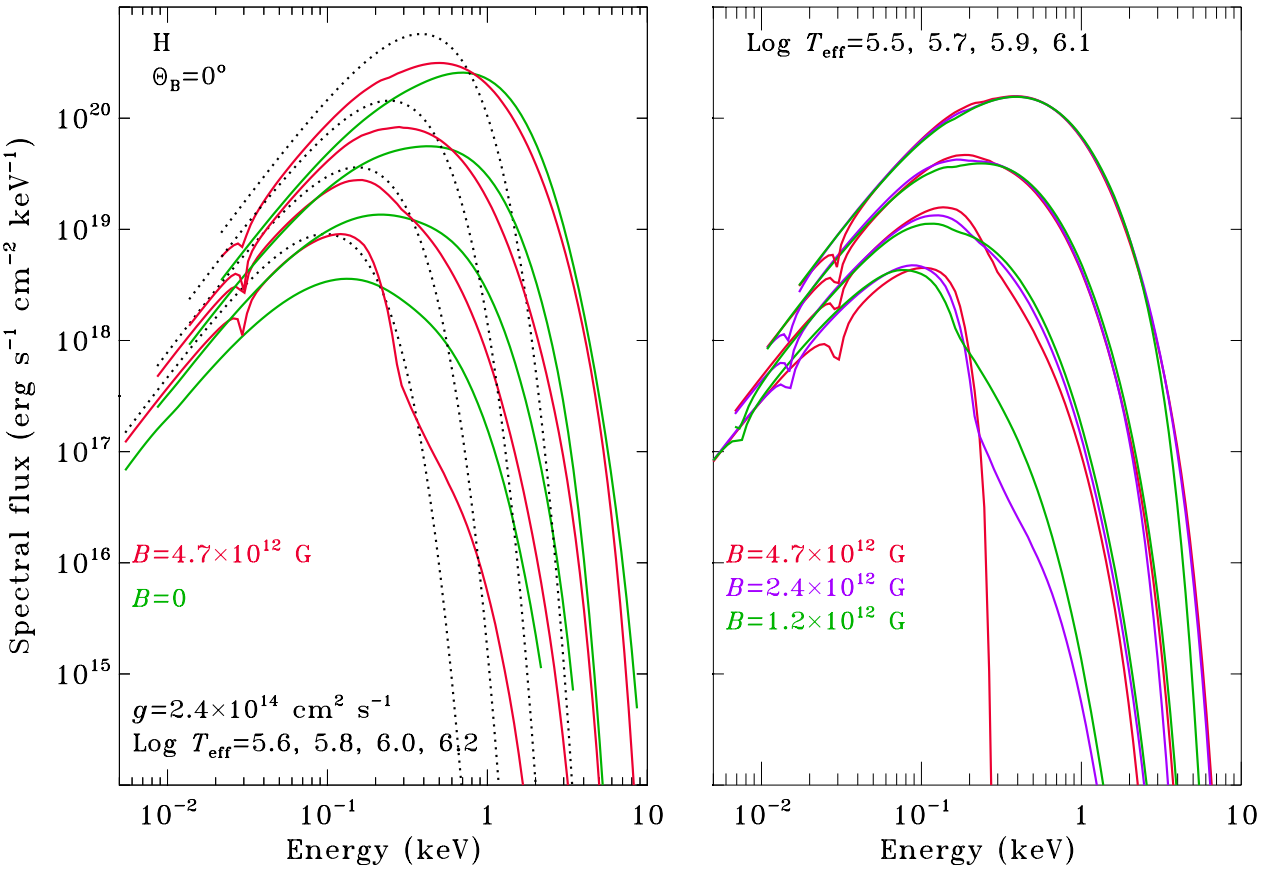


Fig. 7. Spectral fluxes of radiation emerging from magnetic hydrogen atmospheres, for several effective temperatures and magnetic fields perpendicular to the surface.

more pronounced (see the right panel in Fig. 7). The field dependence is most clearly seen, at $T_{\rm eff}$ sufficiently high to provide strong ionization, in the proton cyclotron lines centered at energies $E_{\rm cp} = 6.3\,(B/10^{12}\,{\rm G})$ eV. If the magnetic field is very large, $B \gtrsim 10^{14}$ G, the proton cyclotron line shifts into the X-ray band and can be very strong (see Fig. 8). On the other hand, if the magnetic field is not so large, $B = 10^{10}$–10^{12} G, the NS atmosphere spectra may exhibit the electron cyclotron lines in the X-ray band, at $E_{\rm ce} = 11.6\,(B/10^{12}\,{\rm G})$ keV (see Fig. 9).

First calculations of hydrogen atmosphere models which include bound-bound transitions show that spectral lines, considerably broadened by the motional Stark effect (Pavlov & Mészáros 1993; Pavlov & Potekhin 1995) become prominent at $T_{\rm eff} \lesssim 5 \times 10^5$ K. The strongest line corresponds to the transition between the ground state and the lowest excited state; its energy is $E \approx [75(1 + 0.13\ln(B/10^{13}\,{\rm G}) + 63(B/10^{13}\,{\rm G})]$ eV, at $B \sim 10^{13}$ G (see examples in Fig. 10).

Radiation emerging from a magnetized NS atmosphere is strongly anisotropic. Angular dependences of the local specific intensities, $I_\nu = I_{\nu,1} + I_{\nu,2}$, show a complicated "pencil-plus-fan" structure — a narrow peak along the direction of the magnetic field (where the atmospheric plasma is most transparent for the radiation), and a broader peak at intermediate angles. The widths and strengths of the peaks depend on magnetic field and photon energy (see examples in Fig. 11). Obviously, it is very important to account for this anisotropy while modeling the radiation from a NS with nonuniform surface magnetic field, effective temperature, and chemical composition.

5. Thermal radiation as seen by a distant observer

Results presented in Sections 3 and 4 describe spectral radiation emitted by a *local* element at the NS surface. The effective temperature and/or magnetic field distributions over the NS surface can be nonuniform (for example, if a NS has a dipole magnetic filed, the effective temperature decreases from the magnetic poles to the equator). To calculate the *total* NS emission, one has to integrate the local intensities, computed for local temperatures and magnetic fields, over the visible part of the NS surface S, with account for the gravitational redshift and bending of photon trajectories:

$$F(E) = g_{\rm r}\frac{1}{D^2}\int_S \mu\, I(E/g_{\rm r})\,{\rm d}S\,, \qquad (5)$$

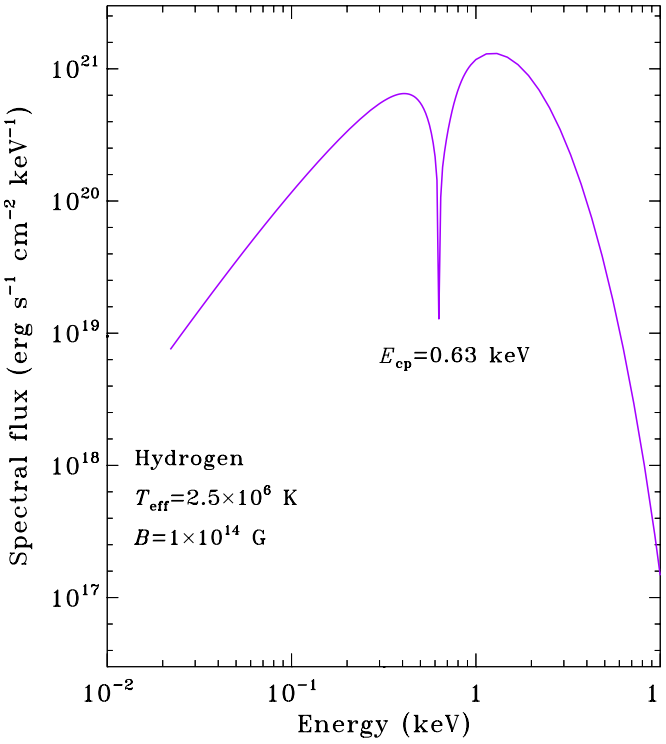


Fig. 8. Spectral flux of radiation emerging from an atmosphere with $B = 10^{14}$ G, with a strong proton cyclotron line.

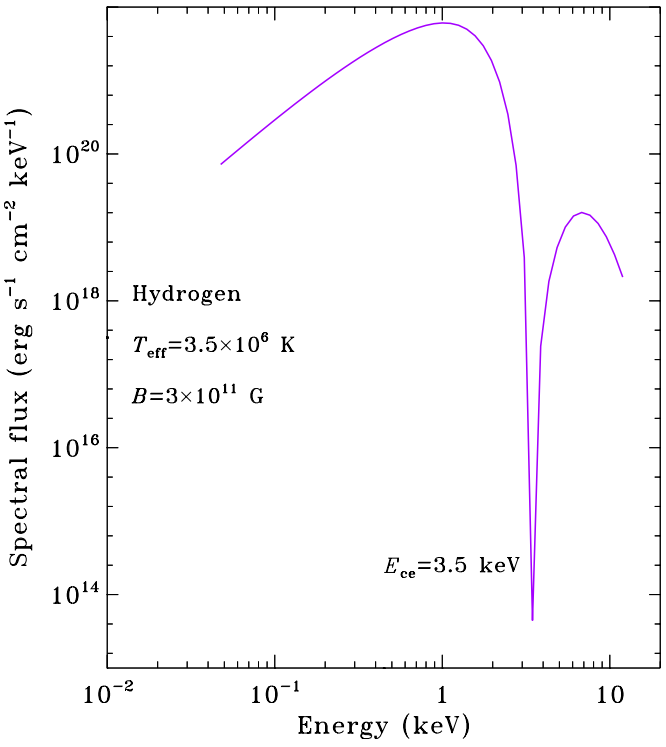


Fig. 9. Spectral flux of radiation emerging from an atmosphere with $B = 3 \times 10^{11}$ G, with a strong electron cyclotron line.

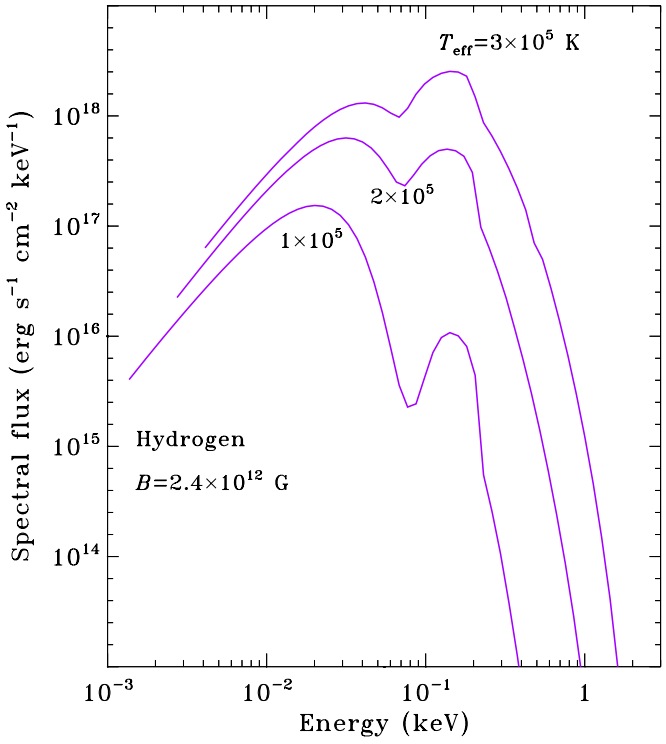


Fig. 10. Spectral fluxes of radiation emerging from hydrogen atmospheres with $B = 2.4 \times 10^{12}$ G and different values of $T_{\rm eff}$, with bound-bound transitions included.

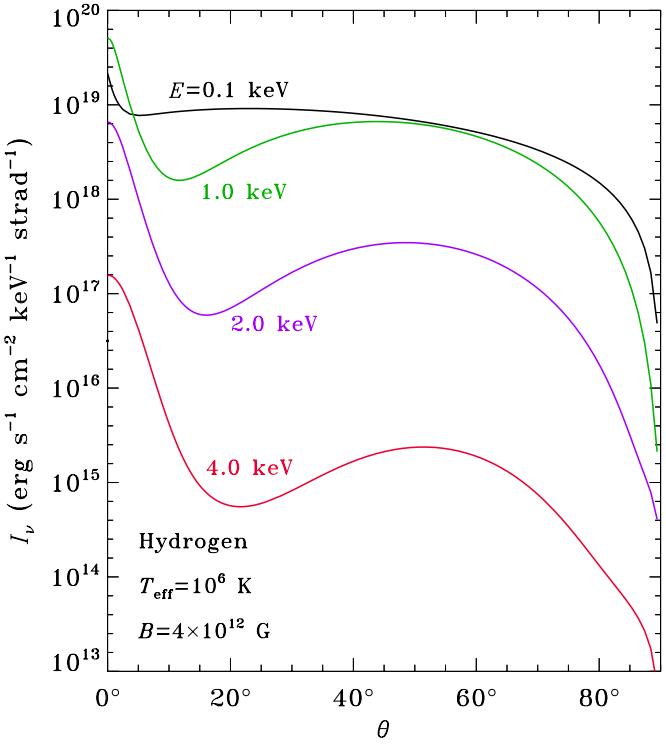


Fig. 11. Angular dependences of polarization-summed specific intensities at different photon energies E in the hydrogen atmosphere model with $T_{\rm eff} = 1 \times 10^6$ K and magnetic field $B = 4 \times 10^{12}$ G, perpendicular to the surface.

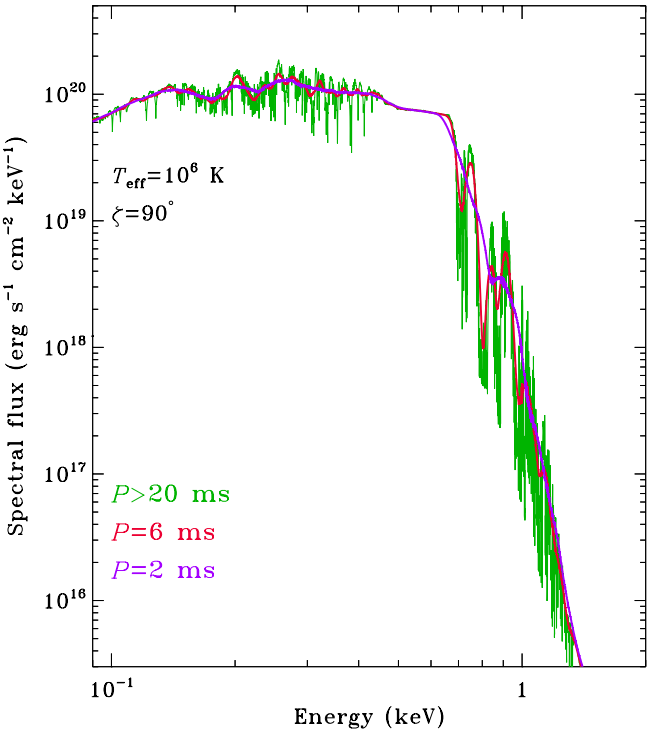


Fig. 12. Spectral fluxes of radiation from the *whole* surface of a nonmagnetic NS covered with an iron atmosphere at $T_{\rm eff} = 1 \times 10^6$ K. The (unredshifted) spectra are calculated for different NS rotation periods P, at the inclination of rotational axis $\zeta = 90^\circ$.

where D is the distance from the NS to the observer, and E is the *observed* (redshifted) energy[3]. More details about the integration over the NS surface can be found in Pavlov & Zavlin (2000b). In should be noted that if a NS has a nonuniform (e.g., dipole) distribution of the magnetic field, the integration broadens the spectral features (in particular, cyclotron resonance lines — see Zavlin et al. 1995b; Pavlov & Zavlin 2000b; Zane et al. 2001).

If the NS is a fast rotator, one should take into account the Doppler shifts of energies of photons emitted from surface elements moving with different radial velocities. Maximum values of these velocities, $v_r = 2\pi R P^{-1} \sin\zeta$ (P is the rotation period, ζ the inclination of the rotation axis), can be as high as 10%–15% of the speed of light for millisecond periods. Figure 12 presents (unredshifted) spectra emitted from the whole NS surface covered with an iron atmosphere (nonmagnetic case). For slowly rotating NSs, $P \gtrsim 20$ ms, there is no significant effect on the emergent radiation. Fast rotation, $P \lesssim 10$ ms, may lead to complete smearing of weak and narrow spectral lines, provided $\sin\zeta$ is large enough, leaving only most prominent spectral jumps around the strongest photoionization edges.

In the case of radio pulsars, a fraction of the observed thermal X-ray radiation is emitted from small hot spots (polar caps) around the NS magnetic poles. These polar caps can be heated up to X-ray temperatures by relativistic particles impinging on the poles from the acceleration zone in the pulsars' magnetosphere. In the case of millisecond pulsars, with characteristic ages of 10^8–10^9 yr, the whole NS surface (except for the polar caps) is believed to be too cold ($T_{\rm eff} \lesssim 10^5$ K) to be observable in X-rays, so the detected thermal emission can be modeled as emitted from small heated spots:

$$F(E) = g_{\rm r} \frac{S_{\rm a}}{D^2} I(E/g_{\rm r},\, \theta^*)\,, \qquad (6)$$

where the apparent spot area $S_{\rm a}$ and the angle θ^* between the wave-vector and the radius-vector to the hot spot are computed with account for the effect of gravitational bending. These quantities depend on the angles α (between the rotational and magnetic axes) and ζ (between the rotational axis and the line of sight — see Fig. 1), and the gravitational parameter $g_{\rm r}$ (see Zavlin et al. 1995a for details).

The flux given by equations (5) or (6) varies with the period of NS rotation. One can obtain a large variety of pulse profiles at different assumptions on the angles α and ζ and the NS mass-to-radius ratio. Examples of pulse profiles computed for radiation from the whole NS surface are shown in Figure 13; pulse profiles of thermal radiation from heated polar caps are presented by Zavlin et al. (1995a).

Although the model atmosphere spectra are different from the blackbody spectra, very often an observed thermal spectrum can be fitted equally well with the blackbody and NS atmosphere models, particularly when the energy resolution is low and/or the energy band is narrow. However, the parameters obtained from such fits are quite different, especially when the hydrogen or helium atmospheres are used. Since the light-element atmosphere spectra are much harder than the blackbody spectra at the same effective temperature, atmosphere model fits give temperatures $T_{\rm atm}$ significantly lower than the blackbody temperature $T_{\rm bb}$, with a typical ratio $T_{\rm bb}/T_{\rm atm} \sim 2$–3 (see, for example, Pavlov et al. 1996; Pons et al. 2002). On the other hand, to provide the same total energy flux, the blackbody fit gives a smaller normalization factor, proportional to S/D^2, than the atmosphere model fit. In other words, the light-element atmosphere fit gives a considerably larger size of the emitting region, $S_{\rm atm}/S_{\rm bb} \sim 50$–200, for the same distance to the source.

6. Conclusions

In the recent decade, substantial progress has been made in modeling atmospheres of isolated NSs. Best investigated cases are nonmagnetic atmospheres and fully-ionized light-element atmospheres with strong magnetic fields. The atmosphere models have been applied to the interpretation of thermal emission from NSs of different types. For instance, Pavlov & Zavlin (1997), Zavlin & Pavlov (1998), and Zavlin et al. (2002) analyzed the X-ray emission from the millisecond pulsar J0437–4715 using the nonmagnetic light-element atmosphere models; Pavlov et al. (2001) applied the magnetic hydrogen models to the analysis of radiation from the Vela pulsar; Zavlin, Pavlov & Trümper (1998) and Zavlin, Trümper & Pavlov (1999) used the magnetic light-element models to interpret the thermal emission from NSs in the supernova remnants PKS 1209–51/52 and Puppis A. More examples are presented in the contribution by Pavlov et al. in this volume.

[3] To take into account the interstellar absorption, a factor of $\exp[-n_{\rm H}\sigma_{\rm eff}(E)]$ should be added in eq. (5) [$\sigma_{\rm eff}(E)$ is the absorption cross section per hydrogen atom].

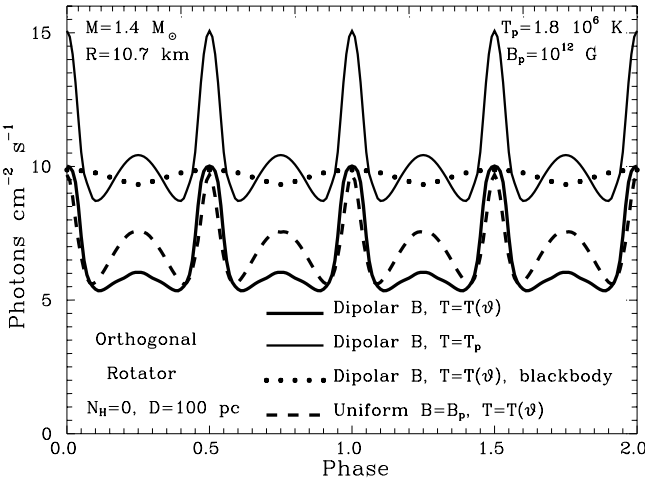


Fig. 13. Energy-integrated light curves of a rotating NS with different distributions of surface temperature and magnetic field (from Shibanov et al. 1995). The temperature is either uniform, $T = T_{\rm p}$, or nonuniform, $T = T(\vartheta)$, as given by computations with account for the anisotropy of the heat conductivity in the NS crust (ϑ is magnetic colatitude, $T_{\rm p}$ and $B_{\rm p}$ are the effective temperature and the field at the magnetic poles). The NS rotational axis is perpendicular to both the magnetic axis and the line of sight ($\alpha = \zeta = 90^\circ$).

However, a number of problems in the atmosphere modeling remains to be solved. First of all, investigations of the structure of various atoms, molecules, and molecular chains in strong magnetic fields, as well as radiative transitions in these species (Pavlov 1998), are necessary to construct magnetic atmosphere models of different chemical compositions. First efforts in this direction are being undertaken (Mori & Hailey 2002). Particularly interesting are the (virtually unknown) radiative properties of matter in superstrong magnetic fields, $B \gtrsim 10^{14}$ G, apparently found in anomalous X-ray pulsars and soft gamma-ray repeaters. Further work is needed on radiative properties of nonideal plasmas and condensed matter. These investigations will eventually result in more advanced models for thermal radiation of isolated NS, needed for the interpretation of high-quality observations of these objects with the *Chandra* and *XMM*-Newton X-ray observatories.

Acknowledgements. The authors gratefully acknowledge the support by the Heraeus foundation and the hospitality of the Physikzentrum Bad Honnef. Work of GGP was partially supported by NASA grant NAG5-10865.

References

Alcock C., Illarionov A.F., 1980, ApJ, 235, 534
Becker W., Pavlov G.G., 2002, in The Century of Space Science, eds. J. Bleeker, J. Geiss & M. Huber (Dordrecht: Kluwer), in press
Bezchastnov V.G., Pavlov G.G., Shibanov Yu.A., Zavlin V.E., 1996, in Gamma-ray Bursts, Proc. 3rd Huntsville Symp., AIP Conf. Proc., v.384, eds. C. Kouveliotou, M. Briggs & G.J. Fishman (NY: Woodbury), p.907
Bulik T., Miller M.C., 1997, MNRAS, 288, 596
Brinkmann W., Ögelman H., 1987, A&A, 182, 71
Cheng A.F., Helfand D.J., 1983, ApJ, 271, 271
Chiu H.Y., Salpeter E.E., 1964, Phys. Rev. Let., 12, 413
Córdova F.A., Hjellming R.M., Mason K.O., Middleditch J., 1989, ApJ, 345, 451
Gänsicke B.T., Braje T.M., Romani R.W., 2002, A&A, 386, 1001
Gnedin Yu.N., Pavlov G.G., 1974, Sov. Phys.-JETP, 38, 903
Greenstein G., Hartke G.J., 1983, ApJ, 271, 283
Grevesse N., Noels A., 1993 in Origin and Evolution of the Elements, eds. E. Prantzos, M. Vaugioni-Flam & M. Gasse (Cambridge University Press), p.14
Ho W.C.G., Lai D., 2001, MNRAS, 327, 1081
Kaminker A.D., Pavlov G.G., Shibanov Yu.A., 1982, Ap&SS, 86, 249
Kellet B.J., et al., 1987, MNRAS, 225, 199
Lai D., Salpeter E.E., 1997, ApJ, 491, 270
Mihalas D., 1978, Stellar Atmospheres (San Francisco: Freeman)
Mori, K., Hailey, C.J. 2002, ApJ, 564, 914
Özel F., 2001, ApJ, 563, 276
Pavlov G.G., 1998, in Atoms and Molecules in Strong External Fields, eds. P. Schmelcher & W. Schweizer (New York: Plenum), p.37
Pavlov G.G., Shibanov Yu.A., 1978, Sov. Astron., 22, 214
Pavlov G.G., Gnedin Yu.N., 1984, Astrophys. Space Phys. Rev., 3, 197
Pavlov G.G., Mészáros P., 1993, ApJ, 416, 752
Pavlov G.G., Potekhin Y.A., 1995, ApJ, 450, 883
Pavlov G.G., Zavlin V.E., 1997, ApJ, 490, L91
Pavlov G.G., Zavlin V.E. 2000a, in Highly Energetic Physical Processes and Mechanisms for Emission from Astrophysical Plasmas, IAU Symp. 195, eds. P.C.H. Martens, S. Tsuruta & M.A. Weber (PASP), p.103
Pavlov G.G., Zavlin V.E., 2000b, ApJ, 529, 1011
Pavlov G.G., Shibanov Yu.A., Ventura J., Zavlin V.E., 1994, A&A, 289, 847
Pavlov G.G., Shibanov Yu.A., Zavlin V.E., Meyer R.D., 1995, in The Lives of Neutron Stars, eds. A. Alpar, U. Kilizóglu & J. van Paradijs (Dordrecht: Kluwer), p.71

Pavlov G.G., Stringfellow G.S., Córdova F.A., 1996, ApJ, 489, L75
Pavlov G.G., Zavlin V.E., Trümper J., Neuhäuser R., 1996, ApJ, 472, L33
Pavlov G.G., Zavlin V.E., Sanwal D., Burwitz V., Garmire G.P., 2001, ApJ, 552, L129
Pechenick K.R., Ftaclas C., Cohen J.M., 1983, ApJ, 274, 846
Pons J.A., Walter F.M., Lattimer J.M., Prakash M., Neuhäuser R., An P., 2002, ApJ, 564, 981
Rajagopal M., Romani R.W. 1996, ApJ, 461, 327
Rajagopal M., Romani R.W., Miller M.C., 1997, ApJ, 479, 347
Rogers F.J., Iglesias C.A., 1994, Science, 263, 50
Romani R.W. 1987, ApJ, 313, 718
Rutledge R.E., Bildsten L., Brown E.F., Pavlov G.G., Zavlin V.E., 2002, ApJ, 559, 1054
Shibanov Yu.A., Zavlin V.E., 1995, Astron. Let., 21, 3
Shibanov Yu.A., Zavlin V.E., Pavlov G.G., Ventura J., 1992, A&A, 266, 313
Shibanov Yu.A., Pavlov G.G., Zavlin V.E., Qin L., Tsuruta S., 1995, in Proc. 17-th Texas Symposium on Relativistic Astrophysics, eds. H. Bohringer, G. Morfill, & J. Trümper, Ann. NY Acad. Sci. 759 (New York), p.291
Tsuruta, S., 1964, Ph.D. Thesis, Columbia Univ., N.Y.
Walter F.M., Matthews L.D., 1997, Nature, 389, 358
Werner K., Deetjen J., 2000, in Pulsar Astronomy — 2000 and Beyond, eds. M. Kramer, N. Wex & R. Wielebinski, ASP Conf. Ser., 202, 623
Zane S., Turolla R., Stella L., Treves A., 2001, ApJ, 560, 384
Zavlin V.E., Pavlov G.G., 1998, A&A, 329, 583
Zavlin V.E., Shibanov Yu.A., Pavlov G.G., 1995a, Astron. Let., 21, 149
Zavlin V.E., Pavlov G.G., Shibanov Yu.A., Ventura J., 1995b, A&A, 297, 441
Zavlin V.E., Pavlov G.G., Shibanov Yu.A., 1996, A&A, 315, 141
Zavlin V.E., Pavlov G.G., Trümper J. 1998, A&A, 331, 821
Zavlin V.E., Trümper J., Pavlov G.G. 1999, ApJ, 525, 959
Zavlin V.E., Pavlov G.G., Sanwal D., Manchester R.N., Trümper J., Halpern J.P., Becker W., 2002, ApJ, 569, 894

Proceedings of the 270. WE-Heraeus Seminar on: *"Neutron Stars, Pulsars and Supernova Remnants"*
Physikzentrum Bad Honnef, Germany, Jan. 21-25, 2002, eds. W. Becker, H.Lesch & J. Trümper, MPE Report 278, pp. 273-286

Thermal Radiation from Neutron Stars: Chandra Results

G.G. Pavlov[1], V.E. Zavlin[2] and D. Sanwal[1]

[1] The Pennsylvania State University, 525 Davey Lab., University Park, PA 16802, USA
[2] Max–Planck–Institut für extraterrestrische Physik, Giessenbachstraße, 85748 Garching, Germany

Abstract. The outstanding capabilities of the *Chandra* X-ray observatory have greatly increased our potential to observe and analyze thermal radiation from the surfaces of neutron stars (NSs). Such observations allow one to measure the surface temperatures and confront them with the predictions of the NS cooling models. Detection of gravitationally redshifted spectral lines can yield the NS mass-to-radius ratio. In rare cases when the distance is known, one can measure the NS radius, which is particularly important to constrain the equation of state of the superdense matter in the NS interiors. Finally, one can infer the chemical composition of the NS surface layers, which provides information about formation of NSs and their interaction with the environment. We will overview the recent *Chandra* results on the thermal radiation from various types of NSs –active pulsars, young radio-quiet neutron stars in supernova remnants, old radio-silent "dim" neutron stars– and discuss their implications.

1. Introduction

Observational study of thermal emission from isolated (non-accreting) neutron stars (NSs) became possible after the launch of *Einstein* (1979) and *EXOSAT* (1983), the first X-ray observatories equipped with X-ray telescopes. Contrary to non-thermal radiation of NSs, generated in the pulsar magnetospheres and observed from radio to γ-rays, thermal emission originates immediately at the surface, with the bulk of the energy flux in the soft X-ray band. Therefore, comparing the spectra and the light curves with the models for NS thermal radiation (see the contribution by Zavlin & Pavlov in these Proceedings; ZP02 hereafter), one can infer the NS surface temperature, magnetic field, gravitational acceleration, and chemical composition, as well as the NS mass and radius. The analysis of such observations allows one to trace thermal evolution of NSs (Tsuruta 1998) and constrain the properties of the superdense matter in the NS interiors (D.G. Yakovlev et al., these Proceedings).

Observational manifestations of NSs are very diverse, and only some of these exotic objects are suitable for observing the NS thermal emission. Most of the *detected* NSs are radio pulsars. Very young, active pulsars (with ages $\tau \lesssim 10^3$ yr — e.g., the Crab pulsar) are quite hot, with expected surface temperatures $\sim$ 1–2 MK, but their non-thermal radiation is so bright that the thermal radiation is hardly observable. The non-thermal component in X-ray emission of middle-aged pulsars ($\tau \sim 10^4$–10^6 yr — e.g., B0656+14, B1055–52) is much fainter, and their thermal radiation, with temperatures 0.3–1 MK, can dominate at soft X-ray and UV energies. The surfaces of old pulsars ($\tau \gtrsim 10^6$ yr — e. g., B0950+08, B1929+10, J0437–4715) are too cold to be seen in X-rays, but their polar caps are expected to be heated up to a few million kelvins, hot enough to emit observable thermal X-ray radiation.

In addition to active pulsars, a number of radio-quiet isolated NSs emitting thermal-like X-rays have been detected, with typical temperatures $\sim$ 0.5–5 MK. They are usually subdivided in four classes: Anomalous X-ray Pulsars (AXPs; see S. Mereghetti et al., these Proceedings), Soft Gamma-ray Repeaters (SGRs; Kouveliotou 1995), "dim" or "truly isolated" radio-silent NSs (i.e., not associated with supernova remnants [SNRs]; Treves et al. 2000), and compact central sources (CCOs) in SNRs (Pavlov et al. 2002a) which have been identified with neither active pulsars nor AXPs/SGRs. Their observational manifestations (particularly, multiwavelength spectra) are quite different from those of "active" pulsars, and their properties have not been investigated as extensively, but the presence of the thermal component in their radiation provides a clue to understand the nature of these objects.

First thermally emitting isolated NSs were detected with *Einstein* (e.g., Fahlman & Gregory 1981; Cheng & Helfand 1983; Helfand & Becker 1984; Seward, Charles, & Smale 1986; Córdova et al. 1989) and investigated with *EXOSAT* (Brinkmann & Ögelman 1987; Kellett et al. 1987). In 1990's, *ROSAT* and *ASCA* detected X-rays from more than 30 radio pulsars, including a few thermal emitters (Ögelman 1995), and discovered several radio-silent NSs (see Becker & Pavlov 2002 for a review). Thermal emission from a few isolated NSs was also detected in the optical-UV range with the *Hubble Space Telescope* (e.g., Pavlov, Stringfellow & Córdova 1996; Walter & Matthews 1997).

The new era in observing X-ray emission from NSs has started with the launch of two currently operating X-ray observatories of outstanding capabilities, *Chandra* and *XMM*-Newton. In this review we present recent results on thermal X-ray emission from isolated NSs of various types observed with *Chandra*. A more general overview of *Chandra* observations of NSs is presented in this volume by M.C. Weisskopf, while the *XMM*-Newton results on NSs are reviewed by W. Becker.

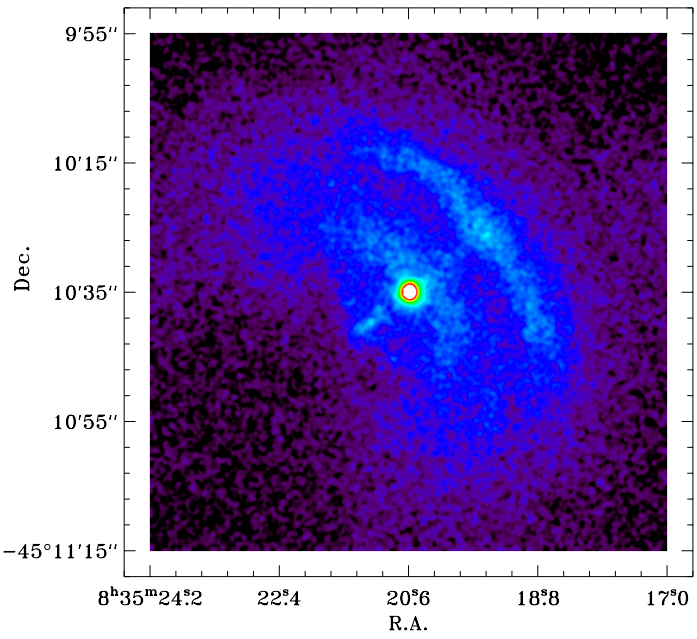


Fig. 1. *Chandra* HRC-I image of the Vela pulsar and surrounding nebula.

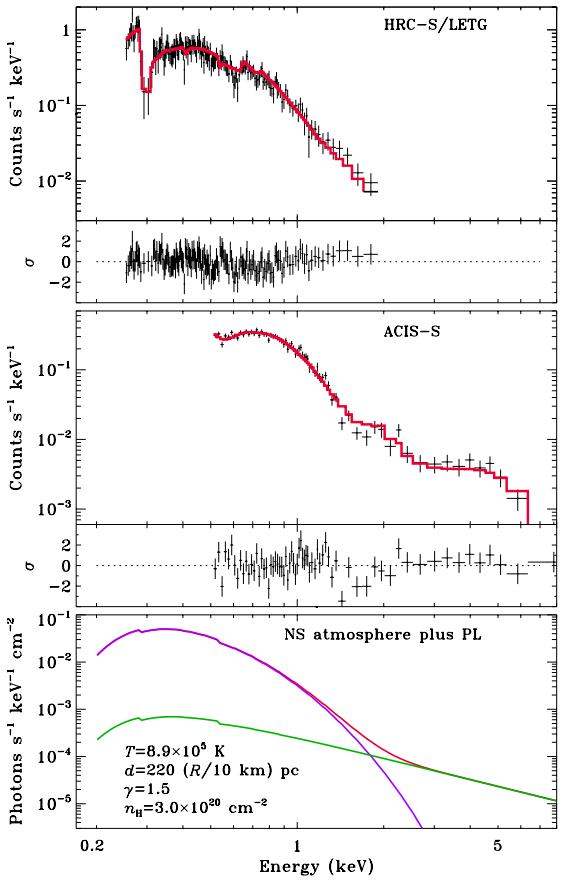


Fig. 2. Two-component (magnetic hydrogen NS atmosphere plus power law) model fit to the combined HRC-S/LETG and ACIS count rate spectra. The bottom panel shows the contributions from the thermal and non-thermal components (lilac and green lines, respectively).

2. Thermal emission from radio pulsars

X-ray emission of rotation-powered pulsars generally consists of two components — thermal and non-thermal. The non-thermal component, generated by relativistic particles in the NS magnetosphere, is, as a rule, strongly pulsed and characterized by a power-law (PL) spectrum. Studying the magnetospheric component is important to understand the mechanisms of the multiwavelength (optical through gamma-rays) pulsar radiation. The thermal component, emitted from the NS surface, can be observed in X-rays if it is not buried under the non-thermal component, as in very young pulsars, and if the temperature is not too low, as in old pulsars. Weak pulsations of the thermal emission can be caused by temperature nonuniformities along the NS surface and/or anisotropy of the radiation intensities in a strong magnetic field (see ZP02). Stronger pulsations of thermal radiation can be observed in old pulsars which emit thermal X-ray radiation from small, hot polar caps around the magnetic poles. In this Section we present the results of our analysis of *Chandra* data on pulsars of different ages: the young Vela pulsar ($\tau_c \equiv P/2\dot{P} = 11$ kyr), the middle-aged pulsars B0656+14 ($\tau_c = 110$ kyr) and B1055–52 ($\tau_c = 500$ kyr), and the very old millisecond pulsar J0437–4715 ($\tau_c = 4.9$ Gyr).

2.1. The Vela pulsar

First *Chandra* observations of this famous 89-ms radio, optical and γ-ray pulsar in the Vela SNR (the distance $d \approx 300$ pc — Caraveo et al. 2001) were carried out with the imaging array of the High Resolution Camera (HRC-I) in January and February 2000. These observations revealed a very complicated structure of the PWN around the pulsar (see Fig. 1) studied by Helfand, Halpern & Gotthelf (2001) and Pavlov et al. (2000, 2001a). The superb spatial resolution of *Chandra* made it possible, for the first time, to resolve the pulsar from its surroundings and investigate the pulsar's radiation.

The spectral data on the Vela pulsar were obtained in two observations (Pavlov et al. 2001b). A 25 ks HRC-S observation with Low Energy Transmission Grating (LETG) of January 2000 provided the high-resolution pulsar spectrum in the energy range $E = 0.25$–2.0 keV. The analysis of the LETG spectrum ($\approx 7,000$ source counts) did not reveal statistically significant spectral lines. The spectrum is best fitted with thermal models (blackbody, hydrogen NS atmosphere), but the observed spectrum somewhat exceeds the model spectra at $E \gtrsim 1.5$ keV (see upper panel in Fig. 2), indicating the presence of a second component with a harder spectrum. The spectrum at higher photon energies was provided by a 37 ks observation (October 1999) with the Advanced CCD Imaging Spectrometer (ACIS), taken in the Continuous Clocking (CC) mode that allows timing at the expense of imaging capability in one dimension. The 1-D count distributions of the pulsar and the

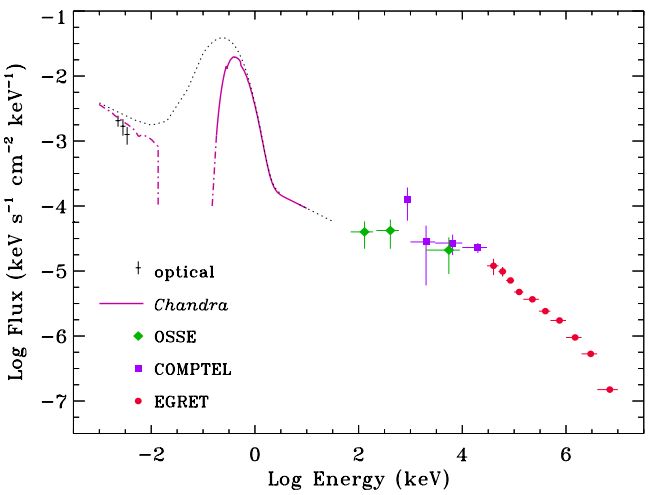


Fig. 3. Multiwavelength energy spectrum of the Vela pulsar. The solid line shows the NS atmosphere plus PL fit to the observed LETG and ACIS spectra. The dotted line corresponds to same model spectrum corrected for the interstellar absorption and extrapolated to lower and higher energies. The dash-dot lines show the extrapolated optical and EUV absorbed spectra (see Pavlov et al. 2001b for details and references).

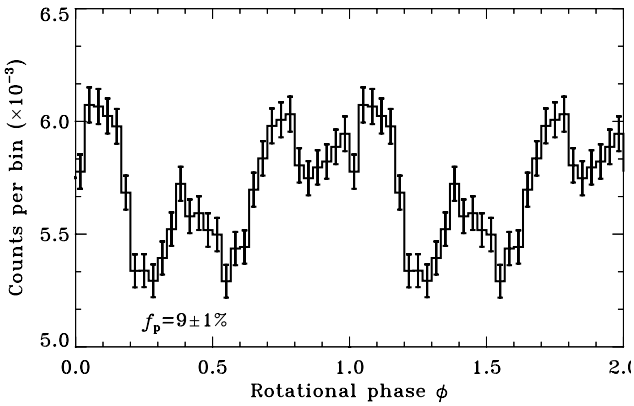


Fig. 4. Light curve of the Vela pulsar from two HRC-I observations of January and February 2000. The zero phase corresponds to the radio peak.

nebula show that the pulsar is much brighter than the PWN background at $E \lesssim 1.5$ keV, and it is discernible up to 8 keV, where the charged particle background takes over (see Fig. 1 in Pavlov et al. 2001b). The pulsar spectrum in the 0.5–8 keV band ($\approx 9,000$ source counts) does not fit one-component models, but it fits fairly well two-component models (e.g., a PL plus a thermal component — see the middle panel in Fig. 2).

The analysis of the combined (LETG plus ACIS) spectra proves that the pulsar's soft X-ray emission, at $E \lesssim 1.8$ keV, is indeed dominated by a thermal component (see bottom panel in Fig. 2). The parameters of this component are drastically different for the blackbody fit ($T_{\rm bb}^{\infty} = 1.4$–$1.5$ MK, $R_{\rm bb}^{\infty} = [2.3$–$2.9]\, d_{300}$ km) and the NS hydrogen atmosphere fit ($T_{\rm eff}^{\infty} = 0.65$–$0.71$ MK, $R^{\infty} = [17$–$20] d_{300}$ km). Such strong difference is explained by the fact that the spectrum of a hydrogen atmosphere decreases with increasing photon energy slower than the ideal Wien spectrum because the radiation at higher energies comes from hotter layers. As a result, the blackbody fit to a hydrogen atmosphere spectrum yields a temperature higher than the true effective temperature and an area smaller than the true emitting area (see ZP02 for more details).

The small blackbody radius might hint that the observed radiation is emitted from hot spots (e.g., polar caps heated by relativistic particles produced in the pulsar magnetosphere), whereas the radius obtained in the hydrogen atmosphere fit implies radiation emitted from the entire NS surface. Rigorously speaking, the surface (atmosphere) of a NS is not a black body, but a blackbody spectrum could mimic the spectrum of a heavy-element (e.g., iron) atmosphere if it is observed with low spectral resolution. However, the lack of significant spectral lines in the LETG spectrum indicates that there are no heavy elements, neither He nor metals, in the radiating atmospheric layers. On the other hand, even strongly magnetized hydrogen does not have spectral features in the investigated energy band (all the hydrogen features are below 0.17 keV for the field of $B = 3 \times 10^{12}$ G, adopted for the Vela pulsar). Therefore, the hydrogen atmosphere interpretation looks more plausible. With this interpretation, the effective temperature of the Vela pulsar is well below the predictions of the "standard" models of the NS cooling (e.g., Tsuruta 1998).

An important result of this analysis is the detection of the hard spectral component which dominates at $E \gtrsim 1.8$ keV. The slope (photon index) of this PL component is $\gamma = 1.2$–1.8 if the NS hydrogen atmosphere model is adopted for the soft component. With this interpretation, the overall X-ray spectrum of the the Vela pulsar is quite similar to those of the three middle-aged pulsars, Geminga, B1055–52 and B0656+14 (see below), where the thermal component was detected, although the ratio of the nonthermal X-ray luminosity to the spin-down energy loss rate, $L_{\rm x}/\dot{E} \simeq 3 \times 10^{-6}$ in the 0.2–8.0 keV range, is a factor of 10^3 smaller than observed for typical X-ray detected pulsars (Becker & Trümper 1997). If the $L_{\rm x}/\dot{E}$ ratio were as high as for other pulsars, the thermal radiation would be undetectable in the phase-integrated spectrum.

It is illuminating to compare the non-thermal X-ray spectrum of the pulsar with those in other energy ranges. Figure 3 shows the spectral flux of the pulsar from optical to gamma-rays. Remarkably, the extrapolation of the PL spectrum obtained in the atmosphere-plus-PL fit matches fairly well with the optical and hard-X-ray (soft-γ-ray) time-averaged fluxes. Moreover, under the hypothesis that the PL spectrum has the same slope in the optical through X-ray range, we can constrain the photon index very tightly: $\gamma = 1.35$–1.45.

The multicomponent structure of the pulsar radiation is also seen from its pulse profile. The HRC-I light curve is shown in Figure 4 (see also Helfand et al. 2001; Sanwal et al. 2002a). It has at least three peaks — quite unusual for a pulsar, but not so surprising for the Vela pulsar which shows up to four peaks in the hard X-ray bands observed with *RXTE* (Harding et al. 2002).

So far, only the analysis of phase-integrated spectra and energy-integrated light curves has been possible. Phase-resolved spectral analysis and energy-resolved timing would be of crucial importance to elucidate the complicated emission

mechanism(s) of both the non-thermal and thermal components. In particular, the analysis of the phase-energy dependence of the thermal emission, based on the NS atmosphere models can make it possible to determine the surface distributions of the temperature and the magnetic field.

2.2. Middle-aged pulsars B0656+14 and B1055–52

Among about 40 rotation-powered pulsars detected with the previous and currently operating X-ray missions, middle-aged pulsars ($\tau \sim 0.1$–1 Myr) are of special interest because their thermal emission is expected to dominate in soft X-rays. The best studied objects of this class are the "Three Musketeers"[1]: PSR B0656+14, Geminga, and PSR B1055–52.

2.2.1. PSR B0656+14

PSR B0656+14 ($\tau_c = 110$ kyr) is the brightest of the Three Musketeers. Observations with *Einstein*, *ROSAT*, and *ASCA* have shown that its X-ray spectrum consists of at least two components. The thermal component ($E \lesssim 1$ keV) resembles a soft blackbody spectrum with an apparent temperature of about 0.9 MK. Because of the narrow energy band of *ROSAT* and poor angular resolution of *ASCA*, the shape of the hard component (at $E \gtrsim 1$ keV) could hardly be determined from those data. For instance, the *ASCA* spectra above 1 keV can be fitted equally well with a hard blackbody with temperature of about 2.5–4.0 MK or a PL with photon index $\gamma = 1.3$–3.0. IR-optical-UV observations of the pulsar (Pavlov et al. 1997; Koptsevich et al. 2001) revealed a nonthermal PL component with $\gamma = 1.4$–1.5, presumably emitted from the pulsar magnetosphere.

To search for spectral features in the X-ray spectrum of PSR B0656+14 and investigate the shape of its high-energy tail, the pulsar was observed with HRC-S/LETG in November 1999 (38 ks exposure) and ACIS-S (in CC mode) in December 2001 (25 ks exposure). The analysis of these data showed no significant features in the source spectrum. To obtain a good fit to the combined X-ray spectrum in the 0.2–6 keV band, a three-component model is required. The high-energy tail ($E \gtrsim 2$ keV) fits best with a PL spectrum with a slope close to that of the optical spectrum. To constrain it more tightly, we assumed that the slope does not change from optical to X-rays, included the optical data in the fit, and obtained $\gamma = 1.5$. The low-energy part of the spectrum ($E \lesssim 0.7$ keV) fits well with a blackbody spectrum with temperature $T_{\rm s}^{\infty} = 0.85$ MK and equivalent radius of emitting sphere $R_{\rm s}^{\infty} = 12.0\,(d/500\,{\rm pc})$ km. This thermal soft (TS) component is presumably emitted from the whole visible NS surface. To fit the spectrum at intermediate energies, one more component is required (see Fig. 5). Very likely, this is a thermal hard (TH) component with temperature $T_{\rm h}^{\infty} \simeq 1.65$ MK (as given by the blackbody model) emitted from pulsar's polar caps of radius $R_{\rm pc} = R_{\rm h}^{\infty} \simeq 1.0\,(d/500\,{\rm pc})$ km heated by relativistic particles streaming down from the pulsar acceleration zones. The bolometric luminosity of the TS component is $L_{\rm bol,s} \simeq 5.5 \times 10^{32}\,(d/500\,{\rm pc})^2$ erg s^{-1}, vs. $L_{\rm bol,h} \simeq 4.9 \times 10^{31}\,(d/500\,{\rm pc})^2$ erg s^{-1} for the TH component. The luminosity of the non-thermal component is $L_{\rm x} \simeq 5.3 \times 10^{30}\,(d/500\,{\rm pc})^2$ erg s^{-1} in the 0.1–10.0 keV range. This three-component model fits the data from IR through X-ray energies (Fig. 6).

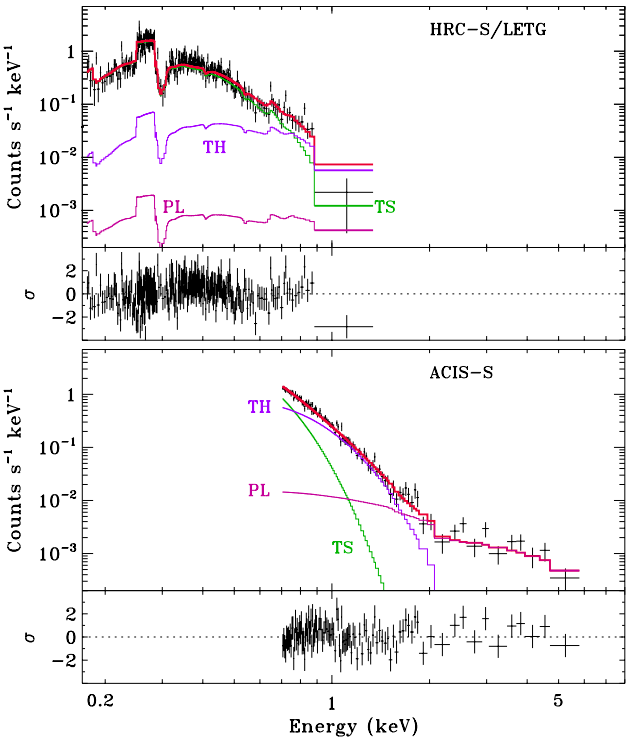


Fig. 5. Three-component, TS+TH+PL, fit to the combined LETG and ACIS-S spectra of PSR B0656+14. The red curves show the model countrate spectra for the two instruments.

Using the magnetic hydrogen atmosphere models (ZP02), instead of blackbodies, for the thermal components gives formally acceptable fits, with effective temperatures lower by a factor of about 2 (e.g., $T_{\rm eff}^{\infty} \simeq 0.4$–0.5 MK for the TS component). However, these fits imply either very small distances, ~ 70–130 pc for $R = 10$ km, or very large radii, $R_{\rm s} \sim 40$–70 km for the TS component, at $d = 500$ pc. Therefore, applicability of these models to PSR 0656+14 is questionable.

The multicomponent structure of the pulsar X-ray radiation is also seen from the behavior of the pulse profiles shown in Figure 7. The shape of the light curves is energy dependent, with a significant phase shift (~ 0.2 of the period) at 0.5–0.7 keV. The source pulsed fraction $f_{\rm p}$ shows a complex behavior: it decreases with increasing energy from about 20% at $E \sim 0.1$–0.3 keV down to about 7% at E around 1 keV and increases again to $f_{\rm p} \simeq 35\%$ at $E \gtrsim 1$ keV. The X-ray peak lags the radio peak by 0.2–0.4 of the period, depending on energy (Fig. 7).

To establish the origin of the peak and the parameters of the X-ray radiation, one should analyze the spectra and the light curves together, with the aid of realistic models for X-ray emission. However, the spectra of the pulsar observed with the pre-*Chandra* X-ray observatories, and even the *Chandra* ACIS-S spectrum observed in CC mode, potentially have a contaminating component — synchrotron radiation from a PWN of a small angular size around the pulsar, which could not be resolved in those observations.

[1] As dubbed by Becker & Trümper 1997

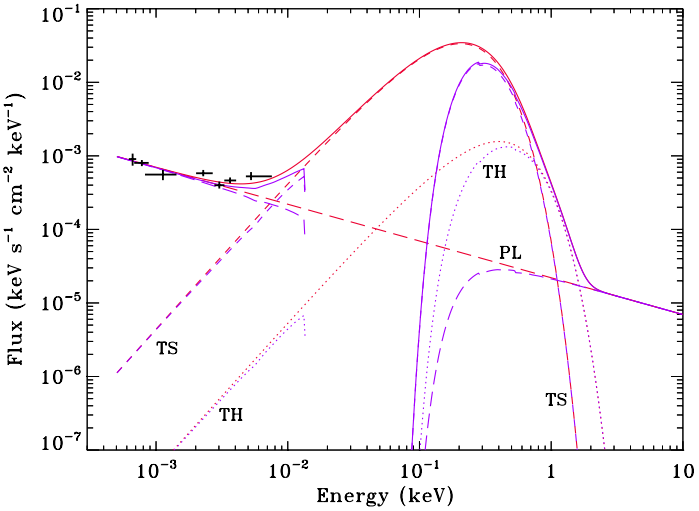


Fig. 6. Spectral flux for the TS+TH+PL model for PSR B0656+14 extrapolated to the optical range. Blue and red curves show the absorbed and unabsorbed spectra, respectively. Crosses are the IR-optical-UV fluxes (Koptsevich et al. 2001).

A hint on extended emission around PSR 0656+14 is seen in the zero-order LETG/HRC-S image (Marshall & Schulz 2002), but that image is strongly contaminated by the diffraction spikes. The pulsar was also observed in a 5 ks exposure with ACIS-S3 in Timed Exposure mode (December 2001) providing the data for spatial analysis of the X-ray emission in the vicinity of the pulsar. The analysis reveals a $3''$–$4''$ extended structure around the piled-up image of the pulsar — first strong indication on PWN around a middle-aged pulsar (see Fig. 8). The pulsar's image, confined within a small, slightly elongated area of about $1''$ diameter (at the center of Fig. 8) is surrounded by a putative PWN of rather complicated morphology. The estimated luminosity of the PWN is $L_{\rm x,pwn} \sim 2\times10^{31}\,(d/500\,{\rm pc})^2$ erg s^{-1} in the 0.1–10.0 keV range. A considerable fraction of the PWN radiation can contaminate the pulsar's radiation observed with the pre-*Chandra* observatories and even with ACIS in CC mode. Therefore, to unambiguously separate the PWN contribution, one should observe the pulsar and its surroundings in high-resolution imaging mode for longer time. The above estimates of the pulsar spectral parameters should be considered with caution until the properties of the putative PWN are studied and its radiation is separated from that of the pulsar.

2.2.2. PSR B1055–52

Analysis of the *Chandra* data on PSR B1055–52, taken in January 2000 with ACIS-S in CC mode (42 ks exposure), yields results very similar to those obtained for PSR B0656+14 (see Sanwal et al. 2002c for details). First, the ACIS spectrum, combined with that obtained with the *ROSAT* PSPC, requires a three-component model (Fig. 9). The high-energy tail of

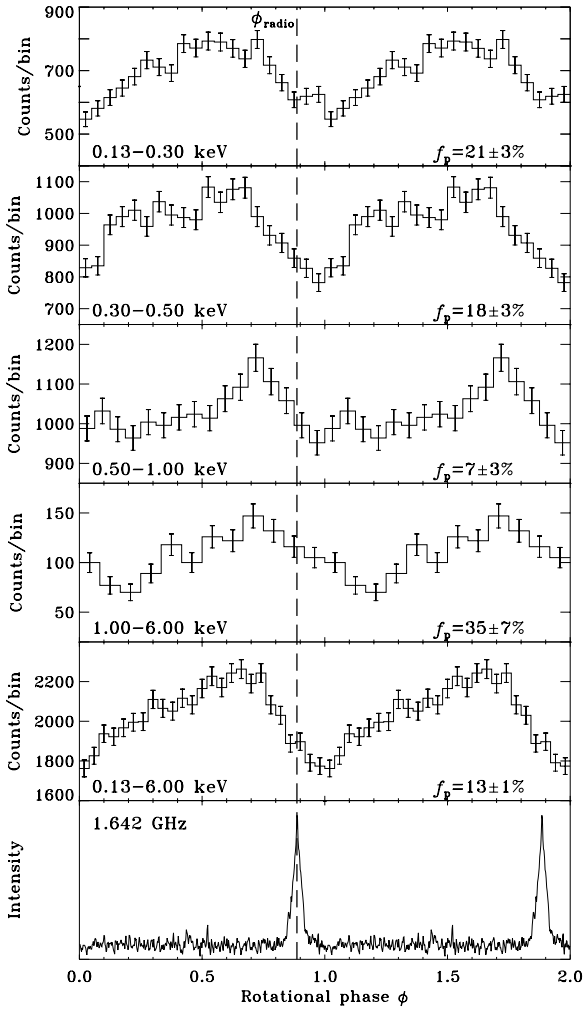


Fig. 7. X-ray pulse profiles for PSR B0656+14 in different energy bands (four upper panels). The radio pulse profile at 1.642 GHz (Gould & Lyne 1998) demonstrates the phase difference between the X-ray and radio peaks. The X-ray data are from the *Chandra* ACIS observation in the CC mode (December 2001).

the spectrum ($E\gtrsim 2$ keV) is best described with a PL with $\gamma = 1.66$; such a component smoothly connects optical (*HST* FOC) and gamma-ray (*CGRO* EGRET) data (Fig. 10). The spectrum at lower energies fits well with two thermal (blackbody) components, soft and hard. The best-fit model parameters to the phase-integrated spectrum are $T_{\rm s}^{\infty} = 0.84$ MK and $R_{\rm s}^{\infty} = 12.0\,(d/1\,{\rm kpc})$ km for the soft thermal component, $T_{\rm h}^{\infty} = 1.62$ MK and $R_{\rm h}^{\infty} = 0.8\,(d/1\,{\rm kpc})$ km for the hard thermal component, $n_{\rm H} = 1.3\times10^{20}$ cm^{-2}.

The energy-resolved light curves of the pulsar derived from the ACIS data reveal energy-dependent variations in the pulsed fraction, the phase of the pulse, and the pulse shape (Fig. 11). In particular, the pulsed fraction increases from $\sim 15\%$ at about 0.3–0.4 keV to $\sim 50\%$ at $\gtrsim 1.0$ keV. For this pulsar, the X-ray pulse at $E\gtrsim 0.3$ keV is in phase with the main radio pulse, contrary to PSR B0656+14.

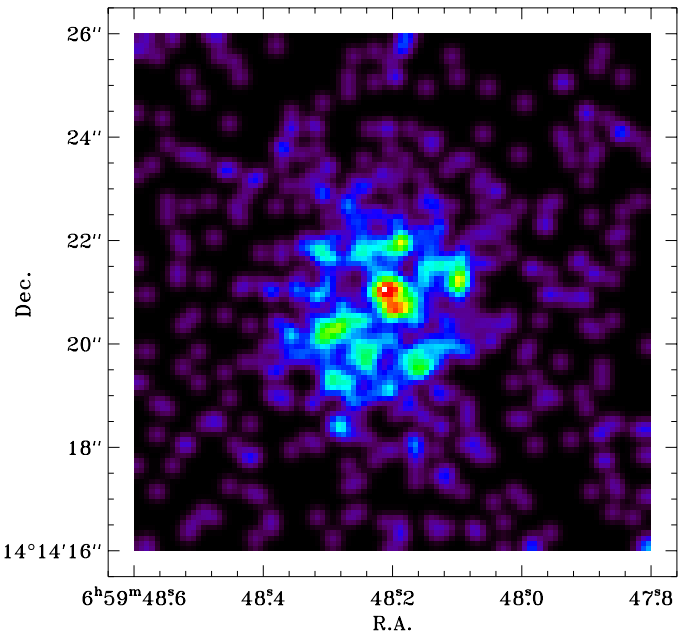


Fig. 8. Image of a $10'' \times 10''$ area around PSR B0656+14 from the 5 ks ACIS observation in the Timed Exposure mode (December 2001).

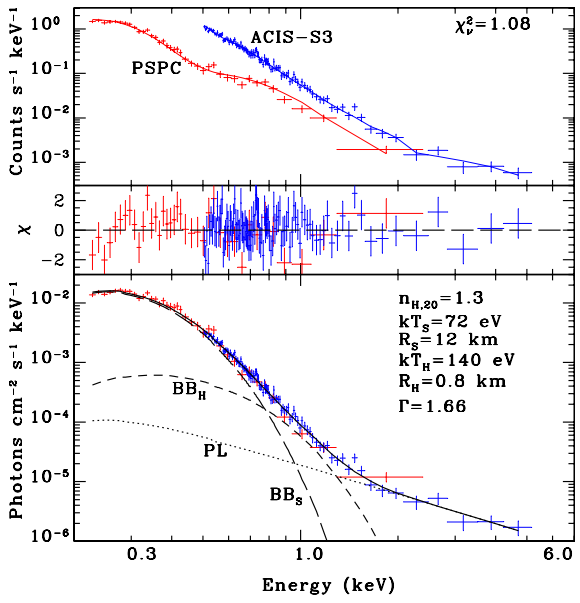


Fig. 9. Three-component model fit to the *Chandra* ACIS and *ROSAT* PSPC spectra of PSR B1055–52.

The phase-resolved spectroscopy shows small variations in the parameters of the soft thermal component, whereas the emitting area for the hard thermal component varies significantly with the rotational phase ($R_{\rm h}^{\infty}$ changes between about 0.5 and 1.5 km), which can be interpreted as changing projection of the hot spot area.

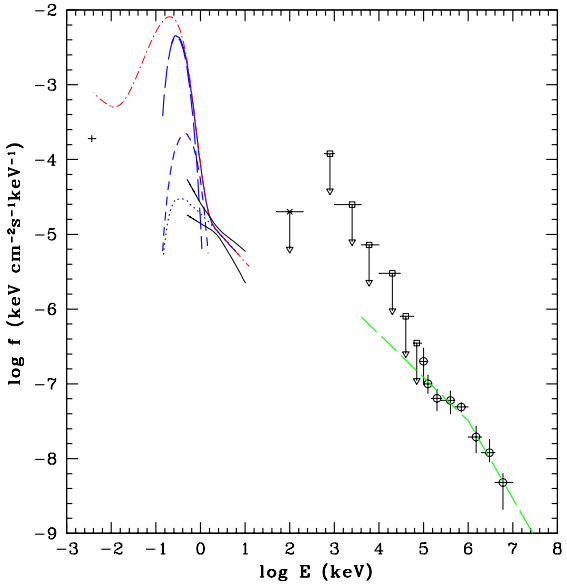


Fig. 10. Spectral flux from PSR 1055–52 for the TS+TH+PL model extrapolated to the optical and γ-ray ranges, together with the data from *HST*, *OSSE*, *COMPTEL* and *EGRET*. The blue and the red curves give the absorbed and unabsorbed spectra, respectively.

Thus, we see remarkable similarity in the X-ray properties of the two middle-aged pulsars, B0656+14 and B1055–52. Interestingly, the temperature of the soft thermal component is approximately the same for these pulsars, although the characteristic age, $\tau_c = P/2\dot{P}$, is a factor of 5 larger for B1055–52. A possible explanation of this fact is that these NSs have different properties (e.g., the mass of B1055–52 is lower — see D.G. Yakovlev et al., this volume). An alternative explanation is that the true age of a pulsar can be quite different from its characteristic age (see below), so that one should be very cautious comparing the NS cooling models with the observations of pulsars.

2.3. Millisecond pulsar J0437–4715

Millisecond (recycled) radio pulsars are distinguished from ordinary pulsars by their very short and stable periods, $P \lesssim 10$ ms, $\dot{P} \sim 10^{-20}$ s s^{-1}. They are presumably very old objects, with spin-down ages $\tau \sim 10^9$–10^{10} yr and low magnetic fields, $B \sim 10^8$–10^{10} G. Similar to ordinary pulsars, a millisecond pulsar can emit non-thermal X-rays from its magnetosphere. Additionally, thermal X-rays can be emitted from pulsars' polar caps heated up to X-ray temperatures by relativistic particles generated in the pulsar acceleration zones.

At a distance $d \simeq 140$ pc, PSR J0437–4715 ($P = 5.75$ ms) is the nearest and brightest millisecond pulsar known at both radio and X-ray wavelengths. It is in a 5.74 d binary orbit with a low-mass white dwarf companion. Optical observations in H_α have revealed a bow-shock PWN, caused by the supersonic motion of the pulsar through the interstellar medium, with the bow-shock apex at about $10''$ south-east of the pulsar, in the

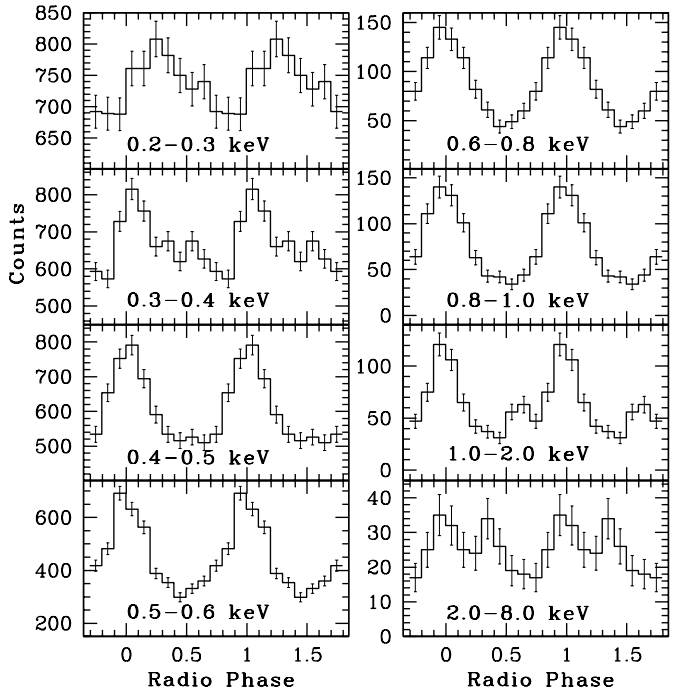


Fig. 11. Energy-resolved light curves of PSR B1055–52 plotted vs. radio phase.

direction of the pulsar's proper motion. Its X-ray radiation was discovered with *ROSAT* (Becker & Trümper 1993). The pulsar was also observed with *EUVE* (Halpern, Martin, & Marshall 1996). The pre-*Chandra* data, obtained in a narrow energy range of 0.1–2.0 keV, can be well fitted with a PL with photon index $\gamma = 2.2$–2.5, or with a polar cap model with a nonuniform temperature distribution (Zavlin & Pavlov 1998 [ZP98]). To discriminate between these two competing models, the pulsar

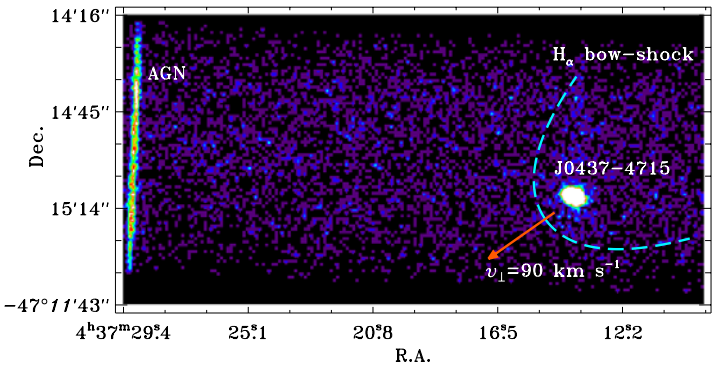


Fig. 12. ACIS image of PSR 0437–4715. The bright strip is the trailed image of a nearby AGN. The dashed curve marks the leading edge of the H$_\alpha$ bow-shock. The arrow shows the direction of the pulsar's proper motion.

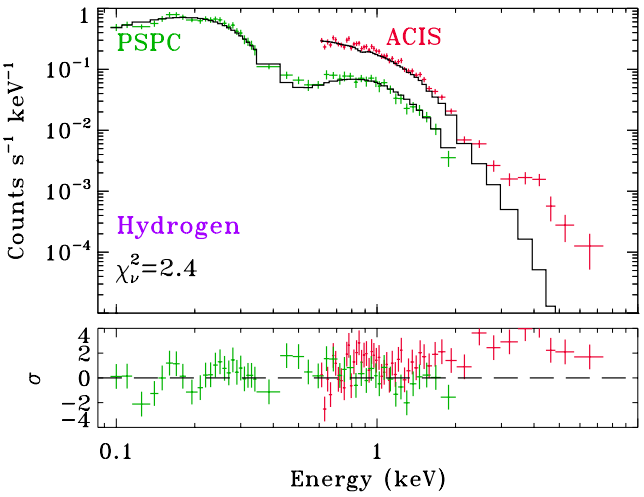


Fig. 13. Two-temperature hydrogen polar cap model fit to the combined ACIS and PSPC data on PSR J0437–4715.

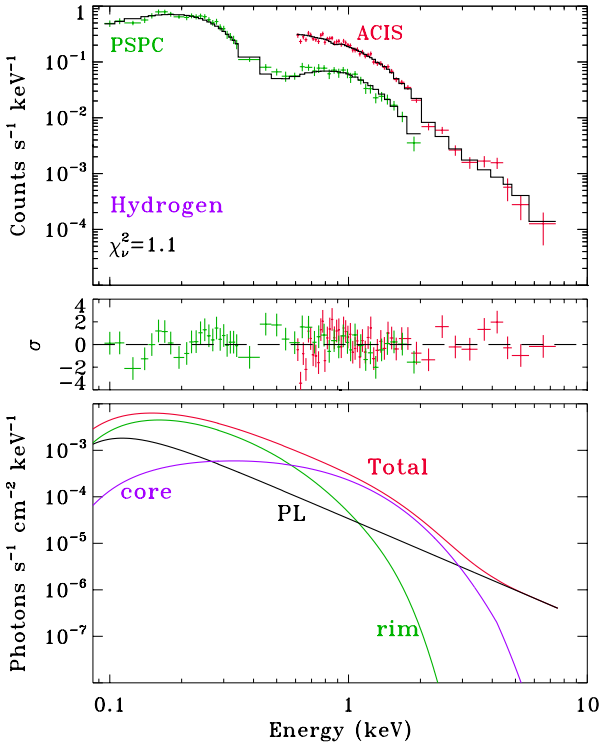


Fig. 14. Power-law plus two-temperature hydrogen polar cap model fit to the combined ACIS and PSPC spectrum of PSR J0437–4715.

was observed with *Chandra* ACIS (May 2000; 26 ks exposure; see Zavlin et al. 2002).

The source spectrum prevails over background at energies up to 7 keV and reveals no significant spectral features. No structures which could be associated with the bow shock observed in H$_\alpha$ are found (see Fig. 12).

The combined analysis of the ACIS and *ROSAT* PSPC data rules out a single PL model (min $\chi^2_\nu = 3.8$), indicating

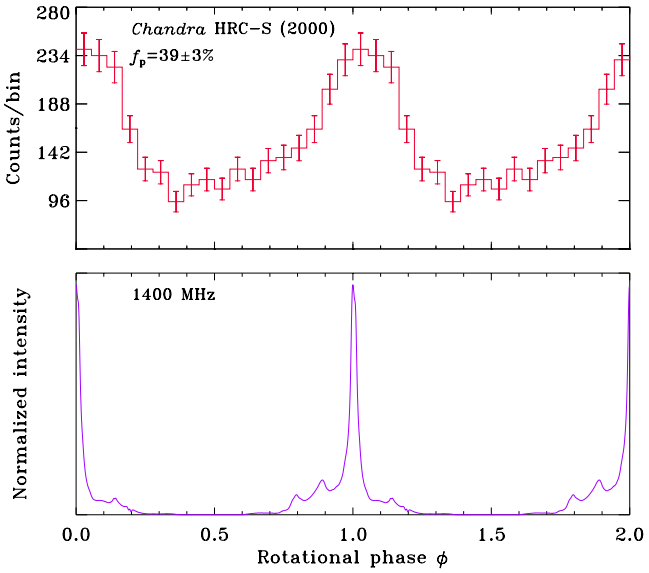


Fig. 15. Pulse profiles of PSR 0437–4715 from the *Chandra* and radio observations.

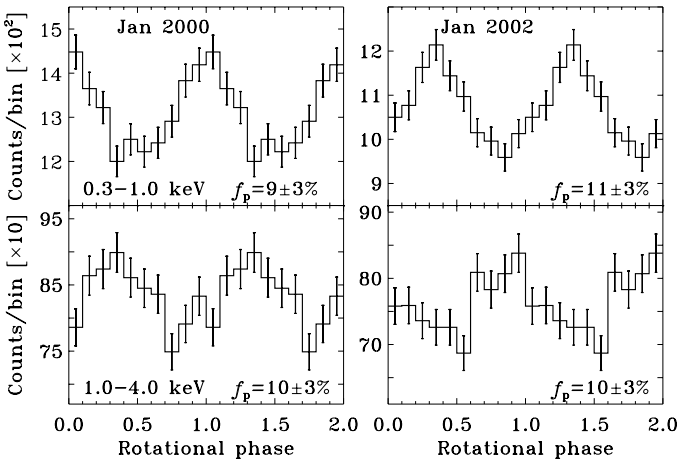


Fig. 16. Light curves of CXO J1210–5226 from two *Chandra* observations.

that more components are needed to get a satisfactory combined fit.

A two-component model, PL plus two polar caps of uniform temperature, provides an acceptable fit to the combined data. However, comparison with the *EUVE* data shows that this model is only marginally acceptable. In addition, the inferred values of hydrogen column density exceed the values $n_{\rm H} = (1–3) \times 10^{19}$ cm^{-2} derived from independent measurements of the interstellar absorption towards objects in the vicinity of the pulsar (see ZP98 for more details).

ZP98 suggested that the temperature distribution in a polar cap should be nonuniform because the heat, released by decelerating magnetospheric particles in subphotospheric layers, propagates along the surface out from the small polar areas, where the energy is deposited, and heats a larger area. They used a two-zone approximation for the polar cap temperature distribution, a hot "core" plus a colder "rim". When applied to the ACIS data, this model shows that the observed spectrum significantly exceeds the model at $E > 2$ keV, i.e., one more component is required (Fig. 13). A natural choice for the additional component is a PL. Adding the nonthermal component greatly improves the fit (Fig. 14). At fixed $n_{\rm H} = 2 \times 10^{19}$ cm^{-2}, the best fitting parameters are $T_{\rm core} = 2.1$ MK, $T_{\rm rim} = 0.54$ MK, $R_{\rm core} = 0.12$ km, $R_{\rm rim} = 2.0$ km, and $\gamma = 2.2$. The bolometric luminosity of two polar caps is $L_{\rm bol} = 2.3 \times 10^{30}$ erg s^{-1} $\sim 0.6 \times 10^{-3} \dot{E}$, and the PL luminosity in the 0.1–10 keV band is $L_{\rm x} = 0.7 \times 10^{30}$ erg s^{-1} $\sim 0.2 \times 10^{-3} \dot{E}$. This model is in good agreement with the *EUVE* data.

In the polar cap model with temperature decreasing outwards from the cap center, the thermal component dominates between 0.1 keV and 2.5 keV, providing about 75% of the X-ray flux, while the PL component dominates outside this band. An important point here is that this model requires the thermal radiation to be emitted from a hydrogen (or helium) NS atmosphere. The high spectral resolution of the ACIS data rules out an atmosphere comprised of heavier chemical elements.

The pulsar was also observed with the HRC-S detector (October 2000; 20 ks exposure) in the timing mode that provides accurate timing results. Figure 15 presents the HRC-S and radio pulse profiles. The phases of the X-ray and radio pulses are found to be virtually the same — their difference (0.3% of the pulsar's period) is smaller than the absolute timing accuracy of *Chandra*. This implies that, if the main contribution to the HRC-S band is due to the thermal polar cap radiation, then the radio emission must be generated close to the NS surface — e.g., the time difference of < 0.1 ms between the X-ray and radio phases corresponds to a distance of < 30 km, much smaller than the light cylinder radius of 275 km.

3. Compact central objects in supernova remnants

Chandra has observed five CCOs. Their most important characteristics are listed in Table 1. Although some properties of CCOs (in particular, their spectra) are very similar to each other, it does not necessary mean that they represent a uniform class of objects. The most outstanding is J1617–5102 in RCW 103, with its highly variable flux (time scales hours to months), putative 6.6 hr period, and a possible optical counterpart ($J \simeq 22.3$). One can presume that this source is not a truly isolated NS (i.e., it is powered by accretion, at least in its high state), although it is not a standard accretion-powered pulsar. The other four CCOs have shown neither long-term variabilities nor indications of binarity. If, based on the observed spectra, we adopt a plausible hypothesis that their radiation is thermal and assume that it can be adequately described by the same spectral model (e.g., BB or hydrogen NS atmosphere), then we have to conclude that the emitting area is growing with age. If the radiation emerges from a hydrogen atmosphere, then the effective radius is consistent with a NS radius for two oldest CCOs, J0821–4300 and J1210–5226, being smaller for two youngest ones, J2323+5848 and J0852–

Object	Host SNR	Age kyr	Period	$T^{\infty}_{\rm bb}$ MK	$R^{\infty}_{\rm bb}$ km	$L^{\infty}_{\rm bol,bb}$ 10^{33}erg s^{-1}	$T^{\infty}_{\rm eff}$ MK	R^{∞} km	$L^{\infty}_{\rm bol}$ 10^{33}erg s^{-1}
J2323+5848	Cas A	0.32	...	5.7	0.5	1.6	3.5	1	2
J0852–4617	G266.1–1.2	∼1	301 ms [?]	4.6	0.3	0.3	3.1	1.5	0.8
J1617–5102	RCW 103	1–3	6.6 hr [?]	4.6–7.0	0.2–1.6	0.5–30	3.5	1–8	1–60
J0821–4300	Pup A	1–3	...	4.4	1.4	4.2	2.0	10	8
J1210–5226	G296.5+10.0	3–20	424 ms	2.9	1.6	1.3	1.6	11	1

Table 1. Compact central objects in SNRs with best-fit parameters for blackbody (columns 5–7) and hydrogen NS atmosphere models (columns 8–10). The periods marked with "[?]" require confirmation. More details on these objects can be found in Pavlov et al. (2002a).

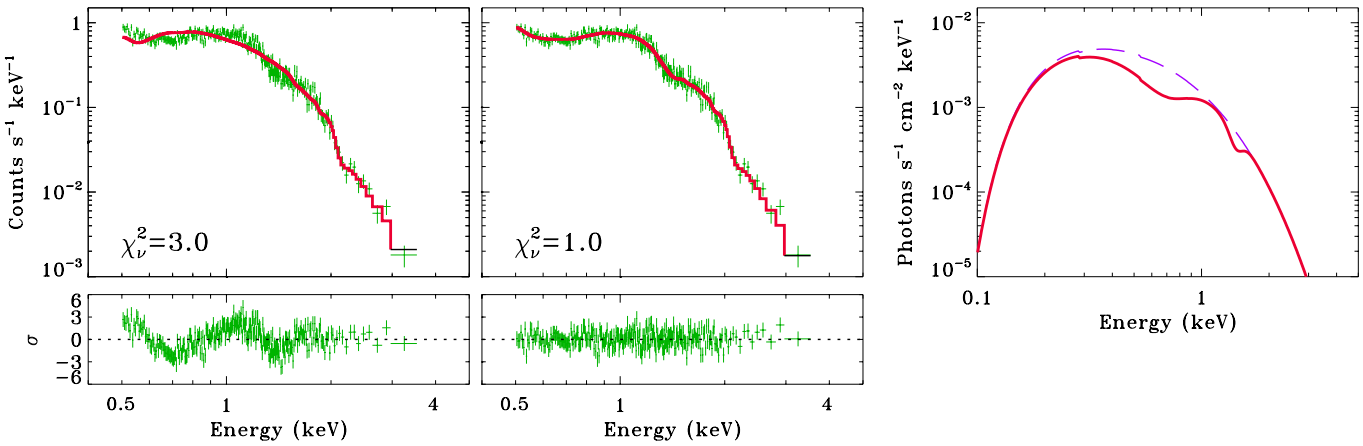


Fig. 17. *Left:* Fit to the *Chandra* spectrum of J1210–5226 with a blackbody model. *Middle:* The same model with two absorption lines added (at energies of 0.7 keV and 1.4 keV). Notice the significant improvement in the fit quality. *Right:* The two-line model for the photon flux (see text).

4617. One might assume that the latter two are black holes, not NSs, but then one would have to invoke accretion as the energy source, which does not look consistent with the lack of variability.

A recent review on CCOs, including the *Chandra* results, has been presented by Pavlov et al. (2002a). Therefore, here we will describe only the most recent results on the best-investigated CCO, J1210–5226 (a.k.a. 1E 1207.4–5209), the first isolated NS which shows spectral lines.

3.1. J1210–5226: the puzzling pulsar in G296.5–10

This radio-quiet X-ray source at the center of G296.5+10.0 (a.k.a. PKS 1209–51/52) was discovered by Helfand & Becker (1984). Mereghetti, Bignami, & Caraveo (1996) and Vasisht et al. (1997) fitted the *ROSAT* and *ASCA* spectra of J1210–5226 with a blackbody model of $T^{\infty}_{\rm bb} \simeq 3.0$ MK from an area with radius $R^{\infty}_{\rm bb} \simeq 1.6\,(d/2\,{\rm kpc})$ km. Zavlin, Pavlov & Trümper (1998) interpreted the observed spectra as emitted from a light-element (hydrogen or helium) atmosphere. For a NS of mass $1.4\,M_{\odot}$ and radius 10 km, they obtained a NS surface temperature $T^{\infty}_{\rm eff} = (1.4–1.9)$ MK and a distance of 1.6–3.3 kpc, consistent with the distance to the SNR, $2.1^{+1.8}_{-0.8}$ kpc (Giacani et al. 2000).

Zavlin et al. (2000) observed J1210–5226 with *Chandra* ACIS-S in CC mode in January 2000 (32 ks exposure) and discovered a period of about 424 ms, which proved that the source is a NS. Second *Chandra* observation with the same observational setup (January 2002; 30 ks) provided an estimate of the period derivative, $\dot{P} \sim (0.7–3) \times 10^{-14}$ s s^{-1} (Pavlov et al. 2002b). This estimate implies that the characteristic age of the NS, $\tau_c \sim 200–1600$ kyr, is much larger than the 3–20 kyr age of the SNR (Roger et al. 1998), while the "canonical" magnetic field, $B \equiv 3.2 \times 10^{19}(P\dot{P})^{1/2}\,{\rm G} = (2–4) \times 10^{12}$ G, is typical for a radio pulsar. These observations revealed smooth pulsations of the X-ray flux from J1210–5226, with pulse shape depending on photon energy (Fig. 16).

The analysis of the ACIS spectra (Sanwal et al. 2002b) shows that continuum models (e.g., blackbody, power-law, fully ionized NS atmosphere) fail to fit the source spectrum, which deviates very significantly from any of the models, revealing two absorption features near 0.7 keV and 1.4 keV (Fig. 17). Including absorption lines in the spectral model improves the quality of the fit substantially. Assuming Gaussian profiles

for the absorption coefficients, we obtain the central energies 0.73 ± 0.01 and 1.40 ± 0.01 keV, equivalent widths 108 ± 15 and 112 ± 24 eV, and central optical depths 0.40 ± 0.06 and 0.43 ± 0.06, respectively.

Attempts to explain the absorption features as caused by the intervening interstellar (or circumstellar) material lead to huge overabundance for some elements. Therefore, the observed lines are most likely intrinsic to the NS.

One could assume that the observed lines are cyclotron lines produced in a strongly ionized NS atmosphere. If one assumes these are electron cyclotron lines, the features might be interpreted as the fundamental and the first harmonic of the electron cyclotron energy $E_{ce} = 1.16 B_{11}$ keV in a magnetic field $B_{11} \equiv B/(10^{11}\,\mathrm{G}) \sim 0.6\,(1+z)$ (z is the neutron star redshift parameter), or as two fundamentals emitted from two regions with different magnetic fields, $B_{11} = 0.6\,(1+z)$ and $1.2\,(1+z)$, broadened by the radiative transfer effects and/or nonuniformity of the magnetic field. However, it is difficult to reconcile this interpretation with the expected strength of the surface magnetic field $B > 3 \times 10^{12}$ G. In addition, the oscillator strength of the first harmonic is smaller than that of the fundamental by a factor of $\sim E_{ce}/(m_e c^2) \sim 2 \times 10^{-3}$ (at $E_{ce} \gg kT$), so that it is hard to explain why the 1.4 keV feature is as strong as the 0.7 keV feature if we assume the two lines are associated with the same magnetic field.

One can assume that the spectral features are associated with ion cyclotron energies, $E_{ci} = 0.63(Z/A)B_{14}$ keV, where Z and A are the ion's charge and mass numbers. The surface magnetic field needed for this interpretation is $\gtrsim 10^{14}$ G, much larger than the conventional magnetic field inferred for a centered dipole from the P, $\dot{P}$ measurements. Such a strong *surface* magnetic field can be consistent with the magnetic moment $\mu = 3 \times 10^{30}$ G cm^3 if the magnetic dipole is off-centered to about 3 km below the surface. However, the ion-cyclotron interpretation of the observed features is not straightforward even in this case (see Sanwal et al. 2002b for more details).

Thus, the most viable possibility is that the observed lines are atomic lines formed in the NS atmosphere. The features cannot be explained as emerging from a hydrogen atmosphere because, at any magnetic field and any reasonable gravitational redshift, there is not a pair of strong hydrogen spectral lines whose energies would match the observed ones. Pavlov et al. (2002c) suggest that these are the strongest lines of once-ionized helium in a superstrong magnetic field, $(1.4\text{–}1.7)\times 10^{14}$ G. In this interpretation, the observed line energies correspond to the gravitational redshift $z = 0.12$–0.23, which corresponds to $R/M = 8.8$–14.2 km $M_\odot^{-1}$. To confirm this result, deep observations with high spectral resolution are needed.

4. "Dim" isolated neutron stars

ROSAT discovered seven objects which are often called "dim" or "truly isolated" NSs. These sources, listed in Table 2, are characterized by blackbody-like spectra with temperatures around 1 MK. Low values of hydrogen column densities, $n_{\rm H} \sim 10^{20}$ cm^{-2}, suggest small distances to these objects. Their X-ray fluxes, $f_{\rm x} \sim 10^{-12}$–10^{-11} erg s^{-1} cm^{-2}, correspond to rather low (bolometric) luminosities, $L \sim 10^{30} - 10^{31}$ erg s^{-1} for a fiducial distance of 100 pc. The fluxes do not show variations on either short (minutes-hours) or long (months-years) time scales, and they are much higher than the optical fluxes, $f_{\rm x}/f_{\rm opt} \gtrsim 10^3$. Such properties strongly suggest that these objects are isolated, nearby NSs. Rotational periods in

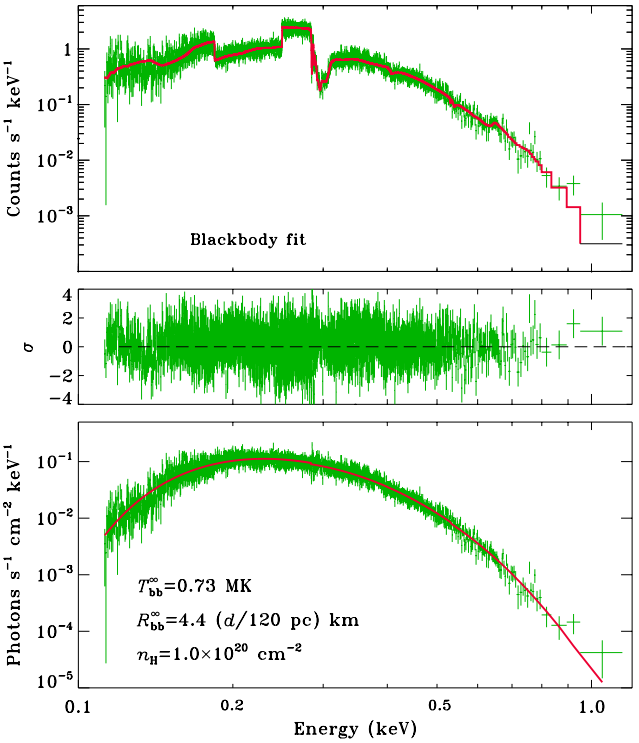


Fig. 18. *Chandra* LETG/HRC-S spectrum of RX J1856.5–3754 collected in a 500 ks exposure. The red curves represent the best blackbody fit to the observational data (the model parameters are given in the bottom panel).

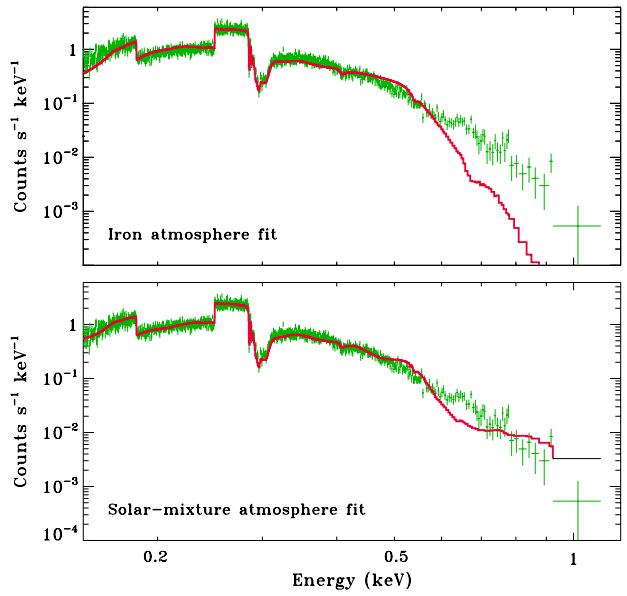


Fig. 19. Fits to the LETG spectrum of RX J1856.5–3754 to NS atmosphere models of heavy-element compositions assuming that the NS is a fast rotator (the models are from ZP02).

Object	$T_{\rm bb}^{\infty}$ MK	$f_{\rm x}$ [a]	$n_{\rm H}$ 10^{20} cm^{-2}	Period s	B mag	Ref.
RX J1856.5–3754	0.7	14	1.3	...	25.8	1
RX J0720.4–3125	0.9	11	1.1	8.37	26.6	2,3
RX J1605.3+3249	1.1	9	1.1	...	> 25	4
RX J0806.4–4123	0.9	3	2.5	11.37[?]	> 24	5,6
RX J0420.0–5022	0.7	1	1.7	22.69[?]	> 25.2	7
RX J1308.8+2127	1.4	5	2.1	5.16	> 26	8,9
RX J2143.0+0654	1.1	9	4.6	...	> 22.8 [b]	10

Table 2. Main properties of the seven "dim" NSs discovered with *ROSAT*. The spectral parameters are obtained from blackbody fits to the *ROSAT* PSPC data. The periods marked with "[?]" require confirmation.
Refs.: 1 - Walter et al. (1996); 2 - Haberl et al. (1997); 3 - Kulkarni & van Kerkwijk (1998); 4 - Motch et al. (1999); 5 - Haberl et al. (1998); 6 - Haberl & Zavlin (2002); 7 - Haberl et al. (1999); 8 - Schwope et al. (1999); 9 - Hambaryan et al. (2001); 10 - Zampieri et al. (2001).
[a] Absorbed flux in 0.1–2.0 keV, in units of 10^{-12} erg cm^{-2} s^{-1}.
[b] R magnitude.

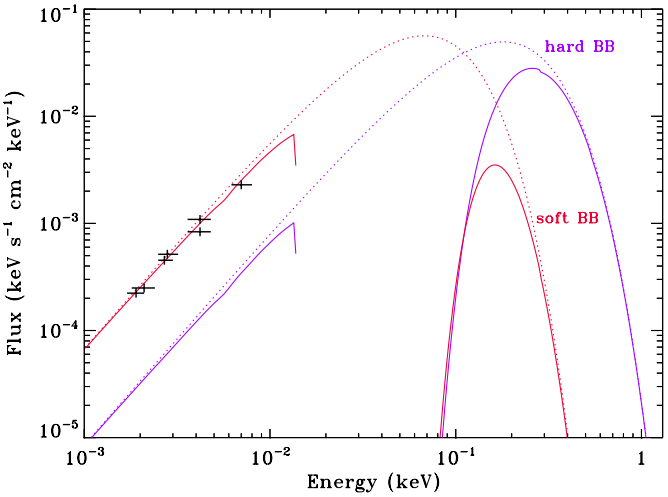


Fig. 20. Spectral flux of RX J1856.5–3754 as given by the best blackbody fit to the LETG data (blue curves, marked "hard BB"), with $T_{\rm bb}^{\infty} = 0.73$ MK and $R_{\rm bb}^{\infty} = 4.4\,(d/120\,{\rm pc})$ km. The red curves give an example of a blackbody fit with $T_{\rm bb,s}^{\infty} = 0.30$ MK and $R_{\rm bb,s}^{\infty} = 18.2\,(d/120\,{\rm pc})$ km ("soft BB") to the optical data (crosses). Solid curves show the absorbed spectra at $n_{\rm H} = 1.0 \times 10^{20}$ cm^{-2} (dots are the unabsorbed models).

J0720.4–3125 and J1308.8+2127 were discovered with *ROSAT* and *Chandra*, respectively (see refs. in Table 2). There are also indications on periodicities in J0420.0–5022 and J0806.4–4123, although those periods are to be confirmed yet. The source powering the thermal radiation of these NSs has been a matter of debate (e.g., Treves et al. 2000). Two main options under consideration are the internal heat of a cooling NS and accretion from the interstellar medium (ISM). A standard estimate on the luminosity powered by the Bondi-Hoyle accretion, $L_{\rm x} \sim 2 \times 10^{31} n v_{10}^{-3}$ erg s^{-1} (here n is the number density of the ISM in cm^{-3}, v_{10} is the relative NS velocity in units of 10 km s^{-1}), requires rather low NS velocities. Recent estimates on the distance to J1856.4–3754 and its proper motion (see below) imply a transverse velocity $v_{\perp} \simeq 185$ km s^{-1}. Therefore, accretion cannot be the energy source for this object unless the star moves in a surprisingly dense medium (a cloud?) with $n \sim 10^2$ cm^{-3}. First estimates of period derivatives for J0720.4–3125 (Zane et al. 2002; Kaplan et al. 2002b) and J1308.8+2127 (Hambaryan et al. 2002) imply surface magnetic fields[2] $\sim 10^{13} - 10^{14}$ G, which favors models invoking young (or middle-aged) cooling NSs rather than accreting NSs.

Below we present results from *Chandra* observations of the most famous (and best-investigated) objects of this class, J1856.5–3754 and J0720.4–3125.

4.1. RX J1856.5–3754

This object (we will call it J1856 throughout this Section) was first observed with *Chandra* in March 2000 in a 55 ks exposure with the HRC-S/LETG instrument. A detailed analysis of this observation is given by Burwitz et al. (2001), who reported no detection of any significant features in the high-resolution spectrum. They also concluded that the combined X-ray and optical data rule out all the available NS atmosphere models: light-element models overpredict the actual optical fluxes (as first estimated by Pavlov et al. 1996), whereas heavy-element models do not fit the LETG spectrum. In October 2001 this source was observed for 450 ks, with the same instrument. However, even this very deep observation revealed no spectral features. The spectrum excellently fits a blackbody model of $T_{\rm bb}^{\infty} = 0.73$ MK and $R_{\rm bb}^{\infty} = 4.4\,(d/120\,{\rm pc})$ km,[3] with the hydrogen column density of $n_{\rm H} = 1.0 \times 10^{20}$ cm^{-2} (Fig. 18; see also Drake et al. 2002).

All attempts to find pulsations from J1856 have been unsuccessful so far (e.g., Ransom et al. 2002). However, since time resolution of both the *ROSAT* and *Chandra* data on J1856 was not sufficient to search for periods shorter than ≈ 10 ms, one could assume that the period of J1856 is shorter than that. Such a hypothesis might also explain the featureless spectrum

[2] We note that these results are preliminary and require further confirmation.
[3] The distance to J1856, $d \simeq 120$ pc, has been recently established by Kaplan et al. (2002a) and Walter & Lattimer (2002).

of J1856 — spectral lines in radiation of a fast-rotating NS can be smeared out because of the Doppler effect (rotational broadening; see ZP02 for more details). However, atmosphere models for a fast-rotating NS fail to fit the detected spectrum because of strong deviations at energies around most prominent absorption edges (see Fig. 19 and Fig. 12 in ZP02).

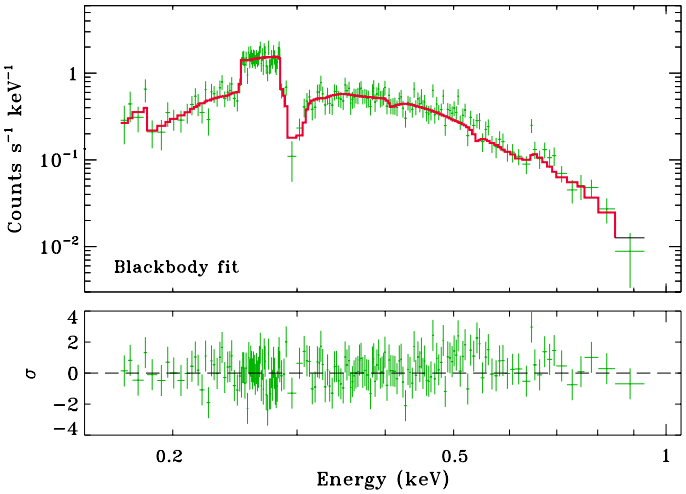


Fig. 21. *Chandra* LETG spectrum of RX J0720.4–3125. The red curve shows the best blackbody fit to the observational data (model parameters are given in the text).

Thus, we have to admit that the blackbody spectrum is the best model for the X-ray spectrum of J1856. In principle, such a blackbody spectrum could mimic the actual spectrum in the relatively short band of 0.15–1.0 keV if the NS surface is in a condensed form (according to Lai & Salpeter 1997, this can happen if the magnetic field is very strong at the NS surface, $B \gtrsim 10^{14}$ G). However, the radius of the emitting area, $R_{\rm bb}^{\infty} \simeq$ 4–5 km, is too small to be the NS radius. Moreover, taking into consideration the optical fluxes detected from J1856 (van Kerkwijk & Kulkarni 2001a; Pons et al. 2002), one encounters one more problem — the extrapolation of the blackbody model inferred from the X-ray data into the optical band falls well below the actually detected fluxes. One may assume (Pons et al. 2002) that the X-ray radiation is emitted from a hot area on the NS surface, while the optical radiation is emitted from the rest of the surface, with a lower temperature. The optical spectrum is well described by the Rayleigh-Jeans law (van Kerkwijk & Kulkarni 2001a) and gives the following relation between the temperature and the radius of the NS surface emitting the soft blackbody radiation: $R_{\rm bb,s}^{\infty} \simeq 8.3\,(T_{\rm bb,s}^{\infty}/1\ {\rm MK})^{-1/2}(d/100\ {\rm pc})$ km (with allowance for the contribution of the "hard blackbody"). On the other hand, a 3σ upper limit on the temperature of the soft component, $T_{\rm bb,s}^{\infty} < 0.39$ MK, found from the X-ray data, corresponds to a lower limit for the radius $R_{\rm bb,s}^{\infty} > 16.3$ km for $d = 120$ pc. Figure 20 shows an example of the two-blackbody fit to the optical and X-ray data on J1856. In this two-temperature picture, it is tempting to interpret the hot area as a pulsar polar cap. This seems to be consistent with the recent discovery of the H_α nebula surrounding J1856 (van Kerkwijk & Kulkarni 2001b), presumably a bow shock in the ambient medium created by the supersonic motion of a NS with a relativistic (pulsar?) wind. However, the hot spot is unusually large and luminous [$L_{\rm bol}^{\infty} = 4 \times 10^{31}(d/120\,{\rm pc})^2$ erg s^{-1}] for a standard pulsar polar cap. This could be explained by a very strong magnetic field localized in the spot region (i.e., essentially different from a centered dipole). Such a field can quench the pair cascade in the wind of primary particles pulled out from the NS surface, which explains the lack of X-ray/optical synchrotron radiation. On the other hand, the strong field can increase the heat flux from the core/crust to the surface. The large size of the hot spot, together with the GR effects (ZP02), can explain the nondetection of pulsations (pulsed fraction $f_{\rm p} \lesssim 4\%$ from the *Chandra* data), particularly if the hot spot is close the rotational pole or the direction of the rotational axis is close to the line of sight. If the new observation of J1856 with *XMM*-Newton (conducted in April 2002) reveals pulsations of this objects, it will support the two-temperature interpretation and provide constraints on the magnetic moment, hot spot position and inclination of the rotational axis.

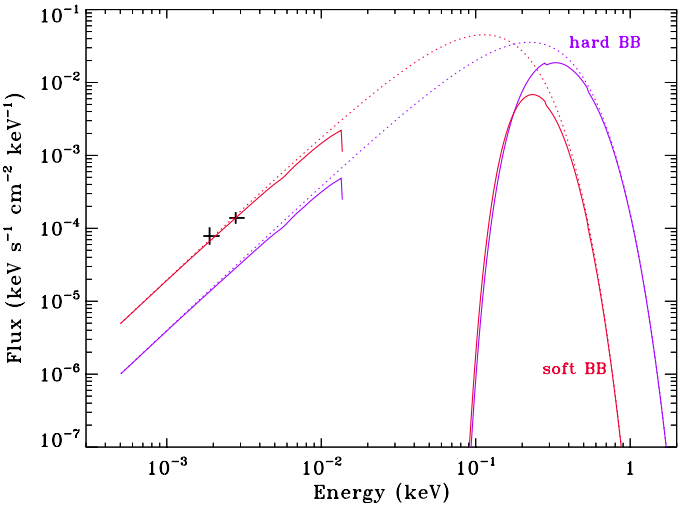


Fig. 22. The same as in Fig. 20, for RX J0720–3125. The parameters for the model spectra are given in the text. The optical data (crosses) are from Kulkarni & van Kerkwijk (1998).

4.2. RX J0720.4–3125

Chandra observed this object in February 2000 for 38 ks with the HRC-S/LETG instrument. Fitting various spectral models to these data gives results remarkably similar to those for J1856. Although the light-element (hydrogen and helium) NS atmosphere models provide acceptable fits (but the models are somewhat harder than the observed spectrum at $E > 0.75$ keV), the predicted optical fluxes (e.g., $B = 23.7$ and 23.3 for the hydrogen and helium nonmagnetic models, respectively) are much brighter than observed ($B \simeq 26.6$ — see Kulkarni & van Kerkwijk 1998). Neither iron nor solar-mixture mod-

els fit the data because of numerous features in the model spectra. The best fit is provided by a blackbody model of $T_{\rm bb}^{\infty} = 0.92$ MK and a radius of the emitting area of $R_{\rm bb}^{\infty} = 2.2\,(d/100\,{\rm pc})$ km, absorbed with the hydrogen column density $n_{\rm H} = 1.7\times10^{20}$ cm^{-2} (Fig. 21). However, similar to J1856, the best blackbody model inferred from the X-ray data underpredicts the optical fluxes which can be interpreted as emitted by a "soft blackbody" with $R_{\rm bb,s}^{\infty} \simeq 4.3\,(T_{\rm bb,s}^{\infty}/1\ {\rm MK})^{-1/2}(d/100\,{\rm pc})$ km. To obtain an acceptable fit of the two-blackbody model to the X-ray data, one should keep $T_{\rm bb,s}^{\infty} \lesssim 0.50$ MK, that results in $R_{\rm bb,s}^{\infty} \gtrsim 6.1\,(d/100\,{\rm pc})$ km. Figure 22 shows an example of the two-blackbody fit to the optical and X-ray data, with $T_{\rm bb,s}^{\infty} = 0.45$ MK and $R_{\rm bb,s}^{\infty} = 6.4\,(d/100\,{\rm pc})$ km for the soft component. If future optical observations provide the distance to J0720.4–3125, it will be possible to evaluate the NS radius and, based on the X-ray light curves, estimate the mass-to-radius ratio.

5. Concluding remarks

Because of the limited space, we described the observational results on only a handful of observed thermally emitting isolated NSs. We only briefly mentioned AXPs and SGRs, whose X-ray radiation almost certainly contains a thermal component, with temperatures of 5–10 MK and equivalent radii of 1–5 km. The current status of AXPs, including their comparison with SGRs, is reviewed by S. Mereghetti et al. (this volume). From the observational perspective, the nature of these enigmatic objects can hardly be understood without deep multiwavelength observations, particularly in the IR and hard X-ray bands, which would help elucidate the origin of the nonthermal component and separate the thermal component more precisely. We did not touch "elderly" nearby pulsars (e.g., B1929–10, B0950+08), mostly because they have not been observed with *Chandra*. If future deep observations show that their X-ray radiation is indeed thermal (emitted from hot, small polar caps), as suggested by the *ROSAT* and *ASCA* observations, the analysis of the spectra and light curves will help establish the strength and geometry of their magnetic fields and the NS mass-to-radius ratio. We did not mention important non-detections of thermal radiation from very young pulsars, the Crab (Tennant et al. 2001; M.C. Weisskopf, this volume) and the recently discovered PSR J0205+6449 in the SNR 3C 58 (Slane et al. 2002), which put upper limits on the NS surface temperature. Finally, very interesting results on thermal radiation from transiently accreting NSs in quiescence have been reported recently (Rutledge et al. 2001, and references therein). Although these old NSs are not truly isolated, their radiation in quiescence resembles that of young isolated NSs because of additional heating due to pycnonuclear reactions in the compressed accreted material.

The *Chandra* observations described above have shown a few important things. First of all, they left no doubts that thermal emission indeed dominates in the soft X-ray radiation of quite a few isolated NSs, and the analysis of this radiation allows one to measure the NS temperatures[4] and, in some cases, the radii or mass-to-radius ratios. Particularly important is the conclusion that the simple picture of a NS with a centered dipole magnetic field and uniform surface temperature is, most likely, an oversimplification. We see that whenever the data allow a detailed analysis, the temperature is not uniform, in both active pulsars and radio-quiet NSs. Moreover, the radius of X-ray emitting area is, as a rule, considerably smaller than the "canonical" NS radius. The example of J1210–5226 (Sec. 3.1) shows that the characteristic age ($\tau_c = P/2\dot{P}$) of a pulsar can differ from its true age by a large factor, and the conventional "pulsar magnetic field" can be quite different from the actual magnetic field at the NS surface. Therefore, any inferences on the properties of NSs and the superdense matter obtained without taking this into account should be considered with caution. For example, adopting the X-ray emitting radius to be the NS radius, a number of authors hurried to conclude that NSs are strange quark stars. Another example is the numerous comparisons of the NS cooling curves with observations of thermal X-rays from pulsars postulating that the pulsar's characteristic age is the true age and the empirical temperature of one of the "thermal components" is a single effective temperature. If we want to understand the real objects, we should abandon the naive paradigm and answer the basic questions raised by the observations:

- What is the true explanation of the small, hot areas in many, if not all, NSs, such as J2323+5848 (CCO of Cas A), RX J1856.5–3754, etc? If these small heated areas are associated not with (unseen) pulsar activity, but with superstrong local magnetic fields, how such fields affect the thermal evolution of NSs?
- What is the relation between the various kinds of NSs — CCOs, AXPs, SGRs, active pulsars, dim NSs? For instance, why do CCOs, AXPs and SGRs show similar properties of thermal radiation, being so different in the other observational manifestations? Can it be that the members of different subclasses are intrinsically similar objects at different stages of their evolution (e.g., AXPs are descendants of CCOs) or viewed from different directions (e.g., dim NSs are usual middle-aged pulsars whose pulsar radiation is not seen because of unfavorable geometry)?
- What is the actual temperature distribution over the NS surface? Does the two-component model for thermal radiation we have used (thermal soft + thermal hard) describe the distribution adequately?
- What is the actual mechanism(s) of the surface emission? Are there any gaseous atmospheres at all? Why does the blackbody model describes the observed spectra so well in many cases?

These are the questions to be addressed (and, hopefully, answered) by future observations of NSs.

Acknowledgements. We gratefully acknowledge the support by the Heraeus foundation and the hospitality of the Physikzentrum Bad Honnef. The work of GGP and DS was partly supported by NASA grant NAG5-10865 and SAO grants GO2-3089X, GO2-3088X and SP2-2001C. We thank Marcus Teter and Vadim Burwitz, who participated in the analysis of some of the above-described *Chandra* observations.

[4] See Fig. 5 in Mereghetti et al. (this volume) which demonstrates current estimates for the temperatures and luminosities of 22 thermally emitting NSs.

References

Becker W., Pavlov G.G., 2002, in The Century of Space Science, eds. J. Bleeker, J. Geiss & M. Huber (Dordrecht: Kluwer), in press

Becker W., Trümper J., 1993, Nature, 365, 528

Becker W., Trümper J., 1997, A&A, 326, 682

Brinkmann W., Ögelman H., 1987, A&A, 182, 71

Burwitz V., Zavlin V.E., Neuhäuser R., Predehl P., Trümper J., Brinkman A.C., 2001, A&A, 379, L35

Caraveo P.A., De Luca A., Mignani R.P., Bignami G.F., 2001, ApJ, 561, 930

Fahlman G.G., Gregory P.C., 1981, Nature, 293, 202

Cheng A.F., Helfand D.J., 1983, ApJ, 271, 271

Córdova F.A., Hjellming R.M., Mason K.O., Middleditch J., 1989, ApJ, 345, 451

Drake J.J., Marshall H.L., Dreizler S., Freeman P.E., Fruscione A., Juda M., Kashyap V., Nicastro F., Pease D.O., Wargelin B.J., Werner K., 2002, ApJ, in press

Giacani E.B., Dubner G.M., Green A.J., Goss W.M., Gaensler B.M., 2000, AJ, 119, 281

Gould D.M., Lyne A.G., 1998, MNRAS, 301, 235

Haberl F., Zavlin V.E., 2002, A&A, in press (astro-ph/0205460)

Haberl F., Motch C., Buckley D.A.H., Zickgraf F.J., Pietsch W., 1997, A&A 326, 662

Haberl F., Motch C., Pietsch W., 1998, Astronom. Nach., 319, 97

Haberl F., Pietsch W., Motch C., 1999, A&A, 351, L53

Halpern J.P., Martin C., Marshall H.L., 1996, ApJ, 462, 908

Hambaryan V., Hasinger G., Schwope A.D., Schulz N.S., 2002, A&A, 381, 98

Harding A.K., Strickman M.S., Gwinn C., McCulloch P., Moffet D., 2002, ApJ, in press (astro-ph/0205183)

Helfand D.J., Becker R.H., 1984, Nature, 307, 215

Helfand D.J., Gotthelf E.V., Halpern J.P., 2001, ApJ, 556, 380

Kaplan D.L., van Kerkwijk M.H., Anderson J., 2002a, ApJ, 566, 378

Kaplan D.L., Kulkarni S.R., van Kerkwijk M.H., Marshall H.K., 2002b, ApJ, 570, L79

Kellett B.J., Branduardi-Raymont G., Culhane J.L., Mason I.M., Mason K.O., Whitehouse D.R., 1987, MNRAS, 225, 199

Koptsevich A.B., Pavlov G.G., Zharikov S.V., Sokolov V.V., Shibanov Yu.A., Kurt V.G., 2001, A&A, 370, 1004

Kouveliotou C., 1995, Ap&SS, 231, 49

Kulkarni S.R., van Kerkwijk M.H., 1998, ApJ, 507, L49

Lai D., Salpeter E.E., 1997, ApJ, 491, 270

Marshall H.L., Shultz N., 2002, ApJ, in press (astro-ph/0203463)

Mereghetti S., Bignami G.F., Caraveo P.A., 1996, ApJ, 464, 842

Motch C., Haberl F., Zickgraf F.J., Hasinger G., Schwope A.D., 1999, 351, 177

Ögelman H., 1995, in The Lives of the Neutron Stars, eds. M.A. Alpar, Ü. Kiziloglu and J. van Paradijs NATO ASI Ser. (Dordrecht: Kluwer), p.101

Pavlov G.G., Stringfellow G.S., Córdova F.A., 1996, ApJ, 489, L75

Pavlov G.G., Zavlin V.E., Trümper J., Neuhäuser R., 1996, ApJ, 472, L33

Pavlov G.G., Welty A.D., Córdova F.A., 1997, ApJ, 489, L75

Pavlov G.G., Sanwal D., Garmire G.P., Zavlin V.E., Burwitz V., Dodson R.G., 2000, AAS Meeting 196, #37.04

Pavlov G.G., Kargaltsev O.Y., Sanwal D., Garmire G.P., 2001a, ApJ, 554, L189

Pavlov G.G., Zavlin V.E., Sanwal D., Burwitz V., Garmire G.P., 2001b, ApJ, 552, L129

Pavlov G.G., Sanwal D., Garmire G.P., Zavlin V.E., 2002a, in Neutron Stars in Supernova Remnant, ASP Conf. Series, eds. P.O. Slane & B.M. Gaensler, in press (astro-ph/0112322)

Pavlov G.G., Zavlin V.E., Sanwal D., Trümper J., 2002b, ApJ, 569, L95

Pavlov G.G., Sanwal, D., Teter, M.A., Zavlin, V.E, 2002c, AAS Meeting 200, #80.01

Pons J.A., Walter, F.M., Lattimer J.M., Prakash M., Neuhäuser R., An P., 2002, ApJ, 564, 981

Ransom S.M., Gaensler B.M., Slane P.O., 2002, ApJ, 570, L75

Rutledge R.E., Bildsten L., Brown E.F., Pavlov G.G., Zavlin V.E. 2001, ApJ, 559, 1054

Sanwal D., Pavlov G.G., Kargaltsev O.Y., Garmire G.P., Zavlin V.E., Burwitz V., Manchester, R.N., Dodson R., 2002a, in Neutron Stars in Supernova Remnants, eds. P.O. Slane and B.M. Gaensler, in press (astro-ph/0112164)

Sanwal D., Pavlov G.G., Zavlin V.E., Teter M.A., 2002b, ApJ, submitted

Sanwal D., Pavlov G.G., Zavlin V.E., Teter M.A., Tsuruta S., Manchester R.N., 2002c, ApJ, submitted

Slane P.A., Helfand D.J., Murray S.S. 2002, ApJ, 571, L45

Seward F.D., Charles P.A., Smale A.P., 1986, 305, 814

Schwope A.D., Hasinger G., Schwarz R., Haberl F., Schmidt M., 1999, A&A, 341, L51

Tennant A.F., Becker W., Juda M., et al., 2001, ApJ, 554, L173

Treves A., Turolla R., Zane S., Colpi M., 2000, PASP, 112, 297

Tsuruta S., 1998, Phys. Rep., 292, 1

van Kerkwijk M.H., Kulkarni S.R., 2001a, A&A, 378, 986

van Kerkwijk M.H., Kulkarni S.R., 2001b, A&A, 380, 221

Vasisht G., Kulkarni S.R., Anderson S.B., Hamilton T.T., Kawai N., 1997, ApJ, 476, L43

Walter F.M., Matthews L.D., 1997, Nature, 389, 358

Walter F.M., Lattimer J.M, 2002, ApJ, submitted (astro-ph/0204199)

Walter F.M., Wolk S.J., Neuhäuser R., 1996, Nature, 379, 233

Zampieri L., Campana S., Turolla R., Chieregato M., Falomo R., Fugazza D., Moretti A., Treves A., 2001, A&A, 378, L5

Zane S., Haberl F., Cropper M., Zavlin V.E., Lumb D., Sembay S., Motch S., 2002, MNRAS, in press

Zavlin V.E., Pavlov G.G, 1998, A&A, 329, 583 [ZP98]

Zavlin V.E., Pavlov G.G., 2002, this volume [ZP02]

Zavlin V.E., Pavlov G.G., Trümper J., 1998, A&A, 331, 821

Zavlin V.E., Pavlov G.G., Sanwal D., Trümper J., 2000, ApJ, 540, L25

Zavlin V.E., Pavlov G.G., Sanwal D., Trümper J., Manchester R.N., Halpern J.P., Becker W., 2002, ApJ, 569, 894

Proceedings of the 270. WE-Heraeus Seminar on: *"Neutron Stars, Pulsars and Supernova Remnants"*
Physikzentrum Bad Honnef, Germany, Jan. 21-25, 2002, eds. W. Becker, H.Lesch & J. Trümper, MPE Report 278, pp. 287-299

Cooling of Superfluid Neutron Stars

D.G. Yakovlev[1], O.Y. Gnedin[2], A.D. Kaminker[1], and A.Y. Potekhin[1]

[1] Ioffe Physical Technical Institute, Politekhnicheskaya 26, 194021 St. Petersburg, Russia
[2] Space Telescope Science Institute, 3700 San Martin Drive, Baltimore, MD 21218, USA
yak@astro.ioffe.rssi.ru, ognedin@stsci.edu, kam@astro.ioffe.rssi.ru, palex@astro.ioffe.rssi.ru

Abstract. Cooling of neutron stars (NSs) with the cores composed of neutrons, protons, and electrons is analyzed. The main cooling regulators are discussed: opening of direct Urca process in a NS central kernel; superfluidity of nucleons in NS interiors; surface layers of light (accreted) elements; strong surface magnetic fields. An emphasis is paid on the cooling scenario with strong $^1S_0$ pairing of protons and weak $^3P_2$ pairing of neutrons in the NS core, as well as strong $^1S_0$ pairing of neutrons in the NS crust. The theory predicts three types of isolated cooling middle-aged NSs with distinctly different properties: low-mass, slowly cooling NSs; medium-mass, moderately cooling NSs; massive, rapidly cooling NSs. The theory is compared with observations of isolated NSs — pulsars and radio quiet NSs in supernova remnants. The constraints on physical properties of NSs which can be inferred from such a comparison are outlined.

1. Introduction

Cooling of neutron stars (NSs) depends on the properties of dense matter in their crusts and cores. These properties are still poorly known and cannot be described unambiguously by contemporary theories. For instance, calculations of the equation of state (EOS) of the NS cores (e.g., Lattimer & Prakash 2001) or the superfluid properties of NS cores and crusts (e.g., Lombardo & Schulze 2001) give a large scatter of results which depend on a model of strong interaction and a many-body theory employed. However, these properties can be studied by comparing the results of simulations of NS cooling with the observations of thermal emission from isolated NSs. We will describe some recent results of such studies. The history of NS cooling theory is reviewed, for instance, by Yakovlev et al. (1999)

For simplicity, we consider the NS models with the cores composed mainly of neutrons with an admixture of protons and electrons. We discuss the basic ideas of the cooling theory, and the main cooling regulators, paying special attention on the effects of superfluidity of nucleons in NS interiors. Our consideration will be based on recent simulations of the cooling of superfluid NSs by Kaminker et al. (2001), Potekhin & Yakovlev (2001), Yakovlev et al. (2001b), and Kaminker et al. (2002, hereafter KYG).

2. Equations of thermal evolution

Neutron stars are born very hot in supernova explosions, with internal temperature $T \sim 10^{11}$ K, but gradually cool down. In about 30 s after the birth a star becomes fully transparent for neutrinos generated in its interiors. We consider the cooling in the following neutrino-transparent stage. The cooling is realized via two channels, by neutrino emission from the entire stellar body and by heat transport from the internal layers to the surface resulting in the thermal emission of photons. For simplicity, we neglect the possible reheating mechanisms (frictional dissipation of rotational energy, or Ohmic decay of internal magnetic field, or the dissipation associated with weak deviations from the chemical equilibrium as reviewed, e.g., by Page 1998).

The internal structure of NSs can be regarded as temperature-independent (e.g., Shapiro & Teukolsky 1983). The general relativistic equations of thermal evolution include the energy and flux equations obtained by Thorne (1977). For a spherically symmetric NS,

$$\frac{1}{4\pi r^2 \mathrm{e}^{2\Phi}} \sqrt{1-\frac{2Gm}{c^2 r}}\, \frac{\partial}{\partial r}\left(\mathrm{e}^{2\Phi} L_r\right) = -Q - \frac{c_v}{\mathrm{e}^{\Phi}} \frac{\partial T}{\partial t}, \qquad (1)$$

$$\frac{L_r}{4\pi\kappa r^2} = -\sqrt{1-\frac{2Gm}{c^2 r}}\, \mathrm{e}^{-\Phi} \frac{\partial}{\partial r}\left(T\mathrm{e}^{\Phi}\right), \qquad (2)$$

where Q is the neutrino emissivity [erg cm^{-3} s^{-1}], c_v is the heat capacity per cm^3 [erg cm^{-3} K^{-1}], κ is the thermal conductivity [erg cm^{-1} s^{-1} K^{-1}], and L_r is the "local luminosity" [erg s^{-1}] defined as the non-neutrino heat flux transported through a sphere of radius r. The gravitational mass $m(r)$ and the metric function $\Phi(r)$ are determined by the stellar model.

It is conventional (e.g., Gudmundsson et al. 1983) to subdivide the calculation of heat transport in the neutron-star interior ($r < R_\mathrm{b}$) and in the outer heat-blanketing envelope ($R_\mathrm{b} \le r \le R$), where R is the stellar radius, and the boundary radius R_b corresponds to the density $\rho_\mathrm{b} \sim 10^{10}$ g cm^{-3} (~ 100 meters under the surface). In the presence of superstrong surface magnetic field, it is reasonable to shift ρ_b to the neutron drip density, 4×10^{11} g cm^{-3} (Potekhin & Yakovlev 2001). The thermal structure of the blanketing envelope is studied separately in the stationary, plane-parallel approximation to relate the effective surface temperature T_s to the temperature T_b at the inner boundary of the envelope. We discuss the T_s–T_b relation in Sect. 3. It is used as the boundary condition for solving Eqs. (1) and (2) at $r < R_\mathrm{b}$.

The effective temperature determines the photon luminosity $L_\gamma = 4\pi\sigma R^2 T_s^4(t)$. Both, L_γ and T_s refer to the locally-flat reference frame on the surface. A distant observer would register the "apparent" luminosity $L_\gamma^\infty = L_\gamma(1 - r_g/R)$ and the "apparent" effective temperature $T_s^\infty = T_s\sqrt{1 - r_g/R}$, where $r_g = 2GM/c^2$ is the Schwarzschild radius and $M = m(R)$ is the total gravitational mass.

The main goal of the cooling theory is to calculate *cooling curves*, $T_s^\infty(t)$, to be compared with observations. One can distinguish three main cooling stages: (i) the internal relaxation stage ($t \lesssim 10$–100 yr; Lattimer et al. 1994; Gnedin et al. 2001), (ii) the neutrino cooling stage (the neutrino luminosity $L_\nu \gg L_\gamma$, $t \lesssim 10^5$ yr), and (iii) the photon cooling stage ($L_\nu \ll L_\gamma$, $t \gtrsim 10^5$ yr).

After the thermal relaxation, the redshifted temperature $\widetilde{T}(t) = T(r,t)\ \mathrm{e}^{\Phi(r)}$ becomes constant throughout the stellar interior. Then Eqs. (1) and (2) reduce to the equation of global thermal balance,

$$C(\widetilde{T})\,\frac{\mathrm{d}\widetilde{T}}{\mathrm{d}t} = -L_\nu^\infty(\widetilde{T}) - L_\gamma^\infty(T_s), \tag{3}$$

$$L_\nu^\infty(\widetilde{T}) = 4\pi\int_0^{R_b} \frac{\mathrm{d}r\, r^2\, Q(\widetilde{T})\,\mathrm{e}^{2\Phi}}{\sqrt{1-2Gm/(c^2 r)}}, \tag{4}$$

$$C(\widetilde{T}) = 4\pi\int_0^{R_b} \frac{\mathrm{d}r\, r^2\, c_v(\widetilde{T})}{\sqrt{1-2Gm/(c^2 r)}}, \tag{5}$$

where C is the total NS heat capacity, and L_ν^∞ is the total neutrino luminosity.

3. Physics input

We describe the results obtained using a fully relativistic non-isothermal cooling code (Gnedin et al. 2001). The code solves the heat diffusion equations (Sect. 2) in the NS interior.

The physics unput is as follows. The EOS in the NS crust is taken from Negele & Vautherin (1973) (assuming spherical atomic nuclei everywhere in the crust). The core-crust boundary is placed at the density 1.5×10^{14} g cm^{-3}. In the core, we use two phenomenological EOSs (EOS A and EOS B) proposed by Prakash et al. (1988).

EOS A is model I of Prakash et al. (1988) with the compression modulus of saturated nuclear matter $K = 240$ MeV. EOS B corresponds to $K = 180$ MeV and to the simplified form of the symmetry energy suggested by Page & Applegate (1992). It has been used in many papers (e.g., Page & Applegate 1992, Yakovlev et al. 1999, 2001a, and references therein).

The masses, central densities, and radii of two stellar configurations for EOSs A and B are given in Table 1. The first configuration corresponds to the maximum-mass NS. The values of $M_{\max}$ reveal that EOS A is stiff, and EOS B is moderate. The second configuration has a central density ρ_c at which the direct Urca process switches on (the process is allowed at $\rho_c > \rho_D$, which corresponds to $M > M_D$). EOS B is based on a smaller symmetry energy and opens the direct Urca process at a higher ρ.

The cooling code includes all important neutrino emission processes in the NS core (direct and modified Urca processes, neutrino bremsstrahlung in nucleon-nucleon scattering, neutrino emission due to Cooper pairing of nucleons) and in the crust (plasmon decay, neutrino bremsstrahlung due to scattering of electrons off atomic nuclei, electron-positron annihilation into neutrino pairs, neutrino emission due to Cooper pairing of neutrons in the inner crust). These processes are reviewed, for instance, by Yakovlev et al. (2001a). The effective masses of protons and neutrons in the core and free neutrons in the crust are taken to be 0.7 of the bare nucleon masses. The values of the thermal conductivity in the NS crust and core are the same as used by Gnedin et al. (2001).

Table 1. NS models employing EOSs A and B (from KYG)

Model	Main parameters	EOS A	EOS B
Maximum mass model	$M_{\max}/\mathrm{M}_\odot$	1.977	1.73
	$\rho_{\mathrm{cmax}}/10^{14}$ g cm^{-3}	25.75	32.5
	R km	10.754	9.71
Direct Urca threshold model	$M_D/\mathrm{M}_\odot$	1.358	1.44
	$\rho_D/10^{14}$ g cm^{-3}	7.851	12.98
	R km	12.98	11.54

Table 2. Parameters of superfluid models in Eq. (6); from KYG

Pairing	Model	$T_0/10^9$ K	k_0 fm^{-1}	k_1 fm^{-1}	k_2 fm^{-1}	k_3 fm^{-1}
$^1S_0$	1p	20.29	0	1.117	1.241	0.1473
$^1S_0$	2p	17	0	1.117	1.329	0.1179
$^1S_0$	3p	14.5	0	1.117	1.518	0.1179
$^1S_0$	1ns	10.2	0	0.6	1.45	0.1
$^1S_0$	2ns	7.9	0	0.3	1.45	0.01
$^1S_0$	3ns	1800	0	21	1.45	0.4125
$^3P_2$	1nt	6.461	1	1.961	2.755	1.3

The T_s–T_b relationship is taken from Potekhin et al. (1997) and Potekhin & Yakovlev (2001). It is relevant either for the surface layers made of iron (without any magnetic field and with the dipole surface magnetic fields $B \lesssim 10^{15}$ G), or for the non-magnetic surface layers containing light elements. In addition, we have modified the relationship by incorporating our new results which take into account the combined effects of accreting envelopes and magnetic fields. It is assumed that the surface magnetic field induces an anisotropic heat transport in the heat-blanketing envelope but does not violate the isotropic (radial) heat diffusion in the deeper NS layers. This preserves the scheme of solving the radial heat diffusion equations (Sect. 2). In this case, T_s varies over the NS surface, and the cooling theory deals with the mean surface temperature $\bar{T}_s$ that determines the NS photon luminosity. For brevity, we denote $\bar{T}_s$ as T_s. It is also assumed that a NS may have a hydrogen atmosphere even if the heat-blanketing envelope is mostly made of iron. The majority of cooling curves are calculated for the non-magnetized heat-blanketing envelopes made of iron. The exceptions are discussed in Sect. 6.3.

We will focus on the effects of nucleon superfluidity on NS cooling. The superfluid properties of NS matter are characterized by the density-dependent critical temperatures $T_c(\rho)$ of nucleons. Microscopic theories predict (e.g., Lombardo & Schulze 2001, Yakovlev et al. 1999) superfluidities of three types: singlet-state ($^1S_0$) pairing of neutrons ($T_c = T_{\mathrm{cns}}$) in the inner crust and outermost core; $^1S_0$ proton pairing ($T_c = T_{\mathrm{cp}}$) in the core; and triplet-state ($^3P_2$) neutron pairing ($T_c = T_{\mathrm{cnt}}$) in the core. Superfluidity of nucleons suppresses neutrino processes involving nucleons, initiates a specific mechanism of

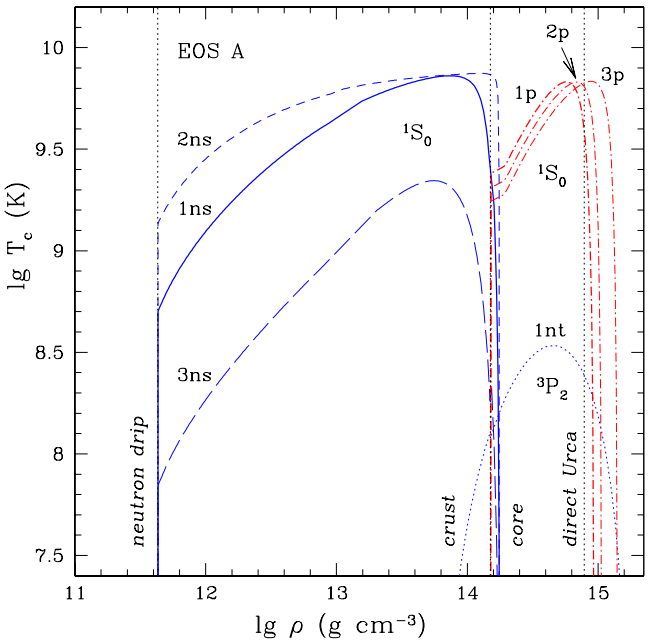


Fig. 1. Density dependence (from KYG) of the critical temperatures for three models 1p, 2p, and 3p of the proton superfluidity (dots-and-dashes) in the core (with EOS A); three models 1ns, 2ns, and 3ns of $^1S_0$ neutron superfluidity (solid, short-dashed, and long-dashed lines); and one model 1nt of $^3P_2$ neutron superfluidity (dots) used in cooling simulations. Vertical dotted lines indicate the neutron drip point, core-crust interface, and direct Urca threshold.

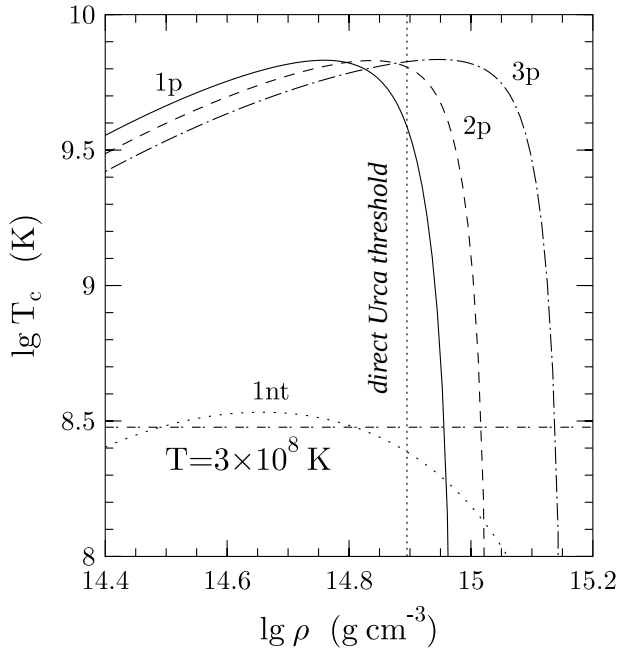


Fig. 2. Density dependence of the critical temperatures of superfluidity of protons (models 1p, 2p, and 3p — solid, dashed, and dot-and-dashed lines) and neutrons (model 1nt — dotted line) in the NS core for EOS A on a larger scale than in Fig. 1. Vertical dotted line indicates direct Urca threshold. Horizontal line is the temperature of matter, $T = 3 \times 10^8$ K, adopted in Fig. 3.

neutrino emission associated with Cooper pairing of nucleons (Flowers et al. 1976), and affects the nucleon heat capacity. All these effects are incorporated into the cooling code as described by Yakovlev et al. (1999, 2001a) and Gnedin et al. (2001).

The microscopic calculations of superfluid critical temperatures $T_c(\rho)$ give a large scatter of results (e.g., Lombardo & Schulze 2001), but some common features are clear. For instance, $T_c(\rho)$ increases with ρ at sufficiently low densities (due to an increasing strength of the attractive part of nucleon-nucleon interaction), reaches maximum and then decreases (due to a short-range nucleon-nucleon repulsion), vanishing at a rather high density. For $T_{cns}(\rho)$, the maximum occurs at subnuclear densities, while the switch off takes place at $\rho \sim \rho_0$, where $\rho_0 \approx 2.8 \times 10^{14}$ g cm^{-3} is the saturated nuclear matter density. For $T_{cp}(\rho)$ and $T_{cnt}(\rho)$, the maxima take place at a few ρ_0 and the fall occurs at the densities several times higher. The maximum values of T_c range from about 10^8 K (or even lower) to $(2-3) \times 10^{10}$ K, depending on the microscopic theoretical model. The maximum values of T_{cnt} are typically lower than those of T_{cp} and T_{cns}, due to the weaker nucleon-nucleon attraction in the $^3P_2$ state.

Instead of studying T_c as a function of ρ, it is often convenient to consider T_c as a function of the nucleon Fermi wavenumber $k = k_{FN} = (3\pi^2 n_N)^{1/3}$, where n_N is the number density of nucleon species N=n or p (neutrons or protons). Moreover, instead of $T_c(k)$ one often considers $\Delta(k)$, the zero-temperature superfluid gap. For the $^1S_0$ pairing, assuming BCS theory, one has $\Delta(k) = T_c(k)/0.5669$. In the case of $^3P_2$ neu-

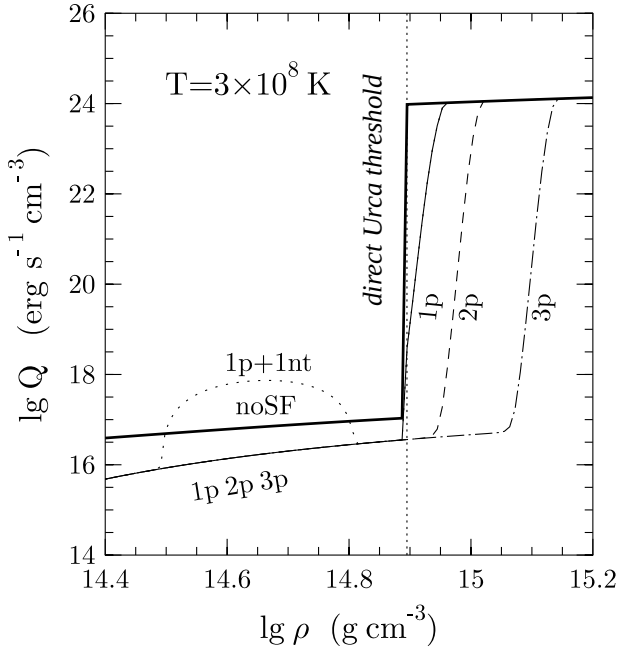


Fig. 3. Density dependence of the neutrino emissivity Q in the NS core at $T = 3 \times 10^8$ K and EOS A. Solid, dashed and dot-and-dashed lines 1p, 2p, and 3p are plotted for proton superfluidity models displayed in Fig. 2. The dotted line shows Q in the presence of proton superfluidity 1p and neutron superfluidity 1nt. The thick solid line is Q in non-superfluid matter.

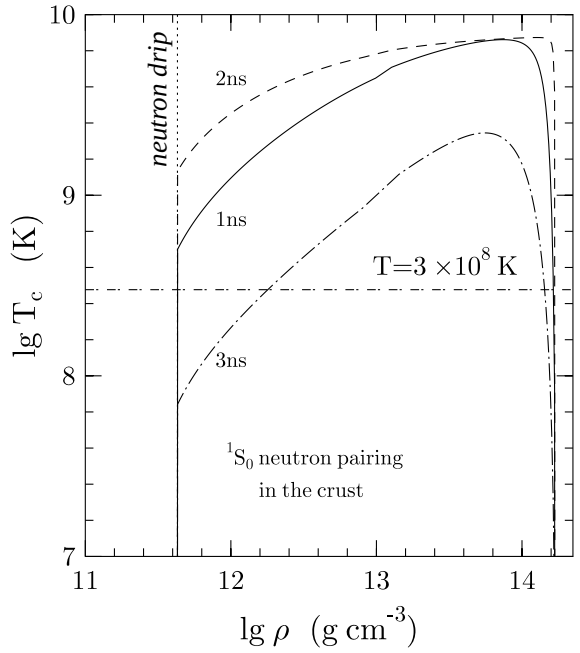


Fig. 4. Density dependence of the critical temperatures of superfluidity of neutrons (models 1ns, 2ns, and 3ns) in the NS crust (cf. Fig. 1). Vertical dotted line indicates neutron drip point. Horizontal line is the temperature of matter, $T = 3 \times 10^8$ K, adopted in Fig. 5.

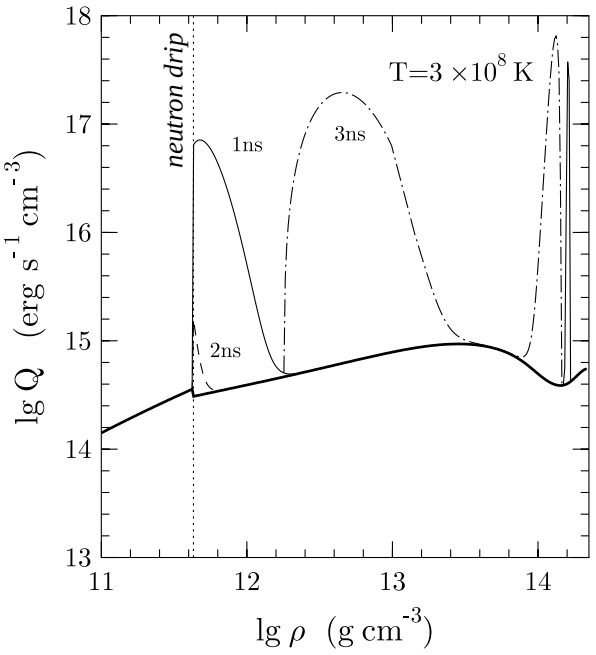


Fig. 5. Density dependence of the neutrino emissivity Q in the NS crust at $T = 3 \times 10^8$ K. Thin solid, dashed, and dot-and-dashed lines 1ns, 2ns, and 3ns are calculated for neutron superfluidity models displayed in Fig. 4. The thick solid line is for non-superfluid matter. The core-crust boundary is artificially shifted to higher ρ for a better visualization of the effects of neutrino emission associated with $^1S_0$ Cooper pairing of neutrons.

tron pairing, the gap depends on the orientation of nucleon momenta with respect to the quantization axis. Following the majority of papers, we adopt the $^3P_2$ pairing with zero projection of the total angular momentum on the quantization axis. In that case $\Delta_{\rm nt}(k) = T_{\rm cnt}(k)/0.8416$, where $\Delta_{\rm nt}(k)$ is the minimum value of the gap on the neutron Fermi surface (e.g., Yakovlev et al. 1999). The dependence of the gaps on k for the selected superfluidity models is plotted in KYG.

Taking into account large scatter of theoretical values of $T_{\rm c}(k)$ it is instructive to consider $T_{\rm c}(k)$ as unknown functions and analyze (Sect. 6) which of them are consistent with observations. In this paper, following KYG, we adopt the parameterization of $T_{\rm c}$ of the form:

$$T_{\rm c} = T_0 \, \frac{(k-k_0)^2}{(k-k_0)^2 + k_1^2} \, \frac{(k-k_2)^2}{(k-k_2)^2 + k_3^2} \, , \qquad (6)$$

for $k_0 < k < k_2$; and $T_{\rm c} = 0$, for $k \le k_0$ or $k \ge k_2$. The factor T_0 regulates the amplitude of $T_{\rm c}$, k_0 and k_2 determine positions of the low- and high-density cutoffs, while k_1 and k_3 specify the shape of $T_{\rm c}(\rho)$. All wave numbers, k, k_0, ... k_3 are expressed in fm^{-1}. KYG verified that by tuning T_0, k_0, ... k_3, the parameterization accurately describes numerous results of microscopic calculations.

Following KYG we use three models of $^1S_0$ proton superfluidity, three models of $^1S_0$ neutron superfluidity, and one model of $^3P_2$ neutron superfluidity. The parameters of the models are given in Table 2, and the appropriate $T_{\rm c}(\rho)$ are plotted in Figs. 1, 2, and 4. One has $k_0 = 0$ for $^1S_0$ pairing. At any given ρ it is reasonable to choose the neutron superfluidity ($^1S_0$ or $^3P_2$) with higher $T_{\rm c}$.

Models 1ns and 2ns of neutron pairing in the crust correspond to about the same, rather strong superfluidity (with maximum $T_{\rm cns} \approx 7 \times 10^9$ K). Model 2ns has flatter maximum and sharper decreasing slopes in the wings (near the crust-core interface and the neutron drip point). Model 3ns represents a much weaker superfluidity, with maximum $T_{\rm cns} \approx 2.4 \times 10^9$ K and a narrower density profile.

The proton superfluidity curves 1p, 2p, and 3p in Figs. 1 and 2 are similar. The maximum values of $T_{\rm cp}$ are about 7×10^9 K for all three models. The models differ by the positions of the maximum and decreasing slopes of $T_{\rm cp}(\rho)$. The decreasing slope of model 1p is slightly above the threshold density of the direct Urca process (for EOS A), while the slopes for models 2p and 3p are shifted to higher ρ. Our models 1p, 2p, and 3p are typical for those microscopic theories which adopt a moderately strong medium polarization of proton-proton interaction.

Finally, the dotted curve in Figs. 1 and 2 shows $T_{\rm cnt}(\rho)$ for 1nt model of $^3P_2$ neutron pairing (used by Kaminker et al. 2001). The curve falls within a wide scatter of $T_{\rm cnt}(\rho)$, provided by microscopic theories.

4. Main regulators of neutron-star cooling

Theoretical cooling curves depend on many features of NS models. Below we discuss four main regulators of the cooling of middle-aged NSs: (1) central kernels, where neutrino emission is enhanced by direct Urca process; (2) the effects of nucleon superfluidity on neutrino emission; (3) surface envelopes of light elements; and (4) surface magnetic fields. The effects of these factors are illustrated in Figs. 2–7. The effects (1) and (2) are the strongest, although (3) and (4) can also be important.

Table 3. Surface temperatures of eight isolated middle-aged neutron stars inferred from observations

Source	lg t [yr]	lg T_s^∞ [K]	Model[a)]	Confid. level	References
RX J0822–43	3.57	$6.23^{+0.02}_{-0.02}$	H	95.5%	Zavlin et al. (1999)
1E 1207–52	3.85	$6.10^{+0.05}_{-0.06}$	H	90%	Zavlin et al. (1998)
RX J0002+62	3.95[b)]	$6.03^{+0.03}_{-0.03}$	H	95.5%	Zavlin & Pavlov (1999)
PSR 0833–45 (Vela)	4.4[c)]	$5.83^{+0.02}_{-0.02}$	H	68%	Pavlov et al. (2001)
PSR 0656+14	5.00	$5.96^{+0.02}_{-0.03}$	bb	90%	Possenti et al. (1996)
PSR 0633+1748 (Geminga)	5.53	$5.75^{+0.05}_{-0.08}$	bb	90%	Halpern & Wang (1997)
PSR 1055–52	5.73	$5.88^{+0.03}_{-0.04}$	bb	[d)]	Ögelman (1995)
RX J1856–3754	5.95	$5.72^{+0.05}_{-0.06}$	[e)]	[d)]	Pons et al. (2002)

[a)] Observations are interpreted either with a hydrogen atmosphere model (H), or with a black body spectrum (bb)

[b)] The mean age taken according to Craig et al. (1997).

[c)] According to Lyne et al. (1996).

[d)] Confidence level is uncertain.

[e)] Analytic fit with Si-ash atmosphere model of Pons et al. (2002).

4.1. Direct Urca process in non-superfluid NSs

The NS cooling is strongly affected by the presence of the central NS kernels ($\rho > \rho_{\rm D}$, Table 1), where direct Urca process – the most powerful neutrino emission mechanism – is open. The effect is especially pronounced in the absence of nucleon superfluidity. For instance, Fig. 3 shows the density profile of the total neutrino emissivity throughout the NS core at a temperature $T = 3 \times 10^8$ K. The emissivity of non-superfluid matter is shown by the thick line. The jump by about 7 orders of magnitude is associated with the direct Urca threshold, $\rho_{\rm D}$. The NSs with the central density $\rho_{\rm c} < \rho_{\rm D}$ have no kernels with the enhanced neutrino emission and show *slow* cooling. The NSs with $\rho_{\rm c} > \rho_{\rm D}$ will have these kernels and show *fast* cooling. The presence of the kernels has dramatic effects on the NS cooling (Lattimer et al. 1991).

4.2. The effects of superfluidity on neutrino emission

First we discuss the effects of superfluidity in the NS cores. The adopted models of proton and neutron critical temperatures (Sect. 3) in the core are shown in Figs. 1 and 2. The appropriate neutrino emissivities are displayed in Fig. 3. A proton superfluidity drastically changes the density profiles of the neutrino emissivity, $Q(\rho)$, as compared with the non-superfluid case (lines 1p, 2p, and 3p in Figs. 2 and 3).

At not too high density, $\rho \lesssim \rho_{\rm I}$ (the threshold density $\rho_{\rm I}$ is specified in Sect. 6), a strong proton superfluidity almost switches off all neutrino processes involving protons, particularly, modified Urca process and even the most powerful direct Urca process. In this regime, the main neutrino emission is provided by neutrino-pair bremsstrahlung in neutron-neutron scattering; its level is *lower* than in a slowly cooling non-superfluid NS regulated by non-suppressed modified Urca process. Since strong proton superfluidity 3p extends to higher ρ, this regime persists to higher ρ, for this superfluidity.

At rather high $\rho \gtrsim \rho_{\rm II}$ (the value $\rho_{\rm II}$ is also specified in Sect. 6) the proton superfluidity dies out and we have the neutrino emissivity fully enhanced by direct Urca process. Again, $\rho_{\rm II}$ is higher for proton superfluidity 3p.

At $\rho_{\rm I} \lesssim \rho \lesssim \rho_{\rm II}$ the neutrino emissivity is determined by direct Urca process partly suppressed by proton superfluidity. Evidently, this regime is absent in non-superfluid NSs. In this regime, the emissivity is sensitive to the decreasing slope of the $T_{\rm cp}(\rho)$ profile and to EOS in the NS core.

Thus, in any $Q(\rho)$ profile, we can distinguish three distinctly different parts: (I) $\rho \lesssim \rho_{\rm I}$; (II) $\rho_{\rm I} \lesssim \rho \lesssim \rho_{\rm II}$; (III) $\rho \gtrsim \rho_{\rm II}$. They will lead (Sect. 6) to three types of cooling superfluid NSs.

Now we switch on neutron superfluidity in the core (model 1nt) in addition to the proton one. For $T = 3 \times 10^8$ K, this superfluidity occurs in a density range from $\sim 3 \times 10^{14}$ g cm^{-3} to $\sim 6 \times 10^{14}$ g cm^{-3} (Fig. 2). It creates a powerful splash of neutrino emission associated with Cooper pairing of neutrons as shown in Fig. 3 by the dotted line. This splash is actually the same for any model of proton superfluidity (1p, 2p, or 3p).

In addition, we discuss the effects of the neutron superfluidity in the crust. The density profiles of the critical temperature $T_{\rm cns}(\rho)$ (models 1ns, 2ns, and 3ns; Table 2; Figs. 1 and 4) and the appropriate neutrino emissivities $Q(\rho)$ at $T = 3 \times 10^8$ K are shown in Fig. 5. The thick line in Fig. 5 exhibits the emissivity of the non-superfluid crust provided mainly by neutrino-pair bremsstrahlung in electron-nucleus scattering. One can observe strong additional peaks of neutrino emission from superfluid crust produced by Cooper pairing of neutrons. The peaks are very sensitive to the models of $T_{\rm cns}(\rho)$. However, since the NS crust contains a small fraction of NS mass (about 1–5 % or smaller, for the adopted NS models) this additional neutrino

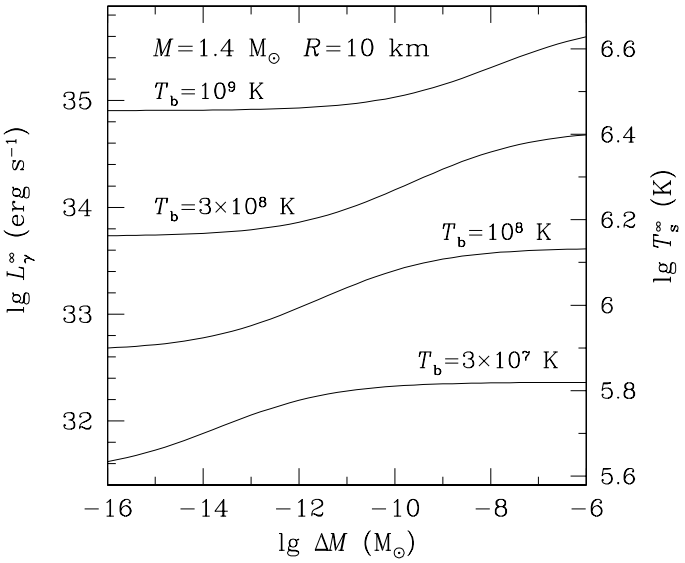


Fig. 6. Photon surface luminosity (redshifted as detected by a distant observer, left vertical axis) or redshifted effective surface temperature (right vertical axis) of a "canonical" NS model ($M = 1.4\,\mathrm{M}_\odot$, $R = 10$ km) for four values of the "internal" temperature T_b (at the bottom of the heat blanketing layer, $\rho_\mathrm{b} = 10^{10}$ g cm^{-3}) versus the mass of accreted material, ΔM.

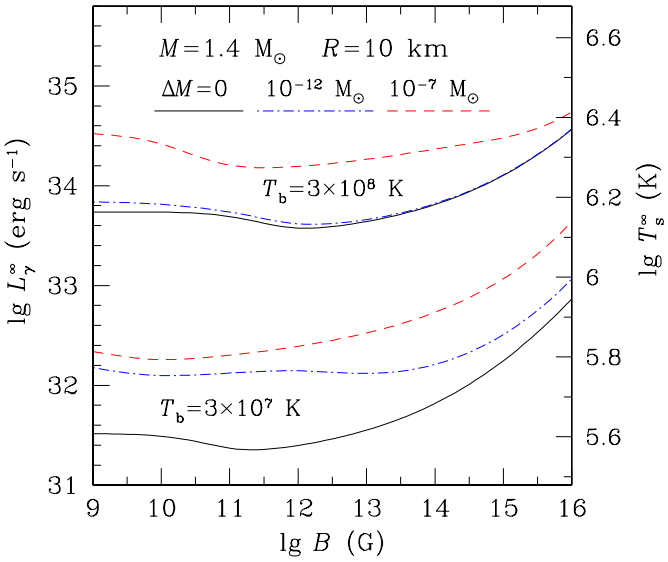


Fig. 7. Redshifted photon surface luminosity (left vertical axis) and mean effective temperature (right vertical axis) of a "canonical" NS with a dipole magnetic field, for two values of T_b and three models of the heat-blanketing envelope (accreted mass $\Delta M = 0$, $10^{-12}\,\mathrm{M}_\odot$, and $10^{-7}\,\mathrm{M}_\odot$) versus magnetic field strength B at the magnetic pole.

emission is important only in those NSs (Sect. 6.3) whose cores produce low neutrino luminosity.

4.3. Accreted surface layers

A heat-blanketing envelope (Sect. 2) is traditionally assumed to be made of iron (e.g., Gudmundsson et al. 1983). However, the envelope may partly contain light elements (H, He) provided, for instance, by accretion. In the heat-blanketing layers, the heat is mainly carried by degenerate electrons. The thermal conductivity of electrons which scatter off light ions is higher than the conductivity limited by scattering off iron ions. Thus, the accreted envelope is more heat transparent. The appropriate $T_\mathrm{s} - T_\mathrm{b}$ relationship was calculated by Potekhin et al. (1997). It depends on ΔM, the mass of accreted hydrogen or helium. The calculation takes into account nuclear burning of light elements in a hot and/or dense plasma, i.e., ΔM is the total accreted mass which may partly be processed into heavier elements due to nuclear transformations in accreted matter. The dependence of the photon NS luminosity on ΔM for four values of the temperature at the bottom of the heat-blanketing envelope ($T_\mathrm{b} = 3\times10^7$, 10^8, 3×10^8, and 10^9 K) is shown in Fig. 6. If the heat-blanketing envelope is fully replaced by accreted material, the NS luminosity can increase by about one order of magnitude, i.e., the surface temperature T_s can increase by a factor of 2.

4.4. Surface magnetic field

The effects of strong magnetic field on the heat conduction through the blanketing NS envelope have been reviewed, for instance, by Ventura & Potekhin (2001). These effects depend on ρ, T, and the field strength B. One can distinguish (i) *classical effects* of electron *Larmor rotation*, and (ii) the *effects of quantization* of electron orbits across the field lines (Landau states).

The classical effects require lower magnetic fields. They become pronounced at $\omega_\mathrm{g}\tau \gtrsim 1$, where ω_g is the electron gyrofrequency, and τ is the effective electron relaxation time. Then the conduction becomes anisotropic. The electron thermal conductivity along the field lines remains equal to its non-magnetic value κ_0, while the conductivity in the perpendicular direction becomes $\kappa_0/[1+(\omega_\mathrm{g}\tau)^2]$.

The conditions of electron quantization are determined by characteristic density ρ_B and temperature T_B,

$$\rho_B \approx 7.045\times10^3\,(A/Z)\,B_{12}^{3/2}\ \mathrm{g\,cm^{-3}}, \quad (7)$$

$$T_B \approx \frac{1.343\times10^8\,B_{12}}{\sqrt{1+1.018(\rho_6 Z/A)^{2/3}}}\ \mathrm{K}, \quad (8)$$

where Z is the mean charge number of atomic nuclei, A is the number of nucleons per a nucleus, $\rho_6 = \rho/10^6$ g cm^{-3}, and $B_{12} = B/10^{12}$ G. The magnetic field remains non-quantizing as long as $T \gg T_B$.

If $\rho \gtrsim \rho_B$ and $T \lesssim T_B$, then the magnetic field acts as *weakly quantizing*. In this regime, the conductivities exhibit de Haas – van Alphen oscillations around their classical values. The field becomes *strongly quantizing* at $\rho \lesssim \rho_B$ and $T \lesssim T_B$;

it substantially modifies all components of the conductivity tensors well as the equation of state.

The thermal structure of the NS envelopes composed of iron at B up to 10^{16} G was studied, e.g., by Potekhin & Yakovlev (2001). Consider, for instance, the dipole field. Near the magnetic pole, the heat is carried away from the NS interior along the field lines. The electron-quantization effects amplify this conduction and make the polar regions of the heat-blanketing envelope more heat-transparent, increasing the local effective surface temperature for a given $T_{\rm b}$. On the contrary, near the magnetic equator the heat propagates across the magnetic field. If $\omega_{\rm g}\tau \gg 1$, the classical Larmor-rotation effects strongly reduce the corresponding transverse conductivity. The equatorial regions become less heat transparent, which lowers the local effective temperature for a given $T_{\rm b}$. In an arbitrary element of the envelope, the heat conduction is affected by both (longitudinal and transverse) conductivities. The NS photon luminosity is obtained by integration of the local radiated flux over the entire NS surface – see Potekhin & Yakovlev (2001) and references therein for the case of the envelopes composed of iron. Here, we supplement these results with new results obtained for partly accreted envelopes with magnetic fields. The details of the new calculations will be presented elsewhere. Figure 7 displays the photon luminosity versus B for two selected values of $T_{\rm b}$ and three selected values of ΔM. The magnetic field affects the luminosity at $B \gtrsim 3 \times 10^{10}$ G. In the range of B up to $B \sim 3 \times 10^{13}$ G, the equatorial decrease of the heat transport dominates, and the NS luminosity is lower than at $B = 0$. For higher B, the polar increase of the heat transport becomes more important, and the magnetic field increases the photon luminosity. The variation of the photon luminosity by the magnetic field $B \lesssim 10^{15}$ G does not exceed a factor of 30.

The joint effect of the accreted envelope and the magnetic field is demonstrated by the dot-dashed and dashed lines. As in the non-magnetic case, the accreted material makes the envelope more heat-transparent, thus increasing the luminosity at given $T_{\rm b}$. Therefore, at $B \sim 10^{10}$–10^{13} G, the magnetic field and the accreted envelope affect the thermal insulation in opposite directions. At higher field strengths, both effects increase the luminosity. However, as evident from Fig. 7, the dependence of this increase on B and ΔM is complicated. In particular, at $B \gtrsim 10^{14}$ G, the effect of the accreted envelope is generally weaker than in the non-magnetic case.

5. Observational data

We will confront theoretical cooling curves with the results of observations of thermal emission from eight middle-aged isolated NSs. In discussing the observations and their theoretical interpretation we closely follow the consideration in KYG.

The observational data are the same as KYG. They are summarized in Table 3 and displayed in Figs. 8–13. The three youngest objects (RX J0822–43, 1E 1207–52, and RX J0002+62) are radio-quiet NSs in supernova remnants. The oldest object, RX J1856–3754, is also a radio-quiet NS. The other objects, Vela, PSR 0656+14, Geminga, and PSR 1055–52, are observed as radio pulsars. The NS ages are either pulsar spindown ages or the estimated supernova ages. The age of RX J1856–3754 was estimated by Walter (2001) from the kinematical data (by identifying a possible companion in the binary system existed before the supernova explosion). We use the value $t = 9 \times 10^5$ yr mentioned in the subsequent publication by Pons et al. (2002).

For the four youngest sources, the effective surface temperatures $T_{\rm s}^{\infty}$ are obtained from the observed X-ray spectra using hydrogen atmosphere models. Such models are more consistent (e.g., Pavlov & Zavlin 2002) with other information on these sources (distances, hydrogen column densities, inferred NS radii, etc.) than the blackbody model of NS emission. On the contrary, for the next three sources we present the values of $T_{\rm s}^{\infty}$ inferred using the blackbody spectrum because the blackbody model is more consistent for these sources. Finally, for RX J1856–3754 we adopt the values inferred using the analytic fit with Si-ash atmosphere model of Pons et al. (2002). We expect that the large error bar of $T_{\rm s}^{\infty}$ provided by this model reflects poor understanding of thermal emission from this source (e.g., Pons et al. 2002, Burwitz et al. 2001, Gänsicke et al. 2001, Kaplan et al. 2001, Pavlov et al. 2002).

6. Theory and observations

6.1. Non-superfluid neutron stars

There is a large scatter of observational limits on $T_{\rm s}^{\infty}$ for the eight sources. Three sources, the youngest RX J0822–43, and two oldest, PSR 1055–52 and RX J1856–3754, seem to be hot for their ages, while the other ones, especially Vela and Geminga, look much colder. We can interpret all observational data with the cooling curves using the fixed (the same) EOS and models of the critical temperatures $T_{\rm c}(\rho)$ (Sect. 3) for all objects. The results are presented in Figs. 8–13.

In the *absence of any superfluidity* there are *two* well-known, distinctly different cooling regimes, *slow* and *fast* cooling. The slowly cooling NSs have low masses, $M < M_{\rm D}$. They mainly loose their energy via neutrino emission in modified Urca processes. For given EOSs in the NS core, the cooling curves of middle-aged NSs are almost the same for all M from about $\rm M_{\odot}$ to $M_{\rm D}$ (e.g., Page & Applegate 1992, Gnedin et al. 2001), being not very sensitive to EOS. The fast cooling occurs via a very powerful direct Urca process (Lattimer et al. 1991) if $M > M_{\rm D} + 0.003\,\rm M_{\odot}$. The cooling curves are again not too sensitive to the mass and EOS. The middle-aged rapidly cooling NSs are much colder than the slowly cooling ones. Two examples, 1.35 and 1.5 $\rm M_{\odot}$ non-superfluid NSs (EOS A), are displayed in Fig. 8. The transition from the slow to fast cooling takes place in a very narrow mass range, $M_{\rm D} < M \lesssim M_{\rm D} + 0.003\,\rm M_{\odot}$. In order to explain these observational limits with the non-superfluid NS models one should make an unlikely assumption that at least the masses of the Vela and Geminga pulsars fall in that narrow mass range. Thus, several sources exhibit the intermediate case between the slow and fast cooling. In the absence of superfluidity, this is highly unlikely.

6.2. Proton superfluidity and the three types of cooling neutron stars

The next step is to interpret the observations (Fig. 9–13) by cooling of superfluid NSs. It turns out that various superfluids affect NS cooling in different ways. Our main assumptions would be that the *proton superfluidity is rather strong* at $\rho \lesssim \rho_{\rm D}$, while the $^3{\rm P}_2$ *neutron superfluidity is rather weak* (Sect. 6.4). We start with the effects of proton superfluidity.

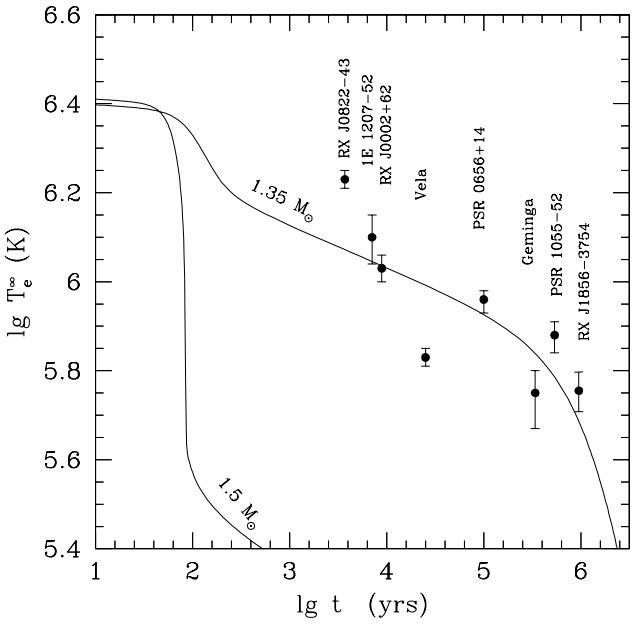


Fig. 8. Observational limits on surface temperatures of eight NSs (Table 3) compared with cooling curves of non-superfluid NSs (EOS A) of $M = 1.35$ and 1.5 $M_\odot$.

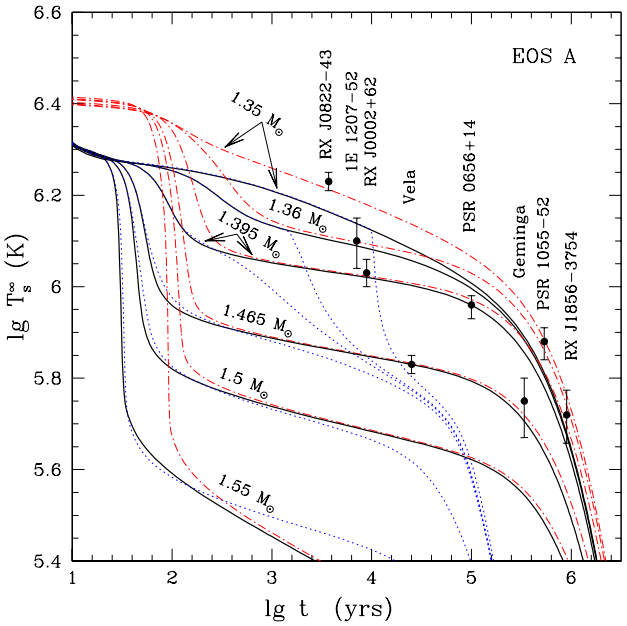


Fig. 9. Observational limits on surface temperatures of eight NSs compared with cooling curves of NSs (EOS A) with masses from 1.35 to 1.55 $M_\odot$ (after KYG). Dot-and-dashed curves are obtained including proton superfluidity 1p alone. Solid curves include, in addition, model 1ns of neutron superfluidity. Dotted lines also take into account the effect of neutron superfluidity 1nt.

The dot-and-dashed cooling curves in Figs. 9–11 are computed assuming the proton superfluidity alone. The proton pairing 1p is adopted in Fig. 9, 2p in Fig. 10, and 3p in Fig. 11. EOS A is used in the models in Figs. 9 and 10, and EOS B in Fig. 11.

As seen from Figs. 9–11, the proton superfluidity leads to the *three* cooling regimes (instead of two in non-superfluid NSs): *slow*, *moderate*, and *fast*. They reflect three neutrino emission regimes from the NS cores discussed in Sect. 4.2 (Fig. 3). Accordingly, there are *three types* of cooling NSs with distinctly different properties.

(I) *Low-mass, slowly cooling* NSs. Their central densities ρ_c and masses $M = M(\rho_c)$ obey the inequalities

$$\rho_c \lesssim \rho_I, \quad M \lesssim M_I = M(\rho_I), \tag{9}$$

where ρ_I, introduced in Sect. 4.2, is discussed below in more detail.

(II) *Medium-mass, moderately cooling* NSs, with

$$\rho_I \lesssim \rho_c \lesssim \rho_{II}, \qquad M_I \lesssim M \lesssim M_{II} = M(\rho_{II}), \tag{10}$$

where ρ_{II}, also introduced in Sect. 4.2, is specified below.

(III) *Massive, rapidly cooling* NSs,

$$\rho_{II} \lesssim \rho_c \leq \rho_{cmax}, \quad M_{II} \lesssim M \leq M_{max}, \tag{11}$$

where ρ_{cmax} and M_{max} refer to the maximum-mass configuration (Table 1).

The threshold values of $\rho_{I,II}$ and $M_{I,II}$ depend on a proton superfluidity model $T_{cp}(\rho)$, EOS in the NS core, and on a NS age. The main properties of regimes I, II, and III are as follows.

(I) *The slowly cooling NSs* are those where the direct Urca process is either forbidden by momentum conservation ($\rho_c \leq \rho_D$) or greatly suppressed by the strong proton superfluidity (Fig. 3).

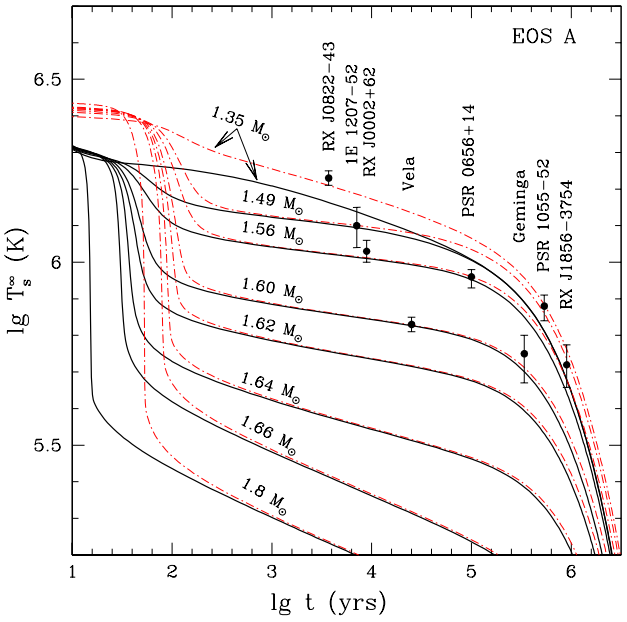


Fig. 10. Observational limits on surface temperatures of NSs compared with cooling curves of NSs (EOS A) with several masses M in the presence of proton superfluidity 2p (from KYG). Dot-and-dashed curves are obtained assuming non-superfluid neutrons. Solid curves include, in addition, model 1ns of neutron superfluidity. $^3P_2$ neutron pairing is neglected.

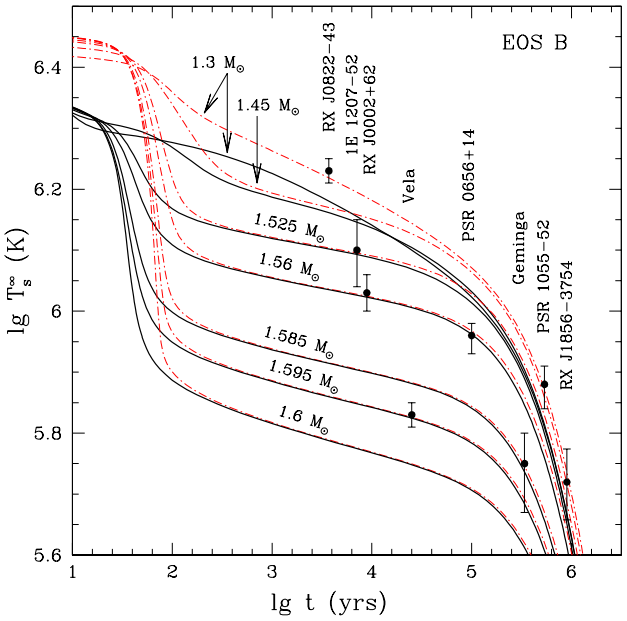


Fig. 11. Observational limits on surface temperatures of NSs compared with cooling curves of NSs (EOS B) with masses from 1.3 to 1.6 $M_\odot$ (from KYG). Dot-and-dashed curves are obtained using model 3p of proton superfluidity. Solid curves include, in addition, model 1ns of neutron superfluidity.

In particular, the cooling is slow for $\rho_c < \rho_D$ and $M < M_D$ in the absence of proton superfluidity. This is the well-known *ordinary slow cooling* which is mainly regulated by the neutrino emission produced by the modified Urca process (Sect. 6.1). However, for the conditions displayed in Figs. 9–11, the proton superfluidity in regime I is so strong that it almost switches off both, the modified Urca process everywhere in the NS core and the direct Urca process at $\rho > \rho_D$. Then the neutrino emission is mainly produced by neutrino bremsstrahlung in neutron-neutron scattering (Sect. 4.2) unaffected by the neutron superfluidity in the NS core (that is assumed to be weak). The bremsstrahlung is less efficient than the modified Urca process and leads to a slower cooling than in a non-superfluid NS. It can be referred to as the *very slow* cooling.

The analysis shows (KYG) that, for the selected models, the regime of very slow cooling holds as long as the proton critical temperature in the NS center is higher than a threshold value:

$$T_{cp}(\rho_c) \gtrsim T_{cp}^{(I)}(\rho_c). \qquad (12)$$

Comparing the neutrino emissivities of the indicated reactions (e.g., Yakovlev et al. 1999), KYG obtained the simple estimates: $T_{cp}^{(I)}(\rho) \sim 5.5\,T$ for $\rho \le \rho_D$, and $T_{cp}^{(I)}(\rho) \sim 17\,T$ for any ρ which is several per cent higher than ρ_D, where T is the internal NS temperature. There is a continuous transition (Fig. 9 in KYG) between the presented values of $T_{cp}^{(I)}(\rho)$ in the narrow density range near ρ_D.

To make the analysis less abstract we notice that in a very slowly cooling NS the internal temperature is $T \sim 5.5 \times 10^8$, 4×10^8, and 1.5×10^8 K at $t \sim 4\times10^3$, 2.5×10^4, and 4×10^5 yr, respectively.

Now we can explicitly specify the maximum central densities ρ_I and masses M_I of very slowly cooling NSs in Eq. (9) for the cases of study, in which $\rho_I \gtrsim \rho_D$ ($M_I \gtrsim M_D$). If $\rho_c > \rho_D$, then we can define ρ_I as the density value on the decreasing, high-density slope of $T_{cp}(\rho)$ (Figs. 1 and 2) which corresponds to $T_{cp}(\rho_I) = T_{cp}^{(I)}(\rho_I)$. It gives the central density of the NS and $M_I = M(\rho_I)$.

For the conditions displayed in Figs. 9–11, the cooling curves (dot-and-dashed lines) of all low-mass NSs with any proton superfluidity (1p, 2p, or 3p) are very similar. For instance, the 1.35 $M_\odot$ curve in Fig. 3 is plotted just as an example; all the curves are almost identical in the mass range $M_\odot \lesssim M < M_I$. Moreover, the cooling curves are not too sensitive to EOS and are *insensitive to the exact values of the proton critical temperature* T_{cp}, as long as the inequality (12) holds. These curves are noticeably higher than the curves which describe the ordinary slow cooling in the absence of superfluidity (e.g., Fig. 8). It is remarkable that they seem to be almost model-independent.

For the conditions in Figs. 9–11, the three relatively hot sources, RX J0822–43, PSR 1055–52, and RX J1856–3754, can be treated as these very-slow-cooling (low-mass) models.

(II) *The moderately cooling stars* are the NSs which possess central kernels where the direct Urca process is allowed but moderately suppressed by proton superfluidity. The existence of a representative class of these NSs is solely due to proton superfluidity.

According to KYG, for the selected cooling models, the proton critical temperature in the center of a medium-mass NS should roughly satisfy the inequality

$$T_{cp}^{(II)}(\rho_c) \lesssim T_{cp}(\rho_c) \lesssim T_{cp}^{(I)}(\rho_c), \qquad (13)$$

with $T_{cp}^{(II)} \sim 3\,T$. Thus, one can find ρ_{II} which corresponds to $T_{cp}(\rho_{II}) = T_{cp}^{(II)}(\rho_{II})$ and determines M_{II}, the maximum mass of moderately cooling NSs in Eq. (10).

The surface temperatures of these medium-mass NSs are governed by proton superfluidity in the NS central kernels, $\rho \gtrsim \rho_I$. One can observe (Figs. 9–11) a steady decrease of the surface temperatures with increasing M. Fixing the proton superfluidity and EOS, one can determine (Kaminker et al. 2001 and Yakovlev et al. 2001b) the masses of moderately cooling NS, which means "weighing" NSs. In this fashion one can weigh five isolated NSs (1E 1207–52, RX J0002+62, Vela, PSR 0656+14, and Geminga) as shown in Figs. 9–11. For instance, adopting EOS A and proton superfluid 1p (Fig. 9) KYG obtain the masses in the range from $\approx 1.36\,M_\odot$ (for 1E 1207–52) to $\approx 1.465\,M_\odot$ (for Vela and Geminga). For EOS A and proton superfluid 2p (Fig. 10) KYG obtain higher masses of the same sources. Obviously, the properties of moderately cooling NSs are *extremely sensitive* to the decreasing slope of $T_{cp}(\rho)$ in the density range from ρ_I to ρ_{II} (and insensitive to the details of $T_{cp}(\rho)$ outside this range).

(III) *Massive* NSs show *fast* cooling similar to the fast cooling of non-superfluid NSs. These stars have central kernels where the direct Urca process is either unaffected or weakly suppressed by the proton superfluidity. In such kernels, $T_{cp}(\rho) \lesssim T_{cp}^{(II)}$. The central densities and masses of these NSs lie in the range given by Eq. (11). Their thermal evolution is not very sensitive to the model of $T_{cp}(\rho)$ and to EOS in the stellar core. Note that if $\rho_{cmax} < \rho_{II}$, the rapidly cooling

NSs do not exist. In the frame of this interpretation, no NS observed so far can be assigned to this class.

6.3. Crustal superfluidity and slow cooling

At the next step, we retain proton superfluidity and add $^1S_0$ neutron superfluidity 1ns in the NS crust. These models are shown by the solid curves in Figs. 9–11. For the moderately or rapidly cooling middle-aged NSs, they are fairly close to the dot-and-dashed curves. This is quite expected (e.g., Gnedin et al. 2001): the $^1S_0$ neutron superfluidity is mainly located in the NS crust which is much less massive than the NS core. Thus, the crustal superfluidity does not affect noticeably the proposed interpretation of 1E 1207–43, RX J0002+62, Vela, PSR 0656+14, and Geminga in terms of moderately cooling NSs.

However, as pointed out by Yakovlev et al. (2001b), this crustal superfluidity strongly affects the slow cooling of low-mass NSs, and the effects are twofold. First, at $t \lesssim 3 \times 10^5$ yr the neutrino luminosity due to $^1S_0$ pairing of neutrons may dominate the sufficiently low neutrino luminosity of the stellar core. Second, at $t \gtrsim 10^5$ yr the $^1S_0$ neutron superfluidity reduces the heat capacity of the crust. Both effects accelerate NS cooling and decrease T_s^∞ (Figs. 9–11) violating the interpretation of the three sufficiently hot sources, RX J0822–43, PSR 1055–52, and RX J1856–3754. The interpretation of RX J1856–3754 is affected to a lesser extent, as a consequence of the rather large error bar of T_s^∞ for this source (Sect. 5).

However, the interpretation can be rescued by the appropriate choice of $T_{\rm cns}(\rho)$. It is sufficient to focus on the interpretation of RX J0822–43, PSR 1055–52, and RX J1856–3754, as the very slowly cooling NSs. For certainty, we take EOS B, $M = 1.3\,M_\odot$, and proton superfluid 3p. The results are presented in Figs. 12 and 13. The dot-and-dashed line is the same as in Fig. 11 and neglects the crustal neutron superfluidity. Thick solid line is also the same as in Fig. 11. It includes an additional effect of crustal superfluid 1ns and lies below the observational limits on T_s^∞ for the sources in question (or almost below in case of RX J1856–3754). To keep the proposed interpretation of the three sources one must raise the cooling curves calculated including the crustal superfluidity. To this aim, one should suppress the neutrino emission associated with $^1S_0$ pairing of neutrons (Fig. 5). Recall that in a middle-aged NS this emission is mainly generated (Fig. 5) in two relatively narrow layers, near the neutron drip point and near the crust-boundary interface, where the local NS temperature T is just below $T_{\rm cns}(\rho)$. Since the Cooper-pairing neutrino luminosity is roughly proportional to the widths of these emitting layers, one can reduce the luminosity by reducing the widths. This can be done by setting $T_{\rm cns}^{\rm max}$ higher and by making the sharper decrease of $T_{\rm cns}(\rho)$ in the wings.

For example, taking crustal superfluid 2ns instead of 1ns (Figs. 4 and 5) one obtains the dashed cooling curve in Fig. 12 which comes much closer to the dot-and-dashed curve than the thick solid curve (model 1ns). Note that the cooling curves are insensitive to the details of $T_{\rm cns}(\rho)$ profile near the maximum, as long as $T_{\rm cns}^{\rm max} \gtrsim 5\times10^9$ K, but they are extremely sensitive to the decreasing slopes of $T_{\rm cns}(\rho)$. On the other hand, by taking the smoother and lower $T_{\rm cns}(\rho)$, model 3ns, one obtains a colder NS than needed for the interpretation of the observations (long-dash line in Fig. 12). Therefore, $^1S_0$ neutron superfluidity with maximum $T_{\rm cns}^{\rm max} < 5 \times 10^9$ K and/or with smoothly decreasing slopes of the $T_{\rm cns}(\rho)$ profile near the crust-core interface and the neutron drip point *violates* the proposed interpretation of the observational data.

Moreover, the observations of RX J0822–43, PSR 1055–52, and RX J1856–3754 can be fitted even with the initial model 1ns of the crustal superfluidity (Fig. 13). The high surface temperature of RX J0822–43 can be explained assuming additionally the presence of a low-mass ($2 \times 10^{-11}\,M_\odot$) heat-blanketing surface envelope of hydrogen or helium. This effect is modeled using the results of Potekhin et al. (1997) described in Sect. 4 (Fig. 6). Light elements raise T_s^∞ at the neutrino cooling stage (curve *acc* in Fig. 13). In order to explain the observations of PSR 1055–52 and RX J1856–3754, one can assume again model 1ns of crustal superfluidity, iron surface and the dipole surface magnetic field ($\sim 10^{12}$ G at the magnetic pole; line *mag* in Fig. 13). Such a field makes the NS surface layers overall less heat-transparent (Fig. 7), rising T_s^∞ at $t \gtrsim 3\times10^5$ yr. Note that the dipole field $\gtrsim 3 \times 10^{13}$ G has the opposite effect, resembling the effect of the surface envelope of light elements.

To summarize, one can additionally vary cooling curves by assuming the presence of light elements and the magnetic field on the NS surface (line *acc-mag* in Fig. 13). However, these variations are less pronounced than those due to nucleon superfluidity. For instance, one cannot reconcile the cooling curves with the present observations of PSR 1055–52 assuming model 3ns of the crustal superfluidity with any surface magnetic field.

6.4. $^3P_2$ pairing of neutrons in the NS core

Now we focus on the $^3P_2$ neutron pairing neglected so far. Its effects are illustrated in Fig. 9, as an example. They are qualitatively similar for the other cooling models in Figs. 10 and 11. In Fig. 9 we take the cooling models obtained including proton superfluidity 1p and crustal superfluidity 1ns, and add the $^3P_2$ neutron superfluidity (model 1nt, Table 2) in the core. This gives the same (solid) cooling curves for the young NSs which have the internal temperatures T above the maximum value of $T_{\rm cnt}^{\rm max} \approx 3 \times 10^8$ K. However, when T falls below $T_{\rm cnt}^{\rm max}$, one obtains (dots) a strong acceleration of the cooling associated with the powerful neutrino emission due to $^3P_2$ neutron pairing (Fig. 3). This emission greatly complicates the proposed interpretation of older sources, PSR 0656+14, Geminga, PSR 1055–52, and RX J1856–3754. The complication arises for a wide class of $T_{\rm cnt}(\rho)$ profiles with $T_{\rm cnt}^{\rm max}$ from $\sim 10^8$ K to $\sim 3\times10^9$ K (in this way, it can be regarded as model-independent). The Cooper-pairing neutrino emission of neutrons induces *really fast cooling* of older sources even if their mass is *low*, $M < M_{\rm D}$ (Sect. 6.2). To avoid this difficulty one can assume (Kaminker et al. 2001) *weak* $^3P_2$ *pairing*, $T_{\rm cnt}(\rho)$, with maximum $T_{\rm cnt}^{\rm max} < 10^8$ K; it does not affect the proposed interpretation.

7. Summary

Following KYG we summarize the effects superfluids on NS cooling.

(a) Strong proton superfluidity in the NS cores, combined with the direct Urca process at $\rho > \rho_{\rm D}$, separates (Sect. 6.2) the cooling models into three distinctly different types: (I) slowly

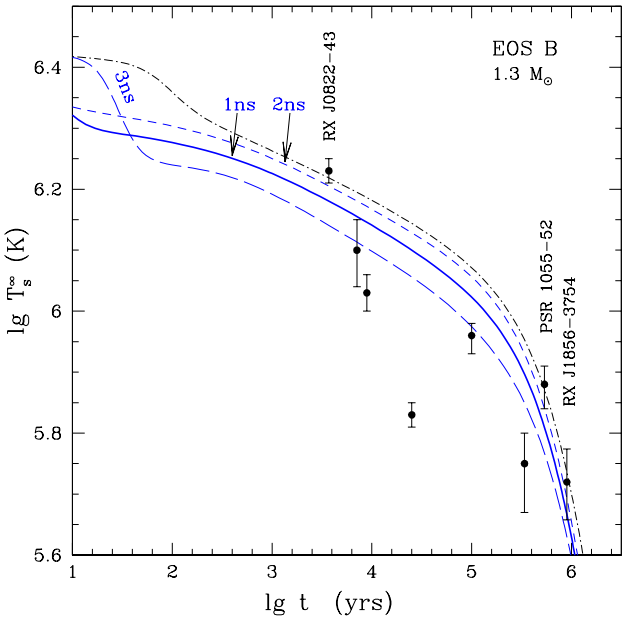


Fig. 12. Cooling curves of 1.3 $M_\odot$ NS model (EOS B) versus observations of RX J0822–43, PSR 1055–52, and RX J1856–3754 (after KYG). Dot-and-dashed curve: proton superfluidity 3p in the NS core. Solid, short-dashed, and long-dashed curves include, in addition, models 1ns, 2ns, and 3ns of crustal neutron superfluidity, respectively. Thick solid line is the same as in Fig. 11.

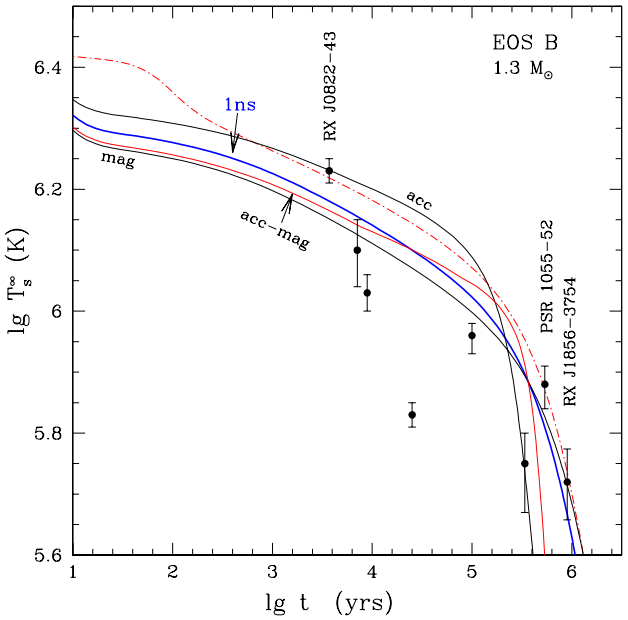


Fig. 13. Cooling curves of 1.3 $M_\odot$ NS model versus observations of RX J0822–43, PSR 1055–52, and RX J1856–3754. Dot-and-dashed curve: proton superfluidity 3p in the NS core. Solid curves include, in addition, model 1ns of crustal neutron superfluidity. Thick solid line is the same as in Figs. 11 and 12. Thin solid curve *acc* is calculated assuming the presence of 2×10^{-11} $M_\odot$ of hydrogen on the NS surface. Thin solid curve *mag* is obtained assuming the iron surface and dipole magnetic field (10^{12} G at the magnetic pole). Thin solid curve *acc-mag* is obtained assuming both, the magnetic field (10^{12} G) and accreted envelope (2×10^{-11} $M_\odot$).

cooling, low-mass NSs ($M \lesssim M_{\rm I}$); (II) moderately cooling, medium-mass NSs ($M_{\rm I} \lesssim M \lesssim M_{\rm II}$); (III) rapidly cooling, massive NSs ($M \gtrsim M_{\rm II}$). The regime of moderate cooling cannot be realized without the proton superfluidity.

(b) Strong proton superfluidity in the NS core is required to interpret the observational data on the three sources, RX J0822–43, PSR 1055–52, and RX J1856–3754, hot for their ages, as the very slowly cooling NSs (Sects. 6.2 and 6.3). Within this interpretation, all three sources may have masses from about $M_\odot$ to $M_{\rm I}$; one cannot determine their masses exactly or distinguish EOS in the NS core from the cooling models.

(c) Strong proton superfluidity is needed to interpret observations of the other sources, 1E 1207–52, RX J0002+62, Vela, PSR 0656+14, and Geminga, as the medium-mass NSs. One can "weigh" these NSs, i.e., determine their masses, for a given model of $T_{\rm cp}(\rho)$ and a given EOS. The weighing is very sensitive to the decreasing slope of $T_{\rm cp}(\rho)$ in the density range $\rho_{\rm I} \lesssim \rho \lesssim \rho_{\rm II}$ (Sect. 6.2).

(d) Strong or moderate $^3P_2$ neutron superfluidity in the NS core initiates rapid cooling due to the neutrino emission resulted from neutron pairing. This would invalidate the proposed interpretation of the old sources like PSR 0656+14, Geminga, PSR 1055–52, and RX J1856–3754. One can save the interpretation assuming a weak $^3P_2$ neutron superfluidity, $T_{\rm cnt}^{\rm max} < 10^8$ K (Sect. 6.4).

(e) $^1S_0$ neutron superfluidity in the crust may initiate a strong Cooper-pairing neutrino emission, decrease substantially $T_{\rm s}^\infty$ of the slowly cooling NSs, and weaken the interpretation of RX J0822–43, PSR 1055–52, and RX J1856–3754 (although it does not affect significantly the moderate or fast cooling). The interpretation can be saved by assuming that the maximum of $T_{\rm cns}(\rho)$ is not too small ($T_{\rm cns}^{\rm max} \gtrsim 5 \times 10^9$ K) and the profile of $T_{\rm cns}(\rho)$ decreases sharply in the wings (Sect. 6.3).

(f) The interpretation of the slowly cooling sources is sensitive to the presence of the surface magnetic fields and/or heat-blanketing surface layer composed of light elements (Sect. 6.3).

(g) No isolated middle-aged NSs observed so far can be idenfied as a rapidly cooling NS. In the frame of the proposed models, these NSs do not exist for those EOSs and $T_{\rm cp}(\rho)$ profiles for which $M_{\rm max} < M_{\rm II}$.

If the proposed interpretation is correct, one can make the following conclusions on the properties of dense matter in NS interiors.

(i) Strong proton superfluidity is in favor of a not too large symmetry energy at supranuclear densities (Kaminker et al. 2001). A very large symmetry energy would mean a high proton fraction which would suppress proton pairing. On the other hand, the symmetry energy should be not too small to open the direct Urca process at $\rho > \rho_{\rm D}$.

(ii) Weak $^3P_2$ neutron pairing is in favor of a not too soft EOS in the NS core (Kaminker et al. 2001). The softness would mean a strong attractive neutron-neutron interaction and, therefore, strong neutron pairing.

(iii) The adopted features of the crustal neutron superfluidity are in favor of those microscopic theories which predict $T_{\rm cns}(\rho)$ profiles with $T_{\rm cns}^{\rm max} \gtrsim 5\times10^9$ K. This is in line with many microscopic calculations of the superfluid gaps which include the medium polarization effects in neutron-neutron interaction (e.g., Lombardo & Schulze 2001). However, the reduction of the gap by the medium polarization should not be too strong, and the decreasing slope of $T_{\rm cns}(\rho)$ should be rather sharp. These requirements constrain the microscopic theories.

The proposed interpretation of the observations relates the inferred NS masses to the superfluid properties of NS interiors. By varying EOS and the proton critical temperature, one can attribute different masses to the same sources. If, on the other hand, one knew the range of masses of the cooling middle-aged NSs it would be possible to draw definite conclusions on the superfluid state of their interiors, first of all, on the proton critical temperature, $T_{\rm cp}(\rho)$.

The presented analysis may seem too simplified because it neglects a possible presence of other particles in the NS cores (muons, hyperons, quarks). It is expected that the inclusion of other particles and the effects of superfluidity of hyperons or quarks will complicate theoretical analysis but will not change the basic conclusion on the existence of the slowly, moderately, and rapidly cooling NSs.

The calculations show that the cooling of middle-aged NSs with $M < M_{\rm I}$ is sensitive to the density profile of free neutrons near the crust bottom and neutron drip point. The presented calculations used only one model of the free-neutron distribution in the crust, assuming spherical atomic nuclei at the crust bottom. It would be interesting to consider the models of crust matter with non-spherical nuclei (e.g., Pethick & Ravenhall 1995) and the effects of superfluidity of nucleons confined in the atomic nuclei in the NS crust.

The determination of $T_{\rm s}^{\infty}$ from observational data is a very complicated problem (as described, e.g., by Pavlov & Zavlin 2002). It requires very high-quality data and theoretical models of NS atmospheres. Thus, the current values of $T_{\rm s}^{\infty}$ may change substantially after the forthcoming observations and new theoretical modeling. These changes may affect the proposed interpretation of the observational data, first of all, of RX J0822–43, PSR 1055–52, and RX J1856–3754. For instance, RX J1856–3754 may have a colder surface ($T_{\rm s}^{\infty} \sim 0.25$ MK), than assumed in the above analysis, with a hot spot (e.g., Pons et al. 2002, Burwitz et al. 2001, Gänsicke et al. 2001). If confirmed, the lower $T_{\rm s}^{\infty}$ might be explained by the effect of ^{3}P$_2$ neutron pairing (Fig. 9).

The future observations of the thermal emission from these sources will be crucial for understanding the superfluid properties of NS matter.

The proposed theory can explain the existence of NSs within a broad range of $T_{\rm s}^{\infty}$. However, it would be unable to explain too hot and too cold objects (with $T_{\rm s}^{\infty}$ essentially higher than the highest cooling curve and essentially lower than the lowest curve in Figs. 9-11). A discovery of such hot or cold isolated NSs would be of special interest.

Acknowledgements. We are grateful to G.G. Pavlov for encouragement, to M.E. Gusakov and K.P. Levenfish, for useful comments. The work was partially supported by RFBR (grants No. 02-02-17668 and 00-07-90183).

References

Burwitz V., Zavlin V.E., Neuhäuser R., Predehl R., Trümper J., Brinkman A.C., 2001, A&A 327, L35

Craig W.W., Hailey Ch.J., Pisarski R.L., 1997, ApJ 488, 307

Gänsicke B.T., Braje T.M., Romani R.W., 2001, A&A (submitted, astro-ph/0110130)

Gnedin O.Y., Yakovlev D.G., Potekhin A.Y., 2001, MNRAS 324, 725

Gudmundsson E.H., Pethick C.J., Epstein R.I., 1983, ApJ 272, 286

Flowers E.G., Ruderman M., Sutherland P.G., 1976, ApJ 205, 541

Halpern J.P., Wang F.Y.-H., 1997, ApJ 477, 905

Kaminker A.D., Haensel P., Yakovlev D.G., 2001, A&A 373, L17

Kaminker A.D., Yakovlev D.G., Gnedin O.Y., 2002, A&A 383, 1076 (KYG)

Kaplan D.L., van Kerkwijk M.H., Anderson J., 2001, ApJ (submitted; astro-ph/0111174)

Lattimer J.M., Pethick C.J., Prakash M., Haensel P., 1991, Phys. Rev. Lett. 66, 2701

Lattimer J.M., Van Riper K.A., Prakash M., Prakash M., 1994, ApJ 425, 802

Lattimer J.M., Prakash M., 2001, ApJ 550, 426

Lyne A.G., Pritchard R.S., Graham-Smith F., Camilo F., 1996, Nature 381, 497

Lombardo U., Schulze H.-J., 2001, in *Physics of Neutron Star Interiors*, ed. D. Blaschke, N. Glendenning, A. Sedrakian (Springer, Berlin) p. 30

Negele J.W., Vautherin D., 1973, Nucl. Phys. A207, 298

Ögelman H., 1995, in *The Lives of the Neutron Stars*, ed. M.A. Alpar, Ü. Kiziloğlu, J. van Paradijs, NATO ASI Ser. C, vol. 450 (Kluwer, Dordrecht) p. 101

Page D., 1998, in *The Many Faces of Neutron Stars*, NATO ASI Ser. C, vol. 515, ed. R. Buccheri, J. van Paradijs, M.A. Alpar (Kluwer, Dordrecht) p. 538

Page D., Applegate J.H., 1992, ApJ 394, L17

Pavlov G.G., Zavlin V.E., 2002, an invited talk at WE-Heraeus Seminar No. 270 (21–25 January 2002, Physikzentrum Bad Honnef, Germany)

Pavlov G.G., Zavlin V.E., Sanwal D., Burwitz V., Garmire G.P., 2001, ApJ 552, L129

Pavlov G.G., Sanwal D., Garmire G.P., Zavlin V.E., 2002, in *Neutron Stars in Supernova Remnants*, ed. P.O. Slane, B.M. Gaensler, ASP Conf. Ser. (accepted, astro-ph/0112322)

Pethick C.J., Ravenhall D.G., 1995, Ann. Rev. Nucl. Particle Sci. 45, 429

Pons J., Walter F., Lattimer J., Prakash M., Neuhäuser R., An P., 2002, ApJ 564, 981

Possenti A., Mereghetti S., Colpi M., 1996, A&A 313, 565

Potekhin A.Y., Chabrier G., Yakovlev D.G., 1997, A&A 323, 415

Potekhin A.Y., Yakovlev G.G., 2001, A&A 374, 213

Prakash M., Ainsworth T.L., Lattimer J.M., 1988, Phys. Rev. Lett. 61, 2518

Shapiro S.L., Teukolsky S.A., 1983, *Black Holes, White Dwarfs, and Neutron Stars* (Wiley, New York)

Thorne K.S., 1977, ApJ 212, 825

Ventura J., Potekhin A.Y., 2001, in *The Neutron Star – Black Hole Connection*, NATO ASI Ser. C, v. 567, ed. C. Kouveliotou, J. Ventura, E. van den Heuvel (Kluwer, Dordrecht) 393
Walter F.M., 2001, ApJ 549, 433
Yakovlev D.G., Levenfish K.P., Shibanov Yu.A., 1999, Physics–Uspekhi 42, 737 (astro-ph/9906456)
Yakovlev D.G., Kaminker A.D., Gnedin O.Y., Haensel P., 2001a, Phys. Rep. 354, 1
Yakovlev D.G., Kaminker A.D., Gnedin O.Y., 2001b, A&A 379, L5
Zavlin V.E., Pavlov G.G., Trümper J., 1998, A&A 331, 821
Zavlin V.E., Pavlov G.G., 1999, private communication
Zavlin V.E., Trümper J., Pavlov G.G., 1999, ApJ 525, 959

Proceedings of the 270. WE-Heraeus Seminar on: *"Neutron Stars, Pulsars and Supernova Remnants"*
Physikzentrum Bad Honnef, Germany, Jan. 21-25, 2002, eds. W. Becker, H.Lesch & J. Trümper, MPE Report 278, pp. 300-302

Neutron Stars, Pulsars and Supernova Remnants: concluding remarks

F. Pacini[1,2]

[1] Arcetri Astrophysical Observatory, L.go E. Fermi, 5, I-50125 Firenze,Italy
[2] Dept. of Astronomy and Space Science, University of Florence, L.go E. Fermi, 2, I-50125 Firenze, Italy

1. Introduction

More than 30 years have elapsed since the discovery of pulsars (Hewish *et al.* 1968) and the realization that they are connected with rotating magnetized neutron stars (Gold 1968; Pacini 1967, 1968). It became soon clear that these objects are responsible for the production of the relativistic wind observed in some Supernovae remnants such as the Crab Nebula.

For many years, the study of pulsars has been carried out mostly in the radio band. However, many recent results have come from observations at much higher frequencies (optical, X-rays, gamma rays). These observations have been decisive in order to establish a realistic demography and have brought a better understanding of the relationship between neutron stars and SN remnants.

The Proceedings of this Conference cover many aspects of this relationship (see also previous Conference Proceedings such as Bandiera *et al.* 1998; Slane and Gaensler, 2002). Because of this reason, my summary will not review all the very interesting results which have been presented here and I shall address briefly just a few issues. The choice of these issues is largely personal: other colleagues may have made a different selection.

2. Demography of Neutron Stars: the role of the magnetic field

For a long time it has been believed that only Crab-like remnants (plerions) contain a neutron star and that the typical field strength of neutron stars is 10^{12} Gauss. The basis of this belief was the lack of pulsars associated with shell-type remnants or other manifestations of a relativistic wind. The justification given is that some SN explosions may blow apart the entire star. Alternatively, the central object may become a black hole. However, the number of shell remnants greatly exceeds that of plerions: it becomes then difficult to invoke the formation of black holes, an event much more rare than the formation of neutron stars.

The suggestion that shell remnants such as Cas A could be associated with neutron stars which have rapidly lost their initial rotational energy because of an ultra-strong magnetic field $B \sim 10^{14} - 10^{15}$ Gauss (Cavaliere & Pacini, 1970) did receive little attention. The observational situation has now changed: a compact thermal X-ray source has been discovered close to the center of Cas A (Tananbaum, 1999) and it could be the predicted object. Similar sources have been found in association with other remnants and are likely to be neutron stars. We have also heard during this Conference that some shell-type remnants (including Cas A) show evidence for a weak non-thermal X-ray emission superimposed on the thermal one: this may indicate the presence of a residual relativistic wind produced in the center. Another important result has been the discovery of neutron stars with ultra-strong magnetic fields, up to $10^{14} - 10^{15}$ G. In this case the total magnetic energy could be larger than the rotational energy ("magnetars"). This possibility had been suggested long time ago (Woltjer, 1968). It should be noticed, however, that the slowing down rate determines the strength of the field at the speed of light cylinder and that the usually quoted surface fields assume a dipolar geometry corresponding to a braking index $n = 3$. Unfortunately the value of n has been measured only in a few cases and it ranges between $1.4 - 2.8$ (Lyne *et al.*, 1996).

The present evidence indicates that neutron stars manifest themselves in different ways:

- Classical radio pulsars (with or without emission at higher frequencies) where the rotation is the energy source.
- Compact X-ray sources where the energy is supplied by accretion (products of the evolution in binary systems).
- Compact X-ray sources due to the residual thermal emission from a hot surface.
- Anomalous X-ray pulsars (AXP) with long periods and ultra strong fields (up to 10^{15} Gauss). The power emitted by AXPs exceeds the energy loss inferred from the slowing down rate. It is possible that AXPs are associated with magnetized white dwarfs, rotating close to the shortest possible period ($5 - 10$ s) or, alternatively, they could be neutron stars whose magnetic energy is dissipated by flares.
- Soft gamma-ray repeaters.

In addition it is possible that some of the unidentified gamma ray sources are related to neutron stars. The present picture solves some previous inconsistencies. For instance, the estimate for the rate of core-collapse Supernovae (roughly one every 30-50 years) was about a factor of two larger than the birth-rate of radio pulsars, suggesting already that a large fraction of neutron stars does not appear as radio pulsars.

The observational evidence supports the notion of a large spread in the magnetic strength of neutron stars and the hypothesis that this spread is an important factor in determining the morphology of Supernova remnants. A very strong field would lead to the release of the bulk of the rotational energy during a short initial period (say, days up to a few years): at

later times the remnant would appear as a shell-type. A more moderate field (say 10^{12} Gauss or so) would entail a long lasting energy loss and produce a plerion.

3. Where are the pulses emitted ?

Despite the great wealth of data available, there is no general consensus about the radiation mechanism for pulsars. The location of the region where the pulses are emitted is also controversial: it could be located close to the stellar surface or, alternatively, in the proximity of the speed of light cylinder.

The radio emission is certainly due to a coherent process because of the very high brightness temperatures (T_b up to and above 10^{30} K have been observed). A possible model invokes the motion of bunches of charges sliding along the curved field lines with a relativistic Lorentz factor γ such that the critical frequency $\nu_c \sim \frac{c}{\rho}\gamma^3$ reaches or exceeds the radio band. Typically, this would entail $\gamma \gtrsim 10^2$.

If we assume $T_b \sim 10^{30}$ K and $\gamma \sim 10^2 - 10^3$, the thermodynamical limitation $kT_b \sim mc^2\gamma F$ requires a coherence factor F (number of electrons in the bunch) of order $\sim 10^{17}$. At least one of the sizes of the bunch must be smaller than the emitted wavelength. The radio spectrum is determined by the distribution in size of the bunches and the effect of coherence is gradually lost at very high radio frequencies (Aloisio & Blasi 2002). This may possibly explain the up-turn of the spectrum observed in some sources in the millimeter range, as reported here by Sieber.

Unfortunately the radio emission does not give sufficient information about the parameters of the source since many of them are affected by the degree of coherence. The situation is different if we consider pulsars which emit at higher frequencies (optical and X-ray bands), where the observed brightness is compatible with an incoherent process.

A striking aspect of the optical pulses is the very strong dependency of the power upon the period (they are emitted only from a few sources).

A possible scenario assumes that the optical radiation is normal synchrotron radiation, emitted from particles which gyrate with a small pitch angle Ψ around the field lines. Such a model, applied to the Crab pulsar, PSR 0531, can explain the observations with parameters compatible with those expected at the speed of light cylinder distance $R_L = \frac{cP}{2\pi}$: $\Psi \sim 10^{-2}$; $B_\perp \sim 10^4$ G; $\gamma \sim 10^2 - 10^3$.

The model leads to the expectation of a very fast decrease of the synchrotron intensity with period because of the combination of two factors: *a)* the reduced particles flux when the period increases; *b)* the reduced efficiency of synchrotron losses (which scale $\propto B^2 \propto R_L^{-6} \propto P^{-6}$) at the speed of light cylinder (Pacini, 1971; Pacini & Salvati 1983, 1987). The prediction fits the observed secular decrease of the optical emission from the Crab Nebula and the magnitude of the Vela pulsar. A recent re-examination of all available optical data confirms that this model can account for the luminosity of the known optical pulsars (Shearer and Golden, 2001).

If so, the optical radiation supports strongly the notion that the emitting region is located close to the speed of light cylinder.

4. A speculation: can the thermal radiation from young neutron stars quench the relativistic wind?

My final remarks concern the possible effect of the thermal radiation coming from the neutron star surface upon the acceleration of particles. This problem has been investigated for the near magnetosphere (Supper & Truemper, 2000) and it has been found that the Inverse Compton Scattering (ICS) against the thermal photons is important only in marginal cases. However, if we assume that the acceleration of the relativistic wind and the radiation of pulses occur close to the speed of light cylinder, the situation becomes different and the ICS can dominate over synchrotron losses for a variety of parameters.

The basic reason is that the importance of ICS at the speed of light distance R_L scales like the energy density of the thermal photons $u_\gamma \propto R_L^{-2} \propto P^{-2}$; on the other hand, the synchrotron losses are proportional to the magnetic energy density in the same region $u_B \propto R_L^{-6} \propto P^{-6}$.

Numerically, one finds that ICS losses dominate over synchrotron losses if

$$T_6 > 0.4 \frac{B_{12}^{1/2}}{P_s}$$

where T_6 is the temperature in units 10^6 K; $B_{12} = \frac{B}{10^{12}\,\mathrm{G}}$; P_s is the pulsar period in seconds).

The corresponding upper limit for the energy of the electrons, assuming that the acceleration takes place for a length of order of the speed of light distance and that the gains are equal to the losses is given by:

$$E_{\max} \simeq 1.2 \times 10^3 {T_6}^{-4}\ P_s \text{ GeV}.$$

Provided that the particles are accelerated and radiate in proximity of the speed of light cylinder distance, we conclude that the thermal photons can limit the acceleration of particles, especially in the case of young and hot neutron stars. It becomes tempting to speculate that this may postpone the beginning of the pulsar activity until the temperature of the star is sufficiently low. The main manifestation of neutron stars in this phase would be a flux of high energy photons in the gamma-ray band, due to the interaction of the quenched wind with the thermal photons from the stellar surface. This model and its observational consequences are currently under investigation (Amato, Blasi, Pacini, work in progress).

References

Aloisio, R., & Blasi, P. 2002, Astrop. Phys.,
Bandiera, R., *et al.* 1998, Proc. Workshop "The Relationship between Neutron Stars and Supernova Remnants", Mem. Societ Astronomica Italiana, vol. 69, n. 4
Cavaliere, A., & Pacini, F. 1970, ApJ, 159, 170
Gold, T. 1968, Nature, 217, 731
Hewish A., *et al.* 1968, Nature 217, 709
Lyne, G., *et al.* 1996, Nature, 381, 497
Pacini, F. 1967, Nature, 216, 567
Pacini, F. 1968, Nature, 219, 145
Pacini, F. 1971, ApJ, 163, L17
Pacini, F., & Salvati, M. 1983, ApJ, 274, 369
Pacini F., & Salvati, M. 1987, ApJ., 321, 447
Shearer, A., and Golden, A. 2001, ApJ, 547, 967

Slane, P. , Gaensler, B. 2002, Proc. Workshop "Neutron Stars in Supernova Remnants"ASP Conference Proceedings (in press)
Supper, R., & Trumper, J. 2000, A&A, 357, 301
Tananbaum, B, *et al.* 1999, IAU Circular 7246
Thompson, C., Duncan, R.C. 1996, ApJ, 473, 322
Woltjer, L. 1968, ApJ, 152, 179